BESSY II
Annual Report
2008
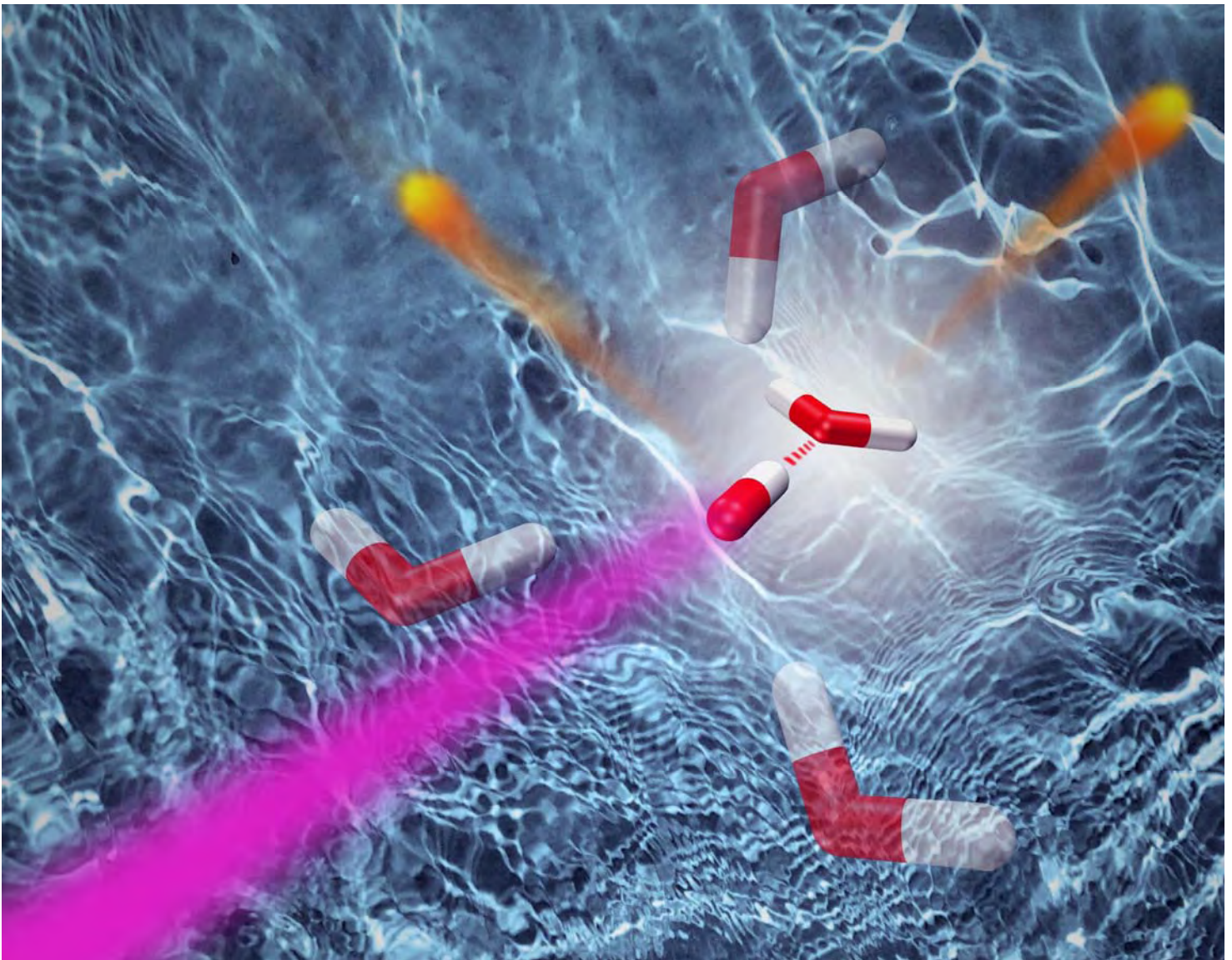
Published by:

Helmholtz-Zentrum Berlin
für Materialien und Energie GmbH

Hahn-Meitner-Platz 1
14109 Berlin
Tel. +49 30 6392 2999
Fax +49 30 6392 2990
www.helmholtz-berlin.de

Edited by:
Dr. Kai Godehusen
Dr. Markus Sauerborn

Transitions –

BESSY has been in a major "phase transition" during the last 24 months. By merging with the former Hahn-Meitner-Institut Berlin, we became the new "Helmholtz Zentrum Berlin für Materialien und Energie", which is a member of the Helmholtz Association, Germany's largest research alliance.

The new organization will be crucial for keeping the development of the Synchrotron radiation source BESSY II on track and for opening new opportunities for a next generation user facility as we are now on the roadmap to build an Energy Recovery Linac Prototype (BERLinPro).

Joining the synchrotron radiation source BESSY-II and the neutron source BER-II within one research center we will be able to strengthen our user support. Additionally we have the opportunity to support the complementary use of photons and neutrons.

The transition of BESSY and the re-organization of the new centre is also the reason for the delayed appearance of the last "BESSY Annual Report". Unfortunately, there will be no BESSY Highlights 2008. Please accept our apologies, especially if you have written a contribution in anticipation of a Highlights brochure.

Finally, we would like to thank our users and our staff for their ongoing enthusiasm and their patience during this transition.

Sincerely

Wolfgang Eberhardt   Anke Rita Kaysser-Pyzalla

Scientific Director (Energy)   Scientific Director (Science with Neutrons
Former Scientific Director BESSY   and Photons, Large Scale Facilities)
                                             Chief Executive

Characterization of new EUV stable silicon photodiodes

F. Scholze, C. Laubis

Physikalisch-Technische Bundesanstalt, Abbestraße 2-12, 10587 Berlin, Germany

F. Sarubbi, L. K. Nanver, S.N. Nihtianov

DIMES, TU Delft, P.O.box 5053, 2600 GB, The Netherlands

Development of EUV lithography equipment has triggered a growing interest in EUV radiation detection. Several types of sensors are needed for evaluating and optimizing the imaging performance. The radiation-sensitive surface of the sensors is exposed to high photon flux doses and is affected by hydrocarbons contamination. Consequently, quite aggressive cleaning is required. Therefore, ruggedness to high photon flux and aggressive environments is a key feature of these EUV sensors alongside extreme requirements for stability, reliability, high and spatially uniform responsivity, large dynamic range, and low noise, i.e. low dark current. To meet these requirements, a new EUV photodiode technology is presently being developed and optimized for the requirements of EUV lithography systems at TU Delft in cooperation with ASML. PTB has long experience in the characterization of detectors using synchrotron radiation[1,2]. We characterized the EUV performance of p+ n photodiodes fabricated by using a novel doping technology[3] regarding their spatial homogeneity, spectral responsivity and high-dose irradiation stability. With respect to the combination of high spectral responsivity and irradiation stability, they are already in the present state of development superior to other commercially available detectors.
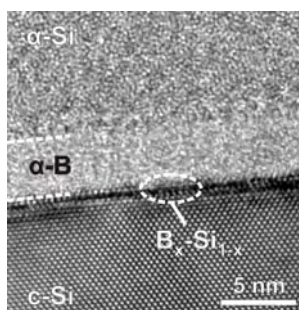
Figure 1 HRTEM image of a B-layer formed after a 2.5 min B2H6 exposure at 700 ºC. The sample has been covered with PVD a-Si for TEM analysis.
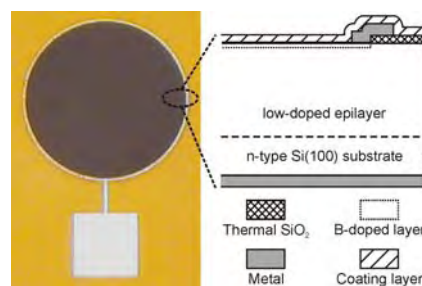
Figure 2 Image and cross-section of a boron-doped EUV photodiode.

For EUV diodes, the stability of responsivity under irradiation is known to be an issue[4]. Figure 3 and Figure 4 show the result of irradiation testing with a rather high dose 200 kJ/cm². No significant change in responsivity is observed for the boron-doped photodiode (Figure 3), while the state-of-the-art EUV photodiode suffered some responsivity loss, which might, however, partly be due to a higher susceptibility of the surface coating of this diode to carbon contamination, (Figure 4). Regarding the spectral responsivity, the boron-doped photodiode are as good as the best state-of-the-art EUV photodiodes, see Figure 5. It must be noted, that the diodes with nitrided oxide passivation shown for reference are not irradiation resistant while the more stable diodes as shown in Figure 4 have a lower responsivity.
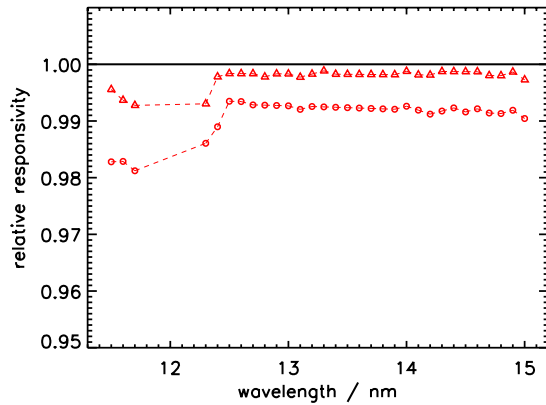
Figure 3 Responsivity of a boron-doped photodiode after irradiation with 200 kJ/cm² normalized to the initial responsivity. The circles represent a diode actually exposed to the radiation while the triangles are a witness diode which was placed under the same vacuum and atmosphere conditions but was shadowed during exposure.
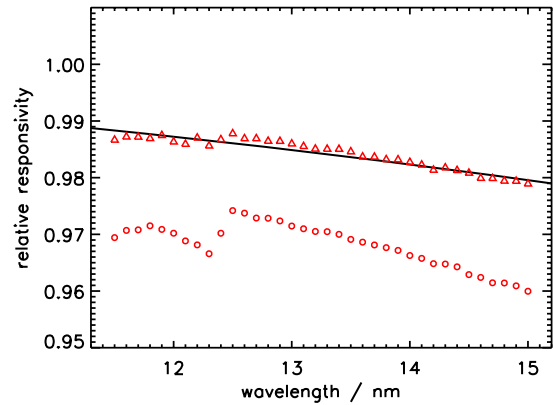
Figure 4 Responsivity of a state-of-the-art EUV photodiode after irradiation with 200 kJ/cm² normalized to the initial responsivity. Symbols same as in Figure 3. The solid line represents the effect of 2.5 nm carbon contamination.
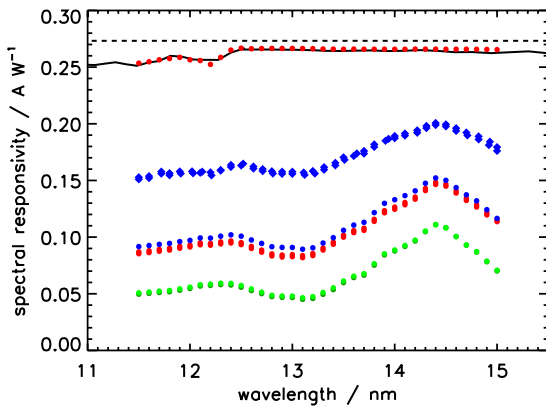
Figure 5 Spectral responsivity of boron-doped silicon diodes. The highest responsivity is for a diode with no additional top layer. The lower responsivity values are for top layers of 15 nm, 30 nm, and 50 nm AlN. The dashed black line shows the theoretical limit[5] for silicon responsivity of 1/3.66 A/W and the solid black line is the best state-of-the-art silicon detector with a very thin nitrided oxide passivation.

These results prove that the technology for the production of planar diffused silicon p-n diodes for EUV detection is capable of achieving the same nearly ideal responsivity as the best state-of-the-art detectors. Due to their almost ideal efficiency, the diodes also show good spatial homogeneity. A particular challenge for EUV photo sensors is the stability under irradiation. Here also the benchmark of the best state-of-the-art detectors is already met.
Summarizing, the development of pure boron-doped photodiodes is proven to be a promising approach toward the improvement of EUV photo sensor performance.

References

[1] R. Klein, C. Laubis, R. Müller, F. Scholze, G. Ulm, The EUV metrology program of PTB, Microelectronic Engineering 83 707 (2006)

[2] F. Scholze, R. Klein, R. Müller, Characterization of detectors for extreme UV radiation, Metrologia 43 S6 (2006)

[3] F. Sarubbi, L. K. Nanver, and T. L. M. Scholtes, CVD delta-doped boron surface layers for ultra-shallow junction formation, ECS Transactions **3**, 3544 (2006)

[4] F. Scholze, R. Klein, T. Bock, Irradiation Stability of Silicon Photodiodes for Extreme-Ultraviolet Radiation Appl. Opt. 42 5621 (2003)

[5] F. Scholze, H. Rabus, and G. Ulm, Mean energy required to produce an electron-hole pair in silicon for photons of energies between 50 and 1500 eV, J. Appl. Phys. 84 2926 (1998)

Pilot comparison for spectral responsivity in the spectral range 11 nm to 20 nm

Frank Scholze, Gerhard Ulm

Physikalisch-Technische Bundesanstalt, Abbestraße 2-12, 10587 Berlin, Germany

Terubumi Saito

NMIJ, 1-1-1 Umezono, Tsukuba-Shi 305-8563 Ibaraki, Japan

Robert Vest

NIST, 100 Bureau Drive, Stop 8411, Gaithersburg, MD 20899-8411, USA

Development of EUV lithography equipment has triggered a growing interest in EUV radiation detection. To improve the metrological environment for emerging technologies using short-wavelength radiation, a pilot comparison for the spectral responsivity of photo diodes in the 11.5 nm to 20 nm spectral range was started between NMIJ, NIST and PTB. The comparison was carried out through the calibration of a group of transfer standard detectors. These detectors have been shown to have reasonable stability to be used to transfer a spectral responsivity scale maintained in a participating laboratory to that of PTB, acting as the pilot laboratory. It incorporated the comparison of different primary detector standards, ionization chamber and electrical substitution radiometer (ESR). Silicon photodiodes with different front passivation layers were used (see Figure 1); AXUV diodes having almost ideal responsivity (see Figure 2) but being sensitive to radiation damage, and SXUV diodes with an irradiation stable metal-silicide passivation. A total of six diodes, three AXUV and three SXUV, have initially been calibrated at PTB, sent to NIST for measurements, re-calibrated at PTB, sent to NMIJ for measurements and were finally re-calibrated at PTB. The re-calibrations at PTB revealed that both types of diodes were sufficiently stable. All measurements are finalized and the partners exchanged their uncertainty budgets and agreed on the final calibration results for each as collected by the pilot laboratory.

		PTB	NIST	NMIJ
Primary detector		ESR	ESR	Ionization chamber
Radiation source		monochromatized SR		
Band width	/nm	0.025	0.07 to 0.4	0.3
Beam divergence	/mrad	1.	1.2	11
Beam spot size	/mm	2 by 2	2.7 by 3	3 by 3
Typical radiant power	/µW	0.2	0.01	2.5

Table 1   Main parameters of the experimental stations used by the pilot comparison participants.

The uncertainty for the comparison (see Figure 3) is determined by the measurement uncertainty of the participating laboratories and the uncertainty attributed to the transfer detectors, due to their limited homogeneity and stability. The measurement uncertainty of the

participating laboratories can be separated into two major contributions, arising from the primary standard detector which is an ESR in the case of PTB[1] and NIST[2] and an ionization chamber for NMIJ[3], and uncertainties attributed to monochromator and beamline (see Table 1). For the ionization chamber, the primary standard detector dominates the uncertainty budget, while for the ESR with its intrinsically low measurement uncertainty the total uncertainty is dominated by the contributions from monochromator and beamline. For this comparison, the uncertainty attributed to the transfer detectors is of the same order as the measurement uncertainty of PTB and NIST using an ESR. Thus further success in EUV radiometry also requires advanced detectors.
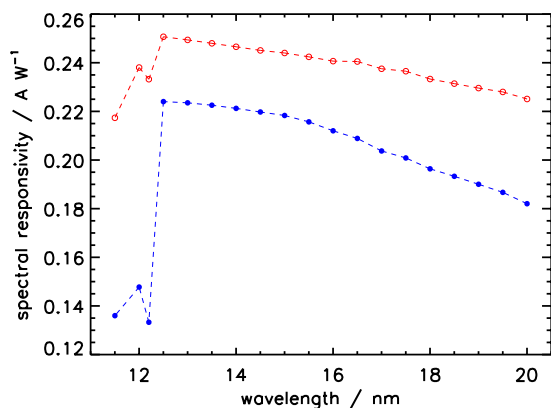
Figure 1 Spectral responsivity of the AXUV (open circles) and SXUV (closed circles) type diodes. The lines are only to guide the eye.
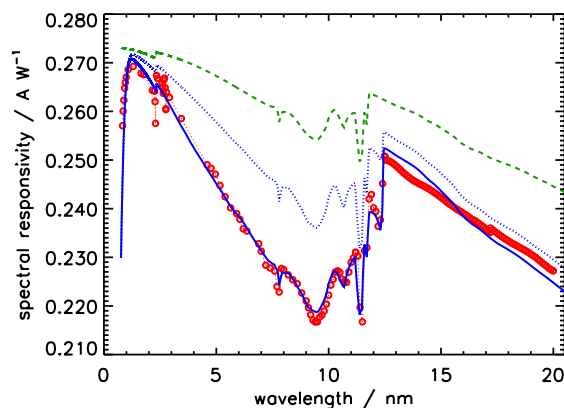
Figure 2 Responsivity of an AXUV diode from 0.827 nm (1500 eV) to 20 nm (red circles). The green dashed line shows the transmittance of 7.5 nm SiO_2 and solid and dashed blue lines the responsivity for different levels of incomplete charge collection.
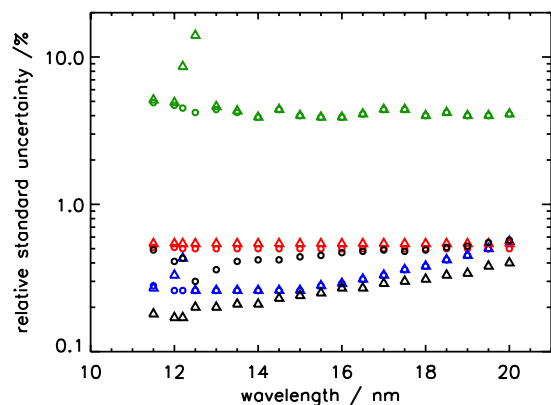
Figure 3 Compilation of the relative measurement uncertainties (k=1) for the spectral responsivity; AXUV (circles) and SXUV (triangles). Data of PTB, NIST, and NMIJ are shown in blue, red, and green, respectively. The black symbols show the uncertainty resulting from the transfer detectors, mainly due to their limited homogeneity and stability.

References

[1] Rabus H., Persch V., and Ulm G., "Synchrotron-Radiation Operated Cryogenic Electrical-Substitution Radiometer as High-Accuracy Primary Detector Standard in the Ultraviolet, Vacuum Ultraviolet and Soft X-ray Spectral Ranges", Appl. Opt. 36, 5421-5440, 1997

[2] Vest R. E., Barad Y., Furst M. L., Grantham S., Tarrio C., and Shaw P. S., "NIST VUV metrology programs to support space-based research", Advances in Space Research 37, 283-296, 2006.

[3] Saito T. and Onuki H., "Detector calibration in the 10-60 nm spectral range at the Electrotechnical Laboratory", J. Optics 24, 23-30, 1993

UV and VUV Radiometry at PTB's Metrology Light Source

A. Gottwald, R. Fliegauf, U. Kroth, W. Paustian, M. Richter, H. Schöppe, R. Thornagel, and G. Ulm

Physikalisch-Technische Bundesanstalt, Abbestr. 2-12, 10587 Berlin

In the UV and VUV spectral ranges, the main work of PTB with synchrotron radiation can be divided into (a) the calibration of radiation sources within the framework of source-based radiometry using an electron storage ring as a primary source standard of calculable synchrotron radiation, (b) the calibration of photodetectors with the aid of cryogenic radiometers as primary detector standards, and (c) reflectometry [1]. Started at the former electron storage ring BESSY I, these activities were continued from 2000 at BESSY II. However, in 2008 started the concentration of UV and VUV radiometry at PTB's new low-energy storage ring MLS [2], profiting there from the almost ideal measurement conditions in the UV and VUV with a characteristic wavelength which can continuously be varied from 3.4 nm to 735 nm. Moreover, the UV and VUV measurement capabilities will considerably be extended towards polarization dependent methods and photon metrology at high radiant power.

The calibration of photodetectors based on cryogenic radiometry and the characterization of optical components and materials via reflectometry in the UV and VUV has been performed at BESSY I and BESSY II by using a McPherson type normal-incidence monochromator (NIM) for the wavelength range from 40 nm to 400 nm [3]. In 2008, this beamline has been transferred from BESSY II to MLS (Figure 1), together with the cryogenic radiometer SYRES II and a reflectometer system. The gracing incidence refocusing mirror was replaced by a double reflector unit for the suppression of higher spectral orders in the range from 80 nm to 120 nm. The beamline output is generally by 50 % to 100 % higher compared to BESSY II (Figure 2) when operated with the same stored electron current.
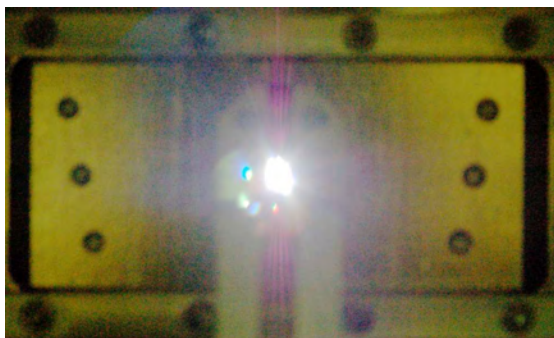
Fig. 1. Synchrotron radiation of PTB's Metrology Light Source passing the exit slit of the normal-incidence mochromator beamline for UV and VUV detector calibration and reflectometry.
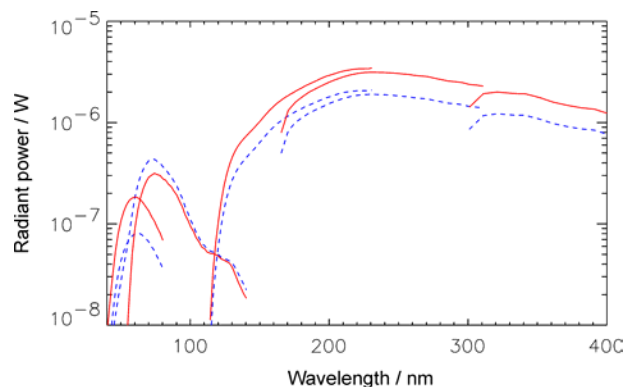
Fig. 2. Radiant power into the respective bandpass available at the normal-incidence mochromator beamline for UV and VUV detector calibration and reflectometry for open monochromator slits (2 mm) and a storage ring current of 100 mA at MLS (solid curves, electron energy: 600 MeV) and BESSY II (dashed curves, electron energy: 1,700 MeV).

For the calibration of radiation sources at MLS, a new spectrometer is under construction which combines a Seya-Namioka type NIM with a toroidal grating monochromator (TGM) under gracing incidence (Figure 3). The spectrometer covers the wavelength range from 7 nm to 400 nm and will be put into operation at MLS in 2010. In a first step, spectral radiance and spectral radiant intensity will be the radiometric quantities of a secondary source standard that can be determined by comparison with the calculable flux of MLS. In a second step, also spectral irradiance calibrations are scheduled to be realized.

Within a straight section of MLS, an undulator with a periodic length of 180 mm (U180) [4] will be put into operation at the end of 2008. It provides radiation in the wavelength range from 4 nm to 20 µm. In the UV and VUV range, the radiant power available will be about two orders of magnitude higher compared to ordinary bending magnet synchrotron radiation. At the exit of a plane grating monochromtor (PGM) currently under construction, an output of 50 µW within a spectral bandpass of 0.1 % of the wavelength is expected. This PGM, again, combines a normal incidence with a gracing incidence branch and covers the spectral range from approx. 4 nm to 400 nm. It is scheduled to start operation in 2010. Since undulator radiation is also 100 % linearly polarized, the PGM undulator beamline will enable UV and VUV radiometry to be extended to high flux and polarization dependent measurements.
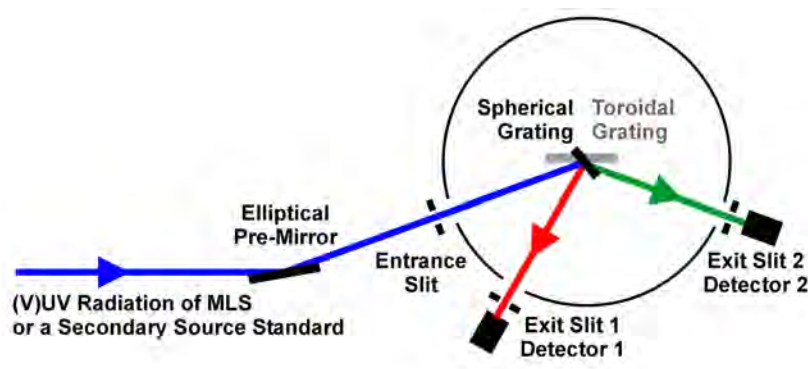
Fig. 3. Scheme of the spectrometer for the calibration of radiation sources in the UV and VUV at MLS.

REFERENCES

[1] M. Richter, J. Hollandt, U. Kroth, W. Paustian, H. Rabus, R. Thornagel, G. Ulm, Metrologia **40**, S107-S110 (2003)

[2] G. Brandt, J. Eden, R. Fliegauf, A. Gottwald, A. Hoehl, R. Klein, R. Müller, M. Richter, F. Scholze, R. Thornagel, G. Ulm, K. Bürkmann, J. Rahn, G. Wüstefeld, Nucl. Instr. and Meth. B **258**, 445-452 (2007)

[3] M. Richter, J. Hollandt, U. Kroth, W. Paustian, H. Rabus, R. Thornagel, G. Ulm, Nucl. Instr. and Meth. A **467-468**, 605-608 (2001)

[4] R. Klein, J. Bahrdt, D. Herzog, G. Ulm, J. Synchrotron Rad. **5**, 451-452 (1998)

Absolute determination of cross sections for resonant Raman scattering on silicon carbide

M. Müller[1], M. Kolbe[1], B. Beckhoff[1], K. Feldrapp[2], S. Storm[2], A.-D. Weber[2]

1 Physikalisch-Technische Bundesanstalt, Abbestr. 2-12, 10587 Berlin, Germany
2 SiCrystal AG, Günther-Scharowsky-Str. 1, 91058 Erlangen, Germany

Reference-free total-reflection x-ray fluorescence analysis for the quantification of surface contamination requires the accurate knowledge of all experimental values as well as of the fundamental parameters involved [1]. Besides the fundamental parameters of the contaminants also the parameters of the substrate affect the result. To reduce the impact of tabulated data with unknown or estimated relative uncertainties the resonant Raman scattering of X-rays in the vicinity of the K absorption edge of silicon carbide (SiC) has been studied. The investigation was carried out at the plane grating monochromator beamline for undulator radiation of the PTB laboratory at BESSY II in Berlin.

SiC is a wide-band-gap semiconductor and offers outstanding material properties for high-power electronics and optoelectronic applications. Non-destructive analytical methods like reference-free TXRF are necessary for process control. For the investigation a SiC wafer was thinned to a thickness of about 10 μm to allow for transmission measurements. We determined absolute cross sections for the energy range below the silicon K absorption edge employing calibrated instrumentation.

Theory

The resonant Raman scattering is an inelastic scattering process, which exhibits a strong resonant behavior as the energy of the incident radiation approaches from below the absorption edge of an element [2]. The KL-RRS proceeds through:

- the intermediate state, where a virtual hole is created in the K-shell and the corresponding electron is transferred to an unoccupied state either in the continuum or in a bound excited state,

- the final state, where an electron from one of the L subshells fills the hole and a photon is emitted.

Experimental Set-up

For this experiment we employed monochromatized undulator radiation provided by the plane grating monochromator beamline in the PTB laboratory at BESSY II. The experimental setup (Fig.1) ensures that the scattered radiation can be measured in a well defined solid angle by means of a Si(Li) detector. The incident radiant power can be absolutely determined by using a calibrated photo diode placed behind the exit diaphragm, if the sample is out of the beam. The Si(Li) detector in use is also calibrated with respect to both its efficiency and its response behavior [3]. Additionally, in the same arrangement the thickness of the measured 2" SiC wafer and the corresponding absorption factors can be experimentally determined by employing transmission measurements.
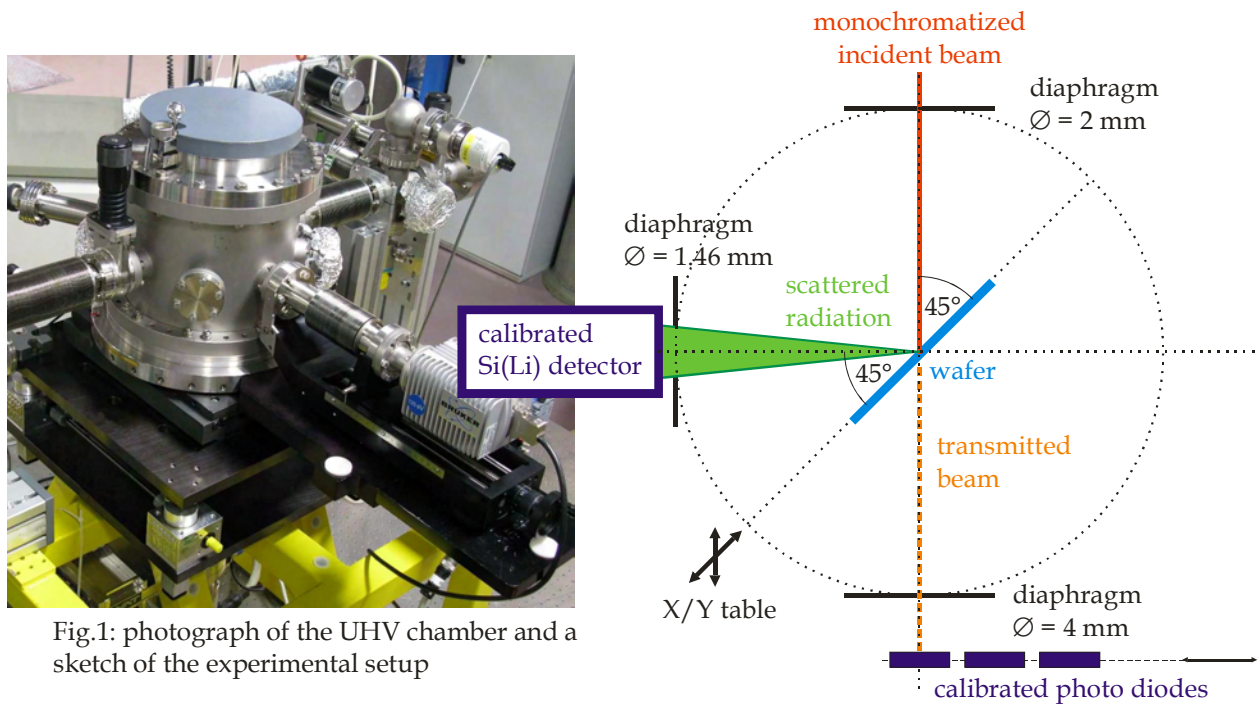
Fig.1: photograph of the UHV chamber and a sketch of the experimental setup

Data Analysis

Because a direct deconvolution of the measured spectrum with the response functions of the Si(Li) detector was not possible, we adopted a different approach to determine the resonant Raman scattering cross section with respect to the scattered photon energy: The theoretically calculated RRS spectral distribution was at first convoluted with the Si(Li) detector's response functions, then the resulting spectra were fitted to the measured spectra [4]. All necessary parameters, such as radiant power, sample thickness, solid angle, absorption coefficients were experimentally deduced.

Results

We determined the cross sections of the resonant Raman scattering on SiC for three photon energies of the incident radiation and compared it with cross

Fig.2: XRF spectrum of the thinned SiC wafer, excited below the Si-K edge (1622 eV). The spectrum was deconvoluted by detector response functions at the energies of fluorescence lines, continuous bremsstrahlung background and spectral distribution of the Resonant Raman Scattering in a least square optimization.
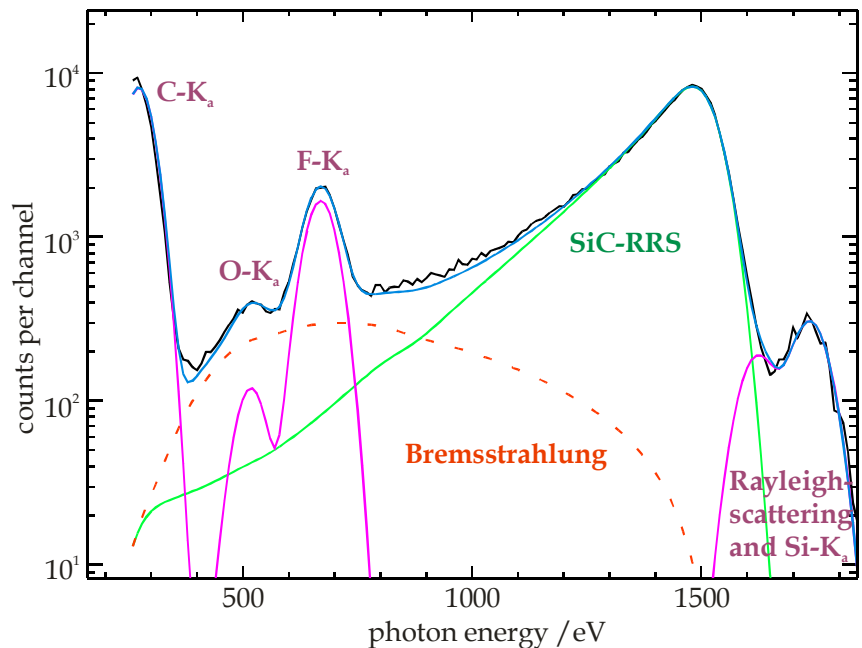
sections of pure silicon [4]. The RRS cross sections of Si and SiC are the same apart from a difference of 2 eV between the resulting values of the Si-K absorption edges. This difference is also found in the transmission measurements of both samples.

Conclusions

The RRS cross sections of SiC are not strongly influenced by chemical bonding, merely the chemical shift of the Si-K absorption edge has an impact on the cross sections. The results suggest that the cross sections for pure Si may be used for SiC as well, if the chemical shift is taken into account. For other Si compounds further investigations are necessary, e.g. Szlachetko et al.[5] reported that there is still a difference of about 20% between the RRS cross sections of Si and SiO_2 after including the K edge shift.

The relative uncertainties of the determined cross sections are only 7%[4]. Therefore the impact of the resonant Raman scattering background contribution on quantitative TXRF can be considered very accurately. This will improve the reliability of the analysis of Si and SiC wafers employing soft X-ray radiation.

References

[1] B. Beckhoff, R. Fliegauf, M. Kolbe, M. Müller, J. Weser, G. Ulm, Anal. Chem., **79** 7873-7882 (2007)

[2] Ch. Zarkadas, A.G. Karydas, M. Müller, B. Beckhoff, Spectrochim. Acta B **61**, 189-195 (2006)

[3] F. Scholze, B. Beckhoff, M. Kolbe, M. Krumrey, M. Müller, G. Ulm, Microchim. Acta **155**, 275–278 (2006)

[4] M. Müller, B. Kanngießer, B. Beckhoff, G. Ulm, Phys. Rev. A **74**, 012702 (2006)

[5] J. Szlachetko, J.-Cl. Dousse, M. Berset, K. Fennane, M. Szlachetko, Phys. Rev. A **75**, 022512 (2007)

Characterization of self-assembled monolayers on germanium surfaces with GIXRF

M. Lommel, B. O. Kolbesen
Institute for Inorganic and Analytical Chemistry, Goethe-Universität, Frankfurt/Main, Germany
P. Hönicke, M. Kolbe, M. Müller, F. Reinhardt, B. Beckhoff,
Physikalisch-Technische Bundesanstalt, Abbestraβe 2-12, 10587 Berlin, Germany

Introduction

Germanium has gained interest in recent years as a promising material for high-performance CMOS applications. However, Ge does not form a robust passivation layer on its surface – germanium oxide is water-soluble [1]. The formation of self-assembled monolayers (SAMs) by suitable organic molecules with appropriate anchor groups on semiconductor surfaces may be used to probe the chemical state and quality of the surface or to achieve surface passivation. Molecules with thiol anchor groups are able to bond to hydrogen-terminated germanium surfaces (Ge-S bond). We have prepared SAMs of alkylthiols with different head groups on germanium.

Figure 1: The thiol (HS-) group is the so called "anchor group" with the sulphur bonding to the germanium. The long chain is the motor of self-assembly. The "head" group, here –OCOCF$_3$, makes a detection of the monolayer easily possible.
Distance: sulphur – fluorine: 1.8 nm

The germanium surface prior to and after SAMs formation has been characterized by AFM, XPS, SR-TXRF and -NEXAFS. Since the surface preparation of germanium is neither well understood nor developed, the controlled preparation of an oxide-free completely H-terminated surface which is a prerequisite for SAM formation of alkylthiols turned out to be a major challenge. Several approaches have been studied [2]. Best results for H-termination of germanium have been obtained by HF treatment The immediate immersion of the HF treated germanium into a 1-mmol solution of thiol, e.g. di-chloroethane, leads to self-assembly of thiol monolayers.

Results and discussion

The success of the formation of the monolayer on the substrate depends largely on several factors during its preparation e.g., the solvent used for the formation of the monolayer has to be free of water as well as traces of oxygen and has to dissolve the thiol of choice. Attempts were made to form monolayers with several 11-mercaptoundecyls [HS-(CH$_2$)$_{11}$-R] with differing head groups (-R). In this case the head groups were chosen to facilitate detection by SR-TXRF (Synchrotron Total reflection X-ray Fluorescence), GIXRF (Grazing Incidence XRF) and NEXAFS (Near Edge X-ray Absorption Fine Structure) and hence determine the degree of coverage as well as to determine the properties of the monolayer, e.g. its height and the bonding angle. The preparation was performed in an argon atmosphere. The sample with the H-terminated surface was blown dry with N$_2$ and immediately immersed into a 1mmol solution of the thiol in dichloroethane (DCE). DCE meets the needs of a
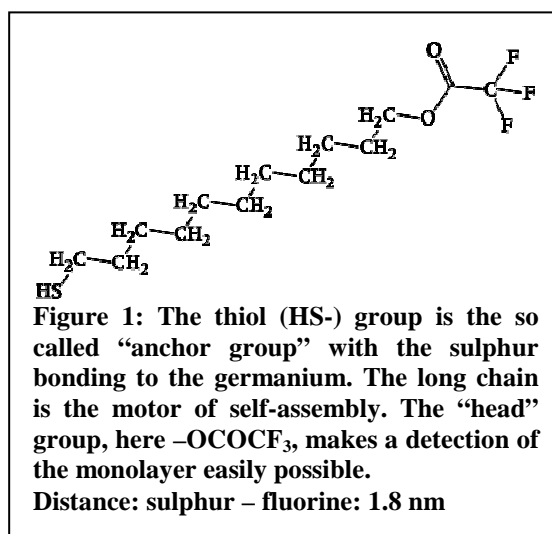
solvent that does not contain water, dissolves both hydrophilic and hydrophobic molecules, does not contain oxygen in its structure and has adequate vapour pressure. The thiol adsorbs onto the germanium surface about 10 seconds after immersion into the precursor solution but the process of self-assembly takes hours if not days to be finished [3]. To distinguish between physisorbed and therefore "horizontal" thiols and the chemisorbed "vertical" thiols we measured the coverage of sulphur on the substrate after different immersion times and performed GIXRF measurements.

The incident angle dependant modulation of the X-ray standing wave field (XSW) above the sample surface allows for the determination of the amount as well as the distance in a vertical direction with respect to the sample surface of so-called marker atoms [4]. Here, the head group with fluorine was used as the marker (Fig.1). The GIXRF curves for different immersion times are shown in fig. 2a. The angle dependant XSW field was calculated with IMD [5] and convoluted with the model shown on fig. 2b and then fitted to each GIXRF curve [6, 7, 8].

sample	laying	standing	background
1h	54.2 %	5.3 %	40.5 %
1d	48.3 %	14.0 %	37.7 %
2d	55.2 %	14.0 %	30.8 %
5d	88.3 %	0 %	11.7 %
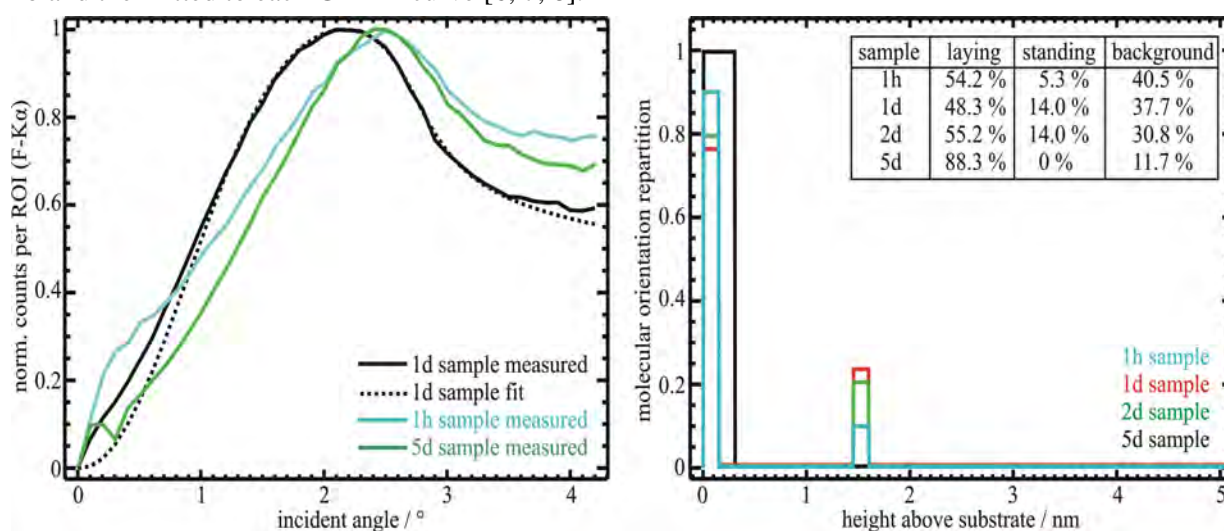
Figure 2: a) GIXRF measurements on F-SAMS for different immersion times and the fitted curve for the 1d sample. b) Different repartitions, which best fitted the respective measurements.

It assumes that the molecules either lie on the germanium surface or that they are bound, resulting in an F-layer at a certain height. The bonding angle, the normalized fraction of vertical thiols and background parameters were used as fitting parameters. The background originates from clustering of the molecules and was assumed to be a constant fluorine distribution. The results shown in fig. 2 led to the conclusion that the fraction of self assembled molecules is optimal after a period of one day. It is lower if immersion times are shorter or significantly longer than one day. A constant background was necessary to fit the GIXRF curves. The fraction of fluorine in the background or rather in clusters is relatively high. This means that clustered molecules cannot be neglected. The curve obtained on the sample treated for five days could only be fitted by increasing the surface layer thickness. This indicates that this sample is covered with a double layer of the lying molecules. The height of the fluorine above the surface was determined to be 1.4 nm, which corresponds to a bonding angle of the Ge-S bond of 47.5°. Beyond this, we determined the coverage of the substrate by AFM [2] and NEXAFS [9]. However, time and concentration are obviously not the only factors to influence the degree of coverage, as the AFM results were not reproducible. Nevertheless, with these results we proved that under the given conditions it is possible to prepare SAMs on germanium.

Summary

Treatments to achieve a controlled surface state of germanium, in particular with H-termination, prior to the preparation of alkylthiol SAMs have been tested and characterized. The immersion of HF treated germanium in a 1-mmol solution of thiol, e.g. dichloroethane, leads to self-assembly of thiol monolayers. The duration of exposure to the solution is a critical factor as too long treatments lead to molecule clusters. The coverage of germanium by self-assembled monolayers is a good proof of an H-terminated surface.

Acknowledgement

References

[1] J. He, Z.-H. Lu, S. A. Mitchell, D. D. M. Wayner; J. Am. Chem. Soc. **120** (11) 2660 (1998)

[2] M. Lommel, E. Mankel, B. O. Kolbesen, ECS Transactions **11** (20) 83-90 (2008)

[3] D. K. Schwartz, Annu. Rev. Phys. Chem. **52** 107 (2001)

[4] M. Krämer, Dissertation, Dortmund (2007)

[5] D.L. Windt, Computers in Physics, **12** 360-370 (1998)

[6] D. K. G. de Boer, Phys. Rev. B **44**(2), 498 (1991)

[7] B. Pollakowski, B. Beckhoff, F. Reinhardt, S. Braun, P. Gawlitza, Physical Review B **77**, 235408 (2008)

[8] P. Hönicke, B. Beckhoff, M. Kolbe, S. List, T. Conard, H. Struyff, Spectrochim. Acta B **63,** 1359 (2008)

[9] M. Lommel, F. Reinhardt, P. Hönicke, E. Mankel, M. Müller, M. Kolbe, B. Beckhoff, B.O. Kolbesen, ECS Transactions, to be published, (2009)

Calibration of the NASA instrument EUNIS

W. Paustian, M. Richter, R. Thornagel

Physikalisch-Technische Bundesanstalt (PTB) , Abbestraße 2-12, 10587 Berlin, Germany

B. Kent

Rutherford Appleton Laboratory (RAL), Chilton, Didcot, Oxfordshire OX11 0QX, UK

Solar radiation in the VUV strongly influences the photochemical processes in the upper atmosphere and, thus, also the earth climate. Space-based observations of the sun in this spectral range have, therefore, attracted increasing interest during the last years. In this context, the reliable characterization of the corresponding space instruments is of high significance. In the BESSY laboratories of PTB, work on solar telescope calibration has a long tradition [1]. In the mid 1990s, the SUMER (Solar Ultraviolet Measurements of Emitted Radiation) and CDS (Coronal Diagnostic Spectrometer) instruments of the SOHO (SOlar and Heliospheric Observatory) mission were calibrated, via hollow cathode gas discharge plasma sources as the transfer standards, and in 2004 the EIS (Extreme-ultraviolet Imaging Spectrometer) instrument of the Solar-B/Hinode mission. The absolute VUV emissions of the source standards used are traceable to calculable synchrotron radiation. In the following, several underflight calibrations of these and further solar instruments were performed by means of short-term rocket missions like SERTS (Solar Extreme-ultraviolet Research Telescope and Spectrometer), MOSES (Multi Order Solar EUV Spectrograph), and EUNIS (Extreme Ultraviolet Normal Incidence Spectrometer) whose own calibrations were performed at the Rutherford Appleton Laboratory (RAL) using PTB's CDS calibration source.
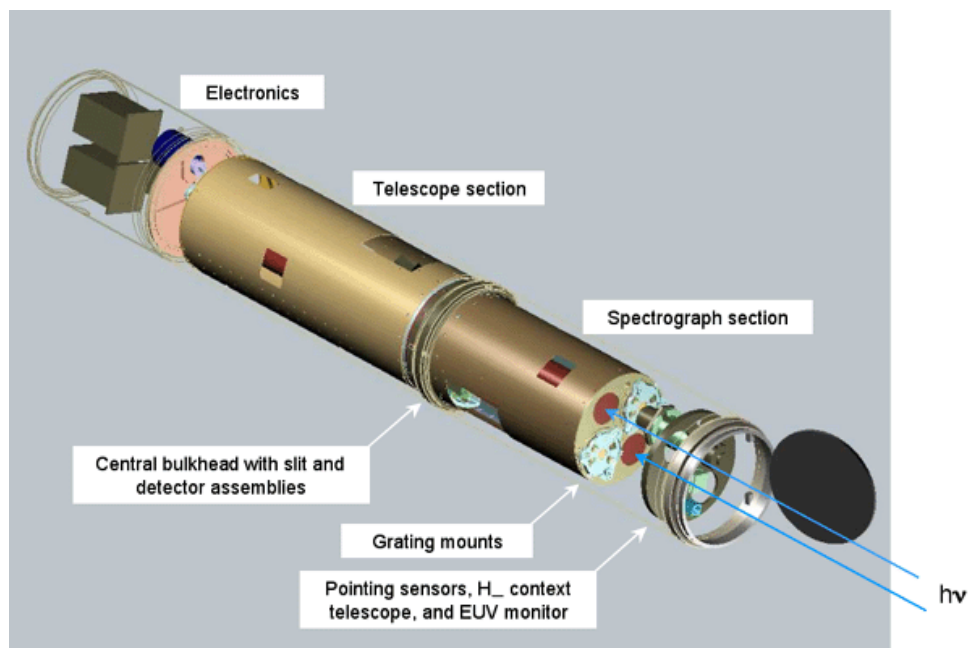
Fig. 1. Scheme of the EUNIS instrument.

The EUNIS instrument (Fig. 1) uses two independent optical systems in two wavelength regions: 17 nm to 21 nm with 3.5 pm resolution and 30 nm to 37 nm with 7 pm resolution. There are only two reflections in each optical channel, from a superpolished, off-axis paraboloidal pre-mirror and a toroidal grating, each coated with a high-efficiency multilayer. Hence, the throughput of EUNIS is much higher than for SERTS that have preceded it. The detector in each channel is a microchannel plate image intensifier fiber-coupled to three pixel sensors. EUNIS is supported by NASA and was launched in April 2006 and November 2007.

Each EUNIS flight was accompanied by an afterflight calibration campaign within a PTB-RAL cooperation, the first in October 2006 and the second in May 2008. As an example, Fig. 2 shows a part of the Ne III spectrum as emitted from the CDS calibration source and measured with the EUNIS instrument. Instrument calibration is obtained by comparing its signal output with the absolute radiant power emitted from the calibration source. For this purpose, integration along the wavelength intervals indicated by the vertical lines in Fig. 2 has to be performed which represent the ranges of integral emission of the source as calibrated at BESSY. Next flight and calibration within the very successful EUNIS program are scheduled for 2010.
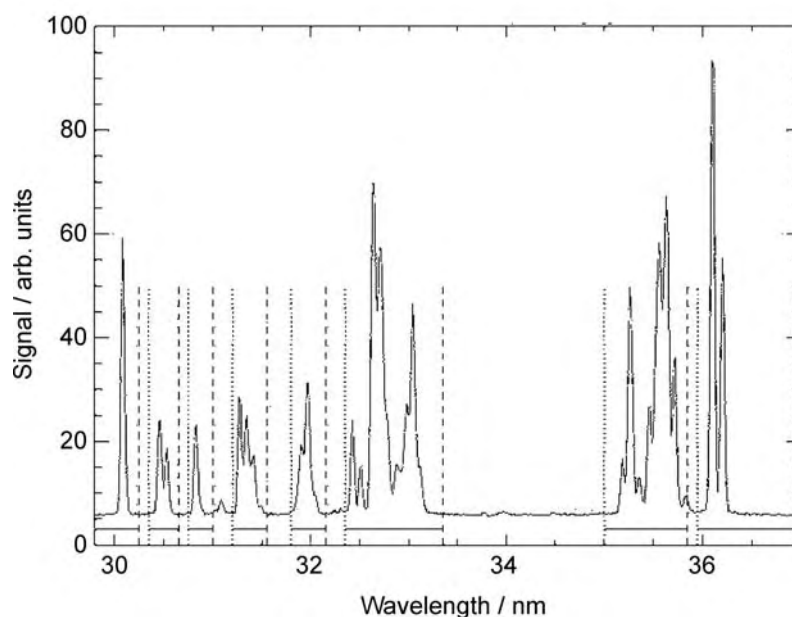
Fig. 2. Part of the Ne III spectrum as emitted from the CDS calibration source and measured with the EUNIS instrument.

REFERENCES

[1] M. Richter, A. Gottwald, F. Scholze, R. Thornagel, G. Ulm, *Calibration of Space Instrumentation with Synchrotron Radiation*. Advances in Space Research **37**, 265-272 (2006).

High-resolution X-ray absorption and emission spectroscopy on binary titanium compounds

F. Reinhardt[1,2], B. Beckhoff[1], H. Eba[3], B.Kanngießer[2], M. Kolbe[1], M. Mizusawa[3],
M. Müller[1], B. Pollakowski[1], K. Sakurai[3] and G. Ulm[1]

[1]*Physikalisch-Technische Bundesanstalt, Abbestr. 2-12, 10587 Berlin, Germany*
[2]*Technische Universität Berlin, Institut für Optik und Atomare Physik, Hardenbergstr. 36, 10623 Berlin, Germany*
[3]*National Institute for Materials Science, Sengen, Tsukuba, Ibaraki 305-0047, Japan*

Introduction: While the elementary composition of samples is readily determined by use of X-ray fluorescence analysis (XRF), the chemical state of a probed atom is only accessible by techniques employing high resolution in either the excitation or the detection channel.

For the chemical speciation of binary compounds of tri- and tetravalent titanium high-resolution X-ray absorption and emission spectra were recorded in different energy regimes in order to evaluate and to qualify both near-edge X-ray absorption fine structure (NEXAFS or XANES) spectroscopy and wavelength-dispersive X-ray emission spectroscopy (WDXES) as spectroscopic methods for this analytical task [1]. For a comparison of the information gained from the various methods, the titanium compounds were classified according to the bonded titanium's oxidation state. Thus, it was possible to distinguish between inner atomic effects due to different oxidation states and external effects related to the respective ligand and the surrounding structure. It becomes evident, that only the combined use of the complementary methods both in the soft and the hard X-ray range allows for a reliable speciation of tri- and tetravalent titanium compounds.

Instrumentation: All measurements in the soft X-ray regime, i.e. Ti-L shell absorption and emission spectroscopy, were carried out at the plane-grating monochromator (PGM) beamline for undulator radiation [2] in the PTB laboratory at BESSY II. For the Ti-K absorption spectra the measurements took place at the four-crystal monochromator (FCM) beamline [3] in the same laboratory. Soft X-ray emission spectra were obtained employing a wavelength-dispersive spherical grating spectrometer in Rowland geometry with 1200 $^{lines}/_{mm}$ [4]. By aligning the CCD-detector to the focus position of the Ti-$L\alpha$ fluorescence line, a resolving power of E/ΔE = 430 is achieved in the Ti-$L\alpha,\beta$ energy range, leading to an energy resolution of about 1 eV.

For all samples the incident photon energy was set to 520 eV, well above the $L_{II,III}$ edges in a non-resonant regime. The incident photon energy was below the Ti-L_I edge to create vacancies only in the Ti-$2p$ orbitals and not in the $2s$ Orbital as well. With energy values for Ti-$L\alpha$ and Ti-$L\beta$ of pure titanium taken from the Elam database, (451.8 eV and 458.2 eV [5]) an energy axis was set for the recorded section of the spectrum.

Complementary to the results obtained in the soft X-ray regime, additional measurements were carried out at SPring-8, beamline BL40XU with NIMS instrumentation optimized for wavelength-dispersive detection in a very broad range of hard X-ray photon energies [6, 7].

Experiment: Because of self-absorption of emitted fluorescence radiation all emission features with an energy above the Ti-L_{III} edge energy are reduced in intensity relative to the Ti-$L\alpha$ emission and all features below. In figure 1 the X-ray emission spectra of titanium and its oxides are shown. A chemical shift is visible for all emission features consistent with the increasing oxidation state of the titanium. The asymmetry of all Ti-$L\alpha$ lines is caused by self-absorption since the L_{III} absorption edge energy is close by [1, 8]. On the low-energy side of the Ti-$L\alpha$ emission line a satellite structure appears in the spectra of the titanium oxides.
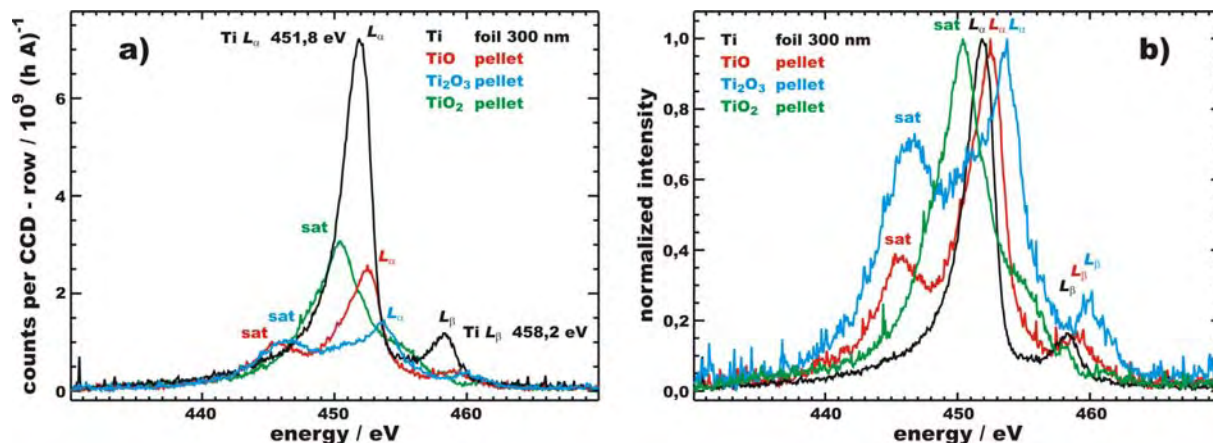
Figure 1: Ti-*L* X-ray emission spectra of pure titanium and the titanium oxides. The CCD-rows were converted to an energy axis by use of database values for Ti-*Lα* and Ti-*Lβ* of pure titanium. a) normalized to current induced in a calibrated reference diode by the incident radiation. b) normalized to 1.

Absorption spectra were recorded for different titanium compounds, i.e. TiO, Ti_2O_3, TiO_2, TiS_2, TiN and TiC, in both the soft and the hard X-ray regime. A comparison shows the well-known correlation between oxidation state and absorption edge energy position and an additional dependence on the ligand. Compounds with titanium in the same oxidation state and with ligands similar in Z (Ti_2O_3 and TiN or TiO_2 and TiC) are hardly distinguishable by their *K* near-edge spectra. In contrast, the X-ray emission is characteristic for those compounds due to the different chemical properties of those ligands (fig. 2). Compounds where the ligand shows similar chemical properties (TiO_2 and TiS_2) give rise to a similar X-ray emission (fig. 2) but with O and S having a considerably different atomic number and hence a very different electron backscattering ability, their XANES spectra clearly differ.
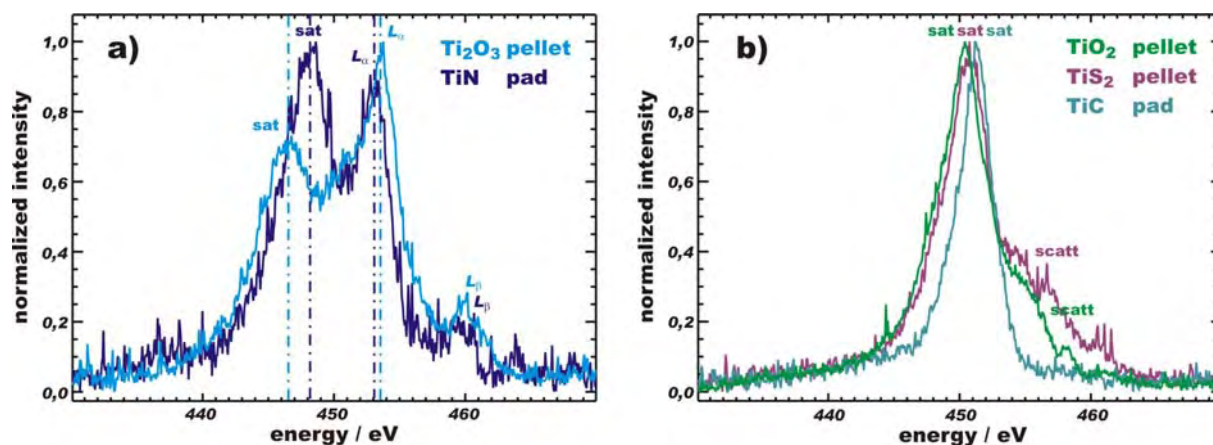
Figure 2: High-resolution X-ray emission spectra of Ti-*Lα,β* a) of Ti_2O_3 and TiN. b) of TiO_2, TiS_2 and TiC.

Conclusion: To evaluate the capabilities of high-resolution X-ray absorption and X-ray emission spectroscopy for chemical speciation, spectra were recorded for a set of binary titanium compounds.

Other compounds, where titanium is in the same oxidation state, exhibit significant differences in their Ti-*K* near-edge absorption spectra only if the atomic number of the ligand itself differs significantly from the one of oxygen.

The Ti-$L\alpha,\beta$ emission spectra are, in general, not a reliable indicator for different ligands. If titanium is present in a defined oxidation state, the chemical properties of the ligand play a major role for the structure of the emission spectrum. As shown for the Ti-L emission spectra of TiO_2 and TiS_2, X-ray emission spectroscopy hardly gives any indication to the species if the chemical bonding is similar.

It is obvious that the combination of both spectroscopic methods yields a larger amount of information than each of these approaches themselves. The information from occupied and unoccupied density of states give access to complementary information and therefore allow for a reliable chemical speciation.

References

[1] F. Reinhardt, B. Beckhoff, H. Eba, B. Kanngießer, M. Kolbe, M. Mizusawa, M. Müller, B. Pollakowski, K. Sakurai, and G. Ulm, Anal. Chem. (2009), in print, DOI 10.1021/ac8018069

[2] F. Senf, U. Flechsig, F. Eggenstein, W. Gudat, R. Klein, H. Rabus, and G. Ulm, J. Synchrotron Rad. **5**:780-782, 1998.

[3] M. Krumrey, J. Synchrotron Rad. **5**:6-9, 1998.

[4] M. Müller, B Beckhoff, R. Fliegauf, and B. Kanngießer, submitted, 2009.

[5] W. T. Elam, B. D. Ravel, and J. R. Sieber, Rad. Phys. Chem. **63**:121-128, 2002.

[6] K. Sakurai, H. Eba, K. Inoue, and N. Yagi, Nucl. Instr. Meth. A **467**:1549, 2001.

[7] K. Sakurai and M. Mizusawa, Rev. Sci. Instr. **78**:066108-1-3, 2007.

[8] B. Stoyanov, F. Langenhorst, and G. Steinle-Neumann, American Mineralogist **92**:577-586, 2007.

VAMAS projects on reproducibility in X-ray reflectometry

M. Krumrey

Physikalisch-Technische Bundesanstalt, Abbestr. 2-12, 10587 Berlin, Germany

X-Ray Reflectometry (XRR) is a well-established technique to evaluate quantitatively electron density, thickness and roughness of thin layers. Due to the interference of X-rays reflected from different interfaces, layers and multilayers on flat substrates give rise to oscillations. The period of the oscillations depends on the layer thickness, the fringe amplitude depends on surface and interface roughness and the relative electron densities of the materials.

During the last years, two worldwide XRR round-robin experiments were performed within the framework of the VAMAS project "X-ray reflectivity measurements for evaluation of thin films and multilayers". The reproducibility of measurements obtained using different equipments has been investigated. VAMAS (Versailles Project on Advanced Materials & Standards – www.vamas.org) is an international organization that supports trade in products using advanced materials through international collaborative projects aimed at providing the technical basis for harmonized measurements, testing, specifications, and standards.

For one of the round robins, a thin TaN/Ta bilayer was deposited on a 300 mm silicon wafer at the Albany NanoTech facility in the College of Nanoscale Science and Engineering (CNSE) at the University at Albany [1]. Unlike conventional Ta-based barrier metallizations, this sample was prepared with the tantalum metal being deposited first and the TaN deposited last; this was done in order to passivate the tantalum metal surface with a relatively non-reactive TaN compound layer. On the basis of the previously mapped lateral uniformity, four samples in near-center region were chosen for the round-robin analyses and delivered to the participating laboratories. The 4 samples were measured by 6 different laboratories (Table 1). While most participants used conventional X-ray sources, PTB applied synchrotron radiation at the four-crystal monochromator beamline at BESSY II [2]. The measurements were performed using the PTB UHV X-ray reflectometer [3].

The analysis of the specimens was based on the average of up to five independent XRR experiments performed, removing and mounting the sample between each measurement. Auto-correlation functions of the derivative of the density profile were obtained by Fourier transform of the ratio of reflectivity data and Fresnel reflectivity [4]. The layer thicknesses have been evaluated by a Gaussian fit of the peaks in the Fourier spectra (Fig. 1).

LAB	X-ray source	Monochromator	Slit size / μm	Detector
A	Cu K_α rot. anode	Göbel mirror	100	NaI:Tl scintillator
B	BESSY II storage ring	4 Si (111) crystals	300	Si photodiode / Photon count. Si drift
C	Cu K_α	Göbel mirror	300	scintillator
D	Cu K_α	Göbel mirror	600	
E	Cu K_α	Parabolic multilayer	100	
F	Cu K_α	Si(111) channel cut crystal	200	scintillator

TABLE 1 Experimental setups of the laboratories involved in the TaN/Ta round-robin.
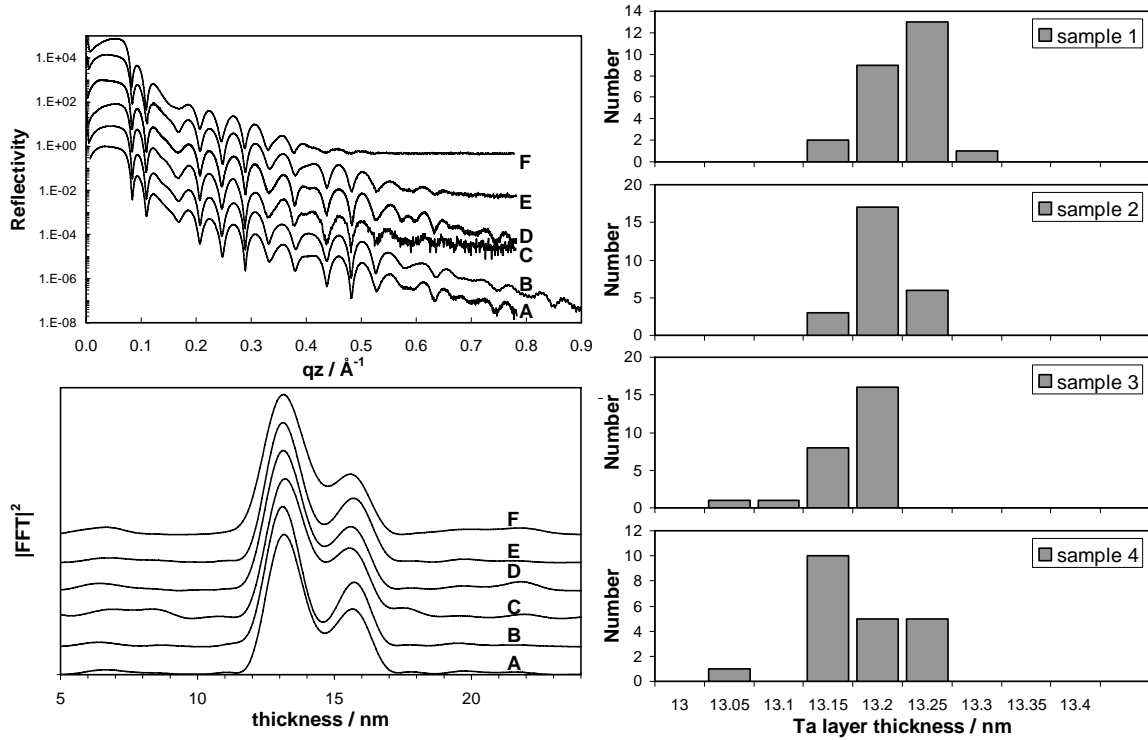
FIGURE 1. Upper left: Experimental XRR profiles acquired by different laboratories on TaN/Ta sample 1. XRR curves are scaled by one order of magnitude for clarity. Measurements in the PTB laboratory at BESSY II are labelled with B.
Lower left: Relative auto-correlation function of the derivative of the electronic density profile obtained by Fourier transform. The peaks correspond to the thickness of the Ta layer and to the total layer thickness of the bilayer, respectively.
Right: Distribution of thicknesses of Ta layer for different samples obtained from the peak in the auto-correlation function.

The maximum discrepancy between thickness values obtained in different labs is less than 0.2 nm. For all the samples standard deviation on the Ta layer thickness is less than 0.04 nm corresponding to about 0.3 %, despite the fact that the XRR measurements were performed using different instruments and in particular with different characteristics in terms of their angular resolution and their maximum and background intensity levels.

For another round-robin with 20 participating laboratories, GaAs/AlAs multilayer samples were chosen because GaAs and AlAs readily grow epitaxially without relaxing. This kind of sample has already been considered as a possible XRR reference standard. However, a top surface oxide developed during the round robin, meaning that only the thicknesses of buried layers can be meaningfully compared. GaAs/AlAs multilayer samples were supplied from the Surface and Thin Film Standards Section of the National Metrology Institute of Japan (NMIJ), AIST Japan. Three pairs of GaAs/AlAs bilayers (Fig. 2) were fabricated on four 4-inch GaAs (100) wafers simultaneously, using a molecular beam epitaxy technique. Fabrication conditions were optimized via structural evaluation of multilayers by TEM and XRR. Uniformities of thicknesses across a wafer and from wafer to wafer were confirmed by XRR.

For the analysis of the measured reflectance data for this complex structure, a modelling and fitting procedure based on the Parratt recursive formalism of the Fresnel equations was applied [6]. Each laboratory applied its own fitting procedure to obtain values for the layer thickness. In order to compare the raw data, excluding the influence of the refinement procedure and the operator choices, simulations of all datasets were also performed starting from the same model and using the same simulation routine (IMD [7]). Each XRR spectrum was fitted over the whole data range. In some cases, the scans were truncated at an angle at which the Kiessig fringes were no longer distinguishable

because of the low signal to noise ratio. For each experimental curve, 18 parameters (seven layer thicknesses, eight roughness values, n and k for the top layer and reflectance scaling factor) were fitted together. Logarithmic fitting was performed using the Marquardt algorithm with statistical weighting. Thickness distributions for buried layers do not differ significantly from the free-fitted ones having a sharp distribution with mean values between 9.49 nm and 9.58 nm and standard deviation values from 0.06 nm to 0.16 nm, respectively. The topmost GaAs layer thickness show a broader distribution of around 0.3 nm centred on a thickness of about 9.5 nm. In general, thickness values measured on a GaAs/AlAs multilayer proposed as a reference sample show a good intra-laboratory reproducibility of about 0.03 nm and an inter-laboratory reproducibility of about 0.1 nm for the buried layers.
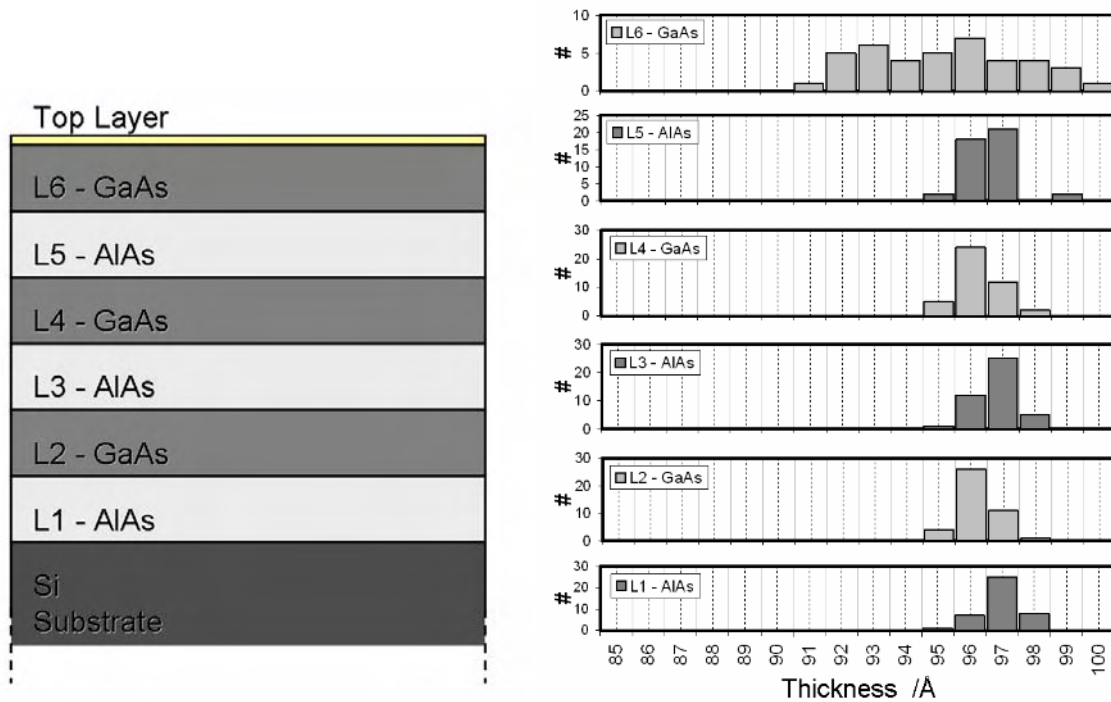
FIGURE 2. Left: Schematic view of the GaAs/AlAs sample structure employed for the round-robin.
Right: Distribution of thicknesses obtained by a common fitting approach (IMD) for all data measured by all participating laboratories.

REFERENCES

[1] R.J. Matyi, L.E. Depero, E. Bontempi, P. Colombi, A. Gibaud, M. Jergel, M. Krumrey, T.A. Lafford, A. Lamperti, M. Meduna, A. Van der Lee and C. Wiemer, Thin Solid Films **516**, 7962 – 7966 (2008)
[2] M. Krumrey and G. Ulm, Nucl. Instr. and Meth. A **467-468**, 1175 - 1178 (2001)
[3] D. Fuchs, M. Krumrey, P. Müller, F. Scholze and G. Ulm, Rev. Sci. Instrum. **66**, 2248 - 2250 (1995)
[4] S. Banerjee, S. Ferrari, D. Chateigner and A. Gibaud, Thin Solid Films **450** (2004) 23–28
[5] P. Colombi, D. K. Agnihotri, V.E. Asadchikov, E. Bontempi, D.K. Bowen, C.-H. Chang, L. E. Depero, M. Farnworth, T. Fujimoto, A. Gibaud, M. Jergel, M. Krumrey, T. A. Lafford, A. Lamperti, T. Ma, R. J. Matyi, M. Meduna, S. Milita, K. Sakurai, L. Shabel'nikov, A. Ulyanenkov, A. Van der Lee and C. Wiemer, J. Appl. Cryst. **41**, 143 – 152 (2008)
[6] L. G. Parratt, Phys. Rev. **95**, 359-369 (1954)
[7] D. L. Windt, Computers in Physics **12**, 360-370 (1998)

Cryogenic radiometry in the hard X-ray range

M. Gerlach, M. Krumrey, L. Cibik, P. Müller, H. Rabus and G. Ulm

Physikalisch-Technische Bundesanstalt, Abbestr. 2-12, 10587 Berlin, Germany

For many applications in radiometry, spectroscopy or astrophysics, absolute measurement of radiant power with low uncertainty is essential. Cryogenic electrical substitution radiometers (ESRs) are regarded as the highest-accuracy primary standard detector in radiometry, from the infrared to the ultraviolet region; in combination with tuneable monochromatized synchrotron radiation from electron storage rings, their range of operation has been extended to the soft X-ray region [1]. ESRs are absolute thermal detectors, based on the equivalence of electrical power and radiant power that can be traced back to electrical SI units and be measured with low uncertainties. The core piece of an ESR is its cavity absorber, which is thermally linked to a fixed temperature heat sink kept at liquid helium temperature via a heat resistance. The absorber is equipped with a thermometer and a heater that allows for the supply of electrical heating power (Fig. 1). The absorber temperature is kept constant by an active control. When radiation is provided, the electrical heating power required to keep the absorber at a constant temperature undergoes a reduction equivalent to the incident radiant power so that the radiant power is obtained through the measurement of the electrical heating power. Cavity absorbers are typically made of copper which provides excellent thermal conductivity at liquid helium temperature in combination with a moderate heat capacity, which in turn ensures a short response time suitable for the measurement of monochromatized synchrotron radiation. However at photon energies above 20 keV, the use of copper absorbers, typically 100 µm in thickness, prevents the operation of the ESR due to increasing transmittance.
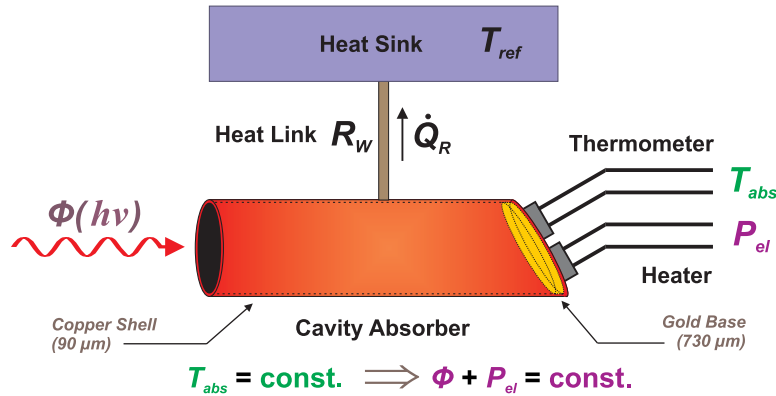
FIGURE 1. Operating principle of an electrical substitution radiometer. The new cavity absorber developed at PTB consists of a gold base and a copper shell to ensure complete absorption up to a photon energy of 60 keV.

To develop a new absorber design for hard X-rays, simulations were carried out using the Monte Carlo simulation code Geant4 [2]. Extensive simulations were performed for a large variety of absorber materials including Cu and Au as well as Ag, Pt and W. Alternative absorber geometries including different thickness of base and shell were investigated as well. Also, thermal aspects had to be taken into account, such as high thermal conductivity and low heat capacity at liquid helium temperatures. Concerning these aspects, metals with low atomic number, such as Cu and Ag, show the best performances, and it became obvious that no single metal would meet all requirements. Furthermore, an appropriate way of fabrication, such as electroforming, had to be applied for the respective metal. The simulations and experiments resulted in a final design of an absorber with a gold base, 730 µm in thickness, inclined 30°, and a cylindrical shell made of copper, 90 µm in thickness, to reduce losses caused by fluorescence and scattered photons. The cavity absorber was manufactured by electroforming at PTB and was implemented into the existing ESR SYRES I [3].

The spectral absorptance of the new and the former cavity absorber is shown in figure 2 (left) in comparison to a pure gold plate, 500 µm in thickness, that would cause significant losses due to Au L fluorescence. These can be totally prevented by applying a copper shell of 100 µm thickness. With this cavity absorber, an absorptance close to 100 % can be achieved in the full energy range from 250 eV, which is the low energy limit for the Monte Carlo simulations using Geant4 and 60 keV, which in turn, is the maximum photon energy with fairly high photon flux at the BAMline using the double-crystal monochromator [4]. The remaining losses are depicted in figure 2 (right). For photon energies above the Au K absorption edge of 80.75 keV, Au fluorescence is the dominant contribution. At 60 keV scattering contributes with 0.4 %, whereas transmitted radiation becomes the key factor for losses in the photon energy range between 75 keV and 80.75 keV.
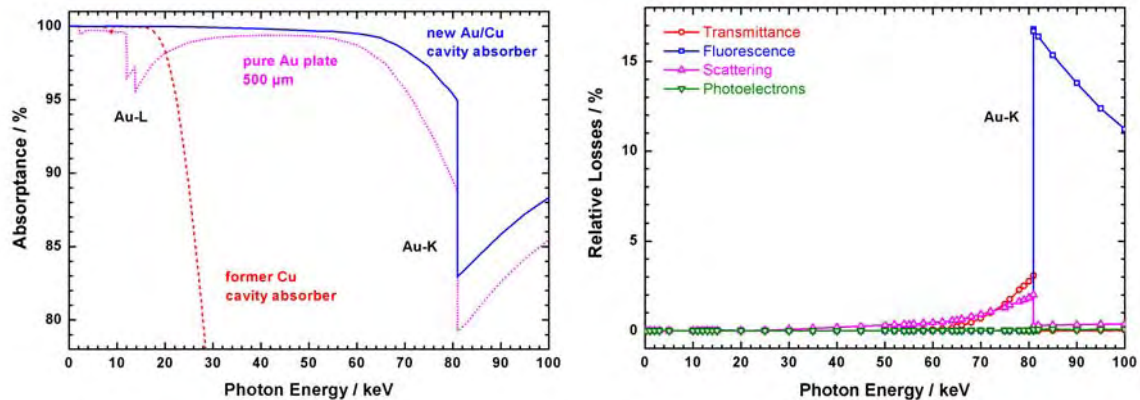
FIGURE 2. Left: Simulated absorption of the former copper absorber, 100 µm in thickness, compared to a pure gold plate, 500 µm in thickness, and the new absorber with gold base and copper shell.
Right: Simulated losses of the new absorber caused by transmittance, fluorescence, scattering and photoelectrons including Auger electrons.

An important application of the newly developed cryogenic radiometry in the hard X-ray range is the calibration of X-ray detectors such as semiconductor photodiodes. Monochromatized synchrotron radiation of high spectral purity was used to calibrate different silicon photodiodes against the ESR for photon energies up to 60 keV. The spectral responsivity of these photodiodes was determined with relative standard uncertainties below 0.3 %. The spectral responsivity in the photon energy range from 1.75 keV to 10 keV was measured at the PTB four-crystal monochromator beamline [5] and from 8 keV to 60 keV at the BAMline. The results for three different types of silicon photodiodes are shown in figure 3: AXUV 100 (International Radiation Detectors, IRD, USA), S3590 (Hamamatsu, Japan) and PIPS 50-500 (Canberra, Belgium).

In the energy range from 4 keV to 10 keV, the photodiodes of the Hamamatsu S3590 type and the Canberra PIPS type exhibit a high responsivity close to the theoretical maximum of 0.273 A/W for silicon [6]. The responsivity declines significantly for photon energies greater than 10 keV, caused by increasing transmittance. By applying a model calculation for the energy absorption in silicon, the thickness of the active volume of the respective photodiode can be determined as 320 µm and 510 µm, respectively, and be compared to the manufacturer's specifications, which are 300 µm and 500 µm, respectively. The thickness of the active volume of the IRD AXUV 100 photodiode is 27 µm, resulting in a much lower responsivity at photon energies greater than 4 keV. In the photon energy range just above the K absorption edge of silicon at 1.839 keV, the photodiodes of type S3590 have a reduced responsivity caused by the absorption in their thick passivation front layer, whereas the IRD AXUV 100 photodiodes exhibit high responsivity due to their SiO_2 front layer thickness of only a few nm. The Canberra photodiodes of type PIPS combine both advantages, a thick active layer of 510 µm and a thin front layer, ensuring a high responsivity and making this type the most suitable for use as secondary standard in the entire photon energy range. The photodiodes of Hamamatsu type S3590 exhibit a discontinuity in their spectral responsivity at a photon energy of 25.5 keV, which is caused by the fluorescence radiation of the conductive silver with that the photodiode is attached to its mounting [7].
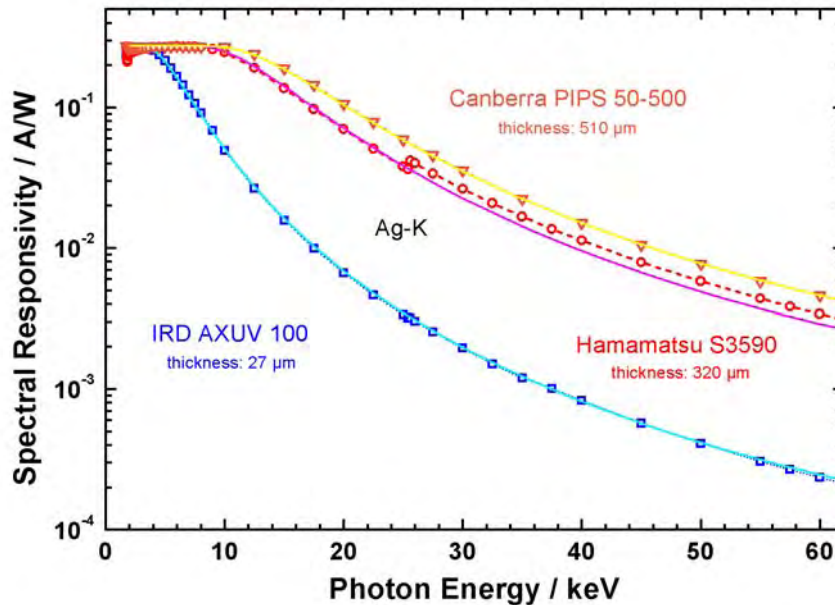
FIGURE 3. The spectral responsivity of three different semiconductor photodiodes calibrated against the ESR in the soft and hard X-ray ranges. Thicknesses of the active volume were derived from a model for photon absorption in silicon (solid lines).

In the photon energy range above 20 keV, a cryogenic radiometer was used for the first time as a primary standard detector to calibrate photodiodes. Whereas the relative uncertainty was about 2 % at PTB by calibration against a free-air ionization chamber due to the uncertainty of the mass energy absorption coefficients [8], for the present measurement with SYRES I relative standard uncertainties between 0.18 % and 0.30 % were achieved in the entire photon energy range, including hard X-rays with photon energies of up to 60 keV [9].

REFERENCES

[1] A. Gottwald, U. Kroth, M. Krumrey, M. Richter, F. Scholze and G. Ulm, Metrologia **43**, S125 – S129 (2006)
[2] S. Agostinelli et al., Nucl. Instr. and Meth. A **506**, 250 – 303 (2003)
[3] H. Rabus, V. Persch and G. Ulm, Appl. Opt. **36**, 5421 – 5440 (1997)
[4] W. Görner, M.P. Hentschel, B.R. Müller, H. Riesemeier, M. Krumrey, G. Ulm, W. Diete, U. Klein and R. Frahm, Nucl. Instr. and Meth. A **467-468**, 703 - 706 (2001)
[5] M. Krumrey and G. Ulm, Nucl. Instr. and Meth. A **467-468**, 1175 - 1178 (2001)
[6] F. Scholze, H. Rabus and G. Ulm, J. Appl. Phys. **84**, 2926 - 2939 (1998)
[7] M. Krumrey, L. Büermann, M. Hoffmann, P. Müller, F. Scholze and G. Ulm, AIP Conf. Proc. **705**, 861 – 865 (2004)
[8] L. Büermann, B. Grosswendt, H.-M. Kramer, H.-J. Selbach, M. Gerlach, M. Hoffmann and M. Krumrey, Phys. Med. Biol. **51**, 5125 – 5150 (2006)
[9] M Gerlach, M Krumrey, L Cibik, P Müller, H Rabus and G Ulm, Metrologia **45**, 577-585 (2008)

First commissioning results in the IR/THz range at the electron storage ring Metrology Light Source

Ralph Müller[1], Arne Hoehl[1], Roman Klein[1], Gerhard Ulm[1],

Jörg Feikes[2], Michael von Hartrott[2], Ulrich Schade[2], Godehard Wüstefeld[2]

[1]*Physikalisch-Technische Bundesanstalt, Abbestraße 2-12, 10587 Berlin, Germany*
[2] *Helmholtz-Zentrum Berlin für Materialien und Energie GmbH Elektronen-Speicherring
BESSY II, Albert-Einstein-Str. 15, 12489 Berlin, Germany*

In April 2008, the PTB's new electron storage ring, the Metrology Light Source (MLS), went into user operation [1-3]. Synchrotron radiation sources have major advantages in the IR range compared to conventional thermal sources, higher photon flux in the far-IR, higher brilliance, pulsed radiation in the ps range, and polarized radiation. Additionally, electron storage rings in a special operation mode with short electron bunches can deliver intense coherent synchrotron radiation (CSR) in the lower energy part of the far-IR (sub-THz to THz) with gain up to 6 to 9 orders of magnitude compared to conventional, incoherent synchrotron radiation emission. The MLS is the first electron storage ring worldwide designed and prepared for low-α operation mode based on the octupole correction scheme, for the production of CSR in the far-IR and THz region. This option strengthens the MLS as a strong THz radiation source [1 -6].

At the MLS two beamlines dedicated to the use of IR and THz synchrotron radiation are under commissioning respectively operational: (1) the MLS-IR beamline optimized for the MIR to FIR [6], and a dedicated THz beamline optimized for the FIR/THz spectral range. The commissioning of the IR beamline started in April 2008. The construction of the THz beamline was finished in the end of 2008.

The IR beamline and THz beamline consist of an arrangement of mirrors which allows - in combination with a special port of the dipole chamber – the transport of the beam to the experiment (see Fig.1). After all mirror reflections the σ-polarization of the electrical wave vector of the radiation is horizontally oriented. First measurements at the IR beamline with calibrated filter radiometers and an IR camera in the visible and near infrared spectral range reveal the good adjustment of the optical path of the beamline. All the flux expected from theoretical calculations is measured at the experiment. The shape and size of the focus is also as good as expected. With this adjusted IR beamline we were able to make first measurements in the THz spectral range. The inset of Fig. 1 shows the focus of the THz radiation (all radiation with a wavelength longer than 500 mm) in the low α mode. Its FWHM size is approximately 3 mm in diameter and is located nearly at the same position as the focus of the visible and near infrared light.
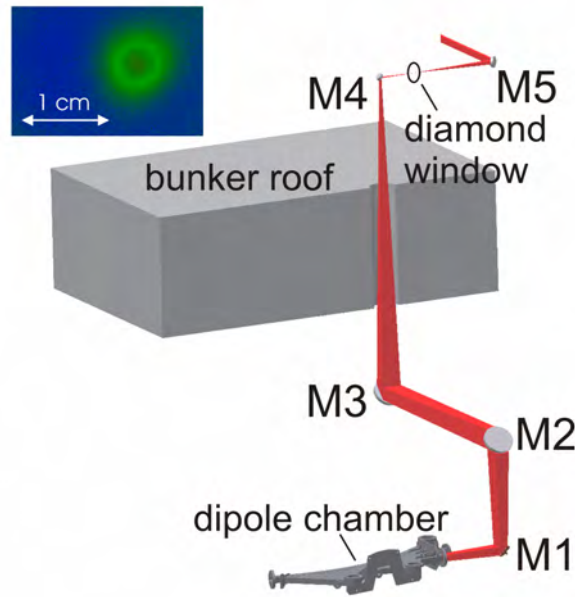
Fig. 1. Optical design of the MLS-IR beamline. The inset shows the focus of the CSR taken with an infrared camera in the THz spectral range in the low α mode.

The MLS has a unique capability to control the higher orders of α and to achieve bunch length reductions by a factor 10 in the sub-mm range. The higher orders of α are controlled by suitably placed sextupoles and octupoles [4]. By careful tuning of the optics, stable CSR is generated at the MLS. A first proof of stable CSR has been obtained. Fig 2. shows the results for the low α mode at 630 MeV and a ring current of 19 mA. Fig. 2a shows the chopped detector signal in the THz spectral region. Without chopping, the signal amplitude is smooth and shows no signs of bursting instabilities (see Fig. 2b). So the THz radiation is stable within the time resolution of a liquid-helium-cooled InSb hot electron bolometer of few micro-seconds.
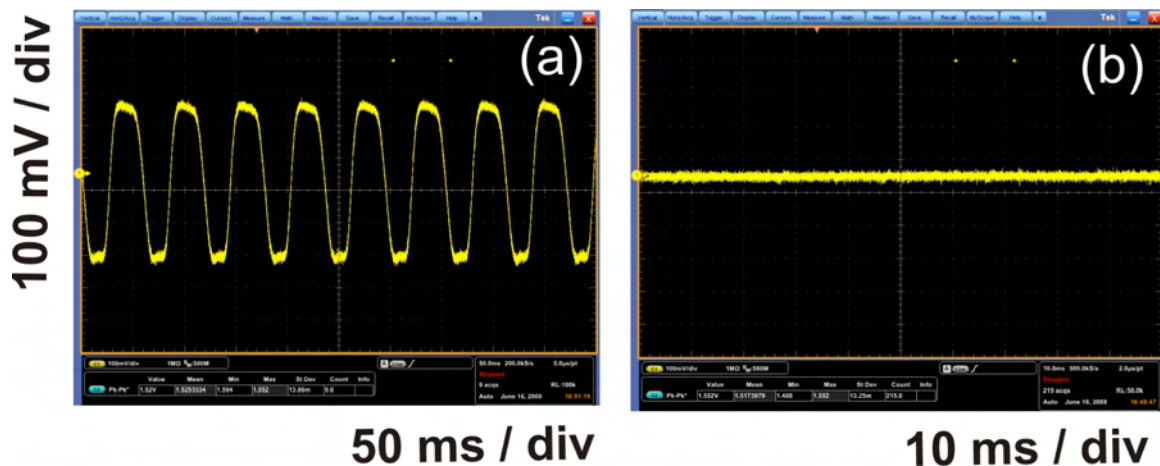
Fig. 2. Oscilloscope traces of stable THz signals at the MLS for 630 MeV electron energy, low α optics, 19 mA ring current, and a cavity voltage of 200 kV measured with an InSb-detector: (a) The chopped THz signal amplitude. (b) The unchopped THz signal amplitude is constant and shows no bursting instabilities.

Additionally we measured the absolute THz power in the focus of the IR beamline. The measured power is depending on the chosen α in the range of a few hundred micro-watts. However, the propagation of sub-terahertz and terahertz electromagnetic waves from the source point to the experiment through such a typical IR beamline is strongly affected by diffraction. This is why we decided to build a dedicated THz beamline with larger optical elements and different transmission windows compared to the IR beamline [6]. First measurements at this new beamline show up to two orders of magnitude more power in the THz range compared to the results at the IR beamline.

In summary, the IR project at the MLS is well under way. The MLS-IR beamline is well adjusted and ready for measurements in the infrared and THz spectral range. The THz beamline and the undulator IR beamline are under commissioning.

[1]   G. Brandt et al., Nucl. Instr. and Meth. B 258, 445 (2007)

[2]   G. Ulm et al., Nucl. Instr. and Meth. A 582, 26 (2007)

[3]   J. Feikes et al., Proc. of EPAC08, 2010 (2008)

[4]   G. Wüstefeld, Proc. of EPAC08, 26 (2008)

[5]   R. Müller et al., Proc. of EPAC08, 2058 (2008)

[6]   R. Müller et al., Infrared Physics & Technology 49, 161 (2006)

In-situ analysis of the Zn(S,O)-buffer layer preparation for chalcopyrite solar cells in the liquid phase using Zn edge X-ray absorption spectroscopy

Iver Lauermann, Timo Kropp, Ahmed Ennaoui, and Emad F. Aziz

Helmholtz-Zentrum Berlin für Materialien und Energie, Berlin, Germany

In chalcopyrite solar cells, a CdS buffer layer is needed between the p-doped absorber and the ZnO window layer. To replace CdS, Zn(S,O) has been introduced as adequate replacement buffer material. However, the chemical bath deposition (CBD) process for depositing Zn(S,O) from an aqueous solution, containing $ZnSO_4$, ammonia, and thiourea ($(NH_2)_2CS$), is not understood in detail.

The LIQUIDROM station at the BESSY II U 41 beamline allows the spectroscopic characterization of liquids and solids under ambient pressure by X-ray absorption spectroscopy (XAS). We used in-situ near edge XAS (NEXAFS) to examine the solution chemistry and to identify the species present in a Zn(S,O) CBD solution at every step of the reaction. Experimental details of the setup for soft X-ray spectroscopy of liquid solutions have been described previously [1].

In Figure 1a (red curve) the Zn L-edge spectrum of Zn^{2+} ions (1M $ZnSO_4$) in pure water is presented. Three main features at 1024.3 eV, 1026.5 eV and 1034.5 eV are visible. These features are due to the transition of electrons from the p-type molecular orbitals (MOs) to the d- and s-type valence MOs localized on the Zn^{2+} ions according to the dipole allowed selection rules [2]. In order to elucidate the nature of the unoccupied MOs, unrestricted Hartree Fock (UHF) calculations were applied to Zn^{2+} with a coordination shell of 6 water molecules. In addition, Tomasi's polarized continuum model (PCM) was used to calculate the effect of the solvent [3]. Although nominally the d-MOs of Zn^{2+} are fully occupied (d10), upon dissolving the ions in water the d- and s-MOs hybridize with the valence MOs of the water molecules and form partially empty MOs, which can be filled by the excited p-electrons upon X-ray absorption. Comparing the XA spectrum of Zn^{2+} ions with the calculated MOs, the local electronic picture of the unoccupied states could be qualitatively drawn in Figure 1.a. The nature of the MOs under the first peak is s-type, the 2nd peak is $d_{xy,\,xz,\,yz}$-type, and the third peak is $d_{x^2-y^2}$, d_{z^2}-type. Upon diluting the $ZnSO_4$ solution to a concentration of 0.15 M (the actual concentration in the CBD solution), the s-type MOs are decreased in intensity relative to the d-type as shown in Figure 1a, black curve. This can be due to the ion-pairing between the Zn^{2+} and SO_4^- which can take place at 1M but is reduced significantly upon dilution to 0.15 M according to our previous investigation. [4]
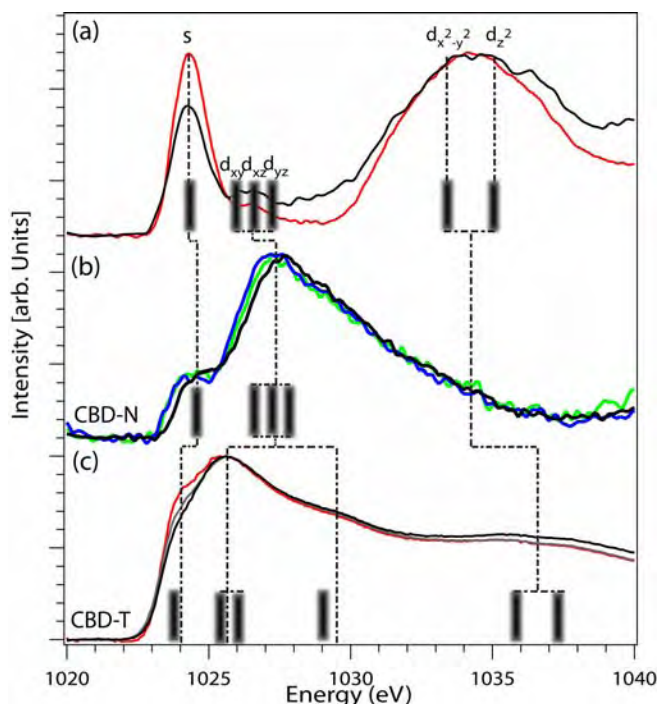
Figure 1. XAS L-edge of Zn in solution, a) Zn^{2+} in water, 1 M (red), and 0.15 M (black). (b) 0.15 M Zn^{2+} in 0.13 M aqueous NH_3 solution (green). Addition of thiourea to a concentration of 0.6 M (blue), followed by heating to 80° C for 3 min, then cooling to room temperature (black curve). (c) 0.15 M Zn^{2+} in 0.6 M aqueous solution of thiourea (red), heated to 80° C (gray). Cooling down to 50° C and addition of NH_3 to yield 0.13 M (black). The dashed vertical lines are presenting the experimental peak shift and splitting. The results of UHF calculations for the energies of the MOs are shown as vertical grey bars for the following models; (a) Zn^{2+} surrounded by 6 H_2O, (b) Zn^{2+} surrounded by 5 H_2O and one NH_3, (c) Zn^{2+} surrounded by 5 H_2O and one molecule of thiourea.

Replacing one water molecule with ammonia in the theoretical model causes the disappearance of the $d_{x^2-y^2}$ and d_z^2 valence MOs as shown in Figure 1b. Furthermore, the s and $d_{xy,\,xz,\,yz}$ valence MOs are shifted to higher energies by approximately 1 eV. This qualitatively explains the change in the experimental spectrum of Zn^{2+} in a solution with added ammonia (0.13 M NH_3), as shown in Figure 1b (green curve). This is due to electron transfer from the ammonia molecule to the empty valence $d_{x^2-y^2}$ and d_z^2 MOs upon complex formation; therefore they are no longer available to receive excited electrons from oxygen p-orbitals upon XA. A second consequence of this complex formation is an increase in the intensity of the valence $d_{xy,\,xz,\,yz}$ relative to the s-MOs. Adding thiourea to the previous solution does not affect the local electronic structure of Zn^{2+} as shown in Figure 1b (blue curve). Heating this solution to 80° C and subsequent cooling to room temperature leads to a shift of the spectrum by 0.3 eV to higher energy as shown in Figure 1b (black curve) but no further change of the overall shape. Thus we conclude that the chemical environment of the Zn^{2+} in the CBD-N remains almost unchanged after addition of thiourea, i.e. it is still surrounded by ammonia molecules and the main interaction is between nitrogen and the zinc ion. However, adding thiourea first to the 0.15 M $ZnSO_4$ solution (as in the CBD-T process) instead of ammonia, leads to a significantly different spectrum as shown in Figure 1c (red curve). The calculated MO energies for Zn^{2+} with 5 water molecules and one molecule of thiourea are in a satisfactory agreement with the experimental XAS peak positions. The optimized model shows that the main interaction between the Zn^{2+} and thiourea is through the C=S group rather than the NH_2-groups of thiourea. This can explain the drastic difference between spectra obtained by the CBD-N method (Figure 1.b) and the CBD-T method (Figure 1.c). Heating this solution to 80° C causes a decrease in the s-valence MOs as shown in Figure 1c (grey curve). Cooling down the solution to 50° C and adding ammonia (to 0.13 M NH_3 as in the actual CBD process) causes a further small decrease in the s-valence MOs intensity compared to the $d_{x^2-y^2}$ and d_z^2

MOs as shown in Figure 1c (black curve). However, the final spectrum obtained from CBD-T is different from the one obtained by CBD-N, where the concentration of all components is identical. The XA spectrum obtained from the final CBD-T process is similar to the XA spectrum of a zinc tris(thiourea) sulphate complex (ZTS) in solution, which was synthesized chemically, crystallised, and re-dissolved in water. In this complex the zinc forms a complex with the thiourea via the sulphur atom [5]. This result confirms further that in the CBD-T process, the complex formation between the zinc and thiourea is via the sulphur atom. Comparing the CBD-N and CBD-T process, one can conclude that in the CBD-N the formation of the zinc thiourea complex is inhibited by the presence of ammonia in solution but that this complex, once formed, as is the case in the CBD-T, is not re-dissolved by ammonia. In both, the CBD-T solution and zinc tris(thiourea) complex in solution, the appearance of the peak corresponding to $d_{x^2-y^2}$ and d_z^2 MOs is due to the back-donation of electrons from the zinc ion to the C=S bond. The electron back donation from metal to ligand results in a decrease of electron density in the MOs localized on the metal, which increases the transition probability of excited p-electrons.

This work clearly shows the chemical background behind the observed differences in solar cell efficiency depending on deposition conditions. Furthermore, it demonstrates the value of the set-up for in-situ examinations of chemical deposition reactions and opens the door for the investigation of further preparation routes to organic and inorganic solar cells. The results described here have been published in [6].

References

1. N. Ottosson, M Henrik Bergersen, Wandared Pokapanich, Gunnar Oehrwall, Svante Svensson, Wolfgang Eberhardt, and Olle Bjoerneholm
2. J. Stöhr, *NEXAFS spectroscopy* (Springer-Verlag, Berlin; New York, 1992).
3. J. Tomasi, M. Persico, *Chem. Rev*. **1994,** *94*, 2027-2094.
4. E.F. Aziz, et al., *J. Phys. Chem. B*, **2007**, 111, 4440-4445.
5. Venkataramanan, M. R. Srinivasan, H. L. Bhat, *J. Raman Spect*., **1994**, 25, 805-811
6. I. Lauermann,T. Kropp, D. Vottier, A. Ennaoui, .E. F. Aziz, *ChemPhysChem*, in print

XAFS study of structural position of Mn impurity in $SrTiO_3$

A.I. Lebedev[1], I.A. Sluchinskaya[1], A. Erko[2]

[1] *Physics Dept., Moscow State University, Moscow, 119992, Russia*
[2] *BESSY GmbH, Albert Einstein Str. 15, 12489 Berlin, Germany*

It has been generally accepted for many years that Mn impurity atoms substitute for Ti sites in as-grown strontium titanate and are there in Mn^{4+} oxidation state [1]. Annealing in reduced atmosphere could transform Mn ions into lower oxidation states (Mn^{3+}, Mn^{2+}) [2]. Recently Lemanov et al. [3] revealed unusually strong dielectric relaxations in Mn-doped $SrTiO_3$ at low temperatures. These relaxations were explained by a model, in which Mn^{2+} ion at the Ti site form a defect of $\{Mn_{Ti}^{2+}\text{-}O^-\}$ type. Later the other group of authors [4-8] found the conditions, in which the Mn impurity can be incorporated into the Sr sites and stay there in Mn^{2+} oxidation state. In such samples all unusual dielectric phenomena were observed; in samples with Mn atoms located at the Ti sites these phenomena were absent. To explain dielectric properties of Mn-doped samples these authors proposed that Mn^{2+} ions located at Sr sites are off-centre [6].

The purpose of this work was to study the local environment of Mn impurity atoms in $SrTiO_3$ prepared in different conditions to determine directly their structural position.

Two samples with a nominal composition of $(Sr_{0.97}Mn_{0.03})TiO_3$ and $Sr(Ti_{0.97}Mn_{0.03})O_3$ were prepared by solid-state reaction from $SrCO_3$, nanocrystalline TiO_2 and $Mn(CH_3COO)_2 \cdot 4H_2O$. Reagents were weighed in necessary proportions, grinded and annealed in air at 1100°C for 8 h. The intermediates were grinded again and annealed finally in the same conditions. One of the samples was additionally annealed in air at 1500°C for 1 h.

X-ray absorption spectra were collected in fluorescent mode at the Mn K edge (6.539 keV) on the station KMC-2. The intensity of monochromated radiation was measured with an ionisation chamber; the intensity of fluorescent radiation was measured by an energy-dispersive RÖNTEC detector. For each sample 5–6 spectra were recorded at 300 K, they were then independently processed and the obtained spectra were finally averaged. The EXAFS data analysis was performed in the traditional way using the models that assume on-centre and off-centre positions of Mn atoms at Sr and Ti sites.

EXAFS spectra for $Sr(Ti_{0.97}Mn_{0.03})O_3$ sample annealed at 1100°C and for $(Sr_{0.97}Mn_{0.03})TiO_3$ sample annealed at 1500°C are shown in Fig. 1. The conditions of preparation of these samples enable us to assume that Mn impurities enter into different sites and are in different oxidation states. The analysis of EXAFS spectra for $Sr(Ti_{0.97}Mn_{0.03})O_3$ sample annealed at 1100°C showed that the spectra are well described by a model, in which Mn atoms enter the Ti sites (see Table). To get a good agreement between experimental and calculated spectra (Fig. 1a) it was necessary to take into account two additional multiple scattering paths: Mn-O-O-Mn and Mn-Ti-O-Mn.

The analysis of EXAFS spectra for $(Sr_{0.97}Mn_{0.03})TiO_3$ sample annealed at 1500°C appeared more difficult. These spectra could not be described within the model with on-centre Mn atom at Sr site. Good agreement between experimental and calculated EXAFS spectra (Fig. 1b) was obtained only for the model, in which there are two distances between Mn and Ti atoms in the second shell (3.095 and 3.467 Å). The contribution from the oxygen atoms in the first shell is characterised by a large Debye-Waller factor, thus giving evidence for a wide dispersion of Mn–O distances in this shell. The "local" lattice parameter (3.78 Å) and displacement of Mn atom from the Sr site (0.32 Å) were estimated from the two Mn-Ti distances given above. Small deviation of the "local" lattice parameter from that obtained from X-ray diffraction (3.90 Å) can be explained by the lattice relaxation around the Mn atom, the size of which is smaller than that of Ti one.
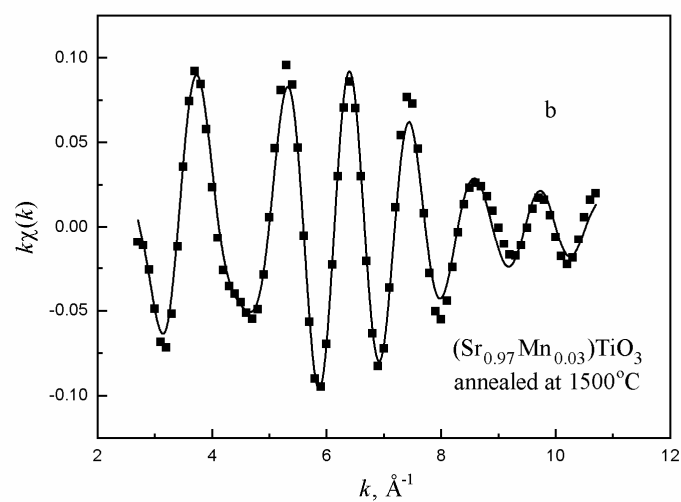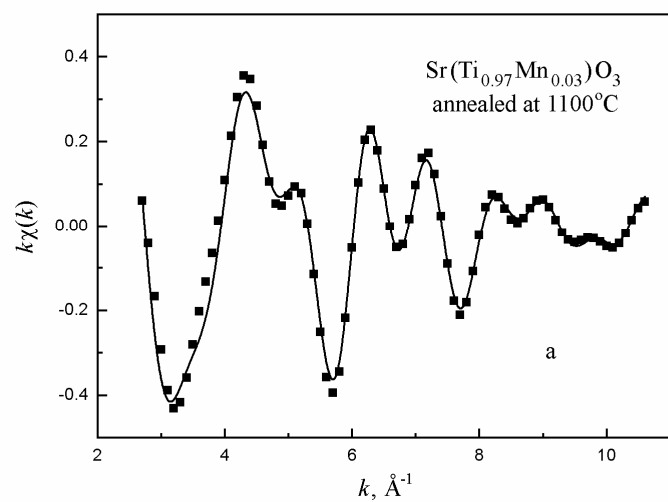
Fig. 1. EXAFS spectra for two Mn-doped $SrTiO_3$ samples. Squares are experimental points, solid lines are their best fit.
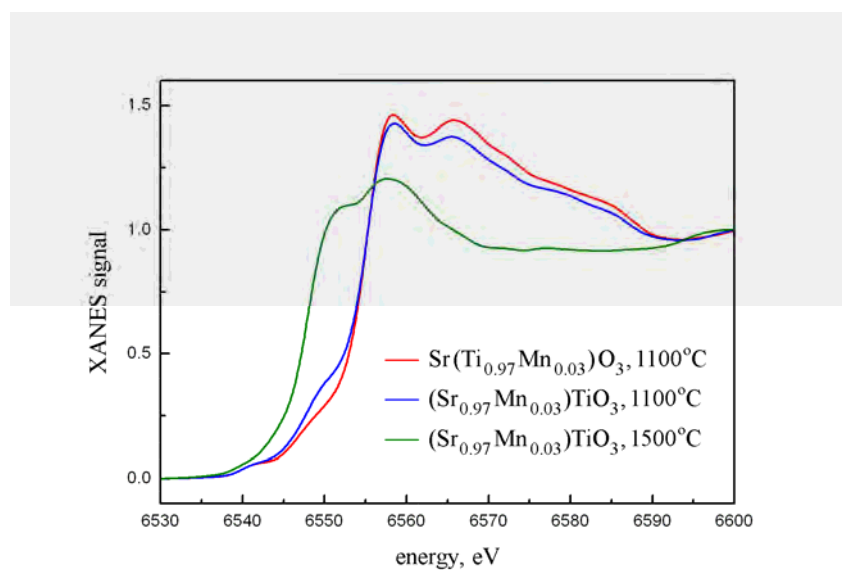
Fig. 2. XANES spectra for three Mn-doped $SrTiO_3$ samples recorded at the Mn K edge.

Table. Structural parameters obtained from the EXAFS data analysis for three samples.

Sample	Shell	R_i, Å	σ^2_i, Å^2	Atom
Sr(Ti$_{0.97}$Mn$_{0.03}$)O$_3$, 1100°C	1	1.916	0.002	O
	2	3.313	0.001	Sr
	3	3.67	−0.006	Ti
(Sr$_{0.97}$Mn$_{0.03}$)TiO$_3$, 1100°C	1	1.914	0.002	O
	2	3.38	0.002	Sr
	3	3.70	−0.004	Ti
(Sr$_{0.97}$Mn$_{0.03}$)TiO$_3$, 1500°C	1	2.32; 2.86	0.031	O
	2	3.095; 3.467	0.008	Ti
	3	3.84	0.014	Sr

XANES region of the X-ray absorption spectra for Mn-doped samples are shown in Fig. 2. Their comparison shows that absorption edges for (Sr$_{0.97}$Mn$_{0.03}$)TiO$_3$ sample annealed at 1500˚C and for Sr(Ti$_{0.97}$Mn$_{0.03}$)O$_3$ one are shifted by ~7 eV. This proves that Mn atoms in these two samples not only occupy two different crystallographic positions, but also are in two different oxidation states. The absorption edge energy for the sample, in which Mn is at the Sr site, is lower than for the sample, in which it is at the Ti site. This means that the Mn atom at the Sr site has lower oxidation state. Comparison of the observed shift with that obtained in [9] between Mn^{2+} and Mn^{4+} oxidation states (7.9 eV) enable to suppose that the oxidation states of Mn atoms in SrTiO$_3$ are +2 for the Sr site and +4 for the Ti site.

XANES spectrum for (Sr$_{0.97}$Mn$_{0.03}$)TiO$_3$ sample annealed at 1100°C (Fig. 2) can be regarded as a superposition of XANES spectra for two samples, for which the EXAFS analysis was made. This means that Mn in this sample is present in both oxidation states, and so actually one can speak only about predominant incorporation of Mn impurity in this or that site of the lattice.

From the presented results it follows that from two models proposed for an explanation of unusual dielectric phenomena in Mn-doped SrTiO$_3$ samples, the model with off-centre Mn$_{Sr}^{2+}$ ion seems to be more adequate. Future systematic investigations are needed to study the effect of the preparation conditions on crystallographic positions of Mn in SrTiO$_3$ and to develop a method of quantitative determination of Mn concentration and its oxidation state at different sites.

References
[1] K.A. Müller. Phys. Rev. Lett. **2**, 341 (1959).
[2] R.A. Serway, W. Berlinger, K.A. Müller, R.W. Collins. Phys. Rev. B **16**, 4761 (1977).
[3] V.V. Lemanov, E.P. Smirnova, A.V. Sotnikov, M. Weihnacht. Phys. Solid State **46**, 1442 (2004).
[4] A. Tkach, P.M. Vilarinho, A.L. Kholkin. Acta Mater. **53**, 5061 (2005).
[5] A. Tkach, P.M. Vilarinho, A.L. Kholkin. Ferroelectrics **304**, 87 (2004).
[6] A. Tkach, P.M. Vilarinho, A.L. Kholkin. Appl. Phys. Lett. **86**, 172902 (2005).
[7] A. Tkach, P.M. Vilarinho, A.L. Kholkin. Acta Mater. **54**, 5385 (2006).
[8] A. Tkach, P.M. Vilarinho, A.L. Kholkin, A. Pashkin, S. Veljko, J. Petzelt. Phys. Rev. B **73**, 104113 (2006).
[9] A. Hagen, L. Mikkelsen. In: *Solid State Electrochemistry* (Proceedings of the 26th Risø Int. Symp. on Materials Science), Risø National Laboratory, Roskilde, Denmark, p. 197 (2005).

In-situ XPS study of adsorbed oxygen species on (La,Ba,Sr)(Fe,Co)O_{3-d} perovskites

Rotraut Merkle, Joachim Maier

Max-Planck-Institut für Festkörperforschung, Stuttgart

Introduction

Mixed conducting perovskites are used as cathode materials in Solid Oxide Fuel Cells (SOFC). In order to elucidate the mechanism of the oxygen incorporation, we performed impedance spectroscopy on well-defined dense microelectrodes [1]. These experiments are complemented by DFT calculations [2]. Knowledge about the type of adsorbed oxygen species (superoxide O_2^- or peroxide O_2^{2-}, or atomic charged adsorbate species O^-) and their concentration is important for a mechanistic understanding of the oxygen incorporation reaction into these materials.

To examine such oxygen adsorbates, the samples have to be studied by XPS under a certain oxygen pressure (typically up to 1 mbar) which required the use of synchrotron radiation. The variation of sample temperature 300-600°C, pO_2, $p(H_2O)$, as well as depth resolution is important for a reliable assignment of the observed peaks. The oxygen adsorbate coverages are expected to be rather small because of their negative charge (buildup of a surface dipole layer) [3], but dependent on applied DC bias.

(La,Ba,Sr)(Fe,Co)O_{3-d} dense thin films were prepared by pulsed laser deposition on YSZ oxide-ion conducting substrates and equipped with a counter electrode so that an electrical current can be drawn through the film corresponding to a steady flux of oxygen incorporated into or generated at the film surface. Thus fuel cell operation can be mimicked and adsorbate concentrations can possibly be modified by the applied electrical bias [3].

Results
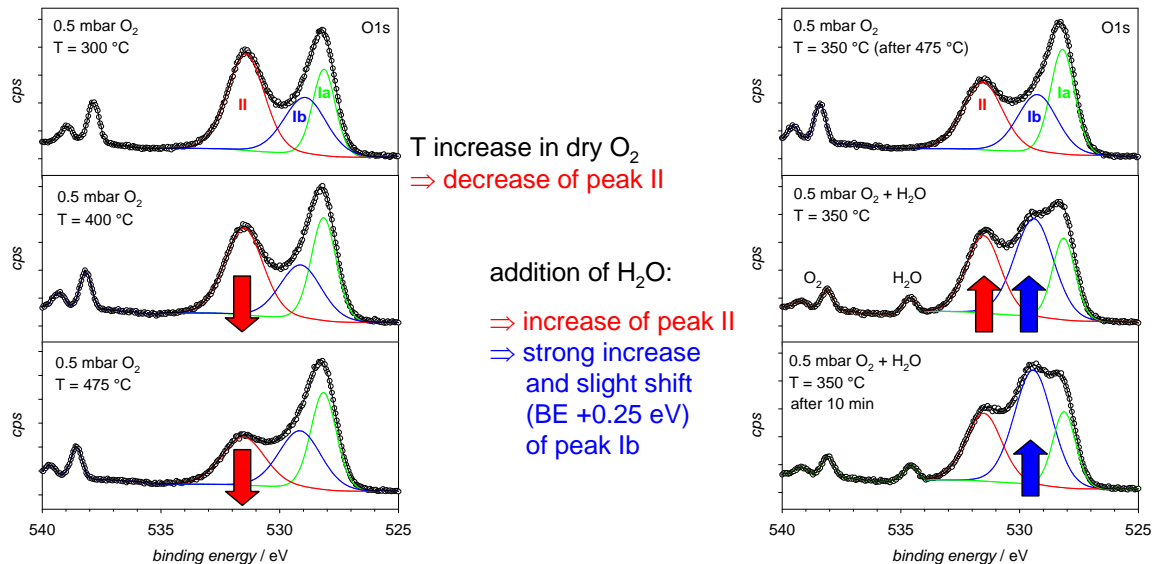
Figure 1: In-situ XPS of dense $La_{0.6}Sr_{0.4}CoO_{3-d}$ "LSC" films at different temperatures and under applied gas pressure (pO_2, $p(H_2O)$).

As exemplified in Fig.1 for LSC, the O1s region typically contains at least two peaks: II at high BE and Ia+Ib at lower BE. Peak II decreases on increasing temperature, and can at least partially be restored by H_2O exposure. During hydratation, also peak Ib seems to increase, but its BE-shift indicates that a new component develops. Based on binding energy, T- and $p(H_2O)$-dependence, peak II and the new component close to Ib are now assigned to OH^-. Depth-resolved spectra (not shown here) indicate that oxygen peak II is surface-related. They also indicate that the surface region is depleted in La^{3+} and enriched in Sr^{2+}. The lower

average cation charge in the Sr-rich surface layer can at least partially be compensated by the presence of H$^+$ in the hydroxide groups.
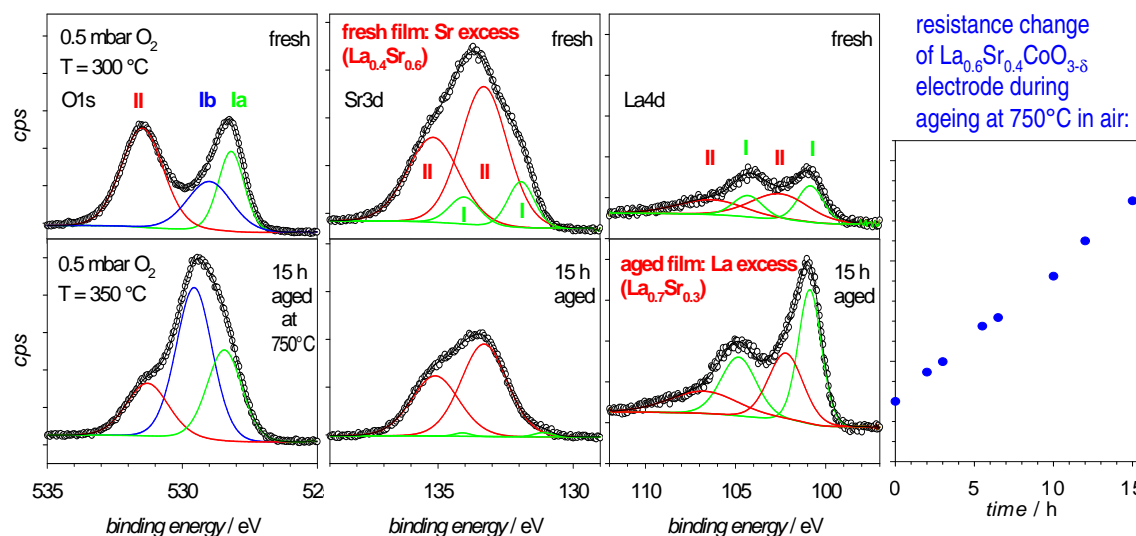
Figure 2: In-situ XPS of freshly prepared and aged (15 h at 750 °C) dense La$_{0.6}$Sr$_{0.4}$CoO$_{3-d}$ films (E$_{kin}$ = 200 eV). Right: evolution of La$_{0.6}$Sr$_{0.4}$CoO$_{3-d}$ electrode resistance during ageing.

Fig. 2 demonstrates the effect of thermal ageing on the film properties. The aged film surface (E$_{kin}$ = 200 eV = 0.7 nm depth) not only shows a different oxygen peak shape, but also a decrease of Sr and increase of La compared to the fresh film (quantitative analysis of cation ratios is in progress). The right panel shows the significant increase of the electrode resistance (which is determined by the oxygen incorporation rate at the LSC film surface) during the 15 h ageing time. Since the oxygen incorporation reaction is sensitive to the material's composition and defect concentrations directly at the surface, this increase must be interrelated to the observed cation redistribution.

Measurements under applied electrical current (which is expected to increase adsorbate concentrations, especially under anodic conditions when oxygen is generated at the perovskite surface) were also performed, but the samle design still requires improvements. A large temperature gradient between backside counter electrode and frontside working electrode (LSC film) repeatedly lead to contact loss. Thus, so far no peak was detected that can explicitly be assigned to adsorbed oxygen species.

Summary and Outlook
The presence of significant amounts of OH$^-$ even at 500 °C and its accumulation close to the surface rise the question of proton involvement in the oxygen incorporation reaction (formation of HO$_2^-$ etc.). This motivates further electrochemical measurements of oxygen reaction kinetics under varying p(H$_2$O). The different surface cation compositions in fresh and aged films will help to understand the frequently observed performance decrease of these electrode materials after prolonged heating. To overcome the contact problem in the DC current measurements, a new sample design with both electrodes on the frontside will be used in the next beamtime. Then the measurements are expected either to yield evidence for molecular oxygen adsorbates, or - if not - to give an upper limit for their concentration.

References:
[1] F. S. Baumann, J. Fleig, H.-U. Habermeier, J. Maier, Solid State Ionics 177 (2006) 1071
[2] E. A. Kotomin, Y. A. Mastrikov, E. Heifets, R. Merkle, J. Fleig, J. Maier, A. Gordon, J. Felsteiner, ECS Transactions 13 (2008) 301
[3] J. Fleig, Phys. Chem. Chem. Phys. 7 (2005) 2027; J. Fleig, R. Merkle, Phys. Chem. Chem. Phys. 9 (2007) 2713

In-situ X-Ray Diffraction Study of the Influence of Sulphur on Phase Formation during the Heat-Treatment of Porphyrin-based Oxygen Reduction Catalysts

U.I. Kramm[1], G. Zehl[1], I. Zizak[2], I. Herrmann[1], I. Dorbandt[1], P. Bogdanoff[1], S. Fiechter[1]

Helmholtz-Zentrum Berlin für Materialien und Energie (HZB)
[1] Lise-Meitner-Campus Wannsee, Glienicker Str. 100, D-14109 Berlin
[2] Conrad-Röntgen-Campus Adlershof, Albert-Einstein-Str. 15, D-12489 Berlin

1. Introduction

During the last decades polymer electrolyte membrane fuel cells (PEM-FC) have been optimized using platinum based catalysts. However, platinum is scarce and expensive. Hence, catalyst costs have a significant impact on the market price of fuel cell units. Therefore, the continuously growing Pt price is impeding the production of less expensive PEM fuel cells and protracting the commercial breakthrough of this technology. Thus, there is a soaring interest in the development of materials with reduced amounts of noble metals and, most promising, of Pt free oxygen reduction catalysts.

It is known for decades that metal chelates can be used as catalysts for the oxygen reduction reaction (ORR) [1]. Using rotating disc electrode (RDE) measurements it has been shown recently, that heat-treated N_4-metallomacrocycles reveal catalytic activities at 0.75 V even comparable to commercial Pt/C catalysts [2]. Henceforth, they are seriously considered as promising noble metal free alternatives to Pt based catalysts.

 However, the pyrolysis of metal-chelate compounds as a necessary preparation step leads to glassy carbon like carbonization products and only a small number of catalytic centres can participate in the ORR. Therefore, current preparation approaches are aimed to increase this side density. To prevent sintering effect, carbon blacks were impregnated with the metal chelates followed by a heat-treatment at temperatures of $\geq 700°C$ in an inert atmosphere. This preparation approach, however, is only suited for low amounts of metal chelate due to the limited support capacity of carbon black. Above a critical loading the excess chelate will sinter as in the case without additional carbon support, leading to similar activity losses. Therefore, using impregnation techniques the catalytic activity cannot be raised beyond a certain level because the catalysts will always be diluted by a specific amount of the auxiliary carbon [3,4].

To overcome this limitation the so called foaming agent technique was developed at the Helmholtz-Zentrum Berlin which works without the addition of auxiliary carbon [2,5,6]. Porphyrins are pyrolysed in the presence of iron-oxalate (and sulphur). The oxalate decomposes under release of CO and CO_2. Simultaneously the porphyrin melts and carbonizes; therefore, the gaseous products cause a foaming effect to the in-situ forming carbon matrix. After the inert heating step is completed the product is allowed to cool down. Finally, a leaching process is applied to remove inorganic by-products. It was found that the addition of sulphur leads to higher catalytic activity towards the oxygen reduction and to a more complete removal of catalytically inactive inorganic metal constituents [2]. To get a better understanding of the role of sulphur during pyrolysis, the heat-treatment process of the porphyrin/Fe oxalate and the porphyrin/Fe oxalate/sulphur catalyst precursors (with optimized sulphur content) was investigated by *in-situ* high temperature X-ray diffraction analysis (HT-XRD).

2. Experimental

In-situ X-ray diffraction measurements were performed at BESSY II beamline KMC-2 using a stainless steel reaction chamber with Kapton® windows at the beam entry and exit slits and equipped with an electric graphite heater encapsulated in pyrolytic boron nitride (pBN) from Tectra GmbH. This newly developed reaction chamber allows measurements under constant Ar gas flow at reduced pressures in a temperature range from RT to 800°C. A two dimensional detector array (HiStar – Bruker AXS) was used to record the spectra. Detector, sample and synchrotron radiation beam were aligned to meet Bragg-Brentano geometry. Measurements were carried out under Ar flow of 200 ml/min at reduced pressure of $p = 400$ mbar with synchrotron radiation energy of 8.731 keV. Calibration of the system was done using an alumina standard for the used beam energy.

A detailed description of the catalyst preparation is given elsewhere [7]. Briefly, an amount of 1.3 mmol FeTMPPCl is mixed with 28.6 mmol iron oxalate dihydrate in a mortar until a homogeneous precursor mixture is obtained. For the preparation of sulphur containing precursor mixture 1.2 mmol sulphur (S_8) are

grounded previously before mixing with oxalate and porphyrin. The powders of the precursor mixtures were pelletized (Ø: 10 mm) and placed onto a pBN sample holder.

3. Results

A detailed description of the chemical processes involved in the foaming agent technique can be found elsewhere based on the results of TG-MS measurements [2,5,6]. As described above, our Foaming Agent Technique (FAT) enables the preparation of a highly porous carbon structure with embedded catalytic centres. As already published for the CoTMPP system (plus Fe oxalate dihydrate and sulphur) [7], also for FeTMPPCl and for H_2TMPP the kinetic current densities in RDE measurements were found to increase by one order of magnitude compared to the sulphur free catalysts, and hydrogen peroxide formation is decreased to less then 5 %. In RRDE measurements sulphur containing catalysts reveal a catalytic activity towards ORR in the same order of magnitude as commercial Pt/C catalysts. Beside this, the method allows us to achieve the fourfold of catalytic site density compared to similar non noble metal catalysts [8]. However, for further optimization it is essential to understand in which way the sulphur affects the pyrolysis of Foaming Agent catalysts. Therefore, the applied temperature range and the involved phase transformations have to be determined and differences compared to the sulphur free precursor should be compiled.

Our newly developed *in-situ* HT-XRD cell allows measurement conditions comparable to the processes involved in the standard catalyst preparation. In Figure 1 the HT-XRD measurement of sulphur free (a) and sulphur containing (b) precursor mixtures are shown in a temperature range from RT to 800°C.
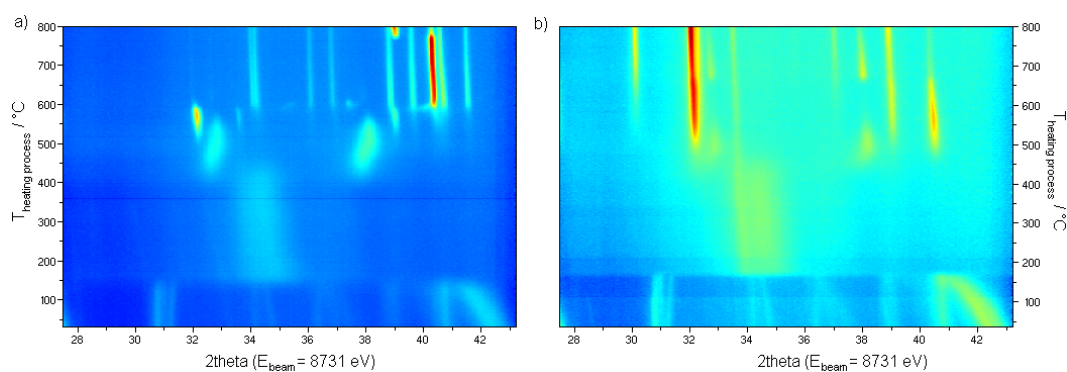
Figure 1: HT-XRD measurements of porphyrin/Fe oxalate precursors heat-treated without (a) and with the addition of sulphur.

Figure 1 clearly demonstrates that above temperatures of approx. 350°C the processes involved during heat-treatment start to differ. To investigate this in more detail the spectra for selected heat-treatment temperatures were extracted and plotted against 2theta (as calculated for Cu K_α wave length) in Figure 2. To improve the signal to noise ratio the average of 10 consecutive measurements around the designated temperature was used. Due to the continued heating-up the error in temperature is slightly increased but still restricted to ≤ 5 °C.

The room temperature spectra of both precursor mixtures are dominated by the reflexes related to iron oxalate dihydrate whereas the porphyrin (and sulphur) did not contribute to the spectra. This can be explained by the much higher amount of oxalate compared to porphyrin (and sulphur). As confirmed by HT-XRD and TG-MS earlier, the oxalate releases its crystal water within T-range from 140 °C to 190 °C (e.g. Ref. 5). Up to 350 °C, diffractograms remain similar, independently of the precursor mixture. Above this temperature structural changes are different for both precursors.

Analysing first the heat treatment process of the sulphur free precursor (Fig. 2a) formation of Wuestite and Hematite can be followed in the temperature range from 435 °C to 545 °C. In parallel to a second decomposition step these oxides are reduced to a Cohenite modification, whereas above 700 °C a high-temperature phase of iron carbide is visible. This high-temperature phase, however, transforms back into Cohenite or into elemental iron and graphite during the subsequent cooling process.

In contrast, the addition of sulphur (Fig. 2b) affects spectra exhibiting amorphous behaviour in a temperature range between 435 °C to 545 °C. At this temperature also Wuestite can be detected but beside this there is another phase with a main reflex at 2theta = 44.4° that might be related to an iron carbide phase. Above 545 °C this signal is decreasing and spectra of the sulphur added sample are mainly amorphous depicted in much smaller intensities of the present reflexes (Hematite and Magnetite).

Taking into account the findings of Grabke et al. [9] it is likely that at temperatures > 435 °C the sulphur is firmly bonded to iron, surpressing a further formation of iron carbide. Indeed, also our results of HT-XRD measurements evidence this effect. Above 600 °C the amount of iron carbide is reduced. Therefore, an amorphous carbon structure is formed that was found to enhance the catalytic properties.
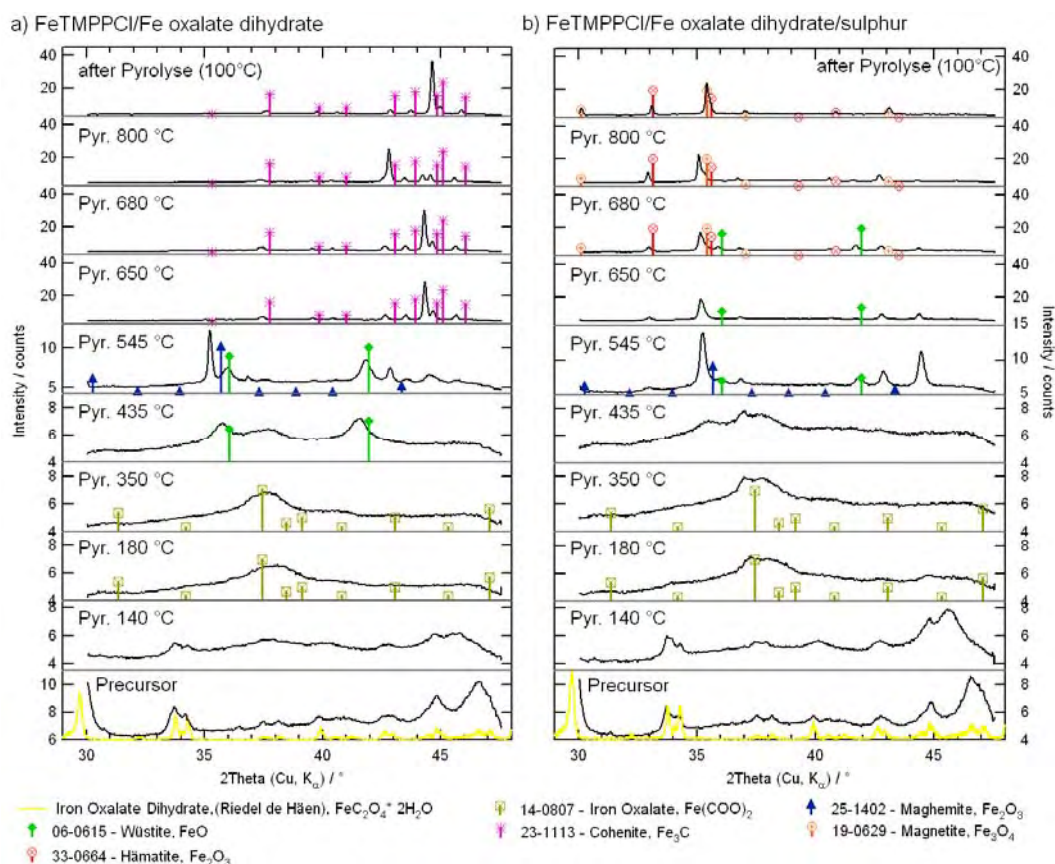
Figure 2: X-ray diffractograms of porphyrin/Fe oxalate precursors heat treated without (a) and after addition of sulphur.

4. Conclusions and outlook

The use of an improved reaction chamber for *in-situ* HT-XRD investigation under gas flow conditions allowed the study of processes involved in activation of porphyrin-type oxygen reduction catalysts under standard preparation conditions. The comparison of sulphur free and sulphur containing precursors let us conclude that the effect of "iron blocking" by sulphur preventing the formation of iron carbides starts at temperatures of 435 °C. This effect significantly enhances activity of Pt-free oxygen reduction catalysts. It was monitored for the first time by *in-situ* HT-XRD analysis. Further work is planned to investigate the pyrolysis processes of precursors using cheaper starting materials.

5. References

(1) Jahnke, H.; Schönborn, M.; Zimmermann, G. *Topics in Current Chemistry* **1976**, *61*, 133.
(2) Herrmann, I.; Koslowski, U.; Radnik, J.; Bogdanoff, P.; Fiechter, S. *ECS Trans.* **2008**, *13*, 145.
(3) Bouwkamp-Wijnoltz, A. L.; Visscher, W.; Veen, J. A. R. v. *Electrochimica Acta* **1998**, *43*, 3141.
(4) Herrmann, I. Entwicklung und Optimierung neuer Präparationsverfahren für Übergangsmetall-basierte Elektrokatalysatoren für die Sauerstoffreduktion. Doktorarbeit, Freie Universität Berlin, 2005.
(5) Bogdanoff, P.; Herrmann, I.; Hilgendorff, M.; Dorbandt, I.; Fiechter, S.; Tributsch, H. *J. New. Mat. Electrochem. Systems* **2004**, *7*, 85.
(6) Herrmann, I.; Bogdanoff, P.; Schmithals, G.; Fiechter, S. *ECS Trans.* **2006**, *3*, 211.
(7) Koslowski, U.; Herrmann, I.; Bogdanoff, P.; Barkschat, C.; Fiechter, S.; Iwata, N.; Takahashi, H.; Nishikoro, H.; Abs-Wurmbach, I. *ECS Trans.* **2008**, *13*, 125.
(8) Koslowski, U.; Abs-Wurmbach, I.; Fiechter, S.; Bogdanoff, P. *J. Phys. Chem. C* **2008**, *112*, 15356
(9) Grabke, H. J.; Moszynski, D.; Müller-Lorenz, E. M.; Schneider, A. *Surface and Interface Analysis* **2002**, *34*, 369.

Interaction of CO_2 with thin nickel oxide layers on Cu(111)

M. P. A. Lorenz, R. Streber, M.-M. Walz, A. Bayer, and H.-P. Steinrück

Lehrstuhl für Physikalische Chemie II,
Universität Erlangen-Nürnberg, Egerlandstraße 3,91058 Erlangen

Nickel oxide is an important material for optical storage media and in heterogeneous catalysis. However, under ambient conditions, impurities such as carbonates can easily be formed by reaction with CO_2. Behm and Brundle [1] for instance reported the formation of a carbonate layer on Ni(100) by simultaneously dosing molecular oxygen and CO_2. As the catalytic activity of nickel oxide could be strongly influenced by the formation of carbonate, we studied the interaction of CO_2 with thin NiO layers on Cu(111) by high resolution XPS applying synchrotron radiation. Cu(111) acts as inert substrate for the growth of NiO layers with defined thickness. The experiments were performed at beamline U49/2-PGM1, using a transportable apparatus described elsewhere [2].

To form NiO, first the appropriate amount of nickel was evaporated onto the Cu(111) surface at 120 K, followed by heating to 300 K to produce flat Ni films [3]. Subsequently, the Ni films were completely oxidised by dosing 120 L of molecular oxygen at 300 K, followed by flashing to 500 K. As result, no metallic component could be detected in the Ni 2p XP spectra (data not shown).
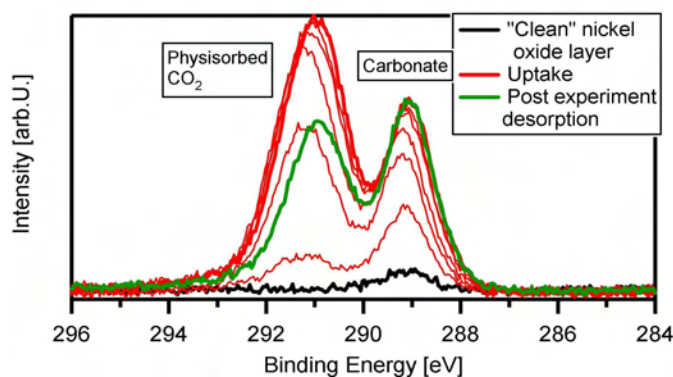
Figure 1: Series of C 1s XP spectra while dosing CO_2 onto 2 ML NiO/Cu(111) at 110 K; carbonate saturation coverage: 0.14 ML.

Figure 1 shows a series of C 1s XP spectra, recorded while dosing CO_2 onto 2 ML NiO/Cu(111) at 110 K. Two characteristic peaks arise at binding energies of 289.0 and 291.1 eV, with the former attributed to carbonate according to Behm and Brundle [1]. Its thermal stability (see Figure 2) rules out a weakly bonded physisorbed species. The other peak at 291.1 eV is assigned to physisorbed CO_2; its intensity is drastically reduced, when decreasing the CO_2 partial pressure (green spectrum). The corresponding O 1s binding energies are 531.6 eV (carbonate) and 534.8 eV (physisorbed CO_2) (Figure 2 b).

Subsequently, we also studied the thermal evolution of the carbonate layers during heating to elevated temperatures, by recording C 1s and O 1s XP spectra. As can be seen in Figure 2 a (C 1s) and 2 b (O 1s), the components at binding energies of 291.1 and 534.8 eV disappear completely up to 200 K, due to desorption, further confirming their assignment to physisorbed CO_2. In contrast, the component attributed to carbonate is thermally much more stable, although its intensity decreases continuously with increasing temperature. But even at 500 K, a temperature range, where NiO already starts to decompose, small amounts of carbonate are still left on the surface. Therefore it is not possible to clean NiO layers, which were contaminated by carbonate (formed from e.g. CO_2 from the residual gas) by simply heating to elevated temperatures.
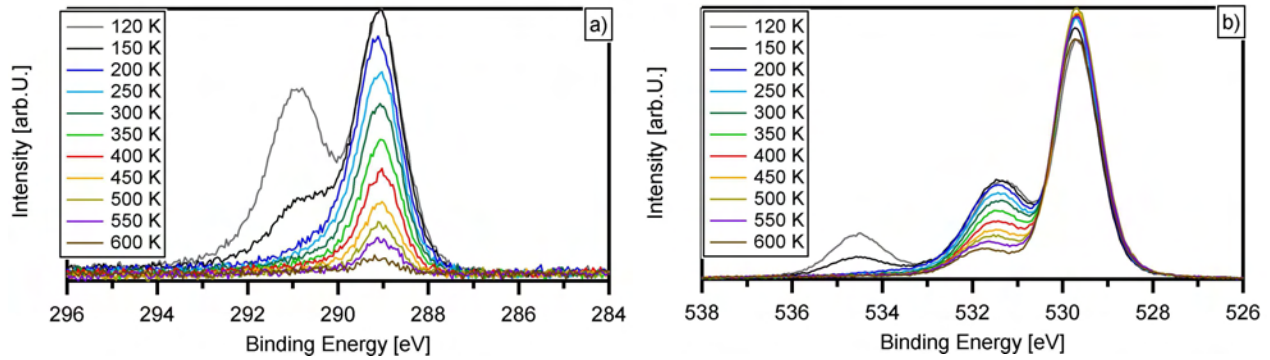
Figure 2: Selected a) C 1s and b) O 1s XP spectra of CO_2 and carbonate adsorbed on 2 ML NiO/Cu(111) recorded during heating to denoted temperatures.
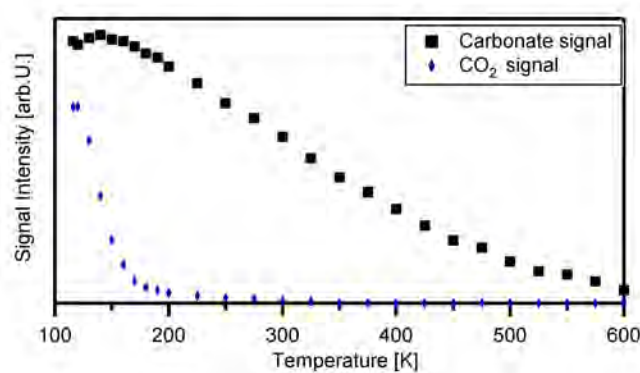
Figure 3: Quantitative analysis of C 1s XP spectra of CO_2 and carbonate adsorbed on 2 ML NiO/Cu(111) during heating.

The quantitative analysis of the C 1s data (Figure 3) clearly shows a nearly linear decay of the carbonate coverage with raising temperature. Note that the increase of the carbonate coverage for temperatures below 150 K is either caused by further formation of carbonate from CO_2 and surface O and/or by reduced damping as consequence of desorbing CO_2 in this temperature regime. The analysis of the O1s data (not shown) shows an overall similar behaviour. Interestingly, at 600 K the O 1s peak assigned to carbonate (not shown) shows still ~25 % of its original intensity, whereas the corresponding C 1s intensity in Fig. 3 has vanished. A possible explanation for this apparent excess of "carbonate" in the O 1s data could be the simultaneous formation of hydroxyl groups. It is known [4] that NiO surfaces are very reactive towards water, e.g., from residual gas, forming Nickel hydroxide. Dosing water onto NiO layers on Cu(111) indeed lead to the formation of NiOH, with the corresponding O 1s peak at the same binding energy (~531.6 eV) than that for the carbonate (data not shown).

[1] R. J. Behm, C. R. Brundle, Surf. Sci. 255 (1991) 327

[2] R. Denecke, M. Kinne, C. M. Whelan, H.-.P. Steinrück, Surf. Rev. Lett. 9 (2002) 797.

[3] R. Domnick, G. Held, H. Koschel, Ch. Ammon, H.-P. Steinrück, Surf. Sci. 482-485 (2001) 1292

[4] N. Kitakatsu, V. Maurice, C. Hinnen, P. Marcus, Surf. Sci. 407 (1998), 36-58

Propylene oxidation over palladium: *Operando* XPS-MS study

Vasily V. Kaichev[1], Andrey V. Matveev[1], Vladimir V. Gorodetskii[1], Valerii I. Bukhtiyarov[1], Bernard E. Nieuwenhuys[2]

[1]Boreskov Institute of Catalysis of SB RAS, Novosibirsk, Russia, E-mail: vvk@catalysis.ru
[2]Leiden Institute of Chemistry, Leiden, the Netherlands

Palladium is well known as the most active catalyst in a number of key industrial processes such as the total oxidation of hydrocarbons in automotive exhausts, the natural gas combustion in gas-powered turbines, as well as selective hydrogenation of alkynes to alkenes. Its practical importance has stimulated a vast amount of works devoted to the study of adsorption, oxidation and hydrogenation of hydrocarbons over palladium. To date, most of the works was performed at high pressure under realistic catalytic conditions by monitoring the reaction products in the gas phase. Unfortunately, this approach has difficulty in unraveling the details of the reaction mechanisms that are very important for the purposeful synthesis or improvement of catalysts. Other studies were carried out under UHV conditions by surface science techniques. Certainly, these UHV studies significantly developed our understanding of the mechanisms for different catalytic reactions, however, the questions about the state of the active catalyst, as well as the reasons for catalyst activation and deactivation, remain very often under discussion. Indeed, the active state of a catalyst exists only during the catalysis and can «die» in UHV. For investigation of really «living» catalysts, different spectroscopic techniques must be applied at elevated pressure *in situ, i.e.,* while the catalysis takes place [1,2]. Moreover, it is essential to combine the spectroscopic characterization of a catalyst surface with simultaneous monitoring of its catalytic performance. In the last several years, such an approach is usually called as *operando*. Here we demonstrate how the application of the *operando* techniques can be used to provide additional insight into the mechanism for heterogeneous catalytic reactions.

The aim of our work was to elucidate the mechanism of activation and deactivation of Pd surface in the propylene oxidation. Pd is chosen as a highly active metal, used in three-way catalysts for utilization of the tailing gases. Propylene is a good model unsaturated hydrocarbon, which can be easily studied by surface science methods. We use a combination of *in situ* X-ray photoelectron spectroscopy and mass-spectrometry. XPS is one of the powerful tools to investigate both the surface composition and the nature of adsorbed species. When *in situ* XPS is coupled with mass-spectrometry, it becomes a particularly effective *operando* technique, which makes it possible to correlate surface properties with the catalytic performance. The experiments were performed at the ISISS beam line at BESSY in Berlin. The construction of this setup was described in detail elsewhere [2]. A differentially pumped system of electrostatic lens is the key feature of this setup, which allows investigation of the

1

catalytic reactions *in situ* in the mbar pressure range. The gas-phase analysis was carried out using a quadruple mass-spectrometer connected through a leak valve to the experimental cell. A Pd(551) single crystal was used as a catalyst. It was mounted onto a sapphire sample holder with a SiC plate heated from the back with a NIR laser. The main advantage of this heating method is the absence of any hot details, which may have a high catalytic activity. The sample temperature was monitored with a chromel-alumel thermocouple spot-welded directly to the crystal edge. The partial pressure of propylene during the experiments was 5×10^{-4} mbar, the propylene/oxygen ratio was 1:1, 1:10, and 1:100.

The reaction was studied using the temperature-programmed-reaction (TPR) techniques based on mass-spectrometric analysis of the gas phase during heating and subsequent cooling with the constant rate of 1 K/s in the range between 100 and 500ºC. The TPR results show a very complex kinetic behavior of this reaction. In all cases, the main reaction products were CO_2 and water. Fig. 1 shows the CO_2 yield during the complete heating/cooling cycle as a function of the sample temperature for the different propylene/oxygen ratios. One can see at least three temperature hysteresis loops in the TPR curves. The most pronounced hysteresis loop was observed at low temperature. For example, during a heating ramp, the activity in propylene oxidation sharply increases at 285, 230 and 210ºC, for the propylene/oxygen ratio 1:1, 1:10, 1:100 correspondingly, whereas a quick decrease in the activity is observed at 150-160ºC during the subsequent cooling ramp. Two other hysteresis loops appear in the oxygen excess. Certainly, such dynamic behavior is determined by strong change in the surface composition. It is well-known that depending on reaction temperature, pressure and hydrocarbon/oxygen feed, palladium surface can be covered with oxide, carbon or hydrate layers. In order to determined the reason, which causes the first hysteresis loop, we recorded under the same conditions the C1s, O1s, and Pd3d core-level spectra during stepwise heating from 100 to 250, 300, 400, and 500ºC and during the following cooling in the same manner. All the experiments showed consistent results, and therefore only the C1s spectra obtained in the equimolar propylene/oxygen mixture are presented bellow.

The C1s spectrum obtained at 100ºC consists of at least 5 marked features. A small peak at 285.7 eV is due to CO, which adsorbs from the background gas or forms over palladium surface as a product of the propylene oxidation. Two weak features at the higher binding energy could be attributed to more strongly oxygenated carbon species like formate, acetate, etc. Two major spectral features at 283.9 and 284.6 eV could be attributed to carbon species located in the near-surface region. The dissolution of carbon in the Pd bulk and following formation of the PdC surface phase [1] at low temperature was also evidenced by $Pd3d_{5/2}$ spectra (not shown). After heating to 250ºC, both the C1s and $Pd3d_{5/2}$ spectra

essentially remained constant. In contrast, at 300ºC all the C1s features and PdC component in the Pd3d$_{5/2}$ spectrum disappear that points out to full removing of carbon from the near-surface region. During cooling to 250ºC, we again observed a similar C1s spectrum, but with very low intensity. Further cooling leads to restoration of the C1s spectrum as well as of the PdC component in the Pd3d$_{5/2}$ spectrum.
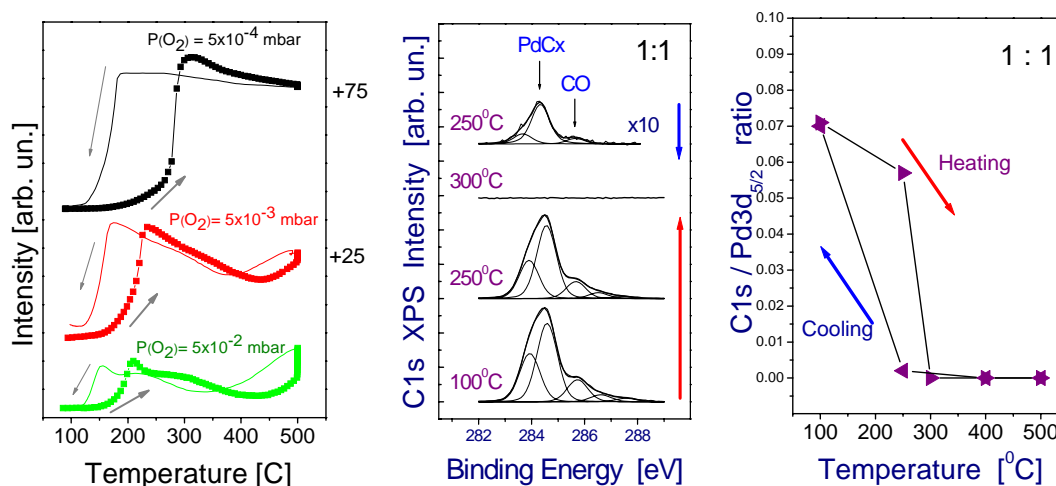
Figure 1. Temperature dependence of CO_2 yield in the propylene oxidation for different propylene/oxygen ratios (left) as well as *in situ* C1s spectra (center) and temperature dependence of C1s intensity observed in the equimolar reaction mixture (right).

Comparing the XPS and TPR data, we can postulate that the first activity hysteresis in the propylene oxidation is closely coupled with the hysteresis in the carbon content in the near-surface region. The state with the lower activity corresponded to the PdC surface phase, which is formed over the palladium surface due to carbon deposition and the following partial carbon dissolution in the Pd bulk. The PdC phase is formed even in an oxygen excess at low temperature, leading to the immediate catalyst deactivation. During heating, the carbon clean-off reaction with oxygen proceeds, which restores the adsorption properties of the palladium surface, and, as a consequence, the propylene oxidation starts above 210-285ºC. Another interesting point of this study is an observation of strong dependence of the propylene conversion on the propylene/oxygen ratio. The higher level of propylene conversion was detected in the equimolar mixture. This phenomenon is explained by the inhibiting effect of oxygen adsorption and formation of the surface oxide. High oxygen content extinguishes the reaction. It means that the presence of oxygen-free metal surface, where propylene can adsorb and dissociate, is necessary for high catalytic activity.

References

[1] V.I. Bukhtiyarov, V.V. Kaichev, I.P. Prosvirin, *Topics Catal*. 32 (2005) 3.
[2] H. Bluhm, M. Hävecker, A. Knop-Gericke, E. Kleimenov, R. Schlögl, D. Teschner, V.I. Bukhtiyarov, D.F. Ogletree, M. Salmeron, *J. Phys. Chem. B* 108 (2004) 14340.

3

An *operando* XPS-MS study of the oscillations in the propane oxidation over nickel foil

Vasiliy V. Kaichev[1], Alexey Yu. Gladky[1], Igor P. Prosvirin[1], Valerii I. Bukhtiyarov[1],
Raoul Blume[2], Michael Hävecker[2], Axel Knop-Gericke[2], Robert Schlögl[2]

[1]*Boreskov Institute of Catalysis of SB RAS, Novosibirsk, Russia, E-mail: vvk@catalysis.ru*
[2]*Fritz-Haber-Institut der MPG, Berlin, Germany*

One of the most interesting and unusual phenomena of catalysis is the rate oscillations [1]. To date, approximately 70 oscillating heterogeneous catalytic systems are known. A classic example is oscillations in CO oxidation over noble metals, which were intensively studied during the last thirty years. At present, a special attention is attracted to oscillations in the oxidation of light alkanes over transition metals. For example, the regular self-sustained oscillations were observed in the methane oxidation over Ni, Co and Pd supported and unsupported catalysts in oxygen-deficient conditions at ambient pressure [2]. Similar oscillations were also observed in the ethane oxidation over Ni and Co foils. In our previous work, it was found that the propane oxidation over Ni can proceed in a self-oscillation regime as well [3,4]. The characteristics of all these oscillations are sufficiently similar to suggest a common origin for the oscillatory behaviour. The stable and repeatable oscillations appear after an induction period of tens minutes, when the catalysts demonstrate very low activity. It points out that the reaction kinetics alone cannot be responsible for the oscillations. Also the oscillation mechanisms, which are in general based on UHV studies [1], cannot be simply extrapolated to the high-pressure conditions. For elucidating the oscillation mechanism in the oxidation of light alkanes over transition metals, it is necessary to apply some *operando* techniques.

Unfortunately, self-oscillations in the methane and ethane oxidation were observed only at atmospheric pressure [2], where most of the surface-sensitive techniques, including XANES and XPS, can not be used. Therefore, as a case reaction, we chose the catalytic oxidation of propane over Ni, where regular oscillations with periods of several minutes can be observed in the mbar pressure range [3,4]. Here we present first results of an *operando* study of the oscillations in the propane oxidation over a Ni foil. We used time-resolved X-ray photoelectron spectroscopy *in situ*, i.e., while oscillations take place, simultaneously with mass-spectrometry (MS) for monitoring gas-phase components. *In situ* XPS is one of the most useful tools to investigate both the surface composition and the nature of adsorbed species on the catalyst surface. When the *in situ* XPS is coupled with mass-spectrometry, it becomes a particularly effective *operando* technique, which makes it possible to correlate the surface properties with the catalytic performance.

The experiments were performed at the ISISS beam line at BESSY in Berlin. The construction of this setup was described in detail elsewhere [5]. A differentially pumped system of electrostatic lens is the key feature of this setup, which makes it possible to investigate the catalytic reactions *in situ* in the mbar pressure range. During the experiments, the total pressure of the reaction mixture in the experimental cell was kept at a constant level of 0.5 mbar. The gas-phase analysis was carried out using a quadruple mass-spectrometer (Prizma, Balzers) connected through a leak valve to the experimental cell. A rectangular piece of a nickel foil ($0.125 \times 6 \times 7$ mm, purity 99.99%, obtained from Advent) was used as a catalyst. It was mounted onto a sapphire sample holder with a SiC plate heated from the back with a NIR laser. The main advantage of this heating method is the absence of any hot details, which may have a high catalytic activity. The sample temperature was monitored with a chromel-alumel thermocouple spot-welded directly to the foil edge.

In this *operando* XPS-MS study, the oscillations were observed at temperatures 550-650°C and for gas mixtures with the propane/oxygen ratios from 1:1 to 20:1. The period, amplitude and waveform of the oscillations were strongly dependent on the temperature and the propane/oxygen ratio. Usually, the catalyst stayed in an inactive state for the most of time with occasional evolution of H_2, CO and H_2O. Such product distribution indicates that both the partial and total oxidation of propane occurred over nickel during the active half-period [4]. The periodic changes in the reactant concentration were accompanied by synchronous fluctuations of the catalyst temperature. Figure 1 shows typical oscillations of the reaction rate, which is demonstrated by the time-induced variation of MS signals at $m/z = 2$ (H_2), $m/z = 18$ (H_2O), $m/z = 28$ (CO) and $m/z = 32$ (O_2). Changes of the catalyst temperature are also detected (Fig.1).
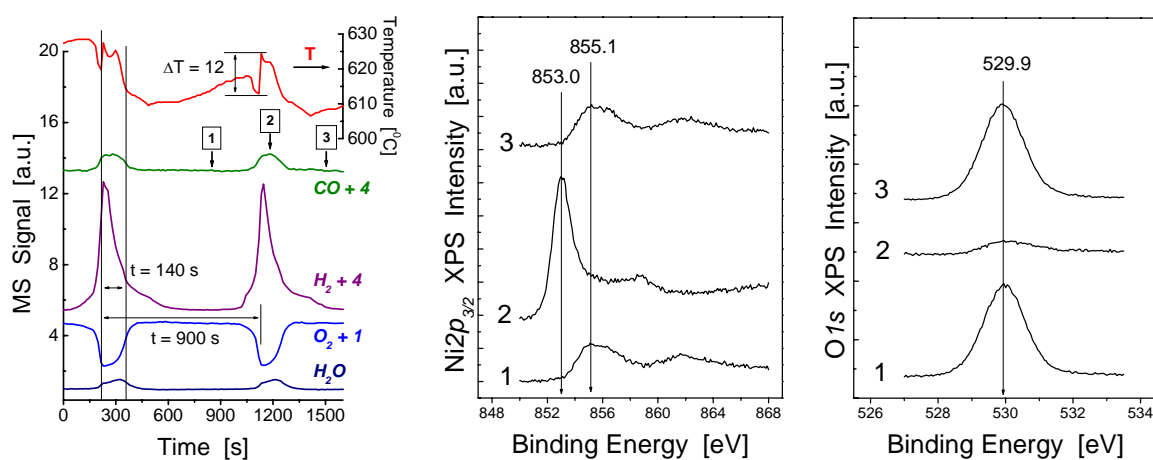
Figure 1. Oscillations of H_2O, O_2, H_2, CO, and temperature (left) as well as Ni$2p_{3/2}$ and O$1s$ core-level spectra taken during inactive and active half-periods of oscillations (centre and right). The propane/oxygen ratio was 3:1.

In order to reveal the nature of the active and inactive state of the catalyst surface, time-resolved XPS spectra were measured *in situ,* directly during the oscillations. Fig. 1 also shows the Ni$2p_{3/2}$ and O$1s$ core-level spectra, which were taken when the system periodically passes through three characteristic points corresponding to the inactive and active states marked as 1, 2, and 3. The Ni$2p_{3/2}$ spectra from the inactive surface (spectra 1 and 3) show the characteristic pattern of NiO with the main Ni$2p_{3/2}$ line at 855 eV and two satellites at higher (by ~1.5 eV and ~7 eV) binding energies. According to previous XPS studies [4], the first satellite, which looks as a prominent shoulder of the main line, is assigned to NiO, while the second strong broad satellite at 862 eV is typical of Ni^{2+} compounds like NiO, Ni(OH)$_2$, NiAl$_2$O$_4$, etc. In contrast, the Ni$2p_{3/2}$ spectrum of the active nickel surface (spectrum 2) consists of a sharp single peak at 853 eV, which corresponds to nickel in the metal state. A wide low-intensive feature at 859 eV in this case is assigned to an energy loss peak due to plasmon excitation. In full agreement with these data, strong changes have been observed in the O$1s$ spectra, when the system periodically passes from the inactive to the active state (Fig. 1). The O$1s$ spectrum from the inactive surface (spectrum 1) exhibits an intense feature at 529.9 eV, which mainly corresponds to oxygen in NiO. Transition to the active state of nickel surface leads to a drop in the O$1s$ intensity (spectrum 2). Again, after subsequent transition to the inactive state, the O$1s$ spectrum is restored in the intensity to the original level (spectrum 3).

Thus, *in situ* XPS spectra clearly indicate that during the inactive half-periods, nickel foil is covered with a nickel oxide layer, which mainly consists of NiO. The transition to the active state is accompanied by the full reduction of nickel oxide to Ni^0. It means that the self-oscillations in the propane oxidation over Ni originate due to the periodic oxidation and reduction of the catalyst surface. The high-activity state is associated with metallic nickel, whereas the low-activity state is characterised by the presence of the nickel oxide layer on the catalyst surface. Considering the propane oxidation as a case reaction, we suppose that the oscillations in the oxidation of other light alkanes over transition metals proceed via a similar mechanism.

References
[1] R. Imbihl, G. Ertl, *Chem. Rev*. 95 (1995) 697.
[2] X. Zhang, C.S.-M. Lee, D.O. Hayward, D.M.P. Mingos, *Catal. Today* 105 (2005) 283.
[3] A.Yu. Gladky, V.K. Ermolaev, V.N. Parmon, *Catal. Lett*. 77 (2001) 103.
[4] A.Yu. Gladky, V.V. Kaichev, V.K. Ermolaev, V.I. Bukhtiyarov, V.N. Parmon, *Kinet. Catal*. 46 (2005) 251.
[5] H. Bluhm, M. Hävecker, A. Knop-Gericke, E. Kleimenov, R. Schlögl, D. Teschner, V.I. Bukhtiyarov, D.F. Ogletree, M. Salmeron, *J. Phys. Chem. B* 108 (2004) 14340.

In-situ investigations of adsorbed benzene on silver-modified Pt(322) surfaces

Sandra Wickert[1], Matthias Schöppke[1], Regine Streber[2], Michael Lorenz[2], Hans-Peter Steinrück[2], Reinhard Denecke[1]

[1] Wilhelm-Ostwald-Institut für Physikalische und Theoretische Chemie, Universität Leipzig, Linnéstraße 2, 04103 Leipzig

[2] Lehrstuhl für Physikalische Chemie II, Universität Erlangen-Nürnberg, Egerlandstr. 3, 91058 Erlangen

The adsorption of molecules on a surface is the first step in heterogeneous catalysis. Thus, detailed knowledge about the adsorption step is necessary for the understanding of the whole catalytic process. In a previous paper by C. Papp et al. the site-specific adsorption of benzene on a Ni(111) surface has been investigated by in-situ X-ray spectroscopy (XPS) [1]. Among other observations, they reported about two specific adsorption sites – hollow and bridge – identified by their C 1s signature. On Pt(111), Wander et al. determined the bridge site for disordered benzene adsorption [2]. An interesting issue is the influence of lateral confinement on the adsorption properties of molecules. So in our work we study the adsorption properties of benzene on stepped Pt surfaces, as an example for larger molecules. We used a regularly stepped Pt(322) surface (with five atomic rows wide (111) terraces and (100) oriented monatomic steps) and modified it with different amounts of Ag. The thermal deposition of Ag on stepped Pt at 300 K results in monatomic rows along the step edges, at least for the first two to three Ag rows [3]. The amount of Ag was varied from 0 to 1 ML (monolayers). The adsorption of benzene was monitored by in-situ XPS; in uptake experiments at 117, 190 and 300 K, the intensity and binding energy of the C 1s signature was determined. In addition, benzene was thermally desorbed, monitored again by in-situ XPS. The experiments were performed at beamline U49/2-PGM1 at BESSY-II.

As a first step, benzene adsorption at different temperatures was characterized on a clean (0 ML Ag) and a completely Ag-covered Pt(322) surface (1ML Ag).
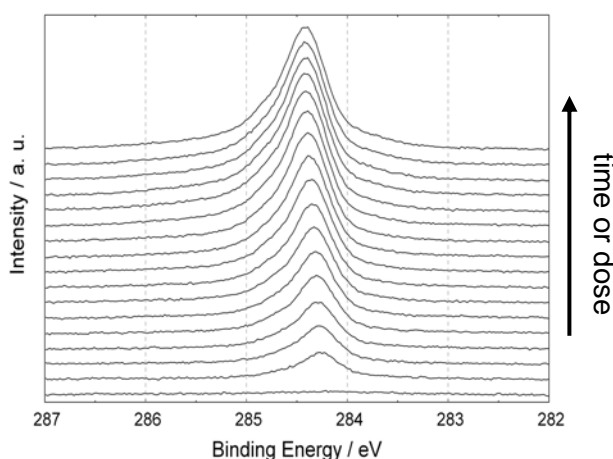
Fig.. 1: C 1s uptake experiment at 190 K for adsorption of benzene on clean Pt(322). Total exposure after 400 s was about 0.8 Langmuir.

At 190 K, benzene chemisorbs on the clean Pt (322) surface, with no physisorption (Fig. 1). There is only one asymmetric C 1s peak, indicating an adsorption site for benzene, where all C atoms have a similar local geometry, i.e., the hollow site is preferred [1]. The observed asymmetry is due to unresolved vibrational splitting. With increasing coverage, the peak maximum shifts to higher binding energies by about 160 meV, because of lateral interactions between the benzene molecules. After 400 s saturation of the benzene coverage was achieved. The same results were obtained for an uptake experiment at 300 K under equal conditions. For 117 K also multilayer adsorption was observed.

On a Pt(322) surface completely covered with Ag one broad C 1s peak at higher binding energies (of about 285.0 eV) is observed during benzene adsorption at 190 K. By removing the benzene gas phase a decrease of the intensity of the C 1s peak identifies this species as physisorbed benzene. For 300 K there is no adsorption of benzene on the Ag layer.

For the study of the lateral confinement the amount of Ag (and thereby the free Pt surface area) was varied. At 190 K, benzene simultaneous adsorbs on Ag and Pt with different relative amounts, depending on the Ag coverage. In Fig. 2 a) the contributions of chemisorbed and physisorbed benzene on Pt and Ag, respectively, are shown, as derived from a deconvolution of the C 1s spectra, The chemisorbed part decreases with increasing amount of Ag and the physisorbed part increases. At 300 K the adsorption of benzene on Ag is suppressed completely, so only adsorption on free Pt(322) areas takes place (Fig. 2 b).
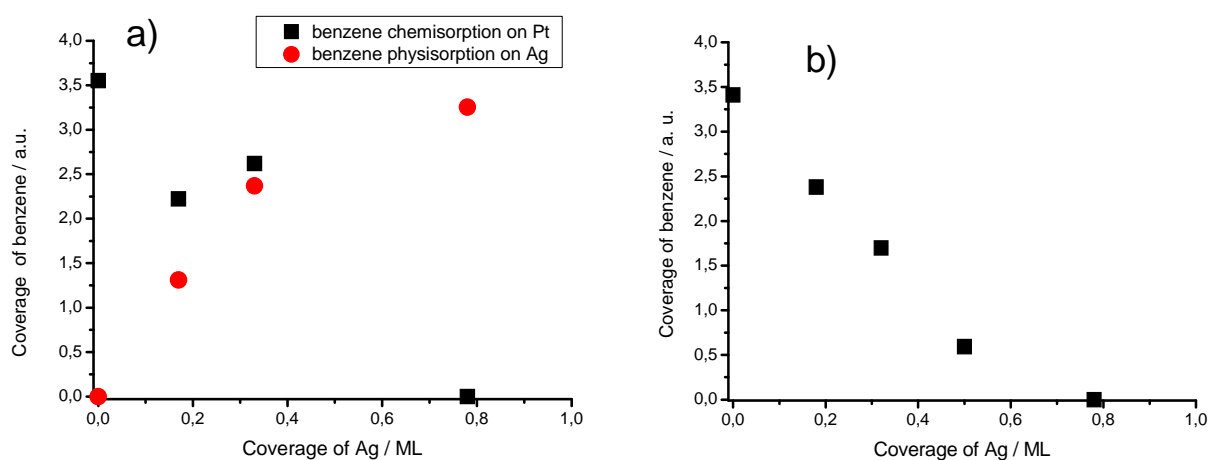
Fig. 2: Benzene coverage (in arbitray units) in dependence of silver coverage. a) Adsorption at 190 K leads to chemisorption (on Pt) and physisorption (on Ag). Data from spectral deconvolution (fit) of C 1s data taken during C_6H_6 exposure. b) Adsorption at 300 K only results in chemisorption on Pt.

In both experiments there is a limiting Ag amount for benzene adsorption on free Pt. At 300 K. where no further data analysis is necessary, extrapolation yields a value of about 0.6 ML Ag for this limit. Obviously, benzene needs at least two rows of Pt to adsorb on it. This implies that benzene adsorbs in flat adsorption geometry, as expected [2]. It also agrees with results by Campbell et al. who found an ensemble of at least six Pt atoms necessary for benzene dissociation [4].

[1] C. Papp, T. Fuhrmann, B. Tränkenschuh, R. Denecke, H.-P. Steinrück, Phys. Rev. B 73 (2006) 235426.
[2] A. Wander, G. Held, R.Q. Hwang, G.S. Blackman, M.L. Xu, P. de Andres, M.A. Van Hove, G.A. Somorjai, Surf. Sci. 249 (1991) 21.
[3] P. Gambardella, M. Blanc, H. Brune, K. Kuhnke, K. Kern, Phys. Rev. B 61 (2000) 2254.
[4] J.M. Campbell, S. Seimanides, C.T. Campbell, J. Phys. Chem. 93 (1989) 815.

Simultaneous Synchrotron X-ray Scattering and Optical Spectroscopy: The first fivefold in situ-coupling technique for on-line monitoring of catalyst synthesis

J. Radnik[a], U. Bentrup [a], J. Leiterer [b], F. Emmerling [b], A. Brückner [a]

a: Leibniz-Institut für Katalyse, Branch Berlin, Richard-Willstätter-Str. 12, 12489 Berlin, Germany
b: Bundesanstalt für Materialforschung und –prüfung, Richard-Willstätter-Str. 12, 12489 Berlin, Germany

The first fivefold coupling of in situ techniques was established at BESSY allowing simultaneous on line monitoring of precipitation processes with X-ray scattering and optical spectroscopy like Raman, UV-Vis and ATR-FTIR. The combination of these methods provides information about the species in the precipitate and the solution, the phases and the particles in the precipitate. This equipment was used for detailed investigation of the precipitation of ammonium iron molybdates used as precursor material for selective oxidation catalysts. Depending on the reaction conditions, the formation of different phases with Anderson- or Keggin-like structure could be observed during the precipitation.

Introduction

Heterogeneous Mo-based complex oxides are versatile catalysts for the selective oxidation of alkanes and olefins to the corresponding aldehydes, anhydrides or acids [1,2] and, in particular iron molybdates, for the selective oxidation of methanol to formaldehyde [3].

In general, a specific phase composition and structure in the mixed oxide catalysts is necessary for good catalyst performance. Usually, the synthesis of such catalyst material comprises different steps like the synthesis of suitable precursors by e.g. precipitation, isolation of the precipitate, drying and subsequent calcination. During the synthesis of the precursor, the preparation method as well as the nature of the used components and the reaction conditions play an important role and affect the final composition, structure and performance of the catalytic material. Systematic investigations with sophisticated methods for on-line monitoring of the synthesis process are required to understand and distinguish the influence of these different parameters.

For this purpose, an experimental setup was established at the µ-spot Beamline at BESSY allowing simultaneous *Small Angle* and *Wide Angle* X-ray scattering (SAXS/WAXS), Raman, UV-VIS and ATR spectroscopy. While the structural changes of molybdate species within solution and precipitate were observed by optical spectroscopy, the scattering experiments provide information on the precipitate, such as particle and crystallite size and nature of crystalline phases formed during precipitation.

Experimental

An experimental setup presented formerly [4] was enhanced at the µ-spot Beamline at BESSY and is schematically shown in Fig. 1. Generally, an ammonium heptamolybdate (AHM) solution and a metal nitrate solution were prepared separately. Than, the nitrate solution was slowly added to the AHM solution by vigorous stirring. This mixture was stirred for 60 min at room temperature. In a second step, concentrated H_3PO_4 or a solution of diammonium hydrogenphosphate $(NH_4)_2HPO_4$ were added, followed by further stirring for 30 min. Finally, the suspension was heated to 50°C and stirred for another 60 min.
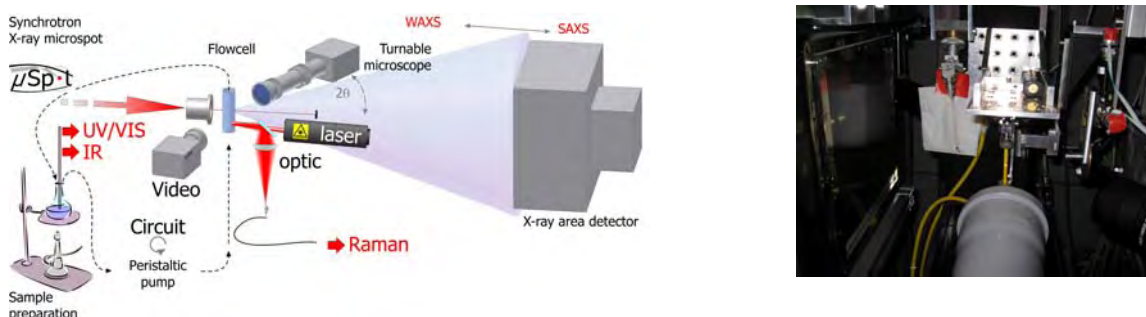
Fig.1: Scheme of the experimental setup and image of the flowcell with the X-ray area detector and the Raman spectrometer

The UV-vis and ATR measurements were carried out by using respective probes directly dipped into the reaction solution. The UV-vis spectra were recorded in reflection mode using an Ava Spec 2048 fiber optic spectrometer (Avantes). Mid infrared ATR spectra were collected using a fiber optical diamond ATR probe (ifs Aachen) coupled to a FTIR spectrometer Avatar 370 (Thermo Electron). The slurry was transported by a peristaltic pump within a closed circuit of flexible tubes through a borosilicate capillary with an inner diameter

of 5 mm and a wall thickness of 100 μm used for Raman and X-ray scattering measurements. The Raman investigations were performed by focussing the laser beam onto the suspension flowing through this capillary using a fiber optical RXN spectrometer (Kaiser Optical Systems) equipped with a 70 mW diode laser at a wavelength of 785 nm. For the scattering experiments the capillary was irradiated with highly monochromatic X-rays (λ = 1.0336 nm). The scattered intensities were collected 20 cm behind the capillary with a two-dimensional X-ray detector (MarMosaic 225). The scattering data were transformed into diagrams of scattered intensities, I, as function of the scattering vector $q = 4\pi/\lambda \sin\theta$ with θ being the scattering angle.

Results

To obtain information about the influence of component concentration and pH-value on the formation of different molybdate phases, the system Mo/Fe/phosphate was exemplarily chosen, and the Mo/Fe ratio and the nature of the phosphate compound were varied.

In Fig. 2 the X-ray scattering results of mixing AHM with the iron nitrate solution and addition of $(NH_4)_2HPO_4$ aq. are presented. Bragg reflections indicating crystalline phases could be observed in all curves.
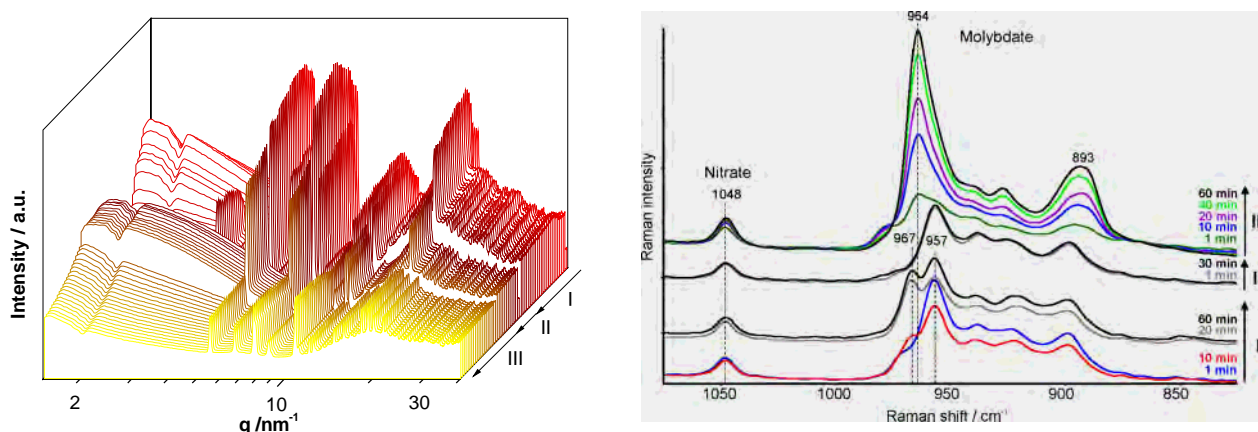
Fig. 2: X-ray scattering curves and Raman spectra after mixing the AHM with the nitrate solutions (I), adding of $(NH_4)_2HPO_4$ aq. (II) and heating at 50°C (III). The scattering curves were obtained every 120 sec.

In the first step one phase is formed immediately after mixing the solutions, further reflections appeared after 20 min indicating the formation of another phase. The latter phase disappears after admixture of the $(NH_4)_2HPO_4$ solution. During heating at 50°C the crystallinity of the remaining solid phase lowers.

The scattering results are confirmed by Raman spectroscopy. In the first step, the formation of two molybdate species is observed indicated by a band at 967 cm^{-1} which is due to an Anderson-type phase containing $[H_6FeMo_6O_{24}]^{3-}$ species [5] and another one with a band at 967 cm^{-1} possibly correlated with $[Mo_8O_{26}]^{4-}$ species. The latter band disappears after addition of $(NH_4)_2HPO_4$ due to the increase of pH. During heating at 50°C the band at 957 cm^{-1} shifts to 964 cm^{-1} and a further band appears at 893 cm^{-1}. The nature of the corresponding species is yet unclear. From inspection of the phosphate bands visible in the ATR spectra it can be concluded that a mixed molybdatophosphate or a mixture of Anderson-type molybdate and phosphate is possibly formed.

If H_3PO_4 is added instead of $(NH_4)_2HPO_4$, a Raman band at 980 cm^{-1} is observed typical for the Keggin-type anion $[PMo_{12}O_{40}]^{3-}$. The results of SAXS/WAXS measurements shown that the Mo/Fe ratio influences the crystallinity of this Keggin structure: a lower amount of Fe leads to an amorphous phase, whereas higher amounts seem to facilitate the formation of a crystalline phase.
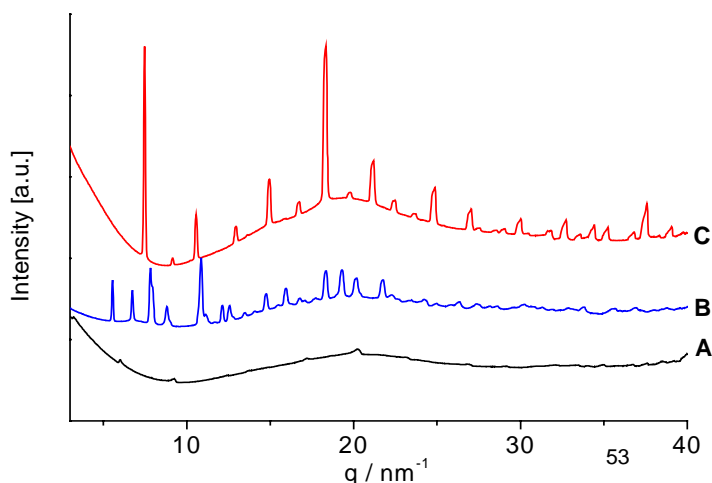
Fig. 4: X-ray scattering curves of the final precipitate obtained under different preparation conditions: A) Mo/Fe=0.12/0.01 + H_3PO_4 B) Mo/Fe=0.12/0.01 + $(NH_4)_2HPO_4$; C) Mo/Fe=0.12/0.02 + H_3PO_4.

Conclusions

The combination of X-ray scattering with synchrotron radiation and optical spectroscopic methods like Raman, UV-Vis and ATR-FTIR allows a comprehensive insight into the synthesis of mixed oxide catalyst precursors in the liquid phase under realistic synthesis conditions. This specific method combination proved to be a valuable tool to elucidate structural changes of the complex anions during precipitation process an on molecular scale together with changes of nanoscopic properties of respective precipitate such as agglomeration and crystallization.

Acknowledgements

References

[1]   R.K. Grasselli, Catal. Today 49 (1999) 141.
[2]   G. Centi, F. Cavani, F. Trifirò, Selective Oxidation by Heterogeneous Catalysis, Kluwer Academic Publishers, New York 2001.
[3]   A.P.V. Soares, M.F. Portela, A. Kiennemann, Catalysis Reviews 47 (2004) 125.
[4]   U. Bentrup, J. Radnik, U.Armbruster, A. Martin, J. Leiterer, F. Emmerling, A. Brückner, Topics in Catalysis, *in press*
[5]   I.L. Botto, A.C. Garcia, H.J. Thomas, J. Phys. Chem. Solids 53 (1992) 1075.

EXAFS study of Redox-active Metal-organic frameworks
Report on application 2008_2_80132

Markus Tonigold and Dirk Volkmer

Ulm University, Institute of Inorganic Chemistry 2, Materials and Catalysis, Albert-Einstein-Allee 11, D-89081 Ulm (Germany), Fax: +49 (0)731-50-23039, Tel: +49 (0)731-50-23921, E-mail: dirk.volkmer@uni-ulm.de

measurements performed during 28th calendar week in 2008 on beamline KMC-2

Introduction

Three metal-organic frameworks (MOFs), named **MFU-1**, **MFU-2** and **MFU-3**, were investigated by EXAFS and XANES to gain deeper insights into the behaviour of these MOFs during catalysis. The structures of the untreated samples as determined by single crystal X-ray analysis are given in Fig. 1 and 2.[1]
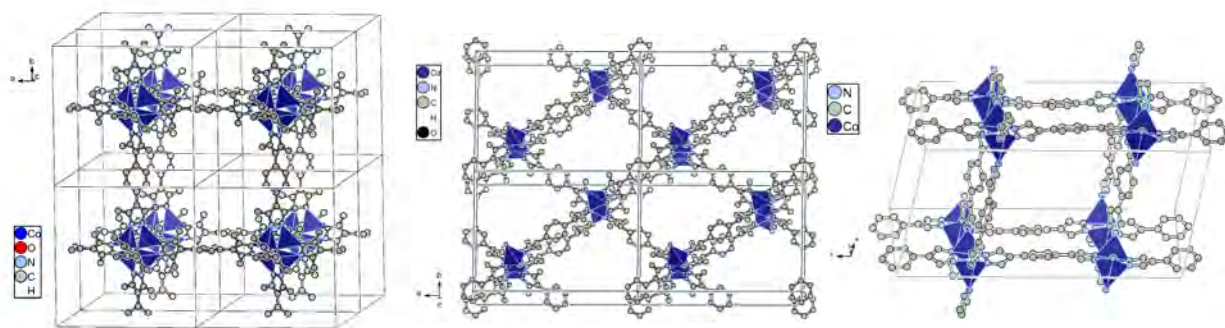
Fig. 1: Crystal packing diagram of **MFU-1** (left), **MFU-2** (middle) and **MFU -3**. {CoON$_3$} in **MFU-1** and {CoN$_4$} in **MFU-2** and **MFU-3** coordination units are represented as blue polyhedrons. Hydrogen atoms are omitted for clarity.

Fig. 2: Left: schematic drawing of **MFU-1**, represented by linearly connected octahedral nodes as secondary building units; Right: **MFU-2** and **MFU-3,** represented by linearly interconnected one-dimensional Co(II) as secondary building units.

All three MOFs catalyse the reaction of cyclohexene with tert-Butylhydroperoxide and show an intensive colour change during reaction. On the other hand, the XRD patterns after catalysis are unchanged for **MFU-1**, whereas **MFU-2** and **MFU-3** get amorphous during catalysis. Additionally, further experiments proofed that **MFU-1** is in fact a heterogenous catalyst, whereas the Co ions of **MFU-2** and **MFU-3** are bleeched out from the networks, and thus homogenous catalysis is observed. Therefore, EXAFS and XANES studies were performed to gain deeper insights into the changes of the novel catalyst materials during catalysis.

Experimental

EXAFS and XANES measurements were conducted at room temperature, using the doublecrystal monochromator (SiGe (111) graded crystals, E/ΔE=4200) at the beamline KMC-2 of the electron storage ring at the Berliner Elektronenspeicherring-Gesellschaft für Synchrotronstrahlung m.b.H. (BESSY II, Berlin, Germany).[2] The XANES and EXAFS spectra were recorded at the Co-K-edge, energy calibration was performed with cobalt metal foil. Measurements were performed in transmission mode using ion chambers, additionally the fluorescence using a fluorescence yield detector (Si-PIN photodiode) was recorded.

Results and Discussion

XANES and EXAFS of **MFU-1**, **MFU-2** and **MFU-3** were recorded for the untreated samples as well as the samples after catalysis. The Co K-edge EXAFS spectra are analyzed using the standard Athena and Artemis FEFF XAFS analysis codes.[3]

The raw and fitted Fourier transforms of the k^2-weighted $\chi(k)$ spectra (calculated in the k-range 2.0–12.0 Å^{-1}) at the Co-K-edge are shown in Fig. 3-5. The Co-K edge spectra were fitted using models derived from the single crystal structure data of **MFU-1**, **MFU-2** and **MFU-3**.
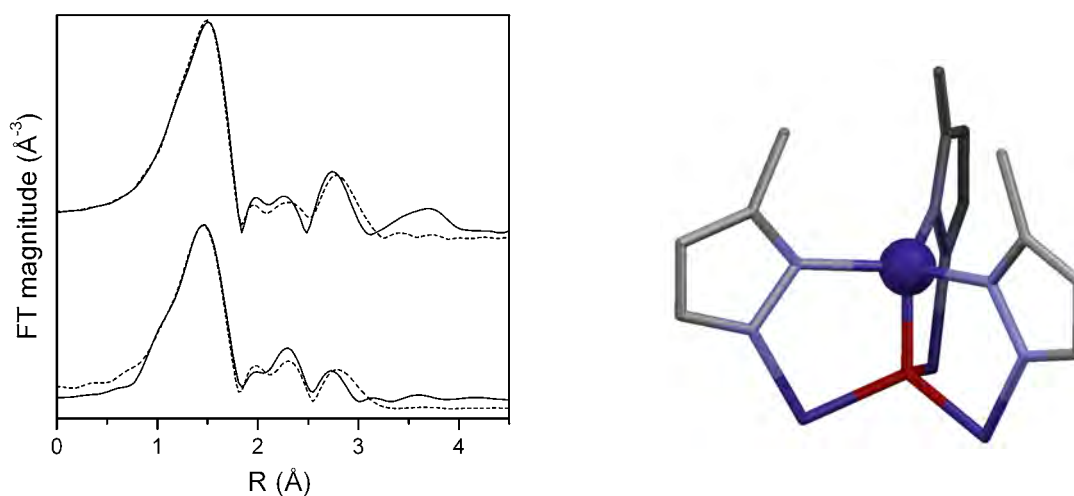
Fig. 3: Left: k^2-weighted Fourier transformation of the EXAFS spectra of MFU-1 before catalysis (top) and after catalysis (bottom) fitted from 1.0-3.5 Å with 10 variables for 19 independent points, R = 0.004 and reduced χ^2 = 762. The raw data and the fitting are shown in solid and dashed lines, respectively. Right: Stick representation of the cluster used for EXAFS data analysis. The absorbing Co atom is highlighted as a ball.
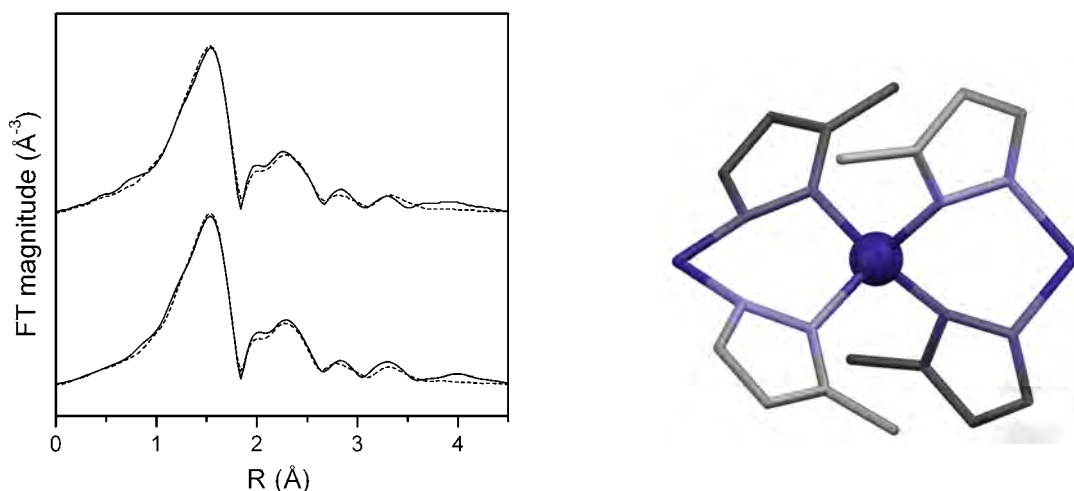
Fig. 4: Left: k^2-weighted Fourier transformation of the EXAFS spectra of MFU-2 before catalysis (top) and after catalysis (bottom) fitted from 1.1-3.5 Å with 7 variables for 18 independent points, R = 0.002 and reduced χ^2 = 213. The raw data and the fitting are shown in thin and thick solid lines, respectively. Right: Stick representation of the cluster used for EXAFS data analysis. The absorbing Co atom is highlighted as a ball.
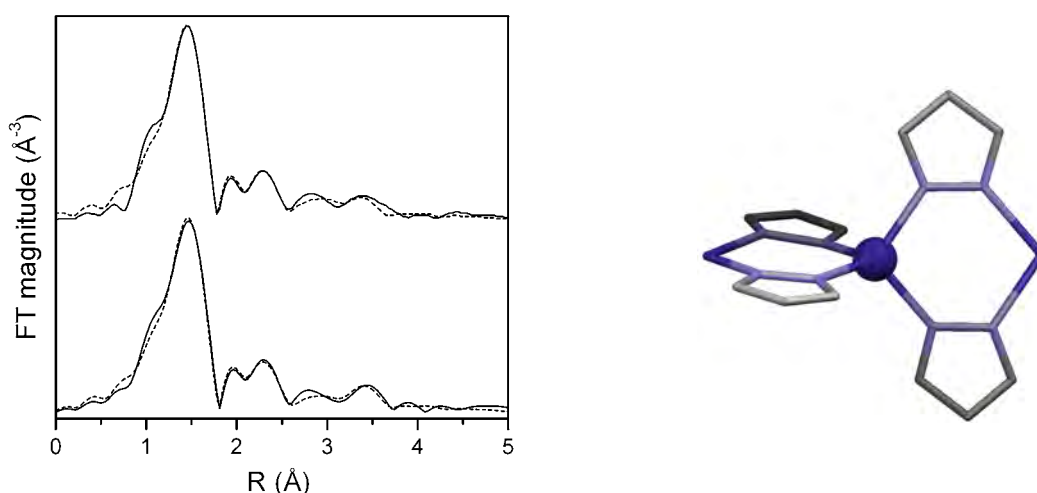
Fig. 5: Left: k^2-weighted Fourier transformation of the EXAFS spectra of MFU-3 before catalysis (top) and after catalysis (bottom) fitted from 1.0-4.0 Å with 12 variables for 19 independent points, R = 0.003 and reduced χ^2 = 146. The raw data and the fitting are shown in thin and thick solid lines, respectively. Right: Stick representation of the cluster used for EXAFS data analysis. The absorbing Co atom is highlighted as a ball.

The excellent fits to the EXAFS data for all three compounds confirm the validity of the structure obtained from single crystal x-ray structure analysis. Particularly no further Co-containing species are observable, proofing that the catalytic activity is due to the metal sites in these three metal-organic frameworks (and not due to further unknown Co-containing impurities or side-products in the voids of the network).

Whereas **MFU-1** shows obvious changes between the sample before and after catalysis (especially above 2 Å in the Fourier transformed spectrum), **MFU-2** and **MFU-3** maintain the local structure during catalysis. Despite the obvious changes in the **MFU-1** spectrum, the fit to the molecular cluster as it is before catalysis is still satisfactory (though with slightly changed bond lengths and Debye-Waller factors). Since also the XRD pattern of **MFU-1** is unchanged during catalysis, we assume that due to diffusion limitation of the catalytic reaction, only a small part of the Co centers

close to the surface of the crystal is structurally changed. This fact is complicating the search for the structure of the catalytic center after the catalytic reaction.

For **MFU-1**, bleeching experiments showed already that the catalysis is homogenous. The next question thus was if the catalysis is maybe only performed by defects on the external surface of **MFU-1**. The obvious change in the EXAFS signal for **MFU-1** after catalysis now additionally proofs that the catalysis is performed on the {Co$_4$O} cluster centres of the framework and not only by defects on the external surface. For **MFU-2** and **MFU-3**, on the other hand, the catalysis is due to bleeching of the Co ions into solution, and the material gets amorphous due to XRD measurements. In contrary, the EXAFS analysis for these two materials reveals that the molecular fragment is still unchanged after catalysis. Therefore, the catalyst is decomposing during catalysis into smaller, stable fragments with still the same local environment.

These results are in accordance with the structural features of the three frameworks: The Co centres in **MFU-1** are still accessible to potential further ligands, whereas the linker in **MFU-2** and **MFU-3** completely "shields" the metal centres from coordination of potential ligands. Altogether, these results indicate that only **MFU-1** type catalysts are promising candidates for catalytic reactions.

Since the EXAFS data for **MFU-1** indicate at least a partial structural change after the catalytic process, XANES spectra were examined to obtain further information upon the valence state for **MFU-1** before and after catalysis. Fig. 6 shows the XANES spectra of MFU-1 before and after catalysis together with Co$_3$O$_4$ and Co^{III}-pyrazolate as references with higher valences, showing that the edge energy is the same for MFU-1 after and before catalysis. The peak edge should be shifted to higher energy for Co of larger oxidation-state, which is often utilized to estimate the oxidation state of Co,[4] and a linear dependence of the chemical shift on the average valence can be assumed.[5] Thus the unchanged position of the peak edge indicates that the oxidation state of Co in **MFU-1** is not changed throughout the catalytic cycles.
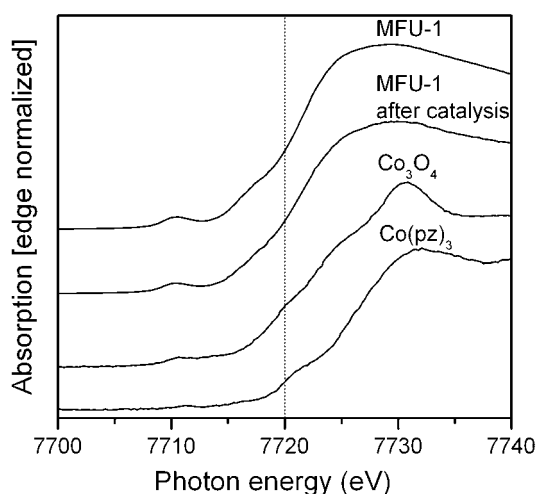
Fig. 6: Normalized Co K-edge XANES spectra.

Acknowledgements

[1] The structure of **MFU-1** is similar to the one of MOF-5, which has a CaB_6 type framework topology. It encloses octahedrally-shaped $\{Co_4O(dmpz)_6\}$ nodes reminiscent of the $\{Zn_4O(CO_2)_6\}$ secondary building units of MOF-5, and phenylene rings constituting the edges of the cubic 6-connected CaB6 net. **MFU-2** and **MFU-3** show PtS-type framework which contains prismatic tunnels running through the crystal, the walls consisting of layers of 1D Co(II) chains and dianionic BDPD ligands. Each Co(II) center adopts a distorted tetrahedral coordination geometry through binding to nitrogen donor atoms from four different ligands.

[2] a) A. Erko, I. Packe, C. Hellwig, M. Fieber-Erdmann, O. Pawlitzki, M. Veldkamp, W. Gudat, *AIP Conference Proc.* 2000*, **521**, 415-418; b) A. Erko, I. Packe, W. Gudat, N. Abrosimov, A. Firsov**, *SPIE* 2000, **4145,** 122-128.

[3] a) B. Ravel, M. Newville, *J. Synchrotron Rad.* 2005, **12**, 537-541; b) M. Newville, *J. Synchrotron Rad.* 2001, **8**, 322-324; c) B. Ravel, *J. Synchrotron Rad.* 2001, **8**, 314-316; d) J. J. Rehr, R. C. Albers, *Rev. Mod. Phys.* 2000, **72**, 621-654.

[4] a) L. Barbey, N. Nguyen, V. Caignaert, F. Studer, B. Raveau, *J. Solid State Chem.* 1994, **112**, 148.

[5] a) M. Croft, D. Sills, M. Greenblatt, C. Lee, S.-W. Cheong, K. V. Ramanujachary, D. Tran, *Phys. Rev. B* 1997, **55**, 8726; b) M. C. Sánchez, J. García, J. Blasco, G. Subías, J. Pérez-Cacho, *Phys. Rev. B* 2002, **65**, 144409; c) M. C. Sánchez, G. Subías, J. García, J. Blasco, *Phys. Rev. B* 2004, **69**, 184415; d) A. H. de Vries, L. Hozoi, R. Broer, *Int. J. Quantum Chem.* 2003, **91**, 57.

In-situ investigation of sulfur oxidation on stepped Pt(355)

R. Streber, C. Papp, M.P.A. Lorenz, A. Bayer, R. Denecke[a], and H.-P. Steinrück

Lehrstuhl für Physikalische Chemie II, Universität Erlangen-Nürnberg, Egerlandstraße 3, 91058 Erlangen
[a] Wilhelm-Ostwald-Institut für Physikalische und Theoretische Chemie, Universität Leipzig, Linnéstraße 2, 04103 Leipzig

Heterogeneously catalyzed reactions are often performed at highly dispersed particles, exhibiting a variety of defect sites, which are proposed to be very reactive. Poisoning of the active sites is a major issue in large scale applications of heterogeneously catalyzed reactions. One very efficient poison for catalysts is sulfur, which is supposed to lead to the blocking of reactive sites.

We studied the reaction of sulfur with oxygen on the stepped Pt(355) surface by in-situ high-resolution XPS applying synchrotron radiation. The Pt(355) surface has five atom row wide (111) oriented terraces and (111) oriented monatomic steps. Sulfur was deposited via hydrogen sulfide adsorbed at ~130 K, followed by heating to 700 K, which leads to the decomposition of H_2S, with hydrogen desorbing as H_2 and S remaining on the surface. The experiments were performed at beamline U49/2-PGM1, using a transportable apparatus described elsewhere [1].

Fig. 1 a shows a series of S 2p XP spectra collected during heating a mixed S and O layer prepared at 250 K by dosing molecular O_2 on Pt(355), precovered with 0.02 ML sulfur. The topmost spectrum (orange) exhibits only one doublet in the S 2p region assigned to atomic S, which shows that preparation of the layer at 250 K leads almost exclusively to the coadsorption of atomic oxygen and sulfur.

Heating the mixed S and O layer to elevated temperatures leads to subsequent appearance of two new doublets in the S 2p spectra, due to the formation of SO_x species during heating. The S $2p_{1/2}$ peak at 166.0 eV (green spectrum), which appears around 300 K, is assigned to SO_2 and the one at 166.9 eV (blue spectrum), that arises at 350 K, is assigned to SO_4, due to their characteristic binding energies and desorption temperatures [2,3]. SO_4 decomposes above 500 K.

Fig. 1: Selected S 2p spectra taken a) during heating a mixed layer of 0.02 ML S and 0.37 ML O, prepared by dosing the appropriate amounts of H_2S and molecular oxygen and b) during oxygen dosing on 0.02 ML S at 350 K; $p(O_2) = 6*10^{-7}$ mbar, $h\nu = 260$ eV

Fig. 1 b shows S 2p XP spectra recorded during dosing of oxygen at 350 K. Initially, the adsorption of oxygen leads to a shift in binding energy of the S 2p doublet assigned to elemental sulfur (see difference between red and orange spectrum in Fig. 1 b). This shift is caused by the displacement of sulfur by oxygen from step to terrace sites. A similar change of adsorption sites was also observed for coadsorbed CO and S on Pt(355) and Pt(322) during heating [4, 5]. After an induction period, the formation of SO_2 (green spectrum) is observed, followed by a time-delayed oxidation of SO_2 to SO_4 (see blue spectrum).
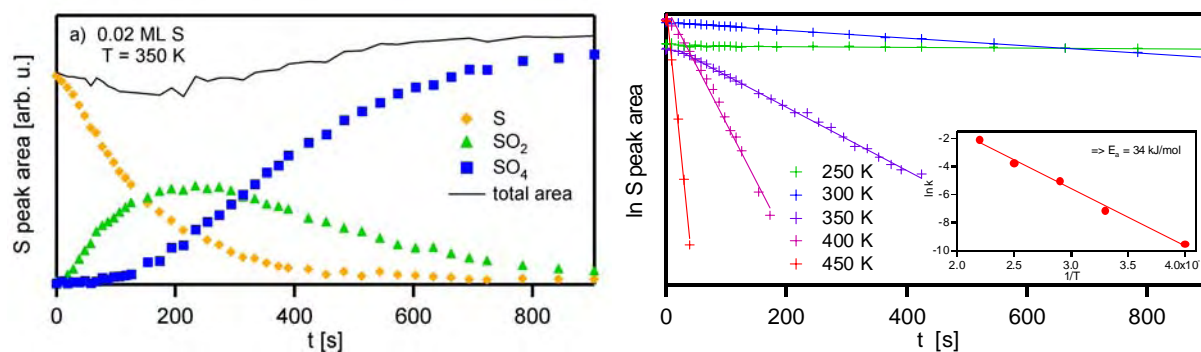
Fig. 2: a) Quantitative analysis S 2p XP spectra recorded during oxidation of 0.02 ML S at 350 K; b) Change of S peak area (logarithmic scale) versus oxygen dosing time during oxidation of 0.02 or 0.03 ML S at different temperatures between 250 and 450 K, inset: ln k versus 1/T.

Fig. 2 a shows the quantitative analysis of the reaction of S with O at 350 K. After the short induction period the S coverage decreases exponentially with time and SO_2 is formed. At ~100 s the subsequent reaction to SO_4 starts and nearly all SO_2 has reacted after 900 s. To determine the kinetic parameters of the reaction, the oxidation has been studied at different temperatures. For small S coverages the plot of S peak area (logarithmic scale) vs. time shows a linear decrease at all chosen temperatures, as can be seen in Fig. 2 b. The negative slopes, i.e., the rate constants k, increase with temperature, indicating pseudo first order reaction kinetics with respect to the oxidation of elemental S. Applying the Arrhenius equation, the plot of ln k vs. 1/T then reveals an apparent activation enthalpy of about 34 kJ/mol for the rate determining step in the oxidation of S to SO_2 on Pt(355).

[1] R. Denecke, M. Kinne, C. M. Whelan, H.-.P. Steinrück, Surf. Rev. Lett. 9 (2002) 797.
[2] M. Polcik, L. Wilde, J. Haase, B. Brena, G. Comelli, G. Paolucci, Suf. Sci.181 (1997) L568.
[3] St. Astegger, E. Bechtold, Surf. Sci. 122 (1982) 491.
[4] R. Streber, C. Papp, M.P.A. Lorenz, A. Bayer, S. Künzel, M. Schöppke, R. Denecke, H.-P. Steinrück, J. Phys.: Condens. Matter (in press).
[5] R. Streber, C. Papp, M. P. A. Lorenz, A. Bayer, R. Denecke, H.-P. Steinrück, Chem. Phys. Lett., 452 (2008) 94.

Structural and Electronic Properties of Mono- and Divalent Thiols Bound on Isolated Gold Nanoparticles

R. Lewinski, C. Graf, B. Langer, E. Antonsson, A. Hofmann, X. Gong, B. Grundkötter,
E. Rühl

Institut für Chemie und Biochemie - Physikalische und Theoretische Chemie, Freie
Universität Berlin, Takustr. 3, D-14195 Berlin

A multivalent linker is defined as a molecule containing identical functional groups binding to acceptor sites. It has been observed in thermodynamic and kinetic studies that the stability of the complexes which are formed between multivalent linkers and substrates is significantly increased, when the binding of multivalent systems is compared to the corresponding monovalent species.[1] Moreover, the number of binding sites are not additive to the enhanced stability, implying a highly non-linear binding behavior of multivalent linkers.[1] However, these effects are not yet fully understood on a molecular level. Nanoparticles functionalized with small mono- and multivalent organic linker molecules are simple model systems for investigations of multivalent interactions.

In the present study high-resolution core-level excitation is used to investigate the local electronic properties of mono- and bivalent thiols which are bound to free gold nanoparticles. For a comparison also the corresponding free ligands are studied in solid nanoparticle samples. The thiol ligands (see Figure 1) are commercially available or prepared by organic syntheses.[2] Gold nanoparticles of 25-50 nm diameter are prepared by colloidal chemistry[3] and functionalized with the mono- or bivalent ligands. The solutions of the ligands or dispersions of the functionalized nanoparticles are sprayed into the gas phase at ambient pressure by using an atomizer. Subsequently, the solvent is evaporated in a diffusion dryer. The nanoparticle beam is focused by an aerodynamic lens in the size regime r < 200 µm in the interaction region with synchrotron radiation.[4] Total electron yields are measured in the S $L_{3,2}$ absorption regime in order to probe the local electronic surroundings of the absorbing sites as a function of chemical binding. This approach relies on a short interaction time of the nanoparticles with X-rays, so that radiation damage is avoided (cf. [5,6]).

We investigate the binding of the three bivalent compounds lipoic acid (LA), its open form dihydrolipoic acid (DHLA), and the amino analogon of lipoic acid, 5-(1,2-dithiolan-3-yl)-butan amine. 11-mercaptoundecanoic acid (11-MUDA) is used as a monovalent reference (see Figure 1). Total electron yield (TEY) spectra of the unbound molecules 11-mercaptoundecanoic acid, dihydrolipoic acid, and lipoic acid in the S $L_{3,2}$-absorption regime are displayed in Figure 2.
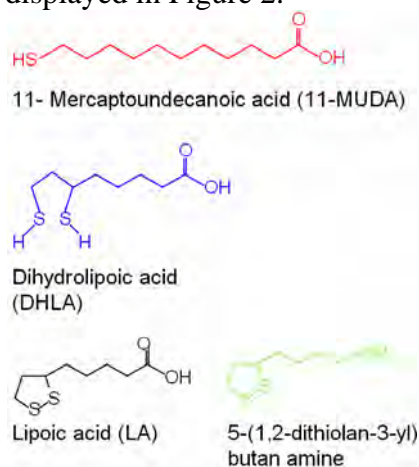
Figure 1: Mono- and bivalent sulfur containing compounds investigated in this study.
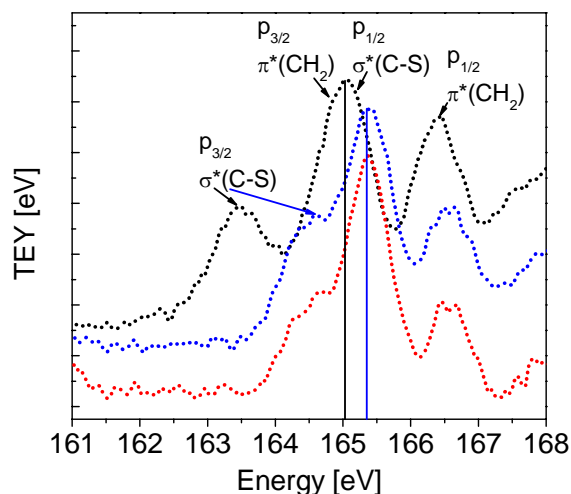
Figure 2: Total electron yield spectra of 11-MUDA (red line), DHLA (blue line) and LA (black line) in the S $L_{3,2}$ absorption regime. The two vertical lines indicate the shift of the S $L_{3,2}$ spectrum of LA compared to that of DHLA.
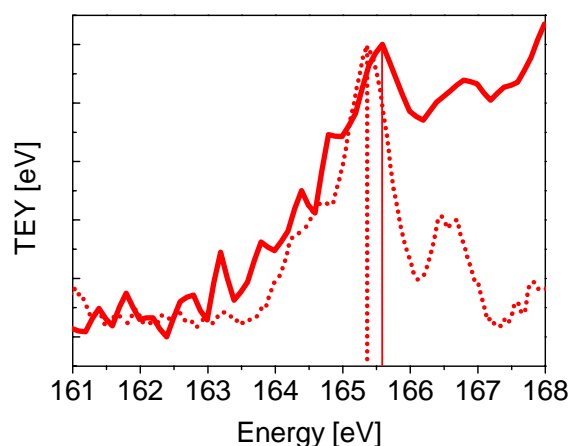
Figure 3: Total electron yield spectra of 11-MUDA bound to gold nanoparticles (red solid line) and free 11-MUDA (red dotted line) in the S $L_{3,2}$-absorption regime. The vertical lines indicate the shift between spectra of the free and the gold-bound 11-MUDA.
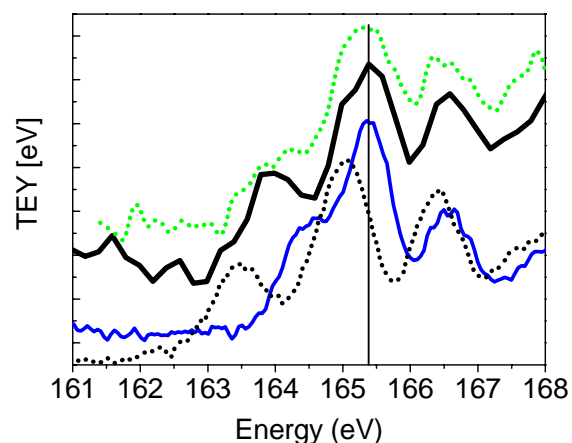
Figure 4: Total electron yield spectra of LA (black solid line) and its amino analogon (green dotted line, see chemical formula in Figure 1) both bound on gold nanoparticles in the S $L_{3,2}$ absorption regime. For a comparison the spectra of free DHLA (blue solid line) and free LA (black dotted line) are also displayed. The vertical line indicates that the spectra of gold-bound LA and 5-(1,2-dithiolan-3-yl)butan amine are not shifted compared to free DHLA.
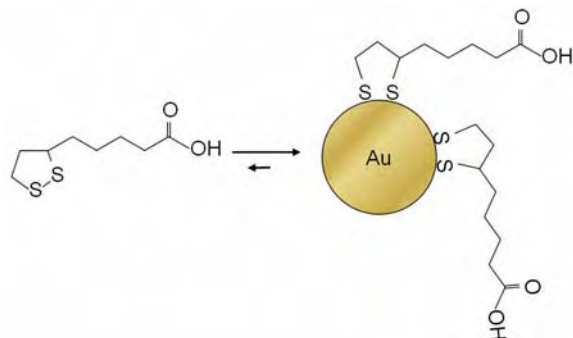
Figure 5: Schematic view of the binding of lipoic acid (LA) to a gold nanoparticle.

11-MUDA shows the typical S $L_{3,2}$-spectrum of a monovalent thiol,[6] whereas the spectrum of DHLA is slightly broadened. This can be explained by the fact that in this dithiol the two sulfur atoms are in slightly different chemical environments (see Figure 1). In contrast, in the spectrum of LA the S $p_{3/2}$ σ^*(C-S) peak is shifted to significantly lower energies and the overall of the spectrum is significantly different, as it is expected for a disulfide.[6] The S $L_{3,2}$-spectrum of 5-(1,2-dithiolan-3-yl)butan amine, also measured in this study (not shown here), is practically identical with that of the analogous acid because the 1,2-dithiolan ring is identical in both molecules.

The free nanoparticles consisting of the pure ligands yield relative intense electron yield spectra. In the case of the functionalized gold nanoparticles only monolayers on the nanoparticle surface are measured. As expected, the TEY-signal of the monolayer in the in near-edge spectra is weak and superimposed to a huge electron signal from the valence continuum. Nevertheless, it turned out that the signal strength is sufficient to take near-edge spectra of such species. Even though these experiments require relatively long acquisition times, no radiation damage was observed because continuously fresh sample entered the ionization region.

Figure 3 shows the S $L_{3,2}$-spectrum of 11-MUDA bound on 25 nm gold nanoparticles. The spectrum is shifted by about 0.2 eV to higher energies compared to the spectrum of free 11-MUDA. This result clearly indicates that also monolayers of organic ligands bound to gold nanoparticles can be investigated by this approach and that these measurements are sensitive to changes in the local electronic structure between thiol-ligands bound to free gold nanoparticles and free thiol ligands in solid nanoparticle samples.

The total electron yield spectrum of lipoic acid in the S $L_{3,2}$-absorption regime is displayed in Figure 4. Lipoic acid is a 1,2-dithiolan (a five-membered ring with two sulfur, see Figure 1). Hence, it can in principle bind on the gold nanoparticles as a closed ring forming a dative bond or by ring opening (as DHLA, see Figure 1) binding as a dithiolate. A comparison with the free lipoic acid shown in Figure 4, indicates that the gold-bound lipoic acid is significantly shifted to higher energies. Besides this, the TEY spectrum of the gold-bound lipoic acid

appears narrower and the lowest energy peak is more shifted than the other peaks. By contrast, the S $L_{3,2}$-spectrum of DHLA (blue solid line) matches much better with the S $L_{3,2}$-spectrum of the particle-bound lipoic acid. Further, particle-bound lipoic acid has a more substantially redshifted shoulder (S L_3 σ^*(C-S) resonance). Therefore, we conclude that lipoic acid mainly binds by ring opening on gold. The redshifted S L_3 peak is most likely due to a small fraction of lipoic acid, which is still present in the sample. It is well-known that the binding of thiols on gold nanoparticles in dispersion is an equilibrium process.[9] Therefore, we expect that this fraction is mainly due to free lipoic acid (see Figure 5). The S $L_{3,2}$-spectrum of 5-(1,2-dithiolan-3-yl)butan amine (the amino analogon of lipoic acid, green dotted line in Figure 4) has a similar shape as that of lipoic acid. However, the shift of the S L_3-resonance is even less pronounced. Hence, in this case the fraction of the 1,2-dithiolan (closed ring) is even lower. The binding of lipoic acid on macroscopic gold surfaces and deposited gold nanoparticles has already been studied before.[7,8] Also, the results published in refs. 7 and 8 indicate that it preferably binds as an open dithiolate by ring opening on gold. This confirms that the present approach yields reliable information on the binding of divalent thiol ligands on isolated gold nanoparticles.

Remarkably, neither the spectrum of lipoic acid, nor that of its amino analogon are shifted in energy compared to the near-edge spectrum of DHLA (see Figure 4), whereas the S $L_{3,2}$-spectrum of the monovalent gold-bound 11-MUDA is clearly blueshifted compared to the unbound 11-MUDA. This also indicates that NEXAFS is sensitive to changes between mono- and multivalent bound organic molecules. A detailed analysis of the spectral shifts and the binding of the ligands to nanoparticles are currently in progress.

In conclusion, the present results show that the high sensitivity of the experimental approach permits studies on the binding of mono- and multivalent ligands to free nanoparticles. It is possible to identify the particle-bound species by inner-shell excitation. Moreover, the present approach is sensitive to changes in the electronic structure between bound and free ligands as well as mono- and bivalent ones.

References
1. J. Rao, J. Lahiri, L. Isaacs, R.M. Weis, and G.M. Whitesides, *Science* **1998**, *280*, 708; P.I. Kitov, and D.R. Bundle, *J. Am. Chem. Soc.* **2003**, *125*, 16271; J.D. Badjic, A. Nelson, S.T. Cantrill, W.B. Turnbull, and S. Fraser-Stoddart, *Acc. Chem. Res.* **2005**, *38*, 723.
2. A. Hofmann, C. Graf, and E. Rühl, in preperation **2009**.
3. G. Frens, *Nat. Phys. Sci.* **1973**, *241*, 20.
4. H. Bresch, B. Wassermann, B. Langer, C. Graf, R. Flesch, U. Becker, B. Österreicher, T. Leisner, and E. Rühl, *Faraday Discuss.* **2008**, *137*, 389.
5. Y. Zubavichus, M. Grunze, O. Fuchs, L. Weinhardt, C. Heske, E. Umbach, and J. D. Denlinger, *Radiation Res.* **2004**, *161*, 346.
6. J. Jalilehvand, *Chem. Soc. Rev.* **2006**, *35*, 1256.
7. T.M. Willey, A.L. Vance, C. Bostedt, T. van Buuren, R.W. Meulenberg, L.J. Terminello, C.S. Fadley *Langmuir* **2004**, *20*, 4939.
8. S. Roux, B. Garcia, J.L. Bridot, M. Salome, C. Marquette, L. Lemelle, P. Gillet, L. Blum, P. Perriat, O. Tillement, *Langmuir* **2005**, *21*, 2526.
9. M. Montalti , L. Prodi , N. Zaccheroni , R. Baxter , G. Teobaldi , F. Zerbetto, *Langmuir* **2003**, *19*, 5172.

Spectroscopic characterization of self-assembled monolayers of benzylmercaptan and p-cyanobenzylmercaptan on Au(111) surfaces

T. Strunskus[a], L. Hallmann[b], V. Staemmler[d], Ch. Wöll[c], and F. Tuczek[b]

[a]Lehrstuhl für Materialverbunde, Technische Fakultät der Christian-Albrechts-Universität zu Kiel, Kaiserstr. 2, 24143 Kiel

[b]Institut für Anorganische Chemie der Christian-Albrechts-Universität zu Kiel, Otto Hahn Platz 6/7, 24098 Kiel

[c]Lehrstuhl für Physikalische Chemie 1, Ruhr-Universität Bochum, Universitätssstr. 150, 44801 Bochum

[d]Lehrstuhl für Theoretische Chemie, Ruhr-Universität Bochum, Universitätssstr. 150, 44801 Bochum

XPS

Benzylmercaptan (BM) and p-cyanobenzylmercaptan (pCBM) were deposited via a self-assembly process onto gold covered silicon wafers from ethanolic solutions. After rinsing with ethanol and drying in a stream of nitrogen gas the samples were transferred into a UHV system; then XPS and NEXAFS spectra were acquired. XPS and NEXAFS experiments were performed at the HE-SGM beamline. XPS spectra were acquired in normal emission geometry at photon energies of 500 eV for the N 1s, 400 eV for the C 1s and 300 eV for the S 2p region, respectively.

The XPS spectra are in accordance with the chemical formulas of the deposited molecules. The intensity of the cyano carbon in the C 1s spectrum in Fig. 1 amounts to 20%, which appears to be enhanced as compared to the stoichiometric ratio of 1:7 applying to pCBM. The deviation from stoichiometry can be explained by the high orientational order of the film, where all the cyano groups are located on the outermost layer, and by the relatively small electron mean free path of only 0.9 nm for photoelectrons at a kinetic energy of about 115 eV. In addition, our calculations indicate that the C 1s lines of the carbon atom in para position to the cyano group and of the methylene carbon should be shifted by 0.5 and 0.7 eV to higher binding energy relative to the other carbon atoms in the benzene ring. The XP spectra do not show any additional oxidized species indicating the stability of the prepared films against oxidation in air.
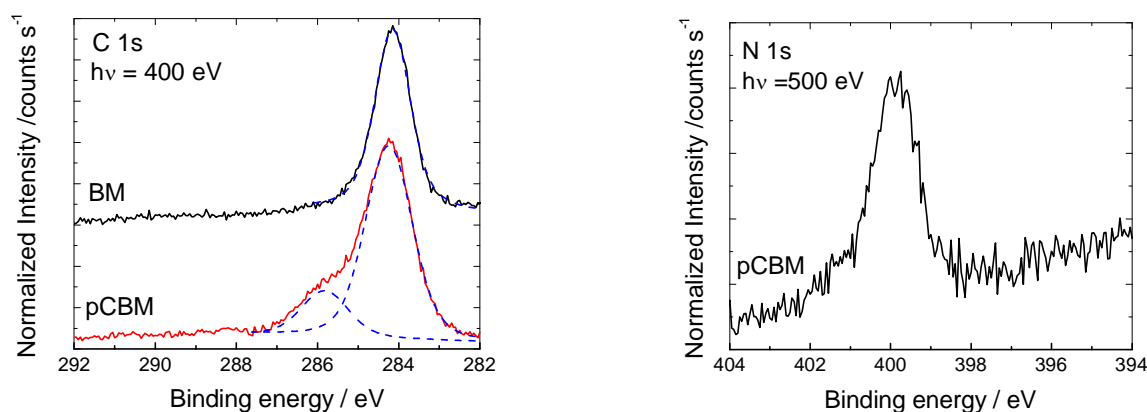
Fig.1 Synchrotron C 1s and N 1s spectra of a benzyl mercaptane (BM) and p-cyano benzyl mercaptane (pCBM) self assembled monolayer on a Au(111) surface.

NEXAFS

NEXAFS spectra were acquired in the partial electron yield mode with a retarding voltage of –150 V at the C K-edge and –250 V at the N K-edge. Linear polarized synchrotron light with a polarization factor P of $\approx 82\%$ was used. Energy resolution was ≈ 0.40 eV. The incidence angle of the light was varied from 90° (E-vector in surface plane) to 30° (E-vector near surface normal). The raw NEXAFS spectra were normalized to the incident photon flux by

division through a spectrum of a clean, freshly sputtered gold sample. The energy scale was referenced to the pronounced π^* resonance of highly oriented pyrolytic graphite at 285.38 eV. NEXAFS spectra measured at the C edge for BM and pCBM are displayed in Figures 2a and 2b, respectively. The assignments of the resonances are summarized in Table 1. BM and pCBM essentially show the same resonances at the carbon edge, but the presence of the cyano group leads to three additional π^* resonances in the case of pCBM. It is interesting to note that the intensity of the first π^* resonance of the benzene ring appears to be more pronounced for BM as compared to pCBM. This could indicate that intensity is shifted to the resonances at higher photon energies due to the presence of the cyano group. More detailed assignments of the resonances are given below. For both SAMs the dichroism of pronounced π^* resonance of the benzene ring has been used to determine the orientation of the phenyl ring relative to the surface normal. The angular analysis was performed as described in ref. [1]. For BM the molecular backbone shows a tilt angle of $19\pm5°$ relative to the surface normal whereas for pCBM a tilt angle of $21\pm5°$ was determined.

In the NEXAFS spectrum of pCBM at the N K edge spectrum three π^* resonances are observed. Their positions and assignments are summarized in Table 2. The angular dependence of the π^* resonance of the nitrile group has been analysed in the same way as the π^* resonance of the benzene ring. In this case a tilt angle of $18\pm5°$ was obtained which is close to the $21\pm5°$ observed for the benzene ring at the C K edge.
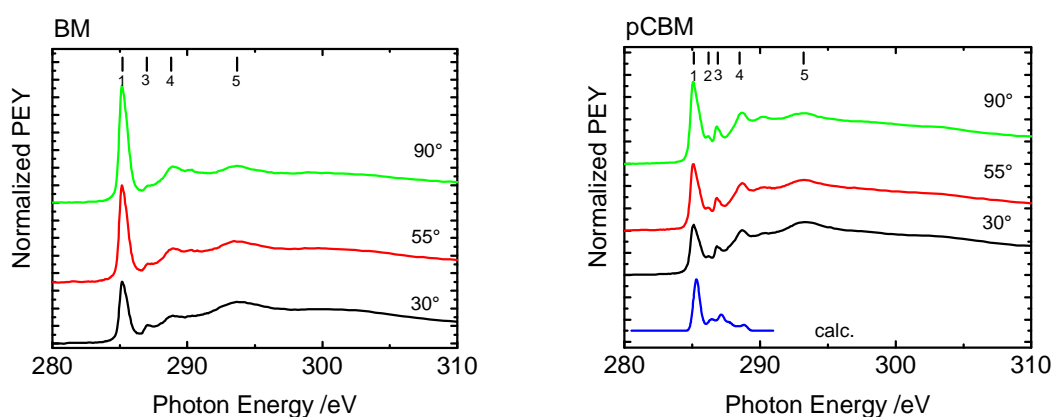
Fig .2 NEXAFS spectra measured at the C K edge for a) BM and b) pCBM. The angles at the curves specify the angles of light incidence relative to the surface. The lines on the top indicate the positions of the resonances and are summerized in table 1. In b) also the calculated spectrum is included for comparison (the calculated transitions were broadened by Gaussian curves with 0.2 eV FWHM).

Table 1.

Resonance	Energy/eV BM	Energy/eV pCBM	Assignment
1	285.2	285.1	π_1^* benzene ring
2	-	286.2	π_1^* cyano carbon
3	287.0	286.9	C-H*, π_2^* cyano carbon
4	288.8	288.5	π_2^* benzene ring, π_3^* cyano carbon
5	293.7	293.2	σ^* benzene ring

The calculations of the NEXAFS spectra were performed using the Bochum suite of open-shell wave function based quantum chemical ab initio programs in a similar way as in our previous studies of NEXAFS spectra [2]. The NEXAFS spectra for BM and pCBM at the carbon K edge closely resemble the spectra expected for benzene and benzonitrile, respectively. There is only a small contribution of the methylene carbon to the spectra which is also supported by the results of our theoretical calculations for pCBM. The C atom of the CH_2SH group has only single bonds to its neighbours and therefore no strong π^* transitions.

The NEXAFS spectrum of the C K edge of pCBM shows a pronounced fine structure indicating the presence of several distinct resonances. The reason is that pCBM contains six types of non-equivalent C atoms which give rise to slightly different ionization thresholds and consequently also to different NEXAFS spectra. The calculated total spectrum shown in Fig. 2b (bottom) is a superposition of the spectra of all eight C atoms. The C atoms in the benzene ring give rise to only one strong NEXAFS transition of π^* character and some weaker π^* and σ^* transitions.

The spectrum for the nitrile C atom closely resembles the one of the N K edge spectrum presented below, with three strong peaks possessing π^* character. Two of the resonances overlap with resonances present also in BM (see Table 1). Therefore the most pronounced contributions of the cyano group lead to the new resonances at 286.2 eV and a pronounced intensity increase of the resonance located at 286.9 eV.

pCBM

N K

90°

55°

30°

Calc.

1 2 3
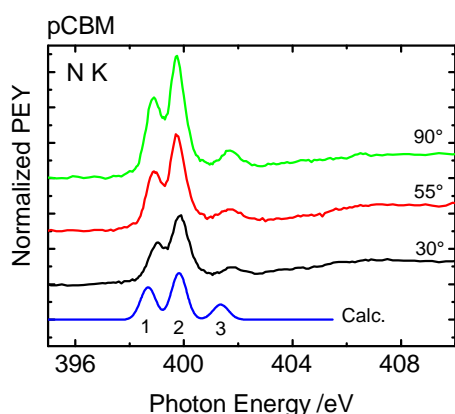
Table 2. Resonances of pCBM at the nitrogen K edge and assignments

Resonance	Energy/eV	Assignment
1	398.9	CN π^*, out-of-plane*
2	399.8	CN π^*, in-plane*
3	401.7	CN π^*, out-of-plane*

* "out-of-plane" = perpendicular to the plane of benzene ring; "in-plane" = in the plane of benzene ring

Fig .7 NEXAFS spectra measured at the N K edge for pCBM. The angles at the curves specify the angles of light incidence relative to the surface. Numbers indicate the resonances as assigned in table 2. A calculated spectrum is included for comparison (the calculated transitions were broadened by Gaussian curves with 0.4 eV FWHM to mimic the experimental resolution.

At the nitrogen K edge there is a very good agreement between experiment and calculation. The N K edge NEXAFS spectrum of pCBM shows three strong bands positioned at 398.9, 399.8 and 401.7 eV. All of them are C-N π^* valence excitations. The second, strongest band at 399.8 eV can be assigned to the excitation from N 1s into the "in-plane" component of the two-fold degenerate C-N π^* orbital, perpendicular to the long axis of the molecule. In the other two bands the excitation leads from N 1s into two linear combinations of the "out-of-plane" π^* orbital of C-N and the π^* orbitals of the benzene ring. The orbital in the lower state at 398.9 eV is primarily localized at CN and has therefore a higher intensity, while the one at 401.7 eV is mainly localized at the benzene ring. It should be noted that the sum of the intensities of the out-of-plane excitations at 398.9 eV and 401.7 eV matches almost exactly the one of the in-plane excitation at 399.8 eV. These three resonances appear only when the cyano group is electronically coupled to the π-system of the benzene ring. For an isolated cyano group as in a nitrile functionalized alkanethiol only one π^* resonance is observed at the N K edge at 400.8 eV [3].

References
1. Dmitriev, A.; Spillmann, H.; Stepanow, S.; Strunskus, T.; Wöll, Ch.; Seitsonen, P. A.; Lingenfelder, M.; Lin, N.; Barth, V. J; Kern. K. *Chem. Phys. Chem.* **2006**, *7*, 2197.
2. Reiss, S.; Krumm, H.; Niklewsi, A.; Staemmler, V.; Wöll, Ch. *J. Chem. Phys.* **2002**, *116*, 7704.
3. Frey, S.; Shaporenko, A.; Zharnikov, M.; Harder, P.; Allara, L. D. *J. Phys. Chem. B,* **2003**, *107,* 7716.

Characterization of a novel water-oxidizing cobalt catalyst by X-ray absorption spectroscopy

M. Risch, V. Khare, A. Grundmeier, O. Sanganas, L. Gerencser, I. Zaharieva, S. Löscher, P. Chernev, M. Haumann, H. Dau[*]

Freie Universität Berlin, Institut für Experimentalphysik, 14195 Berlin, Germany
*holger.dau@physik.fu-berlin.de

Water oxidation occurs by the abstraction of four electrons and four protons from two water (H_2O) molecules resulting in O_2 formation. In nature, only one enzyme, a photosynthetic protein complex termed photosystem II (PSII), is capable of this reaction, delivering the O_2 of the atmosphere [1,2]. Efficient water oxidation is also of prime interest for the production of hydrogen (H_2), the fuel of the future. Therefore, in a worldwide strive, chemists search for synthetic catalysts for efficient water oxidation by low-cost catalysts.

Recently several new transition-metal based synthetic compounds for water oxidation have been reported [3]. In particular, a recently introduced system using cobalt as the active metal [4,5] has attracted much interest. This catalyst is "spontaneously" assembled as a thin layer by electrodeposition on ITO electrodes from aqueous solution of cobalt and phosphate salts. Its self-assembly and self-repair mechanism bears similarities to the biological formation of the manganese complex of water oxidation in PSII [6]. The atomic structure of the cobalt catalyst so far has been unknown.

For the first time, we studied the cobalt catalyst by X-ray absorption spectroscopy (XAS) and determined the Co oxidation state and coordination environment. The results enable us to postulate possible structural features, e.g. Co-Co bridging by di-µ-oxo bridges, which may be related to the function of the catalyst. A respective publication is in preparation [7].

Experimental. The cobalt catalyst was prepared as described in [2]. The catalytic film was either scratched off the ITO electrode and dried to yield XAS samples or the wet native film on the ITO support was directly studied after freezing (quasi *in-situ*). $Co^{II}(OH_2)_6(NO_2)_3$ and $Co^{III}(NH_3)_6$ samples served as oxidation state standards. XAS at the Co K-edge (7709 eV) was performed at beamline KMC-1 at 20 K using a liquid-helium cryostat. A photodiode shielded by Fe foil against scattered incident X-rays served as an X-ray fluorescence detector.
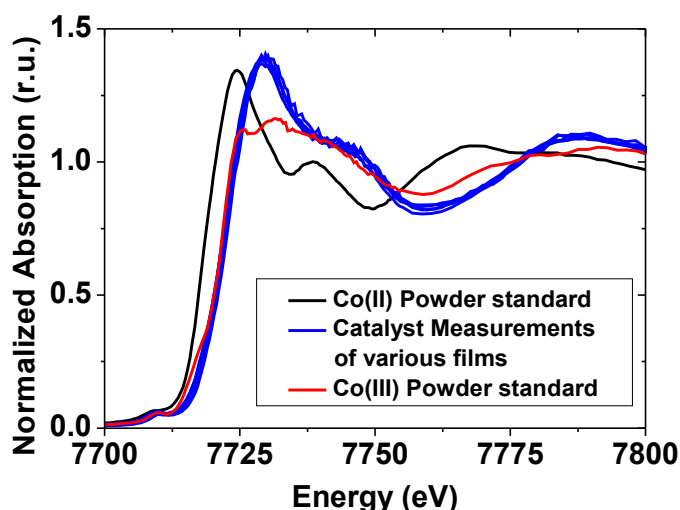
Figure 1: XANES spectra of the Cobalt catalyst and of Co(II) and Co(III) standards. The Co in the catalyst was in the Co(III) oxidation state, as apparent from the similar edge energy as in the Co(III) standard, no matter whether the native film on the ITO electrode or a dried powder of the scratched-off film was studied. Accordingly, the material of the catalytic film appears to be 'robust' against mechanical treatment and dehydration.

Figure 1 shows XANES spectra of the Co catalyst. The edge energies of the native wet Co film on the ITO electrode and the dried scratched-off powder were similar to that of a Co(III) standard. Thus, the Co film almost exclusively contains Co(III). If at all, Co(IV) was present only in very minor amounts. The unchanged K-edge of the Co catalyst in the two conditions suggests that it is robust against dehydration, air-exposure, and mechanical treatment.
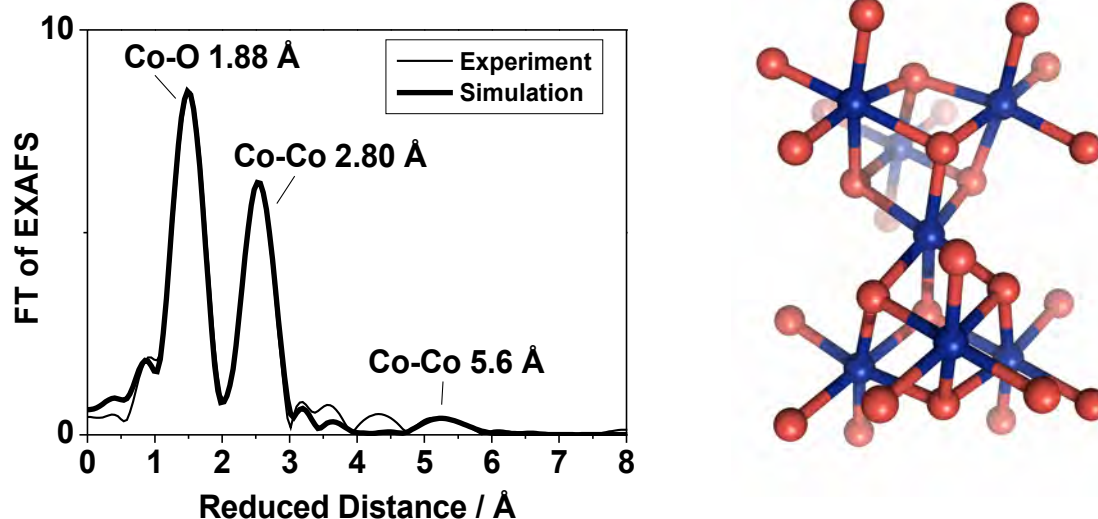
Figure 2: (left) Fourier-transform of an EXAFS spectrum of the native Co catalyst. The main Co-Co distance (2.8 Å) is well determined. (right) Possible structural motif of the Co catalyst in agreement with the XAS-detected interatomic distances and Co coordination numbers (blue, Co; red, O).

Figure 2 shows the FT of an EXAFS spectrum of the native Co catalyst on ITO. The primary Co ligation by ~6 oxygen atoms at a distance of 1.89 Å was determined from a simulation and is well compatible with Co(III). A prominent Co-Co distance of 2.80 Å accounted for at least 3-4 metal-metal interactions per Co ion. There was also evidence for longer Co-Co distances. Interestingly, no positive evidence for the presence of phosphorus in the 1st and 2nd coordination spheres of Co was obtained. However, it can not be fully excluded that 1-2 Co-P interactions at ~2.9 Å may be hidden in the Co-Co FT peak (Fig. 2). This result is remarkable as phosphorus may have a key function in the self-assembly of the catalyst [4].

In summary, first XAS measurements on a novel water-splitting cobalt catalyst have been performed successfully. Our results allow construction of atomic models for the overall structure of the Co(III) catalyst, which may comprise complete or incomplete Co-oxo cubanes ($Co_4(\mu_3\text{-}O)_4$ or $Co_3(\mu_3\text{-}O)_4$ units) [7]. Further XAS experiments at KMC-1, inter alia to follow the assembly of the Co catalyst, are in preparation.

[1] Dau H and Haumann M, *Coord. Chem. Rev.* **2522**, 273-295 (2008).
[2] Haumann M, Grundmeier A, Zaharieva I, Dau H, *Proc. Natl. Acad. Sci. USA* **105**, 17384 (2008).
[3] Meyer TJ, *Nature* **451**, 778 (2008).
[4] Kanan MW, Nocera DG, *Science* **321**, 1072-1075 (2008).
[5] Kanan MW, Surendranath Y, Nocera DG, *Chem. Soc. Rev.* **38**, 109-114 (2009).
[6] Barra M, Haumann M, Loja P, Krivanek R, Grundmeier A, Dau H, *Biochemistry* **45**, 14523 (2006).
[7] Risch M, Khare V, Dau H et al. Manuscript in preparation (2009).

X-ray study of the fluorinated double-wall carbon nanotubes produced using different fluorination methods

Yu.V. Lavskaya[a], L.G. Bulusheva[a], A.V.Okotrub[a], V.O. Koroteev[a], A. Felten[b], E. Flahaut[c], D.V. Vyalikh[d]

[a]*Nikolaev Institute of Inorganic Chemistry, SB RAS, Novosibirsk, Russia*
[b]*Laboratoire Interdisciplinaire de Spectroscopie Electronique, Facultes Universitaires Notre Dame de la Paix, Belgium*
[c]*Centre InteruniVersitaire de Recherche et d'Ingenierie des Materiaux, UniVersite Paul-Sabatier, France*
[d]*Institute of Solid State Physics, Dresden University of Technology, Germany*

Near-edge x-ray absorption fine structure (NEXAFS) spectroscopy and x-ray photoelectron spectroscopy (XPS) have been applied to investigate how synthetic conditions influence on the electronic structure of the fluorinated double-wall carbon nanotubes (DWNTs). The DWNTs were produced by catalytic chemical vapor deposition technique [1] in the result of CH_4 decomposition over $Mg_{0.9}Co_{0.1}O$ containing additions of molybdenum oxide. The fluorinated DWNTs were prepared using three different methods. The sample denoted with F-DWNT (BrF_3) was produced using the fluorination procedure described in [2]. The DWNTs were held in the vapor over a solution of Br_2 and BrF_3 for 7 days and thereafter, the sample was dried by a flow of N_2 until the removal of Br_2. The F-DWNT (CF_4) sample was obtained by CF_4 plasma treatment (plasma frequency is 13.56 MHz, power is 15 Watt, a chamber pressure is 0.1 Torr, exposure time is 10 min) [3]. The sample F-DWNT (F_2) was synthesized using elemental fluorine flow at 200ºC.

The C K- and F K- edge NEXAFS and C 1s XPS spectra were measured at the Berliner Elektronenspeicherring für Synchrotronstrahlung (BESSY) using radiation from the Russian-German beamline. The C 1s XPS spectra were measured at the energy of monochromatized synchrotron radiation equals to 350 eV with energy resolution of 0.2 eV. The NEXAFS spectra were acquired in a total electron yield mode and normalized to the primary photon current from a gold-covered grid. The monochromatization of the incident radiation was ~100 meV in the carbon absorption region and ~410 meV in the fluorine absorption region. Before the experiments the samples were annealed at 70°C during 12 hours to removal a residual gas.

Figure 1 compares the C1s XPS spectra of the initial and the fluorinated DWNTs. The spectrum of the initial DWNT has a single assymetric peak at 284.5 eV. All spectra of the fluorinated DWNTs show three main peaks corresponding to different chemical states of carbon atoms. The peak C at 284.5 eV is referred to non-grafted carbon, the peak C-F in the range 288.0÷288.5 eV is attributed to the carbon atoms covalently bonded to the fluorine atoms and the feature in the range 285.2÷285.7 eV corresponds to the carbon atoms positioned near the CF groups. It should be noted that the features corresponding to CF_2 and CF_3 groups are absent in the spectra. One can see that the intensities of the selected peaks are varied depending on the fluorination method. The C 1s XPS spectra were fitted using a combination of three components with a Gaussian-Lorentzian peak shape with a Doniach-Sunjic high energy tail. The

Fig. 1. C 1s XPS spectra of pristine DWNTs (1) and those fluorinated by CF_4 plasma (2), BrF_3 (3) and F_2 (4).

Table 1. The position of main components in the C 1s XPS spectra and chemical composition of the fluorinated DWNTs

	E_C	E_{C-CF}	E_{C-F}	CF_x
F-DWNT (CF_4)	284.5	285.2	288.0	$CF_{0.17}$
F-DWNT (BrF_3)	284.5	285.4	288.2	$CF_{0.22}$
F-DWNT (F_2)	284.5	285.7	288.5	$CF_{0.33}$

component positions E_C, E_{C-CF}, E_{C-F} and chemical compositions CF_x of the fluorinated DWNTs are presented in the Table 1. The integral intensities of the components, S_C, S_{C-CF}, and S_{C-F}, were used to estimate the sample composition CF_x by a formula $x=S_{C-F}/(S_C+S_{C-CF}+S_{C-F})$. The largest amount of fluorine is attached to DWNT surface using F_2 as a fluorinating agent. The energy of C-CF and C-F components increases when sample contains more fluorine that indicates stronger C-F bond for high fluorinated nanotubes.

The C K-edge NEXAFS spectra of the initial and fluorinated DWNTs are shown in Fig. 2 (top series). The all spectra exhibit three main features and peaks at ~285.4 and ~291.7 eV correspond to π^* and σ^* resonances, respectively. The peak labeled with D positioned between 286.5 and 290.5 eV is attributed to $1s\rightarrow\sigma^*$ transition included C-F bond. The largest reduction of π^* resonance is observed in the spectrum of F-DWNT (F_2) sample. In case of F-DWNT (CF_4), intensity of π^* resonance increases compared to that of pristine DWNTs. We associate this effect with removal of defects in the DWNTs shells after CF_4 plasma treatment. The F K-edge NEXAFS spectra of the fluorinated samples (Fig.2 bottom series) were aligned to the C K-edge spectra using the C 1s and F 1s core levels energies. The spectra show three peaks at the energies 690.4, 692.7 and 695.8 eV labeled with A, B and C, respectively. Position of the peak C coincides with the σ^* resonance of the C K-edge NEXAFS spectrum and, hence, can be attributed to the σ^* absorption edge. The peaks A and B, which are aligned with the peak D of the C K-edge spectra, correspond to the C-F interactions. Our quantum-chemical calculations showed that the peak B corresponds to the σ-type antiboding between fluorine and carbon atoms from the CF-group, the peak A is formed due to interaction of fluorine with carbon atoms situated at the CF-group. The lack of the peak A in the F K-edge NEXAFS spectrum of the F-DWNT (F_2) sample is due to high fluorine coverage of nanotube surface.
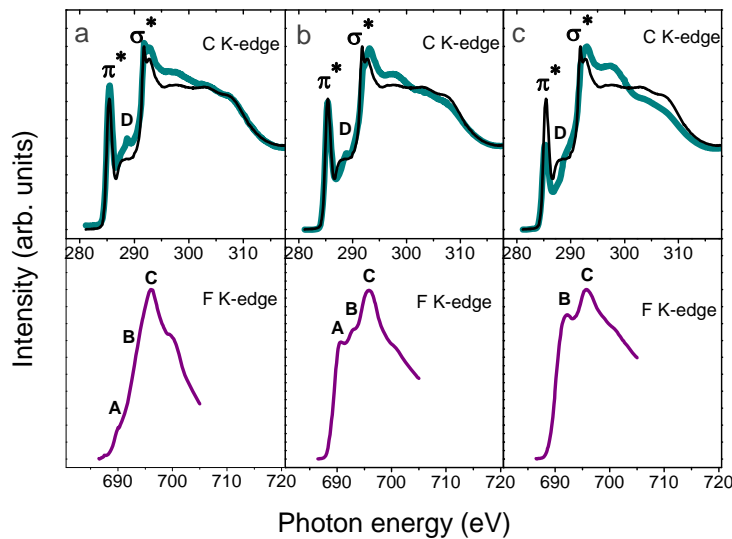
Fig. 2. NEXAFS near C K-edge (dark cyan line) and near F K-edge (purple line) spectra of F-DWNT(CF_4) – a, F-DWNT(BrF_3) – b, F-DWNT(F_2) – c. C K-edge spectrum of the initial DWNTs showed by black line.

[1] E. Flahaut, R. Bacsa, A. Peigney, Ch. Laurent. Chem. Commun. (2003) 1442-1443.
[2] N.F. Yudanov, A.V. Okotrub, Yu.V. Shubin, L.I. Yudanova, L.G. Bulusheva, A.L. Chuvilin, et al. Chem. Mater. 14 (2002) 1472-1476.
[3] A. Felten, C. Bittencout, J.J. Pireaux, G. Van Lier, J.C. Charlier. J. Appl. Phys. 98 (2005) 074308.

XAFS study of the local structure and oxidation state of Cu impurity atoms in doped CdSe and CdSe/CdS core/shell quantum dots

A.I. Lebedev[1], I.A. Sluchinskaya[1], S.G. Dorofeev[2], P.N.Tananaev[2], A. Erko[3]

[1] *Physics Dept., Moscow State University, Moscow, 119992, Russia*
[2] *Chemistry Dept., Moscow State University, Moscow, 119992, Russia*
[3] *BESSY GmbH, Albert Einstein Str. 15, 12489 Berlin, Germany*

Quantum dots (QD) conjugated to biological molecules are promising luminescent markers, which can be used for molecular recognition of antigens and for labeling of specific compartments of cells in nanobiotechnology [1,2]. Unfortunately, conjugates with undoped quantum dots cannot be used *in vitro* because of strong absorption of luminescence by biological tissue and closeness of the luminescence decay times of QD and biological tissue. Shifting of luminescence spectra to red and infrared regions and slowing down of luminescence decay can greatly improve the sensitivity of this method. Doping of CdSe/CdS core/shell quantum dots with copper enables to achieve this purpose. However the nature of copper-containing luminescence centers is not known, and the first step in their investigation is the determination of the local structure and oxidation state of Cu in doped CdSe quantum dots.

The aim of our experiment was to determine the location and oxidation state of Cu atoms in doped CdSe and CdSe/CdS core/shell quantum dots using XAFS technique.

The samples studied were Cu-doped colloidal CdSe and CdSe/CdS core/shell quantum dots capped with oleic acid [3,4]. The samples were doped by three different routes: by using of copper stearate or $Cu_4I_4(PPh_3)_4$ as precursors during the QD synthesis, and by "etching" of undoped quantum dots in the copper stearate solution. For XAFS studies concentrated solutions of QD in dodecane were placed into silica tubes with very thin walls.

X-ray absorption spectra were collected at the Cu K edge (8.979 keV) in fluorescent mode on the station KMC-2. The intensity of monochromated radiation was measured with an ionisation chamber; the intensity of fluorescent radiation was measured with a p-i-n-diode or an energy-dispersive RÖNTEC detector. For each sample 5–7 spectra were recorded at 300 K, they were then independently processed and the obtained spectra were finally averaged. A few additional EXAFS spectra were collected at the Se K edge (12658 eV) to check the structure of QD. The analysis of EXAFS spectra was performed in the traditional way.

The X-ray fluorescence analysis of ten Cu-doped samples of CdSe and CdSe/CdS core/shell colloidal quantum dots was used to determine the concentration of copper in them. Six samples with highest concentration of Cu (0.3–4.5%) were selected for further EXAFS experiments. It was observed that the larger was the radius of quantum dots, the larger amount of Cu could be incorporated into them.

To estimate the oxidation state of Cu in QD, XANES spectra for five Cu-containing reference samples (CuSe with klockmannite structure, Cu_2Se with berzelianite structure, $CaCu_3Ti_4O_{12}$, Cu metal and copper stearate) were measured. The spectra for two typical samples of QD are compared with XANES spectra for Cu_2Se and copper stearate reference compounds in Fig. 1. It is seen that the XANES structure for QD prepared in different conditions have a different shape. In most of QD the Cu oxidation state was +1; only two samples prepared using copper stearate as a precursor demonstrated a shoulder at 8986 eV (see Fig. 1), thus indicating that 15–20% of Cu atoms in QD were in the +2 oxidation state. It is interesting that in the samples "etched" in the copper stearate solution all Cu atoms remained in +1 oxidation state.

The analysis of EXAFS spectra obtained at the Cu K edge revealed two types of local structures. In samples, in which all Cu atoms were in +1 oxidation state, the neighboring Se atoms were located at a distance of 2.38±0.01 Å. For samples with both +1 and +2 oxidation states of Cu the Cu-Se distance was shorter and equal to 2.31–2.33 Å and an additional signal from oxygen atoms at a distance of 1.93–1.94 Å was detected (see Fig. 2). The number of O neighbors was 4–8 times smaller than the number of Se neighbors.
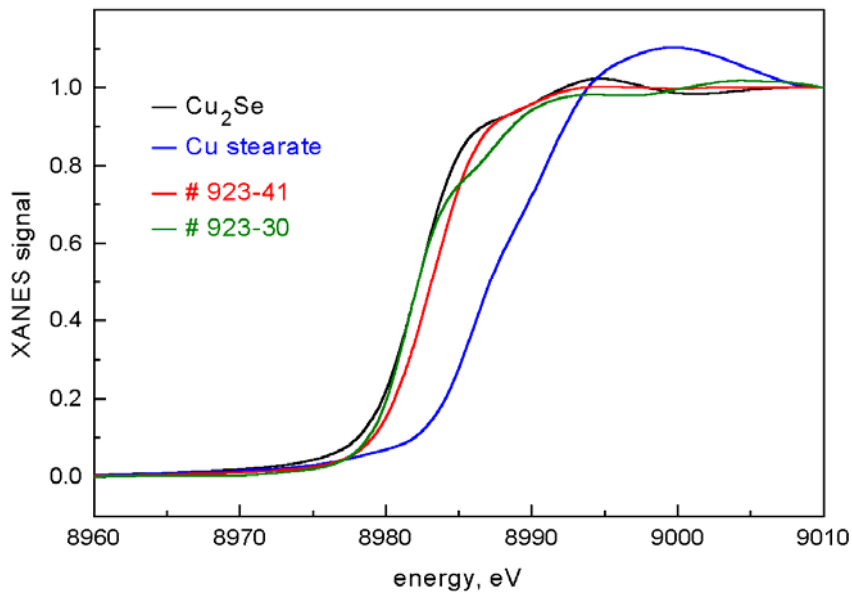
Fig. 1. XANES spectra obtained at the Cu K edge for two reference compounds (Cu$_2$Se and copper stearate) and two Cu-doped CdSe colloidal quantum dots.
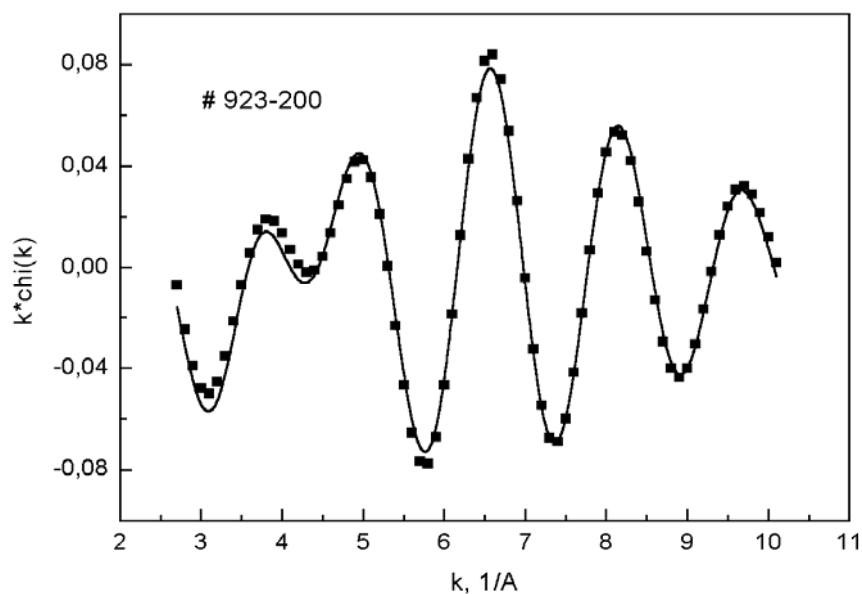
Fig. 2. EXAFS spectra obtained at the Cu K edge for CdSe colloidal quantum dots doped using copper stearate precursor.

We think that in the samples, where a part of Cu atoms are in +2 oxidation state, copper atoms are located on the surface of QD and are bounded with oxygen atoms of oleic acid. As a result of Cu-O interaction, the oxidation state of Cu changes from +1 to +2. In all other samples the Cu atoms are located in the inner part of quantum dots and are in +1 oxidation state.

Another interesting feature of most of studied colloidal QD is a very small contributions from the second and more distant shells to EXAFS spectra obtained at the Cu K edge. Debye-Waller factor for Cu-Se bond (the first shell) was about 0.008 Å^2, which is typical for thermal motion at 300 K, and so the local distortion of Cu atom in tetrahedra can be excluded. This means that some unusual kind of static disorder is present in CdSe QD. The only exclusion was

the sample # 923-42, the QD of which had a tetrapod shape; strong contributions from the second and more distant shells were observed in EXAFS spectra for this sample.

The data analysis of EXAFS spectra obtained at the Se *K* edge revealed very similar Se-Cd distances of 2.61 Å in the first shell for all samples, independent of whether QD had a round or tetrapod shape. An interesting effect of increasing of coordination number in the first shell by about 20% was observed for CdSe quantum dots covered by CdS (core/shell QD). We suppose that in pure CdSe quantum dot some Se atoms are located on its surface, and so they have a decreased (2–3) number of Cd neighbors. After covering its surface with a few atomic layers of CdS, the number of Cd atoms that surround Se increases to 4, and the average coordination number also increases.

References

1. M.J. Bruchez, M. Moronne, P.Gin et al. Science **281**, 2013 (1998).
2. W.C.W. Chan, S. Nie. Science **281**, 2016 (1998).
3. R.B. Vasiliev, S.G. Dorofeev, D.N. Dirin, D.A. Belov, T.A. Kuznetsova. Mendeleev Commun. **14**, 169 (2004).
4. P.N. Tananaev, S.G. Dorofeev, R.B. Vasiliev, T.A. Kuznetsova. Inorg. Mater. **45**, N 3 (2009) (in press).

Effective control of palladium catalytic selectivity by surface doping and structure

Dmitry Zemlyanov[1,2], Bernhard Klötzer[3], Axel Knop-Gericke[4], Robert Schlögl[4]

[1] *Materials and Surface Science Institute, University of Limerick, Limerick, Ireland*
[2] *Birck Nanotechnology Center, Purdue University, West Lafayette, IN 47907-2057, USA*
[3] *Institut für Physikalische Chemie, Universität Innsbruck, A-6020, Innsbruck, Austria*
[4] *Fritz-Haber-Institut der Max-Planck-Gesellschaft, Faradayweg 4-6, D-14195 Berlin, Germany*

Palladium is considered as the best catalyst for the catalytic combustion/partial oxidation of methane and other small hydrocarbons, which is an environmentally benign process for power generation with low NO_x emissions and for removal of residual methane from the emission gases of methane-powered vehicles [1]. Investigation of the oxidation mechanism of palladium and the mechanism of oxide decomposition is critical for developing/improving Pd-based catalysts. Palladium oxidation was found to consist of formation of several partly metastable surface oxide phases [2-4]. The methane/ethylene total oxidation mechanisms were proposed based on this study [5, 6]. Doping is also effective tool to control activity/selectivity of a catalytic reaction can be ruled. We have studied the subsurface-carbon doped Pd [5] and the intermetallic Pd/Zn formed on Pd(111) because an ordered PdZn surface alloy forms an valence band structure similar to those of Cu(111), explaining the similar catalytic activity of PdZn and Cu in methanol steam reforming (MSR) and water gas shift reaction.

The goal is to investigate how the palladium chemistry depends on the stereo-electronic influence of these different dopants. Investigation of the electronic state of palladium and the mechanism of formation/decomposition of Pd-O, Pd-C and intermetallic Pd surfaces is critical for developing/improving Pd-based catalysts. This project continues our *in-situ* XPS study of model palladium catalysts for selective ethylene/methanol oxidation, methanol steam reforming, water gas shift and selective hydrogenation. PdZn and PdGa surface alloys formed on the surface of Pd(111) and Pd(110) serve as novel model catalysts.

First, we investigated thermal stability of the PdZn alloy in vacuum. Zinc was deposed on Pd(111) surface at room temperature and then heated in vacuum. Two Pd 3d components corresponding to Zn-rich and Zn-lean phase were monitored as shown in Figure 1. The transformation from the Zn-rich phase to the Zn-lean phase occurred above 260°C
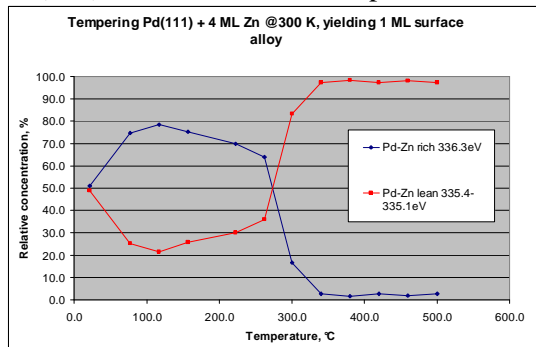
Figure 1. Heating PdZn alloy in vacuum.

We found that on Zn-doped Pd, both methanol decomposition and MSR yield mainly CO_2 and H_2CO up to 260°C, in contrast to Zn-free Pd, mainly yielding CO and strongly deactivating with carbon. Above ~260°C the selectivity of the Zn-doped Pd also changes toward CO due to carbon dissolution in the Pd bulk and progressive decomposition of the PdZn alloy. The surface most active toward CO_2 consists of regular arrays of PdZn islands of 180 - 200 nm size. Above 300°C the regular PdZn structure decomposes and large, likely Zn-rich, islands segregate and Pd/C "alloy" forms.
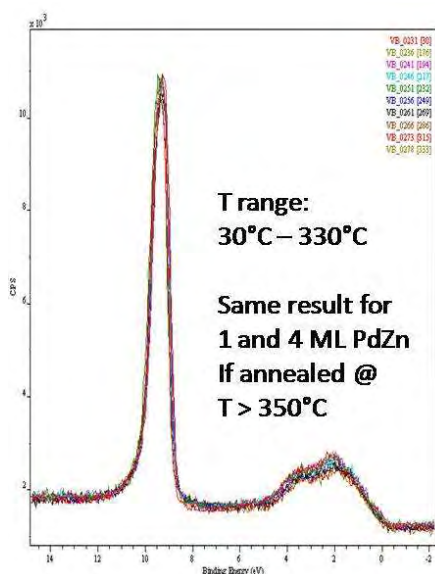
Figure 2. The valence band spectra obtained from PdZn-alloy during heating in 0.25 mbar MeOH/H$_2$O.

The pressure gap was localized in between 0.25 and 30 mbar. Thus, the PdZn-alloy becomes structurally strongly altered during the catalytic measurements at ~30 mbar: (i) the originally densely arranged alloy islands spatially separate at 230°C; (ii) at higher successive deactivation of the CO$_2$ + HCHO formation and activation of steady CO-formation, due to increasing Pd metal surface was detected; (iii) at 350°C larger amounts of C become deposited and dissolved, successively deactivating the surface in analogy to clean Pd. At low MeOH/H$_2$O pressure of 0.25 mbar the alloy is stable and the deactivation is much slower. The valence band does not change up to 300°C (Figure 2).

Since gallium might have similar to zinc electronic effect on Pd, Zn doping was replaced with Ga. First, we developed the procedure of preparation of PdGa alloyed surface: (i) Ga$_2$O$_3$ was deposed on the surface of Pd foil and Pd(111) and then (ii) gallium oxide was reduced in vacuum or in H$_2$ (Figure 3). Actually, at 250°C reduction is kinetically limited: The sharp Ga 3d peaks appear after 40min in H$_2$ (inset of Figure 2). PdGa alloy formation on Pd(111) surface occured at 350°C. The higher temperature compare with palladium foil points to importance of the surface packing on alloy formation. Pd foil surface is supposed to have a lot of defects and therefore PdGa alloy forms at lower temperature.

The valence band regions of PdZn, PdGa and pure Pd are compared in Figure 4. The spectra from the PdZn and PdGa surface alloy are very similar, therefore catalytic behavior for this surfaces is expected to be similar. The kinetic measurements are in the progress now.

Figure 3. The valence band/Ga 3d spectra demonstrating PdGa alloy formation on Pd foil. Keeping in H$_2$ at 250°C for 40 min resulted in PdGa alloy appearance as shown in inset.

References

[1]   G. Zhu, J. Han, D.Y. Zemlyanov and F.H. Ribeiro, Journal of the American Chemical Society 126 (2004) 9896.

[2]   H. Gabasch, W. Unterberger, K. Hayek, B. Klötzer, G. Kresse, C. Klein, M. Schmid and P. Varga, Surface Science 600 (2006) 205.

[3]   D. Zemlyanov, B. Aszalos-Kiss, E. Kleimenov, D. Teschner, S. Zafeiratos, M. Haevecker, A. Knop-Gericke, R. Schloegl, H. Gabasch, W. Unterberger, K. Hayek and B. Kloetzer, Surface Science 600 (2006) 983.

[4]   H. Gabasch, W. Unterberger, K. Hayek, B. Kloetzer, E. Kleimenov, D. Teschner, S. Zafeiratos, M. Haevecker, A. Knop-Gericke, R. Schloegl, J. Han, F.H. Ribeiro, B. Aszalos-Kiss, T. Curtin and D. Zemlyanov, Surface Science 600 (2006) 2980.

[5]   H. Gabasch, E. Kleimenov, D. Teschner, S. Zafeiratos, M. Havecker, A. Knop-Gericke, R. Schlogl, D. Zemlyanov, B. Aszalos-Kiss, K. Hayek and B. Klotzer, Journal of Catalysis 242 (2006) 340.

[6]   H. Gabasch, K. Hayek, B. Kloetzer, W. Unterberger, E. Kleimenov, D. Teschner, S. Zafeiratos, M. Haevecker, A. Knop-Gericke, R. Schloegl, B. Aszalos-Kiss and D. Zemlyanov, J. Phys. Chem. C FIELD Full Journal Title:Journal of Physical Chemistry C 111 (2007) 7957.

[7]   H. Gabasch, W. Unterberger, K. Hayek, B. Kloetzer, E. Kleimenov, D. Teschner, S. Zafeiratos, M. Haevecker, A. Knop-Gericke, R. Schloegl, J. Han, F.H. Ribeiro, B. Aszalos-Kiss, T. Curtin and D. Zemlyanov, Surface Science 600 (2006) 2980.
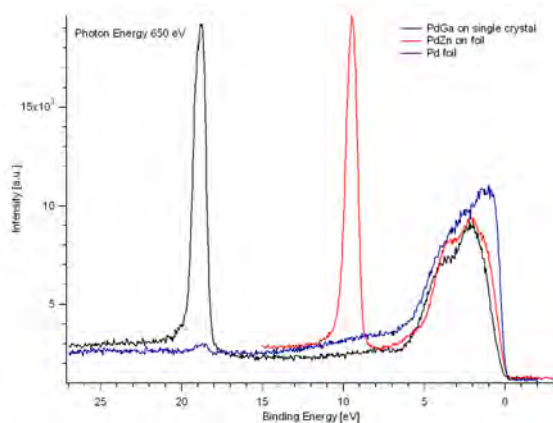
Figure 4. Comparison PdZn and PdGa valence band regions.

Photoemission study of monodispersed Pt nanoparticles deposited onto carbon substrate for PEMFC application

L.V. Yashina[1], S.A. Gurevich[2], M.M. Brzhezinskaya[3], V.S. Neudachina[1,4],
Yu.A. Dobrovolsky[4], E.Gerasimova[4]

[1] Department of Chemistry, M.V. Lomonosov Moscow State University, Leninskie gory 1-3,
119991 Moscow, Russian Federation
[2] Ioffe Physical Technical Institute, 26 Polytekhnicheskaya st., 194021 St Petersburg,
Russian Federation
[3] BESSY GmbH, Albert-Einstein-Str. 15, 12489 Berlin, Germany
[4] Institute of Problems of Chemical Physics RAS, 142432 Chernogolovka, Moscow Region,
Russian Federation

Recent progress in power engineering is closely connected with the low-temperature proton-exchange membrane fuel cells (PEMFC). In comparison with traditional systems, PEMFCs have many advantages, e.g. high fuel conversion efficiency and low noise level. PEMFC includes a cathode, an anode, and PEM. The catalysts deposited onto the electrode surface activate hydrogen ionization at the anode and interaction of the transferred protons with oxygen at the cathode. Nanosize particles of platinum-coated high-disperse carbonaceous substrate can be used as a catalyst for the cathode and the anode processes in the polymer electrolytes. The catalyst support material should have high specific surface area, ability to activate the catalyst, high electrical conductivity, corrosion stability and optimal hydrophobic/hydrophilic properties. In our research, we employed Toray TGP-H-060 carbon paper, which meets all of these requirements.
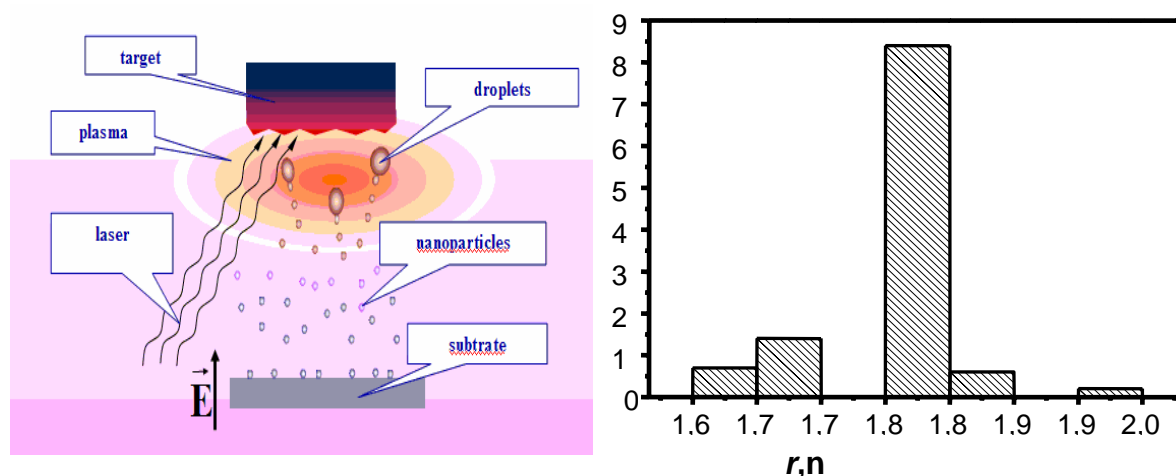
Fig.1. Schematic view of laser electrodepositon setup (left) and size distribution of the obtained Pt clusters (right)

The surface of metal nanoparticles is often charged due to numerous reasons, which are directly related to their catalytic properties; among such reasons electron transfer between the metal granules and the substrate and temperature-activated charge transfer (fluctuations) between the metal granules are worth noting. It is known from experiments that there is an optimal surface coverage, at which the surface charging effect (and hence the catalytic activity) increases drastically [1]. In order to study the nanoparticles/support system in detail, it is necessary to use a model system, in which the size distribution of the particles is very narrow (i.e. the particles are of almost the same size). In our study, we employed laser electrodispersion to obtain monodispersed spherical amorphous Pt granules 1.8 nm in diameter. The schematic representation of the method is given in fig. 1(left); fig.1 (right) represents the size distribution of the Pt particles. The method allows to deposit nanoparticles

uniformly over the surface of the substrate. Samples with different platinum loads were obtained (Pt load from 2 to 24 $\mu g/cm^2$). The catalytic performance of the samples was measured in a test PEMFC; the obtained data indicate that the dependence of catalytic performance on the Pt load has a maximum at approx. 4 $\mu g/cm^2$ (see fig. 2 for detail). In order to explain this behavior, we have performed photoemission studies of the samples with different Pt load.

The photoemission experiments have been undertaken at the Russian-German beamline (RGBL). The spectra were recorded using MUSTANG end station equipped with Phoibos 150 electron energy analyzer

Fig.2. The performance dependence of the PEMFCs with Pt anode catalysts of different metal load (2 $\mu g/cm^2$ -red, 3.9 - $\mu g/cm^{2-}$ green and 6 $\mu g/cm^2$- blue). The cathode is E-TEK Pt/C 20%, Pt load 0.4 mg/cm^2).

(Specs). The Pt 4*f*, O 1*s* and C 1*s* spectra were recorded at a variety of photon energies (330-1030 eV). For the data analysis, the spectra were fitted by the Gaussian – Lorentzian convolution functions with simultaneous optimization of the background parameters. The line asymmetry was described with Doniach-Šunjić (DS) function. Alongside with the monodispersed Pt/carbon paper samples, we also studied a metallic bulk Pt sample as a reference (Fig. 3a).

It is well known that the core-level photoemission spectra of metals have several size-dependent parameters, e.g. peak position or the binding energy, asymmetry index, Auger parameters, plasmon losses etc. The spectra of Pt monodispersed nanoparticles obtained at $h\nu$=485 eV, which corresponds to high surface sensitivity, are shown in Fig. 3b-e. The sample with a minimal Pt load does not have any Pt particles at the surface of the support, since no Pt is observed in the spectra at $h\nu$=485 eV, and the spectra measured at higher energies (e.g. $h\nu$=1030 eV) include two components corresponding to Pt nanoparticles and bulk platinum which can be related to the metallic behavior of the aggregates. Hence we suppose that at low coverages Pt is aggregated in the pores of the carbon paper, thus not being detected by photoemission under high surface sensitivity conditions. The samples with higher Pt load (Fig. 3c-e) include at least two components; though the particles do not conglomerate after laser electrodispersion [1], one of these components is definitely related to the bulk Pt metal (71.2 eV, asymmetry parameter α=0.23). This component most probably appears due to a good contact between the particles, since, according to the data obtained within the framework of the present study, they are not covered with an oxide or any surface contaminant. The second broader component shifted 0.6 eV towards higher binding energies corresponds to Pt in separate clusters with the diameter of 1.8 nm, which is in line with the dependence of the Pt 4*f* binding energy on the particle size [2,3].

The spectral data indicate that the contact between Pt clusters (i.e. the relative intensity of the first component) is minimal for the sample with Pt load 3.95 $\mu g/cm^2$ (Fig. 3b); for this sample the maximum of catalytic activity is also observed. Thus we can conclude that the catalytic activity is influenced by the size effect of the second order, i.e. not only by the size of the particles themselves, but also by the intercluster spacing, which influences the number

Fig.3. Pt 4f photoemission spectra obtained at photon energy of 485 eV

of contacts between the clusters. If there are a lot of direct contacts between the particles, their behavior similar to large clusters or even to bulk metals, which annuls the nanosize effect in catalysis.

It should be noted that the catalyst obtained by laser electrodispersion may help decrease platinum load in PEMFCs, since their specific catalytic performance per 1g of Pt is two orders higher than for standard electrode materials.

[1] T.N. Rostovschikova, V.V. Smirnov, V.M. Kozhevin, D.A. Yavsin, S.A. Gurevich, Nanotechnologies in Russia 1-2 (2007) 47-60.

[2] J. H. Tian, F. B. Wang, Zh. Q. Shan, R. J. Wang, J. Y. Zhang, J. Appl. Electrochemistry 34 (2004) 461-67.

[3] T. You, O. Niwa, M. Tomita, S. Hirono, Anal. Chem. 75 (2003) 2080-85.

Photoemission study of multi-wall carbon nanotubes functionalized by physiologically active substances

L.V. Yashina[1], M.M. Kirikova[1], M.M. Brzhezinskaya[2], A.S.Ivanov[1], S.V. Savilov[1], V.S. Neudachina[1], A.Yu. Filatov[1]

[1]Department of Chemistry, M.V. Lomonosov Moscow State University, Leninskie gory 1-3, 119991 Moscow, Russian Federation
[2]BESSY GmbH, Albert-Einstein-Str. 15, 12489 Berlin, Germany

Development of drugs delivery systems is one of the ways to improve pharmacological properties of many existing medicals, as well as to develop new pharmaceuticals. Carbon nanotubes (CNTs) can potentially serve as a drug delivery system due to their unique ability to penetrate through cell membranes without any damage [1]. This is apparently due to their hydrophobic nature and affinity to bilipid layer which forms the cell walls. To decrease hazard to the living cells, recently it was proposed to modify the CNTs with different functional groups in order to provide their affinity to the inner content of cells. The present report is devoted to the experimental investigation of CNTs functionalization with izadrine (a one-substituted amine, which is a pharmaceutical analog of adrenaline) by means of SXPS and NEXAFS.

The MWNTs were obtained by catalytic pyrolysis of benzene using a patented procedure [2], then purified by annealing in air atmosphere. The samples were characterized by SEM, HREM and Raman spectroscopy. The obtained MWNTs were in a shape of coaxial cylindrical or conic graphene sheets.

Pristine MWNTs were treated with concentrated HCl for 6-8 h, then with 6M nitric acid for 6 h under ultrasonic or with 30% hydrogen peroxide, and finally washed by water until neutral washing solution was obtained. MWNTs were also centrifuged after each washing. The obtained carboxylated MWNTs underwent chemical modification (functionalization) with isadrine. For this purpose, a mixture of izadrine and carboxylated CNTs treated by $SOCl_2$ (to obtain CNT-COCl) were heated up in a sealed ampoule under argon up to 50^0C for 6 h, then treated with ultrasound; the obtained product was washed and dried. The scheme of MWCNT functionalization is presented in Fig. 1.
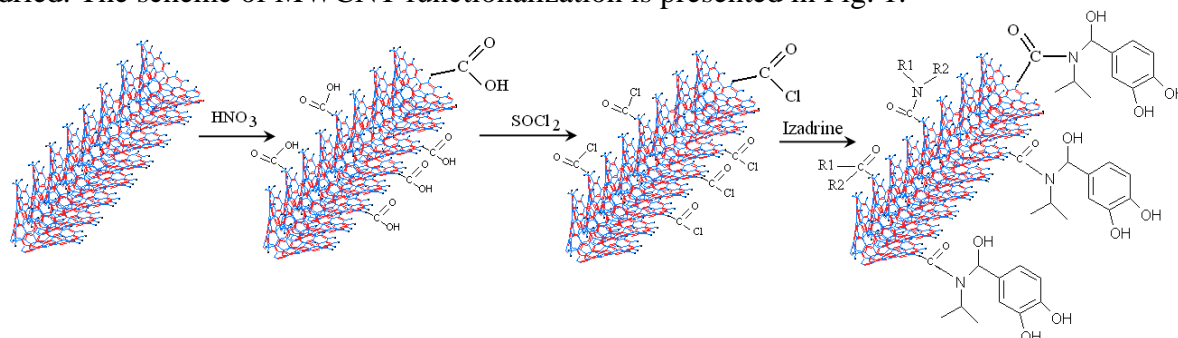
Fig. 1. Scheme of MWCNT functionalization (conic nanotubes are illustrated)

The photoemission spectra have been recorded at the Russian-German beamline (RGBL) using MUSTANG end station equipped with Phoibos 150 electron energy analyzer (Specs). The O 1s, C 1s and N 1s spectra were recorded at a variety of photon energies (330-1030 eV). For the data analysis, the spectra were fitted by the Gaussian–Lorentzian convolution functions with simultaneous optimization of the background parameters.

Photoemission spectra of the pristine nanotubes (Fig. 2a, spectra for conic nanotubes are shown), as well as Raman and NEXAFS spectra (Fig. 3) for conic and cylindrical CNTs indicate that both CNT forms include defects (non-sp^2-hybridized carbon atoms). The C 1s spectra include several components, the major of which correspond to the sp^2- and sp^3-

hybridized carbon atoms; minor ones indicate that the surface includes some –OH and –COOH groups. The corresponding spectral parameters are given in Table 1.
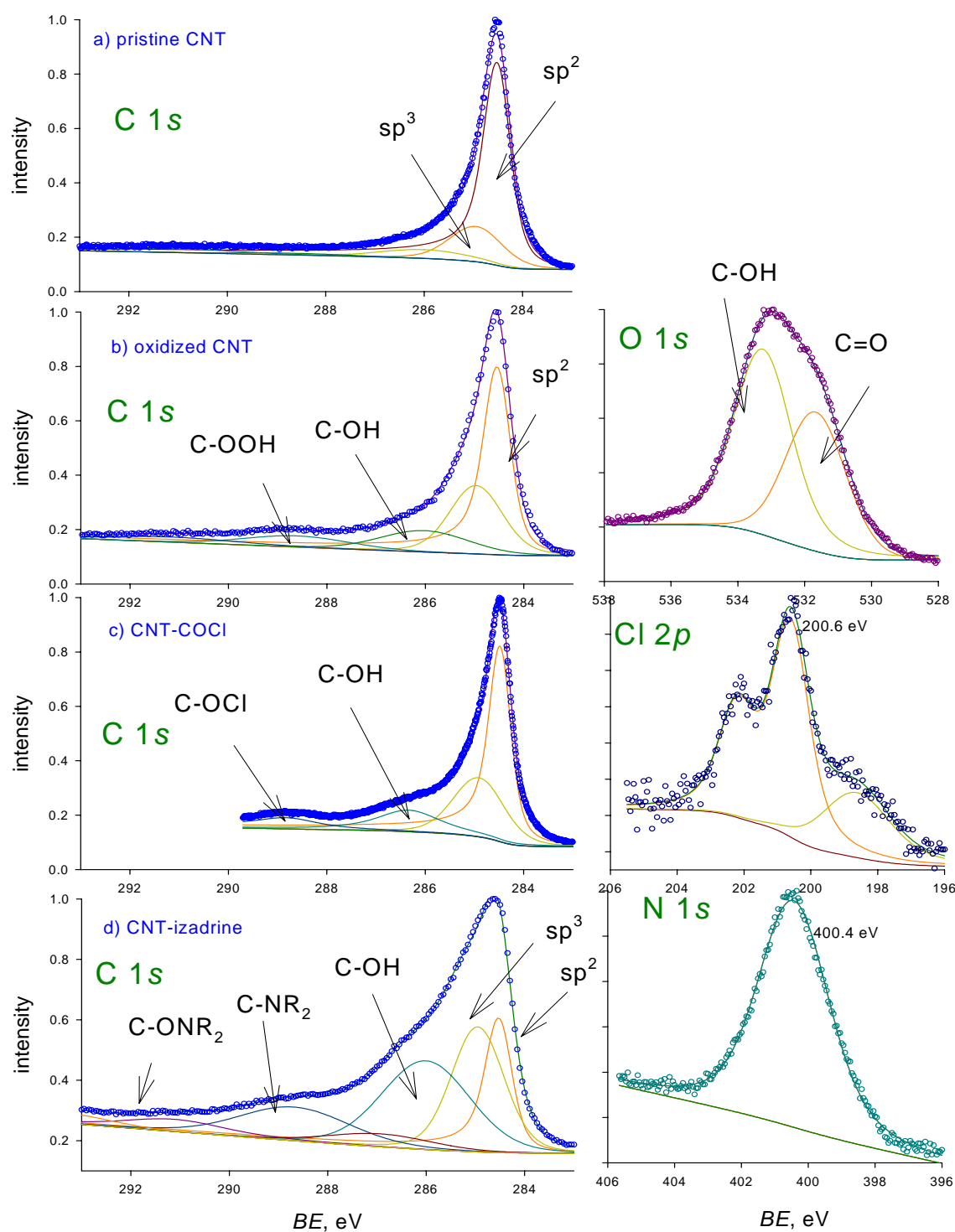
Fig. 2. Photoemission spectra of C1s (hv=355 eV), O1s (hv=600 eV), Cl2p (hv=500 eV), and N 1s (hv=500 eV)

Spectra for the carboxylated (oxidized) CNTs are shown in Fig. 2b. Carboxylation leads to the increase of the number of –COOH and –OH groups at the surface, which is confirmed by the C 1s spectra. The spectra obtained at different photon energies show that oxidation affects not only for the upper atomic layer, but also several sublayers, as it follows from Fig. 4.

The spectra of the izadrine-functionalized CNTs have the most complex character. At least four different components are observed in the C 1s spectra; additional component related to C-ONR$_2$ bond appears in the O 1s spectra, and additionally the N 1s spectrum is registered for this material. The parameters of the intensive components in C 1s spectra differ from those observed for carboxylated or pristine CNTs; we interpret them as C-NR$_2$ and –CONR bonds. The presence of N 1s spectra (BE=400.4 eV) and the components in C 1s spectra shown in Fig. 3d clearly indicate that izadrine is chemically bonded to the surface of CNTs. The essential broadening of the N 1s peak can be attributed to different geometrical displacement of izadrine fragments at the surface.

Table 1. Summary of spectral parameters for C 1s spectra obtained at photon energy 355 eV.

Peak (attribution)	BE, eV	Relative intensities (for conic CNTs)		
		pristine	oxidized	functionalized
sp^2	284.5	0.71	0.51	0.20
sp^3	284.9	0.16	0.24	0.24
C-OH	286.0	0.07	0.12	0.28
C-OOH/ C-OCl/C-NR$_2$	288.6-288.8	0.02	0.08	0.14
C-ONR$_2$	291.2	0	0	0.05
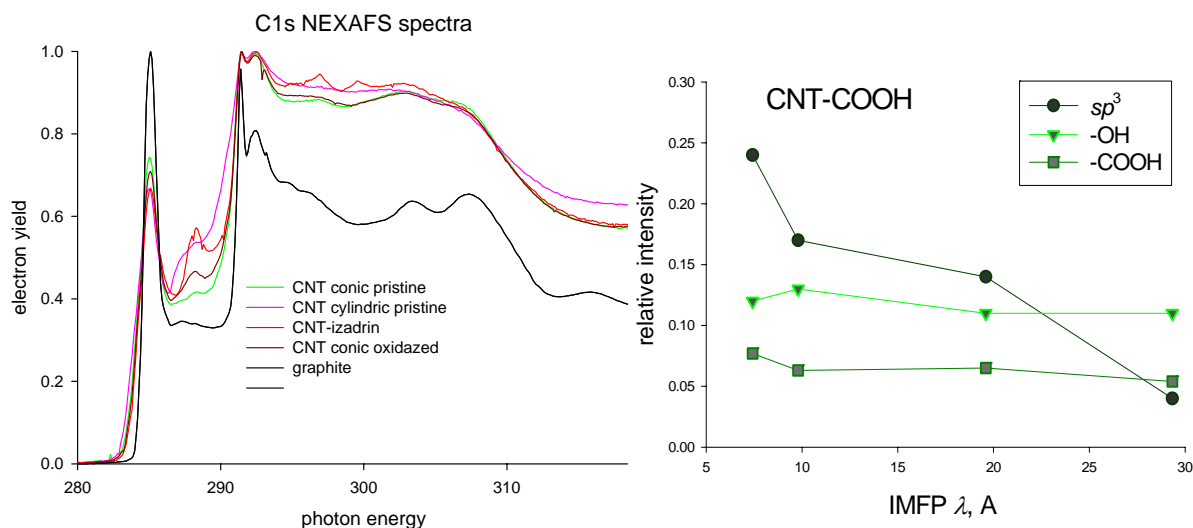
Fig. 3. NEXAFS-spectra C1s

Fig.4. The relative intensities of the spectral components for the C 1s oxidized CNT spectra obtained at different photon energies

By comparing the photoemission and NEXAFS spectra, it was confirmed that conic CNTs are more reactive than cylindrical CNTs due to many end-atoms of graphene layers. During carboxylation up to 3 atomic layers are modified, with partial oxidation of carbon atoms to –COOH and –OH groups. Izadrine fragments are effectively anchored to the disordered structure, and fragments apparently demonstrate different displacement at the CNT surface. Such izadrine-functionalized CNTs can be potentially applied as a drug-delivery system.

[1] B. Kateb *et al*, NeuroImage 37 (2007) S9.
[2] S.V. Savilov, G.A. Zosimov, V.V. Lunin, Application for Patent of the Russian Federation no. 2 005 132 267 (in Russian).

Al doped ZnO for methanol reforming catalyst: characterization and in-situ synchrotron study

Giulio Lolli*, Detre Teschner, Malte Behrens and Robert Schlögl

*Fritz Haber Institute, Max Planck Society, Department of Inorganic Chemistry, Faradayweg 4-6, 14195 Berlin (Germany) *lolli@fhi-berlin.mpg.de*

Introduction

The $Cu/ZnO/Al_2O_3$ catalyst for methanol production/reforming is a well industrially-established catalyst but the exact synergistic mechanism between the Cu metallic phase and the mixed oxide had not been understood in detail. Considering the potential importance of such catalyst in a hydrogen-based economy - methanol is a promising lightweight H_2-carrier molecule [1] - it is important to understand the nature of the active site and optimize its performance to the specific application. In this contribution we want to elucidate the importance of Al doping for the properties of the ZnO substrate. It was recently shown that for extremely low Al content (in the range 2-4 mol%) the Al^{3+} ions are preferentially located in the zincite lattice, whereas for higher Al content a segregation of Al-rich phases ($ZnAl_2O_4$, Al_2O_3) is observed [2]. The typical industrial catalyst ranges between 15 and 20 mol% Al.

Materials and Methods

The ZnO/Al_2O_3 support was prepared with Al contents ranging from 0–15 mol% by coprecipitation. The support was then characterized by synchrotron based environmental XPS and X rays absorption techniques at the Al and O K-edges and Zn L3-edge under several different working conditions: in reducing environments (H_2 @ 250°C), followed by exposure to CO_2 at the same temperature. This was performed at the in-situ setup at the Bessy-II beamline ISISS. Further sample characterization includes XRD, ^{27}Al-MAS-NMR, UV-VIS and EPR spectroscopy.

Results and Discussion

The Al doped ZnO with low Al content presents a different electronic structure than the same support with no or high amount of Al. The band gap energy varies from 3.3 to 3.1 eV with the Al content. The range 2-4 mol% is characterized by a minimum of band gap, which is correlated to the amount of Al atoms in the ZnO lattice and might be due to the creation of interband states. To verify this hypothesis we studied the aluminum K-edge NEXAFS spectra (shown in figure 1). The edge transitions represents the 1s→3p transitions inside the Al atom.

Two features at 1565 and 1567 eV can be ascribed to aluminum in tetrahedral and octahedral coordination respectively [3]. A third broad feature at 1570 eV is a multiple scattering contribution. In our samples the two peaks at 1565 and 1567 eV were not individually resolved, but convoluted in a single peak centered between the two previous values, so a reliable fitting and quantification of the 2 components, like suggested by Shimizu [3], cannot be performed. Nevertheless many differences between the 3% and 15% Al content spectra can be seen (figure 1). The low Al content sample presents a visible shoulder at low energies (highlighted by an arrow) and the convoluted peak is very close to the value for tetrahedral-Al. This suggest that the 4-fold coordinated Al component in this sample is sensibly higher than in the 15% Al that looks more similar to the NEXAFS spectra of transitional alumina with a distribution of T and O sites [3,4]. Indeed the 15 mol% Al sample presents some forms of alumina segregation. This result is in perfect agreement with the idea that at low doping level the Al ions substitute the Zn in the Tetrahedral sites of the HCP ZnO Wurtzite structure. We believe this to be responsible of the band gap energy contraction of these samples.

This different electronic structure can also lead to different properties and behavior of the material under operational conditions. By mean of environmental XPS at different excitations energies we measured the surface and near-surface composition of the material looking at the Zn3p – Al2p photoemission lines in the range 100-70 eV B.E. We can see from figure 2 that the low Al content sample shows a pronounced migration of the Al on the surface during reduction and also in contact with CO_2, during the simulated reaction conditions. This evolution is extremely pronounced and is not observed in higher Al content samples. These results are consistent with a modification of the band gap energy under these conditions (not shown here). Partial surface reduction of ZnO may attract more Al to the surface and can be assumed as the driving force for formation of this newly reconstructed material, which also interacts strongly with the gas phase reactants like CO_2. This suggests that a similar support can actually participate actively in the catalysis or modify the properties of the metal (Cu) that is neighboring. Again all these properties are not observed in high Al content supports, which do not modify themselves during the reaction.

Conclusions

Nanocristalline Al doped ZnO (2-4 mol% Al) represents a promising material as support for methanol steam reforming catalysts. By mean of NEXAFS we were able to find that, at low concentrations, the Al occupies preferentially the tetra-coordinated sites inside the HCP ZnO framework. This however tends to migrate towards the surface if exposed to H_2 environment,

probably due to the formation of Oxygen vacancies that favor the ion mobility. All these aspects should be considered in engineering the catalyst support.
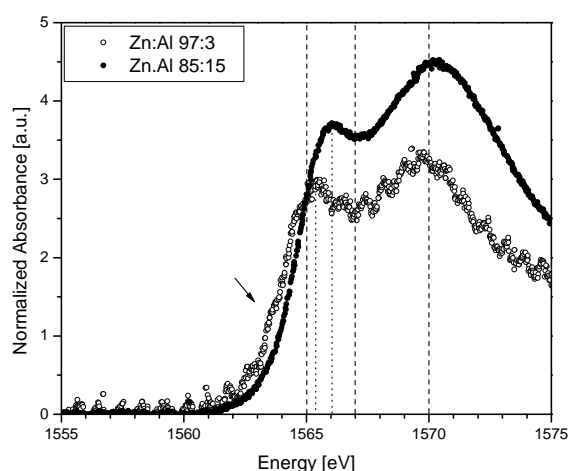
Figure 1. NEXAFS Al-K edge showing Tetrahedral and Octahedral Al coordination 1s→3p transitions.
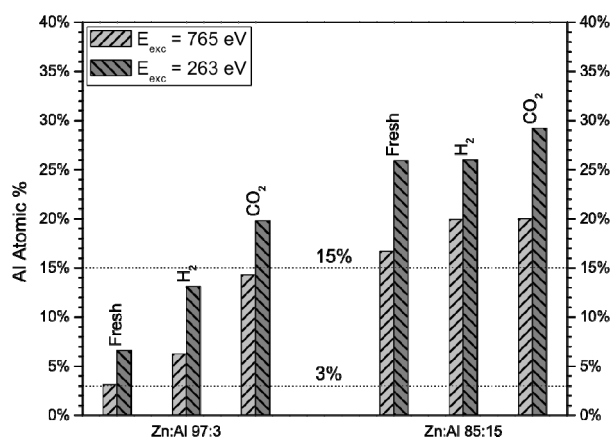
Figure 2. Al atomic % calculated from XPS spectra of the Zn3p and Al2p photoemission regions.

References

1. Turco M., Bagnasco G., Costantino U., Marmottini F., Montanari T., Ramis G., Busca G. *J. Catal.* 228(1), 43-55 (2004).
2. Miao S., Naumann d'Alnoncourt R., Reinecke T., Kasatkin I., Behrens M., Schlögl R., Muhler M. *Eur. J. Inorg. Chem.*, accepted.
3. Shimizu K., Kato Y., Yoshida T., Yoshida H., Satsuma A., Hattori T. *Chem. Commun.* 1681-82 (1999).
4. Bancroft G.M., Fleet M.E., Feng X.H., Pan Y. *Am. Min.* 80, 432-40 (1995).

In situ XPS study of selective oxidation reactions on Ag

T. C. R. Rocha, A. Oestereich, M. Hävecker, R. Blume, D. Teschner, A. Knop-Gericke, R Schlögl

Department of Inorganic Chemistry, Fritz-HaberInstitut der MPG, Faradayweg 4-6, 14195 Berlin, Germany

Introduction

The remarkable catalytic activity of Ag in partial oxidation reactions has been known for decades. Particularly, the ethylene epoxidation and formaldehyde synthesis are two industrially important reactions which received most attention in the past years [1,2]. Both reactions result in important primary chemicals used to produce a wide variety of materials, which find applications in different areas.

It is generally accepted that the key to comprehend the catalytic activity of Ag begins with a deep understanding of the interaction of oxygen with Ag. But the formation of different oxygen species on Ag is a complex function of temperature, gas phase composition, pressure and also the structure (defects, grain boundaries) and morphology (exposed facets, particle sizes) of the Ag catalyst [2,3]. This fact makes the correlation between the surface electronic structure of the catalyst with its activity/selectivity a very difficult task.

In order to shed light on this question, we have investigated the ethylene epoxidation and methanol oxidation reactions under realistic temperatures (180 °C – 650 °C) and in the mbar pressure range by *in situ* X-Ray Photoelectron Spectroscopy (XPS) combined with *in situ* Mass Spectrometry (MS).

Experimental

The experiments were performed using a high pressure XPS endstation at ISISS beamline. The catalyst samples were mounted inside the reaction cell, 1.3 mm away from the first aperture to the differentially pumped stages of the lens system of the hemispherical analyser. The samples were heated from the back side using an infrared laser system. The total pressure for both reactions was kept constant at 0.50 mbar by a pressure controlled valve. The partial pressure of the gasses was regulated by calibrated mass flow controllers. The O1s, Ag3d, C1s core-levels and the valence band were recorded under working conditions by XPS together with the gas phase composition, which was monitored on-line by an electron impact Quadrupole MS (QMS) and a Proton Transfer Reaction MS (PTRMS).

Results and discussion

The selective oxidation of methanol to formaldehyde was investigated on Ag foils with different methanol-to-oxygen mixing ratios at 450 C. Figure 1a shows the O1s core level for mixing ratios of 1:1, 2:1 and 6:1. Since the incident x-ray beam irradiates not only the catalyst surface but also the gas phase molecules, the spectra show gas phase peaks (E_b >534 eV) together with surface peaks. Three oxygen components could be distinguished by fitting the spectra, namely O_a (529.7 eV), O_b (531.2 eV) and O_c (532.8 eV). Comparing to the literature, O_a could be assigned to embedded oxygen, the so called O-gamma and O_b to dissolved O species in the Ag bulk (O-beta). Accordingly, O_c can be assigned to a combination of H_2O and OH species formed during the reaction and SiO_2, a contaminant deposited on the Ag surface.

For the ethylene epoxidation reaction, unsupported Ag powders were used as catalysts and the investigation was done under different reaction mixtures at 180 C. In this case (figure 1b), mainly two components in the O1s XPS spectra were distinguished by fitting. They were addressed as the electrophilic (530,9eV) and nucleophilic (529,5eV) oxygen species, according to the literature [4], although the corresponding binding energies are slightly shifted.
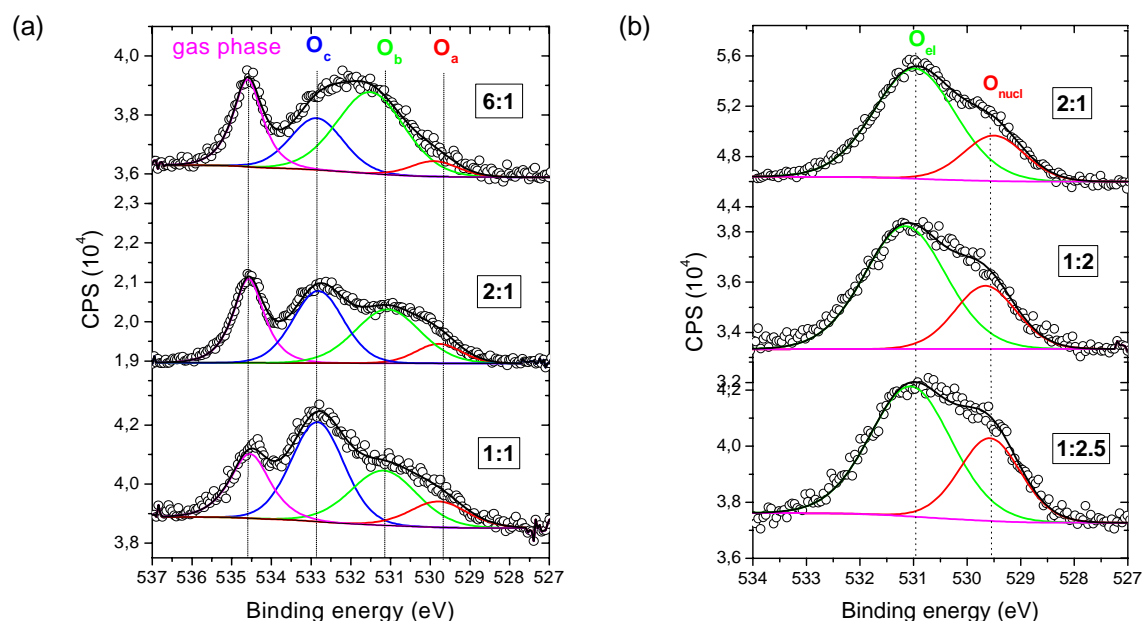
Figure 1: (a) XPS O 1s core level for the methanol oxidation reaction under working conditions (0.5 mbar, 450 C) for different mixing ratios ($CH_3OH : O_2$) 6:1 (top), 2:1 (middle), 1:1 (bottom). (b) XPS O 1s core level for the ethylene epoxidation reaction under working conditions (0.5 mbar, 180 C) for different mixing ratios ($C_2H_2 : O_2$) 2:1 (top), 1:2 (middle), 1:2.5 (bottom).

An important point is that the relative amounts of the different oxygen species in the silver surface formed under working conditions were found to depend on the gas phase composition. This can be qualitatively seen comparing the different spectra in figure 1a for the methanol

oxidation and figure 1b for the ethylene epoxidation. In order to better assign these oxygen species for both reactions, additional studies are being held to gain further information about their physical/chemical characteristics.

Although the nature of the O species under methanol oxidation is still not fully addressed, they can be compared with catalytic aspects. Figure 2b shows the relative selectivity (CH_2O to CO_2 signal ratio) for different mixing ratios (black dots) together with the ratio of the areas of the XPS peaks O_b and O_a measured under working conditions (figure 2a). A good correlation can be observed, indicating that higher selectivities are obtained when the O_b/O_a ratio is higher.
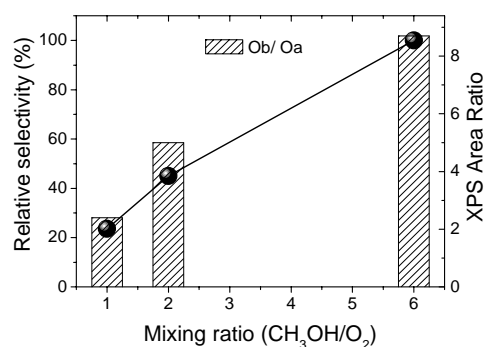
Figure 2: Relative selectivity (CH_2O/CO_2) and XPS area ratios for low binding energy peaks (O_b/O_a) for different feed ratios.

Conclusions

The surface of Ag catalysts under working conditions was characterized for the methanol oxidation and ethylene epoxidation. The oxygen species found in each case were found to be dependent on the gas phase composition. Additionally, in the case of methanol, the changes in the oxygen species present a good correlation with the variations in the selectivity of the reaction. These new insights on the role of different oxygen species can contribute to better understand the mechanisms of selective oxidation reactions over silver, what might lead to the development of improved catalysts.

Acknowledgement

References

[1] X. Bao, M. Muhler, B. Pettinger, R. Schloegl and G. Ertl, Catalysis Letters 22 (1993) 215-225.

[2] V.I. Bukhtiyarov, A.I. Nizovskii, H. Bluhm, M. Hävecker, E. Kleimenov, A. Knop-Gericke, R. Schögl, J. Catal. 238 (2006) 260.

[3] X. Bao, M. Muhler, T. Schedel-Niedrig, R. Schlögl, Phys. Rev. B 54 (1996) 2249-2262

[4] V. I. Bukhtiyarov, M. Hävecker, V. V. Kaichev, A. Knop-Gericke, R. W. Mayer, R. Schlögl, Phys. Rev. B 67 (2003) 235422.

The role of carbon and hydrogen in palladium catalyzed hydrogenation

D. Teschner[1], J. Borsodi[1,2], M. Hävecker[1], A. Knop-Gericke[1], Zs. Révay[2], A.Wootsch[2],
S. D. Jackson[3], D. Torres[4], P. Sautet[4], R. Schlögl[1]

[1] *Fritz-Haber-Institut der Max-Planck-Gesellschaft, Faradayweg 4-6, 14195 Berlin, Germany*
[2] *Institute of Isotopes, CRC, Budapest, Hungary*
[3] *WestCHEM, Department of Chemistry, University of Glasgow, Glasgow, Scotland, UK*
[4] *Laboratoire de Chimie, Université de Lyon, Lyon, CNRS, France*

Introduction

Catalytic hydrogenations are one of the most important processes of the chemical industry. In heterogeneous hydrogenations the majority of catalysts include palladium that is known to be very active in hydrogenating both alkynes and alkenes. Previously we have shown that carbon dissolves in the top few layers of palladium (PdC; Pd 3d peak at 335.6 eV) in the initial stage of alkyne hydrogenation and this enables selective hydrogenation [1]. Herein, we extend our previous studies addressing the fundamental differences of carbon-carbon double or triple bond hydrogenation over Pd. Furthermore, the role of carbon and hydrogen is discussed.

Experimental details

In situ high-pressure XPS investigations were conducted at BESSY, while in situ Prompt Gamma Activation Analysis was performed at the cold neutron beam of the Budapest Neutron Centre, Hungary. Density Functional Theory based calculations on slab models have been carried out to investigate the accumulation of carbon on/in Pd(111). The energetics of surface and subsurface hydrogen was calculated, as well.

Results

We have studied the near-surface region of palladium under various alkyne and alkene hydrogenation reactions. Figure 1 summarizes the state of palladium under 1 mbar alkene or alkyne hydrogenation conditions. Clearly, all investigated alkynes induce the formation of PdC since the higher binding energy component dominates the spectra. On the other hand, hydrogenating alkenes generate much weaker signal at the higher binding energy side of bulk Pd. According to our fitting procedure this peak corresponds roughly 1/3 of the whole signal intensity, which might indicate that some carbon is indeed dissolved in the upper part of the metal lattice, but we attribute the lack of a clearly distinguishable high binding energy component to the absence of PdC. Therefore, as a general rule, the result emphasizes the

widely different nature of the surface under alkyne or alkene feed: alkynes are hydrogenated on PdC while no carbon is incorporated in palladium under alkene hydrogenation.
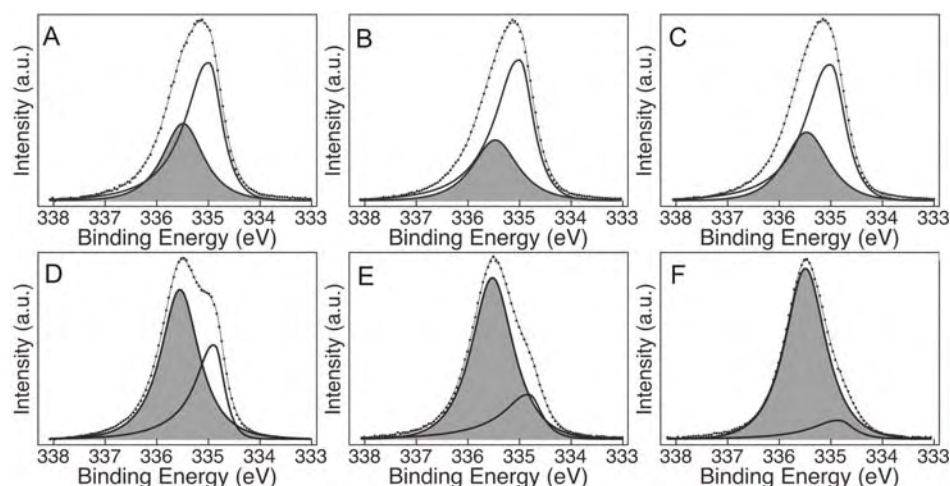
Figure 1: Comparison of in situ Pd $3d_{5/2}$ spectra of Pd foil under alkyne and alkene hydrogenation at 1 mbar (H_2/C_xH_y: 9/1) and 343-353 K. **A**: 1-pentene; **B**: propene; **C**: ethylene; **D**: 1-pentyne; **E**: propyne; **F**: acetylene. [2]

By the help of in situ Prompt Gamma Activation Analysis, we followed the hydrogen content of palladium during hydrogenation. The results indicated that unselective hydrogenation proceeds on hydrogen saturated β-hydride, while during selective hydrogenation the activity was not a function of the hydrogen content. Furthermore, the hydrogen content of Pd during alkene hydrogenation was always high, in line with the absence of PdC that would hinder the equilibration of hydrogen between surface and bulk.

In order to achieve an atomistic understanding for the formation of the PdC phase we addressed the incorporation of C into the Pd substrate. The initial stages in the formation of the PdC phase proceeds via C incorporation from the surface to the first interlayer. Independently of Θ_C, structures involving C atoms adsorbed only in the subsurface are energetically favored (Figure 2 top left panel) with respect to structures involving C adatoms on the surface or on both the surface and subsurface. The most stable conformation corresponds to a √3x√3 distribution of C in the first interlayer. Regarding the C distribution between the first and second interlayer the situation changes. Placing the C atoms in the second interlayer is roughly as favorable as placing them in the first. For coverage higher than ~0.3 ML, distribution of the C atoms on both first and second interlayer is energetically more favored than the population of a single interlayer, hence creating the thermodynamic driving force for the growth of the PdC phase. We considered C incorporation into deeper interlayers and, as a general rule, we observed a significant weakening of the average C binding when an increasing number of interlayers were populated; hence this will limit for deeper extension of the PdC phase.

Figure 2: (Top): Contour maps showing the average binding energy (colour coded, in eV) of carbon as a function of total C coverage (X axis) and the distribution of carbon atoms between interlayers (Y axis) using a Pd(111) substrate. C atoms are distributed between surface and 1st interlayer sites (left panel) or between 1st and 2nd interlayer (right panel). **(Bottom)**: Contour maps showing the average binding energy (colour coded, in eV) of hydrogen as a function of total H coverage (X axis) on Pd(111) (left) or on the model PdC phase (right). H atoms are distributed between surface and 1st interlayer sites. [2]
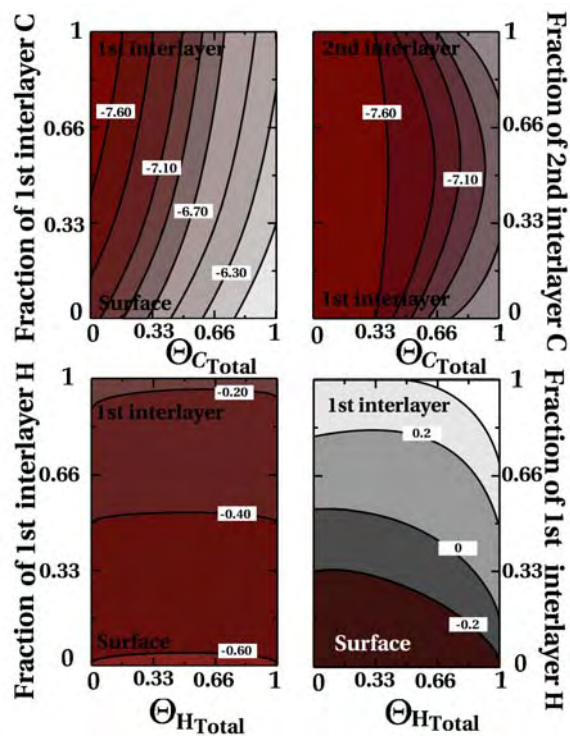
Finally, the presence of C in the subsurface affects the properties of surface hydrogen. The average binding energy of H (E^H_b) as a function of total H coverage (Θ_H) was calculated with respect to the gas phase H_2 molecule. On the clean Pd(111) surface, the binding energy does not strongly depend on the coverage (Figure 3 bottom left panel). H is most stable on the surface, but the penetration into the subsurface is more favored than desorption. In contrast, the bonding properties of H are strongly modified for PdC (Figure 3 bottom right panel): adsorption on the surface is weakened and, most importantly, the accumulation of H into the subsurface is thermodynamically disfavored. Thus one role of the PdC phase is to hinder the migration of H to the subsurface, hence decreasing the H^{sub} / H^{on} ratio in the sample. The PdC phase will, in addition, prevent the migration of bulk H toward the surface. Hence, alkynes are hydrogenated selectively by surface hydrogen, since hydrogen cannot emerge from the bulk, if present at all. On the other hand, alkene hydrogenation occurs using subsurface hydrogen, as its concentration is high and no energetic barrier is built up by a subsurface carbon population.

Acknowledgement

References

[1] a) D. Teschner, J. Borsodi, A. Wootsch, Zs. Révay, M. Hävecker, A. Knop-Gericke, S. D. Jackson, R. Schlögl, Science 2008, 320, 86; b) D. Teschner, E. M. Vass, M. Hävecker, S. Zafeiratos, P. Schnörch, H. Sauer, A. Knop-Gericke, R. Schlögl, M. Chamam, A. Wootsch, A. S. Canning, J. J. Gamman, S. D. Jackson, J. McGregor, L. F. Gladden, J. Catal. 2006, 242, 16.

[2] D. Teschner, Zs. Révay, J. Borsodi, M. Hävecker, A. Knop-Gericke, R. Schlögl, D. Milroy, S. D. Jackson, D. Torres, P. Sautet, Angew. Chem. 2008, 47/48, 9274.

Methodology for the structural characterisation of silica supported V_xO_y species by means of in situ O K-edge X-ray absorption spectroscopy and its application to V_xO_y/SBA-15

Michael Hävecker[1], Matteo Cavalleri[1], Rita Herbert[1], Rolf Follath[2], Axel Knop-Gericke[1], Christian Hess[1,3], Klaus Hermann[1], and Robert Schlögl[1]

[1] *Fritz-Haber-Institut der Max-Planck-Gesellschaft, Faradayweg 4-6, 14195 Berlin, Germany*

[2] *Helmholtz-Zentrum Berlin für Materialien und Energie GmbH, Elektronen-Speicherring BESSY II, Albert-Einstein-Str. 15, 12489 Berlin, Germany*

[3] *Eduart-Zintl-Institut für Anorganische und Physikalische Chemie, Technische Universität Darmstadt, Petersenstr. 20, 64287 Darmstadt, Germany*

mh@fhi-berlin.mpg.de (M. Hävecker)

Introduction

Oxide supported vanadia particles merit special attention due to their large structural flexibility combined with chemical and physical properties that make them interesting for a wide range of applications. It has been controversially debated since years which chemical bonding configuration (terminal vs. bridging) in supported V_xO_y is active in various catalytic reactions. Vibrational spectroscopy is one of the most prominent probes to draw conclusions about which vanadium-oxygen bond constitutes the active site [1, 2]. However, the initially accepted view of the identification of differently coordinated oxygen species in vibrational spectra of supported vanadia catalysts has been challenged recently by a systematic experimental and theoretical study [3]. Thus, there is a strong motivation for an additional probe allowing to tackle the problem of relating structural peculiarities of silica supported vanadium oxide to their functionality. Being a functional material, supported vanadium oxide is very sensitive to the ambient conditions [4]. Thus, the probe should not only provide direct access to the molecular structure of the vanadium oxide species but it must also be applicable under reaction conditions at evaluated temperature, i.e. in situ. We introduce in situ oxygen K-near edge X-ray absorption fine structure (NEXAS) measurements based on the Auger electron yield (AEY) technique as a characterisation tool to assist vibrational spectroscopy that has been applied extensively in earlier work on this system.

Experimental details

The silica SBA-15 supported vanadium oxide samples were prepared by a controlled grafting/ion-exchange procedure consisting of (i) surface functionalisation of silica SBA-15, (ii) ion exchange of ammonium decavanadate and (iii) a final calcination step at 550°C. In situ NEXAFS measurements have been performed at BESSY II using monochromatic radiation of the ISISS (Innovative Station for In Situ Spectroscopy) beamline as a tuneable X-ray source. High pressure soft X-ray absorption spectra were obtained in the presence of oxygen at elevated temperature using the high pressure endstation designed and constructed at the FHI. Details of the set-up are described elsewhere [5].

Results
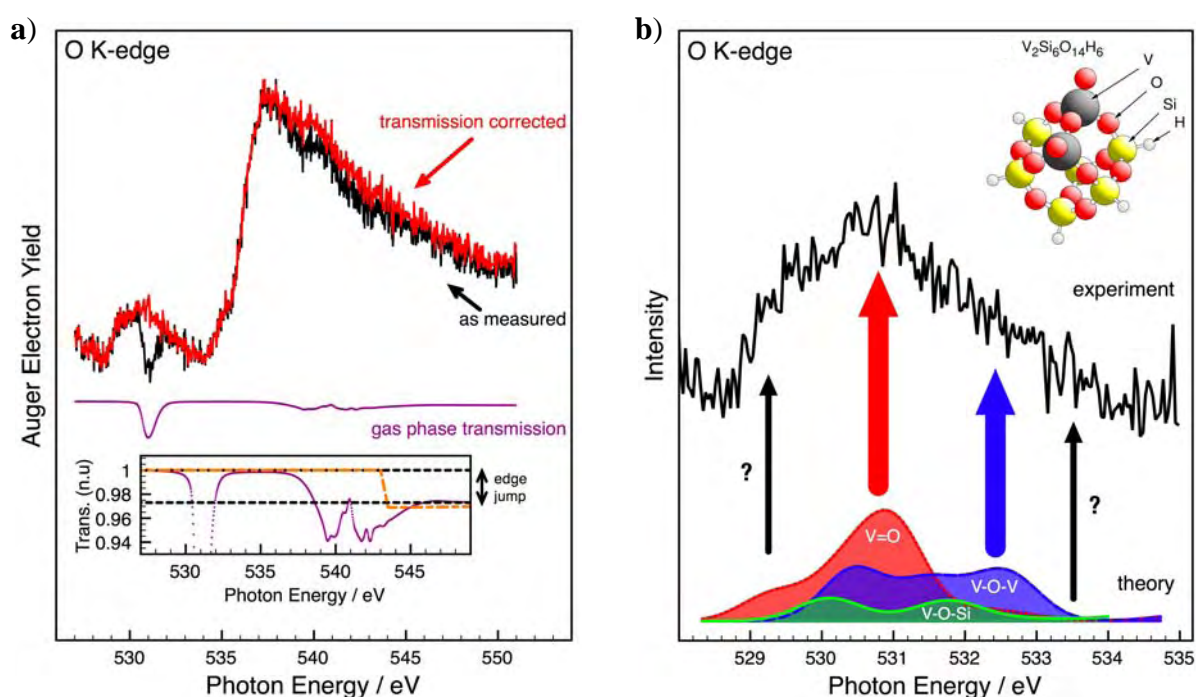
Figure 1: a) presents the Auger electron yield spectrum of V_xO_y(10.8wt%V)/SBA-15 before (black, "as measured") and after (red, "transmission corrected") the reconstruction, respectively. The O_2 gas phase transmission function used for the analysis procedure is shown as well. In **b)** a comparison of the experimental O K-edge NEXAFS spectrum of 10.8wt%V/SBA-15 between 528eV and 535eV (black solid line, "experiment") with theoretically obtained partial spectra of a $V_2Si_6O_{14}H_6$ dimer cluster representing the contribution of different oxygen coordinations ("theory") is shown.

Fig. 1a shows the O K-NEXAFS of V_xO_y/SBA-15 in 0.5mbar O_2 at 400°C. Absorption of X-rays in the gas phase modifies the photon flux impinging on the sample, visible mainly in the dip at 531eV in the "as measured" spectrum. This energy dependent variation of the photon flux is proportional to the total electron yield signal of the gas molecules for the case of thin samples i.e. low gas pressures. Thus, to obtain the non-distorted NEXAFS the "as measured" spectrum has to be corrected by the O_2 gas phase transmission as depicted in Fig. 1a.

The analysis of the O K-NEXAFS allows a clear distinction between separate vanadia, silica and interface contribution in contrast to vibrational spectroscopy with strongly

overlapping contributions due to vibrational coupling. A study of catalysts with different V loadings (0wt%, 2.7wt%, and 10.8wt% vanadium) shows that the contributions of silica to the NEXAFS appear in an energy region (above 534eV) well separated from the spectral signature of oxygen bound to vanadium (approximately 528-534eV) [6]. Differently coordinated oxygen can be identified in the O K-NEXAFS spectrum by comparison with theoretical spectra obtained by state of the art density-functional theory (DFT) calculation [7]. Fig. 1b shows a detailed region of the onset of the O K-edge where the experimental curve (solid black line, "experiment") is compared with theoretical spectra ("theory") obtained by DFT calculations of a $V_2Si_6O_{14}H_6$ model cluster (displayed as inset in Fig. 1b). Contributions of V-O-V and V=O to the experimental spectrum as derived from the theoretical spectra are indicated by thick blue and red arrows, respectively. The comparison of the experiment with the theoretical spectra shows clearly that a complete interpretation requires consideration of oxygen in bridging coordination (V-O-V). Therefore, O K-edge NEXAFS spectra together with theoretical support allow to conclude on the presence or absence of specific oxygen bonds in V_xO_y/SBA-15. Thus the comparison facilitates a detailed analysis of the molecular structure of silica supported vanadium oxide.

Acknowledgement

References
[1] B. M. Weckhuysen, D. E. Keller, Catal. Today **78**, 25 (2003).

[2] I. E. Wachs, Catal. Today **27**, 437 (1996).

[3] N. Magg, B. Immaraporn, J. B. Giorgi, Th. Schroeder, M. Bäumer, J. Döbler, Z. Wu, E. Kondratenko, M. Cherian, M. Baerns, P. C. Stair, J. Sauer, H.-J. Freund, J. Catal. **226**, 100 (2004).

[4] D. E. Keller, T. Visser, F. Soulimani, D. C. Koningsberger, B. M. Weckhuysen, Vibrational Spectr. **43**, 140 (2007).

[5] E. M. Vass, M. Hävecker, S. Zafeiratos, D. Teschner, A. Knop-Gericke, R. Schlögl J. Phys.: Condens. Matter **20**, 1 (2008).

[6] M. Hävecker, M. Cavalleri, R. Herbert, R. Follath, A. Knop-Gericke, Christian Hess, Klaus Hermann, and Robert Schlögl, Phys. Stat. Solidi b, submitted.

[7] M. Cavalleri, K. Hermann, A. Knop-Gericke, M. Hävecker, R. Herbert, C. Hess, A. Oestereich, J. Döbler, R. Schlögl, J. Catal. (2009), doi:10.1016/j.jcat.2008.12.013.

Cobalt as methanol oxidation catalyst: The effect of the reaction mixture composition to the surface oxidation state.

S. Zafeiratos[1], T. Dintzer[1], D. Teschner[2], R. Blume[2], M. Hävecker[2], A. Knop-Gericke[2], R. Schlögl[2]

[1]*LMSPC, UMR 7515 du CNRS, 25 Rue Becquerel, 67087 Strasbourg, France*
[2]*Fritz-Haber-Institut der Max-Planck-Gesellschaft, Faradayweg 4-6, 14195 Berlin, Germany*

Introduction

Cobalt and its oxides (CoO and Co_3O_4) exhibit interesting electronic and magnetic properties and are used as catalysts in a range of reactions. Perhaps the major application of cobalt-based catalysts is in the Fischer-Tropsch synthesis, since cobalt has been shown to efficiently convert syn gas ($CO+H_2$) to methane or liquid fuels [1].Recently cobalt has been proposed as a very promising catalyst to replace noble metals for H_2 production by steam reforming of ethanol [2]. Pure cobalt oxide surface phases have been scarcely investigated with respect to their catalytic properties [3, 4] and always by *ex-situ* methods. In the present work, high pressure photoelectron and soft x-ray absorption spectroscopy are applied under working catalytic conditions, to investigate methanol oxidation reaction on cobalt.

Experimental

In situ x-ray photoelectron and absorption spectroscopy (XPS and XAS respectively) were performed at ISISS beamline at BESSY in Berlin. The soft X-ray absorption spectra of the Co $L_{3,2}$ edges were recorded in the Total Electron Yield (TEY) mode. The Co crystal was pre-treated in the XPS reaction cell by oxidation (0.2 mbar O_2 at 520 K) and reduction (0.2 mbar H_2 at 520 K) cycles, until all residual surface carbon disappeared.

Results

Figure 1 displays photoemission and absorption spectra of Co 2p core level ($L_{3,2}$ edge in absorption spectroscopy nomenclature) obtained from pre-oxidized cobalt surfaces at 520 K, under various gas phase environments. The already available photoemission and absorption data of cobalt oxides in the literature provide the necessary basis for identification of the cobalt oxidation states [5,6,7,8] in figure 1. In pure O_2, the Co $2p_{3/2}$ photoemission peak at 779.6 eV has a weak, broad satellite (S in figure 1a) characteristic of the Co_3O_4 spinel phase [5, 6]. In agreement, the $L_{3,2}$ edge fine structure (figure 1b) is very similar to that previously obtained on Co_3O_4 reference compounds [7, 8]. Finally, the Co/O atomic ratio calculated from the Co 2p and O 1s peaks was 0.69, close to the nominal value of 0.75 for Co_3O_4.
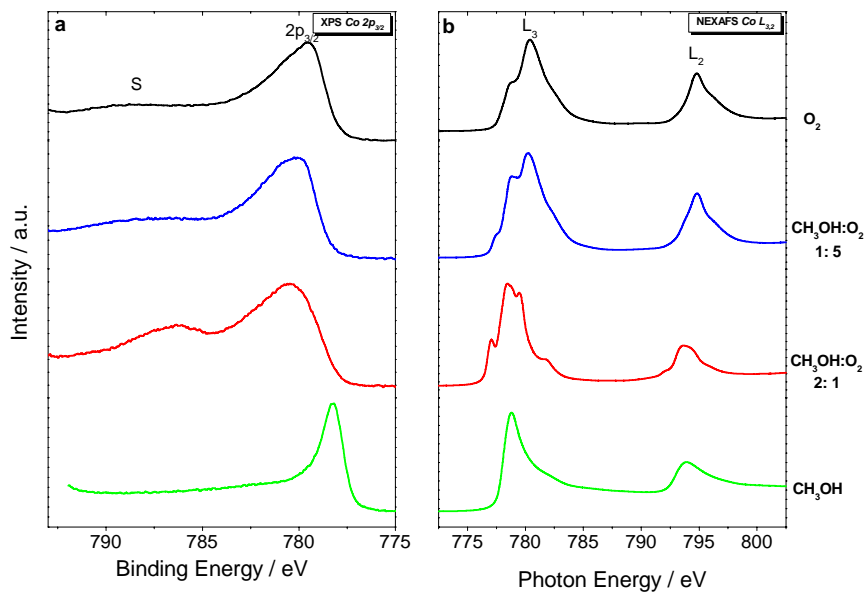
Figure 1. (a) Co $2p_{3/2}$ XPS (*hv= 965 eV*) and **(b)** Co $L_{3,2}$ XAS spectra of Co (0001) at 520 K under 0.2 mbar O_2, 0.3 mbar $CH_3OH:O_2$ =1:5, 0.2 mbar $CH_3OH:O_2$ =2:1 and 0.1 mbar CH_3OH.

All spectroscopic results are consistent with the complete transformation of cobalt surface to Co_3O_4 when heated in O_2 at 520 K. The thickness of the oxide layer is not possible to be determined, but definitely exceeds 4 nm which is the estimated probing depth of the absorption spectra [9].

The spectroscopic characteristics undergo significant modification in oxygen-methanol mixtures (MR is defined here as the $CH_3OH:O_2$ ratio). The Co $2p_{3/2}$ photoemission peak (fig. 1a) is shifted to higher energies (780.6 eV) and the satellite structure becomes broader and more intense, especially for MR=2. These are clear indications for partial reduction of Co_3O_4 to CoO [6]. Additionally, in pure methanol stream, the Co $2p_{3/2}$ peak (binding energy 778.3 eV) is indicative of cobalt in metallic state, verifying that methanol is a very effective reducer for cobalt oxides. The XAS spectra presented in fig. 1b confirm the photoemission results. In particular, for MR=0.2 the Co L-edges are the sum of CoO and Co_3O_4 reference spectra, indicating that under these conditions both cobalt oxide phases co-exist. For MR=2 and pure methanol atmosphere, the Co L-edges are very much alike to that found in previous measurements for CoO [7] and metallic cobalt [8] respectively.

From the discussion above, it is evident that the composition of the gas phase significantly influences the surface chemical state of cobalt. The key in catalysis is to combine spectroscopic and catalytic data, in other words to correlate the surface chemical state to the catalytic activity and selectivity. Relative selectivities of the main products, as well as methanol conversion, were calculated based on *on-line* QMS data (Table 1).

Methanol-to-oxygen Ratio	Maximum Methanol Conversion %	S(CO)	S(CO$_2$)	S(CH$_2$O)	S(H$_2$)	S(H$_2$O)
1:5	26	6	58	13	0	23
2:1	2	25	13	35	16	11
1:0	14	47	0	9	44	0

Table 1. Normalized product selectivities and methanol conversion rates on cobalt, derived by *on-line* QMS results. Data are recorded at 520 K under CH$_3$OH:O$_2$ reactant gas with mixture ratios 1:5, 2:1 and 1:0.

Depending on the reaction conditions CO, CO$_2$, CH$_2$O, H$_2$O and H$_2$ were detected. Selectivities are referring to constant temperature and pressure conditions (520 K, 0.1-0.3 mbar) and are expressed as the percentage in the overall (CO, CO$_2$, CH$_2$O and H$_2$) production. The maximum activity was obtained just after reaching the 520 K (500 K for pure methanol) and afterwards gradual deactivation was observed, as was evident by the decrease of methanol consumption. Comparison of spectroscopic and catalytic data presented in figure 1 and table 1 provide direct indications for the catalytic behaviour of cobalt in oxide and metallic form. In particular for MR=0.2, were Co$_3$O$_4$ is the dominant phase, the CH$_3$OH consumption is high and total oxidation to CO$_2$ is favoured. In contrast, for MR=2, partial oxidation products (CO, CH$_2$O and H$_2$) are detected, accompanied with significantly lower methanol conversion rates (almost ten times). As showed in figure 1, in that case the pre-oxidized cobalt surfaces were reduced to CoO. Finally, in a pure CH$_3$OH stream, metallic cobalt favours methanol decomposition to CO and H$_2$. It is worth mentioning that above 500 K, high rate of coke deposition was observed on metallic cobalt, which is the cause of fast deactivation of this catalyst.

In summary combination of *in situ* spectroscopy and *on-line* gas phase analysis testifies for the dynamic response of the cobalt surface to the reaction mixture, indicating also the effect at the catalytic behaviour.

References

[1] J. Zhang, J. Chen, J. Ren, Y. Sun, Appl. Catal. A 243 (2003) 121.

[2] Meng Ni, Dennis Y.C. Leung, Michael K.H. Leung, International Journal of Hydrogen Energy 32 (2007) 3238

[3] S. Tuti, F. Pepe, Catal Lett 122 (2008) 196

[4] M. M. Natile, A. Glisenti, Chem. Mater. 14 (2002) 3090

[5] M. A. Langell, J. G. Kim, D. L. Pugmire, W. McCarroll, J. Vac. Sci. Technol. A 19 (2001) 1977

[6] H.A.E. Hagelin-Weavera, G. B. Hoflunda, D. M. Minahanb, G. N. Salaitac, Applied Surface Science 235 (2004) 420

[7] D. Bazin, I. Kovacs, L. Guczi, P. Parent, C. Laffon, F. De Groot, O. Ducreux, J. Lynch, Journal of Catalysis 189 (2000) 456.

[8] T. J. Regan, H. Ohldag, C. Stamm, F. Nolting, J. Luning, and J. Stohr, R. L. White, Phys. Rev. B 64 (2001) 214422.

[9] M. Abbate, J. B. Goedkoop, F. M. F. de Groot, M. Grioni, J. C. Fuggle, S. Hofmann, H. Petersen, M. Sacchi, Surf. Interface Anal. 18 (1992) 65.

In situ XPS study of methanol decomposition on Pd/Ga$_2$O$_3$ catalysts and Pd foil

K. Föttinger[a], A. Haghofer[a, b], G. Rupprechter[a], D. Teschner[b], A. Knop-Gericke[b], R. Schlögl[b]

[a]*Institute of Materials Chemistry, Vienna University of Technology, A-1210 Vienna, Austria*
[b]*Fritz-Haber-Institute of the Max-Planck-Society, D-14195 Berlin, Germany*

Background and Objectives

Methanol steam reforming is a promising reaction in terms of hydrogen production for use in PEM fuel cells. The main criterion for a catalyst in this reaction is its selectivity to CO$_2$ and H$_2$. The common byproduct CO, formed by side or follow-up reactions such as methanol decomposition and reverse water-gas shift (RWGS) is problematic due to its poisoning effect on the electrode of a downstream fuel cell. It was previously shown [1] that palladium supported on certain reducible oxides (ZnO, Ga$_2$O$_3$, In$_2$O$_3$) provides high selectivity combined with thermal stability. As a reason for the improved selectivity the formation of an alloy or intermetallic compound (IMC) between Pd and the reduced support has been suggested [1].

The aim of this work was the investigation of alloy formation on a 5 wt% Pd/Ga$_2$O$_3$ powder catalyst in different atmospheres. In-situ XRD had been used previously to determine the temperature of formation of a bulk alloy/IMC under reducing conditions. In-situ XPS allowed for a surface characterization under the conditions of methanol decomposition as well as reduction in hydrogen. In addition, we studied methanol decomposition on pure (unalloyed) Pd foil as well as on Ga$_2$O$_3$ (without Pd) for comparison of the carbon-containing intermediates formed on the catalyst surface.

Experimental

In situ X-ray photoelectron spectroscopy was performed at BESSY II at the ISIS-PGM beamline. Pure Ga$_2$O$_3$ and a 5 wt% Pd/Ga$_2$O$_3$ powder catalyst were mounted onto a temperature controlled sample holder in the form of pressed pellets. During reduction in 0.25 mbar H$_2$, Ga3d and Pd3d regions were recorded at increasing sample temperatures and different excitation energies (160, 400 and 800 eV for Ga3d and 480, 720 and 1120 eV for

Pd3d) , yielding information from different depths. During methanol decomposition, the C1s region was recorded additionally. Methanol decomposition reaction was also carried out on a Pd foil at different temperatures (400, 500 and 600 K, 0.13 mbar methanol). During the reaction the Pd3d and C1s signals were followed at different excitation energies (420, 540, 660 and 1060 eV for C1s; 480, 600, 720 and 1120 eV for Pd3d). The gas phase was analyzed by online mass spectrometry.

Results

Pd-Ga₂O₃:

Previous in-situ XRD measurements under flowing H_2/He had indicated that bulk alloy formation set in at 548 K. Hydrogen reduction in the in-situ XPS system was performed at temperatures of 448, 523 and 623 K and a H_2 pressure of 0.25 mbar. Starting at 523 K and more pronounced at 623 K, metallic Ga appeared in the surface region, indicated by an XPS signal at binding energies 2 eV lower than that of Ga^{3+} in Ga_2O_3 (see Fig. 1). The ratio of Ga^0 to Ga^{3+} did not strongly depend on the information depth. Methanol decomposition was investigated at temperatures of 448, 523 and 623 K as well, with similar amounts of reduced Ga species appearing as in the reduction experiment. While it can be assumed from the combination of XRD and XPS measurements that the reduced Ga is present at least partly in form of an alloy or intermetallic compound of Pd and Ga, the presence of reduced (by the atomic H supply from Pd) but unalloyed Ga cannot be excluded.
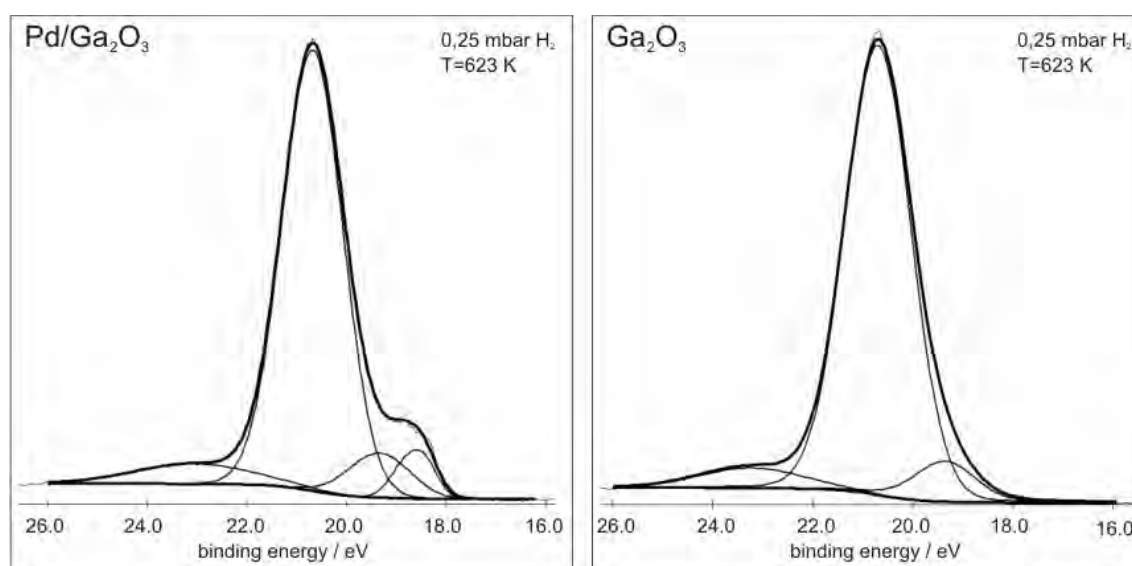
Figure 1: Ga3d region of Pd/Ga₂O₃ (left) and pure Ga₂O₃ (right) recorded at 0.25 mbar H_2 and 623 K. Excitation energy: 160 eV

Pd-foil:

For methanol decomposition reaction on Pd, two different reaction pathways can occur, with or without cleavage of the methanolic C-O bond, leading either to CO and H_2 or to formation of carbon(aceous) species. Using in situ XPS, we aimed at a quantification of these two pathways at different reaction temperatures. C1s signals at 285.3 eV are attributed to adsorbed CO, CH_x species give rise to XPS peaks at ~284.1 eV (see Fig. 2). At the lower reaction temperature (400 K) a significantly larger amount of adsorbed CO was detected on the Pd surface compared to 600 K (CH_x:CO ratio =3 at 400 K and =6 at 600 K), but this does not result in a lower activity due to CO-blocking. At 400 K an additional Pd3d species appeared, shifted by 0.6 eV to higher binding energies, which can be attributed to an adsorbate-induced shift or to a Pd-C phase. Inclusion of such a compound was not required at 600 K reaction temperature, which rather supports the first explanation (adsorbate-induced shift). Additional C1s peaks appeared between 286 and 288 eV binding energies due to various oxygen-containing carbon species.
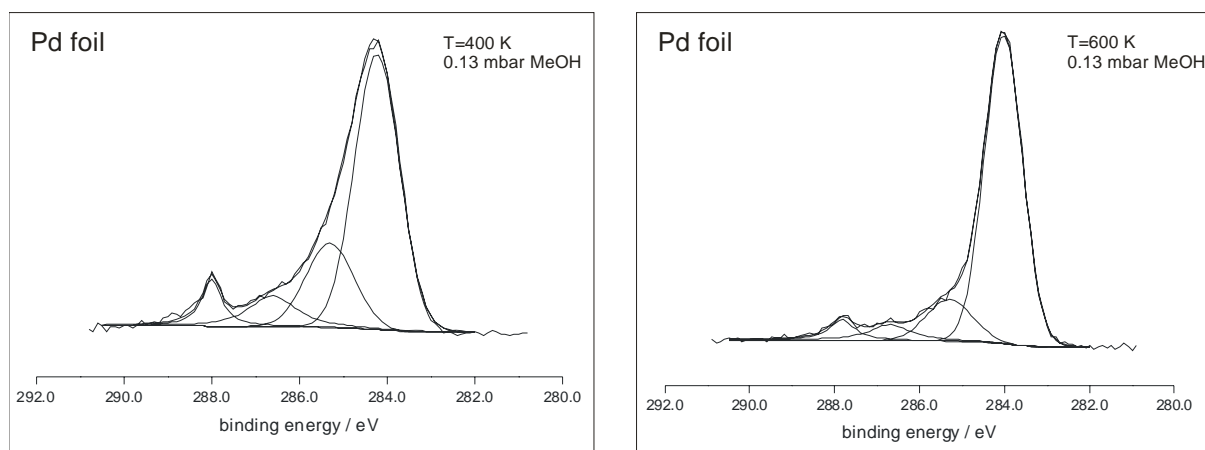
Figure 2: C1s region during methanol decomposition reaction on the Pd foil at 400 K (left) and 600 K (right). Excitation energy: 420 eV

References:

[1] Iwasa, N., Mayanagi, T., Ogawa, N., Sakata, K., Takezawa, N., Catalysis Letters, 54(3) (1998), 119-123.

Magnetic-field induced effects on the electric polarization in DyMnO$_3$

R. Feyerherm, E. Dudzik, A. U. B. Wolter[*], S. Valencia, O. Prokhnenko, A. Maljuk,
S. Landsgesell, N. Aliouane[**], and D. N. Argyriou

Helmholtz Zentrum Berlin für Materialien und Energie, Berlin, Germany
* IPKM, TU Braunschweig, now at IFW, D-01069 Dresden, Germany
** now at IFE, NO-2027 Kjeller, Norway

Continuing our research program [1] on the series of magneto-electric multiferroics RMnO$_3$, in 2008 we have performed x-ray resonant magnetic scattering (XRMS) studies of the rare earth magnetic ordering in DyMnO$_3$, using the new superconducting magnet at the MAGS beamline for the first time. This compact magnet (Fig. 1), based on high-T_c superconductor technology, supplies a maximum field of 50 kOe and is combined with a 4 K base-T cryostat.

DyMnO$_3$ undergoes three stages of magnetic ordering of the Dy and Mn moments as function of T. At the Neel temperature $T_N = 39$ K, a Mn sinusoidal order arises with a gradual shift of the propagation vector τ^{Mn} as T is reduced. At $T_{lock} = 18$ K, τ^{Mn} stabilizes simultaneously with the emergence of a spontaneous electric polarization $P\|c$. In our previous work, we determined the commensurate Dy ordering with propagation vector $\tau^{Dy} = \frac{1}{2} b^*$ below 6.5 K. We also demonstrated that above 6.5 K the ferroelectric polarization of DyMnO$_3$ is enhanced by a Mn-induced Dy spin order with $\tau^{Dy} = \tau^{Mn} = 0.385\, b^*$ [2, 3].

Fig. 1: The new compact 50 kOe super-conducting magnet at MAGS, mounted to the Euler cradle of the diffractometer together with the cryostat holder (right hand side).

DyMnO$_3$ exhibits interesting effects induced by external magnetic field. Below 10 K, DyMnO$_3$ shows a significant enhancement of the electric polarization $P\|c$ by a factor of up to 3.5 for magnetic fields between 10 and 50 kOe applied along a (Fig. 2). This enhancement is related to a two-step metamagnetic behavior with transitions around 20 and 50 kOe observed for $T = 2$ K. This suggests that a modification of the Dy magnetic ordering takes place at these transitions that, in turn, has an effect on the ferroelectric polarization. To verify this hypothesis, DyMnO$_3$ was studied by XRMS at the Dy L$_3$
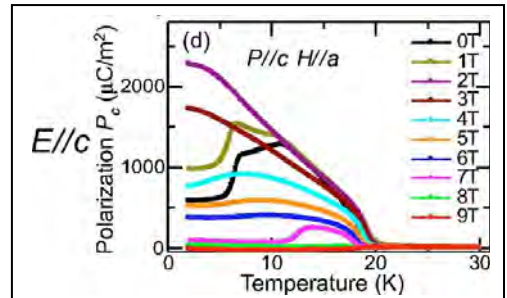
Fig. 2: Temperature dependence of the electric polarization P_c measured at various applied magnetic fields $\mu_0 H\|a$ (from [4]).

resonance in magnetic fields $H\|a$ with scattering vectors (0 k 0). First, we have measured k-scans at 4.5 K in zero field and in 20 kOe, with k values around $2+\tau$ (Fig. 3, top). The Bragg reflection related to the individual Dy ordering $\tau^{Dy} = \frac{1}{2}$ does vanish in an applied field of 20 kOe. Simultaneously, another reflection with $\tau^{Dy} = 0.385$ appears. This value coincides with the Mn-induced Dy ordering observed for $T > 6.5$ K in zero field. We conclude that the field-induced suppression of the $\tau^{Dy} = \frac{1}{2}$ Dy ordering is accompanied by a re-emergence of the Mn-induced ordering and is directly linked to the increase of the electric polarization.

From the magnetic field dependence of the (0 2+τ^{Dy} 0) and (0 2+τ^{Mn} 0) reflection intensities at base temperature (Fig. 3, bottom) we derive a critical field of $H^* = 18$ kOe for the transition of the Dy ordering from $\tau^{Dy} = \frac{1}{2}$ to $\tau^{Dy} = \tau^{Mn} = 0.385$. The related Bragg reflection has its maximum intensity around 20 kOe and rapidly decreases for larger fields. Thus the Mn-induced ordering of Dy is gradually suppressed for magnetic fields above 20 kOe.

Above 40 kOe the intensity levels off, probably marking a second transition. The position of the $(0\ 2+\tau^{Mn}\ 0)$ reflection does not vary significantly with the strength of the applied magnetic field (not shown), which implies that the Mn propagation vector is field-independent.

These observations confirm that the first metamagnetic step in the magnetization data is indeed related to a breakdown of the independent Dy ordering. Above this transition, however, the Dy moments still carry an antiferromagnetic modulation with the same propagation vector as the Mn-induced ordering. The magnetization can only be saturated (forced ferromagnetic alignment) when this modulation is also suppressed. This point is reached above the second transition at ~50 kOe.

It is also interesting to compare the magnetic field dependence of the induced ordering (Fig. 3) with the field dependence of the electric polarization (Fig. 2). There is a direct correspondence between the intensity of the induced-ordering related Bragg reflection and the magnitude of the electric polarization at 4.5 K. We performed a quantitative analysis based on the assumption that the μ_y and μ_z

Fig. 3: (top) XRMS k-scans along (0 k 0) measured at 4.5 K in zero field and in 20 kOe applied magnetic field **H**||a; (bottom) Magnetic field dependence of the integrated intensities of the (0 2.5 0) and (0 2.385 0) reflections at 4.5 K. Open circles show the square of the polarization enhancement ΔP_c defined within the text. The scaling factor is fixed to give a match at 20 kOe. Lines in the bottom figure are guides to the eye.

components of the Mn-cycloid stay unchanged (or change only slightly) under application of a magnetic field. In this case, the field-dependent electric polarization enhancement ($\Delta P_c(H)= P_c(H) - P_0$) should be proportional to the size of the induced Dy moment, justified by the model presented in our previous report [3]. The related Bragg intensity is expected to be proportional to the square of the induced moment. Thus, the square of the polarization enhancement should scale with the $(0\ 2+\tau^{Mn}\ 0)$ Bragg intensity. The experimental data follow this scaling well (Fig. 3, bottom) except for $H \geq 40$ kOe. One possible explanation for the mismatch in this field-region is that the above assumption becomes invalid when the flop of the electric polarization at $H \sim 65$ kOe is approached, since this is related to changes on the Mn-sublattice.

To conclude, we have shown that for **H**||a the intermediate field region with enhanced electric polarization for $T < 6.5$ K is characterized by the re-occurrence of an induced Dy ordering with τ^{Mn}. Only for fields large enough to fully suppress the AFM arrangement of Dy moments with τ^{Mn}, the enhancement of the electric polarization by the Dy vanishes. These observations confirm our previous conjecture [3] that this Mn-induced ordering of Dy is responsible for any enhanced electric polarization in $DyMnO_3$.

References

[1] BESSY Highlights 2006, p. 9; BESSY Annual Report 2007, pp. 164 and 243.
[2] R. Feyerherm *et al.*, Phys. Rev. B **73**, 180401(R), (2006)
[3] O. Prokhnenko *et al.*, Phys. Rev. Lett. **98**, 057206 (2007)
[4] T. Kimura *et al.*, Phys. Rev. B **71**, 224425 (2005).

Counterion distribution around charged proteins in solution studied using ASAXS

Fajun Zhang[1], Luca Ianaselli[1], Maximilian W. A. Skoda[2], Robert M. J. Jacobs[3], Armin Hoell[4], Dragomir Tatchev[4], Frank Schreiber[1]

[1]*Institut für Angewandte Physik, Universität Tübingen, Auf der Morgenstelle 10, D-72076 Tübingen*
[2]*ISIS, Rutherford Appleton Laboratory, Chilton, Didcot, OX11 0OX, UK*
[3]*Chemistry Research Laboratory, University of Oxford, 12 Mansfield Road, Oxford, OX1 3TA, UK*
[4] *Hahn-Meitner-Institut, Department of Structural Research, Glienicker Str. 100, 14109 Berlin*

For the interaction of proteins, the distribution of charges is crucial. In fact, salt ions are ubiquitous in biological media, and the folding of DNA as well as protein is intimately coupled to the counterions that neutralise these macroions. Thus, a detailed understanding of the counterion distribution is essential for many biological systems. However, little is known experimentally about the counterion distribution around charged proteins. ASAXS provides the only way to study this issue by selecting the energies away and near the absorption edge of the target ions, which has been proved by recent successful studies [1-3]. The present work is devoted to the characterization of the counterion distribution around globular proteins, BSA and lysozyme, in aqueous solution using ASAXS.

In the present experiment, we intend to study the ion distribution around proteins as a function of protein and salt concentrations as well as temperature and pH (as a way to control the charge) for BSA and lysozyme in solutions. Proteins with mono-, di- and trivalent salts will be studied by using ASAXS technique. Using the different valencies we will address the question to what extent the higher valency-ions are more localized and the related length scales as well as the effect of protein-ion interaction on the effective protein-protein interactions in solution. During this beamtime, we focused on BSA with trivalent salt, yttrium chloride, in solution. Our goal is to get reliable ASAXS signal for the counterions by optimizing the sample and measurement parameters, such as protein/salt concentration, measuring time and number of energies, etc. and establish the data analysis and fitting protocol for a direct description on the ion distribution around proteins in solution.

Anomalous small-angle X-ray scattering (ASAXS) measurements were carried out at station 7T-MPW-SAXS of BESSY, Berlin. The detector response was calibrated using the scattering from Niobium foil at 18860 and 18800 eV. The angular scale was calibrated using the scattering peaks of Silver Behenate. We have determined the experimental absorption K-edge of yttrium in solution with and without the existence of protein as shown in Figure 1. The absorption edge is 16932 eV, with $\Delta E= -106$ eV compared to the theoretical value (17038 eV). Five energies were selected for ASAXS measurement: with $\Delta E = -4, -14, -48, -152$ and -538 eV.

Protein solutions were filled into capillaries from Hilgenberg GmbH, Malsfeld, Germany. The capillaries are made of borosilicate glass with an inner diameter of 4.0 mm and a wall thickness of 0.05 mm. The scattering of a salt solution was measured as the background, in exactly the same way as the protein solutions and was subtracted from the sample scattering. All measurements were carried out at room temperature. The raw data were corrected for transmission, fluctuation of primary beam intensity, exposure time, and the response of the detector.

Bovine serum albumin (BSA) with protein concentration of 5, 10, and 20 mg/mL and salt concentration (YCl_3) 30 mM, 50mM and 100 mM were measured at five energies with two sample-to-detector distance in order to cover a large q-range. Figure 2 presents the merged scattering profiles of a sample with BSA 20 mg/mL and 30 mM yttrium chloride and the deduced pure resonant term.

The pure resonant term was calculated from the following equation [3]:

$$S_{ion}(q) = \frac{1}{F(E_1, E_2, E_3)}\left[\frac{\Delta I(q, E_1, E_2)}{f'(E_1) - f'(E_2)} - \frac{\Delta I(q, E_1, E_3)}{f'(E_1) - f'(E_3)}\right] \tag{1}$$

Where $F(E_1, E_2, E_3) = f'(E_2) - f'(E_3) + \dfrac{f''^2(E_1) - f''^2(E_2)}{f'(E_1) - f'(E_2)} - \dfrac{f''^2(E_1) - f''^2(E_3)}{f'(E_1) - f'(E_3)}$

In this study, the energies were selected that the imagery part of the scattering factor, f' remains constant for all energies. Hence the observed ASAXS signal will be determined mainly by the real part f'. The successful separation of pure resonant signal for the multivalent ion makes it possible for further understanding the binding number and thickness of counterion around charged protein molecules. Detailed data analysis and model fitting will be carried out imminently. Together with SANS measurements on the same solution, the structure of bind-ion shell around proteins can be evaluated.
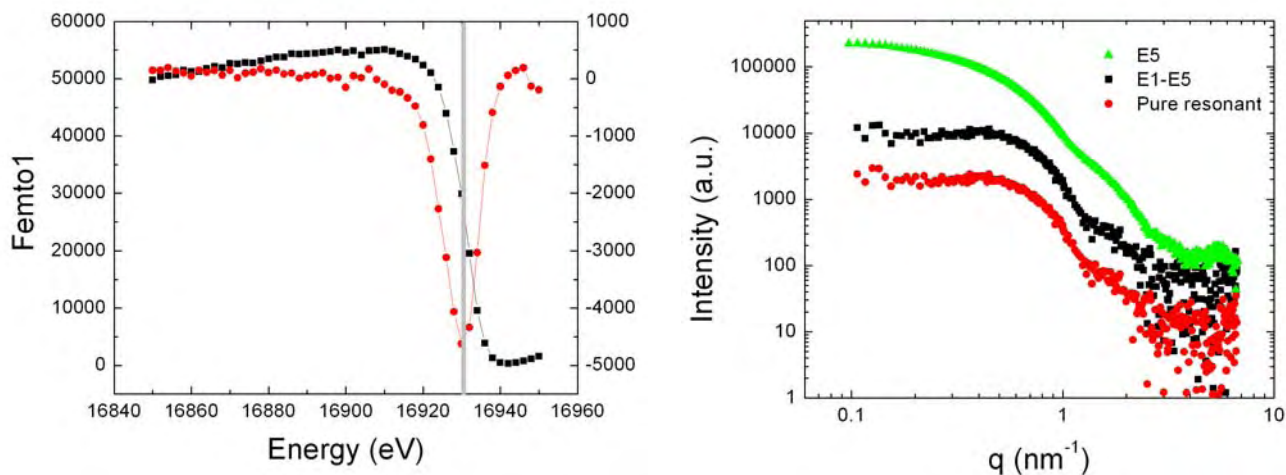
Figure 1 (left). Determination of the absorption edge for yttrium chloride in solution. **Figure 2** (right). Typical ASAXS curves measured at different energies (only one was shown, E5) and the separated ASAXS curve from two energies (E1-E5). The pure resonant term deduced from the separated forms according to Eq. 1.

Nevertheless, we have demonstrated that the ASAXS measurements on the counterion distribution around charged protein molecules are feasible and that information on the ionic cloud can be obtained. The present results encourage us to continue our research on proteins with other counterions, such as Br and Rb.

References

[1] R. Das et al. Counterion distribution around DNA probed by solution X-ray scattering. Phys. Rev. Lett. 2003, 90, 188103
[2] K. Andresen, et al. Spatial distribution of competing ions around DNA in solution. Phys. Rev. Lett. 2004, 93, 248103
[3] G. Goerigk, et al. The distribution of Sr2+ counterions around polyacrylate chains analyzed by anomalous small-angle X-ray scattering. Europhys. Lett. 2004, 66, 33

Characterization of fluorinated singlewalled carbon nanotubes with X-ray absorption and photoelectron spectroscopies

M.M. Brzhezinskaya[1,2], A.V. Krestinin[3], G.I. Zvereva[3], A.P. Kharitonov[3] and A.S. Vinogradov[2]

[1] HZB, 12489 Berlin, Germany
[2] V.A. Fock Institute of Physics, St. Petersburg State University, 198504 St. Petersburg, Russia
[3] Institute of Problems of Chemical Physics RAS, 142432 Chernogolovka, Russia

The graphene layer forming the wall of a single-wall carbon nanotubes (SWCNTs) is a structure that is extremely stable against chemical treatment. Several problems exist, the solution to which urgently demands techniques to chemically modify the nanotube surface to be designated. First, chemical functionalization is required for the use of SWCNTs as the additive in a polymer matrix for the improvement of polymer binder in mechanical properties. Second, for the effective use of SWCNTs in many applications, it is necessary to achieve the best nanotube disintegration in the various media possible, down to the isolated tubes. Fluorination only can potentially become basis for the industrial technology of the chemically modified SWCNT production [1]. In this work, the high-resolution near edge X-ray absorption fine structure (NEXAFS) and X-ray photoelectron (XPS) spectroscopies are used to elucidate the nature of chemical bonding between carbon and fluorine atoms on the surface and inside fluorinated SWCNTs. These methods are very suitable for probing the chemical bonding in polyatomic systems due to their atomic selectivity and high chemical sensitivity [2,3].

SWCNTs were synthesized by an electroarc method using nickel-yttrium catalyst. The purified nanotubes had a narrow diameter distribution with an average value of ~1.5 nm. High-purity SWCNTs (~ 98 wt.%) are obtained in the form of paper (SWCNT paper). The direct fluorination was carried out at a temperature 222 °C for 5 hours [4]. The fluorinated SWCNTs had ~ 35 wt.% fluorine (SWCNTs+F35%). Measurements were performed at the Russian-German beamline at the BESSY II. NEXAFS spectra of all samples were recorded at the C $1s$ and F $1s$ absorption edges in the total electron yield mode with photon energy resolution of 75 and 150 meV, respectively. The XPS spectra were recorded with the exciting photon energies of 385 - 1030 eV with the total energy resolution of 200 meV using Phoibos 150 analyzer.

The NEXAFS spectrum of the pristine SWCNTs (Fig. 1) corresponds well to the spectra of HOPG and MWCNTs. Small distinctions in these spectra usually appear as consistent changes in the relative intensities of the most typical features of the
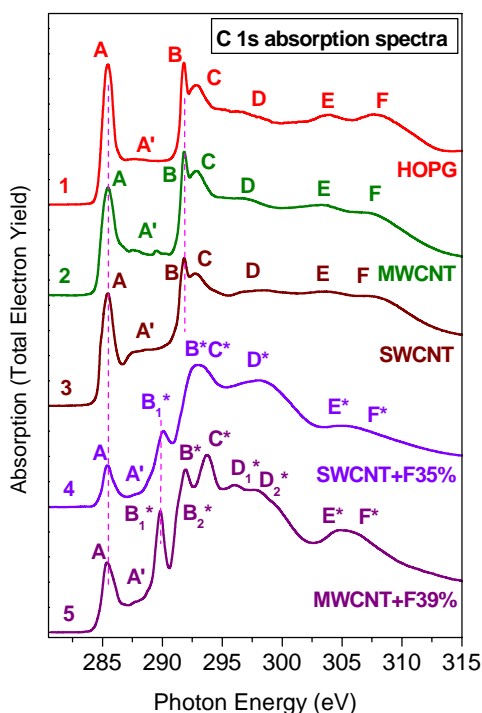
Fig. 1. C $1s$ NEXAFS spectra of HOPG, initial MWCNTs and SWCNTS, SWCNTs+F35% and MWCNT+F39%.

A-B-C structure and inefficient broadening, resulting in "puttying" when turning from HOPG to MWCNTs and SWCNTs. First, the agreement in the spectra of HOPG and SWCNTs indicates the high structural perfection of nanotubes and a lack of any appreciable contribution of the amorphous or other phases of carbon in the samples. Next, this agreement clearly proves the key

role of a single graphene layer in the formation of the C1*s* absorption spectra in HOPG, MWCNTs and SWCNTs [5]; it also certifies the assumption that the dependence of SWCNT conductivity band from tube bending is weak. Hereby, in both the C1*s* absorption spectra of nanotubes and in the HOPG spectrum, the main structures *A–A'* and *B–F* reflect transitions of 1*s* electron of carbon atoms into the free states of the conductivity band, which are formed from the 2*p* electron state of carbon atoms and have π and σ symmetry, respectively [5].

Significant differences in the structure of C1*s* spectra of the pristine and F-SWCNTs are observed. There is a strong decrease in *A* peak intensity, the emergence of new features for structures B_1^*, B^*, C^*, D^* instead of *A'–D* structures, and isolated band *E*–F** formation. We mention that, in addition to new absorption bands in F-SWCNT spectra, *A* band from the spectrum of the original nanotube is retained, proving the fact of incomplete nanotube fluorination.

It is logical to associate the changes observed in C1*s* spectra of F-SWCNTs with the chemical interaction between F atoms and the nanotube wall and, subsequently, the rearrangement of the free-state spectrum in the tubes being explored by X-ray absorption. The appreciable similarity in F-SWCNT and F-MWCNT spectra allows supposing that the chemical binding of fluorine with carbon occurs in both cases, for the most part, by fluorine atoms bonding to carbon atoms on a nanotube sidewall, forming σ(C–F) bonds at the expense of the covalent mixing of F2*p*- and C2p_z-valent electron states [5]. Obviously, such binding of fluorine atoms modifies the coordination of carbon atoms, from triangular in original nanotubes to nearly tetrahedral in fluorinated nanotubes, and it is possible only when sp^2 valent state hybridization of carbon atoms changes for sp^3 hybridization in F-SWCNTs.
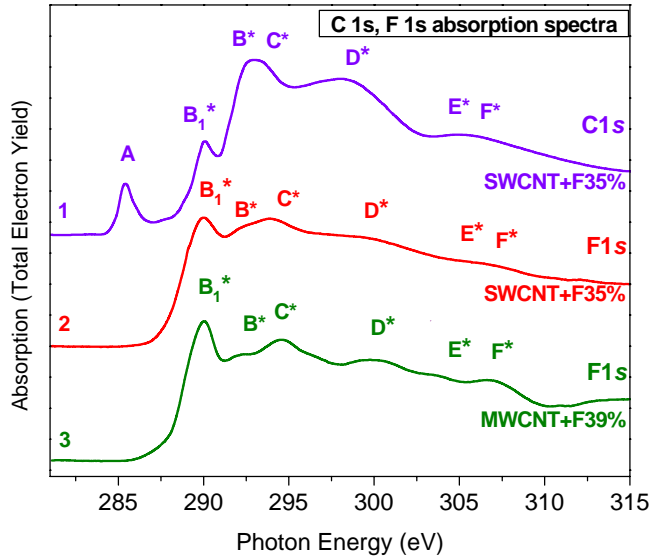
Fig. 2. Comparison of C 1*s* and F 1*s* absorption spectra of SWCNT+F35% and MWCNTs+F39%.

In Fig. 2, the C1s and F1s absorption spectra for F-SWCNTs (curve 2) and F-MWCNTs (curve 3) are shown. Fluorine spectra were reduced to the energy scale of photons in the carbon spectrum using the energy distance $\triangle E$(F1s-C1s) = 398.4 eV between the ground 1*s* levels of F and C atoms in F-SWCNTs, which was measured by the X-ray photoemission method at photon energy of 1030 eV. The F1s-spectra for F-SWCNTs and F-MWCNTs are characterized by very similar fine structures which, in the case of F-MWCNT spectrum (like for carbon spectra), have more relief.

F1*s* absorption spectrum of F-SWCNTs, energetically matched by the C1*s* spectrum, demonstrates a fine structure whose features perfectly correlate to new B_1^*–*F** features, appearing in C1s spectrum as a result of SWCNT fluorination. Such correlation of F1s and C1s spectra had already been observed for F-MWCNTs [5]. This correlation means that both spectra reflect the transitions of ground F1*s*- and C1*s*-electrons into the same vacant electron states of the F-SWCNT conductivity band. New electron states are formed as a result of covalent bonding of carbon and fluorine atoms; therefore, they have a mixed (hybridized) F2*p* – C2p_z character.

C1s photoelectron spectra for F-SWCNTs are presented in Fig. 3. In accordance with the universal curve of the dependence of the electron mean free path from their kinetic energy [3], the escape depth is limited by ~0.5 to 1.5 nm, for all practical purposes restricting the sounding

depth of the sample by means of the near-surface layer, which is as thick as one nanotube diameter by an order of magnitude. As it can be seen from Fig. 3, the signal belonging to carbon atoms of the graphene layer of the initial CNTs (band *A*) partially remains in all spectra. Moreover, in the series of spectra in Fig. 3, an explicit strengthening of this band is observed after increasing of probing depth up to ~1.5 nm from the surface of nanotube rope. That fact unambiguously indicates an appreciable decrease in the fluorination degree of CNTs located inside the rope, i.e., of all nanotubes which do not form the coating surface of the nanotube rope. This result correlates well to the previously discovered increase in the SWCNT fluorination degree upon the improvement of their dispersion, i.e., with the reduction of nanotube rope lateral size formed by them. Comparing C1s spectra of F-SWCNTs, we will mention that all of them except for the signal from the graphene layer (*A* band) contain three additional higher-energy *B-D* bands. The most interesting change in spectra that happens when the energy of exciting photons (and, therefore, the probing depth) increases from ~0.5 nm up to ~1.5 nm is the reduction of the relative intensity of the B band: it decreases more than twice in regard to C band intensity.
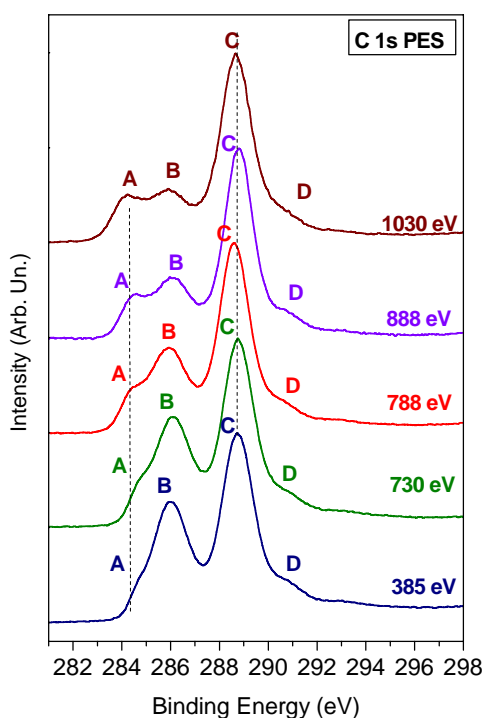
Fig. 3. C 1*s* photoelectron spectra of pristine SWCNT+F35% taken at the different photon energy.

In conclusion, the combined investigation of the F-SWCNTs by highly chemically sensitive X-ray methods is presented. It was observed that fluorination process of SWCNTs is accompanied by chemical bonding between fluorine and carbon atoms on the tube side walls. Fluorine atoms do not substitute carbon atoms in graphene layers of MWCNTs but they add perpendicularly to them as a result of covalent mixing between C $2p_z$ and F $2p$ states. In this case the coordination of carbon atoms changes from sp^2-triangular to sp^3-tetrahedral. The photoelectron spectra showed that the surface of SWCNT ropes is practically fully fluorinated. On the other hand, as deep as ~1.5 nm inside the nanotube ropes, the degree of nanotube fluorination significantly drops.

References

1. E.T. Mickelson, C.B. Huffman, A.G. Rinzler, R.E. Smalley, R.H. Hauge, J.L. Margrave, Chem. Phys. Lett. **296** (1998) 188.
2. J.G. Chen, Surf. Science Report **30** (1997) 1.
3. S. Hüfner, Photoelectron spectroscopy: Principles and Applications (Springer, Berlin 1996).
4. A.V. Krestinin, A.P. Kharitonov, Yu.M. Shul'ga, O.M. Zhigalina, E.I. Knerel'man, M. Dubois, M.M. Brzhezinskaya, A.S. Vinogradov, A.B. Preobrazhenskii, G.I. Zvereva, M.B. Kislov, B.M. Martynenko, I.I. Korobov, G.I. Davydova, V.G. Zhigalina, N.A. Kiselev, Nanotechnologies in Russia, **4** (2009) 60.
5. M.M. Brzhezinskaya, N.A. Vinogradov, V.E. Muradyan, Yu.M. Shul'ga, N.V. Polyakova, A.S. Vinogradov, Phys. Solid State **50** (2008) 587.
6. Carbon Nanotubes, Ed. by M. S. Dresselhaus, G. Dresselhaus, Ph. Avouris (Springer, Berlin, 2000).

Effect of methanol on lignosulfonate macromolecules studied using small-angle x-ray scattering

U. Vainio[*], R. A. Lauten[†], S. Haas[‖], K. Leppänen[‡], L. Veiga[*1],
R. Serimaa[‡], A. Hoell[‖], and R. Gehrke[*]

[*]HASYLAB, DESY, Germany, e-mail: ulla.vainio@desy.de, [†]Borregaard Lignotech, Sarpsborg, Norway,
[‖]Helmholtz-Zentrum Berlin für Materialien und Energie, Berlin, Germany, [‡]Department of Physics, University of Helsinki, Helsinki, Finland

Lignosulfonate, or sulfonated lignin, is a globular polyelectrolyte obtained from wood *via* chemical processing. During sulfite pulping lignin is removed from the wood and transformed into lignosulfonate. Sulfonate groups make the lignosulfonate highly soluble in water, while the rest of the macromolecule is mostly hydrophobic due to aromatic groups. The polymer has been determined to be branched, but also differing views have been presented. In aqueous solution low molecular-weight lignosulfonate has been found to exist as compact flat platelets about 2 nm in thickness. [1]

Lignosulfonate has been tested as a component in low cost methanol fuel cell membranes [2]. To find out more about the inner structure of lignosulfonate and its behaviour in non-polar solvents, we added lignosulfonate into a binary mixture of alcohol and water and varied the concentration of lignosulfonate within the semi-dilute range. It is known that for some polymers the solution properties such as association into larger complexes depend on the order in which methanol and solute are added in the solution [3]. Since lignosulfonate has an overall aromatic nature a solvent with lower polarity might modulate the intra and/or intermolecular bonds. Changes in the structure of the solutions were studied using small-angle X-ray scattering (SAXS) at the 7T-MPW-SAXS beamline at BESSY. Counterions of the charged sulfonate groups are also affected by the polarity of the solvent and they were expected to attach to the sulfonate groups. With anomalous small-angle X-ray scattering (ASAXS) at the same beamline also the counterions, such as rubidium, can be seen and so the location of the charged groups can in theory then be determined.

Experimental

Sodium and rubidium salts of lignosulfonate were prepared at Borregaard Lignotech. The average molecular weights were 7600 g/mol and 9100 g/mol, respectively. The molecular weight of Rb-lignosulfonate is higher only due to the higher mass of Rb with respect to Na. Samples were prepared by dissolving different amount of lignosulfonate in either pure water or in water-methanol mixtures of ratio 3:1 and 1:1. (The lignosulfonate fractions were not soluble in pure methanol.) The volume fractions of lignosulfonate salts in each solution mixture were carefully adjusted to 1.0, 3.7, 7.5, 10.9, 14, and 17 %. The samples were placed in Hilgenberg glass mark tubes with about 4 mm inner diameter and 50 μm wall thickness. SAXS measurements were made with the mark tubes placed in air to avoid leakage of the methanol solution to vacuum. Due to the large background from air scattering, filters needed to be used to guard the 2D gas detector from too high intensities. Measurement time per sample at each sample-to-detector distance and photon energy was about 10 min in SAXS measurements and 30 min in ASAXS measurements. Two sample-to-detector distances were used: 1435 mm and 3804 mm. The measurements were made well below Rb K-absorption edge (15200 eV) at energies 14803, 15085 and 15166 eV to avoid fluorescence and other energy dependent

---

[1]Present address: University of Campinas, Brazil

backgrounds. The magnitude of the scattering vector is defined here as $q = 4\pi \sin\theta/\lambda$, where θ is half of the scattering angle and λ is the wavelength. The data were normalized into absolute units (1/cm) using a glassy carbon of 90 μm thickness as calibration standard.

Results

X-ray absorption near edge structure (XANES) measurements of rubidium lignosulfonate solutions showed that no significant difference is seen in the chemical state of the rubidium in different solutions and concentrations of lignosulfonate within the measurement accuracy (Fig. 1).
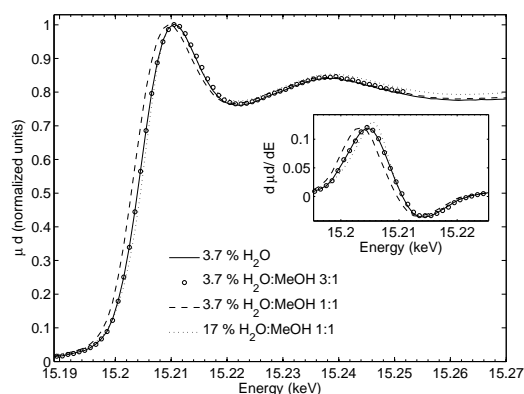
Figure 1: X-ray absorption spectra of lignosulfonate samples of different volume fraction (3.7 % and 17 %) in water, in water–methanol 3:1 and in water–methanol 1:1. μ is the linear absorption coefficient and d is the sample thickness. The inset shows the derivative of μd as a function of energy. The first inflection point of the absorption curve gives the position of the edge.

The ASAXS results for the Rb-lignosulfonate are presented in Fig. 2. A minimum visible in the separated ASAXS data of lignosulfonate in water solution is not seen for methanol–water mixtures. This feature is related to the distribution of rubidium around the lignosulfonate particles in the solution. The two lignosulfonate salts, even though prepared in the same way and having the same valency of +1, had very different behaviour in the methanol–water mixtures according to the SAXS measurements. Therefore the results obtained from ASAXS for the rubidium-lignosulfonate cannot be directly applied to other lignosulfonate salts and may not present the behaviour of the natural state of lignosulfonate.
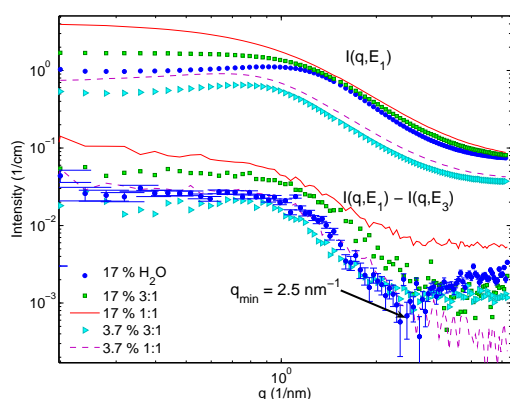
Figure 2: SAXS intensities of some of the rubidium lignosulfonate samples at 14803 eV ($I(q, E_1)$) and the difference of SAXS intensities measured at 15166 and 14803 eV ($I(q, E_1) - I(q, E_3)$). The tail part of the separated curves differs from the total scattering and a strong minimum appears for the concentrated sample in water solution at $q = 2.5$ 1/nm.

References

[1] U. Vainio, R. A. Lauten, and R. Serimaa. Small-angle x-ray scattering and rheological characterization of aqueous lignosulfonate solutions. *Langmuir*, 24(15):7735–7743, 2008.

[2] X. Zhang, J. Benavente, and R. Garcia-Valls. Lignin-based membranes for electrolyte transference. *Journal of Power Sources*, 145:292–297, 2005.

[3] I. Tho, A.-L. Kjøniksen, K. D. Knudsen, and B. Nyström. Effect of solvent composition on the association behavior of pectin in methanol-water mixtures. *European Polymer Journal*, 42(5):1164 – 1172, 2006.

Sub-Terahertz excitations of Charge Density Waves in manganites

A. Nucara, P. Maselli, R. Sopracase, P. Calvani

CNR-INFM Coherentia and Dip. di Fisica, Università di Roma La Sapienza, Roma, Italy

M. Ortolani, U. Schade

Berliner Elektronenspeicherring-Gesellschaft für Synchrotronstrahlung m.b.H., Berlin, Germany

The optical conductivity of La-Ca and Nd-Sr manganites with commensurate charge order (CO) has been first studied in the sub-THz region, by use of the Coherent Synchrotron Radiation of BESSY. Below the ordering temperature T_{CO} of each material, well-defined peaks are observed, associated with side bands. They have been assigned to collective excitations of the Charge Density Waves, namely, pinned phasons and combinations of phasons and amplitudons.

PACS numbers:

Several manganites, like $La_{1-x}Ca_xMnO_3$ (LCMO) with $x \geq 1/2$, exhibit charge ordering (CO) phenomena below a transition temperature T_{CO} [1]. Recent results point toward [2] a weak-coupling, or Charge Density Wave (CDW) [3, 4], approach to the CO phenomena in these materials, even if the collective excitations typical of the CDW have never been observed up to now. One of the CDW modes predicted by the theory is the phason, an infrared-active, acoustic-like, excitation with $\omega_p(\vec{k}=0) = \Omega_p = 0$. Either if the CDW is pinned to lattice impurities, or if it is commensurate with the lattice, one has $\Omega_p > 0$ and the phason can be observed in the very far infrared. The second collective mode is the Raman-active, optically-dispersed amplitudon at $\omega_a(\vec{k}=0) = \Omega_a$. CDW excitations at finite energies have been indeed detected in the subterahertz range (1 THz = 33 cm^{-1}) in one-dimensional metals like the "blue bronze" family[5] $K_{0.3}Mo_{1-x}W_xO_3$. The manganite family offers the opportunity to study the excitation spectrum of a multi-dimensional CDW, provided that one can reach sub-THz frequencies with the desired signal-to-noise ratio.

We have obtained the above result by using the Coherent Synchrotron Radiation (CSR) emitted by the storage ring BESSY when working in the "low-α" mode. We have thus studied, down to frequencies ω_{min} which range from 4.5 to 10 cm^{-1}, the optical conductivity of four manganites. One of them is a $Nd_{1/2}Sr_{1/2}MnO_3$ (NSMO) single crystal, grown by the floating zone method, and here measured in the *ab* plane. Its T_{CO} is 150 K. A second one is a single crystal of $Bi_{0.5}Sr_{0.5}MnO_3$, also grown by the floating zone method [6], and here measured both in the *ab* plane and along the *c* axis. The remaining three samples are polycrystalline pellets of $La_{1-n/8}Ca_{n/8}MnO_3$ with $n = 5,6,7$, and with $T_{CO} = 270$, 230, and 150 K, respectively [7]. The reflectivity $R(\omega)$ of all samples, 2-mm thick, was measured at nearly normal incidence after accurate polishing with sub-micron-thick powders. Conventional radiation sources were used between 20 and 6000 cm^{-1}, the CSR of the BESSY storage ring [10, 11] from ω_{min} to 30 cm^{-1}. $R(\omega)$ was extrapolated to $\omega = 0$ by accurate Drude-Lorentz fits and $\sigma(\omega)$
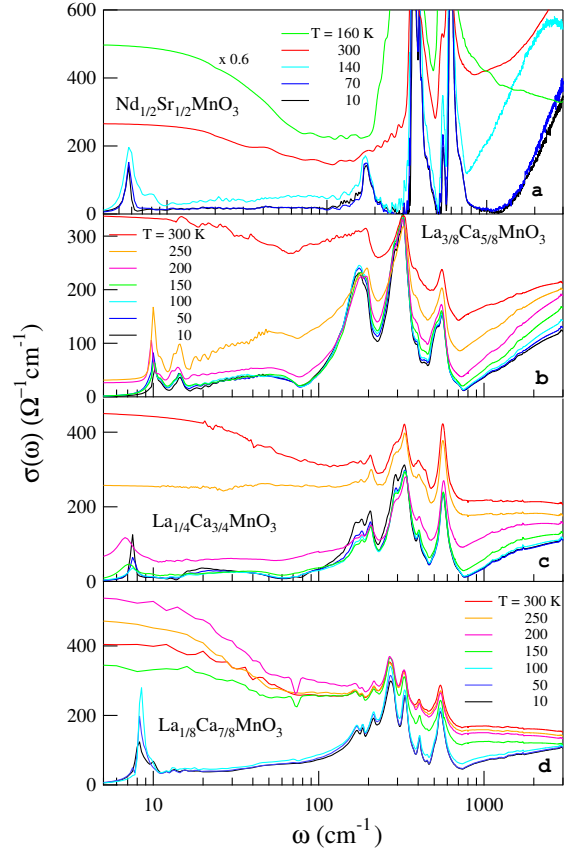
FIG. 1: Optical conductivity at different temperatures of the single crystal of $Nd_{1/2}Sr_{1/2}MnO_3$ and of the polycrystalline pellets of $La_{1-n/8}Ca_{n/8}MnO_3$.

was obtained by standard Kramers-Kronig transformations.

The optical conductivity of the four samples is shown in Fig. 1. At the highest T's it exhibits a weak Drude term, while below T_{CO} an optical gap 2Δ opens in the spectra of all samples. By smooth extrapolations of the lowest-T curves to $\sigma = 0$, one finds $2\Delta(T \simeq 0) \sim 800$ cm^{-1} or 0.1 eV in the polycrystalline samples of LCMO,
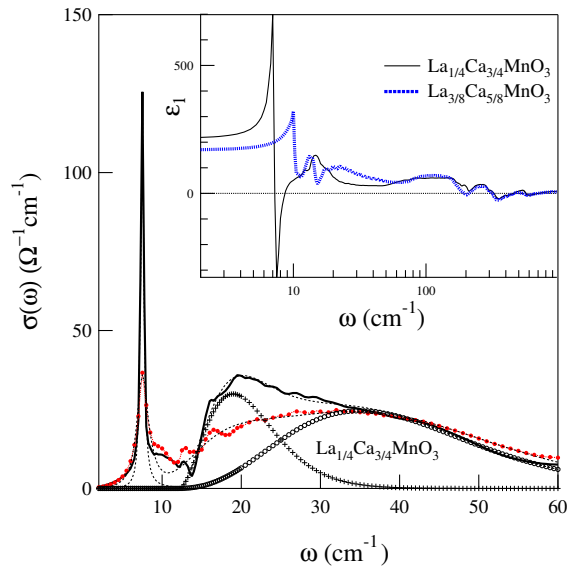
FIG. 2: Low-energy conductivity of $La_{1/4}Ca_{3/4}MnO_3$ at 10 K (solid line) and 100 K (dots) with the corresponding best fits (thin-dotted lines). The side band is the sum of the overtone $2\Omega_p$ and of the combination band $\Omega_p + \Omega_a$, as shown at 10 K by crosses and open circles, respectively. The inset shows the CDW contribution to the real part of the dielectric function $\epsilon_1(\omega)$ in two samples at 10 K.

~ 0.2 eV in NSMO. Correspondingly, sharp conductivity peaks appear at the lowest frequencies in all panels of Fig. 1. We assign the peaks in the sub-THz range to phasons in a "pinned state", consistently with the presence in our samples of both impurities and commensurability. Their frequencies Ω_p are all larger than in [5] $K_{0.3}MoO_3$ (3.3 cm^{-1}) and, in the three samples with CE-type charge order, are found to scale with T_{CO}.

In the La-Ca manganites with $n = 5,6$ a broad side band is also detected below 100 cm^{-1}. It shows the same T-dependence as the main peak and disappears into the Drude continuum above T_{CO}. Fig. 2 shows in further detail both sub-THz bands of $La_{1/4}Ca_{3/4}MnO_3$, indicating that the side band is in fact the sum of two contributions. One of them broadens with T like the phason peak at 7.5 cm^{-1}, while the other one is nearly T-independent. A similar fit was obtained for $La_{3/8}Ca_{5/8}MnO_3$. We assign those two features to the overtone $2\omega_p$ and to a phason-

amplitudon combination band $\omega_p + \omega_a$, respectively, basing on several arguments [12].

Both the pinned-phason mode and the amplitudon have a high density of states close to $\vec{k}_a = 0$, where their dispersion is nearly flat. If therefore $\omega_p + \omega_a$ is peaked at $\Omega_p + \Omega_a$, and $\delta_{p+a} \simeq \delta_{2p}$, one obtains for Ω_a 40 (30) cm^{-1} for $x = 5/8$ (3/4) which provides and electron-phonon interaction strength $\lambda = 0.8$ (0.7) . These moderately low values show that the assumptions of the CDW model are thus justified _a posteriori_.

By using further relations which link the frequencies and the CO gap here measured to the charge dynamics, one can obtain [12] the effective mass of the CDW. It turns out to be $m^*/m_b \simeq 400$ (700) for $x = 5/8$ (3/4) at 10 K, to be compared with $m^*/m_b \simeq 800$ reported for the one-dimensional CDW of $K_{0.3}MoO_3$ [5]. Also the CDW contribution to the dielectric constant ϵ_0^{CDW} can be determined. As here ω_{min} is lower than any CDW absorption, the experimental $\epsilon_1(\omega_{min})$ at low T measures ϵ_0^{CDW}, after one subtracts the phonon contributions and the high-frequency term ϵ_∞. From the inset of Fig. 2 one obtains $\epsilon_0^{CDW} = 100$ (150) at $x = 5/8$ (3/4). These results can be compared with the theoretical prediction of the CDW theory [4], which in the present case[12] gives $\epsilon_{0,calc}^{CDW} = 90$ (120) at $x = 5/8$ (3/4). Therefore, also under this respect the CDW theory is in very good agreement with the experiment.

In conclusion, we have first explored in the sub-THz range the optical conductivity of four manganites with T_{CO} spanning from 130 to more than 500 K, by using a coherent, sub-Terahertz radiation source. In all samples with $T_{CO} < 300$ K we have found sharp peaks which disappear above T_{CO} and are similar to those reported for one-dimensional CDW's. They have been assigned to pinned phasons, followed by broad combinations of phasons and amplitudons. In two La-Ca manganites, a detailed analysis based on the CDW theory has allowed us to determine the electron-phonon coupling, the CDW effective mass, and the CO-phase contribution to the dielectric constant. These parameters are consistent with a description of the charge order in La-Ca manganites in terms of charge density waves, even at commensurate doping.

[1] C. H. Chen and S.-W. Cheong, Phys. Rev. Lett. 76 , 4042 (1996).
[2] G. C. Milward, M. J. Calderón, and P. B. Littlewood, Nature (London) 433 , 607 (2005).
[3] P. A. Lee, T. M. Rice, and P. W. Anderson, Solid State Commun. 14 , 703 (1974).
[4] G. Grüner, Rev. Mod. Phys. 60 , 1129 (1988).
[5] L. Degiorgi and G. Grüner, Phys. Rev. B 44 , 7820 (1991).
[6] C. Frontera, J. L. García-Munoz, A. Llobet, M. A. G. Aranda, C. Ritter, M. Respaud, and J Vanacken, J. Phys.: Cond. Matt. 13, 1071 (2001).
[7] M. Pissas and G. Kallias, Phys. Rev. B 68 ,134414 (2003).
[8] A. Douy and P. Odier, Mat. Res. Bull. 24 , 1119 (1989).
[9] K. Tobe, T. Kimura, and Y. Tokura, Phys. Rev. B 69 , 014407 (2004).
[10] M. Abo-Bakr et al., Phys. Rev. Lett. 90 , 094801 (2003).
[11] M. Ortolani et al., Phys. Rev. Lett. 97 , 097002 (2006).
[12] A. Nucara et al., Phys. Rev. Lett. 101, 066407 (2008).

Characterisation of Bone Mineral Density around Modified Titanium Implants in an Osteoporotic Rat Model with Synchrotron Microcomputed Tomography (SRμCT)

R. Bernhardt, J. Dudeck, D. Scharnweber, St. Rammelt[1], J. Goebbels[2], G. Vollmer[3], H. Worch

Max Bergmann Center for Biomaterials, Technische Universität Dresden, Germany
[1]Department of Trauma and Reconstructive Surgery, University Hospital "Carl Gustav Carus", Dresden, Germany
[2]Federal Institute for Materials Research and Testing (BAM), Berlin, Germany
[3]Institute for Zoology, Technische Universität Dresden, Germany

Introduction

Synchrotron microcomputed tomography (SRμCT) has been applied successfully to analyse quantitatively the bone formation around biofunctionalised titanium implants resulting in a higher bone volume content in relation to uncoated implants in a goat model [1].

As the mineral content of the newly formed bone indicates the stadium of the remodelling process, a three dimensional investigation of this parameter is a promising tool to understand how biofunctionalised implant surfaces influence the local bone mineralisation in their surrounding, especially if the overall bone quality is week or influenced by bony diseases.

Goal of the present work was to describe the mineral structure of bone for selected areas of explants in an osteoporotic rat model including a hormone therapy. Based on SRμCT data, the local distribution of bone mineralisation should be determined three dimensionally as a function of the conditions ‚healthy', ‚osteoporotic' and 'hormone treated osteoporotic'. New knowledge is expected for the osseointegration of biofunctionalised titanium implants for normal as well as for disordered bone regeneration.

Materials and Methods

As the animal model, ovariectomised rats with and without hormone treatments were used for the analytical investigations. Titanium wires with a diameter of 0.8 mm with biofunctional coatings of Chondroitin Sulphate (CS), Bone Morphogenetic Protein 4 (hBMP 4) and a blank control (cp-Ti) were placed in the tibia of ovariectomised rats for 4 weeks. After the animal experiments, the rat tibiae were freed from adherent soft tissue, fixed in paraformaldehyde and dehydrated in ethanol in a graded series of increasing concentrations. The embedding was performed in Polymethyl-metacrylate (PMMA). At the BAMline (BESSY II) 27 specimens, with 3 samples for each condition, were evaluated with Synchrotron microcomputed tomography (SRμCT). For each sample 720 X-ray attenuation projections with a local resolution of 9 μm were acquired using a monochromatic X-ray energy of 30 keV.

Results and Discussion

The SRμCT reconstruction of the explants shows a detailed visualisation of bone formation around the titanium implants and directly on the implant surface (Fig. 1). Assigning different colours to the x-ray absorption values (grey levels), local areas of higher and lower mineral content could be visualised for the bony tissue. On the implant surface a network of newly formed bone with different thickness and mineralisation could be observed. This findings indicate a specific reaction of the organism to the functionalised titanium wires.

The analysis of relations between different implant surfaces, bone conditions and/or hormone therapy to the characteristics of the three-dimensional network around the implants is still under investigation. A suitable imaging procedure for a volumetric analysis related to this specific model was developed (Fig. 2).
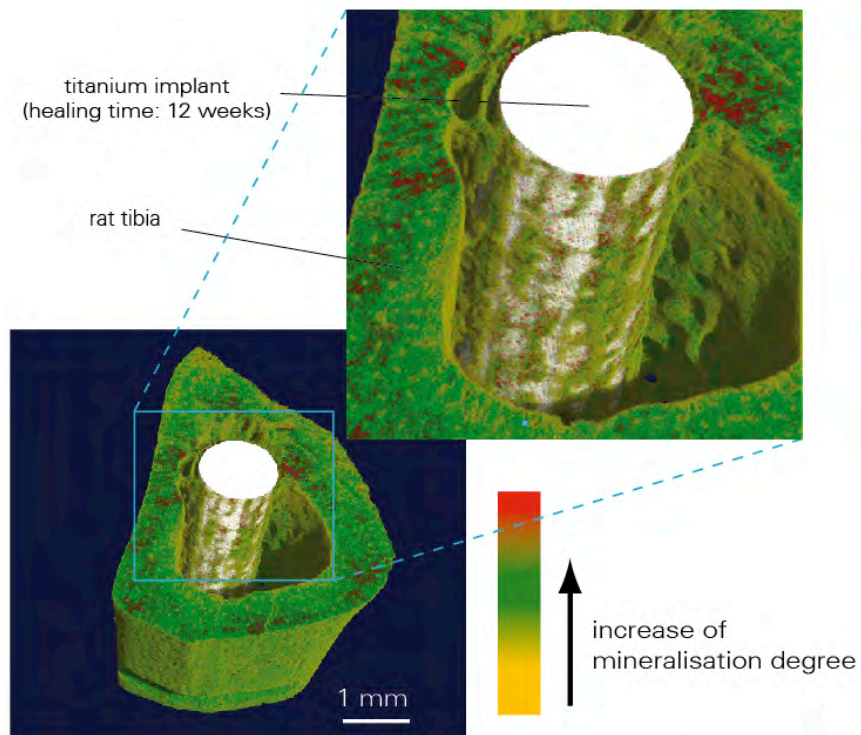
Fig. 1: SRµCT visualisation of different mineralised bone on a biofunctionalised titanium wire (white) after a healing time of 4 weeks in a rat tibia.
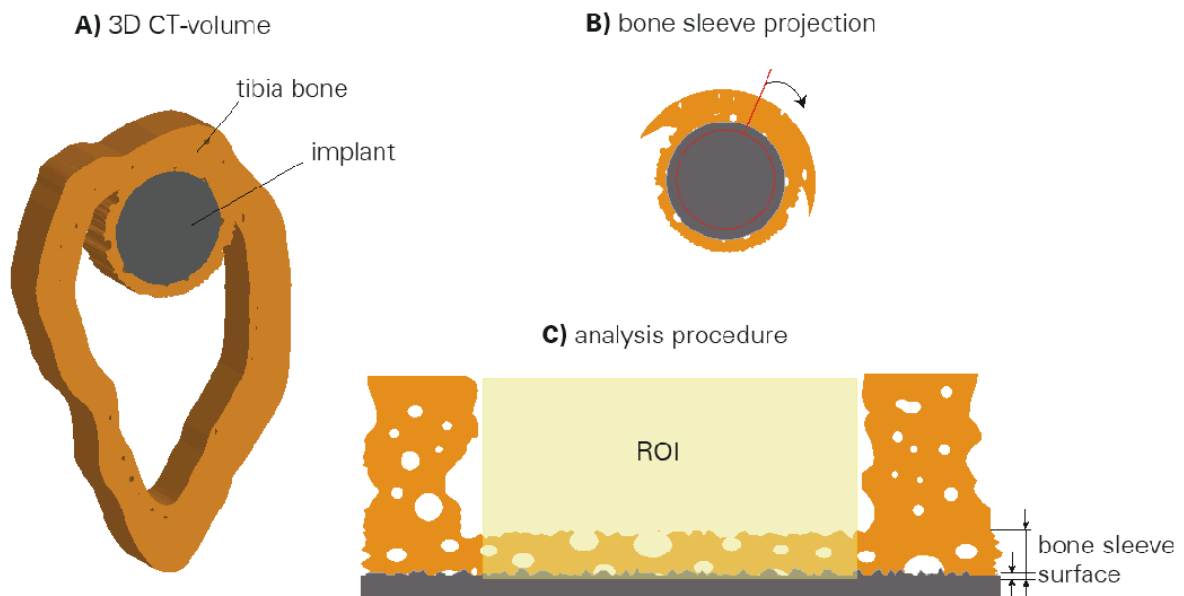
Fig. 2: Adapted analysis procedure to obtain 3D-information of newly formed bone from SRµCT-measurements around cylindrical implants.

Acknowledgments

References:
[1] Bernhardt et al., Biomaterials 26, 3009 (2005)

Vacuum Ultra-Violet Spectroscopic Ellipsometry of DNA Layers Covalently Attached to Diamond and Silicon

Sylvia Wenmackers, Patrick Wagner,
Hasselt University, IMO, Wetenschapspark 1, 3590 Diepenbeek, Belgium

Veronique Vermeeren, Luc Michiels,
Hasselt University, BIOMED, Agoralaan Building C, 3590 Diepenbeek, Belgium

Simona D. Pop, Christoph Werner, Christoph Cobet, and Norbert Esser.
Institute forAnalytical Sciences-ISAS, Albert-Einstein-straße 9, 12489 Berlin, Germany

Our group has developed a prototype DNA sensor on diamond. The DNA probes are covalently attached to diamond surfaces using an effective two-step protocol [1], and the location of the DNA probes can be predetermined by photopatterning the linker layer. This platform is sensitive for point mutations, as was demonstrated using fluorimetric read-out [1] as well as real-time, label-free impedance spectroscopy [2].

In the framework of this project, we are interested in the molecular organisation of DNA probe layers (brushes), both in single and double stranded form. One technique to study DNA brushes on diamond is "nano-shaving" with an atomic force microscope [3]. To study the orientation of immobilised, short DNA strands (8-36 bases) in a non-destructive way, we apply vacuum UV spectroscopic ellipsometry (SE).

We demonstrated that this technique can indeed be used to detect (sub-)monolayers of short DNA strands on ultra-nanocrystalline diamond (UNCD) surfaces. Based on the 4.74 eV transition due to the π-π^* transition dipole moments of the DNA bases, the orientation of the DNA strands could be calculated: we found average tilt angles ranging from 45° to 52° [4].

Since UNCD has an root-mean-square surface roughness of 17 nm, the interpretation of the obtained tilt angles is not straightforward for biological layers thinner than that. Hence, we performed additional 'mapping SE' experiments on UNCD samples, to qualify the lateral spread on the average DNA tilt angles. This made clear that the roughness of the DNA layer can vary from point to point: in Figure 1 and Table 1, three spots have been compared of the same UNCD sample functionalised with double stranded DNA of 29 base pairs. We also collected spectra on atomically flat surfaces to examine tilt angles caused only by the inter-molecular interactions of DNA in dense layers, not by the topography of the underlying surface. At first we opted for DNA-modified single crystalline diamond (SCD). Typically, SCD samples have a surface area limited to (2 mm)². Taking spectra on such small areas is far from trivial. Therefore, we examined additional DNA-layers covalently coupled to single crystalline Si: these substrates are also atomically flat, but larger in surface area, *e.g.* (1 cm)².

The reference spectra collected on clean SCD and Si samples correspond well with UV spectra found in literature. The additional features in the spectra of linker- and DNA-modified SCD and Si samples are similar to those previously recorded on UNCD. Further calculations based on the new data are ongoing, to reveal possible variations in the average orientation of the DNA strands between the previously analysed UNCD samples on the one hand, and the SCD and Si samples on the other, as well as between different spots on the same SCD or Si sample.
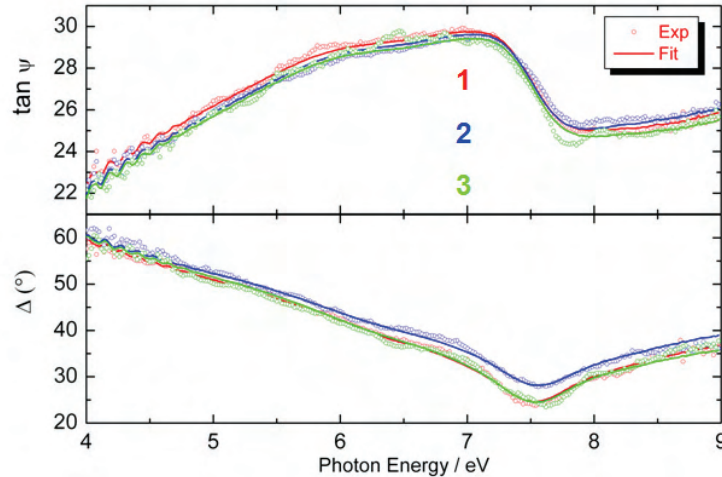
Figure 1: Vacuum UV ellipsometry on UNCD with double-stranded DNA of 29 base pairs. Measured (open symbols) and fitted (lines) spectra of three spots on the same sample.

Table 1: Layer thickness and roughness of the DNA layer (29 base pairs) of the three spots considered in Figure 1, calculated from the fitted spectra.

Film Thickness (nm)	Roughness (nm)
12.7	2.5
12.8	0.5
12.7	1.0

References
[1] Vermeeren, V.; Wenmackers, S.; Daenen, M.; Haenen, K.; Williams, O. A.; Ameloot, M.; vandeVen, M.; Wagner, P.; L. Michiels, L. *Langmuir* **2008**, *24*, 9125.
[2] Vermeeren, V.; Bijnens, N.; Wenmackers, S.; Daenen, M.; Haenen, K.; Williams, O. A.; Ameloot, M.; vandeVen, M.; Wagner, P.; L. Michiels, L. *Langmuir* **2007**, *23*, 13193.
[3] Rezek, B.; Shin, D.; Uetsuka, H.; Nebel, C. E. *physica status solidi (a)* **2007**, *204*, 2888.
[4] Wenmackers, S.; Pop, S. D.; Roodenko, K.; Vermeeren, V.; Williams, O. A.; Daenen, M.; Douhéret, O.; D'Haen, J.; Hardy, A.; Van Bael, M. K.; Hinrichs, K.; Cobet, C.; vandeVen, M.; Ameloot, M.; Haenen, K.; Michiels, L.; Esser, N.; Wagner, P. *Langmuir* **2008**, *24*, 7269.

Near-Surface Stress Gradient in Shot Peened Ti-Alloys Measured by Energy-Dispersive Synchrotron Radiation

Proposer: **Emad Maawad**
Institute of materials science and engineering, TU Clausthal, Germany.
Co-Proposer: **H.-G. Brokmeier**
Institute of materials science and engineering, TU Clausthal, Germany.
GKSS resarch center, Geesthacht, Germany.
Experimental Team: M. Klaus, C. Genzel, J. Gibmeier
BESSY, 12489 Berlin, Germany.

Objective

Mechanical surface treatments such as shot peening (SP) or ball-burnishing lead to changes in the near-surface material states. This is mainly the result of induced plastic deformation which results in work-hardening and the generation of residual stresses. Residual compressive stresses are well known to enhance the fatigue performance and corrosion resistance of a number of metallic materials by retarding or even suppressing micro-crack growth from the surface into the interior. The shot peening-induced residual stresses in shot peened titanium alloys Ti-2.5Cu and Timetal LCB were evaluated by applying energy-dispersive (ED) diffraction using synchrotron radiation because of a higher penetration depth compared to conventional X-ray diffraction [1,2]. The main objective of this study is to measure the compressive residual stresses in deeper region below the surface of aforementioned alloys.

Experiment

Residual stress measurements were performed by applying hard X-rays using synchrotron radiation. Stresses are evaluated by means of the $\sin^2\psi$ method. Energy dispersive X-ray diffraction technique using synchrotron radiation allows the non-destructive measurement of residual stress depth-profile. This technique uses white X-ray beam with various energy ranges, 20 ~ 120 keV in general. Table 1 shows the required parameters of hard x-ray diffractometer.

Table 1. Diffractometer parameters

Beam size	0.50 mm x 0.50 mm
Detector slit	0.03 (H) x 8.00 mm (V)
Beam energy	Up to 120 keV
2-Theta	8° (for Ti-2.5Cu) and 6° (for LCB)
Phi	0°
Psi	0° to 80° (~21 steps)
Exposure time	300 sec.

The residual stress depth profiles were measured in shot peened samples, Ti-2.5C and Timetal LCB. Peening was done to full coverage at Almen intensities of 0.11 and 0.20mmA. Blanks ($20x20x5-10mm^3$) were cut. Some layers (50, 100, 150, 200 µm) were removed by using electro-polishing to reach the stress-free zone.

Achievements and Main Results

Fig. 1 shows examples of the relation between lattice spacing (d) and $(\sin^2\Psi)$ for Ti-2.5Cu. No steep residual stress gradient was found.
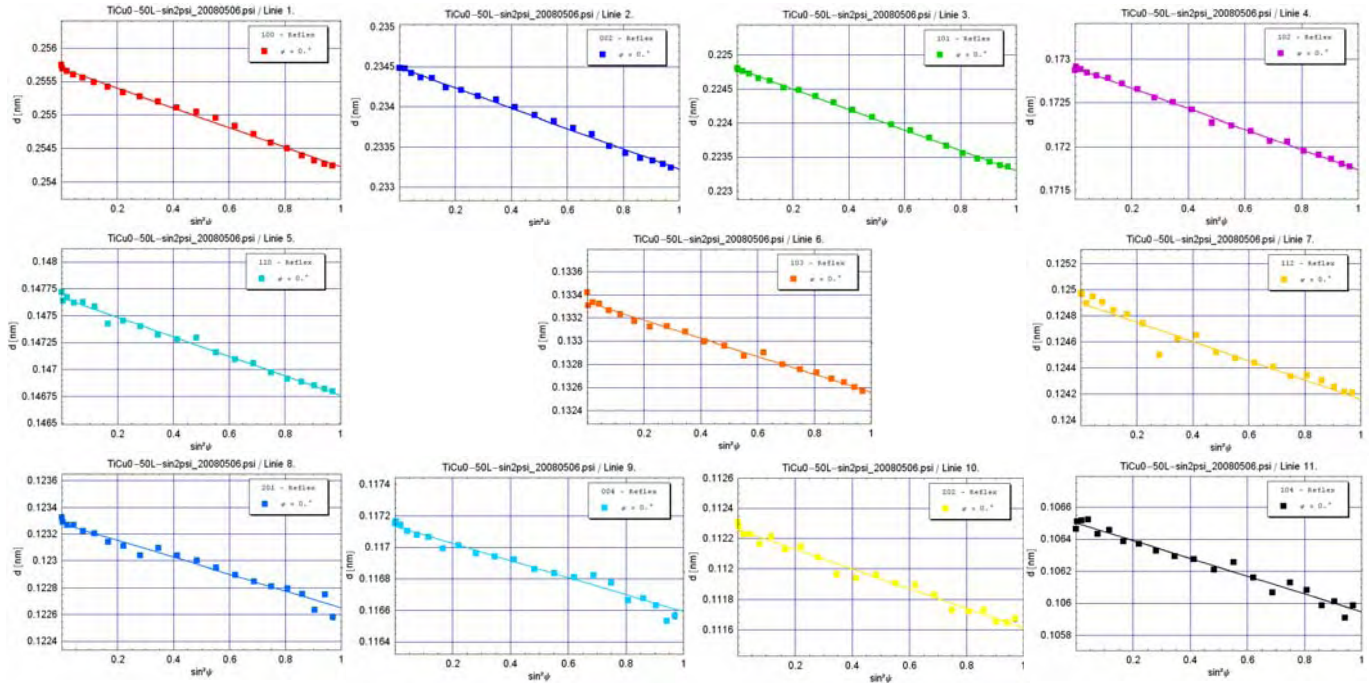
Fig. 1 The relation between lattice spacing (d) and $(\sin^2\Psi)$ for Ti-2.5Cu

Fig. 2 and Fig. 3 show the residual stresses profiles $\sigma(\tau)$ of shot peened Ti-2.5Cu at Almen intensities of 0.11 and 0.20mmA, respectively. It is observed that the residual stress-depth profile obtained from the synchrotron radiation is exponentially damped transform of the actual or real space stress depth. This is explained by the *'modified multi wavelength method'* used in the synchrotron radiation measurements yields the residual stress depth profiles in the Laplace space, i.e. sigma(τ). In addition, The tensile residual stress is located deeper than 300 μm.

$RS = -473.846-4.272T+0.007T^2-5.008(10^{-4})T^3+1.603(10^{-6})T^4-2.019(10^{-9})T^5$
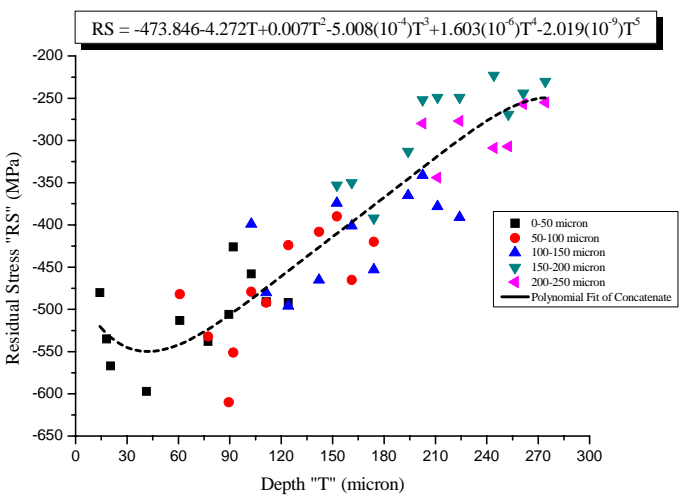
Fig. 2 Residual stress profile of SP (0.11 mmA) Ti-2.5Cu

$RS = -567.102-3.292T+0.058T^2-4.6388(10^{-4})T^3+1.851(10^{-6})T^4-2.645(10^{-9})T^5$
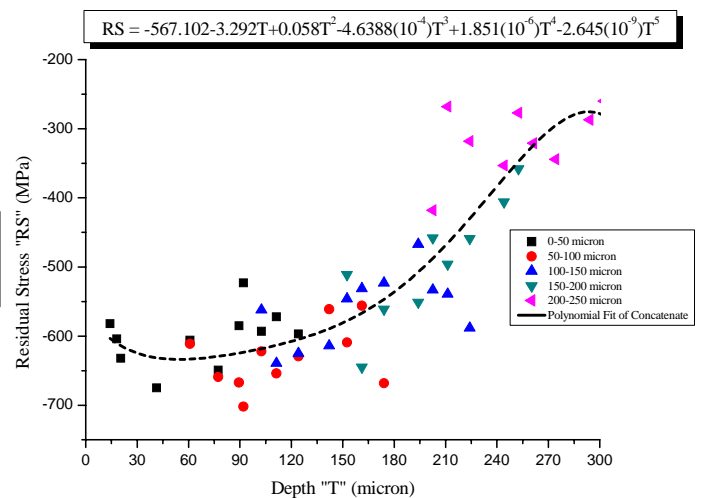
Fig. 3 Residual stress profile of SP (0.20 mmA) Ti-2.5Cu

Fig. 4 shows examples of the relation between lattice spacing (d) and (sin²Ψ) for α-phase and β-phase of TIMETAL LCB.

Alpha **Beta**
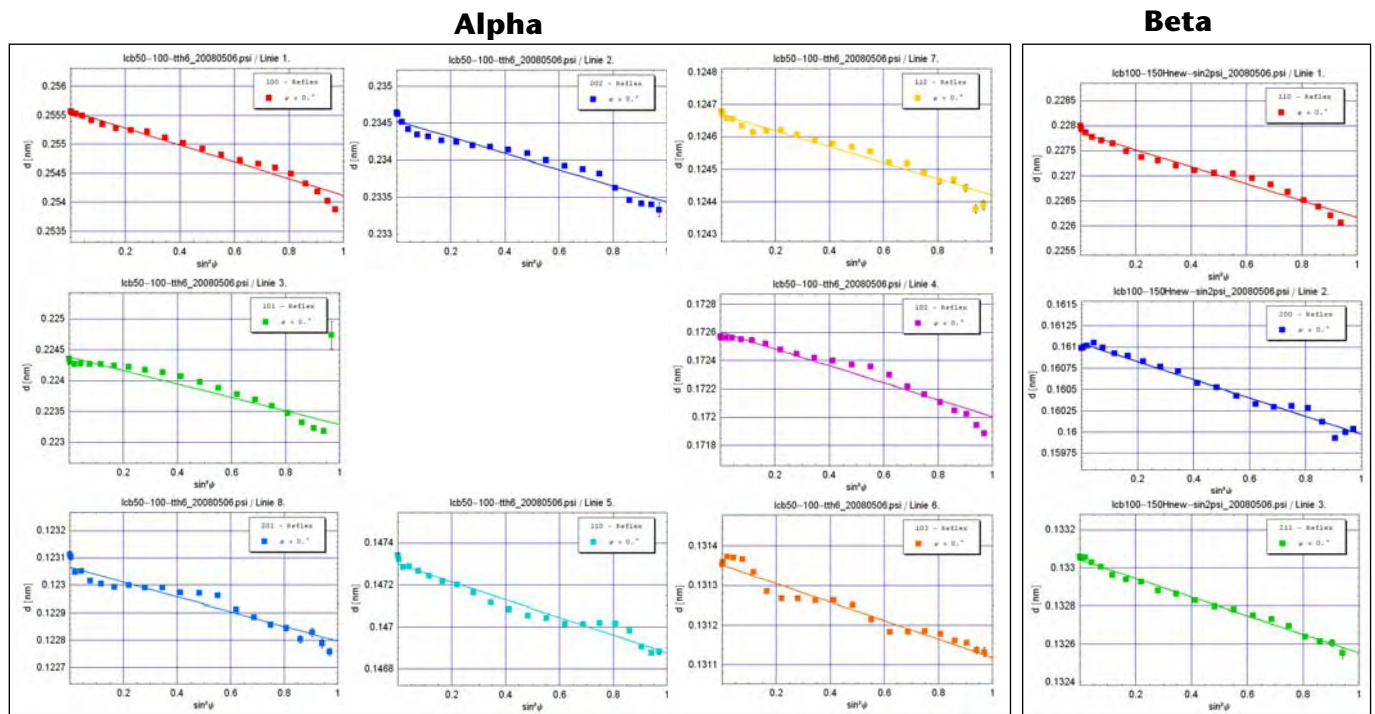
Fig. 4 The relation between lattice spacing (d) and (sin²Ψ) for Timetal LCB

Fig. 5 and Fig. 6 show the residual stresses profiles of shot peened (0.11 mmA) α and β in Timetal LCB, respectively. It is observed that the free stress point is 270 (approx.) μm in depth for β-phase.

$$RS = -411-10.363T+0.202T^2-0.001T^3+2.913(10^{-6})T^4-2.615(10^{-9})T^5$$

$$RS = -510.340-37.820T+0.670T^2-0.005T^3+1.470(10^{-5})T^4-1.657(10^{-8})T^5$$
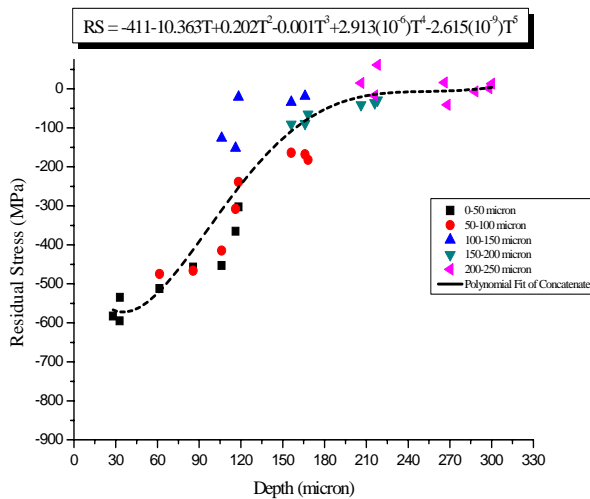
Fig. 5 Residual stress profile of SP (0.11 mmA) α-phase of LCB
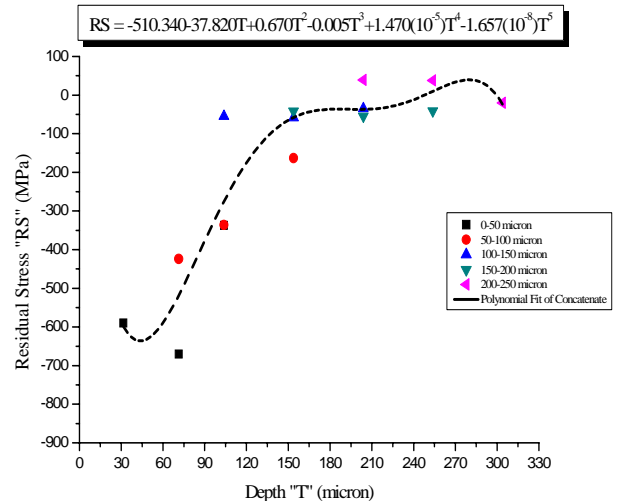
Fig. 6 Residual stress profile of SP (0.11 mmA) β-phase of LCB

The difference of residual stresses between α and β phases is explained by the difference in the yield strength. The β Ti-alloys have in general larger yield strength comparing to that of α alloys, so that the potential maxima of the induced residual stress by plastic deformation is larger in the β phase.

Fig. 7 and Fig. 8 show the residual stresses profiles of shot peened (0.20 mmA) α and β in Timetal LCB, respectively. Also, it is observed that the residual stresses induced in α and β phases are different.

$$RS = -405.840 - 8.122T + 0.066T^2 - 8.483(10^5)T^3 - 4.168(10^7)T + 1.01(10^9)T^5$$

$$RS = -400 - 47.420T + 0.739T^2 - 0.005T^3 + 1.501(10^5)T^4 - 1.707(10^8)T^5$$
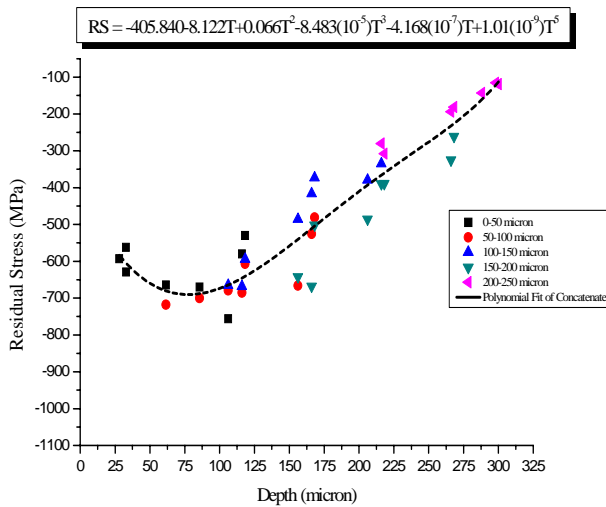
Fig. 7 Residual stress profile of SP (0.20 mmA) α-phase of LCB
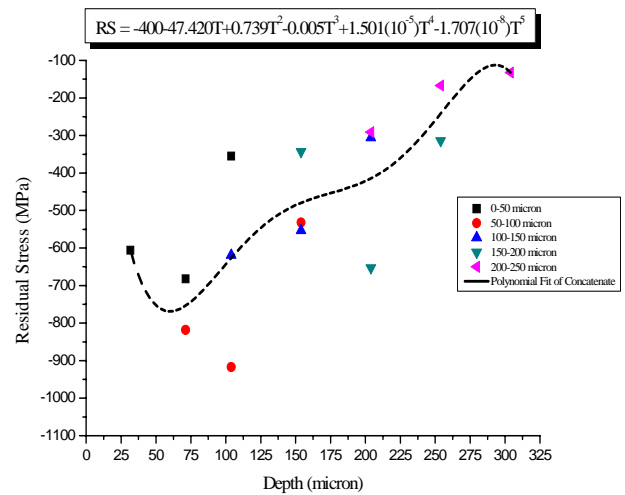
Fig. 8 Residual stress profile of SP (0.20 mmA) β-phase of LCB

A difficult problem concerns the neumerical inverse Laplace transformatiom (NILT), which has to be applied in order to obtain the residual stress profiles **σ(z)** in the real z-space from the experimentally determined Laplace space stressses **σ(τ)** [1].

Acknowledgements

References

[1]Ch. Genzel, C. Stock, W. Reimers, Materials Science and Engineering A 372 (2004) 28-43.
[2]Ch. Genzel,C. Stock, B. Wallis, W. Reimers, Nuclear Instruments and Methods in Physics Research A 467-468 (2001) 1253-1256.

In situ observation of liquid water evolution and transport in PEM fuel cells

Ph. Krüger[1], R. Kuhn[1], H. Riesemeier[3], J. Banhart[2], I. Manke[2], Ch. Hartnig[1]

[1]Centre for Solar Energy and Hydrogen Research (ZSW)

[2]Helmholtz Centre Berlin for Materials and Energy (HZB)

[3]Federal Institute for Materials Research and Testing (BAM)

Abstract:

Liquid water transport has been visualized in situ with a so far unique spatial and temporal resolution. For the synchrotron studies two different viewing directions have been chosen in order to get a pseudo-3D insight in processes on a microscopic scale.
The water content of the different components in a fuel cell and diffusion barriers for the reactant gases have been determined. The different components show a sufficiently different absorption coefficient to distinguish them. Liquid water appears at first close to the catalyst layer; the adjacent micro-porous layer is free of liquid water. In the porous gas diffusion media, water condenses and is from there transported in an eruptive manner to the channel of the flow field.
Component providers and fuel cell developers will benefit from these insights for optimization and design purposes.

Detailed report:

Water management is the key problem in state-of-the-art hydrogen driven fuel cells. Considerable efforts have already been reached by new designs of flow field structure which allow a well-balanced distribution of reactants and help to avoid the formation of large amounts of liquid water. Still the performance suffers from excess water in the gas diffusion layer or drying-out phenomena, e.g. at dynamic operating conditions. These problems can be addressed by, e.g., fine tuning of diffusion materials. A fundamental understanding of water distribution and transport in gas diffusion media features the key pathway to achieve the target of well distributed water content.
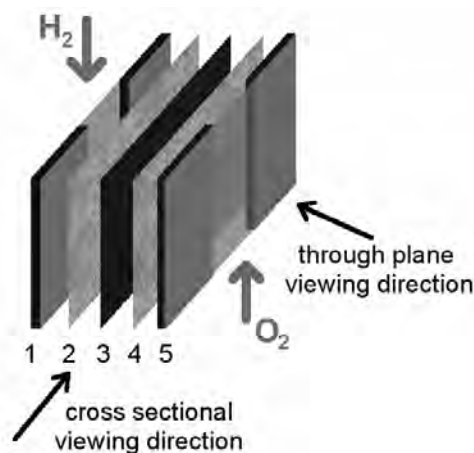
Figure 1: Insight in fuel cells from two different directions.

The observation of liquid water evolution and transport in PEM fuel cell under operating conditions is realized on a microscopic level with a resolution down to 3 µm [1, 2]. By means of synchrotron X-ray radiography the initial formation of small water clusters in the gas diffusion layer and the transport from the diffusion media to the channel of the flow field are detected. The employed fuel cell setup allows for an unperturbed and unbiased insight to the evolution and transport mechanisms of liquid water under operating conditions.

In figure 1, two different viewing directions have been chosen, the through-plane view and the cross-sectional view.
Through-plane imaging allows for a differentiation between areas under the land and the channel of the flow field (Fig. 2). Water evolution starts under the land of the flow field; from a certain pressure onwards the water clusters are transported in an eruptive mechanism from the GDL to the gas channel.
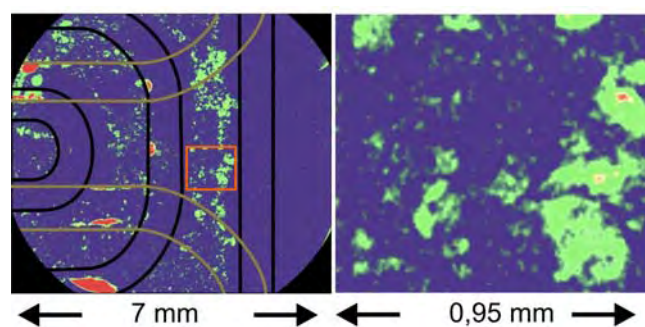
Figure 2: Though plane view in an operation fuel cells. On the right side liquid water clusters under the ribs can be distinguished.

The cross-sectional viewing direction allows a separate investigation of the different components: Gas diffusion layer (GDL), micro porous layer (MPL) and membrane electrode assembly (MEA). It helps to clarify transport mechanisms from the source of water evolution to the gas channel (Fig. 3).
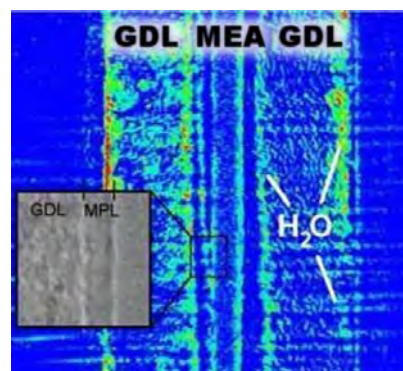
Figure 3: Cross sectional view on liquid water formations in an operating PEM fuel cell.

The dynamic formation of water cluster at changed operating conditions is monitored and the increase of water content in the gas diffusion media can be described. Based on the experimental findings previous results from modeling and simulation approaches are confirmed, which consider the area under the ribs as the primary source of liquid water. A recently proposed eruptive mechanism for the water transport from the gas diffusion layer to the channel, which was observed in *ex situ* experiments, is now supported by the presented *in situ* results.

NEXAFS characterization of electronic structure for CuI@SWCNT nanocomposite

M.M. Brzhezinskaya[1,2], A.V.Generalov[2], R. Püttner[3], A.S. Vinogradov[2],
M.V. Chernysheva[4], A.A. Eliseev[4], N.A. Kiselev[5], A.V. Lukashin[4], and Yu.D. Tretyakov[4]

[1] HZB (BESSY GmbH), Albert-Einstein-Str. 15, 12489 Berlin, Germany
[2] V.A. Fock Institute of Physics, St. Petersburg State University, St. Petersburg, Russian Federation
[3] Institut für Experimentalphysik, Freie Universität Berlin, 14195 Berlin, Germany
[4] Department of Material Science, Moscow State University, Moscow 142432, Russian Federation
[5] A.V. Shubnikov Institute of Crystallography of RAS, Moscow 119333, Russian Federation

Encapsulated single-walled carbon nanotubes (SWCNTs) with inner channels filled by different compounds present the new class of composite materials. Such CNTs are of a big interest because of an opportunity to form 1D nanocrystals as well as quantum nanowires with new physical and chemical properties inside the tubes. Electronic properties of modified CNTs determine substantially the field of their application. As a consequence different spectroscopic methods are important for studying the electronic structure of composites. The NEXAFS [1] spectroscopy probing the partial density of empty electron states that are localized near the absorbing atom is one of the powerful methods for investigating the local atomic and electronic structure as well as the chemical bonding in various nanosystems. Therefore, the present study is aimed to characterize the possible chemical interaction between CuI and SWCNTs in CuI@SWCNTs and electronic structure of the latter.

All measurements have been performed at the Russian-German beamline (RGBL) using experimental station Mustang. The CuI@SWCNT nanocomposite was produced by the filling of metallic single-walled carbon nanotubes with inner diameter of 1.1-1.4 nm by wide-gap semiconducting CuI nanocrystals using so-called capillary technique [2]. Approximate loading value of CuI equals 72.6 wt. % (i.e. one CuI molecule corresponds to about 6 C atoms.). CuI@SWCNT sample was prepared in air by rubbing powder of it into the scratched surface of stainless steel plate. Evaporated layer of CuI, powder of CuO and initial SWCNTs were used as reference samples. Thin (20-25 nm) CuI layers were prepared *in situ* in the preparation chamber by thermal evaporation of thoroughly dehydrated CuI powder (Alfa Aesar) from a water-cooled effusion cell onto a polished stainless-steel plate in a vacuum of $\sim 3 \times 10^{-7}$ mbar. Powders of CuO and SWCNTs were rubbing into the scratched substrates. NEXAFS spectra at the Cu $2p$ and C $1s$ edges were obtained in the total electron yield mode by detecting a sample current. All spectra were normalized to the incident photon flux, which was monitored by recording the photocurrent from a gold mesh placed at the outlet of the beamline. The photon energy at Cu $2p$ and C $1s$ edges was calibrated using Au 4f photoemission lines (E_{bind}(Au $4f_{7/2}$)=83.9 eV and E_{bind}(Au $4f_{5/2}$)=87.6 eV) from gold plate fastened on the same holder with sample under study. The accuracy of this procedure is evaluated to be of 0.1-0.2 eV. The total energy resolution of monochromator at C $1s$ and Cu $2p$ edges was about 100 meV and 300 meV respectively. Measurements of absorption and photoemission spectra were carried out at a pressure in the measuring chamber $\sim 2 \cdot 10^{-10}$ mbar.

Cu $2p$ spectra for CuI@SWCNTs, and reference samples CuI and CuO are presented in Fig. 1. All spectra were normalized to the absorption edge jump at hν=966 eV. Structures corresponding to the electronic transitions from Cu $2p_{1/2}$ and Cu $2p_{3/2}$ core levels to the same empty electron states are denoted by the primed and unprimed letters, respectively. If the dipole rules for $2p$ electron transitions are taken into account, so these spectra reflect local density of empty electron states that have mainly Cu $4s$- and Cu $3d$-character. It can be seen from the Fig.1 that the Cu $2p_{3/2}$ NEXAFS spectra of CuI@SWCNTs and CuI show appreciable differences between their absorption structures. The main distinctions are an appearance of narrow (FWHM=1.1 eV) low-energy peak A, a broadening of all and merging (c_1 and c_2, e_1 and e_2) as well as disappearing (d, f) of some absorption structures in the CuI@SWCNT spectrum. Moreover, all structures in the spectrum of the composite have low-energy shift of order of

0.3 eV in comparison with their counterparts in the spectrum of CuI. It is natural to relate these distinctions to changes in electronic structure of CuI owing to its encapsulation into SWCNTs or to weak chemical interaction between the filler and the CNT in CuI@SWCNT.

Clearly, these changes are accompanied by an electron density transfer between copper, iodine and carbon atoms in the composite. With consideration for the valence electron configuration of the Cu^+ ion ($3d^{10}4s^0$) in CuI, the appearance of narrow low-energy peak A in the Cu $2p_{3/2}$ spectrum of the composite is reasonable to associate with Cu $2p_{3/2}$ electron transitions to empty $3d$ electron states that are lacking in pristine CuI and appear in CuI@SWCNTs as a result of changes in electronic structure of CuI. This is accompanied by the change in the valence electron configuration of the Cu^+ ion from $3d^{10}4s^0$ for CuI to $3d^{10-x}$ for CuI@SWCNTs. The direct comparison of Cu $2p_{3/2}$ spectra for the composite and CuO confirms this interpretation. It is easy to see (Fig.1) that the spectrum for CuO with the valence electron configuration of Cu^{2+} ion, $3d^9$, has the similar narrow (FWHM=1.0 eV) low-energy peak A as well. It is well known that this peak is due to the Cu $2p_{3/2}$ - $3d$ electron transition [3]. The energy of the latter in CuI@SWCNTs (931.25 eV) is in good agreement with the one in CuO (931.3 eV) [3]. Comparison of relative intensities of peaks A from the spectra for CuO and CuI@SWCNTs, that were normalized equally, gives the magnitude of x= 0.06 e for the decrease of the Cu $3d$ charge in the composite. Right now, there is no way to unambiguously indicate a direction of the electron transfer from the copper atoms to the iodine or carbon atoms. As for the other differences between the spectra of CuI@SWCNTs and CuI, they are most likely due to the changes in crystal and electronic structure of CuI owing to its encapsulation into SWCNTs. The general resemblance of absorption structures for spectra of CuI and CuI@SWCNTs, except for the peak A, is probably evidence for conservation of a tetrahedron coordination of absorbing Cu ion as well as relatively small magnitude of effects under consideration. In this case, the broadening and smearing of some absorption structures can be related to a distortion of the tetrahedron environment of Cu ions by iodine atoms.

Fig. 1. Cu 2p NEXAFS spectra for CuI@SWCNTs, CuI and CuO.
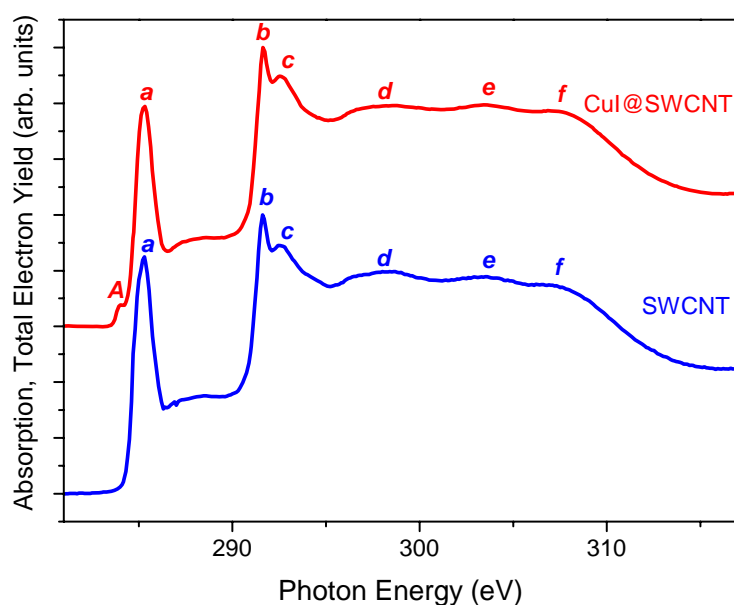
Fig. 2. C 1s NEXAFS spectra for CuI@SWCNTs and SWCNTs.

C 1s spectra for nanocomposite CuI@SWCNTs and pristine SWCNTs normalized to the absorption edge jump at hν=317 eV are shown in Fig. 2. The main structures in the spectrum of the pristine SWCNTs are narrow (FWHM = 1.3 eV) resonance a and bands b, c that are caused by C 1s electron transitions to empty electron states of π and σ symmetry with C $2p_z\pi$ and C $2p_{x,y}\sigma$ character. These states are very similar to the corresponding states of graphite and strongly localized perpendicular and parallel to the carbon hexagon [4]. From Fig.2 it is seen that C 1s absorption spectrum for CuI@SWCNTs is practically identical to the one for pristine SWCNTs except for an additional small shoulder-like peak A at the low-energy side of the π-resonance a. Besides, it is observed the decrease of total spectral weight of π-states of about 12% and the narrowing of π-resonance a of about 0.1 eV for the composite spectrum relative to the one of pristine SWCNTs. It is obvious that such a new peak reflects the interaction between valence electrons of the filler and π electron subsystem of the nanotubes. Cu $2p_{3/2}$ and C 1s

Fig. 3. C 1s and Cu $2p_{3/2}$ NEXAFS spectra for CuI@SWCNTs aligned in energy.

spectra for CuI@SWCNTs, which have been aligned in energy by using the binding energy separation of 648.0 eV between the Cu $2p_{3/2}$ and C 1s core levels, are represented in Fig. 3. It is easy to see that the positions of the peaks A in both spectra are nearly coincide within 1 eV. In the framework of quasimolecular approach [5], this coincidence of the absorption peaks A in both the energetically aligned spectra can be regarded as a result of the transitions of Cu $2p_{3/2}$ and C 1s electrons to the same empty state of CuI@SWCNTs which has hybridized Cu 3d-C$2p_z$ character. In this case, a slightly different position of peak A in C 1s and Cu $2p_{3/2}$ spectra can be associated with a different influence of C $1s^{-1}$ and Cu $2p_{3/2}^{-1}$ holes on the core-excited state under consideration.

In conclusion, the present study has shown that encapsulation of CuI into SWCNTs is accompanied by the changes in electronic structure of CuI because of the ones in atomic structure of CuI in the composite and the chemical interaction between the filler and carbon nanotubes.

References
1. J. Stöhr. NEXAFS Spectroscopy. Springer Verlag, Berlin. (1992). 403 p.
2. M.V. Chernysheva, A.A. Eliseev, A.V. Lukashin, Yu.D. Tretyakov, et al. Physica E **37**, 62 (2007).
3. M. Grioni, J.B. Goedkoop, R. Schoorl, F. M. F. de Groot, et al. Phys. Rev. B **39**, 1541 (1989).
4. P.A. Brühwiler, A.J. Maxwell, C. Puglia, et al. Phys. Rev. Lett. **74,** 614 (1995).
5. A.S. Vinogradov, S.I. Fedoseenko, S.A. Krasnikov, et al. Phys. Rev. B **71**, 045127, (2005).

Synchrotron-based, depth-resolved analysis of elemental gradients in chalcopyrite solar cell absorbers using angle-dependent x-ray emission spectroscopy

H. Mönig[1], Ch.-H. Fischer[1,2], R. Caballero[2], C.A. Kaufmann[2], A. Grimm[2], B. Johnson[2], T. Kropp[2], M. Ch. Lux-Steiner[1,2], C. Jung[2], and I. Lauermann[2]

[1]Freie Universität Berlin, Berlin, Germany,
[2]Helmholtz-Zentrum Berlin für Materialien und Energie, Berlin, Germany
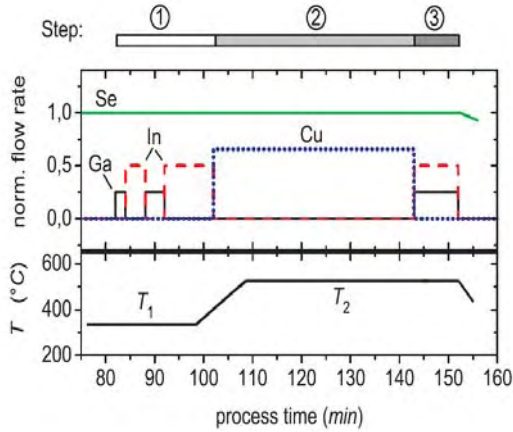
Figure 1: Absorber preparation by 3-stage physical vapour deposition (PVD)

Synchrotron excited soft x-ray emission spectroscopy (XES) is a technique which provides bulk sensitive information[1] with an information depth in the range of 0.1 to 1 µm, depending on the energy of exciting and emitted radiation and the material.. When used angle-resolved, we call this method AXES[2]. We quantify results from angle-resolved XES and use a simple layer model to extract depth profiles from these data. Here we examined $Cu(InGa)Se_2$ solar cell absorbers prepared in the 3-stage process[3] (Figure 1) by the technology department (SE3) of the HZB using different temperatures T2 during the deposition:
T2 = 525°C (standard temperature)
T2 = 425°C
T2 = 330°C (suitable for polyimide substrates)

We analysed these samples with AXES at the U 41 PGM beam line at BESSY II and recorded Cu $L_{2,3}$ and Ga $L_{2,3}$ spectra at different exit angles β to change the depth sensitivity. These spectra are shown in Figure 2. Peaks originating from Cu and Ga were then integrated and plotted vs. the exit angle. The results are shown in Figure 3 (right).
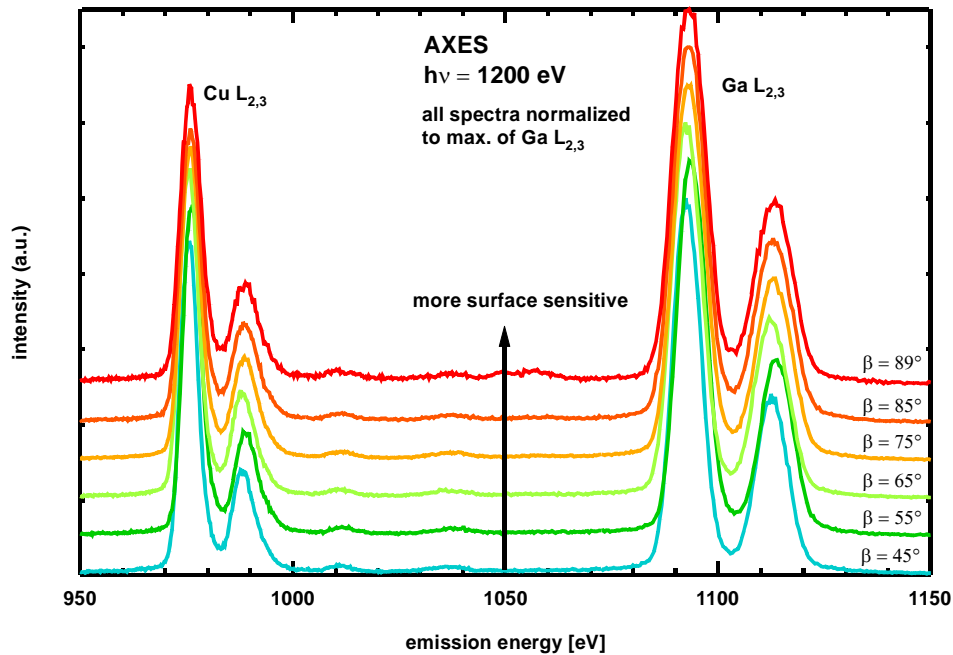
Figure 2: XES spectra with Ga $L_{2,3}$ and Cu $L_{2,3}$ peaks, obtained at different exit angles β, normalised to the maximum of the Ga $L_{2,3}$ peak. For evaluation, peaks are integrated and area ratios plotted vs. β.
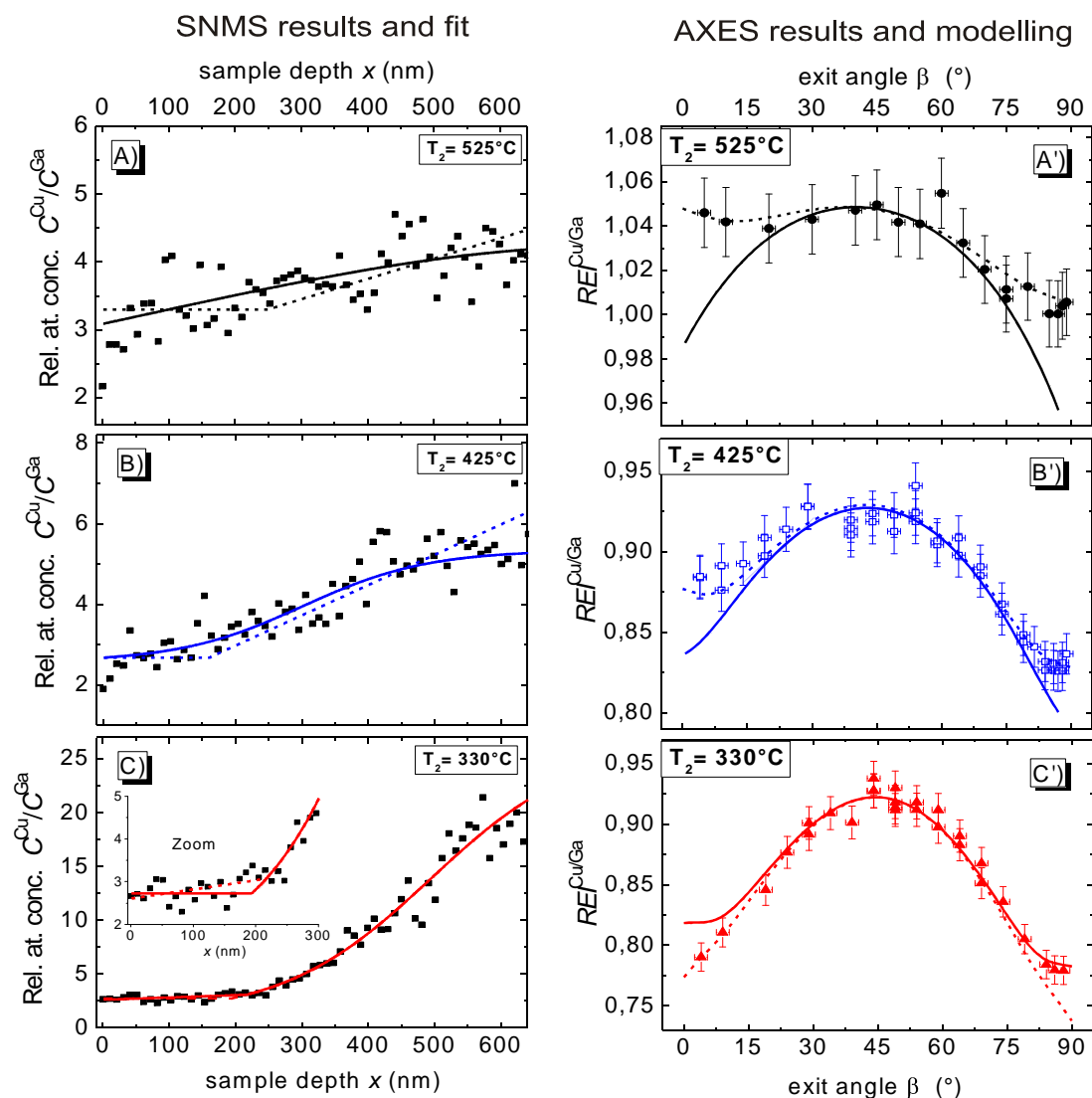
Figure 3: *Comparison of SNMS profiling with AXES results from 3 samples with different processing temperatures T2. Left: Experimental Cu/Ga-ratio from SNMS (dots) and two fitted depth profiles, solid line: best fit of SNMS data, dotted lines: best fit of AXES data. Right: Intensity ratios Cu/Ga from integrated AXES peaks (dots) and calculated based on literature values for x-ray absorption (solid and dotted lines as on the left).*

On the left of Figure 3 we show the comparison with sputtered neutral mass spectrometry SNMS data (done at the ZSW Stuttgart) from the same samples. This method yields absolute elemental concentrations[4]. The results can be summarised as follows: There is a clear influence of T2 on the Cu/Ga-distribution: lower T2 leads to Ga-depletion within the space charge layer. The AXES-results confirm the SNMS-profiles and allow some refinement of the elemental distribution up to a sampling depth of 500 nm. At extreme angles (high surface sensitivity), the AXES results are not consistent with a Cu/Ga gradient in the first 150 nm in samples A) and B) as suggested by SNMS. AXES results point towards a constant Cu/Ga-ratio in that region. These results prove the value of AXES for the analysis of thin films up to several hundred nm.

References

1. C. Heske et. al., Appl. Phys. Lett. **74**, 1451 (1999); Appl. Phys. Lett. **75**, 2082 (1999)
2. H. Mönig, A. Grimm, Ch. Jung, Ch.-H. Fischer, I. Lauermann, C. Camus, C. A. Kaufmann, T. Kropp and M. C. Lux-Steiner, Applied Surface Science 255, 2474-2477 (2008)
3. C.A. Kaufmann, A. Neisser, R. Klenk, R. Scheer, Thin Solid Films 480/481, 515 (2005)
4. K. Herz, A. Eicke, F. Kessler, R. Wächter, M. Powalla, Thin Solid Films 431/432, 392 (2003)

Soft X-Ray Channeling in Policapillary Structures at the Condition of Anomalous Dispersion Region of Si L – Edge Absorption

M. I. Mazuritskiy, P.V. Makhno

Physics Department, Southern Federal University, Sorge, 5, Rostov-on-Don, Russia, 344090

Researches of the X-ray transmission through microcapillary structures aimed at the development of a new focusing devices in particular for long-wavelength X-ray radiation is a high-priority physics problem. Its solution would lead to the appearance of a long-awaited techniques, instruments and technologies for physics, materials science, biology, and medicine. The microchannel plate (MCP) systems have been applied to focus and collimate x-rays and multiply reflection properties of the microchannel surfaces are extremely important to research particularly for ultra soft x-ray radiation.

Great scientific and applied interest have grazing x-ray methods based on the analysis of the secondary response of a solid to the absorption/reflection of incident radiation. If the incident photons are capable to excite the atomic levels then X-ray fluorescence is observed together with elastic scattering if the grazing angle is less than critical one. It was shown [1,2] that under certain conditions x-ray fluorescence emitted inside microcapillaries due to the excitation of atomic levels can affect the spatial distribution of the radiation intensity. We have researched channeling of the X-ray fluorescence (secondary radiation) in the anomalous dispersion region of energy range near SiL – absorption edge. In fact transportation of X-ray can be in the mode regime [3] associated in particular with the surface channeling of photons inside microcapillary structures.

The MCP samples were thin ($\approx$0.5 mm) "perforated" (with 8 μm - diameter channels) plates consisting of mainly silicate glass. Samples were electrically insulated from the metal surface of the holder. The scheme in Fig. 1 shows rays (1) directed almost perpendicularly to the plate surface and corresponding to the grazing incidence onto the microchannel walls. Radiation (3) passed through the microchannel plate (2) absorbed by the plate (4) and detected in the current mode. The angle of incidence was varied by rotating the sample around the x, y axes.
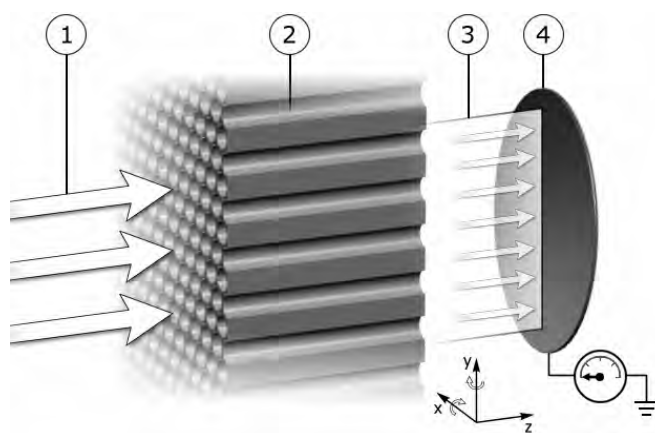
Fig. 1 Experimental scheme

The XANES spectra were excited by monochromatic radiation whose photon energies were varied in the vicinity of the corresponding absorption edges. The total intensity of the X-ray radiation passed through the microchannels of the sample was measured. XANES Si $L_{2,3}$ spectra (see Fig. 2,3) for the various grazing incidence of radiation onto the channel walls have been detected at the outgoing from polycapillary structures. The spectra were obtained with a resolution of 0.1 eV on spectrometer MUSTANG, RGBL-PGM at the BESSY synchrotron center.

The fine structure was observed for the angles of incidence of less than 8°, i.e., under the conditions of total external reflection. The critical angle corresponds to the experimental data [4] for glass in the vicinity of the $L_{2,3}$ edge of silicon absorption (100–140 eV). The L_1 edge of silicon absorption is at the photon energy range of about 160 eV.

The structure of spectra 2,3 in Fig. 2 corresponds to the one obtained in [5,6] for a plane SiO_2 surface. However for MCP samples radiation was incident into long and narrow channels, so the reflected rays could not directly exit outside. Fig. 3 shows the spectra obtained from the MCP preliminarily subjected to thermal hydrogen reduction. The fine structure of spectra 3–5

differs from that seen in Fig. 2. The modified glass surface has an oxide silicon state SiO_x, where $1<x<2$. Note that the fine structure of the spectra measured at the channel outputs remains the same as in the reflection spectra.
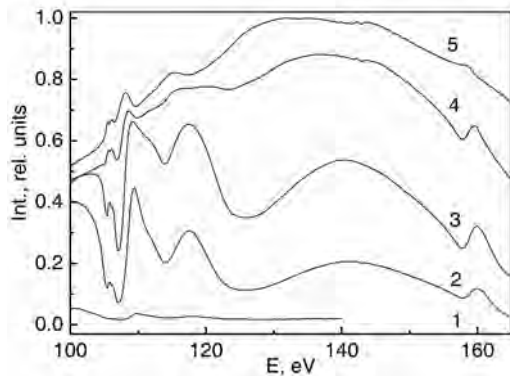
Fig.2 Spectra of white MCP in the vicinity of the L edge of silicon absorption obtained for various angles of radiation incidence onto the channel walls: 1-8.5°, 2-6.5°, 3-5.5°, 4-4.5°, 5-3.5°
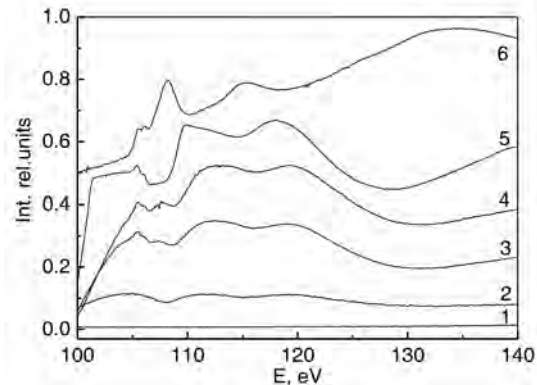
Fig.3 Spectra of microchannel plates subjected to thermal reduction with hydrogen for various angles of incidence of the radiation onto the channel walls: 1-10°, 2-7°, 3-6°, 4-5.5°, 5-5°, 6-4°

As the angle becomes about 3.5° (see Fig.2, spec. *5*) the fine structure unambiguously determines the SiO_2 spectra of the fluorescence yield published earlier ([7,8]). The spectrum 6 on Fig.3 has the similar fine structures for angle about 4°. It is known that the spatial distribution of the fluorescence is almost isotropic. The intensity can increase during fluorescence-radiation transport inside the channels. The surface-bound channeling takes place in the case of transverse wavelength $\lambda_\perp = \lambda / \theta$. We assume that the fluorescence radiation excited inside the channels is transported in such a way that its spectral composition remains almost unchanged. In fact the excited fluorescence is trapped by microchannels and channels along them. is much larger than the wavelength of incident radiation. Channeling of Si L x-ray fluorescence excited in the structure formed by microchannels and interaction of standing waves in a media with unoccupied electronic states is investigated. The surface-bound propagation of X-ray fluorescence excited inside microchannels is observed for angles of incidence of less than $\theta \approx \theta_c/2$.

Actually result of interaction an incident beam with surface is: scattered (or mirror reflection) and refracted radiation which can be selectively absorbed by atoms. X rays are reflected by an extended surface segment, i.e. in a macroscopic field described by a permittivity. The radiation propagates freely along the channels at grazing angles less than the critical angle of total external reflection θ_c. Mirror surfaces are not perfectly smooth. The interaction of the X-ray radiation with the surface layer should be described taking into account that the spatial variation in the permittivity varies with the depth [9]. Various factors including roughness form a transition or contaminated layers. It was shown in [10] that in the case of surface-bound channeling the peak of angular distribution at the capillary output is at angle of less than the angle on which the radiation enters in the channels. In the considered case the radiation is partially scattered to angles of less than 4° and absorbed by the transition layer of the glass. The fluorescence radiation of silicon is selectively trapped by microchannels and propagates inside hollow silicate capillary systems. As a result the reflection spectra transform into the spectra of fluorescence yield. The data of [11] on the absorption cross section in SiO_2 at energies above the L absorption edge make it possible to estimate the mean free path of an excited photon amounting to about 500 Å. In this case of the grazing incidence the fluorescence is excited from a depth of about 50 Å.

The excitation of the silicon L fluorescence can be schematically outlined as follows. The initial stage includes the absorption of a photon resulting in the formation of a hole on an atomic level. Here exist a photonless intermediate state which includes a hole at the inner level and a virtual photoelectron. The lifetime of this excited state is finite and determined by

the time in which a photoelectron wave is scattered in the environment and then a photon is emitted upon the recombination of an electron–hole pair, i.e., the electron system returns to the initial state. The processes of the excitation (absorption) and emission of a photon are conventionally assumed to be of a pure atomic nature, i.e., to proceed independently inside equivalent atoms. However, it was shown in [12] that the interference of photons emitted by atoms of the same kind is possible for the silicon L spectra and the criteria for the interference of the fluorescence radiation were pointed out. In this case the interaction between the excited atomic states is possible during the surface bound channeling of the emitting radiation. An electromagnetic wave acts on electrons and polarizes silicon atoms as a result a time-dependent dipole moment appears. In addition, the phasing of the elementary emitters, i.e., excited silicon atoms distributed over the microchannel walls, induces a macroscopic moment of the transition. The induced correlation between the transition moments of spatially diverse emitters interacting through a radiation field is responsible for the collective emission. As a result, such atoms in a macroscopic volume can emit coherently. One of the conditions ensuring the interference of fluorescence radiation emitted by spatially diverse atoms is that the coherence length exceeds the mean free path of an exciting photon.

Let us estimate the coherence length for fluorescence radiation emitted as a result of the excitation of the silicon L_3 absorption edge. According to [13] the width of an excited L_3 level for silicon atoms is 0.014 eV and the corresponding lifetime is $\tau = 0.5 \cdot 10^{-13}$ s. The maximum size of the coherence region in which the emitters can be phased can be estimated as follows: $l_c \approx \tau \cdot c = 0.14\,mm$. This is much larger than the mean free path (500 Å) of the exciting photon. A specific regime called superradiance can be achieved if a medium is excited (and the emitters are phased) directly by the channeling radiation. In this case, ordering appears due to the narrowness of the atomic-transition lines. The modes of the field are discriminated by the long-wavelength radiation which is propagated along the microchannel axes.

The propagation of radiation in capillary systems depends on its interaction with the inner walls of the channels and is determined by the permittivity. Resonance phenomena in X-ray spectroscopy are observed near the atomic-absorption edges if the photon energies of the incident radiation are close to the energy of the electron transition from an inner electron shell to unoccupied free states. Correct calculations of capillary systems in this region require reliable information on the real and imaginary parts of the permittivity obtained from experimental spectra (XANES/reflection).

One of the important applications is the use of bent MCP to achieve the high density of microfocal sources of coherent fluorescent X-ray radiation.

References
[1] M.I. Mazuritskiy, JETP Lett. **84**, 381 (2006).
[2] M.I. Mazuritskiy, P.V. Makhno JETP Lett. **88**, 351 (2008).
[3] S.B. Dabagov, Physics Uspekhi **46**, 1053 (2003)
[4] P. Tripathi, G. S. Lodha, M. H. Modi, et al Opt. Comm. **211**, 215 (2002).
[5] E.O. Filatova, A.S. Shulakov et al. Sov. Phys. Solid State **40**, 1237 (1998).
[6] A.S. Vinogradov, E.O. Filatova et.al. Sov. Phys. Solid State **25**, 643 (1983).
[7] D. Li, G.M. Bancroft, M. Kasrai et al., Amer. Mineralog. **79**, 785 (1994).
[8] B. Gilbert, B.H. Frazer, F. Naab et al., Amer. Mineralog. **88**, 763 (2003).
[9] R.M. Fechtchenko, A.V. Popov et al. J. Russ. Laser Res. **21**, 62 (2000).
[10] S.B. Dabagov, A. Marcelli et al., Nucl. Instrum. Methods Phys. Res. B **187**, 169 (2002).
[11] NIST Scientific and Technical Databases, http://www.nist.gov/srd/online.htm.
[12] Y. Ma, K. E. Miyano, P.L. Cowan, et al., Phys. Rev. Lett. **74**, 478 (1995).
[13] M. Ohno, G.A. van Riessen, J. Electr. Spectr. Rel. Phen. **128**, 1 (2003).

Local structural understanding of the glass formation process in Zr-based glasses, using XAFS

1. Lahiri Debdutta, Bhabha Atomic Research Centre, India. 2. Schumacher Gerhard, Helmholtz Zentrum Berlin fur Materialien und Energie 3. Riesemeier Heinrich, Institute Bundesanstalt f. Materialforschung und -prüfung, Germany. 4. Schrieb Tobias, Helmholtz Zentrum Berlin fur Materialien und Energie5. Radtke Martin, BAMline (BESSY). 6. Reinholz Uwe, BAMline (BESSY).

Metallic glasses have been of scientific interest for their unique engineering application potential that arises from this amorphous structure. The formation of glass rather than crystalline phase is challenging and varies with alloy composition. Understanding the causes of such preferential glass formation is important for the successful synthesis of a wide variety of metallic glasses and points to an understanding of the nucleation (of crystalline phase) process. The glass-forming ability is negatively correlated with the nucleation of crystalline phases. The preferential nucleation of crystalline (rather than quasi-crystalline) phases is speculated to be correlated with different nature of pre-existing short-range order (SRO) in the corresponding glassy phases. The object of this XAFS work is to probe the role of SRO on the nucleation process by measuring XAFS on the glassy and annealed (quasi-crystalline, from XRD) phases of Zr(69.5)Al(7.5)Cu(12)Ni(11). We have measured XAFS at Cu, Ni, Zr K-edges at BAMline.

Our analysis has focused on the first coordination shell (nearest neighbor) fitting. The shells farther out, although show structure, are extremely disordered to allow for error-free analysis. Moreover, our first shell analysis has been sufficient in establishing the structural model for the material. The fit parameters are listed in Table I. Comparison of the structure before and after annealing (Fig. 1) shows that the structural evolution with annealing mainly involves expansion of bond-length (by 0.1 Å), coordination increase and reduction of DWF (=enhanced degree of order). The low coordination for the different bonds seems unrealistic at the first sight. However, these results seem logically plausible by realizing that XAFS yields the weighted average result from the neighborhood around various sites. Low coordination due to finite size effect is well reported in the XAFS literature of nano-clusters. Considering several possible models for this result, we have realized that icosahedral cluster best represents the structure in this glass. Our interpretation of the XAFS data, henceforth, was targeted at determining (1) the size of the icosahedral cluster; (2) the centers of nucleation (whether Al, Ni, Cu, Zr); (3) the stoichiometric composition of the clusters; (4) the deviation of the cluster from perfect icosahedron.

We first proceeded by generating the geometric coordinates for 13-atom, 55-atom and 147-atom icosahedral clusters corresponding to a desired radial distance from the centre of cluster to the first atomic shell. [Note that icosahedral clusters come in sizes of 13-, 55- and 147-atoms.] For each cluster size and different nucleation centers (viz. Al, Ni, Cu, Zr), we calculated the weighted average of Ni-Ni, Cu-Ni, Cu-Cu, Ni-Zr, Cu-Zr, Zr-Zr, Zr-Cu and Zr-Ni coordination for all the atomic sites, over the fit range (2-3 Å) and compared with our XAFS results. Our analysis yields the structure for the metallic glass $Zr_{69.5}Ni_{11}Cu_{12}Al_{7.5}$ to be (1) disordered icosahedral clusters; (2) the system is heterogeneous, consisting of at least 3 types of clusters: Zr-centered 13-atom Zr-rich cluster, Ni and Cu-centered 55-atom stoichiometric clusters; (3) Ni and Cu-centered clusters have a larger diameter (1 nm)

compared to Zr-centered clusters (0.6 nm); (4) assumption of the given stoichiometry for cluster composition is compatible with our XAFS results; (5) the structural evolution with annealing (for 2 hours at 300^oC) is purely that of improvement in the degree of order of the cluster rather than any phase transition into a new structure. This structure does not improve with prolonged annealing; (6) the improving in order with annealing is the least for Ni-centered cluster and highest for Zr-centered cluster.

The implications of these results are as following:

(1) Our results are in concert with theoretical predictions that more stable clusters are formed around smaller sized atoms. Thus, 55-atom cluster is formed around Ni, Cu while 13-atom cluster is formed around Zr. Moreover, the least change in order of the Ni-centered cluster with annealing indicates that Ni-centered cluster is most stable while Zr-centered cluster is the least stable.

(2) There exists a critical (cluster) size of nucleation: the probability of nucleation of crystalline phase is low for cluster sizes smaller than critical size i.e. the probability of glass formation is high. The fact that the smallest cluster is built around Zr may be indicative of Zr being the preferential site of glass formation. The cluster sizes of 0.6 nm and 1 nm, determined from our XAFS results, may be used to obtain an estimate of the critical size of nucleation. The critical size must be greater than 1 nm since the annealed phase is quasi-crystalline.

(3) The fact that the structural evolution with annealing involves only an improvement in order of cluster rather than diffusion-mediated increase in cluster size or interlocking of different clusters indicates that the clusters in the glassy phase must already have been thermodynamically stable.

We plan to pursue this work by measuring XAFS on a glass that yields crystalline phase with annealing. We can then estimate the critical size of nucleation more accurately.

Table I

Fit parameters for the data of glassy phase and annealed phase of the samples

		Bond-length (Å)	N	DWF (Å^2)	
Ni-Zr	Glassy phase	2.6	2	0.013	
	Post-Annealing	2.7	2.33	0.012	
Cu-Zr	Glassy phase	2.72	2	0.01	
	Post-Annealing	2.8	3	0.005	
Zr-Ni	Glassy phase	2.6	0.5	0.006	
	Post-Annealing	2.66	0.5	0.002	
Zr-Zr	Glassy phase	3.07	5.5	0.022	
	Post-Annealing	3.13	5.5	0.012	
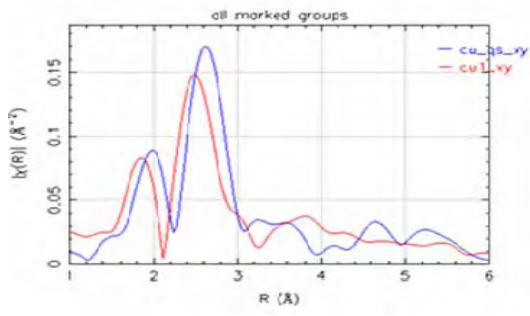
Cu K-edge
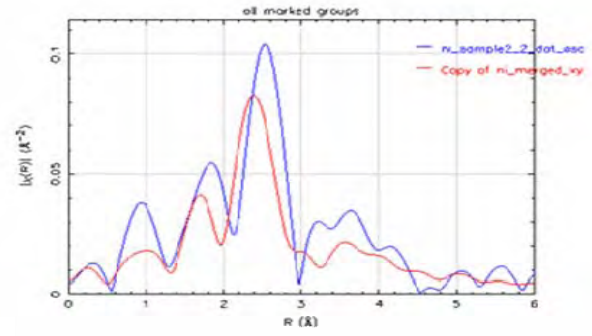
Ni K-edge
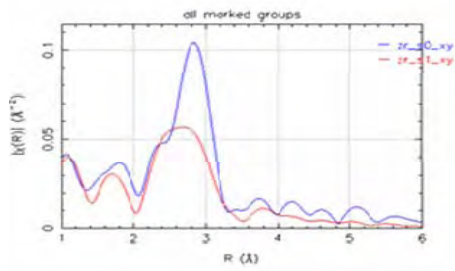
Zr K-edge

There is clear change in structural parameters with annealing.

Fig. 1 XAFS for glassy phase (red curve) and annealed phase (blue curve).

TXM-NEXAFS study of individual carbon nanotubes

Alexandre Felten and Jacques Ghijsen

University of Namur (FUNDP), LISE, 61 rue de Bruxelles, Namur 5000, Namur, Belgium

Xiaoxing Ke and Gustaaf Van Tendeloo

University of Antwerp, EMAT, Groenenborgerlaan 171, B2020 Antwerpen, Belgium

Peter Guttmann

Helmholtz-Zentrum Berlin für Materialien und Energie, Elektronenspeicherring BESSY II, Albert-Einstein-Str. 15, 12489 Berlin, Germany,

Carla Bittencourt

University of Mons-Hainaut, Parc Initialis, Av. Nicolas Copernic 1, Mons 7000, Belgium

1. Introduction

Conventional spectroscopies such as photoemission spectroscopy and x-ray absorption spectroscopy have shown to be particularly well-adapted probes to study electronic properties of pristine and modified carbon nanotubes. However, these conventional techniques typically sample an area of some mm^2 thus preventing the analysis of a single nanostructure. Moreover, signal originating from impurities that are usually present in the nanotube powder (amorphous carbon, onion-like particles, and catalysts) cannot be avoided. In order to overcome these problems, one must carry out the spectroscopy at high spatial resolution. In this context, Scanning Transmission X-ray Microscopy (STXM) has recently been shown to be one of the most appropriate techniques to study carbon nanotubes since it combines both spectroscopy and microscopy with a spatial resolution better than 30 nm allowing studies of isolated nanotubes [1,2,3].

In this work, electronic, structural and chemical properties of isolated multiwall carbon nanotubes (MWCNTs) were studied using the BESSY Transmission X-ray Microscope (TXM). Analysis of the C 1*s* near-edge absorption fine structure (NEXAFS) spectroscopy was performed on individual carbon nanotubes.

2. Method

Carbon nanotube powders were purchased from SES research [4]. The raw powders were sonically dispersed in ethanol and a drop of the solution deposited on a holey Formvar TEM grid. The first sample is non-modified CNT while the second is a CNT decorated with gold nanoparticles and immersed for 24 hours in a DNA (with S-terminated groups) solution. It is assumed that DNA will attach to the side walls of the nanotubes via gold sulphur bonding.

NEXAFS spectroscopy was performed on individual nanotubes using the TXM-NEXAFS end station located at the BESSY beamline U41. In order to prevent degradation, the DNA/CNT sample was cooled using liquid nitrogen during the measurements.

3. Results

Figure 1a shows a TXM image where we can observe an isolated carbon nanotube. NEXAFS spectra were extracted from two different regions of the nanotube, corresponding to the horizontal and vertical part of the nanotube (figure 1b). The spectra show a strong polarization

dependence [3]; the intensity of the C $1s \rightarrow \pi^*$ transition is found to be the highest when the E vector is perpendicular to the tube axis, while it almost completely vanishes when the E vector is parallel to the tube axis. This result shows that the directional electric field of the x-rays can be used as a "search tool" for the direction of chemicals bonds of the atom selected by its absorption edge.
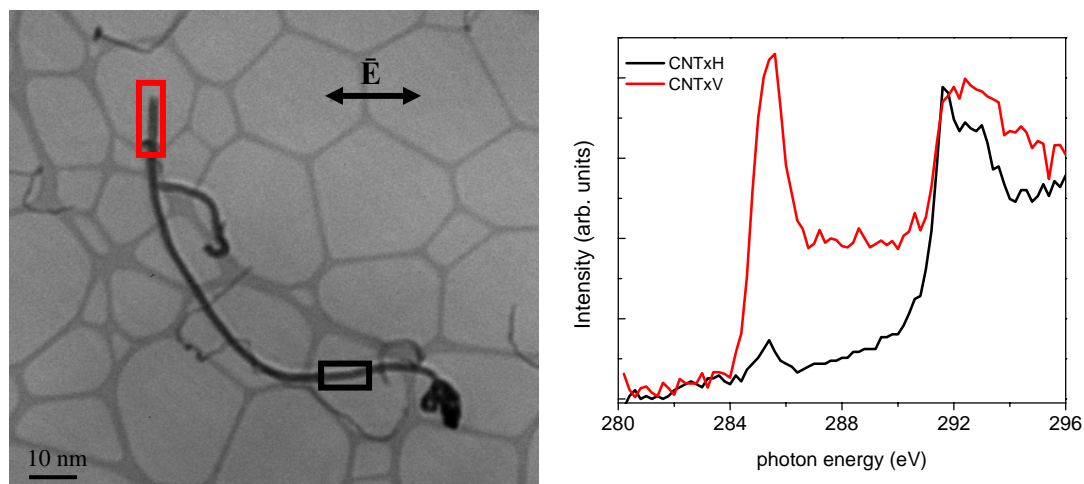
Figure 1. (a) TXM image of a region with one isolated MWCNT. (b) Spectra extracted from the coloured region of the isolated nanotube. In red, the nanotube is perpendicular to the E vector and in black it is parallel.

Figure 2 shows TXM images of the CNT/DNA sample with a nanotube decorated with gold nanoparticles and immersed for 24 hours in a DNA solution taken at 281.0 eV (below the C $1s \rightarrow \pi^*$ transition) and at 285.5 eV (at the C $1s \rightarrow \pi^*$ transition). At 281.0 eV, the intensity of the nanotube is equal all along the nanotube axis meaning that the density is also constant. But at the C $1s \rightarrow \pi^*$ transition, black spots can be observed in some regions of the nanotube revealing the presence of carbon materials attached to the nanotube surface.
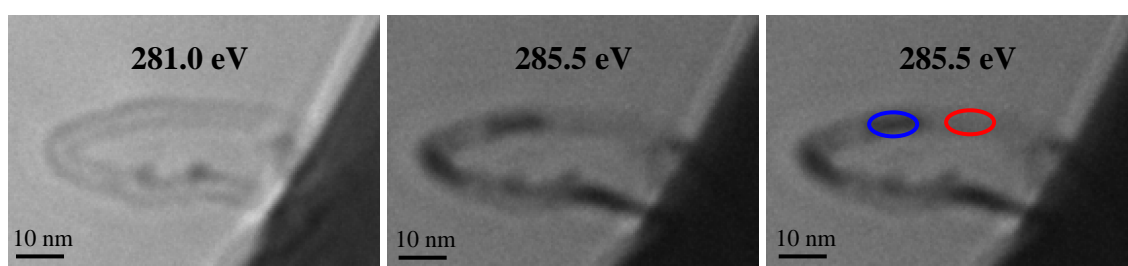
Figure 2. TXM images of a MWCNT taken at 281.0 and 285.5 eV. The nanotube was decorated with gold nanoparticles and immersed for 24 hours in a DNA solution.

NEXAFS spectra of two regions of the nanotubes are shown in figure 3. Due to the horizontal orientation of the nanotube, the signal of the π^* peak of the bare CNT is almost equal to 0 (red curve). This unique property is very useful to detect small amount of carbon material attached to the CNT surface. The blue curve corresponds to the signal coming from the black spot on the nanotube. It can be seen that the intensity at 285.5 eV increases by a factor of three confirming the presence of carbon on the darker regions of picture 2.
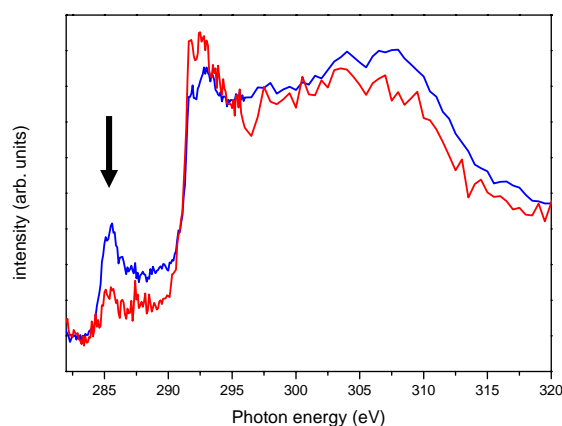
Figure 3. NEXAFS spectra extracted from the blue and red region of the TXM image in figure 2. The arrows shows the increase in the π* transition.

Using TXM we were able to record spectra from an isolated carbon nanotube and to confirm the importance of its orientation compared to the x-ray electric field. We took advantage of the polarization dependence in order to detect carbon material attached at the surface of the nanotube. We are able to distinguish bare regions from regions covered with carbon material on the same individual nanotube. However, at the present stage, we cannot confirm that the carbon signal originates from the DNA chains. In order to confirm it, the next step of our project will be to record the nitrogen edge on the same nanotube.

1. A. Felten, H. Hody, C. Bittencourt, J.-J. Pireaux, D. Hernandez-Cruz, and A. P. Hitchcock, Appl. Phys. Lett. 89 (2006) 093123.
2. A. Felten, C. Bittencourt, J.-J. Pireaux, M. Reichelt, J. Mayer, D. Hernandez-Cruz, and A. P. Hitchcock, Nano Letters 7 (2007) 2435.
3. E. Najafi, D. Hernández Cruz, M. Obst, A.P. Hitchcock, B. Douhard, J.-J. Pireaux and A. Felten, Small 4 (2008) 2279-2285.
4. http://sesres.com/Nanotubes.asp

Polarization-dependent and resonant photoemission spectroscopy on doped and undoped transition metal oxyhalides

S. Glawion, M. Scholz, G. Berner, K. Goß, M. Sing, and R. Claessen
Experimentelle Physik 4, Universität Würzburg, D-97074 Würzburg

The physics of strongly correlated electron systems represent one major topic in current condensed matter research, especially against the background of high-T_C superconductors and colossal magnetoresistance manganites [1]. Photoemission spectroscopy (PES) is a powerful tool in the investigation of the electronic structure of these systems. Some variants of this technique can only be applied using certain advantages of synchrotron radiation, namely energy tunability and its high degree of polarization. Thus, one can make use of the resonant enhancement of states related to specific orbitals (*e.g.*, Ti 3d) and their respective symmetry. We applied these techniques at beamline UE56/2 using the MUSTANG end station to transition metal oxyhalides of the form TiOX (X=Cl,Br). These are layered Mott insulators with features characteristic for low-dimensional systems, *e.g.*, a spin-Peierls ground state in the low-T phase [2], and serve as an electron analogue to the cuprates because of their 3d^1 configuration. Their crystal structure is of the FeOCl type and consists of buckled Ti-O bilayers separated by halide ions. These bilayers interact along the crystallographic c-axis only weakly through van-der-Waals forces. Due to an increased overlap of electron clouds along the b-axis, electronically and magnetically one-dimensional Ti chains are formed. Additionally, neighboring chains along the a-axis are shifted by half a lattice constant, which leads to a triangular lattice in the ab-plane and introduces magnetic frustration into these S=1/2 systems. Intensive research has been performed on the nature and driving force of the observed unconventional spin-Peierls scenario involving two transitions at T_{c1}=66K and T_{c2}=91K in the case of TiOCl [2]. It was found that the incommensurate modulation in the intermediate phase is intimately connected to frustrated interchain interactions [3]. Recent infrared optical absorption and transmittance measurements have indicated a possible metal-insulator transition under pressure [4], which however is still under debate [5]. Investigations of the electronic structure have been performed using photoemission spectroscopy (PES) and suitable band structure and model calculations, namely LDA+U and GGA+U [6], cluster-DMFT [7], DDMRG [8] and VCA [9]. The importance of interchain interactions, *i.e.*, the non-negligible degree of two-dimensionality, for the electronic structure has been evidenced via a quantitative comparison of phenomenological band widths from experiment along the a- and b-axis in both TiOCl and TiOBr [10], as well as by VCA calculations [9].

Recently, we focus our attention on the investigation of doping induced changes in the electronic structure. The van-der-Waals gaps between the layers allow for an intercalation of alkali metal atoms (Na, K) into the crystals, which donate their outer electron to the host system and thus lead to electron doping. From a model point of view, this is expected to lead to a filling-controlled Mott insulator-metal transition, as opposed to the band-width controlled pressure-dependent changes hinted at above. However, spectroscopic signatures of a metallic phase, namely a Fermi edge or quasi-particle peak at the chemical potential, are missing in our PES data, although successful doping was evidenced from a charge transfer to the Ti atom discernible in core-level spectroscopy. Recent molecular dynamics calculations combined with LDA+U have indicated that multi-orbital effects are responsible for a trapping of the additional electrons at specific Ti sites, thus suppressing metallic conductivity [11].

Two major questions have to be addressed experimentally to justify the above scenario: (*i*) To which degree are the additional electrons localized at Ti sites and (*ii*) which orbital do they occupy. The first question was addressed using resonant photoemission spectroscopy (ResPES). With this method it is possible to estimate the degree of hybridization or admixture of the different species (Ti/O/Cl) in the valence band. Measurements were performed on pristine TiOCl crystals at slightly elevated temperatures (~350K) in order to minimize charging effects due to the insulating nature of the samples. Varying the excitation energy over several eV across the Ti 2*p*-3*d* edge a clear resonance behavior of the Ti 3*d* weight closest to the chemical potential was observed, while the high-binding-energy valence band shows only moderate enhancement (see Fig. 1). This is in line with partial density of state (pDOS) calculations which predicted a negligible admixture of O and Cl bands to the Ti 3*d* spectral weight [6] and also supports the picture of electrons localized at (single) Ti sites and a low significance of hybridization for the basic electronic properties of TiOCl. Results considering changes upon doping, however, could not yet be unambiguously related to physical origins because of experimental issues.

The second, maybe even more important question can be answered using polarization-dependent PES (PolPES). Using a special geometry with the incoming beam and outgoing electrons lying in a crystal mirror plane allows a switching between different Ti 3*d* orbitals by exploiting the symmetry dependence of the dipole matrix element involved in photoemission. Thus, one can effectively quantify the degree of orbital polarization also in doped crystals. As one can see in Fig. 2, new spectral weight appears upon doping in the charge gap at ca. 1eV beloe the chemical potential. This weight displays clearly different shapes for horizontal and vertical polarization of the incoming light. Applying an iterative independent component analysis, it was possible to untangle two different contributions identifiable as the two lowest Ti 3*d* orbitals, in agreement with molecular dynamics calculations combined with LDA+U [11, 12].
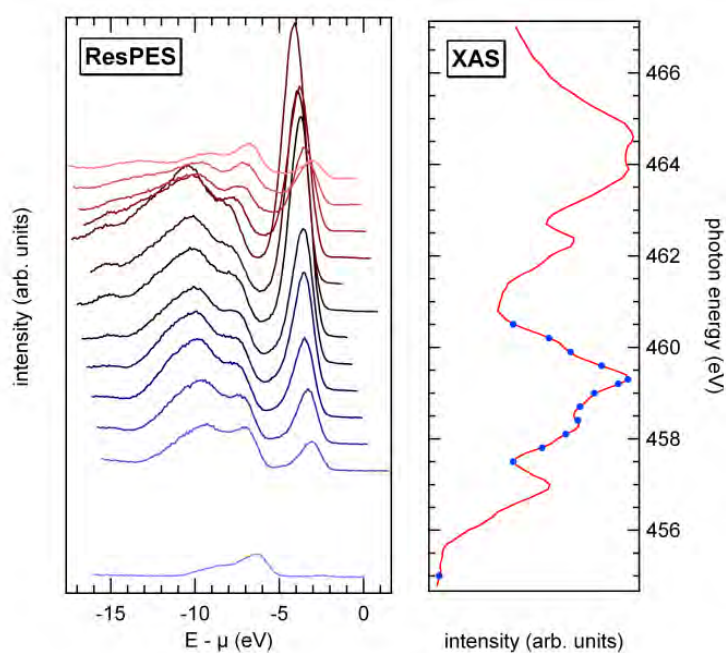
Fig. 1: (left) ResPES spectra of the undoped TiOCl valence band with increasing photon energy from bottom to top. The strongly resonating structure between ca. -5eV and the chemical potential μ is the Ti 3*d* spectral weight, while the high-binding-energy structure corresponds mostly to O 2*p*/Cl 3*p* bands. (right) Ti 2*p* edge X-ray absorption spectrum, with the energetic positions of the ResPES spectra marked.
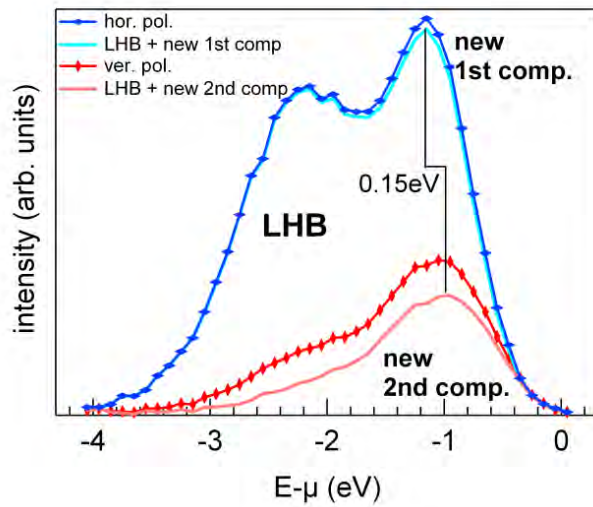
Fig. 2: Deconvolution of the Ti 3*d* spectral weight of a Na doped TiOCl crystal measured with different polarizations of the incoming light. Clear differences between horizontal and vertical polarization on the high-binding-energy side ('LHB') are in line with results from pristine TiOCl [8]. The additional peak appearing upon doping ('new 1st/2nd comp') consists of two components whose separation of ca. 0.15eV is in agreement with molecular dynamics calculations [11]. From their polarization dependence they can be identified as two different Ti 3*d* orbitals.

References:

[1]   M. Imada *et al.*, Rev. Mod. Phys. **70**, 1039 (1998)

[2]   A. Seidel *et al.*, Phys. Rev. B **67**, 020405(R) (2003)

[3]   R. Rückamp *et al.*, Phys. Rev. Lett. **95**, 097203 (2005)

[4]   C. A. Kuntscher *et al.*, Phys. Rev. B **74**, 184402 (2006)

[5]   M. K. Forthaus *et al.*, Phys. Rev. B **77**, 165121 (2008)

[6]   T. Saha-Dasgupta *et al.*, Europhys. Lett. **67**, 63 (2004)

[7]   T. Saha-Dasgupta *et al.*, New J. Phys. **7**, 74 (2005)

[8]   M. Hoinkis *et al.*, Phys. Rev. B **72**, 125127 (2005)

[9]   M. Aichhorn *et al.*, submitted for publication

[10]   M. Hoinkis *et al.*, Phys. Rev. B **75**, 245124 (2007)

[11]   Y. Z. Zhang *et al.*, unpublished

[12]   M. Sing *et al.*, unpublished

NEXAFS C1s, N1s and Co2p spectra potassium-doped CoPc.

V.N. Sivkov[a], S.B. Nekipelov[a], O.V. Molodtsova[b], V.Yu. Aristov[b,d], D.V. Vyalich[c], S.L. Molodtsov[c]

[a]*Komi Science Center, Russian Academy of Science, Ural Division, Syktyvkar 167982, Russia*
[b]*Leibniz Institute for Solid State and Materials Research, D-01069 Dresden, Germany*
[d]*Institute for Solid State Physics, Russian Academy of Sciences, Chernogolovka, Moscow District 142432, Russia*
[c]*Institut für Festkörperphysik, Tehnische Universität Dresden, D-01062 Dresden, Germany*

The wide of possible applications of the 3d transition metal phthalocyanines (MePc's), which are organometallic complexes, in electronic and optoelectronic devices such as organic lightemitting diodes, organic field effect transistors, organic photovoltaic cells, fuel cells radiation and gas sensors, low dimensional molecular magnets and organic based spintronics has initiated substantial research activities in previous years. In particular, cobalt phtalocianine (CoPc) is often utilized in the fields of gas and radiation sensors [1], optoelectronics [2], in medical applications [3, 4]. Nowadays, CoPc is considered as a material for development of low dimensional molecular magnets [5]. The potential applications give a strong motivation to characterize and investigate the electronic structure of cobalt phthalocyanine thin films since this determines the performance.

The ability to incorporate electron acceptors and donors into molecular crystals enables to control of their electronic properties by introducing charge carriers. This special aptitude represents a promising route for technology as well as for the investigation of the fundamental properties of molecular crystals.

Recently the electronic structure of the organic semiconductor CuPc and of potassium doped CuPc at different levels of doping have been studied by means of photoemission and photoabsorption spectroscopy [6-8]. An analysis of the spectra shows strong diffusion of potassium atoms into the Pc films and profound chemical interaction between adsorbed potassium and nitrogen atoms linked to pyrrole carbon. That investigation indicates that the density of states in the energy region of the LUMO is reduced as a consequence of electron doping and filling of the LUMO with electrons that stem from potassium. This demonstrates that the potassium ions sit closely to nitrogen atoms of the CuPc molecule. The transfer of electrons from the potassium to MePc molecule is an effective method of the investigation the hybridization of C1s, N1s and Me2p atomic orbitals and density of unoccupied states. However, the absolute absorption cross section and oscillator strength of X-ray transitions, which is proportional density of unoccupied states, need to be measured.

The present article is dedicated to the evolution of the unoccupied electronic levels of the CoPc as a function of potassium doping. We have studied the absolute absorption cross section spectral dependences in the region of the near edge x-ray absorption fine structure (NEXAFS) N1s, C1s and Co2p edge by using Ti – filter method [9]. The Ti - filter method was used to suppress and measure the monochromatic stray and high-order radiation [9]. Ti - filter was prepared in the form of free film (diameter 14 mm) on Au – grid with small mesh. The total electron yield (TEY) is proportional to the product of the intensity of x-ray monochromatic radiation and absorption cross section. So the absorption cross section in arbitrary units can be obtained by means of the division the TEY by the monochromatic radiation intensity in arbitrary units. At that the intensity of the incident synchrotron radiation (SR) was measured using the TEY from the clean Au photocathode. A TEY was divided into cross section value of the atomic Au [10].

The acquired spectra were energy calibrated using photoionization spectra of CO_2 and N_2 gases. In the NEXAFS experiments the photon incidence angle was selected to be 35° relative to the sample surface normal. The pressure in the experimental system during data acquisition was always better than $1.5 \cdot 10^{-10}$ Torr. The Au(100) surface of a gold single crystal was used as a substrate for CoPc film deposition. The surface was prepared by repeated sputtering and annealing cycles. The CoPc film was deposited in a sample preparation chamber (base pressure of $2.5 \cdot 10^{-10}$ Torr) directly connected to analyzer

chamber. The CoPc deposition rate, monitored by a quartz microbalance, was 1–2 Å/min. The CoPc films used for our studies were about 70 Å thick. Potassium was evaporated onto the CoPc film at rates ranging from 1 to 50 Å/min from a properly outgassed SAES alkali metal dispenser, without detectable pressure increase during deposition. The K concentration in the CoPc films was deduced from a comparison of the relative surface area of the partial K2p-absorption spectrum.
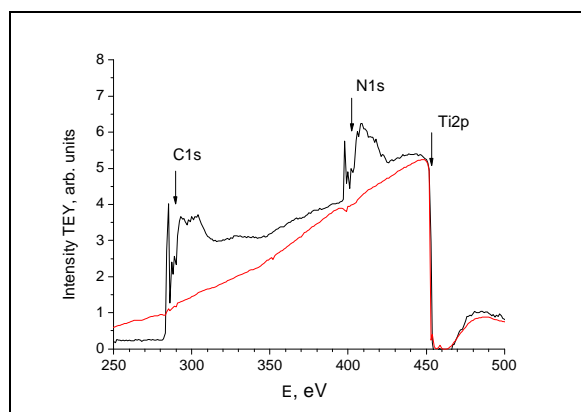
Fig.1. *TEY signal CoPc (black) and TEY signal Au divided cross section Au atom (red) obtained by using Ti-filter.*
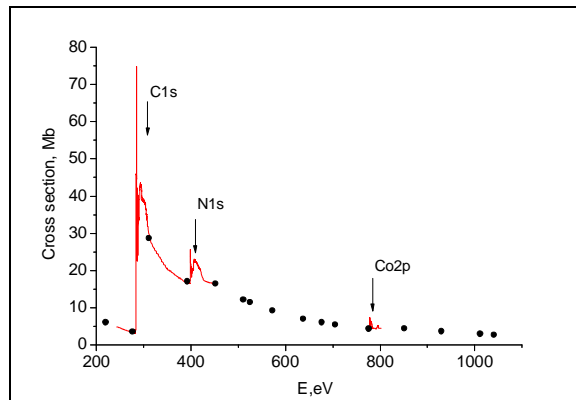
Fig.2. *The spectral dependence cross section CoPc (red) and the calculate sum atomic cross section of CoPc – molecule (black point).*

The TEY signal CoPc and the intensity of the incident SR in wide region 280-500 eV are shown in Fig.1. The intensity SR in the arbitrary units was obtained from the TEY curve of the clean Au dividing by the well-known atomic X-ray absorption cross section of Au [10]. Between 250 and 450 eV photon energy the extracted flux curve varies monotonically. At 450 eV a sharp drop in intensity is observed when passing the Ti 2p absorption edge.

Fig. 2-3 show the TEY signal obtained from the CoPc layer after normalization to the intensity incident SR. It was reduced to the absolute scale by means of the calibration using the known values of the atomic cross section [10]. The normalization was carried out by alignment with the sum atomic cross section of CoPc – molecule.
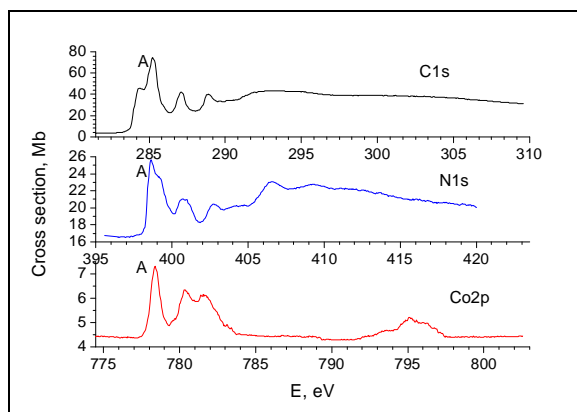
Fig.3. *The spectral dependence cross section CoPc in the regions C1s, N1s and Co2p edges.*
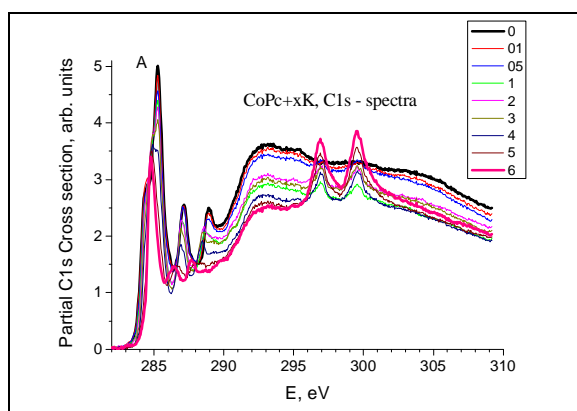
Fig.4. *NEXAFS spectra of CoPc taken at the C 1s edge as a function of K doping, x – K concentration (arb. units). Thick lines marked x=0 (black) and x=6 (red).*

Fig. 4-6 shows the NEXAFS spectra of CoPc at the C1s, N1s and Co $2p3/2$ absorption edges as a function of K doping. The C1s, N1s and Co $2p3/2$ NEXAFS data exhibit the main feature A and some significantly different structures prior to the continuum, which is not discuss in present article. It is obvious that oscillator strength of the main feature A decrease with the increasing of the doping potassium dose x up to practical full disappearance in C1s, N1s and Co $2p_{3/2}$ spectra. At that C1s spectra have a feature (284.8 eV), which may be identified as C1s-π^* in the
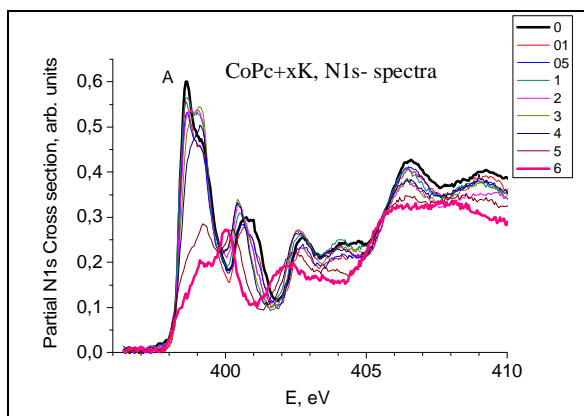
Fig.5 *NEXAFS spectra of CoPc taken at the N 1s edge as a function of K doping, x – K concentration (arb. units). Thick lines marked x=0 (black) and x=6 (red).*
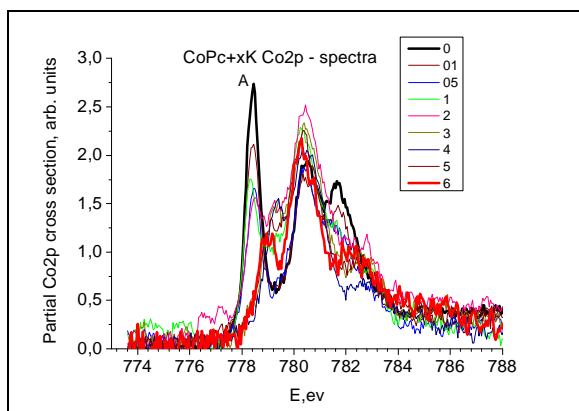
Fig.6. *NEXAFS spectra of CoPc taken at the Co 2p edge as a function of K doping, x – K concentration (arb. units). Thick lines marked x=0 (black) and x=6 (red).*
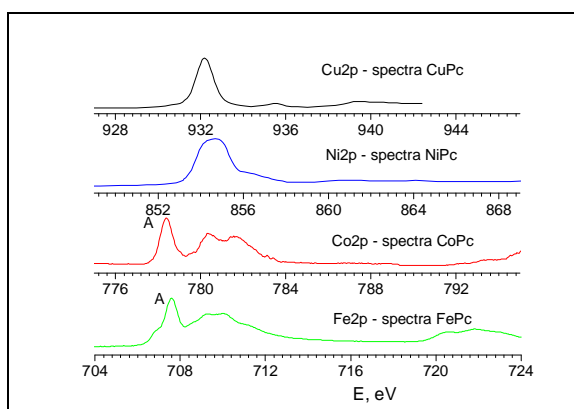
Fig.7. *The NEXAFS Me2p - spectra CuPc [7], NiPc[12], CoPc and FePc.*

aromatic cycles. That synchronous decreases of A features oscillator strength indicate, that the filling LUMO is strongly hybridized orbital. The LUMO, probably, is an incompletely filled MO $1e_g(d_\pi)$ – symmetry which appears due to

decrease of d-electrons number from CuPc to CoPc and FePc (Fig.7). It is agreed with the theoretical data [11].

Acknowledgements:

References

1. M. Trometer, R. Even, J. Simon, A. Dubon, J.-Y. Laval, J.P. Germain, C.Maleysson, A. Pauly, H. Robert, Sens. Actuators B **8**, 129 (1992)
2. C.C. Leznoff, A.B.P. Lever, Phthalocyanines: Properties and Applications, Vols. 1–4 (VCH, New York, 1989–1996)
3. A.R. Harutyunyan, A.A. Kuznetsov, O.A. Kuznetsov, O. Kaliya, J. Magn. Magn. Mater. 194, 16 (1999)
4. A.A. Kuznetsov, V.I. Filippov, R.N. Alyautdin, N.L. Torshina, O.A. Kuznetsov, J. Magn. Magn. Mater. **225**, 95 (2001)
5. A. Zhao, Q. Li, L. Chen, H. Xiang, W. Wang, S. Pan, B. Wang, X. Xiao, J. Yang, J.G. Hou, Q. Zhu, Science 309, 1542 (2005)
6. T. Schwieger, H. Peisert, M. S. Golden, M. Knupfer, and J. Fink, Phys. Rev. B 66, 155207 (2002)
7. O. V. Molodtsova, V. M. Zhilin, D. V. Vyalikh, V. Yu. Aristov, and M. Knupfer, J. Appl. Phys. 98, 093702 (2005)
8. O. V. Molodtsova, M. Knupfer, V. Yu. Aristov, D. V. Vyalikh, V. M. Zhilin, and Yu.A. Ossipyan J. Appl. Phys. 103, 053711 (2008)
9. V. N. Sivkov, A. S. Vinogradov, S. V. Nekipelov, D. V. Sivkov, D. V. Vyalykh, S. L. Molodtsov, Optika i Spektroskopiya 101,N5 782 (2006)
10. B.L. Henke, E.M. Gullikson, J.L. Devis,. At.Data.Nucl.Data.Tables. 54, 181(1993).
11. M.-Sh. Liao, S. Sheiner. J. Computationa Chemistry. 23, 1391 (2002)
12. A.S. Vinogradov, A.B. Preobrajenski, D.A. Zverev, E.V. Nikolaeva, D.V. Vyalikh, S. L. Molodtsov. BESSY Ann. Report, p.201 (2004)

Excellence of refraction enhanced micro-CT for materials characterization

Bernd. R. Müller, Axel Lange, Michael Harwardt, Manfred. P. Hentschel

Federal Institute for Materials Research and Testing (BAM), Berlin, Germany

In computed tomography the contrast at interfaces within heterogeneous materials can be strongly amplified by effects related to X-ray refraction. Such effects are especially useful for materials of low absorption or mixed phases showing similar X-ray absorption properties which produce low contrast. X-Ray refraction is an Ultra Small-Angle Scattering (USAXS) phenomenon [1, 2] which occurs whenever X-rays interact with interfaces (e.g. of cracks, pores, particles, and phase boundaries) especially at low angles of incidence. Due to the short X-ray wavelength below 0.1 nm X-ray refraction is sensitive to inner surfaces and interfaces of nanometre dimensions. Refraction enhanced micro-CT measurements have been conducted [3] at the hard X-ray experimental station (BAM*line*) [4, 5]. By exploring the same specimen with and without the refraction technique the potential of the Synchrotron Refraction Computed Tomography can be shown impressively.

The specimen was a cylindrical (3.5 mm diameter) Low Cycle Fatigue (LCF) test sample provided by MTU Aero Engines, Germany, in an aircraft project. It consists of a titanium base Ti-6242-alloy reinforced by SCS6-fibres from Textron [6]. Static and cyclic forces were applied in parallel to the fibres in order to obtain the values of several mechanical parameters.

After the mechanical treatments absorption based Synchrotron CT measurements were carried out. The nominal Pixel size of the detector system was 1.7 µm x 1.7 µm. Fig. 3 shows a radiograph taken at a distance of 25 mm between the specimen and the detector system. In opposite to film radiographs weak absorption appears bright while strong absorption appears dark. In the centre left of Fig. 3 a bright horizontal stripe indicates the main crack of the specimen caused by cyclic loading. Vertical dark stripes are caused by the reinforcing fibres. Horizontal stripes at the top and bottom are due to monochromator artefacts. Increasing the distance between the specimen and the detector system to 1128 mm effectuates a contrast enhancement of the crack and fibre interfaces (see Fig. 4). Because of the great distance between the specimen and the detector the deflected X-rays are now resolved. This leads to the observable contrast enhancement. Thus some additional small cracks are visible, but the spreading out of the main crack remains the same as in Fig. 3. Thus, by varying the distance between the specimen and the detector the contrast in the radiograph can be adjusted to improve the recognition of damage relevant details!
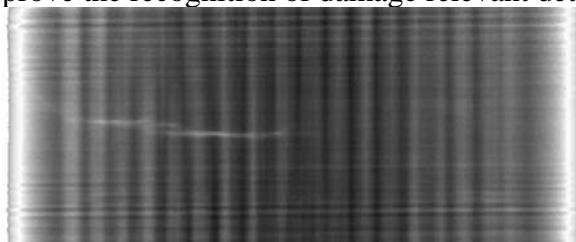
Figure 3: Radiograph of the LCF specimen at 50 keV photon energy. The distance between the specimen and the detector is 25 mm. The nominal Pixel size is 1.7 µm x 1.7 µm. The bright horizontal stripe in the middle left shows a crack caused by cyclic loading. Vertical stripes are caused by the reinforcing fibres. Horizontal stripes at top and bottom are due to monochromator artefacts.
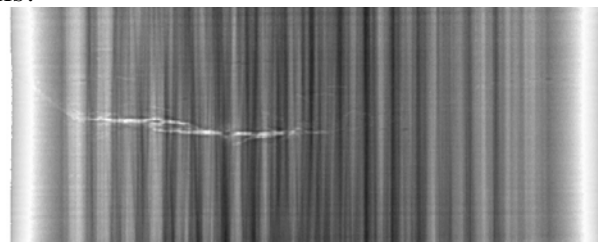
Figure 4: Radiograph of the LCF specimen at 50 keV photon energy. The distance between the specimen and the detector is now 1128 mm. The nominal Pixel size is 1.7 µm x 1.7 µm. The bright and well contrasted horizontal stripe in the middle left shows a crack caused by cyclic loading. Around the main crack few small cracks are visible. The well contrasted vertical stripes are caused by the reinforcing fibres.

Fig. 5 shows the radiograph of the same specimen as before, but archived by the Synchrotron Refraction Computed Tomography technique. Due to technical circumstances the nominal Pixel size during the measurement was only 5.6 µm x 5.6 µm. In contrast to the ab-

sorption measurement the crack interfaces appear dark (nearly black)! This is because the analysing crystal was set to the maximum of its Rocking-curve, therefore all X-rays deflected at the crack interfaces due to refraction and total reflection are not reflected and hence missing at the detector. Thus the crack appears as if it were a strong absorbing material. In comparison to the absorption measurement the spreading out of the main crack shows up much larger. Even though the Pixel size is about three times larger than it was in the absorption case much more details are visible! Above and below the main crack additional small cracks are identifiable (compare Fig. 4 and 5).
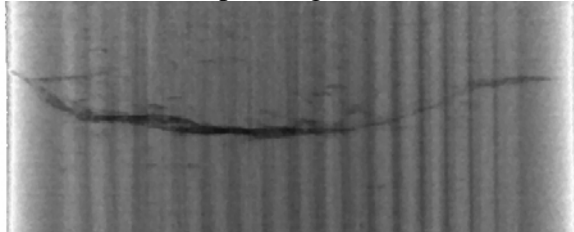
Figure 5: Radiograph of the LCF specimen at 50 keV photon energy recorded in refraction geometry and fibre orientation parallel to the scattering plane of the analysing crystal. The nominal Pixel size is 5.6 µm x 5.6 µm. The horizontal main crack appears dark. Around the main crack several small cracks are identifiable. Vertical stripes are caused by the reinforcing fibres.
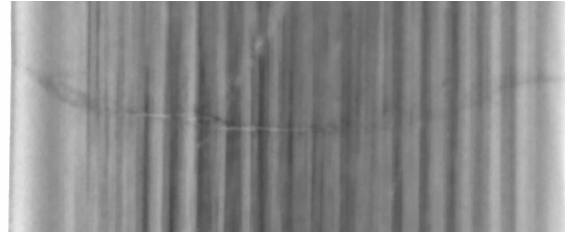
Figure 6: Radiograph of LCF specimen at 50 keV photon energy recorded in refraction geometry and fibre orientation perpendicular to the scattering plane of the analysing crystal. The nominal Pixel size is 5.6 µm x 5.6 µm. The horizontal main crack appears dark. The vertical stripes are caused by the reinforcing fibres.

A further feature of the analysing crystal is its orientation dependent suppression of the scattered X-rays. That means only the vector component of the refracted X-rays (due to the specimen interfaces) is suppressed, which is parallel to the scattering plane of the analyser crystal. The component perpendicular to the scattering plane of the analyser crystal remains unaffected. For this reason the above described refraction technique is an excellent tool to suppress scattered X-rays dependent on there orientation. E.g. the radiograph shown in Fig. 5 was measured while the scattering plane of the analysing crystal was parallel to the fibre orientation. That means scattered X-rays from the crack interfaces perpendicular to the fibre orientation (and the load direction) are mainly suppressed. For the radiograph shown in Fig. 6 the scattering plan of the analyser crystal was perpendicular to the fibre orientation. The contrast of the main crack is less pronounced than in Fig. 5, because the crack interfaces are mainly oriented perpendicular to the load direction.
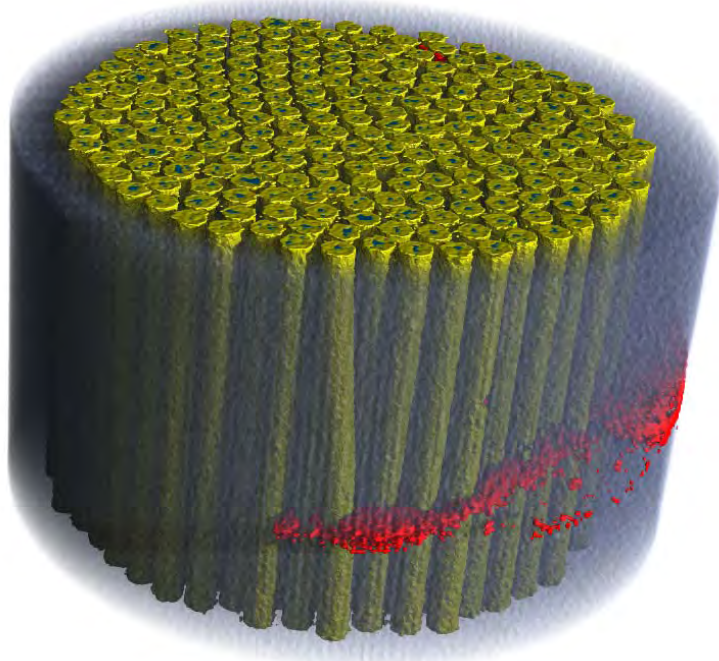
Figure 7: Reconstruction of the data set taken by Synchrotron Refraction Computed Tomography Measurement (scattering plane of the analysing crystal is parallel to the fibre direction). The Ti matrix is shown semi transparent, while the fibres and its Carbon core are solid. The main fatigue crack in the matrix is clearly visible.

Fig. 7 shows a three-dimensional visualization of the reconstruction by filtered back projection of the Synchrotron Refraction Computed Tomography Measurement. The orientation of the scattering plane of the analysing crystal was parallel to fibre direction. Like in the case of absorption CT measurements (not shown here) the visualization contains all the information about the fibre distribution and orientation in the Ti matrix. The main fatigue crack is clearly visible (horizontal structure in the semitransparent matrix). For a better visualization of the crack distribution in the specimen the crack is extracted from the data set and shown separately in Fig. 8. It shows all cracks, which have its main interface component perpendicular to the load direction. In contrast Fig. 9 shows only the distribution of cracks, which have its main interface component parallel to the load direction. From the data analysis it is clearly perceived, that the main crack is oriented perpendicular to the load direction and located in the Ti matrix. The fatigue cracks are oriented parallel to the load direction and located at the fibre/matrix interfaces. During the fatigue test the fibres deboned from the matrix. This led to the partial failure of the specimen.

Figure 8: Visualization of the main fatigue crack of the LCF sample without matrix and fibres. The scattering plane of the analysing crystal was parallel to the fibre direction.

Figure 9: Visualization of fatigue cracks along the fibre surfaces of the LCF sample without matrix and fibres. The scattering plane of the analysing crystal was perpendicular to the fibre direction.

Conclusion

The above described novel Synchrotron Refraction Computed Tomography Technique combines analytical capabilities of sub-micrometer structure detection with the requirements of non-destructive full volume characterization. It is capable to detect and visualize cracks even beyond the spatial resolution of the detector. Furthermore it can detect the orientation of the cracks. The technique is expected to close an essential gap in the spectrum of non-destructive techniques for a better understanding of micro structures of materials down to the nanometre scale and their behaviour under thermal and mechanical loads. Therefore the novel X-ray refraction technique might help accelerating materials development, leads to a better understanding of meso-structures and partly replace micro analysis and mechanical testing in advanced materials science.

[1] A.H. Compton, S.K. Allison, X-rays in Theory and Experiment, Macmillan, London, 1935.
[2] M.P. Hentschel, R. Hosemann, A. Lange, B. Uther, R. Bruckner, Röntgenkleinwinkelbrechung an Metalldrähten, Glasfäden und hartelastischen Polypropylen, Acta Crystallographica Section A 43 (1987) 506-513.
[3] A.C. Kak, M. Slaney, Principles of Computerized Tomographic Imaging, IEEE Press, 1988.
[4] W. Görner, M.P. Hentschel, B.R. Muller, H. Riesemeier, M. Krumrey, G. Ulm, W. Diete, U. Klein, R. Frahm, BAMline: the first hard X-ray beamline at BESSY II, Nucl. Instrum. Methods Phys. Res. Sect. A-Accel. Spectrom. Dect. Assoc. Equip. 467 (2001) 703-706.
[5] A. Rack, S. Zabler, B.R. Müller, H. Riesemeier, G. Weidemann, A. Lange, J. Goebbels, M. Hentschel, W. Görner, High resolution synchrotron-based radiography and tomography using hard X-rays at the BAMline (BESSY II), Nuclear Instruments and Methods in Physics Research Section A: Accelerators, Spectrometers, Detectors and Associated Equipment 586 (2008) 327–344.
[6] B.R. Müller, A. Lange, M. Harwardt, M.P. Hentschel, B. Illerhaus, J. Goebbels, J. Bamberg, F. Heutling, Refraction computed tomography - Application to metal matrix composites, Materialprufung 46 (2004) 314-319.

Hydrogen zoning in zinc-bearing staurolite from a high-P, low-T diasporite (Samos, Greece): a combined EMP-SIMS-FIB-FTIR study

Anne Feenstra[1], Dieter Rhede, Monika Koch-Müller, Michael Wiedenbeck, and Wilhelm Heinrich

Deutsches GeoForschungsZentrum Potsdam, Department 3, Telegrafenberg, D-14473 Potsdam, Germany. E-mail: mkoch@gfz-potsdam.de

Staurolite is an important index mineral for determining the metamorphic grade of Al-rich rocks with the ideal formula $Fe_4Al_{18}Si_8O_{46}(OH)_2$. It has a flexible structure and the crystal chemistry is complex due to variably occupied lattice sites resulting in various coupled vacancy-cation and other complex intracrystalline cation substitutions, which may induce local ordering. Further complexity arises from the fact that staurolite may incorporate highly variable amounts of light elements such as hydrogen and lithium. Li-rich zincostaurolite occurs locally as mm-long crystals at the marble footwall of a meta-karstbauxite on eastern Samos. The Samos rocks have been metamorphosed during an early Alpine high-P, low-T metamorphism (M1) followed by a late Alpine greenschist-grade overprint (M2). Textures and mineral chemistry indicate that staurolite formed from gahnite, cookeite and pyrophyllite during the early M1 stage.

In this contribution we report the chemical composition of the above mentioned natural metamorphic Li- and Zn-rich staurolite single crystal formed at low temperature-high pressure conditions. We present chemical zoning by detailed electron microprobe (EMP) work and secondary ion mass spectrometry (SIMS) by which lithium and hydrogen concentrations were quantified. Staurolite crystals show growth zoning with cores enriched in Zn, Fe, Mg, Co, and to a minor extent Li concentrations increase towards the rims (Fig. 1). Hydrogen concentrations were analyzed by SIMS and calibrated with natural staurolite and cookeite standards. Concentrations are significantly higher in cores (up to 5.97 atoms H per 48O) compared to rims (3.9 to 4.5 atoms H) and clearly anti-correlated with Al (Fig. 1).

Hydrogen concentrations measured by SIMS were compared with those obtained by FTIR spectroscopy (Fig. 2). The high absorption in the OH stretching region requires very thin (< 10 µm) samples for IR measurements. Therefore several 3-5 µm thick and 10 x 20 µm wide oriented foils (Fig. 3) were cut close to the locations of measured EMP-SIMS profiles using

---

[1] Deceased on April 9, 2007

Focused Ion Beam (FIB) technology (Wirth, 2004), by applying a Ga-ion beam at 30 kV and 2.7 nA. The beam current of 2.7 nA was about four times higher than that used for routinely prepared thin foils of 120 nm thickness. Polarised FTIR spectra were collected on this foils at the synchrotron IR-beamline at Bessy II.
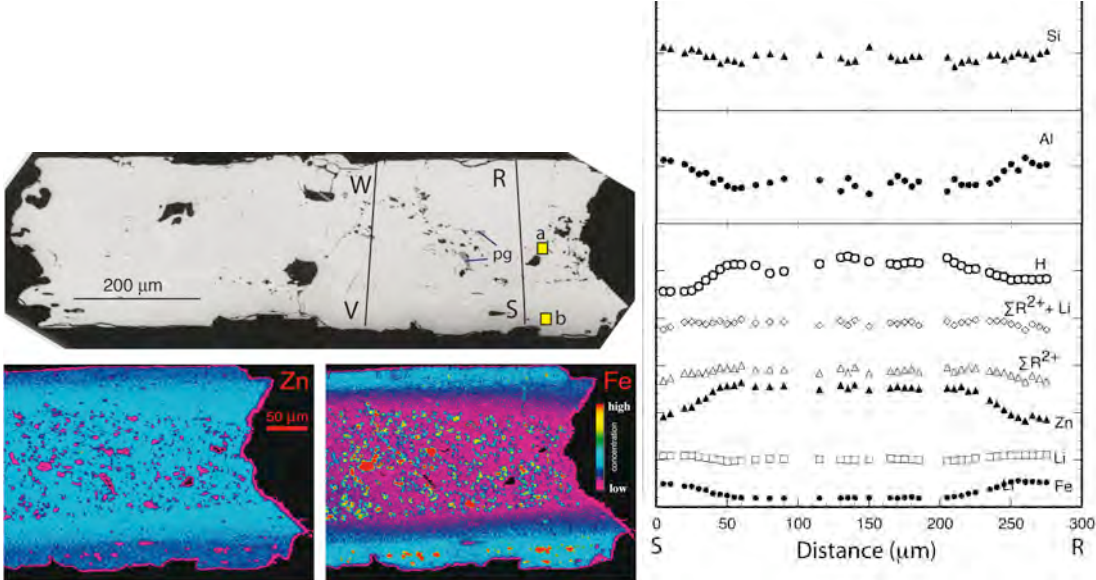
Figure 1: Staurolite crystal Sa9aE: (i) back-scattered electron micrograph (left top); R-S indicate profiles along which EMP and SIMS analyses have been performed; a and b denote locations where FIB-foils have been cut (see IR-spectra a and b in Fig. 2). (ii) selected X-ray element maps for Zn and Fe (left bottom); central part of the crystal contains numerous inclusions of Ca- (Fe, Mn, Mg) carbonate and a few paragonite (pg) solid inclusions., and (iii) variations in major and trace elements along profile S-R (right); Atoms calculated on the basis of 48 oxygens; H and Li measured by SIMS, all other elements by EMP.
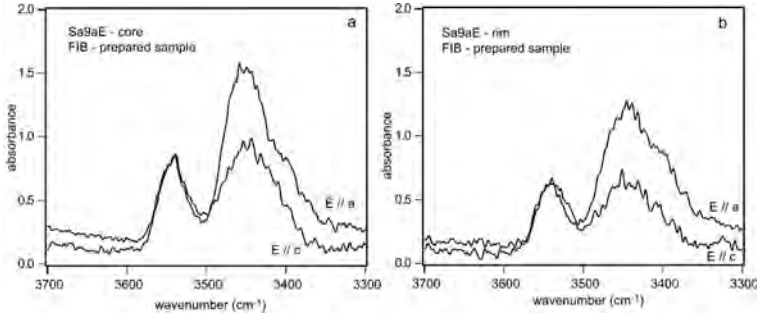
Fig. 2 a, b: Polarized IR-spectra of staurolite Sa9aE (normalized to an effective thickness 10 µm). a, b: FIB prepared samples from core and rim, respectively.
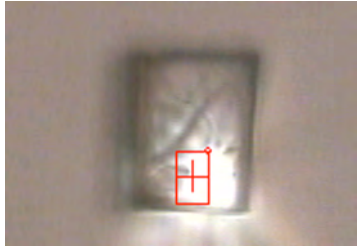
Fig. 3: FIB prepared sample 10 x 20 µm in size; in red is shown size and location of the measure spot.

Applying an IR calibration for OH in Fe-rich staurolite (Koch-Müller and Langer, 1998) the hydrogen zoning profile by SIMS was well reproduced, however, the absolute hydrogen concentrations were systematically lower by about 25%. To see whether this discrepancy is due to water loss during the foil preparation, foils taken on an oriented plate of staurolite from Pizzo Forno with a well-known content of 2.05 wt% H_2O (Koch-Müller and Langer 1998) were cut parallel *a* and parallel *c* at identical focused ion beam conditions as for the unkown staurolite sample. Interestingly, quantification of the water content using the IR calibration yields also 25% less water then obtained on the original sample. Thus, the discrepancy must be caused by sub-micron scale hydrogen loss at the staurolite surface during FIB-thinning. To use the promising focused ion beam techniques in future to prepare very thin site specific IR samples further test with variations in beam current and/or cutting time are necessary.

The observed zonation in hydrogen in this special staurolite is interpreted as reflecting the two-stage growth. M1-staurolite that formed at low T of about 400-450 °C and high P of >1.5 GPa incorporated nearly the maximum amount of hydrogen allowed by the staurolite structure (6 H pfu) and was subsequently overgrown and marginally replaced during the M2 stage by less hydrous, Fe-Co richer staurolite. Hydrogen zoning in staurolite is facilitated by the sensitivity of its structure to changing P-T conditions. Water in staurolite is maximized at high P and low T. Cores of staurolite from Samos represent the most hydrous staurolite compositions reported to date.

References

Koch-Müller, M. & Langer, K. (1998): Quantitative IR-spectroscopic determination of the component H_2O in staurolite. European Journal of Mineralogy 10: 1267-1273.

Wirth R. (2004) Focused Ion Beam (FIB): A novel technology for advanced application of micro-and nanoanalysis in geosciences and applied mineralogy. European Journal of Minerlaogy 16: 863 – 876.

3

Valence state of Co ions in nanostructured LiCoO$_2$ obtained by high pressure torsion method

V. R. Galakhov[1]*, **N. A. Ovechkina**[1], **B. A. Gizhevskii**[1], **C. Taubitz**[2],
M. Raekers[2], **A. R. Cioroianu**[2], **M. Neumann**[2], **A. S. Semenova**[3], **D. G. Kellerman**[3],
R. Ovsyannikov[4], and **S. L. Molodtsov**[5]

[1] *Institute of Metal Physics, Russian Academy of Sciences —
Ural Division, 620041 Yekaterinburg GSP-170, Russia*
[2] *Fachbereich Physik, Universität Osnabrück, D-49069 Osnabrück, Germany*
[3] *Institute of Solid State Chemistry, Russian Academy of Sciences —
Ural Division, 620041 Yekaterinburg GSP-145, Russia*
[4] *BESSY GmbH, Albert-Einstein-Str. 15, D-12489 Berlin, Germany*
[5] *Institut für Festkörperphysik,Technische Universität Dresden, D-01062 Dresden, Germany*

Oxides Li$_x$CoO$_2$ have served as cathode materials for Li batteries. Most of the electrochemical and physical properties would be affected by the electronic structure of these compounds.

The electronic ground state of Co^{3+} ion in LiCoO$_2$ can be written as $t_{2g\uparrow}^3 t_{2g\downarrow}^3 e_g^0$. We have found that the deficiency of oxygen in LiCoO$_{2-\delta}$ give rise of the divalent cobalt ions and this fact can be detected by Co $2p$ and Co $3s$ X-ray photoelectron spectra [1]. In lithium deintercalated cobaltites Li$_{1-x}$CoO$_2$ ($x > 0$) the charge compensation occurs through the formation of holes in the O $2p$ states, whereas the electron configuration of the cobalt ions remains unchanged [2, 3]. Here we present the results of X-ray absorption (XAS) and X-ray photoelectron (XPS) spectroscopy studies of nanostructured LiCoO$_2$.
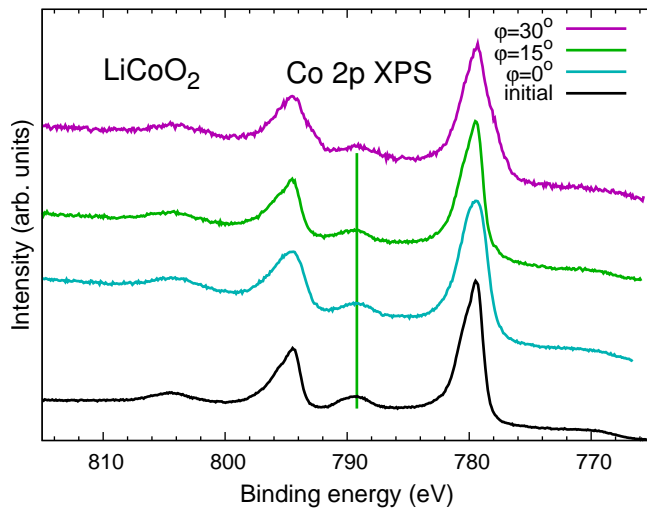
Fig. 1: Co $2p$ X-ray photoelectron spectra of nanostructured LiCoO$_2$ obtained by high pressure torsion method. The anvil rotation angles φ indicate deformation degrees. For comparison, the spectrum of initial LiCoO$_2$ is presented.
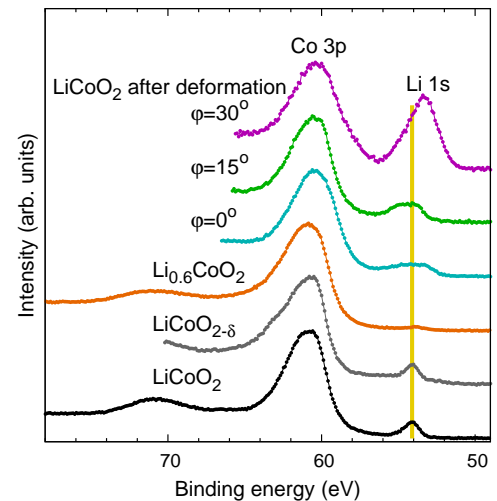
Fig. 2: Co $3p$ and Li $1s$ X-ray photoelectron spectra of LiCoO$_2$ subjected to plastic deformation. For comparison, the spectra of initial LiCoO$_2$ and defective cobaltites Li$_{0.6}$CoO$_2$ and LiCoO$_{2-\delta}$ are presented.

A single-phase, homogeneous ceramic sample of LiCoO$_2$ was prepared by sintering a mixture of Co$_3$O$_4$ and Li$_2$CO$_3$. Nanostructured LiCoO$_2$ samples were obtained by high pressure torsion method.

---

*e-mail: galakhov@ifmlrs.uran.ru

High pressure torsion was realized by means of a 100-t press and Bridgman anvils. Initial powders of $LiCoO_2$ were placed between anvils and pressed at 3–8 GPa. Shear deformation was achieved by rotation of one of the anvils. The degree of strain was specified by the anvil rotation angle φ. Powder X-ray diffraction was used to confirm single-phase specimens. All the nanostructured samples contain 100 % of hexagonal $LiCoO_2$.

The X-ray photoelectron spectra of the defective and nanostructured lithium cobaltites were obtained with a PHI 5600 ci Multitechnique System XPS spectrometer using monochromatized Al $K\alpha$ radiation. The energy resolution was about 0.4 eV. The Co $2p$ X-ray absorption spectra (XAS) were measured at the Russian-German Beam Line at the BESSY storage ring.

Deformation of $LiCoO_2$ can lead either to defects in oxygen and therefore to the formation of Co^{2+} ions or to defects in lithium, nominally accompanied by Co^{4+} ions. According to Co $2p$ X-ray photoelectron spectra presented in Fig. 1, there is no difference between the Co $2p$ X-ray photoelectron spectra (XPS) of nanostructured and initial (coarse grain) samples of $LiCoO_2$ obtained at the anvil rotation angles $\varphi \leq 30°$ (see Fig. 1). This means that the valence state of the Co ions is not changed. Note, Co $2p$ XPS and XAS and Co $3s$ X-ray photoelectron spectra of defective cobaltites $Li_{1-x}CoO_2$ are nearly identical to the spectrum of the initial oxide $LiCoO_2$ [2, 3].

On the other hand, the increase of the anvil rotation angles lead to an increase of the relative intensity of Li $1s$ / Co $3p$ XPS lines (see Fig. 2). Note that photoelectron spectra give an information about the surface of materials. This means that the relative concentration of Li atoms is increased at the sample surface region. One can see that the maximum of the Li $1s$ line in defective $LiCoO_2$ is shifted to the low-binding-energy side. We suggest that it is evidence of the formation of Li_2O.
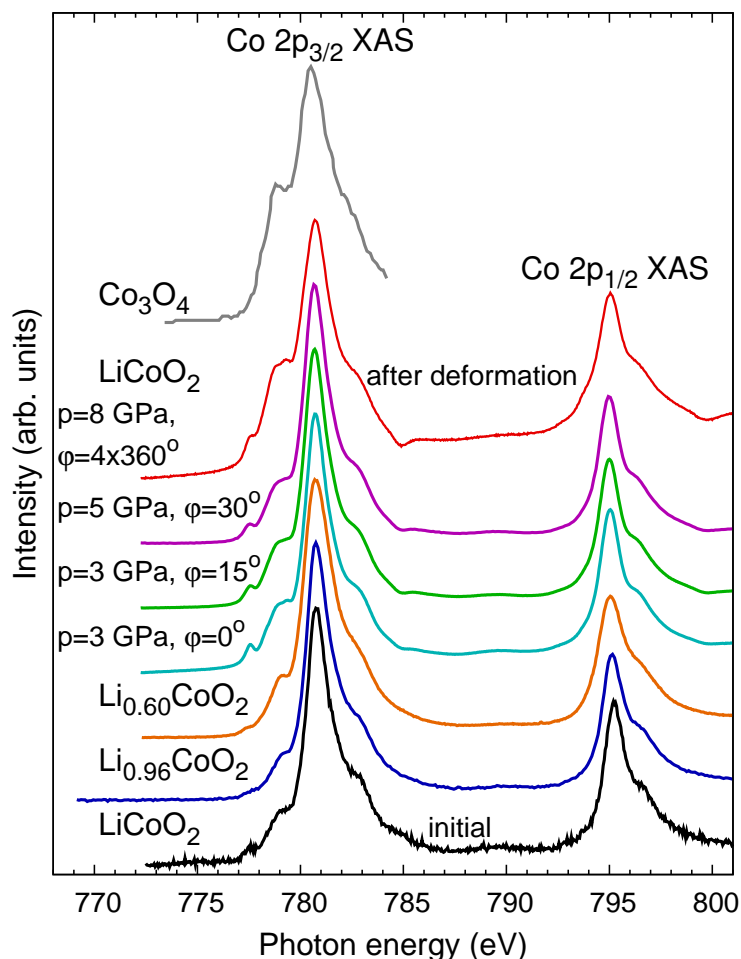
Fig. 3: Co $2p$ X-ray absorption spectra of $LiCoO_2$ subjected to plastic deformation, initial $LiCoO_2$, defective cobaltites $Li_{0.6}CoO_2$, $Li_{0.96}CoO_2$, and Co_3O_4. The spectrum of Co_3O_4 is reproduced from [4].

Fig. 3 shows Co $2p$ X-ray absorption spectra of LiCoO$_2$ subjected to by high pressure torsion deformation. The spectra of the samples obtained at pressures of 3–5 GPa and the anvil rotation angles $\varphi \leq 30°$ present only minor changes indicating that the Co ions are not changed. The absence of changes shows that the Co ions remain in a trivalent Co^{3+} low-spin state. An increase of pressure to 8 GPa leads to radical changes of the Co $2p$ spectrum. The spectrum of nanostructured LiCoO$_2$ obtained at a pressure of 8 GPa and $\varphi = 4 \times 360°$ shows the presence of Co^{2+} ions.

XPS and XAS measurements in TEY mode are surface sensitive to a few hundred Angstroms. We suggest that after deformation, a change of the composition of lithium cobaltite occurs. The concentrations of oxygen as well of lithium decrease: Li$_{1-x}$CoO$_{2-\delta}$ ($\delta > x/2$). The surface of the samples is enriched by Li. Such situation is described in Ref [5]. Note that extration of Li from coarse-grained LiCoO$_2$ occurs only at temparatures higher than 1200 K.

[1] V. R. Galakhov, V. V. Karelina, D. G. Kellerman, V. S. Gorshkov, N. A. Ovechkina, M. Neumann, Phys. Solid State **44**, 266 (2002).

[2] V. R. Galakhov, N. A. Ovechkina, A. S. Shkvarin, S. N. Shamin, E. Z.Kurmaev, K. Kuepper, A. Takács, M. Raekers, S. Robin, M. Neumann, G.-N. Gavrilă, A. S. Semenova, D. G. Kellermann, T. Käämbre, J. Nordgren, Phys. Rev. B **74**, 045120(6) (2006).

[3] V.R. Galakhov, M. Neumann, D.G. Kellerman, Appl. Phys. A **94**, 497 (2009).

[4] D. Bazin, P. Parent, C. Laffon, O. Ducreux, J. Lynch, I. Kovacs, L. Guczi, and F. De Groot, J. Synchrotron Rad. **6**, 430 (1999).

[5] E. Antolini, J. Eur. Ceram Soc. **18**, 1406 (1998).

Nanostructural characterization of TiN-Cu films using EXAFS spectroscopy

F. Pinakidou[1], M. Katsikini[1], E.C. Paloura[1], P. Patsalas[2], G. Abadias[3]

[1] *Aristotle University of Thessaloniki, School of physics, 54124 Thessaloniki, Greece*
[2] *University of Ioannina, Department of Materials Science & Engineering, 45110, Ioannina, Greece*
[3] *Laboratoire de Métallurgie Physique, UMR CNRS 6630, Université de Poitiers, SP2MI, Téléport 2, BP 30179, 86962 Futuroscope-Chasseneuil Cedex, France*

Transition metal-TiN_x material systems have been a subject of extensive scientific and engineering studies since they exhibit excellent mechanical properties as well as wear and corrosion resistance. The problem of toughness in superhard nanocomposites can be addressed by the formation of hard nanocrystalline phases within a metal matrix, such as TiN in Ni or Cu.[1] In such coatings, one of the metals can form a hard nanocrystalline nitride phase while the other one remains unreacted. Here we apply X-ray absorption fine structure (XAFS) measurements at the Cu-*K*-edge in order to identify composition dependent changes in the bonding environment of Cu in TiN-Cu and $Ti_{1-x}Cu_x$ films.

The studied nanocomposite TiN-Cu and $Ti_{1-x}Cu_x$ films were deposited at room temperature on Si substrates by reactive magnetron co-sputtering. In particular, the deposition of the former films occurred under Ar+N_2 atmosphere and of the latter films under inert gas (Ar) atmosphere. Details on the growth conditions have been reported previously.[2] The Cu-*K*-EXAFS spectra of the studied samples were recorded at the KMC2 beamline in the fluorescence yield (FLY) mode. A Cu film, 203 nm-thick, deposited on quartz under the same conditions as the $Ti_{1-x}Cu_x$ films was used as reference.

The $\chi(k)$ EXAFS spectra of the $Ti_{1-x}Cu_x$ and TiN-Cu studied films were subjected to Fourier filtering in the distance range 1.6-2.6Å and the corresponding Fourier Transforms (FTs) (k range: 3.5-12.0Å^{-1}) are shown in Fig. 1(a) and (b), respectively. The analysis of the EXAFS spectrum of the reference Cu film reveals that Cu is coordinated with 12.8 ($\pm$0.8) Cu atoms and the respective Cu-Cu bondlength is equal to 2.55Å ($\pm$0.01), i.e. crystalline Cu is detected. On the contrary, in the studied $Ti_{1-x}Cu_x$ and TiN-Cu samples, the nanostructure of Cu changes as a result of the different chemical composition.

More specifically, as shown in the upper panel of Fig. 2, in the $Ti_{1-x}Cu_x$ samples the total coordination number of Cu, i.e. the sum of both Cu and Ti first neighbours (N_{Cu} and N_{Ti}, respectively), increases from $\cong$6 to $\cong$11 when the Cu increases from 24.1 to 52.7 at%. This change can only be attributed to the systematic increase of the number of Cu atoms bonded to Cu (N_{Cu}). Indeed, as shown in the middle panel of Fig. 2, N_{Ti} is practically constant (within the error bar) and ranges between 3.5 and 4.1 ($\pm$0.4-0.3), while on the contrary, as depicted in the lower panel of Fig. 2, N_{Cu} increases linearly from 2.2 to 7.1 ($\pm$0.4-0.5). Additionally, the EXAFS analysis reveals that the coordination number of Cu does not depend on the substrate and is practically equal between the samples with the same composition (35.5 at% Cu) grown on Si and quartz: in the former case the 1st nn shell consists of 4.2$\pm$0.6 Cu and 3.6$\pm$0.4 Ti atoms while in the latter case Cu is bonded to 3.5$\pm$0.6 Cu and 3.7$\pm$0.3 Ti atoms. In all studied $Ti_{1-x}Cu_x$ samples, the Cu-Ti bondlength is equal to 2.45-2.47Å ($\pm$0.01) while the Cu atoms are located at 2.54-2.56Å
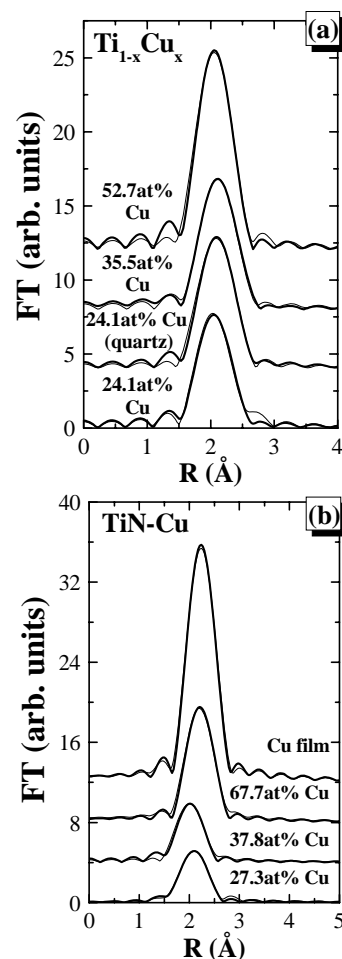
Fig. 1: Fourier Transforms (FTs) of the filtered $k^3*\chi(k)$ Cu-*K*-EXAFS spectra of (a) the $Ti_{1-x}Cu_x$ and (b) the TiN-Cu films. The raw data and the fitting are shown in thin and thick solid lines, respectively.

1

($\pm$0.02), i.e. as in the reference Cu film. Thus, it is revealed that independently of the Cu content, Cu belongs to an amorphous Cu-matrix where Ti partially substitutes Cu atoms while also forms intermetallic TiCu. As the Cu content increases, the total coordination number of Cu increases linearly. More specifically, Cu belongs to intermetallic TiCu nanocrystallites and prefers to segregate when the Cu concentration exceeds 40 at%.

The EXAFS analysis of the TiN-Cu films reveals that only in the sample with the intermediate Cu concentration (37.8 at% Cu), Cu is bonded to both Cu and Ti. The 1st nn shell consists of 1.9$\pm$0.2 Ti and 2.6$\pm$0.3 Cu atoms that are located at 2.47Å ($\pm$0.01) and 2.55Å ($\pm$0.02) respectively, i.e. at the same distance as in the Ti$_{1-x}$Cu$_x$ samples. However, in this sample fewer Ti atoms (1.9$\pm$0.2) are bonded to Cu, compared to the respective number of Ti atoms in the Ti$_{1-x}$Cu$_x$ sample with 35.5 at% Cu (3.6$\pm$0.4). This modification in the TiN/Cu sample with 37.8 at% Cu can be attributed to formation of TiN crystallites, which have also been detected by XRD measurements.[3] Thus it can be proposed that, when the films are grown under Ar-N$_2$ atmosphere, Ti prefers to form TiN and any excess Ti atoms bond to Cu. On the contrary, in the sample with the lowest Cu concentration (27.3 at%), only Ti atoms comprise the 1st nn shell. Cu is bonded to 6.1$\pm$0.4 Ti atoms and the Cu-Ti bondlength is equal to 2.45Å ($\pm$0.01), i.e. the formation of intermetallic Ti-Cu bonds is identified. Finally, in the sample with the highest Cu content (67.7 at%) Cu is coordinated with 10.6$\pm$0.4 Cu atoms located at 2.53Å ($\pm$0.01), i.e. Cu belongs to an amorphous Cu matrix. Therefore, it is concluded that in the TiN-Cu samples, the different Cu content results in significant modifications in the nanostructure of Cu: in the lowest Cu concentration limit, Cu forms intermetallic TiCu, in the sample with the intermediate Cu concentration both TiCu nanocrystallites and Cu-Cu bonds are detected while finally, in the highest Cu concentration limit, Cu belongs to an amorphous Cu matrix.

Fig. 2: Modification of the coordination number of Cu as a function of the Cu content in the Ti$_{1-x}$Cu$_x$ films.

To conclude, the effect the different chemical composition on the nanostructure of Cu in Ti$_{1-x}$Cu$_x$ and TiN-Cu nanocomposite films was studied using EXAFS measurements at the Cu-*K*-edge. It is disclosed that in all studied Ti$_{1-x}$Cu$_x$ films, Cu belongs to amorphous Cu regions and to intermetallic TiCu nanocrystallites. However, the coordination number of Cu increases as a function of the Cu content in the samples, which can be attributed only to the systematic increase in the number of Cu atoms bonded to Cu. On the contrary, in the TiN-Cu films, the alteration in the chemical composition affects both the coordination number and type of atoms in the 1st nn shell. In particular, Cu is coordinated with both Cu and Ti atoms only in the sample with intermediate Cu concentration (37.8 at%). In the sample with the highest Cu content (67.7 at%), Cu belongs to pure, amorphous Cu regions, while in film with the lowest Cu content (27.3 at%), only intermetallic Cu-Ti bonds are identified.

References

[1] J. Musil, P. Zeman, H. Hruby, P.H. Mayrhofer, Surf. Coat. Technol. **120-121**, 179 (1999).
[2] G. Abadias, Y.Y. Tse, J. App. Phys. **95** 2414 (2004).
[3] G. Abadias, private communication

μ-XRF and μ-EXAFS studies of an Al matrix Fe-Ni composite

F. Pinakidou, M. Katsikini, E.C. Paloura.

Aristotle University of Thessaloniki, School of Physics, 54124, Thessaloniki, Greece

The mechanical properties of metals can be improved by either alloying with other metals or by chemical reactions which lead to the formation of intermetallic products.[1] When the surface of a Fe-Ni alloy is exposed to liquid Al, dissolution occurs followed by growth of intermetallic layers at the alloy-aluminium interface.[2,3] The growth of these phases is controlled by chemical reactions at the interfaces and the interdiffusion of Fe and Ni. The strength of the matrix can be further improved via a direct reaction synthesis in which reactant powders are directly added into the molten metal. The reinforcing particles are formed in situ through reactions between reactants or between the reactant and a component of the metal. For example, a mixture of K_2TiF_6 and KBF_4 is added in to the molten Al matrix resulting in the formation of Ti-B particles which are well incorporated in the metallic matrix.

Here we report on the distribution of the metals and the local coordination of Ni in a Fe-Ni rod (97 wt% Fe and 3 wt% Ni) which was dissolved in liquid Al. A 5 wt% mixture of K_2TiF_6 and KBF_4 was added at 1060^oC and stirred for 30min. The μ-XRF and μ-Ni-K-EXAFS measurements were conducted at the KMC2 beamline which is equipped with a double-crystal monochromator and capillary optics that reduce the beam diameter to 5μm. The μ-XRF maps were recorded using excitation photons of 9500eV, i.e. higher than the Fe-K and Ni-K absorption edges, using an energy dispersive (Röntec) fluorescence detector. The μ-Ni-K-EXAFS spectra were recorded from different positions of the sample surface while an Ni-K-EXAFS spectrum was recorded from a random sample spot, after removing the capillaries. The spectra were recorded in the fluorescence yield (FLY) mode using a Röntec detector.

The XRF maps of the studied sample reveal that the distribution of both Fe and Ni is inhomogeneous. More specifically, as shown in Fig.1, Ni-rich (H-regions) and Ni-poor (L-regions) regions are detected. It should be noted that in the Ni-rich islands the corresponding Fe concentration is low, while in the Ni-poor regions, Fe segregates. On the contrary, the μ-XRF spectra recorded from the H- and L-regions reveal that the distribution of both Mn and Cr, which are contaminants in the Fe-Ni alloys, is homogeneous (Fig. 2).
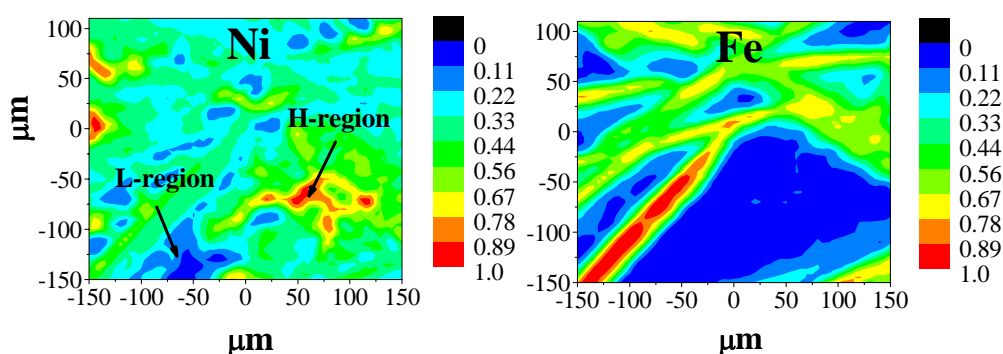
Fig. 1: $300x250μm^2$ μ-XRF maps of the Fe and Ni distributions. The regions denoted L and H, correspond to Ni-poor and Ni-rich regions, respectively.

In order to investigate the possible changes in the bonding environment of the Ni atoms as a function of the Ni segregation or depletion, we recorded μ-Ni-K-EXAFS spectra from the H- and L-regions, respectively. The Fourier transforms (FT) of the k^3-weighted χ(k) μ-Ni-K-EXAFS spectra (k-range 2.5-9.0Å^{-1}) are shown in Fig.3. In the same figure we include the FT of the Ni-K-EXAFS spectrum (k-range 2.5-9.0Å^{-1}) recorded after removing the capillaries. As shown in Fig.3, in the FTs of both the μ-EXAFS and EXAFS spectra, only the 1st nearest

1

neighbor (nn) shell is resolved, indicating that the bonding environment of Ni is amorphous.[4] The µ-EXAFS and EXAFS spectra were fitted assuming that Ni is bonded only to Al. However, the crystalline models used in the fitting process were modified for the Ni-rich and Ni-poor regions: in the Ni-rich regions it is assumed that Al atoms substitute Ni in the structure of crystalline Ni, while in the Ni-poor regions, Ni is assumed to form intermetallic NiAl nanocrystallites.

The µ-EXAFS analysis reveals that the bonding environment of Ni changes as a result of the inhomogeneous distribution of Ni. More specifically, in the Ni-rich regions (H-region), the Ni atoms are bonded to 11.5 ± 0.7 Al atoms that belong to an amorphous Ni matrix. On the contrary, in the region with low Ni content (L-region), Ni is coordinated with 8.8 ± 0.5 Al atoms. In this region, the Ni atoms occupy sites in an amorphous Al matrix. Furthermore, the Ni-K-EXAFS analysis discloses that the coordination number of Ni is equal to 9.7 ± 0.8, i.e. equal to the average number of Al atoms in the L- and H-regions of the sample. Additionally, the µ-EXAFS and EXAFS analysis reveal that the Ni-Al bondlength is equal to 2.47-2.49Å (±0.01), i.e. independent of the inhomogeneous distribution of Ni.

The modification in the bonding environment of Ni can be explained on the basis of the different phases formed in the sample. In particular, in the H-region, Ni belongs to a pure amorphous Ni phase where the Al atoms have partially substituted Ni atoms (Ni is bonded with 12 Ni atoms in metallic Ni). On the contrary, in the L-region, the number of Al atoms in the 1st nearest shell of Ni is smaller. Since in the cubic structure of intermetallic NiAl, each Al atom is bonded with 8 Al atoms, it can be proposed that in this region, Ni belongs to intermetallic NiAl nanocrystallites. Finally, the coordination number of Ni, as determined by the EXAFS analysis is, as expected, equal to the average number of Al atoms in the H- and L- regions.

Fig. 2: µ-XRF spectra recorded from the H- and L-regions, respectively. The low energy region (1 to 6.5 keV) is shown at the inset of the figure.
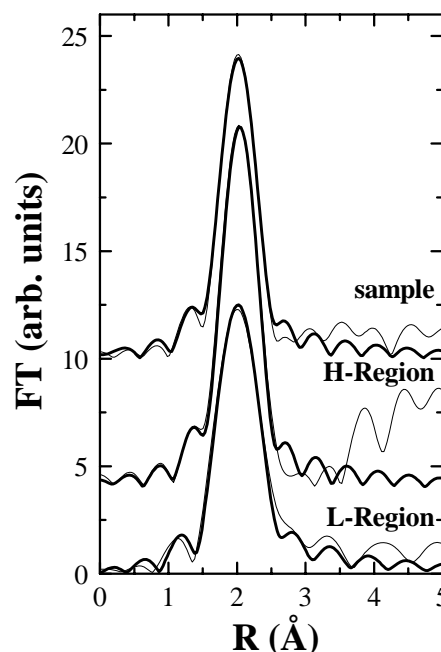
Fig. 3: Fourier Transforms (FT) of the µ-Ni-K-EXAFS spectra recorded from the Ni-rich (H-region) and Ni-poor regions (L-region). The FT shown on the top (denoted "sample") corresponds to the Ni-K-EXAFS spectrum recorded without the capillaries. The raw data and the fitting are shown in thin and thick solid lines, respectively.

References

[1] F.L. Mathews, R.D. Rawlings, "Composite Materials: Engineering and Science", Cambridge: CRC Press, Woodhead (1999).
[2] V.I. Dybkov, J. Mat. Sci., **21**, 3078 (1986).
[3] V.I. Dybkov, J. Mat. Sci., **25**, 3615 (1990).
[4]. F. Pinakidou et al., J. App. Phys., **102**, 113512 (2007).

2

Two kinds of interfaces in SrTiO$_3$/LaAlO$_3$ superlattices revealed by resonant soft x-ray scattering

H. Wadati[1], J. Geck[1], D. G. Hawthorn[1], T. Higuchi[2], M. Hosoda[2], C. Bell[2], Y. Hikita[2],
H. Y. Hwang[2], C. Schüßler-Langeheine[3], E. Schierle[4], H.-H. Wu[3,5], E. Weschke[4],
S.-W. Huang[5], D. J. Huang[5], H.-J. Lin[5], I. Elfimov[1], G. A. Sawatzky[1]

[1]*Department of Physics and Astronomy, University of British Columbia, Vancouver, Canada*
[2]*Department of Advanced Materials Science, University of Tokyo, Kashiwa, Japan*
[3]*II. Physikalisches Institut, Universität zu Köln, Köln, Germany*
[4]*Helmholtz-Zentrum Berlin für Materialien und Energie, Berlin, Germany*
[5]*National Synchrotron Radiation Research Center, Hsinchu, Taiwan*

Introduction: The interfaces of hetero-junctions composed of transition-metal oxides have recently attracted great interest. Among them, the interface between two band insulators SrTiO$_3$ (STO) and LaAlO$_3$ (LAO) is especially interesting due to the metallic conductivity [1] and even superconductivity [2]. Several reports suggest that n-type (LaO/TiO$_2$/SrO) interface is metallic and the p-type (LaO/AlO$_2$/SrO) interface is insulating. In this study we investigated the electronic structure of the STO-LAO superlattice (SL) by resonant soft x-ray scattering [3], which has recently been used to study SrMnO$_3$-LaMnO$_3$ SLs [4].

Experiment: The superlattice sample consisted of seven periods of 12 unit cells (uc) of STO and 6 uc of LAO. The present samples was grown on a STO (001) substrate by the pulsed laser deposition technique at an oxygen pressure of 1.0×10^{-5} Torr and a substrate temperature of 700 $^{\circ}$C. A schematic view of the fabricated superlattice is shown in Fig. 1. The resonant soft x-ray scattering experiments were performed at the BESSY undulator beam line UE46-PGM. The spectra were taken at room temperature. The incident light was polarized in the vertical direction (σ polarization) or in the horizontal direction (π polarization) with the detector integrating over both final polarizations.
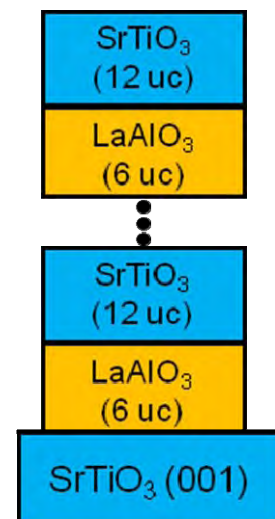
Figure 1: Schematic view of the SrTiO$_3$/LaAlO$_3$ superlattice sample.

Results and discussions: Figure 2 shows the photon-energy dependence of the (002) and (003) peaks near the O 1s absorption edge measured with σ (a) and π (b) polarizations. The structure factor for this (003) peak is proportional to $(f_{TiO2, \text{ int}} - f_{TiO2} + f_{AlO2, \text{ int}} - f_{AlO2})$, where f_{TiO2} and f_{AlO2} are the scattering factors of the TiO$_2$ and AlO$_2$ planes of the STO and LAO layers, respectively, and the subscript "int" means the scattering factor for the interface. The (003) reflection is forbidden by symmetry as long as the interface form factor is the same as the bulk. The existence of this peak in Fig. 2 therefore means that some kind of reconstruction occurs at the interface. From top and middle panels, we can see strong polarization

Figure 2: Photon-energy dependence of the (002) and (003) peaks near the O 1s absorption edge measured with σ (a) and π (b) polarizations. Top and middle panels show intensity maps of (002) and (003) regions, respectively. Here, bright parts correspond to high intensities. Bottom panels show the (002) and (003) peak heights together with the XAS spectra.

dependence. Also we notice that there are two structures in the energy region of 530 – 532 eV, which comes from hybridization with Ti 3d t_{2g} states. The relative intensities of these two structures depend on polarizations. The value of the energy splitting is about 1 eV. From linear dichroism in Ti 2p x-ray absorption, Salluzzo et al. [5] concluded that the xy orbital is stabilized at the interface, and the value of the energy splitting between xy and the other two t_{2g} orbitals (yz and zx) is about 50 meV, which is much smaller than the 1 eV splitting observed in this study. Now we are performing band-structure calculations to explain this 1 eV splitting.

References:

[1] A. Ohtomo and H. Y. Hwang, Nature **427**, 423 (2004).

[2] N. Reyren et al., Science **317**, 1196 (2007).

[3] H. Wadati et al., arXiv:0810.1926v1.

[4] S. Smadici et al., Phys. Rev. Lett. **99**, 196404 (2007).

[5] M. Salluzzo et al., arXiv:0812.1444.v1.

Doping of organic semiconductors to improve electronic interface properties of hetero-junction solar cells.

Thomas Mayer, Corinna Hein, Eric Mankel, and Wolfram Jaegermann
Darmstadt University of Technology, Institute of Materials Science
Petersenstr. 23, D-64287 Darmstadt, Surface Science Division
BMBF Initiative "Organic Photovoltaics"

Due to low dielectric constants and strong intra and extra-molecular relaxation in organic semiconductors optically generated electron hole pairs form strongly bound excitons of 0.5 to 1eV binding energy. In organic solar cells hetero-junctions of electron donor and acceptor materials are used for dissociation of the excitons and charge separation (Fig.1). Even after injection of the electron from the donor to the acceptor electron hole pairs may be bound across the hetero-junction forming so called geminate pairs still likely to undergo recombination. Therefore the electronic structure of such organic hetero-interfaces concerning band/orbital line up and potential gradients is of basic importance for the cell efficiency.
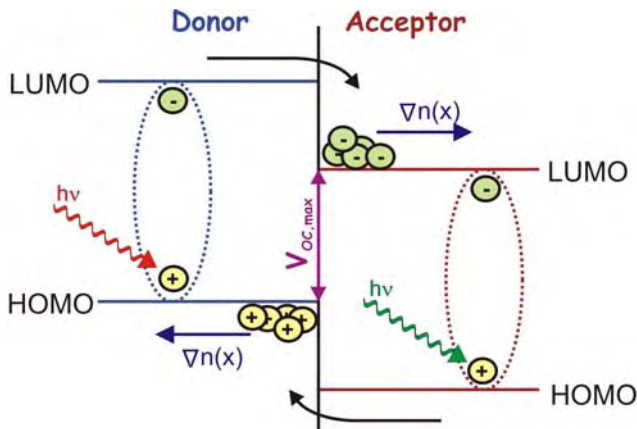
Fig.1: Exciton dissociation and charge separation at the donor acceptor hetero-junction interface in organic solar cells.
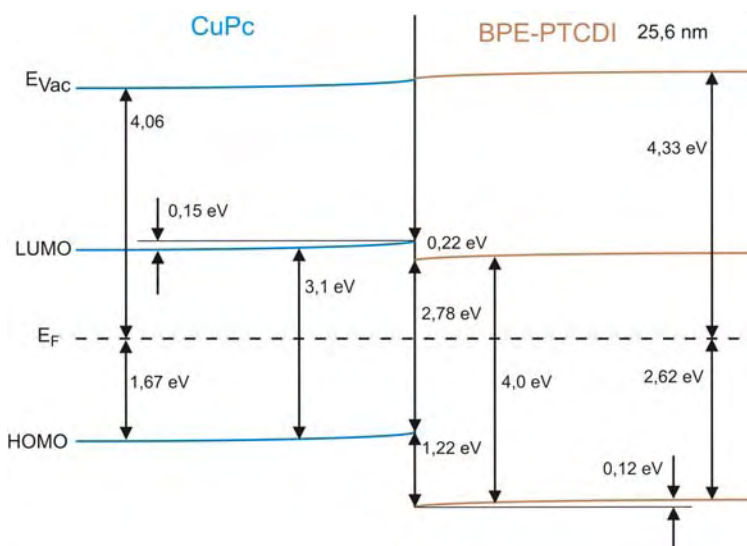
Fig.2: Band diagram of the electronic structure of the donor/acceptor CuPc/BPE-PTCDI hetero-junction. The potential gradients retain charge carriers at the interface whereby the efficiency of the photovoltaic device is reduced.

We investigate the electronic structure of the CuPc/BPE-PTCDI donor/acceptor interface and the changes induced by p-doping of CuPc with WO_3 using SXPS on step wise in situ prepared interfaces. CuPc and BPE-PTCDI were provided by the project partner BASF. The measurements are performed at the BESSY undulator beamline U49 using the SoLiAS end-station. The electronic structure of the donor/acceptor system CuPc/BPE-PTCDI indicates unfavorable potential gradients that retain the separated charge carriers at the interface instead of driving them towards the external contacts (Fig.2). In order to reverse the interface band bending p-doping of CuPc and/or n-doping of BPE-PTCDI is suggested. We tested p-doping of CuPc with WO_3 as an inorganic molecule of high electron affinity. Due to a high number of trap states in the energy gap of organic semiconductors much higher dopant content is necessary in order to shift the Fermi level as compared to inorganic semiconductors[1].
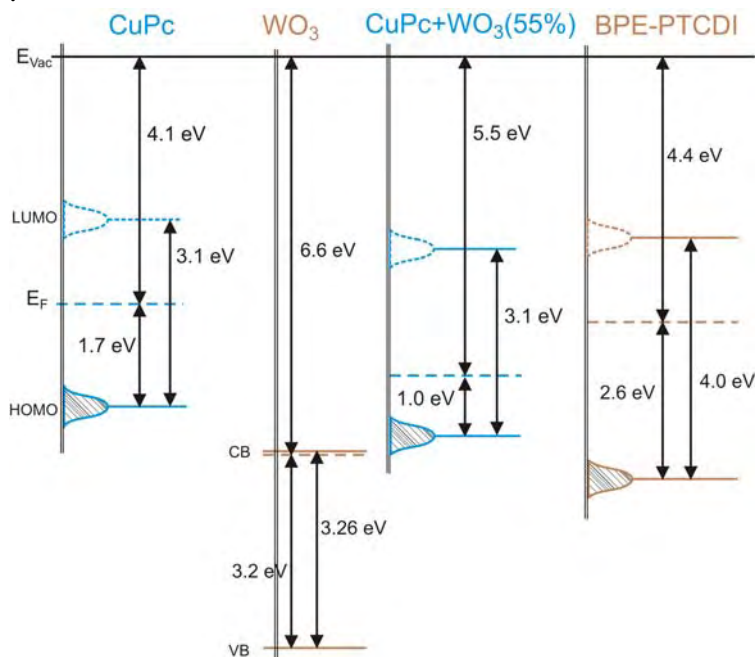
Fig.3: Band diagram of the single materials CuPc, WO₃, BPE-PTCDI and a CuPc+WO₃ blend. For the organic materials values for HOMO photoemission maxima have been determined using SXPS on in-situ prepared films. For HOMO LUMO energy gaps data from inverse photoemission are used. The work function is derived from the valence band spectra secondary edge.

With increasing WO_3 content, the Fermi level position in CuPc changes up to 0.7 eV towards the valence band as derived from 1s core level positions of C and N in CuPc. The band diagrams of the single materials and the CuPc+WO₃ blend as derived with SXPS are given in Fig.3. In the Anderson model that just compares work functions, p doping of CuPc with WO₃ and the reversal of the band bending at the CuPc+WO₃/BPE-PTCDI interface compared to bare CuPc can be expected. The photo-emission set Fig.4 taken in the course of stepwise deposition of BPE-PTCDI onto WO₃ doped CuPc delivers the information for drawing the band diagram of the CuPc+WO₃/BPE-PTCDI interface Fig.5.
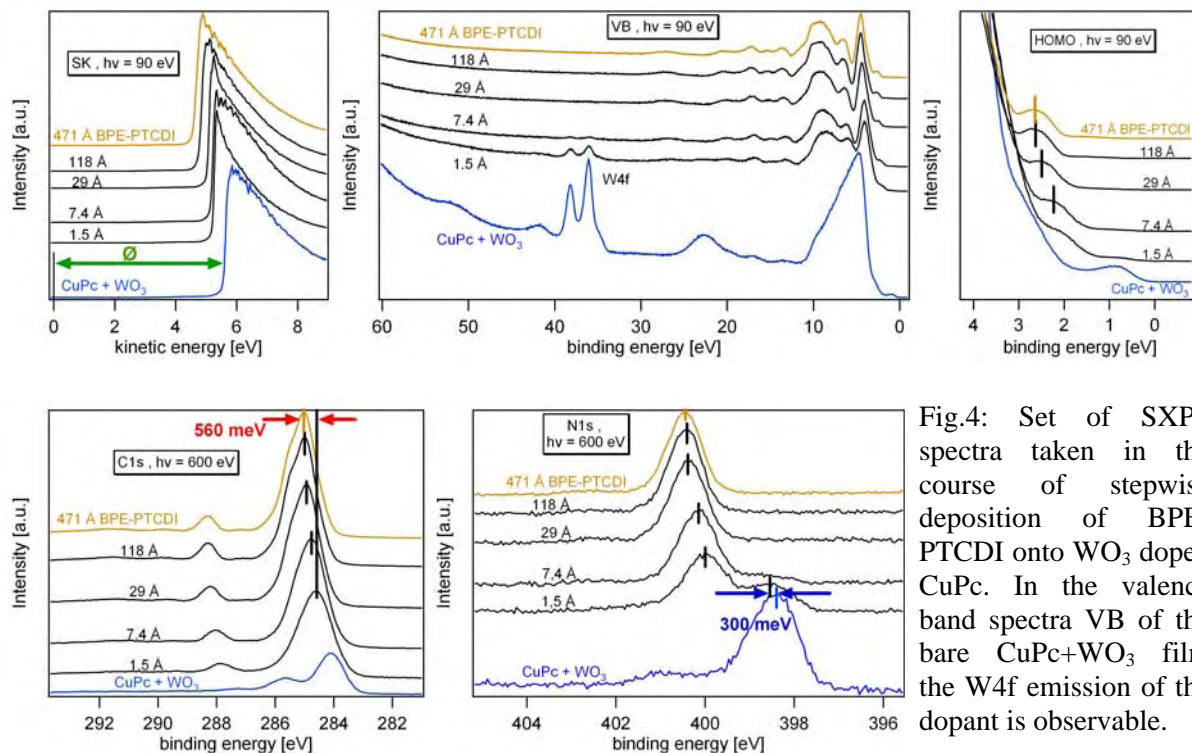
Fig.4: Set of SXPS spectra taken in the course of stepwise deposition of BPE-PTCDI onto WO₃ doped CuPc. In the valence band spectra VB of the bare CuPc+WO₃ film the W4f emission of the dopant is observable.

The line up of the CuPc and BPE-PTCDI HOMO bands can directly be read from the HOMO section of the valence band spectra Fig. 4 top right. The change in work function is derived from the secondary edge (SK top left). Band bending in the substrate and adsorbate film is

taken from induced shifts in the respective core level emissions in the course of stepwise interface formation (Fig.4 bottom).
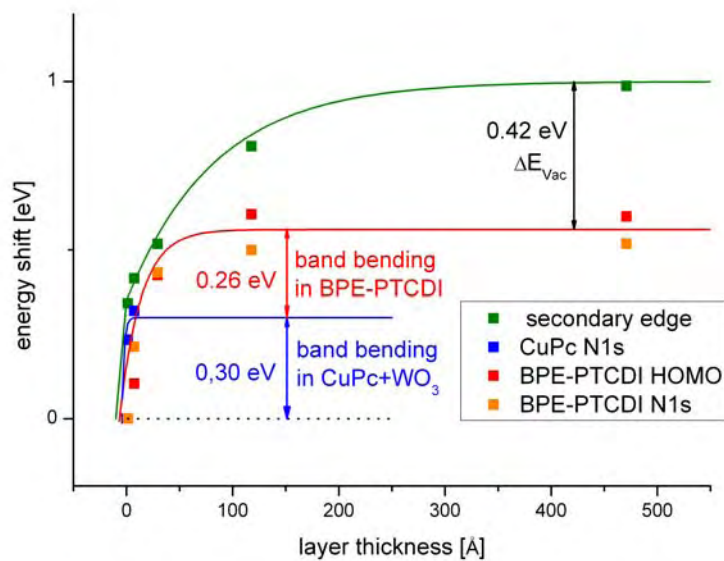
Fig 5: Band bending in the WO$_3$ doped CuPc substrate and in the BPE-PTCDI stepwise adsorbed film as derived from CuPc N1s and BPE-PTCDI HOMO and N1s levels. In addition the change in the energy position of the secondary edge i.e. of the work function is shown and the change in of ΔE_{vac} which is interpreted as interface dipole is indicated.

The band diagram of the WO$_3$ doped CuPc/BPE-PTCDI interface is displayed in Fig.6. As compared to the undoped case Fig.2, the band bending is reversed to the intended direction, supporting the transport of electrons in BPE-PTCDI and holes in CuPc towards the external contacts.

Summary: Applying SXPS p-doping of CuPc using WO$_3$ has been demonstrated to improve the potential distribution at the CuPc/BPE-PTCDI interface for solar cell applications.
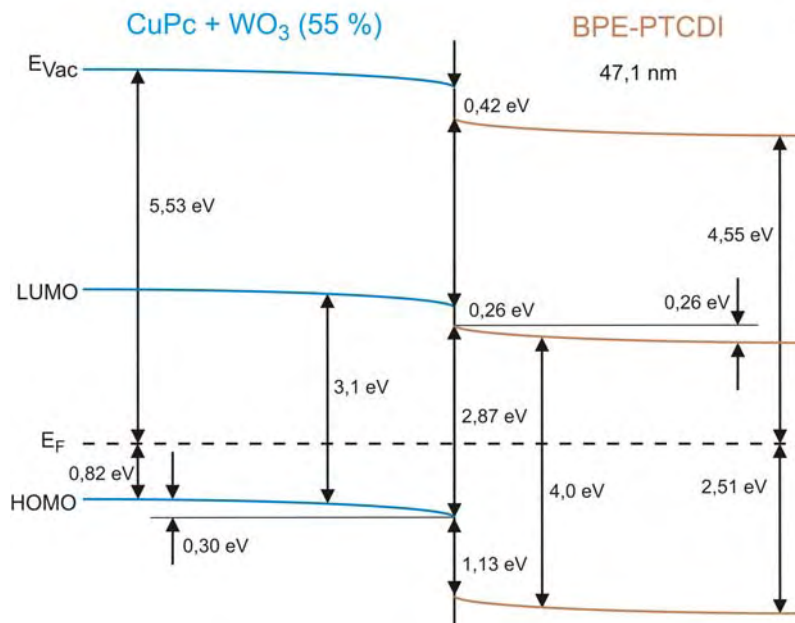
Fig.6: Band diagram of the CuPc+WO$_3$/BPE-PTCDI hetero-junction. P-doping of CuPc with WO3 leads to potential gradients in the favourable direction that promotes the transport of charges away from the interface.

1.   Mayer, T., C. Hein, J. Haerter, E. Mankel, and W. Jaegermann, *A doping mechanism for organic semiconductors derived from SXPS measurements on co-evaporated films of CuPc and TCNQ and on a TCNQ/CuPc interface*. Proc. SPIE 2008. **7052,** : p. 705204

On the electronic structure of the oxypnictide family

T. Kroll[*,1], S. Bonhommeau[2], T. Kachel[2], H.A. Dürr[2], F. Roth[1], R. Kraus[1], J. Werner[1], G. Behr[1], A. Koitzsch[1], A. K. Ariffin[3], R. Manzke[3], F.M.F. de Groot[4], J. Fink[1, 2], H. Eschrig[1], B. Büchner[1], and M. Knupfer[1]

1 IFW Dresden P.O. Box 270016, 01771 Dresden, Germany

2 BESSY, Albert-Einstein-Strasse 15, 12489 Berlin, Germany

3 Institut für Physik, Humboldt-Universität zu Berlin, Newtonstrasse 15, 12489 Berlin, Germany

4University Utrecht, Sorbonnelaan 16, 3584 CA Utrecht, Netherlands

We investigated the recently found superconductor $LaFeAsO_{1-x}F_x$ by X-ray absorption spectroscopy (XAS). A shift in the chemical potential is visible in both the Fe $L_{2,3}$ and O K edge spectra which emphasizes the importance of band effects and moderate correlations in these compounds. From experimental Fe $L_{2,3}$ edge spectra and charge transfer multiplet calculations we gain further information on important physical values such as hopping parameters, the charge transfer energy Δ, and the on-site Hubbard U. Furthermore we find the system to be very covalent with a large amount of ligand holes.

Measurements of the absorption and photoemission spectra of undoped $LnFeAsO$ (Ln=La, Ce, Sm, Gd) reveal no significant changes when exchanging the rare-earth ion or when varying the temperature below and above the magnetic/structural transition temperature.

KEYWORDS: Oxypnictides, Spectroscopy, Electronic Structure

Core level spectroscopic measurements such as X-ray absorption spectroscopy (XAS) are appropriate experimental methods to shed new light on the electronic structure of the recently discovered superconductor $LaFeAsO_{1-x}F_x$[1]. In XAS, a core electron is excited into an unoccupied state near the Fermi level, i.e. one probes the empty states. In this article, we present experimental data from Fe $L_{2,3}$ and O K absorption edges together with theoretical descriptions such as charge transfer multiplet and local density approximation (LDA) calculations. For the presented measurements we chose undoped LaOFeAs and electron doped $LaFeAsO_{1-x}F_x$ polycrystalline samples in a doping range between *x=0.0* and *0.15*. Polycrystalline samples were prepared as pellets as described in Ref. 2, the XAS signal has been taken by recording the fluorescence signal. Fe L and O K edge spectra have been normalized at 750 eV and 610 eV, respectively. Further experimental details are given in Ref. 3.

According to the dipole selection rules, the Fe $L_{2,3}$ absorption edges correspond to excitations of Fe $2p$ core level electrons into unoccupied Fe $3d$ electronic states. In Fig. 1(a) the experimental Fe L_3 edge XAS spectra for different doping levels are shown. Two main changes appear with F doping. The energy position of the main peak around 708 eV shifts slightly with doping towards lower energies. This shift amounts to ≈150meV on going from *x=0.0* to *x=0.15* and

can be explained by the observation that the XPS Fe $2p$ core level excitations do not shift relative to the chemical potential with doping within the experimental resolution[4], while the chemical potential shifts by 200meV with doping from x=0.0 to x=0.2[5]. In other words, this excitation
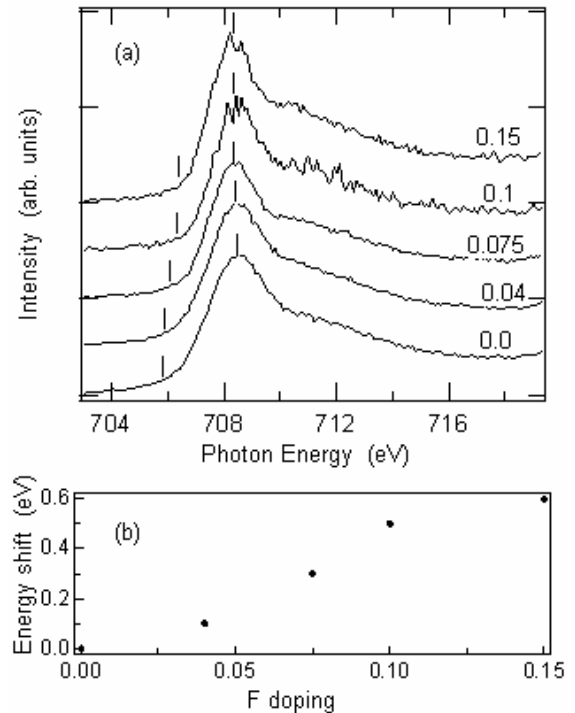
Fig. 1. $LaO_{1-x}F_xFeAs$: Doping dependence of the Fe *L*-edge. (a) Experimental L_3-edge for various doping levels. (b) Shift of the onset of the main peak in eV relative to *x=0.0* as a function of F doping *x*.
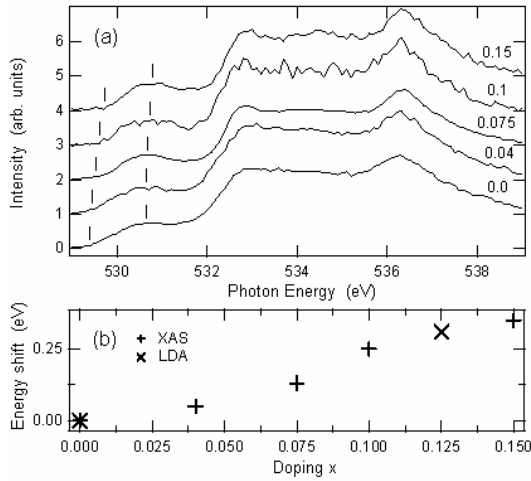
Fig. 2. LaFeAsO$_{1-x}$F$_x$: (a) Doping dependence of XAS O K edge spectra. (b) Energy shift of the onset of the 1st peak as compared to $x=0.0$ for experimental and theoretical results.

energy as seen in Fig. 1 decreases upon doping.

Moreover, the onset of the L$_3$ edge[6] shifts to higher photon energies by ≈ 600 meV. Note that such a shift could also cause an asymmetric peak narrowing and affect the position of the peak maxima. A shifted onset is consistent with additional electrons at the Fe sites, which diminishes the number of holes, i.e. the total intensity at the Fe L-edge. Therefore, the doped electrons reside (partially) at the Fe sites, which is supported by valence band photoemission spectroscopy (PES) [5]. The observed shift of the onset of the Fe L edge spectra is especially remarkable since it emphasizes the importance of band effects and the absence of strong correlations as they have been observed for e.g. the cuprates. The onset of the spectra shifts monotonically to higher photon energies (see Fig. 1(b)) caused by a shift of the chemical potential as it has been observed by PES measurements[5].

Simulations of the Fe $L_{2,3}$ edge require consideration of multiplet splitting, hybridization, and crystal field effects. We performed charge transfer multiplet calculations for divalent Fe^{2+} (d^6) in tetrahedral (T$_d$) symmetry. Note that a band effect such as the shift of the chemical potential is beyond this local approach. The parameter set that reproduces the experimental data best (not shown here, e.g. Ref. 3) is $10Dq=0.2$ eV, $\Delta=E(d^7\underline{L})-E(d^6)=1.25$ eV ($\underline{L}$ denotes a ligand hole), $U=1.5$ eV, and $pd\pi=0.27$ eV. The core hole potential Q has been set to $Q=U+1$ eV. The Slater-Condon parameters have been reduced to 80% of their Hartree-Fock values as it is reasonable in solids, which leads to the two Hund's couplings $J_{eg}=0.90$ eV and $J_{t2g}=0.78$ eV

for the ground state. Such a parameter set leads to a highly covalent system and a high spin state of $S=2$. The shoulder at ≈ 712 eV is provoked by charge transfer effects and emphasizes the hopping values above. Since the core hole potential is rather small (Q=2.5 eV), the excited states are not shifted far out of the Fe 3d band[7], and therefore band effects become visible in the experimental spectra.

A second edge that is worth to investigate is the O K edge. Note that the O ions are located within the LaO$_{1-x}$F$_x$ layer, and therefore do not behave like ligands at the transition metal ion contrary to cuprates or cobaltates. In Fig. 2(a), O K edge spectra for different doping levels are shown for photon energies between 529 and 539 eV. This region can be assigned to excitations from the O 1s core level into unoccupied O 2p states. In the XAS spectra, the onset of the 1st peak shifts by 350 meV towards higher photon energies with doping[6], whereas the 1st peak itself (at 531 eV) shifts only by ≈ 100meV and the 2nd peak (at 532.7 eV) does not shift.

When comparing the experimental spectra to the partial density of states (PDOS) as gained from LDA calculations, one observes that the overall agreement is good[3], and LDA is able to explain all main features, and assign the 1st peak to hybridizations between O and Fe states and the 2nd peak to hybridizations between O and La states. From X-ray photoemission spectroscopy (XPS) experiments[5] it has been observed that the La 4d level shifts relative to the chemical potential by about 200 meV from $x=0.0$ to $x=0.1$ while the As 3d level hardly shifts. This can be ascribed to a change of the Madelung potential between the As and La layers upon doping, in agreement with O K XAS. When focussing on the onset of the 1st peak, i.e. on the change in the chemical potential, a clear doping dependence is observed. This is further illustrated in Fig 2(b) where the shift of the onset of the 1st peak as compared to $x=0.0$ is shown. Such an increase is supported by the PDOS since the shift in the onset of the 1st peak between $x=0.0$ and $x=0.125$ matches well the slope found from the experimental data. This agreement between theory and experiment stresses the observation that the experimental O K edge is strongly affected by the shift of the chemical potential with doping.

In LDA no Coulomb energy U is taken into account. When switching it on at the Fe site, this will have an effect on the energetic position of the Fe 3d spectral weight. As the relative position of the O K XAS peaks matches those determined by LDA calculations within 1 eV,

together with the observation that the LaFeAsO valence-band spectrum can be explained by the DOS as derived from LDA (Ref. 5) but does not match the DOS as derived from LDA+U[8] or DMFT[9], we conclude that U is small as compared to the conduction-band width. Note that the strong electronic correlations in cuprates such as $La_{2-x}Sr_xCuO_2$, are clearly visible in the O K absorption edges[10].

Furthermore, we performed X-ray absorption spectroscopy at the Fe L2,3 edge as well as core level Fe 2p and valence band photoemission spectroscopy on various undoped rare-earth oxypnictides LnFeAsO (Ln=La, Ce, Sm, Gd) at temperatures above and below the phase transition temperatures. In none of our results we find significant change of the spectral shape which leads to the conclusion that the electronic structure of the FeAs layers as seen by these experiments, does not change by exchanging the rare-earth ions or varying the temperature[11]. Exemplarily we show the Fe L absorption and Fe $2p$ excitation spectra at 20 K for different rare-earth oxypnictides (Fig. 3).

In summary, from X-ray absorption spectroscopy measurements together with LDA and charge transfer multiplet calculations, deeper insight into the electronic structure of $LaO_{1-x}F_xFeAs$ has been proposed. The O K-edge is well described by LDA calculations. The shift in the chemical potential is clearly visible in the absorption edge. Furthermore, the band width could be assigned as an upper limit of the on-site Hubbard U.

Band effects have a significant influence also on the shape of the Fe L edge absorption spectra. A shift in the chemical potential towards higher energies is observed in agreement with the results of the O K edge, which stresses the existence Hubbard U significantly smaller than the bandwidth W. Further valuable information could be extracted from Fe $L_{2,3}$ absorption edge absorption together with charge transfer multiplet calculations in tetrahedral symmetry. The low Hubbard U fits to the upper bound as concluded from the comparison between O K-edge XAS spectra and DOS. Furthermore, due to small values of the charge transfer energy Δ and the Hubbard U the system turns out to be very covalent.

Measurements of the XAS and PES spectra of undoped LnFeAsO (Ln=La, Ce, Sm, Gd) reveal no significant changes when exchanging the rare-earth ion or when varying the temperature below and above the magnetic/structural transition temperature.

Fig. 3. LnFeAsO: (a) Fe $L_{2,3}$ absorption edge and (b) Fe 2p photoemission excitation spectra at 20 K.

*) E-mail: t.kroll@ifw-dresden.de
1) Y. Kamihara *et al.*, J. Am. Chem. Soc. **130**, 3296 (2008).
2) S. Drechsler *et al.*, Phys. Rev. Lett. **101**, 257004 (2008).
3) T. Kroll *et al.*, Phys. Rev. B **78**, 220502 (2008).
4) A. Koitzsch *et al.*, to be published.
5) A. Koitzsch *et al.*, Phys. Rev. B **78**, 180506 (2008).
6) The onset of the peak has been defined as the photon energy at which the intensity reaches 10% of its value at the peak maximum
7) H. Eschrig, arXiv:0804.0186
8) C. Cao, P. J. Hirschfeld, and H.-P. Cheng, Phys. Rev. B **77**, 220506(R) (2008)
9) K. Haule, J. H. Shim, and G. Kotliar, Phys. Rev. Lett. **100**, 226402 (2008)
10) J. Fink *et al.,* J. Electron Spectrosc. Relat. Phenom. **66**, 395 (1994)
11) T. Kroll *et a.l*, accepted at New Journal of Physics

Evidence for static, site centered stripe order by photoemission on $Bi_2Sr_{1.2}La_{0.8}CuO_6$

Valentina Scherer, Christoph Janowitz, Beate Müller, Lenart Dudy, Alica Krapf,
Helmut Dwelk and Recardo Manzke
Humboldt-Universität zu Berlin, Institut für Physik, Newtonstr. 15, 12489 Berlin

Taichi Okuda and Akito Kakizaki
Institute of Solid State Physics (ISSP), University of Tokyo, Japan

Antiferromagnetic spin correlations play an important role especially for hole under-doped cuprate superconductors. The vicinity of the Mott–insulating parent compound phase and the metallic phase in this regime requires a description beyond Fermi liquid theory. Possibly the most striking evidence is the occurrence of spin-and charge separation in form of the so called static stripe phase at a hole doping of $n_H = 1/8$ as observed first by Tranquada [1] in a (Nd)-LaSrCuO- cuprate by neutron scattering. Photoemission measurements on cuprates of the same family revealed a dual nature of the Fermi-surface: features due to itinerant as well as due to static, localized electrons from the stripe phase were observed [2]. Since up to now most of these observations were reported on members of the LaSrCuO- family with one CuO_2- layer per unit cell, it is promising to extend these studies on another single CuO_2- layer cuprate from a different family. $Bi_2Sr_{1.2}La_{0.8}CuO_6$ single crystals with a single CuO_2-layer per unit cell, a nominal hole doping around $n_H = 0.10$ and vanishing Tc were therefore grown, characterized and studied by high resolution photoemission.

Measurements at BESSY were performed at the *BEST*-beamline equipped with a 5m-Normal Incidence Monochromator and a high-resolution photoelectron spectrometer SES-2002 and at the Photon Factory (Japan) at BL-18A at the *angle-resolved photoelectron spectroscopy station for surfaces and interfaces*. Spectra recorded at both locations were comparable. The spectra shown below were measured at a photon energy of 22eV and 20 K sample temperature at BESSY. A total resolution of 30meV was found sufficient to resolve the essential details. Due to the very low count rates this was a compromise to collect sufficient data without surface degradation within 48 hours.

High quality single crystals of $Bi_2Sr_{1.2}La_{0.8}CuO_6$ were grown out of solution. The crystals were characterized using several techniques, e.g. x-ray emission (EDX), ac susceptibility, Laue diffraction and LEED, to obtain information on the chemical composition, the superconductivity, and the quality of the crystals. The five samples investigated by photoemission showed in AC susceptibility no transition to the superconducting state down to 2 Kelvin. The exact hole concentration (n_H) was determined from the linear relation between La content and n_H derived from X-ray absorption spectroscopy data [3,4]. This alternative method for the quantitative evaluation of the hole content uses the signal of the CuL3 edge. It consists of a so called "white line", representing the excitation of Cu-2p-electrons into Cu-3d states, and a satellite peak, appearing as a high energy shoulder, with an intensity varying according to the hole content of the sample. To obtain a numerical value for the hole content the ratio of the intensity of the satellite peak to the intensity of white line plus satellite peak has to be evaluated.

Photoemission intensity maps obtained by integrating 200meV (upper picture) and 30 meV (lower picture) spectral intensity below the Fermi energy are shown in FIG. 1. The very low count rate near the Fermi energy at these doping levels posed a challenge to the experiment. It is nevertheless clearly evident, that along the nodal ΓX and ΓY lines the Fermi surface has vanished, while a buildup of spectral weight around the antinodal M-point occured. This electronic structure is decisively different from any hitherto reported one of Bi-cuprates in the underdoped regime. While no spectral weight, dispersion or Fermi surface crossings along the nodal line could be detected, a diffuse but, when compared to the missing intensity along the nodal line, clearly detectable buildup of spectral weight around the antinodal M-point occurred. Interestingly the comparison to a theoretical Fermi surface obtained by cluster perturbation theory for a static, site centered stripe model at 0.10 hole doping, i.e. at the same doping level as in our experiments, gave good qualitative correspondence [5]. The measurements will be continued at elevated temperatures, i.e. above the stripe ordering temperature and for crystals at different doping levels, especially $n_H = 1/8$.
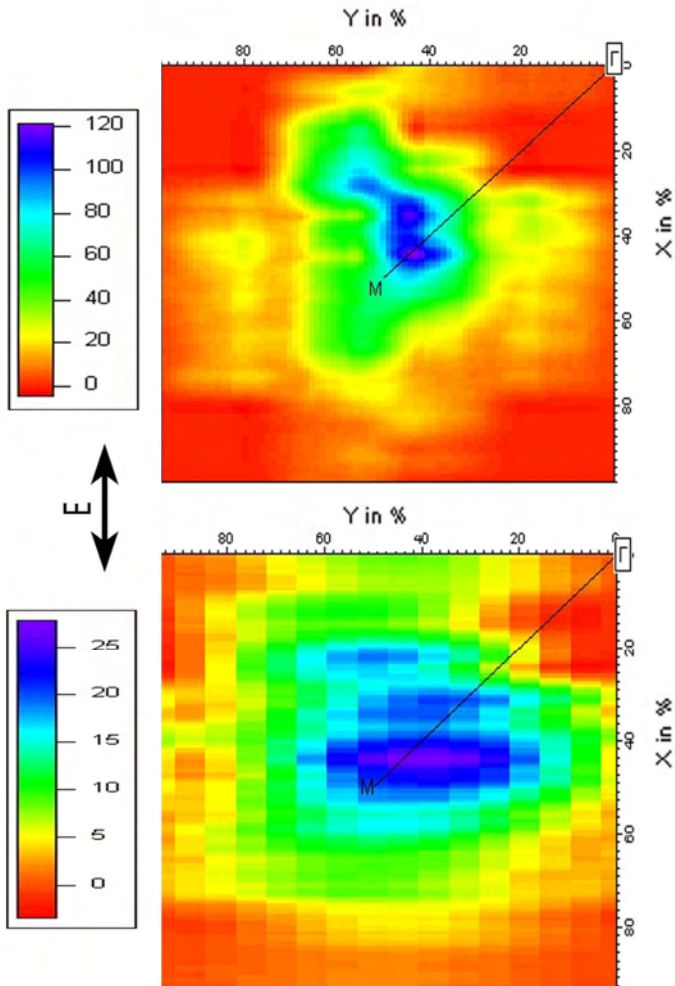
Figure 1.

Photoemission intensity map of the ΓXΓYΓ quadrant with the M-point in the center. The polarization vector and the intensity scale is shown on the left. The upper picture was obtained by integrating all counts 200 meV below the Fermi energy and the lower picture by integrating 30 meV below the Fermi energy.

References:

1) J.M. Tranquada, B.J. Sternlieb, J.D. Axe, Y. Nakamura, S. Uchida, Nature **375**, 561 (1995)

2) X.J. Zhou, T. Yoshida, S.A. Kellar, P.V. Bogdanov, E.D. Lu, A. Lanzara, M. Nakamura, T. Noda, T. Kakeshita, H. Eisaki, S. Uchichida, A. Fujimori, Z. Hussain, Z.-X. Shen, Phys. Rev. Lett. **86**, 5578 (2001)

3) M. Schneider, R.-S. Unger, R. Mitdank, R. Müller, A. Krapf, S. Rogaschewski, H. Dwelk, C. Janowitz, and R. Manzke, Phys. Rev. B **72**, 014504 (2005)

4) A. K. Ariffin, C. Janowitz, B. Müller, L. Dudy, P. Sippel, R. Mitdank, H. Dwelk, A. Krapf and R. Manzke, Journal of Physics: Conference Series (in print) (2008)

5) M. G. Zacher, R. Eder, E. Arrigoni, and W. Hanke,
Phys. Rev. B **65**, 045109 (2002)

Quantitative ASAXS studies of carbon supported RuSe$_x$/C fuel cell catalysts for oxygen reduction reaction

S. Haas[1], A. Hoell[1], G. Zehl[2], I. Dorbandt[2], S. Fiechter[2]

Helmholtz-Zentrum Berlin für Materialien und Energie (HZB)
[1] Conrad-Röntgen-Campus Adlershof, Albert-Einstein-Str. 15, D-12489 Berlin
[2] Lise-Meitner-Campus Wannsee, Glienicker Str. 100, D-14109 Berlin

1. Introduction

Anomalous small-angle X-ray scattering (ASAXS) represents a powerful tool for the evaluation of structural parameters from element sensitive analysis of nano-materials [1, 2]. Recently, based on the use of adequate experimental setups and capable equipment, ASAXS has been proven to provide also useful data on the chemical composition even in the sub-nanometer scale. Heterogeneous precious metal catalysts consist in most instances of nanometer sized metal particles supported on chemically inert carriers. Therefore, they represent very suited model substances for demonstrating the potential of this technique and for further improvement of its skills.

Currently, to meet future energy demands, there is an urgent need for higher performing heterogeneous catalysts for fuel cell applications, distinguishing by reduced amounts of nobel metals or, most promising, by replacing Pt with less expensive metals. Accordingly, selenium modified ruthenium nano-particles supported on activated carbon (RuSe$_x$/C) have been found to catalyze the oxygen reduction reaction (ORR) in acidic media with high activity and superior selectivity [3]. Therefore, this material is now in focus as methanol tolerant electro-catalyst replacing Pt at the cathode side of Direct Methanol Fuel Cells (DMFC) [4-6]. Nevertheless, a better understanding of this novel catalyst system is believed to be the prerequisite for its further optimization to pave the way towards commercial application.

To reveal the structure of such highly complex materials involving constituents ranging from tens of nm down to the sub-nanometre region, comprehensive ASAXS measurements were performed. Using ASAXS one takes advantage of the so-called anomalous or resonant behaviour of the atomic scattering amplitude of an element near its absorption edge to separate its scattering contribution from other elements in the sample. The main targets were to provide a more elaborate structural investigation of novel RuSe$_x$/C fuel cell catalysts by using the possibility of separating the scattering contributions of the carbon black carrier and the different metallic constituents of the thereon supported nano-particles by means of ASAXS measurements. Based on these data a structural model of the catalytically active particles was derived.

2. Experimental

Highly active RuSe$_x$/C catalysts were prepared in a multistep procedure starting from ionic metal precursors [7]. Commercially available carbon black (Black Pearls 2000 from Cabot) was used as support material. In brief, a calculated amount of RuCl$_3$·xH$_2$O was dissolved in water, previously purged with argon. A weighted amount of carbon black was placed inside the quartz tube, heated from room temperature to 950°C while purging with CO$_2$ and held at this temperature for 20 min for activating the carbon support prior to impregnation. After cooling down the activated carbon sample was transferred into the round-bottomed flask with the Ru precursor solution. The solvent was rotary evaporated and the dried powder was treated under forming gas (5% H$_2$/95% N$_2$) at 200°C to form the Ru nano-particles. This Ru/C-intermediate was transferred into an acetonic solution of SeCl$_4$ for selenization. After ultrasonic conditioning the solvent was removed by rotary evaporation and, finally, a reductive treatment under forming gas for 30 min at 800°C was performed.

Anomalous small-angle X-ray scattering has been performed on the SAXS beamline 7T-MPW-SAXS at the synchrotron facility BESSY [8]. The contrast variation was performed at different energies near the Se-K ($E_{Se} = 12658$ eV) and Ru-K ($E_{Ru} = 22117$ eV) absorption edges (see table 1). To cover the full accessible q-range two sample-detector distances (800 mm and 3750 mm) have been selected. The scattering were recorded using an area sensitive gas-filled multi-wire proportional counter. These raw data were corrected for the dark current, dead time and sensitivity of the detector as well as the incoming photon-flux, sample transmission, scattering background and geometrical effects like the projection of the detector plane on the sphere with radius equal to the sample-detector distance. To increase the statistics of the scattering intensity the two-dimensional corrected data were circularly averaged over rings with a certain width. In order to have direct control of statistical errors and to take care of possible time dependent variations of the beam conditions the measurements were separated into several short runs and

then averaged [9]. The scattering of a reference sample (1 mm glassy carbon) were measured at the beginning of each run to scale the intensities obtained at different energies relative to each other. The norm of the scattering vector was calibrated using the d-spacing of silver behenate as reference.

3. Results

In Fig. 1 two scattering curves for the Ru/C sample at energies E6 and E10 are shown together with the obtained scattering curve for the carbon black sample. It can be seen that the scattering curves of the Ru/C sample has a broad shoulder at q ~ 1 nm^{-1} compared to pure carbon black. A noticeable intensity variation with respect to the energy in this q-domain can be seen. At higher q-values a crossover of the curves occurs, being due to isotropic resonant-raman scattering (RRS) close to the absorption edge.

	E (eV)	$\Delta E = E - E_K$ (eV)
E1	12220	-438
E2	12524	-134
E3	12614	-44
E4	12643	-15
E5	12653	-5
E6	21675	-442
E7	21840	-277
E8	22034	-83
E9	22091	-26
E10	22109	-8

Table 1: Numeration of the X-ray energies used in the experiment. The E_K is the energy of the corresponding absorption edge Se-K for E1-E5 and Ru-K for E6-E10.
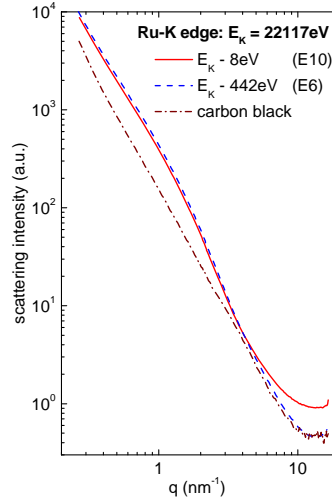
Figure 1: Scattering curves of the Ru/C sample at two energies near the Ru-K absorption edge (E6 and E10). The SAXS curve of the carbon black is shown for comparison
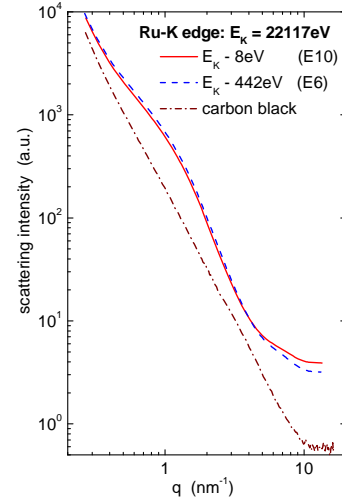
Figure 2: Scattering curves of the RuSe$_x$/C sample at two energies near the Ru-K absorption edge (E6 and E10). The SAXS curve of the carbon black is shown for comparison.

In Fig. 2 scattering curves for the active catalyst sample RuSe$_x$/C at energies E6 and E10 are shown. The scattering seems to be very similar to the scattering from the sample without Se (Fig. 1) but at high q-values above 7 nm^{-1} a second weaker shoulder occurs. Therefore, the corresponding structure element seems to be connected with the Se arrangement. Considering the theoretical calculated energy-dependent correction factors $f'(E)$ and $f''(E)$ of the atomic scattering factor, the three energy-independent partial scattering contributions $I_0(q)$, $I_{0R}(q)$ and $I_R(q)$ can be calculated by solving a set of linear equations [10]

$$I(q, E_i) = I_0(q) + 2f'(E_i)I_{0R}(q) + \left\{ f'^2(E_i) + f''^2(E_i) \right\} I_R(q) \tag{1}$$

where the partial scattering contribution $I_R(q)$ contains information on the spatial arrangement of the resonant scattering element alone. The $I_0(q)$ describing the scattering behaviour if one measures at energies far from any absorption edge of the elements present in the sample. This partial scattering contribution contains information of all structure components. The $I_{0R}(q)$ is the cross term of $I_0(q)$ and $I_{0R}(q)$. The $I_R(q)$ will represent the partial scattering contribution of the Ru distribution only by solving the system of linear equation (1) for energies close to the Ru-K edge and considering the theoretical values f' and f'' listed in [11] and calculated by the method of Cromer & Liberman [12]. In order to check the reliability of the solution, the calculation was repeated several times using three, four or five different energies. The result using the five energies $E_i=E6,...,E10$ is shown in Fig. 3. In addition the obtained ASAXS curve at 21675 eV is also shown after subtraction of the isotropic background level which was determined at q values above 10 nm^{-1}. The main results of this analysis were: (i) the behaviour of the non-resonant contribution $I_0(q)$ is very similar to the ASAXS curve obtained far the Ru-K absorption edge. (ii) the so-called resonant scattering contribution $I_R(q)$ behaves completely different at small and large q-values. In the limit to small q-values the $I_R(q)$ curve converges to a constant intensity contrary to the $I_0(q)$ curve which shows a strong increase. This indicates the presents of a larger non ruthenium containing structure element. In the other limit to large q-values the $I_R(q)$ curve shows a nearly linear decrease in the double logarithmic plot contrary to the $I_0(q)$ curve which shows a weak shoulder in this q-domain. Therefore, the causing structure has nearly nothing to do with the Ru present in the sample. Moreover, the shoulder deduced in

the $I_0(q)$ curve at large q-values has to be considered as an indication for a much smaller mainly ruthenium free structure.

Discussing the measurements near the Se-K absorption edge of the Se containing sample RuSe$_x$/C, it must be noticed that the sensitivity of the ASAXS-technique to Se is much lower in contrast to Ru. Fig. 4 shows two scattering curves obtained for sample RuSe$_x$/C at energies E1 and E5 as well as the SAXS curve for the carbon black. Within in the error no variation of the intensity with respect to the different energies has been ascertained for q-values less than 4 nm^{-1}. Only at larger q-values an increasing intensity with increasing energy has been observed. This energy-behaviour can be explained by a superposition of two effects: (i) the resonant Raman scattering effect caused by the Se-atoms. This effect gives rise to a increase in the intensity while moving the incident energy closer to the Se-K absorption edge; (ii) the anomalous scattering effect of Se-enriched small nano-structures which have a scattering contribution in the larger q-domain.
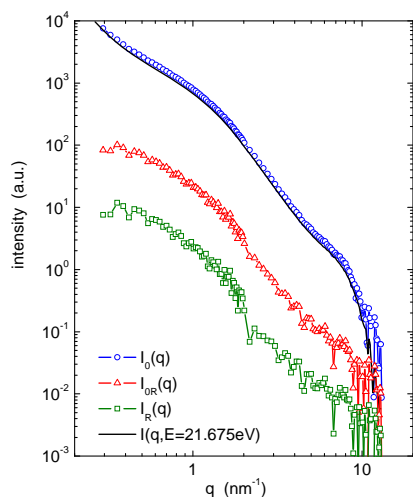
Figure 3: Partial scattering contribution for sample RuSe$_x$/C calculated using the five energies close to the Ru-K absorption edge. Therefore, the $I_R(q)$ represents the scattering of the resonant scattering Ru-atoms. As comparison one measured scattering curve is shown as well.
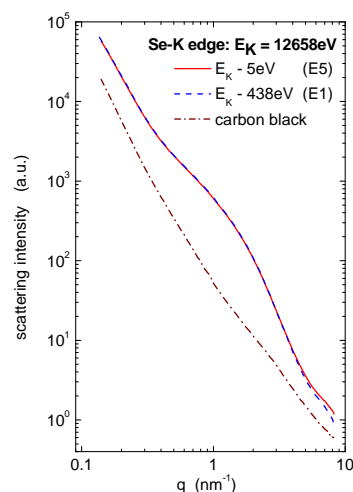
Figure 4: Scattering curves of the RuSe$_x$/C sample at two energies near the Se-K absorption edge (E1 and E5). The SAXS curve of the carbon black is shown for comparison.

The result of the analysis of the energy dependencies of the SAXS curves is that for RuSe$_x$/C catalysts a structure model with three independent types of particles (in size and composition) must be assumed. The three contributions are assumed to be connected with the following structures: (i) the carbon black support nano-particles with a mean radius of 15.00 ± 5.70 nm; (ii) the Ru nano-particles with a mean radius of 1.25 ± 0.60 nm; (iii) the selenium aggregates with a mean radius of 0.30 ± 0.02 nm [11]. This structural model is not just supported by previous results of conventional characterisation techniques (e.g. XRD, TEM and EXAFS [13]). In fact, current ASAXS measurements revealed for the first time that Se-modified Ru nanoparticles on RuSe$_x$/C catalysts are not completely covered by Se on the particle surface as formerly assumed (core-shell model). The Se rather forms clusters on the Ru surface while the rest of the surface is covered by oxygen. Thus, ASAXS successfully demonstrated its potential as future powerful characterisation technique in the field of heterogeneous catalysis, when using adequate experimental setups.

4. References

[1]   G. Goerigk, H.-G. Haubold, O. Lyon, and J.-P. Simon, J. Appl. Crystallogr. 36 (2003) 425-429.
[2]   A. Hoell, F. Bley, A. Wiedenmann, J.P. Simon, A. Mazuelas, and P. Boesecke, Scripta Mater. 44 (2001) 2335-2339.
[3]   S. Fiechter, I. Dorbandt, P. Bogdanoff, G. Zehl, H. Schulenburg, H. Tributsch, M. Bron, J. Radnik, and M. Fieber-Erdmann, J. Phys. Chem. C 111 (2007) 477-487.
[4]   M.A. Priestnall, V.P. Kotzeva, D.J. Fish, and E.M. Nilsson, J. Power Sources 106 (2002) 21-30.
[5]   D.C. Papageorgopoulos, F. Liu, and O. Conrad, Electrochim. Acta 52 (2007) 4982-4986.
[6]   A.E. Comyns, Focus on Catalysts 2007 (2007) 1.
[7]   G. Zehl, I. Dorbandt, G. Schmithals, J. Radnik, K. Wippermann, B. Richter, P. Bogdanoff, and S. Fiechter, ECS Trans. 3 (2006) 1261-1270.
[8]   A. Hoell, I. Zizak, H. Bieder, and L. Mokrani. 2007.
[9]   S. Haas. 2007. Technical University, Berlin.
[10]   H.B. Stuhrmann, Advances in Polymer Science 67 (1985) 123-163.
[11]   S. Haas, A. Hoell, G. Zehl, I. Dorbandt, and S. Fiechter, J. Phys. Chem. C (2009) submitted.
[12]   D.T. Cromer, and D. Libermann, J. Chem. Phys. 53 (1970) 1891-1898.
[13]   G. Zehl, G. Schmithals, A. Hoell, S. Haas, C. Hartnig, I. Dorbandt, P. Bogdanoff, and S. Fiechter, Angew. Chem., Int. Ed. Engl. 46 (2007) 7311-7314.

Magnetic moments of Fe in oxide-free FePt nanoparticles as a monitor for compositional inhomogeneities

C. Antoniak[1,*], A. Trunova[1], M. Spasova[1], K. Fauth[2], M. Farle[1], and H. Wende[1]

[1]*Fachbereich Physik and Center for Nanointegration Duisburg-Essen (CeNIDE), Universität Duisburg-Essen, Lotharstr. 1, D–47048 Duisburg*

[2]*Experimentelle Physik IV, Universität Würzburg, Am Hubland, D–97074 Würzburg*

Introduction – Fe_xPt_{1-x} nanoparticles are currently the object of intense research activities, driven both by fundamental interest and their possible use as new ultra-high density magnetic storage media. For the latter case, nanoparticles with a high magnetocrystalline anisotropy (MCA) are needed to overcome the superparamagnetic limit, i.e. data loss caused by thermally activated magnetisation fluctuations. In addition, the magnetic moments of the nanoparticles should be low to prevent magnetisation switching caused by magnetic dipole interactions.

One of the prime candidates for future application is Fe_xPt_{1-x} in the chemically ordered state around the equi-atomic composition due to its high MCA density of about $6 \times 10^6 J/m^3$[1]. Interestingly, the magnetic moments in FePt nanoparticles in both the chemically disordered and chemically ordered phase are rather small compared to the bulk material [2,3]. The x-ray absorption spectroscopy is a powerful tool to investigate both local structure around the absorbing atoms by the analysis of the extended x-ray fine structure (EXAFS) and magnetic properties, e.g. by measuring the x-ray magnetic circular dichroism (XMCD) as presented here.

The standard Fourier based analysis of EXAFS oscillations of oxide-free $Fe_{0.56}Pt_{0.44}$ nanoparticles give not only evidence for a lattice expansion with respect to the corresponding bulk material [4], but also a clear local deviation from the averaged composition. A visualisation of this compositional inhomogeneity is given by the Wavelet transformation (WT) method. It may be used to distinguish between different atomic species in an alloy due to their different positions of maximum backscattering amplitude in k-space (Fig. 1). This is possible since in these transformations employing wavelets both localised in real space and k-space, the resolution in k-space is not lost in contrast to a Fourier transformed signal [5].

Fig. 1 shows a contour plot of the difference between wavelet transformed EXAFS of nanoparticles and bulk material measured at the Pt L_3 edge at the ID-12 undulator beamline at the ESRF indicating a reduced number of Fe nearest neighbours (nn.) and an enhanced number of Pt nn. around the Pt probe atoms in FePt nanoparticles with respect to the corresponding bulk material. Note, that the slightly different positions in r and the different inclination of the WT data are due the different EXAFS phase shifts.
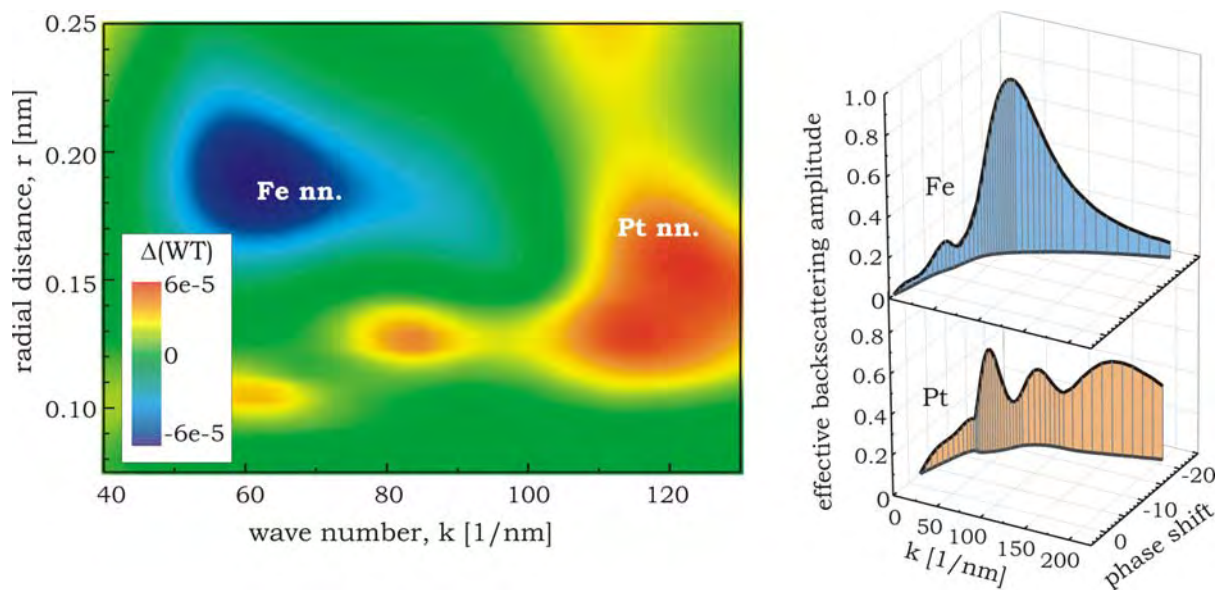
Fig. 1: Contour plot of the difference between wavelet transformed EXAFS measured at the Pt L_3 absorption edge of nanoparticles and bulk material (left), effective backscattering amplitude of Fe (upper right graph) and Pt (lower right graph) and EXAFS phase shift as a function of the photoelectron wave number. In both cases Pt is the absorber atom. The grey line in the coordinates plane at the bottom refers to the dependence of the phase shift on the wave number.

*e-mail: carolin.antoniak@uni-due.de
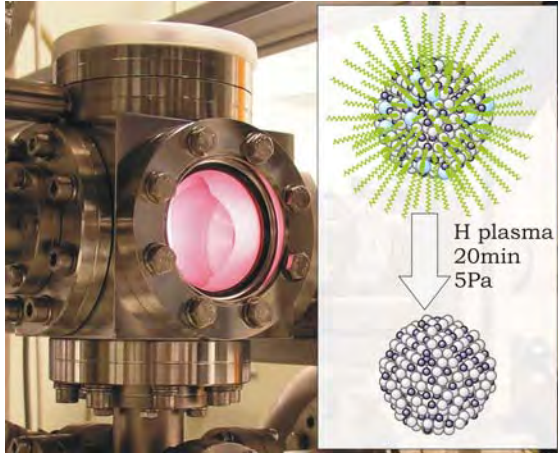
FIG. 2: Picture of the plasma chamber with ignited hydrogen plasma; Inset: schematic drawing of the FePt nanoparticles before and after plasma treatment, e.g. with and without Fe oxides and organic ligands

In this work, the influence of an inhomogeneous composition within FePt nanoparticles with a diameter around 4.4nm on the magnetic properties, especially on the element-specific magnetic is discussed. Since the magnetic moments at the Pt sites are almost independent of the local composition and distortions of the crystal lattice [2,6], we focussed on the magnetic moments at the Fe sites which are a sensitive monitor for structural changes. As reference, the magnetic moments of chemically disordered Fe_xPt_{1-x} alloys were probed as a function of Fe content by XMCD of different samples, i.e. bulk material and 50 nm thick films. In addition, band structure calculations were performed using the spin-polarized relativistic Korringa-Kohn-Rostoker (SPR-KKR) method [7].

Experimental – The x-ray absorption near-edge structure (XANES) and its associated XMCD was measured in the soft x-ray regime at the Fe $L_{3,2}$ absorption edges at the PM3 bending magnet beamline at BESSY II in total electron yield (TEY) mode. The measurements were performed at T = 15K in magnetic fields of $\mu_0 H_{ext} = \pm 2.8T$ at fixed photon helicity in an energy range of 680eV $\leq$ E $\leq$ 790eV. After each scan, either the magnetic field or the circular polarisation was reversed.

Induced magnetic moments at the Pt sites were evidenced in the soft x-ray regime at the $N_{6,7}$ absorption edges of Pt in the energy range 65eV $\leq$ E $\leq$ 85eV.

A portable plasma chamber [8] was attached to the experimental endstations for an in situ cleaning of the samples (Fig. 2). An exposure to a hydrogen plasma at a pressure of p = 5Pa for 20min was found to be sufficient for the complete reduction of Fe oxides and organic ligands, i.e. oleic acid and oleyl amine surrounding the wet-chemically synthesised particles [1] in the as-prepared state.

The efficiency of the plasma cleaning procedure was proven by XANES measurements at the carbon K edge and the Fe $L_{3,2}$ absorption edges [6]. After plasma treatment, no absorption was detected at the carbon edge and at the Fe $L_{3,2}$ absorption edges, pure metallic spectra were obtained.

The size distribution of the nanoparticles is log-normal around a mean diameter of 4.4nm and a standard deviation of about 0.14. In order to prevent the particles from agglomeration during the plasma treatment, less than one monolayer of particles was brought onto the substrate.

Results and Discussion – The deviation of the local composition from the averaged value may strongly influence the magnetic properties of the Fe_xPt_{1-x} nanoparticles, e.g. the element-specific magnetic moments. In order to rate these values experimentally found in nanoparticles, the corresponding magnetic moments of 50nm thick films were measured for different compositions. In addition, SPR-KKR band structure calculations were done for different Fe_xPt_{1-x} bulk systems. We found both experimentally and theoretically that the magnetic moment at the Fe sites is decreasing with increasing Fe content [5]. This decrease can be essentially explained by the decrease of the lattice constant with increasing Fe content which usually yields smaller magnetic moments. Due to an enhancement in the hybridisation of Fe d-states, the decrease of the magnetic moment at the Fe sites is connected to a broadening of the density of states (DOS).
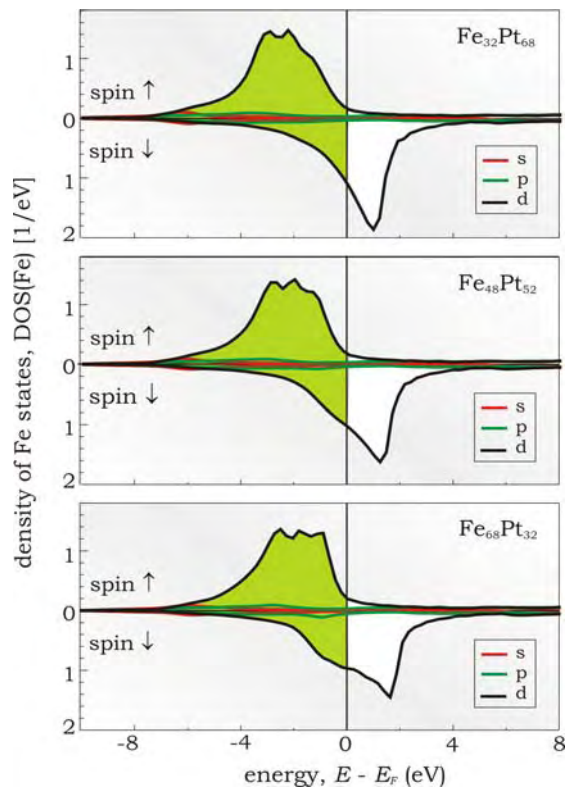
FIG 3: Spin and angular momentum resolved density of states at the Fe sites calculated for three different compositions of Fe_xPt_{1-x} bulk alloys using the Munich SPR-KKR package

172
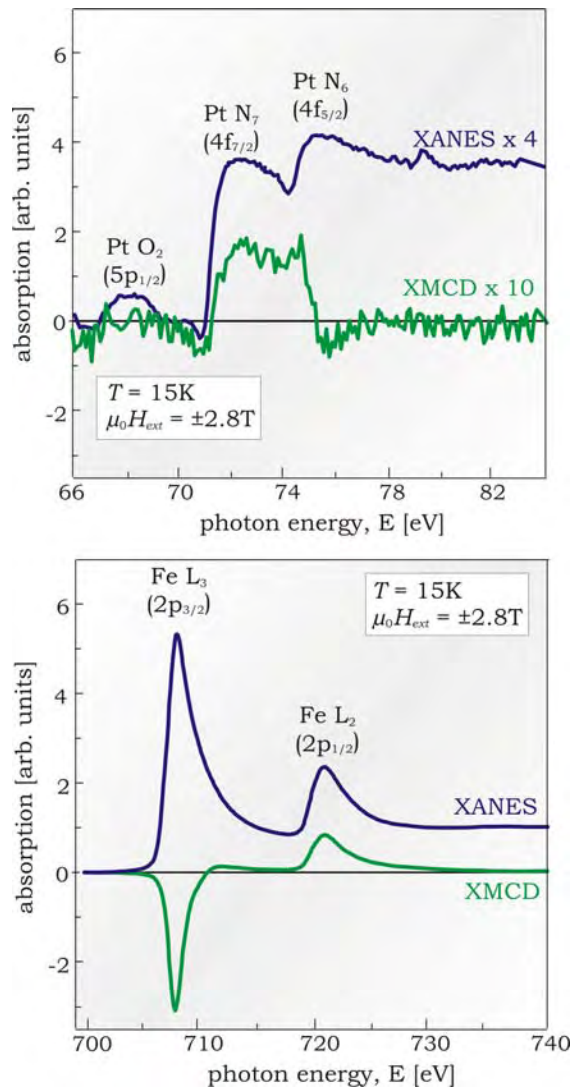
Fig. 4: XANES and XMCD of FePt nanoparticles measured at the Pt $N_{6,7}$ absorption edges (upper panel) and Fe $L_{3,2}$ absorption edges (lower panel)

The calculated spin and angular momentum resolved DOS at the Fe sites is shown in Fig. 3 for three different compositions, $Fe_{0.32}Pt_{0.68}$, $Fe_{0.58}Pt_{0.42}$, and $Fe_{0.68}Pt_{0.32}$.

The relatively narrow d-bands are strongly exchange split. A clear broadening of the DOS at the Fe sites for the Fe-rich alloy is visible and the difference between the majority and the minority band becomes smaller indicating decreasing magnetic moments in agreement to the experimental values obtained from XMCD analysis of Fe_xPt_{1-x} bulk-like films with different compositions [5].

One example of XANES and the corresponding XMCD of FePt nanoparticles are shown in Fig. 4. The XMCD at the Pt $N_{6,7}$ absorption edges clearly indicates some induced magnetism at the Pt sites. Since there is no standard analysis method for spectra obtained at these edges, only qualitative conclusions about the ratio of orbital-and-spin magnetic moments can be made [9]. In regard to the magnetism at the Fe sites, we found from the

XMCD shown in the lower panel of Fig. 4 that the magnetic moments at the Fe sites are reduced by 20-30% with respect to the values of the corresponding bulk material with the same averaged composition. This can be explained by the fact, that the magnetic moment strongly depends on the local environment, e.g. the number of Fe nearest neighbours which is not reflected by an *averaged* composition in the case of the nanoparticles examined here since the Fe atoms were found to be located in Fe-rich environments as summarised in the introduction.

Conclusion – By the analysis of absorption spectra in the EXAFS regime and XMCD measured in the XANES regime, oxide-free FePt nanoparticles were structurally and magnetically characterised. By the combination of the different x-ray absorption techniques, the reduced magnetic moments obtained at the Fe sites can be explained by an inhomogeneous composition within the particles.

[1] S. Sun et al. Science **289**, 1989 (2000)
[2] O. Dmitrieva et al., Phys. Rev. B **76**, 064414 (2007)
[3] C. Antoniak et al. , Phys. Rev. Lett. **97**, 117201 (2006)
[4] C. Antoniak et al., Phys. Rev. B **78**, 0401406 R (2008)
[5] C. Antoniak et al., submitted (2009)
[6] C. Antoniak and M. Farle, Mod. Phys. Lett. B **21**, 1111 (2007)
[7] H. Ebert et al., The Munich SPR-KKR package version 3.6
[8] H.-G. Boyen et al., Adv. Mater. **17**, 574 (2005)
[9] T. Shishidou et al., Phys. Rev. B **55**, 3749 (1997)

DIELECTRIC PROPERTIES OF $(NH_4)_2SO_4$ CRYSTALS IN THE RANGE OF ELECTRONIC EXCITATIONS

B. Andriyevsky [a)], C. Cobet [b)], A. Patryn [a)], N. Esser [b)]

a) Koszalin University of Technology, Śniadeckich Str. 2, PL-75-453, Koszalin, Poland
b) ISAS – Institute for Analytical Sciences, Department Berlin, Albert-Einstein-Str. 9, 12489 Berlin, Germany

Ammonium sulfate, $(NH_4)_2SO_4$, is a dielectric crystal with a first-order ferroelectric phase transition (PT) at the temperature $T_C = 223$ K [1]. The crystal exhibits unusually large relative change in the dielectric constant at T_C [1], a very low value (≈ 15 K) of the Curie-Weiss constant [2, 3] and a very large spontaneous strain [1]. The main aim of the study was the experimental investigation of the dielectric functions of a $(NH_4)_2SO_4$ crystal in the photon energy range of electronic excitations, $4 - 9.5$ eV, and its temperature changes in the range of $170 - 295$ K. The experimental results obtained in this study could be useful for better understanding of peculiarities related to the chemical bonding and phase transition in the crystal.

Measurements of the pseudo-dielectric functions $<\varepsilon_1>(E)$ and $<\varepsilon_2>(E)$ ($\varepsilon = \varepsilon_1 + i\varepsilon_2$) of $(NH_4)_2SO_4$ crystals were performed by spectroscopic ellipsometry [4, 5] using synchrotron radiation of the Berlin Electron Storage ring for Synchrotron radiation BESSY II in the range of $4.0 - 9.5$ eV with a resolution of $\delta E < 0.1$ eV. The angle of incidence was $\sim 68°$, while the polarization of the incident beam was chosen $\sim 20°$ tilted with respect to the plane of incidence during the measurements. A MgF_2 polarizer and rotating analyzer ensured more than 99.998% degree of polarization. The ellipsometric measurements were conducted for mechanically polished $(NH_4)_2SO_4$ crystals of three cuts perpendicular to a-, b-, and c- orthogonal axes of the unit cell and the corresponding dielectric functions $<\varepsilon_1(E)>$ and $<\varepsilon_2(E)>$ were subsequently calculated with an isotropic two layer model.

The susceptibility $<\chi_2>(E)$ [$\chi = \chi_1 + i\chi_2 = (\varepsilon_1 - 1) + i\varepsilon_2$] shows an increasing quasi monotonously behavior with a maximum at 9.37 eV (for the temperature 25 °C) and at 9.50 eV (for the temperature -98 °C) (Fig. 1). This looks very similar to the corresponding theoretical dependences of $RbNH_4SO_4$ crystals obtained from the first principles calculations using the CASTEP code [6]. An analysis of the density of electronic states of $RbNH_4SO_4$ crystals indicates that the big maximum of $<\chi_2>(E)$ at 9.37 eV in case of $(NH_4)_2SO_4$ mainly corresponds to the excitation of oxygen p-electrons.

Distinct and big anomalies of the temperature dependences of pseudo-susceptibilities $<\chi_1>(T)$ and $<\chi_2>(T)$, and reflectance intensity $I_R(T)$ have been obtained at the temperature of discontinuous ferroelectric phase transition for the c-cut of $(NH_4)_2SO_4$ for the superior light polarization $\mathbf{E}\|\mathbf{a}$ studied (Fig. 2, 3). Much smaller anomalies were seen for the samples of a- and b-cuts. One can distinguish here two types of anomalies: (1) broad band with broad and small extremum in $<\chi_1>(T)$ and $<\chi_2>(T)$ near T_C, and (2) narrow peak-like dependences of $<\chi_1>(T)$ and $<\chi_2>(T)$ with extremum position 5 °C lower than the corresponding position of the broad extremum. The maximum of the broad anomaly in $<\chi_1>(T)$ corresponds to the minimum of the narrow and big anomaly in $<\chi_1>(T)$, and vice versa, the minimum of the broad anomaly in $<\chi_2>(T)$ corresponds to the maximum of the narrow and big anomaly in $<\chi_2>(T)$ (Fig. 2, 3).
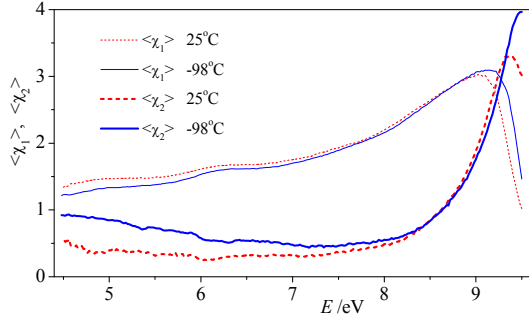
Fig. 1. Spectra of the real and imaginary parts of the susceptibility $<\chi_1>(E)$ and $<\chi_2>(E)$ of c-cut of $(NH_4)_2SO_4$ crystal for the superior light polarization $\mathbf{E}||\mathbf{a}$ at the temperatures 25 °C and -98 °C.
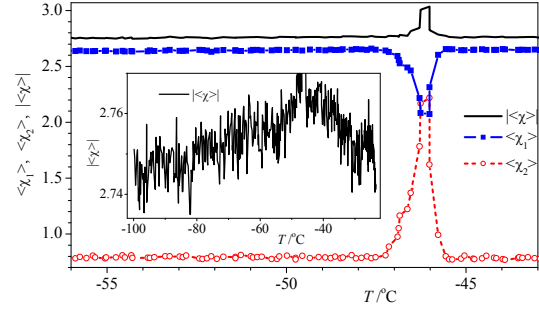
Fig. 2. Temperature dependences of the real ($<\chi_1>$), imaginary ($<\chi_2>$) part and modulus ($|<\chi>|$) of the susceptibility $<\chi>$ of $(NH_4)_2SO_4$ crystal during heating at $E = 8.5$ eV. The insertion shows the temperature dependence of the modulus of the susceptibility $|<\chi>|(T)$ in a larger temperature range.

Therefore, two different temperature dependent processes can be suggested for $(NH_4)_2SO_4$ crystals. The first process is a discontinuous phase transition at $T_C^{(1)}$ taking place in the narrow temperature range of approximately $1 - 2$ °C. The sharp maximum of $<\chi_2>$ and the minimum of $<\chi_1>$ is associated with this process (Fig. 2). The second, continuous process is associated with the slower variation in $<\chi_1>(T)$ and $<\chi_2>(T)$ which creates a maximum in $<\chi_1>$ and a minimum in $<\chi_2>$ at the temperature $T_C^{(2)}$, approximately 5 °C higher than $T_C^{(1)}$ (Fig. 3).

The presence of these two processes agrees with results of dielectric constant measurements on $(NH_4)_2SO_4$ for frequences $10 - 10^2$ kHz [7]. In this study, a small anomaly in the dielectric constant ε was found between 6 and 12 K below the well-known ferroelectric transition at -49.5 °C. It is proposed that this new anomaly is due to the appearance of a spontaneous polarization, which is produced by the secondary order parameter and is in an anti-parallel direction to the spontaneous polarization due to the primary order parameter, which produces the well-known ferroelectric transition. According to this model, ammonium sulfate is ferroelectric just below the transition at -49.5 °C, but it gradually changes into a weak ferrielectric material below this new anomaly temperature.

An interesting result has been obtained when analyzing the temperature dependence of the light intensity $I_R(T)$ reflected from the sample and the temperature dependence of the normal incidence reflection coefficient $R(T)$ (Fig. 4). The normal incidence reflection coefficient R has been calculated according to the known relationship [8],

$$R = \frac{(n-1)^2 + k^2}{(n+1)^2 + k^2} \; , \qquad n = \sqrt{\frac{(\varepsilon_1^2 + \varepsilon_2^2)^{1/2} + \varepsilon_1}{2}} \; , \qquad k = \sqrt{\frac{(\varepsilon_1^2 + \varepsilon_2^2)^{1/2} - \varepsilon_1}{2}} \; . \tag{1}$$

Taking into account the great spontaneous deformations in the crystal and the piezo(elasto)optical effect mentioned, the big and abrupt decrease of the reflectance intensity $I_R(T)$ observed for c-cut (Fig. 4) can be explained as a result of light scattering on a domain-like structure grid. This structure is generated by the non homogeneity of refractive index caused by the abrupt increase of spontaneous deformation.
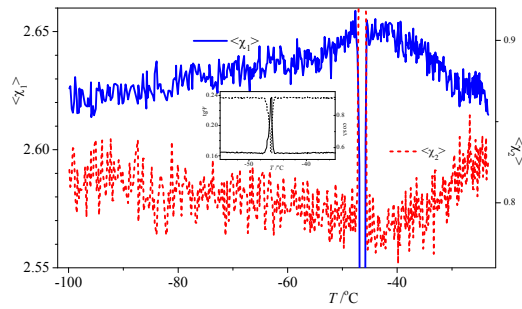
Fig. 3. Temperature dependences of the real $<\chi_1>(T)$ and imaginary $<\chi_2>(T)$ part of the susceptibility of $(NH_4)_2SO_4$ crystal during heating at $E = 8.5$ eV in more fine vertical scale than in Fig. 2. The insertion shows the temperature dependences of the standard ellipsometric parameters $tg\Psi(T)$ and $cos\Delta(T)$.
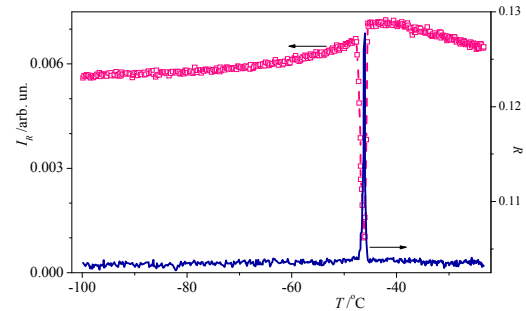
Fig. 4. Temperature dependences of the intensity of reflected light $I_R(T)$ and normal incidence reflectance $R(T)$ calculated from the dielectric functions $<\varepsilon_1>(T)$ and $<\varepsilon_2>(T)$ of $(NH_4)_2SO_4$ for the superior light polarization $\mathbf{E}\|\mathbf{a}$ measured at $E = 8.5$ eV during heating.

Taking into account that the photon energy $E = 8.5$ eV corresponds to the excitation of p-electrons of oxygen in $(NH_4)_2SO_4$ crystal the temperature changes described above can be attributed mainly to the SO_4 group. Finally, one can state that the module of complex susceptibility $|<\chi>|$ of $(NH_4)_2SO_4$ crystal in the range of oxygen p-electrons excitation display maximum at the temperature $T \approx 223$ K of ferroelectric phase transition. For the narrow temperature range $\Delta T \approx 1 - 2$ K near the main maximum of $|<\chi>|(T)$, the big relative increase $\Delta\chi_2/\chi_2 \approx 1.8$ of the imaginary part of the susceptibility $<\chi_2>$ takes place together with simultaneous relative decrease $\Delta\chi_1/\chi_1 \approx -0.25$ of the real part of the susceptibility $<\chi_1>$ (see Fig. 2). This result agrees qualitatively with conclusion of [9] that a considerable part of spontaneous polarization of $(NH_4)_2SO_4$ crystal arises from the SO_4 groups. According to [9] the main driving interaction of the phase transition has its origin in S-O bonds of SO_4^{2-} ion which triggers the transition by getting more distorted structure of lower symmetry; the NH_4^+ ions simply follow an appropriate change. This is probably the reason that the studies related only with NH_4^+ ions indicate that the phase transition has the characteristics of second order [10, 11].

Taking into account the sharp spontaneous deformations at phase transition of $(NH_4)_2SO_4$, which even destroy the crystal, it would be interesting to perform first principal calculations of the complex susceptibility for different unit cell dimensions and arrangements of constituent atoms and to compare results obtained with present experiment.

[1] S. Hoshino, K. Vedam, Y. Okaya, and R. Pepinsky, Phys. Rev. **112** (1958) 405.
[2] H. Ohshima and E. J. Nakamura, Phys. Chem. Solids **27** (1966) 481.
[3] H.-G. Unruh, Solid State Commun. **8** (1970) 1951.
[4] R. M. A. Azzam and N. B. Bashara, *Ellipsometry and polarized light*, Amsterdam: North-Holland Personal Library, 1987.
[5] T. Wethkamp, K. Wilmers, N. Esser, W. Richter, O. Ambacher, H. Angerer, G. Junqk, R. L. Johnson, and M. Cardona, Thin Solid Films **313-314** (1998) 745.
[6] B. Andriyevsky, W. Ciepluch-Trojanek, V. Stadnyk, M. Tuzyak, M. Romanyuk, and V. Kurlyak, J. Phys. Chem. Solids **68** (2007) 1892.
[7] A. Yoshihara, T. Fujimura, and K. I. Kamiyoshi, Phys. stat. sol. (a) **34** (1976) 369.
[8] H. R. Philipp and H. Ehrenreich, Phys. Rev. **129** (1963) 1550.
[9] Y. S. Jain and H. D. Bist, Phys. Stat. Sol. (b) **62** (1974) 295.
[10] D. E. O'Reilly and T. J. Tsang, Chem. Phys. **46** (1967) 1291.
[11] B. H. Torrie, C. C. Lin, O. S. Binbrek, and A. Anderson, J. Phys. Chem. Solids **33** (1972) 697.

Residual Stress Profiles in Friction Stir Welds of 2024Al Alloy and 2124Al-25vol%SiC Composite

Ferreira-Barragáns S.[1], Gesto D.[2], Rey P.[2], Fernández R.[1], González-Doncel G.[1]

[1] Dept. of Physical Metallurgy, National Centre for Metallurgical Research, CENIM-CSIC, Av. Gregorio del Amo 8, 28040 Madrid, SPAIN
[2] AIMEN Technology Centre, Relva 27A-Torneiros, Porriño, 36410 Pontevedra, SPAIN

1. Introduction

Metal Matrix Composites (MMCs) are known to have better mechanical properties than the corresponding unreinforced metallic alloys. However, their wide application as structural materials needs proper development of suitable joining processes. The application of the solid state welding technique known as Friction Stir Welding (FSW) to MMCs seems very attractive. On the other hand, the presence of a residual stress (RS) in welded components may have a significant influence of components performance. Thereby, knowing its magnitude and distribution is very important [1].

In this work, the sub-surface RS profile across the butt weld in a 2124Al-25vol%SiC composite plate obtained by FSW, has been studied from measurements conducted by synchrotron radiation diffraction. For comparative purposes, the RS has been also calculated on a butt weld of 2024Al alloy obtained under similar joining conditions.

2. Experimental details

2.1 Welded samples

The welds were performed on 15 mm thick plates of 2024Al and 2124Al-25vol%SiC$_p$ in T6 condition. Welding process in two passes and butt joint configuration without edge preparation was carried out. A fix pin tool with threaded pin with three grind flats at 120º was used. This pin was fabricated from H13 Steel (Q&T, 49 HRc). The materials investigated were welded at AIMEN Technology Centre (Pontevedra, Spain). The joints parameters are reported in Table 1.

Material	Rotation rate (rpm)	Welding Speed (mm/min)	Force (kN)
2024Al-T6	400 Counter- clockwise	100	Position Control (23 kN)
2124Al-25vol%SiC-T6	300 Counter-clockwise	75	Position Control (8-9 kN)

Table 1: Joints parameters.

2.2 Residual stress measurements

The residual stress distribution across the weld has been measured by energy dispersive diffraction using X-ray synchrotron radiation on the beam line EDDI at BESSY, Berlin, Germany, which operate in the range 10-150 keV. The experimental set up is shown in Figure

1(a). The measurements were carried out in reflection mode. The use of energy dispersive allows detecting many diffraction peaks. At present only the Al-(311) and SiC-(311) reflections have been analyzed. This is a very suitable peak since it shows low plastic anisotropy and has a fairly linear relationship between stress and lattice strain. An angle $2\theta = 8°$ was used. The incoming beam was defined by slits of 1 mm height and 1 mm width, while the diffracted beam size was adjusted by slit of 30 μm. (gauge volume: 1 mm × 1 mm × 0.03 mm). Both the longitudinal (along the weld) and transverse (across the weld) RS components were calculated. The biaxial $sen^2 \psi$ method was used [2].

The strain state was calculated using the conventional relationship

$$\varepsilon = \frac{d - d_0}{d_0} \tag{1}$$

where d is the lattice spacing measured at different locations of the weld, and d_0 is the unstrained lattice spacing measured at equivalent points in a stress-free "comb" sample, Figure 1(b). In the welded sample, it is very important to measure the point to point variation of d_0, since this value can vary due to changes in chemical or structural composition resulting from the welding process [3]. The stress state was calculated from the two measured strain components under the assumption that there is not an out of plane component in the stress tensor ($\sigma_N = 0$), *i.e.*, a biaxial stress state is assumed [2]. Hence;

$$\sigma_L = \frac{E}{1+v}\left(\varepsilon_L + \frac{v}{1-2v}\varepsilon_T\right) \tag{2}$$

where ε_L and ε_T are the values in the weld longitudinal and transverse directions, E is the Young's Modulus and υ Poisson's ratio. σ_T is obtained by exchanging the two strain parameter in Eq. (2).

(a)   (b)
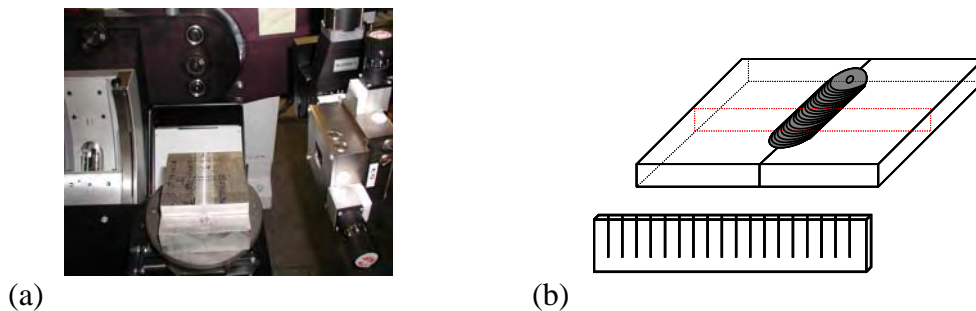
Figure 1: (a) Experimental set up and welded plate, and (b) comb sample.

3. Results and Conclusions

Figure 2 shows the variation of lattice parameter across the stress-free comb samples in both alloy and composite. It can be seen that the distribution reveals structural changes as a consequence of the FSW process. The RS in the materials, Figure 3, presents the typical "M" distribution across the welds [4]. The RS state is more isotropic than in the alloy. In the latter one, the longitudinal component is clearly higher that the transverse one. On the other hand, the RS in the composite is higher than in the alloy. This should be attributed to the additional contribution of the micro-RS associated to the presence of the reinforcement in the composite material.
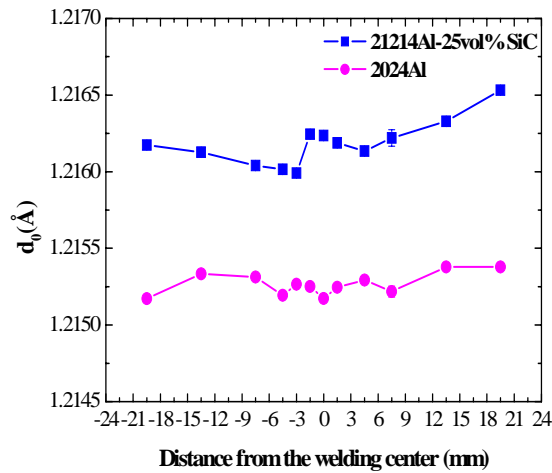
Figure 2: Variation of 311 lattice spacing across the welds in the comb samples in the composite material and the aluminium alloy.

(a)

(b)
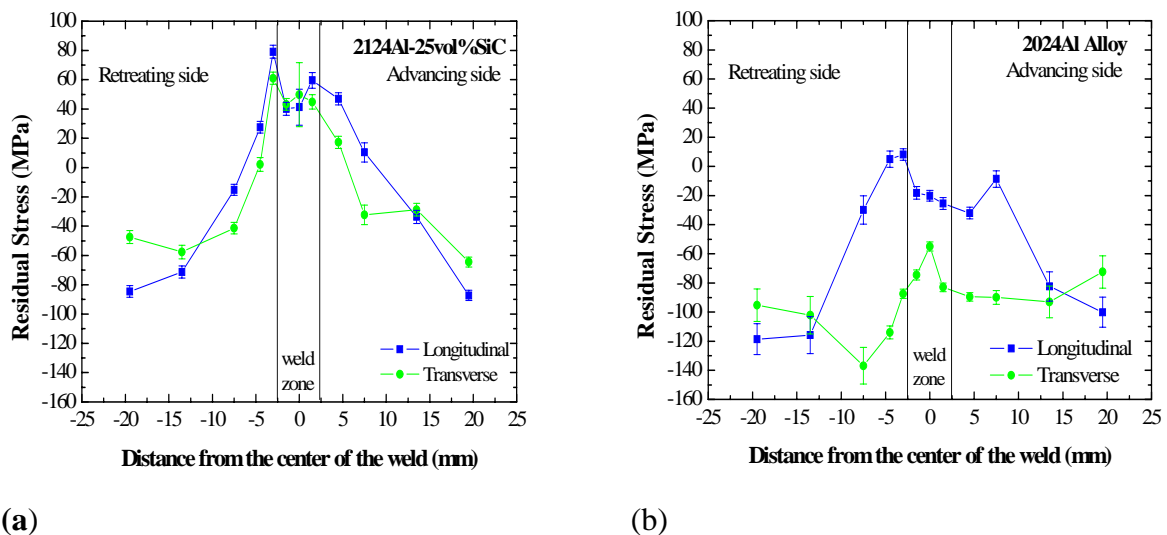
Figure 3: Total residual stress distribution across the welds. (a) Composite (b) Alloy.

4. Acknowledgements

5. References

[1] M.N. James, D.J. Huges, Z. Chen, H. Lombard, D.G. Hattingh, D. Asquith, J.R. Yates, P.J. Webster, Engineering Failure Analysis 14 (2007) 384.
[2] I. C. Noyan and J. B. Cohen. "Residual Stress: Measurements by Diffraction". Springer Verlag, 1987.
[3] S. Pratihar, V. Stelmukh, M.T. Hutchings, M.E. Fitzpatrick, U. Stuhr, L. Edwards. Materials Science and Engineering A 437 (2006) 46.
[4] R.S. Mishra, Z.Y. Ma, Material Science and Engineering R 50 (2005) 1-78.

Imaging of magnetization dynamics in $Fe_{19}Ni_{81}$/Cu/Co trilayer microstructures

J. Kurde[1], J. Miguel[1], D. Bayer[2], J. Sánchez-Barriga[3], A. Rzhevskiy[3], F. Kronast[3],
M. Aeschlimann[2], H. A. Dürr[3], W. Kuch[1]

[1]Institut für Experimentalphysik, Freie Universität Berlin, Arnimallee 14, D-14195 Berlin, Germany

[2]Technische Universität Kaiserslautern, Erwin Schrödinger Str. 46, D-67663 Kaiserslautern, Germany

[3]BESSY GmbH, Albert Einstein Str. 15, D-12489 Berlin, Germany

Modern recording devices contain a stack of two thin magnetic layers separated by a non-magnetic spacer layer. Their fastest operation can be achieved by applying a magnetic pulse, which may induce the magnetization reversal of one of the layers by precession. With the aim of studying this magnetization reversal process we have imaged $Fe_{81}Ni_{19}$/Cu/Co trilayer microstructures with sizes in the range of 5x5 to 10x20 µm². We have investigated the influence of i) the thickness of the Co layer, ii) a static, external field, and iii) a magnetic field pulse in the ps time scale. In the following we will refer to $Fe_{81}Ni_{19}$ as permalloy (Py).

The magnetic structures were magnetron-sputtered in Ar^+ atmosphere at MAGSSY. Sizes range from 5x5 to 10x20 µm² and film thicknesses are Py (4 nm) / Cu (t_{Cu}) / Co (15 nm), with t_{Cu} = 1.5, 2.0, 2.5 and 3.0 nm. During growth a static magnetic field of ~100 mT is applied to induce a uniaxial anisotropy. To image the magnetic domains, photoelectron emission microscopy (PEEM) is used combined with x-ray magnetic circular dichroism (XMCD). These two techniques together provide lateral resolution and element-sensitive magnetic contrast. The latter is essential for studies of systems consisting of different materials. The static images were acquired at the UE49-PGMa, a microfocus beamline with an Elmitec SPPEEM (resolution ~50 nm). A static magnetic field was applied with a special sample holder equipped with magnetic coils. The time-resolved images were acquired at the UE56/2-PGM1 beamline with a Focus PEEM (resolution ~400 nm). To apply a magnetic field pulse, the structures were deposited onto a Au stripline, which is connected to a photoconductive switch. By focusing a fs laser onto the switch, a current pulse through the stripline is generated and thereby a magnetic pulse in the vicinity of the structures [1]. Synchronization of the magnetic pulse (pump) with the x-ray
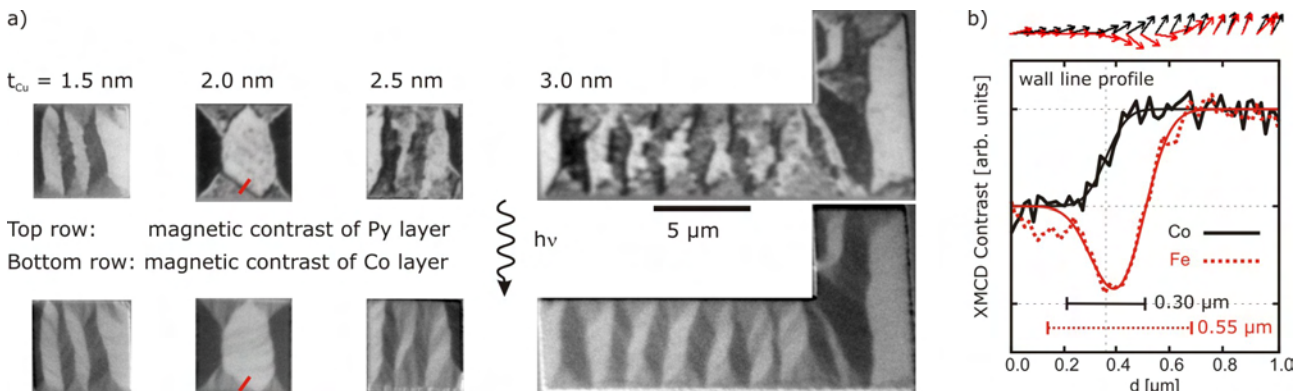
Fig. 1 a) Domain patterns in Py/Cu/Co trilayer microstructures with different Cu thicknesses. b) Line profile of a domain wall in a structure with t_{Cu} = 2.0 nm.

pulses of the BESSY single bunch operation mode (probe) realizes a stroboscopic pump probe experiment.

To gain detailed knowledge about the coupling behavior of the two magnetic layers through the non-magnetic spacer, the domain patterns in Py/Cu/Co trilayer microstructures with different Cu thicknesses were imaged (Fig. 1a). The magnetic domains of the two ferromagnetic layers are coupled parallel, via exchange interaction and orange-peel coupling for all measured Cu thicknesses. For increasing Cu thicknesses, an antiparallel alignment in the domain walls (DW) of the two magnetic layers becomes favorable due to stray fields: At the DWs the dipolar coupling competes with exchange and orange-peel coupling. Similar behavior had been found previously in 180° and head-on walls [2]. Here this effect is also observed at 90° walls: The magnetization inside a wall in the Py layer first turns opposite to the Co layer before it turns back. Detailed statistics of the DW widths at different Cu thicknesses in the two magnetic layers as shown in Fig. 1b will reveal more information about the coupling behavior. Stray fields originating from ripples in the Co layer also lead to strong irregularities in the magnetization of the Py layer for $t_{Cu} > 2.0$ nm.
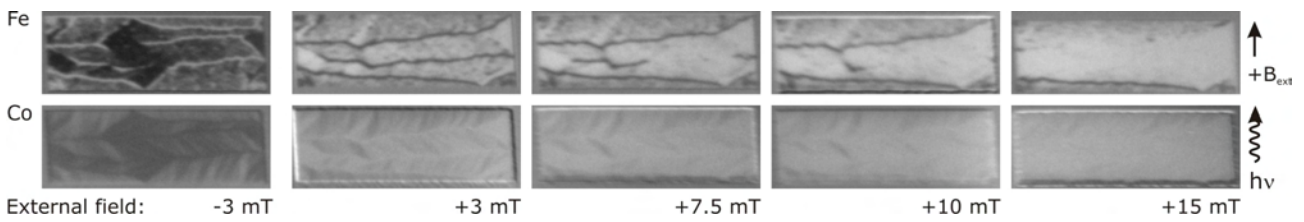
Fig. 2 Influence of an external field on a 5x15 μm Py/Cu/Co structure with $t_{Cu} = 2.5$ nm.

The strength of the antiparallel coupling inside the walls can be investigated with an external field. A trilayer structure with $t_{Cu} = 2.5$ nm and uniaxial anisotropy parallel to the long side (tilted by about 15°) was imaged after applying an external magnetic field along the hard axis (Fig. 2). When reversing the field, domains are switched (domain pattern changed slightly). While switching, the walls in the Py layer keep their antiparallel alignment to the Co layer, hence they are also aligned antiparallel to the applied field. In an external field of ~7.5 mT the walls start to turn partly along the field. Finally, at ~15 mT they are almost completely switched. Even higher fields are necessary to saturate the magnetization along the hard axis of the structure.

Another important aspect is the dynamics of the magnetization in the ps time range. Consequently, a trilayer structure with $t_{Cu} = 2.0$ nm was imaged while applying a magnetic field pulse of ~3 mT amplitude and ~200 ps FWHM perpendicular to the long edge of the structure. Pump-probe delay times with respect to the magnetic field pulse from -100 to 2000 ps in steps of 50 ps where imaged (Fig. 3a). To analyze the magnetization dynamics, the XMCD contrast
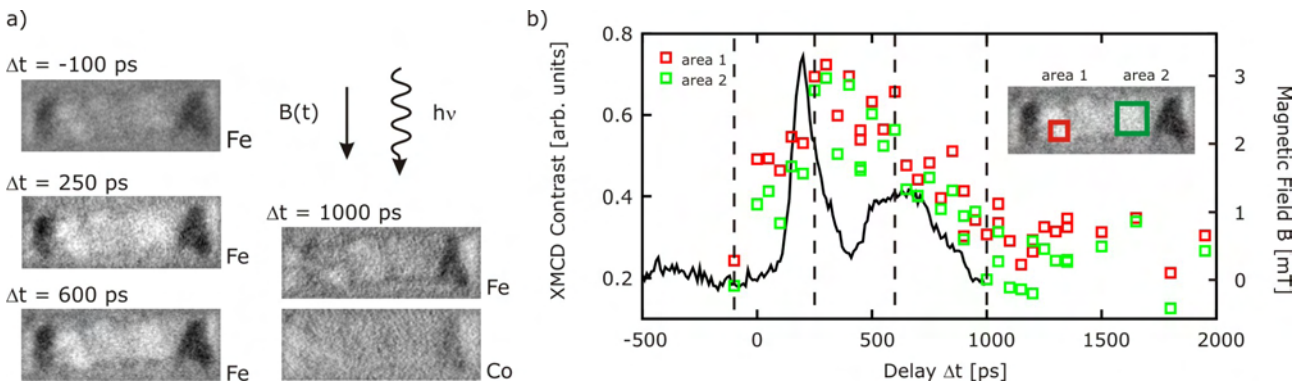
Fig. 3 Time dependence of a 5x15 μm Py/Cu/Co structure with $t_{Cu} = 2.0$ nm. a) Magnetic domains at different delay times. b) Magnetic field pulse (line) and XMCD contrast integrated over two areas on the structure as a function of delay time (squares).

of two areas on the structure has been integrated and displayed as a function of delay time (Fig. 3b). The magnetization is mainly following the external magnetic field. In addition a long-term change in the Py magnetization is visible due to domain wall motion in the magnetically harder Co layer. These preliminary results are being contrasted with micromagnetic calculations (OOMMF).

In summary, the following facts have been observed: An antiparallel coupling in the domain walls of the magnetic layers for spacer thicknesses $t_{Cu} > 1.5$ nm is found, which can be explained by a dipolar interaction. The switching behavior of a trilayer structure with $t_{Cu} = 2.5$ nm is studied in detail, revealing a coupling field of ~15 mT across the walls. First time-resolved measurements of a 5x15 µm² trilayer structure show a repeatable reaction of the Py layer on the magnetic field pulse. For future time-resolved measurements the setup of a new laser system at the UE49-PGMa beamline is in progress. This will combine the high lateral resolution of the Elmitec SP-PEEM with time-resolved pump probe experiments in the ps regime.

[1]   J. Miguel, M. Bernien, D. Bayer, J. Sánchez-Barriga, F. Kronast, M. Aeschlimann, H. A. Dürr, and W. Kuch, Rev. Sci. Instrum. **79**, 033702 (2008)

[2]   J. Vogel, S. Cherifi, S. Pizzini, F. Romanens, J. Camarero, F. Petroff, S. Heun and A. Locatelli, J. Phys.: Condens. Matter **19**, 476204 (2007)

High-resolution XPS study of Fluorinated Carbon Nanotubes

Carla Bittencourt

University of Mons-Hainaut, Parc Initialis, Av. Nicolas Copernic 1, Mons 7000, Belgium

Xiaoxing Ke and Gustaaf Van Tendeloo

University of Antwerp, EMAT, Groenenborgerlaan 171, B2020 Antwerpen, Belgium

Alexandre Felten and Jacques Ghijsen

University of Namur (FUNDP), LISE, 61 rue de Bruxelles, Namur 5000, Namur, Belgium

1. Introduction

Fluorination is a promising method for expanding the use of carbon nanotubes (CNTs) to several areas where the tailoring of properties such as wettability, adhesion, chemical stability, permeation, electrical conductivity, and biocompatibility are important[1]. Due to fluorine's high electronegativity, fluorination drastically modifies the nanotube surface chemistry, changing the electronic properties depending on the degree of fluorination and the specific addition pattern of the fluorine atoms on the nanotube surface[2,3].

Fluorination in fluorine gas generally results in a high reaction ratio and a deep penetration into carbon-related materials which prevents a good control of sidewall fluorination[1]. In this context, plasma fluorination has the potential to limit the fluorination area to the external surface of the nanotubes if performed at room temperature; in addition it requires a reaction time orders of magnitude shorter than other fluorination methods.[4,5]

In this work, CF_4 plasma functionalization of multiwall carbon nanotubes are investigated using high-resolution x-ray photoelectron spectroscopy.

2. Method

Samples were prepared using commercial MWCNT powder synthesized via catalytic chemical vapour deposition (CCVD)[6]. The functionalization was performed in a homemade chamber using inductive coupled plasma at the RF frequency of 13.56 MHz.[4] A controlled flow of CF_4 was introduced inside the chamber; the treatment was performed at gas pressure of 0.1 Torr, using 10 W.

The changes induced in the CNT electronic states due to the grafting of fluorine atoms by the rf-plasma treatment were investigated by XPS. X-ray photoemission experiments were performed at UE56 beam line BESSY II (Berlin) using the Mustang end-station.[7] Photon energies were selected so that all spectra were recorded at similar kinetic energies corresponding to high surface sensitivity, namely 400 eV for recording C $1s$, 800 eV for F $1s$, and 110 eV for valence bands. The selected photon energy for valence band studies, together with a favourable cross-section ratio[8], will lead to a higher contribution of the fluorine states on the valence band spectra. The Au $4f_{7/2}$ peak at 84.0 eV binding energy, recorded on a reference sample, was used for calibration of the binding energy scale.

Results

Table 1 presents the parameters used for the plasma treatment and the resulting F/C ratio evaluated by XPS analysis. As mentioned before, the photon excitation energy was chosen to generate photoelectrons with kinetic energy of the order of 100 eV, for which the inelastic electron mean free path was reported to be ~ 5 Å [9]. Therefore, considering the distance between the CNT walls (~ 3.45 Å); the outer wall contributes 50% of the intensity of the carbon peak. Thus the F/C ratio as determined by XPS includes contribution of photoelectrons belonging to the two outer walls, meaning that the actual fluorine/carbon ratio of the surface will be twice the measured F/C ratio.

Sample	Treatment time (s)	F/C (XPS)	F/C ratio coverage of the outer wall
1	2	0.25	0.50
2	5	0.22	0.44
3	15	0.19	0.38
4	30	0.16	0.32
5	45	0.17	0.34
6	60	0.16	0.32
7	300	0.12	0.24

Table 1 Parameters used for the plasma treatment of MWCNTs, together with the F/C ratio evaluated by XPS and the actual surface coverage on the outer wall. The F/C ratio as determined by XPS includes contribution of photoelectrons belonging to the two outer walls, so the quoted fluorine/carbon ratio of the surface is twice the measured F/C ratio.

Chemical modification by the plasma treatment is revealed by the appearance of new structures contributing to the C 1s line shape at higher binding energies. These structures are generated by photoelectrons emitted from carbon atoms participating in C-F bonding or from carbon atoms neighbour to a carbon atom bound to a fluorine atom: Due to its high electronegativity, fluorine has a very strong effect on the electronic screening of the element to which it is bound. In addition, when a C atom not bound to fluorine is first neighbour of another carbon atom bound to one or several fluorine atoms, an inductive effect arises.[10] The main peak in the C 1s spectrum of the plasma functionalized samples is generated by photoelectrons emitted from the carbon atoms that do not interact directly with fluorine atoms. From the reported results[1], we can suggest the following attribution for the peaks observed in Figure 1: C_2F at 286.4 eV, C_3F at 287.5 eV, C_4F at 288.8 eV, CF at 291.0 eV, and CF_2 at 293.0 eV.

The maximum F/C ratio of 0.25 (equivalent to C_2F surface coverage) is obtained after 2s of functionalization; for increasing functionalization time this ratio decreases (table 1). Figure 1 shows that for increasing functionalization time the relative intensity of the different components varies. This trend suggests that certain bond configurations are more stable and/or are less influenced by the interaction with the CF_4 plasma. We believe that the reduction in the F/C ratio for increasing functionalization time is mainly due to the chemical interaction between the CF_4 plasma and

Figure 1 : C 1s XPS spectrum recorded using hv = 400 eV on CF_4 plasma functionalized for a) 60 s and b) 300 s.

the less stable bond configuration — fluorine plasmas are characterized by high-rate chemical interaction.[11] As the ions in the plasma interacts with carbon atoms in the graphite layer of MWCNTs, fluorine atoms can either bond to carbon atoms or cut C-C bonds.

Because valence electrons are involved in bond formation, subtle differences in surface chemistry may be observed by studying the valence band region. The valence band structure of the pristine CNTs is characterized by features appearing close to 3.5 eV associated with photoelectrons emitted from the 2p-π band, extending from 5.5 to 8.0 eV associated with 2p-σ states and the mixed 2s-2p hybridized states at 13.6 eV. The σ-π hybridization resulting from the formation of the CNTs gives rise to the intensity at 11.5 eV.[12] The CNT spectrum is dominated by an intense C 2s region around 18 eV and a broad C 2p region in the range 9-15 eV.

The impact of the CF_4 plasma treatment on the CNT electronic valence states can be seen in the spectrum recorded on the sample treated for 2 seconds (Figure 3). Notably the MWCNT electronic states are significantly attenuated. Photoelectrons emitted from the valence states of the plasma treated samples generate new structures in the binding energy range of 5 to 16 eV. The broad feature appearing close to 8.3 eV was reported to be generated by photoelectrons emitted from anti-bonding orbitals of the C-F bonds with contribution of F $2p$ states at high binding energy. [13] The main contribution of the photoelectrons emitted from the F $2p$-like states appears at 10 eV. The structure close to 15 eV originates from bonding orbitals of C $2s$-F bonds.
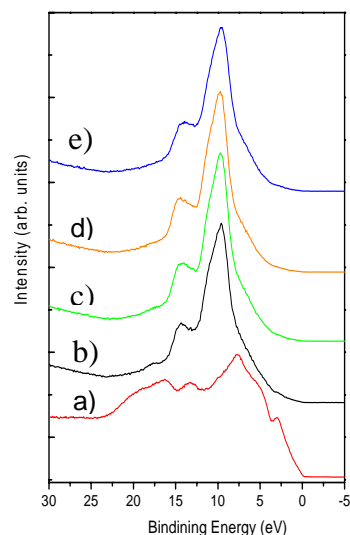
Figure 2: Valence band spectra recorded using hv = 110 eV on (a) pristine MWCNTs compared with those CF_4-plasma treated for (b) 2, (c) 30, (d) 60 and (e) 300 s.

Summary

CF_4 rf-plasma treatment of CNTs effectively grafts fluorine at the CNT surface, inducing changes in the CNT valence electronic states due to the formation of C-F bonds.

For increasing treatment time the relative intensity in the UPS spectra close to the Fermi energy level decreases suggesting that the functionalization of the CNT-surface can be tailored. The fluorine atomic concentration depends on the plasma exposure time.

Acknowledgements

References

(1) A. Tressaud, E. Durand, C. Labrugère, J. Fluorine Chem. **2004**,125, 1639-1648.

(2) H.Touhara, F. Okino, Carbon **2000,** 38, 241-267.

(3) K.N. Kudin, H.F. Bettinger, G.E. Scuseria, Phys. Rev. B **2001**, 63, 045413

(4) A. Felten, C. Bittencourt, J.J. Pireaux, G. Van Lier, J.C. Charlier, J. Appl. Phys. **2005**, 98, 074308.

(5) S. Kaoru, S. Takeda, Jap. J. Appl. Phys. **2007**, 46, 7977-7982.

(6) www.nanocyl.com

(7) http://www.bessy.de/upload/bitpdfs/mustang.pdf

(8) J.J. Yeh, I. Lindau, At. Data and Nucl. Data Table **1985**, 32, 1-155.

(9) S. Hüfner, Photoelectron Spectroscopy, third ed., Springer-Verlag, Berlin **2003**

(10) G. E. Nansé, P. Papirer, F. Fioux, A. Moguet, A. Tressaud, Carbon **1997**, 35, 515-528.

(11) T.E.F.M. Standaert, M. Schaepkens, N.R. Rueger, P.G.M. Sebel, G.S. Oehrlein, J.M.J. Cook, J. Vac. Sci. Technol. A **1998**, 16, 239-249.

(12) A. Felten, J. Ghijsen, J.J. Pireaux, R.L. Johnson, C.M. Whelan, D. Liang, G. Van Tendeloo, C. Bittencourt, J. Phys. D Appl. Phys. **2007**, 40, 7379-7382.

(13) E. Morikawa, J. Choi, H.M. Manohara, H. Ishii, K. Seki, K.K. Okudaira, N. Ueno, J. Appl. Phys. **2000**, 87, 4010-4016.

ASAXS study on the formation of core-shell Ag/Au nanoparticles in glasses

J. Haug[1], H. Kruth[1], M. Dubiel[1], S. Haas[2], D. Tatchev[2], A. Hoell[2]

[1]Martin-Luther-Universität Halle-Wittenberg
[2]Helmholtz-Zentrum Berlin für Materialien und Energie

1 Introduction

Nanosized metal particles embedded in surfaces of glasses are of great interest because of their potential application as nonlinear optical materials for photonic devices. Here, Ag/Au nanoparticles (NPs) were prepared in soda-lime-silica glasses by double ion implantation. By using different ion implantation parameters it is possible to adjust the surface plasmon resonance (SPR) in an extended range of wavelengths. This is possible because for bimetallic nanoparticles the SPR depends on the content of silver and gold. Additionally, core-shell nanoparticles can result in a shift of the SPR to higher values.

With ASAXS, an element specific investigation allows to validate and to quantify the core-shell structure or a bimetallic composition of the Ag/Au nanoparticles. Therefore, we measured at X-ray energies slightly below the Au L_{III}-edge to understand the effects of different implantation sequences on the configuration of the nanoparticles.

2 Experimental

Soda-lime glasses containing (in mol%) 72.4% SiO_2, 14.4% Na_2O, 6.4% CaO, 6.0% MgO, 0.5% Al_2O_3, 0.20% K_2O, 0.3% SO_3, and 0.04% Fe_2O_3 were exposed to Ag^+(200 keV) and/or Au^+(300 keV) ion implantation at room temperature. On glass sheets of 1mm thickness areas of 20x20 mm^2 have been subjected to implantation for each type of ions at doses ranging from 2x10^{16} to 4x10^{16} ions/cm^2. The beam current density was 1 µA/cm^2. Charge buildup reduction at the glass surface during implantation was achieved by electron beam irradiation onto the surface. Two samples with different implantation sequence were produced: 4x10^{16} Au^+ + 4x10^{16} Ag^+ (sample name: 4Au4Ag), 2x10^{16} Ag^+ + 4x10^{16} Au^+ (sample name: 2Ag4Au).

For the ASAXS measurements, the samples were mechanicaly grinded and polished to a thickness of 150µm to achieve an acceptable transmission. The experiment was performed at the 7T MPW SAXS beamline at Bessy, Berlin, near bellow the Au L_{III}-edge (11919 eV). To characterize the SPR due to the metal nanoparticles formed in the implanted areas the optical density of the samples was recorded by means of a Perkin-Elmer spectrometer in the wavelength range of 250-900 nm.

3 Results and discussion

The coherent intensity of a SAXS experiment can be described by

$$\frac{d\sigma}{d\Omega}(Q) = \int \sum_i N_i(R) \Delta \eta_i^2 V(R)^2 \left| F(Q,R) \right|^2 dR$$

where $\Delta \eta_i$ is the scattering contrast, $N_i(R)$ the size distribution, $V(R)$ the volume and $F(Q,R)$ the form factor of NPs of type i. To investigate the chemical composition of
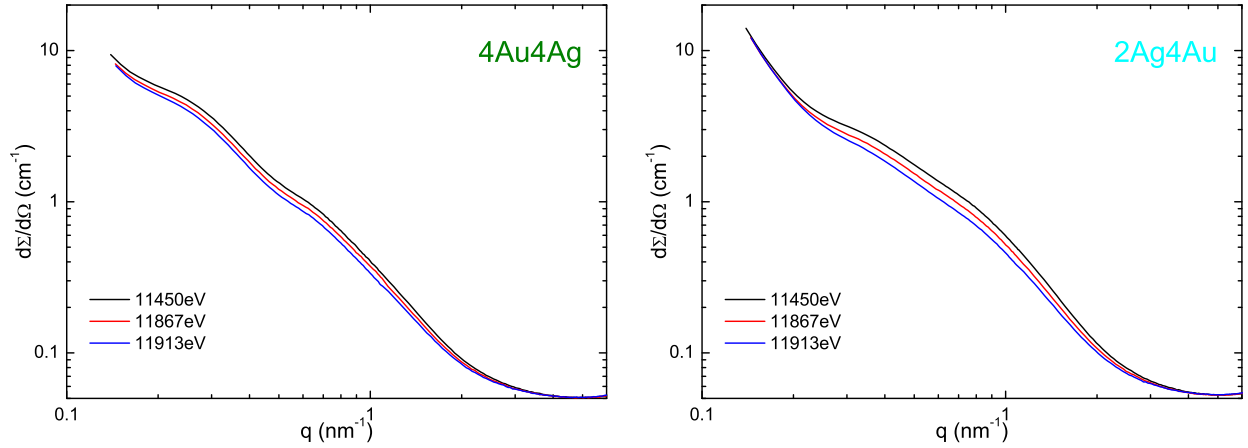
Figure 1: ASAXS measurements of the samples 4Au4Ag (left) and 2Ag4Au (right) at three energies below the Au L$_{III}$-edge.

the NPs, contrast variation was used by utilise the anomalous dispersion at the Au L$_{III}$-edge. Therefore, measurements at three energies near below the edge were performed. In this case, the atomic scattering factor for Au atoms vary with the energy E, $f_{Au}(E) = f_{0Au} + f'_{Au}(E) + if''_{Au}(E)$, and the scattering contrast is defined as $\Delta\eta(E) = \Delta\rho_{Au}f_{Au}(E) + \sum_{j \neq Au} \Delta\rho_j f_j$ where $\Delta\eta_j$ is the difference of the atomic density of element j between matrix and NP and f_j its scattering length.

In Fig. 1 the ASAXS measurements at three energies below the Au L$_{III}$-edge for the two samples are shown. A clear anomalous effect was observed for both samples and the scattering curves indicate the presence of core-shell nanoparticles. From TEM/HRTEM (see Fig. 2) it is known, that the NPs consist of core-shell-particles and additional small homogeneous particles. Therefore, a model with core-shell particles and spherical particles was used for the simultanious fit of the three energy dependent scattering curves.

By using the ratio of the scattering contrast $\Delta\eta(E)$ between the three energies and fitting the ASAXS curves simultaneously with the model, it is possible to compare the results with the calculated contrast values and too get the composition of the sphere and the shell of the NPs (see Fig. 3). For the sample 4Au4Ag the composition is 50%Au and 50% Ag whereas for 2Ag4Au it is 90%Au and 10%Ag.

With this values for the composition, the scattering contrast $\Delta\eta$ for the shell and sphere can be calculated and used in the next fit step. Now, the size distribution, volume concentration and number of particles for all nanoparticles results from the fitting procedure as well as the scattering contrast $\Delta\eta$ for the core (see Tab. 1). Then, the $\Delta\eta$ values from the core can be used to determine the composition of the core. This calculations show that for sample 4Au4Ag the core is completely hollow. For 2Ag4Au, $\Delta\eta$ indicates that the core is not hollow but contains a phase with a density lower than that of Ag.
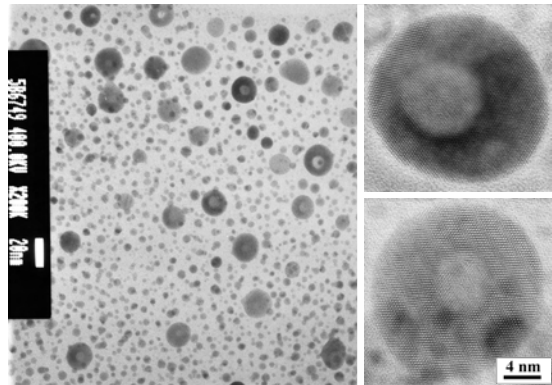
Figure 2: TEM/HRTEM images of Ag/Au nanoparticles with core-shell structure and small spherical particles (4Au4Ag).
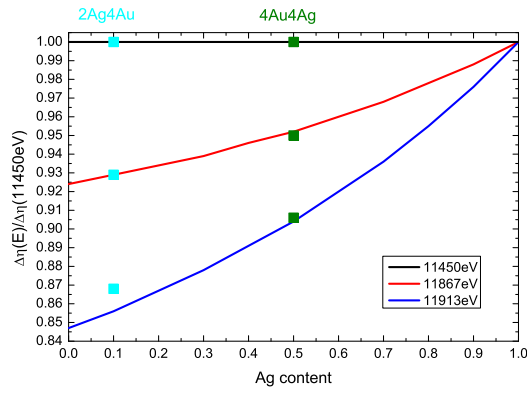
Figure 3: Ratio between the scattering contrasts dependent from the Ag-content and resulting composition of the shell and spherical nanoparticles.
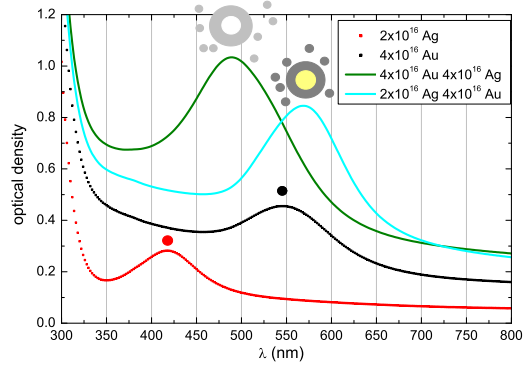
Figure 4: Optical spectra and structure model for the two samples and for pure silver and gold.

		Sphere	Shell	Core
4Au4Ag	Comp.	50%Au/50%Ag	50%Au/50%Ag	hollow
	N	$1.02{\times}10^{16}$	$2.51{\times}10^{13}$	
	fp	0.0082%	0.0035%	
	s	0.43	0.297	
	R	1.14	6.10	2.81
	$\Delta\eta$	$75.55{\times}10^{10}$	$75.55{\times}10^{10}$	$-19.27{\times}10^{10}$
2Ag4Au	Comp.	90%Au/10%Ag	90%Au/10%Ag	unknown
	N	$5.96{\times}10^{15}$	$3.72{\times}10^{13}$	
	fp	0.0113%	0.0045%	
	s	0.434	0.297	
	R	1.25	5.80	2.94
	$\Delta\eta$	$90.72{\times}10^{10}$	$90.72{\times}10^{10}$	$2.27{\times}10^{10}$

Table 1: Values from the simultaneous fit of the three ASAXS curves: composition, number of particles N, volume fraction fp, variance s, mean particle radius R, scattering contrast $\Delta\eta$

4   Conclusion

With the ASAXS measurements it was possible to get information about the size, size distribution, shape and structure of the Ag/Au NPs. Also, the composition of the core-shell NPs can be investigated with this method. The NPs in the sample 4Au4Ag with a composition of 50%Au and 50%Ag results in a SPR between that of pure Ag or Au because of the composition of the shell and the small spherical particles (see Fig. 4). The hollow core did not contribute to the SPR. For the other sample, 2Ag4Au, the composition from the shell and the small spherical NPs of 90%Au and 10%Ag must result in a shift of the SPR near to the SPR of Au. But in this sample the core is not hollow and therefore the SPR is shifted to wavelength values higher than that of pure Au.

These investigations show that it is possible to adjust the SPR between that of pure Ag and Au for hollow NPs by using different ion doses to vary the composition. With different ion implantation sequences it is possible to produce core-shell NPs wich are not hollow and therefore a shift of the SPR to values higher than that of pure Au is possible.

TXM-NEXAFS of Individual Titanate-based Nanoribbon

Carla Bittencourt
LCIA, University of Mons-Hainaut, Mons, Belgium;
Xiaoxing Ke and Gustaaf Van Tendeloo
EMAT, University of Antwerp, Belgium,
Peter Guttmann
Helmholtz-Zentrum Berlin für Materialien und Energie, Elektronenspeicherring BESSY II,
Albert-Einstein-Str. 15, 12489 Berlin, Germany,
Jacques Ghijsen and Alexandre Felten
LISE, University of Namur (FUNDP), Belgium;

1- Introduction

Low dimensional TiO_x- based nanostuctures, such as nanowires, nanotubes, and nanorods bring to reality the possibility to fine-tune chemical reactivity as the system structure and the occupation of the outermost energy levels can be tuned by changing preparation parameters. Several structures have been proposed for these structures, including scrolling of anatase sheets, trititanate $H_2Ti_3O_7$ exfoliated sheets, $(Na,H)_2Ti_2O_4(OH)_2$ based layers, and lepidocrocite titanate-like sheets. Based on x-ray diffraction and transmission electron microscopy experiments, it is currently believed that the structure is closely related to the family of layered titanate $H_2Ti_nO_{2n+1}$ materials, where n = 3,4,5 or even ∞ for the end-member composed of flat layers of octahedra The exact structure is still a matter of debate.

In this work, electronic properties of individual TiO_x-pristine nanoribbons (NR) prepared by hydrothermal treatment of anatase TiO_2 micro-particles were studied using the BESSY TXM-NEXAFS end-station at beamline U41. NEXAFS is ideally suited to study TiO_2-based materials because both the O K-edge and Ti L-edge features are very sensitive to the local bonding environment, providing diagnostic information about the crystal structures and oxidation states of various forms of titanium oxides and sub-oxides. TXM-NEXAFS combines microscopy with spectroscopy allowing the study of the electronic structure of individual nanostuctures with spatial resolution better than 25 nm [*A. Felten et al., Nano Lett., 7, (2007), 2435*]. In addition, the directional electric field vector ($\bar{E}$) of the x-rays can be used as a "search tool" for the direction of chemical bonds of the atom selected by its absorption edge [*J. Stohr in NEXAFS Spectroscopy, Springer Series in Surface Science, vol. 25*]. The electronic structure of these nanoribbons is discussed in terms of the crystal field splitting. Reference anatase and rutile samples are used as template for the interpretation of the spectroscopic signatures of the nanoribbon.

2- Results

NEXAFS spectra are clear fingerprint of titanium oxides. They show significant differences depending on the crystallographic phase as well as on the Ti reduction. TiO_2 single crystal spectra show well-resolved peaks in the range between 455 and 470 eV corresponding to the various Ti $2p \rightarrow 3d$ transitions [*U. Diebold, Surf. Sci. Rep. 48, 53 (2003)*]. The Ti L-edge shows two groups of peaks arising from the spin-orbit splitting of Ti $2p$ core level into $2p_{3/2}$ and $2p_{1/2}$ levels with ~6 eV energy separation. These levels are further split due to crystal-field effects. The Ti $L_{2,3}$ edges recorded on rutile TiO_2 micro-particles (figure 1a), anatase TiO_2 micro-particles (figure 2a), and the ribbon have similar form (figure 3a): the L_3 and L_2 edges are separated by the $2p$ core hole spin orbit coupling around 5 eV. The L_3 and L_2 edges are both split by the strong crystal field splitting arising from the surrounding oxygen atoms. The experimental splitting of the L_2 line for anatase and the nanoribbon are of comparable magnitude (~ 2 eV), splitting for rutile being somewhat larger (~ 2.6 eV). The separation between the t_{2g} and e_g orbitals is about 1.8 eV for anatase and 2 eV for rutile in accordance with reported results [*J. P. Crocombette and F. Jollet, J. Phys.: Condens. Matter 6, 10811 (1994)*].

The O K-edges for the rutile (figure1b), anatase (figure2b), and ribbon (figure 3b) is characterized by two main features. For anatase these are split by 2.5 eV whereas for rutile it is 2.75 eV. For the ribbon the splitting is around 2.5 eV, closer to anatase. This confirms that the crystal field splitting of the titanate ribbons is close to that of the anatase phase.
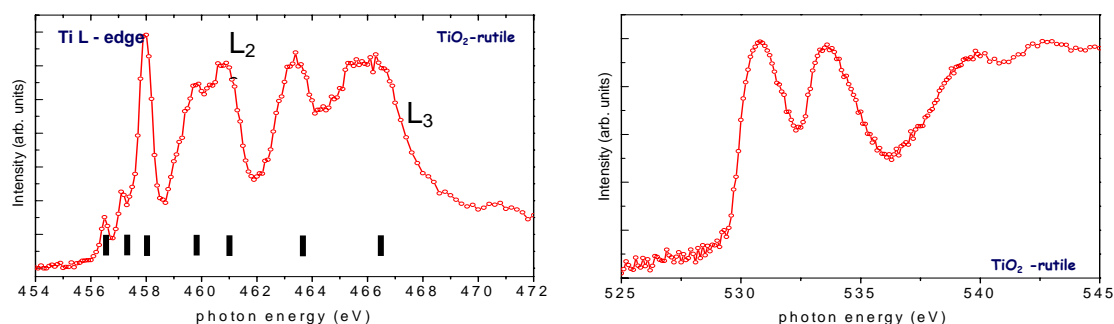
Figure 1: TXM-NEXAFS spectra recorded on TiO_2 rutile powder: a) Ti L-edge b) O K-edge
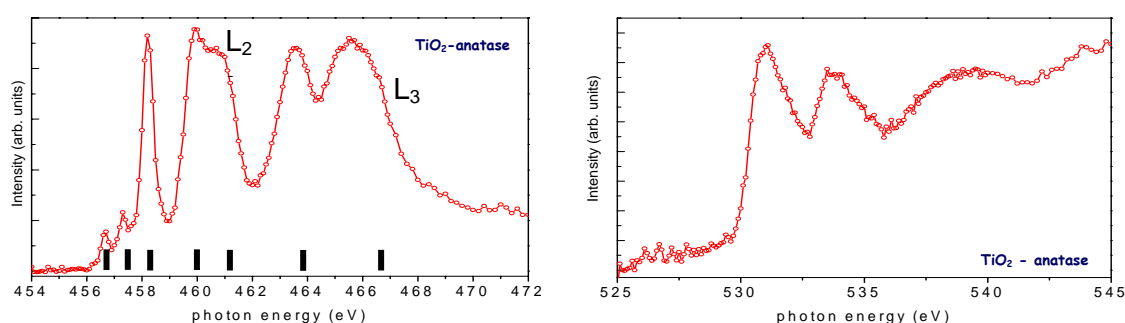
Figure 2: TXM-NEXAFS spectra recorded on TiO_2 anatase powder: a) Ti L-edge b) O K-edge
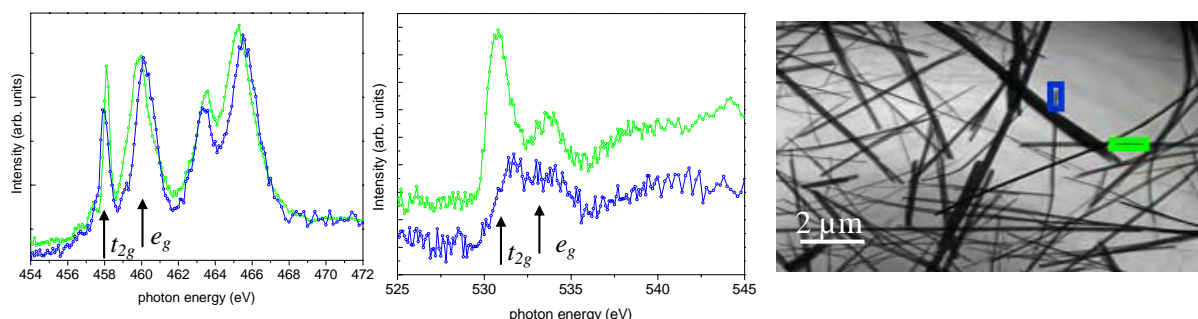
Figure 3 : TXM-NEXAFS spectra recorded on a single TiO_x-nanoribbon: a) Ti L-edge b) O K-edge c) TXM - image at $hv = 464$ eV showing the two experimental geometries used to record the spectra.

Figure 3 illustrates the oxygen 1s (K-edge) and titanium 2p ($L_{2,3}$-edge) absorption edges recorded on the nanoribbon in two experimental geometries: $\bar{E}$ parallel and perpendicular to the principal axis of the nanostructure. The Ti 2p spectra are similar to those reported for the TiO_2 anatase phase [*M.B. Casu et al., Surf. Sci. 602, 1599 (2008)*], with the main discrepancy in the single structure at 460 eV that appears split in the TiO_2. This structure results from transitions to the final state $(2p_{3/2})^{-1}d(3e_g)^1p^6$, the e_g states are formed by $d(z^2)$ and $d(x^2-y^2)$ orbitals, which are directed towards ligand anions and are sensitive to deviations from Ti O_h symmetry. Consequently, the absence of splitting of e_g states into $d(z^2)$ and $d(x^2-y^2)$ suggests that for TiO_x-nanoribbon Ti occupies sites with high O_h symmetry in contrast to sites with distorted O_h symmetry in TiO_2-anatase.

The normal incidence NEXAFS spectra were measured with $\bar{E}$ parallel and perpendicular to the principal axis of the nanostructure. No strong evidence for anisotropic distribution of Ti

sites can be observed. Conversely, the O 1s spectra suggest anisotropic distribution of O sites. The O 1s transitions identified as t_{2g} and e_g in the spectra result from transitions to final states, $3d(2t_{2g})^1(1s)^{-1}p^6$ and $3d(3e_g)^1(1s)^{-1}p^6$. The energy separation between t_{2g} and e_g (crystal field splitting) is 2.5 eV, in close agreement with the value measured in the Ti 2p spectrum.

This work shows the high potential for the TXM-NEXAFS for study isolate low-dimensional nanostrutures.

Electronic structure and bonding in tetrakis-pyridyl porphyrins

S.I.Bozhko[1], V.S.Bozhko[1], M.M.Brzhezinskaya[2,4], G.Dyker,[3] A.M.Ionov[1], L.V. Yashina[5]

[1]*Institute of Solid State Physics, 142432 Chernogolovka, Russia*
[2]*BESSY GmbH, Albert-Einstein-Str. 15, 12489 Berlin, Germany;*
[3]*Ruhr-Universitat Bochum, Universitatstrasse 150, D-44780 Bochum Germany*
[4]*Institute of Physics, St. Petersburg State University, 198904 St. Petersburg, Russia*
[5]*Moscow State University, 119899 Moscow, Russia*

Organic molecular films of porphyrins have attracted attention over the past years in view of potential applications in electronic devices. One of the most exciting properties of compounds is the ability to control electronic properties and spin states of porphyrins by optical excitation and introducing charge carriers which is important for molecular electronics. For understanding and tailoring their properties knowledge of electronic structure and bonding in these compounds is required. As shown in [1-3] in a wide class of porphyrins one can vary electronic state by ligands and metal doping. The occupied and empty states of porphyrins which are involved in chemical bonding are essentially responsible for promising properties and should be studied.

In present project electronic structure and chemical bonding in tetrakis- (tetrakis-3 and -4-pyridyl) porphyrins were studied by UPS and XPS photoemission spectroscopy and XAS spectroscopy. To obtain this information high resolution of N1s, C1s, valence band and absorption spectra were measured at Russian-German beamline at BESSY (MUSTANG Phoibos 150 electron analyzer) in the photon energy range 100-1000 eV. The base pressure in the UHV chamber for measurements was about 5×10^{-10} mbar. The angle of the incident photons was kept fixed at 67° relative to the sample surface normal. We measured normal emission valence band and core level spectra. Total resolution (electron plus photons) was about 120 meV.

Chemically (drop coating chloroform solution of the compounds and UHV *in situ* organic molecular beam deposited films (from oven with temperature at 590K onto Si/Au, In, layered Bi_2Te_3 and SnS surfaces at room temperature) of porphyrins were studied The chemically deposited samples were additionally cleaned *in situ* by resistive heating up to ~ 400 K. Preliminary experiments on possible interaction of porphyrins with Pt under direct UHV deposition also were performed.

We have examined the electronic structure of valence band and core levels of pristine tetrapyridyl-3,4-porphyrins using synchrotron radiation PES.

XPS spectra of N1s levels for TPy4P are shown in Fig.1. Similar results were obtained for TPy3P porphyrin. In TPy-porphyrins XPS spectra three peaks structure of N1s states with binding energies 400.1, 399.2 and 398 eV were assigned to pyrrol, pyridyl, and aza nitrogen

respectively (similar to [3]). Different peaks observed in the C1s spectra are related to the unequivalent C atoms in the porphyrin molecules (aromatic and C-N-C groups) as well as shake-up HOMO-LUMO satellite.
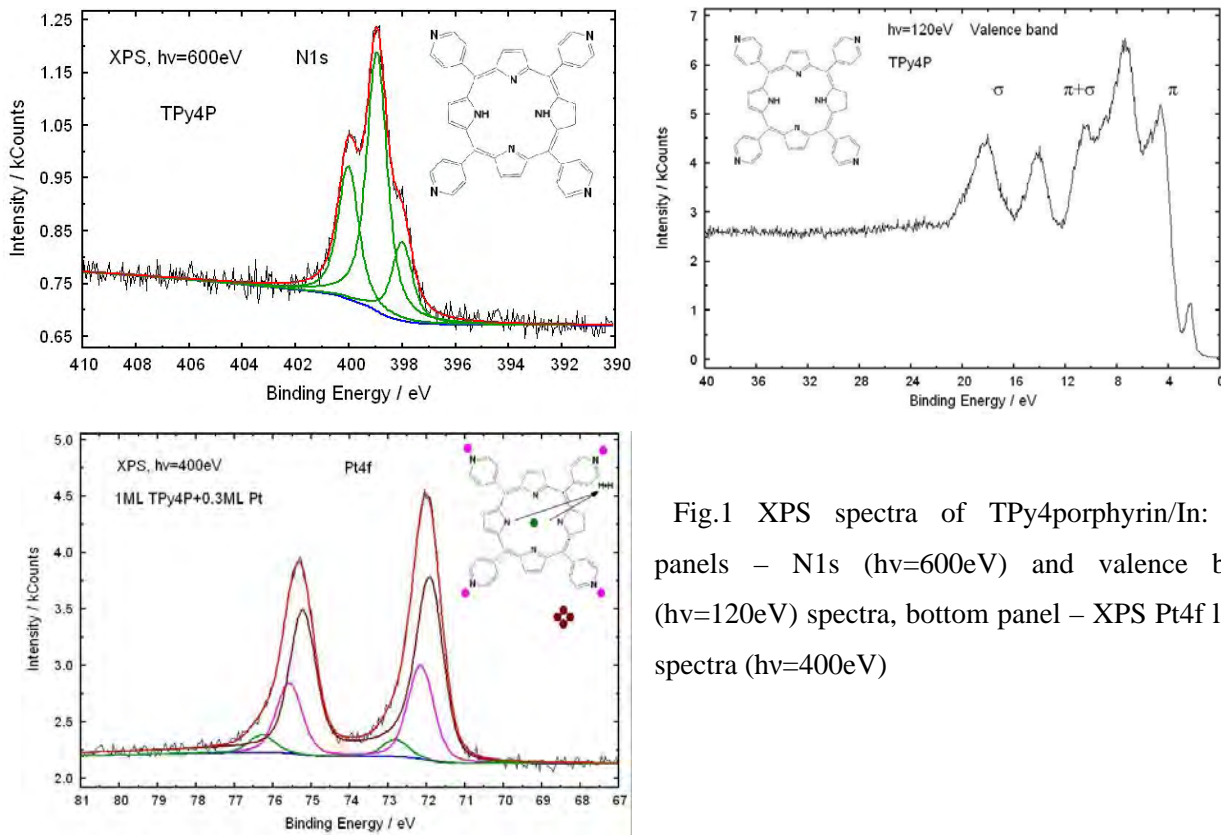
Fig.1 XPS spectra of TPy4porphyrin/In: top panels – N1s (hv=600eV) and valence band (hv=120eV) spectra, bottom panel – XPS Pt4f level spectra (hv=400eV)

UPS studies of VB (performed at photon energy 120 eV) of TPy-porphyrins show that the valence band is mainly formed by peaks corresponding to π (2- 10 eV) and σ states (8-16 eV) of porphyrin macrocycles. Peak of C2s states in lied at about 18 eV in VB spectra.

The C K-edge spectra of NEXAFS spectra of multilayer films (UHV sublimation in situ) of pyridyl-porphyrins exhibit resonances at 284 eV and 287 eV which could be attributed to excitation into unoccupied orbitals located on the porphyrin ring aromatic system. Similar the N three parts K-edge spectra connected with the three different nitrogen atom types were observed in NEXAFS spectra of these compounds.

UHV deposition of a small excess of Pt atoms on this 2HTPyP monolayer results in the complex signal of Pt shown in Fig. 1 and changes in N1s spectra. The simplest possible approach to interpreting the complicated Pt signal assumes that it arises from a mixture of the product of metalation Pt in TPyP (with base and pyridyl group), and unreacted Pt. Further evidence for the existence of this species is provided by the Pt 4f XPS spectra in Figure 1, in which intermediate states of Pt are observed. The respective signal components (Figure 1, magenta line) are located at 72.1 eV), i.e., between the signal of unreacted Pt clusters 71.8 eV, (brown line) and PtTPy4P (72.7 eV, green line).

Preliminary photoemission studies have apparently demonstrated the interaction of monolayered film of TPy4-porphyrin with Pt on the surface after deposition in situ in UHV and changing of Pt4f states and N1s spectra.

Acknowledgement

References.

1.G.Polzonetti et.al. Chem.Phys. 296, (2004) 87.
2.M.P. de Jong et.al. Phys.Rev.B 72 (2005) 035448.
3. F. Klappenberger, A. Weber-Bargioni, W. Auwarter, M. Marschall, A. Schiffrin, and J. V. Barth, JOURNAL OF CHEMICAL PHYSICS **129**, 214702 _2008_

Characterization of self-assembled monolayers of terphenylthiols with amine head groups

P. Dietrich[1], N. Graf[1], T. Gross[1], A. Lippitz[1], B. Schüpbach[2], A. Terfort[2] and W. E. S. Unger[1]*

[1] BAM Bundesanstalt für Materialforschung und -prüfung, VI.43 – Surface and Thin Film Analysis, D-12203 Berlin, Germany

[2] Anorganische Chemie, Philipps-Universität Marburg, , D-35032 Marburg, Germany

Self-assembled monolayers (SAMs) of thiols on gold are unique systems to tailor surface structures and their chemical nature. For this reason they were investigated intensively over the past decades.[1] Especially for high-throughput diagnostic applications thiolate based SAMs on gold can be used as platform to immobilize different biological structures (e.g. peptides, proteins, DNA, carbohydrates). Therefore adequate functional head groups and the knowledge of the basic surface chemistry are a prerequisite.

Within a program to improve microarray performance we studied different aminated surfaces.[2-4] Herein we report on the analysis of SAMs on gold based on ω-aminoterphenyl substituted alkanethiols. These monolayers were analyzed by XPS (X-ray Photoelectron Spectroscopy) and NEXAFS (Near Edge X-ray Absorption Fine Structure) spectroscopy at BESSY to gain deeper insight into their structural and chemical nature.

The surface chemistry and reactivity of the amino groups was tested in a qualitative manner by chemical derivatization using the amine-reactive isothiocyanate reagent **ITC**.
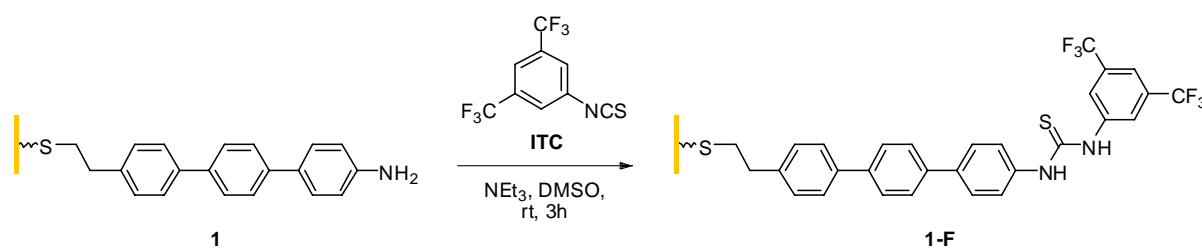
Scheme 1: Derivatization of 2-(4''-amino-1,1':4',1''-terphenyl-4-yl)ethane thiol (**1**) with 1-isothiocyanato-3,5-bis(trifluoromethyl)-benzene (**ITC**).

In Figure 1 high-resolution C1s XP spectrum of thiolate **1-F** after reaction with **ITC** on gold is shown exemplarily.
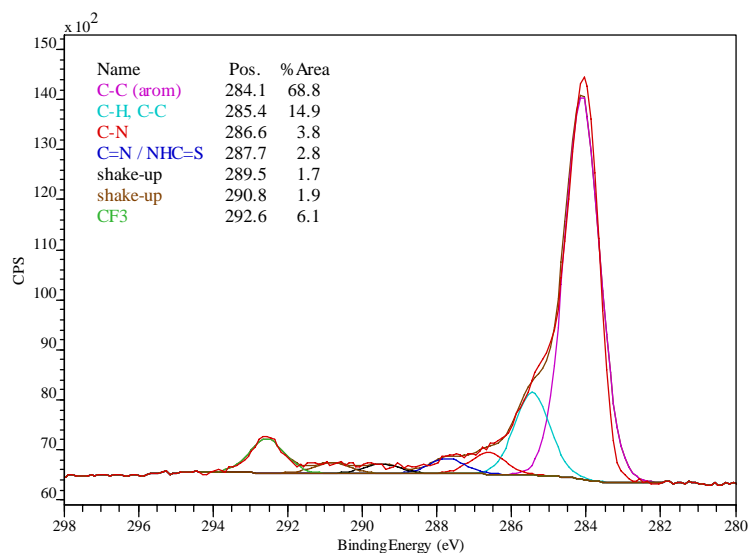
Figure 1: High-resolution C 1s XP spectrum of a derivatized **1-F** SAM.

After chemical derivatization the most distinct peak in the C 1s region of **1-F** is the signal at 292.6 eV originating from newly incorporated CF_3 groups after successful reaction with **ITC**. This interpretation is supported by signals at 287.7 eV in the C 1s and at 399.8 eV in the N 1s (not shown) caused by carbon and nitrogen atoms of the thiourea moiety.

NEXAFS analysis provides both chemical and structural information and can be used to determine a preferential orientation of the molecular moieties within the monolayer with respect to the surface normal. For this purpose NEXAFS measurements were done at BESSY's HE-SGM beam line at different angles (20°, 55°, 90°) of the incidence synchrotron light.

Figure 2 illustrates the C K-edge NEXAFS of the terphenyl SAMs **1** and **1-F**. The most intense resonance of both spectra at 285 eV is associated with transitions to $\pi^{*}_{(C=C,C=N)}$ orbitals of the aromatic backbone. The spectra show further contributions due to σ^{*} resonances at 288 eV (C-H) and 292 eV (C-C, C-N).

After chemical derivatization the C K-edge NEXAFS of the fluorinated SAM **1-F** changes noticeably compared to **1**. The peak at 295 eV can be assigned to excitations into the $\sigma^{*}_{(C-F)}$ orbitals of the CF_3 groups whereas $\pi^{*}_{(C=C-N)}$, $\pi^{*}_{(C=S)}$, and π^{*}_{ring} resonances are found at 286.4 eV, 287.8 eV and 289.0 eV.
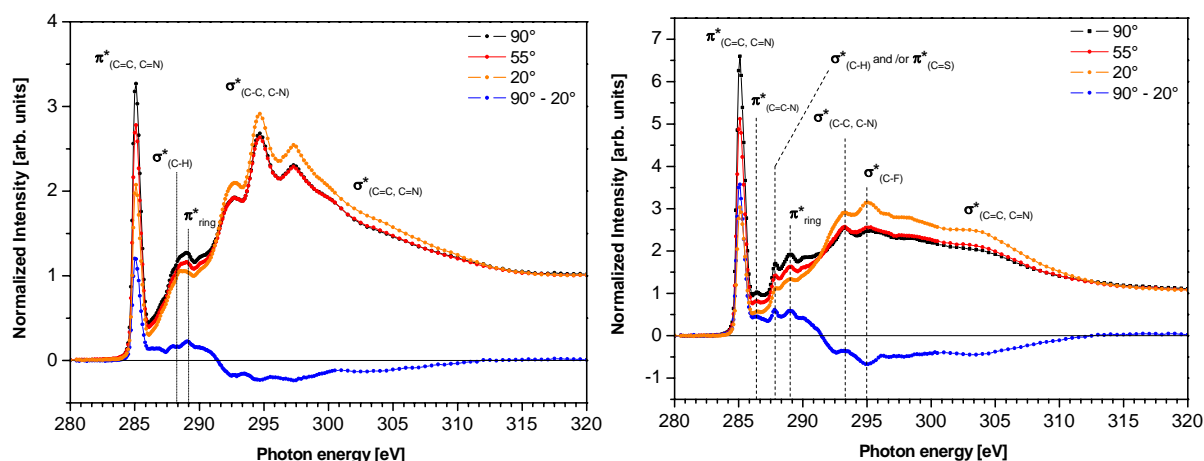
Figure 2: C K-edge NEXAFS at three different angles of incidence of linear polarized synchrotron light (90°, 55°, 20°) and the difference spectrum (90°-20°) of **1** (left) and its fluorinated analog **1-F** (right).

The intensity of the π^* resonance at 285 eV depends on the incident angle of the synchrotron beam[5]. This phenomenon is known as linear dichroism effect.

Using this relation an average tilt angle of $\alpha = 62°$ for the π orbitals of the aromatic ring system in monolayer **1** was determined. And after reaction with the isothiocyanate **ITC** the average tilt angle was slightly increased to 66°. These results indicating that the preferred orientation within the monolayer **1-F** remains unaffected by the chemical derivatization reaction.

These studies will be extended to other SAMs based on aromatic thiols with amino groups in order to quantify the amount of reactive sites on the surface by chemical derivatization XPS.

References

[1]   J. C. Love, L. A. Estroff, J. K. Kriebel, R. G. Nuzzo, G. M. Whitesides, *Chemical Reviews* **2005**, *105*, 1103.
[2]   N. Graf, E. Yegen, T. Gross, A. Lippitz, W. Weigel, S. Krakert, A. Terfort, W. E. S. Unger, *submitted to Surf. Sci.* **2008**.
[3]   N. Graf, E. Yegen, A. Lippitz, D. Treu, T. Wirth, W. E. S. Unger, *Surface and Interface Analysis* **2008**, *40*, 180.
[4]   N. Graf, E. Yegen, A. Lippitz, W. E. S. Unger, in *BESSY Annual Report 2007, Berlin*, **2007**, pp. 107.
[5]   J. Stöhr, *NEXAFS Spectroscopy*, Springer, Heidelberg, Germany, **1992**.

Electronic structure of LaFeAsO$_{1-x}$F$_x$ from Photoemission Spectroscopy

A. Koitzsch[1], D. Inosov[1], J. Fink[1,2], M. Knupfer[1], H.Eschrig[1], S. V. Borisenko[1], G. Behr[1], A. Köhler[1], J. Werner[1], B. Büchner[1], R. Follath[2] , and H. A. Dürr[2]

[1] *Institute for Solid State Research, IFW Dresden, P.O. Box 270116, D-01171 Dresden, Germany.*

[2] *BESSY GmbH, Albert-Einstein-Strasse 15, 12489 Berlin, Germany*

The recent discovery of the superconducting oxypnictides has sparked immediate and intense scientific effort. Superconducting transition temperatures up to T_c = 43 K have been reached for LaFeAsO$_{1-x}$F$_x$ [1, 2]. LaO$_{1-x}$F$_x$FeAs crystals consist of alternating LaO$_{1-x}$F$_x$ and FeAs layers. It is assumed that the LaO$_{1-x}$F$_x$ layers serve as ionic charge reservoirs for the covalently bound metallic FeAs layers where the superconductivity appears. According to band structure calculations the density of states in the vicinity of the Fermi energy is dominated by iron character [3].

Here we report on angle integrated photoemission measurements of LaFeAsO$_{1-x}$F$_x$ (x = 0, 0.1, 0.2). We have measured the photointensity of polycrystalline material for various excitation energies ranging from hν = 15 eV to hν = 200 eV at T = 30 K. Polycrystalline samples of La-FeAsO$_{1-x}$F$_x$ were prepared by using a two-step solid state reaction method, similar to that described by Zhu et al. [4]. The crystal structure and the composition was investigated by powder X-ray diffraction (XRD) and wavelength dispersive X-ray spectroscopy (WDX). Critical temperatures of $T_c \approx$ 23 K and $T_c \approx$ 10 K for x = 0.1 and x = 0.2, respectively, have been extracted from magnitization and resistivity measurements. The undoped sample shows a transition to a commensurate spin density wave below T_N = 138 K [5]. The data were measured using synchrotron radiation at the "1^3" ARPES station with a Scienta R4000 spectrometer at BESSY. The samples have been scraped *in situ* before measurements at a pressure of p = 1 · 10^{-7} mbar. The base pressure in the measurement chamber was p = 1 · 10^{-10} mbar.

Figure 1 presents the valence band of undoped LaFeAsO taken with different photon energies. The spectra have been normalized to the high energy shoulder of the broad peak centered at about E ≈ -5 eV (marked by the arrow). We compare the experimental data to LDA based orbital resolved density of states (DOS) calculations in panel (b). The main features of the valence band for all photon energies are a peak near the Fermi energy at E ≈ -0.25 eV and the broad peak around E ≈ -5 eV. The inset of panel (a) shows a zoom of the vicinity of E$_F$ for hν = 15 eV. The Fermi edge appears as a small slope change at the low energy tail of the spectral weight. In between the near E$_F$ peak and the broad peak a plateau-like region is observed with a small peak at E ≈ 1.7 eV. The broad peak has a complex structure and consists at least of two separate features. The low energy peak and the broad peak, have a significant dependence on the photon energy. The center of gravity of the broad peak shifts towards lower energies due to the intensity increase of the low energy shoulder, which becomes more intense than the high energy shoulder at hν = 95 eV. The presented spectra are taken at T = 30 K, but no major changes are observed when crossing the magnetic ordering temperature T_N = 138 K.

The reason for the hν dependent intensity variations lies in the hν dependence of the photoemission cross section. The opposite behavior of the high energy shoulder of the broad peak and the low energy peak suggests that they arise from different atomic orbitals. We show the energy dependence of the cross section of the potentially important valence orbitals, namely Fe 3d, As 4p, and O 2p as a function of photon energy in Fig 1c. As 4p is important for low

energies (< 25 eV) only. For energies above ~ 25 eV the spectra will be governed by Fe 3d and O 2p emission. For increasing photon energy Fe 3d dominates. Fig 1d shows the ratio of the cross sections Fe 3d/O 2p (blue line). It increases monotonically in the measured range and reaches a value of 6.5 for $h\nu$ = 200 eV. Motivated by the increase of the low energy peak and the decrease of the high energy shoulder with increasing $h\nu$ we assume, that the former is due to Fe 3d and the latter is mainly due to O 2p. We evaluate the intensity of the low energy peak by taking the integral from zero to E = -1 eV without any background treatment (red box). Since we normalized the spectra to the high energy shoulder this integral value corresponds automatically to the experimental intensity ratio. Those values are plotted in Fig. 1d as red points. We find satisfactory agreement and conclude *a posteriori* the correctness of our assumptions.

To conclude we have investigate the electronic structure of the iron arsenide superconductor of $LaFeAsO_{1-x}F_x$ and find gross agreement to band structure calculations. In particular the Fe character of the states near the chemical potential is confirmed.
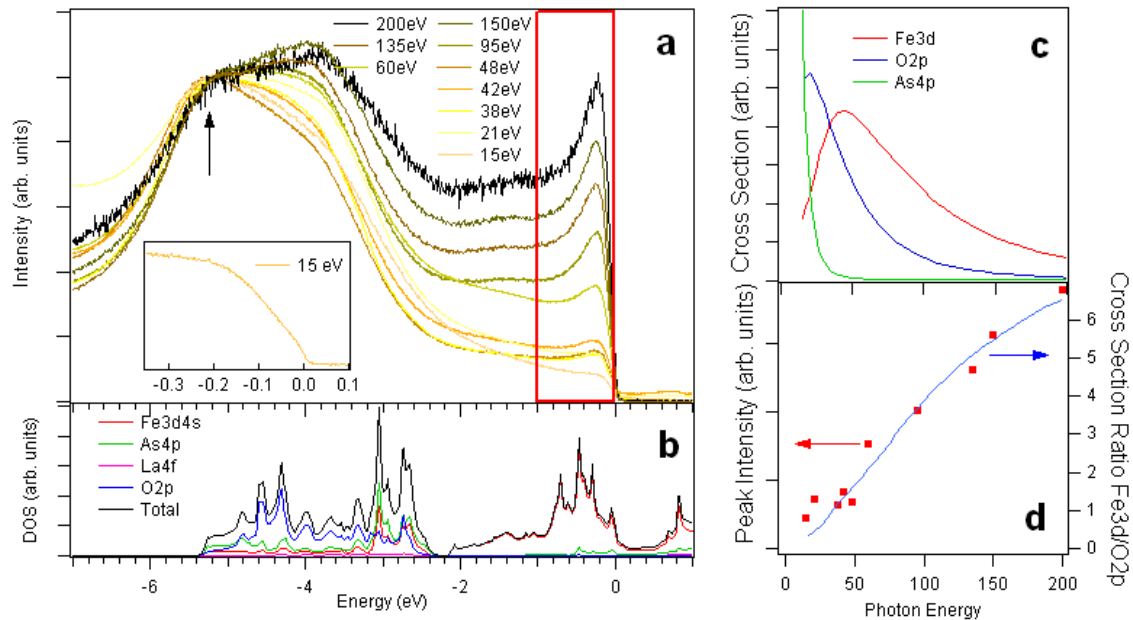
Figure 1: *(a) hv dependent photoemission valence band spectra of LaFeAsO. The arrow marks the point of normalization. The red rectangle is the integration window for the low energy weight shown in panel (d); the inset shows the near E_F region for hv = 15 eV. Note the small change at E = 0 which indicates the Fermi edge. (b) LDA derived orbital resolved. (c) Atomic photoemission crosss section for the relevant orbitals [6]. (d) Ratio of the Fe 3d and O 2p cross section from (c) (blue line) compared to experimental values obtained by integrating the low energy peak.*

[1] Kamihara et al. J. Am. Chem. Soc. **130**, 3296 (2008)
[2] H. Takahashi, Nature **453**, 376 (2008)
[3] H. Eschrig, *arXiv:0804.0186*
[4] X. Zhu et al., Supercond. Sci. Technol. 21 (2008) 105001
[5] H.-H. Klauss et al., Phys. Rev. Lett. 101, 077005 (2008)
[6] J. J. Yeh and I. Lindau, Atomic Data And Nuclear Data Tables **32**, 1-155 (1985)

Temperature dependence of sublattice magnetization in Heusler alloys

M. Kallmayer, P. Pörsch, T. Eichhorn, H. Schneider, C.A. Jenkins, G. Jakob, H. J.Elmers

Institut für Physik, Johannes Gutenberg-Universität Mainz, D-55128 Mainz, Germany

Introduction

NiMn-based Heusler-type intermetallic compounds have recently attracted much attention because Ni_2MnGa has shown huge magnetic shape memory effects [1]. In Ni_2MnGa based Heusler compounds a martensitic transformation from a $L2_1$ parent phase to a martensite phase of lower symmetry occurs at a specific temperature [2]. The martensitic transformation temperature (T_m) of Ni_2MnGa based compounds, being below room temperature for the stoichiometric Ni_2MnGa compound (202 K), is very sensitive to the composition and increases up to 410 K for slightly off-stoichiometric compounds $Ni_{1.96}Mn_{1.22}Ga_{0.82}$. The addition of further constituents, i.e. Fe and Co [3] can remarkably change T_m and further magnetic properties, too. Theoretical investigations [4,] revealed the importance of the electron to atom ratio e/a for the martensitic transformation.

A recent X-ray absorption spectroscopy (XAS) study [5] uncovered the characteristic change of the density-of-states (DOS) function in Ni_2MnGa at T_m as predicted in Ref. [6]. Here, we apply circular dichroism in XAS (XMCD) to investigate changes with temperature and composition of element-specific magnetic moments and of the DOS in order to test theoretical predictions [6,7]

Experimental

Single crystalline Ni_2MnGa based films were prepared as described in Ref. [5].The Ni_2MnGa and $Ni_{1.96}Mn_{1.22}Ga_{0.82}$ films were sputtered from targets with the denoted composition. The $(Ni_2MnGa)_{1-x}(Co_2FeSi)_x$ films were prepared by sequential sputtering of thin layers with subsequent annealing. XAS revealed an intermixing of the latter samples.

Results reported here were derived from transmission measurements unless stated otherwise [8]. The magnetization of the sample was switched at each energy step by applying a magnetic field of 1.6 T perpendicular to the sample. The absorption constant is calculated by $\mu d = \ln(I/I_{ref})$, where d is the thickness of the sample, μ the absorption coefficient and I_{ref} the reference luminescence signal linearly extrapolated from energies below the respective L_3 absorption edges.

Results for Ni_2MnGa

Ni_2MnGa/Al_2O_3(11-20) films show a martensitic phase transition at T_m = 275 K [5] as determined by X-ray diffraction. A satellite peak observed at 3.8 eV above the absorption edge for the austenitic phase is nearly suppressed in the martensitic state (see bottom panel of Fig. 1).To first order absorption intensity at
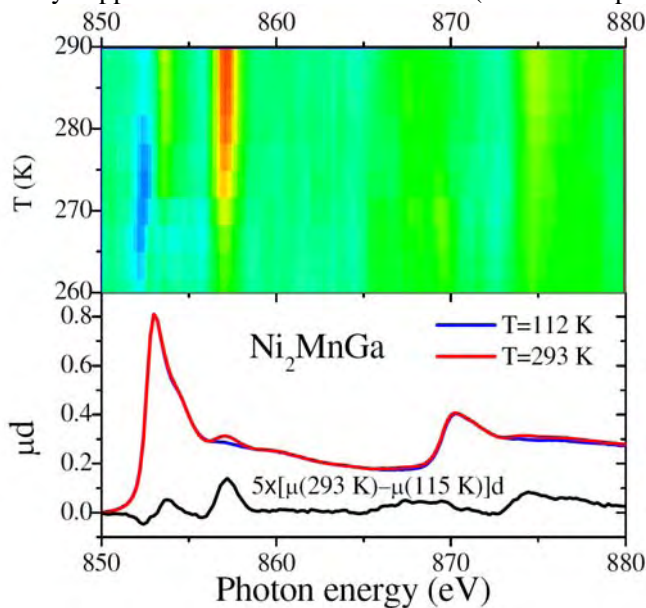
Figure 1. Difference of the Ni XAS spectra (black line) measured at the indicated temperature and at low temperature (115 K) indicated by a color code (blue means negative values, yellow means positive values. Ni XAS spectra for 115 K (blue line) and 293 K (red line) and the corresponding difference spectrum (black line) is shown below.

the L_3 absorption edge is proportional to the DOS of unoccupied states above the Fermi edge. The same holds for the L_2-edge which is, however, broadened compared to the spectra at the L_3 edge. Accordingly, the observed change of the spectra can be explained by a change of the electronic structure. The suppression of the satellite peak in the martensitic state is due to the lift of degeneracies in the Ni 3d related unoccupied electronic states as predicted by ab initio calculations [6] .

For a detailed study of the spectral change we measured XAS for a series of temperatures covering the phase transition region around T_m with data acquisition at 3 K steps. Fig. 1 emphasizes the temperature dependence of the electronic structure in the region of T_m. The Fermi edge is located near the initial increase at the L_3 edge. The difference of the high and low temperature XAS signal reveals a minimum close to E_F and an additional maximum above the L_3 absorption maximum in addition to the appearance of the 3.8 eV satellite discussed before. The initial minimum of the difference indicates a decrease of the local DOS at E_F when the system enters the high temperature cubic phase. This is also in agreement with the theoretical prediction [6]. In order to follow the temperature dependence we plot the difference as a color map with minima indicated in blue and maxima indicated in red. The prominent feature is the rise of the 3.8 eV satellite close to $T_m = 275$ K. In the same temperature region the minimum at E_F reveals a subtle shift of 250 meV to higher energy. The shift of the minimum indicates a shift of electronic states across the Fermi edge which might be the origin of the martensitic phase transition.

Result for $Ni_{1.96}Mn_{1.22}Ga_{0.82}$

Due to the increased Mn content the martensitic phase transition in $Ni_{1.96}Mn_{1.22}Ga_{0.82}$ films, increases to $T_m = 410$ K. The magnetic moment of both Ni and Mn is smaller for the non-stoichiometric compound. The sum rule analysis results in a total reduction of of the magnetic moment of 40 % at 300 K and 10 % at 115 K, also indicating a stronger temperature dependence for $Ni_{1.96}Mn_{1.22}Ga_{0.82}$ (see Table 1). The ratio of the Ni and Mn spin moments of 0.12 remains the same for Ni_2MnGa and $Ni_{1.96}Mn_{1.22}Ga_{0.82}$. A reduction of magnetic moments for non-stoichiometric Ni_2MnGa compounds was predicted by theory [9]. According to this model the magnetization should decrease linearly with the deviation

		Ni_2MnGa		$Ni_{1.96}Mn_{1.22}Ga_{0.82}$	
		115 K	293 K	115 K	293 K
μ_{spin}	Mn	2.50(7)	2.33(7)	2.09(7)	1.44(7)
	Ni	0.31(2)	0.27(2)	0.24(2)	0.17(2)
μ_{orb}	Mn	0.06(5)	0.03(5)	0.01(4)	0.03(3)
	Ni	0.05(1)	0.04(1)	0.02(1)	0.01(1)
μ_{sum}		3.28(11)	2.99(11)	3.08(11)	2.15(11)
μ_{mag}		3.3(3)	at 10 K	3.0(3)	at 10 K

Table 1. Magnetic moments (in µB per atom) for Mn and Ni in Ni_2MnGa and $Ni_{1.96}Mn_{1.22}Ga_{0.82}$ films as derived from a sum rule analysis. The summarized magnetic moment per formula unit μ_{sum} is compared to the magnetic moment per formula unit μ_{mag} measured by SQUID(VSM) magnetometry.

from the average number of valence electrons per atom, e/a, starting from a maximum value of 4 µB per atom at e/a = 7.5 for Ni_2MnGa. For $Ni_{1.96}Mn_{1.22}Ga_{0.82}$ one accordingly expects a value of 3.5 µB per atom [9]. The relative decrease, 3.5/4, is in rough agreement with our result for films, 3/3.3, however, absolute values are considerably smaller for both compounds.

Result $(Ni_2MnGa)_{1-x}(Co_2FeSi)_x$

A composition of $(Ni_2MnGa)_{1-x}(Co_2FeSi)_x$ represents a mixture of two Heusler compounds with an equal number of valence electrons per atom, e/a = 7.5. For a $(Ni_2MnGa)_{1-x}(Co_2FeSi)_x$ film $T_m = 250$ K is reduced compared to the Ni_2MnGa film. We attribute this reduction to the influence of the Co_2FeSi content favoring the cubic structure. The temperature dependence of magnetic moments shown in Fig. 2 reveals a similar behavior as in the case of Ni_2MnGa films (see Ref. [5]). The step-like increase of the Ni spin moment and the peak-like maximum of the Ni orbital moment is well reproduced although the latter appears strongly suppressed. Contrarily the spin moment shows a pronounced maximum and the orbital moment a minimum near T_m. This behavior might be induced by the lowest atomic symmetry present just at the phase transition. The Co and Fe spin moments are smaller compared to moments measured for Co_2FeSi films ($\mu_{spin}(Fe) = 2.5$ µB, $\mu_{spin}(Co) = 1.3$ µB), while the orbital moments are increased. Smaller

spin moments could be intuitively expected for Co and Fe since they are interdiffused into the Ni_2MnGa host with smaller average magnetization.
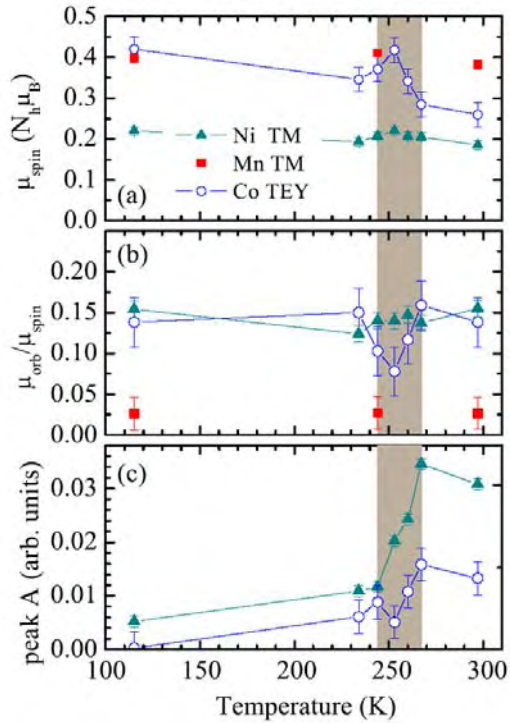
Figure 2.(a) Effective spin moments per d-hole, N_h, for Mn (red squares), Co (blue circles) and Ni (cyan triangles) and (b) orbital to spin momentum ratio for Mn (red squares), Co (blue circles) and Ni (cyan triangles) for a 100 nm $(Ni_2MnGa)_{0.975}(Co2FeSi)_{0.025}$ (110) film on $Al_2O_3(11\text{-}20)$. (c) The increase of the peak area (after linear background subtraction) of the satellite peak A observed 3.8 eV above the Ni L_3 (cyan triangles) and Co L_3 (blue circles) absorption edge indicates the martensitic phase transition. The temperature range of increasing peak area is marked in gray.

In summary we find an almost temperature-independent ratio of sublattice magnetization in Ni_2MnGa based compounds. An increase of the Mn concentration reduces the Mn and Ni moments. An increase of the Co_2FeSi content leads to an increase in the Mn and Ni moment, and to a decrease in T_m.

[1] K. Ullakko, J. K. Huang, C. Kantner, R. C. OHandley, and V. V. Kokorin, Appl. Phys. Lett. 69 1966 (1996).
[2] P. J. Webster, K. R. A. Ziebeck, S. L. Town, and M. S. Peak, Philos. Mag. B 49, 295 (1984).
[3] V. V. Khovailo et al., JSME Int. J., Ser. A 44, 2509 (2003).
[4] A. T. Zayak, W. A. Adeagbo, P. Entel, and K. M. Rabe, Appl. Phys. Lett. 88, 111903 (2006).
[5] G. Jakob, T. Eichhorn, M. Kallmayer, and H. J. Elmers, Phys. Rev. B 76, 174407 (2007).
[6] J. Enkovaara, and R. M. Nieminen, J. Phys.: Condens. Matter 14, 5325 (2002).
[7] M. Lezaic, Ph. Mavropoulos, J. Enkovaara, G. Bihlmayer, and S. BlÄugel, Phys. Rev. Lett. 97, 026404 (2006).
[8] M. Kallmayer et al., Appl. Phys. Lett. 88, 072506 (2006).
[9] J. Enkovaara, O. Heczko, A. Ayuela, and R.M. Nieminen, Phys. Rev. B 67, 212405 (2003).

Residual stress measurements on PVD-multilayers with various designs

H.-A. Crostack, U. Selvadurai-Laßl, G. Fischer

Lehrstuhl für Qualitätswesen; Universität Dortmund, Joseph-von-Fraunhofer Str. 20, 44227 Dortmund, Germany

1. Introduction

PVD multilayer systems are used as hard coatings of cuttings tools [1]. Due to the coating process and the mismatch of thermo-elastic properties between the metallic and ceramic layers of multilayer system and the substrate (Young's modulus, Poisson ratio, thermal expansion coefficient) high residual stresses and residual stress gradients are induced. These stresses and stress gradients can result in microcracks and the delamination of the coatings. In consequence, the life time of concerned cutting tools will be shortened. A better knowledge about the correlation between the process parameters and the residual stresses is a key factor to prevent this life time reduction. For that reason, PVD-multilayer systems were manufactured with various designs [2] and the residual stresses were analyzed in the layer materials and the substrate using Energy Dispersive Diffraction method available at beamline EDDI of BESSY II.

2. Materials and Methods

The residual stress measurements were performed on the ceramic/metal multilayer system TiAlN/Ti manufactured with the four designs schematically shown in Fig. 1
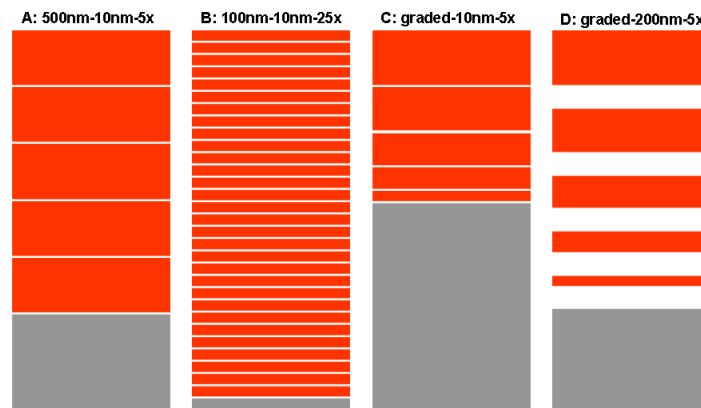
Fig. 1: Designs A - D of analysed PVD-multilayer systems CrAlN/Cr and TiAlN/Cr, ceramic layers -red, metal layer - white, steel substrate - gray, the thickness ratio of layer types is drawn realistically

In case of design A (5 ceramic and metal layers), the metal layer thickness was varied in the range from 10 to 60 nm at a fixed thickness of ceramic layers (500 nm). The multilayer design B (25 ceramic and metal layers) were only studied with the thicknesses of 100 and 10 nm of ceramic and metal layer, respectively. Design C is a multilayer system with graded thickness of ceramic layers and a fixed metal layer thickness (10 nm). In contrast to design C, the metal or amorphous ceramic layer was 200 nm thick. The surface of most substrates were uniform mechanical treated before depositing the multilayer system. To study the effect of mechanical

treatment on the residual stress, the treatment was finished after various grinding and polishing steps for selected. TiAlN/Ti samples with design A.

For X-ray diffraction stress analysis on these multilayers, the materials science beamline EDDI was chosen, which provides X-rays in an energy range between about 10 and 120 keV [3]. The measurements were performed in the energy-dispersive mode which yields diffraction spectra with a multitude of reflections for fixed positions of ω (6°) and 2θ (12°). The residual stresses were analysed by means of the $\sin^2\psi$ -method [4] using X-ray elastic constants calculated from the single crystal constants. Each reflection E(hkl) in the spectrum yield another average information depth and allowed for a depth-resolved analysis of the near surface residual stress fields by extending methods like the multi-wavelength method [5] to the energy-dispersive case of diffraction. By means of these methods, information on the phase-specific in-plane residual-stress state within both layer materials became available. Furthermore, the depth-depending stress states in the subsurface regions of substrate was obtained, too. The subsurface region belongs to the critical failure zones of PVD-coated tools.

3. Results

The diffractograms (Intensity/E) reveal that the crystalline portion of the studied nanocrystalline ceramic and metallic layers is high. Even reflections of 10 nm thin metal layers can be detected. In all samples, the reflections (111) and (200) of TiAlN exist.

In all multilayer systems high compressive residual stresses were found in the ceramic layers (-1.5 and to -5 GPa). The residual stresses in metal layers are also compressive but much lower than in the ceramic layers (-50 and -200 MPa). This effect is due to the stress relaxation by plastic deformation.

A reduction of surface roughness of substrate surface by stepwise finer grinding and polishing before the deposition of the TiAlN/Ti multilayer system increases the compressive residual stress in the TiAlN layers and decreases the compressive residual stress in the substrate region near the coating (Fig. 2). But here the stresses evaluated for TiAlN (111)-reflection are lower than for the TiAlN (200) reflection.
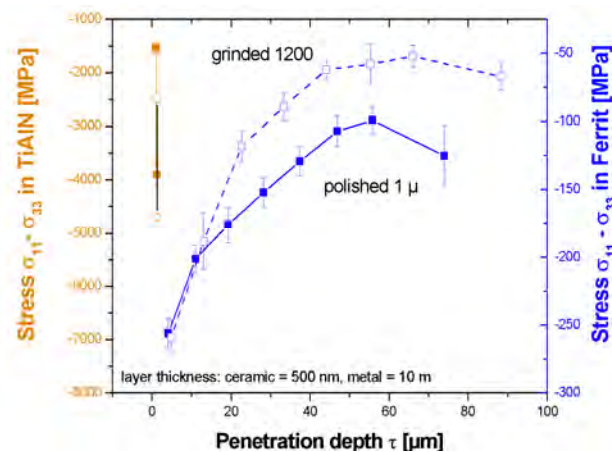
Fig. 2: Effect of substrate preparation on the residual stresses in the TiAlN layer of the multilayer system TiAlN/Ti and the steel substrate, (500 nm ceramic – 10nm metal)

Since in the steel substrate various Fe-reflections could be evaluated, the depth profile of residual stress were analysed near the substrate-multilayer interface. Near the interface similar compressive stresses of about 260± 13 MPa exist in substrate after both preparations. The plot shows that the compressive stresses diminish with increasing distance to the interface (Fig.2). In the sample grinded with 1200 mesh hard particles (open symbols) the stress gradient is steeper. The compressive stress diminishes down to – 60 ± 8 MPa (grinding) and 99 ± 10 MPa (grinding and polishing), respectively.

Correlation between stresses of coating and substrate yields to an influence of substrate preparation on the complete sample. Polishing leads to a decrease of stress values of the ceramic layers, but to an increase of stress values in deeper substrate regions. Further investigations on substrate without any preparation are needed to interpret this effect.

The influence of designs A, B and C was analysed on samples with various TiAlN layer thicknesses (Tab. 1). In thick coating layers with the same thickness (A) the residual stress of ceramic layers are lower than of thin layers (B). But in graded layers (C) the highest value was found. The stress values of metal layer and subsurface substrate behave contrary. Thus in metal and substrate of graded layers the smallest stress values exist. In thin layers the crystal growing process is interrupted in an early stadium and this inhomogeneous state increase residual stresses.

Tab. 1: Residual stresses of TiAlN/Ti multilayers with different design A, B and C.

Design	Layer Thickness of ceramic / metal	Coating thickness [nm]	σ_{11} Fe	σ_{11} TiAlN (111)	σ_{11} Ti (002)
A	500nm / 10nm-5x	500	256±11	-1528±122	-191±43
B	100nm / 10nm-25x	2500	152±12	-3890±117	-144±35
C	Gradiert / 10nm-5x	1500	110±13	-5012±100	-74±27

Multilayer systems with various ceramic and partially amorphous ceramic layer thickness exhibit higher RS (Tab. 2) than systems with thick (500 nm) ceramic and thin metal layers (see design B of Tab. 1).

Tab. 2: Residual stresses of TiAlN/amorph TiAlN multilayers with different design B and D.

Design	thickness TiAlN [nm]	thickness TiAlN amorph [nm]	σ_{11} [MPa] Ferrit	σ_{11} TiAlN 111
B	25x100 nm	25x10 nm	-275±26	-4475±64
D	Σ 1500	5x200 nm	-300±12	-4022±46

4. Acknowledgement

5. References

[1]   T. Hanabusa, K. Kusaka, T. Matsue, M. Nishida, O. Sakata, T. Sato; JSME, Series A, Vol. 47, No. 3, (2004) 312- 317

[2]   W. Tillmann, E. Vogli: Adv. Eng. Mat., 10, No. 1-2, (2008) 79-84

[3]   M. Klaus, I.A. Denks, Ch. Genzel; Mat. Sci. Forum Vol. 524-525 (2006) 601-606

[4]   Ch. Genzel, C. Stock and W. Reimers, Mat. Sci. Eng. A 372 (2004), p. 28.

[5]   Hauk, V., Macherauch, E. (Hrsg.): Eigenspannungen und Lastspannungen (HTM Beiheft), Carl Hanser Verlag München, Wien (1982)

Direct measurement of the electric field in semiconductor junctions using high energy, high resolution x-ray photoemission (HIKE).

Allsop, N.A.; Lauermann, I.; Mönig, H.; Gorgoi, M.; Fischer, Ch.-H.; Grimm, A.; Johnson, B.; Kropp, T.; Lux-Steiner, M. Ch.;

Helmholtz Zentrum Berlin für Materialien und Energie.

One of the key parameters in semiconductor devices is the built-in electric field or band bending which results from the formation of an electronic junction. Band bending is often characterised by capacitance-based methods, however as the defects become more complicated (e.g in thin film solar cells) the interpretation becomes ambiguous.

Traditional PES spectroscopy can only indirectly monitor the band bending in incomplete semiconductor junctions. We have used high kinetic energy PES (HIKE) to directly determine the band bending in completed model semiconductor junctions, including measurements under in-situ applied bias to control the band bending.

High kinetic energy photoemission measurements allow material inspection down to 20 nm depth with high resolution. When measuring semiconductors the emission can change by several 100meV through this depth due to the electric field/band bending. Band bending measurements are not new to the PES community. The shift of the peaks with different doping concentrations [1] or the shift of peaks upon deposition of thin overlayer [2] is often used to follow the band bending. However, these methods involve comparing measurements taken in the presence of unknown surface charges and work function, which are usually presumed to remain constant. Due to the limited depth of conventional PES the normal measurements are rarely able to look at completed semiconductor junctions and therefore the defect occupation can also be substantially different.

Sensitive measurements of the peak shifts are also complicated by changes in the work function or shifts due to realignment of the beam between samples. Therefore we also measured the broadening by fitting the shape of the photoemission peaks, a method which previous studies have argued is not realisable for conventional PES [3].
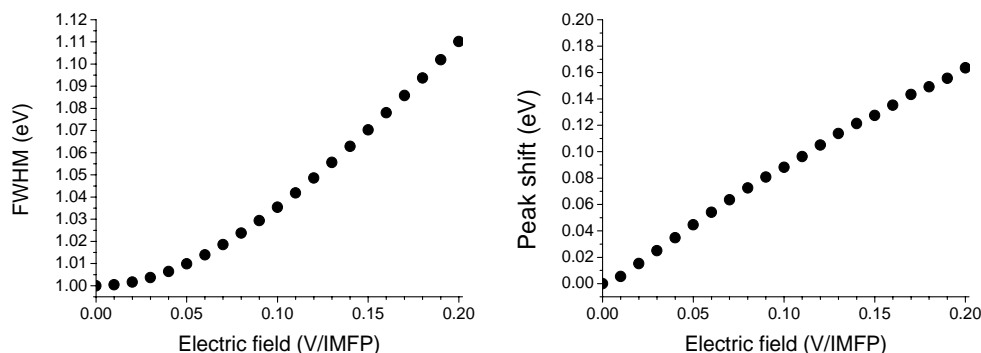
Figure 1. The theoretical broadening and peak shift associated with the electric field in Volts per Inelastic Mean Free Path. A 1eV starting FWHM has been assumed but the field can be normalized to any FWHM.

The samples used were GaAs:Au Schottky contacts (Fig.2). Gold is known to pin the Fermi level at the surface of n-type GaAs to induce a built in voltage of approx. 0.9V. In order to measure the Ga2p and As2p in the completed junction, a very thin 5nm layer of gold was used. In conventional PES this would completely absorb the photoelectrons emitted from the GaAs, however with HIKE we can use an excitation energy of 6keV. The 5nm gold layer is also thick enough to allow a voltage to be applied in-situ.
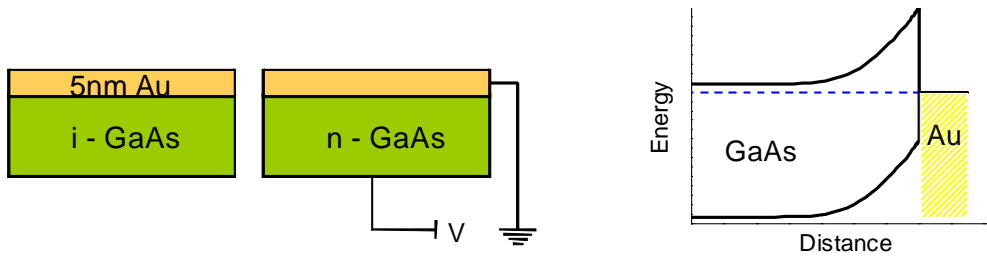
Figure 2. GaAs-Au Schottky contacts

The peak fitting procedure was performed by using the measured peak from the intrinsic GaAs, where no significant field is present, and convoluting this peak with an exponential decay function. The decay function represents the shift in the peak position as the depth increases. An example of the fitting procedure is shown in Fig. 3.
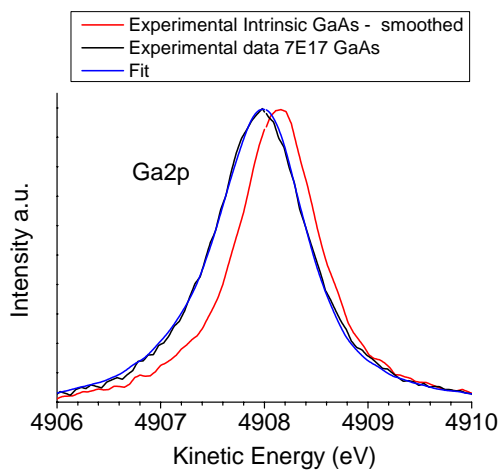
In addition to the intrinsic sample, three n-type GaAs wafers were measured with varying doping concentrations. The doping concentration was independently measured using a capacitance method (Mott-Schottky plot) and the theoretical electric field at the interface calculated using textbook semiconductor equations. The agreement between the field as measured using the peak broadening and the theoretical values based on the capacitance

measurements is shown in Fig 4.

Figure 3. Example of a fitted curve

For the highly doped sample with a strong electric field the agreement is excellent but for the lower doped sample the agreement between the value extracted from the Ga2p and As2p peak is not as good. However, it should not be forgotten that even determining the field strength to within a factor of 2 is often very useful for electronic devices.

In order to further investigate the sensitivity of the technique the peaks were measured under an in-situ applied bias, in order to directly manipulate the electric field at the junction. This time both the shift in the peak position and the broadening was used to estimate the electric field. The results are displayed in Fig 5.
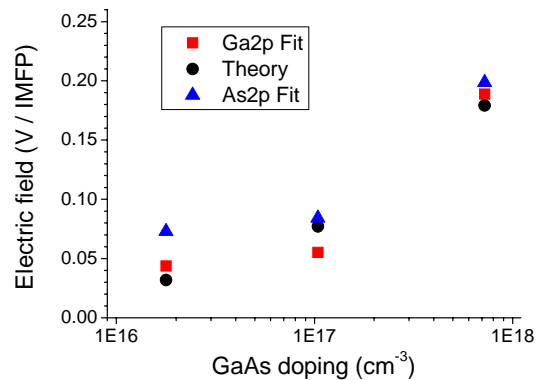
Figure 4. Fitted and theoretical parameters for different GaAs doping levels.
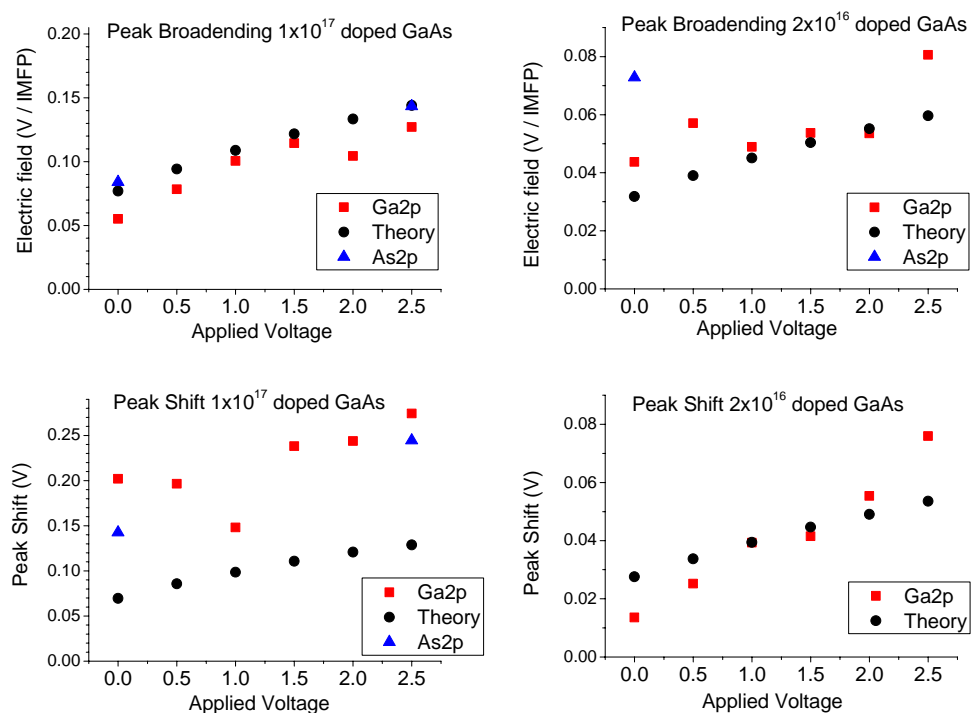
Figure 5. Fitted and theoretical parameters for sample with an in-situ applied voltage. Note that for the peak shift values the slope is most important parameter, a y-axis offset between samples can occur as result of work function changes.

The trends within the plots are clear to see and validate the method as a way of measuring the electric field. However, the number of points which deviate from the trend show that extreme care needs to be taken when making the measurements. We used the 3rd order excitation of the 111 Si crystal on the KMC-1 beamline, with a Be window to reduce the thermal load on the crystal monochromator. This gave the excellent stability which allows shifts of only 10-20meV to be measured under an excitation energy of 6030eV! Any realignment of the system must then be followed by remeasurement of a gold reference peak.

In conclusion we have demonstrated that the measurement of the electric field in a completed semiconductor junction is possible using HIKE. This should provide a new tool to investigate structures such as thin film solar cells and other electronic devices. The technique places a high requirement on the stability of the beam, which the KMC-1 beamline at BESSY is able to provide. Additionally it is clear that when interpreting high kinetic energy PES data of semiconductors and insulators, the effects of band bending and electric field need to be taken into account.

References

[1] W. Eberhardt, G. Kalkoffen, C. Kunz, D. Aspnes, and M. Cardona, Phys. Stat. Sol. (b) 88, pp 135-143, (1978).

[2] E.A. Kraut, R.W. Grant, J.R. Waldrop, and S.P. Kowalczyk. Phys. Rev. Lett, 44, 24, pp1620-1622 (1980).

[3] G. Margaritondo, F. Gozzo and C. Coluzza, Phys. Rev. B, 47, 15, pp 9907-9909 (1993)

Relative Sub-shell Photoionization Cross-sections of Nickel Determined by Hard X-ray High Kinetic Energy Photoelectron Spectroscopy

M. Gorgoi, F. Schaefers, W. Braun, W. Eberhardt

Helmholtz Zentrum Berlin, BESSY II, Albert-Einsteinstr. 15, 12489 Berlin, Deutschland

Recently, high kinetic energy photoelectron spectroscopy has lead to a break-through due to its non destructive way of investigating the bulk electronic properties of materials. However, due to the relatively new development of this technique there is a lack of information concerning the photoionization cross section at high energies. Currently, only calculated atomic cross section data are available [1-4] which have not yet been verified experimentally.

In photoemission, the sub-shell photoionization cross-section is one of the factors that determine the intensity of particular spectral lines and their satellites. In the hard x-ray regime the core level cross-sections are decreasing rapidly, a fact which hinders the experiment considerably. This is now compensated by the photon intensity provided by third generation synchrotron sources. In most of the photoemission experiments ratios of signal intensities or energy shifts in the core levels are followed. For the analysis of these data absolute cross section values are not essential. However, whenever compound materials are investigated or when estimating signal levels and the feasibility of an electron spectroscopy experiment the knowledge of cross sections is essential. Thus the present study concentrates on describing the sub-shell photoionization cross sections of the nickel metal.
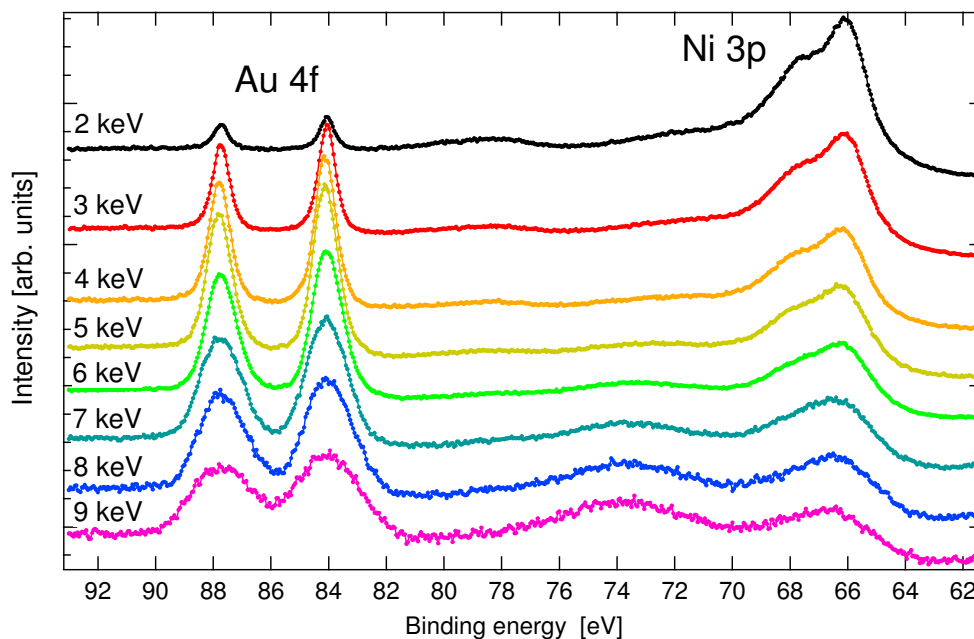
Figure 1. The Ni 3p and Au 4f core level spectra recorded at energies ranging from 2 keV to 9 keV. The normalized spectra were shifted manually on the intensity scale for a better viewing.

Thin layers of Ni were investigated using excitations energies ranging from 2 keV to 9 keV. The measurements were performed at the KMC-1 beamline employing the HIKE end-station. Spectra were recorded in normal emission geometry. The samples were prepared by evaporation in ultra high vacuum (UHV). Ni with a guaranteed purity of 99.999% was purchased from Goodfellow. The thickness of the films was controlled by means of a quartz crystal

microbalance. The final layer thickness was 4 nm. A thick gold film was employed as a substrate. Based on previous experimental studies of Kunz et al. [5] describing the sub-shell cross section for gold, a gold crystal Au(111) sample was also used as reference. In the Ni case the core levels characteristic to the gold substrate were still visible and thus the Au 4f core level was chosen as a reference. The 2s, 2p, 3s, 3p core levels of Ni were recorded in a stepwise like manner. A step of 1 keV in the excitation energy was employed. Moreover, for a thorough intensity calibration of the spectra the flux given by the double crystal monochromator was recorded using the available ionization chamber as well as a GaAs diode that was introduced in the beam for every measurement point.

The following example shows the core level spectra of Ni 3p recorded altogether with the Au 4f core levels corresponding to the gold substrate (Figure 1). As a first evaluation step a normalization procedure to the intensity of the incoming flux was employed. Further on, the level of background on the low binding energy side was subtracted and then for a better viewing of the core level intensity evolution, the spectra were normalized to the high binding energy background side. The intensity evaluation was performed after a thorough fitting of the spectra and after the subtraction of a Shriley background. The peak areas were used in the signal evaluation.
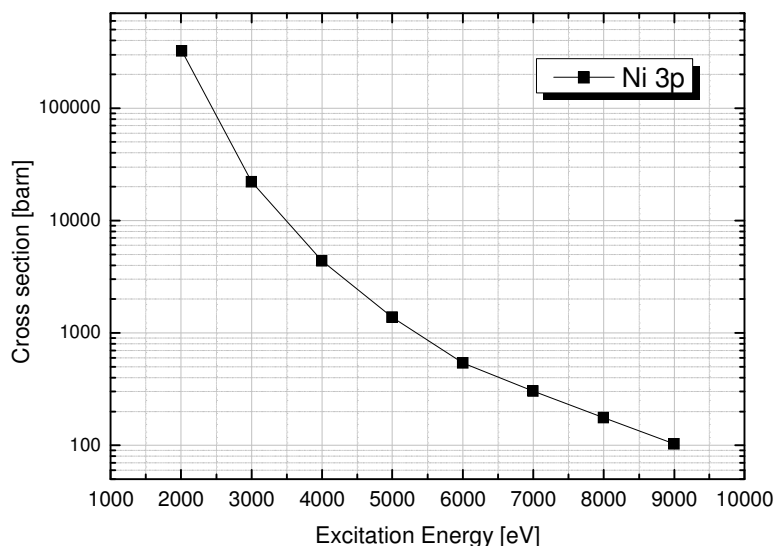
Figure 2. The evaluated cross section of Ni 3p as a function of energy.

In the description of the photoemission signal [6] the angular anisotropy factors were neglected and electron effective attenuation lengths were considered the same for Au and Ni. A preliminary evaluation of the sub-shell photoionization cross sections taking into account the already published values of Au 4f cross sections [5] and the densities of gold and nickel was performed. The result is shown in Figure 2.

For an exact estimation of the sub-shell photoionization cross section values a very good assessment of the electron effective attenuation lengths [5] is required. In order to do that further investigation may be necessary.

[1] J. J. Yeh and I. Lindau, Atomic Data and Nuclear Data Tables **32**, 1-155 (1985)

[2] M. B. Trzhaskovskaya, V. I. Nefedov, and V. G. Yarzhemsky, Atomic Data and Nuclear Data Tables **77**, 97 (2001)

[3] M. B. Trzhaskovskaya, V. I. Nefedov, and V. G. Yarzhemsky, Atomic Data and Nuclear Data Tables **82,** 257–311 (2002)

[4] J.H.Scofield, Lawrence Livermore National Laboratory Report UCRL-51326, 1973.

[5] C. Kunz, S. Thiess, B.C.C. Cowie, T.-L. Lee, J. Zegenhagen, Nuclear lnstruments and Methods in Physics Research A 547, 73-86 (2005).

[6] H. Bubert et al., eds. Surface and Thin Film Analysis. 2001, Wiley-VCH: Weinheim

NEXAFS investigation of graphite-carbon nanotube hybrid system

A.V. Okotrub[a], M.A. Kanygin[a], A.G. Kurenya[a], A.G. Kudashov[a], Yu.V. Lavskaya[a], L.G. Bulusheva[a], S.L. Molodtsov[b]

[a]*Nikolaev Institute of Inorganic Chemistry, SB RAS, Novosibirsk, Russia*
[b]*Institute of Solid State Physics, Dresden University of Technology, Germany*

Angle-resolved near-edge x-ray absorption fine structure (NEXAFS) method has been applied for revealing graphitic layers distribution in the samples of graphene multi-layers and aligned multi-walled carbon nanotubes (CNTs) synthesized by aerosol-assistant catalytic chemical vapor deposition (CCVD) technique.

Arrays of multi-walled CNTs have been grown on the oxidized silicon substrates using an aerosol-assistant CCVD method. A mixture of heptane and ferrocene (2 wt.%) was dispersed into reactor volume with a rate 2 g/h using an injector. The pyrolysis was performed at 800°C and atmospheric pressure in argon flow (150 cm^3/min). The duration of synthesis was 5 min for the sample 1 and 40 min for the sample 2. Short time of the CCVD synthesis resulted in small thickness of the film (Fig. 1(a)). CNTs constituted the sample 1 have length ~1 μm and poor alignment. The thickness of the sample 2 is ~ 12 μm and CNTs have predominantly vertical orientation to the substrate surface (Fig. 1(b)). Bright lines on the image perpendicularly to the direction of CNT growth indicate non-uniform formation of the array. It could be suggested that thin horizontal layer consists of graphenes and iron carbide Fe_3C as it was indicated in [1].

C K-edge NEXAFS spectra were measured at the Berliner Elektronenspeicherring für Synchrotronstrahlung (BESSY) using radiation from the Russian-German beamline. A vertical axis of sample rotation was oriented perpendicular to the electric field vector, which was in the horizontal plane of spectrometer. The spectra were taken for various incidence angles Θ. The NEXAFS data were acquired in a total electron yield mode and normalized to the primary photon current from a gold-covered grid, which was recorded simultaneously. The monochromatization of the incident radiation was better than 80 meV. Before the measurements the sample was heated in the vacuum chamber at ~150°C to remove the adsorbed molecules. The working pressure in the chamber was ~10^{-9} mbar.

NEXAFS spectra measured at the C *K*-edge of the samples 1, 2 for different incidence angles are compared in Fig. 2 (a). The spectra have been normalized to their intensity at 330 eV. The resonances around 285 eV have the π∗-like character, while the features arisen within 291.5–293.0-eV interval correspond to the 1s→σ∗ transitions mainly. The change in the relative intensity of π∗-resonance characterizes orientation of graphitic layers in the samples produced. The inserts in the Fig. 2(a) show the variation in π∗-resonance obtained for different angular positions of sample relative to the incidence beam. One can see that the samples 1 and 2 have opposite angular dependence of π∗-resonance. Increase of the incidence angle Θ causes decrease of the π∗-resonance intensity in the NEXAFS spectrum of the sample 1 and enhancement of that in the spectrum of the sample 2.

Fig. 1. SEM images of the cleavages of sample 1 grown at 800°C for 5 min (a) and sample 2 grown at 800°C for 40 min (b). Thin horizontal layers in the image (b) correspond to graphene layers
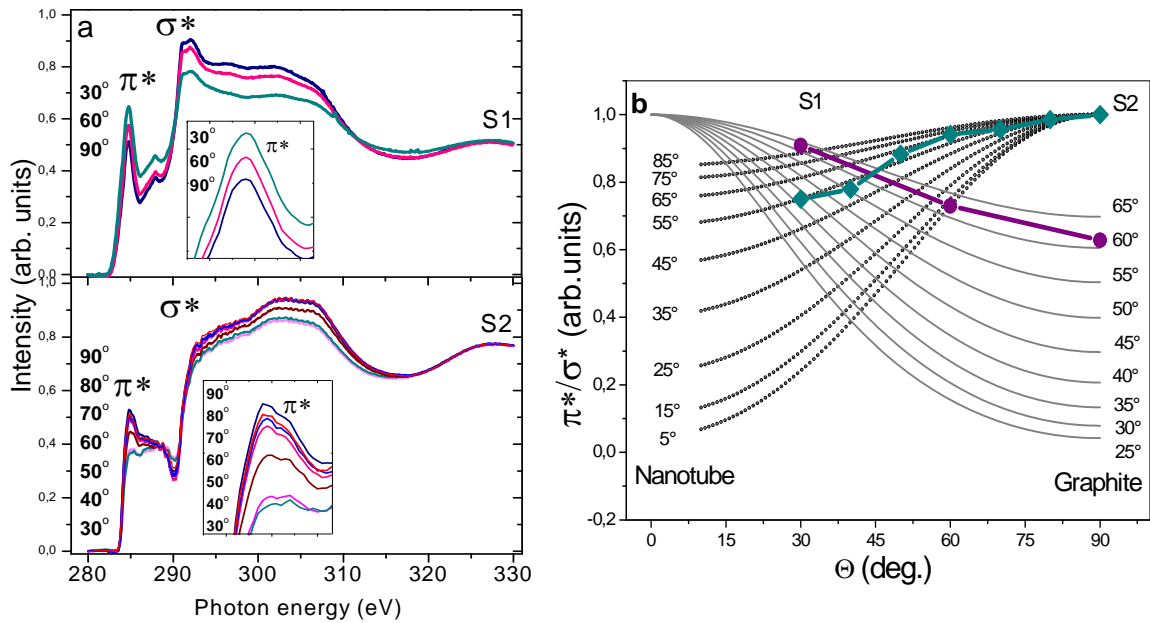
Fig. 2. a – Angular dependence of NEXAFS spectra of the sample 1 (S1 lines) and sample 2 (S2 lines). b – Theoretical dependencies of π*/σ* intensity ratio calculated for different angular distribution of carbon nanotubes and graphite layers in a sample and experimental points derived from the NEXAFS data for the sample 1 (S! line) and sample 2 (S2 line).

To determine the average misalignment of graphitic layers in the samples 1, 2 we used the approaches developed in [2, 3], which consider that graphite consists of crystallites and CNT array is a set of graphitic cylinders. Within these approaches the deviation of crystallites from the basal graphite plane and CNTs from the normal to the substrate surface is described by the Gaussian distributions. The angular dependences of the π*/σ*- intensity ratio calculated for different widths of orientation distribution of graphite crystallites and CNTs are presented in Fig 2 (b). Comparison of the theoretical curves with the experimental data allows making the numerous evaluation of misorientation of graphitic layers in the samples. The angular dependence of the relative intensity of π*-resonance derived from the NEXAFS data of the sample 1 has behavior similar to that of strongly disordered graphite. The width of the angular distribution of graphitic layers equal to ~62° corresponds to the deviation of graphene planes from the silicon surface ±31° in average. The experimental points obtained for the sample 2 follow the dependence expected for aligned CNTs with ~55°-distribution of nanotubes in array (±22.5° deviation from the vertical to the silicon substrate). This dependence is actually characteristic of array of multi-walled CNTs, having a lot of defects and intrinsic texture of the graphitic shells composing a CNT. The angular dependence of π*/σ*- intensity found for the sample 1 was surprised and it undoubtedly indicates formation of graphene layers in the result of CCVD synthesis of CNTs.

In summary, using the angle-resolved NEXAFS method we detected formation of graphitic layers in process of CNT array production. The thickness and perfectness of graphenes could be controlled with changing the parameters (time, temperature, etc.) of the CCVD method.

[1] D. Kondo, S. Sato, Y. Awano, Appl. Phys. Express 1 (2008) 074003.
[2] V.V. Belavin, A.V. Okotrub, L.G. Bulusheva, A.S. Kotosonov, D.V. Vyalykh, S.L. Molodtsov, J. Exp. Theor. Phys. 103 (2006) 604.
[3] A.V. Okotrub, V.V. Belavin, L.G. Bulusheva, A.V. Gusel'nikov, A.G.Kudashov, D.V. Vyalikh, S.L. Molodtsov, . Exp. Theor. Phys. 107 (2008) 517.

2

Local atomic and electronic structure of ferromagnetic AlN_Cu nanorods.

authors: A.V.Soldatov, A.Guda, M.Soldatov
institute: Southern Federal University, Rostov-on-Don, Russia.

Nanostructured AlN – is promising material for nanoelectronics. Its unique properties are well known and can be found somewhere [1]. One can control semiconductor properties of this material and create new ferromagnetic properties by means of doping with transition metal atoms [2,3]. There are already reports about room-temperature ferromagnetic properties of AlN, doped by Fe, Cr and Mn. But there still no realistic theory that can describe ferromagnetism in all kinds of diluted magnetic semiconductors. The main problem is that it is very hard to obtain exact position of dopping atoms in a host lattice. X-ray absorption spectroscopy is unique tool for solving of such problem.
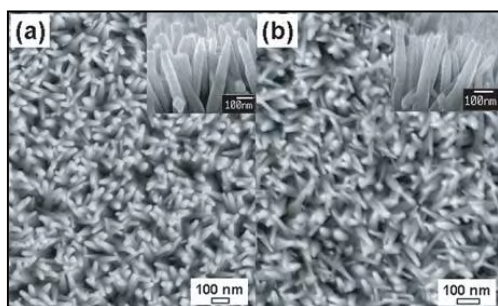
Figure 1. AlN nanorods on Si substrate (a) and Cu doped AlN nanorods on Si substrate (b)
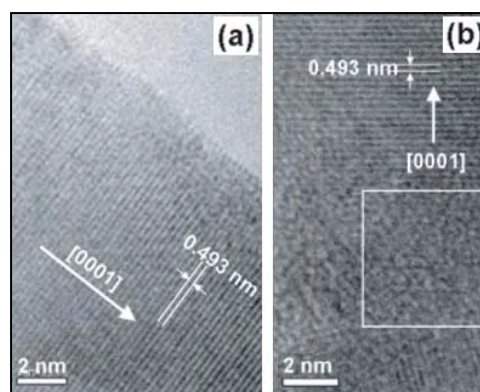
Figure 2. HRTEM image of single AlN nanorod (a) and Cu doped AlN nanorod (b)

AlN:Cu nanorods were prepaired in tube furnace on Si (100) substrate in the presence of $CuCl_2$ during reaction of heating as copper source [5]. The typical diameter and length of the nanorods, as follows from Figure1, is around 20-50 nm and 1 µm respectively. The concentration of the Cu atoms is about 3-5%. The spontaneous magnetization and the coercivity of the AlN:Cu are about 0.38 emu·cm^{-3} and 100 Oe respectively. It is important to note that AlN:Cu material is highly resistive at room temperature ($>10^5$ Ω cm). AlN:Cu nanorod is a single wurtzite AlN crystal with growth direction (0001). HRTEM images of a single nanorod (Figure2) reveal lattice distortions after incorporation of copper atoms.

Cu L2,3 XANES spectra were recorded in a UHV chamber attached to Russian-German beam line (RGBL) of the third generation synchrotron BESSY in Berlin. We used total electron yield (TEY) for absorption signal measurements. Complementary to Cu L2,3 edge also Cu K-edge spectrum from the same sample was measured in NSRL, Hefei, China.

X-ray absorption spectra were simulated, using self-consistent full multiple scattering theory (program package Feff 8.4). It was found that time-dependent LDA works well with Cu L2,3 edges. Magnetic properties of point Cu defects in AlN host lattice using LAPW approximation implemented in Wien2k package were also calculated. Theoretical calculations on Figure3 show that the Cu L2,3 spectrum of AlN_Cu nanorods can not be explained by only Cu point defects, that are embedded into host lattice of AlN. We supposed that small copper clusters can grow during AlN nanorods growing in the presence of $CuCl_2$ in a tube furnace. Theoretical simulations of spectra from clusters in AlN still not finished, but meanwhile we decided to obtain complementary information about atomic structure around Cu atoms from the Cu K-edge. Spectrum for small free Cu clusters was taken from ref [6]. As can be seen from Figure 4 in AlN_Cu nanorods there is a strong probability for cluster creation, but they can have different sizes – from several atoms to several hundred atoms, which resemble bulk copper. A theory of

multidimensional interpolation of spectrum [7] is to be applied for this problem to answer the question about average size of copper clusters inside AlN lattice.
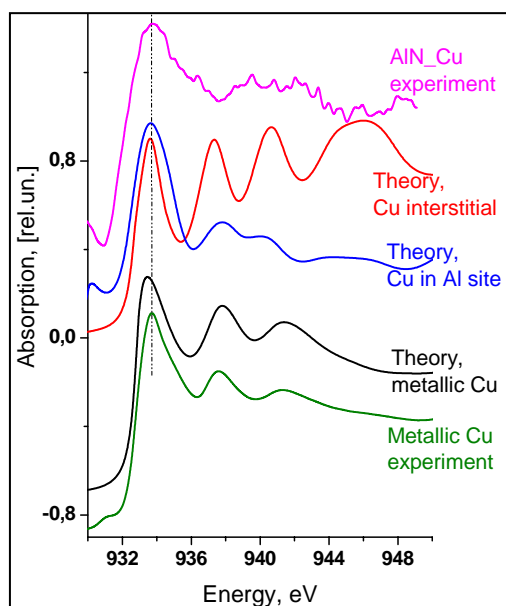
Figure 3. Experimental XANES spectra for Cu L2,3 edges for metallic Cu and AlN_Cu nanorods vs theoretical simulations
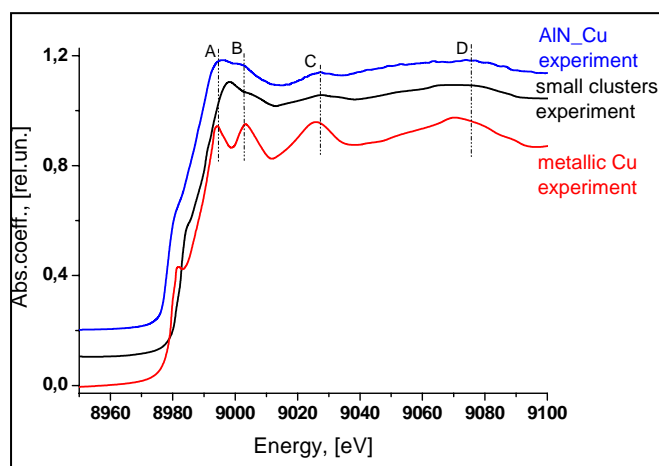
Figure 4. Experimental XANES spectra for Cu K-edge for AlN_Cu nanorods, small Cu clusters and metallic Cu

Finally, spin-polarized band-structure calculations predict, that among all point Cu defects, that are possible in AlN lattice – Cu in N site, Cu in Al site, Cu interstitial – only Cu in Al site is responsible for magnetic moment. We continue our calculations for Cu clusters, embedded in AlN, and first results also predict that they will be magnetized, due to p-d hybridization of Cu atoms and neighboring nitrogen atoms around cluster.

References.

1. A. Siegel, K. Parlinski, and U. D. Wdowik, // Phys. Rev. B – 2006, 74, 104116.
2. Y. Yang, Q. Zhao, X. Z. Zhang, Z. G. Liu, C. X. Zou, B. Shen, and D. P. Yu, // Applied physics letters 90, 092118. - 2007.
3. M.B. Kanoun, S. Goumri-Said, // Physica B 403. – 2008, 2847–2850.
4. Z G Huang, R. Wu and L J Chen // J. Phys.: Condens. Matter 19, - 2007, 056209 – Cu substitutional
5. X.H.Ji, S.P.Lau, S.F.Yu, H.Y.Yang, T.S.Herng and J.S.Chen, 2007. Nanotechnology 18, 105601
6. Sumedha Jayanetti, Robert A. Mayanovic et.al. Journal of Chemical Physics V.115 №2, 2001
7. G. Smolentsev, A.V. Soldatov, Computational Materials Science, 39, p.569, 2007

Synchrotron radiation prevents train crash.

authors: A.V.Soldatov, V.I.Kovesnikov, A.Guda, M.Soldatov
institute: Southern Federal University, Rostov-on-Don, Russia.

Train is the most safety transport. A big work was made to minimize the possibility of crash. But there still some problems that make a lot of harm to railwaymen. One of them is connected with brake blocks. Initially, brake blocks were made from the same material as wheels. This led to fast wear and tear of wheel and to big costs on its repair and replacement. Nowadays soft materials for brake blocks are preferable, such as composites. Last ones usually consist of graphite, synthetic rubber, aluminum oxide and sulfur compounds. Such contents significantly increase the lifetime of wheel but lead to unexpected consequences. During exploitation specific defects arise, because composite materials are aggressive for steel. These defects arise from redistribution of temperature fields on the wheel rim under friction. So, radial cracks, metal dislocations appear and wheel can derail.

In order to investigate, what chemical reactions take place during the process of friction, the x-ray absorption spectra of corresponding materials were measured. This methodic was already successfully applied to exploration of complex chemical interactions between additives in engine oil and metallic surfaces [1]. We focus our attention on definite object – train wheel from crash from railway museum. We took pure steel from the wheel far from its surface – sample1 on Figure1. As can be seen from Figure1, sample3 – damaged steel during friction – has a scaled structure like mica. Millimeter-sized scales were taken from damaged wheel surface, which was in contact with brake block. We also studied a material that adhered to the material of brake block – sample2.

Figure 1. Sample1 – initial state of steel, Sample2 – scaled structure formed on the wheel surface during friction, Sample3 – part of wheel that adhered to the brake block

Spectra were recorded at Russian-German beamline RGBL in high vacuum chamber. All samples were maintained on copper sample holder and a good conducting contact was provided between sample and sample holder. We used total electron yield signal from sample. Size of x-ray beam in experiment was about 50x100mkm^2. Energy resolution was E/ΔE~5000. We studied different points on a sample to find out does it sensitive to heterogeneity of the surface. We also made element analysis to see the distribution of such elements as Cr, Ni, Cu and Mn. Amount of these elements tells us how steel state is changed during its exploitation. This information is additional to the information about Fe atoms chemical state, analyzed with x-ray absorption

spectroscopy. Quantitative analysis of Cr, Ni, Cu and Mn distribution was made in BAM institute by means of laser induced breakdown spectroscopy [2] and results of this analysis are presented in Table1.
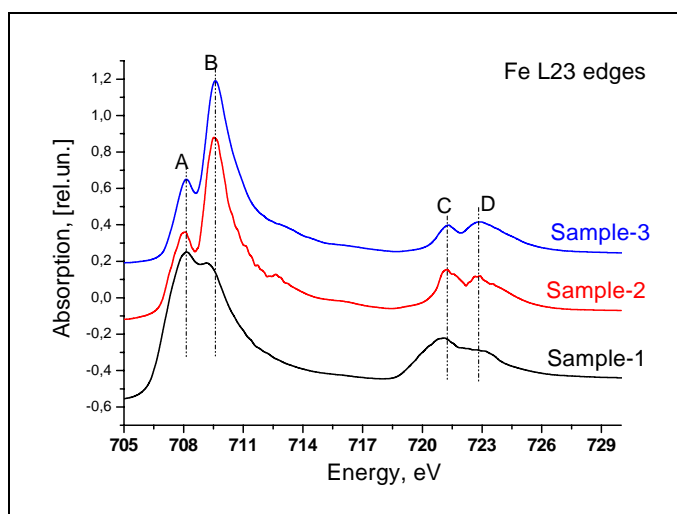
Figure 2. XANES spectra Fe L2,3 edge form initial state of wheel steel (sample1), scale from wheel surface after long time friction (sample2 and sample3).

Figure2 represents the Fe L2,3 XANES spectra for initial state of steel (from a railway wheel) and steel after the exploitation. We can clearly identify the changes that took place during the reactions. Sample-2 and Sample-3 have identical spectra with small changes in relative intensities of features C and D. Intensities of peaks A and B shows chemical state of Fe atoms [3] within thin layer near surface. One can say that during a friction of the wheel with the brake blocks due to high temperatures and high pressure a chemical reaction between wheel steel and composite material takes place. Scaled structure is formed and only then follows mechanical separation of the scales. Part of them forms a layer on a wheel and other part adheres to brake block. We suppose that certain fraction of Fe atoms react with sulfur atoms of composite material, that diffuse due to high temperature from volume of brake block. Having high temperature steel surface has a contact with the air, so part of Fe atoms oxidizes, that can be seen from the features A and B in Figure1. Principle component analysis within multidimensional expansion [4] of these spectra can be applied to identify the phases that present in samples. Now we continue calculations of Fe L2,3 edges within multiplet theory [5].

Table 1. Fractions of Cr, Ni, Cu and Mn atoms in samples. Sample3 was extremely inhomogeneous, which can be seen from intervals for fractions.

	Cr(%)	Ni(%)	Cu(%)	Mn(%)
Sample1	0.25	0.2	0.17	1.2
Sample2	0.1	0.38	0.17	3
Sample3	0.03-0.25	0.02-0.5	0.03-0.13	0.6-2.8

Literature
1. M.Nicholls, M.N.Najman, et,al., Can.J.Chem. 85:816-830, 2007
2. http://www1.messe-berlin.de/vip8_1/website/MesseBerlin/htdocs/www.laseroptics/ pdf/1.4_Panne_-_10.20.pdf
3. S. Anders, M.Toney, et,al., J. Appl. Phys., Vol. 93, No. 10, 15 May 2003
4. G. Smolentsev, A.V. Soldatov, Computational Materials Science, 39, p.569, 2007
5. Frank de Groot, Coordination Chemistry Reviews 249 (2005) 31–63

Scanning SAXS/WAXS measurements of dentine and bone sections

P. Zaslansky, A. Maerten, C. Lange, C. Li, S. Siegel, P. Fratzl, O. Paris

Max Planck Institute of Colloids and Interfaces, Research Campus Golm, 14424 Potsdam

The structure of mineral crystals in human teeth and murine bone was studied using the scanning SAXS/WAXS and XRF setup at the µ-spot beamline [1].

SAXS measurements of human-tooth dentine sections

Dentine in human teeth, is known to have a graded structure, that varies by depth, as one moves away from the enamel and into the tooth bulk (closer to the pulp) [2,3]. Composed of mineralized collagen fibrils, dentine exhibits a highly anisotropic structure, with micron-sized tubules running outward from the pulp, radiating in all directions through the tissue towards enamel. Dentine is tough, withstands many years of service in the mouth, yet much remains unknown about how the variation in the structure contributes to the excellent performance.

We have used a micron-sized beam on the µ-Spot beamline to look closer at the structural variations. We prepared and scanned thin (100 micron thick) slices from different sides of teeth, to study how the microstructure at the lengthscale of the mineral crystals (carbonated hydroxyl-apatite crystals sized 30~50 nm) varies spatially. Variation in dentine seems to follow the outer curvature of enamel, with gradual transitions between particle orientations. The degree of particle co-alignment (Rho parameter, Fig 1, *left*) also varies spatially: crystals are not well aligned. The thickness T parameter, which gives a good indication about the thin dimension of the mineral platelets also varies spatially and systematically (Fig 1, *right*): particles become smaller at greater distances from the dentin-enamel junction.

Such systematic evaluations of the particle arrangement in representative tooth samples will help to better understand the microstructure and how it is adapted to the loading forces in teeth.
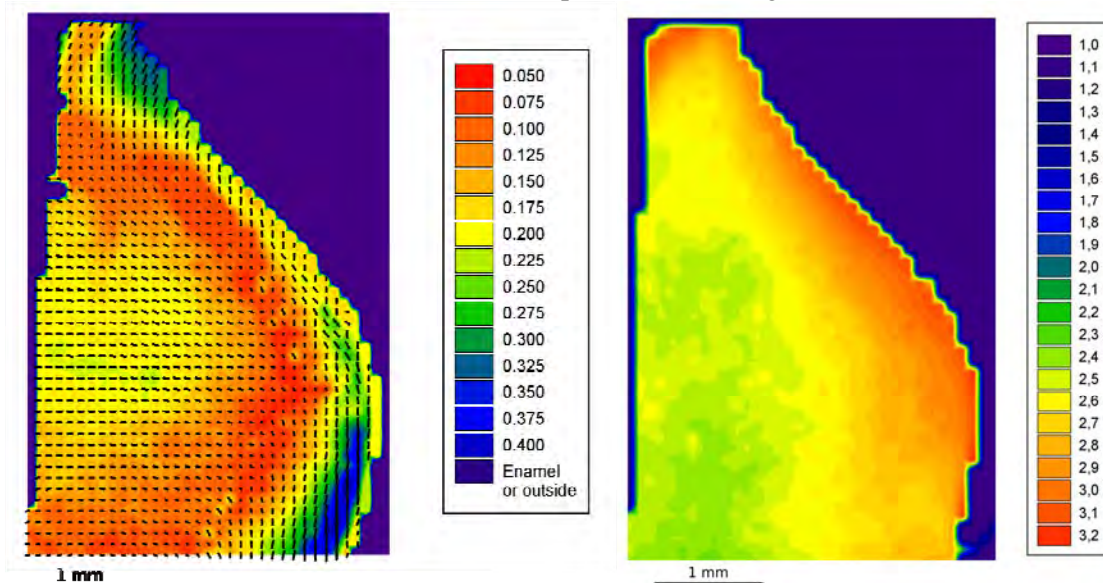
Fig. 1: (*Left*) Rho parameter values (color coded) where 1 indicates perfect crystal co-aligning and 0 indicates complete randomness of particle orientations. The orientation is indicated by small bars. (*Right*) T parameter indicating the particle thickness in it's thinnest dimension. Enamel is not shown but is located on the upper right side of the sample.

Mineral deposition and growth during embryonal bone development in mice

The knowledge how mineral crystals in bone nucleate, grow and organise themselves from the "birth of bone" (embryonal) is still poor. Therefore the aim of this study is to understand the development of the

mineral properties, the mineral deposition and organisation in growing bones (tibia, femur) from embryonal to mature stages using mouse as a model system (strain C57 BL6). This work is carried out in cooperation with the group of Prof. Stefan Mundlos (Charité and MPI for Molecular Genetics). We used a multi-method approach including optical microscopy and environmental scanning electron microscopy (ESEM) to get an overview of the mineralized sample areas. Especially, scanning small-angle X-ray scattering (sSAXS) that provides quantitative information about the crystal size, shape and orientation was used for detecting local structural changes in bone material. For very small samples like embryonal bone the SAXS facility at the µ-Spot beamline at BESSY II (Berlin) with a beam size of 25 µm is very well suited. To detect the very low amounts of mineral it is possible to measure the X-ray fluorescence (XRF) signal of calcium and to create a calcium distribution map of the sample. SAXS and WAXS maps or scans from selected regions give information on orientation and thickness of the mineral particles. Longitudinal sections of embedded bones of embryonal mice at day 16.5 as well as bone of a 6 week old mouse were measured.
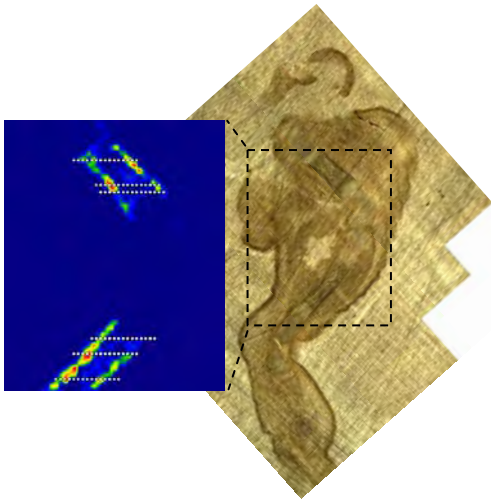
Fig. 2: Light microscopy image *(right)* and Ca X-ray fluorescence map *(left)* for a typical sample. SAXS/WAXS data were collected at the spots of high Ca content, where bone mineral can be expected (dotted lines).

The embryonal bone at day 16.5 displays the first stage of mineralization revealed by the ESEM- and the X-ray images whereas the bone of the 6 week old mouse displays mature bone. The analysis of the data is in progress.
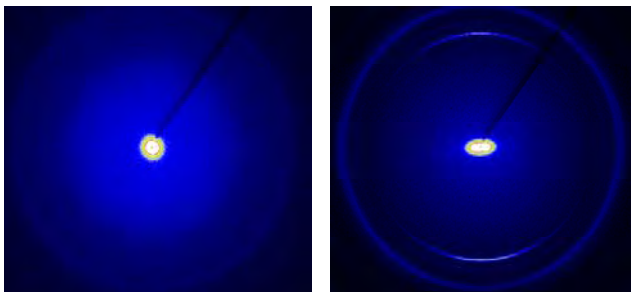
Fig. 3: Typical SAXS/WAXS patterns for an early mineralization site *(left)* and mature bone *(right)*.

1. O. Paris, C. Li, S. Siegel, S., G. Weseloh, F. Emmerling, H. Riesemeier, A. Erko, P. Fratzl. *A new experimental station for simultaneous X-ray microbeam scanning for small- and wide-angle scattering and fluorescence at BESSY II.* J. Appl. Cryst. **40**, S466-S470 (2007).
2. W. Tesch, N. Eidelman, P. Roschger, F. Goldenberg, K. Klaushofer, P. Fratzl., *Graded microstructure and mechanical properties of human dentin.* Calcif. Tissue Int. **69**, 147-157 (2001).
3. P. Zaslansky., 'DENTIN' in *Collagen: Structure and Mechanics* (Ed. P Fratzl), Springer, New York (2008)

In – situ studies of deformation in byssus fibers

H. S. Gupta[1], M. Harrington[2], S. Siegel[1], C. Li[1] and P. Fratzl[1]

[1]Biomaterials Department, Max Planck Institute of Colloids and Interfaces, MPIKGF Golm, D-14424 Potsdam, Germany

[2] Department of Biology, University of California at Santa Barbara, Santa Barbara CA, USA

Biocomposite tissues like bone (mineralized collagen) and tendon (collagen/proteoglycan composites) consist of stiff and ductile components at the nanoscale, whose functioning is essential for understanding the mechanics of the whole system. Such systems exhibit phenomena like molecular scale self – healing due to as yet incompletely understood processes. We investigated the molecular origins of the stress healing phenomena in the byssus fiber, which attached mussel shells to the rocks on wave swept shores. They exhibit elastic behaviour followed by a long inelastic plateau region, and more remarkably have the ability to self – heal mechanically after being stretched into the inelastic zone.

We applied *in – situ* tensile testing combined with time – resolved synchrotron small angle X – ray scattering (SAXS) to byssus fibers kept in a wet state and under applied tensile strain. Molecular strain was measured by shifts of the collagen diffraction peaks.
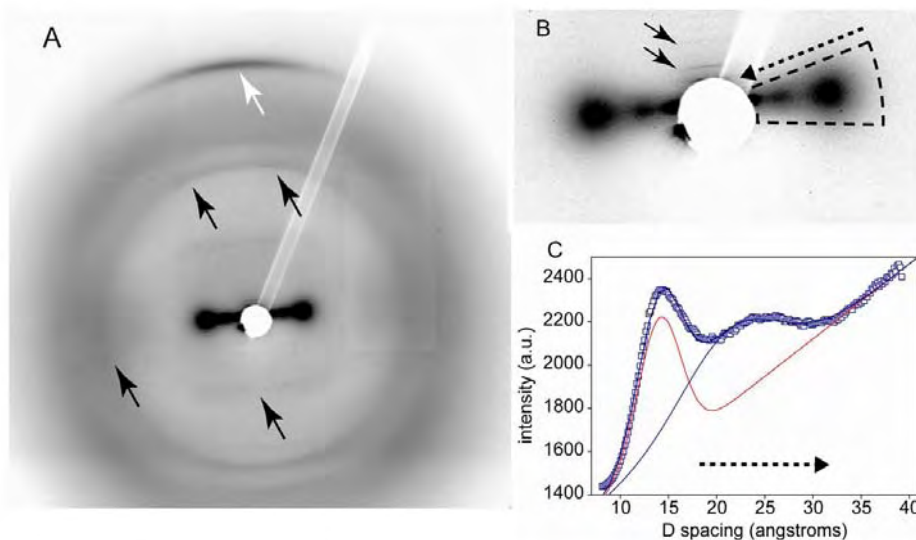
Figure: (A) 2D wide angle X-ray diffraction pattern of the byssus fiber: white arrow indicates collagen molecular peak (B) small angle X-ray scattering diffraction pattern (arrows) (C) integrated profile of the equatorial pattern (dashed sector in B).

Plotting molecular strain against stress shows that the collagen domain is elastic with a Young's modulus of 2.97±0.19 GPa (mean ± s.e.m.), consistent with previously measured moduli of collagen from tendon. Cyclic loading shows an elastic response at the molecular level indicating that no damage is occurring in the collagen helical domains. It is suggested that in the yield region unfolding and breakage of crosslinks in domains flanking the collagen domain in the byssal fiber occurs. A deeper understanding of selfhealing in such systems may make it possible to modify inelastic proceeses in engineered fibers.

Microbeam SAXS/WAXS studies on biogenic and biomimetic calcite single crystals

C. Gilow, A. Schenk, B. Aichmayer, C. Li, S. Siegel, O. Paris and P. Fratzl

Department of Biomaterials, Max Planck Institute of Colloids and Interfaces, Research Campus Golm, D-14424 Potsdam

Due to their complex structure, biogenic minerals have fascinating properties. Molluscs, as an example, produce seemingly effortless high-quality minerals with an astounding degree of control. This is achieved via an organic matrix which directs and regulates the mineral deposition.

We investigated calcitic prisms from the shell of *Pinna nobilis* in co-operation with Professor Emil Zolotoyabko (Technion, Haifa, Israel). These prisms diffract like single crystals. Additionally, a strong small angle X-ray scattering (SAXS) signal reveals a pronounced nanostructure, presumably due to intracrystalline proteins, that were previously isolated and characterized by (Marin et al. 2005). These interesting properties act as a source of inspiration for materials science and nanotechnology. In co-operation with Dr. Helmut Cölfen (MPI of Colloids and Interfaces, Potsdam, Germany) we additionally produced bio-inspired calcite crystals grown in the presence of a negatively charged polyelectrolyte (PSS, Aldrich) via a gas diffusion technique (Wang et al. 2006). In this process the macromolecules are incorporated into the crystals and create inner surfaces between the mineral and the polymer phase. SAXS as a non-destructive technique probing a comparatively large sample volume is an ideal tool to explore the nano-structure of biogenic and biomimetic minerals. By recording the wide-angle X-ray scattering simultaneously with the SAXS-signal, it is possible to determine the orientation relation of the nanostructures of the crystals with respect to the crystalline lattice.

The µ-Spot beamline is equipped to perform simultaneous SAXS and WAXD measurements (Paris et al. 2007). We have extended this setup, which now can be used for single crystal diffractometry. To accomplish this, the sample is placed in the axis of rotation of a goniometer with the help of a long-distance microscope. A sequence of diffraction patterns are then recorded for different rotation angles. The wavelength of the beam is chosen by a 111-Si monochromator. To calibrate the distance between the sample and the detector, a silicon-oxide powder standard (NIST-SRM 1878a) is used.
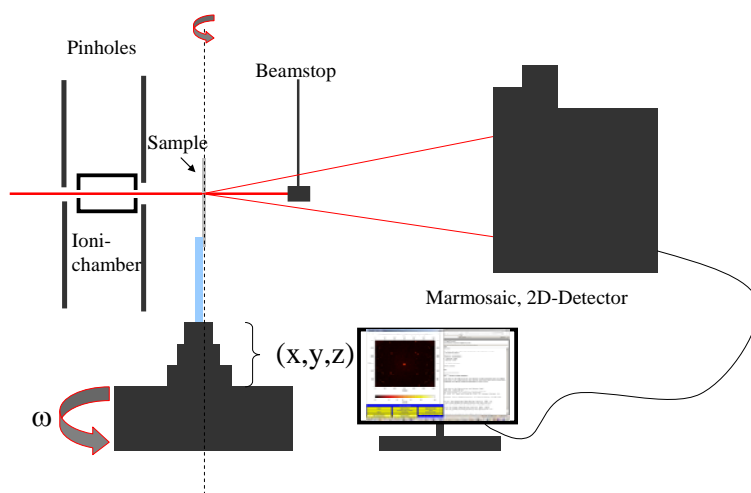
Fig. 1: Schematic experimental setup at the µ-Spot beamline for SAXS/WAXS on single crystals

Figures 2a and 2b each show typical frames from a sequence for biogenic and biomimetic calcite, respectively (100 s acquisition time). The diffraction peaks correspond to a single-crystalline pattern of calcite. The inset shows a higher magnification of the anisotropic SAXS signal which is oriented in the direction of the indicated (104) peak. The corresponding WAXD peak is excited at a different angle of sample rotation. Taking into account geometrical corrections necessary to compare the SAXS and WAXD orientation (Lichtenegger et al. 1998), we could show that the nanostructure, which presumably arises from the organic inclusions, is preferentially oriented along both the (104) and the (006) plane. Furthermore the spherically averaged SAXS signals of the biogenic and the biomimetic calcite particles do not follow Porod's law (decay with Q^{-4}), but instead decay slower, which is characteristic for rough inner surfaces.

In summary this setup is a versatile tool to probe the nanostructure of crystals. Especially the orientations of inner structures with respect to the crystal lattice can be probed in an effective manner. Our study of biogenic and biomimetic single-crystal calcite particles with organic inclusions serves as a proof of principle but also revealed interesting similarities between both systems, which will help to deepen the understanding of the processes involved in biomineralization. Future work will also include a three-dimensional reconstruction of the reciprocal space of both the SAXS and the WAXD signal.
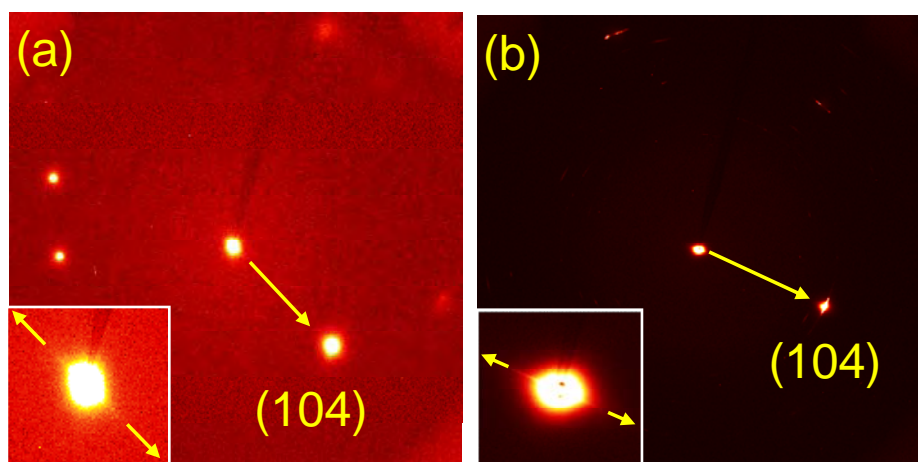
Fig. 2: Typical diffraction images from a calcitic prism of the pinna nobilis (a) and the biomimetic calcite particles (b). The insets show the anisotropic SAXS signals which point towards the indicated peaks.

Lichtenegger, H., Reiterer, A., Paris, O., et al. (1998). *Determination of spiral angles of elementary fibrils in wood cell walls: Comparison of small-angel X-ray scattering and wide angle X-ray diffraction.* Proceedings of the International Workshop on the Influence of Microfibril Angle to Wood Quality, West Port, New Zealand.

Marin, F., Amons, R., Guichard, N., et al. (2005). *Caspartin and calprismin, two proteins of the shell calcitic prisms of the Mediterranean fan mussel Pinna nobilis.* Journal of Biological Chemistry **280** (40): 33895-33908.

Paris, O., Li, C., Siegel, S., et al. (2007). *A new experimental station for simultaneous X-ray microbeam scanning for small- and wide-angle scattering and fluorescence at BESSY II.* Journal of Applied Crystallography **40**: S466-S470.

Wang, T. P., Antonietti, M., Cölfen, H. (2006). *Calcite mesocrystals: "Morphing" crystals by a polyelectrolyte.* Chemistry-a European Journal **12** (22): 5722-5730.

Microstructure and Chitin/Calcite Orientation Relationship in the Lobster Cuticle Using Microbeam Synchrotron X-ray Diffraction

Ali Al-Sawalmih, Chenghao Li, Stefan Siegel, Helge Fabritius[1], Dierk Raabe[1], Peter Fratzl, Oskar Paris

Department of Biomaterials, Max Planck Institute of Colloids and Interfaces
14424 Potsdam, Germany
[1] Max-Planck-Institut für Eisenforschung, Max-Planck-Str. 1, 40237 Düsseldorf

The exoskeleton of the lobster *Homarus* americanus is a chitin–protein-based nano-composite, reinforced with calcite crystallites[1] and amorphous $CaCO_3$ (ACC)[2, 3]. Earlier studies identified that two components of chitin/protein fibers networks exist in the cuticle: in-plane fibers (i) which exhibit the well known twisted plywood structure[4], and out-of-plane fibers (o) which run vertically toward the surface through the pores of the former.[5] We employed microbeam X-ray diffraction to investigate the local microstructure, the orientation relationship between the organic (α-chitin) and the inorganic (calcite) components, and their corresponding spatial distribution.[6] Our synchrotron measurements were performed at the μ-Spot beamline[7] of the BESSY synchrotron facility in Berlin.

We found that calcite exhibits a simple fiber texture (preferred orientation) with the c-axis perpendicular to the cuticle surface, as well as parallel to the chitin c-axis. Fig. 1a shows a microbeam diffraction pattern from the lobster exocuticle recorded with the X-ray beam parallel to the cuticle surface. In Fig. 1b, the azimuthal coincidence of the calcite 00.6 reflection and the chitin 013 pair indicates that the calcite c-axis and the chitin c-axis of the vertical fiber component are collinear. Detailed analysis of the microdiffraction patterns reveals that calcite is associated with the out-of-plane chitin/protein fibers, rather than the in-plane fibers.[6]

The spatial distributions of the two major mineral phases, calcite and amorphous calcium carbonate (ACC), as well as chitin were determined by performing line scans across the cuticle cross-section covering exocuticle and endocuticle. Calcite was only found in the distal layers of the exocuticle in a region extending about 20–50 μm from the cuticle surface. However, the whole cuticle is fully mineralized with ACC in the non calcified regions, which can be uniquely concluded from the occurrence of an amorphous halo in the recorded X-ray profiles of the area of interest, Fig. 3.[6]

For a better understanding of the functional role of amorphous calcium carbonate and its stability in the cuticle, the temperature induced transformation of ACC into calcite was studied. We employed *in-situ* heat treatment of the cuticle cross section using a custom made lamp-furnace [8]. Figure 3 shows diffraction profiles for three different temperatures from the same representative region within the endocuticle. The crystalline chitin decomposed completely at temperatures between 250–300 °C, and only a broad hump from ACC remained in the diffraction profile at 325 °C. At about 425 °C, the amorphous halo from ACC started to vanish, and calcite reflections appeared. The whole cuticle was fully calcified at 450 °C indicating that ACC has fully transformed into calcite (see Fig. 3). The details of the transformation behavior, in particular the changes of the cuticle nanostructure and the formed crystalline phases at even higher temperatures allow drawing conclusions about the mechanisms of ACC stabilization in the lobster cuticle[9].
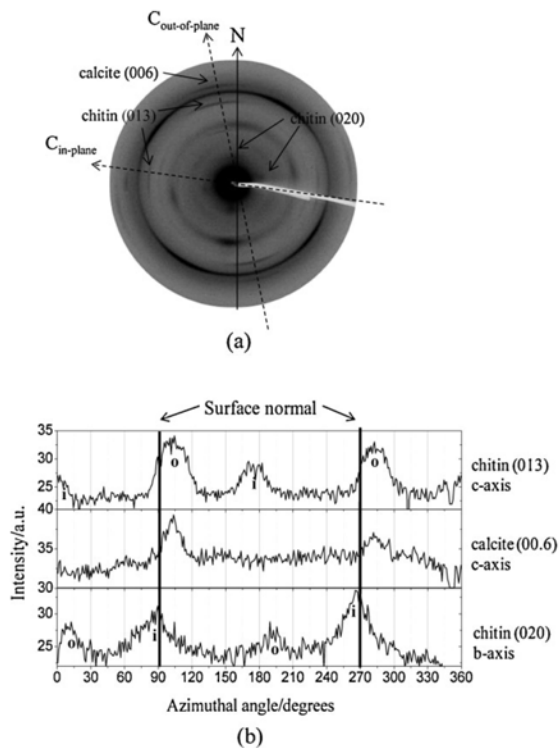
Fig. **1**: a) Diffraction pattern from the mineralized lobster exocuticle recorded with the X-ray microbeam, b) Azimuthal integration of selected X-ray diffraction rings of chitin and calcite.
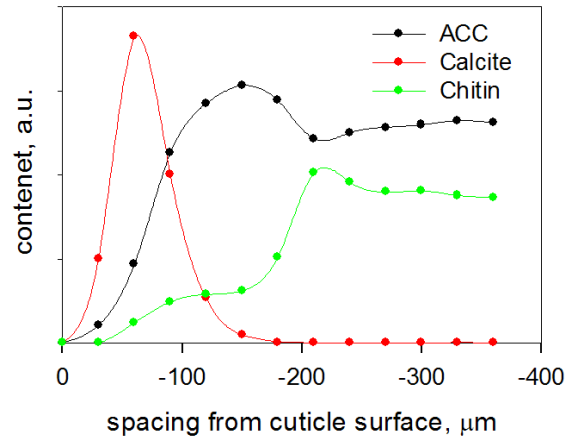
Fig. **2**: Amount of chitin, calcite and ACC, based on the integrated intensity from the corresponding diffraction peaks.
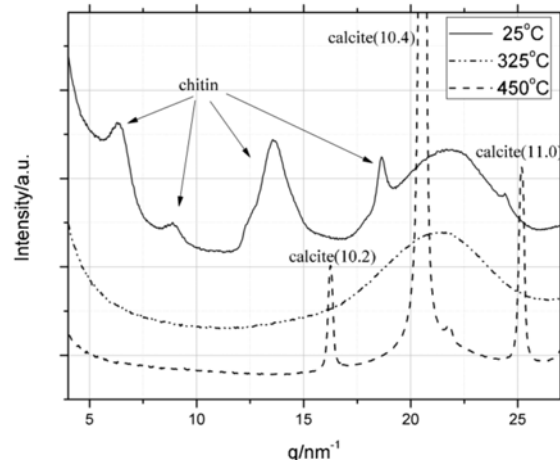
Fig. **3**: Microbeam X-ray diffraction profiles from the endocuticle as a function of temperature

[1]   A. Neville, *Biology of fibrous composites*, Cambridge University Press, **1993**.
[2]   F. Boßelmann, P. Romano, H. Fabritius, D. Raabe, M. Epple, *Thermochim Acta* **2007**, *463*, 65.
[3]   A. Becker, U. Bismayer, M. Epple, H. Fabritius, B. Hasse, J. M. Shi, A. Ziegler, *Dalton Transactions* **2003**, 551.
[4]   Bouligan.Y, *Tissue & Cell* **1972**, *4*, 189.
[5]   D. Raabe, A. Al-Sawalmih, S. B. Yi, H. Fabritius, *Acta Biomaterialia* **2007**, *3*, 882.
[6]   A. Al-Sawalmih, C. H. Li, S. Siegel, H. Fabritius, S. Yi, D. Raabe, P. Fratzl, O. Paris, *Advanced Functional Materials* **2008**, *18*.
[7]   O. Paris, C. H. Li, S. Siegel, G. Weseloh, F. Emmerling, H. Riesemeier, A. Erko, P. Fratzl, *Journal of Applied Crystallography* **2007**, *40*, S466.
[8]   G. A. Zickler, W. Wagermaier, S. S. Funari, M. Burghammer, O. Paris, *Journal of Analytical and Applied Pyrolysis* **2007**, *80*, 134.
[9]   A. Al-Sawalmih, C. Li, S. Siegel, P. Fratzl, O. Paris, **submitted**.

Widening the fullerene band gap in fluorination

V.M. Mikoushkin[1], V.V.Bryzgalov [1], S.Yu. Nikonov[1], V.V. Shnitov[1], Yu.S. Gordeev[1], Boltalina[2,3],
I.V. Gol'dt[2], M.M. Brzhezinskaya[4]

[1]) *Ioffe Physical-Technical Institute RAS, St.-Petersburg, 194021, Russia*
[2]) *Chemistry Department, Moscow State University, Moscow, 119899, Russia*
[3]) *Chemistry Department, Colorado State University, Fort Collins, 80523, USA*
[4]*BESSY, German-Russian laboratory*

Abstract. Study of valence band structure of highly fluorinated fullerenes $C_{60}F_{48}$ in comparison with that of ordinary fullerenes C_{60} was performed at the conditions of negligible static charging of samples. It was shown that the band gap of carbon clusters becomes wider in fluorination due to disappearance of molecular levels starting from the highest ones which takes place due to participation of π-electrons in creation of C-F bonds. The project was supported by the bilateral program "Russian-German Laboratory at BESSY" and by the by the Russian Academy of Sciences (Program "Quantum physics of condensed matter").

Introduction

Fluorinated fullerenes $C_{60}F_x$ have been extensively studied last fifteen years in many laboratories by different techniques, as these objects make possible investigating the influence of fluorination on the electronic structure and basic properties of well defined carbon clusters [1-9]. In the comprehensive research of several groups [5] the following important conclusion was made that the highest occupied electron levels (HOMO) on highly fluorinated fullerenes, such as $C_{60}F_{46}$, are shifted compared to the levels of ordinary fullerene C_{60} to higher binding energies due to inductive effect of electronegative fluorine atoms, which makes the band gap wider. Shifts of HOMO levels of less fluorinated fullerenes were observed also in our former research [8-10]. But these shifts were of different origins. One of them was directed to lower binding energies and was shown to be connected with fragmentation of fluorofullerenes induced by radiation. Another one was directed to higher binding energies analogous to the result of Ref. [5], but contrary to it, the shift was explained by systematic fault, namely, by static charging of films under irradiation due to photoemission. The main objective of this research was to study the HOMO and valence band electronic structure of highly fluorinated fullerenes $C_{60}F_{48}$ in conditions of negligible radiation degradation and charging, to compare it with the electronic structure of ordinary fullerenes C_{60} and to attempt answering the question whether HOMO levels shift or not. Conductive organic thing films were used as a solid solvent of fluorinated fullerenes $C_{60}F_{48}$ to prevent charging of these wide band gap dielectric molecules. We have found signs that electron levels do not shift, and that the band gap becomes broader in fluorination due to depletion of π-electron system and disappearance of the upper π-electron derived HOMO levels.

Experimental details

Films of $C_{60}F_{48}$ were grown on the surfaces of conductive n-Si(100) wafer and Au. Silicon substrate was annealed in high vacuum before the deposition of the film to remove thick layer of native oxide and to create ultra-thin SiC layer which was expected to prevent chemical interaction of $C_{60}F_{48}$ molecules with Si substrate. Powder consisting of molecules with certain and known number of fluorine atoms was used in the experiment. This material was synthesized at Chemistry department of Moscow State University by the technology described in [1]. Thin composite films were grown by co-evaporation of $C_{60}F_{48}$ molecules together with molecules of phthalocyanine PcCu in ratio 1:2 which was controlled by C1s photoemission lines. PcCu semiconductor matrix was expected to provide charge outflow and to prevent static charging of the sample surface under irradiation. Thickness of the films was estimated by the weakening of SiLVV Auger- and Au4f photoemission lines and did not
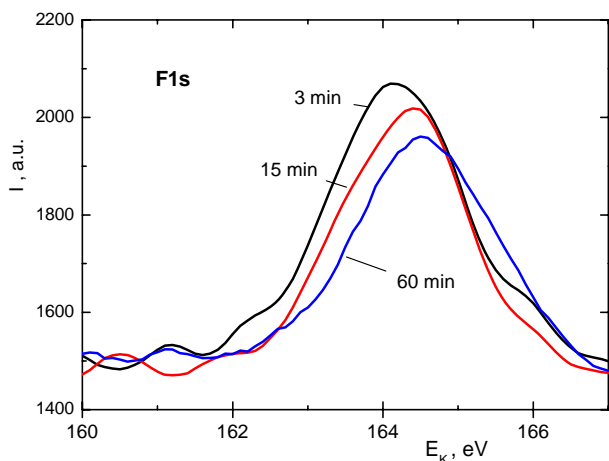
exceed 2-3 monolayers. Photoemission spectra of the films were measured using monochromatic synchrotron radiation of the German-Russian beamline equipped with the plane-grating monochromator (PGM) and the photoelectron spectrometer with hemispherical analyzer VG CLAM-4 whose total energy resolution was better than 300 meV [11].

Fig.1. F1s photoelectron spectra of $C_{60}F_{48}$ measured after 3, 15 and 60 min of irradiation by diagnostic x-ray beam (hν ~ 850 eV).

Experiment duration was short enough to prevent essential degradation of studied films resulting in shift of photoemission lines towards to the Fermi-level. The photon energy scale of the monochromator was calibrated using the photoemission Au $4f_{7/2}$ line of gold (E_b = 84.0 eV).

Results and discussion

X-ray photoemission spectra of core-electrons C1s and F1s were measured and the corresponding binding energies of $C_{60}F_{48}$ molecules in the organic matrix were obtained relative to the Fermi level: E_b (C1s, C-F) = 288.5 eV and E_b (F1s) = 687.1 eV. These values proved to be very close to the values obtained by us earlier for pure thing film of $C_{60}F_{36}$ [10]. The value of the binding energy E_b (C1s, C-F) = 288.5 eV corresponding to carbon atoms bound with fluorine practically coincides with that (288.4 eV) obtained in Ref. [5]. This fact evidences absence of static charging in experiments with thing (~10 nm) pure films of highly fluorinated fullerenes in photoemission experiments [5,10]. Though, the compensation of static charging effect by the effect of degradation of fluorofullerenes under irradiation also can result to the agreement of the experiments. The scale of the degradation effect is illustrated by Fig.1 presenting the radiation induced shift of F1s line of $C_{60}F_{48}$ observed in this work. Fig.1 demonstrates low radiation stability of highly fluorinated fullerenes $C_{60}F_{48}$ as compared to $C_{60}F_{18}$ [8]. Visible shift of about 0.1-0.2 eV is observed after irradiation of the sample by diagnostic x-ray beam during several minutes. After one hour the shift exceeds 0.4 eV. The shift must be large by the value of static charging the sample surface, if there is a case, because of increasing conductivity of the material in the course of its degradation [10]. Therefore measurements of photoemission spectra of highly fluorinated fullerenes need careful analysis of static charging and degradation effects.
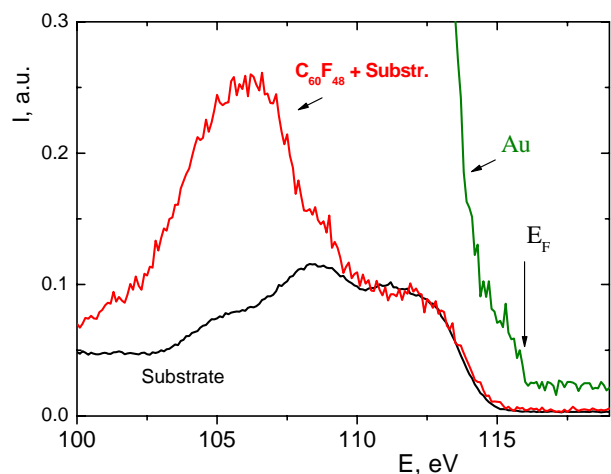
Fig.2. Valence band photoelectron spectra of gold, of Pc on Si substrate and composite PcCu+$C_{60}F_{48}$ thing film grown on Si substrate. Photon energy is hν = 120.6 eV.

Fig.2 shows the photoemission spectra of valence band of the studied composite film and the film of organic matrix of smaller but comparable thickness. Contribution of the spectrum of the Si substrate is seen because of low thickness of the studied films. The valence band photoemission spectrum of
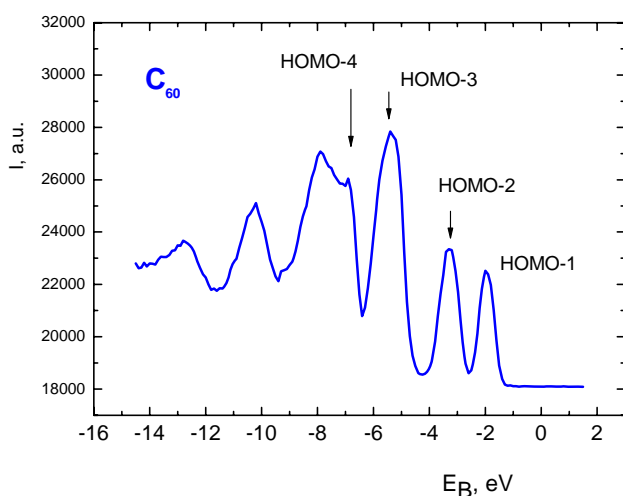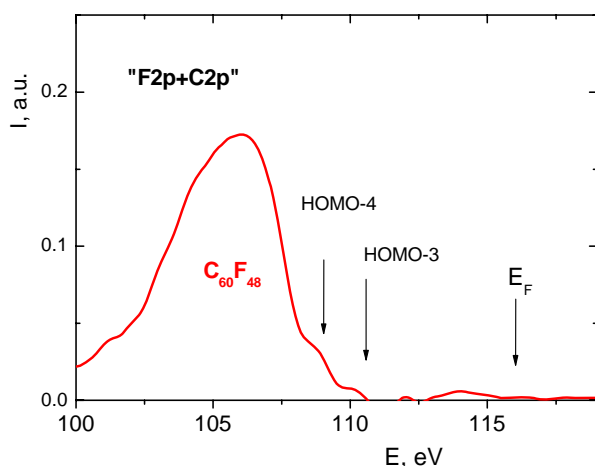
$C_{60}F_{48}$ was obtained as a difference between these two spectra. Fig.3 demonstrates the obtained spectrum of $C_{60}F_{48}$.

Fig.3. Valence band photoelectron spectrum of $C_{60}F_{48}$ without contribution of substrate. Photon energy is $h\nu = 120.6$ eV.

Position of the Fermi-level corresponds to the valence band edge of Au. Unfortunately the fine structure of the spectrum is not seen because of the residual contribution of the matrix. Comparison of this spectrum with the corresponding spectrum of ordinary fullerite C_{60} (Fig.4) shows the grate difference of the electronic structure of these molecules.

Fig.4. Valence band photoelectron spectra of C_{60} film. Photon energy is $h\nu = 120.6$ eV.

One can see that lines of the upper molecular states of fullerene HOMO-1, HOMO-2 and HOMO-3 completely disappear and the line HOMO-4 radically decreases when 48 fluorine atoms attach to fullerene C_{60} and form $C_{60}F_{48}$. As a result, the band gap of $C_{60}F_{48}$ becomes wider than that of ordinary fullerite C_{60} by ~5 eV. Fig. 3 does not show any shifts of molecular lines: the line HOMO-4 saves its position. Therefore we came to the conclusion that the reason of widening of the band gap of carbon clusters in fluorination is disappearance of the upper π-electron states due to participation of π-electrons in creation of C-F bonds. These former π-electrons contribute to the "F2p+C2p" peak in the photoemission spectrum of $C_{60}F_{48}$.

References:

[1] O.V.Boltalina, S.H.Strauss, "Fluorinated Fullerenes", in Dekker Encyclopedia of Nanoscience and Nanotechnology: New York, Marcel Dekker, 2004, eds. J. A. Schwarz, C. Contescu, K. Putyera, p. 1175-1190.

[2] P.J.Benning, T.R.Ohno, J.H.Weaver, et al., *Phys. Rev. B* **47**, 1589 (1993).

[3] D.M.Cox, S.D.Cameron, A.Tuinman, et al., *J.Am. Chem. Soc.* **116**, 1115 (1994).

[4] Y. Matsuo, T.Nakajima, S.Kasamatsu, et al., *J. Fluor. Chem.* **78**, 7 (1996).

[5] R. Mitsumoto, T. Araki, E. Ito, et al., *J. Phys. Chem. A* **102**, 552 (1998).

[6] A.P.Dement'ev, O.V.Boltalina et al., *Proceeding Electrochemical Society* **2001-11**, 559 (2001).

[7] S.V.Amarantova, V.N.Bezmelnitsyn et al., *Nucl.Instrum Meth.A* **470**, 318 (2001).

[8] V.M. Mikoushkin, et al., *Bulletin of the BESSY Annual Report (2006)*, Berlin, 202 (2007).

[9] V.V. Shnitov, et al., *Fullerenes, Nanotubes and Carbon nanostrucrutes* **14**, 297 (2006).

[10] V.M.Mikoushkin, V.V.Shnitov, V.V.Bryzgalov, Yu.S. Gordeev, O.V. Boltalina et al., "Core-level structure of $C_{60}F_{18}$ and $C_{60}F_{36}$ studied by photoelectron spectroscopy", this book.

[11] S.I.Fedoseenko, D.V.Vyalikh, et al., *Nucl. Instr. and Meth. A* **505,** 718 (2003).

The oscillator strength distributions in the NEXAFS spectra of bacterial surface protein layers: X-ray damage.

V.N. Sivkov[a], S.V. Nekipelov[a] , D.V. Vyalikh[b], K. Kummer[b], V.V. Maslyukc, A. Bluher[d], I. Mertig[c], M. Mertig[d], S.L. Molodtsov[b]

[a]*Komi Science Center, Russian Academy of Science, Ural Division, Syktyvkar 167982, Russia*
[b]*Institute of Solid State Physics, Dresden University of Technology, D-01062 Dresden, Germany*
[c]*Martin-Luther-Universit¨at Halle-Wittenberg, Fachbereich Physik, D-06099 Halle, Germany*
[d]*BioNanotechnology and Structure Formation Group, Max Bergmann Center of Biomaterials and Institute of MaterialsScience, Dresden University of Technology, D-01062 Dresden, Germany*

The possible applications of the regular bacterial surface layers (S layers), which are the self-assembly biomolecular structures with well-defined structural and physico-chemical surface properties [1], for the organization of inorganic material at the nanometer scale have stimulated the spectroscopic researches of the surface protein layer of the bacteria *B. sphaericus* NCTC 9602 in previous years. The S layer protein is known to be absorbed in a regular, two-dimensional structure onto solid surfaces which is formed via self-assembly [2, 3]. At that, surface coverage of up to 90% is routinely achieved as had been demonstrated by scanning electron microscopy. The S layer shows a *p4* symmetry and reveals a lattice constant of 12.5 nm, and a complex pattern of pores and gaps that are 2–3 nm wide. The thickness of such protein layer amounts to approximately 5 nm. According to its presently known primary structure a single S layer protein molecule is composed of 1228 amino acids, including 1517 nitrogen atoms and has a molecular weight of ~130 kDa [4]. With the exception of Cysteine all 20 standard amino acids are present. The protein contains 3.91 carbon, 1.22 oxygen, 7.7 hydrogen and the neglectable amount of 0.0027 sulfur atoms per one atom of nitrogen. The 83.1% of the nitrogen, 21.4% of the carbon and 64.8% of the oxygen atoms are bounded in the peptide backbone of the protein. Details of the sample preparation are described elsewhere [5].

Recently, we have performed photoemission (PE) and near edge x-ray absorption fine structure (NEXAFS) experiments in order to characterize electronic properties of the regular two dimensional S layer of *Bacillus sphaericus* NCTC 9602 [5-7]. Both PE and NEXAFS at the C 1*s*, N 1*s*, and O 1*s* core levels showed similar chemical states for each oxygen atom and also for each nitrogen atom, while carbon atoms exhibited a range of chemical environments in backbone and different functional groups of the amino acids. A series of characteristic NEXAFS peaks was assigned to particular molecular orbitals of the amino acids by applying a phenomenological building-block model.
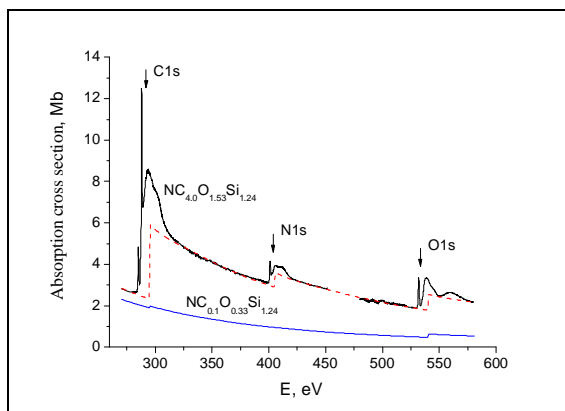
Fig. 1. *Spectral dependence of the TEY signal of S layer after normalization to the incident photon flux (black). Comparing with tabulated atomic cross sections [12] we found the best agreement for a chemical composition $NC_{4.0}O_{1.53}Si_{1.24}$ (dotted line). The additional signal $C_{0.1} O_{0.33} Si_{1.24}$ is easily assigned to contributions by the SiOx/Si substrate (blue).*

In the issue of the researches had shown that the radiation induced damage of the protein samples can substantially change the line shape of the data also resulting in appearance of new intense spectral feature [8]. Therefore the valid irradiation doses data are of severe importance for researches allowing feasible adjustment of experimental conditions and provide perspectives of measurements of biological samples with spectroscopic methods applying soft x-ray radiation.

The goal of the project is to carry out the study of the radiation-induced decomposition of the S-layer by the analysis of the oscillator
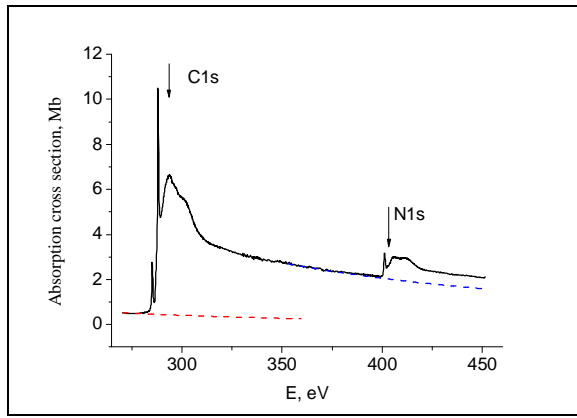
Fig.2. *The absorption cross section spectral dependences of S layer. The dash lines are extrapolated curves.*

Fig.3. *The photon-flux density of the monochromatic synchrotron radiation had normalized at the beam current.*

strength distributions in the C1s, N1s and O1s NEXAFS-spectra as a function of the gained skin dose. An irradiation doses gained by the surface area of the samples that is much thinner than the light penetration depth (skin doses, D) were calculated:

$$D = \frac{s}{M} \, \sigma \, N \, E \, dt = \frac{s}{M \, V_E} \, \sigma \, N \, E \, dE \qquad (1)$$

where σ is absorption cross section of the single S layer protein molecule, N denotes the photon-flux density of the monochromatic synchrotron radiation, S is the light spot size at the sample position, E is the photon energy, t is the exposure time, V_E is the energy scanning velocity and M is weight of a single S layer protein molecule (~130 kDa). The absolute absorption cross sections were measured by Total electron Yield (TEY) method with using Ti-filter for suppressed nonmonochromatic background [9].

All presented data were obtained at the BESSY-II using radiation from the Russian–German beamline (RGBL) [5, 6]. The light spot size at the sample position was 200×87 μm^2 [10] which allowed to study homogeneous parts of the S layer. All spectra were acquired in TEY mode by recording the sample drain current. The spectral dependence of the photon flux was determined using a clean Au photocathode. The flux curve exhibits huge dips in the region of the O 1s absorption threshold (530-570 eV) due to extensive oxygen contamination of the optical elements. Hence, we decided to repeat measurements in the O 1s range at the beamline D1011 of the MAX II storage ring at MAXlab (Lund University, Sweden).

Fig. 1 shows the TEY signal obtained from the surface-adsorbed protein layer after normalization to the incident photon flux. The

curve features distinct jumps when passing the C, N and O 1s edge. More precisely, at each absorption edge it exhibits a near-edge fine structure followed by a monotonically descending tail. While the NEXAFS reflects transitions into free molecular states, the structureless tail is due to transitions into continuum states far beyond the vacuum level [11]. However, beside the strong evidence in the already mentioned previous studies, our data itself indicates direct proportionality between the curve in Fig. 1 and the total X-ray absorption cross section of the sample. In fact, using atomic calculations of absorption cross-sections, we were able to reproduce the full measured spectrum. The best agreement was found assuming an average atomic composition of $NC_{4.0}O_{1.53}Si_{1.24}$. The corresponding curve is included in Fig. 1 as a blue line. It should be noted that the close similarity in the regions of continuum transition where atomic calculations hold validity from the energies of the synchrotron radiation. The values of the atomic absorption cross section were selected from tabulated data [12]. Fig. 2 shows the absorption cross section of S layer which had measured as difference between the curves (1) and (2) in fig.1. The photon-flux density of the monochromatic synchrotron radiation was measured by TEY clean Au-photocathode with using the front-surface total quantum yield data of Au [13] which show in fig.3. The exposure doses gained by the S-layer samples were calculated by formula (1) for the any certain time and energy position. The dose was obtained for monochromatic radiation only, because Ti-filter full suppressed higher order radiation. The researches had shown that higher order radiation induced strong damage of the protein samples. X-ray damage effects were studied at C 1*s* and N

1*s* thresholds of excitation upon scan-by-scan irradiation of the S-layer proteins and in the extreme case of irradiation by outmost high flux-density nonmonochromatized ("zero-order") synchrotron radiation. Only the S-layer signal was used to describe the radiation damage. In the fingers 4 and 5 showed the irradiation-induced changes of NEXAFS C1s and N1s spectra of S layer. Fig.4-5 are shown that the oscillator strength of the C1s - π_{CONH} and N1s - π_{CONH} transitions decrease with increased the exposure doses gained by the S-layer sample. At that sum oscillator strength for C1s spectrum is unvaried (unshow), but for N1s spectrum is obvious decrease. The two structures (**a, b**) developed in the N1s edge with increasing irradiation doses. The analysis of the NEXAFS 1s spectra and the chemical structure of S layer have shown that 90% from area A resonance in N1s spectra fit from the nitrogen atoms of peptic group and 82% in from area A resonance C1s spectra fit from the carbon atoms of peptic group. This observation indicates that, while the peptic bonds get damaged by the applied radiation, N atoms partially leave from the sample surface,
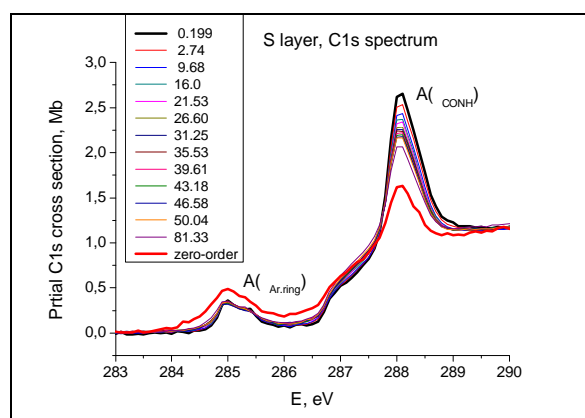
C atoms - in contrast to nitrogen – remain at the sample surface, and interact presumably with N atoms likewise released from the peptide units or resided by cracking at the surface of the Si wafer. We suspect that also in the case of radiation-damaged proteins some of the dispensed N atoms may interact with C atoms forming carbon-nitride compounds.

References

1. Mann, S. Nature **1993**, 365, 499.
2. U.B. Sleytr, P. Messner, D. Pum, M. Sara, Crystalline Bacterial Cell Surface Proteins (Academic Press, San Diego, 1996).
3. [3] Sleytr, U.B.; Sara, M. Trends Biotechnol., 15, 20 (1997).
4. UniProt database, www.uniprot.org
5. Vyalikh D.V.; Kirchner, A.; Kade, A.; Danzenbacher, S.; Dedkov, Yu.S.; Mertig, M.; Molodtsov, S.L. J. Phys. Condens. Matter, 18,131 (2006).
6. Vyalikh D.V.; Danzenbächer S.; Mertig, M.; Kirchner, A.; Pompe, W.; Dedkov, Yu.S.; Molodtsov, S.L. Phys. Rev. Lett., 93, 238103 (2004).
7. Vyalikh D.V.; Kirchner, A.; Danzenbächer, S.; Dedkov, Yu.S.; Kade, A.; Mertig, M.; Molodtsov, S.L. J. Phys. Chem. B, 109, 18620 (2005).
8. Kade, A.; Vyalikh D.V.; Danzenbächer S.; Kummer K.; Bluher A., Mertig, M., Scholl A,, Doran A., Molodtsov, S.L., J. Phys. Chem., B, 111, 13491 (2007).
9. Sivkov V. N., Vinogradov A. S., Nekipelov S. V., Sivkov D. V., Vyalykh D. V., Molodtsov S. L., Optika i Spektroskopiya 101, N5, 782 (2006)
10. Fedoseenko S.I., Vyalikh D.V., Iossifov I.F., Follath R., Gorovikov.S.A., Püttner R., Schmidt, J.-S., Molodtsov S.L., Adamchuk V.K.; Gudat W., Kaindl G., Nucl. Instr. and Meth. in Phys. *Res.* A, 505,718 (2003).
11. Stohr, J. NEXAFS Spectroscopy (Springer, Berlin, 1992).
12. J.J. Yeh, Atomic Calculation of Photoionization Cross-Sections and Asymmetry Parameters (Gordon and Breach Science Publishers, Langhorne, PE (USA), 1993). J.J. Yeh, I.Lindau, Atomic Data and Nuclear Data Tables, 32, 1-155 (1985)
13. Henke B.L., Knauer J.P., Premaratne K.,J. Appl. Phys., 52,1509 (1981)

Fig.4. *Irradiation-induced changes of the Partial C1s absorption cross section for S layer.*

Fig.5. *Irradiation-induced changes of the Partial N1s absorption cross section for S layer.*

Analysis of 3D Microstructure and Deformation of Multiphased Materials by Micro Computertomography

H.-A. Crostack, J. Nellesen[1], G. Fischer[1], K. Ehrig[2], H. Riesemeier[2] and J. Goebbels[2]

Lehrstuhl für Qualitätswesen, TU Dortmund, D-44221 Dortmund, Germany

[1]RIF e.V., Joseph-von-Fraunhofer-Str. 20, D-44227 Dortmund, Germany

[2]BAM Bundesanstalt für Materialforschung und -prüfung,
Unter den Eichen 87, D-12205 Berlin, Germany

1. Introduction

Comprehension of micro deformation and micro damaging processes running before the macroscopic failure of metal materials is essential in order to predict the material behavior and to tailor materials with respect to desired mechanical properties. To gain this understanding one has to analyze these processes in the course of loading and to study the impact of microstructure. In case of *multiphased* materials for example the effect of volume fraction, shape, orientation and arrangement of the phase dispersed in the matrix on these processes has to be considered. Micro deformation which precedes the micro damaging is often accompanied by strain localisation. This phenomenon affects tremendously the locus and the type of the successive failure, the behavior during machining the material, the roughness of the surface and the fracture strain.

2. Materials and Methods

For this reason, in this work strain localisation is analysed *non-destructively* by mapping 3D microstructure of multiphased materials in different stages of deformation with synchrotron radiation based micro-tomography. The 3D tomograms are evaluated by digital image correlation to get strain tensor and displacement vector fields: Exploiting gray value gradients (i.e. contrast between the phases), an affine and radiometric transform between a less deformed and a more deformed state are iteratively optimized for a set of corresponding tomogram subvolumes. From the final affine transform of each subvolume pair the Lagrangian strain tensor γ is calculated. After a principal axis transformation of this tensor the scalar equivalent strain ε_{equ} can be gained. In order to guarantee a sufficient number of sites with a high gray value gradient for the digital image correlation algorithm the size of the subvolumes has to be adapted to the characteristic microstructural length which is given by the mean distance between vicinal microstructural objects. A detailed description of this approach can be found in [1].

500 μm
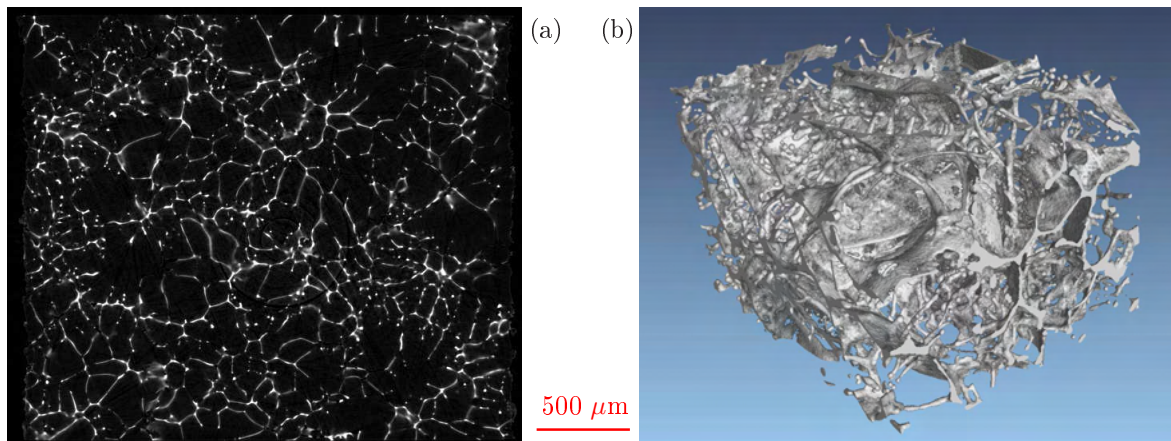
Figure 1: (a) 2D-image of microstructure from the bulk of a plain tensile specimen made of the multiphased material $Al_{98}Sn_2$, tin segregations (white) at the grain boundaries; (b) 3D-representation of the segregated tin.

In the scope of the experiments tiny plain dog-bone shaped tensile specimens with a cross-sectional area $A = 2 \times 1 \text{ mm}^2$ made of the alloy $Al_{98}Sn_2$ were investigated which were manufactured by spark cutting. The experiments were performed at BAM*line* at BESSY II [2, 3]. Monochromatic photons of $E = 35$ keV were selected by a double multilayer monochromator. After each deformation step the gauge length of the tensile specimen was imaged by microtomography in the unloaded state. During image acquisition the specimen was turned on its longitudinal axis 2000 times through an angle increment of 0.09 ° yielding the semi circle. Due to parallel beam geometry the reconstruction was done slice-by-slice. The 3D tomogram was formed by the stack of 2D slices.

3. Results

From the 2D-image (*xy*-slice) in fig. 1(a) extracted from the 3D-tomogram of the undeformed specimen it is obvious that tin segregates at the grain boundaries. For this reason, tin serves as a marker for the 3D image correlation algorithm. Thus, in this case the characteristic microstructural length is given by the mean grain size. The spatial distribution of the segregated tin can be grasped in fig. 1(b).

Since the characteristic microstructural length in the investigated material approximately amounts to 100 µm a cubic tomogram subvolume with an edge length of about 250 µm was chosen for the correlation analysis.
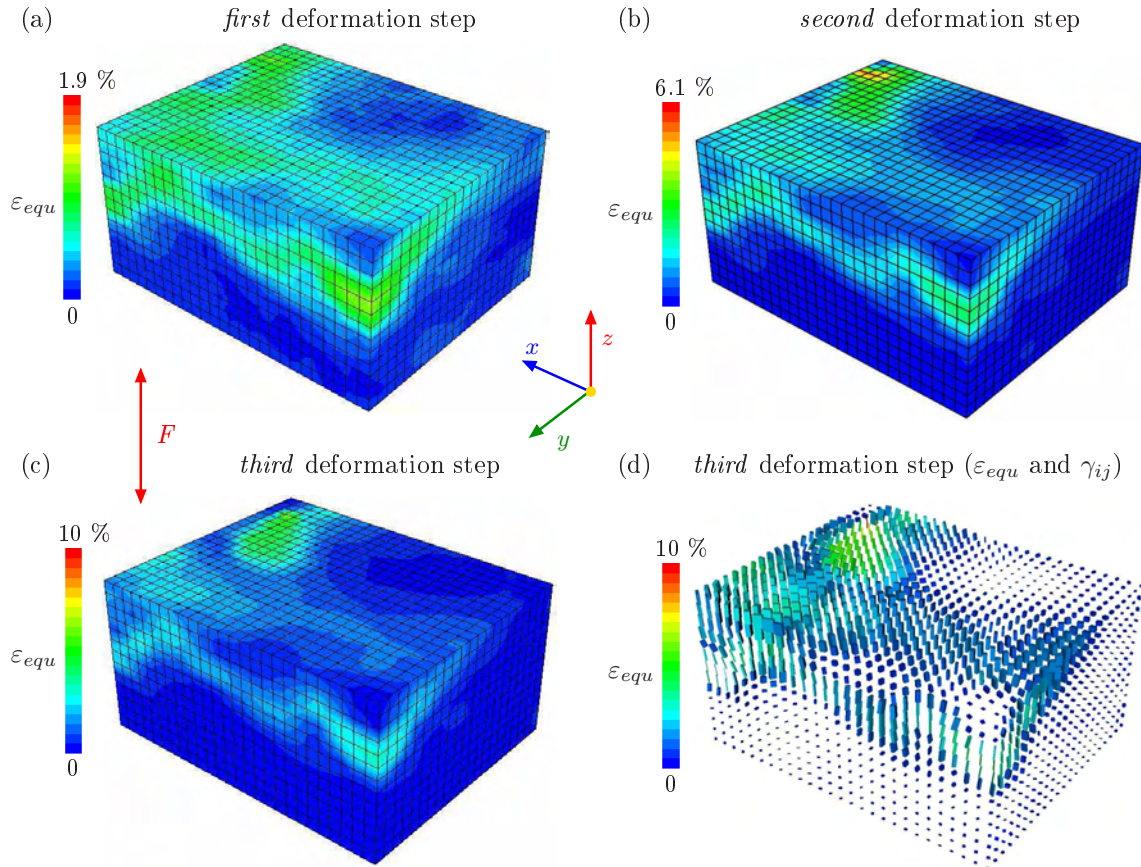
Figure 2: (a)-(c) 3D representation of the color-coded equivalent strain in the course of loading, (d) 3D representation of the field of Lagrangian strain tensors γ with cuboids; cuboids are color-coded according to the scalar equivalent strain ε_{equ}; only the tensor cuboids of the planes visible in subfigure (c) are shown.

In the subfigures 2(a)-(c) the development of equivalent strain ε_{equ} in the first, second and third deformation step are visualized. In order to achieve the smooth representation of equivalent strain the distribution of the discretely sampled scalar field was tesselated. From the comparison of these subfigures it can be deduced that bands of elevated equivalent strain which emerge already in the first deformation step retain their position but the strain values increase. In subfigure 2(d) the 3D field of Lagrangian strain tensors γ in the third

deformation step is depicted by cuboids. For the sake of clearness only the tensor cuboids of the planes visible in subfigure 2(c) are shown. The bricks which are color-coded according to the scalar equivalent strain are oriented and scaled according to the Lagrangian strain tensor. The comparison of subfigures 2(c) and 2(d) reveals that in the band of elevated strain which can be seen in the facing *xz*-plane the largest edge of the cuboids (maximum principal strain) is preferentially aligned with the direction of global load indicated by the red line with arrows at both ends. Up to now the effect of microstructure on the initiation and growth of bands has not been studied but will be analyzed in future work.

4. Acknowledgment

5. References

[1] H.-A. Crostack, J. Nellesen, G. Fischer, S. Schmauder, U. Weber, F. Beckmann, *3D analysis of MMC microstructure and deformation by μCT and FE simulations*, Developments in X-ray Tomography VI, edited by Stuart R. Stock, Proceedings of SPIE 7078, 70781I-1-12, 2008 (SPIE, Bellingham, WA).

[2] H. Riesemeier, K. Ecker, W. Görner, B.R. Müller, M. Radtke, M. Krumrey, *Layout and first XRF Applications of the* BAM*line at BESSY II*, X-ray Spectr. 34 (2005) 160-163

[3] A. Rack, S. Zabler, B. R. Müller, H. Riesemeier, G. Weidemann, A. Lange, J. Goebbels, M. Hentschel, W. Görner, *High resolution synchrotron-based radiography and tomography using hard X-rays at the* BAM*line (BESSY II)*, Nucl. Instr. Meth. A 586 (2008) 327-344

Valence Electronic Structure of Ruthenium Based Complexes Probed by Photoelectron spectroscopy at High Kinetic Energy (HIKE)

E. M. J. Johansson[1], M. Odelius[2], M. Gorgoi[3], O. Karis[1], R. Ovsyannikov[3], F. Schäfers[3], S. Svensson[1], H. Siegbahn[1], H. Rensmo[1]

[1]Dept. of Physics, Uppsala University
[2]Fysikum, Stockholm University
[3]BESSY GmbH, Berlin

Different ruthenium-polypyridyl complexes are extensively investigated today due to their potential use in photoconversion, e.g. in dye-sensitized solar cells. Some ruthenium-polypyridine complexes such as $Ru(dcbpy)_2(NCS)_2$ have resulted in solar cell systems having very high photon to current conversion efficiency in the visible region. In most of the ruthenium based dyes, the dominant absorption process is traditionally considered as a metal to ligand electron transfer, induced by absorption of the incoming photon. In for example the dye-sensitized solar cell, the electron is thereafter transferred from the ligand to the oxide nanoparticle. The efficiency of the photoconversion process is largely dependent on the properties of the interfacial region and specifically the molecular properties of the dye molecule. Insight into the detailed electronic structure of the dye molecule will thus facilitate the understanding of the mechanisms determining observed functions and efficiencies. Photoelectron spectroscopy (PES) is a technique that can be used to obtain element specific information on the electronic and molecular surface structure at the interfaces in the dye-sensitized solar cell. In the present report we use photoelectron spectroscopy at high kinetic energy (HIKE) using hard X-ray as an experimental tool to understand the bulk valence electronic structure of such metal-centered complexes. We report a series of ruthenium polypyridine complexes with CN^-, or Cl^- or NCS^- ligands. The different ligands are exchanged stepwise to follow how the metal-ligand interactions develop. Such experimental information is of general interest in the design of such inorganic coordination complexes. The experimental results are modeled well by DFT calculations in a crystalline environment whereas the gas phase models show distinct differences in the mixing of ruthenium and ligand orbitals.

The bulk sensitivity using HIKE is particularly useful for measurements of valence structures on molecular films that are difficult to prepare in-situ (in a UHV environment) due to difficulties in evaporation of the material without decomposition. For such ex-situ samples the valence electron spectra may contain contributions from a contamination layer making, for example, the interpretation of traditional ultraviolet photoelectron spectroscopy (UPS) measurements difficult. However, at a kinetic energy of 2800 eV, as used in this study, the mean free path is in the range of 5 nm, that is, about 5 molecular layers. This means that about 40 percent of the signal originates from layers buried deeper than 5 nm and that the contribution from the surface contamination in the interpretations therefore is substantially diminished.

Another important feature when using hard X-rays compared to UPS or PES based on soft X-rays, is the general influence of the cross section of the different energy levels. Specifically, in the ruthenium based dyes, the cross section of Ru 4d relative C 2p, N 2p, O 2p, Cl 3p or S 3p will increase considerably when using hard X-rays. Photoelectron spectroscopy with HIKE in the valence region will therefore mainly probe the Ru 4d partial density of states (PDOS) and can be used as an experimental tool to delineate the molecular orbital character for the highest occupied orbitals in the complexes. The figure shows the experimental valence spectra of the different Ru-polypyridyl complexes. The frontier orbital structures of these kinds of ruthenium complexes are often interpreted within an octahedral symmetry in which the highest occupied molecular orbital contains three degenerate orbitals mainly localized at the Ru center
(The t_{2g} set).

However, experiments on Ru(dcbpy)$_2$(NCS)$_2$ (N719 in the figure), Ru(tcterpy)(NCS)$_3$ (BD in the figure) indicate that the t$_{2g}$ Ru 4d levels split substantially due to the symmetry and the interaction with the different ligands and accordingly that other orbitals than those from the metal center have to be mixed into the density of states (DOS) between 0-5 eV.

Comparing the experimental spectra of the different dye molecules, we observe that the highest occupied electronic structure differs substantially. At high photon energies, the ruthenium contribution is high as explained above and the interaction between the Ru 4d and the X-ligands can thus be followed directly for the different dyes. The splitting between the two peaks with lowest binding energy are very similar for dye 1 (BD) and dye 2 (N719), about 1.5 eV, and the intensity ratio in both cases is also similar and slightly below 2:1. For the dye with CN ligands and the dye with Cl ligands, there is no clear large peak close to the peak at lowest binding energy, instead a broad feature at 3-4 eV from the first peak is observed, which suggests that the mixing of the ligand molecular orbitals with the Ru 4d levels is different for these dyes.

Calculations of the electronic structure of single molecules showed that the Ru 4d level splits up. However, the intensity relations for the ruthenium contribution in the highest occupied electronic structure do not agree with experiment. Calculations of the dye molecules in crystal structures were also performed and the agreement with experimental data for these calculations is found to be much better. This showed that the intermolecular interactions in the solid state are important and largely influence the orbital composition in the frontier electronic structure. The precise electronic structure is a key parameter for photoconversion involving charge transfer processes and the result emphasises the importance of intermolecular interaction for modeling the initial conversion process in the dye-sensitized solar cell.
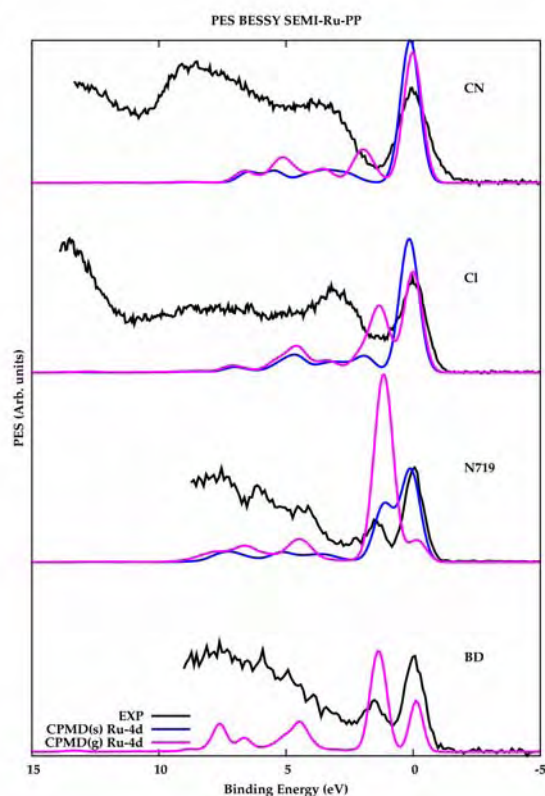
Figure 1: Valence spectra of the ruthenium complexes together with the calculated ruthenium contribution in a gas phase calculation CPMD(g) and in the calculation on a crystal of molecules CPMD(s)

High energy X-Ray photoelectron spectroscopy of HBC-C14

Vajiheh Alijani Zamani, Shahabeddin Naghavi, Andrei

Gloskovskii, Gerhard Fecher and Claudia Felser

Institut für Anorganische Chemie und Analytische Chemie,

Johannes Gutenberg - Universität, Mainz

A charge transfer (CT) complex is defined as an electron donor – electron acceptor complex, characterized by electronic transitions to an excited state. In this excited state, there is a partial transfer of charge from the donor to the acceptor. Almost all CT complexes have unique and intense absorption bands in the UV and visible range. They are good candidates as photovoltaic cells, transistors and superconductors. Hard X-ray photoelectron spectroscopy (HAXPES) is a powerfull tool to investigate the bulk electronic structure of solids. It allows to study the density of occupied states and to estimate the position of HOMO. We started our theoretical and experimental investigations of CTs from HBC-C14 which is a strong polyaromatic donor.

The structure of HBC-C14 is shown in Figure 1. Thin films of HBC-C14 were prepared by spin coating. The concentration of the solution was 3 mg/ml in chloroform as solvent. To reach this concentration, the solvent was heated to 55° C. The optimal rotation speed for the films preparation was 1500 rpm. Lower rotation speeds leads to thicker films but we can see precipitates on the surface of the films, whereas higher rotation speeds results in thinner non-continuous films. The process for cleaning of the Si/SiO_x substrate was acetone ultrasonication for 30 minutes at 35° C followed by rinsing with isopropanol and finally drying with N_2. The thickness of the film measured by using a tencor profiler was estimated to be 30 nm.

AFM images and thickness profile (TP) line of the film chosen for the photoemission studies are shown in Figure 2a, b, respectively. The TP was taken along the line AB drawn through a defect on in the film which most likely is a hole to the substrate. Its depth is 25 nm and can be used as a measure for the film thickness. Generally, the TP line excibits the oscillations with an amplitude of 10 nm. This means that the film consist of two layers: 15 nm thick 2D continious layer and 10 nm thick 3D layer on the top.

Thin film was investigated at KMC-1 beamline of BESSY with different excitation energies between 2.2 keV and 8 keV. Prior to synchrotron measurements, the film was investigated using laboratory XPS (Al Kα with an excitation energy of 1.486 keV). Figure 3 shows survey XPS spectrum. No trace of Si from the substrate and negligible oxygen signal was observed in this measurement. The resolution of the non-monochromatised laboratory X-Ray sources is not enough for valence band studies, therefore HAXPES measurements using tunable synchrotron radiation were done.
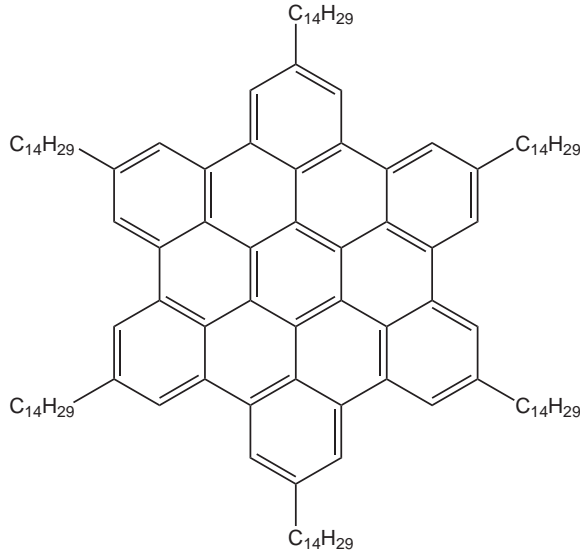
FIG. 1: Structure of HBC-C14.
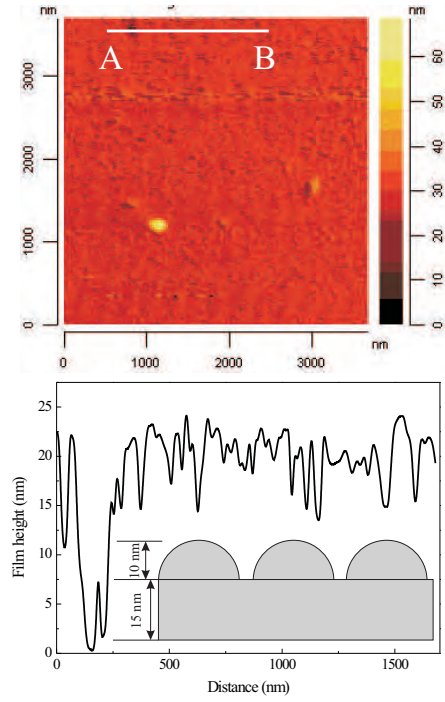
FIG. 2: (a) AFM images of the HBC-C14 film; (b) thickness profile line taken along line AB shown in (a) and a schematic drawing of the structure of the film.
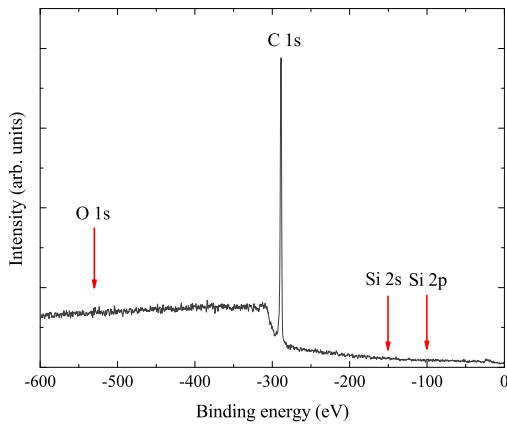
FIG. 3: XPS spectrum of thin film of HBC-C14 on Si/SiO$_x$ substrate. The energy position of Si and O core levels are marked with arrows.
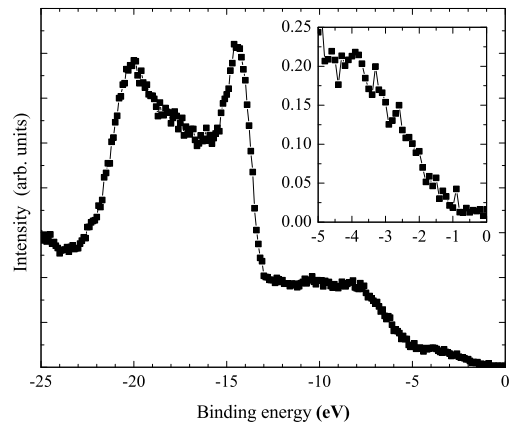
FIG. 4: Valence band spectra of HBC-C14 at E$_{exc}$=3 KeV.

Still at excitation energy of 2.2 keV, the survey spectrum shows mainly C 1s core level emission and Si is not visible. With increasing photon energy the inelastic electron mean free path increases from 5 nm at 2.2 keV to 15 nm at 7 keV and photoemission signal from the Si/SiO$_x$ substrate becomes visible at 7 keV (not shown here). We can conclude that HAXPES measurements at intermediate energies (about 4 keV) are better suited than at high energies (7 keV), in

particular for uncapped thin films with a thickness of several tens of nanometers. Intermediate excitation energies already ensure good bulk sensitivity with a probing depth slightly less than the film thickness. In the case of very high excitation energies the inelastic electron mean free path becomes comparable with the film thickness. This results in the experimental probing depth much larger than the film thickness. The signal from the substrate superimpose with the spectrum from the thin film what makes the data processing much more complicated. Moreover, at very high excitation energies the intensity from p states is moderately low, as their absorption cross section drops down at high kinetic energies much faster than the one of the s states.

The best resolution at high signal to noise ratio was achieved at $E_{exc}=3$ keV (Figure 4). The valence band onset is at about -2 eV. This result is in a good agreement with the calculations predicting the HOMO-LUMO gap of 2.6 eV. Additional inversed photoemission studies are needed to investigate the density of states with positive energies where LUMO is situated.
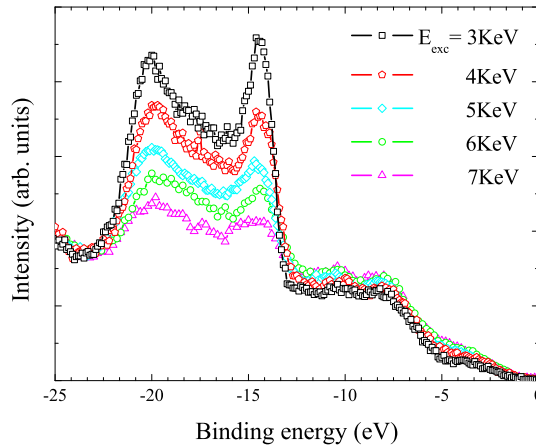
FIG. 5: Valence band spectra of HBC-C14 measured at different excitation energies.

Pronounced excitations are visible from -14 eV to -20 eV that are related to aliphatic chains that exist in the HBC center [1]. The intensity of these excitations decreases with increasing the photon energy. This is, indeed, a prove that those excitations belong clearly to the compound and not to the substrate. At -6 eV to -10 eV excitations with lower intensity and an unresolved structure are visible. The intensity of the excitations between -6 eV and the threshold are even lower. The intensity in the latter two ranges does not change with increasing photon energy (Figure 5).

[1] J. J. Pireaux and R. Caudano, Phys. Rev. B 15, 2242 (1977).

Characterisation of Photonic Band Gap Phosphors

Alan Michette and Matthew Shand
King's College London, Department of Physics, Strand, London, WC2R 2LS, UK
George R Fern, Jack Silver, Robert Withnall and Terry Ireland
Wolfson Centre for Materials Procesisng incorporating the Centre for Phosphors and Display Materials, Brunel Univesity, Kingston Lane, Uxbridge, Middlesex, UB8 3PH, UK.

Several phosphors were characterized using the KMC-2 beamline and a user-provided Jeti Spectroradiometer 1201 linked to a standard PC via a USB cable. This instrument records the luminance of the material over the wavelength range 380–780 nm. The measurements were taken at 1 keV intervals in the range 6–12 keV and in some cases measurements were also taken at smaller energy intervals around the x-ray absorption edges of the activator ions and the host lattice ions. Many samples were investigated to ascertain which materials show the brightest luminance using these excitation conditions. The samples that were studied were powders of: Y_2O_3:Eu 1%, Y_2O_3:Ce 1%, Y_2O_3:Dy 1%, Y_2O_3:Er 1%, Y_2O_3:Gd 1%, Y_2O_3:Ho 1%, Y_2O_3:Nd 1%, Y_2O_3:Pr 1%, Y_2O_3:Sm 1%, Y_2O_3:Tb 1%, Y_2O_3:Tm 1%, Y_2O_3:Yb 1%, Gd_2O_2S:Pr 1%, 2%, 3% and 5%, and the 1% dopant concentration with several deposition thicknesses, Y_2O_3:Eu 2% Tb0.1% Gd0.1%, $Y_{1.2}Gd_{1.8}Al_5O_{12}$:Ce, Y_2O_3:Eu 2% Tb 0.1%, Gd 0.1%, ZnO:Zn, several types of ZnS:Cu, ZnS:Cu,Pb, ZnO:Ga, $Tb_3Al_5O_{12}$:Ce $LaPO_4$:Tb, Y_2O_2S:Tb and of some of these materials deposited as photonic band gap materials comprising of face centred cubic lattices with a cell parameter in the region of 300 nm. Hence around 55 sets of measurements were made.

A significant amount of time was spent optimising the measurements with the Jeti spectroradiometer since this is a non-standard detector and has non-ideal resolution and sensitivity. The spectrometer should have ideally been placed 6–20 cm from the sample but in this range of distances with the first samples measured it was found that no visible light emission could be detected. After some experimentation it was found that the optimised position for the Jeti was as close to the sample as possible without interfering with the x-ray beam, which meant that it had to be around 30° to the incident x-ray beam. A monochromator system would give better resolution, and sensitivity would be greatly enhanced if the detection method was via a photomultiplier tube. It was also found that the mounting of the samples for measurement could be improved. The phosphor powders were mounted onto adhesive tape which resulted in a thin uneven covering of powder and may have been one factor that produced some of the poor emission spectra. By modifying the sample holder it was possible to produce 2 mm thick samples that gave improved emission spectra.

It was surprising that most of the phosphors studied gave poor visible emission spectra, $<1\,\mathrm{Cd\,m^{-2}}$. Most of the materials analysed are well known scintillator materials and have already shown good photo and cathodo-luminescence; the Gd_2O_2S:Pr phosphor had also previously been tested on the King's laser plasma x-ray source where it showed excellent emissive properties.[1] This is likely to be due to the inability of the detector to measure small sample areas, since the x-ray beam spot was smaller than the sampling area of the detector. The most intensely emitting samples measured all contained Tb doping; LAP:Tb, (YGd)$_2$O$_3$:Tb, Y_2O_2S:Tb and Gd_2O_2S:Tb

gave very strong, clean emission spectra with luminance values of $10–60\,\mathrm{Cd\,m^{-2}}$ (see figure 1).
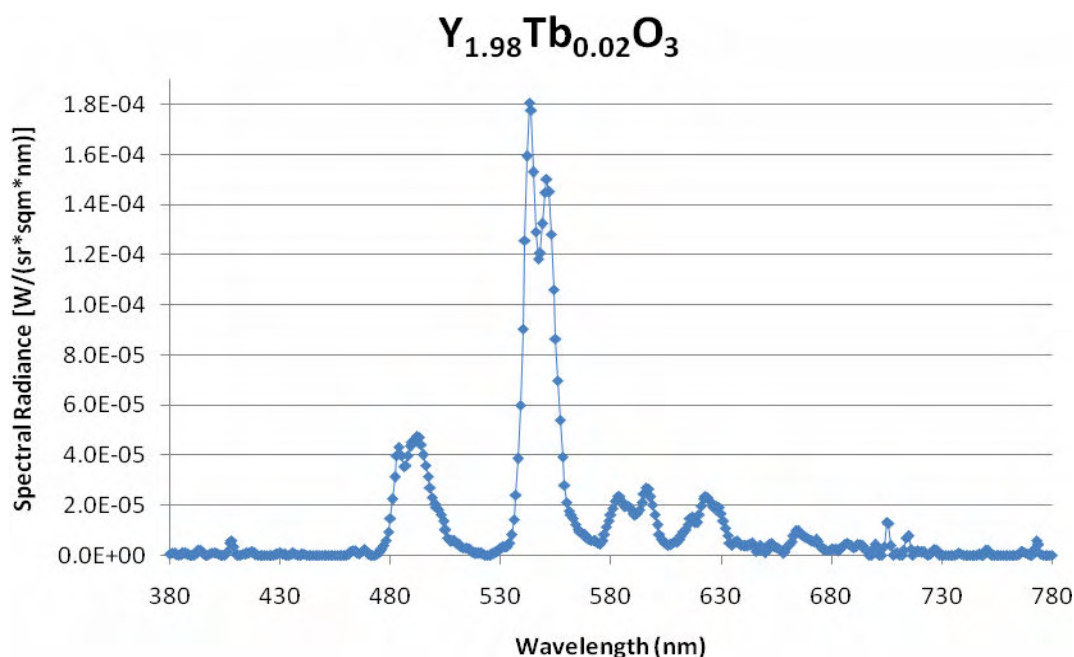
Figure 1. Typical emission spectrum of 1% terbium doped yttria obtained at BESSY in the energy range 6–12 keV.

The use of Tb^{3+} is advantageous since it has many sharp emission bands spanning the visible spectrum (380–780 nm) which will enable the analysis of the effect of photonic band gaps in the structured materials. Attenuation of a Tb^{3+} emission band was observed at 427 nm in the lattice of a small PBG crystal. This coincides with the calculated stop band for this inverse opal phosphor lattice, and requires further investigation since the observed emission was weak.

Hence, future investigations on photonic band gap materials will need to consider the use of a better detector, improved sample mounting and the use of Tb doped scintillator materials.

Acknowledgements

Reference
(1) George Fern, Terry Ireland, Jack Silver, Robert Withnall, Alan Michette, Chris McFaul, Slawka Pfauntsch, Characterisation of Gd_2O_2S:Pr phosphor screens for water window X-ray detection, *Nuclear Instruments and Methods in Physics Research Section A: Accelerators, Spectrometers, Detectors and Associated Equipment*, In Press, Available online 6 December 2008, ISSN 0168-9002, DOI: 10.1016/j.nima.2008.11.116.

Synthesis and material analysis of carbon-nitride nanoparticles

E. Kovacevic[1], J. Berndt[1], Th. Strunskus[2], J. Winter[3], L. Boufendi[1] and Ch. Wöll[4]

[1]*GREMI Université d'Orléans, Polytech'Orleans, Orleans Cedex 2, France*
[2] *Christian-Albrechts-University of Kiel, Institute of Material Science, Kiel, Germany*
[3]*Ruhr University Bochum, Institute for Experimental Physics II, Bochum, Germany*
[4]*Chair of Physical Chemistry I, Ruhr University Bochum, Bochum, Germany*

The aim of the investigations is the production and analysis of nitrogen containing hydrogenated carbonaceous nanoparticles. The incorporation of nitrogen into carbonaceous materials is interesting in a wide area of applications - from technology to astrochemistry. A large variety of nitrogen containing carbonaceous materials have attracted a great interest due to their mechanical and electrooptical properties. Nowadays many of these materials already found applications in industry, e.g. as coatings for hard disks, microelectromechanical elements (MEMs) or emitters. Furthermore nitrogen containing carbon compounds can also be found in astrophysical environments. The existence of nitrogen both in gas and solid phase is clearly seen in observational IR spectra of the interstellar medium and it is known that the prominent feature of Titan's atmosphere is a thick haze region that acts as the end product of hydrocarbon and nitrile chemistry. Carbon-nitride materials miming the Titans aerosols are named tholins and low temperature plasmas can be considered as one of the best sources for their production.

One of the crucial questions for the application and production of plasma produced polymers concerns the stability of these materials. An important point for the production of stable polymers is of course the material temperature - during the production process and afterwards. It was found (see [1] and the references therein) that plasma polymers can be stabilized by thermal annealing, since the thermal treatment enhances the mobility of cross-linked polymer chains and therefore favors the recombination of trapped free radicals. Vice versa, annealing experiments can deliver important information about the stability of the polymer, about the stability of their bonding structure, and thus, indirectly about the conditions during the production process.

The nanoparticles we present in this contribution are produced in a low temperature, low pressure and low power radio-frequency discharge, from nitrogen/methane gas mixture (10% methane). The capacitively coupled discharge was driven by 13.56 MHz , input power 40W at 1mbar total gas pressure. The particle formation is monitored by the analysis of electrical characteristics of the discharge (e.g. self-bias) as well as by emission spectroscopy and laser light scattering. This observation of the plasma allowed the in-situ identification of different growth phases - that are related to specific particle sizes, and thus a controlled production of the particles. Our further analysis was obtained on particles with diameter of about 100nm. The annealing experiments have been obtained in high vacuum chamber at the HEGSM beam-line The effect of the annealing on the polymer material was investigated (in situ i.e. during the annealing) by means of Near Edge X Ray Absorption Fine Structure spectroscopy (NEXAFS). The NEXAFS measurements are obtained in the soft X-ray spectral region where sharp core levels are found for C, N, and O elements contained in our samples.

Figure 1 shows the ex-situ IR spectrum of the particles produced in nitrogen/methane gas mixture. The broad strong features with maximum at about 3300 cm^{-1} can be identified as NH stretching vibrations (NH_2 and NH_3, overlapping with certain small amount of OH stretching bonds due to impurities present in the chamber). The structured shoulder at 2930 cm-1 is identified as CH stretching feature (CH_2 and CH_3, symmetric and asymmetric). The dominant feature in the spectrum is a strong, broad absorption peak centered at about 1625 cm^{-1} (6.15 µm) which can be interpreted mostly by the formation of CN double bonds, with possible C=C presence as well as a superposition of vibrations with different origins (e.g. C=O, CH deformation bands, see [2]). The presence of triple bonds is observable from the feature with maximum at about 2200cm^{-1}. The origin of this feature is C≡N (nitrile, isonitrile) and possibly C≡C stretching vibrations.
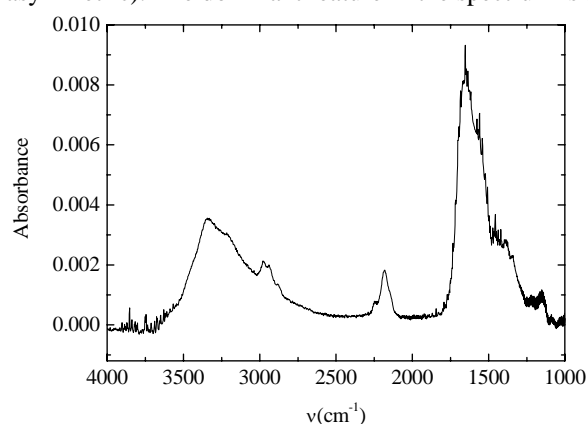
Figure 1 Ex-situ FTIR spectrum of CN dust particles (diameter about 100nm).

NEXAFS measurements on the nanoparticles gave us better insight in the charachteristics of nanoparticles. From normalized C K edge spectra, as in Figure 2, we can see almost negligable presence of C=C bonds at 285 eV (signed within the Figure 2 as C1)). Therefore, and according to explanations proposed in the literature, we can suppose that nitrogen intensified the C=C vibrations in the IR spectrum. This can partially explain the dominant feature in the fingerprint area (1000-1800 cm^{-1}). Further resonance line can be observed at 286.6 eV (C2), in the

literature correlated with C1s→π* (C≡N), and with some π* resonances from C=O [3]. Some authors [4] associate this peak also with some C=N bonds. This possibility can be in our case not excluded, for one reason that we observe C=N in the FTIR spectrum. The other important reason why not to exclude several possibilities is that nanoparticle formation in plasma processes results in complex polymers with large variety of bonding situations. The resonances at 288eV (C3) can be correlated with C-H σ*; although there is also a possible correlation with C=O originating from amide groups.. This peak has a shoulder at about 287.7 eV, correlated with aliphatic and ketonic C-H groups. Around and above 292 eV (edge, C4) we can observe different C1s→σ* resonances, with shape and position, together with previously mentioned σ*(C-H) states, typical for plasma polymerized samples [5]. We observe also a shoulder around 301eV (C5), probably coming from σ* C=C and C=N resonances [5].
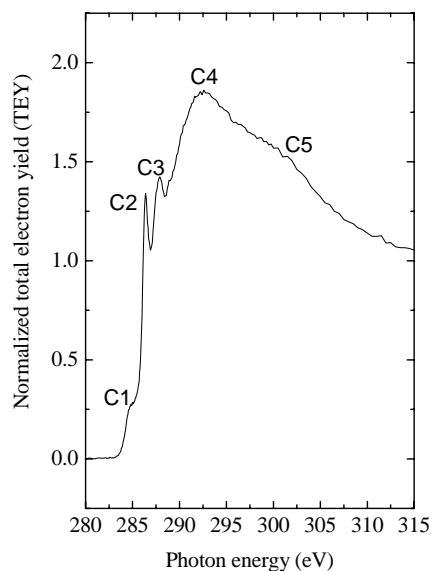
Figure 2 NEXAFS spectrum: C K edge
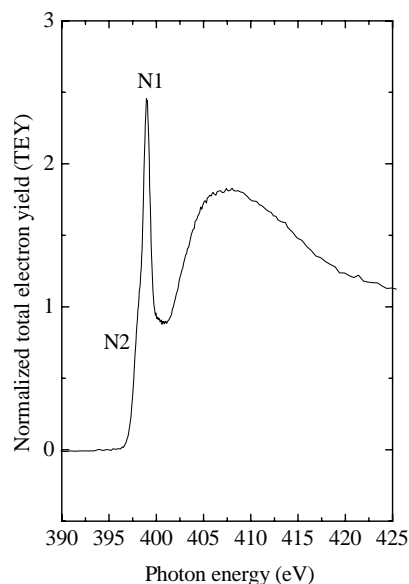
Figure 3 NEXAFS spectrum: N K edge

The dominant pre-edge peak is positioned at 399.7 eV(N2), with a shoulder at about 399 eV. The main peak can present a variety of π nitrogen bonds; hence the unique identification is obviously very complicated. On the basis of calculation data for carbon-nitride films some authors [6] show that such kind of low energy peak can be related to constrained CN bonds, the presence of pyridine-like double bonds (–C=N–), or imines. Some authors ascribe this peak to N≡C bonds (nitriles, isonitriles)[3]. This kind of bonds is, actually, for most of polymer materials in IR spectra (around 2100 cm^{-1}) either not observable or present as a weak feature. One explanation in favor of nitrile presence in the material is: aliphatic nitriles absorb weakly in IR, so it is possible that there is a more significant presence of these groups as assumed. On the other hand, NEXAFS is very sensitive to the presence of these groups and could overemphasize the real picture.

Furthermore we can observe a change of the slope around 402 eV and the strong broad σ* resonance around 407 eV. The presence of σ bonds is observable through the strong broad resonance above 407 eV (N-C, N-H).

The annealing of the above analyzed nanoparticles was performed in several steps, with temperature increase of about 20 K/min. The NEXAFS spectra from annealing experiment are presented without normalization in order to stress losses we could observe from nanoparticle surface and bulk material. Although measurements have been obtained after every 50K step, we present only certain steps, in order to present important changes more clearly.

Figure 4 shows the C K edge at different temperatures. The changes in spectra start first above 550K. Above this temperature we can observe the increase of C=C sites (peaks C1+C5), and a gradual loss of C=O and C-H correlated peaks (C3). After 700K spectra reveal changes in the C2 peak, correlated with nitrogen presence. The changes observed above 550K can be correlated with the behavior of oxygen, i.e. oxygen removal. From the NEXAFS spectra on the O K edge (Figure 5) we can observe the start of this oxygen removal at 550 K. The oxygen presence is negligible above 650 K. Fig. 6 shows the changes of the NEXAFS spectra at certain temperatures for the N K edge. Spectra were unperturbed until 650K (oxygen loss). Above 700K (Figure 7) spectra reveal drastic changes in the peaks N1 and N2 (for identification see Fig 3). N1 increases, while N2 decreases, and new peaks arise, like the feature around 401-402eV. The whole preedge region becomes weaker compared to the 407 eV region (σ* resonances). In comparison with the previous reports on CN film annealing (e. g [7]), where the nitrogen loss starts already around 450K, we observed losses around 800K. After 850 K the material is rather stable.

However, due to the complexity of the material and the complicated identification of spectral features, this work requires further analysis like elemental analysis and especially theoretical calculations of NEXAFS spectra, which are beyond the scope of this report.
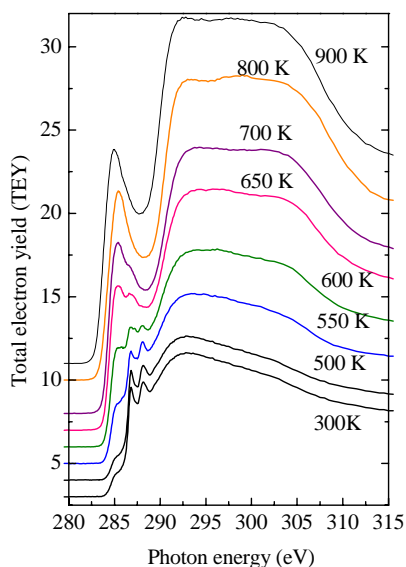
Figure 4 C K edge NEXAFS spectra: annealing
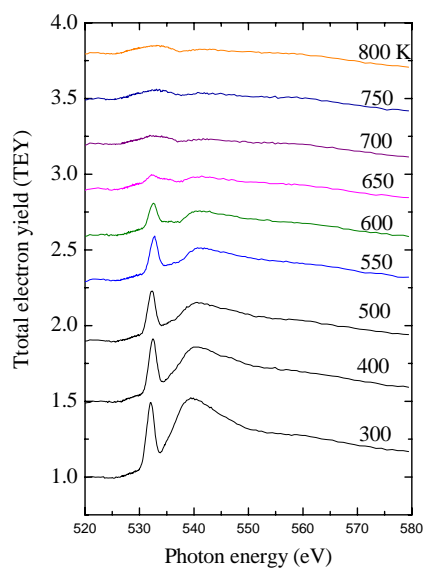
Figure 5 O K edge NEXAFS spectra: annealing
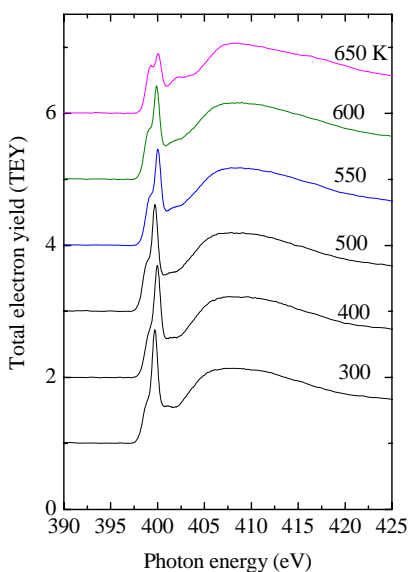
Figure 6 N K edge NEXAFS spectra: up to 650K
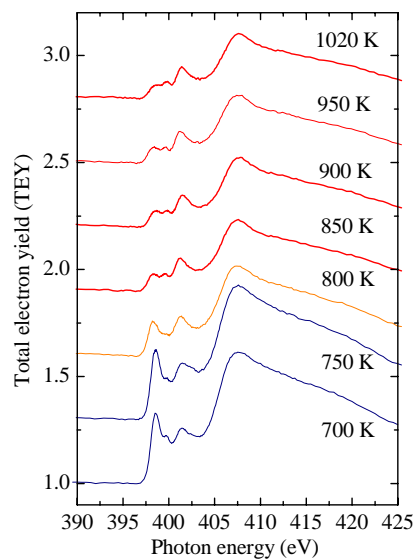
Figure 7 N K edge NEXAFS spectra: above 650K

References
[1] H. Biederman, Plasma polymer films, Imp. Colledge Press, London, UK (2004).
[2] A. C. Ferrari, S.E. Rodil, and J. Robertson, Physical Review B **67**, 155306 (2003).
[3] A.G. Shard, J. D. Whittle, A. J. Beck, P. N. Brookes, N. A. Bullett, R. A. Talib, A. Mistry, D. Barton, S. L. McArthur, J. Phys. Chem. B **108**, 12472 (2004).
[4] C. Lenardi, M.A. Baker, V. Briois, G. Coccia Lecis, P. Piseri, W.Gissler, Surf. Coat.Technol. **125**, 317 (2000).
[5] J. Stöhr, "NEXAFS Spectroscopy", Springer-Verlag, Heidelberg (1992).
[6] F. Alvarez and M.C. dos Santos, Journal of Non-Crystalline Solids **266**, 808 (2000)
[7] G-Q. Yu, S-H. Lee, J-J. Lee, Diamond and Related Materials **11**, 1633 (2002).

Features of resonant F *KLL* Auger spectra from titanium trifluoride TiF$_3$ and fluorinated multi-walled carbon nanotubes F-MWCNTs.

A.S. Vinogradov[1], M.M. Brzhezinskaya[1,2], A.V. Generalov[1], A.Yu. Klyushin[1], and R. Püttner[3]

[1] *V.A. Fock Institute of Physics, St. Petersburg State University, St. Petersburg, 198504 Russia*
[2] *HZB (BESSY GmbH), 12489 Berlin, Germany*
[3] *Institut für Experimentalphysik, Freie Universität Berlin, 14195 Berlin, Germany*

The electronic structure of solid metal fluorides, that present the most ionic crystals, is usually considered in the framework of the simple ionic model. At the same time, the covalent mixing (hybridization) between the fluorine $2p$ electrons and valence electrons of metal atoms has a dramatic effect on the electronic structure of their compounds. Using x-ray absorption spectroscopy at the F $1s$ edge, we have shown previously that even in the case of such strongly ionic compounds of the $3d$ transition-metal (TM) fluorides, covalent bonding plays an important role, causing a mixed TM $3d$ – F $2p$ character of the empty electronic states near the bottom of the conduction band [1]. Recently we also have observed the strong effect of the covalent bonding on electronic structure of multi-walled carbon nanotubes (MWCNTs) upon their fluorination [2]. The main aim of the present study was to gain a deeper insight into the nature of chemical bonding and electronic structure features for the titanium trifluoride, TiF$_3$, and the fluorinated multi-walled carbon nanotubes, F-MWCNTs, using high-resolution measurements of resonant F *KLL* Auger spectra. Resonant Auger spectroscopy is well known to provide a new and powerful method to study the core-electron excitations in atoms and ionic crystals [3-5]. In principle, there is a close analogy between the core-excited states of atoms and those in solids: in both cases the excited electron is bound to the inner hole of the parent atom by electrostatic forces. At the same time, this electron can be localized in solids only in the volume that is confined to neighboring atoms of the parent one for the excited electron. These atoms are chemically bonded to the parent atom and therefore are involved in a formation process of possible excited states for the core electron under consideration. From this it is clear that the covalent bonding between the parent atom and its neighbors can strongly influence the localization character of the excited electron and its localization extent on the parent atom which define resonant spectator and participator Auger-decay processes for the core-excited electron and spectral shape of resonant Auger spectra.

All measurements have been performed at the Russian-German beamline (RGBL) using experimental station Mustang. Thin (20-25 nm) TiF$_3$ layers were prepared *in situ* in the preparation chamber by thermal evaporation of thoroughly dehydrated TiF$_3$ powder from a effusion cell heated by an electron beam onto a polished stainless-steel plate in a vacuum of $\sim 3 \times 10^{-7}$ mbar. A sample of F-MWCNTs (10 wt. % of fluorine) was prepared in air by rubbing powder of it into the scratched surface of a clean stainless-steel plate. NEXAFS spectra at the F $1s$ edges for these samples were obtained in the total electron yield mode by detecting a sample current. The photon energy was calibrated using the known energy position of the first narrow peak in the F $1s$ absorption spectrum of solid K$_2$TiF$_6$ (F $1s \rightarrow t_{2g}$; 683.9 eV [6]) and the photon-energy resolution was set to 200 meV at the F $1s$ edge ($\sim$685 eV). Photoelectron and F *KLL* Auger spectra for TiF$_3$ and F-MWCNTs were collected in the angle-integrated mode with the total energy resolution of 400 meV using a Phoibos 150 electron analyzer. No sample charging effects were observed during the absorption and photoelectron measurements that were carried out at a pressure in the measuring chamber about $2 \cdot 10^{-10}$ mbar.

The F $1s$ absorption spectrum recorded for TiF$_3$ is compared in Fig. 1 with the spectra for other titanium fluorides, K$_2$TiF$_6$ and TiF$_4$, that were measured previously [1]. As is well seen, the spectra for ionic compounds TiF$_4$ and TiF$_3$ as well as for a molecular anion TiF$_6^{2-}$ (in solid K$_2$TiF$_6$) are strongly similar in their spectral shape. Taking into account the similar octahedral fluorine environment of the titanium atom in these compounds and the quasi-molecular analysis of the spectra for TiF$_4$ and TiF$_6^{2-}$ [1], the low-energy absorption band a –

b' in F $1s$ absorption spectrum of TiF$_3$ can be also associated with core-electron transitions to the empty weakly antibonding MOs t_{2g} and e_g of the octahedral TiF$_6$ quasi-molecule formed by the Ti atom and the surrounding fluorine atoms. These MOs result from the covalent mixing between the Ti $3d$ electron states, which are split into $3dt_{2g}$ and $3de_g$ components in the field of the fluorine octahedron, and the $2p$ states of the fluorine atoms. It should be noted that in the context of a simple ionic model these MOs are essentially localized at the central (Ti) atom and are primarily determined by the $3dt_{2g}$ and $3de_g$ states, which can be observed in the F $1s$ absorption spectrum of the TiF$_6^{2-}$ anion due to covalent bonding between the Ti and F atoms. Finally, the variations of the low-energy absorption structures, when going from TiF$_6^{2-}$ to TiF$_4$ and TiF$_3$,.result from a considerable tetragonal and trigonal distortions of the TiF$_6$ octahedra in these titanium fluorides.
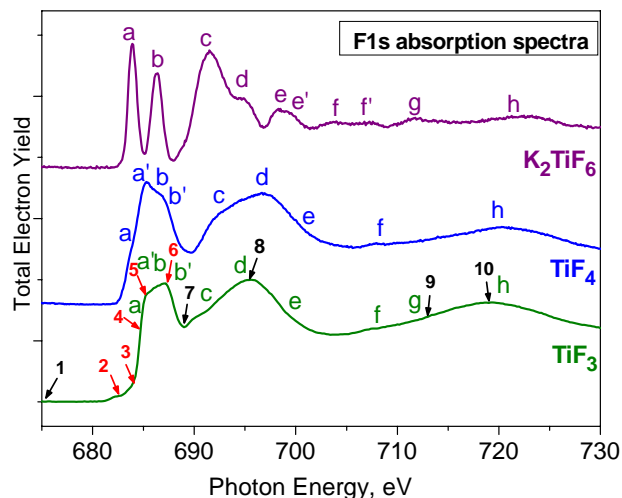
Fig.1. *F 1s absorption spectra of TiF$_3$, TiF$_4$, and K$_2$TiF$_6$.*

The electron (valence-band, core-levels and Auger) spectra for TiF$_3$ excited by photons of various energies in vicinity of the F $1s$ absorption edge (as marked by numbered arrows in the absorption spectrum, Fig.1) are presented in Fig. 2. It is seen from Figure that contributions from the valence-band and core-levels signals to Auger spectra are small. The nonresonant F KLL Auger spectrum excited by photons with energy far above the F $1s$ edge (curve 10; $hv = 719$ eV) exhibits a spectral shape that is typical of the normal Auger spectrum of the neon-like F$^-$ anion in alkali fluorides [4]. It comprises three groups of lines (a and b, cd and e, f) associated with $KL_{2,3}L_{2,3}$ (^1D and ^1S), $KL_1L_{2,3}$ (^3P and ^1P), and KL_1L_1 (^1S) Auger transitions. Examining the series of Auger spectra (curves 2 – 7), it is clear that all the Auger signals change their intensities and energy positions, when the photon energy is scanned across of the low-energy absorption band (resonance) a – b'. All resonant spectra are characterized by a high-energy shift with respect to the normal one that decreases nonlinearly in its magnitude from 5.5 eV to 0.3 eV with increasing the photon energy in the range between 682.5 eV (curve 2) and 689.0 eV (curve 7). Note that the valence-band photoelectron signal VB therewith does not substantially change. Evidently these findings are caused by characteristic features of decay processes for the core-excited F atoms arising from transitions of

Fig.2. *Resonant F KLL Auger spectra of TiF$_3$.*

the F $1s$ electrons to low-energy unoccupied electron states of TiF$_3$ (MOs t_{2g} and e_g; absorption band a - b'). Owing to the appreciable localization of the excited electron on the fluorine atoms, it has effect on the Auger decay processes for $1s$ hole in the fluorine atoms. Only slight modifications on the line shape and intensity of the VB signal upon the resonance excitation are indicative of an absence of participator Auger transitions. In such a situation it

is clear that the low-energy F 1*s* excitations in TiF$_3$ decay predominantly via spectator Auger transitions. In this deexcitation process the electron excited to the Ti 3*d* – F 2*p* hybridized electron state (MOs t_{2g} and e_g) will remain as a screening electron both in the initial and final states, thus causing an increase in the energy of the outgoing electron compared to the normal Auger decay (with a fully delocalized excited electron).
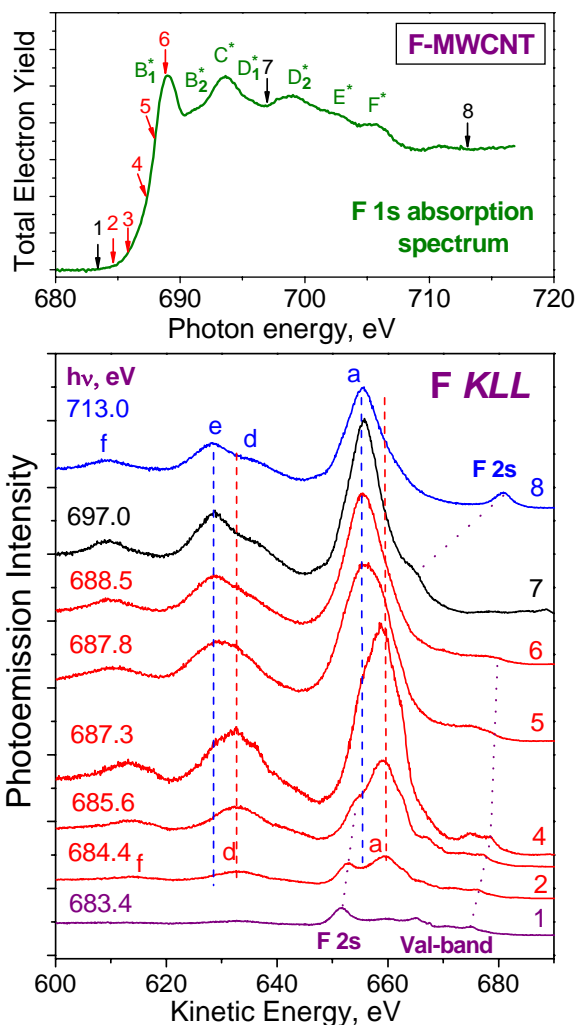
Fig. 3. *Resonant F KLL Auger spectra of F-MWCNTs.*

The observed decrease of this high-energy shift for the resonance Auger transitions, when the photon energy is scanned across of the resonance *a* – *b*′, points to the fact that the localization extent of the low-energy core-excited states is rapidly reduced with increasing the photon energy over the absorption resonance.

Further inspection of the resonant F *KLL* Auger spectra for F-MWCNTs containing 10 wt% of fluorine atoms (Fig. 3) discloses similar regularities that also can be explained by the spectator Auger deexcitation processes of the low-energy core-excited states which have the hybridized C 2*p* – F 2*p* character and are responsible for the band B$_1$* in the F 1*s* absorption spectrum. Differences which are observed in the resonant Auger spectra of F-MWCNTs as compared to those of TiF$_3$ (a lower resolved spectral shape and a lower energy shift of 4.2 eV) can be understood taking into account the presence of two C-F phases [7] and a weaker covalent bonding between the fluorine and carbon atoms in F-MWCNTs.

In conclusion, the analysis of the resonant F *KLL* Auger spectra measured with a high energy resolution for TiF$_3$ and F-MWCNTs has shown that these spectra contain direct and otherwise inaccessible information concerning a localization and hybridization character for the low-energy unoccupied electronic states.

References
1. A.S. Vinogradov, S.I. Fedoseenko, S.A. Krasnikov, et al. *Phys. Rev. B* **71**, 045127 (2005).
2. M.M. Brzhezinskaya, N.A. Vinoradov, V.E. Muradyan, Yu.M. Shul'ga, N.V. Polyakova, A.S. Vinogradov. *Fizika Tverdogo Tela* **50**, 565 (2008). [*Phys. Sol. State* **50**,587 (2008)].
3. H. Aksela, S. Aksela, J. Tulkki, et al. *Phys. Rev. A* **39**, 3401 (1989).
4. H. Aksela, E. Kukk, S. Aksela, et al. *Phys. Rev. B* **49**, 3116 (1994).
5. E. Kukk, S. Aksela, H. Aksela, et al. *Phys. Rev. B* **50**, 9079 (1994).
6. A.S. Vinogradov, A.Yu. Dukhnyakov, V.M. Ipatov, D.E. Onopko, A.A. Pavlychev, and S.A. Titov. *Fizika Tverdogo Tela* **24**,1417 (1982) [*Sov. Phys. Solid State* **24**, 803 (1982)].
7. M.M. Brzhezinskaya, N.A. Vinoradov, V.E. Muradyan, Yu.M. Shul'ga, R. Püttner, A.S. Vinogradov, and W. Gudat. *Fizika Tverdogo Tela* **in print** (2009). [*Phys. Sol. State* **in print** (2009)].

Magnetic domain structure of Heusler/MgO/Heusler trilayer systems

A. Kaiser, C. Wiemann, S. Cramm, C.M. Schneider

Forschungszentrum Jülich, Institut für Festkörperforschung IFF-9, 52425 Jülich, Germany

Heusler alloys [1] are considered as interesting ferromagnetic electrode materials for magnetic tunnel junctions (MTJ). Due to their high spin polarization at the Fermi level they are expected to show extremely high tunnelling magnetoresistance (TMR) values. MgO as a tunneling barrier material has a comparable lattice constant and thus provides the possibility of epitaxial growth of trilayer systems [2]. Due to the reduction of defects and the onset of resonant tunnelling mechanisms an increase of the TMR effect can be expected [3].

Many macroscopic studies of the magnetic, electronic and structural properties of Heusler-based MTJs have been carried out. From a fundamental point of view, but also with respect to technical aspects, the micromagnetic behaviour cannot be neglected. Co_2FeSi (CFS) and Co_2MnSi (CMS) are two protagonists of the class of half-metallic Heusler compounds. They have similar lattice constants providing structural compatibility to MgO. Both materials have very high Curie temperatures around 1000 K [4, 5] and magnetic moments per formula unit of 5.07 μ_B (CMS) and 6 μ_B, respectively. Hysteresis measurements reveal clearly distinguishable coercive fields of 2.8 mT (CMS) and 6.5 mT (CFS).

Single films and trilayer structures with asymmetric electrode configurations have been prepared by magnetron sputtering. The films have been subsequently microstructured by optical lithography and argon ion beam milling into squares with areas ranging from 2×2 to 100×100 μm^2. A more detailed description of the growth conditions and the experimental results can be found elsewhere [6].

The micromagnetic structure of the films has been studied by photoemission electron microscopy (PEEM). PEEM exploiting the XMCD effect is a powerful technique for the element-selective study of magnetic domain configurations [7, 8]. The measurements have been conducted using an Elmitec PEEM III at the beamline UE56/1-SGM at BESSY-II. All measurements shown in this report have been generated by tuning the photon energy to the appropriate L_3 absorption edge and calculating the XMCD asymmetry value $A = (I_{\sigma+} - I_{\sigma-})/(I_{\sigma+} + I_{\sigma-})$ for each pixel with $I_{\sigma\pm}$ being the intensity values for right and left circularly polarized light.

Fig. 1 shows the magnetic domain patterns from single CMS and CFS films. Under the influence of the shape-induced demagnetizing field, the magnetization configuration of elements of comparable size is distinctly different. The CMS film develops a so-called concertina or buckling pattern (shown in fig. 1(c)) also known from Permalloy elements in a similar thickness range [9]. It is formed by alternating low-angle walls with the local magnetization direction varying around the average magnetization. With decreasing element size the effect of the demagnetizing field becomes stronger and successively simpler flux-

(a) CMS 10x10 μm^2

(b) Sketch of domain pattern in CMS 10x10 μm^2

(c) CMS 20x20 μm^2

(d) CFS 20x20 μm^2
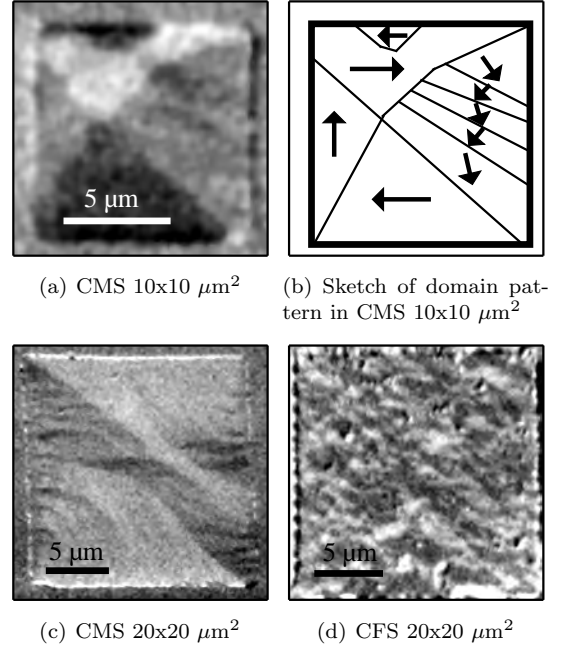
Figure 1: Magnetic domain structures in patterned CMS and CFS elements. The magnetic contrast has been obtained at the Co L_3 edge.

closure patterns reminiscent of Landau states start to form (Fig. 1(a) and 1(b)), which are still accompanied by buckling structures. The latter disappear for elements in the micrometer regime. However, the occurrence of the buckling state is not necessarily the magnetic ground state configuration, but may arise due to a local energetic minimum caused by neighbouring domains blocking each other. A completely different response is observed in the CFS films. Even under the influence of the demagnetizing field in small 10×10 μm^2 elements (Fig. 1(d)) the polycrystalline nature of the film is dominating the magnetization pattern and the fine-grained domain structure remains essentially unchanged from that observed in the extended film (not shown). This result shows that the intrinsic anisotropy of the CFS-film is much stronger than the demagnetizing field of the square element.

In a second step the single Heusler films have been combined into trilayer structures with a MgO interlayer of 3 nm thickness. In order to separate the magnetic response of the individual layers in this stack, the full versatility of soft x-ray PEEM is needed. By tuning the photon energy of the incident beam to the L_3-absorption edges of Fe and Mn the magnetization of both ferromagnetic layers can be investigated independently. Resulting domain images for a square element of CMS(20 nm)/MgO(3 nm)/CFS(2 nm) with an edge length of 10 μm are compiled in fig. 2. Due to the limited escape depth of the photoelectrons, the Mn signal is rather weak and had to be upscaled by a factor
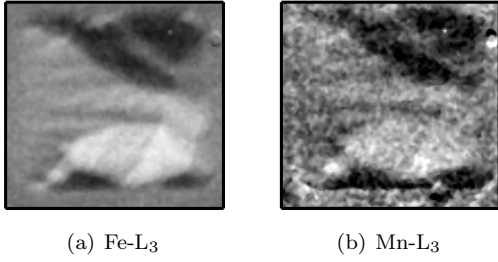
(a) Fe-L$_3$ (b) Mn-L$_3$

Figure 2: Element-selective domain imaging in the layer system CMS/MgO/CFS, revealing a parallel magnetic coupling of the CFS and CMS films.

(a) CMS (20 nm)/ MgO (3 nm)/ CFS (2 nm)

(b) CFS (20 nm)/ MgO (3 nm)/ CMS(2 nm)

Figure 3: Comparison of magnetic domain patterns acquired at the Co L$_3$ edge of $20 \times 20 \ \mu m^2$ square elements of both trilayers.

of five. Comparing the domain patterns of the Fe and Mn data reveals identical structures consisting of Landau flux-closure pattern superposed by concertina features in both films. The reasons for this coupling can be a roughness-induced Néel/orange-peel mechanism [10] or pinholes in the MgO layers, which favour a ferromagnetic contact between the CFS and CMS layer through a direct exchange interaction. The domain patterns of the trilayer film resemble the situation of the single CMS film (fig. 1a). Due to the difference in thickness in both films the micromagnetic structure is strongly dominated by the CMS bottom layer. For larger $20 \times 20 \ \mu m^2$ elements (fig. 3a) the magnetic structure is no longer determined by the flux-closure. Instead the competition between local anisotropy fluctuations and demagnetizing field is won by the anisotropy and a magnetization ripple due to the polycrystalline structure of the films is formed.

In the inverse trilayer system the magnetic microstructures changes drastically. Instead of the anisotropy-dominated ripple pattern we find a different behaviour with higher average domain size and the formation of a low-remanence magnetization pattern consisting of two antiparallel Landau domains, as shown in fig. 3b. Some of the 90°-walls have been replaced by an additional domain with two low-angle walls. This configuration is known as "Tulip" state [11]. The 180°-walls between neighbouring antiparallel domains are modified by a high density of cross-tie structures. By the formation of cross-ties the magnetostatic energy is reduced, since 180°-walls are replaced by energetically more favorable 90°-walls [12].

In this trilayer structure we do not find a magnetic contrast at the Mn edge. This fact is surprising since the CMS film is the top layer and is expected to yield a higher intensity than in the reversed stack. Thus we must conclude that the CMS film is nonmagnetic at room temperature. This behaviour may be attributed to a strong thickness dependence of the CMS magnetic moment in thin films below 8 nm thickness supporting the results of previous XAS and FMR measurements [13, 14, 15]. The strongly reduced Curie temperature in the 2 nm CMS film may be explained by interdiffusion at the interface leading to a higher atomic disorder. Furthermore, this result seems to indicate that the MgO barrier in this layer has only a negligible density of pinholes, because a direct exchange coupling to the bottom CFS layer should also result in a common Curie temperature for both layers.
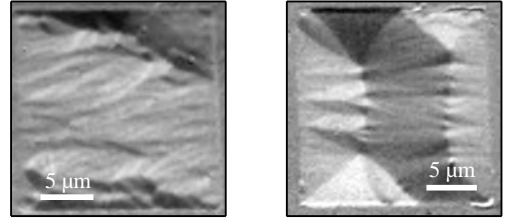
In conclusion our element-selective domain imaging experiments reveal the complexity of the magnetic microstructure in Heusler-based thin film systems. The results also show that the micromagnetic structure depends on fine details of the formation process of the Heusler phases. Analysis of the domain configurations shows that the ferromagnetic coupling observed in the dual-Heusler trilayers can be attributed to roughness-induced Néel coupling. This can be overcome by an improvement of the preparation conditions. The surprising difference of the magnetic behaviour between the CMS/MgO/CFS and CFS/MgO/CMS trilayer structures is due to a strong thickness dependence of the magnetic ordering in CMS and must be taken into account for the construction of magnetic tunnelling junctions.

Acknowledgements

References

[1] Heusler, F. *Verh. Dtsch. Phys. Ges.* **12**, 219 (1903).

[2] Yamamoto, M., *et al.*, *J. Phys. D: Appl. Phys.* **39**, 824 (2006).

[3] Yuasa, S., *et al.*, *Nature Materials* **3**, 868 (2004).

[4] Webster, P. *Contemp. Phys.* **10**, 559 (1969).

[5] Wurmehl, S., *et al.*, *Phys. Rev. B* **72**, 184434 (2005).

[6] Kaiser, A., *et al.*, *J. Magn. Magn. Mater.* (2008). doi:10.1016/j.jmmm.2008.10.037.

[7] Schönhense, G. *J. Phys.: Cond. Matt.* **11**, 9517 (1999).

[8] Stöhr, J. and Anders, S. *IBM J. Res. Develop.* **44**, 535 (2000).

[9] Chumakov, D., *et al.*, *Phys. Rev. B* **71**, 014410 (2005).

[10] Neel, L. *C. R. Acad. Sci.* **255**, 1676 (1962).

[11] Hubert, A. and Rührig, M. *J. Appl. Phys.* **69**, 6072 (1991).

[12] Huber Jr, E., *et al.*, *J. Appl. Phys.* **29**, 294 (1958).

[13] Schmalhorst, J., *et al.*, *Phys. Rev. B* **70**, 24426 (2004).

[14] Wang, W., *et al.*, *Phys. Rev. B* **71**, 144416 (2005).

[15] Rameev, B., *et al.*, *phys. stat. sol.(a)* **1**, 10 (2006).

Effect of the partly filled HOMO in CoPc on formation and decay processes of Co $2p_{3/2}$ excitations from a comparison with NiPc.

A.S. Vinogradov[1], M.M. Brzhezinskaya[1,2], A.V. Generalov[1], A.Yu. Klyushin[1], and K.A. Simonov[1]

[1] *V.A. Fock Institute of Physics, St. Petersburg State University, St. Petersburg, 198504 Russia*
[2] *HZB (BESSY GmbH), 12489 Berlin, Germany*

The 3d-metal phthalocyanines (3d-MPc's) are very stable planar complexes that show various interesting properties and have extensive applications in the areas of catalysis, pigments, semiconductors and sensors [1]. The central part of the 3d-MPc's (including the 3d-atom and its nearest surroundings) is believed to be their most reactive part and to determine the most important applications of these compounds. The occupied and empty 3d electron states of the metal atom, which are located near the Fermi level, are essentially responsible for the unique properties of the 3d-MPc's. Since the practical application of these phthalocyanines is based on the understanding their electronic structure, its investigation remains a subject of intense research over several decades. In particular, the occupied electronic states of 3d-MPc's were investigated by photoemission (PE) spectroscopy [2,3], while x-ray absorption (XA) and inverse photoemission spectroscopy were used for studying the unoccupied states [4-6]. The similar studies are usually performed for the whole series of MPc's (M = Fe, Co, Ni, Cu and Zn) since their electronic structure is mainly characterized by a gradual increase of the 3d electron number for the metal atoms along this series. Further, the metal 3d derived electronic states of MPc's are usually regarded, up to now, as the nearly pure atomic 3d components split by a square-planar (D_{4h}) molecular field of the complex into the e_g ($d_{xz,yz}$), b_{2g} (d_{xy}), a_{1g} (d_{z^2}), and b_{1g} ($d_{x^2-y^2}$) components [7]. As a result, in going from FePc to ZnPc the metal atom 3d electron configuration varies from $e_g^4 a_{1g}^2 b_{2g}^0 b_{1g}^0$ to $e_g^4 a_{1g}^2 b_{2g}^2 b_{1g}^2$. The similar electron configurations are known to be best probed in an x-ray absorption experiment by excitation of metal 2p core electrons to the unfilled 3d derived electronic states [8]. In such the probing, a gradual filling of emty b_{2g} and b_{1g} states must be observed in the metal atom 2p absorption spectra of MPc's. A most interesting situation is expected in the case of Co 2p excitations of CoPc since the 2p electron excited to the unfilled $3db_{1g}$ will interact additionally with the 3d electron in the partly filled b_{2g} HOMO. At the same time this HOMO is fully occupied for the NiPc complex and the LUMO is the empty $3db_{1g}$ state. The main aim of the present study was to gain a detailed information on formation and decay processes for Co 2p excitations from the high-resolution absorption and resonant PE (Res PE) spectra measured at the Co 2p edges and to analyze effects of the partly filled HOMO and 3d-3d electron interaction on decay processes of the Co 2p excitations on the basis of comparison between corresponding spectra for CoPc and NiPc. Below are presented the first results of our measurements performed last December.

All measurements were performed at the Russian-German beamline (RGBL) using experimental station Mustang. The NiPc and CoPc chemicals were purchased from Aldrich Inc.. The samples were thin (30-50 nm) polycrystalline NiPc and CoPc films prepared *in situ* in the preparation chamber by thermal

Fig. 1. *Metal atom $2p_{3/2}$ absorption spectra for NiPc and CoPc.*

evaporation of powders from a Knudsen cell onto a polished stainless-steel plate in a vacuum of ~3×10⁻⁷ mbar The NEXAFS spectra of these samples were obtained in the total electron yield mode by detecting a sample current. The photon-energy resolution was set to 550 meV at the Ni $2p_{3/2}$ edge (~850 eV) and 480 meV at the Co $2p_{3/2}$ edge (~780 eV). The photon energy was calibrated using the known energy position of the first narrow peak in the Ne $1s$ absorption spectrum (Ne $1s \to 3p$; 867.13 eV [5]) and in the F $1s$ absorption spectrum of solid K_2TiF_6 (F $1s \to t_{2g}$; 683.9 eV [6]). Valence-band and core-level photoelectron (PE) spectra for NiPc and CoPc were collected in the angle-integrated mode with a Phoibos 150 electron analyzer. The total energy resolution was about 580 meV and 520 meV for the Res PE spectra at the Ni $2p_{3/2}$ and Co $2p_{3/2}$ edges, respectively. The energy scale was aligned by measuring the $4f_{7/2}$ PE lines of the reference gold or platinum foils. All spectra were normalized to the incident photon flux, which was monitored by recording the photocurrent from a gold mesh placed at the outlet of the beamline. No sample charging effects were observed during the absorption and photoelectron measurements that were carried out at a pressure in the measuring chamber about $2\cdot10^{-10}$ mbar. The long x-ray irradiation of the CoPc sample was found to result in its minor deterioration which was only manifested in small changes of relative intensities of absorption structures in Co $2p_{3/2}$ spectrum. Nevertheless, the position of the light spot on the sample was varied every 2 h in order to ensure insignificance of this photochemical effect.

The metal atom $2p_{3/2}$ absorption spectra recorded for CoPc and NiPc are compared in Fig. 1. As is well seen, the Co spectrum is significantly different from the Ni one and shows two additional low-energy absorption structures A^* and A_1. The more complicated structure of Co $2p_{3/2}$ absorption spectrum can be understood taking into account a presence of the partly filled HOMO $3db_{2g}$ in the cobalt complex. Compared to the spectrum of NiPc, the additional low-energy band A^* is attributed to a Co $2p_{3/2} \to 3db_{2g}$ transition while the main absorption

Fig. 2. *Res PE spectra of NiPc at the Ni 2p3/2 edge.*

transition of Co $2p_{3/2}$ electrons to a $3db_{1g}$ state (band A in the Ni$2p_{3/2}$ spectrum) should be regarded to be split into two triplet and singlet components (A_1 and A_2) due to an $3d$-$3d$ exchange interaction between the electron excited to the $3db_{1g}$ state and the $3db_{2g}$ electron.

PE spectra of NiPc and CoPc excited by photons of various energies in vicinity of the Ni $2p_{3/2}$ and Co $2p_{3/2}$ absorption edges (as marked by numbered arrows in the absorption spectra, Fig.1) are shown in Figs. 2 and 3, respectively. The bottom curves in both figures correspond to photon energies below the Ni $2p_{3/2}$ and Co $2p_{3/2}$ excitations. Structures a' - f in these spectra are superpositions of the valence MO PE signals originating from the nitrogen and carbon $2p$ and $2s$ atomic states as well as from Ni or Co $3d$ states. Examining the series of PE spectra in Fig.2 and 3, it is clear that some of valence-band PE signals are significantly enhanced when the photon energy is scanned across the $2p$ – $3d$ absorption resonances (band A in Ni spectrum and A^*, A_1 and A_2 in Co spectrum). It is of interest that the enhancement effects are different for Res PE spectra of NiPc and CoPc. Evidently these findings are caused by the presence of the partly filled b_{2g} HOMO in CoPc. More detailed analysis of these experimental data is in progress.

Fig. 3. *Res PE spectra of CoPc at the Co $2p_{3/2}$ edge.*

References

1. C.C. Leznoff, A.B.P. Lever, *Phthalocyanines, Properties and Applications.* Vol. 3, VCH Publishers, Inc., NY, 1993.
2. W.D. Grobman, E.E. Koch, in: L.Ley, M. Cardona (Eds.), *Photoemission in Solids II,* Springer-Verlag, Berlin 1979, Chapter 5.; E.E. Koch, in: P. Reineker, H. Haken, H.C. Wolf (Eds.), *Organic Molecular Aggregates,* Springer-Verlag, Berlin 1983, p.35.
3. M. Iwan and E.E. Koch, Solid State Commun. **31**, 261 (1979).
4. E.E. Koch, Y. Jugnet, and F.J. Himpsel, Chem. Phys. Lett. **116**, 7 (1985).
5. M.L.M. Rocco, K.-H. Frank, P. Yannoulis, and E.E. Koch, J. Chem. Phys. **93**, 6859 (1990).
6. H. Yoshida, K. Tsutsumi, N. Sato, J. Electron Spectrosc. Relat. Phenom. **121**, 83 (2001).
7. H. Höchst, A. Goldmann, S. Hüfner, and H. Malter, Phys. Stat. Sol. (b) **76**, 559 (1976).
8. H. Ebert, J. Stöhr, S.S.P. Parkin, M. Samant, A. Nilsson. Phys. Rev. B 53, 16067 (1996).

Charge order in $La_{1.8-x}Eu_{0.2}Sr_xCuO_4$ studied by resonant soft X-Ray diffraction

V. Soltwisch[1], E. Schierle[1], E. Weschke[1], J. Geck[2], D. Hawthorn[2], H. Wadati[2], H.-H. Wu[3], H. A. Dürr[1], N. Wizent[4], B. Büchner[4], P. Ribeiro[5], G. A. Sawatzky[2], J. Fink[1,4]

[1]Helmholtz Zentrum Berlin für Materialien und Energie, [2]University of BC Vancouver Canada, [3]II.Physikalisches Institut, Universität Köln, [4]Leibniz Institute for Solid State and Materials Research Dresden, [5]IFW Dresden
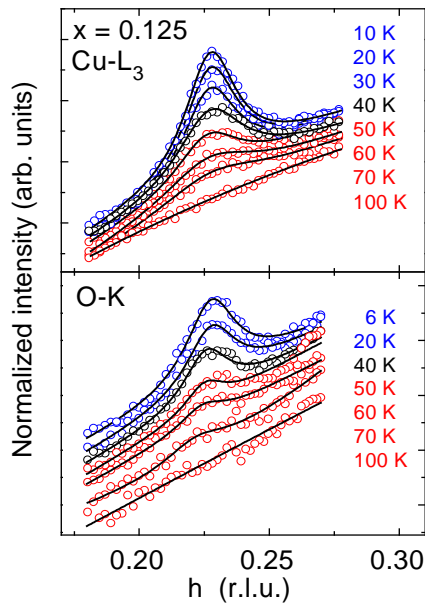
Fig. 1. (ε 0 l) superstructure peaks recorded for various temperatures with photon energies corresponding to Cu-L3 (l=1.6) and the O-K (l=0.75) resonance. The intensity is shown as a function of h in units of the reciprocal lattice parameter a*.

In high-T_c superconductors at low doping concentrations x the doped holes tend to order within the CuO_2 planes. This ordering is determined by a complex interplay between charge, spin and lattice degrees of freedom and results in stripe-like or checkerboard phases. The charge stripes constitute antiphase domain walls between antiferromagnetic domains and their role for the occurrence of superconductivity is not yet understood. Stripe order, observed near x = 1/8, is fluctuating in many hole-doped cuprates, but can be stabilized by corrugation of the CuO_2 planes as in $La_{2-x}Ba_xCuO_4$ (LBCO), $La_{1.6-x}Nd_{0.4}Sr_xCuO_4$ (LNSCO) as well as in the compound $La_{1.8-x}Eu_{0.2}Sr_xCuO_4$ (LESCO). LESCO in particular has a strong corrugation due to the small Eu ions and exhibits static stripes in a large range of x, the superconducting range between 0.08<x<0.2 is almost completely replaced by a stripe-ordered phase [1].

Charge order in regular stripes can be studied by diffraction techniques, such as neutron and x-ray diffraction [2,3]. These techniques are sensitive to accompanying spin order and lattice distortion, respectively. A more direct method to address the charge ordering is resonant x-ray diffraction at the oxygen K resonance, which exploits the increase of the scattering factor of the holes due to resonant dipole transitions from the 1s shell into unoccupied states near the Fermi energy [4]. Fig. 1 displays two series of data recorded from LESCO for x = 1/8 at the Cu-L_3 and the O-K edge for various temperatures. Scans are shown as a function of h parallel to the CuO_2 planes and exhibit clear peaks at h = 0.23 that disappear below 100 K. The value of the modulation period ε fits nicely into a series of neutron scattering results that demonstrate a doping dependence of the modulation wave vector [5]. Analogous results were also obtained for other doping levels between x = 0.1 and x = 0.15.

Figure 2 displays the integrated intensity of this charge-order diffraction peak as a function of photon energy across the O-K resonance (red curve) in comparison to the absorption spectrum measured by the fluorescence yield (black). The intensity of the charge scattering peaks at the energy position corresponding to transitions into the unoccupied hole states. The appearence of this so-called mobile charge carrier peak (MCP) at a photon energy of 528 eV demonstrates that resonant diffraction at this energy directly measures the ordering of the doped holes [4]. The blue curve of this figure was obtained from a Kramers-Kronig transform

Fig. 2: Integrated intensity of the (ε 0 0.75) superstructure reflection as a function of photon energy across the O-K resonance (red). For comparison, the x-ray absorption measured by the total fluorescence yield (black) and calculated intensity obtained from a Kramers-Kronig transform of absorption data (blue) are shown.

of absorption data, assuming a linear dependence of the spectral weight of the MCP from the doping concentration, which is valid for low doping levels. In this calculation (blue), the spectral weight at a photon energy of 529.5 eV is substantially overestimated compared to the data (red). At this photon energy, transitions into electronic states of the upper Hubbard band (UHB) are observed. The fact that the experimental spectral weight is much smaller indicates a deviation from the linear doping dependence of the spectral weight that occurs for doping levels x>0.2 [6]. A large doping concentration per Cu site in the charge stripes was also concluded in [4].

The data of Fig. 1 can be fitted by Lorentzian line shapes (solid lines), the resulting integrated intensities as a function of temperature for doping concentrations ranging from x = 0.1 to x = 0.15 are shown in Fig. 3. Evidently, the intensities tend to vanish at temperatures between 40 K (x = 0.1) and 80 K (x = 1/8). These temperatures are significantly smaller than the transition temperature of the low-temperature tetragonal phase of approximately 120 K [1], indicating that charge order is not driven by this structural transition. More significantly, the charge ordering temperature is substantially larger than the spin ordering temperature [1]. This means that while the charge stripes occur as a periodic arrangement of domain walls between antiferromagnetic antiphase domains, they do no depend on long-range magnetic order.
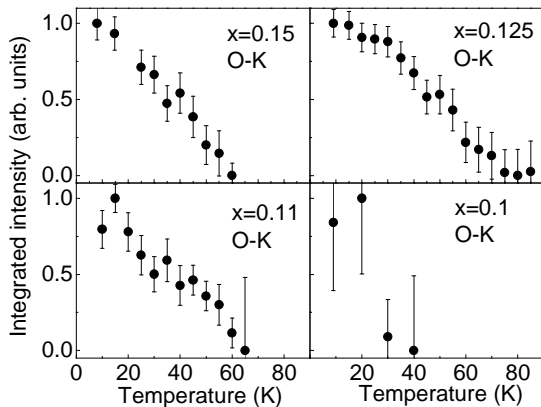
Fig. 3: Integrated intensity of the (ε 0 0.75) superstructure reflection as a function of temperature for various doping levels x as determined from data obtained at the O-K resonance.

References:

[1] H. H. Klauss *et al.*, Phys. Rev. Lett. **85**, 4590 (2000).
[2] J. M. Tranquada *et al.*, Nature **375**, 561 (1995).
[3] M. Von Zimmermann *et al.*, Europhysics Letters **41**, 629 (1998).
[4] P. Abbamonte *et al.*, Nature Physics **1**, 155 (2005).
[5] K. Yamada *et al.*, Phys. Rev. B **57**, 6165 (1998).
[6] J. Fink *et al.*, Phys. Rev. B, accepted (2009).

Charge order in doped $RTiO_3$

A. C. Komarek,[1] H. H. Wu,[1,2] C. Trabant,[1] R. Feyerherm,[3] E. Duzik,[3]
L. H. Tjeng,[1] M. Braden,[1] C. Schüßler-Langeheine[1]

[1]*II. Physikalisches Institut, Universität zu Köln, Zülpicher Str. 77, 50937 Köln, Germany*
[2]*National Synchrotron Radiation Research Center, Hsinchu 30076, Taiwan*
[3]*Helmholtz-Zentrum Berlin, Albert-Einstein-Str. 15, 12489 Berlin, Germany*

Inducing a metal insulator transition by doping into a Mott insulator is intensively studied at the moment due to its relevance for the phase-diagram of the cuprate high temperature superconductors [1]. The titanates $RTiO_3$ are particularly interesting since they posses a single electron in the $3d$-shell compared to the cuprates with a single hole. But in contrast to the cuprates, the orbital degree of freedom plays an important role in the titanates [2] and they exhibit a 3-dimensional crystal structure.

Doping Sr and Ca into $RTiO_3$ allows to render the titanates metallic; concomitantly the magnetic order is suppressed. However, while a small amount of Sr is sufficient to render $RTiO_3$ with larger rare earth ionic radius (like R=La) metallic, $R_{1-x}Ca_xTiO_3$ samples with smaller rare earth ionic radius stay insulating up to much higher doping levels of about 40% of Ca and beyond. This surprising difference has remained unexplained so far. There are several phase diagrams known, where doping into a Mott-insulator does not yield metallic behavior even at high amounts of doping. In such systems charges sometimes order, forming checker-
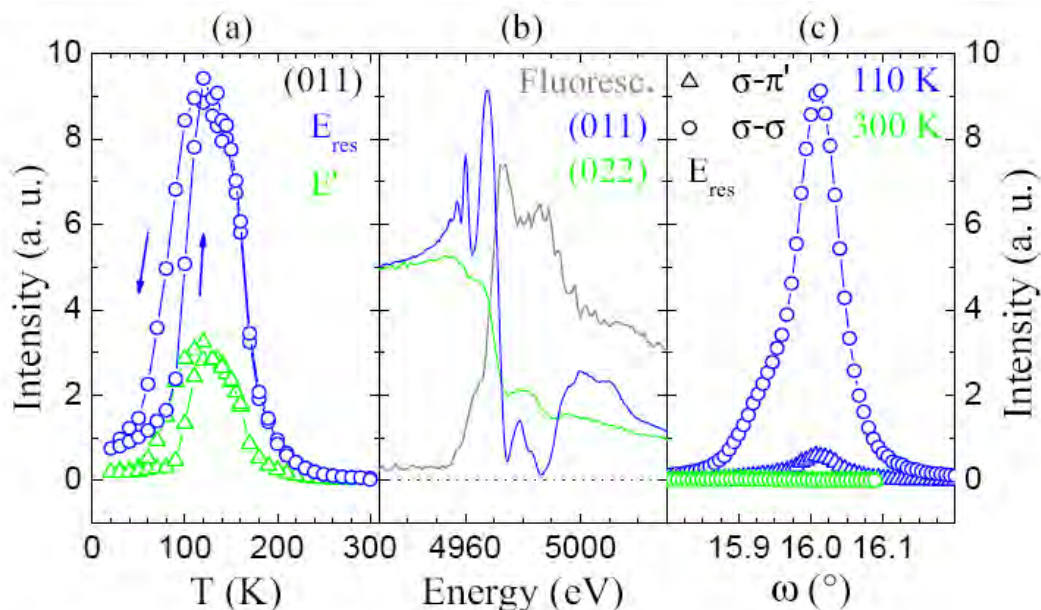
Fig. 1 (a) Temperature dependence of the (011) superstructure reflection from a sample of $Y_{1-x}Ca_xTiO_3$ with $x = 0.36$. (b) Energy scans of the (011) superstructure and the (022) fundamental reflections together with the fluorescence signal ($x = 0.36$). (c) polarization analysis: ω-scans of the (011) reflection for the rotated and unrotated channels ($x = 0.36$).
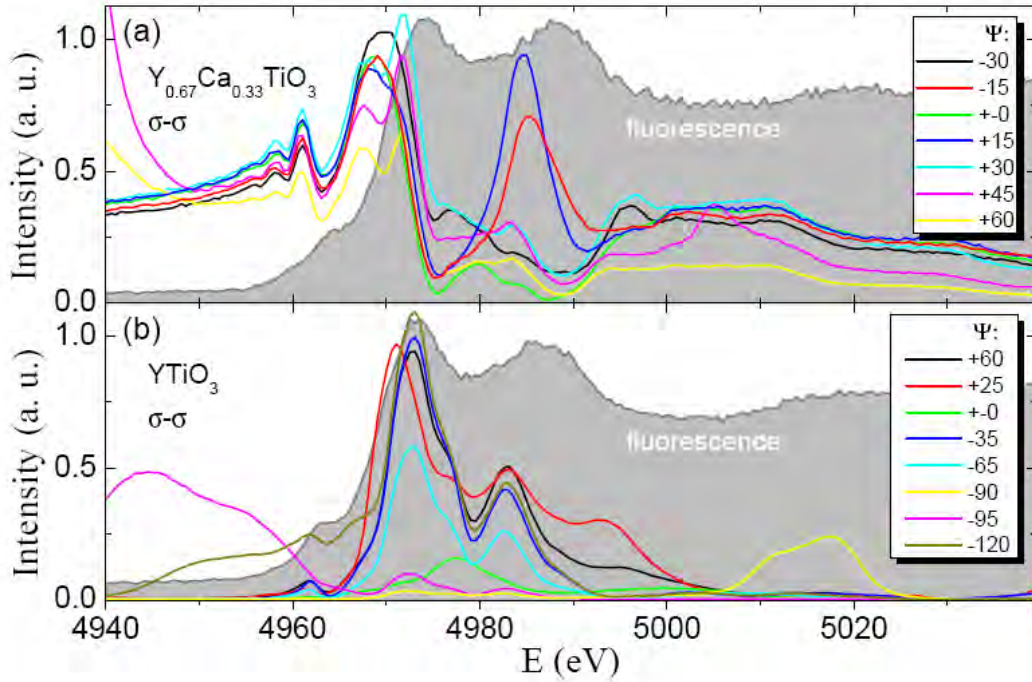
Fig. 2 Energy scans of the (011) superstructure reflection for (a) $Y_{0.67}Ca_{0.33}TiO_3$ and (b) $YTiO_3$ at different azimuthal angles.

board or stripe arrangements, like for example in $Pr_{1-x}Ca_xMnO_3$ or in $La_{2-x}Sr_xNiO_4$ [3,4]. In the titanates, however, so far no evidence for charge ordering has been reported.

We have recently found evidence for charge ordering in $R_{1-x}Ca_xTiO_3$ samples with R=Y, Er, Lu in different single crystal neutron diffraction measurements as well as in single crystal X-ray diffraction measurements using synchrotron radiation. Charge ordering in these systems leads to a symmetry reduction from an orthorhombic to a monoclinic symmetry: *Pbnm* → *P2₁/n*. In the monoclinic phase, two distinct Ti-sites appear. This symmetry reduction was already observed in synchrotron radiation powder X-ray diffraction measurements by K. Kato *et al.* [5] and has been verified in similar synchrotron measurements on our own samples. The structural refinement of various single crystal neutron and X-ray diffraction measurements reveals two different oxygen environments of the two distinct Ti-sites with one TiO_6 octahedron being enlarged. Using these structural data the nominal valence of the two Ti-sites can be calculated by the bond valence sum (BVS) formalism. The difference of the oxidation state of both Ti-ion amounts to 0.3 electrons. In order to verify this finding spectroscopically, we performed resonant X-ray diffraction measurement at the MAGS beamline, where we studied the signatures of charge ordering for several $R_{1-x}Ca_xTiO_3$ samples with R=Y, Er, Lu for the hole-doping regime $0.33 < x < 0.5$.

In Fig. 1(a) the temperature dependence of the (011) charge ordering superstructure reflection of a $Y_{1-x}Ca_xTiO_3$ sample with $x = 0.36$ is shown for two different incident X-ray energies. Below the charge ordering temperature this superstructure reflection intensity increases strongly. In Fig. 1(b) an energy scan of this superstructure reflection is shown together with the fluorescence spectrum and the energy dependence of the fundamental (022) peak. In contrast to the (022) behavior, there is a strong resonant enhancement of (011) at the absorption threshold
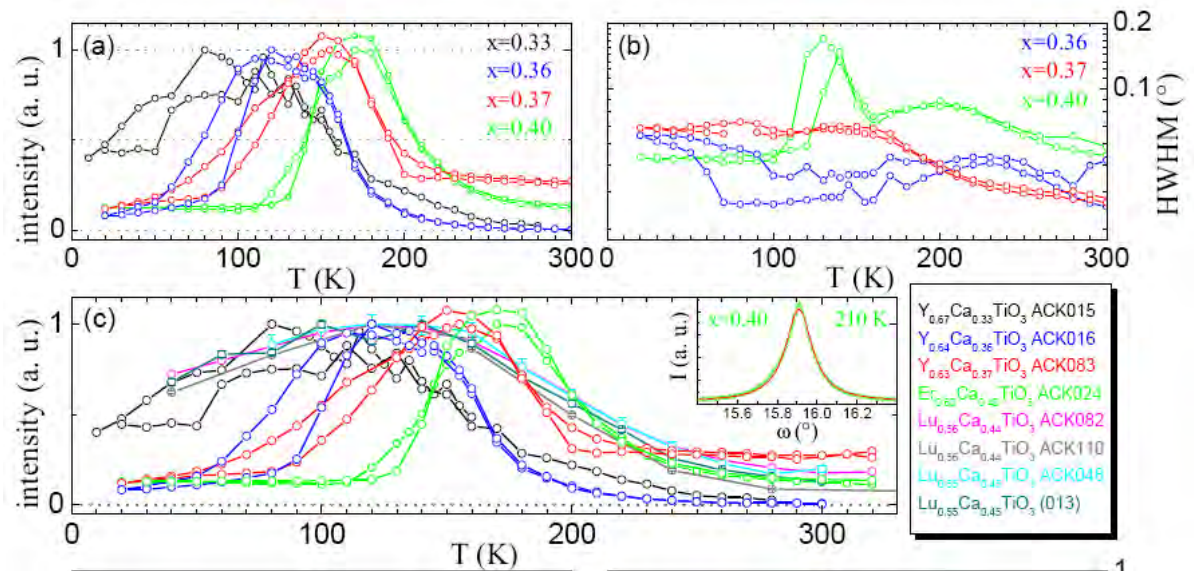
Fig. 3(a,c) Temperature dependence of the (011) superstructure reflection and (b) temperature dependence of the peak width (HWHM) of the (011) reflections for different samples.

with a peak at the maximum of the *derivative* of the fluorescence signal. This is a clear signature of charge ordering.

To corroborated this interpretation, we present in Fig. 2(a) a direct comparison of energy scans of the (011) reflections for $Y_{1-x}Ca_xTiO_3$ ($x = 0.33$) and $YTiO_3$. In the undoped $YTiO_3$ system this reflection is indicative for orbital ordering since the antiferro-orbital ordering scheme is alternating between neighboring Ti-sites. As can be seen in these figures, the maximum intensities can be found at the peak of the absorption in the undoped system, while in stark contrast the maximum (011) intensity for 33% hole-doped system is found at clearly lower photon energies. Furthermore, the polarization analysis reveals the bulk of the (011) signal from the doped samples is found in the unrotated σ-σ channel and not in the σ-π channel where orbital ordering contributions would be expected [Fig. 1(c)]. All these results support the charge ordering picture in the $R_{1-x}Ca_xTiO_3$ system with R=Y, Er, Lu.

In Fig. 3(a) the temperature dependence of the superstructure reflection intensity is compared for different samples with Ca-doping levels 0.33, 0.36, 0.37 and 0.40. Upon cooling the (011) charge ordering superstructure reflection intensity starts to increase at higher temperatures for samples with larger hole-doping level. Hence, the charge ordering seems to be stabilized for samples closer to the optimum/half-doped composition. In Fig. 3(b) the peak widths are plotted as a function of temperature indicating a loss of spatial coherence at the lower transition temperature. Finally, in Fig. 3(c) also the temperature dependence of the (011) superstructure reflection intensities of the higher doped samples are shown. These exhibit a much smoother transition and show signatures of charge order already at room-temperature.

[1] M. Imada *et al.*, Rev. Mod. Phys. **70**, 1039 (1998).
[2] Y. Tokura *et al.*, PRB **48**, 14063 (1993).
[3] Y. Tokura et al., Science **288**, 462 (2000).
[4] J. M. Tranquada *et al.*, Nature **375**, 561 (1995).
[5] K. Kato *et al.*, JPSJ **71**, 2082(2002).

Temperature dependent quasiparticle renormalization in nickel metal

R. Ovsyannikov, J. Sánchez-Barriga, J. Fink, A. Varykhalov, H. A. Dürr

Helmholtz Zentrum Berlin, BESSY II,

Albert-Einstein-Strasse 15, D-12489 Berlin, Germany

Spintronics, also known as magnetoelectronics, is an emerging technology involving detection and manipulation of electron spin for data storage and processing. In order to perform such an operation two primary types of devices are required – a device that could generate a spin polarized current, the so called spin-injector and a device that is sensitive to spin polarization, i.e., a spin detector. One of the known spintronics systems are the giant magnetoresistance (GMR) devices[1]. A typical GMR devices consist of two ferromagnetic layers separated by a metallic nonmagnetic spacer layer. When the magnetization direction of two ferromagnetic layers is aligned the resistance will be smaller than that for antialigned layers. Tunnel magnetoresistance (TMR) devices[2] use a similar idea. In this case the spacer layer is made out of insulating material and the magnetization vector alignment/antialignment will change the tunneling resistance. Such devices find common use as read heads of modern hard drives. Ultimate performance of such devices is determined by spin-dependent lifetimes of spin-polarized charge carriers, thus focusing attention on the electronic structure and the dynamic properties of strongly correlated systems like *3d*-ferromagnets, transition metal oxides and *4f-* rare-earths systems.

One of the fundamental consequences of electron correlation effects is that the bare particles in solids become 'dressed' with the excitation cloud resulting in quasiparticles. Such a quasiparticle will carry the same spin and charge as the original particle, but will have a renormalized mass and a finite lifetime. The properties of many-body interactions are described with a complex function, the called self energy $\Sigma = \Re\Sigma + \Im\Sigma$. The real part of the self energy $\Re\Sigma$ depicts the change of the dispersion or the increase of the effective mass, while the imaginary part of the self energy $\Im\Sigma$ contains the information about the lifetime of the quasiparticle. In case of electron scattering processes due to electron-electron, electron-phonon or electron-impurity interactions their contribution to the lifetime broadening, Γ, is independent of each other and can be expressed as a sum of each contribution: $\Gamma = \Gamma_{el-el} + \Gamma_{el-ph} + \Gamma_{el-imp}$[4]. Γ_{el-imp} represents an energy-independent term arising from the electron-impurity scattering, while Γ_{el-el} and Γ_{el-ph}, which are contributions from electron-electron and electron-phonon scattering respectively, are energy dependent. For *3d*-metals Γ_{el-el} is well described at low energies by a Fermi liquid behavior and depends quadratically on the binding energy. In case of electron-phonon interaction the energy dependence of lifetime broadening is more complicated and will lead to the appearance of a kink – a sudden change in the dispersion below a finite binding energy.

We studied the spin dependent quasiparticle band structure of Ni (111) with high resolution angle-resolved photoemission spectroscopy (ARPES) to obtain detailed insight into self energy. The experiment was performed at the UE-112 beamline in the BESSY-II storage ring using "1³" spectrometer. We grew a thick ($\approx$100Å) Ni(111) layer on a W(110) surface. ARPES spectra were measured at a photon energy of 136 eV. The accessible plane in the Ni bulk Brillouin zone is shown in Fig. 1. The measured Fermi surface is shown in Fig. 2. The solid yellow line indicates the line along which ARPES data were taken. Dashed lines indicates positions of d and sp-like bands. In order to quantitatively analyze the spectral line shape we used Lorentzians on a linear background to fit the momentum distribution curves (MDC's) – the intensity distribution curves as a function of momentum for a given binding energy.

Data measured at low temperature ($\approx$50 K) for sp-like and d bands are presented in Fig. 3. The plots (c) and (d) of Fig. 3 show the intensity distribution of a band while the (a) and (b) plots show the MDC data (symbols) and fits (solid lines) at Fermi level. In the present analysis we used the MDC widths δk to estimate the imaginary part of self energy $\Im\Sigma = \hbar v_f \delta k$, where v_f is the Fermi velocity [4]. The band dispersion in the absence of the kink was assumed to be linear and the Fermi velocity was estimated as
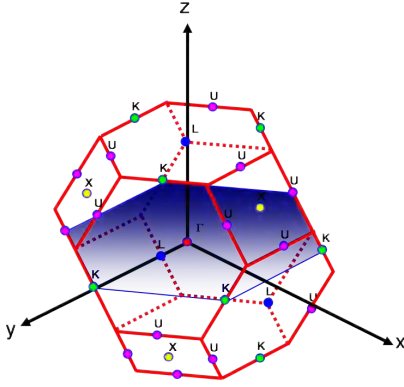
Figure 1: Sketch of the Ni Brillouin zone
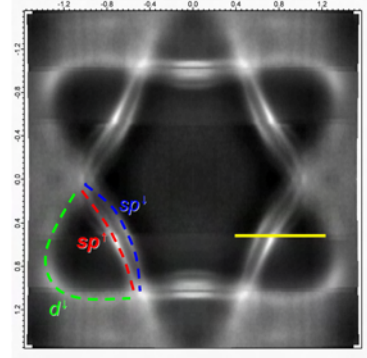
Figure 2: Experimentally obtained Fermi surface of Ni with the assignment of minority d ($d^\downarrow$), majority sp-like ($sp^\uparrow$) and minority sp-like ($sp^\downarrow$) bands.
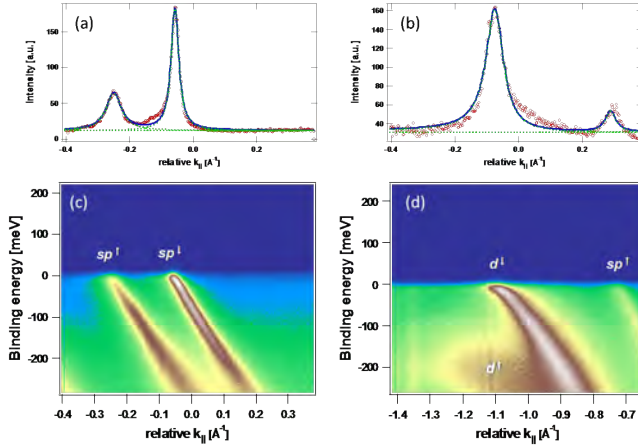
Figure 3: ARPES images measured at low temperature (≈ 50K) of the Ni (111) surface for sp-like bands (c) and d band (d). Corresponding MDC data (symbols) and fits (lines) at Fermi are shown in (a) and (b), respectively

a slope of the linear fit of the first $\approx 50 - 70$ meV of the fitted dispersion. The resulting imaginary and real parts of the self energy of the sp-like minority, sp-like majority and d bands are shown in Fig. 4(a) and Fig. 4(b), respectively. Symbols represent the observed imaginary and real parts of the self energy. Solid and dashed lines display modeled electron-phonon and electron-electron lifetimes, respectively. For binding energies $E \gtrsim 35$meV the lifetimes of minority sp-like and d bands decrease while the majority sp-band does not show any significant change. Such behavior is in a good agreement with literature [3] and has been explained by electron-phonon interaction. The electron-phonon coupling to a phonon of energy Ω can be expressed as:

$$\mathfrak{Im}\, \Sigma^{el-ph} = 2\pi \int\limits_0^{\hbar\Omega_{max}} \alpha^2 F_k\left(E'\right)\left[2n\left(E'\right) + f\left(E' + E\right) + f\left(E' - E\right)\right],$$

where $n(E)$ is Bose-Einstein distribution, $f(E)$ is Fermi-Dirac distribution and $\alpha^2 F_k$ is the Eliashberg function[4]. In the present analysis we used a Debye model to describe the phonon Eliashberg function: $\alpha^2 F_k = \lambda\left(\frac{E}{\hbar\Omega_D}\right)$ for $E \le \hbar\Omega_D$ and $\alpha^2 F_k = 0$ for $E > \hbar\Omega_D$[4], where λ is electron-phonon coupling constant. We obtained $\lambda_{sp\downarrow} \approx 0.21$ for minority sp-like states and $\lambda_{d\downarrow} \approx 0.44$ for d states. In case of majority sp-like states the coupling constant is much smaller $\lambda_{sp\downarrow} \approx 0$. This difference in the λ-values is especially prominent for the dispersion close to the Fermi level in Figs. 3(c) and 3(d).

Measured room temperature data (≈ 320 K) for sp-like and d bands are presented in Fig. 5. At high temperatures kink disappear in line broadening but we still could compare MDCs at the Fermi
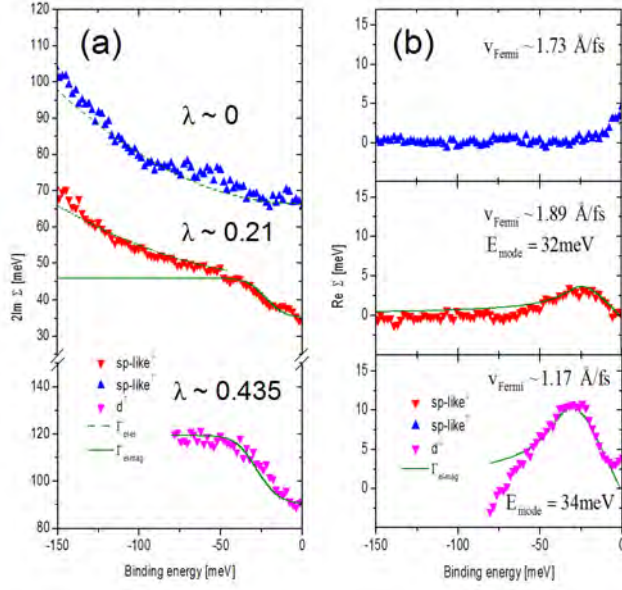
Figure 4: Experimental imaginary (a) and real (b) parts of the self energy of *sp*-like minority, *sp*-like majority and *d* bands. Symbols represent the observed imaginary (real) parts of the self energy. Solid and dashed lines displays modeled electron-phonon and electron-electron lifetimes respectively.
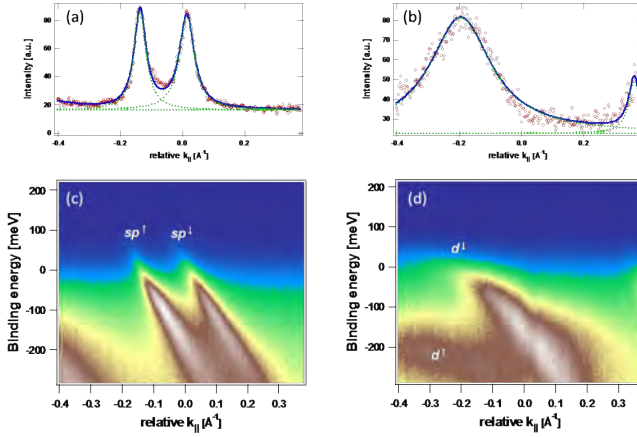
Figure 5: ARPES images measured at room temperature ($\approx$ 320K) of the Ni (111) surface for *sp*-like bands (c) and *d* band (d). Corresponding MDC data (symbols) and fits (lines) at Fermi are shown in (a) and (b), respectively

level. With increasing temperature we observe a decreasing quasiparticle lifetime at the Fermi level for all probed minority spin bands as expected for electron-phonon coupling. The *sp*-like minority spin band displays an increase of lifetime broadening from 0.014Å^{-1} to 0.029Å^{-1}, while *d* minority band lifetime broadening increases from 0.038Å^{-1} to 0.096Å^{-1}. Surprisingly the majority spin states behave differently. We actually observe a slightly increased lifetime at room temperature. The width of the majority band decreases with increasing temperature from 0.029Å^{-1} to 0.023Å^{-1} corresponding to an actual increase of the elastic mean free path from 33Å to 43.5Å. The corresponding increase in Fermi velocity from 1.73Å/fs to 2.06Å/fs points to a temperature dependent reduction of the majority spin quasiparticle renormalization. Although the origin of this novel effect is still unclear it could possibly arise from spin excitations coupling to phonons.

[1] P. Grünberg *et al.*, Phys. Rev. Lett. 57, 2442–2445 (1986)

[2] M. Julliere, Phys. Lett. 54A, 225226 (1975)

[3] M. Higashiguchi *et al.*, Phys. Rev. B 72, 214438 (2005)

[4] S. Hüfner, *Very High Resolution Photoelectron Spectroscopy*, 1st ed. (Springer-Verlag Berlin Heidelberg 2007)

Static and fluctuating stripe order in 1/8-doped LNSCO and LSCO

H. H. Wu,[1,2] M. Buchholz,[1] C. Trabant,[1] F. Heigl,[3] E. Schierle,[4] M. Cwik,[1]

M. Braden,[1] L. H. Tjeng[1] and C. Schüßler-Langeheine[1]

[1]*II. Physikalisches Institut, Universität zu Köln, Zülpicher Str. 77, 50937 Köln, Germany*

[2]*National Synchrotron Radiation Research Center, Hsinchu, Taiwan*

[3]*CELLS-ALBA, 08193 Bellaterra, Barcelona, Spain*

[4]*Helmholtz-Zentrum Berlin, Albert-Einstein-Str. 15, 12489 Berlin, Germany*

In hole-doped layered copper-oxides static and fluctuating stripe order has been considered to be a crucial issue for the understanding of the basic physics of the high-Tc superconductor. Stripe order is a complex collective order involving charge and spin degrees of freedom. While in $La_{2-x}Sr_xCuO_4$ (LSCO) fluctuating stripe order gives rise to peaks in inelastic neutron scattering, partial substitution of La by Nd leads to a pinning of spin and charge order and the formation of static stripes as revealed by peaks in the elastic neutron diffraction signal [1].

Earlier experiments from the isostructural nickelate system gave us strong indications that resonant soft x-ray diffraction RSXD is not only sensitive to static but also to fluctuating stripe order. This finding suggests that RSXD may be an attractive alternative method to study in particular fluctuating charge order, which is difficult to probe by neutron scattering.

For this experiment we chose samples with doping level near 1/8, namely $La_{1.48}Nd_{0.4}Sr_{0.12}CuO_4$ (LNSCO) and $La_{1.88}Sr_{0.12}CuO_4$ (LSCO) single crystals. The samples were cut and polished ex situ. The experiments were performed at the beam line UE46-PGM using the UHV diffractometer built at the Freie Universität Berlin.

As seen in Figs. 1, 2 and 3, both systems exhibit a pronounced incommensurate charge order peak at the oxygen K and copper $L_{2,3}$ edges, thus confirming our basic assumption that fluctuating stripe order can in fact be probed by RSXD. In fact for the LSCO sample this is the first direct observation of charge order. Earlier neutron diffraction work found magnetic order, but no direct evidence for charge order [3].
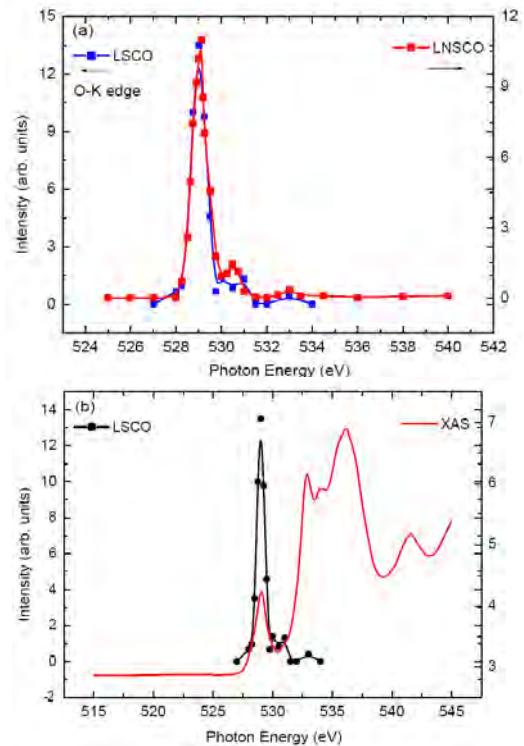
FIG. 1. (a) Photon energy dependence of charge order at oxygen K edge in LNSCO and LSCO. (b) X-ray absorption spectra (XAS) at oxygen K edge (red line) and the resonant x ray scattering intensity of charge order near O-K edge in LSCO (black line).
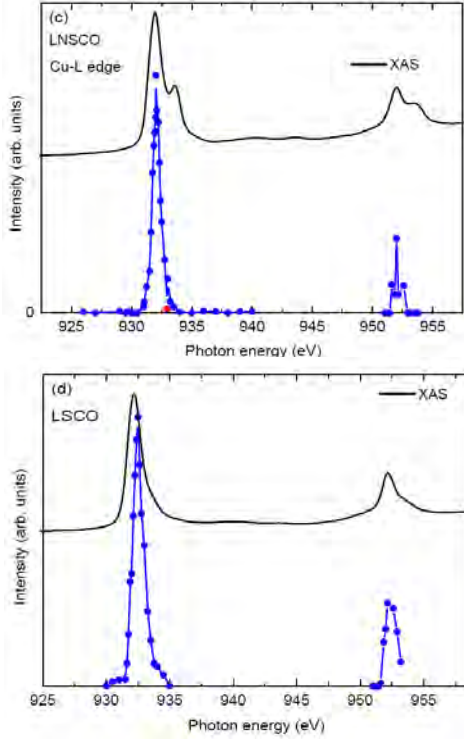
FIG. 2 (c) and (d) Photon energy dependence of charge order near Cu $L_{2,3}$ edge (blue line) and XAS at Cu $L_{2,3}$ edge in LNSCO and LSCO.

In Figure 1(a) and 1(b), the charge order in LNSCO and LSCO shows the strong photon energy dependence near oxygen K edge. The resonance energy for the charge order in both systems is located at photon energy of 529 eV, which is mainly from a $3d^9\underline{L}$ to $1s3d^9$ transition. The resonance behavior at oxygen K edge has similar feature for LNSCO and LSCO supporting a common electronic origin of both diffraction features. As can be seen in Figure 2(c), and 2(d), the two systems have slight difference in the RSXD spectra near Cu $L_{2,3}$ edges, which require further analysis. We studied the temperature dependence of both signals (Fig. 3). The Nd-stabilized system (LNSCO) shows a structural phase transition from low-temperature-orthorhombic (LTO) to low-temperature-tetragonal (LTT) at about 70 K [1,2] while the Nd-free $La_{1.88}Sr_{0.12}CuO_4$ always remains in the LTO phase.

As for LNSCO, static charge order is known to exist in the LTT phase [4], and in fact we find no superstructure peak above the LTT-LTO phase transition temperature. In LSCO, the intensity of charge order vanishes slightly above the critical temperature similar to what has been observed for the magnetic order [5].

[1] J. M. Tranquada *et al.*, Phys. Rev. Lett. **78**, 338 (1997).

[2] J. M. Tranquada *et al.*, Phys. Rev. B **54**, 7489 (1996).

[3] K. Yamada *et al.*, Phys. Rev. B **57**, 6165 (1998).

[4] J. M. Tranquada *et al.*, Nature **375**, 561 (1995).

[5] H. Kirmura *et al.*, Phys. Rev. B **59**, 6517 (1999).
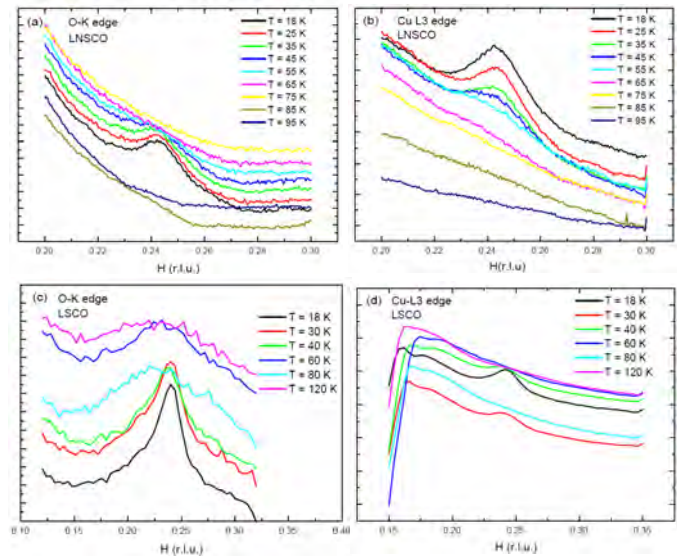
FIG. 3: Temperature dependence of charge order at O-K and Cu L_3 edges in LNSCO and LSCO.

X-ray photoelectron spectroscopic analysis of HfO$_2$/Si structure synthesized by ALD and MOCVD methods

E O Filatova[1], A A Sokolov[1], V V Afanas'ev[2], E Yu Taracheva[1], M M Brzhezinskaya[3] and A A Ovchinnikov[1]

[1]Institute of Physics, St-Petersburg State University, St-Petersburg, 198504, Russia
[2]Department of Physics, University of Leuven, Celestijnenlaan 200D, B-3001 Leuven, Belgium
[3]BESSY, Albert Einstein Str. 15, D-12489 Berlin, Germany

HfO$_2$ is one of the most promising contenders to become the insulating material for the future MOS technology nodes, it combines high dielectric constant (κ=16-45), wide bandgap, and sufficient thermodynamic stability with respect to interaction with silicon to withstand the thermal budget of the MOS device processing [1,2]. Successful implementation of HfO$_2$-based insulating stacks requires basic understanding of the HfO$_2$/Si interface chemistry and its impact on the electrical properties [3,4]. In particular, the properties of the interlayer (IL) between Si and HfO$_2$ are of importance as they have direct effect on the electron transport in the Si surface channel. The main goal of this project consisted in layer-by-layer X-ray photoelectron spectroscopic (XPS) investigation (Hf *4f*, Si *2p*, and O *1s* electron states) of thin layers of HfO$_2$ grown on (100)Si crystal surface using atomic layer deposition (ALD) or metallo-organic chemical vapour deposition (MOCVD) with purpose to receive the information about chemical phase composition of the IL depending on preparation method.

In framework of present work were investigated next samples:
1. The HfO$_2$ (ALD, 5 nm)/n-Si and HfO$_2$ (ALD, 5 nm)/p-Si structures were fabricated at 300°C using ALD from HfCl$_4$ and H$_2$O precursors on the IMEC-cleaned, i.e., covered with 0.8 nm-thick chemical Si oxide, surface of n- and p-type (100)Si crystals, respectively.
2. The HfO$_2$ (MOCVD, 5 nm)/n-Si sample was prepared on the identically prepared n-type (100)Si surface using MOCVD of HfO$_2$ at 485°C from (Hf((CH$_3$)$_2$N)$_4$) and O$_2$ precursors.
3. The HfO$_2$ (ALD, 1.5nm)/p-Si sample was synthesized by ALD at 280°C from (Hf((CH$_3$)$_2$N)$_4$) and H$_2$O precursors on Si-p-type (100) substrate etched prior to deposition in 1% aqueous HF solution for 30 s without final water rinse.

To obtain the depth profiles, the Ar$^+$ ion sputtering was applied using 2.5 keV *in situ* ion beam with the size of the sputtered area being 15 mm x 15 mm. All measurements were

Figure 1. Hf *4f* photoelectron spectra from the HfO$_2$/Si samples before and after different Ar$^+$ ion sputtering steps: a) HfO$_2$(ALD, 5 nm)/n-Si; b) HfO$_2$(MOCVD, 5 nm)/n-Si; c) HfO$_2$(ALD, 5 nm)/p-Si; d) HfO$_2$(ALD, 1.5 nm)/p-Si.

performed at the Russian-German beamline. The XPS spectra were taken at the exciting photon energies of 200 eV and 700 eV using hemispherical electron energy analyzer VG Clam 4 with the energy resolution better than 200 meV. All spectra were collected at the analyser pass energy of 10 eV and the binding energies (BE) were referenced to the bulk Si^0 *2p$_{3/2}$* core level at 99.2 eV [5].

Fig.1 shows the Hf *4f* XPS spectra obtained at the excitation energy of 200 eV from the pristine HfO$_2$/Si samples and those observed after different sputtering steps. Before sputtering, analysis of the Hf *4f* spectra reveals the presence of the Hf *4f* doublet peak with spin-orbit splitting of l.7 eV and intensity ratio between components of 0.8. The BE position of these peaks is varied from

18.6 eV ($4f_{7/2}$) (5-nm thick films) to 17.6 eV ($4f_{7/2}$) (1.5-nm thick layers). The most plausible explanation of these differences is HfO$_2$ thickness-dependent irradiation-induced oxide charging.

During sputtering the Hf $4f$ doublet peak becomes weaker and ultimately disappears. At the same time the new peaks centred at 14.7 eV and 16.4 eV become detectable in the spectra after 40 min sputtering. As these peaks are associated with Hf^0 $4f$ doublet in metallic hafnium [6, 7], this observation suggests that oxygen is preferentially removed by Ar$^+$ ion sputtering and while the remaining hafnium is reduced to Hf^0.

Fig.2 shows the Si $2p$ XPS spectra obtained at the excitation energy of 200 eV. Fig. 2a),b),c) shows the spectra obtained from the HfO$_2$(5nm)/Si samples for sputtering steps after 40 minutes of the sputtering.

Analysis of the Hf $4f$ and Si $2p$ XPS spectra of HfO$_2$(ALD, 5 nm)/Si samples after the 70 minutes of ion sputtering reveals that only Hf^0 $4f$ and Si^0 $2p$ lines remain in the spectra. Further sputtering is found to have no measurable effect on the shape and the intensity of these peaks.

Figure 2. Si $2p$ XPS spectra from the HfO$_2$/Si samples after ion sputtering for different time (given in min): a) HfO$_2$(ALD, 5 nm)/n-Si; b) HfO$_2$(MOCVD, 5 nm)/n-Si; c) HfO$_2$(ALD, 5 nm)/p-Si; d) HfO$_2$(ALD, 1.5 nm)/p-Si.

The intensities of the peaks Hf^0 $4f$ and Si^0 ($2p$) were compared using normalization on the photoionization cross-section yielding the ratio close to 5:1. Apparently, a thin layer of metallic Hf, was formed on the Si-surface during the Ar$^+$ ion bombardment impeding further sample sputtering. Interestingly, as can be seen from figure 2, in the sample with MOCVD HfO$_2$ the Si^0 ($2p$) peak appears after longer sputtering time as compared to the samples with ALD HfO$_2$ suggesting difference in the Ar$^+$ sputtering rate.

All peaks in the Si $2p$ XPS spectra were deposited into peaks which corresponds to different oxidation states Si^{x+} (x=0,1,2,3,4). Figure 3 shows the fit of the Si $2p$ XPS spectra of the HfO$_2$(ALD, 5 nm)/n-Si samples after 45 and 55 minutes of the sputtering. In its turn, figure 4 presents curve fitting of the Si $2p$ emission band in the HfO$_2$(ALD, 1.5nm)/p-Si sample before the sputtering, and after 17 and 32 minutes of the sputtering.

Figure 3. Curve fitting of the Si $2p$ XPS spectra taken after 45 and 55 minutes of ion sputtering of the HfO$_2$ (ALD, 5 nm)/n-Si sample.

Such curve fitting was carried out for all etching steps. Analysis of all curve obtained indicates the presence of small amount of Hf-silicate and SiO$_2$ at the interface for HfO$_2$ (5 nm)/Si samples and substantial quantity of SiO$_2$ and SiO$_x$ for HfO$_2$ (ALD, 1.5 nm)/p-Si sample.
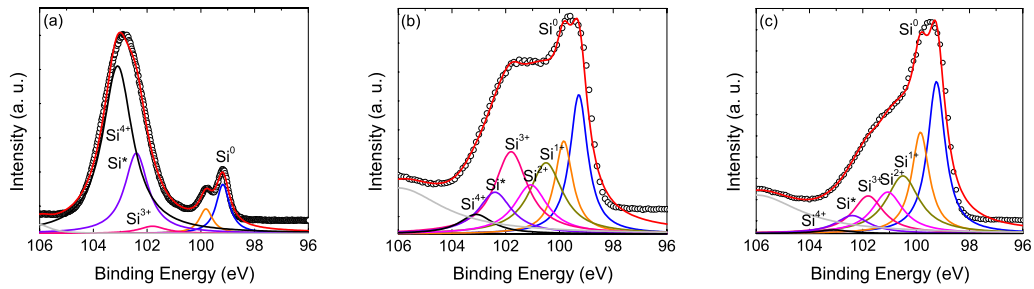
Figure 4. Curve fitting of the Si *2p* XPS spectra from the HfO$_2$ (ALD, 1.5 nm)/p-Si sample before the sputtering (a) and after sputtering for 17 (b) and 32 (c) minutes.

Fig.5 shows O*1s* XPS spectra obtained at the excitation energy of 700 eV. There is observed a shift of the O *1s* peak towards lower BEs as illustrated in figure 3. Importantly, variation of the samples surface charging would result in a correlated shift of the both Hf *4f* and O *1s* peaks energy positions.

Analysis of Hf *4f*, Si *2p* and O *1s* photoelectron spectra in the HfO$_2$/Si samples prepared using different oxide growth techniques indicates the presence of small amount of Hf-silicate and SiO$_2$ at

Figure 5. O*1s* XPS spectra of the HfO$_2$(ALD, 5 nm)/n-Si (a) and HfO$_2$(MOCVD, 5 nm)/n-Si (b) samples before and after different Ar$^+$ ion sputtering steps.

the interface between (100)Si crystal and HfO$_2$ grown on the 0.8-nm thick native oxide under-layer. On the contrary, the presence of considerable amounts of SiO$_2$ and SiO$_x$ is revealed at the interface formed by depositing hafnia on HF-dipped, i.e., hydrogen-passivated, silicon. Further, it is found that Ar$^+$ ion sputtering leads to the formation of a metallic Hf on the Si-substrate with no signs of silicate phase. The sputtering induced formation of metallic Hf may be important not only from the point of view of optimizing dry etching of the HfO$_2$ films, but, at the same time, may also be used to incorporate metallic particles or conducting layers to the Si/HfO$_2$–based heterostructures.

Acknowledgments

References

[1] Kukli K, Aarik J, Aidla A, Siimon H, Ritala M and Leskela M 1997 *Appl. Surf. Sci.* **112** 236
[2] Hsu C T, Su Y K and Yokoyama M 1992 *Jpn. J. Appl. Phys.,* Part 1 **31** 2501
[3] Sayan S, Garfunkel E, Nishimura T, Schulte W H, Gustafsson T and Wilk G D 2003 *J. Appl. Phys.* **94** 928
[4] Misra V, Lucovsky G and Parsons G 2002 *MRS Bull.* **27** 212
[5] Cardona M and Ley L 1978 *Eds., Photoemission in Solids I: General Principles (Springer-Verlag, Berlin) with additional corrections*
[6] Tan R *et al* 2005, Applied Surface Science **241** 135–140
[7] Suzer S *et al* 2003*.,* J. Vac. Sci. Technol. **A21** 106

X-ray reflection spectroscopic characterization of HfO$_2$/Si structure synthesized by ALD and MOCVD methods

E O Filatova[1], A A Sokolov[1], I V Kozhevnikov[2] E Yu Taracheva[1], F Schaefers[3]and W Braun[3]

[1]St-Petersburg State University, Institute of Physics, St-Petersburg, 198504, Russia
[2]Institute of Crystallography, Moscow, 119333, Russia
[3]BESSY, Albert Einstein Str. 15, D-12489 Berlin, Germany

HfO$_2$ is one of the most perspective materials for the nanoelectronics industry to replace SiO$_2$ because it has a high dielectric constant and is expected to be stable in contact with Si. So far one stable monoclinic phase and four metastable phases: cubic, tetragonal, orthorhombic I and orthorhombic II have been identified for HfO$_2$. An amorphous modification can also be fabricated. Although the tetragonal HfO$_2$ structure has the highest dielectrical permittivity an amorphous structure is to be preferred for several reasons. First of all amorphous materials do not contain grain boundaries or dislocations that can trap charge and offer fast diffusion pathways for leakage current. In addition, stresses in amorphous materials can be taken up by small variations in the random network, where they may likewise be taken up by misfit dislocations in a polycrystalline material. Amorphous structures also tend to minimize electronically active defects, but may give rise to shallow traps. Epitaxial films can be produced free of grain boundaries and defects and, therefore, are usually preferred for gate dielectrics. Therefore, most of the work on HfO$_2$ has been focused on manufacturing amorphous films to replace SiO$_2$, but this process is unpredictable, because the microstructure of films is largely depending on thickness, technology of synthesis and utilizable precursors. Therefore the technology of preparing films, i.e. method and condition of synthesis (rate of deposition, temperature of substrate, etc.), also as utilizable precursors are an important issue to fabricate films with the required properties. A further study of the effect of different factors is required. In this work we were focused on the discussion of the crystalline and electronic structure of thin films of HfO$_2$ of different thicknesses and prepared by two different methods (Atomic Layer Deposition (ALD) and Metal Organic Chemical Vapour Deposition (MOCVD)). The HfO$_2$ films were deposited on (100) n-type silicon wafers by ALD, using hafnium tetrachloride (HfCl$_4$) and water at 300 °C substrate temperature. Different film thicknesses (5, 20 and 100 nm) were obtained by varying the number of ALD cycles only. When the MOCVD method was used, the HfO$_2$ films were deposited on (100) n-type silicon wafers using tetrakisdiethylaminohafnium (Hf(N(C$_2$H$_5$)$_2$)$_4$) and O$_2$ at 485 °C substrate temperature.

The angular and spectral dependences of the reflectivity in the vicinity of O K(1s) - absorption edge were measured using s-polarized synchrotron radiation in the reflectometer set-up on the optics beamline (D-08-1B2).

The O1s reflection spectra of HfO$_2$ films of thicknesses 5, 20 and 100 nm synthesized by ALD and measured at grazing incidence angle of 4° are presented in figure 1. The absorption spectra calculated on the basis of the measured reflection spectra by means of the Kramers–Kronig transform using the method described in details in [1] are presented in figure 2.

The molecular orbitals of HfO$_2$ derived from a linear combination of atomic orbitals (LCAO) are characterized by four unoccupied orbitals: e_g(Hf5d+O2$p\pi$), t_{2g}(Hf5d+O2$p\sigma$), a_{1g}(Hf6s+O2p) and t_{1u}(Hf6p+O2p). Peaks a and b (fig.2) reflect core –electron transitions in the oxygen atoms to the lowest unoccupied Hfde_g and Hfdt_{2g} electronic states that are hybridized with the 2p states of the oxygen atoms. Obviously, there is a broadening of the feature a with the growth of the film thickness. Moreover the feature a demonstrates a double structure a –$a´$ in the absorption spectrum of the film of 100 nm thickness. This splitting appears because of Jahn-Teller d-state degeneracy and specifies on presence of monoclinic phase in the film. At that the grains size must be ~/>2 nm. Otherwise it takes place suppression of the Jahn-Teller effect. The manifestation of details c and d is also signature of ordering of structure. The probability of the transitions to the (Hf 6s,6p+O 2p) states is very low and the double structure c-d cannot be observed in the amorphous state of the film.

Above mentioned arguments have allowed concluding that the 100 nm thick film has the polycrystalline structure with a size of the grains ~/>2 nm and its microstructure involves generally the monoclinic phase. At that films of thickness 5 and 20 nm have amorphous structure.

Figure 4 shows the O1s-reflection spectra of films of equal thickness of 5 nm, but fabricated by two different methods (ALD and MOCVD). The O1s - absorption spectra calculated from reflection spectra (figure 4) using a Kramers – Kronig analysis are presented in figure 5.
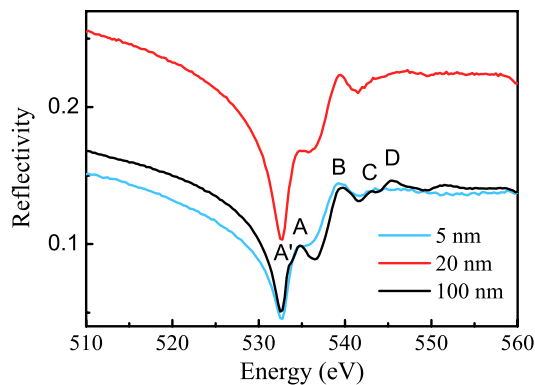
Figure 1. O1s reflection spectra of HfO_2 5, 20 and 100 nm thick films synthesized by ALD and measured at a grazing incidence angle of 4°.
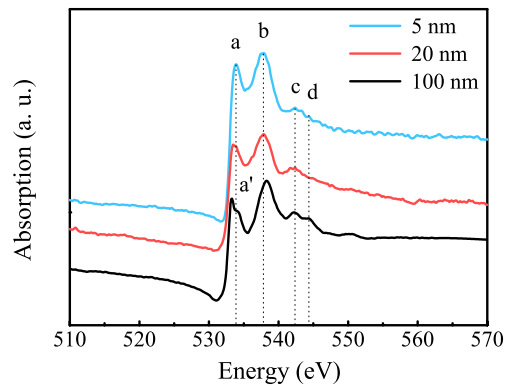
Figure 2. Absorption spectra calculated on the bases of the measured reflection spectra (figure 1) using a Kramers - Kronig analysis.

Analysis of the shape of the reflection and absorption spectra (figure 4, 5) allows concluding, that the film manufactured by ALD is amorphous, whereas the film prepared by MOCVD method has signatures of ordering of the structure because of the pronounced details *c* and *d*. In contrast to the 100 nm thick film manufactured by ALD (figures 1 and 2) there is no sign of a Jahn-Teller splitting in the spectrum of the film prepared by MOCVD that allows assuming that grain size in the film under consideration is < 2 nm. It can be argued that the film prepared by MOCVD shows evidence for crystallization.
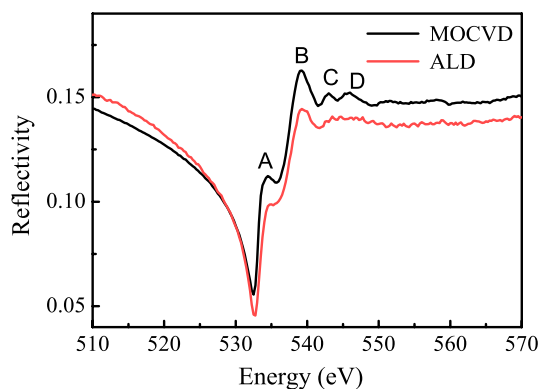
Figure 4. O1s- reflection spectra of films 5 nm thick fabricated by ALD and MOCVD measured at a grazing incidence angle 4°.
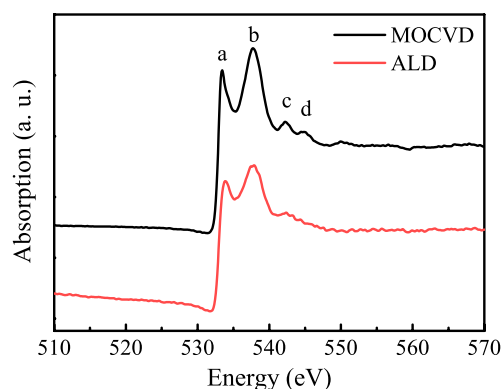
Figure 5. O1s- absorption spectra of 5 nm thick films calculated from reflection spectra (figure 4).

In addition to reflection spectra the reflectivity curves versus grazing angle were measured at different wavelengths of the incident beam for HfO_2 films under consideration. The reflectivity curves versus grazing angle measured at energy 520 eV are shown in figure 6, circles, respectively. The depth-distribution of chemical elements obtained within the framework of the approach developed in [2] is shown in figure 7. The corresponding reflectivity curves are shown in figure 6, curves 3, for the ALD sample, which are in a perfect agreement with the experimental data. The calculated reflectivities of the MOCVD samples are not shown in figure 6, because they cannot be distinguished from curves 2, by applying the fitting procedure. Such situation can takes place when the film is structurally inhomogeneous.
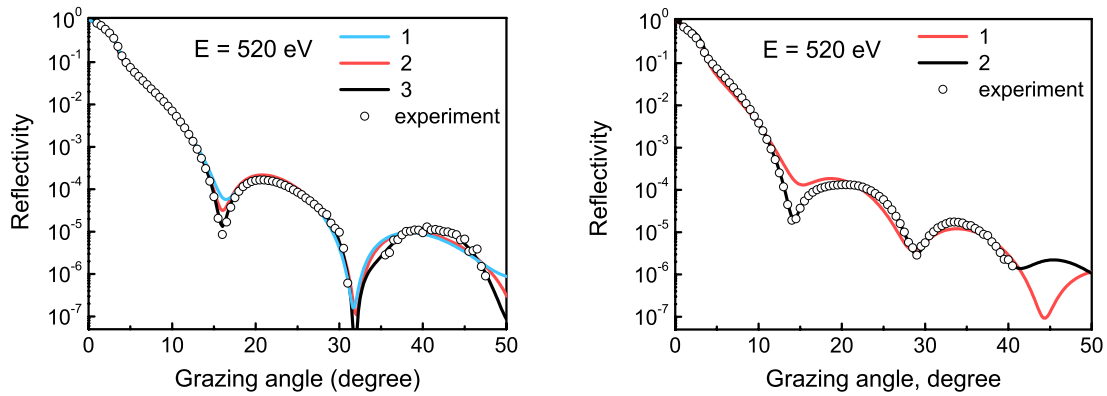
Figure 6 The measured reflectivity curves (circles) versus grazing angle at energy 520 eV of the 5 nm thick HfO$_2$ film deposited onto a Si substrate by the ALD (left) and MOCVD (right) technique. Curves 1 and 2 are the result of fitting with the use of the single-layer (1) or three-layer (2) models. Curves 3 are the result of a numerical refinement of the three-layer model.
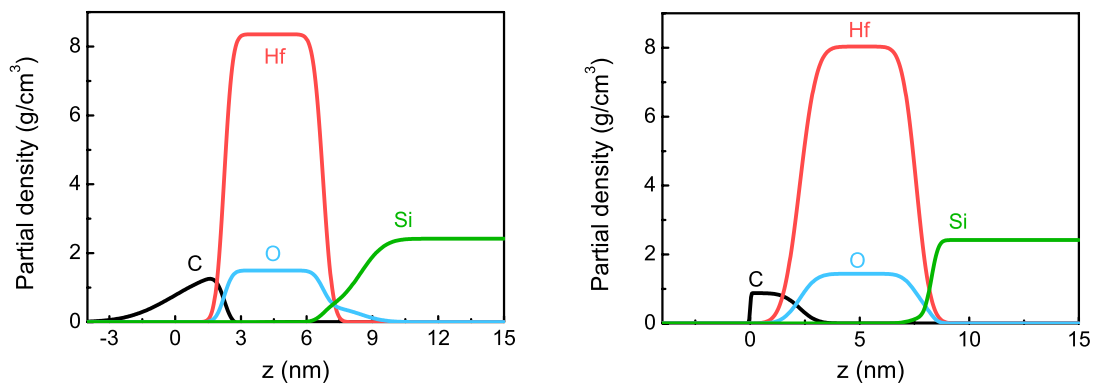
Figure 7 Depth-distribution of chemical elements for the 5 nm thick films deposited onto a Si substrate by the ALD (left) and MOCVD (right) technique: three-layer model.

The microstructure of films of different thickness synthesized by ALD and MOCVD was characterized by reflection spectroscopy and soft x-ray reflectometry techniques. It was shown that near – edge reflection spectra and absorption spectra calculated on the basis of reflection spectra are very sensitive even to signatures of ordering on a subnanometer scale in the film. It was established that the microstructure of the HfO$_2$ film is strongly depends on the film thickness. First results on the reconstruction of the depth-distribution of chemical elements based on the analysis of reflectivity curves were discussed. The element depth profiling shows that there are no measurable differences between 5 nm ALD and MOCVD films would provide a direct support to the importance of structural factor. The calculations carried out allow assuming that MOCVD film is inhomogeneous in depth.

References

[1] Filatova E, Lukyanov V, Barchewitz R, André J-M, Idirk M and Stemmler Ph 1999 *J. Phys.: Condens. Matter* **11** 3355

[2] Kozhevnikov I V 2003 *Nucl. Instrum. Methods A*, **508** 519-541.

Investigations of a structure of thin TiO_2 films by soft x-ray reflectometry techniques

E O Filatova[1], E Yu Taracheva[1], G S Shevchenko[1], A A Sokolov[1], I V Kozhevnikov[2], S Yulin[4], F Schaefers[3], W Braun[3]

[1]Institute of Physics, St-Petersburg State University, St-Petersburg, 198504, Russia
[2]Institute of Crystallography, Moscow, 119333, Russia
[3]BESSY, Albert Einstein Str. 15, D-12489 Berlin, Germany
[4]Fraunhofer Institut Angewandte Optik und Feinmechanik, Albert Einstein Strasse 7,D-07745 Jena

TiO_2 films are extensively studied because of their interesting chemical, electrical and optical properties. TiO_2 is a high bandgap semiconductor that is transparent to visible light and has excellent optical transmittance. TiO_2 has high refractive index, good insulating and catalytic properties as well as it possesses unique wettability and biological compatibility. As a result TiO_2 thin films are widely used in many practical applications (catalysis, photocatalysis, dye-sensitized photovoltaic cell, gas sensors, and etc.) Besides TiO_2 nanofilms are widely used as protective layer for very large scale integrated (VLSI) circuits, for manufacture of optical elements, as antireflective (AR) coatings, for electrochromic displays and planar waveguides. The high dielectric constant of TiO_2 allows its consideration as an alternative to silicon dioxide for ultrathin gate oxide dielectrics used in memory and logic devices. The mechanical, physical, chemical and electrical properties of TiO_2 films in many respects depend strongly on their crystallinity. As it is known, TiO_2 films can be synthesized in different crystal modifications (anatase, rutile and brookite) or in amorphous phase.

Rutile TiO_2 has higher opacity, greater density and greater inertness than the anatase one and it is used as a convertible pigment in paints and dyes industry. Besides because of its highest refractive index TiO_2 rutile type is required for photonic crystals application.

While the anatase type of TiO_2 can enhance the photocatalytic and hydrophilic property of TiO_2 due to its higher photoactivity and more crystal defects than other types of TiO_2.

Fabrication of films with the necessary microstructure depends on different deposition parameters and is the important technological problem. To adjust a technological process it is necessary to use precise technique for thin films characterization. Traditionally XRD technique is applied to identify crystallinity of films. At the same time the sensitivity of this method is limited by the grain size.

The TiO_2 films 10nm and 70 nm thick synthesized by magnetron sputtering method on Si(100) wafers were investigated using X-ray reflection spectroscopy.

The angular and spectral dependences of the reflectivity in the vicinity of O K(1s) - absorption edge and Ti $L_{2,3}$ (2p) - absorption edge were measured using s-polarized synchrotron radiation in the reflectometer set-up on the optics beamline.

Reflection spectra of TiO_2 films 10 and 70 nm thick measured in the vicinity of Ti $L_{2,3}$ (2p) – and O K(1s)- absorption edges at grazing incident angles 4° and 2°, correspondingly, are presented in Fig.1. One can see that both the Ti 2p and the O (1s) spectra for different films thickness correlate well in energy position of main details of the structure and in absolute value of the reflectivity. At the same time, the reflection spectra of films are characterized by different contrast, especially in the case of OK-spectra. Moreover the reflection spectrum for film 70nm thick shows additional details in the structure. The absorption spectra calculated on the bases of the measured reflection spectra with help of Kramers - Kronig relationship described in details in [1] are presented in the Fig.2.

The peaks a and b (fig.2a) in Ti $2p_{3/2}$ spectrum stem from dipole allowed transitions of Ti $2p_{3/2}$ electrons to unoccupied 3d states. These states are split into $3dt_{2g}$ (peak a) and $3de_g$ (peak b) components by octahedral crystal field created by the O ions. What is the most interesting that there is a further splitting of the peak b into two bands b_1-b in the absorption spectrum of thick film (70nm). The manifestation of doubling of the Ti $2p$-$3de_g$- transitions depends on the crystalline structure of TiO_2. The main difference in Ti 2p spectra of different polymorphs is a change in intensities of components of peaks b and b_1. It is important for our investigations that the intensities of components of peaks b_1 and b in the spectrum of thick film (70nm) correlate well with anatase structure. The essential difference between rutile and anatase lies in the secondary coordination. It is shown in [2] that the experimental XAS spectra of anatase and rutile cannot be solely viewed in terms of a localized atomic cluster. According to [2] clearly the effect of the p-d and d-d interactions is important but this must be modified by the crystal field and further longer-range effects.
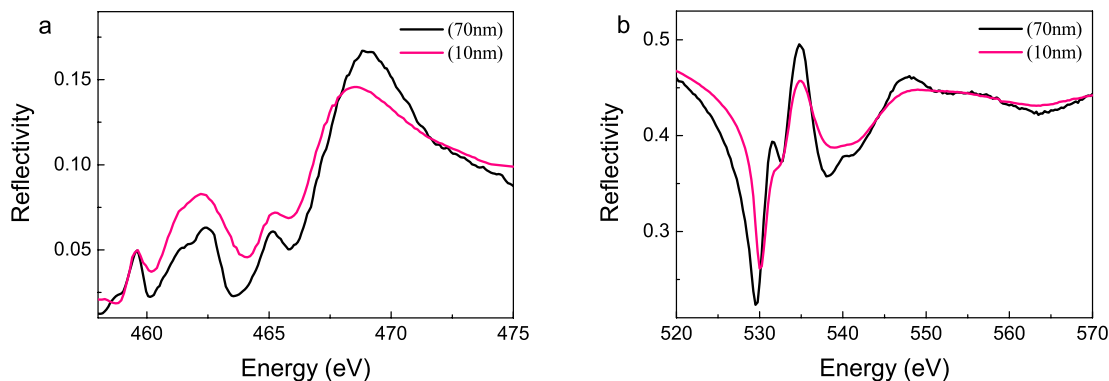
Figure 1. Reflection spectra of TiO_2 films 10 and 70 nm thick measured in the vicinity of (a) Ti $L_{2,3}$ (2p) - and (b) O K(1s)- absorption edges
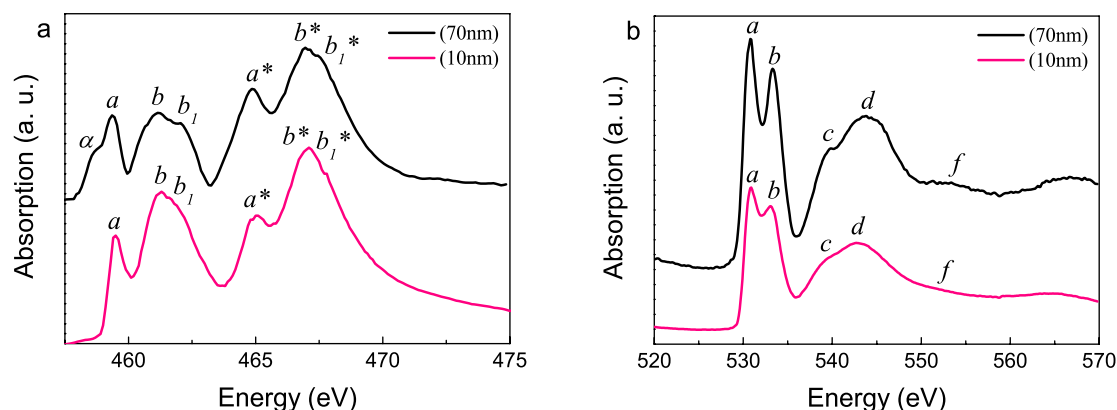
Figure 2. Absorption spectra of TiO_2 films 10 and 70 nm thick in the vicinity of (a) Ti $L_{2,3}$ (2p) - and (b) O K(1s)- absorption edges calculated from reflection spectra (Fig.1). The Ti $2p_{1/2}$ structures are marked by asterisks.

   The OK-edge features (fig.2b) at higher energies are very different for investigated films, too. The structure in the spectrum of TiO_2 film 70 nm thick is characterized by d, c and f peaks and is related with transitions into the empty electronics states with mixed Ti 4s, 4p+O2p character. Analysis of the energy positions of c, d and f peaks in the spectrum of TiO_2 film 70 nm thick shows a good correlation of this structure with the structure of anatase.

   Analysis of the energy positions and intensity of main peaks in the spectra of investigated TiO_2 films shows that the TiO_2 film 70nm thick is characterized by anatase structure and the TiO_2 film 10nm thick is amorphous.

   The TiO_2 film 70nm thick was investigated in the vicinity of OK-absorption edge at different grazing incident angles, which means at different depth formation of the reflected beam. The measured OK-reflection spectra are plotted in the fig. 3. One can see that there is no change in the shape of reflection spectra with growth of the depth formation of the reflected beam that points on the homogeneous of the investigated film.

   In addition to reflection spectra the reflectivity versus grazing angle was measured at λ = 0.154 nm for TiO_2 film 70nm thick. Measured reflectivity versus the grazing angle of a probe beam is shown in Fig.4, black curve.
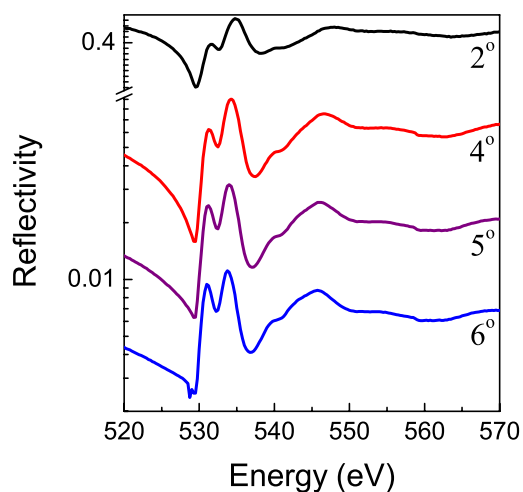
Figure 3. Reflection spectra of TiO_2 film 70 nm thick measured in the vicinity of O K(1s)- absorption edge at different grazing incident angles.

Approach developed in [3] was used to reconstruct the depth-distribution of the dielectric constant basing on the experimental reflectivity curve. The found dielectric constant profile $\delta(z) = 1 - Re[\epsilon(z)]$ is shown in Fig.5, where the Z axis is directed into the depth of a sample. The film density is constant with depth and is equal to 3.6 g/cm^3. An accuracy of fitting process is demonstrated by red curve in Fig.5. So that one can conclude that TiO$_2$ film 70nm thick is homogeneous with depth.
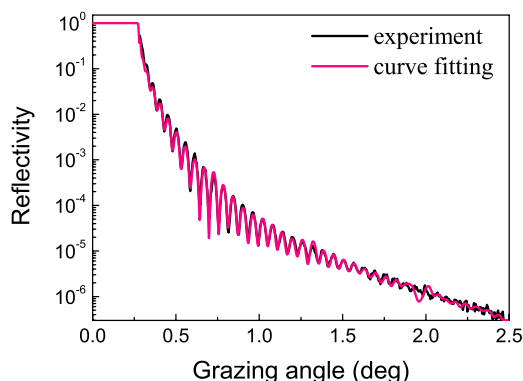
Figure 4. Reflectivitie versus grazing angle, measured at $\lambda = 0.154$ nm for TiO$_2$ film 70nm thick. Measured reflectivity is red curve. Accuracy of fitting process is blue curve.
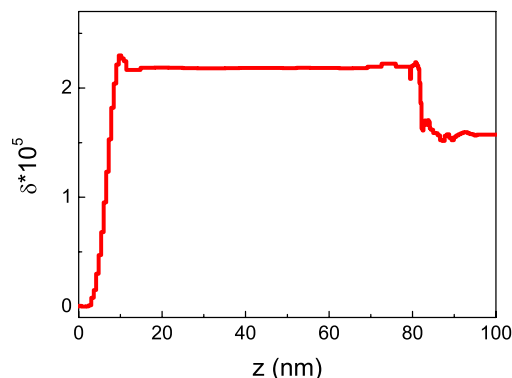
Figure 5 Dielectric constant profile $\delta(z) = 1 - Re[\epsilon(z)]$ reconstructed from measured reflectivity (fig.4).

The x-ray reflection spectroscopy data indicate that TiO$_2$ film 70nm thick is characterized by anatase structure. Following to dielectric constant profile reconstructed from measured reflectivity and angular dependence of the OK-reflection spectra one can conclude that TiO$_2$ film 70nm thick is homogeneous. The TiO$_2$ film 10 nm thick is amorphous. The investigation carried out shows the high sensitivity of the reflection spectroscopy to the middle atomic ordering.

Acknowledgments

References

[1] E. Filatova, V. Lukyanov, R. Barchewitz, J.-M. Andre, M. Idir, Ph.Stemmler. J. Phys.: Condens. Matter **11** (1999) 3355
[2] R Brydson, H Sauer, W Engel, J M Thomas, E Zeitler, N Kosugilland H Kurodall. J. Phys.: Condens. Matter l(1989) 797-812.
[3] I.V.Kozhevnikov, "Physical analysis of the inverse problem of X-ray reflectometry", *Nucl. Instrum. Methods A*, **508** (2003) 519-541.

Chemical and magnetic spectromicroscopy of individual nanoparticles

Florian Kronast[1], Nina Friedenberger[2], Katharina Ollefs[2], Michael Farle[2], Hermann A. Dürr[1]

[1]Helmholtz Berlin, Albert-Einstein-Str. 15, 12489 Berlin

[2]Universität Duisburg-Essen, Lotharstr.1, 47048 Duisburg

Overcoming the superparamagnetic limit represents a mayor challenge in high-density magnetic data storage technology. The bottom-up self-assembly technique for colloidal monodisperse hardmagnetic nanoparticles may provide a new cost effective approach. For instance the magnetocrystalline anisotropy of FePt alloys and nanoparticles can be tuned from zero to about 10^7 J/m^3 depending on the chemical composition and order [1,2].

In self-assembled nanoparticle arrays the "blocking temperature", i.e. the critical temperature below which the magnetization is considered to be stable over the timescale of the measurement [3], depends not only on the magnetic anisotropy of the individual particle but also on the dipolar interaction which in turn depends on the magnetization of the particle and the distance between them. Up to now there have been no experimental results that clearly identify why some results can be interpreted in a way that the dipolar interactions between the nanoparticles result in an enlarged or reduced blocking temperature. While structural properties of such self-assembled particles can be routinely studied using electron microscopy, a magnetic characterization is presently mainly based on ensemble averaging.

Here we use photoelectron emission microscopy (PEEM) to overcome this limitation. 30nm spatial resolution at the spin-resolved photoelectron emission microscope (SPEEM / UE49 PGM1) allows us to measure x-ray absorption spectra and x-ray magnetic circular dichroism (XMCD) of individual nanoparticles. To correlate magnetic properties of the nanoparticle with its shape and configuration, which cannot be resolved by the SPEEM, we match our PEEM data with previously taken high-resolution electron microscopy images (SEM). A grid of Au markers on the sample substrate serves a map to identify identical places. A specially designed sample holder with integrated magnetic yoke allows us to apply magnetic fields up to 33mT during imaging without significant reduction of the spatial resolution of the SPEEM instrument. Therefore we could study the magnetization reversal of individual nanoparticle as a function of applied magnetic field.

During our first study we investigated Fe nanoparticles with a cubic shape, synthesized by the group of Luis M. Liz-Marzan in Vigo [4]. As a result of the colloidal preparation technique the metallic core of the as grown nanoparticles is surrounded by an oxidation shell and organic ligands. The ligand shell also acts as a spacer keeping neighbouring particles at a minimum distance of ~2nm. We performed spectromicroscopy to obtain oxidation state of single nanoparticles in the as grown state. In order to extract local XAS spectra we recorded a stack of PEEM images at photon energies ranging from 700 to 740eV. Fig. 1a) shows a PEEM image taken at an energy close the Fe L_3 resonance. Bright spots in the PEEM image correlate perfectly with the position of single Fe nanoparticles visible in the SEM image Fig.1b). After drift correcting the PEEM image stack we extracted XAS spectra of individual nanoparticles by reading out the intensity from a particular region of interest. The XAS spectrum of the indicated nanoparticle is presented in Fig.1c). In the as grown state we find a spectral line-shape that can be explained by a combination of Fe and Fe_2O_3 contributions. Prior to the magnetic measurements we removed the organic ligands and reduced the iron oxide by a plasma etching technique. Finally we protected the samples by a thin Al layer against re-oxidation.
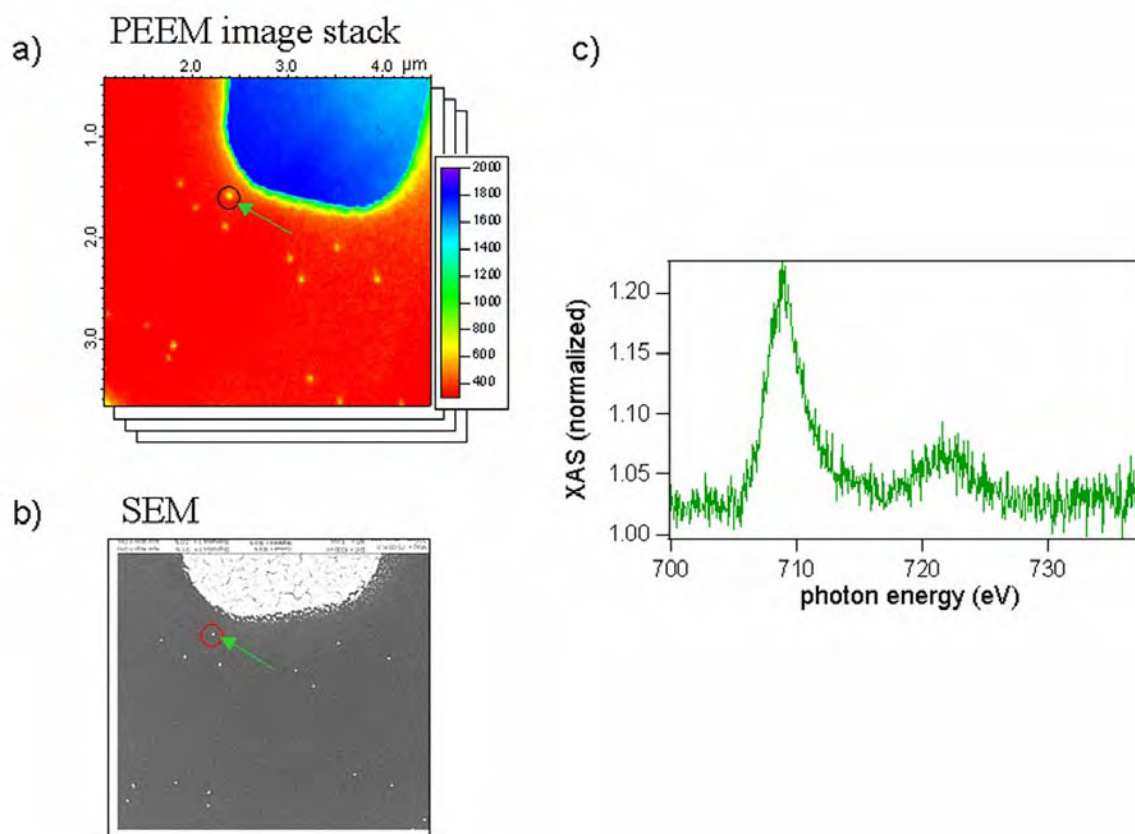
Fig. 1: The PEEM image in panel a) shows the chemical contrast of the Fe nanoparticles recorded at a photon energy close to the Fe L_3 resonance. The field of view is about 3µm. Panel b) shows the corresponding image taken with a scanning electron microscope. Small spots around the centre are nanoparticles; the big structure at the top is part of the Au markers on our substrate. Panel c) shows the XAS spectrum obtained from a single nanoparticle located at the position indicated in a) and b).

We started to investigate the magnetic properties of these Fe nanoparticles at the lowest possible temperature in the SPEEM (~115K). At low temperature we expect less thermal fluctuations and therefore a stronger magnetic contrast. For magnetic imaging we exploited the x-ray magnetic circular dichroism at the Fe L3 resonance. In combination with applied magnetic fields during imaging we could measure hysteresis loops of single nanoparticles. Fig. 2a) shows a PEEM image recorded at a different place of that sample where the nanoparticle coverage was significantly higher than at the position shown in Fig.1a). Due to the preparation we find the particles in different configurations that range from single particle sites to small clusters formed by a few nanoparticles. The red marker indicates a position with single particles. The image with the corresponding magnetic contrast is shown in Fig. 2b). It displays the component of the magnetization vector **M** parallel (red) or antiparallel (blue) to the propagation vector **k** of the incident x-ray beam. The latter differed from the direction of the applied magnetic field **B** only by the grazing incidence angle of 16°. At 12mT external field we observe a few Fe nanoparticles with their magnetization antiparallel to the magnetic field possibly due to a strong dipolar coupling with their neighbours. Variations in the magnetic contrast with the cluster size already indicate the influence of the particle configuration on its magnetic properties. One of the main goals of our study was to measure the hysteresis loops of individual nanoparticle configurations, extracting them from a stack of magnetic images recorded at different magnetic fields. The hysteresis of the single Fe nanoparticle indicated in Fig.2a) is shown in Fig. 2c). For that isolated particle we find a closed hysteresis loop indicating a superparamagnetic state. Comparing hysteresis loops of different nanoparticle configurations we find that the magnetic switching behaviour of the nanoparticles is sensitively influenced by their configuration.

In summary we have shown that chemical and magnetic properties of individual nanoparticles can be measured using X-PEEM in combination with applied magnetic field during imaging. In combination with SEM data also the influence of different particle configurations on the magnetic switching behaviour can be resolved.
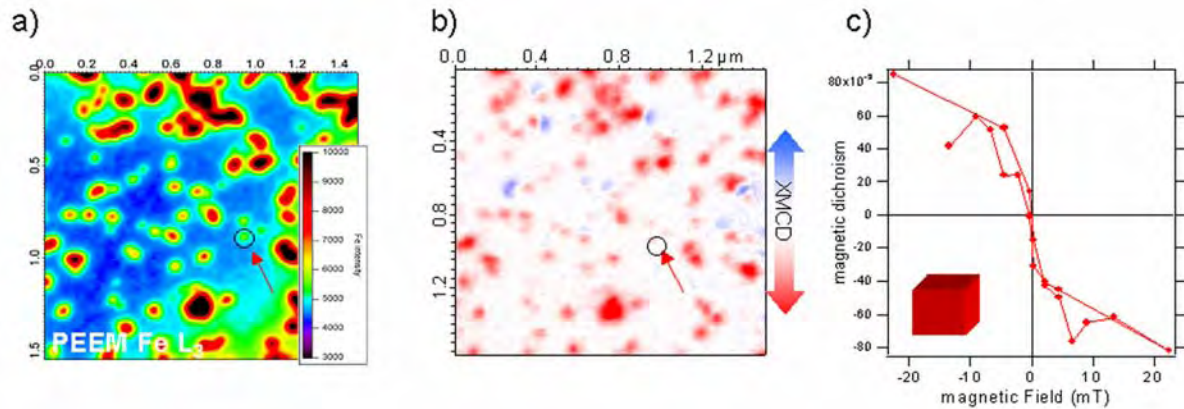
Fig. 2: The PEEM image in panel a) shows different nanoparticle configurations which are mainly clusters consisting of a few particles. The arrow indicates the position of a single nanoparticle. Panel b) shows the corresponding XMCD contrast recorded with an applied field of 12mT at a temperature of 115K. As XMCD contrast we display the difference of two images taken with circular polarization and opposite helicities divided by their sum. In panel c) we present the hysteresis loop of the indicated single nanoparticle extracted from a stack of PEEM images taken at magnetic fields varying from –23 to 23mT.

References:

[1] O. Margeat, M. Tran, M. Spasova, M. Farle, Magnetism and structure of chemically disordered FePt3 nanocubes, Phys. Rev. B 75, 134410 (2007).

[2] C. Antoniak, J. Lindner, M. Spasova, D. Sudfeld, M. Acet, M. Farle, K. Fauth, U. Wiedwald, H.-G. Boyen, P. Ziemann, F. Wilhelm, A. Rogalev, Shouheng Sun, Enhanced Orbital Magnetism in Fe50Pt50 Nanoparticles, Phys. rev. Lett. 97, 117201 (2006).

[3] C. Antoniak, J. Lindner, V. Salgueiriño-Maceira, M.Farle, Multifrequency magnetic resonance and blocking behavior of Fex Pt1-x nanoparticles, phys. stat. sol. (a) 203, 2968 (2006)

[4] Alexey Shavel, Benito Rodríguez-González, Marina Spasova, Michael Farle and Luis M. Liz-Marzán; Adv. Funct. Mat. 17 (2007) 3870-3876

Resonant photoemission at $2p$ edges of magnetic transition-metal oxides exhibiting half-metallic properties

M. C. Richter[1], D. R. Batchelor[2], J.-M. Mariot[3], P. De Padova[4], M. Sabra[1],

O. Heckmann[1], A. Taleb-Ibrahimi[5], and K. Hricovini[1]

[1] LPMS, Université de Cergy Pontoise, 5 Mail Gay-Lussac, 95031Cergy Pontoise, France

[2] BESSY, Albert-Einstein-Str. 15, 12489 Berlin, Germany

[3] LCP-MR (UMR 7614), Université P. et M. Curie, 11 rue P. et M. Curie, 75005 Paris, France

[3] CNR-ISM, via Fosso del Cavaliere, 00133 Roma, Italy

[5] Synchrotron SOLEIL, L'Orme des Merisiers, Saint Aubin, BP 48, 91192 Gif-sur-Yvette, France

1. Introduction

Transition metal (TM) oxides, for instance Fe_3O_4, CrO_2, and $La_{0.7}Sr_{0.3}MnO_4$, have become the most actively studied half metals. The electronic structure of TM oxides is not well understood yet because d electrons are strongly correlated and cannot be adequately described within a standard band theory framework [1]. Moreover, there is a lack of experimental results proving the true half-metallic behaviour. From the experimental point of view, half metallicity does not show any clear electrical signature and therefore it is not easy to determine. The most direct method to measure the spin polarization is based on photoemission because this technique directly probes the occupied electronic states [2]. But the low efficiency of the spin detection severely limits its use. In the case of nickel (not a half-metal) it has already been demonstrated that intensities of the resonant photoemission spectroscopy (RPES) spectra induced by circularly polarized light are sensitive to the sample magnetism [3]. In our experiments, aside from the intensities, we expect to see also a difference in kinetic energies of photoelectrons when switching the circular polarization of the light on a magnetized sample. For a given photon energy, the difference in the kinetic energy for left and right light polarization is a consequence of the energy gap in one of the spin channels. This will be a qualitative proof of half metallicity. Hopefully, we will also be able to obtain a quantitative estimate of the gap width.

Therefore RPES at TM $2p$ thresholds may be used as an alternative technique to direct spin detection. Using left and right hand circular polarisation of the light on magnetized samples, a signature of half metallicity can be extracted.

2. Experiment

With this idea in mind, we have used the dispersive mode available at BESSY on the photoemission endstation of beamline UE52-PGM to obtain image shots [4]. Such measurements in other synchrotron radiation centres require at present a time-consuming recording of individual spectra for different excitation energies. The set-up at BESSY gives opportunity to take, in *one* shot, a complete electron spectrum over an energy range large enough to follow the Raman-Auger behaviour with an unsurpassed accuracy. This opens up new possibilities for the study of electron correlation and of subtle dichroic effects in magnetised samples which are expected to be significant in the Raman region. In the present work, we have been able observe the evolution of three Auger channels after excitation in the vicinity of the $2p$ edges of the TM. This is an important step forward in opening the possibility to use circularly polarised light to investigate such systems.

3. Results

In this test experiment, we have been able to study in great detail the Raman-Auger behaviour in the $2p$-$3p3p$, $2p$-$3p3d$, and $2p$-$3d3d$ non-radiative transitions for Fe and Cr in the half-metallic systems Fe_3O_4 and CrO_2, respectively. In this report, we present only a preliminary analysis of the data obtained on Fe_3O_4.

Figure 1 shows the $2p$ absorption spectra for both light helicities together with the x-ray magnetic circular dichroism (XMCD) which indicates that we successfully magnetised remanently the sample.
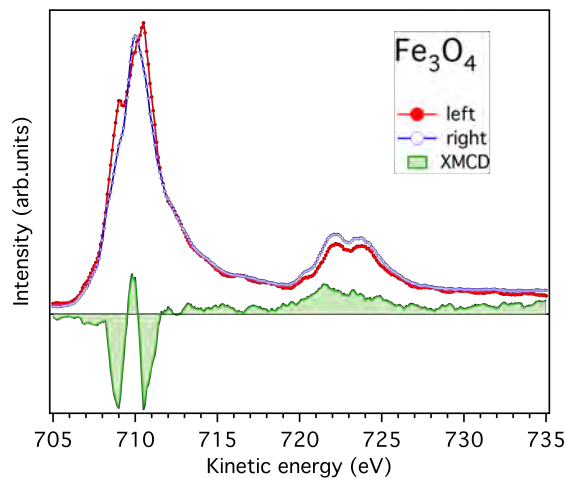
Fig. 1: Fe $2p$ x-ray absorption and XMCD spectra of Fe_3O_4
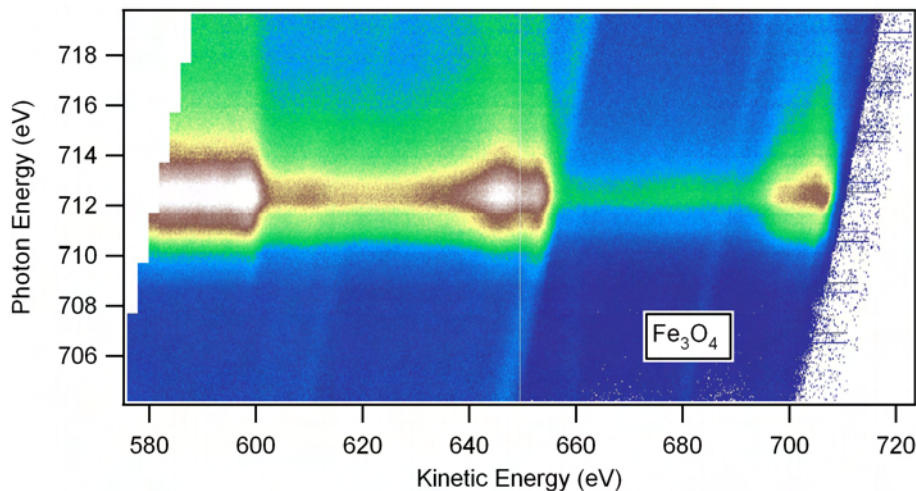
Fig. 2: Intensity of non-radiative Fe $2p$ decays as a function of the excitation energy in Fe_3O_4

In Fig. 2 we show an image of the intensity of the above-mentioned non-radiative processes as a function of the incident photon energy, obtained after normalising the spectra and putting together eight different photon energy intervals. The three Raman-Auger transitions appear as bright spots in the figure. Profiles taken at different photon energies over an energy interval of 0.2 eV fully confirm the presence of the « over-shoot » behaviour for the Fe $2p$-$3p3p$ feature which we have observed and discussed recently [5].

The quality of the image spectra shows that it will be possible to do a subtraction between images taken with different light polarisations in order to extract even only subtle differences. We hope that these studies will establish resonant photoemission as an efficient tool for the determination of magnetic structure in half-metallic systems.

References:

[1] Y. Tokura (ed.), Colossal Magnetoresistive Oxides (Gordon & Breach, London, 2000).

[2] See, e.g., J.-H. Park *et al*., Phys. Rev. Lett. 81 (1998) 1953.

[3] L. H. Tjeng *et al*., Phys. Rev. B 48 (1993) 13378.

[4] D. R. Batchelor *et al*., Nuclear Instrum. Methods Physics Research A 575 (2007) 470.

[5] M. C. Richter *et al*., European J. Phys. (accepted for publication).

NIR-VUV-ellipsometric study of bulk c-GaSb and nano-patterned GaSb surfaces, from 0.7 to 23.6 eV*

M. Kildemo[1], I. S. Nerbø[1], S. Leroy[2], C. Cobet[3], S. Wang[3] and E. Søndergård[2]

[1]Department of Physics, Norwegian University of Science and Technology (NTNU), NO-7491 Trondheim, Norway
[2]Surface du Verre et Interfaces, Unité Mixte de Recherche CNRS/Saint-Gobain Laboratoire, UMR 125, 39 Quai Lucien Lefranc, F-93303 Aubervilliers Cedex, France
[3]ISAS-Institute for Analytical Sciences, Department Berlin, Albert-Einstein-Strasse 9, D-12489 Berlin, Germany

Spectroscopic Ellipsometry (SE) of nano-patterned surfaces has been shown to result in accurate estimates of particularly the height of a uniform nano-pattern, and a reasonable estimate of the average shape of the nano-feature [Nerbø et al. Appl. Opt. **47** (2008) 5130]. In particular, nanostructured GaSb produced by low ion-beam-energy sputtering with high flux, is an interesting model system [Facsko et al. Science **285** (1999) 1551].

The primary idea behind the beam-time at BESSY using the Vacuum Ultra Violet (VUV) Rotating Analyzer Ellipsometer (RAE), was to investigate the fundamental question with regards to the polarimetric optical response of nano-patterned surfaces at shorter wavelengths. Furthermore, through the measurement of the dielectric function of bulk-GaSb, and the estimation of the dielectric function of GaSb-oxide and amorphous GaSb (a-GaSb), it is possible to compare the fitted uv-visible graded anisotropic effective medium model to the results from the VUV region, and possibly deduce empirically at what point effective medium theory breaks down.

The measurement of not previously reported dielectric functions is a continuous matter of research as instrumentation allows the spectral range to be extended. In this study, the dielectric function of c-GaSb has been accurately measured and extended from 6 eV to 23.6 eV using VUV-RAE. Furthermore, in order to compare the VUV results from the effective medium models fitted in the UV-visible range, the dielectric function of thin GaSb-oxide has also been estimated.

Figure 1 shows an overview of the dielectric function of c-GaSb in the range 0.7 to 23.6 eV. In particular, the dielectric function from the reference data from [Aspnes et al. J. Appl. Phys. **48** (1997) 3510] is used in the range 1.5 to 6 eV. Furthermore, the dielectric function was extended from 0.7-1.5 eV using PMSE measurements at 55 and 70 degrees angle of incidence, together with an appropriate overlayer removal. The pseudo-dielectric function measured in this work from Te-doped GaSb in the range 4 to 9.8 eV using a MgF$_2$ rotating analyzer at 68 degrees angle of incidence, and using a triple gold rotating analyzer from 10-23.6 eV at 45 degrees angle of incidence, is also shown in Figure 1. The overlayer from the "clean" HCL etched sample heated in-situ to 300 degrees Celsius was found to be best approximated by a surface roughness, and not by a GaSb-oxide. A 50 % void and 50 % c-GaSb in conjunction with the Bruggeman isotropic effective medium approximation was used to determine an overlayer thickness. The dielectric function of bulk c-GaSb was calculated by inverting (Ψ,Δ) data, and is represented by the full lines overlapping the spectral data from ref. Aspnes from 4 to 6 eV, and covering the new range 6 to 9.8 eV and 10 to 23.6 eV. New features in the dielectric function is observed at 8 eV, 10-11 eV, 15 eV and around 20-23 eV. The most surprising result is a strong feature at 10-11 eV, which experimentally unfortunately falls just in the overlapping region between measurements with the MgF$_2$ rotating analyzer and the triple gold rotating analyzer. By focusing onto the details of the high energy end of the dielectric function of GaSb in Figure 1, the Ga 3d to the conduction band

excitations are clearly observed (not shown here), as recently described for GaN [Rakel et al. Phys. Rev. B **77 (2008)** 115120].

The optical response of random nano-patterned GaSb surfaces consisting of 32 nm high nanocones laterally distributed with an average spacing of 49 nm, was thus investigated by VUV-RAE using synchrotron radiation from 4 to 23.6 eV. The VUV results have been combined with ex-situ ultraviolet-visible spectroscopic ellipsometry. The polarimetric response in terms of the more general Mueller matrix components m12 and m33 has therefore been fitted and compared to the graded uniaxial effective medium model recently reported for nano-patterned GaSb [Nerbø et al. Appl. Opt. **47** (2008) 5130].

The ex-situ SE measurements of m12, m33 and m43 are shown in the left Figure 2, together with the simulated intensities using the graded uniaxial effective medium model. The same nano-patterned surface was also measured by RAE using synchrotron radiation in the range 4-9.6 eV at 68 degrees incidence. The latter RAE measurements of m12 and m33 are shown in the middle Figure 2, together with the simulations using the uv-visible model. The middle Figure 2 additionally shows m43 calculated from m12 and m33 assuming no depolarisation. A future beam-time would preferably include a retarder in order to measure m43 in order to determine depolarisation. The RAE measurements of m12 and m33 in the range 10-20 eV at 45 degrees incidence, are shown in the right Figure 2 together with the simulations using the uv-visible model. The right Figure 2 shows a strong spectral feature from the nano-patterned surface near the region of Bragg condition for ordered surfaces and a strong deviation from the effective medium model.
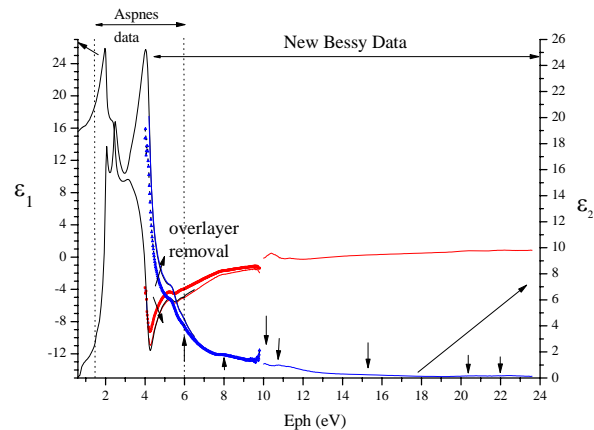
Figure 1. The compiled dielectric function of GaSb from 0.6 to 23.6 eV used in this work. The data from 1.5 to 6 eV is the data from Aspnes et al.
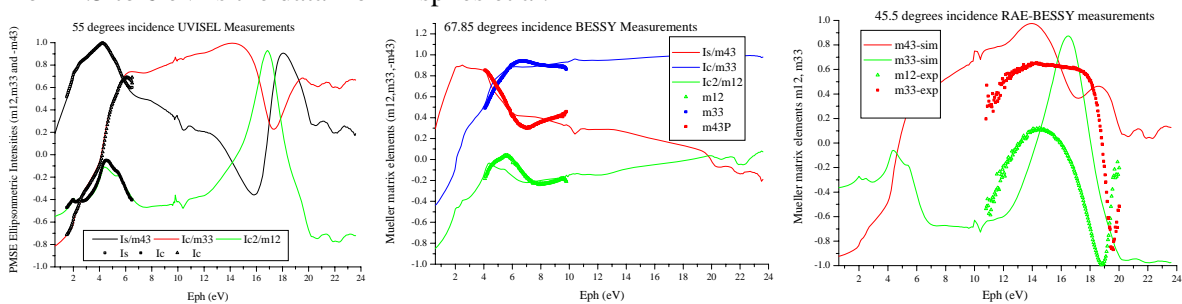
Figure 2. Uv-visible spectroscopic ellipsometric measurements (symbols, left Figure) and VUV Rotating Analyzer spectroscopic ellipsometry at Bessy (symbols, middle and right Figure) of nanostructured GaSb. The full lines are the simulations using the uv-visible fitted graded uniaxal effective medium model.

* This short report is an extract from a manuscript in preparation and will be submitted during 2009.

Pt and Pd-Carbon Nanotube Interaction

Carla Bittencourt

University of Mons-Hainaut, Parc Initialis, Av. Nicolas Copernic 1, Mons 7000 Belgium

Xiaoxing Ke and Gustaaf Van Tendeloo

University of Antwerp, EMAT, Groenenborgerlaan 171, B2020 Antwerp, Belgium

Alexandre Felten and Jacques Ghijsen

University of Namur, LISE, 61 rue de Bruxelles, Namur 5000, Namur, Belgium

Among the metals used to decorate CNTs, Pd and Pt appear to be particularly important since besides the catalytic behavior found for Pt decorated CNTs, Pd is considered the most promising metal to achieve transparent contacts; also, ballistic transmission of electrons was reported for the Pd-CNT contact [1]. Thus, the understanding of the interaction between Pd atoms and CNT-surface is a key issue in the design and optimization of practical applications.

The nature of the metal coating CNTs was reported [2] to depend on the interaction energy of a single metal atom on a CNT as well as on the metal cohesive energy (E_{coh}). The total binding energy of a cluster of size N was estimated to be equal to $E_{cluster} = - E_{coh} + \alpha E_{surface} N^{2/3}$, ($\alpha$ is a geometrical factor and $E_{surface}$ is the average surface energy per atom). Suggesting the existence of a critical cluster size such that metal nanoparticles smaller than such size will efficiently wet the surface, while larger particles will coalesce into still larger clusters.

In the present study of the Pt-CNT and Pd-interaction, pristine and oxygen-plasma, treated MWCNTs with different amounts of metal evaporated onto their surface were analyzed. The morphology of the "overlayer" is observed by transmission electron microscopy; its electronic structure and its interaction with the CNT surface is investigated by photoelectron spectroscopy (PES); the latter measurements were performed at UE56 beam line BESSY II (Berlin) using the Mustang end-station.

Figure 1, shows TEM images of pristine CNT decorated with Pt (figure 1a) and Pd (figure 1b) thermally evaporated. It can be seen that discrete particles form at the CNT-surface.
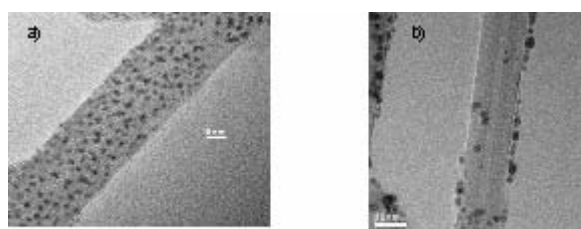
Figure 1, show TEM images of a pristine CNT decorated with 5 Å (a) of Pt and (b) of Pd thermally evaporated. It can be seen that discrete particles form at the CNT-surface.

Figure 2a shows the comparison of the C 1s XPS spectrum before and after the plasma treatment, the chemical modification of the CNT surface produced by the plasma treatment is revealed by the appearance of a broad structure at higher binding energy. This structure was reported to be generated by photoelectrons emitted from C 1s atoms belonging to hydroxyl, carbonyl and carboxyl (or ester) groups that were grafted at the CNT surface by the oxygen plasma treatment. The inspection of the evolution of the C 1s peak for a sequence of Pt (or Pd) evaporations (not shown) revealed that no additional feature can be observed.
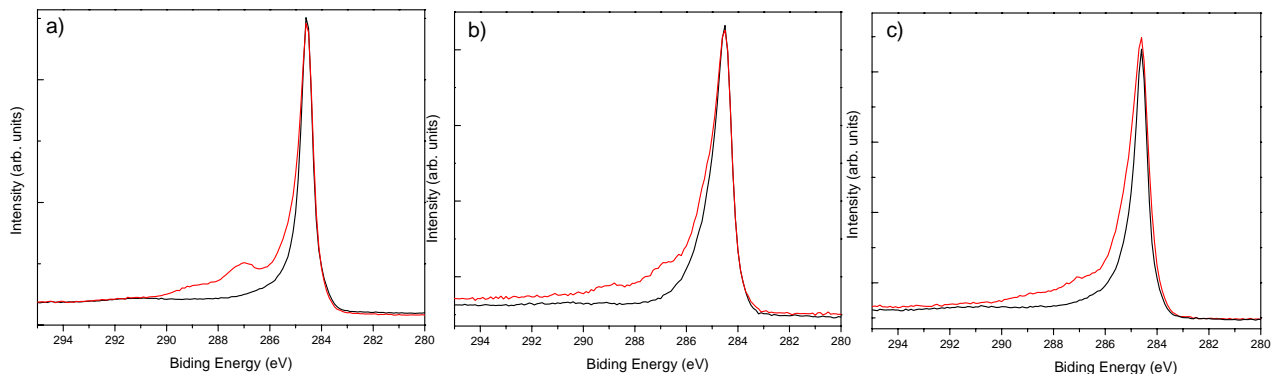
Figure 2: C 1s core-electron spectra recorded on a) CNTs, b) Pt/CNTs and Pd/CNTs. Black line – pristine CNTs and red line oxygen plasma functionalized CNTs

Metal-CNT interaction can be studied by X-ray photoelectron spectroscopy. If there is a chemical reaction at the interface, then the new chemical environment of the atoms at the interface will lead to the appearance of new features at the XPS spectra. The inspection of the evolution of the C 1s peak for a sequence of Pt (or Pd) evaporations (not shown) revealed that no additional feature can be observed.

Figure 2 shows the comparison between the C 1s core-level before and after evaporation of 10 Å of Pt and Pd on pristine and plasma functionalized CNTs. The increase in the asymmetry of the C 1s peak is associated with the many-electron response to the sudden creation of a photohole [2]. Within the Born approximation, it can be shown that the magnitude of this asymmetry is proportional to the square of $\sigma(E_f)$, the density of states (DOS) near the Fermi energy level, as well as to the effective charge of the photohole seen by the conduction electron, χ_q [2]. Hence, changes in the asymmetry of the C 1s peak following the Pt deposition, suggest changes in χ_q and $\sigma(E_f)$ due to Pt-CNT interaction, it affecting the screening process of the C 1s core hole by perturbing the DOS near E_f. Theoretical results have shown that when a metal atom such as Ni and Pd (which belong to the same column of the periodic table as Pt) replaces one C atom of a graphene sheet, a few electronic levels resulting from the metal atom interaction with the sheet appear close to the Fermi energy level. This effect suggests an increase in the metallicity of this system (when compared to the graphene sheet) what explains the increase of the asymmetry in the C 1s peak. In addition, based on these results it can be suggested that a small shift to higher binding energy of C 1s peak following the Pt evaporation corresponds to an upward displacement of the Fermi energy level and consequently a rigid shift of the electronic states [3].

The decrease in the intensity of the structure associated to oxygen groups is less conspicuous for the Pt/CNT samples (figure 2b), this can be associated to the formation of C-O-Pd bonds in the Pd/CNT samples.

References

[1] A. Javey, J. Guo, Q. Wang, M. Lundstrom and H. Dai, Nature, 424, 654 (2003).

[2] A. Maiti, and A. Ricca. Chem. Phys. Lett. 395, 7 (2004)

[3] S. Hüfner, Photoelectron Spectrsocopy, third ed., Springer-Verlag, 173-187, (2003)

[4] F. Banhart, J.C. Charlier, P. M. Ajayan, Phys. Rev. Lett. 84, 686 (2000)

[5] G.K. Wertheim, S.B. DiCenzo and S.E. Youngquist, Phys. Rev. Lett. 51, 2310, (1983)

Internal load transfer in a novel metal/ceramic composite exhibiting lamellar microstructure

Siddhartha Roy, Jens Gibmeier and Alexander Wanner

Universität Karlsruhe (TH), Institut für Werkstoffkunde I, Kaiserstr. 12, D-76131 Karlsruhe

Metal/ceramic composites (MMCs) are technologically important because of their high specific stiffness and strength, high wear resistance, better properties at elevated temperatures etc [1, 2, 3]. The aim of our study is to analyze the mechanics of a new class of metal/ceramic composites on a mesoscopic length scale. These composites are produced by melt-infiltration of freeze-cast and sintered alumina preforms by the eutectic aluminum-base alloy Al-12Si. The as-produced material exhibits a hierarchical domain structure with each domain composed of alternating and interpenetrating layers of metallic and ceramic lamellae. Figure 1 shows a typical microstructure of the face perpendicular to the freezing direction for this composite. The ceramic preform for this composite was freeze-cast at -10°C. After sintering and prior to melt-infiltration the porosity of the preform was 56 vol%. After melt-infiltration the porosity was negligible.

Diffraction-based techniques are most suitable for the in-situ study of internal load transfer in composites because they provide phase-selective information [4]. Such measurements have e.g. successfully been carried out in particle reinforced [5], whisker reinforced [4] and short fiber reinforced [6, 7] MMCs. Our experiments at beamline EDDI@BESSY aim at studying the internal load transfer in composite samples having one single domain under external compressive load using energy dispersive X-ray diffraction.

High-energy synchrotron X-ray diffraction is favoured over laboratory X-ray diffraction or neutron diffraction because this experimental approach combines a large penetration depth with a sufficiently small gauge volume at acceptable measuring times [8, 9]. The energy-dispersive set-up at the EDDI beamline provides a white beam which allows recording the complete diffraction spectra over a wide energy range up to photon energies of 150 keV. Thus several lattice planes of each phase can be taken into account for residual stress analysis and moreover the crystallographic texture can be determined simultaneously [10, 11].

Schematic layout of the beamline components as well as the technical specifications can be found in ref. [12]. For the present study, the energy range 20 – 90 keV was selected for analysis and a scattering angle $2\theta = 7°$ was chosen as it gave good energy separation as well as sufficient peak intensities. A gauge volume having a nominal volume of 0.12 mm³ was defined by the primary and the secondary slits. The slit system as well as the dimension of the gauge volume within the sample is shown in Figure 1. The slit size for the incoming beam (S2 in Figure 1) was maintained at 1 mm × 1 mm while each of the two slits in the diffracted beam (S3 and S4) had dimensions of 60 µm × 5 mm. For in-situ analysis of internal load transfer under external compressive loading, the sample was placed between two hardened steel punches in a miniature mechanical testing rig manufactured by Kammrath & Weiss GmbH, Dortmund, Germany. The testing rig was mounted on the 5 axes sample positioning table of the diffractometer unit. The sample was aligned in a manner that the centre of mass of the gauge volume coincincides with the centre of the sample. Crosshead velocity during compression was maintained at 2 µm·s⁻¹, corresponding to a nominal strain rate of 10^{-3} s⁻¹. The compressive load on the sample was increased stepwise and at every loading step measurements were carried out according to the *sin²ψ* method of X-ray stress analysis [13] by tilting the test rig along with the sample in the inclination angle range $0° \leq \psi \leq 90°$. After each load application and before the corresponding diffraction measurement, sufficient waiting time (in the range of 5-10 minutes) was maintained to minimize the effects of stress relaxation during the single diffraction measurements. At any applied load for each ψ tilt the acquisition time was 1 minute. In diffraction measurements the lattice strain is always measured parallel to the scattering vector. For $\psi = 0°$, the scattering vector is approximately transverse to the loading direction while for $\psi = 90°$ it is almost parallel to the loading direction. A pre-load in the range of 20–30 N (corresponding to a stress of 3–5 MPa) was first applied

to ensure that the sample did not fall down during tilting of the rig and the strain at this initial state was used as the reference value for further calculations. Hence, no effect of processing induced thermal residual stresses (refer to [14]) is considered and only the extent of internal load transfer under an applied external compressive load is measured, irrespective of the process history the sample experienced. Here onwards, lattice misrostrains and stresses would correspond to changes in lattice microstrains and stresses with respect to this reference state. Volume average lattice strain analyses are carried out in all three phases of the composite in transmission mode. Individual diffraction lines were fitted by a "Pseudo-Voigt" function to determine the line positions.
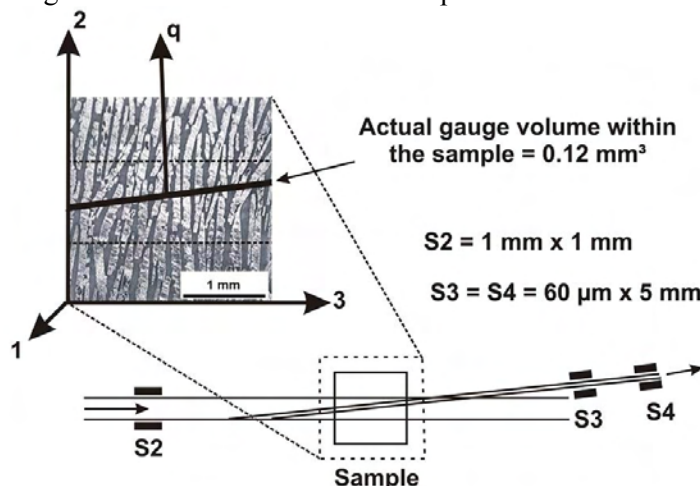
Figure 1: Schematic diagram showing the measurement geometry for energy dispersive synchrotron X-ray diffraction. The zoomed image shows the microstructure of the face perpendicular to the freezing direction for the actual single domain sample used in the study. Actual dimensions and shape of the gauge volume are marked within the sample and "q" shows the orientation of the scattering vector.

Composite samples with varying orientations of the loading axis with the lamellae along with samples with preforms coated prior to melt infiltration were studied (details about the effect of domain orientation on the elastic and elastic plastic flow behavior have been studied by Roy and Wanner [5], Ziegler et al. [15] and Roy et al. [16]). Simple monotonic compression as well as loading – unloading – reloading experiments were performed. Only a brief description of the internal load transfer taking place in the single domain sample with uncoated preform compressed along the freezing direction (actual microstructure shown in Figure 1 with direction 1 being the freezing direction) will be given here. Details of the internal load transfer mechanism operative in this sample are given in ref. [17].
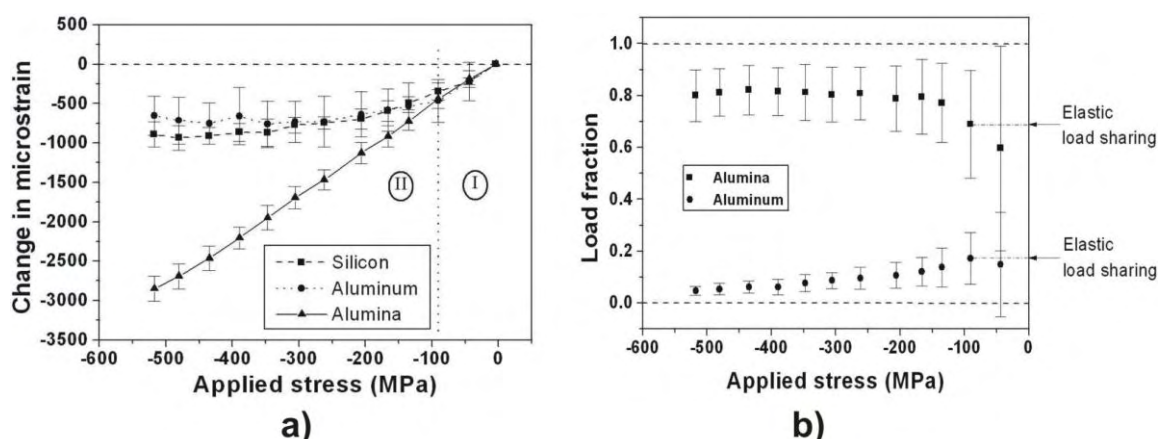
Figure 2: (a) combined plot showing the evolution of continuum mechanics average microstrains for all three phases at different applied stresses and (b) Load fraction vs. applied stress plot for alumina and aluminum phases; minor effects of Si has been neglected (ref. [17])

A typical diffraction spectrum for the composite under study can be found in ref. [14]. 8 diffraction peaks of alumina, 4 of aluminum and 3 of silicon were indexed for analysis. Figure 2a shows the change in continuum mechanics equivalent lattice microstrain measured along the loading direction in all three phases of the composite at different externally applied compressive stresses.

These continuum mechanics equivalent strains for each phase were determined from the analysis of the multiple diffraction peaks according to the method described in [18]. For this calculation the phases were assumed to be texture-free. Two distinct regions can be identified in Figure 2a. Until about 90 MPa (region I), the lattice microstrains in all three phases increase almost linearly. Afterwards, at higher applied stresses, the microstrain vs. applied stress plots for the aluminum and silicon phases reach a plateau while the microstrain in the alumina phase keeps on increasing almost linearly. Figure 2b shows the calculated load fraction in the alumina and aluminum phases (minor effects from the presents of the Si phase have been neglected) at different applied stresses. The plot clearly shows that at all applied stresses, most of the load is being carried by the alumina phase. At low values of applied stress, the load fraction in alumina first increases and correspondingly, the load fraction in aluminum decreases. At higher stresses, the load fraction in alumina reaches a plateau while the aluminum load fraction slowly tends towards zero.

Conclusions

Energy dispersive synchrotron X-ray diffraction has been shown to be a powerful tool for in-situ study of internal load transfer in a lamellar metal/ceramic composite under external compressive load. Load fractions calculated at various applied stresses in alumina and aluminum phases show that as the applied stress is increased, the load fraction in the aluminum phase decreases, while the load fraction in the alumina phase increases to about 80%. The load transfer from the metallic alloy to the ceramic phase is significant but not complete. A plateau well below unity is observed, which may be attributed to the internal damage processes within the ceramic phase. This work gives a first insight into the mechanism of internal load transfer in this novel composite. Further work will concentrate on the effect of domain orientation and interface modification on load transfer behavior.

1. Chawla N, Chawla KK. Metal matrix composites. Springer (2006)
2. Clyne TW, Withers PJ. An introduction to metal matrix composites.Cambridge: Cambridge University Press (1993)
3. Berthelot J-M. Composite materials: mechanical behavior and structural analysis. Springer (1999)
4. Bourke MAM, Goldstone JA, Shi N, Allison JE, Stout MG, Lawson AC, Scripta Met. Mater. 29 (1993) 771 - 776
5. Wanner A, Dunand DC, Met. Mater. Trans. A. 31 (2000) 2949 - 2962
6. Garces G, Bruno G, Wanner A, Scripta Mater. 55 (2006) 163 - 166
7. Garces G, Bruno G, Wanner A, Acta Mater. 55 (2007) 5389 - 5400
8. Wanner A, Dunand DC. Metallurgical and Materials Transactions A. 31A (2000) 2949 - 2962
9. Fitzpatrick ME, Lodini A. Analysis of residual stress by diffraction using neutron and synchrotron radiation. Taylor & Francis (2003)
10. Reimers W, Pyzalla AM, Broda M, Brusch G, Dantz D, Schmackers T, Liss KD. Journal of Materials Science Letters. 18 (1999) 581 - 583
11. Pyzalla A. Journal of Nondestructive Evaluation. 19 (2000) 21 - 31
12. Genzel Ch., Denks IA, Gibmeier J, Klaus M, Wagener M, Nuclear Instruments & Methods in Physics Research: Section A. *578* (2007) 23 - 33
13. Macherauch E, Müller P., Z. f. angewandte Physik. 13 (1961) 305-312
14. Roy S, Gibmeier J, Wanner A, Advances in X-ray Analysis. 2008, submitted
15. Ziegler T, Neubrand A, Roy S, Wanner A, Piat R. Compos. Sci. Technol. doi:10.1016/j.compscitech.2008.12.009
16. Roy S, Butz B, Wanner A. 13th European Conference on Composite Materials (ECCM13), Stockholm, Sweden, June 2 – 5, 2008, paper no. 0303
17. Roy. S, Gibmeier. J, Wanner. A. Adv. Engg. Mater., accepted
18. Daymond MR. Journal of Applied Physics. 96 (2004) 4263 - 4272

Spontaneous capillary filling of silica nanochannels arrays
studied by energy-dispersive small-angle x-ray diffraction measurements

Daniel Rau[1], Stefan Mörz[1], Wolfram Leitenberger[2], and Patrick Huber[1]
[1]Faculty of Physics and Mechatronics Engineering, Saarland University, D-66041
Saarbruecken
[2]Institute for Physics and Astronomy, Potsdam University, D-14476 Potsdam-Golm

We studied the capillary filling (spontaneous imbibition) of silica grains permeated by arrays of hexagonally arranged nanocapillaries (SBA-15, mean channel diameter 7 nm) by time dependent energy-dispersive SAXS measurements. The study was aimed at a quantitative understanding of this filling process, in particular with regard to the filling dynamics.

The Bragg peaks characteristic of the hexagonal arrangement of the empty nanochannels could be resolved by energy-dispersive SAXS measurements (50s exposition time) – see Fig. 1. Upon invasion of the liquid hydrocarbon (n-$C_{25}H_{52}$) the intensity of the hexagonal reflections reduced according to a square root of time power law – see Fig. 2. Such Lucas-Washburn dynamics are expected for a capillarity-driven filling process of the channels, which leads to a reduction in electron density contrast between empty and filled nanochannel. The overall dynamics are significantly slower than expected from the fluid parameters of the n-alkane investigated (viscosity, surface tension, and contact angle), a finding under current further investigation.
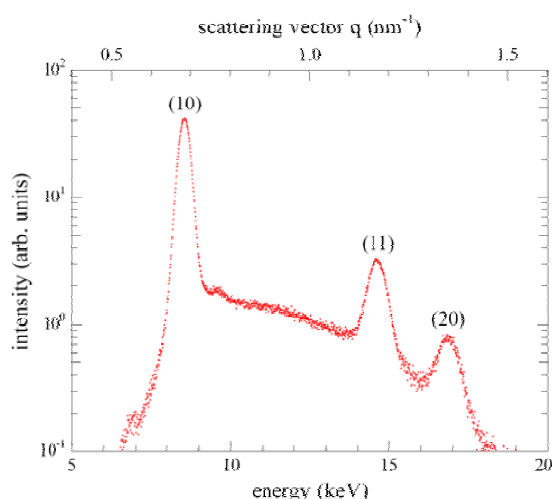
Fig. 1: SAXS pattern of the empty SBA-15 powder. The reflections are indexed based on two-dimensional, hexagonal mesh with lattice parameter a=10.8 nm.
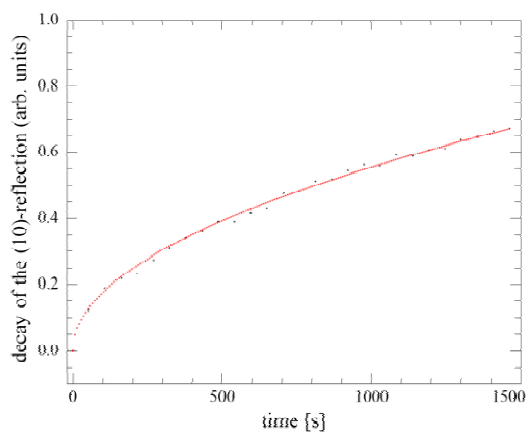
Fig. 2: Relative decrease of the (10) reflection upon of invasion of liquid n-$C_{25}H_{52}$ into the nanochannels of SBA-15 (symbols) in comparison with a square-root-of-time power-law fit.

PEEM of Rb/TaS$_2$: Probing a Metal-to-Insulator Transition with Nanoscale Precision

D. Rahn[1], *E. Ludwig*[1], *J. Buck*[1], *K. Rossnagel*[1], *F. Kronast*[2], *H. Dürr*[2], *and L. Kipp*[1]

[1] *Institute for Experimental and Applied Physics, University Kiel*
[2] *Helmholz Zentrum Berlin für Materialien und Energie*

The effects of alkali metal deposition on layered transition-metal dichalcogenides (TMDCs) are of great interest in basic research and in applications, for example battery development. However, the rather simple question of how the alkali metals adsorb on TMDCs has not been satisfactorily answered yet. On the one hand, a certain amount of alkali atoms intercalates into the van der Waals gaps of the TMDCs, while a small amount also remains on the surface [1]. On the other hand, the formation of nano structures in the uppermost layer is observed [2, 3].

Beside these considerations on the kinetics of the intercalation process, the TMDC 1T-TaS$_2$ is of particular interest. It is a correlated material showing an extraordinarily rich phase diagram including various charge-density-wave (CDW) phases and a first-order metal-insulator transition (MIT) at about 180 K with an increase of in-plane resistivity of about one order of magnitude. This transition is widely understood as a Mott-Hubbard localization caused by the favorable valence band structure created by the CDW. It is also accompanied by a modification of the periodic lattice distortion from a nearly commensurate c($\sqrt{13} \times \sqrt{13}$)R13.9° reconstruction to a commensurate one. This results in an increased splitting of the Ta 4f core levels which provide a very sensitive tool for investigating changes in the atomic distortion pattern associated with the CDW. Using angle-resolved photoemission spectroscopy, it has recently been shown that a similar metal-insulator transition at the surface of 1T-TaS$_2$ can be induced already at room temperature by adsorption of Rb [4].
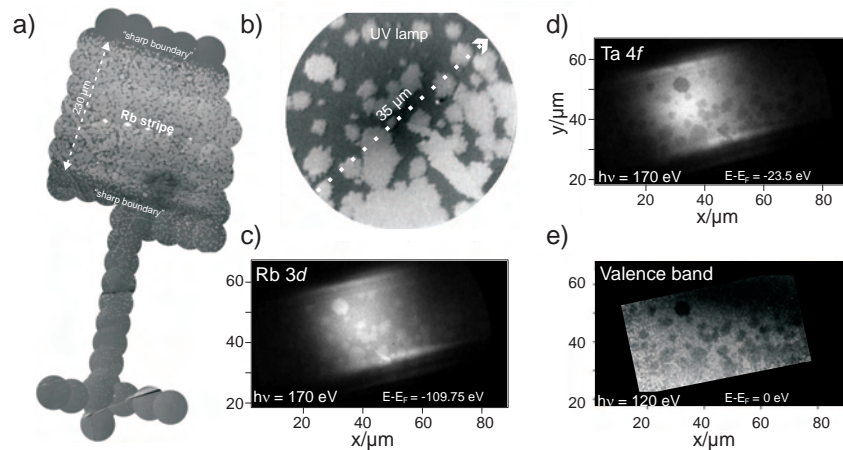
Figure 1: PEEM images of 1T-TaS$_2$ after spatially Rb evaporation. a) Overview image taken with a Hg discharge lamp. b) Enlarged image showing smaller islands. The contrast is due to changes in the work function. c-e) Same sample area as in b) but using the Rb 3d-, and Ta 4f core levels and the Ta 5d valance states for imaging, respectively.

To further investigate the adsorption of Rb and the accompanying structural and electronic transitions, we prepared a spatially sharply defined Rb stripe on the crystal surface. To this end, we developed a new dispenser device which allows a spatially well-defined deposition. It consists of a SAES-Getters dispenser in a liquid nitrogen cooled copper housing. Two apertures are embedded in the housing to collimate the Rb beam to a specific divergence. The first one, directly positioned behind the SAES-Getters dispenser, has a circular shape and a diameter of 2 mm, and the second one, positioned at a distance of 50 mm behind the first one, consists of a slit aperture with the dimensions of roughly 5 mm × 0.3 mm. During the deposition, the exit slit aperture was very close to the sample ($\approx 500~\mu m$) to minimize the divergence of the Rb beam, and the housing was cooled to a temperature of around 150 K. After a spatially well-defined deposition for 390 s at 6 A, photoemission images and spectra were taken with the Elmitec PEEM at beamline UE49 PGMa with an energy resolution of about 350 meV.

Photoemission intensity images of the sample surface taken with a Hg discharge lamp (fig. 1a) show a well defined stripe composed of many differently sized islands. This stripe exhibits a width of approximately 230 μm, which roughly agrees with the 300 μm wide exit slit of the evaporator. The contrast in this image and also in fig. 1b) is due to local changes in the work function induced by the Rb adsorption. High intensity regions reflect a local lowering of the work function. The three images (fig. 1c,d,e) show the same sample area as fig. 1b) using adsorbate and substrate core levels and substrate valance states for the image contrast. The first image (fig. 1c) measured at the Rb 3d core level (E-E$_F$ = -109.75 eV) shows the same contrast as fig. 1b) and therefore reveals a correlation between the work function lowering and the Rb adsorption. The photoelectron spectra in fig. 2b) (along x-direction
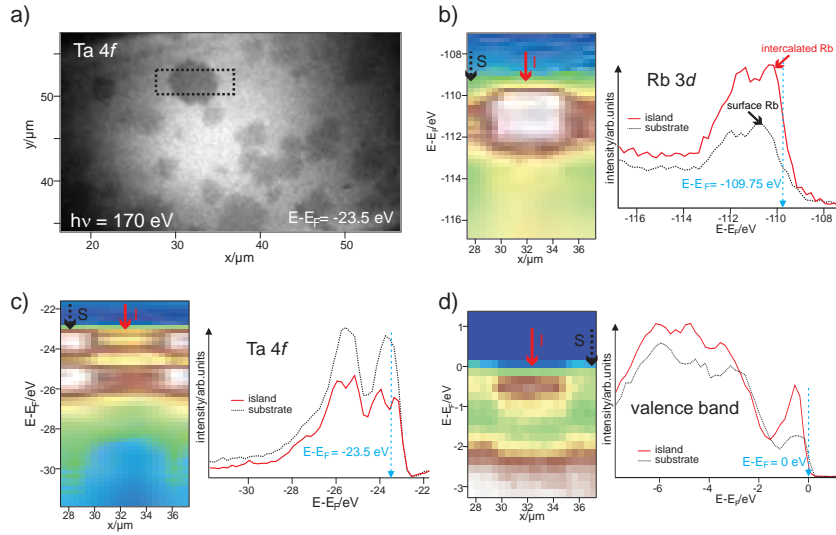
Figure 2: Spatially resolved photoemission spectra. a) Same sample area as in fig. 1b), but slightly enlarged . b) Rb $3d$ spectra (taken in the box in a) from the islands show an increased Rb signal and an asymmetry orginating from intercalated Rb. Corresponding Ta $4f$ (c) and Ta $5d$ (d) spectra reveal an enhanced splitting of the Ta $4f$ CDW components and a shift of spectral weight away from E_F respectively.

in marked box in fig. 2a) show that this contrast is not only due to an overall higher intensity in the island regions. The Rb $3d$ core level spectra on the islands also exhibit an asymmetry on the low binding energy side which can be attributed to Rb atoms intercalated into the van der Waals gap between the TaS$_2$ triple layers. The second image (fig. 1d) displays the same sample region using the Ta $4f$ core level (E-E$_F$ = -23.5 eV) for imaging. This image reveals an inverted contrast in comparison to the Rb $3d$ and the UV lamp images. The Ta $4f$ core level spectra on the islands in fig. 2c) show an overall loss in intensity but also an enhanced CDW induced splitting of the two different Ta $4f$ spin orbit components. To get a comprehensive picture of the electronic changes, the third image (fig. 1e) shows the same sample region again but now using the Fermi edge (E-E$_F$ = 0 eV) for imaging. Similar to the Ta $4f$ image, a lower intensity on the islands is observed. The spectra in fig. 2d) illustrate that this intensity loss is due to a shift of spectral weight away from the Fermi level to higher binding energies.

In conclusion, results of our measurements suggest the following picture. In the sample region directly hit by Rb atoms, a sharp image of the evaporator exit slit could be found. This stripe consists of many smaller concentric islands of intercalated Rb. The different diameters of these islands, especially in the boundary regions of the stripe, and the clustering of intercalation seeds in the directly hit region suggest that these islands orginate from small dot-like intercalation channels generated by one or a few of the fastest Rb atoms that leave the evaporator. After the creation of such an intercalation channel, a concentric expansion probably takes place as long as additional Rb is provided. Thus, the local dimensions of the islands are not correlated with the diffussion length of the Rb atoms inbetween the layers but rather with a spatially varying Rb amount deposited onto the directly hit sample surface.

In addition to the elucidation of the intercalation kinetics, the results of our measurements also suggest a spatial correlation between intercalated Rb, a change in the periodicity of the lattice distortion as evidenced by an enhanced splitting of the Ta $4f$ lines, and the metal-insulator transiton. Moreover, the Ta $5d$ valance states are more intense and narrower on the islands, which supports the picture of a transition driven by a Mott-Hubbard-type localization.

References

[1] S. E. Stolz, L. J. Holleboom, and H. I. Starnberg, Phys. Rev. B **71**, 125403 (2005)

[2] R. Adelung, L. Kipp, J. Brandt, L. Tarcak, M. Traving, C. Kreis, and M. Skibowski, Appl. Phys. Lett. **74**, 3053 (1999).

[3] E. Spiecker, A. K. Schmid, A. M. Minor, U. Dahmen, S. Hollensteiner, and W. Jäger, Phys. Rev. Lett. **96**, 086401 (2006).

[4] K. Rossnagel, E. Rotenberg, H. Koh, N. V. Smith, and L. Kipp, Phys. Rev. Lett. **95**, 126403 (2005).

Photoelectron microscopy of Rb/TaS$_2$: Evidence for a spatially confined 2*H* to 1*T* structural transition

D. Rahn[1], E. Ludwig[1], K. Rossnagel[1], C. Enderlein[2], K. Horn[2], and L. Kipp[1]

[1] *Institute for Experimental and Applied Physics, University Kiel*
[2] *Fritz-Haber-Institut der Max-Planck-Gesellschaft Berlin*

The layered transition metal dichalcogenide TaS$_2$ is of particular interest because it grows in a variety of different polytypes which display effects like superconductivity and charge-density-wave (CDW) formation. The 1*T* polytype, in particular is a correlated material with an extraordinarily rich phase diagram including various CDW phases and a first-order metal-insulator transition (MIT) at about 180 K (T$_{CDW1T}$). This transition is widely understood as a Mott-Hubbard-type localization caused by the favorable valence band structure created by the CDW. It is also accompanied by a modification of the periodic lattice distortion from a nearly commensurate c($\sqrt{13} \times \sqrt{13}$)R13.9° reconstruction to a commensurate one. This 'Star of David' like reconstruction exhibits three non-equivalent tantalum positions (CDW sites a, b, c) 1:6:6. In Ta 4*f* core level spectra emissions from sites b and c are clearly distinguishable by relatively large splitting of the two Ta 4*f* spin orbit components. This CDW induced splitting, which is increased after the MIT, provides a very sensitive tool for investigating changes in the chemical environments of the tantalum atoms, and in particular for changes in the periodicity of the reconstruction.
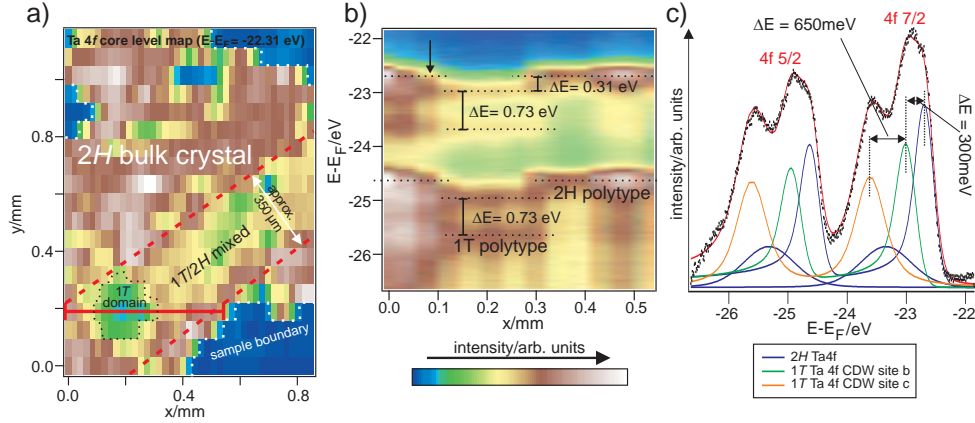
Figure 1: a) Constant binding energy map of the Ta 4*f* photoemission intensity at room temperature (E-E$_F$ = -22.55 eV) after Rb deposition on a liquid nitrogen cooled sample. Red dashed lines indicate the Rb deposited region. b) Ta 4*f* core level spectra (along the solid red line in image a). The spectra show a mixture of 2*H* and 1*T* polytype phases. c) Ta 4f spectrum at black arrow in b) fitted with Doniach Sunjic profiles. The spectrum is composed of two 1*T* related spin orbit doublets (CDW sites b and c) and one 2*H* related feature. The core hole screening induced asymmetry, typical for the 2*H* polytype, is fitted by an additional peak.

The 2*H* polytype of TaS$_2$ shows a less complex phase diagram with only one CDW transition from the undistorted state to a 3×3 superlattice below 70 K (T$_{CDW2H}$) and a superconducting phase below 0.8 K (T$_{SC}$). Recent studies on both show that by intercalation of foreign atoms into the van der Waals gap of these layered compounds one can effectively tune the different transition temperatures [2].

For *in situ* Rb intercalated 1*T*-TaS$_2$, an increased transition temperature of the MIT could be observed, leading to an insulating phase already at room temperature [3]. For the 2*H* polytype, a recent study [4] has shown that Na doping reduces T$_{CDW2H}$ and simultaneously increases T$_{SC}$.

To further investigate the interplay between the different phases, a spatially well-confined stripe shaped Rb deposition on a 2*H*-TaS$_2$ crystal was carried out. The spatially well-defined Rb deposition was achieved with a newly developed evaporator device consisting of a SAES-Getters dispenser inside a liquid nitrogen cooled copper housing. Two apertures are embedded in the housing. The first one, directly positioned behind the SAES-Getters dispenser, has a circular shape and a diameter of 2 mm, and the second one, positioned at a distance of 50 mm behind the first one, is slit-shaped with the dimensions of approx. 5 mm × 0.3 mm. During the deposition the dispenser was running at 6 A for 390 s and the sample was cooled with liquid nitrogen. The exit slit aperture was very close to the sample surface ($\approx 500\ \mu m$) and the housing was cooled to a temperature of around 150 K. The pressure during deposition increased from 9.7×10^{-10} mbar to 5×10^{-8} mbar.

The photoelectron microscopy measurements were carried out at beamline UE112 PGM-1 at BESSY (spot size: $8 \times 11\ \mu m^2$) using a hemispherical electron analyzer (Specs Phoibos 100) and a sample on a stepper motor controlled scanning stage. Photon energies of 80 eV and 180 eV were used. The total energy resolution was about 0.1 eV.
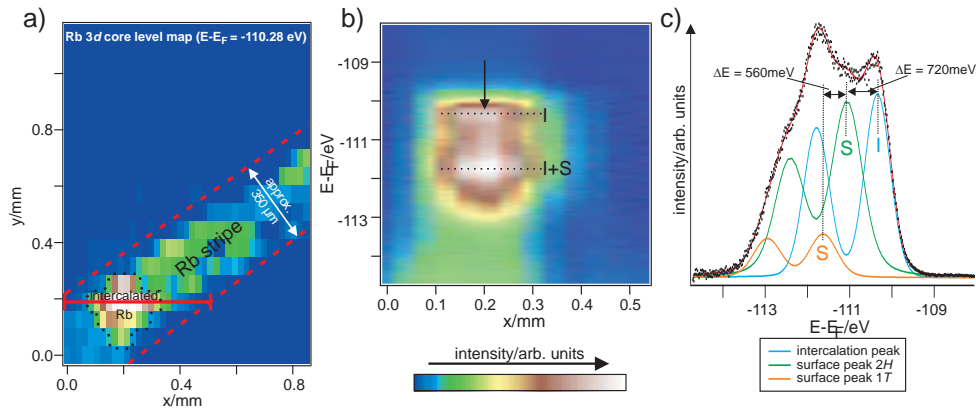
Figure 2: a) Constant binding energy map of the Rb 3d photoelectron intensity at room temperature (E-E$_F$ = -110.28 eV) of the same sample region as in fig. 1 a). b) Rb 3d core level spectra (along the solid red line in a). The Rb signal indicates a sharp Rb stripe c) Rb 3d core level spectrum (at arrow in fig. 1b) fitted with Doniach Sunjic profiles. The spectrum is composed of one surface 1T, one surface 2H and one Rb intercalation related spin orbit doublet.

Figure 1a) shows a Ta 4f photoemission intensity map taken after Rb deposition. A significant reduction of intensity in a stripe shaped sample region is observed, as expected for the deposition with a slit aperture. Taking into account the divergence of the Rb beam, the width of this stripe (350 μm) agrees very well with the one from the slit aperture (300 μm).

The changes of the Ta 4f core level in this low intensity domain (fig. 1b) is visualized by core level spectra taken along the solid red line in fig. 1a). The most striking changes are located between x = 0.15 mm and x = 0.35 mm. Here the Ta 4f core level shows an additional splitting of the spin orbit components typical for the 1T polytype. Between the 2H- and the 1T- like sample regions, a continuous transition is observed. The transition region exhibits three peaks in each spin orbit component (see fig. 1c), the intensity decreases and the emissions shift 310 meV to higher binding energies. This shape of the spin orbit components orginates from a mixture of three Ta 4f spin orbit doublets: one from the 2H and two from the 1T domain. The intensity decrease can be explained by remaining surface Rb. The shift results from a charge transfer between the topmost 1T- like and the underlying 2H- like layer and is an evidence that mainly the topmost layer is of 1T configuration. This core level shift has also been observed for TaS$_2$ crystals of the 4H_b polytype [5, 6], whose unit cell consists of two 1T-like and two 2H-like layers in alternating order.

In fig. 2a) a Rb 3d intensity map of the same region as in fig. 1a) is shown. The high intensity region in this map corresponds to the low intensity region in fig. 1a), which indicates a connection between the Rb distribution and the changes of the Ta 4f core level, especially the polytype transition marked in fig. 1a). Furthermore, the Rb 3d core levels in fig. 2b) show an intercalation related asymmetry only in the 1T region. This suggests that the 2H to 1T transiton may be initiated by Rb atoms intercalated into the van der Waals gap between the topmost and the first underlying layer.
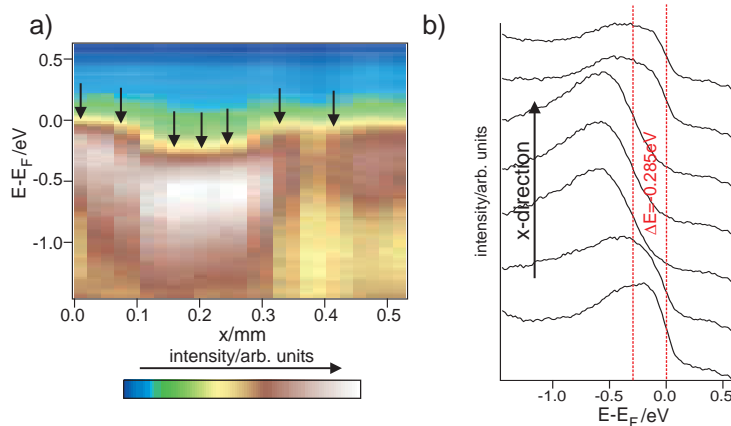
Figure 3: a) Ta 5d spectra (taken along the solid red line in fig. 1 a) near normal emission. In the 1T domain, the Ta 5d peak is shifted to higher binding energies indicating a metal-insulator transition, as expected for Rb intercalation into this polytype. b) The spectra taken at the marked positions in a) show a shift of 285 meV on the 1T domain. The altered peak shape supports the picture of a Mott-Hubbard like transition. Both graphs are slightly filtered with a Gaussian.

The surface feature of the Rb $3d$ core level exhibits a shift (560 meV) between the two polytypes, similar to that of the Ta $4f$. Therefore, the Rb $3d$ core level spectrum consists of two surface and one intercalation related Rb $3d$ spin orbit doublet (fig. 2c). This explains the reduced separation between surface and intercalation related features.

In addition, the spatial confinement of the Rb atoms helps to understand the intercalation process. Since no surface Rb is observed outside the stripe boundaries, already during the adsorption of Rb atoms on the cooled sample some process has to be at work in the directly hit region inhibiting nearly all surface diffusion on warming up. Otherwise surface diffusion would lead to a surface Rb related feature over the entire sample surface. One possible explanation could be that the Rb atoms generate intercalation channels in the directly hit sample area. This would lead to an increased intercalation probability in this local area and thus to a lowering of Rb atoms that leave this region by surface diffusion.

Whether the $1T$ stripe is Rb induced or not, it is expected that this sample area should respond with a MIT when the Rb atoms reach the intercalation sites between the layers [7]. Indeed, a Ta $5d$ core level map (not shown) exhibits a slight intensity decrease in the whole stripe area and an even stronger intensity loss in the $1T$ part of the stripe. Fig. 3a) shows Ta $5d$ spectra (taken along the solid red line in fig. 2a), revealing that this intensity loss is caused by a shift of spectral weight from the Fermi level to higher binding energies ($\Delta E \approx 285$ meV). This may be attributed to a local MIT on the $1T$- domain. In the depleted region the Ta $5d$ peak becomes more intense and slightly narrower, indicating an increased localization of the Ta $5d$ electrons, as expected for the MIT. Furthermore, the Ta $4f$ core levels show an increased CDW splitting ($E_{CDW} = 730$ meV) of the two spin orbit components in this sample region compared to pristine $1T$-TaS$_2$ ($E_{CDW} = 500 - 550$ meV). This serves as evidence for a CDW in the $1T$ domain and a changed CDW periodicity induced by intercalated Rb. We can therefore conclude that there is a close connection between intercalated Rb and the MIT.

References

[1] E. Morosan, H. W. Zandbergen, B. S. Dennis, J. W. G. Bos, Y.Onose, T. Klimczuk, A. P. Ramirez, N. P. Ong and R. J. Cava, Nature Phys. **2**, 544 (2006).

[2] L. Fang, P. Y. Zou, Y. Wang, L. Tang, Z. Xu, H. Chen, C. Dong, L. Shan, and H. H. Wen, Science and Technology of Advanced Materials **6**, 736-739 (2005).

[3] K. Rossnagel, E. Rotenberg, H. Koh, N. V. Smith, and L. Kipp, Phys. Rev. Lett. **95**, 126403 (2005).

[4] L. Fang, Y. Wang, P. Y. Zou, L. Tang, Z. Xu, H. Chen, C. Dong, L. Shan, and H. H. Wen, Phys. Rev. B **72**, 014534 (2005).

[5] S.E. Stolz, and H. I. Starnberg, J. Phys.: Condens. Matter **15**, 52331 (2003).

[6] H. P. Hughes, and J. A. Scarfe, J. Phys.: Condens. Matter **8**, 1457 (1996).

[7] D. Rahn, H. I. Starnberg, M. Marczynski-Buehlow, T. Riedel, J. Buck, K. Rossnagel, and L. Kipp, DPG spring meeting, O27.2 (2008).

Band structure of hard carbon films assessed from the optical measurement

L. Zajíčková[1], D. Franta[1], D. Nečas[1], V. Buršíková[1], C. Cobet[2]

[1] Department of Physical Electronics, Masaryk University, Kotlářská 2, 61137 Brno, Czech Republic
[2] Institute for Analytical Sciences, Department Berlin, Albert-Einstein-Str. 9, D-12489 Berlin

Introduction

Hard carbon materials find many applications in tribology, MEMS and as protective coatings due to their unique properties such as high hardness, chemical inertness and biocompatibily. In case of microcrystalline and nanocrystalline diamond, diamond-like carbon (DLC) and their modifications (doping, nanocomposites) it is important to control the structure of these materials, namely the content of sp^2 and sp^3 bonded carbon. The relative content of sp^2 and sp^3 bonded carbon can be determined from the ratio of pi and sigma electrons. Recently, we published the Kramers-Kronig consistent model of dielectric response based on parameterization of density of states (PDOS) that was employed for various disordered materials (DLC, SiO_x, a-Si) [1, 2]. Using this model the ratio of π-to-σ electrons in the carbon materials can be determined from optical measurements provided that the set of thermally annealed DLC films is studied. While the absorption peak corresponding to π electrons (responsible for the weak graphitic bonds) lies in the visible region, the absorption corresponding to σ electrons (responsible for the strong diamond bonds) lies in the VUV region, with the maximum of absorption at about 13 eV. Therefore, it is necessary to carry out the ellipsometric measurements of the films in the VUV region.

Experimental

The DLC films were prepared by plasma enhanced chemical vapor deposition (PECVD) in radio frequency capacitively coupled discharges. The gas mixture consisted of methane and hydrogen. The substrate was double side polished silicon single crystal (c-Si) wafer that can be used also for transmittance measurements in the IR range. The optical measurement of DLC films was performed by following methods.

- Transmittance data in MIR (0.046–0.62eV) measured with Bruker Vertex80v FTIR spectrophotometer.

- Ellipsometry in the NIR, visible and UV range (1.25–6.5eV) measured with Jobin Yvon UVISEL phase-modulated variable-angle spectroscopic ellipsometer.

- Transmittance in NIR (1.13–1.35eV) measured with PerkinElmer Lambda 45 spectrophotometer.

- Reflectance in NIR, visible and UV region (1.24–6.5eV) measured with PerkinElmer Lambda 45 spectrophotometer.

- Ellipsometry in the UV and VUV range (5.5–9eV) measured with BESSY II synchrotron rotating-analyser ellipsometer.

Results and Discussion

For the optical characterization of films prepared on c-Si it is essential to use reliable optical constants of silicon. Since such data are not available in wide spectral range applied in present investigation it was necessary, as the first step, to characterize the particular silicon wafer used as the substrate in PECVD. Except for the reflectance, the same methods listed above were employed. The overview of obtained data is shown in Fig. 1.
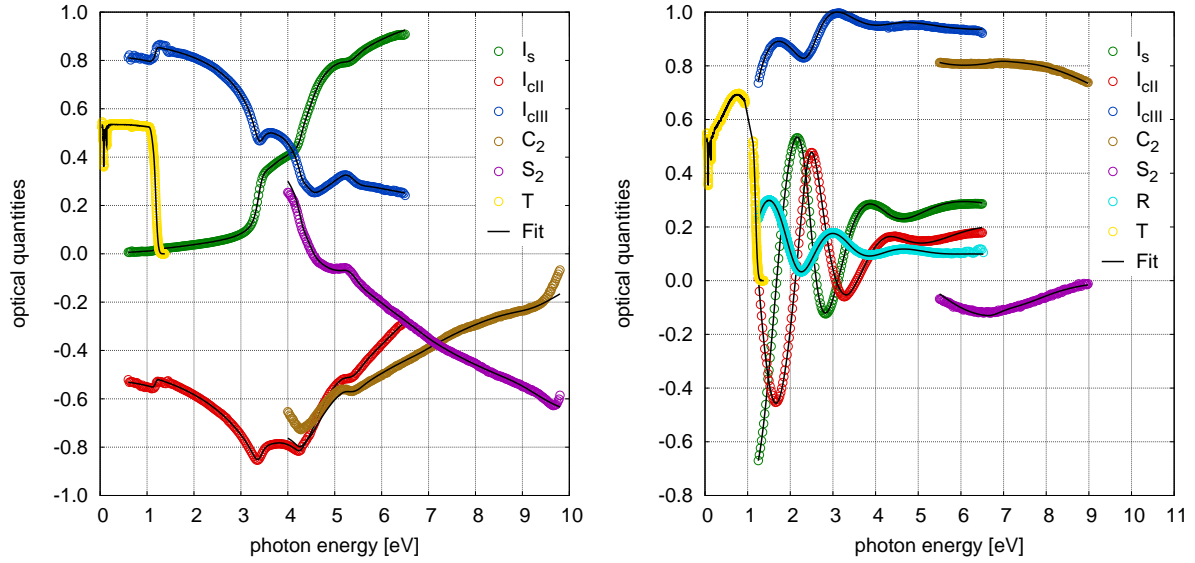
Figure 1: Overview of experimental data for (left) the silicon substrate and (right) selected DLC film obtained by several methods in wide spectral range and their comparison with the proposed model. The abbreviation of the methods used in caption are following: I_S, I_{CII} and I_{CIII} are associated ellipsometric parameters measured with UVISEL ellipsometer, C_2 and S_2 are second harmonics coefficients measured with BESSY ellipsometer, R and T are reflectance and transmittance, respectively.

All experimental data on c-Si were fitted simultaneously by a single Kramers-Kronig (KK) consistent dispersion model covering both interband transitions and phonon absorption. The interband transitions were modelled using true Gaussian-broadened functions describing individual contributions of direct transitions in the one-electron approximation. The indirect transitions forming the indirect band gap were modelled using the parameterized density of states (PDOS) model. The sharp structures at critical points were modelled using hyperbolic excitons. Efficient numerical methods were developed for calculation of true Gaussian broadening of arbitrary functions and for calculation of KK images of such broadened functions. The latter is based on expression of the KK integral using convolutions of the unbroadened function with Dawson integrals. These methods can also be used for modeling of other crystalline materials. Finally, the absorption in MIR region was modelled using a set of Gaussian peaks. The sound agreement between the measurement and the model is apparent from Fig. 1. The determined optical constants of silicon substrate can be seen in Fig. 2.

All experimental data (Fig. 1) on DLC films were fitted simultaneously by a single KK consistent dispersion model covering both interband transitions and phonon absorption. The $\pi \rightarrow \pi^*$ and $\sigma \rightarrow \sigma^*$ interband transitions were modelled using the parameterized density of states (PDOS) model while the absorption in MIR region was modelled using a set of Gaussian peaks.

This model had been already applied to characterization of these samples, however, without the synchrotron ellipsometry data [2]. The extension of the spectral range to 9eV resulted in substantial changes in determined band gaps and transition high energy limits found by this model. The most important change is the increase of the $\sigma \rightarrow \sigma^*$ band gap from 1.6 to 6.7eV – the new value is much closer to the crystalline and polycrystalline diamond band gap. Consequently, the π-to-σ ratio predicted by the model increased considerably. This change also strongly influenced the dielectric function above the measured range, i.e. above 9eV (see Fig. 3): the sharp structure around 13eV resembles the similar structure observed for diamond.
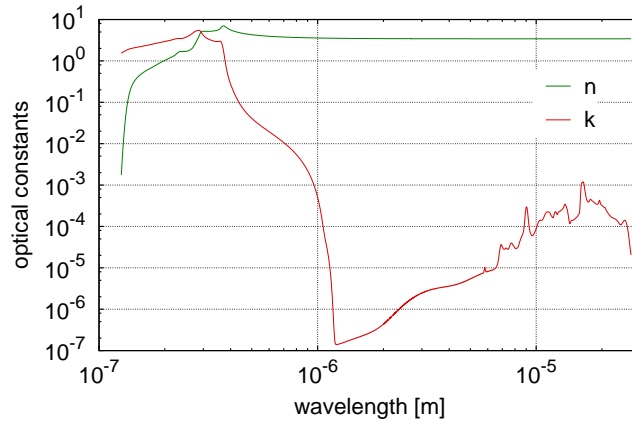
Figure 2: Optical constants on the silicon substrate determined by fitting the measurement with proposed model as shown in Fig. 1.
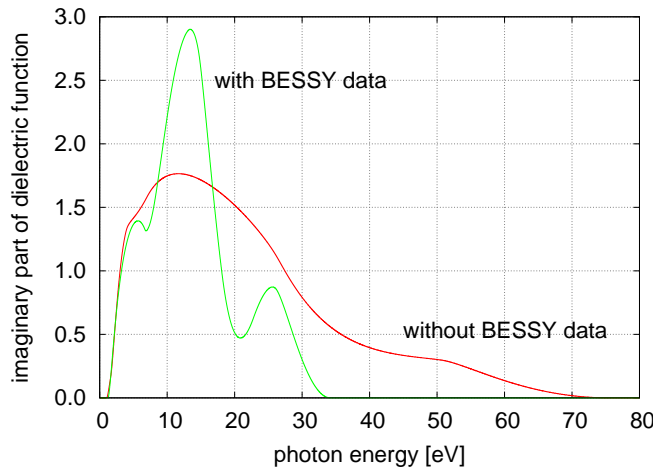
Figure 3: Imaginary parts of dielectric function of the DLC film determined from data including/excluding the VUV synchrotron ellipsometric measurements.

Conclusion

The measurement of DLC films at the synchrotron ellipsometer at BESSY II performed in the range 5–9 eV brought additional information about the band structure of DLC material. This is obvious from the fitting results obtained including these VUV data to the data sets obtained by other methods in the range restricted by the highest energy of 6.5 eV. Therefore, it is important to extend further the measurement range to the XUV region.

Acknowledgment

References

[1] D. Franta, D. Nečas, L. Zajíčková, Opt. Express 15 (2007) 16230–16244.

[2] D. Franta, D. Nečas, L. Zajíčková, V. Buršíková, Diamond Relat. Mater. (2008), doi:10.1016/j.diamond.2008.10.037

Electronic structure studies of $BaFe_2As_2$ by angle-resolved photoemission spectroscopy

S. Thirupathaiah,[1] J. Fink,[1,2] R. Ovsyannikov,[1] H.A. Dürr,[1] R. Follath,[1] Y. Huang,[3] S. de Jong,[3] M.S.Golden,[3]
Yu-Zhong Zhang,[4] R. Valenti,[4] C. Felser,[5] S. Dastjani Farahani,[5] M. Rotter,[6] D. Johrendt[6]

[1] *Helmholtz-Zentrum Berlin, Albert-Einstein-Strasse 15,12489 Berlin, Germany*

[2] *Leibniz-Institute for Solid State and Materials Research Dresden, P.O.Box 270116, D-01171 Dresden, Germany*

[3] *Van der Waals-Zeeman Institute, University of Amsterdam, NL-1018XE Amsterdam, The Netherlands*

[4] *Inst. für Theor. Physik, Goethe-Universität, Max-von-Laue-Straße 1, 60438 Frankfurt, Germany*

[5] *Inst. für Anorg. Chemie und Anal. Chemie, Johannes Gutenberg-Universität, 55099 Mainz, Germany*

[6] *Department Chemie und Biochemie, Ludwig-Maximilians-Universität München, 81377 München, Germany*

.

Introduction

The discovery of high-T_c superconductivity in iron pnictides [1] is a new era which has acquired much attention from the superconductor's community. In the case of cuprates the parent compounds are antiferromagnetic Mott-Hubbard insulators and when doped undergo a metal-insulator transition which leads to the superconducting state. On the other hand the parent compounds of the iron pnictide superconductors are metallic in nature and at low temperature a structural transition accompanied by a spin density wave (SDW) order occurs. When iron pnictides are doped the SDW order is suppressed and superconductivity appears [2]. There are several reports on both electron doping and hole doping into pnictides for the achievement of superconductivity [3-4]. The highest transition temperature, T_c that was achieved so far is 56K in $SmO_{1-x}F_xFeAs$ [5]. There are other iron pnictides containing no oxygen ions. The prototype of one of them is AFe_2As_2 (A = Ba, Sr, etc.). The highest T_c obtained in these compounds is 38 K in $Ba_{1-x}K_xFe_2As_2$ [3]. These materials undergo a structural transition from a high temperature tetragonal paramagnetic phase to an orthorhombic antiferromagnetic phase at low temperatures.
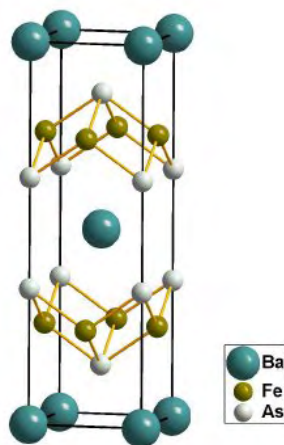
Fig.1. Crystal structure of $BaFe_2As_2$. FeAs tetrahedra form two-dimensional layers, surrounded by the layers of Ba. Fe ions inside the tetrahedra form a square lattice.

Along with these prototypes, two more compounds of simple structure were developed. They are namely LiFeAs with highest T_c = 18K in $Li_{1-x}FeAs$ [6] and FeSe (Te) whose highest T_c is 27 K under pressure of 1.48 GPa [7]. In iron pnictides the existence of SDW ordering is supposed to occur because of a Fermi surface nesting scenario between hole pockets and electron pockets. Interestingly the electronic structure of all these compounds is found to be similar. The clarification of electronic structure of iron pnictides is an important step for the understanding of the physical properties and the mechanism for high-T_c superconductivity.

We report here our results on the electronic structure of $BaFe_2As_2$ using angle-resolved photoemission spectroscopy (ARPES). $BaFe_2As_2$ is the parent compound of the superconductors $Ba_{1-x}K_xFe_2As_2$ and $BaFe_{2-x}Co_xAs_2$. Fig. 1 represents the crystal structure of $BaFe_2As_2$ in its tetragonal form [8].

Experimental Details

Single crystals of $BaFe_2As_2$ were grown out of a Sn flux in Amsterdam and München, using conventional high temperature solution growth techniques. Elemental analysis of the Amsterdam crystals was performed using wavelength dispersive X-ray spectroscopy (WDS). Further elemental analysis was obtained from X-ray induced photoemission spectroscopy on the core levels. Both methods yielded a Sn contamination of approximately 1.6 atomic %. The ARPES experiments were carried out at the BESSY synchrotron radiation facility using the U125/1-PGM beam line and the "1^3-ARPES" end station provided with a SCIENTA R4000 analyzer. Spectra were taken with various photon energies ranging from $h\nu = 30$ to 175 eV. The total energy resolution ranged from 10 meV (FWHM) at photon energies $h\nu = 30$ eV to 20 meV at $h\nu = 175$ eV. The angular resolution was $0.2°$ along the slit of the analyzer and $0.3°$ perpendicular to it. The linear polarization of the radiation could be changed from the horizontal direction to the vertical direction. Due to matrix element effects the experimental results are strongly affected by the orientation of the polarization of the photons relative to the scattering plane (defined by the direction of the incoming photons and that of the outgoing photoelectrons).

Results and Discussion

The ARPES measurements on $BaFe_2As_2$ were focused to two points of the Brillouin zone, the Γ and the X-point. The electronic properties of the material are determined by Fe states located at these points. To obtain information on the character of the antiferromagnetic order we performed measurements in the paramagnetic tetragonal state and the antiferromagnetic orthorhombic state. Typical ARPES data on $BaFe_2As_2$ are depicted in Fig. 2, where we show the measurements near the Γ-point at T = 20 K using 75 eV photons with linear vertical polarization. In the panel (a) of Fig. 2 we have plotted momentum distribution maps for different energies relative to the Fermi level. We see an almost circular Fermi surface which increases with increasing binding energy. This clearly demonstrates that at the Γ-point there is a hole pocket. Comparing our data with band structure calculations indicates that the hole pocket is formed by 3 Fe bands having Fe $3d_{xy}$, Fe $3d_{xz}$ and Fe $3d_{yz}$ character. This assignment is supported by our polarization dependent measurements (not shown). More resolved data show a small splitting between the Fe $3d_{xy}$ and the other two Fe 3d bands. In Fig. 3 we show the measurements near the X-point at T = 20 K using 75 eV photons with linear horizontal polarization. In the panel (a) of Fig. 3 we have plotted momentum distribution maps for different energies relative to the Fermi level. The size of the hole pocket is smaller than the electron pocket near the Fermi level. This is in good agreement with previous reports and with bandstructure calculations. According to bandstructure calculations the in-plane Fermi surfaces around this high symmetry point (X-point) should be caused by two concentric electron pockets. The character of these pockets is supported by the experimental data shown in Fig. 3 near the Fermi level. With increasing binding energy the diameter of the Fermi surfaces at the X-point increases. At higher binding energies the Fermi surfaces transform into a blade-like feature, in good agreement with bandstructure calculations. Performing similar measurements at T = 300 K, no differences relative to the low temperature data could be resolved.
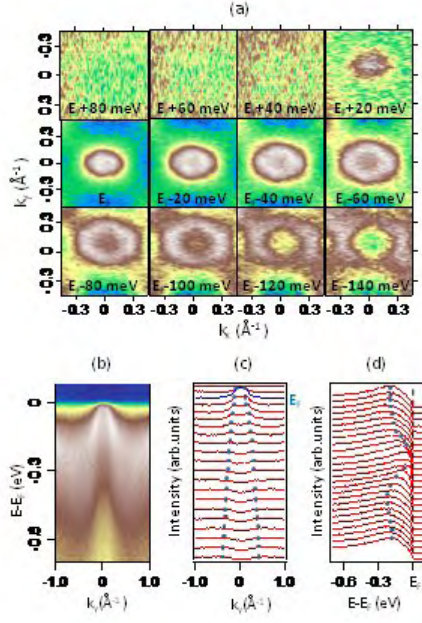
Fig.2. ARPES data around the centre of Brillouin zone (Γ-point) measured with $h\nu = 75$ eV at a temperature of 20 K. The photon polarization was vertical. (a) Momentum distribution maps, (b) spectral intensities as a function of k_y at $k_x = 0$, (c) momentum dispersive curves and (d) energy dispersive curves.
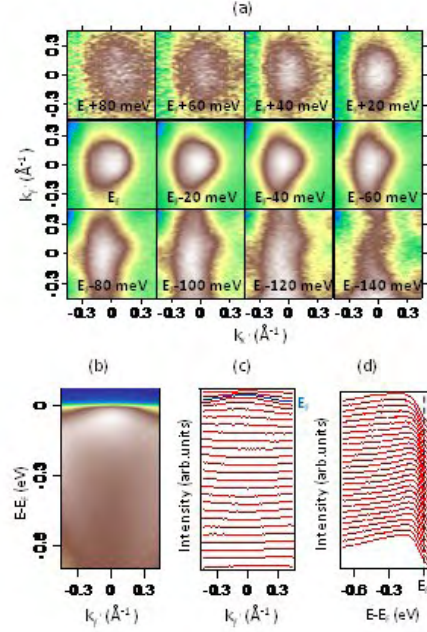
Fig.3. ARPES data around X-point measured with $h\nu = 75$ eV at a temperature of 20 K. The photon polarization was horizontal. (a) Momentum distribution maps, (b) spectral intensities as a function of k_y at $k_x = 0$, (c) momentum dispersive curves and (d) energy dispersive curves.

Summary

In the present ARPES study we have determined the electronic structure of $BaFe_2As_2$, a parent compound of doped FeAs-based high T_c superconductors. Performing temperature dependent measurements, important information has been obtained both for the paramagnetic tetragonal state and the antiferromagnetic orthorhombic state. No significant changes could be resolved between the two phases indicating that the real differences for the electronic structure between the two phases are probably much smaller than that predicted by spin-dependent bandstructure calculations. This supports an itinerant character of the Fe 3d electrons in these systems.

References

[1]. Y. Kamihara, T. Watanabe, M. Hirano, and H. Hosono, J. Am. Chem. Soc. 130, 3296 (2008).

[2]. H. Chen, Y. Ren, Y. Qiu, Wei Bao, R.H. Liu, G. Wu, T. Wu, Y.L. Xie, X.F. Wang, Q. Huang, X.H. Xhen, arXiv: 0807.3950.

[3]. M. Rotter, M. Tegel, and D. Johrendt, Phys. Rev. Lett. 101, 107006 (2008).

[4]. A. S. Sefat, R. Jin, M. A. McGuire, B. C. Sales, D. J. Singh, D. Mandrus, arXiv:0807.2237.

[5]. X. H. Chen, T. Wu, G. Wu, R. H. Liu, H. Chen, and D. F. Fang, Nature (London) 453, 761 (2008).

[6]. X.C. Wang, Q.Q. Liu, Y.X. Lv, W.B. Gao, L.X. Yang, R.C. Yu, F.Y. Li, C.Q. Jin, arXiv: 0806.4688.

[7]. Y. Mizuguchi, F. Tomioka, S. Tsuda, T. Yamaguchi, Y. Takano, arXiv: 0807.4315.

[8]. F. Ma, Z. Y. Lu and T. Xiang, arXiv:0806.3526v1.

Characterization of Carbon Nanotubes Using X-ray Microscopy

J. Sedlmair[1], S.-C. Gleber[1], H. Zänker[2], P. Guttmann[3], Heim[3], J. Thieme[1]

[1]Institut für Röntgenphysik, Georg-August-Universität Göttingen,
Friedrich-Hund-Platz 1, D-37077 Göttingen
[2]Forschungszentrum Dresden-Rossendorf, Bautzner Landstraße 400, 01328 Dresden
[3]BESSY GmbH, Albert-Einstein. 15, 12489 Berlin

Introduction

Carbon nanotubes (CNTs) of different origin have been studied with the Scanning Transmission X-Ray Microscope (STXM) at U41 at BESSY II. The combination of NEXAFS absorption spectra with spatial resolution is ideally suited for a detailed analysis of these samples.

In recent time, CNTs have drawn a lot of attention due to their unique properties. However, to fully understands and make use of these properties, the characterization of CNTs needs to be optimized. In our study, the differences between the species are observable both in the microscopic images and the spectral data. To be more specific, we have investigated two CNT-samples with energies around the C1s K-shell absorption edge (~ 284 eV).

Materials and Methods

We have investigated CNTs from two different productions: the first ones were from Bayer GmbH (in the following called BayCNT), while the other specimen came from the Forschungszentrum Dresden-Rossendorf (in the following referred to as FZD-CNT) [1].

The samples have been treated with ultrasound for several hours. However, they did not do into solution with the water, but rather precipitated at the bottom of the glass vessels we used. Nevertheless, all CNT-samples have been suspended in water (with concentration of 10 – 40 µg per 300 - 1000 ml) for better handling. The dispersion was dropped onto Si_3N_4-foils and left there to dry, so that the CNTs would stick to the foils. The measurements were done at the K-shell absorption edge of carbon, i.e. around 285 eV. This energy range lies in the so-called 'water window', which extends between 280 eV and 523 eV (4.4 nm and 2.1 nm), meaning that here the absorption from water is much lower than from other elements. This is important, as the goal of these studies is to investigate the CNTs in aqueous media.

If a sample is imaged at different energies ascending over an absorption edge, each pixel of this so-called image stack contains its own NEXAFS-spectrum. For the stacks here, we recorded images from 280 eV to 300 eV with a stepsize of 0.2 eV. These data were evaluated with "Stack_analyze", which runs on IDL.

The scanning transmission x-ray microscope used for the studies has been described elsewhere [2] [3], as well as the Stack_analyze [4] software used for further evaluation of the stacks.

Results and Discussion

The first image shows the FZR-CNTs at high resolution ($11 \times 11 \mu m^2$, $220 \times 220 px^2$). The flexible structure of the CNTs is obvious and resembles to the SEM-images we got from the FZD. We also performed a stack of an interesting area of the CNTs on that foil, with a less good resolution ($7 \times 7 \mu m^2$, $30 \times 30 px^2$). The resulting spectrum can be seen in Figure 1b. The program SpecFit, developed in our group, has been used to derive information about single binding states.

The second figure shows the results of the same measurements performed with the BayCNTs. Interestingly, both the visible structure as well as the spectral signature differ immensely, although both samples were expected to be similar.

1a) FZD-CNT

1b)

2a) Bay-CNT

2b)
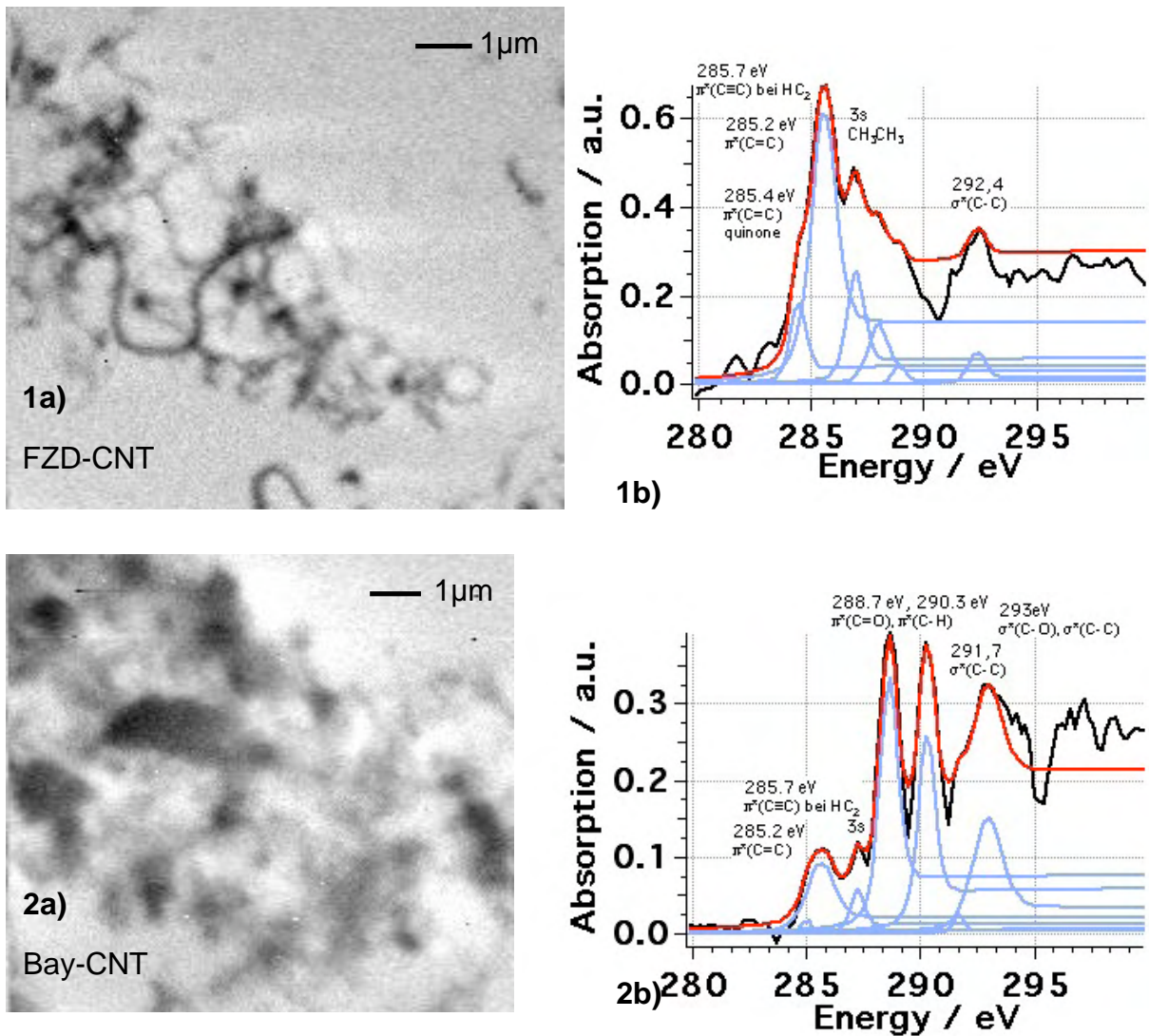
Figure 1 and 2: The images show the x-ray microscopic pictures of the two CNT-samples.
The NEXAFS-spectra show the absorption of the different CNT-sample depending on the energy of the incident x-radiation, from which information about the binding states in the samples can be achieved.

Comparing the spectra it becomes visible, that these CNTs have been fabricated in a way, that functional groups appear differently, thus causing different properties. This makes clear how important it is to have a suitable method to characterize these new materials [5]. The STXM is ideal for this purpose since it combines high spectral resolution with spatial information.

Outlook

In the future, we want to investigate the role of CNTs within material sciences, such as the interaction with concrete. The incorporation of CNTs in this building material makes it a lot more stabile and lighter at the same time.
Since CNTs are applied not only in material sciences, but as well in other fields of research it is also important to know what happens, when they are disposed and get in contact with the environment. This interaction between CNTs with living and non-living organic matter is also subject of our future work.

Acknowledgwments

References

[1] Schierz A, Zänker H.: Aqueous suspensions of carbon nanotubes: Surface oxidation, colloidal stability and uranium sorption. In: Environ Pollut. 2008 Nov 14

[2] U. Wiesemann, J. Thieme, P. Guttmann, R. Früke, S. Rehbein, B. Niemann, D. Rudolph, and G. Schmahl: First results of the new scanning transmission X-ray microscope at BESSY-II. In: J. Susini, D. Joyeux, F. Polack, eds., X-Ray Microscopy 2002, Journal de Physique IV 104 (2003) 95–98.

[3] P. Guttmann, S. Heim, S. Rehbein, S. Werner, B. Niemanns, R. Follath, G. Schneider: X-ray microscopy at the new U41-FSGM beam line. In: BESSY Annual Report 2007, p 297-300

[4] Jacobsen, C., Medenwaldt, R., Williams, S., 1998. A perspective on biological X-ray and electron microscopy. In: Thieme, J., Schmahl, G., Rudolph, D., Umbach, E. (Eds.), X-ray Microscopy and Spectromicroscopy, Springer, Heidelberg, pp. II-93–II-102.

[5] Felten A, Bittencourt C, Pireaux JJ, Reichelt M, Mayer J, Hernandez-Cruz D, Hitchcock AP. Individual multiwall carbon nanotubes spectroscopy by scanning transmission X-ray microscopy. In: Nano Lett. 2007 Aug;7(8):2435-40

Synchrotron-based infrared reflectance microspectroscopy of metamorphosed CM2 carbonaceous chondrite NWA 4757

Lyuba Moroz[1,2], Martin Schmidt[3], Ulrich Schade[4], Marina Ivanova[5]

[1]Westfälische Wilhelms-Universität Münster, Institut für Planetologie, Wilhelm-Klemm-Str. 10, D-48149 Münster, Germany; [2]Deutsches Zentrum für Luft und Raumfahrt e.V. (DLR), Institut für Planetenforschung, Rutherfordstr. 2, D-12489, Berlin, Germany; [3]University of California Berkeley, Berkeley CA 94720, USA; [4]Helmholtz-Zentrum Berlin für Materialien und Energie, BESSY II, Albert-Einstein Str. 15, D-12489, Berlin, Germany; [5] Vernadsky Institute of Geochemistry and Analytical Chemistry, Russian Academy of Sciences, Kosygin St. 19, 119991 Moscow, Russia.

Introduction.

Chondritic meteorites (chondrites) are the most ancient rocks formed in our solar system. They provide unique opportunities to constrain the physical and chemical processes that were active in the accretionary disk (solar nebula) surrounding the ancient Sun ~ 4.57 Ga ago. The most chemically primitive carbonaceous chondrite (CC) class consists of 9 groups with distinct bulk compositional and oxygen isotopic characteristics: CI, CM, CV, CO, CK CR CH, and CB. Several meteorites are ungrouped. Several meteorites found in Antarctica have been thermally metamorphosed in their parent bodies (asteroids), but their mineralogical and chemical characteristics would appear to have classified them as CI or CM chondrites before metamorphism [1]. More recently, two non-Antarctic metamorphosed CM2 carbonaceous chondrites (MCCs) - Dhofar 225 and Dhofar 735 - were found in a hot desert: [2, 3, 4]. They differ from typical CM2 chondrites in mineralogy, oxygen isotopic compositions, H_2O content, bulk chemistry, and infrared spectra of their matrices [3, 4, 5]. The carbonaceous chondrite NWA 4757, recently found in Morocco, has similarities to both groups of carbonaceous chondrites, metamorphosed and normal CM2s [6]. The meteorite contains 1.9 wt.% H_20, 0.68 wt.% C and consists of fine-grained matrix material, round objects sometimes with halos of phyllosilicate and carbonates, and relict aggregates embedded into the altered matrix [6, 7]. Silicates of these objects and the matrix correspond to serpentine in chemical composition [6]. The minor phases are ilmenite, chromite, sulfides, kamacite, taenite, tetrataenite, phosphates, Ca,Mg-carbonates. Average bulk oxygen isotopic compositions are $\delta^{17}O = 12.84$; $\delta^{18}O = 23.83$; $\Delta^{17}O = 0.45$ (all ‰) [7]. The oxygen isotopic composition of NWA 4757 is out of the range of typical CM2 meteorites, and is similar to that of MCCs. The matrix is more homogeneous in chemical composition compared to matrices of metamorphosed and normal CM2 chondrites [6].

In this study we used synchrotron-based IR microspectroscopy at the BESSY IR beamline IRIS [8] to characterize hydration states of NWA 4757 matrix minerals and altered objects.

Experimental procedure

A polished section of NWA 4757 provided by the Meteorite Committee RAS was used for IR reflectance measurements. The IRIS infrared beamline at the electron storage ring facility BESSY II [8] is equipped with a Thermo Nicolet Continuμm IR microscope coupled to a Nexus 870 FTIR spectrometer. We used an LN_2-cooled HgCdTe (MCT) detector, a KBr beam splitter and a 32x Cassegrain objective with a numerical aperture of 0.65. We acquired reflectance spectra in the range between 1.4 and 14 μm. The spectral resolution was 8 cm^{-1}. We probed the meteorite matrix and hydrated objects with a spot size of 15 x 15 μm^2 and 20 x 20 μm^2. To provide gold-plated surfaces for standard measurements, we deposited gold layers 1mm wide and 100 nm thick directly onto the samples. It is also possible to deposit gold onto a polished epoxy next to the polished meteorite surfaces.
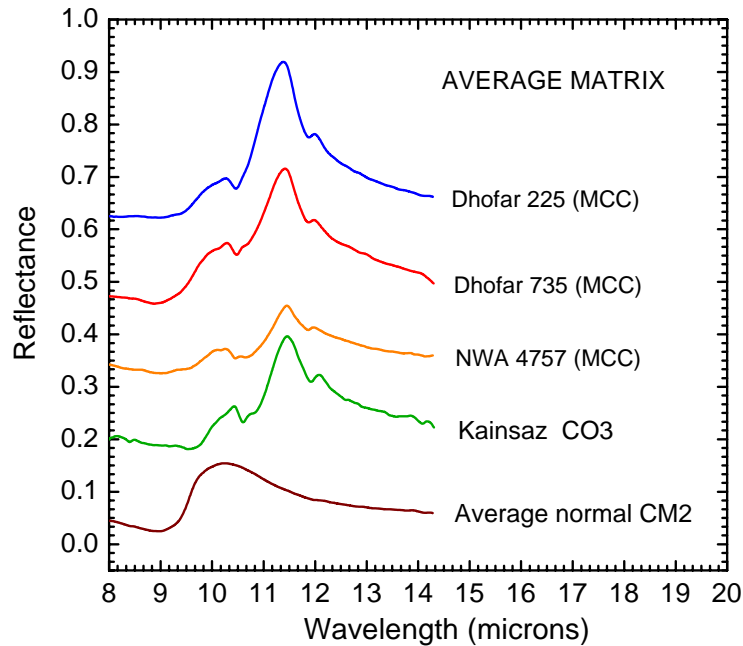
Fig. 1. The average matrix IR reflectance spectra of NWA 4757 compared to the matrix spectra of other non-Antarctic metamorphosed CM chondrites (MCCs), "normal" non-metamorphosed CM2 chondrites and CO3 chondrite Kaisaz. Each spectrum is offset for clarity from the previous one.

Results and discussion:

The spectra of normal (hydrated) CM2 matrices are dominated by smooth broad Si-O peaks of hydrated silicates, observed near 10 µm (Fig. 1). Anhydrous (or nearly anhydrous) matrices of thermally metamorphosed CMs chondrites Dhofar 225 and Dhofar 735 are spectrally dominated by fine-grained Fe-rich olivine, whose spectra are characterized by three Si-O reflectance peaks between 10.5 and 12.5 µm (Fig. 1). The average IR spectrum of anhydrous matrix of CO3 chondrite Kainsaz shown in Fig. 1 also exhibits similar reflectance peaks. Unlike matrices of typical CM2 chondrites, studied previously [5], the matrix of NWA 4757 is depleted in hydrated silicates and is dominated by Fe-rich fine-grained olivines. In this respect, the matrix of NWA 4757 strongly resembles previously studied matrices of metamorphosed CM2 meteorites Dhofar 225 and Dhofar 735 [5], but is somewhat enriched in hydrated silicates compared to the latter two meteorites.

Furthermore, our IR study shows that NWA 4747 contains strongly hydrated objects and halos, absent in Dhofar 225 and Dhofar 735. These objects and halos are significantly enriched in hydrated silicates and carbonates compared to the matrix (Fig. 2). Some of hydrated objects and halos do not show detectable IR signatures of anhydrous silicates, while others contain fine-grained olivines, resembling the matrix olivines in composition. Our study indicates that phyllosilicates in NWA 4757 are more homogeneous in composition than hydrated silicates of typical CM2 chondrite matrices. It is possible that these hydrated objects and halos in NWA 4757 result from terrestrial weathering of the meteorite. A study of trace element distribution will help to understand whether this is the case [6]. Based on our IR study and preliminary mineralogical, chemical and oxygen isotopic analyses [6, 7], NWA 4757 belongs to the metamorphosed CM2 chondrites, and appears to be a mixture of dehydrated matrix material and strongly hydrated objects. If these strongly hydrated objects and halos formed in deep space, they could survive only if the matrix had been dehydrated before their incorporation into the parent asteroid of NWA 4757.
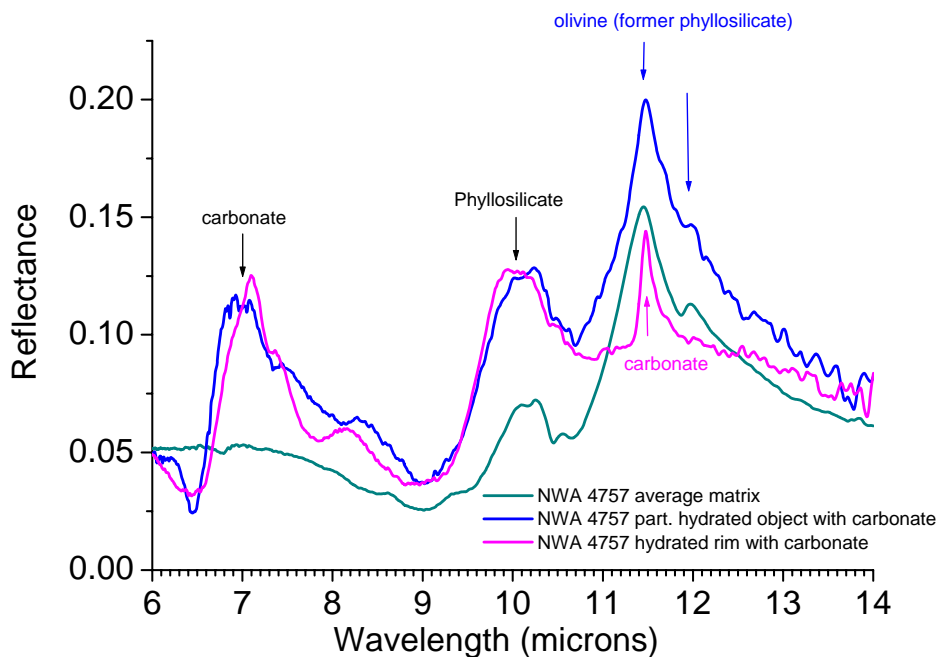
Fig. 2. IR reflectance spectra of (blue) a partly hydrated object containing phyllosilicate, fine-grained olivine and carbonate, and (magenta) a strongly hydrated halo composed of phyllosilicates and carbonates. The average matrix IR spectrum of NWA 4757 is shown for comparison. Characteristic reflectance peaks of phyllosilicates, carbonates and olivine are indicated by arrows.

References

[1] Ikeda Y. 1992. *Proceedings of NIPR Symposium on Antarctic Meteorite:***5**, 49-73.
[2] Ivanova M.A. et al. 2004. *Meteoritics & Planetary Science* **39**. Abstract #5113.
[3] Ivanova M.A. et al. 2005. *36th Lunar & Planetary Science Conference,* Abstract #1054.
[4] Ivanova M.A. et al. Submitted to *Meteoritics & Planetary Science*.
[5] Moroz L.V. et al. 2006. *Meteoritics & Planetary Science* **41**, 1219-1230.
[6] Ivanova M.A. et al. 2004. *Meteoritics & Planetary Science* **43**. Abstract #5103.
[7] Ivanova M.A. et al. 2008. In *Meteoritical Bulletin 93, 2008 March,* 578-579.
[8] Schade, U. et al. 2002 *Rev. Sci. Instr., 73,* 1568-1570.

Dynamics within nanoparticle dispersions from the environment studied by soft X-ray spectromicroscopy

S.-C. Gleber[1], J. Sedlmair[1], S. Heim[2], P. Guttmann[2], J. Thieme[1]

[1] Institut für Röntgenphysik, Georg-August-Universität Göttingen, Friedrich-Hund-Platz 1, 37077 Göttingen
[2] BESSY GmbH, Albert-Einstein-Str. 15, 12489 Berlin

Introduction

It has been pointed out that soft X-ray spectromicroscopy is an important tool for investigations of aqueous colloidal samples from the environment (Thieme et al., 2007 (1), Thieme et al, 2007 b (2)). The BESSY scanning X-ray microscope (STXM) provides a combination of high spatial resolution in the range of $30\,\mu$m to $50\,\mu$m and high spectral resolution of about 3000. This has been used for elemental mapping and chemical analysis of soil samples (Mitrea et al., 2007 (3), Mitrea et al., 2008 (4)). Taking advantage of the natural contrast mechanism, sample preparation is not necessary, it can be imaged in transmission within its original aqueous media up to $10\,\mu$m thickness

In soil science, the element distribution within soil colloid clusters is of great interest. The here presented application of stereo imaging to the STXM provides a tool for that and can be used to reveal the spatial arrangement of e. g. iron oxides in soil colloid clusters. Changing the chemical conditions of aqueous medium leads to changes in the spatial arrangement, which can be done directly in the X-ray microscope. Thus, in combination with stereo imaging, dynamical behaviour of spatial arrangements can be investigated.

The analysis of stereo images is done by the self-written programme `xstereo` based on IDL (Interactive Data Language). It provides the reconstruction of spatial distances, lengths and edge structures and spatial plots of the marked structures (Gleber et al., 2003 (5), Gleber et al., submitted (6)).

Stereo experiments at STXM

Stereo experiments at the STXM required the modification of the STXM object plate (Gleber et al, 2007 (7)). Now, the detachable tilt stage, introduced by Weiß, 2000 (8), is implemented as shown in figure 1 right. To mount it to the STXM object plate, an aluminium adapter is applied. A tapered borocilicate glass capillary is used as tiltable sample holder for aqueous samples. It is tilted via an axle by a stepper motor. The axle is inserted into the STXM object plate due to the small distance of both STXM vacuum vessels for X-ray operation. The insertion causes a difference in z-position between the stepper motor and the axle, resolved by a spring.

Since 2008, a compact digital camera with USB hub is implemented in the STXM setup, allowing for displaying the sight by the visible light microscope (VLM) with a computer and storing the image. The computer display provides a resolution of about $1\,\mu$m when combined with the $40\,$x objective of the VLM. The resulting improve in prealignment reduces focusing efforts with X-radiation, and thereby minimises dosage and expenditure of time. Both effects are important for stereo experiments. Furthermore, the possibility to store the prealignment images is helpfull to recognise the initially imaged sample region after tilting the object holder.

The minimum distance of the capillary from the STXM zone plate is limited by the minimum distance necessary between the capillary and the vacuum window of the zone plate vacuum vessel. The tapered part of capillary has to be quite short for stability reasons. However, the vacuum window of the STXM is not on top of a cone, but of a cylindrical device of about $1.5\,$cm diameter (figure 1 left). Thus, attaching of the part of the capillary increasing in diameter to the cylindrical mount of the vacuum window limits the achievable distance of the tapered capillary tip from the vacuum window. On the other hand, the minimum distance between vacuum window and zone plate is limited due to the limited possible drive of the zone plate in
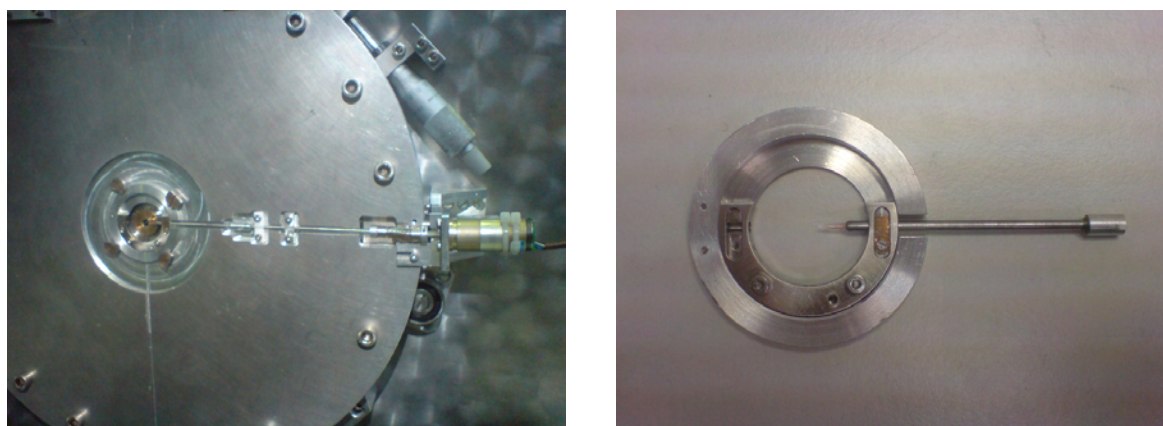
Fig. 1: *Photographs of the STXM object holder plate modified for stereo imaging and the detachable object holder.* **Left:** *Photograph of the STXM object holder plate modified for stereo imaging. The detachable tilt stage is mounted via an adapter (shown right besides) in front of the vacuum window of the zone plate vacuum vessel. The axle is inserted in STXM object plate to connect tiltable sample holder with a stepper motor, divided in two parts for easy object holder demounting.* **Right:** *Photograph of the detachable object holder for stereo imaging with the STXM with a capillary inserted. Detachable object holder on an adapter for mounting to the object plate. Object-side part of the divided axle visible.*

z-direction. Therefore, the capillary tip could not be focused at energies below 300 eV yet. This has to be improved in order to realise carbon mapping in combination with stereo microscopy.

Experimental results

With the actual setup, it is possible to investigate spatial arrangements within aqueous samples with in-situ manipulation. This is demonstrated with an aqueous soil sample (calcaric phaeozem) and an iron oxide abundand in the environment (haematite) (Gleber et al., submitted (6)). To show the influence of haematite added to an aqueous calcaric phaeozem sample as a progression in time, three pairs of stereo micrographs taken at the STXM are presented in figure 2. The tilt angle was 12° for all three stereo pairs, where the upper images and the lower images were taken under equal tilt position, respectively. The first pair on the left side shows a cluster of a dispersion of pure phaeozem filled into a capillary. A cluster of phaeozem particles of different sizes is shown. The image pair presented in the middle of figure 2 shows the same phaeozem cluster, but after the addition of haematite. The lower image is taken 12 min and the upper image 38 min later. Structural changes are visible compared to the images taken before the injection of haematite. The image pair shown on the right of figure 2 is taken from the same phaeozem cluster after third addition of haematite dispersion to the capillary, 2 hrs 40 min after first haematite addition. The image recording started 44 min for the upper image and 55 min for the lower image after third haematite addition. Further changes in the cluster arrangement are visible.

To determine the changes induced by the addition of haematite, the stereo images shown in figure 2 were processed with `xstereo`. The markers applied to the first stereo pair are shown in figure 3. The same structures were marked and the revealed spatial distances are included in the following discussion. The spatial distance between the structures marked as 1 and 2 stays stable at 1.1 µm within the estimated error range of 0.1 µm due to the image quality. The distance between the particle edges marked as 3 and 4 increases after the addition of haematite from 0.6 µm in the first stereo pair (figure 3 left) to 0.8 µm in the second stereo pair and 0.9 µm in the third stereo pair. The plots of the spatial distribution of the marked structures are revealed by `xstereo` , but not presented here.
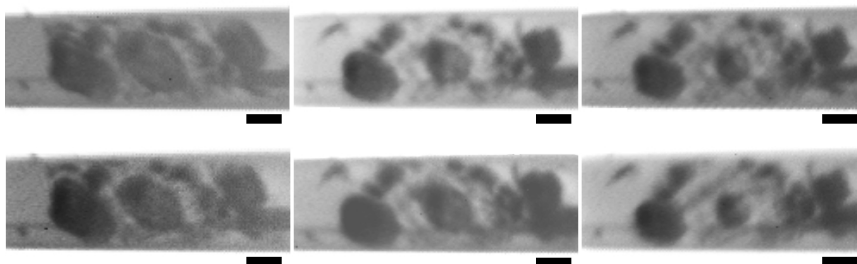
Fig. 2: Three pairs of stereo micrographs of aqueous calcaric phaeozem in a capillary. Upper images were taken at equal capillary position, and lower ones under a tilt angle of 12°. **Left:** Pure aqueous phaeozem sample. **Middle:** Same phaeozem cluster after first addition of a haematite dispersion. Imaging time 12 min (lower image) and 38 min (upper image) after addition of haematite. **Right:** Same phaeozem cluster after third addition of haematite. Imaging time 44 min (upper image) and 55 min (lower image) after third haematite addition. All images taken at $E = 400\,eV$ with 50 nm pxl size and an exposure time of 18 ms per pixel. The scale bars indicate $1\,\mu m$
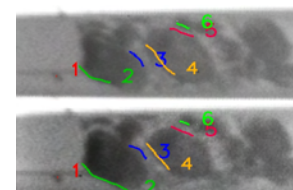
Fig. 3: Sample structures marked for `xstereo` processing of sample shown on the left in figure 2. Only first stereo pair presented.

Outlook

To be able to identify particles within the distribution and relate them with the morphological changes of the colloidal soil structures, it is necessary to combine the stereo experiment with elemental mapping. With further adaption of the STXM, it is possible to perform stereo experiments as presented here at the carbon absorption edge. Then, for example the dynamical behaviour of added carbon nanotubes within aqueous soil samples (Sedlmair et al., this volume (9)) can be spatially investigated.

Acknowledgement

Literature

[1] Thieme J, McNulty I, Vogt S and Paterson D 2007 *Environmental Science and Tecnolology* **41** 1027

[2] Thieme J, Gleber S, Mitrea G and Guttmann P 2007 *Optics and Precision Engineering* **12** 1887–1885

[3] Mitrea G, Thieme J, Novakova E, Gleber S C, Guttmann P and Heim S 2007 *BESSY Annual Report 2006* 190–192

[4] Mitrea G, Thieme J, Guttmann P, Heim S and Gleber S C 2008 *Journal of Synchrotron Radiation* **15** 26–35

[5] Gleber S C, Knöchel C, Thieme J, Rudolph D and Schmahl G 2003 *X-Ray Microscopy 2002* (*Journal de Physique IV Proceedings* vol 104) ed Susini J, Joyeux D and Polack F (EDP Sciences, Les Ulis) p 639

[6] Gleber S C, Thieme J, Chao W and Fischer P *Journal of Microscopy* submitted

[7] Gleber S C, Thieme J, Guttmann P, Heim S and Mitrea G 2007 *BESSY Annual Report 2006* 234–236

[8] Weiß D 2000 *Computed tomography based on cryo X-ray microscopic images of unsectioned biological specimens* Ph.D. thesis Georg-August-Universität Göttingen

[9] Sedlmair J, Gleber S C, Zänker H, Guttmann P, Heim S and Thieme J *BESSY Annual Report 2008*

DEAD SEA SCROLLS:
CHARACTERIZATION OF PARCHMENT SURFACE AND INKS

Admir Masic[1], Emanuel Kindzorra[2], Ira Rabin[2], Ulrich Schade[3], Oliver Hahn[2], Gisela Weinberg[4]

[1]Max Planck Institute of Colloids and Interfaces, Potsdam, Germany
[2]BAM Federal Institute of Materials Research and Testing, Berlin, Germany
[3]BESSY, Berlin, Germany
[4]Fritz Haber Institut der MPG, Berlin, Germany

The Dead Sea scrolls (DSS) were discovered between 1947 and 1956 in eleven caves in and around the settlement Khirbet Qumran at the west shore of the Dead Sea. The texts, of great religious and historical significance, pose a number of historical questions that might be solved with the help of material study. In addition, the scrolls and scroll fragments have experienced complicated and seldom accurately documented post discovery treatments. For long-term preservation and historical study of the scrolls the recognition of the treatment materials is of primary importance. Our previous study was focused on the physical characterisation of parchment surface by means of infra-red external reflection spectroscopy (IR-ERS) [1]. The present study is devoted to the recognition of the various deposits on the parchment surface and characterization of the inks.

The measurements were performed using infrared synchrotron radiation of the BESSY storage ring (IRIS line) and a FT-IR microscope (Nicolet) equipped with a liquid nitrogen cooled MCT detector. The microscope has a computer-controlled XY-mapping stage with a precision of 0.5 microns and a range of 10 cm, hence allowing for reproducible measurements over several selected microscopic areas of quite large fragments. The full mapping of a 3x3 cm fragment takes about 12 hours, with 128 scans acquired in each point with a spectral resolution of 4 cm-1 and a spatial resolution of 5 microns.

For acquiring transmission FT-IR spectra, micro samples were prepared in a Diamond micro compression cell and measured at a room temperature. A 32x Cassegrain objective with an aperture of 20 μm × 20 μm was used to focus the beam on the sample. A total of 256 scans were co-added per sample spectrum (wavenumber range: 4,000–700 cm^{-1}).

Surface characterization.
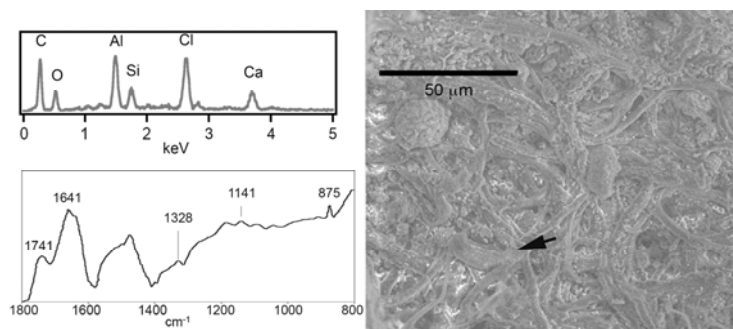
Fig. 1: EDX spectrum (upper left) and Mid μ-FT-IR absorbance spectrum (lower left) of the DSS sample (IQ10_v) obtained from the reflectance spectra by applying Kramers-Kronig transformation measured at the spot indicated by the black arrow in the scanning electron micrograph (right).

In Fig. 1 an example of absorbance spectra of IQ10 sample (verso) is shown. Beside a Reststrahlen band observed at about 1400 cm^{-1} associated to calcite ($CaCO_3$) the spectra is characterised by bands which can be assigned to C=O stretching (1741 cm^{-1}), Amide I (1661 cm^{-1}), Amide II (~1550 cm^{-1}), oxalates (1328 cm^{-1}), silicates (1184 cm^{-1}, 1141 cm^{-1}, 1095 cm^{-1}) and calcite (875 cm^{-1}). Since it is known that this sample has not been treated in the post-discovery period we believe the band due to C=O stretching to be a manifestation of the tannins on the surface of parchment, as suggested by John Poole and Ronald Reed. According to their hypothesis the finishing stage of the production of Jewish parchments in antiquity included surface treatment with vegetable tannins. [2] In many cases, however, appearance of the C=O stretch is due to the treatments of the post-discovery period. The summary of results (Table 1) for a number of the Dead Sea Scroll parchments have shown that the spectral features obtained with the IR microscope are directly related to the specific areas analyzed additionally by means of optical and scanning electron microscopy accompanied by EDX and micro-XRF scans. Fibres are always characterized by enhanced Amide I and

Amide II bands whereas the dusty surfaces show the dominant presence of calcite and silicates. In the same way, the elemental distribution measured by EDX and micro-XRF that reflects the composition of the analyzed area corroborated the results obtained by IR-microscopy.

Table I: Summary of the results obtained by IR mapping of the fragments.

Sample r=recto v=verso	Specific area EDX,XRF,SEM identified	Amide I	Amide II	Calcite	Silicates	$C_2O_4^{2-}$	$C=O$ stretch
I_Q10_r	Fibers	+	+	+	+	+	-
I_Q10_v	Fibers	+	+	+	+	+	+
GA_v	Border	+	+	-	+	+	+
GA_v	Fibers	+	+	-	-	+	+
GA_v	Gelatinized surface	+	+	-	+	-	+
4Q12_r	Fibers	+	+	+	+	-	-
4Q12_v	Gray-yellow deposit	+	+	+	+	-	-
4Q12_v	Fibers	+	+	+	+	+	-
4Q12_v	White deposit	-	-	+	-	-	-
4Q28_r	Glossy surface	+	+	+	+	+	-
4Q28_v	Single fiber	+	-	+	+	-	-
4Q28_v	Fibers and dust	-	-	+	+	-	-
4Q28_v	Fibers	+	+	+	-	-	-

Ink characterization by FTIR transmission spectroscopy.

Mixing carbon black with the gums and distilled water produces a black ink similar to those used in the ancient times. We have also investigated a sample of commercial Chinese inks. Parchment has strong amide absorptions in the finger print region, therefore sample preparation is of paramount importance: presence of parchment in the samples can easily mask the characteristic features of the binding agents. Since the samples for the study must be taken from the inscriptions on parchment the extraction of of inks only, i.e. without parchment becomes one of the greatest limitations of this type of the measurement.

In Fig. 2 we show the spectra of the inks containing rosins of Acacia trees, oak galls. Note that nature of the binding agent in the commercial Chinese ink was unknown to us.
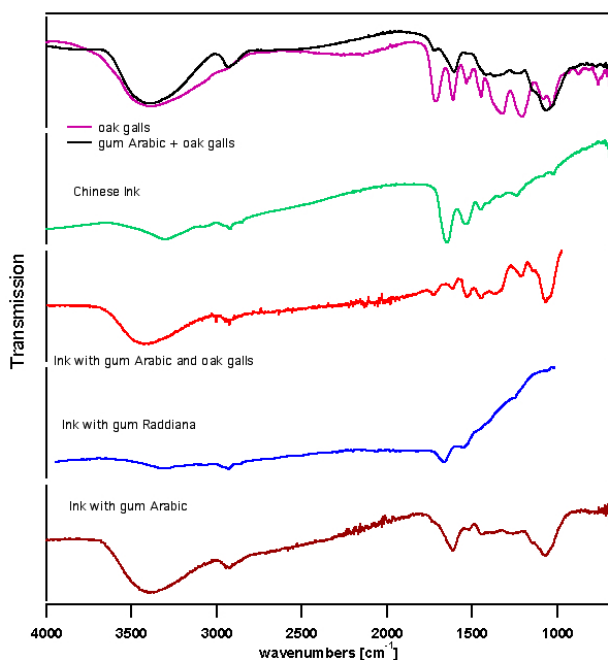
Fig. 2. FTIR spectra of the inks. For comparison two curves in the upper part correspond to the pure binding agents.

The prominent broad peak at 1043 cm^{-1} clearly indicates the presence of Gum Arabic [3].
Hydrolyzable tannins from the oak gall in the same ink manifest themselves through the series of the peaks between C—O stretch 1190 cm^{-1} and C==O stretch at 1715 cm^{-1} (red curve). Bands corresponding to the condensed tannins of acacia Raddiana (around 1000 cm-1) couldn't be resolved in this sample (blue curve) [4,5]. The binding agent of the Chinese ink (green curve) could be clearly identified as animal glue due to the characteristic pattern of the amide bands of the collagen.

Conclusion

FTIR reflection microscopy allows to distinguish between the collagenous portions and inorganic deposits on the surface. The applicability of this method is, however, severely affected by the texture and variable thickness of parchments.
Extraction of minute samples is advantageous in the cases of well preserved fragments or dummy studies. It is extremely useful for the construction of the data base of mixed media. However, with historical fragments in advanced gelatinization stage, and thus highly inhomogeneous, extraction of a minute sample might not lead to representative results.

Bibliography
[1] A. Masic, M. Ortolani, I. Rabin, U. Schade, G. Martra, O. Hahn, S. Coluccia, Dead sea scrolls: From mid to far IR non-destructive characterization of parchments and their conservation treatment materials, in BESSY – Annual report (2007), 257-259
[2] J.B. Poole, R. Reed, The preparation of leather and parchment by the Dead Sea Scrolls community, Technology & Culture **3** (1962)**,** 1-36
[3] P. A. Williams, G. O. Phillips, Gum Arabic, in Handbook of hydrocolloids, eds. G. O. Phillips and P. A. Williams, CRS press, Cambridge 2000
 [4] M. Arshad, A. Beg, Z.A. Siddiqu, Infrared Spectroscopic Investigation of Tannins. *Die Angewandte Makromolekulare Chemie* **7** (1969), 67-78.
[5] M. Giurginca, N. Badea, L. Miu, A. Meghea, Spectral technics for identifying tanning agents in the heritage leather items. *Revista De Chimie* **58** (2007), 923-928

ARCHAEOLOGICAL GOLD PROVENANCE STUDIES – THE CASE OF CARPATHIAN MOUNTAINS NATIVE GOLD

Bogdan Constantinescu[1], Angela Vasilescu[1], Martin Radtke[2], Uwe Reinholz[2]

[1] *Department of Applied Nuclear Physics, "Horia Hulubei" National Institute of Nuclear Physics and Engineering, PO BOX MG-6, Bucharest 077125, Romania*

[2] *Bundesanstalt für Materialforschung und – prüfung (BAM), Richard-Willstätter Strasse 11, 12489, Berlin, Germany*

The study of trace elements in archaeological metallic objects can provide important clues about the metal provenance and the involved manufacturing procedures, leading to conclusions regarding the commercial, cultural and religious exchanges between the old populations [1]. Ancient metallic objects are inhomogeneous on a micrometric scale, containing remains of imperfect smelting and inclusions (small areas with composition different from the surroundings). The goal of the study is to verify if Transylvanian gold was used to manufacture Romanian archaeological objects. This is realized by using information related to trace elements: Sb, Te, Pb - recognized fingerprints for Carpathian Mountains mines and Sn characteristic for the panned river-bed (alluvial) gold [2]. To solve these issues, samples (grains, nuggets, fine gold "sand") from various Transylvanian mines and rivers and some very small (few milligrams) fragments of archaeological objects are measured. Another outcome of this Synchrotron Radiation X-Ray Fluorescence (SR-XRF) experiment is to obtain the elemental characterization (Au, Ag and Cu content) of representative Transylvanian gold mines, subject of interest for the assignment of any other archaeological artifacts to one of the Central European gold sources.

During the 2008 (March) experiment, point spectra for 15 natural gold samples from Transylvania and 12 "micronic" samples from archaeological objects were acquired at 32.5 keV excitation SR energy, using a spatially resolved SR-XRF set-up mounted for analyses at the hard X-ray beam line – BAMline [3] . The beam was focused to a beam size of 100×100 μm^2. The gold samples were mounted in air in a special frame for passe-partouts on a motorized xyz stage at an angle of $45°$ to the X-ray beam. Fluorescence signals were collected for 300 s each by a Silicon Drift Detector (SDD) detector covered with a with respect to the incident beam. Data are performed by means of AXIL software [4]. Relative concentrations of minor components are determined using a procedure based on different metallic standards and fundamental parameter calculations with SNRLXRF.

A summary for the characterization of Transylvanian native gold is the following:

- high (7 - 35%) Ag amounts and low (0.15 - 1%) Cu amounts;
- placer deposits (Valea Oltului, Stanija, Valea Ariesului) contain as fingerprint Sn (150-300 ppm) – most probably from river bed cassiterite, but also palladium (Lipova – Arad);
- primary deposits present as main fingerprints Te (200-2500 ppm), Sb (150-500 ppm) - however, the samples are very inhomogeneous;
- primary deposit of Rosia Montana contains te (500 – 5000 ppm) and a mixture of metallic copper and copper from chalcopyrite;
- primary deposit Fizesti presents a big amount of Pb = 1%, Sb (350 ppm), traces of Te and also Sn.

Practically the native gold samples are inhomogeneous - mixtures of gold-silver-copper metallic alloy with areas of tellurides and antimoniates with galena (lead), pyrite (iron), chalcopyrite (irin, copper) and sphalerite (zinc) inclusions.

Many isolated pieces or large treasures of ancient gold coins (staters) were discovered in Romania, especially around Sarmizegetusa – the capital of Dacia [5]. The coins analyzed in this work (6 pieces) come from the recently discovered treasure (around 1000 kosons) at Târsa-Luncani [6]. This quaint type of coins is usually considered the only kind of gold coins issued by the Dacians. The strangeness of these coins consists in their Roman iconography. The obverse - an eagle standing left on a scepter holding a wreath in one claw - is inspired by the silver denarii issued by O. Pomponius Rufus; while the reverse - three togate male figures advancing left, the first and third of which carry an axe on their left shoulder - seems to be inspired by a silver denarius issued in 54 BC by M. Junius Brutus. The controversies around these coins are connected with the significance of the inscription, the place of mint and the issuer. There are 2 main types of koson coins: with and without monogram, undeciphered up to date. The study intended to determine whether the gold used for the koson coins is native or refined. This study shows that the type "with monogram" is made from refined (more than 97%) gold with no Sb, Te or Sn traces (re-melted gold), and the type "without monogram" is manufactured from native alluvial gold, partially combined with primary Transylvanian gold (Sn and Sb traces detected). For a comparison, the Greek "pseudolysimachus" type staters (contemporary with "kosons") are made of refined re-melted gold (no Sn, Sb, Te presence). Concerning the Early Bronze Age hair ring from the Tauteu hoard and the Late Bronze Age Vulchitrun disk [7] we found that both are made of alluvial gold.

The results obtained in 2007 and 2008 have been presented at the 3rd International Symposium on Synchrotron Radiation in Art and Archaeology - SR2A - Barcelona, Spain, October 2008, and, consequently, submitted to Applied Physics A.

1. E. Pernicka, Nucl. Instr. Meth. B47, 24 (1986)
2. B. Constantinescu, R. Bugoi, V. Cojocaru, D. Voiculescu, D. Grambole, F. Herrmann, D. Ceccato, Nucl. Instr. Meth. B 231, 541 (2005)
3. I. Reiche, M. Radtke, A. Berger, W. Goerner, S. Merchel, H. Riesemeier, H. Bevers, Appl. Phys. A 83, 169 (2006)
4. B. Vekemans, K. Janssens, L. Vincze, F. Adams, P. Van Espen, X-Ray Spectrometry 23, 278 (1994)
5. O. Iliescu, Quaderni ticinesi di numismatica e antichità classiche, 19, 185 (1990)
6. C. M. Petolescu, The treasure of King Koson (Booklet), Romanian National History Museum, Bucharest (2000) (in Rom.)
7. Al. Bonev, The gold treasure of the Vulchitrun village, in D.W. Bailey, I. Panayotov (eds), Prehistoric Bulgaria, Monographs in World Archaeology 22, Madison, 277 (1995).

Toward a better understanding of the use of bone materials in the prehistoric times: micro-XRF/SAXS/WAXS investigations of artificially heated bone samples at low temperatures.

Céline Chadefaux[1], Aurélien Gourrier[2], Oskar Paris[3] and Ina Reiche[1]

[1] Laboratoire du Centre de Recherche et de Restauration des Musées de France, UMR 171 CNRS, Palais du Louvre - 14, quai François Mitterrand, 75001 Paris, France,
supported by EU project R II 3.CT-2004-506008, BESSY-ID.08.1.70810 and ID.08.2.80355 as well as ANR project n°: 07-JCJC-0149-01

[2] Laboratoire de Physique des Solides, UMR 8502 CNRS, Université Paris Sud, Bât 510 Orsay, France.

[3] Max-Planck-Institut für Kolloid- und Grenzflächenforschung, Potsdam, Germany.

Ancient bone materials record information in their structure and in their chemical and isotopic composition about the ways of life in the past. This is particularly true for burnt or boiled archaeological samples as they can represent evidences of the mastering of fire by man in prehistoric times. Therefore, it is very important to get access to this information by chemical and structural analysis.

Bone materials exhibit a high degree of structural hierarchy. They essentially consist of collagen molecules and hydroxyapatite crystallites. Both phases are closely linked at the nanoscale and the complexity of bone structure and composition is enhanced in archaeological bone materials because of *post-mortem* alteration processes in the burial environment. These chemical, physical or biological processes may alter the material and so, the archaeological information may be lost [1]. This is the reason why an exact characterization of the state of conservation of archaeological bone material is required. This investigation of the archaeological bone structure and composition will help us to preserve the material itself, to find characteristic markers of ancient human activities and to evaluate if the information contained in its structure can have a real archaeological signification.

For this reason, an analytical strategy adapted to the complexity of this nanocomposite biomaterial was developed at the LC2RMF in Paris to characterize the state of conservation of the archaeological bone materials at different scales [2]. Micro-XRF/SAXS/WAXS experiments were conducted at the MySpot beamline at BESSY and were complemented by other technique in order to obtain a complete picture of structural and chemical changes at all levels [3].

In particular, micro-SAXS/WAXS experiments provide average values of the thickness and the orientation of mineral particles across a transverse bone section [4,5]. These measurements will be correlated to the morphological and structural analyses conducted by TEM on ultrathin sections at nanoscale [6]. This will allow us to obtain both a precise structural description using the TEM images, although limited to a highly localized part of the samples, and the corresponding average parameters over much larger sampling regions using scanning SAXS/WAXS.

One of the purposes of our project deals with the characterization of structural modifications in bone material induced by heating at low temperatures (100-300 °C). Most of the previous research concerns studies of the heat-induced modifications at high temperature (500-940 °C) and its effect on the mineral part of the bone material [7,8].

Material

In order to investigate the effect of low temperature treatments on the particle size and orientation, three modern sheep bone samples artificially heated have been analysed by micro-SAXS/WAXS. These samples were heated during 60 minutes at 150, 170 and 200°C. A modern sheep sample not submited to any heat treatment was also measured for reference and archaeological samples were also analysed to distinguish alteration features linked to the heating from those linked to the diagenesis.

Experimental

Scanning SAXS/WAXS experiments were conducted at the MySpot beamline [9] by working at an energy of 15 keV using a Si/W multilayer on Si(311) as monochromator. The beam size was reduced by collimation to ~ 30 µm in diameter. Simultaneously, X-Ray fluorescence (XRF) measurements were acquired to correlate the structural crystalline modifications with the elemental distribution across the sample. Two dimensional mappings were performed from the outer part of the bone material section to the inner part to evaluate the structural and chemical modifications. Indeed, during burial, the outer part of the bone section, directly in contact with the soil, is more sensitive to interactions with the environment and will be more intensively modified [10]. Thus, scans were carried out in steps of 30(h) x 30(v) µm^2 across the transverse sections to use the full resolution of the instrument in direct space corresponding, in first approximation, to the beam diameter. The sample-to-detector distance and the detector tilt and centre were calibrated using a Ag behenate standard [11]. The data were reduced using the FIT2D software [12] and analysed with software developed in Python by Aurélien Gourrier using a procedure described in detail elsewhere [5]. The analysis of the radial profiles provides parameters related to the shape and the thickness (so called T-parameter) of the bone crystals while the azimuthal profiles allow deriving orientation parameters [13].

Preliminary results and discussion

The figure 1 presents the results obtained on the bone sample artificially heated at 170°C. A region of the sample indicated in fig. 1.A by a rectangle was scanned and analysed to derive a map of the particle thickness shown in fig.1.B. About 80% of the T-parameter values fall in a range of 2.5-3.2 nm as observed in the histogram of the parameter distribution (fig. 1.C). The lower values seem to correspond to a network of porosity in the sample, which can be related to the channels formed during the remodelling process of the living tissue as observed from fig.1.B. It is not clear, at present, whether this is an effect of the heat treatment. In fact, lower T-parameter values have also been reported to be linked with a late stage of the mineralization process during the remodeling phase [5].

We will process the measurements of the other heated samples to compare them to the modern reference in order to find out characterisic heat induced modifications at low temperature. Last but not least, it is also important to be able to differentiate heating effects from those of diagenesis in ancient bones. Work is in progress to clarify these issues.
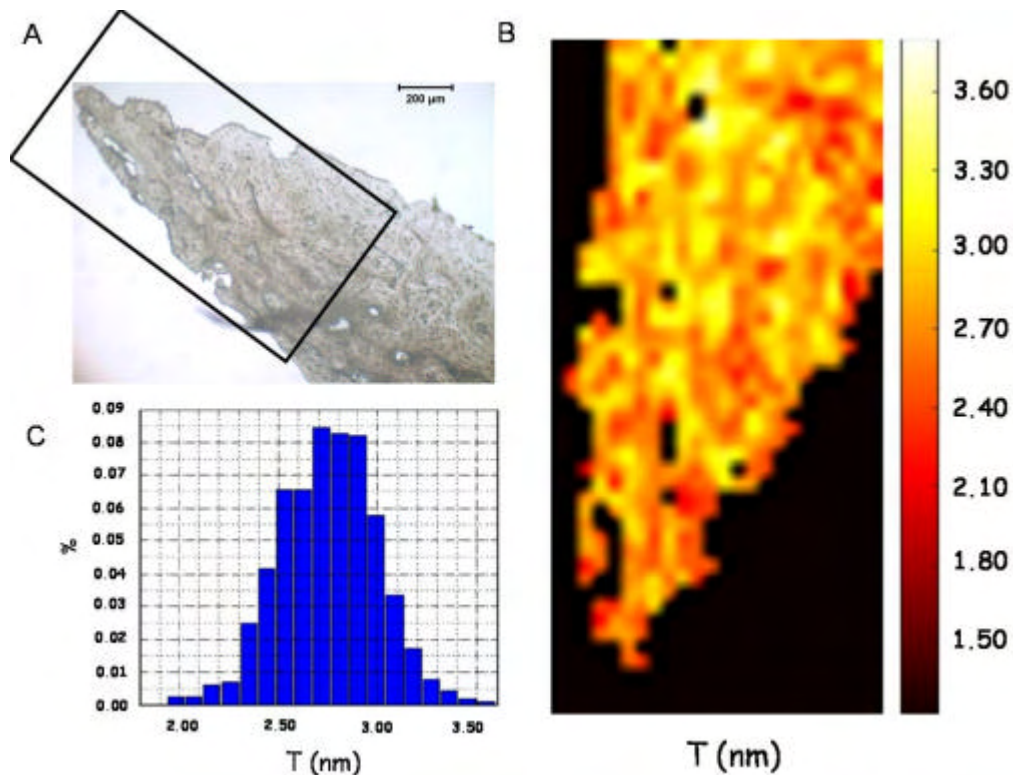
Figure 1: *Evaluation of the thickness of the bone crystals in an artificially heated bone section: A-light microscopy image of the transverse bone section analysed B- map of the T-parameter and C-corresponding % distribution over the scanned area.*

References

[1] R.E.M. Hedges, Archaeometry 44, 3 (2002) 319

[2] I. Reiche, L. Favre-Quattropani, C. Vignaud, H. Bocherens, L. Charlet, M. Menu, Meas. Sci. Technology 14 (2003) 1608.

[3] C. Chadefaux, A. Staude, J. Nötel, H. Riesemeier & I. Reiche, Appl. Phys. A (in prep.)

[4] S. Rinnerthaler, P. Roschger, H.F. Jakob, A. Nader, K. Klaushofer, P. Fratzl, Calcif. Tissue Int. 64 (1999) 422

[5] A. Gourrier, W. Wagermaier, M. Burghammer, D. Lammie, H.S. Gupta, P. Fratzl, C. Riekel, T.J. Wess & O. Paris, J. Appl. Cryst 40 (2007) 78

[6] C. Chadefaux & I. Reiche, J. nano Res. (accepted).

[7] I. Reiche, C. Vignaud, M. Menu, Archaeometry 44, 3 (2002) 447

[8] J. Hiller, T.J.U. Thompson, M.P. Evison, A.T. Chamberlain, T.J. Wess, Biomaterials 24 (2003) 5091

[9] O. Paris, C. Li, S. Siegel, G. Weseloh, F. Emmerling, H. Riesemeier, A. Erko, P. Fratzl, J. Appl. Cryst. 40 (2007) 466

[10] I. Reiche, L. Favre-Quattropani, T. Calligaro, J. Salomon, H. Bocherens, L. Charlet, M. Menu, Nucl. Instr. Meth. Phys. B 150 (1999) 656

[11] T. N. Blanton, T. C. Huang, H. Toraya, C. R. Hubbard, S. B.Robie, D. Louër, H. E. Göbel, G. Will, R. Gilles, & T. Raftery, Powder Diffr 10 (1995) 91

[12] A.P. Hammersley, ESRF Internal report HA02T (1997)

[13] P. Fratzl, S. Schreiber, P. Roschger, M.H. Lafage, G. Rodan & K. J. Klaushofer, Bone Min. Res. 11 (1996) 248

SR-XRF analysis of Pt trace contents in ancient gold alloys at the BAM*line*: a new approach

Maria F. Guerra[1], Martin Radtke[2], Ina Reiche[1], Heinrich Riesemeier[2], Erik Strub[2]

[1] Centre de Recherche et de Restauration des Musées de France, UMR 171 CNRS, Palais du Louvre - 14, quai François Mitterrand, 75001 Paris, France, supported by EU project R II 3.CT-2004-506008, BESSY-ID.07.1.693

[2] Bundesanstalt für Materialforschung und –prüfung (BAM), Richard-Willstätter-Straße 11, 12489 Berlin, Germany.

Queries on the origin and provenance of gold used in the past require for precious and rare items the use of non-destructive analytical techniques providing information on the characteristic elements of the metal.

Gold sources exploited in the antiquity were mainly of secondary type (especially alluvial) and in a few cases of primary type (especially auriferous quartz). The different metallurgical steps from the gold ore to the gold alloy – in the past a gold alloy consisting of a combination of gold with different amounts of silver and copper – results in the loss of information on the original gold both by evaporation or absorption in the cupels of a large number of elements present in the ore and by addition of other different metals. For this reason, together with the fact that gold has always been re-melted and reused to produce other objects, only very few elements are characteristic of the gold source.

Among the characteristic elements of gold, Pt together with elements such as Pd, Sn, Sb,... provides important information on the geological source [1-3]. For example, the presence of Pt in gold, together with Sn, is essential to distinguish secondary from primary gold deposits [4]. In the case of available geo-chemical information on the ancient gold sources, Pt can be used to provenance gold and follow its circulation in the past [5].

Few analytical techniques are at present available to measure Pt directly on the gold object (non-invasive) or, in a few cases, on tiny samplings. Nowadays, the most accepted techniques are ICP-MS, PIXE and PIXE-XRF. However, ICP-MS requires sampling and IBA techniques, in spite of being totally non-invasive, have inadequate detection limits for certain elements such as Pt. We could show that with PIXE-XRF we could only attain a minimum detection limit (MDL) of 80 ppm.

For these reasons, SR-XRF appears to be a good solution for the analysis of goldwork. In fact, SR-XRF fulfils all the necessary requirements, which means MDLs that can be optimised by adapting the excitation energy to the element to be measured, and micro-beams for a non-invasive analysis with good spatial resolution. Our first attempt to develop a protocol in order to measure low contents of Pt in gold alloys [6] was carried out with excitation energy at the Pt L_3-edge (11.564keV). The evaluation of the Pt contents in gold (Z-1 compared to Au) required a specific procedure taking into account the resonant Raman scattering [7,8]. Using a simple model, quantification of the Pt content was carried out by Monte Carlo simulation using the program MSIM7 [9] and by subtraction of the Au and Pt spectra obtained on pure standards. The MDL could be estimated to 20ppm.

In order to solve the problems connected to both the rather poor MDL obtained at low energy and the difficult quantification process of Pt contents, we made new developments of both the analytical SR-XRF set-up and the quantitative calculation procedure at high energy [10]. In the case of the BAM*line*, the continuous radiation ranges from 5keV up to 100keV allowing the use of the K-lines of Pt.

An intense monochromatic photon beam of 0.2x0.2mm² was obtained with a double multilayer monochromator (DMM) leading to a 100 times higher photon flux attaining the sample compared to often used Si 111-Monochromators. Energies for the K-edges of high Z elements can only be reached with reasonable intensities with the DMM excitation. The size of the beam was defined by a slit. We used a 20mm² HPGe detector with nominal resolution of 130eV at photon energy of 5.9keV, placed at a distance of about 2.5cm from the sample, perpendicular to the photon beam in the plane of the electron storage ring, in order to minimize the background contribution from the scattered radiation; the signal delivered by the detector was processed with a Saturn digital signal-processing unit from XIA. An Al foil insulates the detector from the low energy fluorescence spectrum. The sample was inclined by 45° with respect to the photon beam and the detector. All spectra were normalized to the integrated excitation intensity.

A Pt free Au standard was measured under the same experimental conditions as the sample for the estimation of the Pt content. Calculation is carried out by subtraction of the pure Au spectrum from the

spectrum of the sample. The peaks positions and widths of the difference signal and of the Pt sample were compared. Excitation energy of 79.5keV, lying between the Pt and the Au K-absorption edge, respectively at 78.395keV and 80.725keV, was chosen. Because of the limited energy resolution of the DMM, around 1.2keV FWHM at this energy, an Au fluorescence signal is still present in the spectra. The Au Ka2 peak at 66.989keV interferes with the Pt Ka1 peak at 66.832keV. The Raman scattering from the gold is also located in this energy region. Therefore we used the Kß1 line to carry out the calculation.

		Au %	Ag %	Cu %	Pt ppm	MDL K 1 Pt ppm
ancient alloys	S1	98,2	1,7	0,05	61	89
	S4	92,9	3,0	3,9	634	40
	S5	68,3	28,5	3,1	291	67
	S6	90,2	6,3	2,9	2233	73
ancient coins	S2	87,8	9,8	2,3	78	71
	S3	90,3	0,3	9,4	232	74

Table 1: *Composition by ICP-MS and activation analysis of different ancient gold samples of infinite thickness used to evaluate the MDL of Pt using the Kß1 line.*

The MDL for Pt was calculated with the fit of the un-normalised spectra based on the formula suggested by IUPAC [11]. Table1 shows that the Pt MDL calculated for a set of gold coins and plaques with different Pt contents range from 40 to 90ppm. In this table all the samples are of infinite thickness.
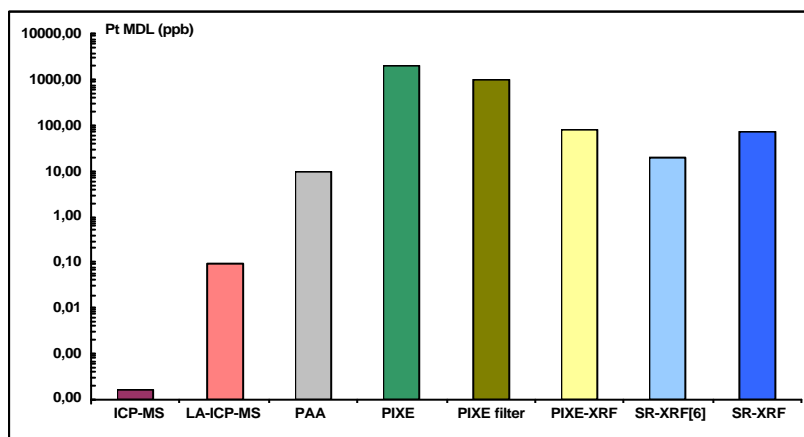
Figure 1: *Comparison of the MDL (in ppb) obtained for Pt by SR-XRF at high and low energy at the BAMline with other analytical techniques usually used for gold provenancing: classical PIXE and with a 75µm Zn selective filter, PIXE-XRF with As primary target and 12 MeV PAA [1] together with ICP-MS and LA-ICP-MS [5,12].*

Figure 1 compares these MDLs with those obtained for other techniques: high energy SR-XRF shows a MDL equivalent to PIXE-XRF whilst at low energy the MDL enhanced by a factor of about 3.

We tested our new protocol with a 79.5keV incident beam of 0.2x0.2mm², based on the fact that gold samplings are usually very tiny and included in resin for non-destructive analysis and that goldwork is of very different type and size: from large statues to mini-beads, from plain objects to thin foils. However, with our set-up only objects or samples with a thickness superior to 300µm (the analytical depth for PtK 1 in gold [13]) can be considered as infinite thick during quantification and only in certain cases the beam is smaller than the sample.

The analysis of 3 thick ancient gold coins showed that the presence of additional elements in the gold alloys, such as Os and Ir, increases the Pt MDL. The analysis of four archaeological gold samples illustrated the difficulties connected to the study of such small or thin items: for two samples included in resin we could calculate 120ppm of Pt for one and 420ppm for the other with a MDL of 80 ppm; for two thin foils of about 50µm thickness Pt concentrations were under the MDL.

Confirming the significant role of SR-XRF in gold provenancing, these results showed that the use of L-edge measurements and of a Si SDD detector accepting higher count rate should simplify the analytical task as samples can be assumed as infinite thick. This assumption does not held for the high-energy measurements and can introduce a significant source of error for quantitative analysis.

The first results at the Pt L-edge are in progress. They were obtained with excitation energy of 11.58 keV. This energy was chosen after a series of test measurements with different energies to optimize the detection limits. DMM and DCM have been used in series to suppress harmonics. An SDD detector was used to get maximum count rate with acceptable energy resolution of 380 eV for Pt with a count rate of typically 70000 cps and a dead time of 50%.

The calculation of the MDL has been done with respect to pure element standards. In Figure 2, the fit for the Standard RM8058 Pt is shown exemplarily. For this case a MDL of 3.1ppm for Pt has been reached, using the standard IUPAC definition. Anyhow, the real detection limit must be assumed a little worse due to the uncertainty of the non standard fit procedure.

Quantification of unknown samples has been done with a rule of proportion, using RM8058 as standard.
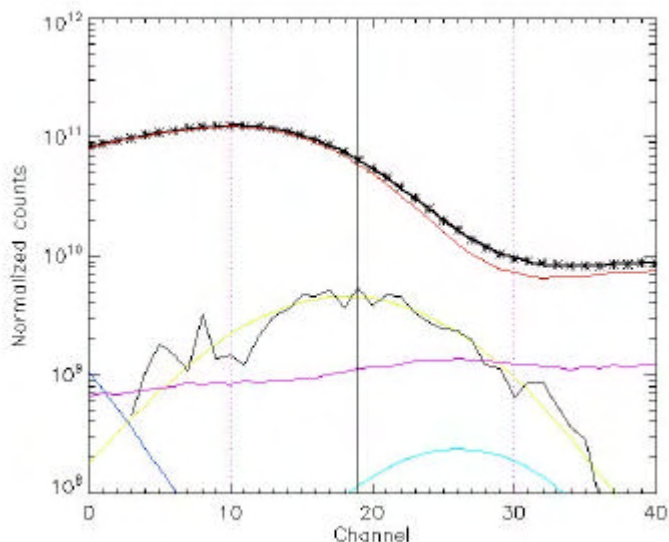
Figure 2: *Fit of the measured signal with a sum of pure Pt, Au, Ag, Zn and Cu measurements. The peak of Pt is located in Channel 19. The yellow line shows a pure Pt signal. The black line shows the fraction of the signal of the sample whish is attributed to Pt. These signals are correlated with a correlation factor of 0.93. This is strengthening the position, that the signal can really be attributed to Pt.*

Standard RM 8058 containing 40.8ppm of Pt was used to calculate the Pt MDL with the new protocol together with two coins analysed by 12MeV proton activation analysis (PAA) and LA-ICP-MS. We could show in table 2 that the Pt MDL ranges from 3.1 to 4.7, attaining 3ppm for standard RM 8058. This value is equivalent to the MDL obtained by PAA at optimised conditions. In this same table we compare the Pt concentrations obtained by SR-XRF at low energy with the expected values of the two coins measured by PAA and ICP-MS. The good agreement between the expected and obtained concentrations is evident.

	SR-XRF Pt / ppm	SR-XRF MDL / ppm	expected Pt ppm
RM 8058	40,6	3,1	40,8
coin NAP	624,8	4,7	630
coin FRA	2665	3,6	2924

Table 2: *Expected Pt concentrations for standard RM 8058 and a set of ancient gold coins measured by ICP-MS and activation analysis compared with the concentrations obtained by SR-XRF at low energy. The Pt MDL is shown for the three samples.*

The application of this new protocol to a few thin ancient gold foils of about 50µm thickness showed that Pt concentrations could be calculated at low energies. A few archaeological samplings included in resin were also analysed and their Pt concentrations could as well be obtained.

References

[1] M.F. Guerra, Nucl. Instr. and Meth. B 226 (2004) 185.

[2] M.F. Guerra, J. Archaeological Sciences 31 (2004) 1225.

[3] A. Gondonneau, M.F.Guerra, Archaeometry 44 (2002) 473-599.

[4] R.K Dubé, Gold Bull. 39 (2006) 103.

[5] M.F. Guerra, in: R. Van Griecken, K. Janssen (Eds.), Cultural heritage conservation and environmental impact assessment by non-destructive testing and micro-analysis, Balkema, London, 2005, 223.

[6] M. F Guerra, T. Calligaro, M. Radtke, I. Reiche, H. Riesemeier, Nucl. Instr. and Meth. B 240 (2005) 505.

[7] T. Fujikawa, T. Konishi, T.Fukamachi, J. Electron Spectrosc. Relat. Phenom. 134 (2004) 195.

[8] P.P. Kane, Physics Reports-Review Section of Physics Letters 218 (1992) 67.

[9] L. Vincze, K. Janssens, F. Adams F, M.L. Rivers, K.W. Jones, Spectrochim. Acta Part B 50 (1995) 127.

[10] M. F Guerra, M. Radtke, I. Reiche, H. Riesemeier, E. Strub, Nucl. Instr. and Meth. B 266 (2008) 2334.

[11] P. Kump, Spectrochim. Acta Part B – Atomic Spectroscopy 52: (1997) 405

[12] A. Gondonneau, M.F. Guerra British Archaeological Reports IS 792 (1999) 262

[13] R.E. Van Grieken, A.A. Markowicz (Eds.). Handbook of X-Ray Spectrometry: Methods and Techniques. Marcel Dekker, Inc., New York, 1993.

Photon-energy calibration for the 10m-NIM beamline by establishing an atlas of H_2 absorption lines between 85 and 72 nm (14.5 – 17.3 eV).

M. Glass-Maujean, , A. Knie*, I. Haar*, R. Hentges*, W. Kielich*, K. Jänkälä*, A. Ehresmann*, and H. Schmoranzer**

Laboratoire de Physique Moléculaire pour l'Atmosphère et l'Astrophysique, Université P. et M. Curie /CNRS, 4, pl Jussieu, F-75252 Paris Cedex 05, France
*Institut für Physik, Universität Kassel, D-34132 Kassel, Germany
** Fachbereich Physik, Technische Universität Kaiserslautern, D-67653 Kaiserslautern, Germany

The U125/2-10m-NIM beamline at BESSY is probably the beamline with the highest resolution world wide in the VUV spectral range. In any case, there is no comparable instrument at the other synchrotron facilities in terms of spectral resolution and light intensity. However, in order to fully use its capabilities, it is necessary to characterize precisely its apparatus function and ultimate resolution and, particularly, to calibrate the energy of the delivered photons in the relevant energy range.

The molecular hydrogen absorption spectrum was used for that purpose as it presents hundreds of lines in the 14.5 – 17.3 eV energy or 85 – 72 nm wavelength range, many of them being still very narrow. At these energies, however, the hydrogen molecule may dissociate and, above 15eV, also ionize; nevertheless, many excited levels still decay via molecular fluorescence connected with a sufficiently long lifetime to lead to very narrow absorption lines.

The absorption spectrum was recorded simultaneously with the ionization, dissociation and fluorescence excitation spectra using a new redesigned target cell (fig. 1). The target
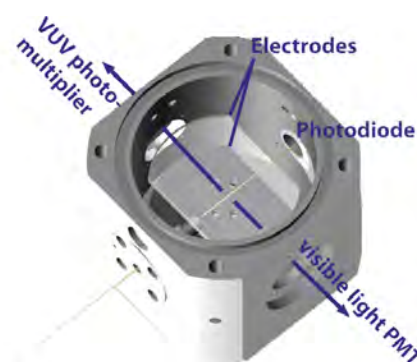
Figure1: redesigned target cell

gas pressure used amounted to 5 or 20 mTorr, at room temperature.

The 10m-normal-incidence monochromator was equipped with a 1200-lines/mm grating and was used at third order with 45μm-wide slits. The translation of the grating had been adjusted to get the best resolution at the third order.

The apparatus function and the resolution were measured on lines known to present a width equal to the Doppler width, i.e. 0.00035nm (HWHM) at 80 nm. In this case, the measured profile was found nearly symmetrical with nearly an expected triangle-shape with

Figure 2: Absorption, dissociation, ionization and fluorescence cross sections, (for the fluorescence, the values are only qualitative).

a width of 0.0016±0.0002 nm (HWHM) which is by 50% larger than last year. The flux transmitted through the monochromator, as measured on the on the last refocusing mirror before the experiment, was around 3 times lower than last year.
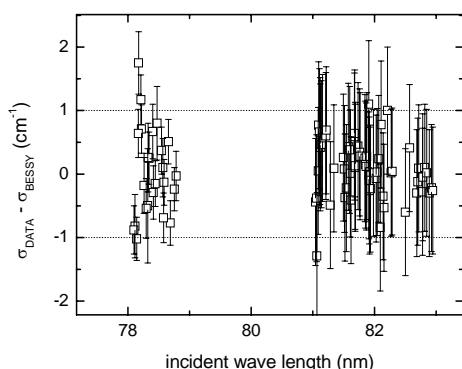
Figure 3: Energy differences between the measured positions and the reference data

We compared the positions of the absorption lines in the 83-81 nm and 79-78 nm spectral ranges with reference data obtained thirty years ago, on photographic plates, at low temperature, with a resolution of 300 000, simultaneously with Ritz standards[1], precise within 1.0 or 0.3 cm-1 (for the data corrected for pressure shift) and confirmed for several lines by recent laser measurements[2]. Obviously, the recent corrections in the 10m-NIM grating drive control loop (Heidemann correction) improved greatly the precision of the measurements. The measured values are now precise within one cm^{-1} at 80 nm (125000 cm^{-1}), instead of six in previous years. As can be seen from figure 3 the measured positions are really much improved and consistent. The complete scan of the lines still contains a few steps much larger than demanded; but these spikes can be easily identified and removed.

As the hydrogen molecule is a simple molecule; the potential curves of the lower states have been calculated at high precision with the adiabatic corrections. It is quite straightforward to solve the Schrödinger equation and calculate the positions of the rovibronic levels in the adiabatic approximation. It is also easy to calculate the intensities of the absorption lines in this approximation. This approach is quite good for the $^1\Pi_u^-$ levels excited from the ground state with $^1\Sigma_g^+$ symmetry through Q lines; most of the levels with a long radiative lifetime belong to the $^1\Pi_u^-$ symmetry. However, this approach is only fair or even poor for the $^1\Sigma_u^+$ levels which are very sensitive to the non-adiabatic perturbations.

Figure 4: Part of the spectrum: in grey the absorption cross section, in blue the dissociation one, with the calculated Q(1) lines (green stars)

The positions of the Q lines were reproduced by the calculations within a few cm^{-1} as tested on the existing reference data. At higher energies, where no precise experimental reference data are available, we compared the computed positions of the Q lines with our measured positions. The calculated positions were found in very good agreement with the observed values of our spectrum[3] and, in most cases, the intensities were also well reproduced; the non-adiabatic couplings affect the intensities of the Q lines. (see figure 4)

The planed energy range could not be fully covered during this beam time. Therefore, the project should be completed during the next beam time in spring 2009.

[1] G. Herzberg and Ch. Jungen, J. Mol. Spectrosc. **41**, 425 (1972) and S. Takezawa, J. Chem. Phys., 52, 2575 (1970)
[2] M. Sommavilla, Diss. ETH Zürich nr 15688 (2004)
[3] M. Glass-Maujean, S. Klumpp, L. Werner, A. Ehresmann, & H. Schmoranzer, Mol. Phys. 105,1535 (2007)

Initial Alignment and Commissioning of an Autocollimator Based Slope Measuring Profiler at the Advanced Light Source

Frank Siewert[a], Valeriy V. Yashchuk[b], Jonathan L. Kirschman[b],
Gregory Y. Morrison[b], Brian V. Smith[b]

[a] *Helmholtz Zentrum Berlin für Materialien und Energie, Elektronenspeicherring BESSY-II, Albert-Einstein-Str. 15, 12489 Berlin, Germany*
[b] *Lawrence Berkeley National Laboratory, One Cyclotron Road, Berkeley, California 94720, USA*

Abstract

We describe the initial alignment of an autocollimator and beam guiding optical components on a carriage–traverse setup to be used as a slope measuring instrument for the inspection of highly precise reflective synchrotron optics at the LBNL/ALS Optical Metrology Laboratory. After the alignment, first commissioning measurements have been performed to characterize the new instrument. A discussion of the results will show the achieved performance and define the direction of future upgrade work to improve the instrument.

Introduction

The use of an autocollimator based slope measuring profiler to measure reflective optical surfaces was first proposed by Debler and Zander in 1979 [1]. Recent developments of the Nanometer Optical Component Measuring Machine (NOM) at BESSY [2, 3, 4] and the Extended Shear Angle Difference (ESAD) Instrument at the Physikalisch Technische Bundesanstalt (PTB) [5, 6, 7] demonstrated a new level of accuracy for slope measuring instruments. Both instruments achieved up to 10-fold superior measurement accuracy, compared to previous instruments, such as the Long Trace Profiler (LTP-II) [8, 9]. 2nd generation slope measuring profilers like the NOM or the ESAD-device are sophisticated engineering solutions combining highly accurate mechanical and motional parts, precise optical components and calibrated sensors. These instruments are operated under defined environmental conditions to guarantee excellent physical stability during the measurements [7, 10]. The Autocollimator- based Slope Measuring Profiler (ASMP)discussed here is a low budget realization of a NOM-like profiler using the Developmental Long Trace Profiler (DLTP) setup at the ALS-OML [11] and an autocollimator "Elcomat 3000 special" (Moeller Wedel Optical [12]) calibrated at the PTB.

Initial Alignment of the DLTP Optical Components

The inspection of reflective optical elements using a scanning pentaprism and an angle measuring sensor is a well known setup [2, 3, 13, 14, 15]. It prevents the measurement from being influenced by the pitch of the moving carriage as a first order error source. An optimal utilization of this setup requires the precise alignment of the autocollimator with respect to the beam guiding optics on the air bearing based carriage. Nevertheless, the accuracy of the carriage movement is an essential point for the achievable measurement accuracy. The test beam and moving direction of the carriage have to be very accurately aligned [14]. Otherwise the yaw movement of the carriage could cause cross-talk effects in the autocollimator. The DLTP setup model is shown in Fig. 1. The main mechanical parts like the carriage-traverse system and the alignment table for the autocollimator are mounted on an optical table. The complete setup is covered by a hutch to enable stable environmental conditions during a measurement. A home-made adjustable laser was used to align the autocollimator parallel to the moving direction of the carriage. A diaphragm at the carriage, mounted telecentric to the measuring axis of the autocollimator, was used for fine alignment. The projection of the diffraction

pattern from the diaphragm onto an image plane showed a stable image while moving the carriage over the entire range of motion of 900 mm.
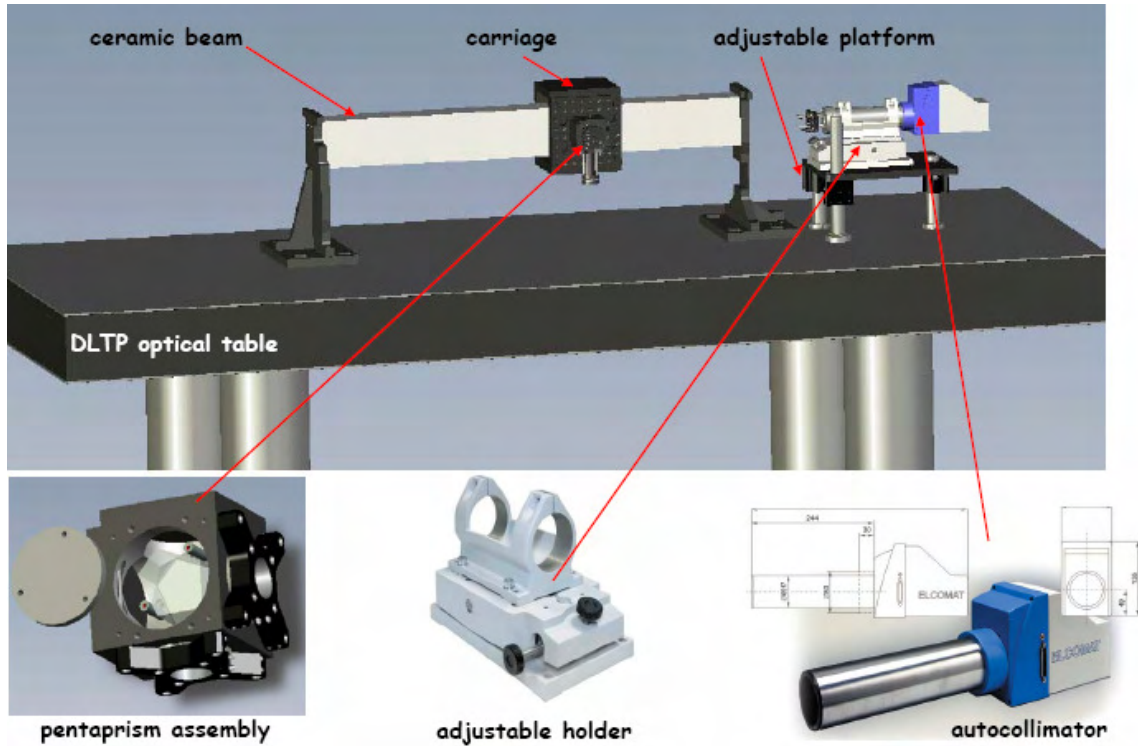
Figure 1:   Mechanical setup of the Autocollimator based Slope Measuring Profiler (ASMP) at the ALS Optical and Metrology Laboratory
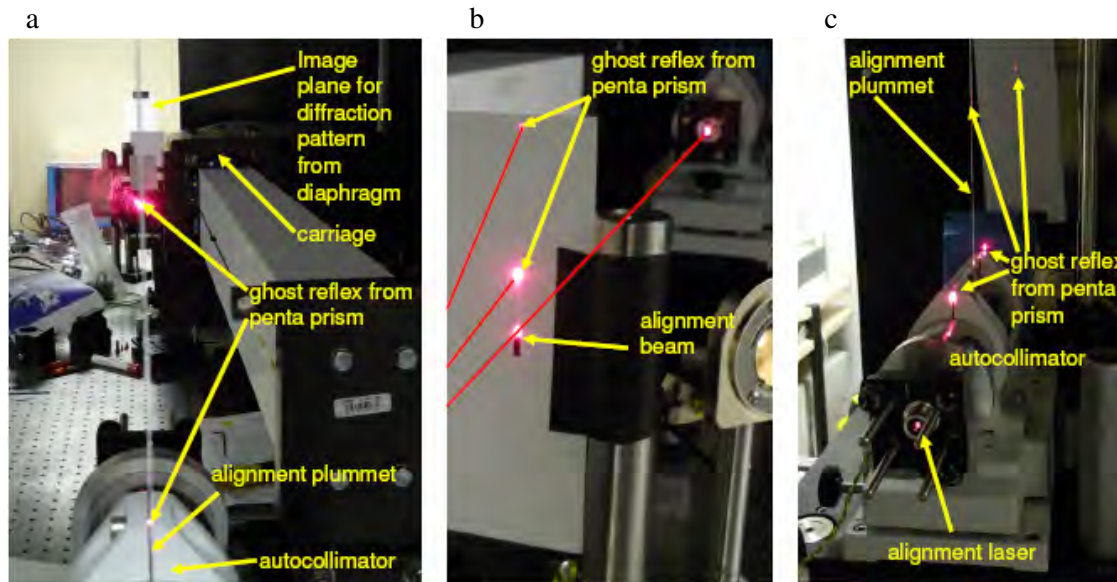
Figure 2:   Setup for the alignment of the autocollimator and pentaprism: a) view from autocollimator to the pentaprism, the image plane for detecting the diffraction pattern of the diaphragm is in the background, b) ghost reflections of the pentaprism at an image plane between pp and autocollimator, c) alignment laser, alignment plumb line and further image plane in the back.

Finally the beam guiding pentaprism was assembled on an alignment stage at the carriage (see Fig. 1). The ghost reflections of the front and reverse side of the pentaprism were used for the alignment, see Figure 2. When alignment is achieved both spots can be detected at the alignment plumb line independently from the current position of the carriage along the complete range of motion. A more sophisticated alignment procedure for a pentaprism, but not used for this first approach, was recently given by R. Geckeler [14].

Inspection of the DLTP Pentaprism

The quality of the beam guiding pentaprism is an accuracy limiting parameter for the performance of the instrument. The inhomogeneity of the glass, the flatness of the pentaprism faces and the angle errors of the faces will have a direct influence on the measurement. Thus, a range of five pentaprisms has been inspected by use of the ZYGO-GPI interferometer in the OML to identify the piece of best quality (see Figure 3). First a plane reference mirror of $\lambda/40$ (15 nm pv) shape accuracy was measured. After alignment of the pentaprism in the beam path the reference mirror was measured again.
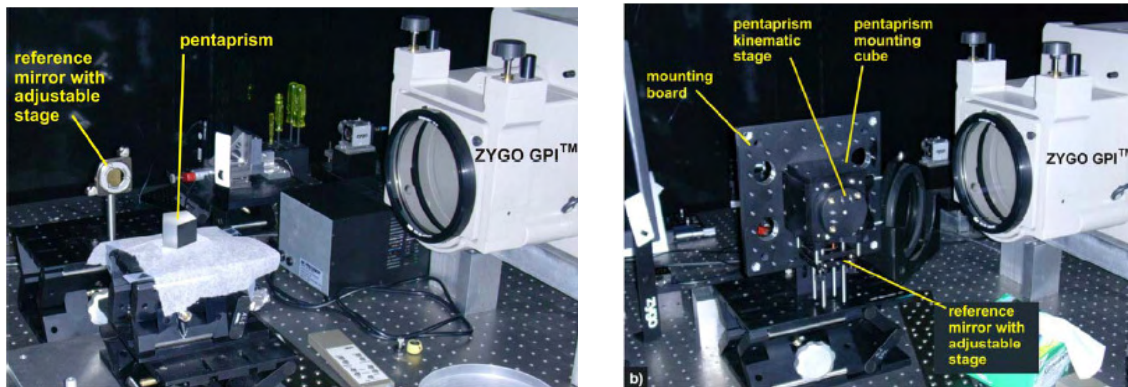
Figure 3:   Set up at the ZYGO-GPI for inspection of penta prisms (left) and for measurement with the penta prism in orientation similar to the mounting at the instrument (right)
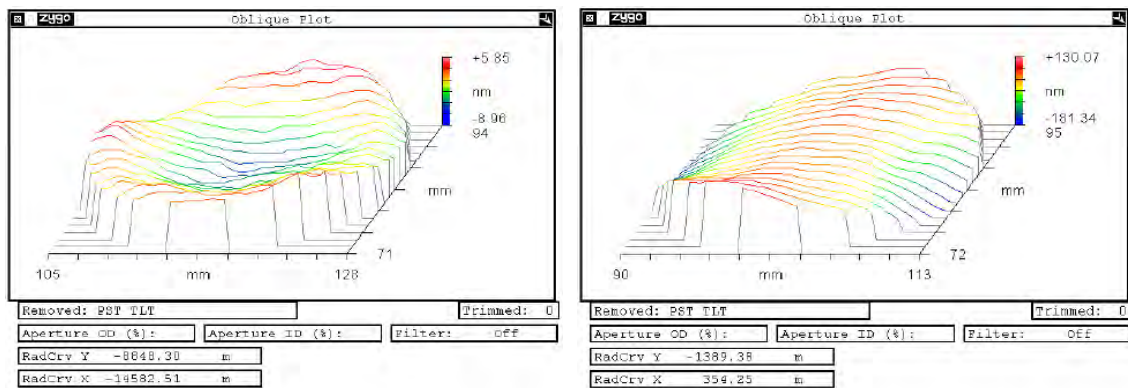
Figure 4:   ZYGO-GPI interferometer measurements, **left**: result for the plane reference mirror, height deviation = 15 nm pv, radii = -8.85 km and -14.58 km, **right:** result with pentaprism in the test beam height deviation 311 nm pv, radii = 0.35 km and -2.43 km

Then the pentaprism was mounted and inspected at an orientation similar to its position in the instrument (see Figure 3, right). Figure 4 shows the strong influence of the pentaprism quality on the measurement. Instead of 15 nm pv shape accuracy, measured for the reference mirror, a shape deviation of about 311 nm pv, more than one order of magnitude, was measured for the aligned pentaprism in the test beam. The values for the radii show a comparable characteristic.

Initial Commissioning

A long term stability scan over 10 hours was chosen for a first step evaluation of the instrumental setup. A plane mirror was placed at a distance of about 200 mm from the autocollimator. Directly after alignment of the mirror and closing the hutch at 6 pm a scan was run overnight. Figure 5 shows the signal of the X- and Y-angles (a strong drift, typical for the system immediately after alignment and a long term transient over the complete measuring time can be seen). In addition the Y-angle for the first 2-3 hours shows a higher noise level, probably caused by other equipment under operation close to the lab. Especially for the Y-angle an oscillation over a time period of about 12 minutes is clearly detected for the entire scan time. It shows a strong correlation to the switching-on/switching-off cycle of the lab air conditioner. Related to the required time for a line scan of about 5 – 30 min this oscillation would be a first order error source and needs to be eliminated by further improvement of the laboratory environment. In general, the noise level of the Y-angle is lower compared to the X-angle. It can be assumed that the pentaprism lessens the "pitch"-part of the random error influencing the measurement.
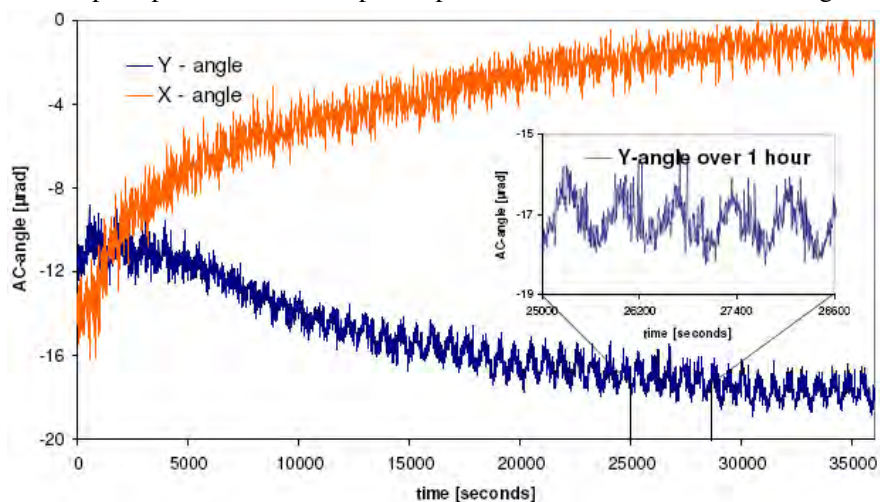
Figure 5:   Stability scan of the autocollimator showing the read out of Y- and X-angles. Variations due to sample alignment and temperature variations in the OML can be seen. The higher frequency oscillations with a period of about 12 min are correlated with the switching on/switching-off cycle of the laboratory air conditioner

The option of cross measurements of well known reference surfaces is a sure method to characterize a new measuring device [**16, 17**]. A spherical mirror R = 10m with a residual slope error of 1 µrad rms and 60mm in length was measured along its tangential center line by use of the BESSY-NOM. The substrate material is quartz glass with a gold coating of 30 nm thickness. The same line of inspection was scanned at the DLTP. The scan-line of interest was measured under different conditions, from mirror edge A to edge B and after a 180° rotation from edge B to edge A. Each measurement consisted of a group of 30 up to 34 line scans traced in the forward and reverse directions. A measuring point spacing of 0.2 mm was chosen to enable a higher angular resolution for an optimal line-array characterization of the autocollimator. All results were obtained by application of a calibration curve, the result of a highly accurate calibration procedure of the autocollimator at the PTB [**18**]. The air conditioner was running during two measurements (Fig. 6) and was switched off during two further measurements (Fig. 6). Like the stability scan, these measurements were performed overnight, starting at about 5 pm, and ending next day between 9 – 10 am. The results of these tests, shown in Figures 6 clearly demonstrate the need of a climate control system to guarantee thermal stability of the sample and instrument during a measurement series. It can be seen in Figure 6 that the system starts drifting after switching off the air conditioner. It takes about 6 hours to achieve a more or less stable state. In the morning around 8 – 9 am the overnight-achieved state of stability has disappeared by initial staff activity in the laboratory and heating up of the building. As in the stability scan, a higher level of random error is identified for the measurement time until about 8-9 pm, see Fig. 6.
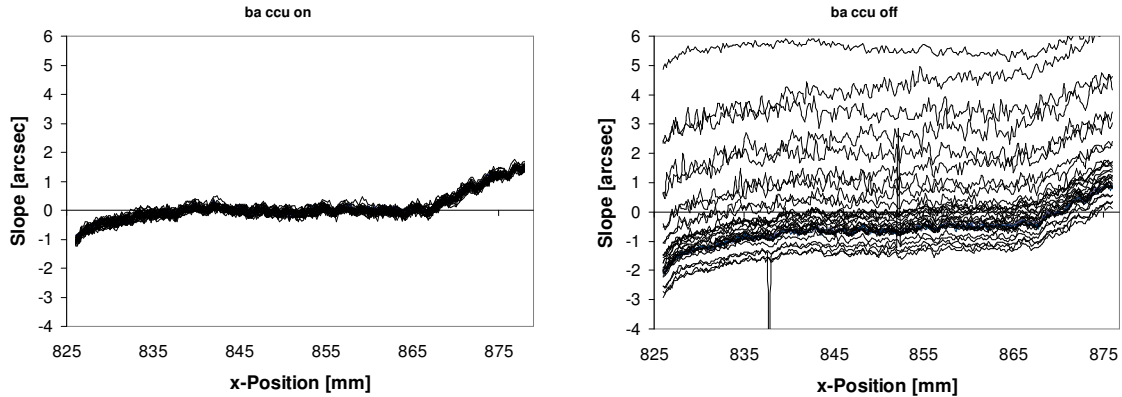
Figure 6: Left: Measurement from edge B (x_B=825mm) to edge A(x_A=878mm), air conditioner switched on, profile of residual slope for 30 single line scans forward and reverse trace.
Right: Measurement from edge B (x_B=825mm) to edge A x_A=878mm), air conditioner switched off, profile of residual slope for 33 single line scans forward and reverse trace.

In general, the noise level at night is clearly lower, see again Fig. 6. When the air conditioner is off the 12-minute periodic error, identified in the stability scan, will not influence the measurement. But this advantage is canceled out by a strong drift in the temperature of the test mirror and the different components of the instrument.

The level of random error of the DLTP is about 2-3 times higher than at the BESSY-NOM. Figure 7 shows 33/34 single line scans traced forward and reverse of the reference sphere by use of the DLTP and the NOM (with running climate control unit). The measurements were started 24 hours after alignment of the sample. Expressed as a 95% standard deviation (k=2) the reproducibility of the 33 DLTP measurements shown in Figure 10 is 0.143 µrad rms. The level achieved with the NOM is 0.053 µrad rms for a comparable set of 34 measurements.
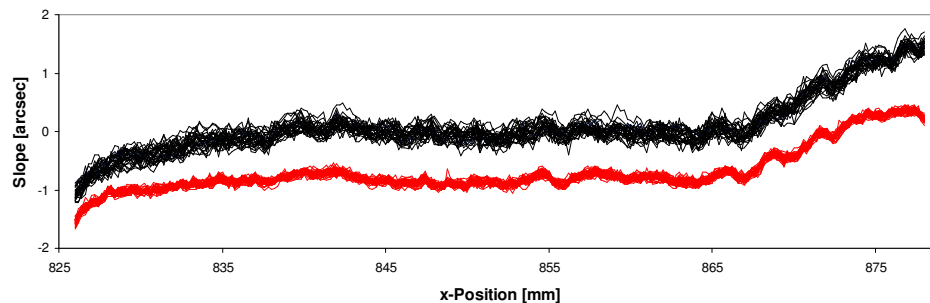
Figure 7: Comparison of BESSY-NOM (read) and ALS-DLTP (black) measurements (reference sphere R=10m, measurement from mirror edge B to edge A, climate control unit switched on), profile of residual slope for 33 single line scans forward and reverse traced, the waiting time before scan start was 24 hours after sample alignment. For a better visualization a shift of 0.8 arcsec is subtracted from the NOM-measurements.

Discussion of Results of First Measurement with the DLTP

Figure 8 shows the results of measurements obtained under different environmental conditions by use of the DLTP and the NOM. Both instruments yield comparable results for the radius of curvature and in part for the residual slope deviation, see also Table 1. The deviation for the measured radius of curvature values is between 0.006 and 0.04 %. Note that unlike the DLTP measurements presented here, the BESSY-NOM reference measurement was achieved by a stitching procedure of 4 times 4 sub-scans. For the reference measurement at the NOM, the well-characterized, linear view field of the autocollimator of ± 200 arcsec was applied. The reference curve is an average of 2 measurements (edge A to edge B and edge B to edge A).

Compared to the NOM measurements, a higher random error is observed for the DLTP measurements. The excellent agreement for the measured radius of curvature is a strong indication of the effective application of the calibration curve generated by the PTB. The subtraction of a measurement, traced

from mirror edge A to edge B, by a measurement traced from edge B to edge A, enables an estimation of the achieved measurement uncertainty and partial identification of the systematic error. Note this method is applicable only if the same x-travel range of the scanning carriage is used and for both scans the slope is detected by the same field of view of the autocollimator. Figure 9 shows the difference curves for the measurements with the DLTP for the air conditioner switched on and off, (shown in Fig 8) and for measurements at the NOM (air conditioner switched on). The differential curves of the DLTP measurements clearly displays systematic error structures in the profile (see Figure 9). Note that a significant part of the systematic error has a periodical (oscillation-like) structure. That is probably a result of a limited performance of the calibration of the autocollimator at a stationary baseline distance. While the standard working state (air conditioner switched on) shows an error level of about 0.5 µrad rms, a slightly lower level of 0.4 µrad rms is achieved for the switched off state. For additional observations see also Figure 11. Subtracting the reference curve, the residual slope profile of the single measurements shows a slightly lower noise level for the switched off state. But the gained improvement for the switched off state is marginal at best. Systematic error sections at both curves are specially labeled. Subtracting the curves for the switched on and off states, the rms value for the achieved deviation profile can be interpreted (very carefully) as the level of random error of the instrument (see Figure 10).
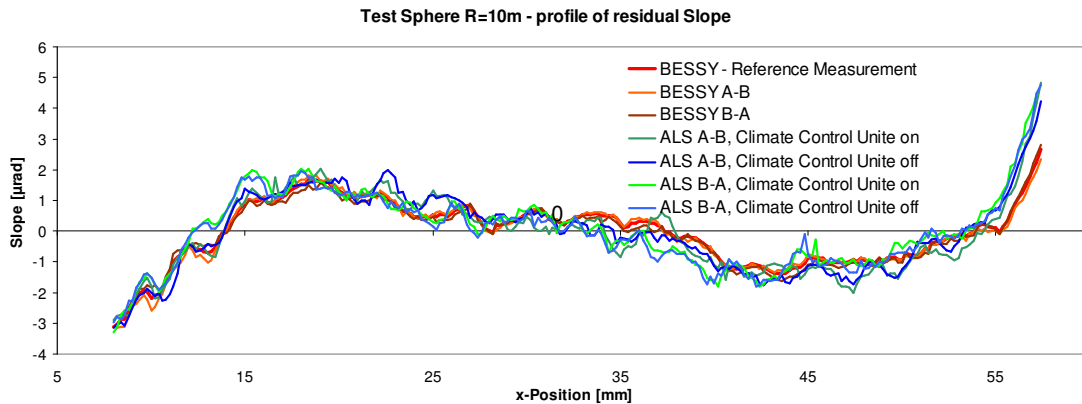
Figure 8: Reference sphere R=10m, profile of residual slope, for different measurements with the BESSY-NOM and the ALS-DLTP. With both instruments the line of interest was measured from edge A to edge B and after realignment from edge B to edge A. The measurements at the ALS were taken with the Climate Control Unit switched both on and off

Figure 12 shows the PSD spectra of the measurements on the 10m test mirror performed with the ALS-DLTP and the BESSY-NOM. Both spectra have very similar high spatial frequency behavior that can be expressed with an inverse power law of the second order. Such behavior is characteristic for a random noise related to air turbulence. Moreover, the same inverse power law describes the spectra of slow drifts.
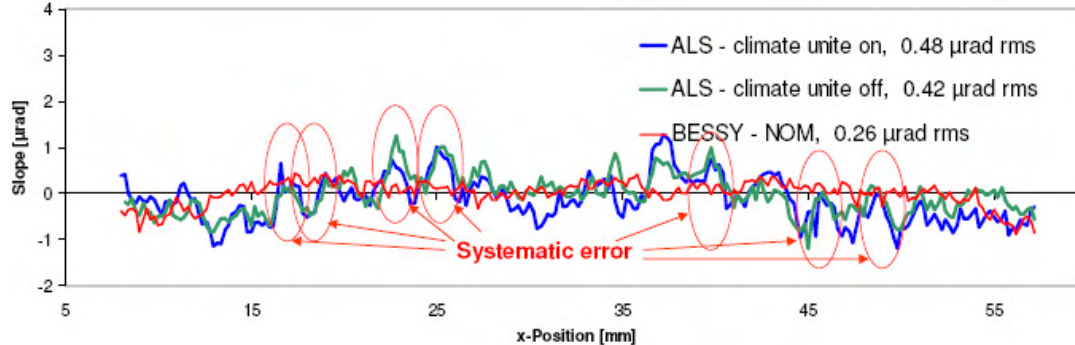
Figure 9: Residual error budget for different measurements with the ALS-DLTP and the BESSY-NOM. The measurements at the ALS were taken with Climate Control Unit switched both on and off.
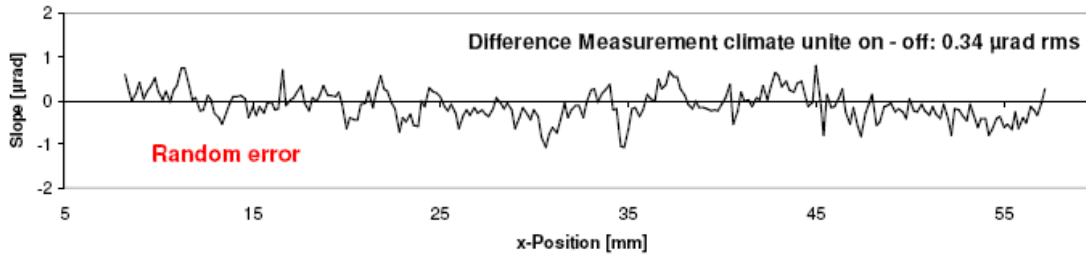
Figure 10: Difference of two measurements with the ALS-DLTP. The difference can be interpreted very carefully as the achieved level of random error for the ASMP of 0.34 µrad rms.

	Residual Slope [µrad rms]	Radius of Curvature [m]
BESSY NOM Reference Curve	1.02	9.9609
BESSY NOM A-B	1.05	9.9614
BESSY NOM B-A	0.97	9.9603
ALS DLTP A-B (CCU on)	1.25	9.9652
ALS DLTP B-A (CCU on)	1.27	9.9645
ALS DLTP A-B (CCU off)	1.22	9.9626
ALS DLTP B-A (CCU off)	1.22	9.9642

Table 1: Measurement results obtained by use of the ASMP and the NOM, for a reference sphere, R=10m, scan length: 50 mm, applied step size: 0.2 mm

The inspection of highly accurate plane mirrors characterized by residual slope errors below the 0.25 µrad rms limit is a specific challenge for metrology. In contrast to the measurement of curved surfaces, a very small field of view of the CCD-array of ± 2 µrad or less is used for the measurement. Thus, the error budget strongly depends on pixel errors and the local homogeneity of the CCD-array in general. Furthermore, vibrations and air-turbulence will limit the achievable accuracy. Figure 13 shows eight scans (blue curves) obtained by DLTP measurements on a super polished plane mirror for the MERLIN-beamline at the ALS [19]. The NOM measurements (red curves) were performed on a 310 mm long super polished mirror for beamline UE46 at BESSY [20]. In both cases the climate control unit was switched on and the measurements were started more than 24 h after alignment. The DLTP measurement shows a 3 times higher noise level than the NOM result. It can be assumed that this is mainly caused by the high level of vibration in the lab and the thermal cycling of the air conditioner. The achieved measurement result for the ASMP of 0.04 arcsec rms (0.2 µrad rms) is dominated by random noise. In this case pixel errors and the local homogeneity of the CCD-array are not relevant to the accuracy achieved. The inspected mirror under test is more accurate than the instrument used. The reproducibility of the 8 DLTP measurements is 0.06 arcsec rms (0.3 µrad rms). This result is obtained
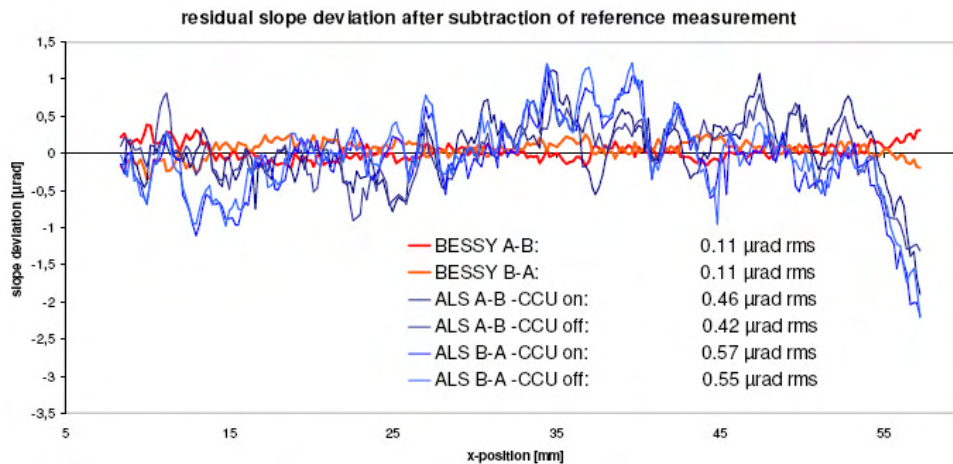
Figure 11: Profile of residual error and rms values for different measurements with the DLTP and the NOM after subtraction of the NOM reference measurement. For the BESSY-NOM measurements the Climate Control Unit was on.

324

when a 0-order fit is used to correct, in part the drift on the measurement. The 8 NOM measurements have a reproducibility of 0.02 arcsec rms (0.1µrad rms) for a 70 mm scan length.
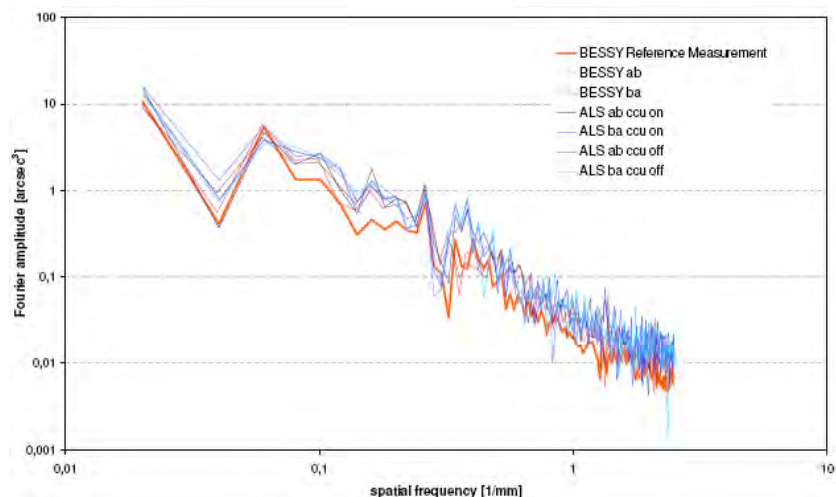
Figure 12:   PSD of residual slope data for different measurements on the R=10m reference sphere
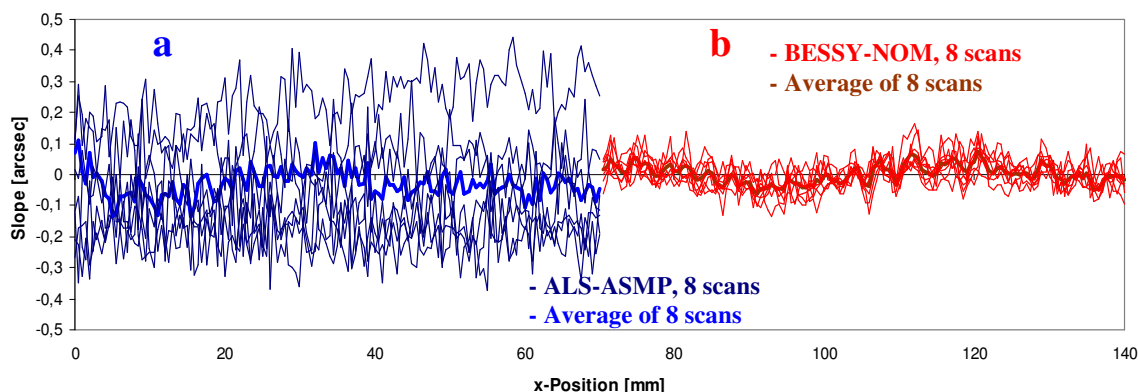
Figure 13: Measurements on plane substrates. Profiles of residual slope, a) 8 scans traced with the DLTP blue curves left and b) 8 scans traced with the NOM red curves right. The reproducibility is 0.06 arcsec rms, after drift correction, for the DLTP and 0.02 arcsec rms for the NOM. Both test substrates are chracterized by a residual slope of better than 0.04 arcsec rms (0.2 µrad rms).

Conclusions and Outlook

The instrumental set up of a Developmental Long Trace Profiler[1] assembled, preliminary aligned, and inspected in June 2008 at the ALS enables the slope metrology of synchrotron optics with an estimated measurement uncertainty of about 0.5 µrad rms for significantly curved optics. A lower measurement uncertainty in the range of 0.25-0.3 µrad rms can be achieved in the case of plane optical elements.

It was shown that the use of calibration curves gained by calibration of the autocollimator at the PTB provides an excellent agreement with measurement results of the BESSY-NOM. Comparing the results for the measured radius of curvature, of a R = 10 m sphere, a deviation of less than 0.04 % is observed. It was shown that the method of curve correction by calibration is applicable in general. Some fitting errors in the software used have been observed during the commissioning (see Figure 6), and will be debugged in the near future.

The achieved performance of the instrument can be improved by further upgrade of the laboratory environment. It is to be noted that the measuring device, data acquisition method, and the surrounding environment have to be understood as one unit of operation. The air conditioning controller located close to the DLTP should be replaced by a more advanced system. A new climate control unit should be placed at a larger distance from the metrological devices in the laboratory, to avoid interfering parasitic effects. The limited quality of the beam guiding optics (pentaprism) was shown. It can be

assumed that a part of the shown systematic error (see Figure 9 and 11) is caused by the inhomogeneity of the pentaprism. It can be easily replaced by a double mirror as done at the NOM. A more accurate traverse and stone pillars instead of metal parts, as currently in use, will improve the physical stability of the instrument. An upgraded hutch to cover the measuring set up will provide better shielding against environmental instability. However, better shielding would significantly increase the characteristic time of the system that describes the temperature transition process after opening/closing the hutch. For an easier alignment of optical components a more robust/stable alignment laser would be helpful. A topic of the future work is the high precision characterization and calibration of the instrument. Highly accurate metrology devices have to be calibrated for the specific conditions during a measurement. Thus, the development of dedicated calibration tools is mandatory. A first set up of a vertical angle comparator has been realized at BESSY [21] and shown to be reasonable in its use for additional calibration of the NOM. A more sophisticated design of Universal Test Mirror (UTM) was proposed recently [22] and is under development by a cooperation of the ALS, BESSY and the PTB. The presented results can not provide a complete characterization of the instrument. Further investigation is required. Additional measurements of well known reference optics, provided by the **G**lobal high accuracy **R**ound **R**obin (GRR) [17] cooperation are recommended. Stability scans for different pentaprism-to-autocollimator distances as well as variations of the diaphragm size and position are recommended. Using the autocollimator the straightforward movement of the carriage system can be characterized.

Recent Developments

After the first DLTP setup was assembled the movable pentaprism was precisely re-aligned by R. Geckeler (PTB) [23] using his original procedure for alignment [14]. The positive effect of the re-alignment [24, 25], was demonstrated by measuring a spherical mirror (R=15 m) supplied by InSync. Inc. In addition, the application of optimal scanning strategies enables a highly accurate metrology by use of the DLTP [25], (related to scanning strategies see also [26]). Finally, the high performance of the ALS-DLTP after the last upgrade [27] was shown by measuring the GRR reference sphere S3 (R=1280 m) [28]. The result of the measurement is shown in Fig. 14. The resulting residual slope traces obtained with the DLTP and the NOM are of excellent coincidence with an absolute deviation of less than 0.1 µrad. A further cross check, of DLTP and NOM by use of the 15 sphere is in preparation. Note: this test will cover a much larger view filed of the sensors than applied for the S3 sphere.
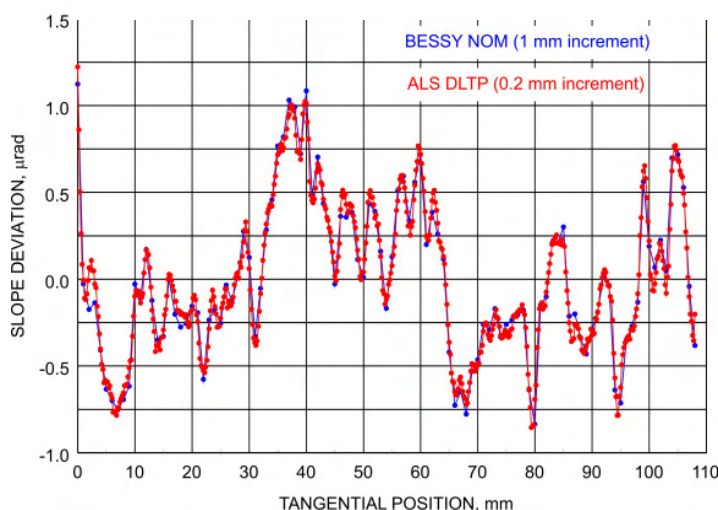
Figure 14: Profile of residual error and rms values for different measurements with the DLTP and the NOM after subtraction of the NOM reference measurement. For the BESSY-NOM measurements the Climate Control Unit was on.

[1] Note the DLTP does not use a LTP-head for performing slope measurements. The used sensor is an autocollimator made by Moeller Wedel GmbH

Acknowledgements

References:

1   E. Debler, K. Zander, *Ebenheitsmessung an optischen Planflächen mit Autokollimationsfernrohr und Pentagonprisma*, PTB Mitteilungen Forschen + Prüfen, Amts und Mitteilungsblatt der Physikalisch Technischen Bundesanstalt, Braunschweig und Berlin, 1979, pp. 339-349

2   Frank Siewert, Tino Noll, Thomas Schlegel, Thomas Zeschke, and Heiner Lammert, *The Nanometer Optical Component Measuring machine: a new Sub-nm Topography Measuring Device for X-ray Optics at BESSY*, AIP Conference Proceedings 705, American Institute of Physics, Mellville, NY, 2004, pp. 847-850

3   H. Lammert, T. Noll, T. Schlegel, F. Siewert, T. Zeschke, *Optisches Messverfahren und Präzisionsmessmaschine zur Ermittlung von Idealformabweichungen technisch polierter Oberflächen*, Patent No.: DE 103 03 659 (28 July 2005)

4   F. Siewert, H. Lammert, T. Zeschke, *The Nanometer Optical Component Measuring Machine*; in: Modern Developments in X-ray and Neutron Optics, Springer 2008

5   R.D. Geckeler, I. Weingärtner, *Sub-nm topography measurement by deflectometry: flatness standard and wafer nanotopography*, Proc. of SPIE, 4779, Bellingham, WA, 2002, pp. 1-12

6   Jens Illemann and Matthias Wurm, *Deflectometric Measurements of Synchrotron-Optics for Postprocessing*, AIP Conference Proceedings 705, American Institute of Physics, Mellville, NY, 2004, pp. 843-846

7   Ralf D. Geckeler, *ESAD Shearing Deflectometry: Potentials for Synchrotron Beamline Metrology*, Proc. of SPIE, 6317, Bellingham, WA, 2006,

8   P. Takacs, S. N. Qian and J. Colbert, *Design of a long trace surface profiler*, Proc. of SPIE, 749, Bellingham, WA, 1987, pp. 59-64

9   P. Takacs, S. N. Qian, *Surface Profiling interferometer*, US patent No.U4884697, Dec. 5, 1989

10 F. Siewert, H. Lammert, T. Noll, T. Schlegel, T. Zeschke, T. Hänsel, A. Nickel, A. Schindler, B. Grubert, C. Schlewitt, *Advanced metrology: an essential support for the surface finishing of high performance x-ray optics*, in Advances in Metrology for X-Ray and EUV Optics edited by Lahsen Assoufid, Peter Z. Takacs, John S. Taylor, Proc. of SPIE, Vol. 5921-01, Bellingham, WA, 2005,

11 J. Kirschmann, E. E. Domning, G. Y. Morrison, B. V. Smith, V.V. Yashchuk, Precision Tiltmeter as a Reference for Slope Measuring Instruments, Scholarship Repository, Univ. of California , Berkeley 2008

12 http://www.moeller-wedel-optical.com/El-Autocolimators/G_Elcomat3000.htm

13 Shinan Qian, Werner Jark, Peter Z. Takacs, *The penta-prism LTP: A long-trace-profiler with stationary optical head and moving penta prism*, Rev. Sci. Instrum. 66 (3), March 1995

14 R.D. Geckeler, *Optimal use of pentaprisms in highly accurate deflectometric scanning*, Meas.Sci.Technol., 18(2007), pp. 115-125

15 J. Susini, R. Baker and A. Vivo, *Optical metrology facility at the ESRF*, Rev. Sci. Instrum. 66 (2), February 1995

16 A. Rommeveaux, M. Thomasset, D. Cocco, F. Siewert, *First report on a European round robin for slope measuring profilers*, Proc. of SPIE, 5921-01, Bellingham, WA, 2005

17 F. Siewert et al., *Global High Accuracy intercomparison of Slope Measuring Instruments*, AIP Conference Proceedings 879, American Institute of Physics, Mellville, NY, 2007, pp. 706-709

18 R.D. Geckeler, I. Weingärtner, A. Just, R. Probst, *Use and traceable calibration of autocollimators for ultra-precise measurement of slope and topography*, Proc. of SPIE, Vol. 4401, Bellingham, WA, 2001, pp. 184-195

19 MERLIN (**M**ili-**E**lectron-volt **R**esolution beam**LIN**e) project developed by the ALS Scientific Support Group, Beamline 4.0.1: www.als.lbl.gov/als/techspecs/ bl4.0.1.html

20 F. Siewert, *BESSY-Meßprotokoll für planen Spiegel M2 – UIE46XM-Beamline*, Berlin, 2007

21 F. Siewert, *Calibration: Calibration and Autocalibration*, 3rd International Workshop on Metrology for X-ray Optics, Daegu, Korea, June 2006

22 V. Yashchuk, W. McKinney, T. Warwick, T. Noll, F. Siewert, T. Zeschke, R. Geckeler, *Proposal for a Universal Test Mirror for Characterization of Slope Measuring Instruments*, Proc. of SPIE, Vol. 5856-121, 2007

23 S. Barber, R.D. Geckeler, Tony Warwick and V. Yashchuk, *Optimal alignment of Pentaprism in DLTP,* LSBL Note LSBL-924 (September 12, 2008)

24 V. Yashchuk, J. Kirschmann, G. Y. Morrison, B. V. Smith, E. E. Domning, F. Siewert, T. Zeschke, R.D. Geckeler, A. Just, *Autocollimator based slope measuring profiler (a la BESSY NOM) under development at the ALS OML ,* LSBL-920 (June 26, 2008)

25 V. Yashchuk, *Optimal Scanning Strategies for Slope Measuring Profilers, (in preparation)*

26 H. Lammert, *Subnanometer Accuracy Measurements with the LTP at BESSY*, Int. Workshop on Metrology for X-ray and Neutron Optics, Chicago 2000

27 V. Yashchuk, *DLTP Performance Test with a 1280-m Spherical Reference Mirror,* LSBL Note LSBL-931 (January 12, 2009)

Time-of-flight electron spectroscopy in multi-bunch mode

Johannes Floß,[1] Marko Förstel,[2,3] Toralf Lischke,[2] Tiberiu Arion,[2] Melanie Mucke,[2] Brandon Jordon-Thaden,[3] Andreas Wolf [3] and Uwe Hergenhahn[2,a]

1: Freie Universität Berlin, Institut für Chemie und Biochemie, Takustr. 3, 14195 Berlin
2: Max-Planck-Institut für Plasmaphysik, EURATOM association, Boltzmannstr. 2, 85748 Garching
3: Max-Planck-Institut für Kernphysik, Saupfercheckweg 1, 69117 Heidelberg

Electron spectroscopy carried out via a time-of-flight (TOF) measurement offers some advantages compared to the use of a conventional dispersive spectrometer. Most notably, the parallel acquisition of a band of electron energies can be accomplished. Additionally, by a suitably shaped magnetic field, a large solid angle acceptance of almost 4π sR is achievable ('magnetic bottle spectrometer', [1,2]). The times-of-flight of the electrons for typical instrument dimensions range from some ns to some µs. The use of a pulsed light source with a low repetition rate, such as a laser or a synchrotron radiation source running in single-bunch mode, therefore seemed a necessity for this type of spectroscopy.

In this report we give first results from an alternative approach, in which the time structure of the fill pattern of BESSY is removed from the TOF spectra by a deconvolution procedure. A typical BESSY fill pattern, as measured by time-correlated single photon counting [3], is shown in Fig. 1. Mathematically the deconvolution of such functions from a signal recorded as a function of time is an exact operation. In practice however the inevitable noise on any experimental data renders a straight-forward inversion of the convolution impossible. Some strategies used to overcome these problems are frequency filtering in Fourier space, deconvolution guided by the maximum entropy principle and least squares analysis of the measured data using a parametrized form of the underlying deconvoluted signal ('peak fitting').

In our experiment, we have measured the TOF photoelectron spectra of He and Ne using a magnetic bottle spectrometer (Fig. 2) at the TGM4 beamline during multi-bunch operation. For analysis, spectra were modelled by 1-4 Gaussian peaks of variable width and position, which were convoluted by the fill pattern recorded simultaneously by the BESSY control system used to monitor the hybrid bunch position. The parameters of the Gaussian curves were adapted to optimally reproduce the measured TOF spectra (Fig. 3).

Results for the photoelectron spectrum of Ne excited with 110 eV photons are shown in Fig. 3. At this photon energy, the spectrum is dominated by photoionization of the 2p main line. Excitation of this feature by the hybrid bunch can be visually distinguished. It is therefore most interesting whether the deconvolution algorithm reveals any further photoelectron lines, such as the 2s inner valence line. The deconvoluted spectrum (Fig. 3 right hand side panel) does show a second, intense photoelectron line, which after time-to-energy conversion (not shown) appears however at a binding energy of 73 eV. This somewhat unexpected result can be explained by a Xe contaminant in the gas inlet system from a preceding experiment – this gas gives rises to an intense photoelectron line from ionization of the 4d orbitals, with reference binding energies of 67.5 and 69.5 eV.

These first results show that deconvolution TOF spectroscopy in multi-bunch mode has some potential, which we will explore further by comparison of identical spectra measured in multi and single bunch.

[1]   P. Kruit and F. H. Read, J. Phys. E **16**, 313 (1983).
[2]   P. Lablanquie, L. Andric, J. Palaudoux, U. Becker, M. Braune, J. Viefhaus, J. H. D. Eland, and F. Penent, J. Electron Spectrosc. Relat. Phenom. **156-158**, 51 (2007).
[3]   K. Holldack, M. v. Hartrott, F. Hoeft, O. Neitzke, E. Bauch, and M. Wahl, in *Advanced Photon Counting Techniques II*, edited by W. Becker (SPIE, 2007), Vol. 6771, p. 677118.

[a] Mail address: IPP, c/o BESSY, Albert-Einstein-Str. 15, 12489 Berlin; email: uwe.hergenhahn@ipp.mpg.de
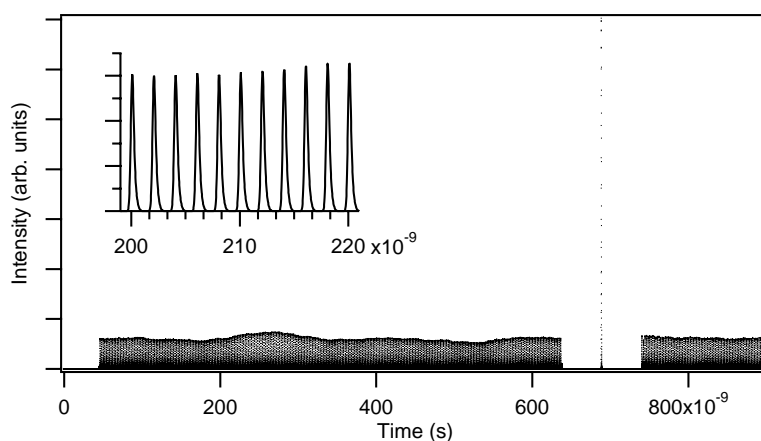
Figure 1: Fill pattern of BESSY in multibunch operation, recorded with an avalanche photodiode (APD). The inset of the figure shows the 2 ns spacing of the individual photon bunches. Here, the true pattern is broadened by the APD risetime of approx. 100 ps.
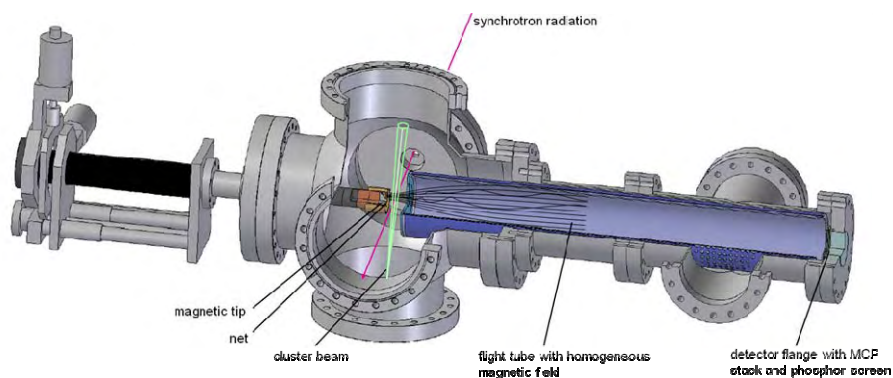
Figure 2: Sketch of the magnetic bottle time-of-flight spectrometer. The synchrotron radiation direction, gas jet and central axis of the spectrometer are all perpendicular to each other. In the set-up actually employed, the spectrometer was mounted vertically pointing upward.
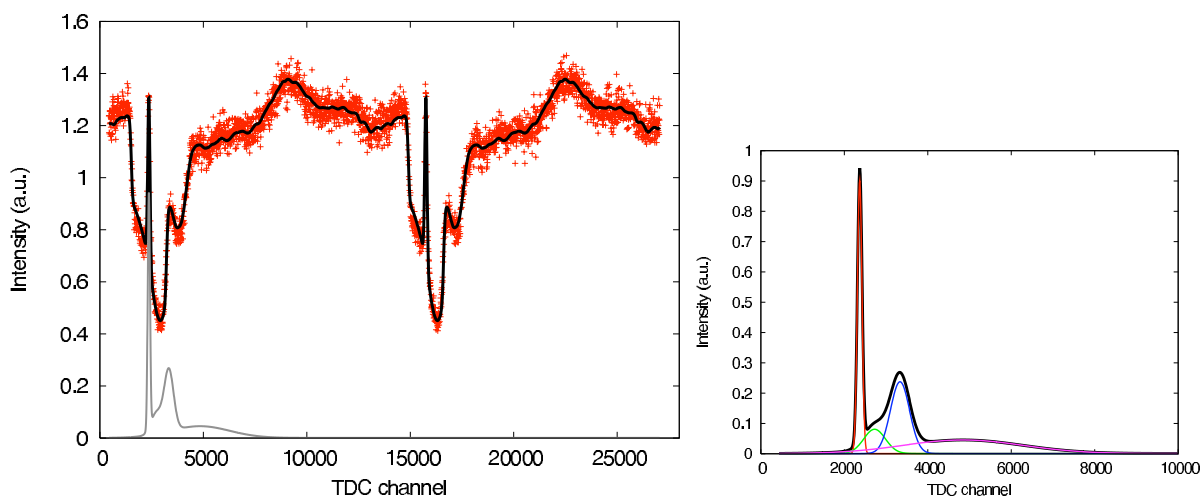
Figure 3: Time-of-flight spectrum of Ne photoelectrons at 110 eV kinetic energy (left panel) and deconvoluted structure consisting of four Gaussians (right panel).

329

The new BESSY TXM for cryo-tomography and nano-spectroscopy

P. Guttmann, S. Heim, S. Rehbein, S. Werner, G. Schneider

Helmholtz-Zentrum Berlin für Materialien und Energie, Elektronenspeicherring BESSY II,
Albert-Einstein-Str. 15, 12489 Berlin

1. Introduction

The BESSY x-ray microscopy group has developed a new full-field transmission x-ray microscope (TXM) which employs an advanced x-ray optical concept [1]. In our new BESSY microscope, a standard monochromator beam line provides a high energy resolution of up to 10,000 which permits NEXAFS studies. An elliptically shaped mono-capillary is used to form the hollow cone illumination necessary for sample illumination and to match the aperture of the objective.

The new TXM also significantly improves the possibilities to study cryogenic or heated samples for life and materials sciences. Taking advantage of the developments over the last decades in cryo electron tomography, the sample stage of the TXM is an adaptation of a state-of-the-art TEM stage. Therefore, the microscope provides the same excellent mechanical accuracy and temperature stability known from cryo TEM, a tilt range of ±80° and lateral travel ranges of ±1mm with a bidirectional reproducibility <15 nm. The translation axes are mounted with respect to the rotation axis in order to make it possible to establish eucentricity for any part of the specimen, i.e. bring any point of the sample onto the spatially fixed tilt axis. Together with the high photon flux and the fully automated operation of the microscope's control software, the acquisition time for a full tomography tilt series is reduced to less than 20 minutes.

2. The way towards sub-10 nm real space x-ray imaging

2.1 Improvements of the condenser
The parameters of the ellipsoidal capillary are determined by the beam divergence of the monochromator and by the desired aperture matching to the high resolution objective of the microscope. Ray tracing calculations show that the slope error of the capillary should be below 100 µrad and the alignment accuracy in the tilt angle of the capillary with respect to the incoming beam should be better than 100 µrad [2]. A single-bounce ellipsoidal glass capillary fabricated and evaluated by optical measurements during and after fabrication by Xradia was applied [3]. The resulting slope error of 80 µrad is well below the limit calculated by ray tracing. The x-ray performance of the capillary was tested with the BESSY x-ray microscope at the U41-FSGM beam line at a photon energy of 510 eV. Firstly, the capillary was adjusted to get the smallest possible focus. Figure 1a shows an x-ray image of the focus which is in size 620 nm x 990 nm (FWHM-values). Secondly, a Siemens star test pattern with structure sizes down to 25 nm was used to demonstrate the imaging capabilities of the x-ray microscope using a capillary as condenser. To obtain a large homogeneously illuminated object field, the condenser is helically scanned. Figure 1b shows the x-ray image of this test pattern using a micro zone plate objective with 30 nm outermost zone width.
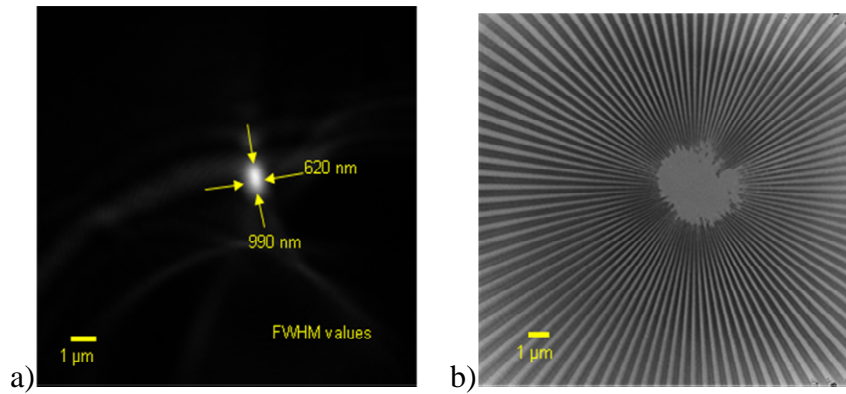
Fig. 1: a) Focus of the capillary imaged by a micro zone plate at $\Delta E/E \approx 9000$, 510 eV, 100 ms exposure time. b) Test pattern imaged by a micro zone plate (both fabricated at BESSY by S. Rehbein, S. Werner) at $\Delta E/E \approx 9000$, 510 eV, 2 s exposure time with scanned condenser.

To analyze the performance of the new condenser, quantitative measurements were performed to measure the efficiency of the capillary. The focusing efficiency of the capillary was measured to be 80% for a photon energy of 510 eV. Note, this value exceeds the efficiency of zone plate condensers by nearly an order of magnitude.

2.2 Developments of the x-ray objective

Fresnel zone plates are the key optical elements for soft and hard x-ray microscopy. The resolving power of zone plates scales with the order of diffraction. By employing high orders of diffraction, it is possible to increase the resolution without the need of manufacturing smaller outermost zone widths. In order to demonstrate the resolution achievable with high order imaging, we used a multi-layer test sample with B_4C/Cr lines and spaces of 5 different widths down to 7.8 nm. Figure 2 shows the result of a resolution test experiment performed with the BESSY TXM at 700 eV photon energy with a 25nm zone plate operating in the 3rd order. Note that lines and spaces of 14.3nm are clearly resolved while the 11.0nm structures still show some modulation.
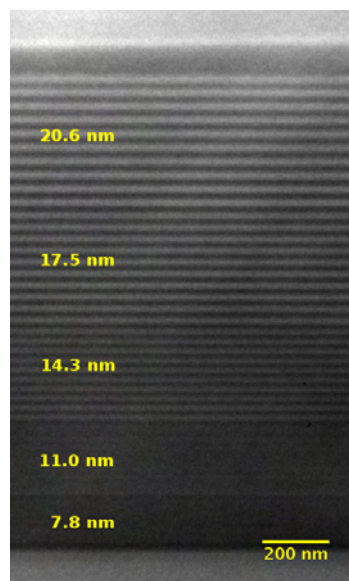
Fig. 2. B_4C/Cr multilayer test structure imaged in the 3rd diffraction order using a $dr_N = 25nm$ zone plate, E = 700 eV, E/ΔE =1732, t_{exp} = 15.7 s

Until now no sub-20 nm (half-pitch) resolution x-ray images were presented in the literature from extended relevant samples. To demonstrate the improved resolution in the 3rd order of diffraction for relevant samples, an advanced copper interconnect stack which was thinned by FIB milling to a thin lamella of about 1.5 µm thickness was imaged at E = 900 eV. In this image the cut-off frequency corresponds to a feature size of about 12 nm which is in good agreement with the obtained resolution demonstrated with the multilayer structures [4].

For short exposure times and minimum radiation load of the specimen the diffraction efficiency of the zone plate objectives has to be maximized. As the efficiency strongly depends on the height of the diffracting zone structures the achievable aspect ratio of the nanostructures determines these limits. To reach aspect ratios ≥ 20:1 for high efficient optics we superimposed zone plates on top of each other [5]. With this approach the final aspect ratio is only limited by the number of stacked zone plate layers. For the stack process several nano-structuring process steps have to be developed and/or improved [6]. In first experiments two layers of nickel zone plates were stacked on top of each other. The height of the single layers was about 160 nm corresponding to a total height of 320 nm for the stacked structures. After electroplating of the second layer, a trench was cut into the nanostructures by FIB to allow a look at the cross section (thanks to Y. Ritz and D. Chumakov, AMD Dresden). The stacked zone plate with an outermost zone width of 30 nm is shown in Fig. 3. A mismatch of about 30 nm between the first and the second zone plate layer is observed. The second layer has not been polished yet and is still slightly overplated. The required overlay accuracy is ≤ 2dr_n/7 to avoid a degradation of the zone plate efficiency and resolution [7]. This means our achieved overlay accuracy has to be improved in order to fabricate efficient high resolution zone plates. Recently, an overlay error of about 2 nm was reported [8] showing that a sufficient accuracy is possible with advanced e-beam lithography. For this reason a new state-of-the-art e-beam writer is ordered and will be setup in the second semester of 2009. The polished zone plates are fabricated on a thick substrate due to the mechanical stability for the Chemical Mechanical Polishing (CMP) process step. For using this zone plates as x-ray optics the substrate has to be thinned afterwards by wet chemical etching. A process to protect the structures during the backside etching is under development.
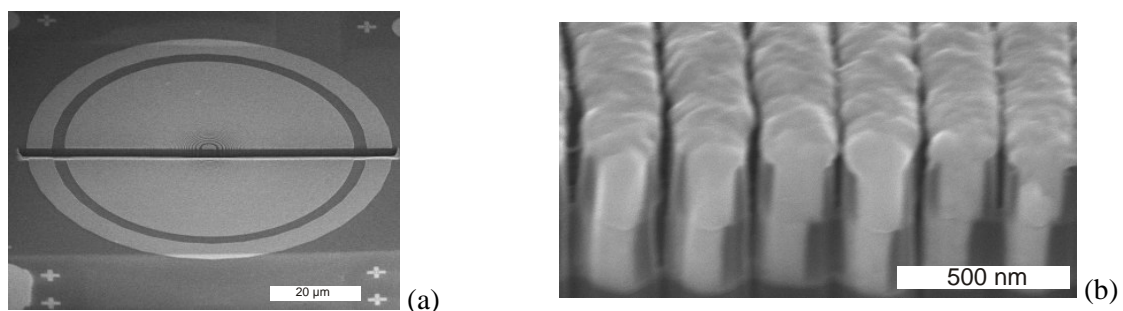
Fig. 3: SEM micrograph of a stacked nickel zone plate with 30 nm outermost zone width. (a) Overview with cross marks and FIB produced trench. (b) Stacked zones are slightly overplated.

3. Cryo-tomography of frozen-hydrated mammalian cells

Full-field x-ray microscopy has proven to be an excellent tool for 3-D studies of whole frozen hydrated biological samples [9, 10, 11]. However, tomography of flat grown mammalian cells was not possible as they do not fit into glass capillary sample holders. Our new TXM overcomes this severe limitation, because its optical concept requires no monochromator pinhole close to the object plane. In the new TXM, it is possible to study adherent cells grown on TEM grids. As an example, Fig. 4 shows one slice of a tomography reconstruction of a frozen-hydrated mouse cell imaged at 510 eV. The voxel size is 9.8 nm, which is also the thickness of the slice. The nuclear membrane with its double structure and internal structures of the nucleus are visualized.
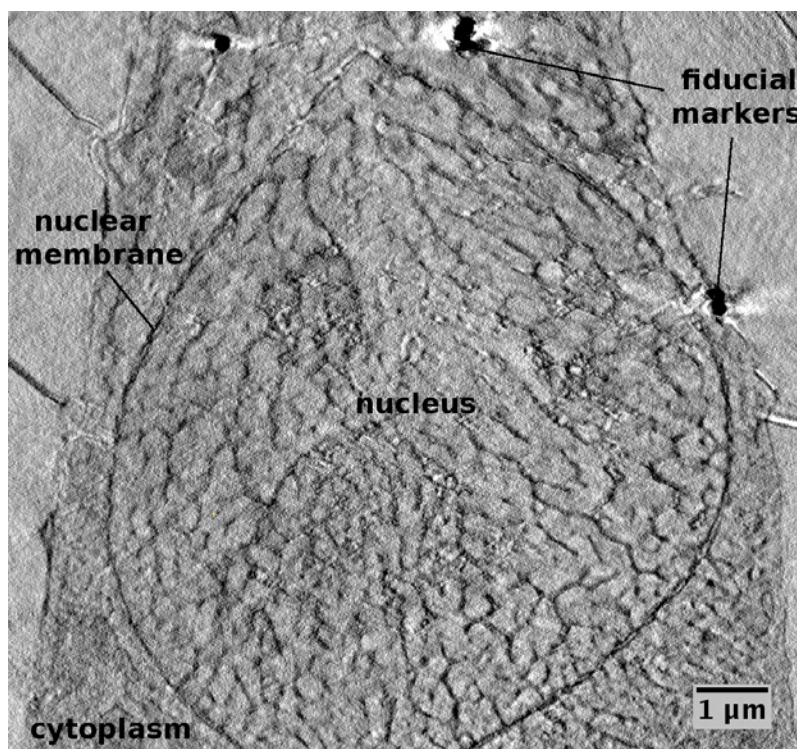
Fig. 4: Slice through the reconstructed local linear absorption coefficient of the nucleus of a mouse adenocarcinoma cell; 131 projections recorded at E = 510 eV.

4. Stress-migration in advanced copper interconnect structures

Besides electromigration in semiconductor devices, stress migration is one of the most important failure mechanisms in advanced copper interconnects. As a result of lattice vacancy migration due to local mechanical stress at the via/plate interface small holes called voids form. However, the void formation mechanism is not fully understood. X-ray microscopy permits to study dynamic void evolution during stress migration. An exemplary micrograph from the stress-migration studies is shown in Fig. 5. This slice through the reconstructed volume of a 1 µm thick IC lamella shows that the void is located in the copper interconnect line directly below the via. Depending on their size, larger voids lead to unacceptable resistance increase and ultimately cause open circuit or other circuit malfunction.
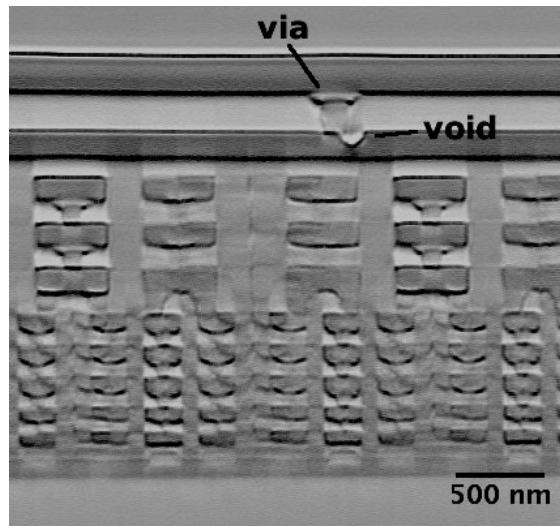
Fig. 5: Slice from a tomographic reconstruction of a stress migration sample imaged at E = 700 eV, visualizing the location of the void close to the via.

5. Nano-spectroscopy of TiO$_2$ particles

The spectromicroscopy capabilities of the new TXM are demonstrated with TiO$_2$ particles. An image stack was taken in the energy range from the Ti L-edge up to the oxygen K-edge with an energy resolution of E/ΔE $\geq$ 7214 (Fig. 6). Note the combined excellent spectral and spatial resolution in a large field of view.
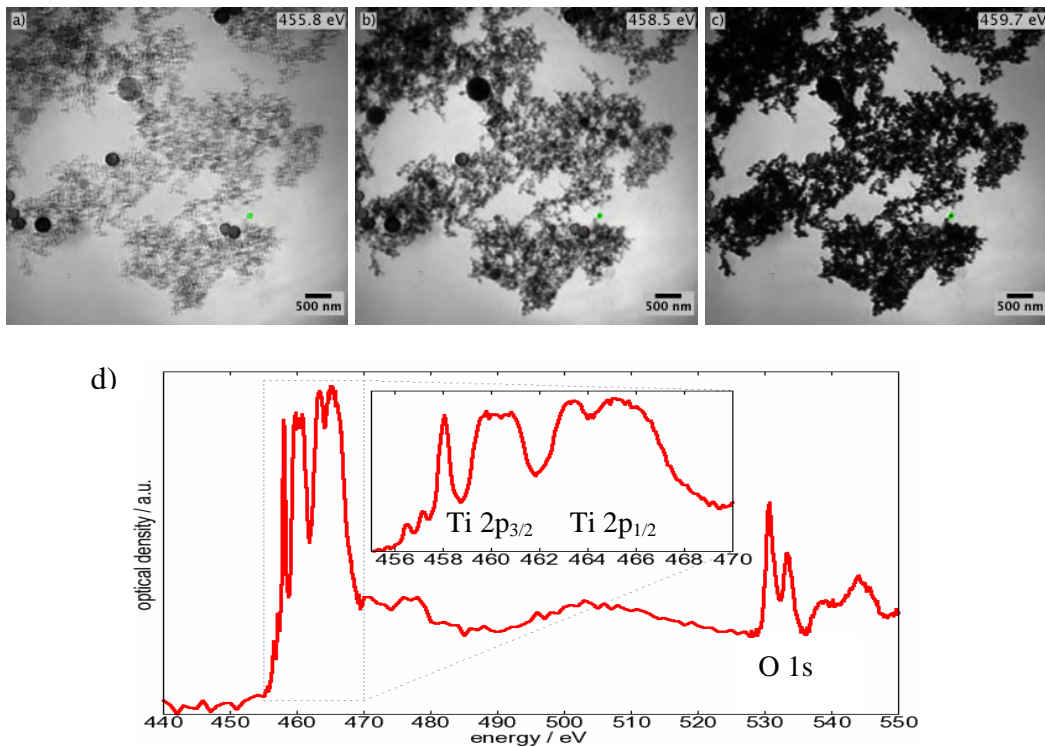
Fig. 6: a) - c) Selected micrographs of TiO$_2$ particles imaged at different photon energies. d) Spectrum at the position of the green dot in a)-c) for the whole energy stack (440 - 550 eV, E/ΔE = 7214, total 380 images).

Acknowledgements

References

1. P. Guttmann, S. Heim, S. Rehbein, S. Werner, B. Niemann, R. Follath, G. Schneider: X-ray microscopy at the new U41-FSGM beam line, BESSY Annual Report 2007 (2008), 297 - 300

2. P. Guttmann, X. Zeng, M. Feser, S. Heim, W. Yun, G. Schneider: Ellipsoidal capillary as condenser for the BESSY full-field x-ray microscope, submitted to XRM 2008 proceedings

3. Zeng X, Duewer F, Feser M, Huang C, Lyon A, Tkachuk A, Yun W., Ellipsoidal and parabolic glass capillaries as condensers for x-ray microscopes, Appl Opt. 2008 May 1; 47(13):2376-81

4. S. Rehbein, S. Heim, P. Guttmann, S. Werner, and G. Schneider: Ultrahigh-Resolution X-Ray Microscopy with Zone Plates in High Orders of Diffraction, submitted

5. S. Werner, S. Rehbein, P. Guttman, S. Heim, G. Schneider: Towards stacked zone plates, submitted to XRM 2008 proceedings

6. S. Rehbein, P. Guttmann, S. Werner and G. Schneider, J. Vac. Sci. Technol. B 25 (1789), 2007

7. G. Schneider, Appl. Phys. Lett. 73, 599 (1998)

8. W.Chao, B. D. Harteneck, J. A. Liddle, E. H. Andersson and D. T. Attwood, Nature (London) 435, 1210 (2005)

9. Schneider G, Ultramicroscopy 75 (1998) 85 - 104

10. Weiss D, Schneider G, Niemann B, Guttmann P, Rudolph D, Schmahl G, Ultramicroscopy 84 (2000) 185 - 197

11. Schneider G, Anderson E, Vogt S, Knöchel C, Weiss D, LeGros M and Larabell C, Surf. Rev. Lett. 9 (2002) 177 - 183

Project title:

X-ray microCT study of *ex vivo* engineered heart tissue

Objectives (max. 200 words)

The aim of this study is to obtain 3D visualization of spatial distribution of injected neonatal rat cardiomyocytes (labelled cells) inside the heart tissue of infracted mice.

Achievements (max. 500 words)

The microCT was used to image and characterize 3D distribution of injected cells plated on collagen scaffolds inside the heart tissue of infracted mice (Fig. 1a). 3D visualization of the spatial distribution of the grafted cells in respect with the host myocardium, veins and capillary system was obtained (Fig. 1b). In particular, the X-ray absorption of the labeled cells by magnetic iron oxide nanoparticles was higher than the other heart tissues, allowing their visualization as bright spots in the 2D images (Fig. 1c). These slice images were compiled and analyzed to render 3D images and to obtain a better visualization of cell distribution within the samples. 3D visualization of the spatial distribution of the grafted cells is shown on Fig. 1d.
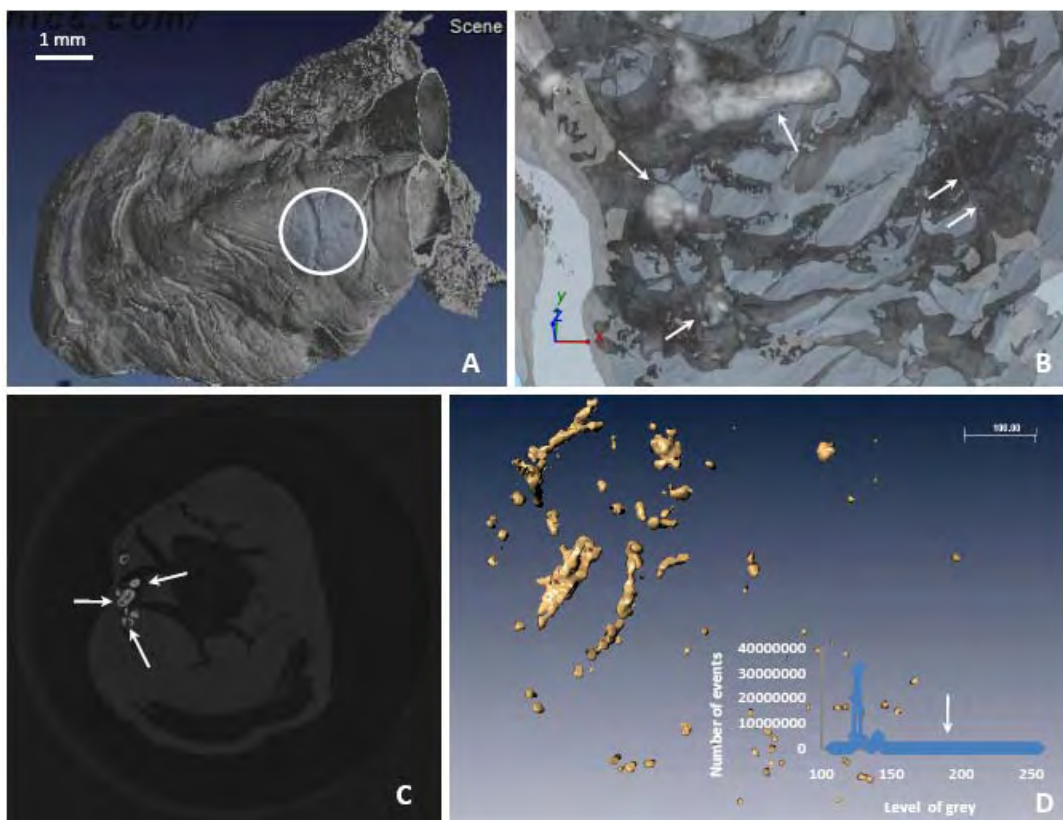
Fig. 1. MicroCT image of the infracted heart (a). 3D image of the spatial distribution of the grafted cells in respect with the host myocardium, veins and capillary system (b). 2D original slice (c). 3D visualization of the spatial distribution of the grafted cells (d).

1

This result is of special importance that after injection cell population is manly heterogeneous distributed at earlier stage as well as was located in one area. The 3D images so obtained constituted a very innovative progress, as compared to the usual 2D histological images, which do not provide the correct position of the cardiomyocytes within the heart. Moreover, this is potentially interesting for future research on determining time variable (early and late differentiation stage), because through the microCT we hope to be able to observe in 3D the migration of cells with respect to the cardiac vessel, with important structural details not observable by the conventional bidimensional imaging techniques. However, we should note that due to a complicate nature of the investigated object the data treatment is still in progress.

2

Morphological Characterization of Articular Cartilage on the Cellular Level

Rolf Zehbe[1], Christoph Brochhausen[2], Astrid Haibel[3], Franziska Schmidt[1], Ulrich Gross[4],

C. James Kirkpatrick[2], Heinrich Riesemeier[3], Helmut Schubert[1]

[1] Technische Universität Berlin, Institute of Materials Science & Technologies, Englische Strasse 20, 10587 Berlin, Germany

[2] GKSS Research Centre at DESY, Petra III, Notkestrasse 85, 22607 Hamburg, Germany

[3] BAM, Federal Inst. for Materials Research & Testing, Division I.3, Richard-Willstätter-Strasse 11, 12489 Berlin, Germany

[4] Charité University Medicine Berlin, Biomaterials Laboratory, Aßmannshauser Strasse 4-6, 14197 Berlin, Germany

[5] Johannes Gutenberg University, Institute of Pathology - REPAIRlab, Langenbeckstrasse 1, 55101 Mainz, Germany

[1] Corresponding author: Rolf Zehbe (rolf.zehbe@tu-berlin.de)

Introduction:

Articular cartilage covers the end of bones allowing their relative movement. It forms a smooth, glassy tissue, also known as hyaline cartilage, showing a characteristic zonal structure of the extracellular matrix components and specialized cells, the chondrocytes. Depending on the localization, the chondrocytes are either stretched along the surface (superficial zone) or are shaped elliptical or rounded in the middle zone, where some cells form isogeneous cell groups. Chondrocytes are generally surrounded by a low density fluidic region called lacuna.

In deeper regions the extracellular matrix proteins become more perpendicularly oriented to the surface. Further below, calcification increases, which is indicated by the so called tide mark. Ultimately, this calcification results in the formation of the subchondral bone. Unlike the cartilagineous tissue region, the subchondral bone is vascularised and varies in cell types (osteoblasts, osteoclasts, osteocytes, fatty cells and cells attributing to the nervous system).

The tissue morphology is well investigated via conventional means, including light microscopy and electron microscopy. Unfortunately, due to the opacity of the tissue for both electrons and optical wavelength, it is only possible to investigate thin tissue slices. To reveal the true 3D morphology, it is therefore required to section and register multiple slices, which is prone to errors due to sectioning losses and sectioning artefacts (**1**).
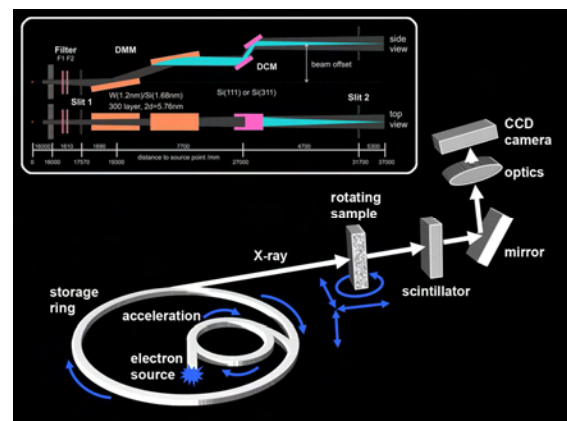
Figure 1: Experimental setup for SR-µCT measurements

Contrary to electrons and optical wavelength, X-rays show only marginal refraction, resulting in poor absorption but high penetration in biological tissues. It is therefore possible to image the true 3D morphology by recording projection images and mathematically transform this data into subsequent slice images (**2**, **3**, **4** & **5**).

Although the resolution offered by X-ray experimental setups and detector systems is sufficient to image structural details down to several nanometers in theory, conventional X-ray tube setups have beam properties not fit well to image biological tissues (e.g. non-monochromaticity, non-

coherence and low photon flux). Even with synchrotron experimental setups, biological tissues are difficult to image due to the very low differences of structures in absorption contrast. Therefore, two different approaches exist; first, elevating the absorption contrast by labelling tissue structures with metals as is common in electron microscopy and second, attenuating the phase contrast which can be achieved with a coherent X-ray beam (**6**, **7**).

While staining might introduce artefacts due to non homogeneous diffusion of the stain or later during data reconstruction (**8**), the use of phase contrast imaging requires an experimental setup with a highly coherent beam. These experimental requirements are met by the BESSY BAMline setup, which is displayed in Figure 1 and consists of a high precision sample stage (rotation table combined with translation tables), with a sample holder, a scintillator and subsequent light optics with a CCD-camera.

Methods:

A cylindrical cartilage-bone plug was harvested from the joint of a 24 month old cow and was immediately fixed in phosphate-buffered formaldehyde.

Afterwards, it was rinsed in distilled water, decalcified using EDTA, followed by dehydration using a series of graded ethanol, exchanging the ethanol with methyl benzoate and finally exchange with xylene as described elsewhere (1).

Using the BESSY BAMline setup, the sample was positioned 15 cm away from the scintillator screen to permit both phase contrast and absorption contrast. The region of interest recorded by the CCD camera was set to 2048 x 1500 pixels allowing for a maximum sample width of 3.3 mm. The sample was rotated in steps of 180°/ 1200 and was exposed to the beam at 14 keV for an exposure time of 2.0 s. Both, darkfield and flatfield corrections were applied to limit formation of ring artefacts during reconstruction. Persistent ring artefacts were compensated later via

sinogram correction. Reconstruction of the obtained projected images was performed using filtered back-projection as described by Basu and Bresler (**9**). The data was tone-mapped to 8-bits while preserving a high contrast between all relevant tissue structures. These data were saved as multi-image TIFF-stack (**1**).

2D-sliced and 3D-rendered data were obtained using the following software OsiriX, VGStudio MAX and ImageJ64. To further enhance the cellular distribution and to more easily distinguish between soft and calcified tissue, the histogram grey values were remapped corresponding to Figure 2.
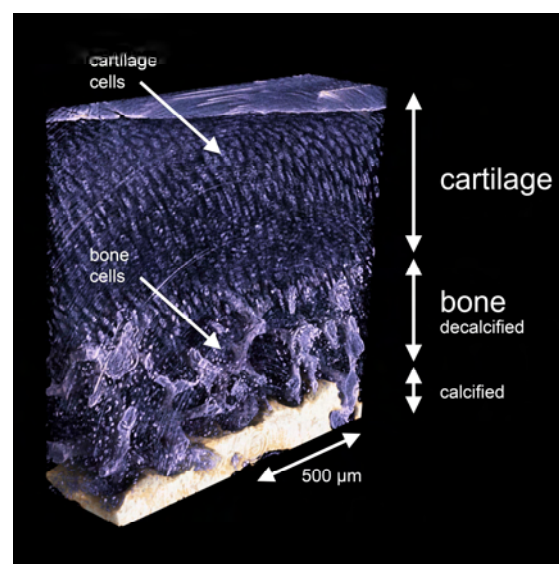
Figure 2: Rendered SR-µCT volume data of bovine articular cartilage

The representation of a single chondrocyte inside its lacunae was achieved by digitally magnifying and median filtering of the cropped TIFF-stack in each axial direction using ImageJ. The filtered data were rendered using OsiriX, while estimating the volume of a single lacuna with its chondrocyte using ImageJ (Figure 3).

To compare the SR-µCT data to a higher resolving methodology, SEM imaging combined with a focussed ion beam for milling was carried out using a Zeiss Cross Beam EsB 1540 with a gallium source. The sample was previously gold sputter-coated, FIB milled to achieve a planar surface and finally imaged in SE-detector mode at a region showing a lacuna doublet.

Results:

The µCT data (voxel size of 1.6 µm), shows both phase contrast and absorption contrast, due to both coherence and monochromacity of the beam. The used beam energy of 14 keV proved sufficiently high to penetrate both soft tissue and hard tissue zones, while achieving good absorption contrast in both. Sample positioning 15 cm away from the scintillator screen favoured the phase contrast mode.

Consequently, all cartilage structures can be revealed. Figure 2 shows the distribution of the slightly arched chondrocytes in the soft tissue region, a region of decalcified bone and the calcified subchondral bone, with its distinct micro- and macro-porosity.
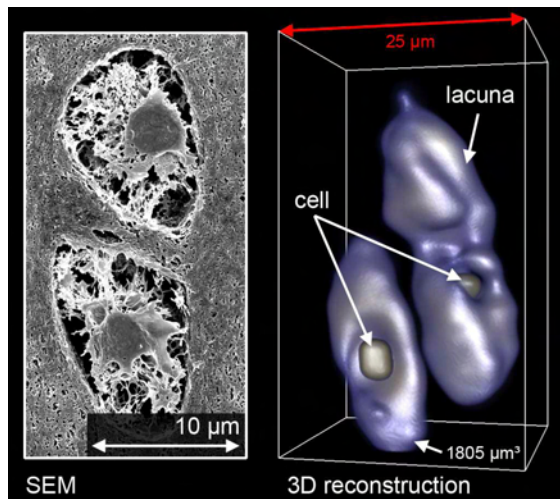
Figure 3: Comparison of a FIB-milled cross-section of a lacuna doublet in SEM with the SR-µCT data showing cells, lacunae and the volume estimation

The magnified spatial data of three independent chondrocytes embedded in their lacuna is shown in Figure 3. One of the lacunae with its cell was analyzed using ImageJ to have a combined volume of 1805 µm³. The SEM data of a similar lacuna doublet corresponds directly to the presented SR-µCT data.

Discussion:

In this study we have demonstrated that SR-µCT reaches a spatial resolution which enables the tomographic representation of single cells inside tissues without any further metal staining using a combination of phase contrast imaging mode and absorption contrast imaging.

References:

(**1**) Zehbe et al., Going beyond Histology: Synchrotron µCT as a Complementary Methodology for Biological Tissue Characterization, Journal of the Royal Society Interface, submitted

(**2**) Hounsfield, G.N., Computerized transverse axial scanning (tomography). Part I: Description of system. Part II: Clinical applications. British Journal of Radiology 46, 1016-1022 (1973).

(**3**) Cormack, A.M., Reconstruction of densities from their projections, with applications in radiological physics. Physics in Medicine and Biology 18, 195-207 (1973).

(**4**) Radon, J. Über die Bestimmung von Funktionen durch ihre Integralwerte längs gewisser Mannigfaltigkeiten, Berichte Sächsische Akademie der Wissenschaften 69. 262-267, (1917).

(**5**) Kak, A.C. & Slaney, M. Principles of Computerized Tomographic Imaging, IEEE Press (1988).

(**6**) Germann, M. et al., Strain fields in histological slices of brain tissue determined by synchrotron radiation-based micro computed tomography, Journal of Neuroscience Methods 170, 149-155 (2008).

(**7**) Cloetens, P. et al., Quantitative phase tomography of Arabidopsis seeds reveals intercellular void network, PNAS 103 (39), 14626-14630 (2006).

(**8**) Zehbe, R. et al., Characterization of oriented protein-ceramic and protein-polymer-composites for cartilage tissue engineering using synchrotron µ-CT. Int J Mat Res 98, 562-568 (2007).

(**9**) Basu, S. & Bresler, Y. O(N2 log2N) Filtered Backprojection Reconstruction Algorithm for Tomography, IEEE Transactions on image Processing, 9 (10), 1760-1773 (2000).

The ββα-Me type II restriction endonuclease Hpy99I

Monika Sokolowska[1,2], Honorata Czapinska[1,2], Matthias Bochtler[1,2,3,§]

[1]*International Institute of Molecular and Cell Biology, Trojdena 4, 02-109 Warsaw, Poland*

[2]*Max-Planck-Institute of Molecular Cell Biology and Genetics, Pfotenhauerstr. 108, 01309 Dresden, Germany*

[3]*Schools of Chemistry and Biosciences, Main Building, Park Place, Cardiff University, Cardiff CF10 3AT, UK*

ββα-Me nucleases have been named for their conserved active site region, which consists of a β-hairpin (ββ) and α-helix (α) that together anchor a catalytic metal ion (Me). They are present in all three kingdoms of life and fulfill diverse biological functions. Structurally characterized members include unspecific nucleases, homing endonucleases and also Holliday junction resolvases. Structures of ββα-Me restriction endonucleases have not yet been reported, even though these enzymes form the second largest group of type II restriction endonucleases after PD-(D/E)XK enzymes and before GIY-YIG, phospholipase-derived and half-pipe endonucleases.

The type II REase Hpy99I from the gastric pathogen *Helicobacter pylori* can be classified as a ββα-Me endonuclease on the basis of statistically significant sequence similarity to the Holliday junction resolvase T4 endonuclease VII, a bona fide ββα-Me endonuclease. The enzyme recognizes the nearly symmetric (pseudopalindromic) recognition sequence CGWCG. At the center of its target sequence, Hpy99I distinguishes A-T from G-C pairs, but not individual nucleotides. Interestingly, the enzyme cleaves its target just downstream of the recognition sequence, i.e. with a unique five base pair stagger not observed previously with this polarity in any structurally characterized restrictase DNA complex.

Starting from synthetic genes, we have overproduced N-terminally histidine-tagged Hpy99I in the presence of its cognate methyltransferase to protect host DNA from the endonuclease activity of Hpy99I. The recombinant restrictase was purified by metal affinity chromatography and confirmed to be active in the presence of Mg^{2+} or Mn^{2+} ions,

but not in the presence of Ca^{2+} ions. Crystals in space group H32 were obtained in the presence of EDTA or Ca^{2+} ions and diffracted to 1.75 and 1.50 Å resolution, respectively. Phases were obtained by the SAD method, exploiting the anomalous signal of structural Zn^{2+} and soaked in Br^- ions. Crystals contained one Hpy99I dimer with bound DNA in the asymmetric unit. Instead of the co-factors Mg^{2+} or Mn^{2+}, the active sites contained a surrogate Na^+ ions of similar size and coordination preference, which do not support DNA hydrolysis.
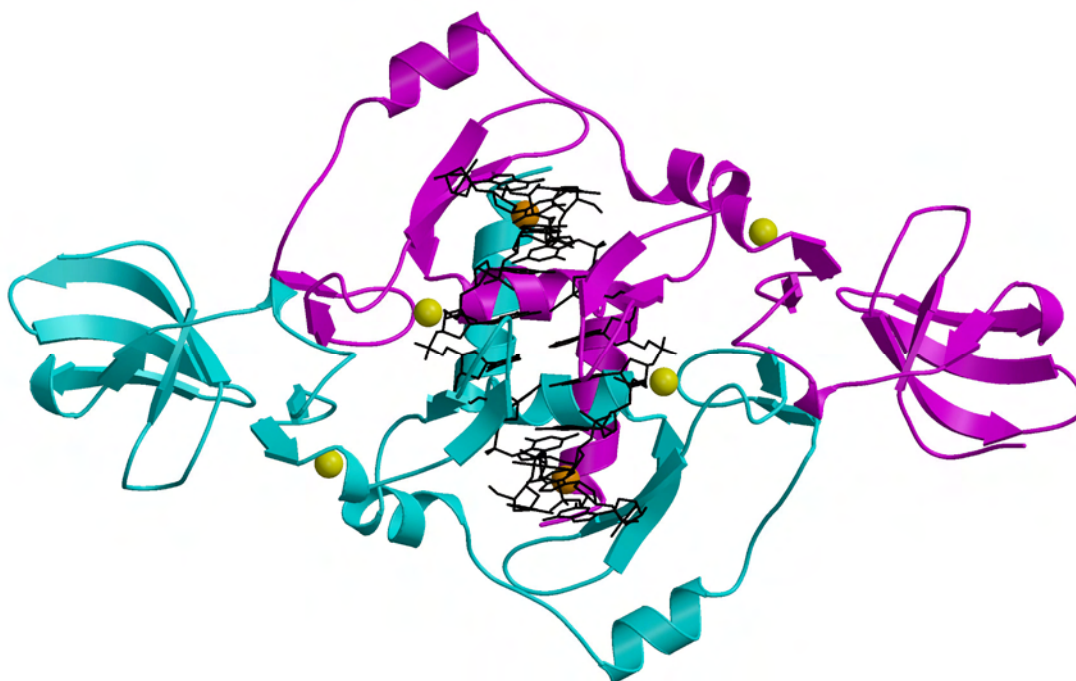
Figure 1: Schematic representation of the Hpy99I-DNA complex. The DNA and protein are shown in all atom and ribbon representations, respectively. The two protein subunits are colored in cyan and magenta, respectively. The metal ions in the active sites are shown in orange, and structural Zn^{2+} ions are presented as yellow balls.

According to the crystal structure, each Hpy99I subunit recognizes one half-site of the DNA and consists of an antiparallel β-barrel and two β4α2 repeats. The β-barrel makes no contacts with DNA and lacks an obvious function. The two β4α2 repeats bind structural zinc ions. The first and second repeats make sequence specific major and minor groove contacts, respectively. The second repeat comprises the ββα-Me active site region and binds the catalytic metal ion (or its surrogate). The crystal structure illustrates the recognition of the CGWCG target sequence and attributes the partial specificity for the central base pair to exclusive minor groove readout by two arginine residues. It provides

the first detailed illustration of the ββα-Me site in REases and complements structural information on the use of this active site motif in other groups of endonucleases, such as homing endonucleases (e.g. I-PpoI) and Holliday junction resolvases (e.g. T4 endonuclease VII). A manuscript describing the above results is currently under consideration by the journal *Nucleic Acid Research*.

Acknowledgment:

Human Cystathionine Gamma-Lyase in complex with DL-propargylglycine (PDB entry 3CO6)

Collins, R., Karlberg, T., Lehtiö, L., Berglund, H., Dahlgren, L.G., Flodin, S., Flores, A., Gräslund, S., Hammarstrom, M., Johansson, I., Kallas, Å., Kotenyova, T., Moche, M., Nilsson, M.E., Nordlund, P., Nyman, T., Olesen, K., Persson, C., Schuler, H., Svensson, L., Thorsell, A.G., Tresaugues, L., Van den Berg, S., Sagermark, J., Busam, R.D., Welin, M., Weigelt, J., Wikström, M.

Structural Genomics Consortium[#], Department of Medical Biochemistry and Biophysics, Karolinska Institutet, Scheeles väg 2, 171 77 Stockholm, SWEDEN
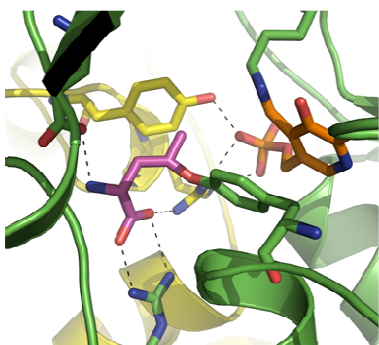
Cystathionine-γ-lyase (EC 4.4.1.1, CTH, CSE, cystathionase) is a pyridoxal-phosphate (PLP) dependent enzyme that catalyses the conversion of L-cystathionine to L-cysteine in the transulfuration pathway. Deficiency of CTH causes the autosomal recessive disease cystathioninemia. CTH can also convert L-cysteine to H_2S, a gas transmitter highly interesting from a medical perspective since it functions as a neuromodulator in the central nervous system and as a smooth muscle relaxant in the vascular system. It has also been suggested to be linked to several cardiovascular diseases, to (anti-) inflammatory responses and to gastric injury caused by non-steroidal anti-inflammatory drugs (*1*). H_2S is produced in the liver, kidney, vascular system and gut by CTH and in the brain by cystathionine beta-synthetase (CBS). Yang *et al. (2)* showed that H_2S is physiologically generated by CTH and that genetic deletion of CTH in mice markedly reduces H_2S levels in the serum, heart, aorta, and other tissues. DL-Propargylglycine (PAG) is one of few known inhibitors acting on CTH (*3*).

Here we present the crystal-structure of CTH in complex with PAG at 2.0Å resolution together with kinetics of H_2S formation and inhibition studies using PAG (*4*). The enzyme is crystallized as a tetramer with PLP observed covalently bound to Lys212 forming a Schiff base. Both monomers in the subunit interfaces contribute to the active site pocket. The inhibitor is observed bound to Tyr114, the interaction of was not predicted based on existing information from known PAG complexes. The structure of the PAG complex highlights the particular importance of Tyr114 in and the mechanism of PAG-dependent inhibition of human CTH. These results provide significant insights, which will facilitate the structure-based design of novel inhibitors to aid in the development of therapies for diseases involving disorders of sulfur metabolism.

References

1. S. Fiorucci, E. Distrutti, G. Cirino, J. L. Wallace, *Gastroenterology* **131**, 259 (Jul, 2006).
2. G. Yang *et al.*, *Science* **322**, 587 (Oct 24, 2008).
3. C. Steegborn *et al.*, *J Biol Chem* **274**, 12675 (Apr 30, 1999).
4. Q. Sun *et al.*, *J Biol Chem* (Nov 19, 2008).

The TIR domain of human Toll-Like Receptor 10 (PDB entry 2J67)

Stenmark, P., Ogg, D., Berglund, H., Busam, R., Collins, R., Ericsson, U.B., Flodin, S., Flores, A., Graslund, S., Hammarstrom, M., Hallberg, B.M., Holmberg Schiavone, L., Hogbom, M., Johansson, I., Karlberg, T., Kotenyova, T., Magnusdottir, A., Nilsson, M.E., Nilsson-Ehle, P., Nyman, T., Persson, C., Sagemark, J., Sundstrom, M., Uppenberg, J., Thorsell, A.G., Van Den Berg, S., Wallden, K., Weigelt, J., Welin, M., Nordlund, P.
Structural Genomics Consortium[#], Department of Medical Biochemistry and Biophysics, Karolinska Institutet, Scheeles väg 2, 171 77 Stockholm, SWEDEN
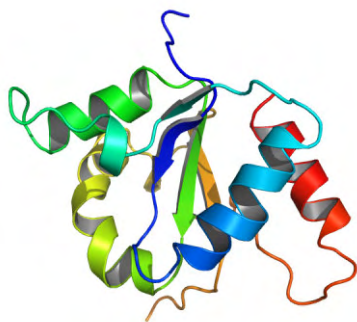
The Toll-like receptors (TLRs) play an essential role in initiating the immune response against pathogens. The 10 identified human TLRs recognize a wide variety of pathogen-associated molecular patterns from bacteria, viruses, and fungi, as well as certain host-derived molecules (*1*). TLRs are type I transmembrane glycoproteins with an extracellular domain composed of numerous leucine-rich repeats and an intracellular region containing a Toll/IL-1 receptor homology (TIR) domain (*2*). The intracellular domains interact with several TIR domain-containing adaptor molecules that conveys the downstream signaling, resulting in transcription factor induction. Dysfunction in the TLRs results in desensitization of the recognition of certain (*3*) pathogenic ligands, and might render the host susceptible for microbial invasion. To date, TLR10 remains the only orphan member among the human TLRs. TLR10 has been reported to homodimerize and also heterodimerize with TLRs 1 and 2, and to directly associate with the common TLR adaptor MyD88 (*4*).

The 2.2 Å crystal structure of the TLR10 TIR domain represents the third TLR TIR-domain structure alongside with those of TLRs 1 and 2 (*5*). The asymmetric unit is comprised of a dimer with a two-fold symmetry axis. The buried surface area of 974 Å² shows a high degree of compatibility between the two monomers, and the structure is in accordance with functional mapping done with TLR10 and other TLR family members. Analysis of the amino acid sequence conservation between members of the TLR family has revealed a sequence that might constitute an adaptor protein recruitment site (Hasan, 2005). In the TLR10 dimer, these residues form an extended patch. It is concluded that this structure might represent the physiological dimer.

References

1. H. Heine, E. Lien, *Int Arch Allergy Immunol* **130**, 180 (Mar, 2003).
2. R. J. Ulevitch, *Nat Rev Immunol* **4**, 512 (Jul, 2004).
3. K. A. Fitzgerald *et al.*, *J Exp Med* **198**, 1043 (Oct 6, 2003).
4. U. Hasan *et al.*, *J Immunol* **174**, 2942 (Mar 1, 2005).
5. T. Nyman *et al.*, *J Biol Chem* **283**, 11861 (May 2, 2008).

Human Cleavage and Polyadenylation Specificity Factor 5 (PDB entry 2CL3/2J8Q)

Moche, M., Stenmark, P., Ogg, D., Berglund, H., Busam, R., Collins, R., Ericsson, U.B., Flodin, S., Flores, A., Graslund, S., Hammarstrom, M., Hallberg, B.M., Holmberg, S.L., Hogbom, M., Johansson, I., Karlberg, T., Kosinska, U., Kotenyova, T., Magnusdottir, A., Nilsson, M.E., Nilsson-Ehle, P., Nyman, T., Persson, C., Sagemark, J., Sundstrom, M., Uppenberg, J., Upsten, M., Thorsell, A.G., Van Den Berg, S., Wallden, K., Weigelt, J., Welin, M., Nordlund, P.

Structural Genomics Consortium[#], Department of Medical Biochemistry and Biophysics, Karolinska Institutet, Scheeles väg 2, 171 77 Stockholm, SWEDEN
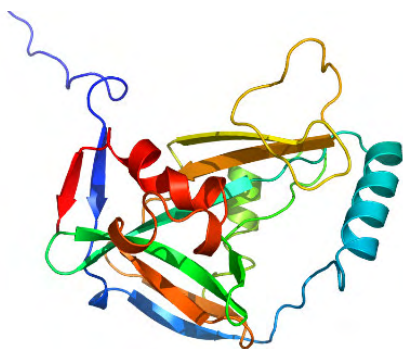
Modifications in the 3´ end of mRNA are carried out in two steps: ii) endonucleolytically cleavage at the polyadenylation site and ii) polyadenylation. One of the factors involved in this process is the pre-mRNA cleavage factor Im which is a heterodimeric protein consisting of one 25 kDa subunit and a subunit of either 68, 59 or 72 kDa (*1*).

We have determined the structure of the 25 kDa subunit called "Cleavage and Polyadenylation Specificity Factor 5" (CPSF5) to a resolution of 1.9 Å using SAD phasing (*2*). It is a member of the NudiX protein family but harbours large structural differences with other members of the family (e.g. several extra beta strands and one additional long helix).

CPSF5 appeared to be a dimer in the crystallographical structure, which opens three possibilities: i) the complex is actually a heterotetramer, ii) one dimer of CPSF5 interacts with one monomer of the large subunit or iii) the CPSF5 dimer dissociates when interacting with the large subunit forming a heterodimer.

A crevice that is very likely to be the RNA binding site of the monomer is prolonged in the dimer making a long continuous crevice over the dimer. Contacts between symmetry-related mates also reveal the existence of a putative protein-binding site.

References

1.	U. Ruegsegger, D. Blank, W. Keller, *Mol Cell* **1**, 243 (Jan, 1998).
2.	L. Tresaugues *et al.*, *Proteins* **73**, 1047 (Dec, 2008).

Human Argininosuccinate synthase (PDB entry 2NZ2)

Karlberg, T., Uppenberg, J., Berglund, H., Busam, R.D., Collins, R., Ericsson, U.B., Flodin, S., Flores, A., Graslund, S., Hallberg, B.M., Hammarstrom, M., Hogbom, M., Johansson, I., Kotenyova, T., Magnusdottir, A., Moche, M., Nilsson, M.E., Nordlund, P., Nyman, T., Ogg, D., Persson, C., Sagemark, J., Stenmark, P., Sundstrom, M., Thorsell, A.G., Van Den Berg, S., Wallden, K., Weigelt, J., Holmberg-Schiavone, L.
Structural Genomics Consortium[#], Department of Medical Biochemistry and Biophysics, Karolinska Institutet, Scheeles väg 2, 171 77 Stockholm, SWEDEN
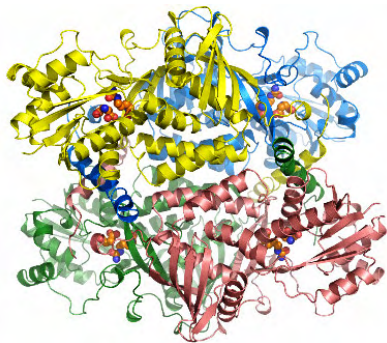
Argininosuccinate synthase (EC 6.3.4.5, ASS, Citrulline-aspartate ligase) is responsible for the condensation reaction between citrulline and aspartate in an ATP-dependent manner to form argininosuccinate, AMP and pyrophosphate. It is the rate-limiting enzyme in the synthesis of arginine and part of the Urea-cycle and also a potential limiting step for the NO-production via the Arginine-citrulline cycle (*1*). The gaseous messenger NO has been widely studied and is of significant importance to human cell physiology (*2*). Deficiency of ASS can lead to the rare autosomal disorders citrullinemia or hyperammonemia where increased levels of citrulline and ammonia could affect the brain or manifest as intermittent ataxia (*3*).

We have solved the structure of the human tetrameric argininosuccinate synthase in complex with two of its substrates, aspartate and citrulline at 2.4Å resolution (*4*). The enzyme comprises two domains, one nucleotide-binding domain and one catalytic domain. The nucleotide domain resembles the Adenine nucleotide alpha hydrolase-like fold, whereas the catalytic domain has a unique fold for this type of enzyme. An additional C-terminal extension, a long α–helix is stretching out from the catalytic domain and is making interactions with neighboring monomers and thus is important for the oligomerization. The overall structure is a homo-tetramer with tight subunit-subunit interactions.

Two of the substrates were found bound to the active site pocket, in a cleft between the two domains. The binding site for the aspartate lies between citrulline and a loop from the nucleotide-binding domain whereas the citrulline is bound to the catalytic domain. The residues in the active site cleft are highly conserved. The structure gives new insights into the function of the numerous clinical mutations identified in patients with type I citrullinemia.

References

1. A. Husson, C. Brasse-Lagnel, A. Fairand, S. Renouf, A. Lavoinne, *Eur J Biochem* **270**, 1887 (May, 2003).
2. M. Mori, T. Gotoh, *Biochem Biophys Res Commun* **275**, 715 (Sep 7, 2000).
3. L. C. Pendleton, B. L. Goodwin, L. P. Solomonson, D. C. Eichler, *J Biol Chem* **280**, 24252 (Jun 24, 2005).
4. T. Karlberg *et al.*, *Acta Crystallogr D Biol Crystallogr* **64**, 279 (Mar, 2008).

Human DEAD-box RNA-helicase DDX19 ADP complex
(PDB entry 3EWS)

Lehtio,L., Karlberg,T., Andersson,J., Berglund,H., Collins,R., Dahlgren,L.G., Flodin,S., Flores,A., Graslund,S., Hammarstrom,M., Johansson,A., Johansson,I., Kotenyova, T., Moche,M., Nilsson,M.E., Nordlund,P., Nyman,T., Olesen,K., Persson,C., Sagemark,J., T horsell,A.C., Tresaugues,l., Van den berg,S., Weigelt, J., Welin,M., Wikstrom,M., Wisniewska,M., Schueler, H

Structural Genomics Consortium[#], Department of Medical Biochemistry and Biophysics, Karolinska Institutet, Scheeles väg 2, 171 77 Stockholm, SWEDEN
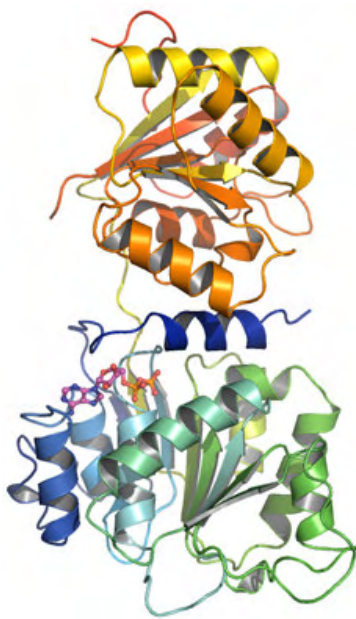
The DExD/H family of RNA-binding helicases consists of a large group of proteins involved in general cellular RNA-metabolism such as transcription, splicing, RNA nucleocytoplasmatic transport, translation and ribosome biogenesis (*1*). All DExD/H helicases bind and hydrolyze ATP, and are believed to unwind RNA-secondary structure or assist in the folding of RNA/RNP complexes thus acting as RNA chaperones. Proteins in this family normally consist of two domains: an N-terminal domain with the conserved DExD/H motif and a C-terminal helicase domain. There are at least eight conserved motifs, based on primary sequence alignments that are involved in coordination and hydrolysis of ATP and binding of RNA (*2, 3*). DDX19 (or Dbp5) is a human DEAD-box helicase that is required for mRNA export from the nucleus (*4*). DDX19 is located primarily in the cytosol, but is recruited to the nuclear pore complex, where it assists in the mRNA export. Futher, the helicase is involved in translation termination and interacts with release factors eRF1 and eRF3 (*5*).

We have solved the structure of the conserved core of DDX19, containing the DEAD-domain and the helicase domain in complex with ADP, at 2.7 Å resolution. DDX19 has a fold that is typical of a DEAD-box helicase with two α-β RecA-like domains connected via a flexible linker. The nucleotide binding site is located in a pocket between the two domains. ATP hydrolysis at this site enables DDX19 to translocate along ssRNA and remove paired strands or proteins (3).

References

1. P. Linder, *Curr Biol* **18**, R297 (Apr 8, 2008).
2. O. Cordin, J. Banroques, N. K. Tanner, P. Linder, *Gene* **367**, 17 (Feb 15, 2006).
3. A. M. Pyle, *Annu Rev Biophys* **37**, 317 (2008).
4. C. Schmitt *et al.*, *Embo J* **18**, 4332 (Aug 2, 1999).
5. T. Gross *et al.*, *Science* **315**, 646 (Feb 2, 2007).

Human FLJ10324 (RADIL), RA domain (PDB entry 3EC8)

Wisniewska, M., Lehtio, L., Andersson, J., Collins, R., Dahlgren, L.G., Flodin, S., Flores, A., Graslund, S., Hammarstrom, M., Johansson, A., Johansson, I., Karlberg, T., Kotenyova, T., Moche, M., Nilsson, M.E., Nordlund, P., Nyman, T., Olesen, K., Persson, C., Sagemark, J., Schueler, H., Thorsell, A.G., Tresaugues, L., van den Berg, S., Weigelt, J., Welin, M., Wikstrom, M., Berglund, H

Structural Genomics Consortium[#], Department of Medical Biochemistry and Biophysics, Karolinska Institutet, Scheeles väg 2, 171 77 Stockholm, SWEDEN
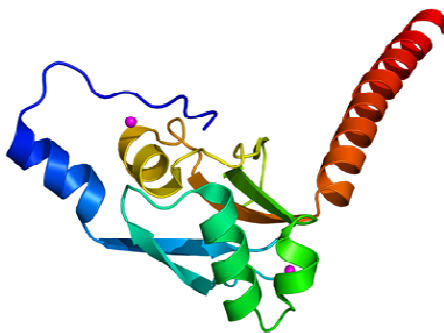
FLJ10324 (also called RADIL, KIAA1849, AF6L) is a multi-domain protein composed of a Ras association (RA) domain, a forkhead-associated (FHA) domain mediating phospho-peptide interactions, a dilute (DIL domain) of unknown function, and a protein-protein interacting PDZ domain. The RA domain is structurally similar to ubiquitin and is present in one or two copies in a number of signalling molecules that bind and regulate a small GTPase called Ras or the Ras-related GTPases, Ral and Rap. RA-containing proteins include RalGDS, AF6, RIN1, RASSF1, SNX27, CYR1, STE50, and phospholipase C epsilon.

At date there is limited knowledge about the specific biological role played by FLJ10342. This protein has a similar domain composition as afadin (AF6), a protein involved in linking membrane-associated proteins to the actin cytoskeleton and in Rap-induced cell adhesion that suggests a related role for FLJ10324.

The RA domain of FLJ10324 has been shown to bind to the small GTPase Rap1 and reduce the exchange rate of the nucleotide but seems not to effect Rap-induced cell adhesion in a similar way as afadin (*1*). Later FLJ10324 has been shown to be required for cell adhesion and migration of neural crest precursors, a highly motile embryonic cell population that give rise to different cell types (*2*).

Here we present the crystal structure of RA domain of FLJ10324 at 2.6Å resolution. The structure was solved by MIRAS phasing using heavy atoms derivatives (lead and mercury). The overall structure reveals the ubiquitin-like fold consisting of five-stranded β-sheet and two α-helices. Additionally, at N- and C- terminus we can observe two α-helices that do not belong to the RA domain.

References

1. Z. Zhang, H. Rehmann, L. S. Price, J. Riedl, J. L. Bos, *J Biol Chem* **280**, 33200 (Sep 30, 2005).
2. G. A. Smolen *et al.*, *Genes Dev* **21**, 2131 (Sep 1, 2007).

Human guanine monophosphate synthetase (PDB entry 2VXO)

Welin, M., Lehtio, L., Andersson, J., Arrowsmith, C.H., Berglund, H., Collins, R., Dahlgren, L.G., Edwards, A.M., Flodin, S., Flores, A., Graslund, S., Hammarstrom, M., Johansson, A., Johansson, I., Karlberg, T., Kotenyova, T., Moche, M., Nilsson, M.E., Nyman, T., Olesen, K., Persson, C., Sagemark, J., Schueler, H., Thorsell, A.G., Tresaugues, L., Van Den Berg, S., Wisniewska, M., Wikstrom, M., Nordlund, P.
Structural Genomics Consortium[#], Department of Medical Biochemistry and Biophysics, Karolinska Institutet, Scheeles väg 2, 171 77 Stockholm, SWEDEN
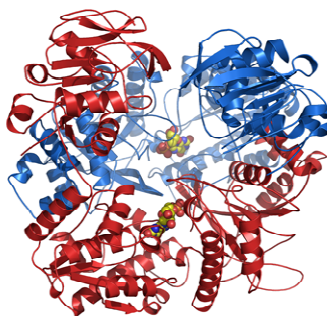
GMP synthetase (GMPS, E.C. 6.3.5.2) is a glutamine amidotransferase involved in the de novo synthesis of purines. It catalyzes the conversion of XMP to GMP in the presence of glutamine and ATP. GMPS is a bifunctional enzyme with an N-terminal glutaminase domain that generates ammonia from glutamine, and a C-terminal synthetase domain that aminates XMP to GMP (*1*).

XMP + ATP + GLN + H2O -> GMP + AMP + GLU + PPi

GMPS is a potential target for anticancer therapies and acivicin is known to inhibit GMPS (*2-4*). The *E. coli* GMPS structure suggested large movements between the two domains, separated by 30 Å, during reaction since no obvious route for ammonia channeling was visible (*1, 5*).

Human GMP synthetase structure was solved to 2.5 Å resolution by molecular replacement using the glutaminase domain of human GMP synthetase (2VPI) and the synthetase domain of Thermus thermophilus (2YWC). GMPS belongs to the class 1 glutamine dependent amidotranferases which has a conserved catalytic triad consisting of a Cys-His-Glu [5]. The asymmetric unit contains a homodimer with XMP bound to each active site. The human GMPS is slightly larger than the *T. thermophilus* and *E.coli* GMPS structures, having an additional domain in the dimer interface stretching from residue 449 to 579. This domain is built up by a three stranded β-sheet flanked by five α-helices. A β-hairpin in this domain is also interacting with the same β-hairpin in the other subunit and involved in binding of the XMP phosphate. The human GMPS dimer is more tightly packed than the bacterial GMPS structures. This is the first GMPS structure of eukaryotic origin and the information regarding substrate binding will aid potential drug design.

References

1.   X. Huang, H. M. Holden, F. M. Raushel, *Annu Rev Biochem* **70**, 149 (2001).
2.   S. V. Chittur, T. J. Klem, C. M. Shafer, V. J. Davisson, *Biochemistry* **40**, 876 (Jan 30, 2001).
3.   M. Hirst, E. Haliday, J. Nakamura, L. Lou, *J Biol Chem* **269**, 23830 (Sep 23, 1994).
4.   J. Nakamura, K. Straub, J. Wu, L. Lou, *J Biol Chem* **270**, 23450 (Oct 6, 1995).
5.   J. J. Tesmer, T. J. Klem, M. L. Deras, V. J. Davisson, J. L. Smith, *Nat Struct Biol* **3**, 74 (Jan, 1996).

Human heat shock 70kDa protein 6 (HSP70B), ATPase domain in complex with ADP (PDB entry 3FE1)

Wisniewska, M., Lehtio, L., Berglund, H., Collins, R., Dahlgren, L.G., Flodin, S., Flores, A., Graslund, S., Hammarstrom, M., Johansson, A., Johansson, I., Karlberg, T., Kotenyova, T., Moche, M., Nilsson, M.E., Nordlund, P., Nyman, T., Persson, C., Sagemark, J., Siponen, M.I., Thorsell, A.G., Tresaugues, L., Van Den Berg, S., Weigelt, J., Welin, M., Wikstrom, M., Schueler, H.

Structural Genomics Consortium[1], Department of Medical Biochemistry and Biophysics, Karolinska Institutet, Scheeles väg 2, 171 77 Stockholm, SWEDEN
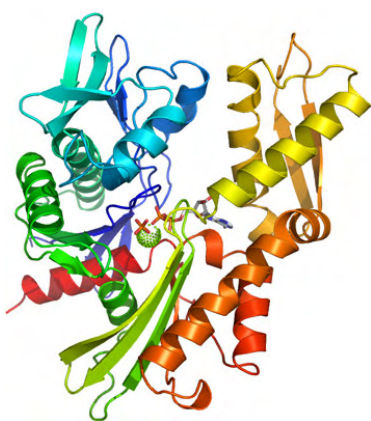
Heat shock-70 proteins (Hsp70) are a family of chaperones involved in the heat shock and unfolded protein response as well as housekeeping functions (*1*). The human genome contains at least eight Hsp70 isoforms – some stress-induced, some constitutively expressed; some cytosolic and some organelle-specific. Hsp70 proteins consist of an N-terminal ATPase domain and a C-terminal peptide binding domain joined by a flexible linker. They bind extended peptide segments with a net hydrophobic character exposed during translation, membrane translocation, or following stress-induced damage, and allow refolding of such peptides. Refolding activity is coupled to ATPase activity of the N-terminal domain, which is also regulated by co-chaperones (*2*).

The human HSPA6 protein (also called Hsp70B') is a stress-induced member of this family that localizes to the nucleus and cytosol (*3-5*). We have determined the crystal structure of the HSPA6 ATPase domain (residues E6 – D385), which shares 85% identity with the corresponding part of the HSPA1AA (Hsp72) protein. Our structure shows the protein with one magnesium ion and the products of ATP hydrolysis (one molecule of ADP and one phosphate group) bound in the cleft between the two major lobes of the ATPase domain. Coordinates and structure factors have been deposited in the pdb (accession code 3FE1).

References

1. M. Daugaard, M. Rohde, M. Jaattela, *FEBS Lett* **581**, 3702 (Jul 31, 2007).
2. T. K. Leung, C. Hall, M. Rajendran, N. K. Spurr, L. Lim, *Genomics* **12**, 74 (Jan, 1992).
3. T. K. Leung, M. Y. Rajendran, C. Monfries, C. Hall, L. Lim, *Biochem J* **267**, 125 (Apr 1, 1990).
4. M. P. Mayer, B. Bukau, *Cell Mol Life Sci* **62**, 670 (Mar, 2005).
5. E. J. Noonan, R. F. Place, C. Giardina, L. E. Hightower, *Cell Stress Chaperones* **12**, 219 (Autumn, 2007).

Human Nudix motif 16 (PDB entry 3COU)

Tresaugues, L., Moche, M., Berglund, H., Busam, R.D., Collins, R., Dahlgren, L.G., Flodin, S., Flores, A., Graslund, S., Hammarstrom, M., Herman, M.D., Johansson, A., Johansson, I., Kallas, A., Karlberg, T., Kotenyova, T.,Lehtio, L., Nilsson, M.E., Nyman, T., Persson, C., Sagemark, J., Schueler, H., Svensson, L., Thorsell, A.G., Van Den Berg, S., Welin, M., Weigelt, J., Wikstrom, M., Nordlund, P.

Structural Genomics Consortium[#], Department of Medical Biochemistry and Biophysics, Karolinska Institutet, Scheeles väg 2, 171 77 Stockholm, SWEDEN

NUDT16 is a 195 aminoacid long protein which belongs to the Nudix hydrolase superfamily (*1*). The activities of these enzymes are targeted against a broad range of substrate containing a nucleoside diphosphate linked to another moiety (NDP-X) leading to NMP + P-X. NUDT16 has a "decapping" activity consisting in removing the 5´cap of the mRNA rendering it accessible for being degradated by a 5´-3´ exonuclease (*2*).

The specificity of NUDT16 and its homologuous from Xenopus laevis X29 has been shown to be dependent of divalent cations required for hydrolysis. In vitro, when Mg2+ is added, the protein is only able to hydrolyze U8snoRNA whereas in presence of Mn2+ or Co2+ the activity is higher and the specificity is extended to other RNAs (*3*). Structures of the both apo and holo- X29 protein of Xenopus laevis in complex with Mn2+ and m7GpppA were available (*4*).

We have solved the structure of human NUDT16 to a resolution of 1.8Å (PDB code : 3COU). Applying a crystallographic symmetry operator on the monomer present in the asymmetrical unit allows retrieving the dimerical quaternary structure previously determined in the Xenopus homologous X29. If the sequence identity between this X29 and NUDT16 is only 54%, residues involved in Mn2+ chelating and CAP binding are strictly conserved. One difference between these structures is that the side-chain of Glu158, involved in Mn2+ chelating, is in the same orientation as the corresponding residues (Glu150) in the holo-X29 despite the lack of a cation in this area.

References

1.   A. G. McLennan, *Cell Mol Life Sci* **63**, 123 (Jan, 2006).
2.   T. Ghosh, B. Peterson, N. Tomasevic, B. A. Peculis, *Mol Cell* **13**, 817 (Mar 26, 2004).
3.   B. A. Peculis, K. Reynolds, M. Cleland, *J Biol Chem* **282**, 24792 (Aug 24, 2007).
4.   J. N. Scarsdale, B. A. Peculis, H. T. Wright, *Structure* **14**, 331 (Feb, 2006).

Human Phosphate Cytidylyltransferase 2 (PDB entry 3ELB)

Karlberg, T., Welin, M., Andersson, J., Arrowsmith, C.H., Berglund, H., Bountra, C., Collins, R., Dahlgren, L.G., Edwards, A.M., Flodin, S., Flores, A., Graslund, S., Hammarstrom, M., Johansson, A., Johansson, I., Kotenyova, T., Lehtio, L., Moche, M., Nilsson, M.E., Nordlund, P., Nyman, T., Persson, C., Sagemark, J., Thorsell, A.G., Tresaugues, L., Van Den Berg, S., Weigelt, J., Wikstrom, M., Wisniewska, M., Schuler, H.
Structural Genomics Consortium[#], Department of Medical Biochemistry and Biophysics, Karolinska Institutet, Scheeles väg 2, 171 77 Stockholm, SWEDEN

Ethanolamine phospholipids (PE) are a major component of cell membranes in eukaryotes and the most abundant in prokaryotic membranes. Three biosynthetic pathways of PE formation are known in eukaryotes: the major route CDP-ethanolamine pathway (Kennedy pathway), decarboxylation of phosphatidylserine and base exchange with phosphatidylserine (*1*). Phosphate cytidylyltransferase 2 (CTP:Phosphoethanolamine cytidylyltransferase, PCYT2; ECT) catalyzes the transformation of CTP and phosphoethanolamine into CDP-Ethanolamine and pyrophosphate using the hydrolysis of CTP to CMP, the penultimate step in the Kennedy pathway of *de novo* synthesis of phospholipids (*1-3*). After which CDP-Ethanolamine:1,2-diacylglycerol ethanolaminephosphotransferase catalyses the final step producing PE. Recent studies suggest that increase in phosphoethanolamine in some breast cancer cells is caused by the down-regulation of PCYT2 (*4*).

Here we present the crystal structure of PCYT2 in complex with CMP at a resolution of 2.0Å. The structure was solved by SAD using selenomethionine-labelled protein. PCYT2 is a monomer which consists of two cytidylyltransferase domains and each domain contains a nucleotide-binding motif HxGH. The N-terminal domain (residues Gly19-Leu155) consists of a five-stranded parallel β-sheet with topology 3-2-1-4-5 flanked by five α-helices and a sixth helix making considerable domain-domain interactions. The C-terminal domain (Trp187-Thr351) has a similar fold. Interestingly, only the C-terminal domain has CMP bound in its nucleotide binding pocket. CTP and MgCl$_2$ were added to the protein in the crystallization trials.

References

1. M. Bakovic, M. D. Fullerton, V. Michel, *Biochem Cell Biol* **85**, 283 (Jun, 2007).
2. O. B. Bleijerveld, J. F. Brouwers, A. B. Vaandrager, J. B. Helms, M. Houweling, *J Biol Chem* **282**, 28362 (Sep 28, 2007).
3. A. Signorell, M. Rauch, J. Jelk, M. A. Ferguson, P. Butikofer, *J Biol Chem* **283**, 23636 (Aug 29, 2008).
4. L. Zhu, C. Johnson, M. Bakovic, *J Lipid Res* **49**, 2197 (Oct, 2008).

Human sorting nexin-17, PX domain (PDB entry 3FOG)

Wisniewska, M., Tresaugues, L., Berglund, H., Collins, R., Dahlgren, L.G., Flodin, S., Flores, A., Graslund, S., Hammarstrom, M., Johansson, A., Johansson, I., Karlberg, T., Kotenyova, T., Lehtio, L., Moche, M., Nilsson, M.E., Nordlund, P., Nyman, T., Persson, C., Sagemark, J., Siponen, M.I., Thorsell, A.G., Van Den Berg, S., Weigelt, J., Welin, M., Wikstrom, M., Schueler, H.
Structural Genomics Consortium[1], Department of Medical Biochemistry and Biophysics, Karolinska Institutet, Scheeles väg 2, 171 77 Stockholm, SWEDEN
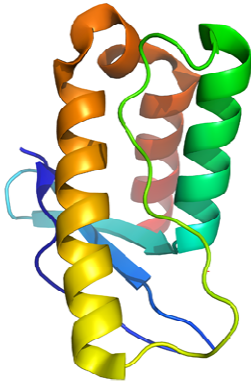
Sorting nexins (SNXs) are a family of membrane associated proteins characterized by the presence of a phox (PX) homology domain. This domain confers specificity towards phosphoinositides, and targets the SNX proteins to membrane domains enriched in specific phospholipids (*1, 2*). Sorting nexin-17 was initially identified as a binding partner for P-selectin (*3*). This interaction accelerates P-selectin internalization and inhibits its lysosomal degradation (*4*). SNX17 is also a binding partner for several members of the low-density lipoprotein (LDL) receptor family such as LDLR, VLDLR, ApoER2 and LDLR-related protein (LRP) (*5*). Recently it was shown that SNX17 interacts with the NPVY motif in the LDL receptor tail (*6*), and is a part of the cellular sorting machinery that regulates cell surface levels of LRP by promoting its recycling (*7*). SNX17 consists of an N-terminal PX domain, followed by a B41 (band 4.1 or FERM) domain.

Here we present the crystal structure of the PX domain at 2.8 Å resolution. The structure was solved by molecular replacement using MOLREP with the cytokine-independent survival kinase CISK-PX (1XTE) as a search model. The asymmetric unit consisted of one polypeptide chain. The overall fold of the SNX17-PX domain is composed of a β-sheet with three antiparallel β-strands and a helical subdomain consisting of three α-helices. Coordinates and structure factors have been deposited in the PDB with accession code 3FOG.

References

1. M. L. Cheever *et al.*, *Nat Cell Biol* **3**, 613 (Jul, 2001).
2. F. Kanai *et al.*, *Nat Cell Biol* **3**, 675 (Jul, 2001).
3. V. Florian, T. Schluter, R. Bohnensack, *Biochem Biophys Res Commun* **281**, 1045 (Mar 9, 2001).
4. R. Williams *et al.*, *Mol Biol Cell* **15**, 3095 (Jul, 2004).
5. W. Stockinger *et al.*, *Embo J* **21**, 4259 (Aug 15, 2002).
6. J. J. Burden, X. M. Sun, A. B. Garcia, A. K. Soutar, *J Biol Chem* **279**, 16237 (Apr 16, 2004).
7. P. van Kerkhof *et al.*, *Embo J* **24**, 2851 (Aug 17, 2005).

Human TULP1 in complex with IP3 (PDB entry 3C5N)

Busam, R.D., Lehtio, L., Collins, R., Dahlgren, L.G., Flodin, S., Flores, A., Graslund, S., Hammarstrom, M., Hallberg, B.M., Herman, M.D., Johansson, A., Johansson, I., Kallas, A., Karlberg, T., Kotenyova, T., Moche, M., Nilsson, M.E., Nordlund, P., Nyman, T., Persson, C., Sagemark, J., Svensson, L., Thorsell, A.G., Tresaugues, L., Van den Berg, S., Weigelt, J., Welin, M., Berglund, H.

Structural Genomics Consortium[#], Department of Medical Biochemistry and Biophysics, Karolinska Institutet, Scheeles väg 2, 171 77 Stockholm, SWEDEN
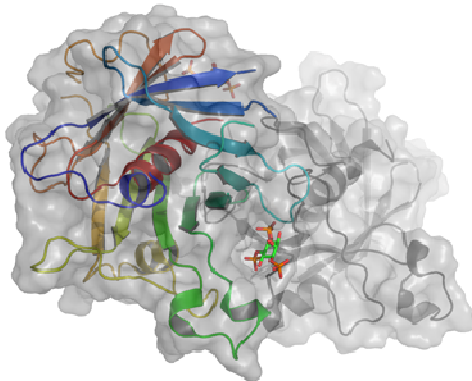
Monogenic murine obesity models are of value for pinpointing genetic causes for obesity (*1*). One murine obesity model is 'tubby' where the phenotype is characterized by increased body-weight at three to six months of age. Once the weight gain is induced it rapidly progresses and results in doubling of weight compared to controls. The phenotype is caused by an autosomal recessive mutation (*2, 3*). Genetic approaches aimed at understanding the molecular basis for the tubby mouse phenotype revealed a family of four genes: the founding member TUB and three Tubby-like proteins (TULP1-3) that share significant sequence homology in a 260 residues long C-terminal domain (*4, 5*). The C-terminal domain of TUB has been found to anchor in the membrane by binding to phosphatidylinositol-(4,5)-bisphosphate (*6*). Upon cleavage of PIP2 by phospholipase C, a nuclear localization signal in the N-terminal part of TUB mediates transport into the nucleus. In the nucleus, TUB may regulate the transcription of one or several so far unknown genes (*7*). Here we solved the structure of TULP1 in complex with IP3 to 1.8Å resolution that is a follow on structure of 2FIM.

References

1.   J. Naggert, T. Harris, M. North, *Curr Opin Genet Dev* **7**, 398 (Jun, 1997).
2.   P. W. Kleyn *et al.*, *Cell* **85**, 281 (Apr 19, 1996).
3.   D. L. Coleman, E. M. Eicher, *J Hered* **81**, 424 (Nov-Dec, 1990).
4.   P. M. Nishina, M. A. North, A. Ikeda, Y. Yan, J. K. Naggert, *Genomics* **54**, 215 (Dec 1, 1998).
5.   M. A. North, J. K. Naggert, Y. Yan, K. Noben-Trauth, P. M. Nishina, *Proc Natl Acad Sci U S A* **94**, 3128 (Apr 1, 1997).
6.   S. Santagata *et al.*, *Science* **292**, 2041 (Jun 15, 2001).
7.   T. J. Boggon, W. S. Shan, S. Santagata, S. C. Myers, L. Shapiro, *Science* **286**, 2119 (Dec 10, 1999).

Human dCMP deaminase (PDB entry 2W4L)

Siponen, M.I., Moche, M., Berglund, H., Collins, R., Dahlgren, L.G., Flodin, S., Flores, A., Graslund, S., Hammarstrom, M., Johansson, A., Johansson, I., Karlberg, T., Kotenyova, T., Lehtio, L., Nilsson, M.E., Nyman, T., Persson, C., Sagemark, J., Schuler, H., Thorsell, A.G., Tresaugues, L., Van Den Berg, S., Weigelt, J., Welin, M., Wikstrom, M., Wisniewska, M., Nordlund, P.

Structural Genomics Consortium[1], Department of Medical Biochemistry and Biophysics, Karolinska Institutet, Scheeles väg 2, 171 77 Stockholm, SWEDEN
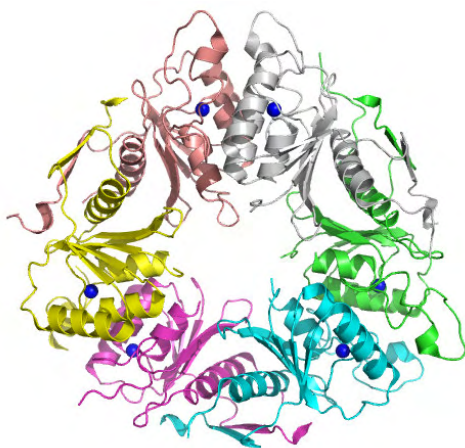
2´-Deoxycytidylate deaminase (dCMP deaminase or dCD) is a key enzyme in the pyrimidine metabolism catalysing the deamination of deoxycytidine monophosphate (dCMP) into deoxyuridine-5´-monophosphate (dUMP). In humans, dCMP deaminase is hexameric and allosterically activated by magnesium associated dCTP (Mg*dCTP) while inhibited by deoxythymidine-5'-triphosphated (dTTP)(*1-3*). In Humans, dCD modifies several anticancer(*4*) and antiviral(*5*) drugs by deamination thereby reducing drug efficiency giving dCD inhibitors therapeutic potential. A crystal structure of the dCD enzyme from *Streptococcus mutans* was recently determined with the active site zinc to 3.0Å resolution (2HVV) and in complex with zinc, Mg*dCTP and the substrate analogue DHOMP to 1.7Å resolution (2HVW) (*6*).

We determined the crystal structure of human dCMP deaminase to 2.1Å resolution with a zinc ion in the active site (2W4L). The enzyme is found to be hexameric and current experiments aim to determine the structural basis for its allosteric mechanism. Comparing this human and *S. mutans* dCD enzymes reveal that the protein part, bridging the allosteric effector and the zinc active sites, is quite different between the two enzymes.

References

1.	G. F. Maley, F. Maley, *Science* **141**, 1278 (Sep 27, 1963).
2.	G. F. Maley, F. Maley, *Biochemistry* **21**, 3780 (Aug 3, 1982).
3.	W. R. Mancini, Y. C. Cheng, *Mol Pharmacol* **23**, 159 (Jan, 1983).
4.	B. Hernandez-Santiago *et al.*, *Antimicrob Agents Chemother* **46**, 1728 (Jun, 2002).
5.	J. Y. Liou, P. Krishnan, C. C. Hsieh, G. E. Dutschman, Y. C. Cheng, *Mol Pharmacol* **63**, 105 (Jan, 2003).
6.	H. F. Hou, Y. H. Liang, L. F. Li, X. D. Su, Y. H. Dong, *J Mol Biol* **377**, 220 (Mar 14, 2008).

Human DEAD box RNA helicase DDX5 (p68) (PDB entry 3FE2)

Karlberg, T., Siponen, M., Berglund, H., Collins, R., Dahlgren, L.G., Flodin, S., Flores, A., Graslund, S., Hammarstrom, M., Johansson, A., Johansson, I., Kotenyova, T., Lehtio, L., Moche, M., Nilsson, M.E., Nordlund, P., Nyman, T., Persson, C., Sagemark, J., Thorsell, A.G., Tresaugues, L., Van Den Berg, S., Weigelt, J., Welin, M., Wikstrom, M., Wisniewska, M., Schuler, H.

Structural Genomics Consortium[1], Department of Medical Biochemistry and Biophysics, Karolinska Institutet, Scheeles väg 2, 171 77 Stockholm, SWEDEN
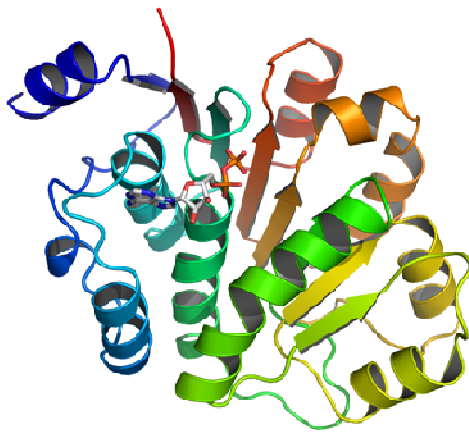
DDX5 (EC=3.6.1.- DEAD box protein 5, RNA helicase p68) belongs to the ATP-dependent DEAD box subfamily of RNA helicases that is characterized by the presence of several conserved motifs, including the signature DEAD sequence. The DEAD box RNA helicases play important roles in all aspects of cellular RNA metabolism e.g. pre-mRNA splicing, transcription, ribosome biogenesis, export, translation (*1*). DDX5 shares 90% protein sequence similarity with DDX17 (p72) in the central core, but the N- and C-terminal extensions are significantly different. DDX5 and DDX17 have been suggested to exist as heterodimers in a variety of complexes in the cell (*2*). Both proteins act as transcriptional co-activators; this has been shown for the activation of transcription of ERα (*3*), MyoD (*4*) and p53 tumor suppressor (*5*). DDX5 and DDX17 may be important for the recruitment of specific components of the transcription machinery, including chromatin remodeling factors, and they may facilitate formation and stabilization of the initiation complex (*6*).

The structure of the DEAD domain of DDX5 was solved and refined to 2.6 Å resolution. It shows the typical DEAD domain structure, with a central 8-stranded β-sheet sandwiched between 5 α-helices on each face, and one ADP molecule in the nucleotide binding pocket.

References

1. O. Cordin, J. Banroques, N. K. Tanner, P. Linder, *Gene* **367**, 17 (Feb 15, 2006).
2. V. C. Ogilvie *et al.*, *Nucleic Acids Res* **31**, 1470 (Mar 1, 2003).
3. H. Endoh *et al.*, *Mol Cell Biol* **19**, 5363 (Aug, 1999).
4. G. Caretti *et al.*, *Dev Cell* **11**, 547 (Oct, 2006).
5. G. J. Bates *et al.*, *Embo J* **24**, 543 (Feb 9, 2005).
6. G. Caretti, E. P. Lei, V. Sartorelli, *Cell Cycle* **6**, 1172 (May 15, 2007).

An Intersubunit Active Site between Supercoiled Parallel β Helices in the Trimeric Tailspike Endorhamnosidase of Shigella flexneri Phage Sf6

Jürgen J. Müller,[1,4] Stefanie Barbirz,[2,4] Karolin Heinle,[2] Alexander Freiberg,[2,5] Robert Seckler,[2] and Udo Heinemann[1,3,*]

[1]Max-Delbrück-Centrum für Molekulare Medizin, Robert-Rössle-Str. 10, 13125 Berlin
[2]Physikalische Biochemie, Universität Potsdam, Karl-Liebknecht-Str. 24-25, 14476 Golm
[3]Institut für Chemie und Biochemie, Freie Universität, Takustr. 6, 14195 Berlin
[4]These authors contributed equally to this work.
[5]Present address: The University of Texas Medical Branch, Department of Pathology, Keiller Building, 3.144, 301 University Boulevard, Galveston, TX 77555-0609, USA.

Sf6 belongs to the Podoviridae family of temperate bacteriophages that infect gram negative bacteria by insertion of their double-stranded DNA. They attach to their hosts specifically via their tailspike proteins.

The structure of Shigella phage Sf6 tailspike protein lacking the head binding domain (Sf6 TSPΔN) was determined to a resolution of 1.25 Å at the EMBL BW7B beamline of DESY (Hamburg), whereas the diffraction data of the Sf6 TSPΔN in complex with the oligosaccharide were measured at the Protein Structure Factory Beamline BL 14.2 at BESSY (Table 1). The final model shows one monomer in the asymmetric unit. The biologically active trimer is built by crystallographic three-fold symmetry.

The monomer structure reveals a conserved architecture with a central, right-handed β helix. In the trimer of Sf6 TSPΔN, the parallel β helices form a left-handed, coiled β coil with a pitch of 340 Å. The C-terminal domain consists of a β sandwich reminiscent of viral capsid proteins. Further crystallographic and biochemical analyses show a Shigella cell wall O-antigen fragment to bind to an endorhamnosidase active site located between two β helix subunits each anchoring one catalytic carboxylate. The functionally and structurally related bacteriophage, P22TSPΔN, lacks sequence identity with Sf6 TSPΔN and has its active sites on single subunits. Sf6 TSP may serve as an example for the evolution of different host specificities on a similar general architecture.

Reference

Mueller, J.J., Barbirz, S., Heinle, K., Freiberg, A., Seckler, R., Heinemann, U. (2008) *Structure* **16***, 766-775.
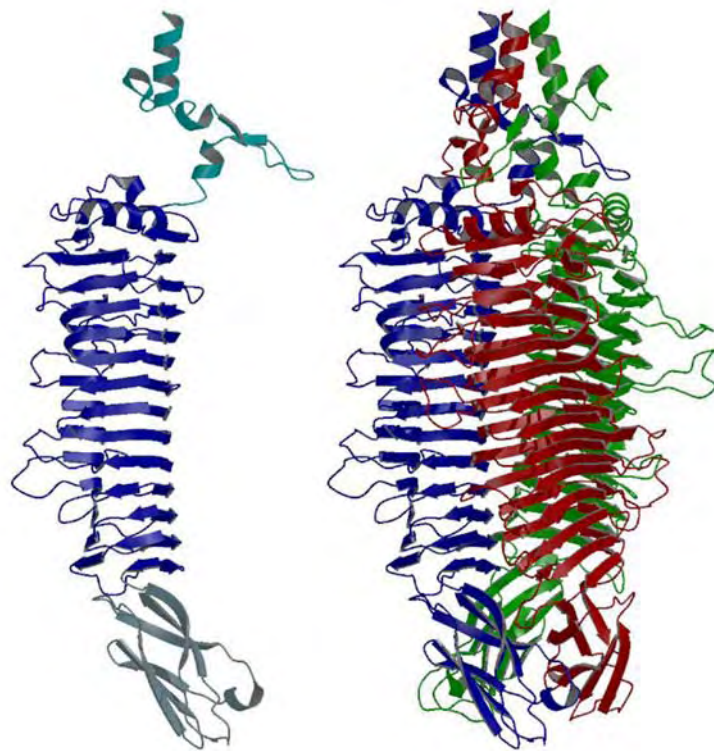
Figure 1. Crystal structures of the monomer (left) and biological active crystallographic trimer (right) of Sf6 TSPΔN. (PDB code 2VBK).
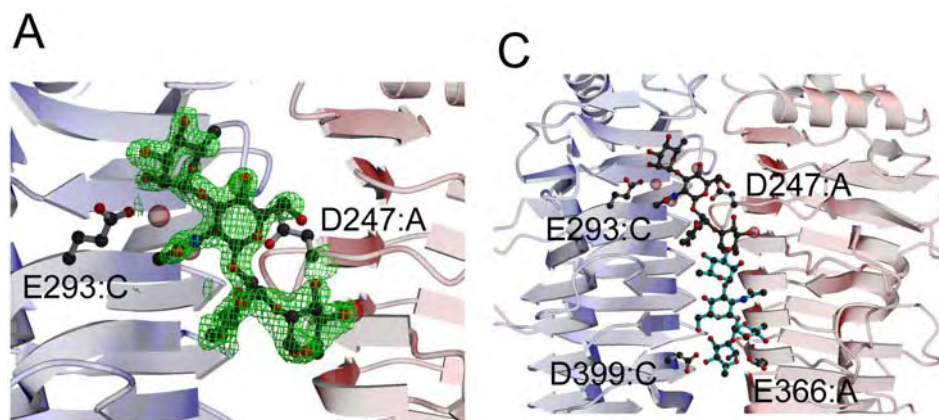
Figure 2. Localization of the Endorhamnosidase Active Site of Sf6 TSPΔN (PDB code 2VBM).

(A) Difference electron density (contoured at 3σ) observed in a complex of the protein with one repeating unit (RU) of an O-antigen hydrolysis product (a-L-Rhap-(1-3)-b-L-GlcpNAc-(1-2)-a-L-Rhap-(1-2)-a-L-Rhap). Glu293 (chain C) and Asp247 (chain A) belong to the binding site.

(C) An octasaccharide (2 RU) modeled into the binding site with its reducing end reaching the catalytic residues Asp399 and Glu366, which lie on different chains, as indicated (right). Bridging water molecules are colored purple.

Table 1. Summary of data collection and refinement statistics of Sf6 TSPΔN, and of the Sf6 TSPΔN-tetrasaccharide complex.

Sample Sf6 TSPΔN	native	complex
A. *Data collection*		
Resolution (Å)	15-1.25 (1.27-1.25)	47-2.0 (2.07-2.0)
Observed / unique reflections	355,196 / 169,746	205,525 / 41,871
Completeness (%)	97.4 (79.8)	99.7 (97.2)
$<I / \sigma(I)>$	11.6 (2.0)	17.4 (7)
R_{sym} (%)	5.1 (25.4)	5.5 (21.5)
Redundancy	2.2 (1.9)	4.9 (4.0)
B (Å^2), Wilson statistics / mean value	9.2 / 11.2	17.6 / 11.5
Mosaicity (°)	0.16	0.2
B. *Refinement*		
Unit cell dimensions a / c (Å)	96.23 / 182.43	95.36 / 182.76
R / R_{work} / R_{free} (%)	12.0 / 11.9 / 14.2	19.2 / 19.0 / 23.2
Overall coordinate error (from R_{work} and R_{free}) (Å)	0.031/0.032	0.164/0.153
Rmsd bond lengths (Å)	0.016	0.012
Rmsd bond angles (°) / torsion angles (°)	1.864 / 7.69	1.362 / 6.77
$<B>$, protein mainchain (Å^2) / sidechain (Å^2)	9.7 / 12.0	19.4 / 21.0
$<B>$, protein all atoms (Å^2)	10.8	20.2
$<B>$, solvent and hetero atoms (Å^2)	24.5	26.3
Ramachandran: Favored / allowed / outlier(%)	95.7 / 4.1 / 0.2	95.9 / 3.9 / 0.2
C. *Structure model*		
Protein: Residue range/atoms	112-622 / 3857	114-622 / 3833
Number of non-hydrogen atoms	4874	4139
Water molecules / phosphate ions	665 / 3	248 / 2
PEG/ethylene glycol/glycerol/tetrasaccharide	2 / 12 / 6 / 0	- / - / - / 1
Mg^{2+} / Mn^{2+}	2 / 0	1 / 2
Alternative conf. / sites of radiation damage	44 / 23	2 / -

Values for the highest resolution shell are shown in parenthesis.

$R_{sym}= \Sigma|I-<I>| / \Sigma I$. $R = \Sigma||F_o|-|F_c|| / \Sigma |F_o|$, where F_o is the observed and F_c is the structure factor amplitude calculated from the model.

Crystal structure of *E. coli* phage HK620 tailspike reveals that Podoviral tailspike endoglycosidase modules are evolutionarily related

Stefanie Barbirz[1*], Jürgen J. Müller[2*], Charlotte Utrecht[1], Alvin J. Clark[3], Udo Heinemann[2,4], and Robert Seckler[1]

[1]**Physikalische Biochemie, Universität Potsdam, Karl-Liebknecht-Str. 24-25, 14476, Golm**
[2]**Max-Delbrück-Centrum für Molekulare Medizin, Robert-Rössle-Str. 10, 13125, Berlin**
[3]**University of Arizona, Department of Molecular and Cellular Biology, Life Sciences South, P.O. Box 210106, Tucson, AZ 85721-0106, USA.**
[4]**Institut für Chemie und Biochemie, Freie Universität, Takustr. 6, 14195 Berlin**
[*]Authors contributed equally to the work

Temperate phages of the λ family possess mosaic genomes as a result of horizontal exchange of genetic material. Their genomes mutate fast, so that structurally and functionally homologous proteins frequently lack detectable sequence homology. The *Podoviridae* HK620, Sf6 and P22 are evolutionarily related. With their tailspike proteins (TSP) they recognize and cleave their host cell receptor, i.e. the O-antigen of gram-negative bacteria. The trimeric TSP have highly homologous N-terminal particle binding domains but no homology in their receptor binding parts, designated TSPΔN.

Single-wavelength anomalous diffraction (SAD) data from HK620 TSPΔN (SeMet) crystals were collected at the selenium peak wavelength of 0.9797 Å under cryo-cooling (100 K) using a MarResearch imaging plate MAR345 at the PSF beamline BL14.2 of the Free University Berlin at BESSY, Berlin. The high resolution native dataset was collected with an ADSC Q4 CCD detector at the beamline ID14-2 at the ESRF (Grenoble, France) (Table1). Crystals of oligosaccharide-HK620 TSPΔN complexes diffracted to 1.6 Å resolution at 100 K at the BESSY BL14.2 beamline using a MAR345 imaging plate (Table 1).

We have determined the crystal structure of the TSPΔN of *Escherichia coli* phage HK620 to 1.38 Å resolution (Fig. 1). The protein has endo-N-acetylglucosaminidase activity and produces hexasaccharides of an O18A1 type O-antigen. Its active site is revealed in the structure of a hexasaccharide bound to HK620 TSPΔN determined at 1.6 Å resolution (Fig.2) (1). As in Sf6 TSP (2) and P22 TSP (3), the main central part of HK620 TSP is a right-handed parallel β-helix. The C-terminal domain forms a β-sandwich, as in Sf6 TSP. Although P22 TSP has a different fold in its C-terminus, sequence alignments with the other TSP C-terminal

domains reveal conserved motifs (1). We therefore propose that the three TSP share conserved functions in the infection process.

References

1   Barbirz, S., Mueller, J.J., Uetrecht, C., Clark, A.J., Heinemann, U., Seckler, R. (2008) *Molecular Microbiology* **69**, 303-316

2   Mueller, J.J., Barbirz, S., Heinle, K., Freiberg, A., Seckler, R., Heinemann, U. (2008) *Structure* **16**, 766-775

3   Steinbacher, S., Seckler, R., Miller, S., Steipe, B., Huber, R. Reinemer, P. (1994) *Science* **265,** 383-386

A   **B**
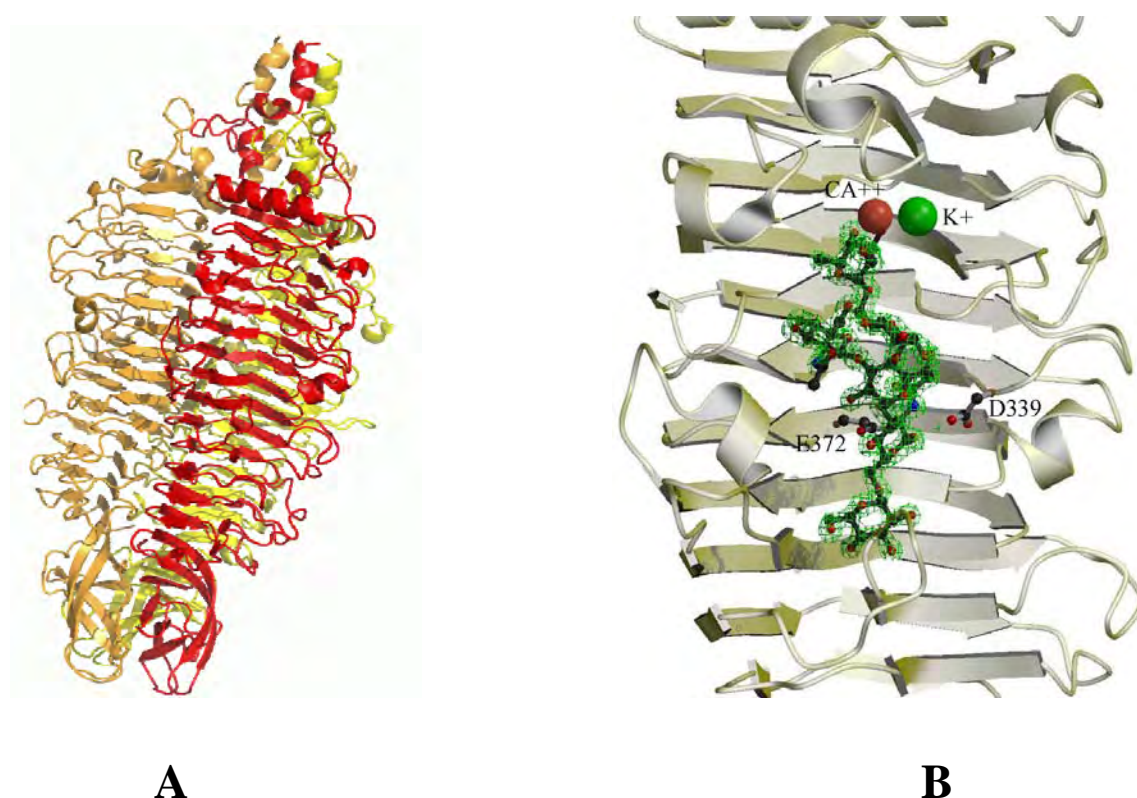
Figure 1.
(A) Crystal structure of the biological active crystallographic trimer of HK620 TSPΔN. (PDB code 2VJI). The monomers are coloured red, yellow, orange
(B) Crystal structure of a hexasaccharide repeat released from the O-antigen of the host cell *E. coli* H TD2158 bound to HK620 TSPΔN in the solvent exposed groove of one monomer. The electron density for the bound hexasaccharide was contoured at 3σ. Putative active-site residues and corresponding hexasaccharide model are shown in ball-and-stick representation (PDB code 2VJJ).

Table 1. Summary of data collection and refinement statistics of HK620 TSPΔ and of the HK620 TSPΔN-hexasaccharide complex at pH 6.0.

Sample HK620 TSPΔN	native	complex
A. *Data collection*		
X-ray source	ESRF ID14-2 ADSC	BESSY BL 14.2
Detector	Q4 CCD	MAR345
Wavelength (Å)	0.9330	0.9500
Resolution range (outer shell) (Å)	20 -1.38 (1.38-1.428)	43.6-1.59 (1.585-1.64)
Wavelength (Å)	0.9330	0.9500
Unique reflections	115,675	73,235
Completeness (%)	97.5 (90.2)	95.6 (83.5)
$I / \sigma(I)$	12.7 (5.1)	26.7 (10.9)
R_{sym} (%)	6.4 (26.3)	4.1 (12.8)
Redundancy	4.6 (4.0)	5.0 (4.1)
Wilson B-factor (Å^2)	14.6	10.9
Mosaicity (°)	0.36	0.30
B. *Refinement and model statistics*		
Unit cell dimensions a / c (Å)	74.22 / 175.16	73.91 / 174.59
R_{work} / R_{free}	0.152 / 0.182 (0.209 / 0.238)	0.133 / 0.165 (0.260 / 0.334)
Rmsd bond lengths (Å)	0.011	0.009
Rmsd bond angles (°)	1.55	1.30
Rmsd torsion angles (°)	5.1	7.1
Averaged main-chain B-factor (Å^2)	17.0	9.2
Ramachandran statistics	87.8 / 12.0 / 0.2 / 0	87.6 / 12.2 / 0.2 / 0
C. *Structure model*		
Protein: Residue range/atoms	112-709 / 4535	112-709 / 4604
Hetero compounds: H_2O	935	731
Ca^{2+}, K^+, Cl^-, HPO_4^{2-}	0, 0, 1, 1	1, 1, 1, 0
cryo components, hexasaccharide	2, 0	7, 1

Values for the highest resolution shell are shown in parenthesis.

$R_{sym} = \Sigma|I-<I>| / \Sigma I$. $R = \Sigma||F_o|-|F_c|| / \Sigma |F_o|$, where F_o is the observed and F_c is the structure factor amplitude calculated from the model.

Preliminary X-ray analysis of a novel haloalkane dehalogenase DbeA from *Bradyrhizobium elkani* USDA94

Tatyana Prudnikova[a], Tomas Mozga[c], Pavlina Rezacova[d,e], Radka Chaloupkova[c], Yukari Sato[f], Yuji Nagata[f], Jiri Brynda[d,e], Michal Kuty[a,b], Jiri Damborsky[c], and Ivana Kuta Smatanova[a,b*]

[a]*Institute of Physical Biology University of South Bohemia Ceske Budejovice, Zamek 136, 373 33 Nove Hrady, Czech Republic*

[b]*Institute of Systems Biology and Ecology, Academy of Science of Czech Republic, Zamek 136, 373 33 Nove Hrady, Czech Republic*

[c]*Loschmidt Laboratories, Institute of Experimental Biology and National Centre for Biomolecular Research, Faculty of Science, Masaryk University, Kamenice 5/A4, 625 00 Brno, Czech Republic*

[d]*Institute of Molecular Genetics, Academy of Sciences of the Czech Republic, Flemingovo nam. 2, 166 37 Prague, Czech Republic*

[e]*Institute of Organic Chemistry and Biochemistry, Academy of Sciences of the Czech Republic, Flemingovo nam. 2, 166 37 Prague, Czech Republic*

[f]*Department of Environmental Life Sciences, Graduate School of Life Sciences, Tohoku University, 2-1-1 Katahira, Sendai 980-8577, Japan*

[*] Correspondence e-mail: ivas@greentech.cz

A novel enzyme, DbeA, belonging to the family of haloalkane dehalogenases (EC 3.8.1.5) was isolated from *Bradyrhizobium elkani* USDA94. This haloalkane dehalogenase is closely related to DbjA enzyme from *Bradyrhizobium japonicum* USDA110 (71% sequence identity), but has different biochemical properties. DbeA is generally less active and has a higher specificity towards brominated and iodinated compounds compared to DbjA. To understand the altered activity and specificity of DbeA enzyme, its mutant variant DbeA1, carrying the unique fragment of DbjA, was constructed. Both the wild type DbeA and the DbeA1 were crystallised using the sitting-drop vapour-diffusion method. The crystals of DbeA belong to the primitive orthorhombic space group $P2_12_12_1$, while the crystals of the mutant DbeA1 belong to

the monoclinic space group *C*2. Diffraction data were collected to the resolution of 2.2 Å for DbeA as well as for DbeA1.

A mutant of DbeA, designated DbeA1, was constructed using inverse PCR to study the importance of the insertion in the N-terminus of the cap domain for activity and specificity of these enzymes. The fragment $_{143}$VAEEQDHAE$_{151}$ equivalent to the unique sequence of DbjA that is not present in DbeA and other HLDs (Ikeda-Ohtsubo et al., in preparation) was inserted between D142 and A143 of DbeA. Crystallographic analysis of DbeA and DbeA1 was initiated to understand the structure-function relationships of the wild type and the insertion mutant. Here we report the crystallisation and diffraction data analysis of DbeA and DbeA1.

The purified sample of DbeA protein (Fig. 1) was used for crystallisation experiments at concentration of 4-6 mg.ml^{-1} in 100 mM Tris–HCl buffer pH 7.5. Sitting-drop procedure (Ducruix & Giege, 1999) for DbeA protein crystallisation was performed in Cryschem 24-well plates (Hampton Research, Aliso Viejo, USA). Reservoir contained 300 – 1000 μl of the precipitant reagent. Each droplet contained 3 μl of DbeA protein solution mixed with 1 μl of reservoir solution (100 mM Tris – HCl pH 7.5, 20% (w/v) PEG 3350 or 4000 and 150 mM calcium acetate). Experiments were carried out at 277 and 292 K temperature. Colourless single needle-shaped crystals with dimensions of approximately 0.05 x 0.05 x 0.3 mm were obtained within two weeks.

Crystallisation of DbeA1 protein was performed using the same crystallisation method and conditions with protein concentrations of 6.5–9 mg.ml^{-1} in 100 mM Tris–HCl buffer pH 7.5. Colourless, well shaped crystals of DbeA1 mutant grew within 5-8 days in drops containing 3 μl of protein solution and 1 μl of reservoir solution composed of 22-25% (w/v) PEG 3350 or 4000, 130 - 150 mM calcium acetate and 100 mM Tris–HCl buffer pH 7.5. Drops were equilibrated over 800 ml reservoir solution.

Freshly prepared single crystals were used to collect diffraction data using synchrotron radiation sources. Diffraction data sets were collected to the 2.2 Å resolution for both the DbeA and DbeA1 (Fig. 3).

DbeA protein crystallised in the primitive orthorhombic space group $P2_12_12_1$ with unit-cell parameters a = 62.7 Å, b = 121.9 Å, c = 161.9 Å. Scaling and merging of data in resolution range 50 – 2.2 Å resulted in completeness of 92 % and an overall R_{merge} of 6.6 %. Diffraction data for the DbeA1 were processed in the centred monoclinic space group $C2$ with unit-cell parameters a = 133.8 Å, b = 75.1 Å, c = 77.6 Å, α = γ = 90°, β = 92°. Scaling and merging of data in resolution range 50 – 2.2 Å resulted in completeness of 98.9 % and an overall R_{merge} of 12.9 %. Evaluation of the crystal-packing parameters indicated that the lattice could accommodate four DbeA proteins in one asymmetric unit with a solvent content of approximately 46 % and two molecules in the asymmetric unit with about 45 % solvent content.

References

Chaloupkova, R., Sykorova, J., Prokop, Z., Jesenska, A., Monincova, M., Pavlova, M., Tsuda, Nagata M. Y. & Damborsky, J. (2003). *J. Biol. Chem.* **278**, 52622–52628.

Ducruix, A. & Giege, R. (1999). *Crystallization of Nucleic Acids and Proteins. A Practical Approach,* 2nd ed. Oxford University Press.

Ikeda-Ohtsubo, W., Goto, Y., Sato, Y., Ohtsubo, Y., Minamisawa, K., Tsuda, M., Damborsky, J. & Nagata, Y. (2009) (in preparation)

Kabsch, W. (1993). *J. Appl. Cryst.* **26**, 795–800.

Kulakova, A. N., Larkin, M. J. & Kulakov, L. A. (1997). *Microbiology* **143**, 109–115.

Minor, W., Cymborowski, M., Otwinowski, Z., Chruszcz, M. (2006). *Acta Cryst.* **D62**, 859-866.

Murshudov, G. N., Vagin, A. A. & Dodson, E. J. (1997). *Acta Cryst.* **D53**, 240–255.

Nagata, Y., Hynkova, K., Damborsky, J. & Takagi, M. (1999). *Protein Expr. Purif.* **17**, 299-304.

Newman, J., Peat, T. S., Richard, R., Kan, L., Swanson, P. E., Affholter, J. A., Holmes, I. H., Prokop, Z., Damborsky, J., Nagata, Y. & Janssen, D. B. (2004). WO 2006/079295 A2.

Prokop, Z., Damborsky, J., Oplustil, F., Jesenska, A. & Nagata, Y. (2005). WO 2006/128390 A1.

Sato, Y., Natsume, R., Tsuda, M., Damborsky, J., Nagata, Y. & Senda T. (2007). *Acta Cryst.* **F63**, 294-296.

Vagin, A. & Teplyakov, A. (1997). *J. Appl. Cryst.* **30**, 1022–1025.
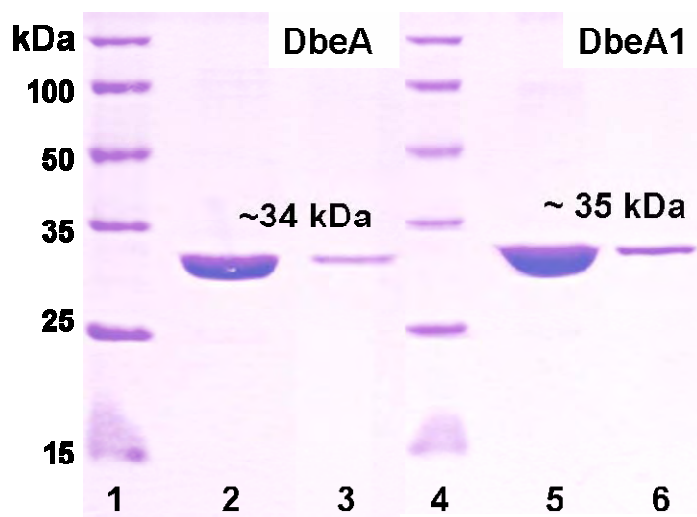
Figure 1

12 % SDS-PAGE stained by Coomassie Brilliant Blue R-250 monitoring the purity of the protein samples and dissolved crystals. Lanes 1 and 4: SDS-PAGE Standards, high range molecular weight marker (Bio-Rad Laboratories), lanes 2 and 5: 3.0 ng of DbeA and 4.0 ng of DbeA1 samples used for crystallisation experiment, respectively; lanes 3 and 6: dissolved crystals of DbeA and DbeA1, respectively.
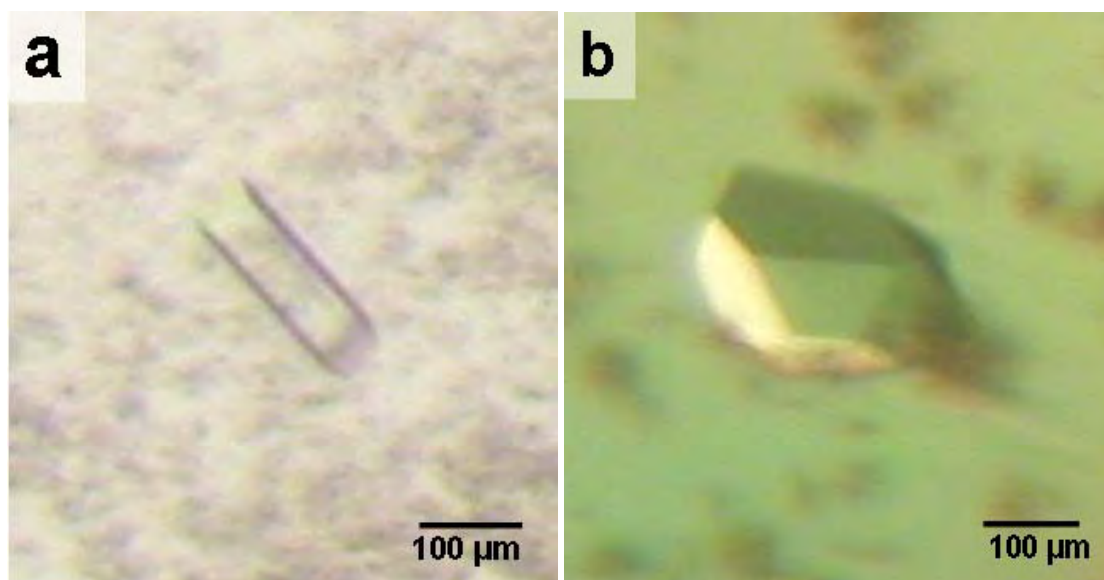
Figure 2

Optimised crystals of (a) DbeA and (b) DbeA1derived from *B. elkani* used for diffraction analysis.
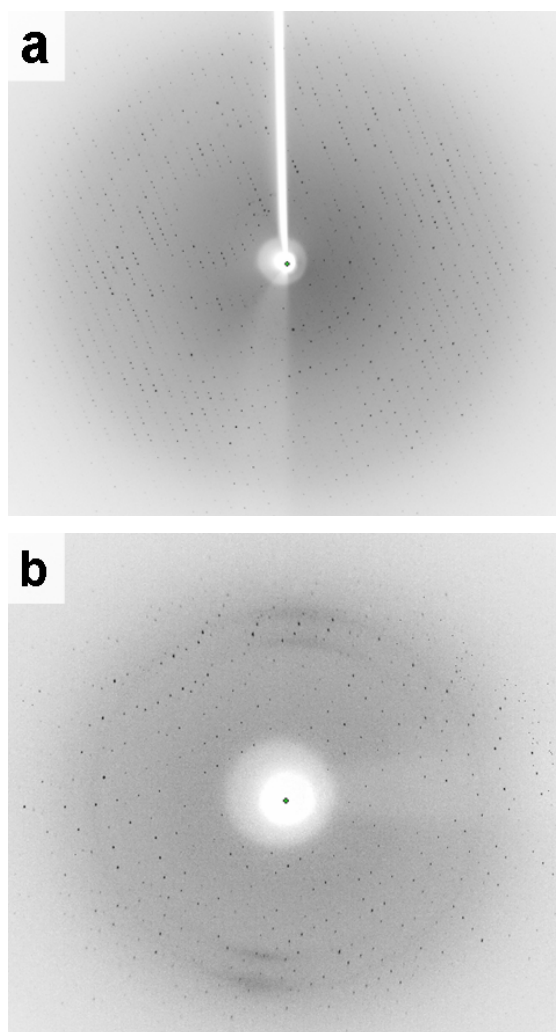
Figure 3

Diffraction images of (a) DbeA and (b) DbeA1 crystals.

Haloalkane dehalogenase DhaA from *Rhodococcus rhodochrous* NCIMB 13064

A. Stsiapanava[1], M. Strakova [3], J. Damborsky[3] and I. Kuta Smatanova[1,2]

[1]Institute of Physical Biology, University of South Bohemia Ceske Budejovice, Zamek 136, CZ-373 33 Nove Hrady, Czech Republic
[2]Institute of Systems Biology and Ecology, v.v.i., Academy of Science of the Czech Republic, Zamek 136,CZ-373 33 Nove Hrady, Czech Republic
[3]Loschmidt Laboratories, Faculty of Science, Masaryk University, Kamenice 5/A4, 62500 Brno, Czech Republic

Haloalkane dehalogenases (EC 3.8.1.5), which are members of the α/β-hydrolase fold family, catalyze hydrolytic conversion of a broad spectrum of hydrocarbons to the corresponding alcohols [1]. Dehalogenation is a key step in the aerobic mineralization pathways of many halogenated compounds that represent environmental pollutants. So haloalkane dehalogenases are potentially important biocatalysts with both industrial and bioremediation applications. Moreover, they can be applied as active components of biosensors or in decontamination mixtures for warfare agents [2]. The haloalkane dehalogenase DhaA was isolated from Gram-positive bacterium *R. rhodochrous* NCIMB 13064 [3]. Besides a wide range of haloalkanes, DhaA can slowly convert serious industrial pollutant 1,2,3-trichloropropane (TCP) [4]. The aim of our project is solve structure of DhaA wild type in the complex with TCP.

Diffraction data for DhaA were collected to 1.04 Å at the BESSY in Berlin. Crystals belong to the triclinic space group *P*1. The known structure of the haloalkane dehalogenase from *Rhodococcus* species (PDB code 1bn6) [5] was used as a template for the molecular replacement. Currently, structure of the DhaA protein is in the process of being further refined and interpreted.

References

[1] Janssen, D.B. (2004). *Cur. Opin. Chem. Biol.* **8**, 150-159.

[2] Prokop, Z., Oplustil, F., DeFrank, J. & Damborsky, J. (2006). *Biotech. J.* **1**, 1370-1380.

[3] Kulakova, A. N., Larkin, M. J. & Kulakov, L. A. (1997). *Microbiology* **143**, 109–115.

[4] Schindler, J. F., P. A. Naranjo, D. A. Honaberger, C.-H. Chang, J. R. Brainard, L. A. Vanderberg, & C. J. Unkefer. (1999). *Biochemistry* **38**, 5772–5778.

[5] Newman, J., Peat, T.S., Richard, R., L., Swanson, P.E., Affholter, J.A., Holmes, I.H., Schindler, J.F, Unkefer, C.J., & Terwilliger, T.C. (1999). *Biochemistry* **28**, 16105-16114.

A CK2α point mutant without backbone tension at the P+1 loop

J. Raaf[1], K. Klopffleisch[1], B. B. Olsen[2], O.-G. Issinger[2], K. Niefind[1]

[1]Institute of Biochemistry, University of Cologne, Zülpicher Straße 47, D-50674, Köln, Germany
[2]Institute of Biochemistry and Molekylær Biology, University of Southern Denmark, Campusvej 55, 5230 Odense, Denmark

The Ser/Thr protein kinase CK2 (former name "casein kinase") is composed of two catalytic subunits (CK2α) attached to dimer of non-catalytic chains (CK2β)[1]. Together with the cyclin dependent kinases and the mitogen-activated kinases, CK2α is a member of the CMGC family of eukaryotic protein kinases (EPKs)[2]. CK2 is involved in several important cellular processes like proliferation and apoptosis and its overexpression is associated with a variety of tumors[3].

In contrast to other EPKs, the regulatory mechanism and the detailed function of CK2 in signaling pathways are not illucidated yet. One remarkable feature of CK2α is that all known structures have the characteristic active kinase conformation including an open activation loop. In CK2α the activation loop is constrained in an open position by the N-terminal segment together with a structural chloride ion and a conserved water cluster.

Another structural speciality of CK2α is an unfavorable backbone conformation of Ala193 within the P+1 loop of the substrate binding site, which is found in all CK2α structures published so far[4] (see Figure 1). This tension is stabilized by hydrogen bonds between the proximate carbonyl groups of Ala193 and Lys198. In closely related kinases of the CMGC group the P+1 loop tension is released in the inactive state and the equivalent position is responsible for their proline preference at the P+1 position of substrates. As this preference and regulatory mechanism is not valid for CK2α, the backbone strain has no evident function and is regarded as an evolutionary remnant[4].

a)   **b)**
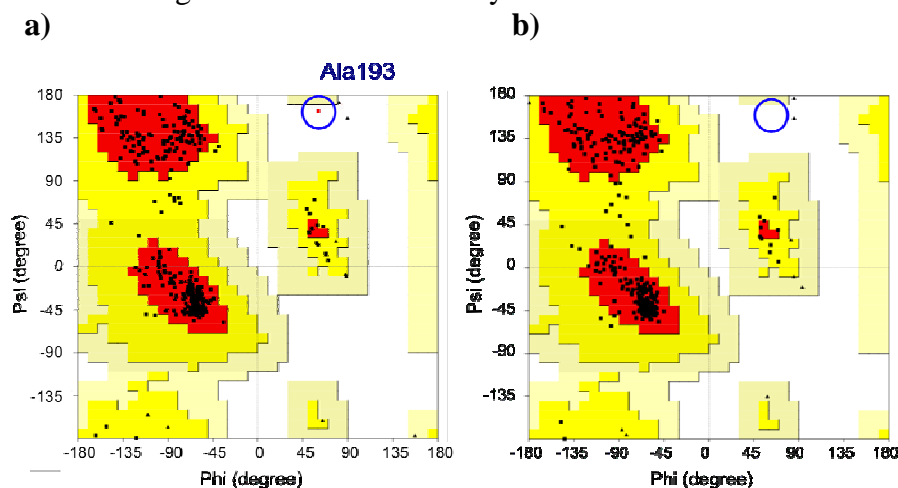
Figure 1: Ramachandran plots of a) *hs*CK2α[1-335] (2pvr[4]) and b) *hs*CK2α[1-335]Ala193Gly. The outlier (Ala193) in the case of *hs*CK2α[1-335] is representative for the backbone strain of position 193 in all published CK2α structures. In the point mutant *hs*CK2α[1-335]Ala193Gly this tension is released.

To study the case of a relaxed P+1 loop of a human CK2α C-terminal deletion mutant (*hs*CK2α[1-335])[5], we replaced Ala193 by a glycine residue. Crystals (Figure 2) were obtained with 1 M Na K phosphate, pH 5, as precipitant. For cryo protection we used a 1 M Na K phosphate, pH 5; 25% glycerol solution. The crystals with the space group $P4_3 2_1 2$ diffracted to 2.29 Å. An X-ray diffraction data set was collected at beamline 14.1 of BESSY. The structure was refined to a final R_{free}-value of 24.04 % and al R_{work}-value of 17, 61 %.
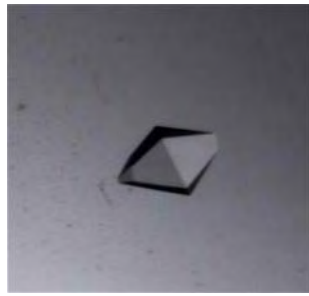
Figure 2: Protein crystal of *hs*CK2α[1-335]Ala193Gly, grown in 1 M Na K phosphate, pH 5.

In the point mutant structure we observed a relaxed backbone in position 193. The hydrogen bonds mentioned above are less strong, so that Lys198 can turn away and releases the backbone (Figure 3). The relaxation is also visible in the corresponding Ramachandran plot (Figure 1). According to this decrease of internal tension we also found an increased thermostability of Δ=+3.1°C of *hs*CK2α[1-335]Ala193Gly in comparison to *hs*CK2α[1-335] in differential scanning calorimetry (data not shown).
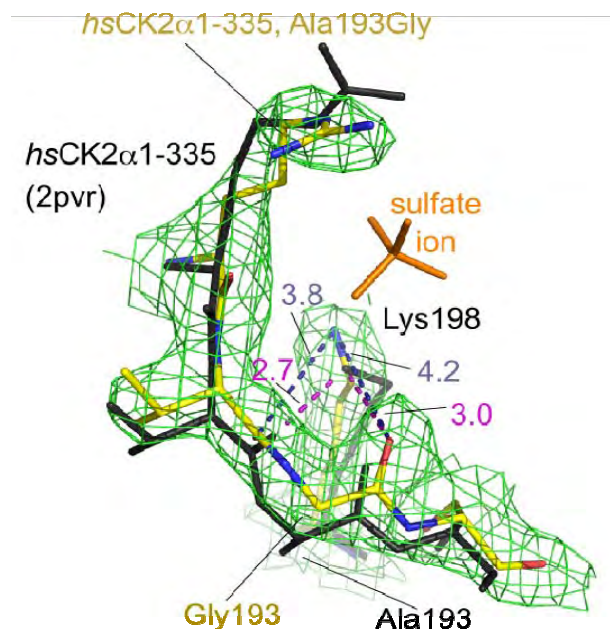
Figure 3: Detailed view on position 193 where alanine was replaced by glycine. The backbone tension which can be observed in all CK2α structures is stabilized by hydrogen bonds between the flanking carbonyl groups of Ala193 and Lys198. In *hs*CK2α[1-335]Ala193Gly Lys198 turns away and releases the backbone. Yellow carbon atoms belong to *hs*CK2α[1-335]Ala193Gly, black atoms belong to *hs*CK2α[1-335](2pvr[4]). Electron densities are drawn with a contour level of 1σ. Dashed lines indicate hydrogen bonds (blue: *hs*CK2α[1-335]Ala193Gly, purple *hs*CK2α[1−335]), distances are given in Å.

References

[1] Niefind, K., Guerra, B., Ermakowa, I. & Issinger, O.-G. , *EMBO J*, **20**, 5320–5331, 2001

[2] Hanks, S.K. & Hunter, T. , *The FASEB Journal*, **9**, 576-596, 1995

[3] Guerra, B. & Issinger, O.-G , *Electrophoresis*, **20**, 391-408, 1999

[4] Niefind, K., Yde, C. W., Ermakova, I. & Issinger, O.-G. , *J Mol Biol*, **370**, 427-438, 2007

[5] Ermakova, I., Boldyreff, B., Issinger, O.-G. & Niefind, K., *J Mol Biol*, **330**, 925-934, 2003

Tomographic insights into evolution.
Microtomographic investigations of the external and internal morphology of male and female insect genitalia

Seidel, Sophia, Museum für Naturkunde
Kühbacher, Markus, Helmholtz Zentrum für Material und Energie
Wessel, Andreas, Museum für Naturkunde
Hartung, Viktor, Museum für Naturkunde
Hilger, Andre, Helmholtz Zentrum für Material und Energie
Choinka, G., Helmholtz Zentrum für Material und Energie
Manke, Ingo, Helmholtz Zentrum für Material und Energie
Riesemeier, Heinrich, BAM
Kyriakopoulos, A., Helmholtz Zentrum für Material und Energie
Hoch, Hannelore, Museum für Naturkunde

Comparative morphology of genital structures in Butterfly Bugs
(Insecta: Hemiptera: Fulgoridae)

The Fulgoridae, or butterfly bugs, are conspicuous, fairly large (up to 10 cm) insects with wings
that are often brightly colored. They feed on trees and wooden shrubs by sucking
plant juices from the phloem. At present ca. 600 species are described worldwide
(Nagai & Porion, 1996). The majority of species are tropical (O'Brien & Wilson 1985).
Interestingly, neither the degree of their diversity (i.e. the exact number of species) or the
boundaries between many of the species already described are sufficiently clear.

In many insects, the male genitalia show a complicated structure and differ in closely related
taxa. Therefore, they are widely used in taxonomy. A combination of established and new
methods like Scanning Electron Microscopy (SEM) and Micro-Computer Tomography
(Micro-CT) provides a more detailed view of the genitalia than was possible previously.
Synchrotron radiation-based X-ray microtomography allows the acquisition of high resolution
images while maintaining the physical integrity of the specimens (which is of immense
importance if unique museum specimens, such as holotypes, are to be studied).
 In the present study we apply these methods to species of the butterfly bug Penthicodes,
which
is widespread in South-East-Asia (10 species described: Nagai & Porion, 1996).

In the bilaterally symmetrical male genitalia, the parameres and the anal tube enclose and
conceal the copulatory organ, the aedeagus.The membranous expandable lobes of the
aedeagus are wrinkled in repose. During copulation they are inflated apparently due to
pumping haemolymph into the aedeagus. As the female gonoporus is very small, inflation
probably happens after insertion of the aedeagus into the female reproductive duct.

In fulgorids, the structure of the aedeagus has never been studied in such detail. It was only
occasionally mentioned or drawn in species descriptions, for example from Lallemand (1963).
Homologising morphological structures and consequently taxonomy above the species level
suffered from the lack of knowledge about the functional morphology.

Preparation of specimens.
Inflating the genital structures with potassium hydroxide (KOH).
For examination the male abdomen is placed in 50 °C KOH solution (10 %) for 45 min (histo-lysis) and then in distilled water: the difference in osmotic pressure leads to inflation of the membranous parts. After inflation the sample is exposed to ascending ethanol series and then critical-point-dried.

 Perspectives:
High resolution Micro-CT enables us to create a virtual 3D-model without destroying the original
specimen, and thus allows us to study unique specimens such as holotypes. Micro-CT will for the
first time help us visualize the internal structures of male and female genitalia, contributing to a deeper knowledge of their functional morphology, and eventually, the copulatory mechanism. This in turn, is subject to sexual selection, and hence, at the root of evolutionary change.

Preliminary results of this study were presented at
- Annual Meeting of the German Zoological Society (DZG, Deutsche Zoologische Gesellschaft), Jena, September 2008 (poster)
- Annual BESSY Users´ Meeting, Berlin-Adlershof, December 2008 (poster; awarded 1st prize)

Microfluidic Mixers for the Investigation of Rapid Protein Folding Kinetics Using Synchrotron Radiation Circular Dichroism Spectroscopy

P. Baumgärtel[1], A.S. Kane[2,3], A. Hoffmann[4], G. Reichardt5[4], R.Seckler[1], O. Bakajin[3], B. Schuler[4]

[1] Department of Physical Biochemistry, University of Potsdam, Germany
[2] Department of Electrical & Computer Engineering, University of California, Davis
[3] BioSecurity and Nanosciences Lab., Lawrence Livermore National Lab., Livermore, CA
[4] Department of Biochemistry, University of Zurich, Switzerland
[5] Helmholtz-Zentrum Berlin, 12489 Berlin, Germany

In the last year we worked on optimizing our microfluidic mixer which we have developed for monitoring rapid protein folding reactions using synchrotron radiation circular dichroism (SRCD) spectroscopy. The detailed design and the fabrication process as well as the quantification of the mixing efficiency and performance SRCD spectroscopy measurements can be found in our newest publication[1]. The SRCD spectroscopy measurements were performed on the small, fast folding, protein cytochrome c (cyt c) at the undulator beamline U125/2-10m NIM at BESSY. Our results show that the combination of SRCD with microfluidic mixing opens new possibilities for investigating rapid conformational changes in biological macromolecules that have previously been inaccessible.

Cytochrome c folding kinetics

The refolding reaction was initiated by a 4-fold dilution of cyt c in 4 M GdmCl (guanidinium hydrochloride) with refolding buffer to a final GdmCl concentration of 0.8 M. The measurement was performed at a total flow rate of 250 µL/min. At the first measurement position (Figure 1C) in the channel, corresponding to 180 µs after mixing, spectra were taken both for the refolding reaction and under equilibrium start (4 M GdmCl) and end (0.8 M GdmCl) conditions (Figure 2B). The reference spectra at 4 and 0.8 M are typical of an unfolded protein and a folded α-helical protein, respectively. A linear combination of both reference spectra shows that the spectrum acquired 180 µs after the start of refolding corresponds to about $28 \pm 6\%$ folded signal. Note that the reference with 4 M GdmCl can be measured down to 205 nm, significantly lower than accessible in conventional stopped-flow CD instrumentation. We also measured the kinetic progress curve of the refolding reaction at 220 nm along the entire observation channel (up to 30 ms, Figure 2A). The refolding trace was fit with a single exponential with a refolding rate of 190 ± 25 s^{-1}. The accessible time window covers $44 \pm 2\%$ of the total signal change. A change of $22 \pm 2\%$ already occurred in the dead time of our instrument, and $33 \pm 2\%$ of the signal is still missing
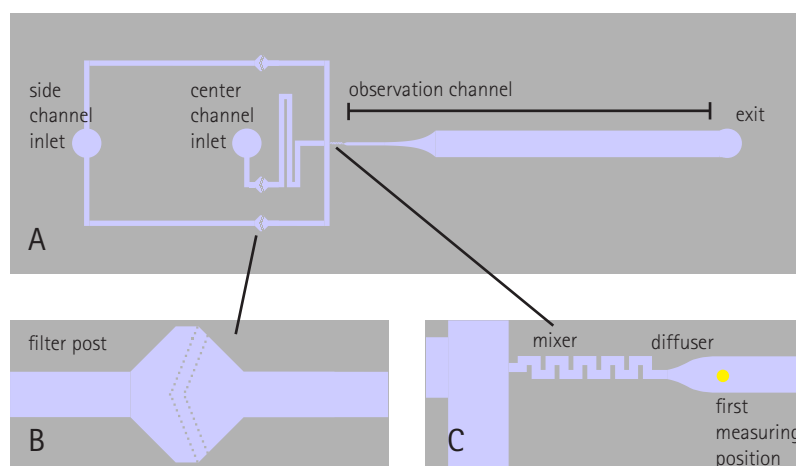
Figure 1: (A) drawing of the optimized SRCD mixer chip. (B) Filter posts are designed to minimize clogging of the mixer. (C) Design details of the optimized serpentine mixer. The smooth curvature of the diffuser minimizes the creation of any recirculation vortices in the observation channel where kinetics are measured.
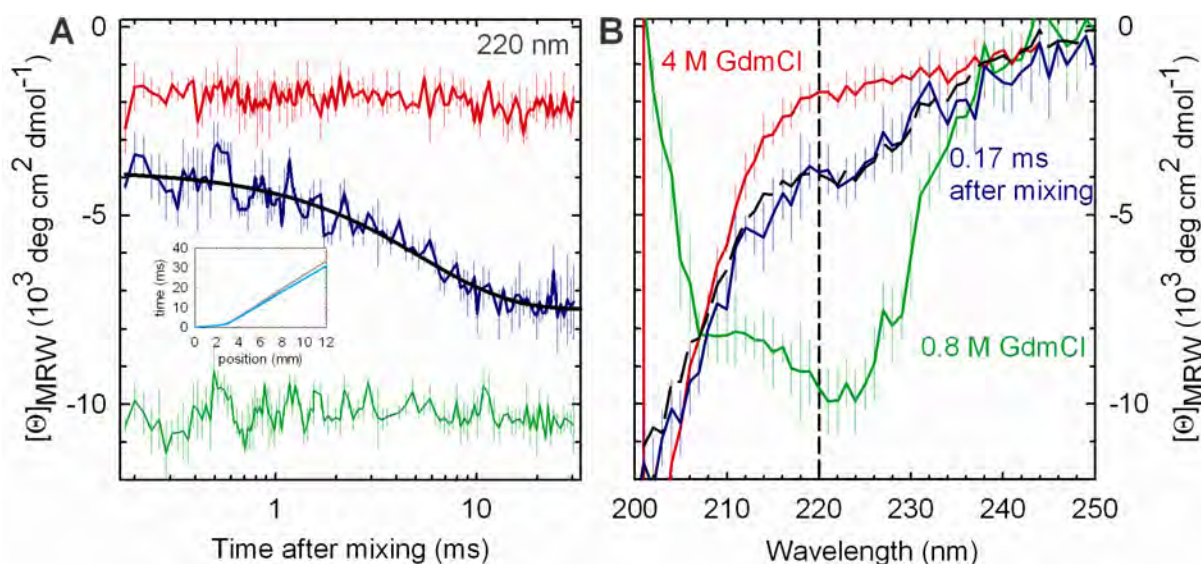
Figure 2: Synchrotron radiation circular dichroism measurements of cyt c in the mixing device. Kinetic measurements under refolding conditions are show in blue, measurements under equilibrium conditions representing the start (4 M GdmCl) and end conditions (0.8 M GdmCl) are shown in red and green, respectively. (A) Refolding kinetics measured at 220 nm and single exponential fit to the data (black). (B) CD spectra measured at 0.18 ms after mixing and linear combination of 28% native and 72% unfolded spectra (black dashed line).

after 30 ms. As expected, the reference spectra under equilibrium conditions are invariant along the channel and show the CD signal characteristic of folded and unfolded protein, respectively. The fast refolding kinetics of cyt c have been studied in great detail,[1] which makes cyt c an ideal reference for rapid mixing experiments.

The novel combination of SRCD spectroscopy with microfluidic mixing devices opens new opportunities to probe structural changes in biomolecules on previously inaccessible time scales and wavelength ranges. Our device provides an unprecedented dead time for CD experiments in the presence of buffers with high absorption (GdmCl) and clearly demonstrates the potential of the method. Future improvements in the approach described here are to be expected, especially with the advent of a dedicated SRCD beam lines, which is currently under construction at BESSY and will be available for users in the second half of 2010. Higher photon flux will improve the signal-to-noise ratio, accelerate data acquisition, thus reduce sample consumption, enable the use of lower protein concentrations, and possibly allow a further extension of the accessible wavelength range and the use of deeper channels. Of particular importance for the combination with microfluidic mixing is the brilliance of synchrotron sources, allowing the efficient focusing of light into microstructures. Also future developments in microfabrication, here we plan to work in cooperation with the "Anwendungszentrum für Mikrotechnik" at the HZB, are thus expected to enable further improvements in dead time and time resolution.

[1] Avinash S. Kane, Armin Hoffmann, Peter Baumgärtel, Robert Seckler, Gerd Reichardt, David A. Horsley, Benjamin Schuler, und Olgica Bakajin. "Microfluidic Mixers for the Investigation of Rapid Protein Folding Kinetics Using Synchrotron Radiation Circular Dichroism Spectroscopy." Analytical Chemistry 80, 9534-9541 (2008)

Structural and functional characterization of human Iba proteins

Jörg O. Schulze [1] , Claudia Quedenau [2] , Yvette Roske [1] , Thomas Adam [3] , Herwig Schüler [1] , Joachim Behlke [1] , Andrew P. Turnbull [1] , Volker Sievert [2] , Christoph Scheich [2] , Uwe Mueller [4] , Udo Heinemann [1,5] and Konrad Büssow [2,6]

1 Max Delbrück Center for Molecular Medicine, Berlin, Germany
2 Max Planck Institute for Molecular Genetics, Berlin, Germany
3 Institute of Microbiology and Hygiene, Charité Medical School, Berlin, Germany
4 Macromolecular Crystallography, BESSY GmbH, Berlin, Germany
5 Institute of Chemistry and Biochemistry – Crystallography, Free University, Berlin, Germany
6 Department of Structural Biology, Helmholtz Centre for Infection Research, Braunschweig, Germany

Iba2 is a homolog of ionized calcium-binding adapter molecule 1 (Iba1), a 17-kDa protein that binds and cross-links filamentous actin (F-actin) and localizes to membrane ruffles and phagocytic cups. Human Iba1 was found to bind calcium ions in overlay assays, but structures solved by NMR and X-ray crystallography revealed a monomeric, Ca(2+)-free protein. In contrast mouse IBa1 showed a homodimeric protein with Ca(2+). Here, we present the crystal structure of human Iba2 and its homodimerization properties, F-actin cross-linking activity, cellular localization and recruitment upon bacterial invasion in comparison with Iba1.
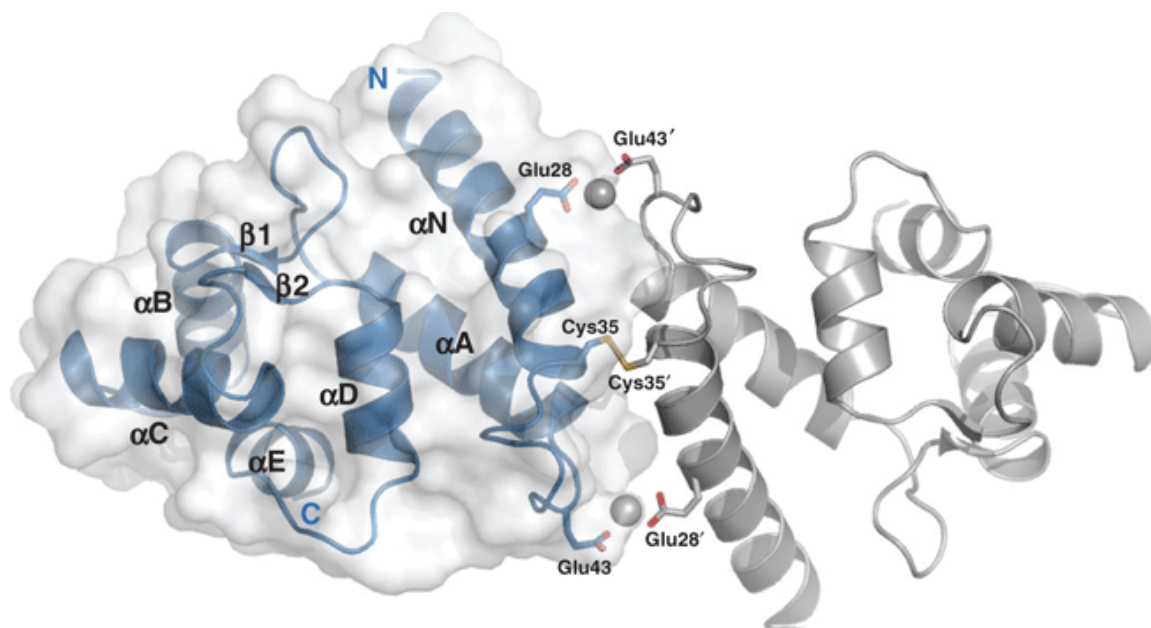
Figure 1. Cartoon representation of the homodimer Iba2. One subunit of the dimer is rendered in gray, the other subunit is shown in blue with a transparent surface. Important residues in the dimerization interface are depicted in stick representation with oxygen atoms in red and sulfur atoms in yellow.

The Iba2 structure comprises two central EF-hand motifs lacking bound Ca(2+). Iba2 crystallized as a homodimer stabilized by a disulfide bridge and zinc ions. These ions are not located in potential dimerization or oligomerization interfaces. Structurally, the Iba2 monomer is very similar to monomeric human Iba1. Both structures differ significantly only in the conformation of EF-hand2. The homodimer of Iba2 has a unusual small dimerization interface of 360A² corresponding to 5% of the total protein surface.
Equilibrium dialysis showed that neither Iba1 nor Iba2 bind Ca(2+) in presence of 100μM Ca(2+). Analytical ultracentrifugation showed that human Iba1 and Iba2 form homodimers

under reducing conditions. The presence of Ca(2+) had only marginal effect on dimerization of both Iba proteins. Sedimentation experiments and microscopy detected pronounced, indistinguishable F-actin binding and cross-linking activity of Iba1 and Iba2 with induction of F-actin bundles. Fluorescent Iba fusion proteins were expressed in HeLa cells and co-localized with F-actin. Iba1 was recruited into cellular projections to a larger extent than Iba2. Additionally, we studied Iba recruitment in a Shigella invasion model that induces cytoskeletal rearrangements. Both proteins were recruited into the bacterial invasion zone and Iba1 was again concentrated slightly higher in the cellular extensions. According to our studies, the most outstanding difference between both Iba proteins seems to be their distinct expression patterns in various tissues of the body.

References:

Imai Y, Ibata I, Ito D, Ohsawa K & Kohsaka S (1996) A novel gene *iba1* in the major histocompatibility complex class III region encoding an EF hand protein expressed in a monocytic lineage. *Biochem Biophys Res Commun* **224**, 855–862.

Kawasaki H, Nakayama S & Kretsinger RH (1998) Classification and evolution of EF-hand proteins. *Biometals* **11**, 277–295.

Ohsawa K, Imai Y, Kanazawa H, Sasaki Y & Kohsaka S (2000) Involvement of Iba1 in membrane ruffling and phagocytosis of macrophages/microglia. *J Cell Sci* **113**, 3073–3084.

Yamada M, Ohsawa K, Imai Y, Kohsaka S & Kamitori S (2006) X-Ray structures of the microglia/macrophage-specific protein Iba1 from human and mouse demonstrate novel molecular conformation change induced by calcium binding. *J Mol Biol* **364**, 449–457

Crystal Structure of KorA Bound to Operator DNA: Insight into Repressor Cooperation in RP4 Gene Regulation

Bettina König[a], Jürgen J. Müller[a], Erich Lanka[b] und Udo Heinemann[a,c]

[a]Max-Delbrück-Center for Molecular Medicine, Robert-Rössle-Straße 10, 13125 Berlin, Germany
[b]Max-Planck-Institute for Molecular Genetics, Ihnestraße 73, 14195 Berlin, Germany
[c]Institute for Chemistry and Biochemistry, Free University, Takustraße 6, 14195 Berlin, Germany

heinemann@mdc-berlin.de

KorA is a global repressor in RP4 which regulates cooperatively the expression of plasmid genes whose products are involved in replication, conjugative transfer, and stable inheritance. The structure of KorA bound to an 18-bp DNA duplex that contains the symmetric operator sequence and incorporates 5-bromo-deoxyuridine nucleosides has been determined by MAD phasing at 1.96-Å resolution (Figure 1, Table I). KorA is present as a symmetric dimer and contacts DNA via a helix-turn-helix motif. Each half-site of the symmetric operator DNA binds one copy of the protein in the major groove. As confirmed by mutagenesis, recognition specificity is based on two KorA side chains forming hydrogen bonds to four bases within each operator half-site. KorA has a unique dimerization module shared by the RP4 proteins TrbA and KlcB. We propose that these proteins cooperate with the global RP4 repressor KorB (1, 2) in a similar manner via this dimerization module and thus regulate RP4 inheritance.
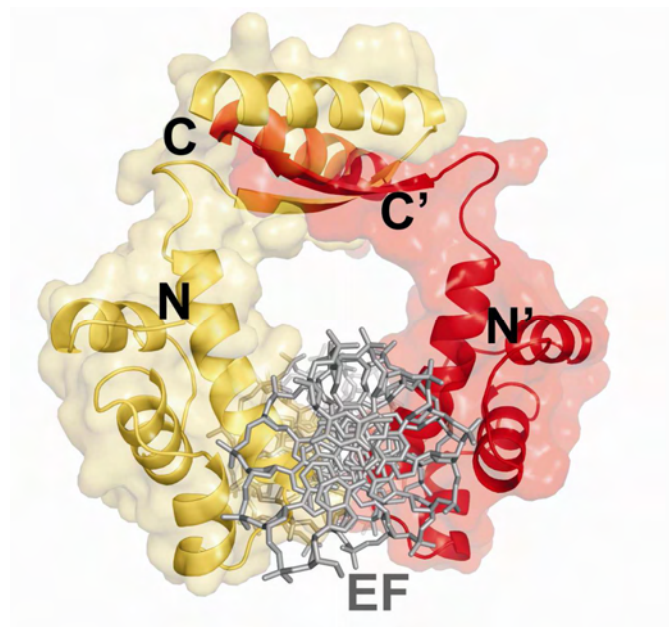
Figure 1. Overall structure of the KorA-O_A* complex.
(A) Image of the KorA dimer (yellow and red) on a semitransparent molecular surface bound to its operator site, looking down the DNA axis. For clarity, the DNA (gray) is shown in only one of the two orientations present in the complex.

Table I. Data collection and refinement statistics

Data collection

Data set	Peak	Inflection point	Native-like merged peak
Wavelength (Å)	0.91991	0.92004	0.91991
Resolution range (Å)[a]	50-1.96 (2.08-1.96)	50-1.96 (2.08-1.96)	50-1.96 (2.08-1.96)
Total reflections[a,b]	229,922 (19,830)	216,313 (18,556)	230,648 (20,085)
Unique reflections[a]	60,942 (7,376)[b]	60,954 (7,347)[b]	31,085 (3,817)
Completeness (%)[a]	92.6 (68.4)	92.5 (68.0)	93.3 (70.1)
$<I / \sigma(I)>$[a]	32.2 (12.7)	37.1 (11.4)	42.5 (17.4)
R_{sym} (%)[a]	2.5 (6.5)	2.2 (7.5)	2.7 (7.4)
R_{meas} (%)[a,c]	2.9 (8.3)	2.5 (9.7)	2.9 (8.2)

Refinement

Resolution range (Å)	50-1.85
R_{work} (%)	17.0
R_{free} (%)	20.1
Reflections in R_{work}	32,666
Reflections in R_{free}	1,753
R.m.s. deviations	
Bond lengths (Å)	0.006
Bond angles (°)	1.522
No. of atoms	
Protein and DNA	2961
Water oxygens	317
Ramachandran (%)	
Most favored	98.8
Additional allowed	1.2

[a]Values in parentheses are for the highest resolution shell.
[b]Friedel pairs not merged.
[c]Multiplicity-corrected R_{sym} as defined by Diederichs and Karplus (41).

References

1. Delbrück, H., Ziegelin, G., Lanka, E. and Heinemann, U. (2002) An Src homology 3-like domain is responsible for dimerization of the repressor protein KorB encoded by the promiscuous IncP plasmid RP4. *The Journal of Biological Chemistry*, **277**, 4191-4198.

2. Khare, D., Ziegelin, G., Lanka, E. and Heinemann, U. (2004) Sequence-specific DNA binding determined by contacts outside the helix-turn-helix motif of the ParB homolog KorB. *Nature Structural & Molecular Biology*, **11**, 656-663.

Funding

Structural basis of S-norcoclaurine synthase enzymatic activity.

Andrea Ilari [1], Stefano Franceschini [1], Alessandra Bonamore [1], Fabio Arenghi [2], Bruno Botta [3], Alessandra Pasquo [4], & Alberto Boffi [1]

1. Dipartimento di Scienze Biochimiche and Istituto di Biologia e Patologia Molecolari (IBPM), CNR, Università "Sapienza" P. Aldo Moro 5, 00185, Rome, Italy.
2. Dipartimento di Studi di Chimica e Tecnologia delle Sostanze Biologicamente Attive, Università "Sapienza" P. Aldo Moro 5, 00185, Rome, Italy.
3. CPC Biotech s.r.l., via dei Mille 111, 80121, Napoli, Italy.
4. ENEA Casaccia Research Centre, Dipartimento BIOTEC, Sezione Genetica e Genomica Vegetale, P.O. Box 2400 I-00100 Rome, Italy

Benzylisoquinoline alkaloids are among the most important plant secondary metabolites and include a number of biologically active substances that are widely employed as pharmaceuticals such as morphine, codeine, berberine and papaverine. The enzymatic pathways leading to the amazing diversity of benzylisoquinoline derivatives have been largely unveiled in several plant species. These pathways have been shown to originate from a common route in which the first committed step consists in the stereospecific Pictet-Spengler condensation of dopamine with 4-hydroxyphenylacethaldehyde (4-HPAA) to yield the benzylisoquinoline central precursor, S-norcoclaurine.

The S-norcoclaurine biosynthesys is catalyzed by the Norcoclaurine synthase (NCS).

We solved he first crystallographic structure of NCS (from *T. flavum*) without substrates and in complex with dopamine and the non-reactive substrate analogue 4-hydroxybenzaldehyde (PHB). A three-wavelength MAD data set was collected from Se-Met -NCS on the BL14-2 beamline at the synchrotron radiation source BESSY, Berlin, Germany, using a CCD detector. Complete data sets (120° of φ rotation each) were collected at the peak (λ= 0.97966 Å), inflection (λ= 0.97984 Å) and remote (λ= 0.97800 Å) wavelengths, at a temperature of 100 K. Each frame was collected with an exposure time of 2 s and a 1.0° oscillation range. The data scaling indicated that the crystal is trigonal (P3$_1$21) with the following unit-cell dimensions: a=b=86.31 Å, c=118.36 Å, α=β=90°, λ=120° (1).

The structure of NCS without substrates was solved by MAD technique using the program SOLVE (PDB code 2VNE) and the structure of NCS in complex with dopamine and the non-reactive substrate analogue PHB was solved at 2.1 Å resolution by molecular replacement using the monomer B of substrate free NCS as search probe (PDB code 2VQ5) (2). Each monomer shows an accessible cleft, located between the seven stranded antiparallel β-sheets and the three α-helices, that extends through the protein matrix forming a 23.4 Å long tunnel. The wider opening (4.2 Å diameter), is formed by an array of hydrophobic residues and a polar patch composed by Tyr108,131,139 and Glu103 side chains located at the entrance of the cavity. Deeper in the cavity, the side chain of Lys122 protrudes towards the interior of the tunnel forming a "hook" capable of intercepting the carbonyl group of the aldehyde substrate.

As shown in Fig.1, the geometry of NCS active site is dominated in addition to Lys122 by the presence of other two strong proton exchanger, Asp141 and Glu110, and of a hydrogen bonding donor, Tyr108. These residues shape the binding site of the two aromatic substrates and dictate the mechanism proposed in Fig.2. The reciprocal orientations of dopamine and PHB and their relationships with neighbouring aminoacid side chains immediately suggest a general acid-base reaction mechanism that matches closely the classical two-steps Pictet-Spengler scheme and

eventually leads to the stereospecific ring closure to yield S-norcoclaurine. The presence of a strong interaction (2.6 Å) between the amino group of Lys122 and the carbonyl oxygen of the aldehyde, coupled to the off-plane position of the carbonyl with respect to the phenyl ring, is suggestive of a proton transfer from the ammonium ion to the carbonyl oxygen and consequent stabilization of a partial positive charge on the carbon atom (Fig.2B). Such a configuration supports the idea that Lys122 is also involved in the water molecule release from the carbinolamine moiety subsequent to the nucleophilic attack of the dopamine amino group to the aldehyde carbonyl. The electrophilicity of the imine double bond thus formed is the driving force of the subsequent Mannich type cyclization that entails a rotameric rearrangement of the iminium ion adduct followed by electrophilic substitution at the C5 position (Fig. 2 (d) and (e)). After deprotonation, assisted by the carboxyl moiety of Glu110, the S-stereospecific product is formed (Fig. 2 (f)). The mechanism thus proposed is exquisitely stereospecific in that, given the position of Glu110 with respect to the dopamine ring orientation, C5 proton abstraction may only occur from a single possible configuration of the intermediate.
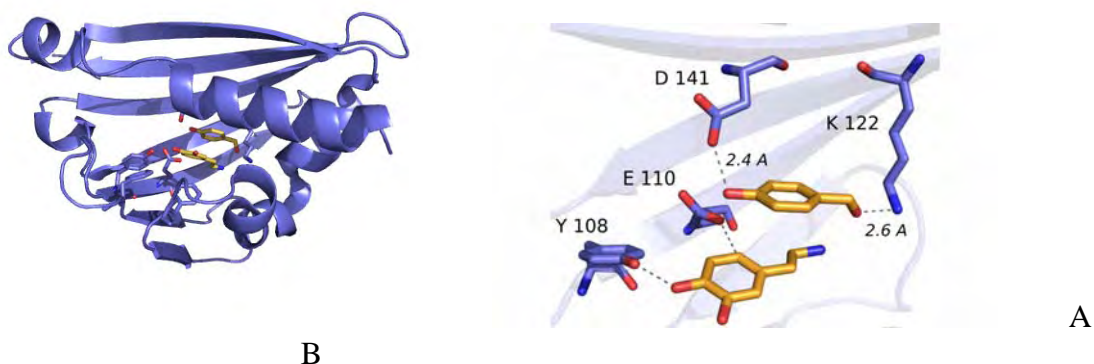
Fig.1 Norcoclaurine synthase (NCS) from *Thalictrum flavum* in complex with dopamine and PHB. (A) Overall fold. (B) Catalytic site. The PHB and dopamine molecules are indicated in yellow-orange. The residues involved in the catalysis are indicated in blue.
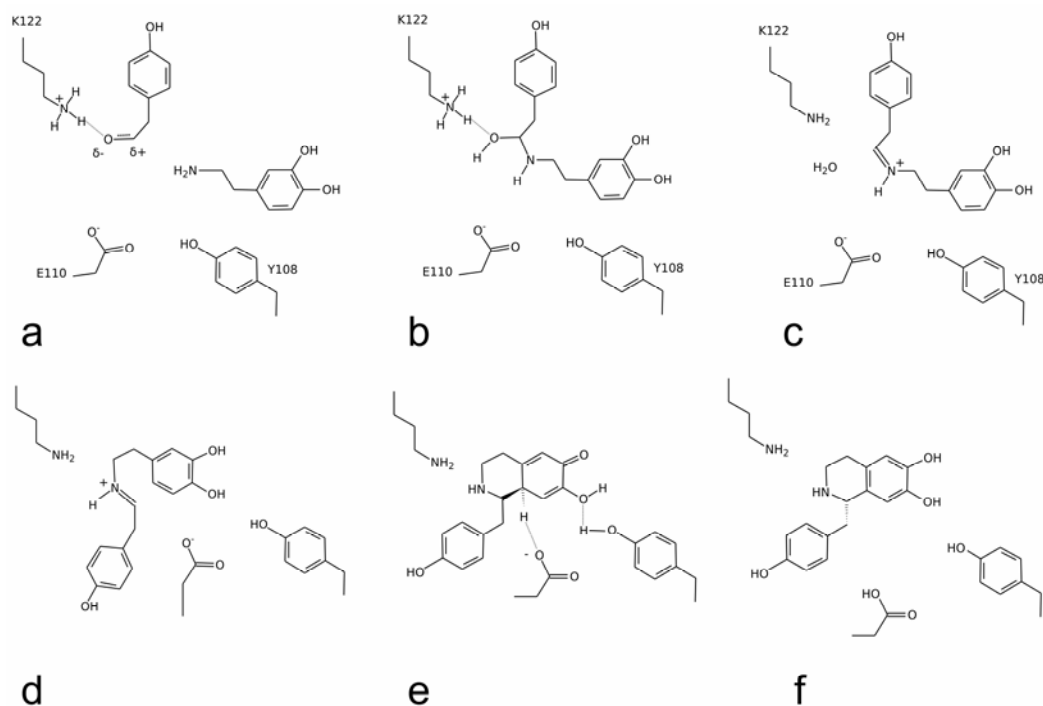
Fig2. **Mechanism of NCS catalyzed S-norcoclaurine synthesis.** The following steps are proposed: (a) binding of p-hydroxyphenylacetaldehyde and dopamine to the catalytic site; (b) nucleophilic attack of the dopamine amino group to the aldehyde carbonyl group; (c) water molecule release, assisted by Lys122 and generation of the imine double bond; (d) rotameric arrangement of the imine intermediate; (e) electrophilic attack of the sp^2 imine-carbon to the C5 of dopamine with concomitant C5 proton abstraction from the quinone intermediate assisted by Glu110 residue; (f) product release .

References
1. Pasquo A, Bonamore A, Franceschini S, Macone A, Boffi A, Ilari A "Cloning, expression, crystallization and preliminary X-ray data analysis of norcoclaurine synthase from Thalictrum flavum." *Acta Crystallogr Sect F Struct Biol Cryst Commun.* (2008) 64:281-3.

2. Ilari A, Franceschini S, Bonamore A, Arenghi F, Botta B, Macone A, Pasquo A, Bellucci L, Boffi A. "Structural basis of enzymatic (s)-norcoclaurine biosynthesis." *J Biol Chem.* 2009 284:897-904.

Crystal structure of Glucose-1-phosphatase (AgpE) from *Enterobacter cloacae.*

Grishkovskaya I[1]., Herter T[2]., Wessner H[1]., Borriss R.[2] & Höhne W.[1]
[1]Institute of Biochemistry, Charite Campus Mitte, Berlin, Germany
[2]Institute of Biology, Bacterial Genetics, Humboldt University, Berlin, Germany

Because of the medical importance of phytate the enzymes involved in its hydrolysis were intensively studied in the last decades. Phytases sequentially hydrolyze five or six phosphate groups from inositol ring. In contrast, glucose-1-phosphatase hydrolyzes only the 3' phosphate of phytate.

Glucose-1-phosphatase (AgpE) from *Enterobacter cloacae* belongs to the group of histidine acid phosphatases with main activity directed towards glucose-1-phosphate, but its phytase activity is two times higher than that reported for *E. coli* Agp.

We collected data at the BL14.2 from the crystals of an inactive mutant of AgpE in complex with myo-inositol hexaphosphate (phytate) at 1.9Å resolution. The data set was obtained with 92 % completeness in the highest resolution shell. The estimated unit cell constants in the space group R3 were a=b= 151.1, c= 86.6 with α=β= 90, γ= 120°. We also collected data at the BL14.1 from the crystals of this mutant in complex with its inhibitor myo-inositol hexasulphate at 1.5Å resolution. The data set was obtained with 86% completeness in the highest resolution shell. The estimated unit cell constants in the space group P1 were a= 47.4 b= 54.5, c= 160.9 with α=β=γ= 90°.

The both structures have been solved with the molecular replacement method using the structure of Agp from *E. coli.* From the refined structures of the complexes we expect information allowing us to explain the unique hydrolysis profile of this enzyme.
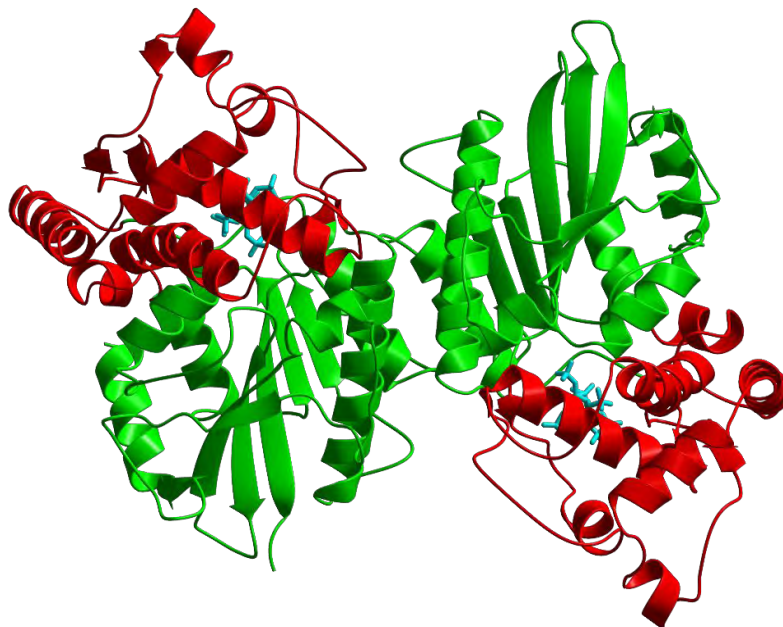
Fig. 1. Crystal structure of AgpE from *Enterobacter cloacae* in complex with phytate.

1) Lee C.D. et al., The Journal of Biological Chemistry (2003), 278, 31412-31418.
2) Herter T. et al., Appl Microbiol Biotechnol (2006), 70, 60-64

Structural studies of β-galactosidase from *Arthrobacter* sp. C2-2

Jan Dohnálek[1], Andrea Štěpánková[1], Tereza Skálová[1], Jindřich Hašek[1], Vojtěch Spiwok[2], Petra Lipovová[2]

[1]*Institute of Macromolecular Chemistry, Academy of Science of the Czech Republic, v.v.i., Heyrovského nám. 2, 16206 Prague 6, Czech Republic*
[2]*Institute of Chemical Technology, Technická 5, 166 28, Prague 6, Czech Republic*
E-mail: dohnalek@imc.cas.cz

Enzyme β-galactosidase catalyses hydrolysis of lactose into galactose and glucose (EC 3.2.1.23). The enzyme is known to be functional as monomer in some bacteria or tetramer in *Escherichia coli*. The *E. coli* enzyme requires participation of a neighboring chain in formation of a fully functional active site. On the other hand β-galactosidase from a psychrophilic bacterium *Arthrobacter* sp. C2-2 belonging to the same family 2 of glycosyl hydrolases has been recently found to form functional hexamers of a total molecular weight reaching 660 kDa (Fig. 1a). The active site of the *Arthrobacter* enzyme is formed solely by amino acid residues of one peptide chain with a total of six active sites present per one hexamer. The active site is located in the TIM barrel domain and contains a pair of catalytic residues Glu442 and Glu521 [1].

Even if no complementation of the active sites, positioned in a central cavity, is required for activity, the active form of the enzyme is hexameric and so far no other oligomeric arrangement has been experimentally observed. The hexamers possess three types of channels making the central cavity of the globule accessible from exterior and one of the first questions raised after the discovery of this structural arrangement was the route of substrates and products. The sizes of the three channel types differ and channel II is the most likely opening for passage of molecules. Structural studies of complexes can answer many questions connected with the specific structural properties of the cold-active enzyme [1].
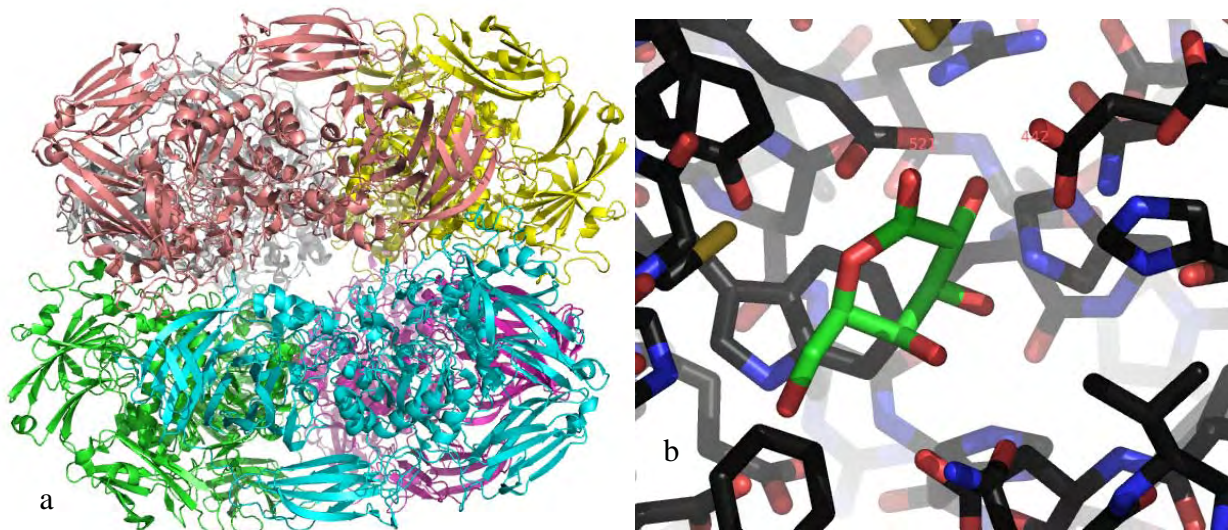
Figure 1. (a) Hexamer of β-galactosidase from *Arthrobacter* sp. C2-2., view along the channel type II, individual chains are color-coded, (b) D-galactonolactone binding in the active site. Created with program PYMOL [4].

X-ray structures of the cold-active enzyme with three ligands have been determined. Ligands can be localized in the electron density within the expected active site [2-3]. As these ligands

were delivered by soaking into the crystalline form of the enzyme the active sites were accessed through a channel or channels (Fig. 1b).

The initial results were followed by many experiments to gain structural information on complexes with a wider spectrum of ligands and X-ray diffraction experiments were in part performed at Bessy, beamline PX 14.1 for macromolecular crystallography.

From the recent results if follows that enzyme hexamers present in solution arrange into crystal lattice in different orientations with "constant" space group $P2_1$ and somewhat varied unit cell dimensions. This variability of possible orientations of hexamers in crystal lattice also explains abundance of non- or weakly diffracting crystals of this β-galactosidase.

[1] Skálová, T., Dohnálek, J., Spiwok, V., Lipovová, P., Vondráčková, E., Petroková, H., Dušková, J., Strnad, H., Králová, B., Hašek, J.: *Cold Active β-Galactosidase from Arthrobacter Sp. C2-2 Forms Compact 660 kDa Hexamers: Crystal Structure at 1.9 Å Resolution.* J. Mol. Biol. (2005) 353, 282-294.
[2] Štepánková A., Skálová T., Dohnálek J., Hašek J., Lipovová P. *Galactonolactone inhibiting the active site of beta-galactosidase from Arthrobacter sp. C2-2. Crystal structure at 2.2 A resolution.* Materials Structure, vol. 15 2a, (2008), k34.
[3] Štepánková A., Skálová T., Dohnálek J.,Dušková J., Kolenko. P, Hašek J., Lipovová P.
The structures of the cold active enzyme β-galactosidase from Arthrobacter sp. C2-2 with three bound ligands. In: The 9th International School on the Crystallography of Biological Macromolecules, Como, Italy, 2008.
[4] DeLano, W.L. *The PyMOL Molecular Graphics System* (2002) DeLano Scientific, San Carlos, CA, USA. http://www.pymol.org.

Structural Genomics of drug target proteins of Schistosoma mansoni

Francesco Angelucci, Adriana E. Miele, Giovanna Boumis, Daniela Dimastrogiovanni,
Maurizio Brunori, and Andrea Bellelli
CNR Institute of Molecular Biology and Pathology and Department of Biochemical Sciences
"A. Rossi Fanelli", "Sapienza" University of Rome, P.le Aldo Moro 5, 00185 Rome, Italy

Schistosomiasis is a severe widespread human parasitic disease affecting 200 million people in tropical and subtropical areas, caused by the helminth parasites of the genus *Schistosoma*. The cure relies mainly on a single chemotherapeutic agent, praziquantel, raising the risk to develop resistant strains; in this view, the search for new drug targets is fundamental. We focused our attention to the detoxification pathway, in particular on Thioredoxin glutathione reductase from S. mansoni (SmTGR).

In animal cells, redox regulation is provided by the Thioredoxin (Trx) and Glutathione (GSH/GSSG) systems, which are reduced by NADPH via specific flavine-oxidoreductases. In Schistosoma the unique enzyme SmTGR represents a molecular shortcut between the two systems: it is a promiscuous selenocysteine-enzyme able to transport reducing equivalents from NADPH to both GSH/GSSG and Trx systems *via* the fusion of Thioredoxin Reductase (TR) and Glutaredoxin (Grx) domains. Very recently SmTGR proved to be a very promising drug target, being essential for the parasite survival and being the target of two previously used schistomicidials, oltipraz and antimonium salts [1].

Due to the difficulty of heterologous expression of selenoproteins, we cloned in *E. coli* cells a truncated form of SmTGR, lacking the last two amino acids (Sec597-Gly598). The protein crystallized in a C2 space group with dimensions: a = 142.32 Å , b = 102.53 Å , c = 59.03 Å , β = 112.638; the structure was solved at 2.2 Å by molecular replacement taking rat TR as first template and Grx from *Populus tremula* as second search model.

The biological unit of SmTGR is a dimer, but crystals contain one monomer per asimmetric unit; the crystallographic dimer was generated by reflection of the twofold symmetry axis, and it is shown in fig.1. The structure of the monomer reveals the unusual fusion of two domains: Grx and TR. Dimerization occurs through the larger TR domains and results in a distorted ''W'' structure, with the two Grx domains, with the redox site represented by Cys27-Cys29, at the top of each outer arm of the W. The large TR domain comprises three subdomains: (i) one N-terminal FAD binding domain, in gold in Fig. 1, with the redox couple Cys154-Cys159; (ii) one central for NADPH-binding, green in Fig. 1, and (iii) one C-terminal involved in the interface with the symmetric monomer in the dimer, magenta in Fig. 1. Moreover, a solvent-accessible insertion loop red in fig. 1, is present; it is peculiar to SmTGR, but we cannot assign a specific funtion to it.

SmTGR has significant activity against DTNB and GSSG both acting as oxidants of NADPH. This redox activity requires access of the substrates to the FAD binding site. In this respect the absence of the two C-terminal residues may be of little relevance. On the other hand, our enzyme displays no thioredoxin reduction activity, in agreement with other truncated TGRs and with the putative function of the Gly-Cys-Sec-Gly motif in the electrons transfer from NADPH to the Grx domain.

Grx activity could be elicited in our enzyme as in other truncated TGRs when exogenous yeast GR and GSSG are added. These experiments confirm that the Grx domain is fully functional.

We propose that the unusual fusion of the two domains in SmTGR allows the Grx activity to be maintained through either GSH or NADPH via the mobile C-terminus, or both. In this way the Grx activity of TGRs, known to regulate some important cell functions, becomes independent of the rapid oscillations of the absolute concentrations of GSH/GSSG or their ratio in the cell. This mechanism may be relevant in schistosomes since they are continuously subjected to oxidative damage caused by the host immune response and may experience sudden peaks of consumption of GSH.

The structure of SmTGR provides the frame for designing new drugs against the disease, given that potential inhibitor lead compounds are already available [1]. Moreover, an antischistosomal treatment based on specific inhibition of SmTGR might present only limited secondary effects in humans, as in mammals TGRs are mainly expressed only in the male reproductive system after puberty, and SmTGR is functionally different from mammalian TR, GR, and TGR enzymes.
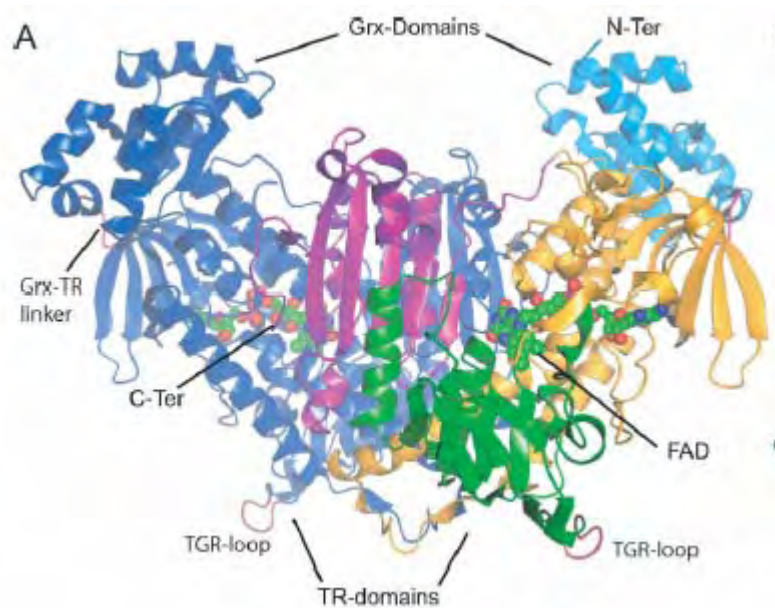
Figure 1: The structure of truncated Schistosoma mansoni TGR in ribbon representation, produced with CCP4MG. Overall structural organization of the biological unit of the enzyme: the W-shaped SmTGR dimer. One monomer is in blue and the other monomer is colored according to the division in domains from N- to C-terminus: Grx domain in light blue (1–107); FAD binding domain in gold (108–257 and 391–461); NADPH binding domain in green (258–358 and 364–390); the interface domain in magenta (462–493). The linker regions between Grx and TR (103–107) domains in magenta and the insertion (359–363) peculiar to SmTGRs in red lie at the top and at the bottom, respectively.

References

1. Kuntz A, Davioud-Charvet E, Sayed AA, Califf LL, Dessolin J, Arner ES, Williams DL. Thioredoxin glutathione reductase from Schistosoma mansoni: an essential parasite enzyme and a key drug target. *PLoS Med* (2007) 4:e206.

2. Angelucci F, Miele AE, Boumis G, Dimastrogiovanni D, Brunori M, Bellelli A. Glutathione reductase and thioredoxin reductase at the crossroad: The structure of *Schistosoma mansoni* thioredoxin glutathione reductase. *Proteins* (2008) 72:936–945.

The 1.8-A crystal structure of alpha1-acid glycoprotein (Orosomucoid) solved by UV RIP reveals the broad drug-binding activity of this human plasma lipocalin.

Dorian L. Schönfeld[1], Raimond B.G. Ravelli[2], Uwe Müller[3], Arne Skerra[1]

[1]Lehrstuhl für Biologische Chemie, Technische Universität München, An der Saatzucht 5, 85350 Freising-Weihenstephan, Germany

[2]European Molecular Biology Laboratory, Grenoble Outstation, 6 rue Jules Horowitz, BP 181, 38042 Grenoble Cedex 9, France

[3]AG Makromolekulare Kristallographie, BESSY GmbH, Albert-Einstein-Strasse 15, 12489 Berlin, Germany

α1-Acid glycoprotein (AGP) is an important drug-binding protein in human plasma and, as an acute-phase protein, it has a strong influence on pharmacokinetics and pharmacodynamics of many pharmaceuticals. We report the crystal structure of the recombinant unglycosylated human AGP at 1.8 Å resolution, which was solved using the new method of UV-radiation-damage-induced phasing (UV RIP). AGP reveals a typical lipocalin fold comprising an eight-stranded β-barrel. Of the four loops that form the entrance to the ligand-binding site, loop 1, which connects β-strands A and B, is among the longest observed so far and exhibits two full turns of an α-helix. Furthermore, it carries one of the five N-linked glycosylation sites, while a second one occurs underneath the tip of loop 2. The branched, partly hydrophobic, and partly acidic cavity, together with the presumably flexible loop 1 and the two sugar side chains at its entrance, explains the diverse ligand spectrum of AGP, which is known to vary with changes in glycosylation pattern.

Structure of two-domain laccase from *Streptomyces coelicolor*

Jindřich Hašek , Jan Dohnálek, Tereza Skálová, Jarmila Dušková, Petr Kolenko, Andrea Štěpánková
Institute of Macromolecular Chemistry, Academy of Sciences of the Czech Republic,
Heyrovského nám. 2, CZ16206 Prague 6, Czech Republic

Laccases (E.C. 1.10.3.2) - multicopper oxidoreductases acting on diphenols and related substances – belong to widely studied class of multicopper blue proteins. The catalytic mechanism of the enzymes was described (Solomon et al., 1996). The evolutionary theory offered by Nakamura and Go (see Fig.1) supposed that the enzymes of present species, i.e. nitrite reductases (two domain, active as trimer), laccases and ascorbate oxidases (three domain, active as monomer), and ceruloplasmins (six domains, active as monomer) developed from a common ancient single domain cupredoxin-like protein precursors.

The structure of the small laccase (SLAC) determined in frame of this project is the first experimental proof of two domain laccase active in the trimeric form (see Fig.2) and confirms one step in the Nakamura evolutionary hypotheses. The structure solved at 2.6 Å resolution is structurally similar to a group of two-domain trimeric nitrite reductases. The SLAC has four copper ions per monomer, similarly as three domain laccases. Type 1 blue copper ion is in domain 2, near central part of the trimer. Trinuclear copper cluster is placed inter domains 1 and 2 of neighbor monomers. The missing middle domain, which conformationally stabilizes three domain laccases, is compensated by trimeric organization of the SLAC.

Special scafold of crystal lattice shown in Fig.3 is responsible for very high contents of solvent (81 %). Long fragments of poly(ethylene glycol)monomethyl ether (MME-PEG550) used in the crystallization solution in high concentration (39 %) was found adsorbed at several places on the protein surface by charge supported hydrogen bonds. Some of the polymer chains play a role of adhesive between neighbor protein molecules in the crystal lattice /3,4,5/. Fig. 4 shows a fragment of MME-PEG550 wound around positive charge at the end of Arg146. More information on the detailed structure of SLAC and comparative analysis of the whole group of structurally related proteins can be found in paper published by Skálová et al in the first issue of J.Mol.Biol. in 2009.

REFERENCES

/1/ Nakamura, K. & Go, N. (2005). *Function and molecular evolution of multicopper blue proteins.* Cell. Mol. Life. Sci, **62(18)**, 2050-2066.

/2/ Skálová T., Dohnálek J., Østergaard L.H., Østergaard P.R., Kolenko P., Dušková J., Štěpánková A., Hašek J., J. Mol. Biol. (2009) *The structure of the small laccase from Streptomyces coelicolor reveals a link between laccases and nitrite reductases,* **385**, 1165-1178.   doi:10.1016/j.jmb2008.11.024

/3/ Hašek J, Dohnálek J, Dušková J, Skálová T, Kolenko P, Koval T, Štěpánková A. (2008).
Polymer and co-polymer surface modifying effects in the protein crystallization.
Acta Cryst., **A64**, C233.

/4/ J. Hašek, P. Kolenko, T. Koval, J. Dohnálek, J. Dušková, T. Skálová, A. Štěpánková
Polymer surface modifying effects in the protein crystallization. An interpretation based on the review of polymer and co-polymer interactions with bio-macromolecules.
The 2nd Annual Congress - Spine2 Complexes. 4 - 6 July 2008, Illkirch (Strasbourg, France).

/5/ P. Kolenko. PhD Thesis. TU University Prague, IMC AV CR, Praha 2009.
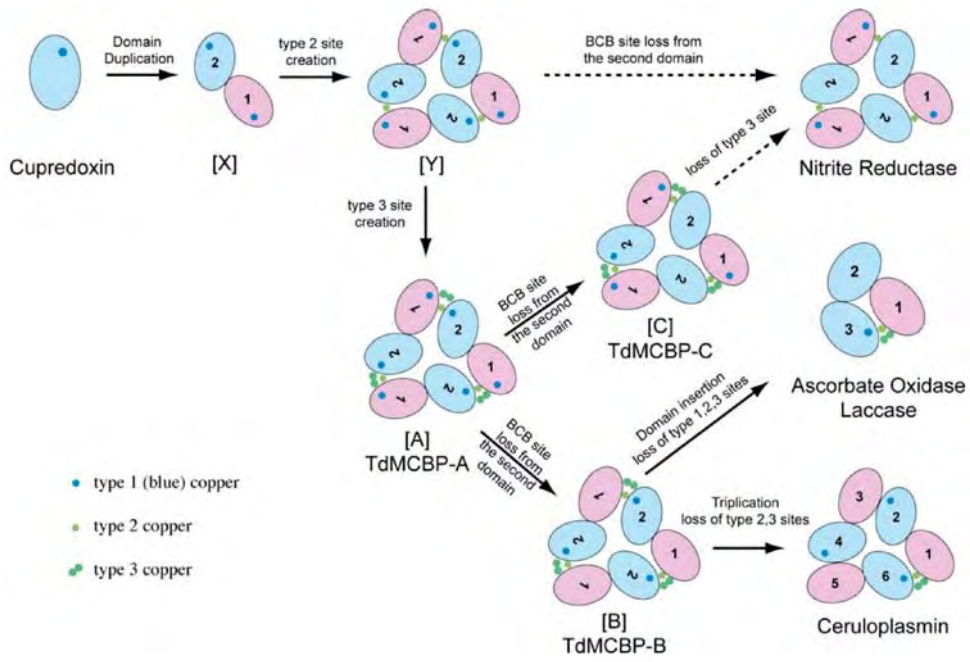
Fig.1. Evolutionary hypotheses of Nakamura (Reprinted from Nakamura et al, 2005).
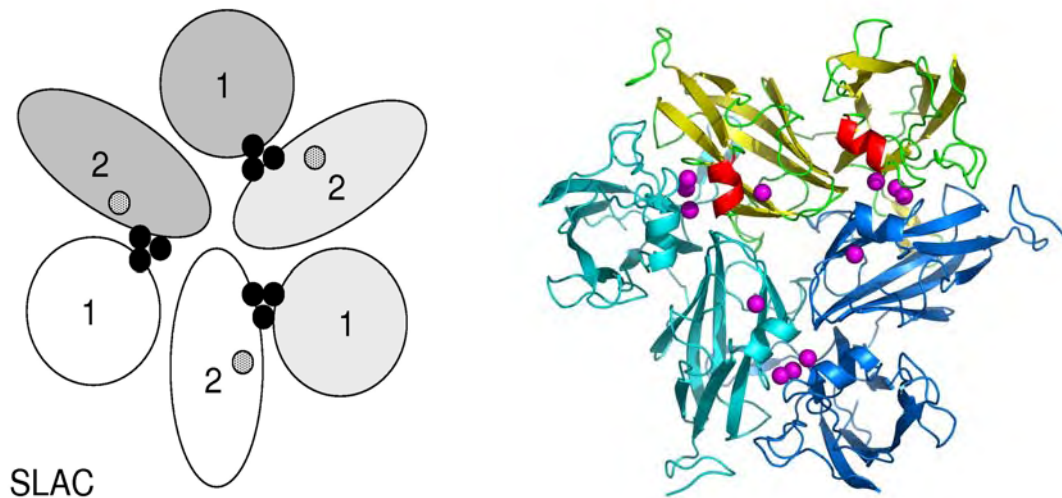
Fig.2. Structure of SLAC (Reprinted from Skálová et al, 2009).
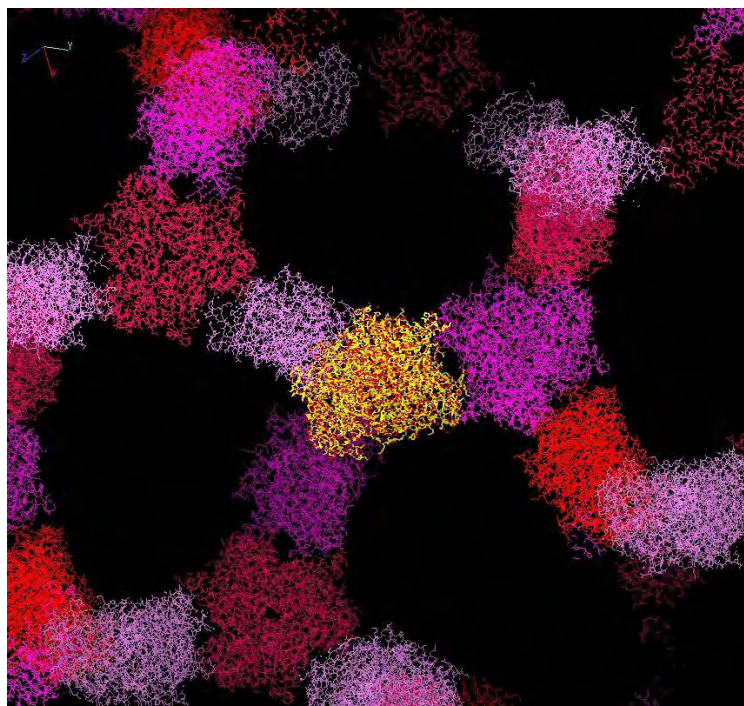
Fig.3. Structure of SLAC has an extreme contents of solvent water in its crystal lattice (Reprinted from Skálová et al, 2009).
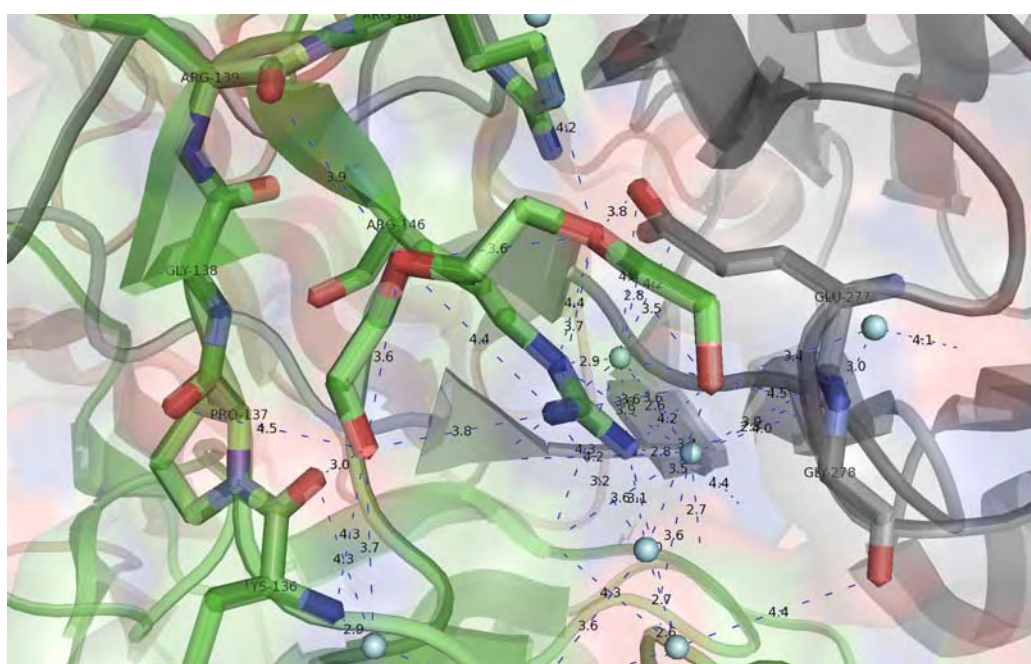
Fig.4. Interactions of poly(ethylene glycol)monomethyl ether with Arg146 of small laccase

Molecular mechanism of the antimonial drugs against Leishmaniasis

Paola Baiocco, Gianni Colotti, Stefano Franceschini and Andrea Ilari

CNR Institute of Molecular Biology and Pathology and Department of Biochemical Sciences "A. Rossi Fanelli", "Sapienza" University of Rome, P.le Aldo Moro 5, 00185 Rome, Italy

Leishmaniasis is a disease that affects 2 million people and kills 70,000 persons every year. It is caused by Leishmania species, human protozoan parasites of the trypanosomatidae family. Trypanosomatidae differ from the other eukaryotes in their specific redox metabolism, since the glutathione/glutathione reductase system is replaced by the unique trypanothione/trypanothione reductase system.

The current treatment of leishmaniasis relies mainly on antimonial drugs (like Pentostam).

However, the molecular mechanisms of these drugs are not completely understood and their use is severely impaired by the side effects related to their toxicity. In addition, an ever increasing number of drug-resistant strains have been identified in Bihar, India, which prevent the use of antimonial drugs in this endemic area. Therefore, on the one hand there is an urgent need to develop novel drugs that target specific metabolic pathways of the parasite; on the other hand it is also necessary to understand the mechanism of action of the most used drugs in order to minimize their severe side effects. Among the potential molecular targets to date, trypanothione synthetase (TS) and the trypanothione reductase (TR) are most promising in that they are involved in the unique thiol-based metabolism of Leishmania, which is common to all parasites of the Trypanosomatidae family but absent in the host. TS synthesizes a glutathione-spermidine conjugate named trypanothione (N1-N8-bis(glutathionyl)spermidine) and TR keeps this molecule reduced. The trypanothione/TR system replaces many of the antioxidant and metabolic functions of the glutathione/glutathione reductase and thioredoxin/thioredoxin reductase systems present in other organisms and, for this reason, it is necessary for the protozoa survival.

Pentavalent antimonials, which are the first choice drugs for the treatment of visceral leishmaniasis, are known to be active only following bioreduction to the trivalent Sb(III) form. Fairlamb and coworkers discovered that trivalent antimonials inhibit TR and that reduction of TR by nicotinamide adenine dinucleotide phosphate (NADPH) is essential for inhibition.

We solved the crystal structure of TR from *Leishmania infantum* in the oxidized state and of the complex of TR with NADPH and Sb(III) in the reduced state. Crystals were obtained at 294 K by the hanging drop vapour diffusion method using ammonium sulfate as precipitant agent and diffract to better than 2.95 Å resolution using a synchrotron radiation source. The datasets from oxidized TR and reduced TR in complex with NADPH and Sb(III) were collected at the synchrotron radiation source Bessy, Berlin, Germany. The crystals exhibit an unusually high solvent content of 74 %, belong to the tetragonal space group $P4_1$ with units cell parameters a=b=103.45 Å, c=192.62 Å and two molecules in the asymmetric unit (1). The crystal structures of oxidized trypanothione reductase (TR) from *Leishmania infantum* and of the complex of reduced TR with NADPH and Sb(III), disclose for the first time the molecular mechanism of action of the antimonial drugs against the parasite. The metal binds directly the two redox-active catalytic cysteine residues (Cys52 and Cys57), one threonine residue (Thr335) and His461' of the two-fold symmetry related subunit in the dimer, thereby disallowing the hydride transfer from the protein to the trypanothione and therefore

trypanothione reduction (Fig. 1). Such interaction is consistent with the modality of cysteine binding of thiophilic metals such as As(III), Sb(III) and Bi(III). Metal-bound cysteines are fully deprotonated thiolate anions, the nucleophilicity of which is greatly attenuated upon formation of metal complexes, with high thermodynamic stability, that dissociate with very slow rates. Sb(III) profoundly perturbs the thiol redox potential of the cell exposing the parasites to the oxidative damage caused by ROS (reactive oxygen species) produced by the host macrophages (2).
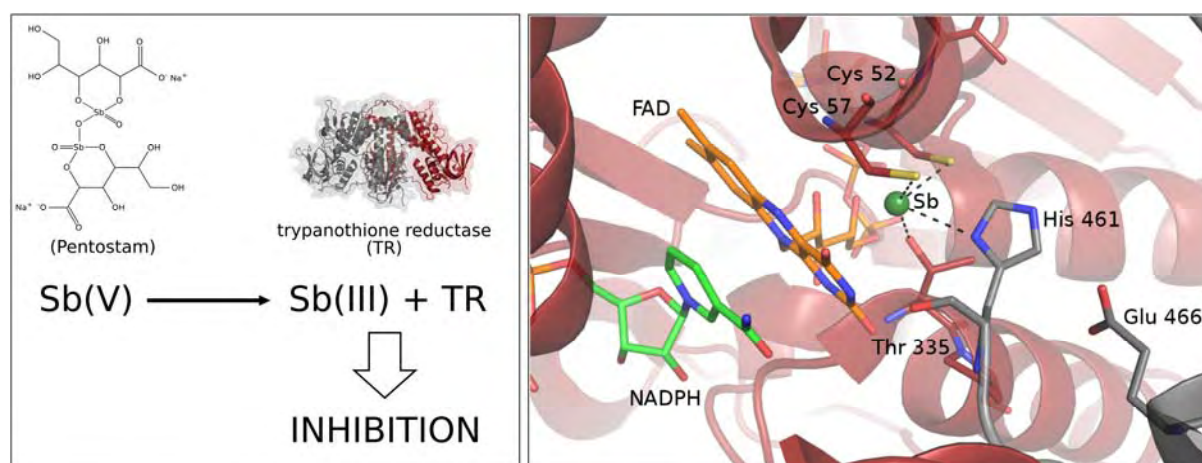
Figure 1: Panel A. Scheme of the mechanism of action of the antimonial drugs. The antimonial drugs (like Pentostam) contains Sb (V). Sb (V) is reduced in the parasites to Sb (III) and Sb (III) binds to Trypanothine reductase (TR) thereby inhibiting its activity. Panel B. Catalytic site of TR. Sb (III) (in green) binds to the TR catalytic site. The ligands (Cys57, Cys 52, Thr 335 and His 461 are indicated).

References

1. Baiocco, P.; Franceschini, S.; Ilari, A.; Colotti, G. Trypanothione reductase from Leishmania infantum: cloning, expression, purification, crystallization and preliminary X-ray data analysis. *Protein and Peptide Letters* (2009) in press.
2. Baiocco, P.,Colotti, G. Franceschini, S. and Ilari, A. Molecular basis of antimony treatment in Leishmaniasis *J. Med. Chem.*(2009) in press.

Analysis of the structure of CYP450 EryK from S. erythraea

Linda C. Montemiglio[1], Adriana E. Miele[1], Beatrice Vallone[1], Carmelinda Savino[2]

[1]Department of Biochemical Sciences - "Sapienza" University of Rome – P.le A. Moro 5 – 00185 Rome - Italy;
[1]CNR Institute of Molecular Biology and Pathology – P.le A. Moro 5 - 00185 Rome - Italy.

Background. EryK is a P450 cytochrome (CYP113A1) that catalyzes the hydroxylation in C-12 of ErD, in a late stage of erythromycin biosynthesis. We have already determined the structures of EryK in two ligand-free, one substrate bound and two inhibitors-bound forms. These structures allowed us to identify the structural and mechanistic features of EryK that are necessary to allow the binding of a bulky macrolide substrate that has two glycosyl groups while discriminating against the mono-glycosylated biosynthetic pathway intermediates or the closely related shunt metabolite ErB.

The two ligand-free forms of EryK were obtained by crystallization conditions with different values of ionic strength [1]. These two structures allowed us to identify "open" and "closed" conformations of EryK with different arrangements of some structural elements that line the heme distal pocket and that are responsible for its accessibility.

We concluded that these two structures are in equilibrium in solution, but we cannot exclude that at least one of them is an artifact due to the crystallization conditions and crystal packing. We are therefore trying to demonstrate that the closing mechanisms of the active site observed in EryK, represents two equilibrium conditions of the enzyme.

In order to answer this question, we attempted to obtain crystals of the substrate complex of EryK in different conditions of ionic strength.

If the crystallization conditions affect the enzyme structure, we would observe open and closed conformations of EryK also in the complex with its substrate, depending on ionic strength.

Results. We obtained some crystals of the EryK-ErD complex in high ionic strength conditions, different data sets were collected at BESSY (BL 14.1) achieving, in the best case, a resolution of 1.8 Å.

The data set was processed and scaled using the HKL2000 suite.

We are comparing the previously obtained structure of EryK-ErD (low ionic strength) with the new form of the enzyme-substrate complex obtained at low ionic strength.

We did not observe relevant differences: since both structures display a tight closure of secondary structure elements around the bulky substrate.

These data support our hypothesis that the different ligand-free forms of EryK are not due to an experimental artefact. In the absence of the ligand, EryK is in equilibrium between the "closed" and the "open" structures and the closed structure is locked by interaction with ErD.

The ionic strength can modulate the relative populations of these two conformers in the unbound state, but it has no effect when a ligand is trapped in the binding pocket.

Statistics of data obtained at BL.14.1 in BESSY

Resolution = 1.8 Å

Space group = P21

$\chi^2 = 0.816$

$R_{fac} = 0.086$

$R_{fac}^2 = 0.061$

Completeness = 100%

Mosaicity = 0.315

Unit cell parameters (Å): a= 54.131 b= 67.812 c= 57.718   β= 101.837°
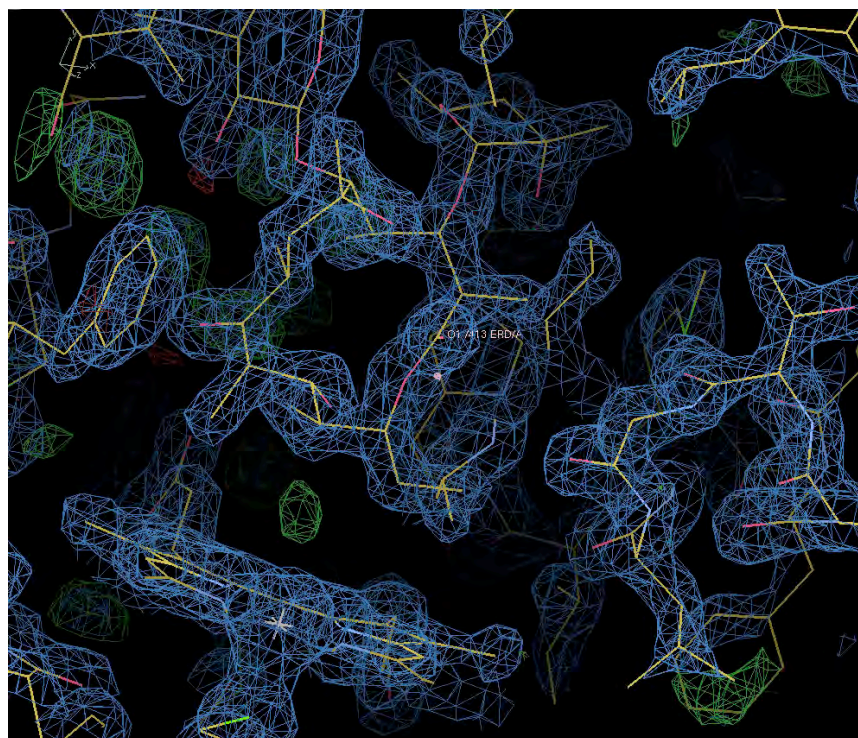
Figure. Electron density ($2F_o$-F_c and F_o-F_c) maps of the heme distal pocket of the complex EryK-ErD at 1.8Å, contoured at 1.0 and 3 σ respectively. The ligand, ErD, is clearly visible.

References

[1] Savino C., Sciara G., Miele A.E., Kendrew S.G., Vallone B. (2008) Cloning, expression, purification, crystallization and preliminary X-ray crystallographic analysis of C-12 hydroxylase EryK from Saccharopolyspora erythraea.   Protein Pept Lett. 15(10):1138-41.

MOLECULAR MECHANISM OF NEUROPROTECTION BY NGB

MOSCHETTI T., ARDICCIONI A., RONDINELLI C., BRUNORI M. AND VALLONE B.
Dept. of Biochemical Sciences, University "La Sapienza", Ple Aldo Moro, 00185 Rome, Italy

Objectives

Neuroglobin (Ngb) is a hexacoordinate globin expressed in vertebrate brain, where it acts as a neuroprotective factor against hypoxic damage ad neurodegenerative diseases; consequently the discovery of the mechanism by which Ngb exerts neuroprotection could lead to design novel therapeutic strategies [1]. We are interested to investigate structure-function relationship in murine Ngb, in order to characterize the molecular mechanism of neuroprotection by Ngb, focusing our attention on: (i) correlation between the iron redox state and 3D structure, since it has been demonstrated that only the unligated ferric form is competent for the interaction with a transduction pathway linked to a trimeric $G_{\alpha\beta\gamma}$-protein [2]; (ii) characterization, also by spectroscopy, of reaction intermediates that occurs in Ngb ferrous derivatives. For this purpose, we used the Carbonmonoxy-Ngb (CO-Ngb) as a model, as previously done for analyzing the binding mechanism in Ngb [3] (iii) evaluation of the huge internal cavity relevance for the interaction with these ligands [4].

Achievements

During 2007, we collected at BESSY synchrotron a dataset of Ngb Fe^{2+}, obtaining a model structure of ferrous Ngb chemically reduced at room temperature (1.87 Å), as referred in the "BESSY Annual Report 2007". During 2008, we concluded the analysis of this structure by means of comparison with data from X-ray Absorption Spectroscopy (XAS) experiments, which were carried out in collaboration with the group of Prof. Arcovito (Institute for Biochemistry and Clinical Biochemistry, Università Cattolica del Sacro Cuore, Rome). This joined approach of X-ray crystallography and XAS experiments demonstrated that the protein is efficiently reduced under X-ray beam and that during the transition from ferric to ferrous state Ngb does not undergo structural rearrangements (Fig.1), in analogy with a well-known oxidoreductase, cytochrome-*c*. Accordingly to data obtained by means of kinetic approach [5], our evidences confirm that endogenous hexacoordination promotes redox processes at the heme iron, and support the hypothesis that redox cycling is part of the still debated functional mechanism of Ngb. These results have been published in 2008 [6], as indicated in the "Publication list 2008".
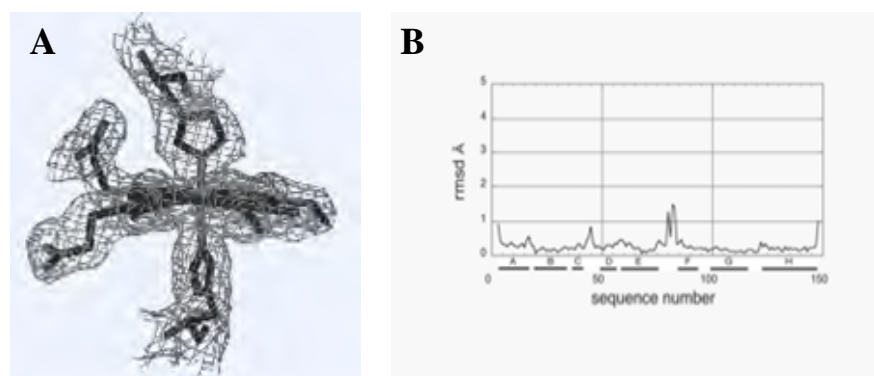
Fig.1 Crystal structure of chemically reduced Ngb
A) Blow-up of electron density map of the active site of dithionite reduced Fe(II)Ngb.
B) RMSD plot comparing the 3D structures of chemically reduced Fe(II) Ngb at 1.87 Å resolution and photoreduced Ngb (reported by Vallone et al. [4] at 1.4 Å resolution).

The study of reaction intermediates of Ngb requires, as a first step, the reduction and CO derivatization of Ngb Fe^{3+} crystals. Therefore, through trial and error procedure, we set up a protocol that allows to obtain at least 95% of molecules in the crystal in the CO-bound form. We

also tried to dissociate CO by means of X-ray illumination at the iron K-edge, based on the results exposed in Arcovito *et al.* [6]. We performed two different data collection: at first we produce a reference measurement of the CO-Ngb structure under xenon (Xe) pressure; subsequently, we have attempted to dissociate CO by means of X-ray induced photolysis at the edge iron wavelength, in the presence of Xe which could have hamper the CO escape to the solvent. Inspection of electron density maps at 2.2Å resolution shows that this process leads to partial CO dissociation (Fig.2).

This result represents not only a useful statement for future photodissociation experiments, but also a part of the project that concerns the analysis of cavity role in Ngb. In fact during 2007, we successfully collected dataset of Xenon (Xe) pressurized crystals for both the unliganded and liganded forms of Ngb. Moreover, in collaboration with the *Macromolecular Crystallography Group* of BESSY, we collected datasets of Ngb crystals derivatized with Krypton (Kr). The preliminary results of this analysis have been cited in the "Murine Neuroglobin in complex with Xenon Report 2007". During 2008 we concluded the refinement of Ngb•Kr structure, and compared the Xe docking sites of Ngb with those of sperm whale Myoglobin (Mb) and human Cytoglobin (Cygb) [7,8]. We show the presence of four docking sites for Xe (but only two for Kr); two of the four Xe sites are within the large internal cavity. Their topology is consistent with a role as ligand pathway and appears similar to that of Mb and Cygb cavities. Moreover, this pathway seems to promote iron accessibility in the ligand bound species, which may be related to function; this is presumed to be by-and-large related to redox chemistry given the internal hexacoordination with His(E7). A paper with these results is almost ready to be submitted for publication.
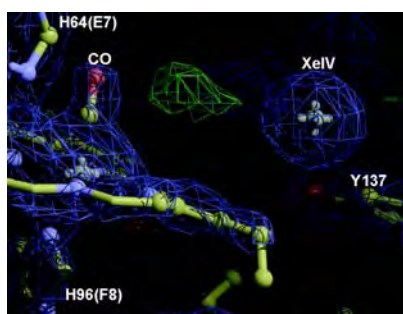
Fig.2: Xenon binding in the distal heme pocket of CO-Ngb
The 2Fo-Fc map contoured at 1.8s on the XeIV niche, in the Carbonmonoxy-Ngb•Xe structure; only the CO-bound heme conformer is depicted. The Fo-Fc map at 3.26s is also displayed, showing the unmodelled positive electron density that we assigned to a putative photodissociated CO. Electron density maps have been calculated using COOT (picture obtained in the RASMOL mode).

References
[1] Brunori M. and Vallone B., FASEB J. 20, 2192-2197, 2006.
[2] Wakasugi T., *et al*., J. Biol. Chem. 278, 36505-36512, 2003.
[3] Vallone B. *et al.* Proc. Natl. Acad. Sci. USA 101, 17351-17356, 2004.
[4] Vallone B. *et al.* Proteins 56, 85-92, 2004.
[5] Weiland, T.R., *et al.,* J. Am. Chem. Soc. 126, 11930-11935, 2004
[6] Arcovito, A., *et al.,* Arch. Biochem. Biophys. 475, 7-13, 2008.
[7] Tilton, R.F., *et al*., Biochemistry 23, 2849-2857, 1984.
[8] de Sanctis, D., *et al.,* Biochem. Biophys. Res. Commun. 316, 1217-1221, 200

Structural investigations of two redox active enzymes (AFR and GatDH) and one aminopeptidase

Y. Carius, H. Christian, M. Schu and A. J. Scheidig

Christian-Albrechts-Universität Kiel, Am Botanischen Garten 1-9, 24118 Kiel, Germany

GatDH is a sugar converting enzyme of biotechnological relevance. One of its reactions is the regioselective oxidation of galactitol to the rare sugar L-tagatose [1]. The enzyme is active as a dimer of dimers, in which two dimers are coordinated through two magnesium ions (figure1).

Figure 1: the dimer of dimers of GatDH. The two coordinating Mg-ions are shown as red balls.
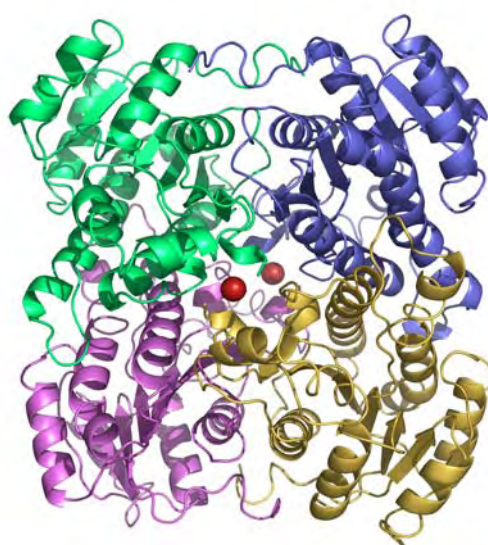
The structure of GatDH with its cofactor NAD^+ has already been solved to a resolution of 1.25 Å. To obtain the structure of GatDH with its cofactor and bound substrate soaking experiments were performed. Unfortunately, no bound substrate molecules could be identified in the active site. Therefore cocrystallisation experiments were performed with different known substrates. Crystals were obtained of GatDH, its cofactor NAD^+ and the substrate 1,2-(S)-pentanediol. From this crystals one data set was collected at the BESSY MX beamline 14.2. The data was processed and scaled with XDS and the structure was refined to a resolution of 1.8 Å.

Electron density found in the active site of all four monomers of GatDH could be interpreted as 1,2-(S)-pentanediol. The superposition of all four monomers shows that the position of the substrate in the active site is quite similar, but not unique (figure 2).

Figure 2: the active site of GatDH with the bound substrate 1,2-(S)-pentanediol superimposed as from all four chains in the dimer of dimers.
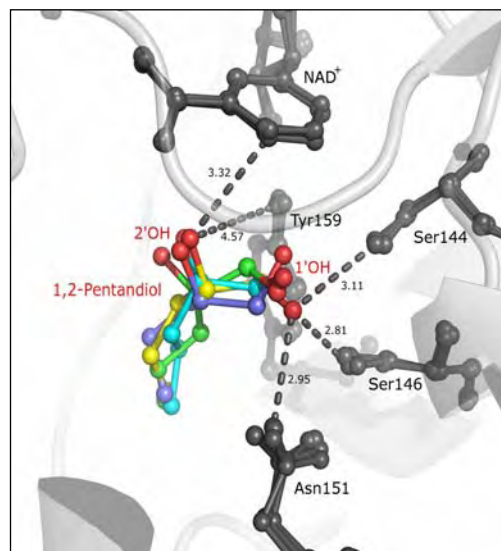
In the next steps, cocrystallisation experiments with other substrates will be done to gain a deeper insight into the catalytic mechanism of GatDH.

AFR is also a sugar converting enzyme of biotechnological relevance and investigated in respect of its usability as a rare sugar sensor in blood diagnostics.

The structure of AFR from *Sinorhizobium morelense* in complex with NADP$^+$ was solved recently [2]. Here, we crystallized AFR from *S. smeliloti*. Furthermore AFR was cocrystallized with its cofactor NADPH as well as with its cofactor and the substrate 1,5-anhydro-D-fructose. The crystals appeared to belong either to space group $P2_12_12_1$ with two copies in the ASU or to $C222_1$ with one copy in the ASU with unit cell parameter a= 70, b= 90 c=95Å, respectively. The crystals diffracted X-rays to a least 2Å. The data was processed and scaled with XDS/XSCALE. The phasing was done by molecular replacement using the structure or AFR from *Sinorhizobium morelense (PDB-ID 2glx)* as a search model. Refinement of the data sets is under progress.
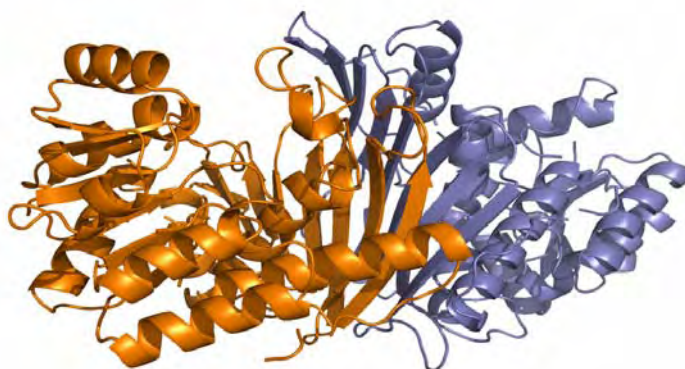
Figure 3: The functional dimer of AFR from *S. smeliloti* is build up by crystallographic symmetry operation (space group $P2_12_12_1$).

The enzyme methionine aminopeptidase Met-AP 1 hydrolyses protein and peptide substrates. Inhibitors for Met-AP display numerous biological effects and are used in a broad spectrum as therapeutics against cancer and inflammations. Furthermore, Met-AP is one potential target for new antibiotic substances. For a rational approach towards the identification of new inhibitors or the optimization of identified lead compounds, screening of potential complexes of Met-AP with new inhibitors is needed.

Within the last beam time period we have tried to obtain high resolution data sets from two newly identified inhibitors in complex with MetAP1. The crystals were grown in co-crystallization experiments under different pH conditions. Depending on the pH we observed different crystal shapes and different diffraction behaviour. Unfortunately those crystals which diffracted best (around 1.7 Å) had no significant inhibitor bound at the active site and those crystals in which bound inhibitor could be verified diffracted not better than 3.4Å. Therefore, further experiments are needed in order to improve the crystals.

References

[1] G.-W. Kohring, P. Wiehr, M. Jeworski and F. Giffhorn, Commun. Agric. Appl. Biol. Sci. 68, 309-312 (2003)
[2] T. R. Dambe, A. M. Kühn, T. Brossette, F. Giffhorn and A. J. Scheidig, Biochemistry 45, 10030-10042 (2006)

Structure determination of *cg*Hle, a homoserine acetyltransferase homologue, from *Corynebacterium glutamicum*

C. Tölzer, S. Pal, H. Watzlawick[1], J. Altenbuchner[1], K. Niefind

Institut für Biochemie, Universität zu Köln, Zülpicher Straße 47, D-50674 Köln (Cologne), Germany
Institut für Industrielle Genetik, Universität Stuttgart, Allmandring 31, D-70569 Stuttgart, Germany

The bacterial strain *Pseudomonas veronii* MEK700 is able to degrade 2-butanone and other alkyl methyl ketones [1]. The corresponding degradation pathways involves the gene *mekB*. Its product MekB shows esterase activity catalyzing the hydrolysis of acetic acid esters. Additionally, however, MekB is homologous to homoserine acetyltransferases (HAT), i.e. it presumably can catalyze the transfer of an acetyl group to coenzyme A or other metabolites rather than to water.

We are currently trying to determine the structures of MekB and of its homologue *cg*Hle from *Coryne-bacterium glutamicum*. For this purpose we crystallized both enzymes (Figure 1).
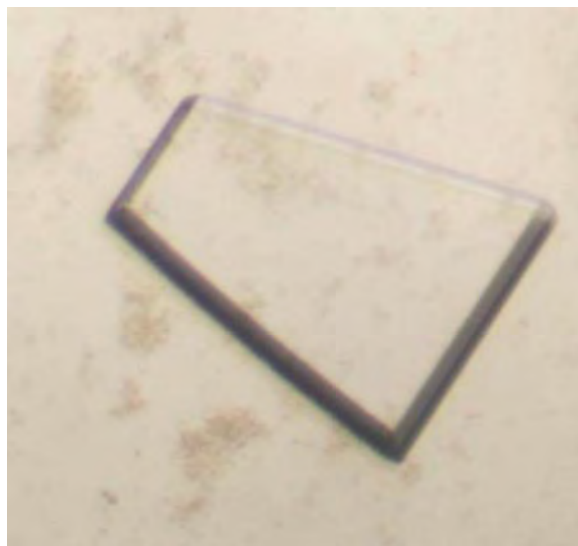
Figure 1: A crystal of *cg*Hle from *C.glutamicum* grown in polyethylen glycol 8000

In the case of *cg*Hle we were able to collect X-ray diffraction data sets of two crystal forms at beam line 14.1 of BESSY. The structure could be solved with molecular replacement techniques and is currently in the refinement process.

References

[1] C. Onaca, M. Kieninger, K.-H. Engesser, and J. Altenbuchner, J. Bacteriol. 189, 3759 (2007)
[2] C. Tölzer, S. Pal, H. Watzlawick, J. Altenbuchner, and K. Niefind. Acta Cryst. F65, 34 (2008)

Synthetic models of biological metal centers studied by
X-ray absorption spectroscopy at V, Mn, Fe, Ni, and Zn K-edges

A. Grundmeier[1], M. Risch[1], O. Sanganas[1], L. Gerencser[1], S. Löscher[1], I. Zaharieva[1],
P. Chernev[1], S. Pfirrmann[2], C. Limberg[2], N. Marinos[3], M. Driess[3], M. Hörnke[4], B. Koksch[4],
V. Kraehmer[6], D. Rehder[5], M. Anderlund[6], A. Magnuson[6], M. Haumann[1*], H. Dau[1*]

[1]Freie Universität Berlin, Institut für Experimentalphysik, 14195 Berlin, Germany
[2]Humboldt-Universität zu Berlin, Institut für Chemie, 12489 Berlin, Germany
[3]Technische Universität Berlin, Institut für Chemie, 10623 Berlin, Germany
[4]Freie Universität Berlin, Inst. f. Chemie und Biochemie, 14195 Berlin, Germany
[5]Universität Hamburg, Inst. f. Anorganische und Angewandte Chemie, 20146 Hamburg, Germany
[6]Uppsala University, Molecular Biomimetics, 75120 Uppsala, Sweden
*holger.dau@fu-berlin.de, michael.haumann@fu-berlin.de

Protein-bound metal centers play a prominent role in numerous biological reactions. Synthetic chemistry aiming at the development of catalysts and systems which mimic relevant features of biological metal sites is a rapidly growing field with strong technological, environmental and medical impact (biomimetics). We study synthetic metal compounds of biological importance by X-ray absorption spectroscopy. In a collaborative approach, encompassing groups from the three Berlin universities, (inter)national collaborations, and being integrated into the Berlin Cluster of Excellence "Unifying Concepts in Catalysis" (Unicat), a wide variety of models with relevance in biocatalysis and medicine is investigated (samples related, e.g., to H_2 production by hydrogenase enzymes, photosynthetic water oxidation, substrate halogenation by haloperoxidases, and peptide aggregation in Alzheimer´s disease) (Fig.1).

In the past years, the research group Dau/Haumann at the FU-Berlin continuously has been developing and improving a set-up for XAS at the beamline KMC-1 at BESSY, in cooperation with F. Schäfers and M. Mertin (BESSY). The next step, in 2009, is the integration of a new 13-element energy-resolving Ge X-ray fluorescence detector into our experiment (detector financed by Unicat cluster of excellence). This will enable us to further expand the XAS activities at BESSY with respect to K- and L-edge studies on metal centers.

Here an overview is presented of recent experiments at KMC-1 on model compounds studied by XAS at the V, Mn, Fe, Ni, Zn K-edges (Fig. 1). Results on a cobalt catalyst for water oxidation and Mn/Fe metalloenzymes are presented in two further reports in this issue.
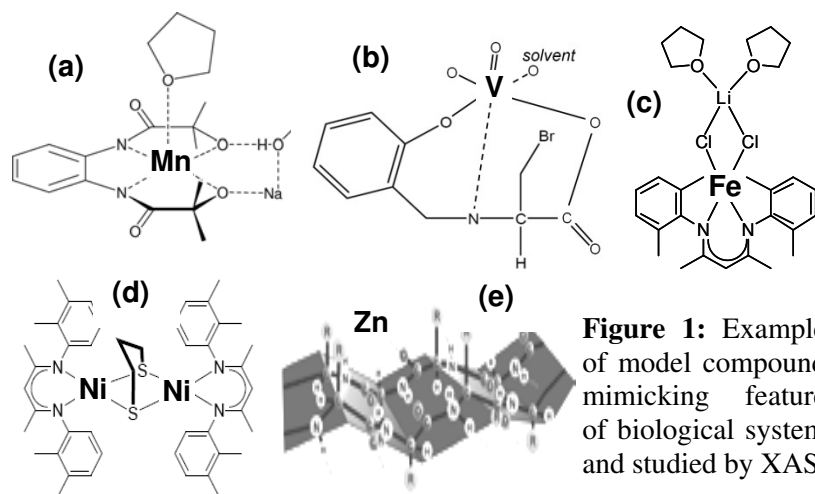
Figure 1: Examples of model compounds mimicking features of biological systems and studied by XAS.
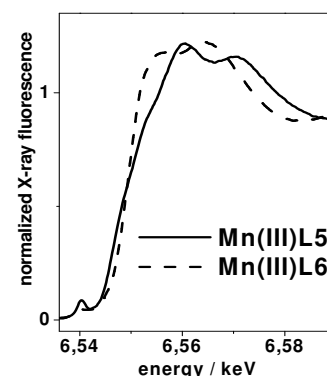
Figure 2: Typical XANES of 5- and 6-coordinated Mn(III) (Fig. 1-a).

Experimental. XAS at KMC-1 was performed in fluorescence and absorption modes using a single-element energy-resolving Ge detector system (Canberra, Xia) and several ion chambers (Physics Dept., FU-Berlin), at 20 K using a liquid helium cryostat. A new data-evaluation program (P. Chernev) was used for rapid on-site processing of XAS data.

(1) Photosynthetic water oxidation at the tetra-manganese complex of photosystem II (PSII) is a challenging chemical task [1-3]. In projects aiming at light-driven H_2 production from water (SolarH2, 6th FP of the EU; BioH2, BMBF), we studied mono- and binuclear Mn compounds mimicking features of the coordination of Mn in PSII (Fig. 2).

(2) H_2 production by hydrogenase enzymes is of high interest for (bio)technological applications and thus has attracted much interest in model chemistry [4]. Novel compounds containing Ni and Fe atoms were synthesized and studied by XAS (Fig. 3A,B).

(3) Vanadium haloperoxidases catalyze the oxidation of halogenides by peroxide. In continuation of previous work [5], we investigated models for the V-side in enzymes (Fig. 3C). A respective joint publication is in preparation [6].

(4) Binding metal ions to peptides is involved in amyloid formation in Alzheimer´s disease. Zn-binding peptides were synthesized [7] and Zn XANES spectra were measured (Fig. 3D). Further XAS experiments with improved samples are planned.
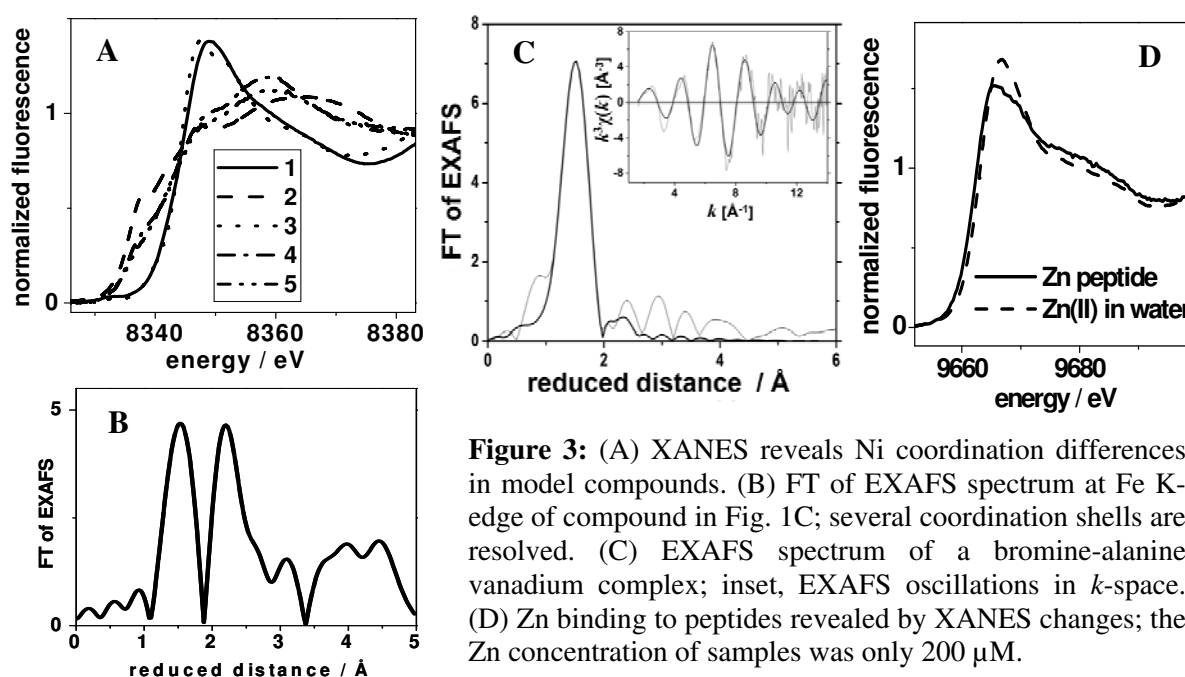
Figure 3: (A) XANES reveals Ni coordination differences in model compounds. (B) FT of EXAFS spectrum at Fe K-edge of compound in Fig. 1C; several coordination shells are resolved. (C) EXAFS spectrum of a bromine-alanine vanadium complex; inset, EXAFS oscillations in *k*-space. (D) Zn binding to peptides revealed by XANES changes; the Zn concentration of samples was only 200 µM.

In summary, successful XAS studies were performed at KMC-1 on a wide variety of systems. These studies will be continued and the results will be integrated into collaborative publications. This beamline and our set-up allow for XAS measurements on most of the transition metals of importance in biology and related model chemistry. Further improvement of the XAS experiment at KMC-1 is desirable and will be approached in 2009.

[1] Dau H and Haumann M, *Coord. Chem. Rev.* **2522**, 273-295 (2008).

[2] Magnuson A, Liebisch P, Högblom J, Anderlund MF, Lomoth R, Meyer-Klaucke W, Haumann M, Dau H, *J. Inorg. Biochem.* **100**, 1234-1243 (2006).

[3] Haumann M, Grundmeier A, Zaharieva I, Dau H, *Proc. Natl. Acad. Sci. USA* **105**, 17384-17389 (2008).

[4] Löscher S, Schwartz L, Stein M, Ott S, Haumann M, *Inorg. Chem.* **46**, 11094-11105 (2007).

[5] Christmann U, Dau H, Haumann M, Kiss E, Liebisch P, Rehder D, Santoni G, Schulzke C, *Dalton Trans.* **21**, 2534-2540 (2004).

[6] Kraehmer V, Grundmeier A, Dau H, Rehder D et al. (2009) manuscript in preparation.

[7] Pagel K, Seri T, von Berlepsch H, Griebel J, Kirmse R, Böttcher C, Koksch B, *Chembiochem.* **9**, 531-536 (2008).

X-ray absorption spectroscopy investigations on binuclear metal sites in proteins and models at the Mn and Fe K-edges

O. Sanganas[1], A. Grundmeier[1], M. Risch[1], I. Zaharieva[1], P. Chernev[1], V. Khare[1], T. Weyhermüller[2], K. Wieghardt[2], N. Voevodskaya[3], A. Gräslund[3], S. Stripp[4], T. Happe[4], H. Dau[1], M. Haumann[1]*

[1]Freie Universität Berlin, Institut für Experimentalphysik, 14195 Berlin, Germany
[2]Max-Planck Institut für Bioanorganische Chemie, 45470 Mülheim a.d.R., Germany
[3]Stockholm University, Department of Biochemistry and Biophysics, 10691 Stockholm, Sweden
[4]Ruhr-Univ. Bochum, Biochemie der Pflanzen, AG Photobiotechnologie, 44780 Bochum, Germany
*michael.haumann@fu-berlin.de

Protein-bound metal centers comprising two closely associated transition metal ions are involved in a wide variety of catalytic reactions in biological enzymes. In particular, such sites are involved in the activation of small molecules, such as hydrogen (H_2) and oxygen (O_2). Two different gross types of di-metal sites may be distinguished, namely (a) complexes comprising metal coordination mainly by sulfur atoms of thiol groups from cysteine amino acids and (b) complexes where metal coordination is mediated mainly by oxygen and nitrogen ligands from aspartate, glutamate, and histidine. Prominent examples of type (a) are hydrogenases (H_2ases), enzymes that catalyze the formation of H_2 by proton reduction, and of type (b) are ribonucleotide reductases (RNRs), which activate O_2 during the formation of deoxyribonucleotides for DNA synthesis.

Particularly interesting are H_2ases from green algae of the di-iron type (Fe-Fe H_2ases), representing the "minimal unit" of biological H_2 formation [1], which are highly appealing for renewable fuel production in biotechnology. For the first time, we studied the Fe-Fe H_2ase (HydA1) from the alga *Chlamydomonas reinhardtii* (Fig. 1A) by XAS at the Fe K-edge.

RNRs are the only enzymes which produce deoxyribonucleotides in all organisms and therefore of key medical interest. Recently a novel RNR type with an Fe-Mn active site (instead of the usual Fe-Fe site, Fig. 1B) has been discovered in the human-pathogenic bacterium *Chlamydia trachomatis* [2]. For the first time, its metal site was studied by XAS both at the Mn and Fe K-edges.

XAS data of high quality were obtained for both enzyme systems, which have been incorporated in recent collaborative publications [3,4].
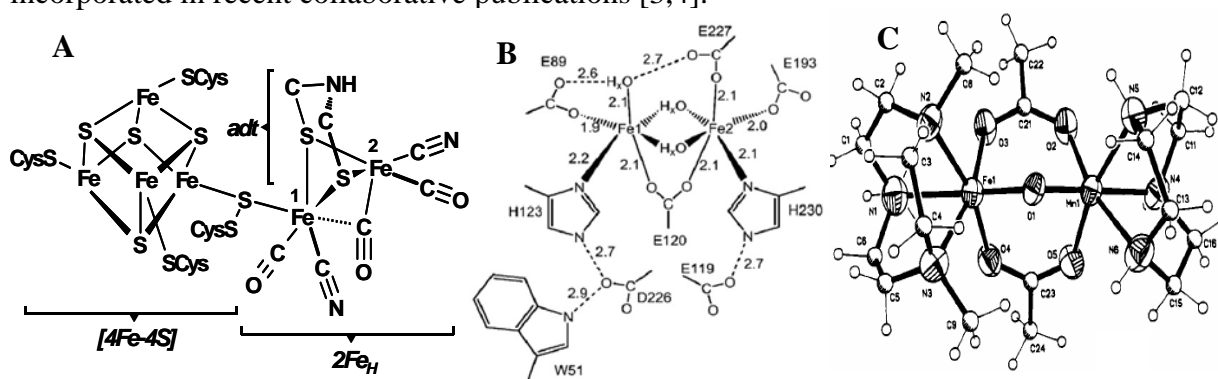
Figure 1: (A) Structure from protein crystallography of the 6Fe-site in Fe-Fe H_2ase [1]. (B) Structure of the metal site in Mn-Fe RNR from *C. trachomatis* reconstituted with an Fe-Fe site [5]. (C) Example of a synthetic Mn-Fe complex [6] containing Mn(IV) and Fe(III), studied here by XAS.

Experimental: XAS was performed at beamline KMC-1 using a double-crystal monochromator and the set-up for XAS of our group at FU-Berlin, comprising a liquid-helium cryostat and a single-element energy-resolving germanium detector. EXAFS scans were done at the Mn K-edge (at ~6550 eV) and at the Fe K-edge (at ~7100 eV) with samples residing at 20 K in the cryostat. Solutions of purified H_2ase and RNR proteins were studied with metal concentrations of about 0.5-1 mM. In addition, synthetic model compounds holding Mn and Fe ions (Fig. 1C [6]) were measured.

(1) For the first time, the active site Fe-complex of Fe-Fe H$_2$ase (HydA1) from *C. reinhardtii* was studied by XAS. XANES and EXAFS spectra of HydA1 protein in the as-isolated state and after treatment with substrate (H$_2$) and inhibitor (CO) were obtained (Fig. 2). Our results show that the 6Fe cluster in the green algae enzyme structurally is similar to the one in H$_2$ases from bacteria [3,7,8]. These studies pave the way for in-depth investigation of H$_2$-formation in H$_2$ases from algae.

(2) XAS on the Mn-Fe site of *C. trachomatis* RNR in several oxidation states of the metals (e.g. Mn(III)Fe(III) and Mn(III)Fe(II)) revealed the Mn-Fe distances and their changes upon site reduction (Fig. 3). Metal-metal distance changes were accompanied by the formation of additional μ-O(H) bridges between the metal ions [4]. First insights into the potential binding of O$_2$ at the Mn-Fe site were obtained. The next step are XAS studies on the crucial Mn(IV)Fe(III) state of catalysis.

(3) XAS data of synthetic Mn-Fe complexes in the Mn(IV)Fe(III) and Mn(III)Fe(III) states revealed the Mn-Fe distances and fine structural details of the metal site, and provided spectroscopic standards for the XAS investigations on the biological metal centers (Fig. 4).
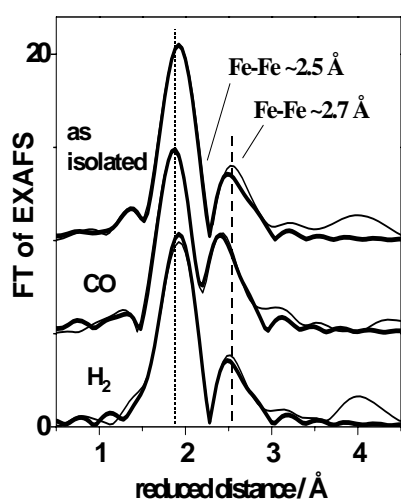
Figure 2: FTs of Fe EXAFS spectra of HydA1 H$_2$ase in three states. Fe-Fe distances in the 4Fe4S cluster and 2Fe unit were resolved [3].
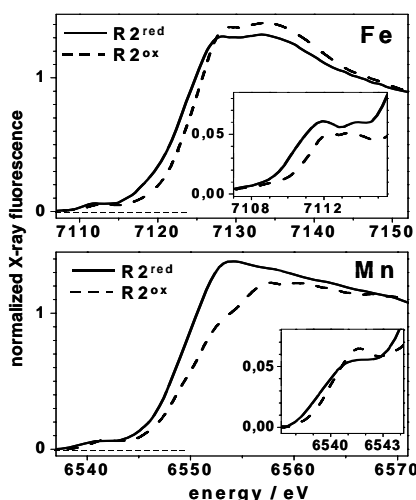
Figure 3: Fe and Mn XANES spectra of Mn-Fe RNR in two states. Edge shifts are due to metal reduction (insets: pre-edges) [4].
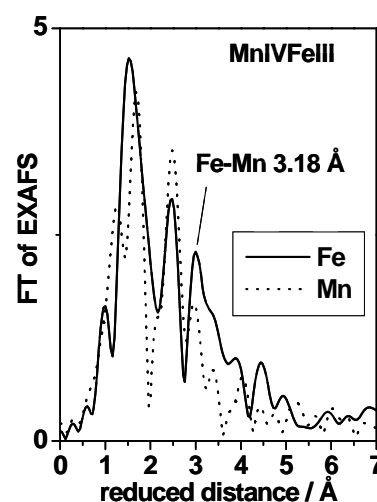
Figure 4: Fe and Mn EXAFS spectra of a hetero-bimetallic synthetic complex (see Fig. 1C) in the Mn(IV)Fe(III) state.

In summary, high-quality XAS data and novel structural and electronic information were obtained for two metalloenzymes and for relevant synthetic models. The results have entered recent publications [3,4]. In 2009, our BioXAS experiment at beamline KMC-1 will be enhanced by a recently purchased 13-element energy-resolving Ge-detector, thus allowing for XAS experiments on proteins and models with even improved signal quality and increased distance resolution.

[1] Peters JW, *Curr. Opin. Struct. Biol..* **9**, 670-676 (1999).

[2] Högbom M, Stenmark P, Voevodskaya N, McClarty G, Gräslund A, Nordlund P, *Science* **305**, 245-248 (2004).

[3] Stripp S, Sanganas O, Happe T, Haumann M, *Biochemistry accelerated*, submitted (2009).

[4] Voevodskaya N, Lendzian F, Sanganas O, Grundmeier A, Gräslund A, Haumann M, *J. Biol. Chem.* Epub, doi:10.1074/jbc.M807190200 (2008).

[5] Voevodskaya N, Narvaez A-J, Domkin V, Torrents E, Gräslund A, *Proc. Natl. Acad. Sci. USA* **103**, 9850-9854 (2006).

[6] Hotzelmann H, Wieghardt K, Flörke U, Haupt H-J, Weatherburn DC, Bonvoisin J, Blondin G, Giererd JJ, *J. Am. Chem. Soc.* **114**, 1681-1696 (1992).

[7] Löscher S, Schwartz L, Stein M, Ott S, Haumann M, Inorg. Chem. 46, 11094-11105 (2007).

[8] Kamp C, Silakov A, Winkler M, Reijerse EJ, Lubitz W, Happe T, *Biochim. Biophys. Acta* **1777**, 410-416 (2008).

The geometry and quality of root-canal fillings in teeth: a phase-enhanced microtomography study on the *BAMline* imaging setup

Paul Zaslansky[a], Alexander Rack[b], Hagay Shemesh[c]

[a]Max Planck Institute of Colloids and Interfaces, Research Campus Golm, Potsdam, Germany, [b]European Synchrotron Radiation Facility, 38043 Grenoble Cedex, France, [c]Department of Cariology Endodontology Pedodontology, Academic Centre for Dentistry Amsterdam (ACTA), Amsterdam, The Netherlands

Human teeth are exposed to harsh working conditions in the mouth for many years. These harsh conditions promote wear and tear - not only due to a cyclic nature of pressure, thermal and hydration loads but also (occasionally primarily) due to damage caused by bacteria. Bacteria often actively destroy all types of tooth tissue, through the formation of caries. When extensive damage ensues and the root regions become affected/infected, the dental surgeon may perform root-canal treatment, so as to remove bacteria and debris from the tooth pulp chamber and inner canals. This is followed by canal sealing/obturation where a filler (e.g. Gutta Percha) is cemented into the empty and disinfected canal.

To date, this procedure remains problematic [1] for a variety of reasons: varying root geometry as well as access, preparation, filling and other treatment limitations. Consequently infection remains or may develop/re-appear in a large number of cases.

In the experiments reported here, single-rooted teeth were prepared according to accepted root-filling procedures as previously reported [2]. Representative samples were visualized under the partially coherent imaging conditions of the BAMline microCT setup, utilizing the propagation radiography method [3,4]. In a preliminary set of experiments, multiple phase-enhanced radiographs were collected in which edges, voids on the supra-micron length-scale and discontinuities can be seen (fig 1).
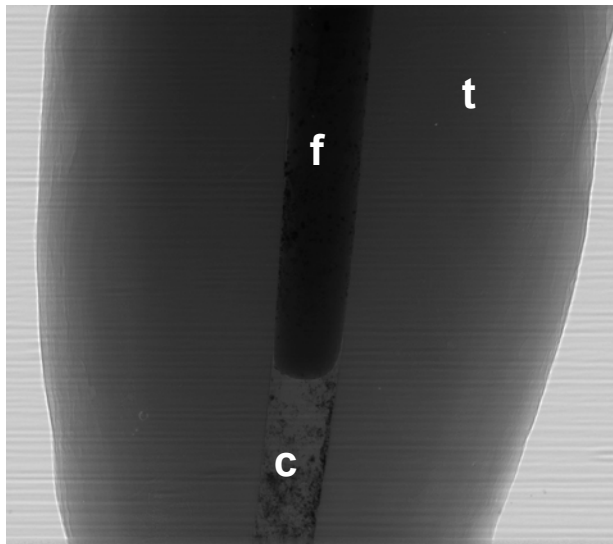
Figure 1: Typical radiograph of root-canal filled tooth; (t) - tooth (f) - filling (c) - cement
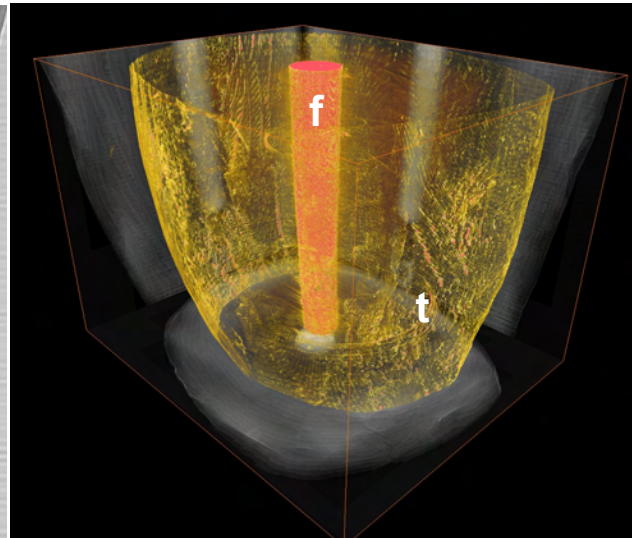
Figure 2: 3D rendering of a typical reconstruction. Red: root canal filling, yellow: outline of root and canal, black/gray: orthogonal side-projection views

The filling features revealed by the phase enhanced images are by no means simple to understand. When reconstructed into 3D tomograms, a large number of details of the canal, cement and tooth-microstructure emerge (fig 2). In such images, the complex structure cannot be represented by unique assignment of colors per region. Thus, only some of the important details are seen, attesting to a complex 3D picture.

When virtual slices are cut in the data, spatial relations between filler, cement and natural tissue are revealed (figs 3,4).

The non-destructive nature of this data and its unique level of detail suggest high potential for important findings in such measurements. Understanding the nature of interaction of the tooth and filling materials and the quality of fit along the canal require additional investigations, so as to be able to interpret the relation between the image and the real state of the materials in the wet tooth. Such information may shed important light on key contributions to the success or failure of this treatment.

Figure 3: Slice across root: low magnification view, revealing tooth root outline and filling of canal. Scale bar: 1 mm
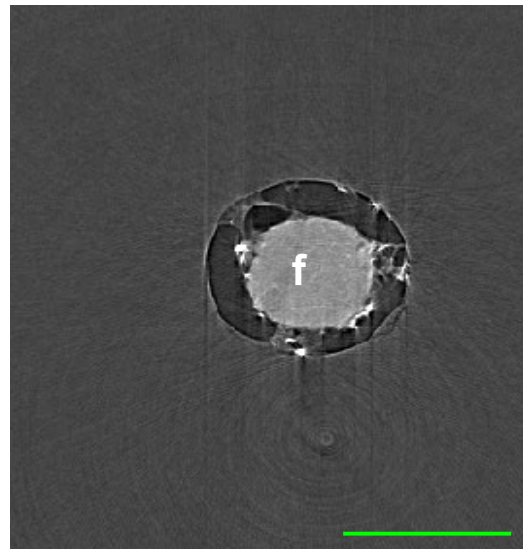
Figure 4: Slice across root: zone of root filling where clear gaps are seen between filling material and canal walls. Scale bar : 200 μm

References:
1. Nair PN. O*n the causes of persistent apical periodontitis: a review*. Int Endod J.;39(4):249-81,(2006).
2. Shemesh H, Wu MK, Wesselink PR. *Leakage along apical root fillings with and without smear layer using two different leakage models: a two-month longitudinal ex vivo study*, Int Endod J. 2006 Dec;39(12):968-76, (2006).
3. A. Rack, S. Zabler, B. R. Müller, H. Riesemeier, G. Weidemann, A. Lange, J. Goebbels, M. Hentschel, W. Görner, *High resolution synchrotron-based radiography and tomography using hard X-rays at the BAMline (BESSY II),* Nuclear Instruments and Methods in Physics Research A vol. 586 (2), pp. 327-344 (2008)
4. S. Zabler, H. Riesemeier, P. Fratzl and P. Zaslansky, *Fresnel-propagated imaging for the study of human tooth dentin by partially coherent x-ray tomography,* Opt. Express 14 (19) 8584-8597, (2006).

Analysis of inhibitor complex structures of human cAMP specific phosphodiesterase 4A

R. Eylenstein, M. Zahn, E. B. Küttner, S. Moschütz, P. Schäfer, N. Sträter
Institut für Bioanalytische Chemie, Biotechnologisch-Biomedizinisches Zentrum,
Universität Leipzig, Deutscher Platz 5, 04103 Leipzig

The second messenger cyclic nucleotide cAMP plays an important role in intracellular signal transduction. Induced by an extracellular signal, cAMP will be produced and lead to the activation of further signal cascades thereby triggering cellular responses. The rapid signal inactivation of the cAMP-mediated cellular response is exclusively provided by cAMP-specific phosphodiesterases (PDE). The PDE4, one of the eleven families of the PDE superfamily hydrolyses the cyclic 3'-5' phosphodiester bond in cAMP to generate the product AMP. The catalytic domain of PDE4A consists of 16 α-helices, which form three subdomains [1]. The intersection of the subdomains forms the active site, which contains a zinc and a magnesium ion (Fig. 1).
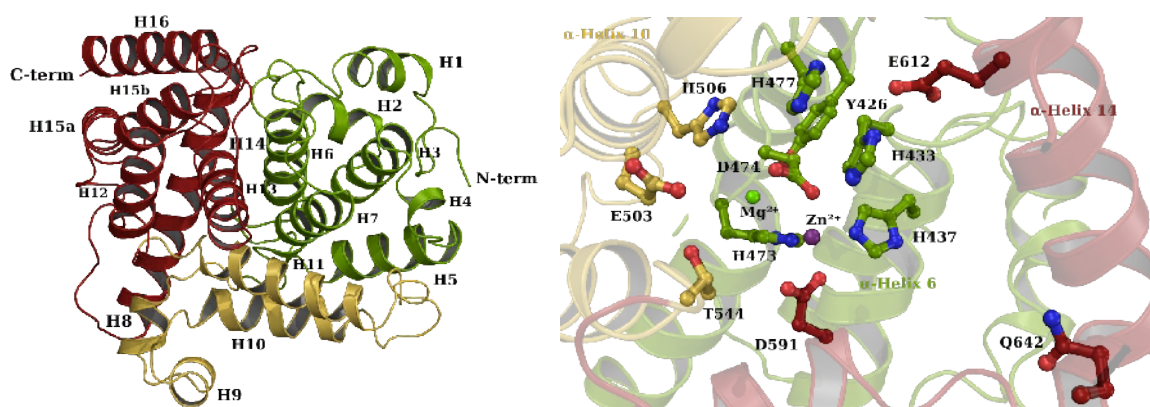
Fig. 1: Structure of the catalytic domain of PDE4A (PDB ID: 2QYK).

Dysfunction of PDE4 can lead to diseases such as asthma and chronic obstructive pulmonary disease. Until today, therapeutic substances which were developed against the PDE4-family show little or no subtype-specificity [2]. A therapeutic application of these substances may thus lead to strong side effects. The determination of the binding mode of new inhibitors (in collaboration with Curacyte AG, Leipzig) is in the focus of our research.

After the insoluble expression of the catalytic domain of human PDE4A in *E. coli* and subsequent renaturation and purification, we could obtain crystals of PDE4A in the presence of 21 % ethylene glycol by the sitting-drop vapour diffusion method at a protein concentration of 7 - 9 mg/ml after ~8 days at 292 K. Crystals were soaked over night with nine different inhibitors with a maximal DMSO concentration of 4 %.

Data collection of inhibitor-soaked crystals was performed at BESSY-MX beamline 14.1 at a wavelength of 0.9184 Å (Table 1). Data analysis was carried out using Mosflm, Scala and Refmac 5.0 of CCP4 program suite [3], where the unliganded structure was used as an initial refinement model.

Table 1: Data collection statistics

inhibitor	CD 110996	CU 130278	CU 150152
space group	$P2_12_12$	$P2_12_12$	$P2_12_12$
resolution range [Å]	26.06 - 1.82	36.49 - 1.95	36.44 - 1.90
completeness [%]	99.6 (99.2)	92.2 (78.3)	96.5 (89.8)
multiplicity	6.7 (6.3)	4.5 (3.7)	4.2 (3.7)
mosaicity [°]	0.53	0.57	0.36
$I/\sigma(I)$	14.6 (3.1)	13.3 (3.6)	11.5 (2.7)
R_{sym} [%]	10.8 (50.3)	8.4 (39.6)	9.4 (51.4)

*Values in brackets correspond to the highest resolution shell.

For the structurally related pharmaceutical inhibitors three different modes of binding were determined. In the first binding mode, the inhibitors interact with the bimetal centre via a reactive hydroxide ion and H433. Furthermore, the inhibitors are stabilized via π-stacking interactions and hydrogen bonds (Fig. 2). In the second binding mode, the inhibitors do not interact with the bimetal centre and show only hydrophobic binding interactions (Fig. 2). Inhibitor CU 150152, which belongs to the third binding mode, is a larger inhibitor with a kink at the non-aromatic heterocyclic ring and displays a larger number of interactions (Fig. 2).

The differences in the binding modes correlate well with the kinetic constants, which were determined by isothermal titration calorimetry.

a) binding mode I: b) binding mode II: c) binding mode III:
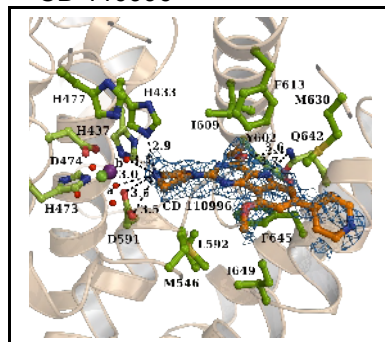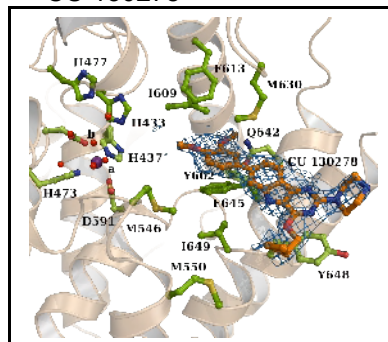
CD 110996   CU 130278   CU 150152
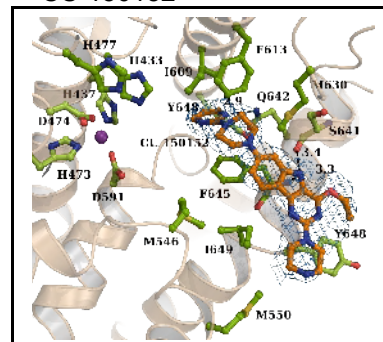
K_i = 10,3 nM K_i = 133 nM K_i = 3,5 nM

Fig. 2: Structure of three different inhibitors exhibiting different binding modes, bound to the active site of PDE4A. a) CD 110996. b) CU 130278. c) CU 150152.

References

[1] Y. H. Jeon *et al*. (**2005**), *Cell. Mol. Life Sci.*, **62**: 1-16.

[2] D. Spina (**2008**), *British Journal of Pharmacology*, 1-8.

[3] Collaborative Computational Project, Number 4 (**1994**), *Acta Cryst.* D50, 760-763.

Study of the peptide/linker interface for biosensors by IR synchrotron mapping ellipsometry

D.-M. Rosu[1], G. Sun[1], N. Esser[1], X. Zhang[2], J. Rappich[2], U. Schade[3], M. Gensch[3], M. Hovestädt[4], R. Volkmer[4], K. Hinrichs[1]

[1] ISAS- Institute for Analytical Sciences, Department Berlin, Albert-Einstein-Str. 9, 12489 Berlin, Germany

[2] Helmholtz Zentrum Berlin für Materialien und Energie GmbH, Institut für Si-Photovoltaik, Kekuléstr.5, 12459 Berlin, Germany

[3] Helmholtz-Zentrum Berlin für Materialien und Energie GmbH, Elektronen-Speicherring BESSY II, Albert-Einstein-Str. 15, D - 12489 Berlin, Germany

[4] Charité Universitätsmedizin Berlin, Institut für Medizinische Immunologie, Abteilung Molekulare Bibliotheken, Hessische Str. 3-4 , 10115 Berlin, Germany

Biosensors on silicon substrates attract great interest due to their possible technological applications in medicine and immunology. In particular the preparation and characterisation of functionalized surfaces for biomolecular identification is important for the design of biosensors. Due to monolayer sensitivity and non-invasivity infrared ellipsometry is well suited for characterization of such biofunctionalized surfaces.

The IR synchrotron ellipsometer at BESSY II, for the mid infrared range, enables investigation of samples with a lateral resolution below 1 mm^2 and it is equipped with a mapping table, allowing therefore the investigation of the homogeneity of organic thin films and biosensors. [1-3]
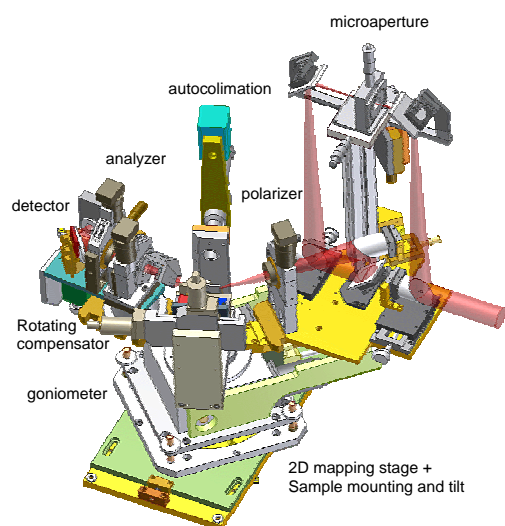
Figure 1: Infrared mapping ellipsometer [1-3] with 2-dimensional mapping stage, autocollimation, rotating compensator and microfocus unit.

An Au surface functionalized by benzoic acid served as model sample. The peptide was immobilized on this surface. The sample was measured at an incidence angle of 65° in the laboratory and with the synchrotron mapping ellipsometer at BESSY, respectively. A satisfying agreement between the lab measurements (probed area ~ 50 mm^2) and the averaged synchrotron measurement (probed area of each spot < 1 mm^2) was found (see Fig. 2). However, since different areas were probed, the difference between the two measurements is most likely caused by the inhomogeneity of the film.

The characteristic bands for the benzoic acid are identified: around 1610 cm^{-1} (benzene ring vibration) and around 1720 cm^{-1} (C=O vibration).
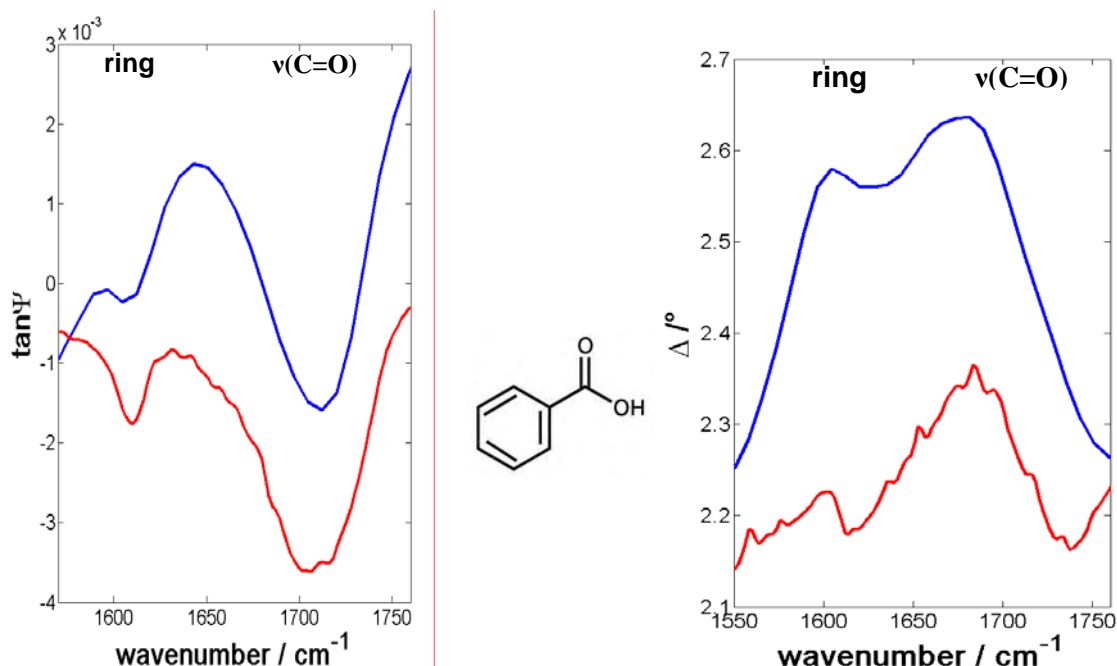
Figure 2: Baseline corrected tan Ψ and Δ spectra of benzoic acid on Au: averaged BESSY measurements of a 4x6 mm^2 area (blue); a lab measurement of ~ 50 mm^2 (red) are shown for comparison

The homogeneity of the film was checked in more detail by synchrotron infrared mapping ellipsometry measurements on a sample area of 4x6 mm^2 (Fig. 3). TanΨ maps are calculated considering the amplitude of the C=O stretching band and Δ maps were calculated by averaging the values of Δ spectra in the nonabsorbing range 1700-1800 cm^{-1}. A delta variation of 0.6° and a 33% variation in tanΨ were determined.
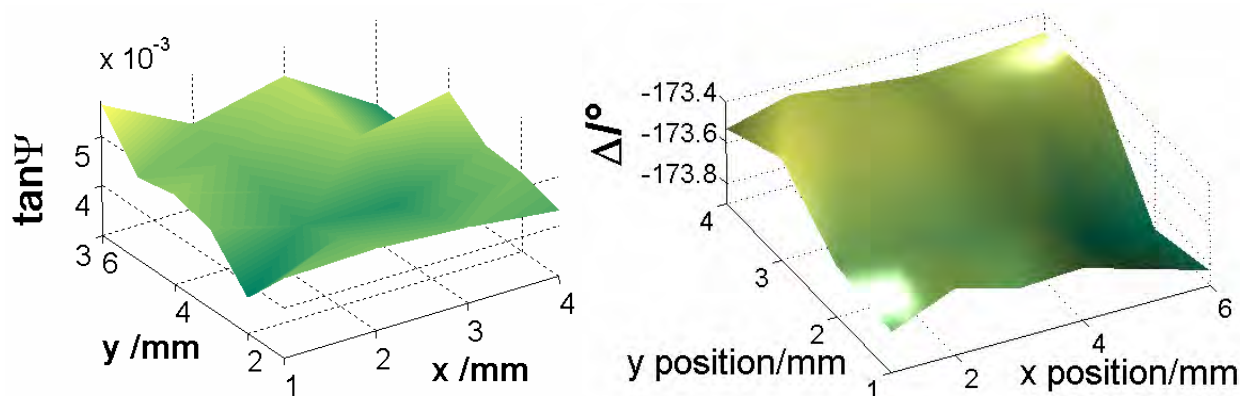
Figure 3: Interpolated 2D t*an Ψ and Δ maps of a 4x6 mm^2 area of benzoic acid on Au*

In a next step, GST peptide was immobilized on the benzoic acid film. The successful binding of the peptide to the benzoic acid was confirmed by the appearance of the amide I and amide II bands in the IR spectra as shown in Fig. 4. Considering the fact that the area investigated with the synchrotron mapping ellipsometer was 5x5 mm^2 and the one in the lab approximately

50 mm^2, the difference between the lab measurements and the mean of the synchrotron ellipsometric spectra is also here explained by the inhomogeneity of the sample.
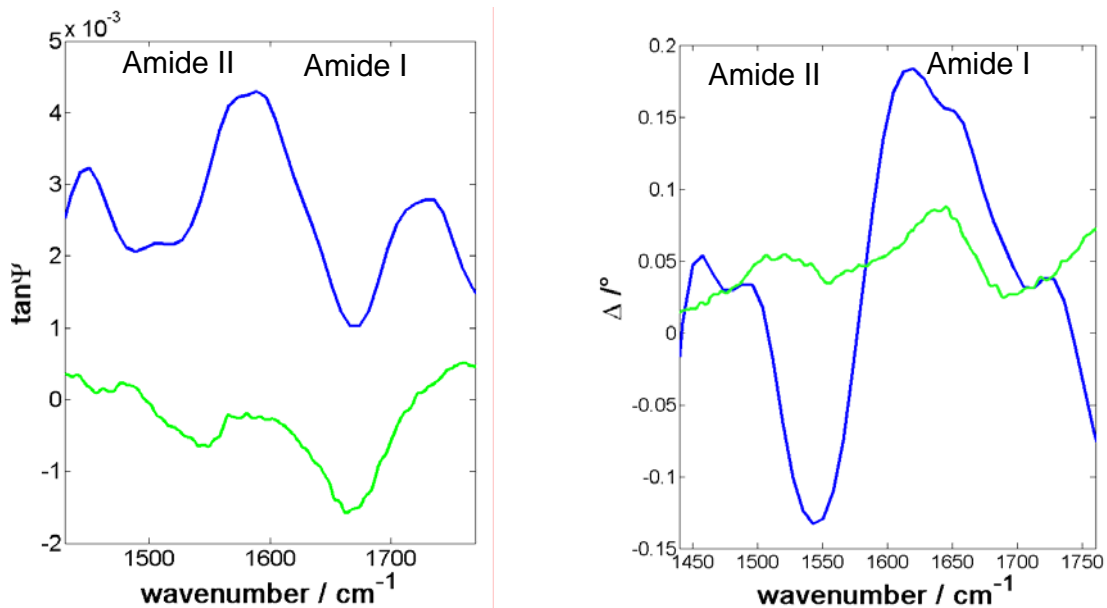
Figure 4: Baseline corrected tan Ψ and Δ spectra of the adsorbed GST peptide: averaged BESSY measurements of a 4x6 mm^2 area (blue); a lab measurement of ~ 50 mm^2 (green) is shown for comparison.

In future, the peptide incubated sample will be used as a template for a third step, the incubation with an antibody.

References:

[1] *"Microfocus-Infrared Synchrotron Ellipsometer for Mapping of ultrathin films",* M. Gensch, N. Esser, E. H. Korte, U. Schade, K. Hinrichs, Infrared Physics and Technology 49 (1-2) (2006) 39-44.

[2] *"Influences of thick film inhomogeneities on the ellipsometric parameters",* K. Roodenko, M. Gensch, H. M. Heise, U. Schade, N. Esser, K. Hinrichs, Infrared Physics and Technology 49 (1-2) (2006) 74-77.

[3] „*Infrared Imaging and Mapping of Biosensors"*; K. Hinrichs, Encyclopedia of Micro- and Nanofluidics, part 9: 824

Understanding the dual specificity of the membrane-bound nucleotidase NTPDase2 from *Rattus norvegicus*

M. Zebisch and N. Sträter

Center for Biotechnology and Biomedicine, Institute of Bioanalytical Chemistry, Faculty of Chemistry and Mineralogy, University of Leipzig, Deutscher Platz 5, 04103 Leipzig, Germany.

NTPDases or *n*ucleoside *tri*phosphate *d*isphosphohydro*lases* are membrane-bound nucleotide-metabolizing enzymes. They are responsible for signal conversion and inactivation in extracellular nucleotide-mediated or "purinergic" signaling, where nucleotides bind to G protein-coupled P2Y receptors or ligand-gated P2X ion channels to induce cellular responses (*1*). The NTPDase enzymes catalyze the sequential hydrolysis of the *γ*- and *β*-phosphates from nucleoside triphosphates to generate the corresponding monophosphate. For their hydrolytic activity, the enzymes require the presence of divalent metal ions at micro- to millimolar concentrations (**Figure 1**).
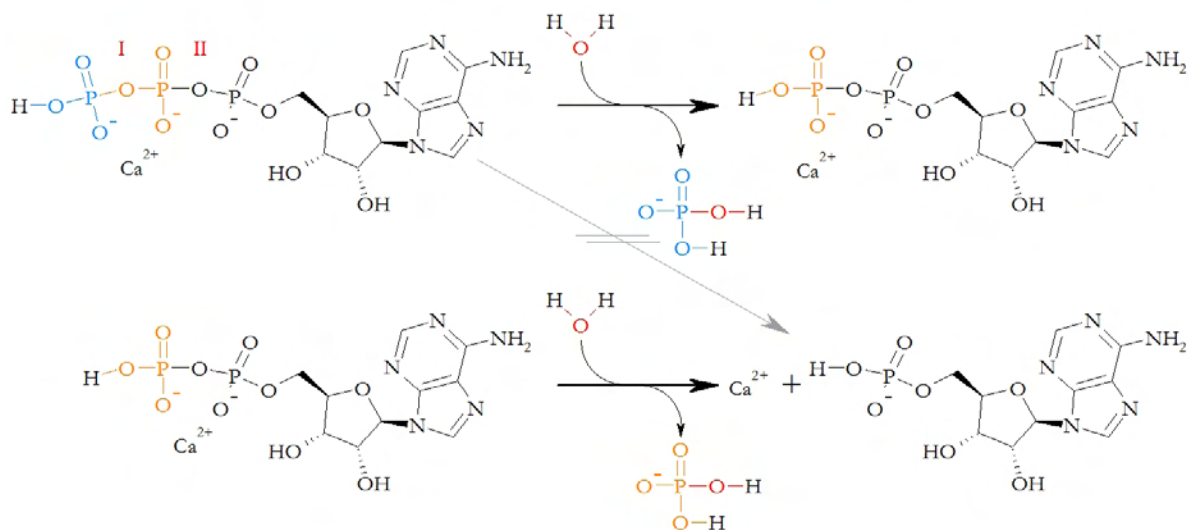
Figure 1: *Reactions catalyzed by NTPDase family proteins. Hydrolysis of the γ- and β-phosphate occurs sequentially. Removal of pyrophosphate by direct cleavage of bond II without prior cleavage of bond I is not observed.*

The structure of the catalytic extracellular domain of NTPDase2 was determined to a resolution of 1.8Å. The phase problem was solved by SIRAS using a tungstate derivative of the protein. The active site of the protein could be identified and the catalytic mechanism be elucidated after a dataset of an AMPPNP (an ATP analog)-soaked crystal had been recorded at BESSY (*2*). However, it was still unclear, how the same active site could be engaged to hydrolyze nucleoside diphosphates such as ADP almost as well. To

answer this question, crystals were again soaked with hydrolysis-stable ADP analogs. The commercially available ADP analogs did either not bind to the active site (AMPCP) or were hydrolyzed by the protein (ADPβS). Only with the ADP analog AMPNP, a complex structure could be determined. Analysis of this structure shows that depending on the length of the substrate's phosphate tail, the α-phosphate adopts different positions so that the terminal phosphate can reach the hydrolytic site in both, nucleoside di- and –triphosphate hydrolysis.

Data collection statictics. Values in parentheses are for the highest-resolution shell.

	Ca^{2+}×AMPNP	Ca^{2+}×UMPPNP
X-ray source	BESSY/BL14.2	BESSY/BL14.1
Wavelength (Å)	0.9184	0.918
Space group	$P2_12_12_1$	$P2_12_12_1$
Crystal-to-detector distance	160	160
Frames recorded; Δφ/frame	312; 0.5°	210; 0.5°
Cell Dimensions		
a, b, c (Å)	41.0, 69.1, 163.8	41.6, 69.0, 164.0
Reflections observed, unique	176038, 27867	131203, 32186
Resolution (Å)	26.70-2.10 (2.15-2.10)	33.00-2.00 (2.05-2.00)
R_{sym} (%)	6.0 (48.8)	5.1 (26.6)
<I/σI>	22.3 (4.4)	19.6 (5.0)
Completeness (%)	99.3 (99.4)	98.1 (92.4)
Multiplicity	6.3 (6.3)	4.1 (3.4)
Mosaicity (°)	0.6	0.6
Wilson B factor	36.8	28.1
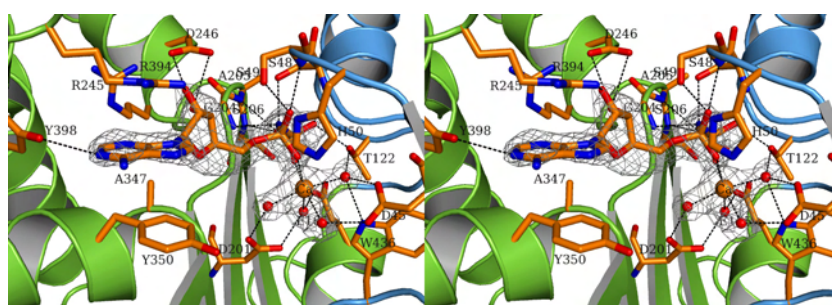
Figure 2: Stereo-view of the active site. The omit electron density map ($\lvert F_o\text{-}F_c\rvert \times \varphi_c$) of the bound ligands AMPNP and Ca^{2+}, and active site waters is contoured at 3σ.

References

1. Schwiebert, E. M. and Zsembery, A. (2003) Extracellular ATP as a signaling molecule for epithelial cells, *Biochim. Biophys. Acta 1615*, 7-32.

2. Zebisch, M. and Strater, N. (2008) Structural insight into signal conversion and inactivation by NTPDase2 in purinergic signaling, *Proc. Natl. Acad. Sci. U. S. A 105*, 6882-6887.

Characterization of Free Macro Algae Bio Mass by Hard X - Ray Fluorescence Measurements–Binding Structure

G. Bunke, A. Erko*, T. Scheydt**, H. Scharf***, W. Jurkowski, J. Paulovics
Technical University of Berlin
*BESSY GmbH, Berlin**TU Berlin, Institut für Angewandte Geowissenschaften
*** BAM, Berlin

Introduction

The Characterization of metal capacity of bio mass by x - ray fluorescence measurements is the most powervul direct method for quantitative estimation of metal loading of wet and swollen immobilized bio mass under real conditions. The use of macro algae bio mass is of particular interest for the removal of heavy metals from contaminated water. The aim of investigation is to provide a cost effective bio mass for sorption of ionic components.

Characterization of Free Macro Algae Bio Mass by Hard X - Ray Fluorescence Measurements

Preparation of samples

Macro algae (Fig. 1) are cultivated in coastal see of France. Fig. 2 shows dried and cut *Undaria pinnatifida*. Particle fraction between 0.2 mm and 0.3 mm was used to estimation of bio sorption isotherms (Fig. 3). Special material (Fig. 4) show the special material, what was used for sample preparation of X – ray analysis. All samples are also shown in figure 4, which were used for the characterization of the free macro algae bio mass fraction between 0.2 mm and 0.3 mm particle diameter of *Undaria pinnatifida*. Samples are labeled with numbers (0 up to 8).

Fig. 1: Wet macro algae (*Undaria pinnatifida*)

Fig. 2: Dried and cut *U. pinnatifida*

Fig. 3: Particle fraction of *Undaria pinnatifida* between 0.2 and 0.3 mm
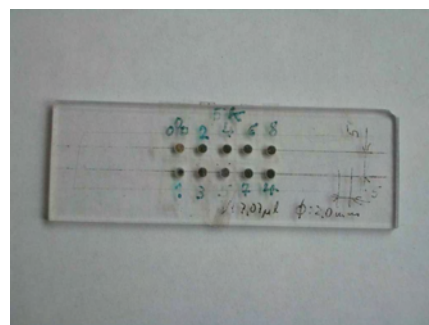
Fig. 4: Sample preparation for X – ray measurements (wet sample)

Figure 5 shows a view in the measuring chamber of the beam line KMC-2 "Berliner Elektronenspeicherring-Gesellschaft für Synchrotronstrahlung m. b. H. (BESSY GmbH, Berlin Adlershof)", which was used for measurements of EXAFS spectra.
Samples were placed 45° to synchrotron beam and detector 90° to synchrotron beam. Measuring was carried out by room temperature and air atmosphere.
The used detector is an Si-PIN photodiode.

Fig. 5: Measuring station (sample, detector (Si-PIN photodiode), synchrotron beam line KMC-2)

Characterization of bio sorbents

Modern methods such as liquid - solid equilibrium estimated by AAS (Fig. 6) , ICP (Fig. 7) and x – ray analysis (Fig. 8 and 9) open the possibility to characterize the loading of ionic components on the surface of bio sorbents.
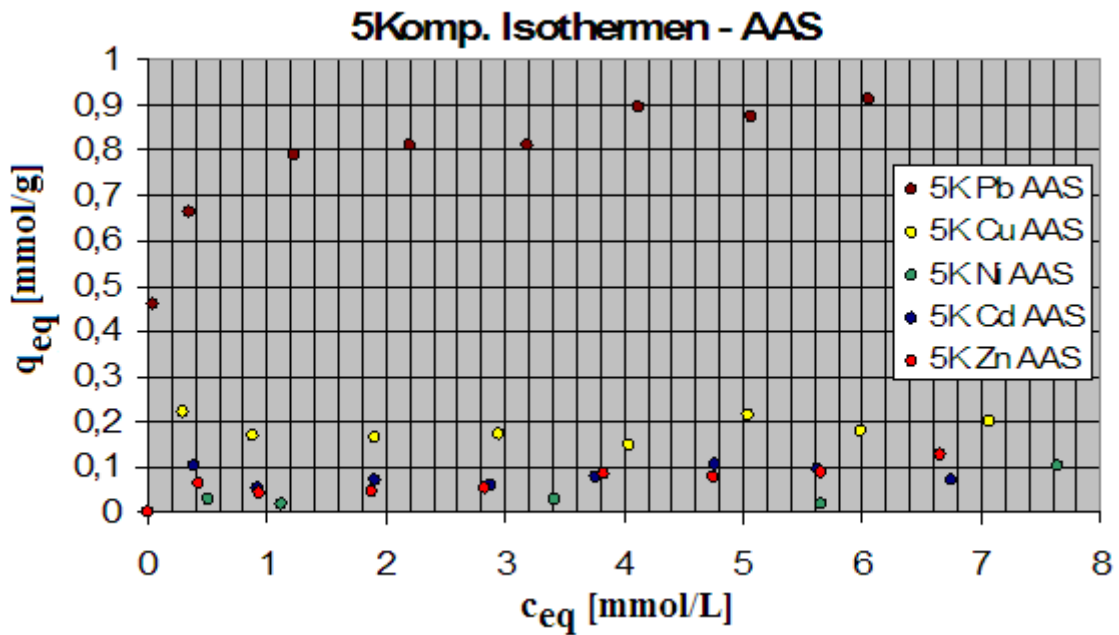
Fig. 6: Fife component isotherms for Pb 2+, Cu 2+, Ni 2+,
Cd 2+, Zn 2+, analyzed by F AAS
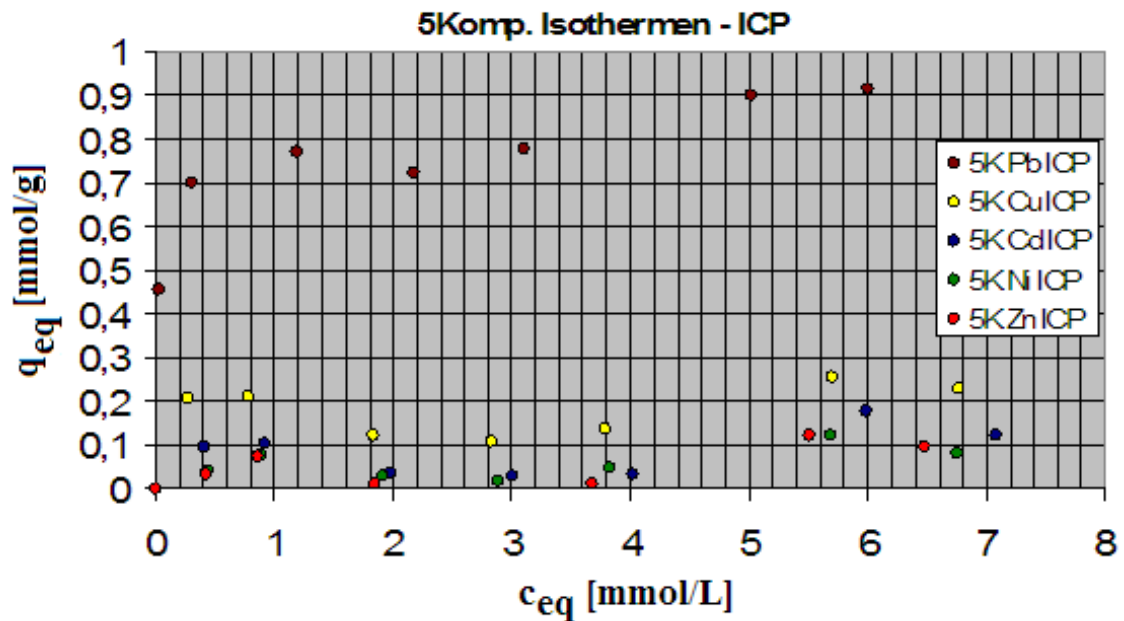
Fig. 7: Fife component isotherms for Pb 2+, Cu 2+, Ni 2+, Cd 2+,
Zn 2+, analyzed by ICP OES

q_eq mmol/g
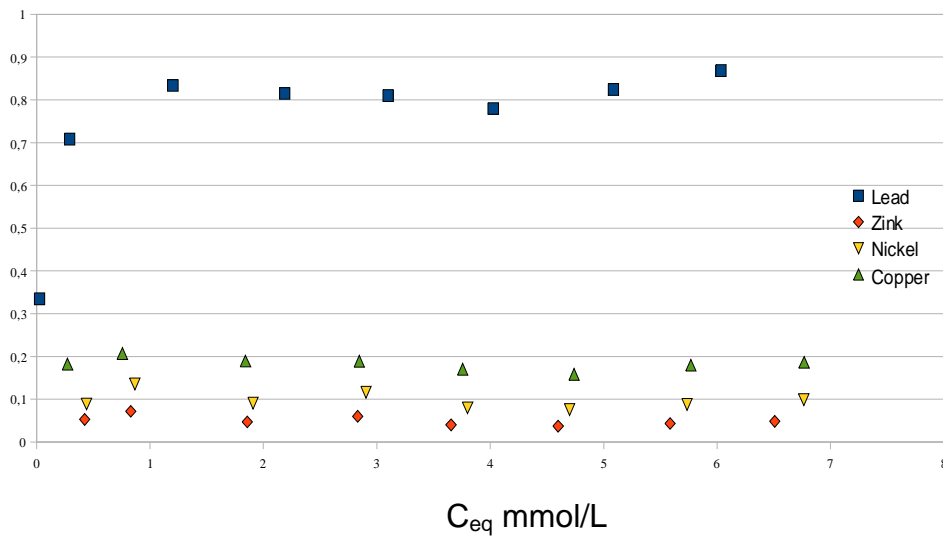
Fig. 8: Fife component system, isotherms for Pb 2+, Cu 2+, Ni 2+, Zn 2+, analysed by x - ray fluorescence mapping measurements
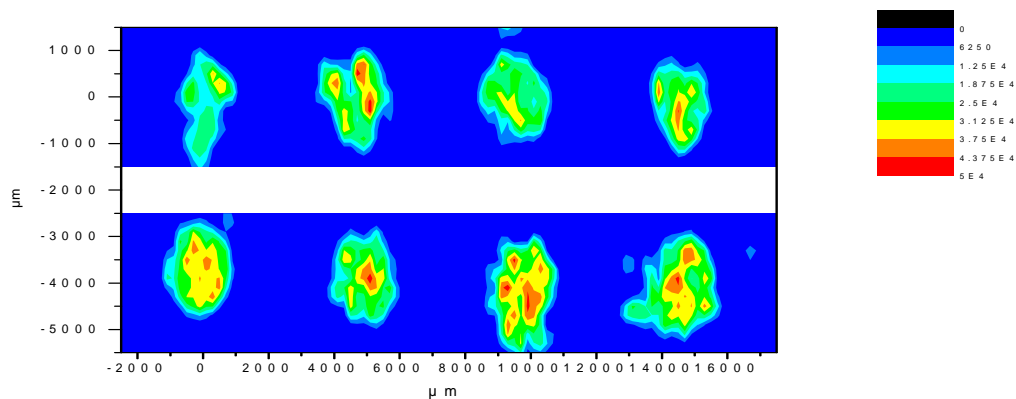
Fig. 9: Example: x - ray fluorescence mapping measurements for Pb 2+, logarithmic scale, 5 component system (Pb 2+, Cu 2+, Ni 2+, Zn 2+)

EXAFS spectra (Fig. 10), open the possibility to characterize the binding structure (Fig. 11) of heavy metals on the surface of bio sorbents. The results show that different binding structures of metals exist inside of bio sorbent. The X – ray measurements were successful for characterization of the binding structure. The right interpretation is not finished. Father X – ray experiments are necessary.
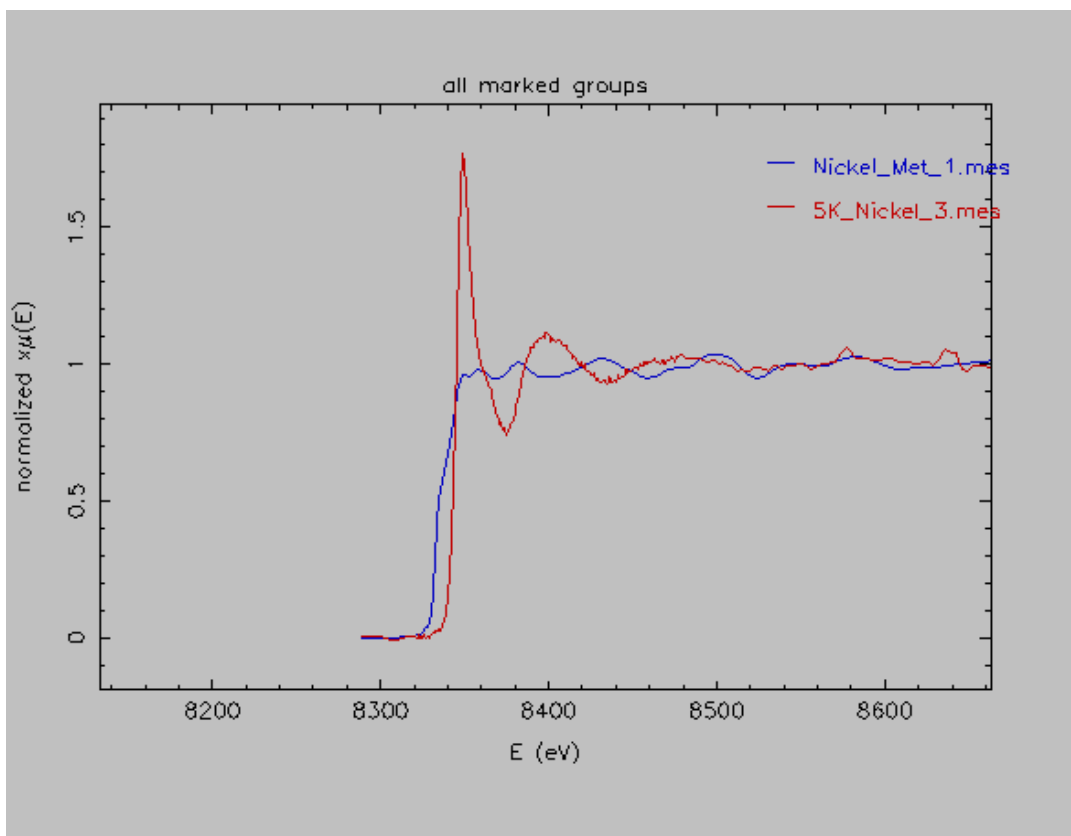
Fig. 10: Example: Result of EXFAS measurements for Ni 2+
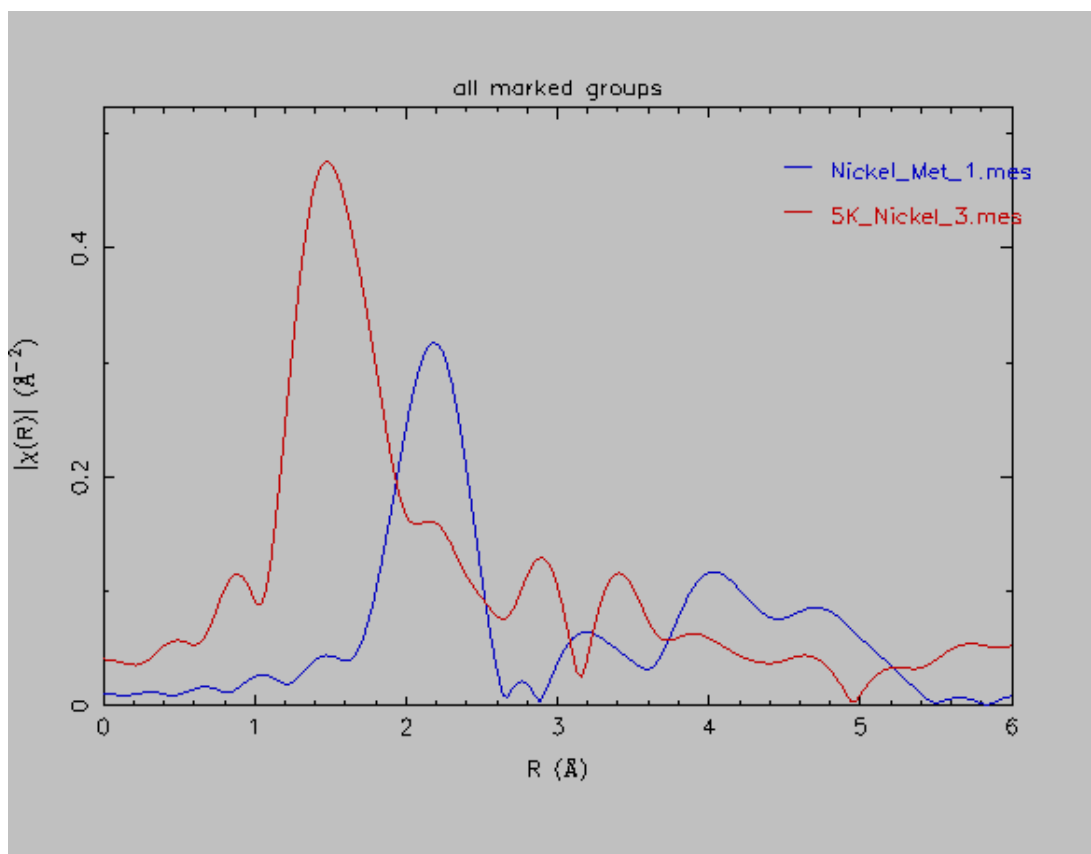
Fig. 11: Example: Result of EXFAS measurements for Ni 2+ binding structure

Fig. 12 shows the loaded samples 2, 4, 6, and 8 in the dried state. The brown color characterize the bio mass particles. Besides the bio mass particles many heavy metal crystals are on the surface. That means, that the concentration on heavy metals in solution was very high. After drying precipitation of heavy metal crystals exists. In future this precipitation is to prevent.

| No. 2 | No. 4 | No.6 | No.8 |
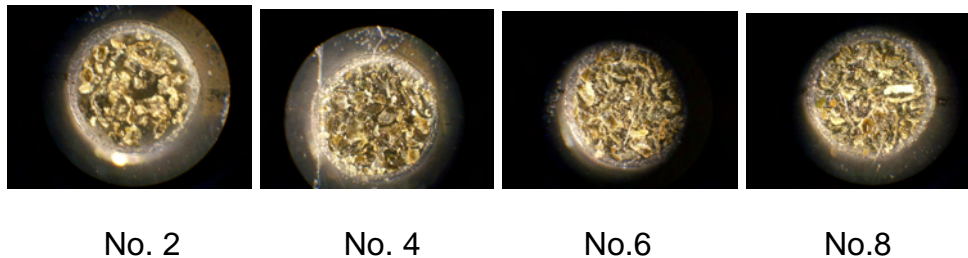
Fig. 12: Free bio mass particle in dried state

Conclusion

The special aim of the investigation is to find inexpensive biosorbents with high capacity for ionic components. Other objectives are the characterization of biosorbents by different methods (porosity, x-ray measurements, binding structure) and mathematical modeling of distribution equilibrium and concentration time curves by dynamic cyclic column experiments.

- X -ray fluorescence measurements
- Advantage: measuring metal components insight of particles (direct method)
- Necessary: Isotherm estimation by measuring the concentration in solution
- Estimation of one and muticomponent isotherms
- Estimation of binding structure by EXAFS Measurements

Supported by BESSY GmbH and DFG

Keywords: bio sorption, bio mass, characterization, Binding structure, desorption, dynamic experiments

Crystal structure analysis reveals how the Chordin family member Crossveinless 2 blocks BMP-2 receptor binding

Jin-li Zhang[1], Li-yan Qiu[1], Alexander Kotzsch[1,2], Stella Weidauer[1,2], Lucy Patterson[3], Matthias Hammerschmidt[3], Walter Sebald[1,4], and Thomas D Mueller[1,2,4]

[1]Department of Physiological Chemistry II, Biocenter, University of Wuerzburg, Am Hubland, 97074, Wuerzburg, Germany

[2]Department of Molecular Plant Physiology and Biophysics, Julius-von-Sachs Institute, University of Wuerzburg, Julius-von-Sachs Platz 2, 97082 Wuerzburg, Germany

[3]Max-Planck Institute for Immunobiology, Stuebeweg 51, 79108 Freiburg, Germany

[4]Rudolf-Virchow-Center, Versbacher Str. 9, 97078 Wuerzburg, Germany

Objectives

Crossveinless 2 (CV-2) is an extracellular BMP modulator protein belonging to the Chordin family. BMPs regulate many processes during embryonal development and have important roles in the tissue and organ homeostasis in the adult. Dysregulation of BMP signaling leads to severe diseases, thus requiring a stringent regulation of its activity at many different levels. Secreted modulator proteins like Noggin, Follistatin or those of the Chordin family are able to interfere with BMP activity through binding to these ligands and competing for receptor binding. During development CV-2 is expressed at sites of high-BMP signaling and like Chordin CV-2 can either enhance or inhibit BMP activity. The pro- and anti-activity of Chordin proteins is unique among BMP modulators indicating that these modulators must exhibit a mechanism different from receptor competition. CV-2 binds to BMP-2 via its N-terminal Von Willebrand factor type C (VWC) domain 1. Here we report the structure of the complex between CV-2 VWC1 and BMP-2. The tripartite VWC1 binds BMP-2 only through a short N-terminal segment, called clip, and the subdomain (SD) 1. Mutational analysis establishes that the clip segment and SD1 together create high-affinity BMP-2 binding. All four receptor-binding sites of BMP-2 are blocked in the complex, explaining that VWC1 acts as competitive inhibitor for all receptor types. In vivo experiments reveal that the BMP-enhancing (pro-BMP) activity of CV-2 is independent of BMP-2 binding by VWC1 showing that pro- and anti-BMP activity are structurally separated in CV-2.

Achievements

We have determined the first structure of a Chordin modulator protein bound to its cognate BMP ligand. The structure of the BMP-2:CV-2 VWC1 complex reveals a new architecture with the VWC1 domain of CV-2 being attached to BMP-2 like a paperclip to a sheet of paper. The 68 residues long CV-2 VWC1 domain exhibits a tripartite architecture with the N-terminus forming a long extended clip, a 34-residue long subdomain 1 (SD1) and a second slightly smaller (23 residue) subdomain 2 (SD2). Both subdomains form a flat extended structure with only SD1 of both subdomains sharing contact with BMP-2. The subdomains form small non-globular structures with very limited secondary structures. Subdomain SD1 comprises three short anti-parallel β-strands, subdomain SD2 contains only a short 2-stranded β-sheet. The rigid structure - despite the lack of large secondary structure elements - can be explained by the large number of disulfide bonds. Ten cysteine residues form five disulfide bonds, which distributed throughout the small VWC domain result in a highly rigidified backbone structure.

BMP signaling is achieved by binding of BMP-2 first to its high-affinity type I receptors, BMPR-IA or BMPR-IB, and subsequently by recruiting the low-affinity type II receptors - three different receptor can be utilized, BMPR-II, ActR-II and ActR-IIB - into the complex. Formation of this heterohexameric complex initiates downstream signaling, which includes transphosphorylation of the receptor serine/threonine-kinases and subsequent phosphorylation of so-called R-SMAD proteins. The latter dimerize upon phosphorylation and translocate into the nucleus where they regulate gene transcription.The unusual paperclip like structure now explains how the rather small VWC domain of CV-2 can simultaneously block binding of BMP-2 to both receptor subtypes. The clip folds into the type I receptor site interacting with many of the (main) binding determinants of BMP-2 thereby competing with type I receptor binding. The subdomain SD1 on the other hand binds to the type II receptor site covering a vast majority of the residues of BMP-2 that also interact with the type II receptors. The subdomain SD2 shares no contact with BMP-2 and thus seems not required for ligand recognition and binding. Truncation/deletion studies indeed show that SD2 can be deleted without consequences for the binding affinity of CV-2 VWC1 to BMP-2 in vitro. In vivo, however, inhibition efficiency of this truncated CV-2 VWC1 seems reduced, whether this is due to additional stabilizing contacts not observed in the crystal lattice or due to enhanced degradation for the truncation product is so far unknown.
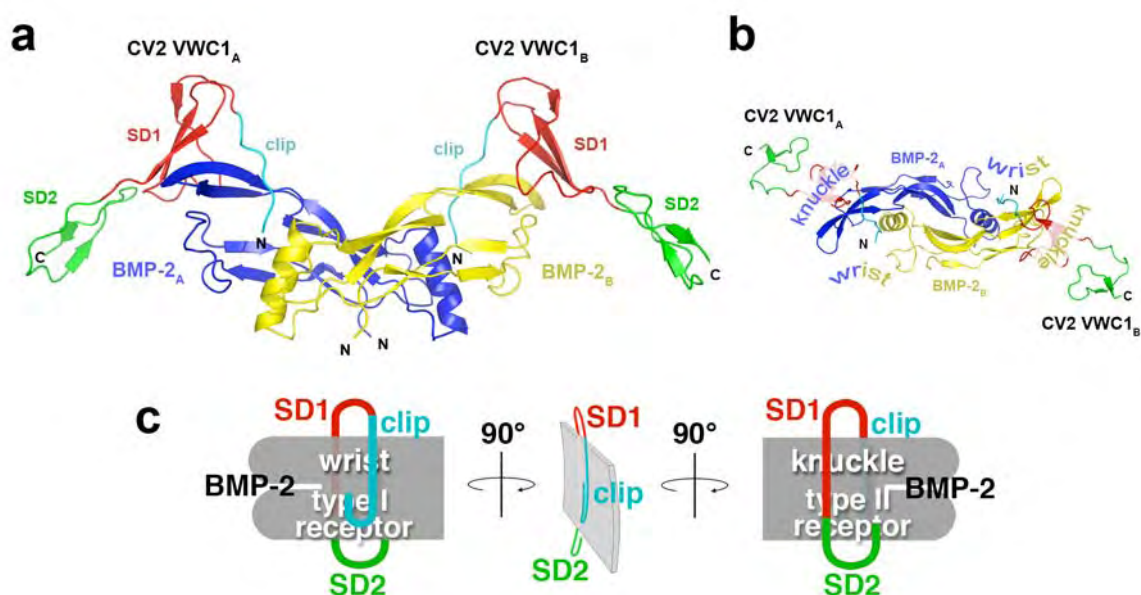
Figure 1: (a) Crystal structure of the complex BMP-2:CV-2 VWC1. BMP-2 is shown in blue and yellow, CV-2 VWC1 is colored with respect to its architecture. The clip region is shown in cyan, subdomain SD1 in red and subdomain SD2 in green. (b) As in (a) but shown from above, the receptor binding sites - wrist (type I receptor epitope) and knuckle (type II receptor site) - are indicated. (c) The binding of CV-2 VWC1 resembles that of a paperclip stacking onto a sheet of paper, with the clip located in the type I receptor epitope and the subdomain SD1 occupying the type II receptor binding site.

One very interesting property of CV-2 is its dual activity with respect to BMP-2 signaling. Whereas other BMP modulator proteins like Noggin, Follistatin or members of the DAN family are purely antagonizing BMP activity, CV-2 and some other members of the Chordin family can also enhance BMP signaling via a so far unknown mechanism. We have studied the effects of mutations in VWC1 in the context of full-length CV-2 via

mRNA microinjection in zebrafish. From our in-vitro and cell-based data CV-2 VWC1 seems to exhibit only a anti-BMP activity, i.e. only antagonizing functions could be observed, which is also consistent with the picture revealed by the crystal structure of the complex. When full-length wildtype CV-2 is injected into zebrafish embryos at the 4-cell stage an ambiguous activity for CV-2 is observed. Some embryos show a weak dorsalizing phenotype (anti-BMP activity), some embryos exhibit a weak ventralizing phenotype, which accounts for the pro-BMP activity. However, mutations in the CV-2 VWC1 domain that strongly abrogate BMP-2 binding show only a ventralizing effect indicating that the anti-BMP activity of CV-2 solely resides in the CV-2 VWC1 domain. Therefore pro- and anti-BMP activity of CV-2 seems to be confined in different regions of the molecule, the molecular mechanism by which it can be switched between these two opposing activities is however unclear at this state.

Crystal structure analysis reveals a spring-loaded latch as molecular mechanism for GDF-5 - type I receptor specificity

Alexander Kotzsch[1], Joachim Nickel[2], Axel Seher[2], Walter Sebald[2], and Thomas D Mueller[1]

[1]Department of Molecular Plant Physiology and Biophysics, Julius-von-Sachs Institute, University of Wuerzburg, Julius-von-Sachs Platz 2, 97082 Wuerzburg, Germany

[2]Department of Physiological Chemistry II, Biocenter, University of Wuerzburg, Am Hubland, 97074, Wuerzburg, Germany

Objectives

Dysregulation of Growth and differentiation factor 5 (GDF-5) signaling, a member of the TGF-β superfamily, is strongly linked to skeletal malformation. GDF-5 mediated signal transduction requires ligand-induced hetero-oligomerization of two types of BMP serine/threonine kinase receptors termed type I and type II, which differ by key sequence signatures in their cytoplasmic part. Whereas many BMP ligand members exhibit promiscuous binding to their type I and type II receptors, GDF-5 seems to rather specifically signal through the type I BMP receptor BMPR-IB. Consequently, mutations in either GDF-5 or BMPR-IB lead to similar phenotypes indicating that in chondrogenesis GDF-5 signaling seems to be exclusively mediated through BMPR-IB. In vitro interaction analyses however show that discrimination between the two BMP type I receptors BMPR-IA and BMPR-IB occurs with only 20-fold difference in binding affinity. Nevertheless, mutations found in the skeletal malformation diseases Symphalangism abrogate the type I receptor specificity of GDF-5 clearly showing that the small difference in affinities for BMPR-IA and BMPR-IB in vitro are highly significant in vivo. The molecular mechanism by which GDF-5 can distinguish between these two receptors is unknown so far. Here we present structural insights into the GDF-5:BMPR-IB complex revealing how binding specificity for BMPR-IB is generated on a molecular level. In BMPR-IB a loop within the ligand-binding epitope acts like a latch allowing high-affinity binding of GDF-5. In BMPR-IA this latch is in a closed conformation leading to steric repulsion. The new structural data now provide also a molecular basis how phenotypically relevant missense mutations in GDF-5 might impair receptor binding and activation.

Achievements

We have determined the structure of the TGF-β ligand GDF-5 (Growth and differentiation factor 5) bound to its high-affinity type I receptor BMPR-IB. Although at first sight the structures of the binary complexes of BMP-2 bound to BMPR-IA and GDF-5 bound to BMPR-IB seems highly similar, a detailed analysis shows remarkable differences that might explain the differences in binding and signaling observed between GDF-5 and BMP-2. Whereas the backbone core of the two type I receptors BMPR-IB and BMPR-IA are almost identical, the loops involved in binding to the BMP/GDF ligands differ significantly. The β1β2-loop and notably the β4β5-loop are exhibiting different backbone conformations in BMPR-IB and BMPR-IA. This is of importance as these two loops contribute more than 80% of the ligand-binding interface of the type I receptor. Mutagenesis data supports this view by showing that the main binding determinants for ligand recognition and binding differ in both receptors despite numerous residues in the binding interface of the receptors are conserved. In BMPR-IA a glutamine residue in the β4β5-loop, which is conserved in BMPR-IB, is the hot spot of binding, contributing more than 3kcal mol^{-1} via an intermolecular bi-dentate hydrogen bond to the binding free energy. Exchange of this conserved residue in BMPR-IB, however, does not alter the binding affinity; instead substitution of the

preceding phenylalanine residue (which is also conserved in BMPR-IA) for alanine completely abolishes binding to BMP ligands. This documents that recognition of BMPR-IB and BMPR-IA by the BMP ligands differs.
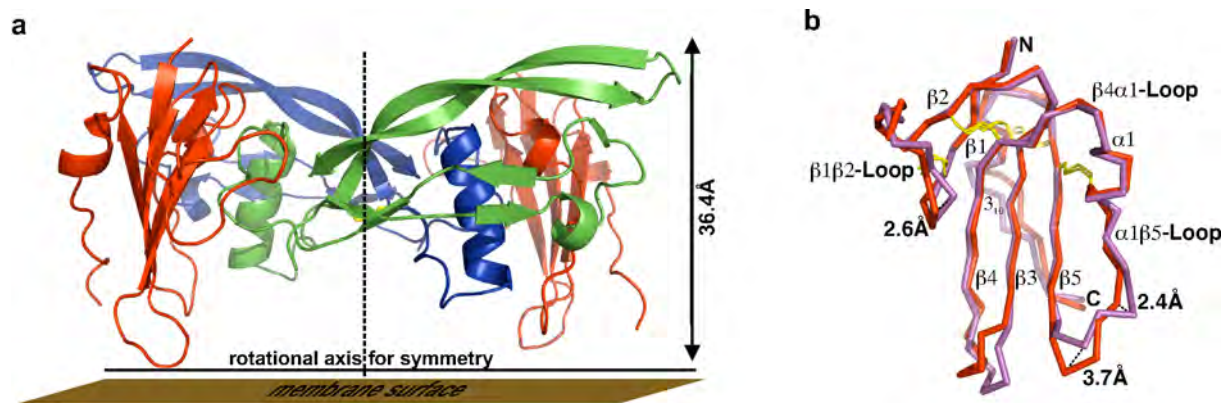
Figure 1: (a) Crystal structure of the complex GDF-5:BMPR-IB. GDF-5 is shown in blue and green, the receptor BMPR-IB is colored in red. Two BMPR-IB molecules bind to the homodimeric ligand GDF-5. Due to its symmetry only half of the complex (1 GDF-5 monomer and 1 BMPR-IB molecule are present in the asymmetric unit) the biological unit is formed by a crystallographic two-fold. (b) A superposition of the two type I receptors BMPR-IB (red) and BMPR-IA (magenta) from the complex structures GDF-5:BMPR-IB and BMP-2:BMPR-IA documenting the high degree of structural similarity. The core regions are almost identical, the main differences are located in the loops, which, however, present 80% of the ligand binding interface.

Mutations in GDF-5 have revealed that the type I receptor specificity of GDF-5 depends on a single residue Arg57 in the pre-helix loop, which is placed in the center of the ligand-receptor interface. Substitution of the bulky arginine by smaller residues such as leucine or alanine result in GDF-5 variants that bind to BMPR-IA and BMPR-IB with identical affinities. Thus the amino acid exchange only benefits the interaction with BMPR-IA whereas binding to BMPR-IB is unaffected. We therefore analyzed the region around Arg57 in the GDF-5:BMPR-IB structure. The β1β2-loop of BMPR-IB, which is in direct contact with Arg57 of GDF-5 adopts two alternative conformations; one that can be termed open and a second that directly lies on top of Arg57 and is therefore called closed. Superposition with BMPR-IA of the BMP-2:BMPR-IA complex structure reveals that the β1β2-loop of BMPR-IA would result in steric clash in the docked situation and exhibit a loop conformation that can be described as locked. Thus in BMPR-IB this loop adopts a backbone conformation that creates enough space for the bulky sidechain of Arg57 of GDF-5. Binding of BMPR-IA however requires a smaller amino acid at this ligand position, e.g. the equivalent residue in BMP-2 is Ala52. Consequently, this loop seems to act like a mechanical latch. To determine the molecular source for the closing and opening of the latch, we observed that a amino acid exchange between BMPR-IB and BMPR-IA is likely restraining the backbone conformation of the β1β2-loop in BMPR-IB. Gly42 of BMPR-IA is exchanged for His23 in BMPR-IB, with Gly42 occupying backbone torsion angles that are no amenable to non-glycine residues. Thus, the torsion angle requirements of the histidine lead to an opening of the loop in comparison to the situation in BMPR-IA suggesting that the latch mechanism involves a spring which actively opens the latch to allow binding of BMPR-IB to ligands with large bulky residues close to the latch.

This documents a nice example how flexibility can be used for implementing ligand-receptor specificity without the requirement to built-in "active" elements like intermolecular hydrogen-bonding for discrimination between two alternative binding partners.
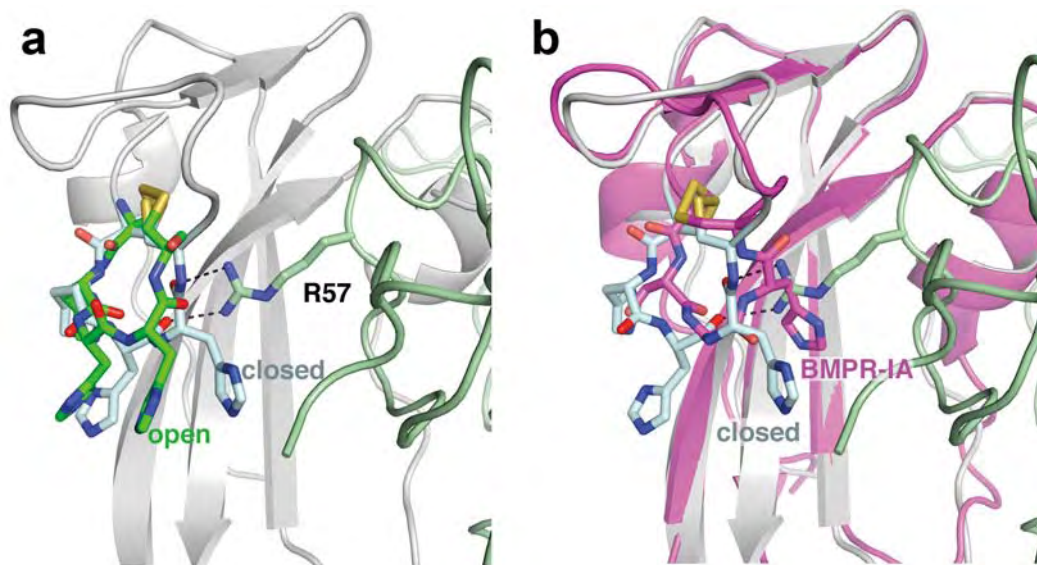
Figure 2: (a) The β1β2-loop of BMPR-IB adopts two alternative conformations (displayed as sticks with C-atoms in cyan for the closed conformer and green C-atoms for the open conformer) in the complex GDF-5:BMPR-IB. The bulky residue Arg57 in GDF-5 is in direct contact with the β1β2-loop in the closed conformation and forms two hydrogen bonds with the backbone of the BMPR-IB β1β2-loop. (b) BMPR-IA from the complex structure of BMP-2:BMPR-IA was docked onto the GDF-5:BMPR-IB complex. The β1β2-loop of BMPR-IA is in a locked conformation that would result in a steric clash of BMPR-IA His24 with the side chain of Arg57 of GDF-5 thereby explaining the lower binding affinity of GDF-5 for BMPR-IA.

Imaging actin filaments of muscle cells at ambient conditions by x-ray spectromicroscopy

J. Sedlmair[1], S.-C. Gleber[1], S. Öztürk[2], S. Heim[3], P. Guttmann[3], T. Pfohl[2], J. Thieme[1]

[1]Institut für Röntgenphysik, Georg-August-Universität Göttingen,
Friedrich-Hund-Platz 1, D-37077 Göttingen
[2]Max-Planck-Institut für Dynamik und Selbstorganisation,
Bunsenstraße 10, D-37073 Göttingen
[3]BESSY GmbH, Albert-Einstein-Str. 15, 12489 Berlin

Introduction

The aim of this study is to image the actin network of muscle cells using the scanning transmission x-ray microscope (STXM). This important part of the cytoskeleton is crucial for the shape and motility of a cell. Since muscle cells contain a large amount of actin filaments they are ideally suited for this kind of experiment. Applying soft x-ray radiation is not only needed to resolve these small structures, it provides natural contrast, too, if wet samples are analyzed in the energy range of the so called water window between 280 and 523 eV.

The actin network of the cytoskeleton is important for the motility of the cell. Many investigations to image these filaments have been made, but most of this work uses scanning electron microscopy and other techniques, which require the cells to be dead, cryo-vitrificated or treated otherwise before measurements.

Materials and Methods

X-ray microscopy plays a key role to achieve imaging of cells at ambient conditions. X-radiation provides the possibility to observe samples of several micrometers of thickness with a resolution in the sub 100nm-regime. The first test experiments to reach this goal have been done in 2008. We imaged VSMCs, which have been dried and fixated on Si_3N_4-foils in dry as well as in aqueous environment. Additionally, we recorded an image-stack of an actin-rich region of a vascular smooth muscle cell (VSMC) treated in that way. That means, spectral information is available for each pixel of the recorded images.

The preparation of the VSMCs was the following: The Si_3N_4-foils were coated with collagen to provide a suitable environment for the cells to grow. After incubating for a few days in medium were dried and fixated with PFA (paraformaldehyde).

Using the STXM (described elsewhere [1]) at undulator U41, the absorption of x-rays passing through the specimen is measured. By tuning the energy with the FSGM [2] monochromator below and above the 1s-absorption edge of carbon, spatial and spectral information are combined to achieve a detailed characterization of the components in the sample.

For the evaluation of the stack, the program stack_analyze was used [3].

Results and Discussion

In a first approach, the feasibility of imaging this important part of the cytoskeleton with the STXM was tested. These experiments were performed with dry and fixated cells initially to test the system.
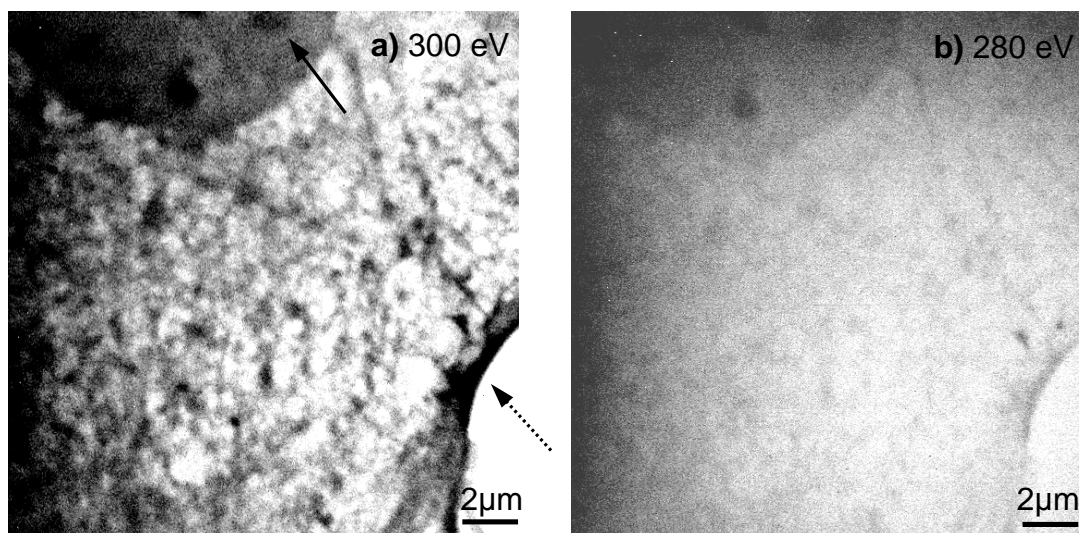
*Fig. 1: Images of vascular smooth muscle cell (VSMC) dried and fixated on Si₃N₄-membranes, taken with the scanning transmission X-ray microscope at **a)** E = 300eV and **b)** E = 280eV. Apart from the network structure in the cell, the actin-rich boarder of the cell-membran can be recognized as (⋯▶) well as the nucleoli in the nucleus (⟶).*

The difference in absorption below (fig. 1a) and above (fig. 1b) the C 1s-absorption edge is clearly. In the first stack, slight differences in the NEXAFS-spectra of the different components could be seen. This needs, however, a more thorough analysis. The intriguing results of the first experiments lead the way for further investigation with the STXM, since this instrument opens the possibility to gain insight into cells at ambient conditions.

Outlook

In future experiments, we want to investigate VSMCs in aqueous media in capillaries. Since we already imaged colloidal systems in water in capillaries, the setup should be realizable. The aim is to image the hierarchical structure of the network with a resolution below 100 nm. The outcome of these experiments will be cross-referenced with the results from recent microfluidic x-ray diffraction studies on actin filaments [5]. Additionally, experiments with pure actin (dry and aqueous) are planned to obtain reference spectra for comparison with the measurements of whole cells.

Acknowledgwments

References

[1] U. Wiesemann, J. Thieme, P. Guttmann, R. Früke, S. Rehbein, B. Niemann, D. Rudolph, and G. Schmahl: First results of the new scanning transmission X-ray microscope at BESSY-II. In: J. Susini, D. Joyeux, F. Polack, eds., X-Ray Microscopy 2002, Journal de Physique IV 104 (2003) 95–98.

[2] P. Guttmann, S. Heim, S. Rehbein, S. Werner, B. Niemann, R. Follath, G. Schneider: X-ray microscopy at the new U41-FSGM beam line. In: BESSY Annual Report 2007, p 297-300

[3] Jacobsen, C., Medenwaldt, R., Williams, S., 1998. A perspective on biological X-ray and electron microscopy. In: Thieme, J., Schmahl, G., Rudolph, D., Umbach, E. (Eds.), X-ray Microscopy and Spectromicroscopy, Springer, Heidelberg, pp. II-93–II-102.

[4] Otten A, Köster S, Struth B, Snigirev A, Pfohl T., Microfluidics of soft matter investigated by small-angle X-ray scattering. In: J Synchrotron Radiat. 2005 Nov;12 (Pt 6):745-50

[5] Köster S, Kierfeld J, Pfohl T. ,Characterization of single semiflexible filaments under geometric constraints. In: Eur Phys J E Soft Matter. 2008 Apr;25(4):439-49.

In-situ synchrotron diffraction study of load partitioning in a surface hardened duplex stainless steel

R. Lin Peng[1], J. Gibmeier[2,*], G. C. Chai[3], S. Johansson[1]

[1]Linköping University, Sweden
[2]Hahn-Meitner-Institut Berlin GmbH, Germany
[3]Sandvik Materials Technology, Sweden

Mechanical treatments such as shot peening and deep rolling are employed to enhance the fatigue resistance of components through the introduction of a strain hardened surface layer with compressive residual stress. In such components the actual stress distribution is a result of complex interactions between the applied and residual stresses and depends on a number of factors, including stress and strength distribution, external loading, microstructure and defects. In the current experiment, we have used in-situ synchrotron X-ray diffraction to study macroscopic load partitioning between the surface and the bulk and microscopic load partitioning between the constituent phases in a surface mechanically treated duplex stainless steel of type SAF 2507.

Experimental details

The duplex stainless steel of SAF 2507 investigated in the experiment is 6.4 mm thick hot rolled plate in solution treated and water quenched condition. Its chemical composition is (in weight %): 24.58 Cr, 6.64 Ni, 3.73 Mo, 0.85 Mn, 0.28 N, 0.017 C and Fe (balanced). Both surfaces of the plate were mechanically treated, a process that introduced strain hardening and compressive stresses to a layer of about 0.2 mm. The 0.2% proof stress and tensile strength are 688 MPa and 867 MPa, respectively. Microstructure characterization using electron back scatter diffraction mapping revealed 55 vol. % γ and 45 vol. % α as well as a strong texture.

The in-situ synchrotron experiment was carried out at the high energy synchrotron beamline EDDI-beamline@Bessy [1]. A tensile specimen with a 5 mm wide gauge section was prepared along the rolling direction of the plate. The surface for synchrotron measurement was slightly polished by electrolytic polishing to remove the oxide scale. A compact loading frame was used for tensile loading and the applied load was monitored by strain gauges attached on both side surfaces of the specimen. Two loading-unloading cycles were successively applied with 0.5% and 0.87% peak strain, respectively. Stress analysis in conventional reflection mode were carried out to obtain stress information in a surface layer of about $\tau_{mean} = 0.026$ mm according to the $\sin^2\psi$-method of stress analysis [2]. The ψ-angle was stepped in 4° from $\psi=0^o$ to $\psi=80^o$ and afterwards in 1° to $\psi=89^o$. Additional measurements were carried out in transmission mode at 0.75 mm depth, the behavior of which can be considered representative for the unhardened bulk of the specimen. 20 ψ angles, spreading evenly between $\sin^2(\psi=0^o)$ to $\sin^2(\psi=89.9^o)$, were used.

Results and analysis

The (hkl)-planes that could be observed in the current experiment and their diffraction elastic constants are listed in Table 1. The first four α reflections and the first five γ reflections given in Table 1 were used for the calculation of the surface phase specific stresses. For measurements in transmission mode, the α-110 interference lines showing only poor intensities are replaced by α-321 in stress analysis. For the same reason, the phase specific stress of the austenite is calculated based on measurements on γ-220, γ-311, γ-222 and γ-420.

---

* now: Universität Karlsruhe, Institut für Werkstoffkunde I, D-76131 Karlsruhe

Table 1 Diffraction elastic constant (DEC) $\frac{1}{2}S_2$ ($\times 10^{-6}$ MPa^{-1})

α-110	α-200	α-211	α-220	α-321	γ-111	γ-200	γ-220	γ-311	γ-222	γ-420
5.8	7.7	5.8	5.8	5.8	5.14	8.86	6.07	7.11	5.14	7.07

Since the stress component normal to the specimen surface (σ^i_{33}) may not be assumed zero in a duplex stainless steel, the $\sin^2\psi$ analysis yields the phase specific stress ($\sigma^i_{11}-\sigma^i_{33}$), in which σ^i_{11} is the axial stress. For uniaxial loading, the axial macrostress could be derived according to the equation [3]: $^M\sigma_{11} = (\sigma^\alpha_{11} - \sigma^\alpha_{33})V^\alpha + (\sigma^\gamma_{11} - \sigma^\gamma_{33})V^\gamma$. The calculated macrostress is plotted in Fig. 1 as a function of applied strain. As can be seen, the surface layer and bulk follow completely different loading paths. While in the surface, the applied load results in a decreased compressive macrostress, in the bulk where a small tensile residual macrostress exists the macrostress increases almost linearly with applied stain. When the bulk yields after reaching 0.2%, a rapid load transfer appears, such that the macrostress increases rapidly in the surface layer that is still elastic but slowly in the bulk. At the peak strain of the first cycle, a somewhat larger macrostress is found in the surface than in the bulk. The occurrence of plastic deformation in the bulk relaxes the compressive stresses of the surface layer and the plastic incompatibility between different regions of the cross section introduces now tensile stresses in the hardened surface layer after unloading. When reloaded beyond 0.62% strain, the surface also yields, accompanied by a slower increase in macrostress. The macroscopic plastic incompatibility resulted in a highly heterogeneous load distribution, marked by a surface stress of 1070 MPa and a bulk stress of 680 MPa at 0.87% applied strain. This difference in macrostress remains as high tensile residual stress in the surface after unloading that leaves a plastic strain of 0.54%.
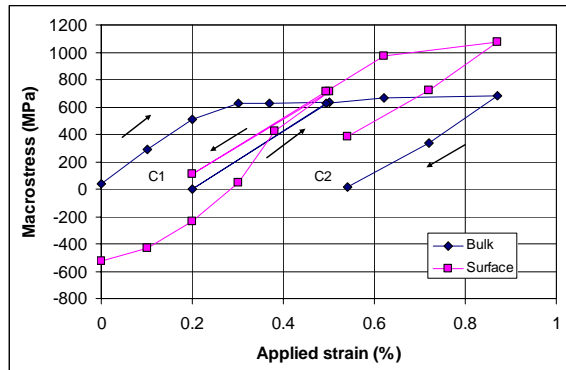
Fig. 1 Macrostress obtained from the in-situ synchrotron measurements in the surface layer (0.026 mm) and bulk (at 0.75 mm depth). The lines are guide for the eyes. C1 and C2 refer to cycle 1 and cycle 2, respectively.
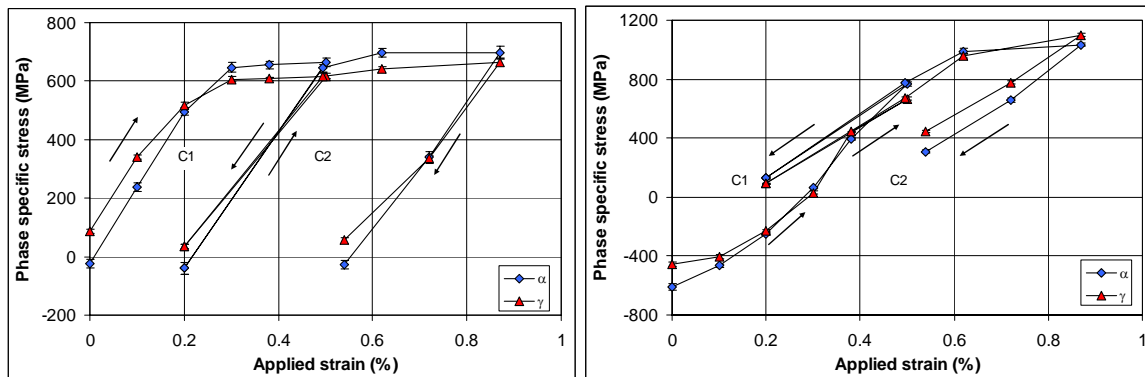
Fig. 2 The evolution of phase specific stresses ($\sigma^i_{11}-\sigma^i_{33}$) with applied strain for 0.75 mm depth (left) and surface (right). C1 and C2 refer to cycle 1 and cycle 2, respectively.

As often observed for such materials [3], the applied load is found distributed unevenly between the constituent phases, which changes with applied load (Fig. 2). The evolution of phase specific stresses (σ^i_{11}-σ^i_{33}) can be considered reflecting mainly the influence of the applied load and phase-incompatibility induced microstresses on the axial stress, σ^i_{11}. In the bulk, γ having a high tensile residual stress yields before α, leading to a slight load transfer from γ to α. The plastic incompatibility between the phases eventually resulted in a higher tensile stress in α than in γ. In the surface layer, the phase microstresses vanish rapidly during initial loading to 0.2% strain but increase again beyond 0.38% strain. Yielding may have occurred first in the ferrite, which leads to a load transfer to the austenite and eventually γ experiences a higher stress than α.

Due to the strong texture, intergranular stresses also develop, resulting in somewhat different stress distributions between different grain-families. Fig. 3 reveals that the grain-orientation-dependent anisotropy is stronger for the austenite phase than for the ferrite, reflected by the larger divergence between the hkl-planes.
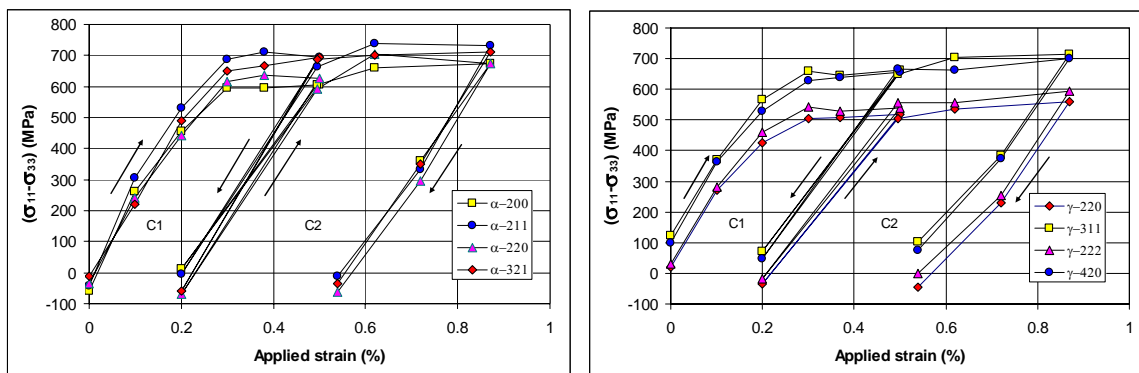
Fig. 3 The evolution of lattice stress with applied strain for ferrite (left) and austenite (right) at 0.75 mm depth. C1 and C2 refer to cycle 1 and cycle 2, respectively.

Summary

The surface layer and bulk are found to follow different loading paths, which could be explained by the influence of initial residual stresses and difference in strength. Inhomogeneous load distributions between the ferrite and austenite as well as between different grain-families due to microscopic incompatibility are also observed. The experiment has shown that in-situ energy dispersive synchrotron X-ray stress analysis offers a potent tool for studying macroscopic and microscopic load partitioning in polycrystalline materials.

Reference

[1]   Ch. Genzel, I.A. Denks, J. Gibmeier, M. Klaus, G. Wagener.: Nucl. Instr. Meth. In Phy. Res. **578** (2007) 23-33
[2]   E. Macherauch, P. Müller: *Z. f. angewandte Physik,* **13** (1961), 305-312.
[3]   R. Lin Peng, Y.D. Wang, G.C. Chai, N. Jia, N., S. Johansson, G. Wang: *Mater.Sci.Forum,* **524-525**, (2006), 917.

Interaction of Gold with Thin Ceria Films and Silica Supported Ceria Nanoparticles.

M. Baron, O. Bondarchuk, H. Abbott, H. Kuhlenbeck, S. Shaikhutdinov, H.-J. Freund

Fritz-Haber-Institut der Max-Planck-Gesellschaft, Faradayweg 4-6, Berlin D-14195

Chemical reactions on gold surfaces have received much attention owing to the unusual catalytic properties of highly dispersed gold [1]. However, the nature of the active sites in Au catalysts remains a controversial issue. Among the reaction mechanisms proposed in the literature, there are some involving positively charged (Au^+, Au^{3+}) species, in particular supported on ceria. Moreover, it has been shown that nanocrystalline ceria ("nano-ceria") as a support remarkably increases the activity of gold as compared to conventional ceria supports [2]. The effect was attributed to the presence of cationic surface species. In this work, the electronic structure of $Au/CeO_2(111)$ and $Au/nano-CeO_x$ systems was studied using photoelectron spectroscopy (PES).

Well-ordered $CeO_2(111)$ films were grown on a Ru(0001) substrate [3]. Ceria nanoparticles were formed by physical vapor deposition onto ice precovered ultra-thin silica films [4] grown on Mo(112) in oxygen ambient.
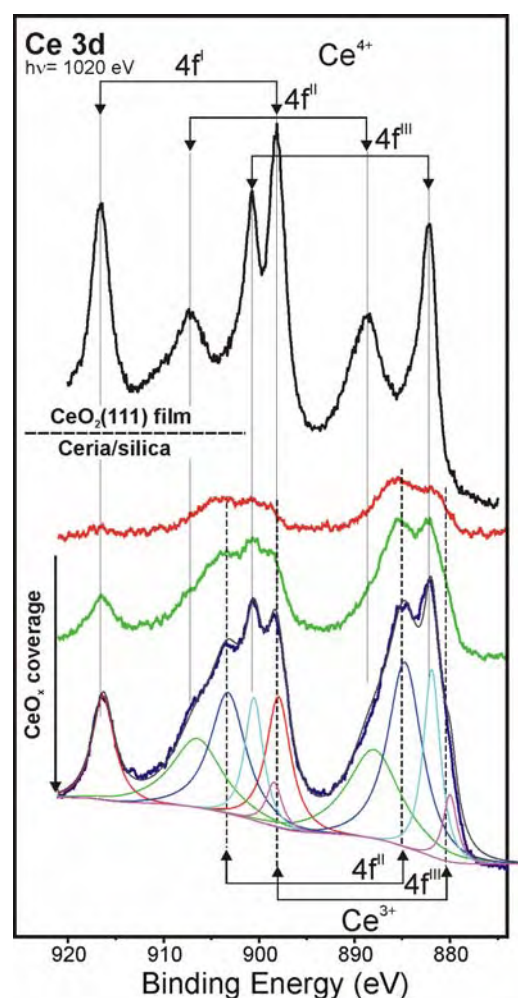
Figure 1. Ce 3d region of PE-spectra (photon energy 1020 eV) measured on $CeO_2(111)$ films (top spectrum) and ceria nanoparticles at increasing coverage (bottom spectra).

Figure 1 shows Ce3d spectra of a thin ceria film and silica supported ceria at increasing coverage. The spectra are typically rationalized in terms of the spin orbital pairs of the $Ce3d^9 4f^0 O2p^6$, $Ce3d^9 4f^1 O2p^5$ and $Ce3d^9 4f^2 O2p^4$ final states of Ce^{4+}, which are labeled in figure as 4f', 4f'' and 4f''', respectively [5]. The spectra of ceria nanoparticles are very different from those of $CeO_2(111)$ films. We found that Ce states in the nanoparticles can in principle be obtained by a superposition of the Ce^{4+} and Ce^{3+} states with a respective weighing factor, whereby broadening reflects different surroundings of the Ce atoms in the nanoparticles. The analysis revealed that the $Ce^{3+}/(Ce^{3+} + Ce^{4+})$ ratio increases from 40 ± 1 to 50 ± 2 and finally to 67 ± 10 % upon decreasing the ceria coverage, while only ~10 % is observed in the films.

The partial reduction of ceria nanoparticles is also reflected in the Ce 4d spectra as shown in Fig. 2. In analogy with Ce 3d spectra, the highest BE peaks at ~123 and ~126 eV are typically assigned to Ce^{4+} with a $Ce4d^9 4f^0 O2p^6$ final state (marked as 4f ') with a spin-orbit splitting of 3.3 eV. There is no agreement for the assignment of the other peaks due to a strong coupling between the Ce4d and Ce4f levels that results in the multiplet splitting, which has a
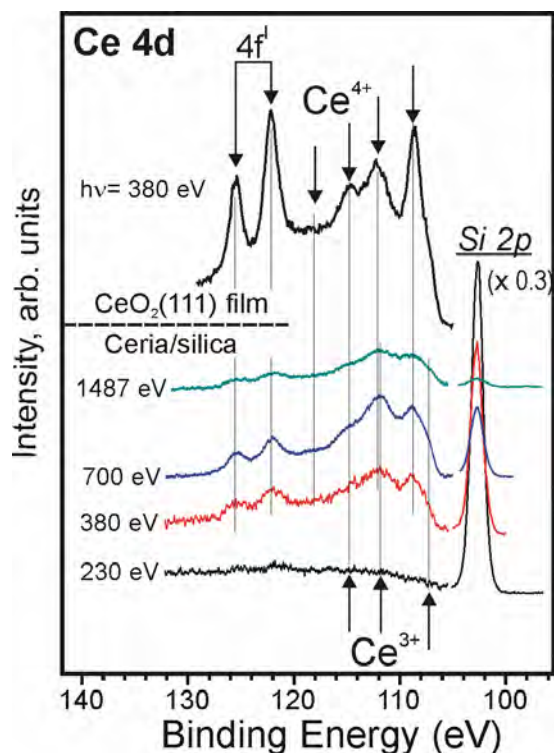
Figure 2. Ce 4d region of XPS spectra measured on $CeO_2(111)$ films (top spectrum) and ceria nanoparticles (bottom spectra) at different photon energies as indicated.

magnitude comparable to the spin-orbit splitting, thus rendering the full analysis very complex [6].

It has turned out that the Ce4d spectra of ceria nanoparticles are strongly dependent on the photon energy. At 230 eV only the Si 2p peak at 102.5 eV could be detected in this region, with no signal corresponding to the Ce 4d levels. With stepwise increasing of the photon energy from 230 to 1487 eV, the Ce 4d signals first grow in intensity and then attenuate, while the Si 2p peak decreases monotonously. Such behavior cannot be explained solely by escape depth effects, thus reflecting the elemental composition depth profile in the surface region. Indeed, at the same kinetic energy (~ 100 eV), the Ce 4d spectrum reveals almost no Ce on the surface while the Ce 3d spectrum does (see Fig. 1). In fact, the photon energy dependence of the Ce 4d spectra can be explained by the non-linear dependence of the photoionization cross section of the Ce 4d level exhibiting the so-called Cooper minimum [7] at low energies (i.e. in variance to the Si 2p that has the highest cross section at low photon energy which monotonously decreases at higher energies [8]).

The presence of the BE states above 120 eV of a relatively high intensity in the Ce 4d spectrum of ceria particles is fully consistent with the corresponding Ce 3d spectrum of the same sample showing primarily Ce^{4+} species. However, the differences in the peak intensity ratios observed in the low BE region as compared to the fully oxidized CeO_2 film indicate a significant contribution of the Ce^{3+} photoelectrons at ~114, ~112 and ~109 eV.

In the next step, we compare electronic properties of gold deposited onto well-ordered $CeO_2(111)$ films and silica-supported CeO_x nanoparticles. Gold deposition on the $CeO_2(111)$ films at 100 K results in the relatively broad Au 4f signal centred at 84.3 eV for the Au $4f_{7/2}$ component, that shifts to 84.0 eV (i.e. characteristic for the bulk gold) upon heating to 300 K due to Au sintering.

The XP-spectra of Au/nano-CeO_x substantially differ from those of Au/$CeO_2(111)$. Fig. 3a shows a Au 4f spectrum measured for "as deposited" gold and subsequent heating to the indicated temperatures. A broad Au $4f_{7/2}$ signal centred at 85.3 eV is at about 1 eV higher energies than for Au particles on ceria films. The signal broadening, which is quite symmetric, can in principle be attributed to a broad size distribution of gold species attached to the ceria nanoparticles. Stepwise heating to 600 K leads to an increasing contribution of the metallic state at 84.0 eV and a simultaneous vanishing of the component at 86.1 eV. Meanwhile, the intensity of the ~ 85 eV component stays relatively constant. This indicates that a significant part of the Au species, even annealed to 600 K, exhibits BEs as high as 85 eV, which is ~ 1 eV higher than in gold nanoparticles formed on the CeO_2 films.

Figure 3. Au 4f (a) and Ce 3d (b) regions of PE-spectra for 0.15 ML Au deposited at 100 K on CeO_x/SiO_2. The spectra were measured at 100 K after heating to the indicated temperatures. The deconvolution of the Au 4f spectra is shown only for the spectra at 100 and 600 K, for clarity. The Ce 3d spectrum for the pristine CeO_x is also shown, for comparison.

In principle, both initial and final state effects can be responsible for the BE shifts observed on small Au clusters. It has previously been shown that the Coulomb energy of the final state is decisive. Since hole screening for Au having a $6s^1 5d^{10}$ configuration should even be more efficient than for Rh ($5s^1 4d^8$), we concluded that the high BE values observed for Au are attributed to initial state effects, indicating the formation of positively charged gold species when deposited on nano-ceria at 100 K.

This finding suggests that gold strongly interacts with ceria nanoparticles. The interaction also manifests itself by that the amount of Ce^{4+} in nano-ceria decreases upon deposition of Au at 100 K and even further upon stepwise heating to 600 K (Fig. 3b). Therefore, the results indicate that gold may reduce ceria nanoparticles at these conditions. This is fully consistent with our analysis of the Au 4f spectra showing significant amounts of oxidized Au species on ceria nanoparticles.

Therefore, in variance to extended ceria surfaces, where only metallic Au nanoparticles are observed at 300 K, the "cationic" gold species are formed in abundance on nano-CeO_x and exhibit enhanced thermal stability. It is clear that nano-ceria stabilizes small Au clusters, which may even be incorporated into the ceria nanoparticles at elevated temperatures as judged by complementary IR spectroscopy studies of CO adsorption [9].

References:
[1] G. Bond, C. Lois, D. Thompson, Catalysis by Gold, World Scientific, 2006.
[2] J. Guzman, S. Carrettin, et al., Angew. Chem. Int. Ed., 44 (2005) 4778.
[3] J.-L. Lu, H.-J. Gao, S. Shaikhutdinov, H.-J. Freund, Surf. Sci., 600 (2006) 5004.
[4] S. Kaya, M. Baron, D. Stacchiola et al. Surf. Sci., 601 (2007) 4849.
[5] P. Burgoughs, A. Hamnett, et al. J. Chem Soc. Dalton Trans. 17 (1976) 1686.
[6] P. Bagus, unpublished
[7] J. W. Cooper, Phys. Rev. 128 (1962) 681.
[8] J.J. Yeh, I. Lindau, Atomic Data and Nuclear Data Tables 32 (1985) 1.
[9] M.Baron, O. Bondarchuk, D. Stacchiola, S. Shaikhutdinov, H.-J. Freund, submitted.

Photoemission spectroscopy of chalcopyrite solar cells

Catherine A. Jenkins[1,2], Christian D.R. Ludwig[2], Thomas Gruhn[2], Gerhard H. Fecher[2], Andrei Gloskovskii[2], Claudia Felser[2], Benjamin Johnson[3], and Christian Kaufmann[3]

1. Department of Materials Science and Engineering, University of California, Berkeley, 94720 USA
2. Institut für Anorganische und Analytische Chemie, Johannes Gutenberg-Universität, D-55099 Mainz, Germany
3. Helmholtz Zentrum Berlin für Materialen und Energie, 14109 Berlin, Germany

This work reports on hard x-ray photoelectron spectroscopy (HAXPES) studies of subsurface interfaces in heterostructures based on solar cells of ZnO:Al/ZnO/Cu(In,Ga)Se$_2$/Mo/SLG (soda lime glass) produced by three-stage co-evaporation, rapid thermal processing and chemical bath deposition. Details of the measured valence band spectra are compared with Wien2k calculations and it is shown that the electronic structure of the buried junctions is clearly resolved by this method.

Solar cell modules based on Cu(In,Ga)Se$_2$ are of great interest during this period of scientific attention to efficient renewable energy sources. The low kinetic energies of soft x-ray spectroscopic methods limit the mean free path of the resulting photoelectrons and thus limit the information depth. Hard x-ray photoemission exploits the brilliance of synchrotron radiation to allow the in situ investigation of junctions in a buffer/absorber or simple absorber [1]. The mean free path of electrons excited by up to 8keV is tens of unit cells, giving a large information depth. Measurements were carried out at the KMC-1 high energy beamline at BESSY II Berlin, Germany. The total resolution (monochromator plus detector) at 2.2 and 3keV was 250meV and slightly lower at higher incident energies. The compound under investigation is unetched Cu(In,Ga)Se$_2$, a known semiconductor with a band gap of 1.15-1.17eV. The Cu(In,Ga)Se$_2$ absorber was fabricated by three stage co-evaporation and crystallizes in the chalcopyrite structure.
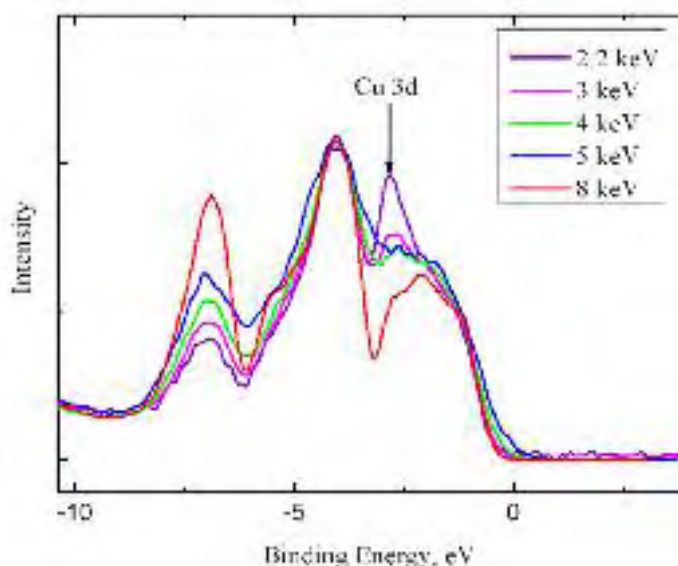
Figure 1: Valence band spectra at incident energies from 2-8keV of Cu(In,Ga)Se$_2$. The difference between the spectra is primarily due to the relative weights of the s, p, and d cross sections with increasing energy. The peak between -3 and -2eV binding energy attenuates more rapidly than other peaks with significant d orbital contributions due to the different symmetry of the orbitals, see Figure 2.

For the self-consistent electronic structure calculations we used Wien2k [2], an implementation of the full-potential linearized augmented plane waves + local orbitals method, based on the density functional theory of Hohenberg and Kohn [3]. Wien2k is appropriate for the ground state and gives no information about ionization, so the electronic correlations in the

real material give rise to a slight shift in peak energy compared with the calculations. The Wyckoff sites Cu 4a, In 4b, Se 8d were used as well as experimentally determined values of the lattice constants. The lattice constants and anion displacement of the chalcopyrites were taken from the literature [4]. A k-mesh of 475 k-points in the irreducible Brillouin zone was used. Convergence was reached with a change in total energy of less than 0.05mRy per iteration.

Figure 2: momentum resolved calculations indicate that primarily d_{z2} and d_{x2-y2} orbitals contribute to the intensity between -3 and -2eV, whereas primarily d_{xy} and $d_{xz}+d_{yz}$ orbitals contribute to the remainder of the states between -5 and 0eV.
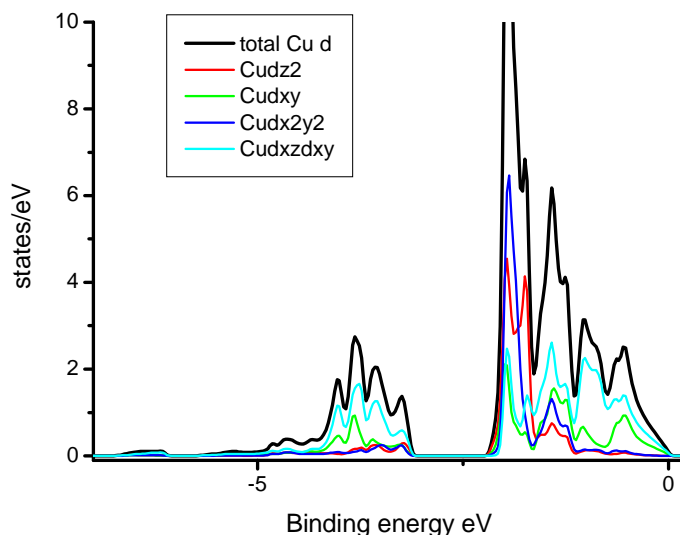
The relative spectral intensity in the valence bands of unbuffered Cu(In,Ga)Se$_2$ shown in Figure 1 changes with increasing kinetic energy. The effective cross section of d states with unique symmetry decreases most quickly as can be seen from the striking decrease in the contribution of Cu d states to the intensity of the peak at -2.5eV as a function of increasing incident energy. The area from -2eV to the Fermi energy and between -5 and -3eV does not attenuate despite significant contribution from d states because of the different symmetry: momentum resolved calculations indicate that primarily d_{z2} and d_{x2-y2} orbitals contribute to the intensity between -3 and -2eV, whereas primarily d_{xy} and $d_{xz}+d_{yz}$ orbitals contribute to the remainder of the states between -5 and 0eV. A positive gradient in the concentration of copper with depth (as in [5]) therefore does not explain the change in the intensity of the peaks arising from the Cu-3d states because of the decrease in intensity only of the d_{z2} and d_{x2-y2} orbitals.

Figure 3 shows the calculated density of states (DOS) for Cu(In,Ga)Se$_2$. Partial DOSs are shown for Cu, In, Ga, and Se, with the bold line indicating total DOS. The maximum in the DOS at -1.8eV below the valence band edge emerges almost entirely from Cu states with a significant d contribution. The calculated band between -5.3 and -2.8eV due to p and d states in the Se and Cu expresses two maxima, the one at -3.2eV roughly a factor of three more intense than that at -5eV. The calculated band between -5.8 and -6.6eV arising almost purely from the In s and Se p contributions appears quite prominently in the measured spectrum (not shown), as the cross sections of s and p states are less curtailed by higher energy photons. However, the double maximum is not clearly resolved as peak splitting, although the hybridization gap of 0.5eV around -6eV is clearly resolved in both the spectra and the calculations. Figure 3 shows the momentum resolved calculations, showing the difference in symmetry between the d orbitals.

The measured photoelectron spectra agree well with the calculated DOS. HAXPES is clearly demonstrated as a technique capable of resolving the valence band of buried interfaces in solar cell component heterostructures.
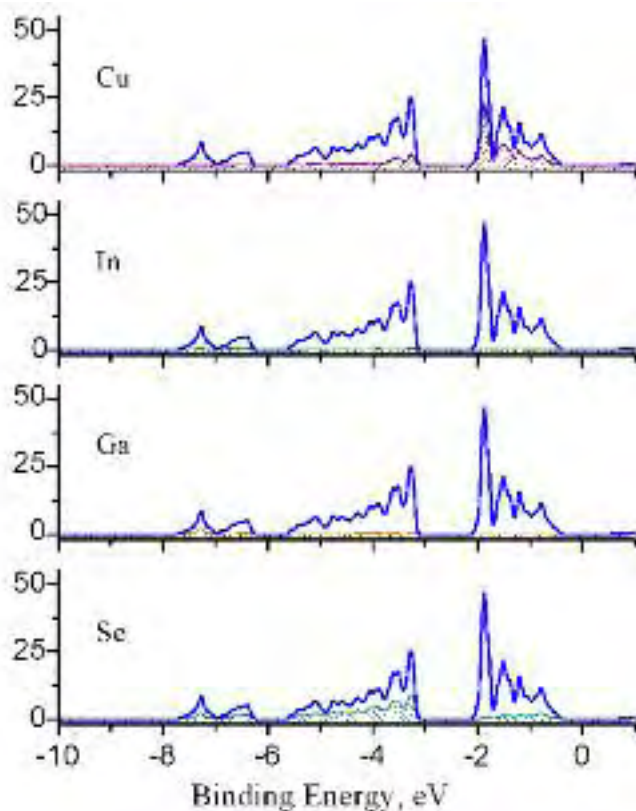
Figure 3: The calculated DOS of each individual element in Cu(In,Ga)Se₂. The maximum in the DOS at -1.8eV below the valence band edge emerges almost entirely from Cu states with a significant d contribution represented by the filled in curve. At 8keV the weighted cross section of the d states is relatively reduced, explaining the low intensity of the broad spectral feature between -3 and -1eV binding energies. Each panel with calculations consists of a solid blue line indicating the total DOS and a thinner hashed area indicating the contribution from the individual element.

References:

[1] G.H. Fecher, A. Gloskovskii, K. Kroth, J. Barth, B. Balke, C. Felser, F. Schäfers, M. Mertin, W. Eberhardt, S. Mähl, O. Schaff, J. Electron. Spectrosc. Relat. Phenom. **156-8** (2007) 97-101.

[2] P. Blaha, K. Schwarz, G.K.H. Madsen, D. Kvasnicka and J. Luitz, "Wien2k, An Augmented Plane Wave + Local Orbitals Program for Calculating Crystal Properties, Vienna, Austria, 2001.

[3] P. Hohenberg and W. Kohn, Phys. Rev., **136**, 1964, pp 864-871.

[4] H.W. Spiess, U. Haeberlen, G. Brandt, A. Räuber, J. Schneider, Phys. Stat. Sol. (b), **62**, 1974, p. 183.

[5] Kötschau and Schock, J. Phys. Chem. Solids **64** p. 1559 (2003).

Stochastic 3D Modeling of the GDL Structure in PEMFCs Based on Thin Section Detection

R. Thiedmann[1], Ch. Hartnig[2], I. Manke[3], H. Riesemeier[4], V. Schmidt[1]

[1]Ulm University, Institute of Stochastics, Ulm

[2]Zentrum für Sonnenenergie- und Wasserstoff-Forschung Baden-Württemberg, Ulm

[3]Helmholtz-Centre for Materials and Energy, Berlin

[4]Federal Institute for Materials Research and Testing, Berlin

Abstract

In order to use hydrogen as an energy carrier, an effective way to convert hydrogen into electricity is necessary, with the fuel cell technology being an appropriate mean due to its high efficiency. A key component of this technique is the gas diffusion layer (GDL). For a better understanding of the physical processes within a GDL, a well-fitted structural model is needed. For constructing a 3D model and for its verification, real measured structural 3D information is absolutely necessary. The 3D image data from GDLs are gained by means of synchrotron X-ray radiography at Bessy. For comparing the developed stochastic model with the real measured 3D structures, statistical characteristics as the spherical contact distribution are applied.

Detailed report

One of the key components of a PEM fuel cell is the GDL, see Figure 1. It is responsible for the transport of hydrogen and oxygen to the electrodes where the electrochemical reaction takes place. Also, its task is to remove the water produced. In this context it is important that just the right water content is achieved, because water is essential for the conductivity of the membrane, whereas excess water in the GDL leads to flooding of the pores, which in turn limits current density. Hence, the balance between water drainage and water storage is the key to high performance. Additionally, the GDL acts as a conductor for the electricity produced.
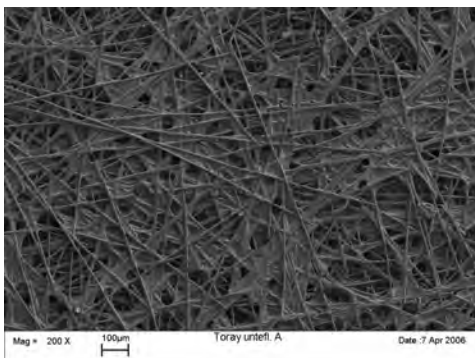
Figure 1: 2D SEM image of a GDL (Toray)
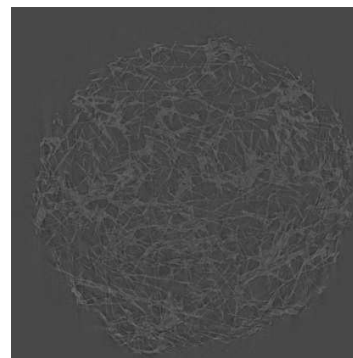
Figure 2: Slice of a 3D image of Toray paper

For a better understanding of the physical processes within the GDL and for an optimization of its design, a well-fitted structural model is needed. We have developed a 3D structural model of the GDL using tools from stochastic geometry, in particular, random tessellations, see [1]. The advantage of this type of stochastic modeling is that the complex morphology of the GDL can be described by few parameters. In our case, the morphology of the GDL is formed by a large number of irregularly located long fibers with negligible curvatures, see Fig. 1. The fundamental idea of our structural model arises from the production process of the GDL considered, where fibers are disposed almost horizontally. This leads to the assumption that a GDL can be seen as a stack of thin sections, i.e., thin separated sub-layers of fibers, which fits the structure shown in Fig.1 quite well. This assumption can be proved by looking at vertical cross sections of real measured 3D synchrotron data, see Fig. 2. Furthermore, Fig. 1 shows that the individual fibers can be approximated by straight cylinders. Therefore, in a first step the thin sections of the GDL are represented by planar random line tessellations, which are built by intersecting lines located at random in the Euclidean plane. Then, these lines are "blown up" to 3D objects, i.e., they are dilated in 3D. Each 3D dilated line tessellation represents a thin section, i.e., a separated sub-layer of the GDL. Finally, a certain number of such dilated line tessellations are stacked together and, in this way, a 3D (structural) model for the whole GDL fiber system is obtained. For modeling the binder in the GDL structure, some cells of the tessellation are chosen at random to contain binder. A realization of the complete 3D model can be seen in Fig. 3.

For the final fitting and verification of the model, the comparison with real 3D data is indispensable. These data are gained by synchrotron X-ray tomography. The great advantage of this method is that 3D structural images with a high resolution (about 1 to 2 µm) can be gained. Such a resolution is required because the diameter of a fiber which is, in our case, the most interesting object in a GDL structure is about 7-8µm. In addition the observation area, i.e., the size of the 3D image, is sufficiently large to contain enough (structural) information for a statistical analysis. Last but not least, the carbon fibers generate a good contrast in the resulting 3D images, i.e., they can be relatively easily detected from the images. A slice of a 3D image can be seen in Fig. 2. The complete 3D image is then a stack of such slices, i.e., a 3D matrix containing grey values.

For verifying the 3D model, a comparison with 3D (synchrotron) data has been done. In [1] we have computed the spherical contact distribution function, i.e., a statistical tool describing the shortest distance of a point in the background (chosen at random) to the foreground. The results show, that the real structure and the structures generated by the model are very similar, see Figure 4.
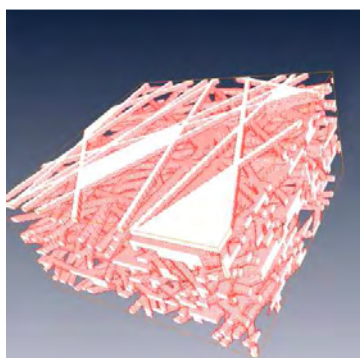
Figure 3: Realization of the 3D model
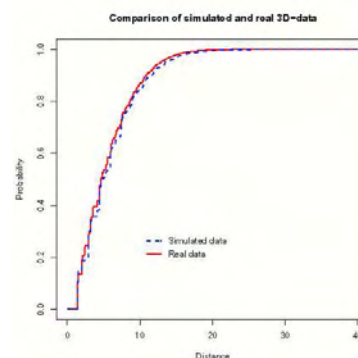
Figure 4: Spherical contact distributions

In the next step, characteristics related to transport processes are investigated in detail, see [2]. Such characteristics are on the one side computed from the model and on the other side computed from real measured 3D synchrotron data. The comparison shows that the (fitted) model of [1] seems to be quite realistic with respect to transport relevant characteristics such as tortuosity properties or the pore size distribution. Without using the real 3D image data to get reference values, a verification of the model would be impossible.

The model developed in [1] and improved in [2] can now be used to simulate different scenarios of fiber and binder configurations and for investigating their physical behavior. This leads to a better understanding of the different processes within the GDL. This is a precondition for the optimal GDL construction and the optimal choice of their application in the fuel cell technology.

References

 [1] R. Thiedmann, F. Fleischer, Ch. Hartnig, W. Lehnert, V. Schmidt. Stochastic 3D-Modeling of the GDL Structure in PEM Fuel Cells Based on Thin Section Detection. *J. Electrochem. Soc.*, **155(4)**, B391 -- B399 (2008).

 [2] R. Thiedmann, Ch. Hartnig, I. Manke, V. Schmidt, W. Lehnert. Local Structural Characteristics of Pore Space in GDLs of PEM Fuel Cells Based on Geometric 3D Graphs. *J. Electrochem. Soc*. (*submitted*).

UV/VIS Fluorescence of O 1s-excited H_2O

M. Meyer [1], J. Plenge [2], E. Serdaroglu [2], R. Flesch [2], and E. Rühl [2]

[1] *LIXAM/CNRS, UMR8624, Centre Universitaire Paris-Sud, Bâtiment 350, F-91405 Orsay Cedex, France*
[2] *Physikalische und Theoretische Chemie, Institut für Chemie und Biochemie, Freie Universität Berlin, Takustr. 3, 14195 Berlin, Germany*

Dispersed fluorescence spectroscopy is a versatile tool to study the dynamics of inner-shell excited atoms, molecules, and clusters [1,2]. It has specific advantages, which include high detection specificity and efficiency as well as high spectral resolution in the ultraviolet/visible regime. As a result, one can easily distinguish different products and electronic states, which are involved in the relaxation process. In the case of molecular fragments, vibrational and rotational resolution can be obtained, which provides additional information about the fragmentation dynamics of the core-excited molecule. Recently, fluorescence emission following core excitations in the water molecule (H_2O) has been observed [3]. We report in this work on the ultraviolet/visible fluorescence (260 nm $\leq \lambda$(fluo) $\leq$ 900 nm) of O 1s-excited H_2O, where we analyze the radiative emission from the fragments H, O, O^+, OH^+, and OH.

The experiments were carried out at the beamline UE-52-SGM at BESSY. Fluorescence is produced in the interaction region of the synchrotron radiation and an effusive gas jet of H_2O. Fluorescence is collected in the direction perpendicular to the synchrotron radiation and is focused on the entrance slit of a high-resolution fluorescence spectrometer (Jobin Yvon HR460) equipped with a liquid nitrogen cooled CCD detector (Spectrum One).

Fig. 1 shows fluorescence spectra of H_2O recorded between 375 nm and 475 nm. The excitation energy was set to 120 eV (Fig. 1(a)), 534.2 eV (Fig. 1(b)), 536 eV (Fig. 1(c)), 537.1 eV (Fig. 1(d)), and 545 eV (Fig. 1(e)), respectively. An excitation energy of 120 eV corresponds primarily to direct photoionization in the valence continua. The other energies are in the O 1s-excitation regime. Here the O 1s→$4a_1$ (E = 534.2 eV) and O 1s→$2b_2$ (E = 536 eV) transitions are excited, where the $4a_1$ and $2b_2$ orbitals have primarily molecular character. At 537.1 eV the Rydberg transition O 1s → $3pb_1/a_1$ (E = 537.1 eV) is excited. The excitation energy of 545 eV lies above the O 1s-ionization threshold. The fluorescence spectra are dominated by atomic lines, which in this wavelength region are mostly assigned to the emission from O^+ ions and excited hydrogen atoms. The fluorescence comes primarily from $2s^2 2p^2(^3P, {}^1D)3d$ and $2s^2 2p^2(^3P, {}^1D)3p$ states of O^+. In addition, fluorescence from $2s^2 2p^2(^3P, {}^1D)4f$ and $2s^2 2p^2(^1D)4d$ states is exclusively observed after O 1s-excitation and is absent in the fluorescence spectrum recorded at 120 eV excitation energy.

Besides fluorescence from atomic fragments, radiative emission has also been observed from the molecular fragments OH and OH^+ (Fig. 2). The feature around 310 nm is assigned to the transition A $^2\Sigma^+ \rightarrow$ X $^2\Pi$ of OH, where the vibrational transitions 0-0, 1-1 and 2-2 can be identified. The spectra indicate significant changes of the vibrational distribution of the OH (A $^2\Sigma^+$) fragment as a function of the excitation energy reflecting the different decay dynamics of the O 1s-core-excited states of H_2O. In addition, after resonant O 1s $\rightarrow 4a_1$ and O 1s $\rightarrow 2b_2$ excitation fluorescence attributed to the A $^3\Pi \rightarrow$ X $^3\Sigma^-$ transition of OH^+ is observed around 360 nm. The formation of OH^+ (A $^3\Pi$) following O 1s $\rightarrow 4a_1$ excitation can be explained in terms of ultrafast decay of O 1s-excited H_2O prior to electronic relaxation [4]. In this context, further rotationally resolved fluorescence spectra of the molecular fragments OH and OH^+ are expected to reveal detailed and complementary information on the fragmentation dynamics of core-excited H_2O similar to previous work on H_2S [2].
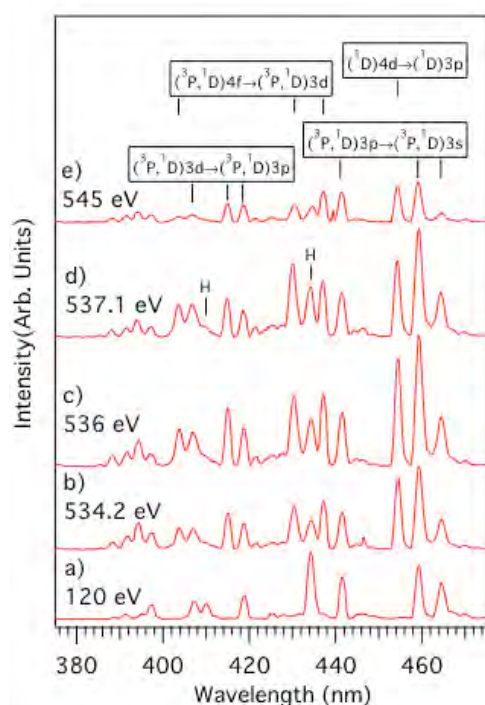
Figure 1: Fluorescence spectra of H_2O recorded at different excitation energies. The spectrum is dominated by atomic lines, which are mostly assigned to the emission of H and O^+.
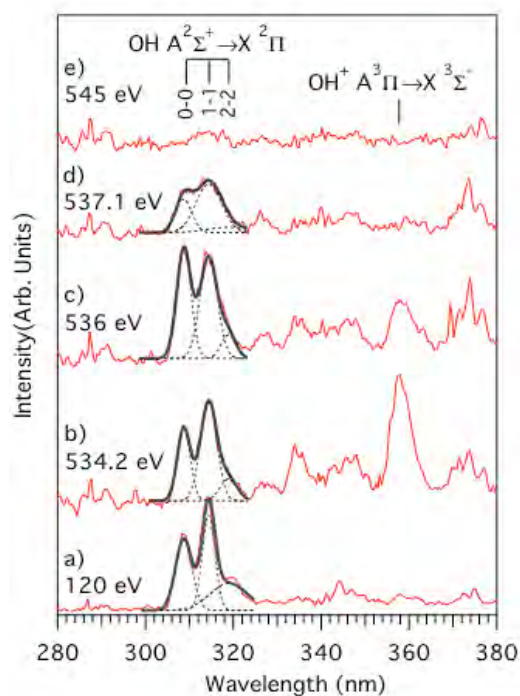
Figure 2: Fluorescence spectra of H_2O recorded at different excitation energies. Fluorescence emission lines from the molecular fragments OH and OH^+ are indicated.

References
[1]   M. Meyer, A. Marquette, A. Grum-Grzhimailo, R. Flesch, and E. Rühl, Surf. Rev. Lett. **9**, 141 (2002); I. L. Bradeanu, R. Flesch, M. Meyer, H. W. Jochims, and E. Rühl, Eur. Phys. J. D **36**, 173 (2005).
[2]   M. Meyer, P. O'Keeffe, J. Plenge, R. Flesch, and E. Rühl, J. Chem. Phys. **125** (2006).
[3]   A. Kivimäki, M. Coreno, R. Richter, J. Álvarez Ruiz, E. Melero García, M. De Simone, V. Feyer, G. Vall-Llosera, and K. C. Prince, J. Phys. B-At. Mol. Opt. **39,** 1101 (2006); E. García, A. Kivimäki, L. Pettersson, J. Ruiz, M. Coreno, M. De Simone, R. Richter, and K. Prince, Phys. Rev. Lett. **96,** 4 (2006).
[4]   I. Hjelte, M. N. Piancastelli, R. F. Fink, O. Bjorneholm, M. Bassler, R. Feifel, A. Giertz, H. Wang, K. Wiesner, A. Ausmees, C. Miron, S. L. Sorensen, and S. Svensson, Chem. Phys. Lett. **334,** 151 (2001).

Cation-Specific Interactions with Carboxylate in Amino Acid and Acetate Aqueous Solutions

Emad F. Aziz[1], Niklas Ottosson[2], Stefan Eisebitt[1], Robert Seidel[1], Wolfgang Eberhardt[1], Barbara Jagoda-Cwiklik[3], Robert Vácha[3], Pavel Jungwirth[3], and Bernd Winter[1]

[1]Helmholtz-Zentrum Berlin für Materialien und Energie, Albert-Einstein-Strasse 15, 12489 Berlin, Germany; [2]Department of Physics, Uppsala University, Box 530, SE-751 21 Uppsala, Sweden; [3]Institute of Organic Chemistry and Biochemistry, Academy of Sciences of the Czech Republic, and Center for Biomolecules and Complex Molecular Systems, Flemingovo nám. 2, 16610 Prague 6, Czech Republic;

Ion-selective interactions play an important role in many chemical, environmental, and biological processes occurring in aqueous solution. The cationic interaction with the protein's carboxylate groups is of special interest due to its effect on protein association and enzymatic activity. It has been established empirically that the tendency for contact ion-pair formation correlates with the match between the hydration enthalpies, i.e., in the present case the cation and anionic carboxylate group. For instance, the hydration enthalpy of sodium matches those of major intracellular anions or anionic groups such as carboxylate, better than potassium.

Observations of ion-specific effects on proteins date back as early as 1888, when Hofmeister recognized[1] that inorganic salts can be ranked by their ability to "salt out" hen egg white protein in aqueous solution. Hofmeister series have since been observed for numerous phenomena in aqueous ion solutions, including their interfaces[2]. Understanding the microscopic origin of this remarkable phenomenon, which is at the heart of aqueous chemistry, calls for a combined experimental and theoretical effort.

On the theoretical side, a recent combined molecular dynamics and quantum chemical study has revealed that sodium interacts more strongly with protein surfaces than potassium, and that the ion-specific interaction is mediated by weak ion pairs $(COO^-:X^+)_{aq}$. This finding and interpretation thereof is awaiting firm experimental confirmation.

Here we report oxygen K-edge X-ray absorption spectroscopy (XAS) measurements from aqueous solutions of X-acetate (X = Li^+, Na^+, K^+, NH_4^+), and of glycine aqueous solutions, with additions of either NaCl or KCl. XAS is highly sensitive to the empty valence states of a given atomic site, and the technique is most suitable for probing orbital changes mediated by ion-ion interactions.

The O1s XA transition investigated here directly probes the atomic site of the -COO_{aq}^- group closest to the cation, and has thus superior sensitivity to differences in counterion interactions. Another important advantage of the present study is that the bonding geometry can be determined, which is information not accessible otherwise. Additionally, certain differences in the O1s XA spectra of neat water and solutions can be assigned to the distortion of the water network.

XAS measurements at the oxygen K-edge of acetate and glycine/salt aqueous solutions were performed at the U41-PGM undulator beamline, BESSY, Berlin[3]. The aqueous solution is circulated (1 L/min) within a stainless steel closed tubing system, inside an UHV chamber, as to warrant continuous renewal of the irradiated liquid sample. In the interaction region, the X-ray radiation hits the sample flowing behind a 150 nm thick Si_3N_4 membrane.
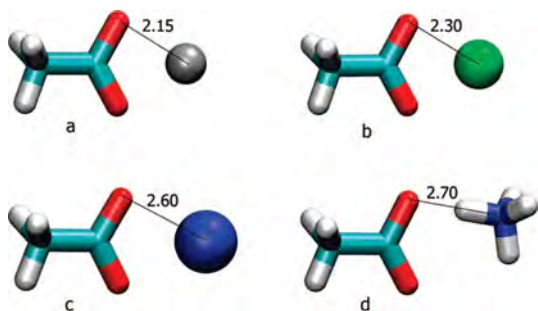
Figure 1: Calculated geometries of contact ion pairs of (a) lithium acetate, (b) sodium acetate, (c) potassium acetate, and (d) ammonium acetate. All distances are given in Ångstrom.
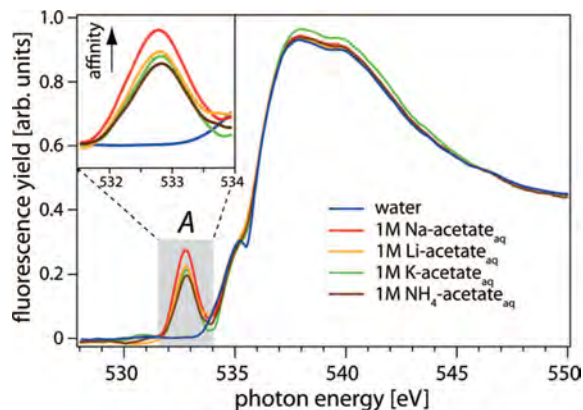
Figure 2: Oxygen 1s XA spectra for different X-acetate (X$=$Li$^+$, Na$^+$, K$^+$, NH$_4^+$) solutions. Enlargement of the region between 531.5 and 534.5 eV is presented on the top left and correlated with the cation binding affinity.

X-ray absorption is recorded by total fluorescence yield (FY) measurements using a 5 × 5 mm^2 GaAsP photodiode. Due to the long attenuation lengths of X-rays, on the order of a few micrometers, the method is primarily bulk sensitive. The setup is readily applicable to more complex molecules than studied here, and for FY measurements, the use of an oxygen-free membrane is equally well suited as a free-vacuum jet experimental setup[4].

The geometries of all investigated contact ion pairs are depicted in Figure 1. In each case, the free energy of ion pairing was evaluated as the difference between the energy of the solvated contact ion pair and the energies of the separately solvated cation and anion in water. Water was described within a polarizable continuum solvent using the COSMO model[5]. The present ab initio calculations were performed using the Gaussian 03 program package.

Figure 2 contrasts the oxygen K-edge X-ray absorption (XA) spectra of a series of 1 M X-acetate aqueous solutions (X = Li$^+$, Na$^+$, K$^+$, NH$_4^+$) as well as of pure liquid water, and Figure 3 shows the analogous data for 1 M glycine in 1 M NaCl and 1 M glycine in 1 M KCl aqueous solutions. All spectra were measured under the same experimental conditions, and slight changes in the photon flux were accounted for by normalizing the spectral intensities. This leads to identical intensities in the (background) region >545 eV photon energy, i.e., sufficiently far away from the absorption edges. The O1s XA spectra of the solutions are dominated by the characteristic water features. These are the pre-edge at 535 eV, and the main- and post-edges at 538 and 540 eV. All XA solution spectra of Figure 2 almost fully overlap with the neat water spectrum, the main differences being the occurrence of a new peak (labeled A) at 532.8 eV photon energy and some systematic intensity changes in the main- and postedge regions.

Peak A is a sole spectral signature of the -COO$_{aq}^-$ group, and arises from the promotion of an O1s core-level electron to the lowest unoccupied molecular orbital (LUMO), of π* character. Intensities of A change considerably. For acetate solutions (Figure 2), the intensities of A decrease in the sequence Na$^+$ > Li$^+$ > K$^+$ > NH$_4^+$, and for the two glycine solutions (Figure 3), A is more intense for NaCl than for KCl.
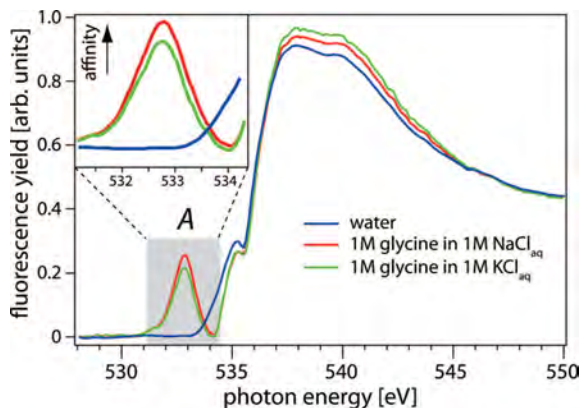
Figure 3: Oxygen 1s XA spectra of 1 M solution of glycine in 1 M NaCl and 1 M glycine in 1 M KCl. Enlargement of the region between 531 and 534.5 eV is presented on the top left and correlated with the cation binding affinity.

Table 1: Free energy change upon replacing sodium with lithium, potassium, or ammonium in a contact ion pair with acetate in water.

	ΔG (sodium $\rightarrow$ other cation) (kcal/mol)
lithium	+0.3
potassium	+2.5
ammonium	+3.4

The observed A-peak intensity changes (Figures 2 and 3) can be attributed to the change of the local density of unoccupied states at the oxygen site of -COO_{aq}^-, induced by interaction with the cations. The observed intensity changes quantitatively correlate with the strength of ion pairing. Intensities of the acetate-specific O1s absorption signal are hence proportional to the total number of empty states of p symmetry in the integration interval. The effect scales with the strength of the COO_{aq}^- to cation(aq) interaction. Contrary to the A-peak intensity changes, an increase of the main/post-edge intensity correlates with the reverse order of X, i.e., $Na^+ < Li^+ < K^+ < NH_4^+$.

Our results show that the width of peak A is independent of the cation used. Hence, for each cation studied, the interaction geometry is essentially of the same bidental nature, in agreement with the calculated structures presented in Figure 1. All alkali cations are observed to take middle positions between the two carboxylate oxygens. Computational results of the relative strength (with respect to Na^+) of cation pairing with acetate in water are summarized in Table 1. We see that sodium forms the most stable ion pair with aqueous acetate, followed by lithium which is only marginally less stable. The tendency for ion pairing with potassium and particularly with the ammonium cation is weaker. The fact that lithium binds slightly less strongly than sodium to acetate is in accord with the empirical law of matching water affinities. It states that ions prefer to pair with counterions or ionic groups which have comparable hydration enthalpies which can be translated in a simple Born solvation picture to surface charge densities. From this point of view, Na^+ matches most closely the COO^- group, followed by Li^+, K^+, and NH_4^+.

References

[1] Lewith, S. *Arch. Exp. Pathol. Pharmakol.* **1888**, *23*, 1.

[2] Cacae, M. G.; Landau, E. M.; Ramsden, J. J. *Q. Rev. Biophys.* **1997**, *30*, 241.

[3] Aziz, E. F.; Freiwald, M.; Eisebitt, S.; Eberhardt, W. *Phys. Rev. B* **2006**, *73*, 75120.

[4] Winter, B.; Faubel, M. *Chem. Rev.* **2006**, *106*, 1176.

[5] Klamt, A.; Schuurmann, G. *J. Chem. Soc., Perkin Trans. 2* **1993**, 799.

Autoionisation in Water Clusters

Melanie Mucke[1], Markus Braune[2], Toralf Lischke[1], Marko Förstel[1,3], Tiberiu Arion[1], Uwe Becker[2] and Uwe Hergenhahn[1a]

1: Max-Planck-Institut für Plasmaphysik, EURATOM association, Boltzmannstr. 2, 85748 Garching
2: Fritz-Haber-Institut der Max-Planck-Gesellschaft, Faradayweg 4-6, 14195 Berlin
3: Max-Planck-Institut für Kernphysik, Saupfercheckweg 1, 69117 Heidelberg

Synchrotron radiation has proven to be a versatile tool for investigating the electronic dynamics of weakly bound systems, such as noble gas and hydrogen-bonded clusters. On moving from monomers to dimers or clusters, the physical properties of the system change, allowing new dynamic schemes to evolve. Here, we report on a non-local autoionisation channel which has hitherto not been observed in water experimentally: After photoionisation of an inner valence electron the remaining hole is filled by relaxation of an outer valence electron. The energy released is transferred to another molecule within the same cluster where it suffices to ionise another outer valence electron. About a decade ago, this process was predicted theoretically for weakly bonded clusters [1] and later, this so-called Interatomic or Intermolecular Coulombic Decay (ICD) was discovered experimentally in rare gas systems [2].

Water clusters were generated by expanding water vapour through a conical nozzle into an evacuated volume. Valence electrons of water were ionised with synchrotron radiation, and the emitted photoelectrons were detected together with the ICD electrons generated in the water clusters. The expected energy range of these ICD electrons lies between 0 and 8 eV [3], but as other processes such as intra-cluster inelastic electron scattering generate an unstructured distribution of "secondary" electrons in this kinetic energy range, it is unlikely that simple non-coincident electron energy spectra will reveal an unambiguous signature of the ICD process. Thus, an electron-electron coincidence measurement set-up was chosen in order to discriminate between low kinetic energy electrons emitted as a result of inner valence photoionisation and secondary electrons resulting from scattering. A magnetic bottle type time-of-flight spectrometer [4] was used to detect electrons of kinetic energies down to 100 meV from an acceptance solid angle of almost 4π sR. Experiments were performed in single bunch mode at the undulator beamline UE112-lowE-PGMa.
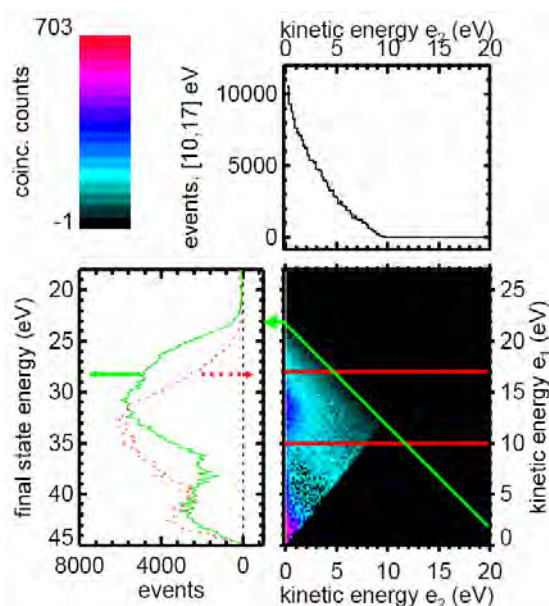
Figure 1: Emission probability of coincident electron-electron pairs from free water clusters with a mean size of $\langle N \rangle = 40$ irradiated with 45 eV photons.

[a] Mail address: IPP c/o HZB, Albert-Einstein-Str. 15, 12489 Berlin; email: uwe.hergenhahn@ipp.mpg.de

In the two-dimensional map of Figure 1 the coincident events detected for any combination of photoelectron kinetic energy (e_1) and corresponding second electron kinetic energy (e_2) are shown. Random coincidences have been subtracted. The two red lines indicate the range of the photoelectron kinetic energies in which ICD electron-photoelectron pairs are expected. Integrating the number of events in this region leads to the energy spectrum of ICD shown in the top panel. Its shape is determined by a convolution of initial and final state energies, the latter being dependent on the nuclear dynamics during the autoionisation process. Calculations for small water clusters at fixed nuclear positions led to a similar spectrum, e.g. peaking at low kinetic energies [3]. The red curve in the left graph displays the total number of coincidences for each photoelectron kinetic energy. Summing-up electron pairs of constant total energy (green line in the coincidence map) results in the green graph, corresponding final state energies being given on the left axis.
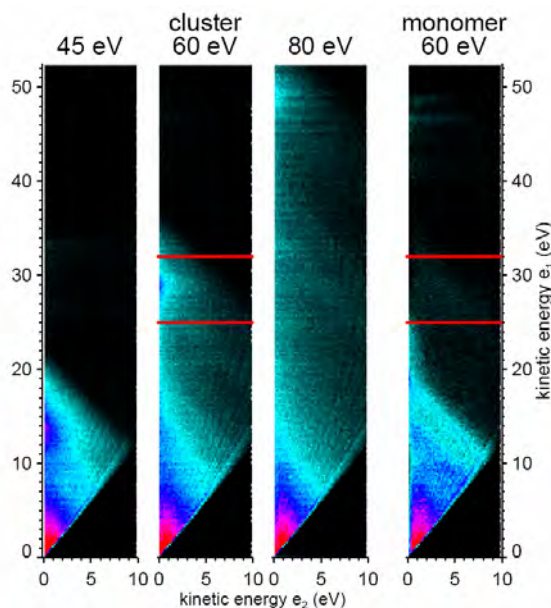
Figure 2: Coincidence maps of water clusters taken at different photon energies and of water monomers at 60 eV.

In figure 2 results obtained in technically identical measurements on water monomers as well as on clusters at three different photon energies are compiled. Please note that in the monomer map there is no intensity in the ICD region because the latter needs two or more participating molecules in the form of a hydrogen-bonded cluster or in a condensed phase. Additionally, the cluster maps show that the high intensity feature at very low e_2-energies and around e_1-energies of 14, 29 and 49 eV respectively does shift linearly with photon energy on the e_1-energy scale, but not in e_2. We can therefore definitively assign these transitions to the ICD of an inner valence vacancy. The origin of the considerable intensity of very low-kinetic energy electron-pairs could not yet be fully determined, but we assume that it partially results from scattering processes with more than two components as well as from the apparative setup.

In conclusion, we note that the existence of ICD in water has been demonstrated experimentally for the first time. The low energetic electrons generated in this autoionisation process may have to be considered in connection with the DNA damage produced by ionising radiation in living cells.

[1] L.S. Cederbaum et.al, PRL 79, 4778 (1997)
[2] S. Marburger et.al, PRL 90, 203401 (2003)
[3] I. Mueller et.al, JCP 125, 204305 (2006)
[4] P. Lablanquie et.al, JESRP 156,51 (2007)

Experimental setup of an ion-trap experiment at BESSY for measuring XMCD spectra of free clusters (GAMBIT*)

S. Peredkov, A. Savci, P. Bischoff, S. Peters, C. Kalus, M. Neeb, W. Eberhardt
Helmholtz-Zentrum Berlin, Röntgen-Campus-Adlershof (BESSY II), 12489 Berlin
B. Hofferberth, A. Lagutschenkov, H. Kampschulte, L. Barzen, G. Niedner-Schatteburg
Technische Universität Kaiserslautern, 67663 Kaiserslautern

A Penning-trap setup is currently under construction at the beamline UE52-PGM which will be used to record X-ray absorption spectra of free mass-selected clusters. The ultimate goal is to record XMCD spectra of free mass-selected transition metal clusters and to determine the spin and orbit contributions as a function of cluster size and temperature. Such data are not available through other methods. So far, only the total magnetic moments of mass-selected free clusters have been recorded by Stern-Gerlach experiments [1]. Our data will be used to compare with recent XMCD data of deposited clusters [2-4].

An FT-ICR mass spectrometer (MS) installed at the beamline serves both as a cluster ion trap and mass analyzer (m/e) [5,6]. A superconducting magnet (4-7 T), that is part of the Penning trap, serves as the magnetic field source for XMCD experiments. Recording the core shell absorption spectra with circularly polarized light (left/right) the XMCD spectra of the magnetically aligned clusters will be measured [7]. Higher charge states of the parent cluster ions or ionic fragments resulting from Auger decay and photodissociation will be used as absorption signal. The different ions or charge states will be registered by their characteristic cyclotron frequencies.

During the last year the ion trap has been built up and tested with a commercial electrospray ion source (ESI). Thereafter a piezo-driven laser vaporisation cluster source (30 Hz) and 90-degree ion deflector [8] has been installed to produce metal cluster ions. A mass spectrum is shown in Fig. 1 for small Nb-clusters (left). The right panel of Fig. 1 shows an isolated single cluster ion (Nb_7^+) after removing all other cluster masses. During the current commissioning period   the   X-
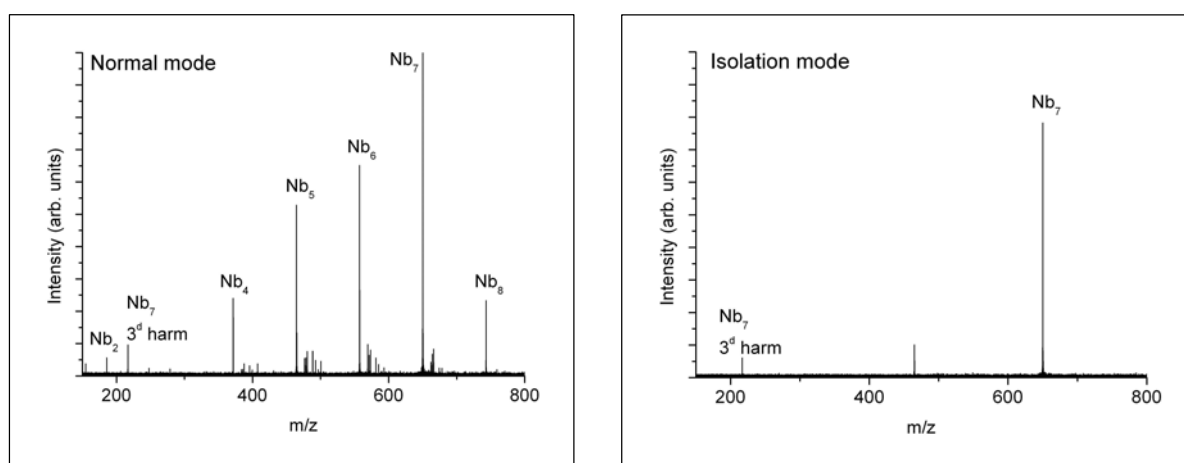
Fig. 1: FT-ICR mass spectrum of Nb_n-cluster cations in normal and isolation mode.

ray beam has been aligned through the whole apparatus including ion trap, ion optics and apertures. Moreover, the synchronization of the monochromator control, pulsed laser source, filling/detection scheme of the ion trap and a pneumatic x-ray beam shutter has been successfully implemented and computer-controlled. In addition, cryogenic cooling of the ion

trap (<20 K) has been tested at TU Kaiserslautern and will soon be integrated into the instrument for measuring temperature-dependent XMCD spectra.

The next crucial step is to find the overlap between the X-ray beam and stored clusters which circulate radially along their combined magnetron/cyclotron orbit. The X-ray beam has a horizontal diameter of 0.5 mm (FWHM) at the trapping center (Fig. 2). Vertically, the beam size can be controlled by the exit slit (20, 40, 100, 200, 500, 5000µm) which is located ~4 m upstream from the trapping center.
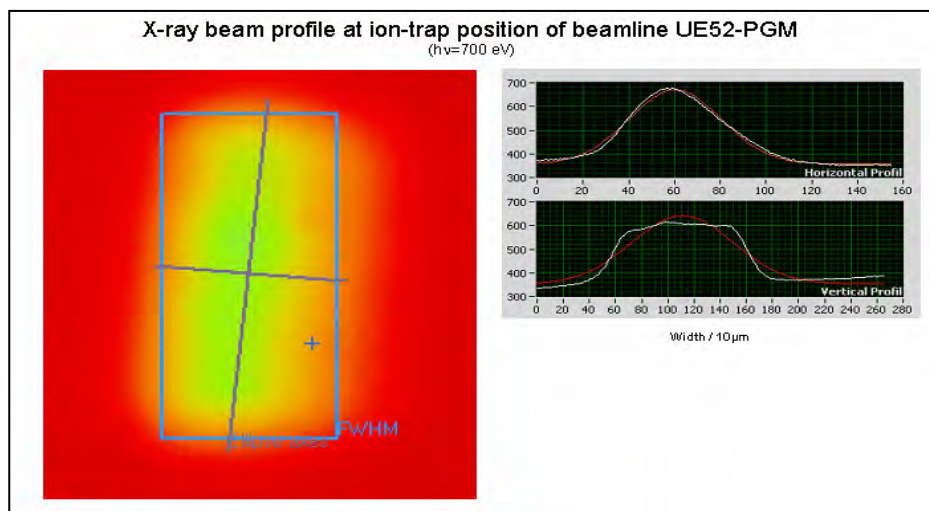
Fig. 2: X-ray beam profile (hν=700 eV) at the ion-trap position ~4 m behind the monochromator exit slit. The horizontal width is fixed by the natural beam divergence to ~0.5 mm (FWHM).

[1] I.M.L. Billas, A. Chatelain, W.A. de Heer, Science **265**, 1682 (1994).
[2] J.T. Lau, A. Föhlisch, R. Nietubyc, M. Reif, W. Wurth, Phys. Rev. Lett., **89**, 57202 (2002).
[3] K. Fauth, M. Heáler, D. Batchelor, G. Schütz, Surf. Sci. **529**, 397 (2003).
[4 P. Gambardella, A, Dallmeyer, K. Maiti, M.C. Malagoli, W. Eberhardt, K. Kern, C. Carbone,
Nature **416**, 301 (2002).
[5] A.G. Marshall, C.L. Hendrickson, G.S. Jackson, Mass Spectrom. Rev. **17**, 1 (1998).
[6] B.M. Reinhard, A. Lagutschenkov, J. Lemaire, P. Boissel, P. Maitre, G. Niedner-Schatteburg, J. Phys. Chem. A **108**, 3350 (2004).
[7] M. Getzlaff, A. Kleibert, R. Methling, J. Bansmann, K.-H. Meiwes-Broer, Surf. Sci. **566**, 332
(2004).
[8] S. Jaberg, Dissertation, Universität Kaiserslautern, 2008.

X-ray absorption and electron yield spectra of water cluster

Marko Förstel[a,b,*], Silko Barth[a], Toralf Lischke[a], Melanie Mucke[a], Volker Ulrich[a],
Tiberiu Arion[a], Axel Reinköster[c], Uwe Hergenhahn[a,*]

[a] Max-Planck-Institute for Plasma Physics, EURATOM Association, Boltzmannstr. 2, 85748 Garching, Germany
[b] Max-Planck-Institute for Nuclear Physics, Advanced Study Group of the Max-Planck-Society,
    Saupfercheckweg 1, 69117 Heidelberg, Germany
[c] Fritz-Haber-Institute of the Max-Planck-Society, Department for Molecular Physics, Faradayweg 4-6,
    14195 Berlin, Germany

Water ice (Ih) is crystalline, with a tetrahedral coordination of the molecules in it. Conventionally, the structure of liquid water is assumed to be similar. In this picture, every water molecule gives rise to four hydrogen bonds (double donor, double acceptor). However, fluctuations which locally distort this ordering on a short time-scale are admitted. Typical water *molecule* bond orders in the conventional picture are therefore 3.xx. Obviously, this value depends on the definition of what a hydrogen bond is [1]. Results obtained by numerous, different experimental techniques support or at least agree with this view [1].

This picture has been challenged by X-ray absorption experiments on liquid water [2]. These authors claim that molecules in the liquid phase act as single donor, single acceptors only. This interpretation rests on a comparison of their measured traces with spectra of ice and with DFT calculations. Here we present the ion yield and electron yield spectra of small water clusters excited with X-rays during two different beamtimes at the beamline UE52 SGM. These data exhibit some of the principal features discussed in Ref. [2]. We will discuss to which extent the interpretation given there is compatible with our new experiments.
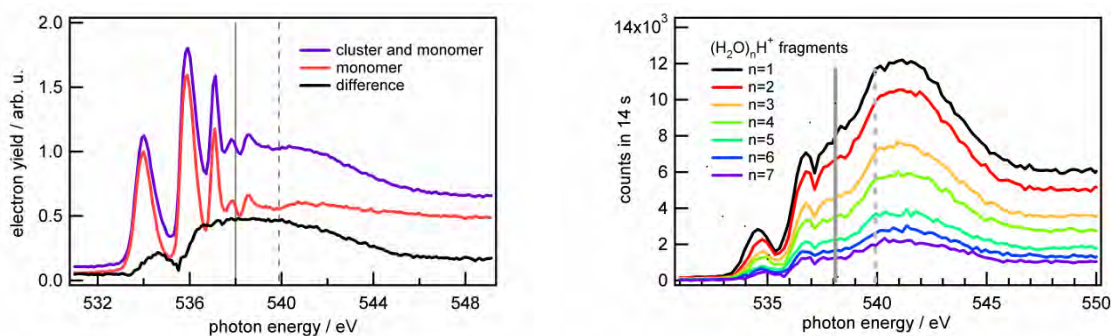
Figure 1: Total Auger-electron yield (left panel) and total ion yield (right panel) of small water clusters after photoexcitation. The grey vertical lines indicate O 1*s* ionization potentials for liquid water surface states (solid) and molecular water (dashed).

The Auger-electron yield spectra (Fig. 1) obtained for small clusters have been compared to those of water and crystalline ice presented by Bluhm *et al*. [3]. We find a great similarity to the Auger yield of a water film as recorded in [3], while the spectra for ice have a significantly different appearance. This is in agreement with the work of Buch *et al*. [4]. These authors conclude on an amorphous structure of the ⟨N⟩ < 200 water clusters from a theory assisted interpretation of vibrational spectra.

The ion yield spectra (right panel, Fig. 1) show a peak at energies higher than the O 1*s* ionization potential. Such a "post peak" has formerly been interpreted as a characteristic of

the crystalline form of water. However we would like to explain this feature in our experiment differently. At excitation energies above the O 1*s* edge two or three positive charges are formed within the clusters due to Auger decay. Due to coulombic repulsion the cluster asymptotically decays into singly charged fragments. The absorption of a single photon can now result in the detection of more than one ion. This enhances the quantum efficiency so it can no longer be used as a direct measure for the absorption. The velocity of these charged fragments will differ depending on their size. When using a pulsed extraction field in such a way that fast ions leave the interaction region before extraction, only slow ions are detected. We can show that the peak at around 541 eV excitation energy of the ion yield spectra strongly decreases (Fig 2), when a pulsed extraction field is used.
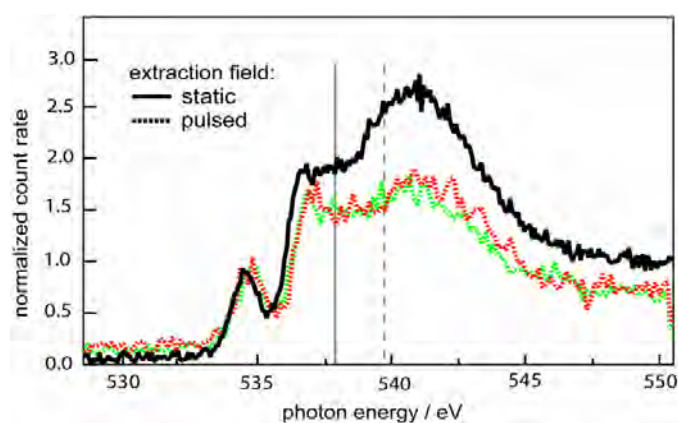
Figure 2: Comparison of the ion yield of small water clusters after photoexcitation using static (solid line) and pulsed (dashed lines, red 112, green 520 V/cm.) extraction fields. Vertical lines: Ionization potentials for molecular and liquid surface water as in Fig. 1.

Summarizing, we have measured Auger-electron yield and ion yield spectra of small and medium-sized water clusters along the oxygen K-edge. The Auger-electron yield is in agreement with expectations for an amorphous, liquid-like structure of the clusters. A distinct peak in the partial ion yield occurs at the same photon energy as in the photoabsorption spectra of crystalline ice. We have pointed out the possible role of variations of the quantum efficiency with photon energy in the formation of this feature.

[1] R. Kumar, J. R. Schmidt and J. L. Skinner, J. Chem. Phys. **126**, 204107 (2007).

[2] P. Wernet, D. Nordlund, U. Bergmann, M. Cavalleri, M. Odelius, H. Ogasawara, L. A. Näslund, T. K. Hirsch, L. Ojamäe, P. Glatzel, L. G. M. Pettersson and A. Nilsson, Science **304**, 995-9 (2004).

[3] H. Bluhm, D. F. Ogletree, C. S. Fadley, Z. Hussain and M. Salmeron, J. Phys.: Condens. Matter **14**, 8, (2002).

[4] V. Buch, B. Sigurd, J. P. Devlin, U. Buck, J. K. Kazimirski, Int. Rev. Phys. Chem **23,** 375-433 (2004).

PHOTOIONIZATION OF THE C_{60} MOLECULES IN THE LOW PHOTON ENERGY RANGE

Sanja Korica, Axel Reinköster, Markus Braune and Uwe Becker
Fritz-Haber-Institut der Max-Planck-Gesellschaft, Berlin

We have performed high-resolution measurements of photoelectrons emitted from the valence shell of C_{60} in the low photon energy region, from 13 to 30 eV and in small steps of 0.1 eV, in order to study the photoionization cross-section behavior of the two highest occupied molecular orbitals HOMO and HOMO-1 in his close threshold regime. In addition, absolute cross-section measurements of the single photoionization of C_{60} were performed in the same energy region.

The measurements were performed at the BESSY beamline U125-2_NIM. We used a vacuum chamber containing a conventional electron time-of-flight spectrometer with a MCP detector unit to which appropriate voltages were applied in order to keep the resolution constant. In addition, an opposing ion time-of-flight mass spectrometer was used for mass analysis and detection of the different ions being created in the photoionization process. The beam of C_{60} molecules was provided by an oven resistively heated to a temperature of aproximately 500°C.
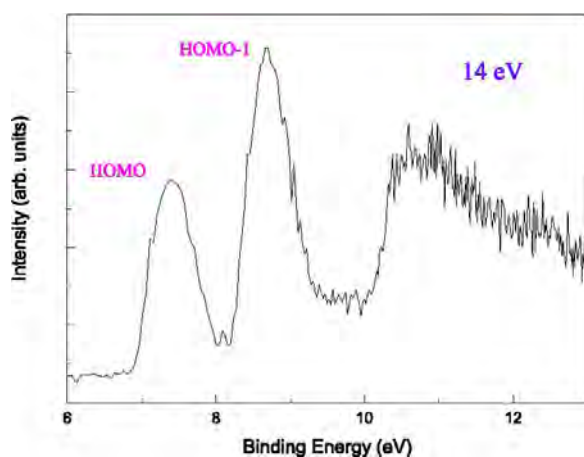
Fig.1. The electron yield of the C_{60} as a function of the binding energy

A typical C_{60} gas-phase spectrum for a photon energy of 14 eV is shown in Fig.1. Our PES results support the photon energy dependent oscillations in the partial cross sections of the two highest occupied molecular orbitals, HOMO and HOMO-1, observed in former experiments. They have been explained within the three-step model of photoemission theory, as an interference between the photoelectrons generated within the molecule [1]. They also carry structural information on the cage size and the delocalized electron distribution [2]. In Fig.2. we show the normalized partial cross sections of the HOMO and HOMO-1 C_{60} orbitals derived from partial cross section and branching ratio measurements during the last years. In contrast to the good overall agreement between theory and experiment, there is still a striking disagreement regarding the predicted discrete resonance structures [3] in the low photon energy region (Fig.3). We assume that these resonances are somehow quenched by the vibrations of the molecule and, as unstable states, do not appear in the photoelectron intensity.
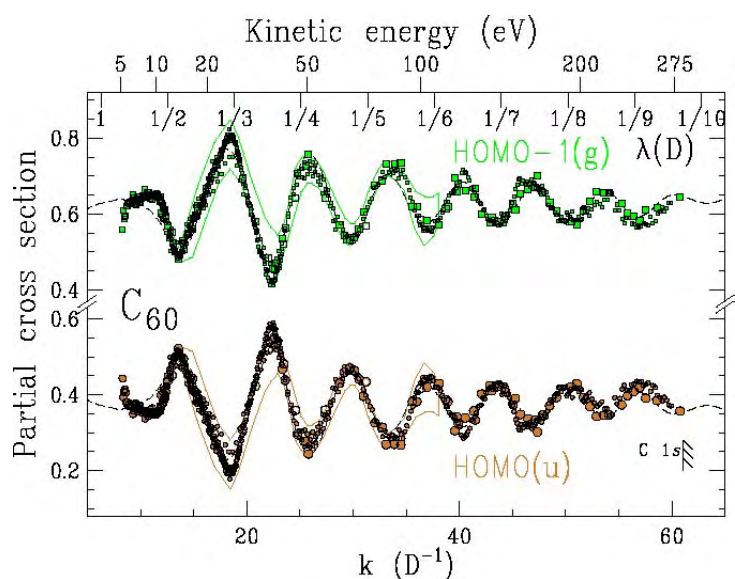
Fig.2. Intensity of C_{60}'s photoelectrons from the two outermost orbitals, HOMO
and HOMO-1. Units correspond to the cage diameter (D=7.1A)
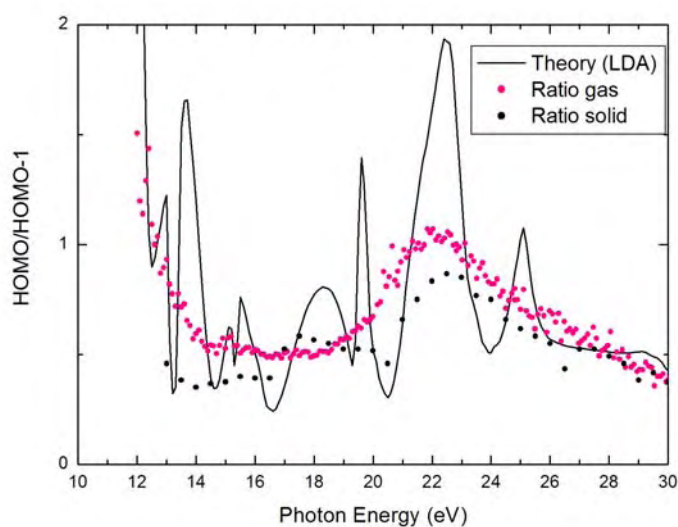
Fig.3. Experimentally determined ratio HOMO/HOMO-1 compared with the
calculated photoionization cross-section ratio[3] and experimental data
for the solid C_{60} [4]

Absolute cross section measurements of the single photoionization of C_{60} give evidence for a giant plasmon resonance around 20 eV with an overall width of about 8eV, as theoretically predicted [5]. This effect arises from collection of the strength of the individual one-electron transitions into a single collective excitation.
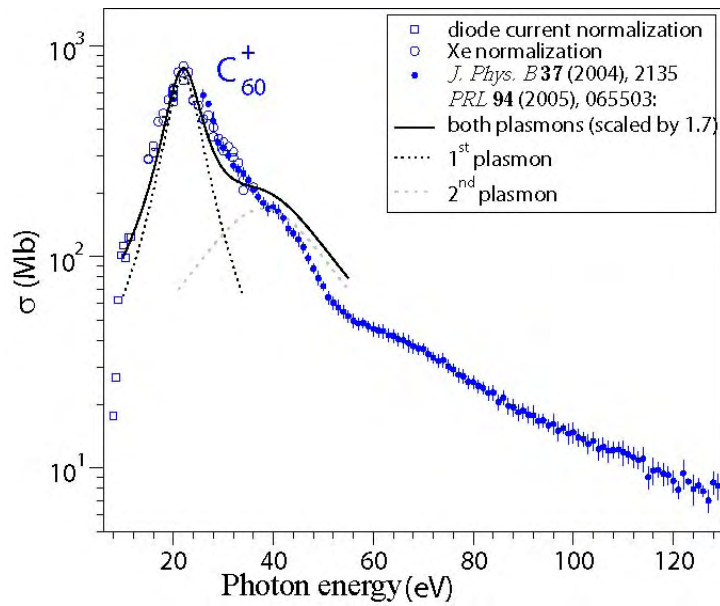
Fig.4. Photoionization cross section of the producing of C_{60}^{+}. We extended our old measurements [6] towards significantly lower photon energies. The data were normalized to the cross section of xenon and, at lower photon energies, to the current measured with the diode at the end of the beamline

[1] Y. B. Xu *et al*., Phys. Rev. Lett. **76**, 3538 (1996)
[2] S. Korica *et al*., Phys. Rev. A **71**, 13203 (2005)
[3] P. Decleva, *private communication*
[4] H. Li *et al*., J. Phys. B **19** 436223
[5] V. K. Ivanov *et al*., J. Phys. B **34**, L669 (2001)
[6] A. Reinköster *et al*., J. Phys. B **37**, 2135 (2004)

ELECTRONIC STRUCTURE OF ENDOHEDRAL METALOFULLERENE La@C$_{82}$

Sanja Korica, Axel Reinköster, Markus Braune and Uwe Becker
Fritz-Haber-Institut der Max-Planck-Gesellschaft, Berlin

Endohedral metallofullerenes, composed of a doped carbon cages, exhibit unique properties driven by the characteristics of the encapsuled metal atoms. They represent a new class of materials with a wide range of potential future applications as molecular and solid state devices. Although they were discovered almost simultaneously with Buckminsterfullerene itself [1], more than twenty years ago, experimental results on them are very rare due to the difficulty to synthesize them in macroscopic quantities and to cleanly characterize them.

Here, we report our first study on the electronic structure of La@C$_{82}$ with synchrotron radiation photoelectron spectroscopy. The experiment was carried out on the beamline TGM4 of BESSY using a small cross chamber equipped with a TOF electron analyzer. La@C$_{82}$ molecules were evaporated from the powder, prepared and purified elsewhere, that was heated in resistively heated oven at ~ 515°C. All spectra have been taken with the normal electron emission. During the measurement the vacuum was better than 6x10^{-7} mbar.

Concerning the theoretical calculations performed up to now, both molecular dynamics (MD) based on density functional theory (DFT)[2] and Hartree-Fock (HF) calculations[3], have predicted that the guest La ion occupies off-center position in the molecule. La d valence electrons are strongly ionized in the C$_{82}$ cage and, to a first approximation, La can be considered to be in the 3+ charge state. These results indicated a strong hybridization between the La 5d orbitals and cage π binding and antibonding orbitals which produces a significant rearrangement of the energy levels and not simply a rigid filling of C$_{82}$ empty states.
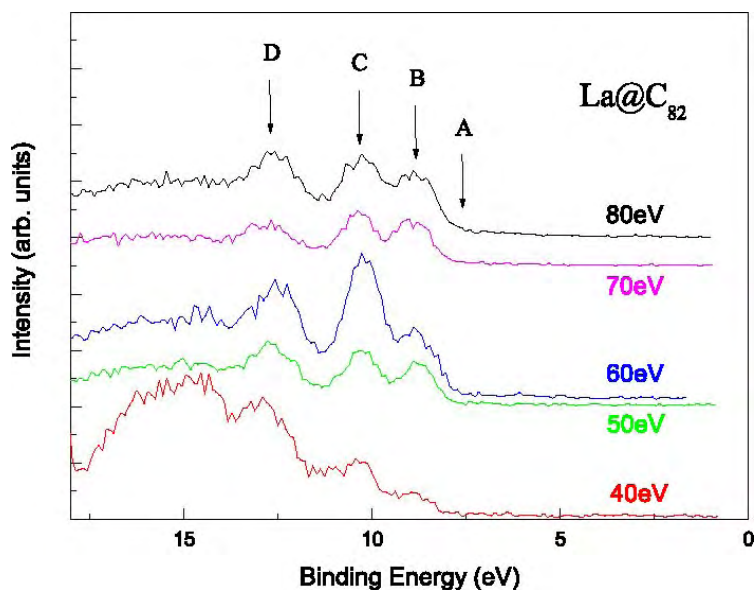
Figure 1. Photoelectron yield as a function of the binding energy for five different photon energies

Figure 1 presents several valence band spectra of La@C_{82} measured in the photon energy range from 40-80 eV. There are four distinct structures observed, marked A-D. Peaks B-D are derived almost entirely from π-bonding states. The shoulder A has no analog in the spectrum of C_{82} and is, according to [4], due to states derived from SOMO of La@C_{82}. The nature of the SOMO is that of a π state of the cage and it arises from the charge transfer from the La atom to the C_{82} cage. Another interesting characteristic of the spectra is oscillatory behavior of photoelectron intensity with incident photon energy. This phenomenon, also found in other fullerenes [5,6,7], has been attributed to intramolecular interference effects. The strength of the oscillations, however, varies between the states depending on the localization of electron density. This suggests that this experiment is a very sensitive probe of electron delocalization for fullerene systems.

[1] J. R. Heath *et al*., J. Am. Chem. Soc. **107**, 7779 (1985)
[2] W. Andreoni *et al*., Appl. Phys. A **66**, 299 (1998)
[3] S. Nagase *et al*., Chem. Phys. Lett. **201**, 475 (1993)
[4] D. M. Poirier *et al*., Phys. Rev. B **49**, 17403 (1994)
[5] J. H. Weaver *et al*., Phys. Rev. Lett. **66**, 1741 (1991)
[6] M. B. Jost *et al*., Chem. Phys. Lett. **184**, 423 (1991)
[7] S. Hino *et al*., Chem. Phys. Lett. **190**, 169 (1992)

X-ray photoionization of deposited Cu-clusters on a native Si-wafer

S. Peters, S. Peredkov, A. Savci, A. Vollmer, M. Neeb, W. Eberhardt

Helmholtz-Zentrum Berlin, Röntgen Campus Adlershof (BESSY II), 12489 Berlin

XPS (Cu 2p), NEXAFS (L_3-edge) and Auger spectra (L_3VV) of mass-selected Cu-clusters have been measured at beamline PM4 (Optics beamline) and compared with the respective spectra of a Cu-crystal [1,2]. The clusters were prepared by a magnetron cluster source and mass selected by a sector dipole magnet. The mass-filtered clusters were softly landed and the ion current was measured during deposition by an electrometer (10-200 pA); cluster deposition was stopped after a coverage of $3*10^{12}$ atoms has been reached. The coverage density spot has been imaged by a new channelplate-phosphor screen device and CCD camera (Fig. 1). From this we conclude for a coverage density of 1-$3x10^{13}$ atoms/cm^2. The deposited cluster samples were transferred from the laboratory to the beamline end station by a mobile UHV chamber.
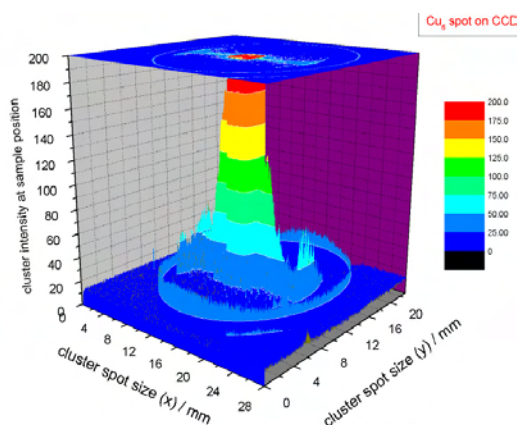
Fig.1. Deposition spot as measured by a Channelplate/CCD device

Our X-ray photoionization experiments reveal that both the XPS and L_3-absorption threshold are higher in energy than the respective bulk value (up to 1 eV). The observed blue shift of the core binding energy is explained by the smaller screening ability of the clusters, i.e. due to the reduced atomic coordination. The reduced screening ability is also apparent in the Auger spectra. The $L_3M_{4,5}M_{4,5}$-Auger spectra of the Cu-clusters were measured as function of photon energy [3]. The Auger energy of the main Auger peak depends clearly on the photon energy, i.e. the kinetic energy of the photoelectron (Fig. 2). The larger the photon energy the smaller the Auger energy which can be explained as PCI shift, i.e the interaction of the outgoing photoelectron with the doubly charged Auger final state. The PCI shift shrinks with increasing cluster size. Cu-bulk does not show any photon energy dependence because in the metal the Auger final state is efficiently screened by the conduction electrons. Our measured energy dependence of the Auger spectra demonstrates that the electronic structure of the clusters is not metal-like but rather molecular or semiconducting like up to 55 atoms, at least. A specially prepared high density sample, which has been approximated by a Poisson distribution as island of ~2nm diameter, has almost converged to the bulk limit.

1
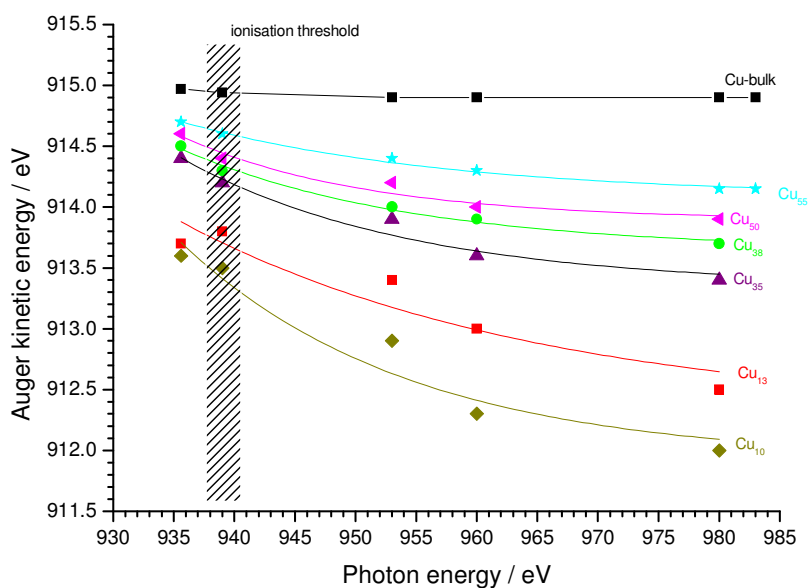
Fig. 2. Photon energy dependence of the main Auger peak (L₃VV) of small deposited Cu-cluster.

After oxidation of Cu_{55} at atmospheric pressure the oxidation of the cluster is clearly visible by the strong excitonic pre-edge feature (ca. 931 eV) as seen in Fig. 3 while the non-oxidised samples do not show any pre-edge XAS peak. The ESCA shift of the $2p_{3/2}$ peak amounts to ca. +1.5 eV.
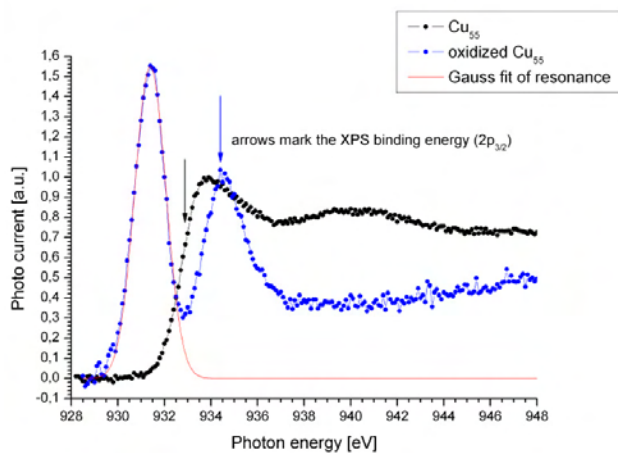
Fig. 3: X-ray absorption spectra (L₃) of oxidized and pristine Cu_{55} on Si-wafer.

[1] N. Ferretti, PhD-Thesis, "Core ionization spectroscopy of deposited Cu clusters", Technische Universität Berlin, Dec. 2008.
[2] S. Peters, Master Thesis, Technische Universität Berlin, in preparation
[3] S. Peters, S. Peredkov, N. Ferretti, B. Balkaya, M. Neeb, W. Eberhardt, submitted.

2

High-Resolution Core-Level Spectroscopy of Sulfur Hexafluoride Clusters

R. Flesch, E. Serdaroglu, A. A. Pavlychev[1], X. Brykalova[1], and E. Rühl
Physikalische Chemie, Freie Universität Berlin, Takustr. 3, 14195 Berlin, Germany
[1]St. Petersburg State University, 198504, St. Petersburg, Russia

Weakly bound clusters bridge the gap between isolated molecules in the gas phase and condensed forms of matter such as liquids, solids, and nanoparticles. Inner-shell excitation has been proven to be a sensitive approach to detect changes in the electronic as well as the geometric structure of molecules bound in clusters.

Fig. 1: (a) The effective potential of an S-2p-electron in SF_6 is described by an inner and an outer well that are separated by a barrier, as taken from ref. [1]. (b) In homogenous SF_6 clusters the outer well potential is significantly modified by additional barriers that come from the cluster environment. This gives rise to spectral changes in S 2p-excited clusters compared to the bare molecule.

The spectroscopy of S 2p-excited sulfur hexafluoride (SF_6) is well-established [1]. It is known that the effective potential of an S 2p electron consists of inner-well- and outer-well regimes. These determine the electronic properties of bound and quasi-bound states below and above the S 2p-ionization edge (see Fig. 1 (a)).

We have studied S 2p-excited sulfur hexafluoride clusters $((SF_6)_n)$ in recent theoretical work using the *quasi-atomic* approach [2], which extends our earlier work [3]. It is found that the cluster environment leads to changes in the outer-well regime of SF_6 (see Fig. 1 (b)). The following changes in the S 2p spectra are expected to occur: (i) inner-well S 2p-excited states *below* the S 2p ionization threshold are essentially unchanged; (ii) inner-well S 2p-excited states *above* the S 2p ionization threshold (shape resonances) are changed in position as well as in their shape; (iii) states that are bound in the outer-well potential (Rydberg states, double excitations) are expected to be strongly perturbed.
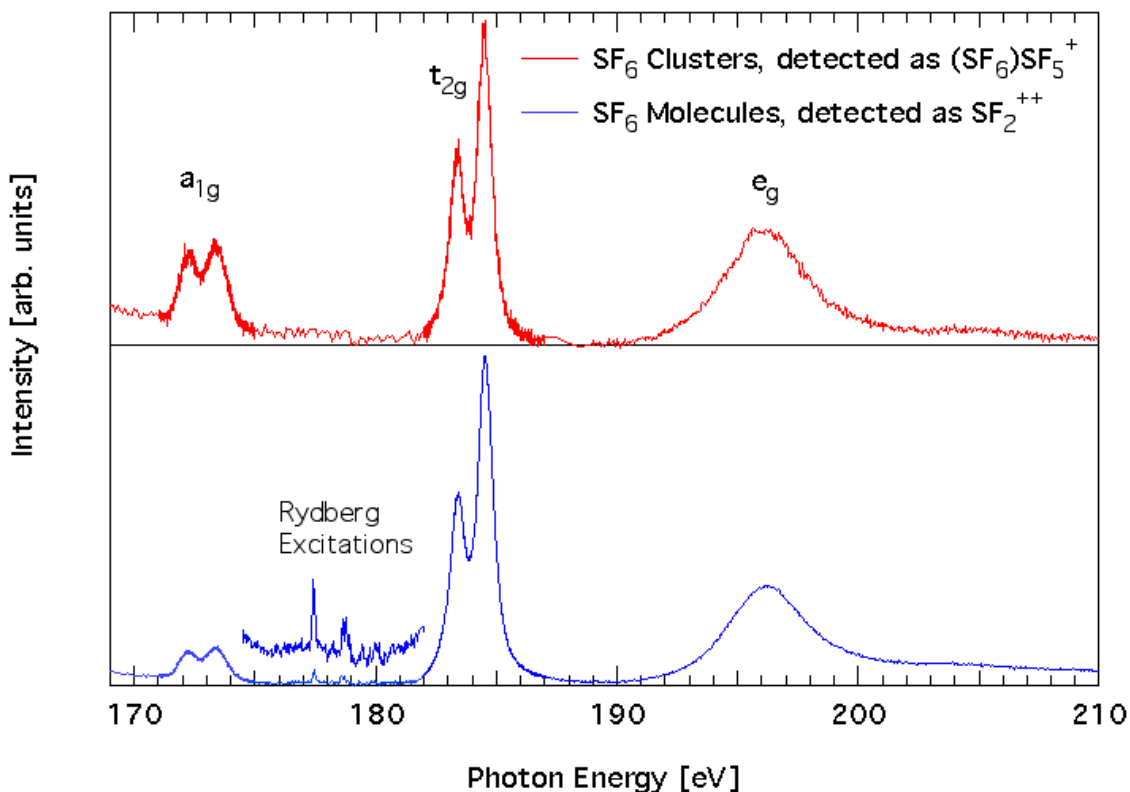
Fig. 2: Inner-shell excitation spectra of SF_6 clusters (top) and isolated SF_6 molecules near the S 2p ionization threshold.

Inner-shell excitation spectra of SF_6 clusters have been measured at the U49/2-PGM-1 beamline at BESSY-II in the energy range near the S 2p ionization threshold (170-210 eV) in order to validate previous theoretical predictions. Spectra of molecular SF_6 are recorded simultaneously, so that all changes in spectral positions and band shapes are revealed, similar to earlier work [2-4]. Overview spectra of clustered and isolated SF_6 near the S 2p edge are shown in Fig. 2. Partial ion yields are utilized to determine the inner-shell excitation spectra of clusters and isolated molecules. Specifically, the $(SF_6)SF_5^+$ yield is used to detect clusters, and SF_2^{++} is used for isolated molecules. It is found that the spectra are quite similar to each other, but the relative intensities are different. For example, transitions into the a_{1g} state occur with higher intensity for clusters. Transitions into Rydberg states that are clearly visible for SF_6 (cf. ref. [1]) are absent in the cluster spectrum, as predicted from theory [5].

Fig. 3 gives a detailed view of the quasi-bound S-2p$\rightarrow e_g$ shape resonance (Fig. 3), where the solid curves represent non-linear least-square fits to the experimental data using exponentially modified Gaussians. It is found that the e_g shape resonance is redshifted by 95±5 meV in clusters (see inset in Fig. 3). The lifetime of the quasi-bound e_g state is essentially determined by its tunneling probability through the internal barrier. It is therefore affected by changes in the outer-well potential. Additionally, changes in the shape of the band are observed, as well. These occur mainly in the range between 198 eV and 205 eV, where additional intensity comes from double excitations [1]. The deconvolution of this spectral range into contributions from the e_g shape resonance and double excitations is currently in progress.

Fig. 4 shows the S 2p$\rightarrow a_{1g}$-band. This band does not show any visible changes upon cluster formation. This is in full accordance with predictions from theory [5] since the a_{1g} band is below the S 2p threshold so that its properties are not affected by changes in the outer-well potential.

We intend in the near future to refine the model shown in Fig. 1 (b) by using the experimental results shown in this work.
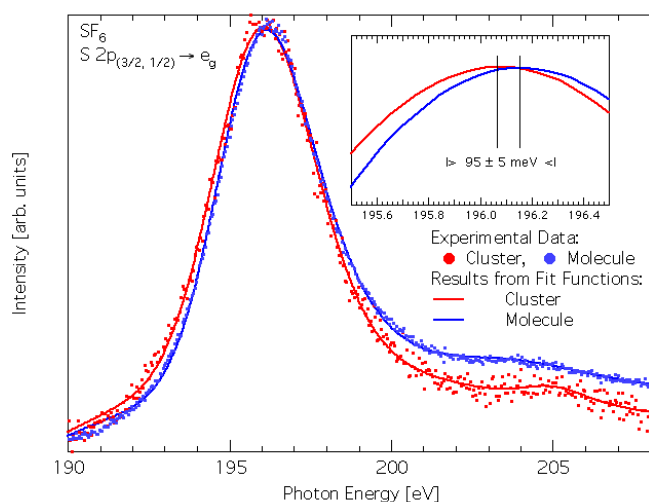
Fig. 3: S 2p→e_g shape resonance of SF_6 in isolated molecules (blue trace) and in clusters (red trace). A red- shift by 95±5 meV as well as changes in the band shape are observed for clusters.
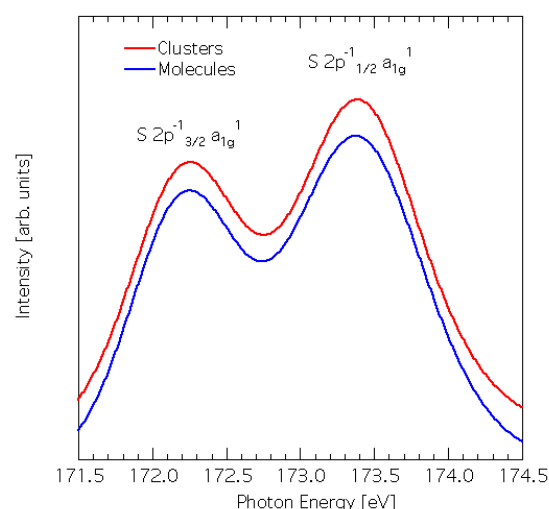
Fig. 4: S 2p→a_{1g} band of SF_6 in isolated molecules (blue trace) and in clusters (red trace). The maxima of both transitions remain constant within ±5 meV.

References

[1] E. Hudson, D. A. Shirley, M. Domke, G. Remmers, A. Puschmann, T. Mandel, X. Xue, G. Kaindl, *Phys. Rev. A* **47**, 361 (1993).

[2] A.A. Pavlychev, X.O. Brykalova, D.A. Mistrov, R. Flesch, E. Rühl, *J. Electron Spectrosc. Relat. Phenom.* **166-167**, 45, (2008).

[3] A.A. Pavlychev, X.O. Brykalova, R. Flesch, E. Rühl, Phys. Chem. Chem. Phys. **8**, 1914 (2006).

[4] R. Flesch, A.A. Pavlychev, J.J. Neville, J. Blumberg, M. Kuhlmann, W. Tappe, F. Senf, O. Schwarzkopf, A.P. Hitchcock, E. Rühl, Phys. Rev. Lett. **86**, 3767 (2001).

[5] A.A. Pavlychev, X.O. Brykalova, D.A. Mistrov, R. Flesch, E. Rühl, to be published.

Linear dichroism in the 2p photoionization of atomic Na

D. Cubaynes [1], M. Meyer [1], E. Heinecke [2], K. Riek [2], P. Zimmermann [2], M. Yalçınkaya [3],
S. Fritzsche [4], E. Gryzlova [5], and A. N. Grum-Grzhimailo [5]

[1] *LIXAM/CNRS, UMR8624, Centre Universitaire Paris-Sud, Bâtiment 350, 91405 Orsay, France*
[2] *Institut für Atomare Physik und Fachdidaktik, Technische Universität Berlin, Hardenbergstrasse 36,
D-10623 Berlin, Germany*
[3] *Istanbul University, Science Faculty, Physics Department, 34118 Vezneciler/Istanbul, Turkey*
[4] *Gesellschaft für Schwerionenforschung (GSI), D-64291 Darmstadt, Germany*
[5] *Institute of Nuclear Physics, Moscow State University, Moscow 119991, Russia*

High-resolution photoelectron spectroscopy on laser-excited atoms provides detailed and valuable information on the complex interactions in the electronic cloud of the atoms [1]. In particular, the well-defined polarization of both laser and synchrotron radiation (SR) can be used to study the dichroism in the photoionization of polarized atoms, i.e. to obtain new information on the dynamics of the ionization process [2]. In these studies, alkaline atoms serve often as prototype targets, since the excitation energy necessary to promote the outer "s"-electron to the lowest excited "p"-state is easily attainable with conventional lasers. In the present study, we investigated the linear dichroism in the 2p photoionization of Na atoms, laser-prepared in the Na*$2p^63p$ $^2P_{3/2}$ or $^2P_{1/2}$ excited state as well as laser-oriented in the Na $2p^63s$ $^2S_{1/2}$ ground state.

The experiments were performed at beamline UE125/2-SGM of BESSY. The counter-propagating laser and SR intersect the sodium vapor, which is produced by a radiatively heated oven, in the source volume of a high-resolution electron energy analyzer (Scienta SES-2002). The excitation of the sodium atoms was obtained by a continuous wave single mode ring laser, which was pumping either the Na $2p^63s$ $^2S_{1/2} \rightarrow 2p^63p$ $^2P_{1/2}$ or the Na $2p^63s$ $^2S_{1/2} \rightarrow 2p^63p$ $^2P_{3/2}$ transition at $\lambda = 589.559$ and 589.995 nm, respectively. With a typical laser power of 800 mW, more than 30% of the sodium atoms could be promoted to the excited level. The emitted electrons were measured at the magic angle (54° 44') with respect to the SR polarization vector. The relative orientation Θ between the linear polarization vectors of the laser and the SR was changed by a rotatable half-wave plate, which was introduced in the optical path of the laser.

As example of our results, Figure 1 presents two high-resolution photoelectron spectra of Na* $2p^63p$ $^2P_{3/2}$ laser-excited atoms recorded at a excitation energy of hν(SR) = 54 eV for parallel ($\Theta = 0°$) and perpendicular ($\Theta = 90°$) orientation of the polarization vectors. The lines in the kinetic energy region between 13.6 and 14.7 eV are attributed to the Na$^+$ $2p^53p$ $^{1,3}L_J$ (except $^1S_0$) final ionic states and have been discussed in detail in an earlier study [3]. A strong variation of the relative line intensities is observed for these Na$^+$ $2p^53p$ $^{1,3}L_J$ multiplet lines,

when comparing the two spectra recorded at different orientations Θ. This effect is directly related to the introduced alignment of the Na*$2p^6 3p$ $^2P_{3/2}$ excited state and is known as linear alignment dichroism [4]. Our theoretical description is based on multi-configuration Dirac-Fock and Hartree-Fock approaches and simple three-parameter 'generalized geometrical model' (GGM) [3,5] accounting for the intermediate coupling in the final ionic states. Within the GGM, the intensity variation of each $2p^5 3p$ $^{1,3}L_J$ multiplet line is expressed as a function of the relative partial cross sections for the photoionization of the 2p electron into the "εs" or "εd" continua, cosine of the relative phase Δ between "εs" and "εd" photoelectrons, the intermediate coupling coefficients of the $2p^5 3p$ $^{1,3}L_J$ state, and the initial alignment A_{20} produced by the laser excitation. In a separate measurement the alignment was determined to about -2/3. Introducing this value for A_{20} into the simulations, the theoretical spectra (Fig. 2) and relative intensity variations of the individual lines are in very good agreement with the experimental results (Fig. 1). The observed intensity variations between the spectra at $\Theta = 0°$ and $\Theta = 90°$ are independent of the relative phase Δ and consistent with dominating cross section for the emission of "d" electrons for this photon energy.
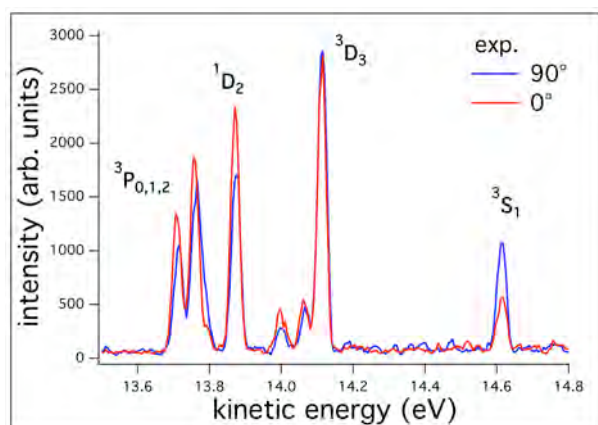
Figure 1: Experimental photoelectron spectrum of laser-aligned Na*$2p^6 3p$ $^2P_{3/2}$ in the region of the Na$^+$ $2p^5 3p$ $^{1,3}L_J$ manifold recorded for parallel (red) and perpendicular (blue) relative orientations of the linear polarization vectors.
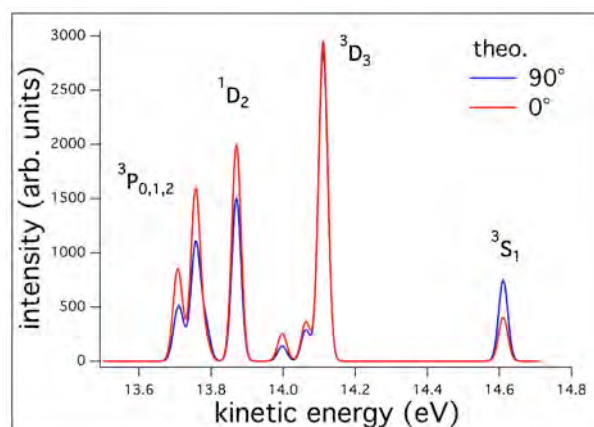
Figure 2: Theoretical simulation of the Na*$2p^6 3p$ $^2P_{3/2}$ photoelectron spectrum in the region of the Na$^+$ $2p^5 3p$ $^{1,3}L_J$ manifold for parallel (red) and perpendicular (blue) relative orientations of the linear polarization vectors.

References
[1]   F. J. Wuilleumier and M. Meyer, J. Phys. B **39**, R425 (2006).
[2]   H. Klar and H. Kleinpoppen, J. Phys. B **15**, 933 (1982).
[3]   D. Cubaynes, M. Meyer, A.N. Grum-Grzhimailo, J.-M. Bizau, E.T. Kennedy, J. Bozek, M. Martins, S. Canton, B. Rude, N. Berrah, F.J. Wuilleumier, Phys. Rev. Lett. **92**, 233002 (2004).
[4]   M. Meyer, D. Cubaynes, F.J. Wuilleumier, E. Heinecke, T. Richter, P. Zimmermann, S.I. Strakhova, A.N. Grum-Grzhimailo, J. Phys. B **39**, L153 (2006).
[5]   A. Verweyen, A.N. Grum-Grzhimailo, N.M. Kabachnik, Phys. Rev. A **60**, 2076 (1999).

Photoelectron recapture and post-collision interaction near the Ar 2p threshold

B. Langer, R. Lewinski, E. Antonsson, U. Becker[†], and E. Rühl

Institut für Chemie und Biochemie - Physikalische und Theoretische Chemie, Freie Universität Berlin, Takustr. 3, 14195 Berlin

[†]*Fritz-Haber-Institut der Max-Planck-Gesellschaft, Faradayweg 4-6, 14195 Berlin*

Particle breakup processes, such as the photon-induced emission of two or more electrons following photoionization, are highly dynamic. This is in particular true for, including the remaining ion, three particle breakup as photoionization with subsequent Auger-decay. In this case each emitted particle can interact with the corresponding partner. As result, an energy exchange between the different breakup partners becomes possible. A nice example of such behavior is the photoelectron recapture and post-collision interaction (PCI) [1,2]. Here the emitted high energetic Auger electron interacts with the low energetic photoelectron. This interaction causes a reduction of the kinetic energy of the energy of the corresponding photoelectron which becomes recaptured. This is the so called photoelectron recapture process. It repopulates high lying Rydberg state and gives rise to subsequent resonant Auger decay.

We have measured the electron emission of argon excited by synchrotron radiation in the Ar 2p threshold regime. The experiments were conducted at the U49/2-PGM1 beam line of BESSY II during the single bunch operation mode. Electron spectra were accumulated
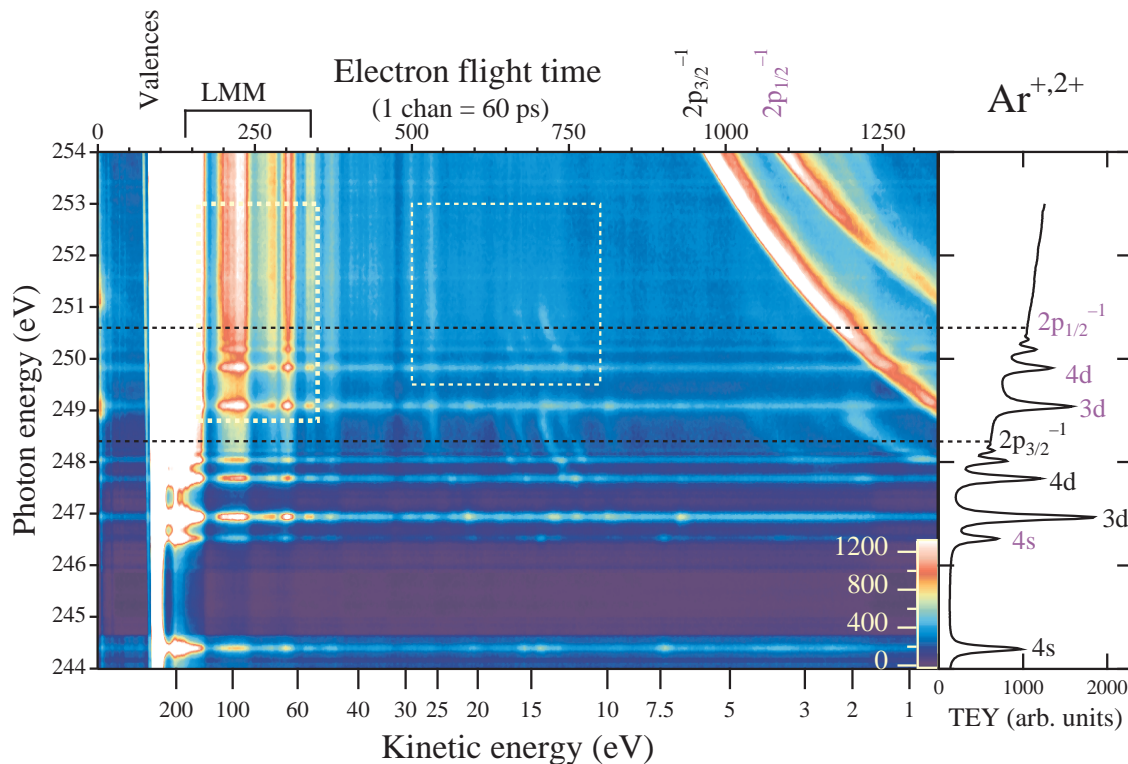
Figure 1: Two dimensional false color map of the electron emission in the Ar 2p thresold region. The intensity is of the emitted electrons is shown as a function of the photon energy and the electron flight time,where the fast electrons are displayed in the left part of the map. In the right part of the Figure the total electron yield (TEY) is shown. The electron recapture process can be observed as intensities of second step Auger lines in the region between 10 and 20 eV kinetic energy and a photon energy just above the Ar $2p_{3/2}$ and Ar $2p_{1/2}$ thresholds, respectively.These are represented by dotted black lines. Similar behavior has been observed in the case of the Ne 1s ionization [4]. The white dotted frames indicate the details shown in Figures 2 and 3, respectively.
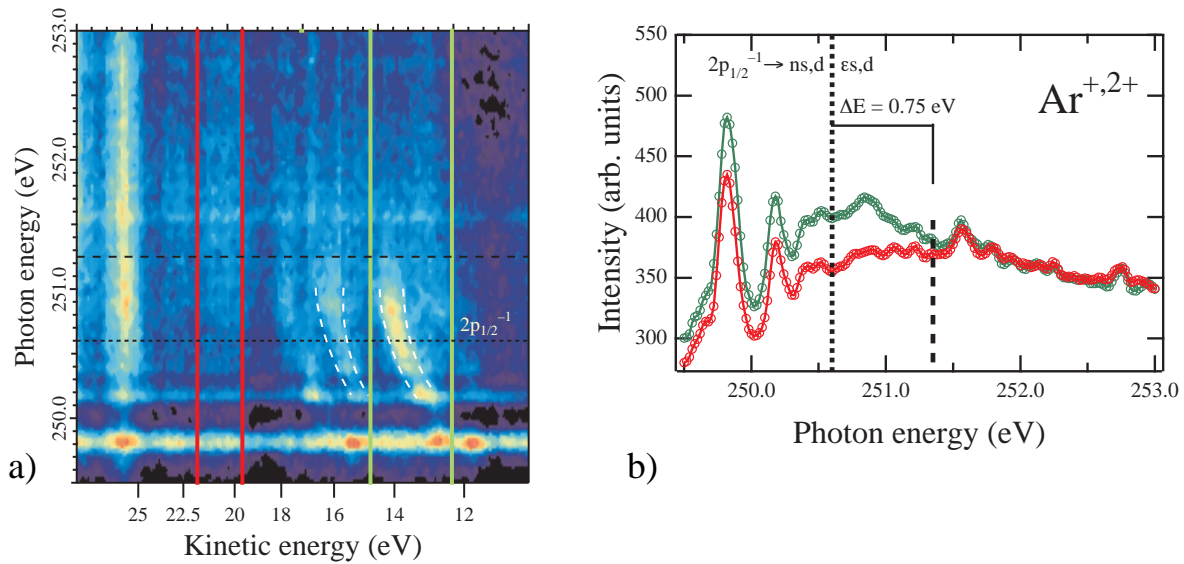
Figure 2 (a) Details of Figure 1 showing the electron recapture regime near the Ar $2p_{1/2}$ threshold. The green vertical lines mark an area that contains a second step Auger line whereas the red vertical lines encloses an area where no such processes can be seen; **(b)** shows the averaged intensity between the respective lines. These are shown as a function of the photon energy. Only in the region between the threshold (dotted line) and the dashed line electron recapture takes place.

using a newly developed magnetic bottle spectrometer, which is similar to recent work [3]. The spectrometer has the advantage that it detects all kinetic energies simultaneously, which is due to the time-of flight detection. Furthermore, the collection efficiency is high. This allows us to study the Ar 2p threshold region between 244 eV and 254 eV in detail, where steps of 20 meV with a collection time of 5 s for each step are sufficient.

Figure 1 shows a two-dimensional false color map of the electron emission processes over the photon energy as well as the kinetic energy of the photoelectrons. The photoelectron recapture process is clearly seen above the corresponding Ar 2p thresholds. This process which is due to shake-down, converges continuously into the so-called post collision interaction (PCI) regime. The slow photoelectrons are not recaptured in the PCI regime, they are rather retarded in their kinetic energies. This retardation is clearly seen in the two dimensional plots of the Auger intensity (Fig. 1). These results provide a high resolution representation of three particle breakup in the low kinetic energy region. A new and unexpected result concerns the time dependance of these processes. Recapture and post collisions are highly time dependent. This time dependence is contained in the

Figure 3: Detail of Figure 1 showing the LMM Auger groups indicating a change in the life time dependent line width in the region between the $2p_{1/2}$ threshold (dotted horizontal line) and the end of the recapture processes (dashed line).

two-dimensional spectra, as shown in Fig. 3. Between the threshold of the Ar 2p photoelectron emission and the normal Auger emission beyond the recapture region there is a clear change of the emission life time visible (Fig3). This change reflects the time needed by the photo- and Auger electrons for recapture and the post-collision interaction. The recapture of the photoelectron is particularly reflected by the second step Auger electron. Taking the instrumental resolution into account we estimate a 20% decrease of the natural Auger line width (114 meV), which corresponds to an additional life time of 1-2 fs. This charge transfer effect is in agreement with corresponding observations on surfaces where the higher density of atoms causes a faster transfer process [4]. In general, most of these Auger channels are energetically not allowed, since the binding energy difference is too small for emission of a further Auger electron. However, if a slow Ar 2p photoelectron becomes recaptured into a high lying Rydberg state as result of emission of the first Auger electron, the second step Auger decay becomes possible. This has been observed for the first time for Ne 1s photoionization [5]. The inset of Fig. 1, shown in enlarged form in Fig. 2, displays the kinetic energy behavior of these „forbidden" lines in a distinct way. They die out beyond the recapture regime giving rise to the much slower fluorescence decay of the corresponding initial hole states. The life time of these states represents the undisturbed Auger life time of approx. 6 fs. These processes may be studied in real time on an attosecond time scale, if suitable light sources become available.

References
[1] W. Eberhardt, S. Bernstorff, H. W. Jochims, S. B. Whitfield, B. Crasemann, Phys. Rev. A**38**, 3808 (1988).
[2] J. Tulkki, T. ÅBerg, S. B. Whitfield, B. Crasemann, Phys. Rev A**41**, 181 (1990).
[3] J. H. D. Eland, O. Vieuxmaire, T. Kinugawa, P. Lablanquie, R I. Hall, and F. Penent, Phys. Rev. Lett. **90**, 053003 (2003).
[4] A. Föhlisch, P. Feulner, F. Hennies, A. Fink, D. Menzel, D. Sanchez-Portal, P. M. Echenique, W. Wurth, Nature **436**, 373 (2005).
[5] R. Hentges, N. Müller, J. Viefhaus, U. Heinzmann, U. Becker, J. Phys. B: At. Mol. Opt. Phys. **37**, L267 (2004).

Satellites Of Atomic Transitions Induced By Vibrational Modes In Molecules.

V.A. Alekseev

Institute of Physics, St.Petersburg State University, Peterhof, 198504 Russia

N. Schwentner

Institute für Experimental Physik, Freie Universität Berlin, Arnimallee 14, D-14195, Germany

INTRODUCTION.

We have reported on   satellites of dipole-forbidden transitions (SDFT) in spectra of gas phase mixtures of Xe with CF_4 [1]. SDFT appear in spectra as spectrally narrow bands ($\Delta v \sim 10$ cm^{-1}) coinciding with energies of the dipole-forbidden np- and nd-states of the Xe atom increased by the energy of one v_3 *quantum* of CF_4 (v_3=1281 cm^{-1}) . The observed process may be written as follows

$$Xe(GS) + CF_4 (v_3=0) + hv \rightarrow \ Xe (DFS) + CF_4 (v_3=1),$$
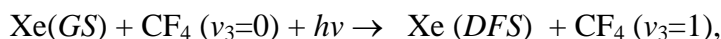
where *GS* and *DFS* denote respectively the ground and dipole-forbidden states of the Xe atom. Studies of Xe/C_2F_6 mixtures revealed similar satellites due to strong IR-active v_{10}-mode of C_2F_6 (v_{10}=1250 cm^{-1}). Also, it has been shown that only the IR-active vibrational modes of CF_4 and C_2F_6 induce satellites. Along with the satellites of forbidden transitions, spectra also display satellites of resonance transitions (SRT)

$$Xe(GS) + CF_4 (v_3=0) + hv \rightarrow \ Xe(RS) + CF_4 (v_3=1).$$
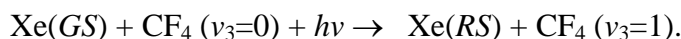
where *RS* denotes resonance state.   In this contribution we report recent results on studies of SDFT and SRT in rare gas - molecular gas mixtures.

EXPERIMENTAL.

Synchrotron radiation was dispersed by the 10m normal incidence monochromator. After passing a gas cell SR emission was recorded by luminescence of sodium salicillate screen. Fluorescence excited in the gas mixture by SR was detected via a Mg_2F side-on window with use of a solar blind photomultiplier. The second photomultiplier was use to record undispersed fluorescence in the UV and visible spectral regions.

RESULTS AND DISCUSSION

 The most interesting example of this effect was observed in the spectral region between the Xe 8d [1/2]$_1$ and Xe 5d' [3/2]$_1$ resonance states. Spectrum in Figure 1a shows several SDFT to the 7d-states and a more intense SDFT to the 8p[1/2]$_0$ state.   A striking feature of SDFT is the large strength of these transitions. The most intense SDFT are readily seen at pressure of few mbar.   The strength combined with their small spectral width implies that the transitions occur   at large distances where the lower and upper potentials are nearly parallel. The most intense satellites were observed on the wings of resonance transitions, i.e. when the energy between given resonance and dipole-forbidden states is close to the v_3 quantum energy, E(*RS*)-E(*DFS*)$\sim hv_3$. Another factor is the optical coupling between *RS* and *DFS* states. SDFT is intense when *DFS* and *RS* states are coupled by a dipole-allowed IR transition.

In contrast to SDFT, SRT are spectrally broad bands closely resembling in shape their parent

resonance bands. Figure 2a shows spectra of the Xe $6s[3/2]_1$ and Xe $7s[3/2]_1$ resonances in mixture with CF_4 and their satellites. The large spectral width suggests that SRT are molecular transitions at relatively small Xe-CF_4 distances where the upper and lower potentials are not parallel. The intensity of SRT is three orders of magnitude weaker in comparison with the strongest SDFT. Similar satellites have been observed in spectra of Kr/CF_4 and Xe(Kr)/C_2F_6 mixtures. For the first resonance transitions in the Xe and Kr atoms SRT have very similar shape. These bands are compared in Figure 2b. The intensities of SRT correlate qualitatively with the intensity of a resonance transition in the atom (Xe $6s[3/2]_1$ is ~ 1.3 times stronger than Kr $5s[3/2]_1$) and a vibrational transition in the molecule (the v_{10} band of C_2F_6 is a factor of 1.3 stronger than the v_3 band of CF_4).

SUMMARY

SRT and SDFT are due to simultaneous electronic and vibrational excitation of atom and molecule by one photon. On the other hand, these bands differ in spectral shape and intensity implying different intensity borrowing mechanisms. SDFT appear owing to long range interaction of $RS \leftrightarrow DFS$ electronic and vibrational dipoles. SRT may be viewed as molecular transitions at relatively small atom-molecule distances. Recent observation of

$Na(3s) + CF_4 (v_3=0) + hv \rightarrow$ Na $(3d) + CF_4 (v_3=1)$
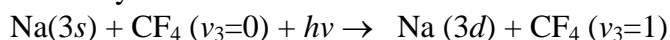
satellite transition in static cell and cross-beam experiments [2,3] confirms that the SDFT effect is of general nature and it appears very likely that similar vibrationally induced transitions may be observed for many other atom - molecule pairs.

ACKNOWLEDGMENTS

REFERENCES

1.V.A.Alekseev, and N.Schwentner, Annual BESSY Report 2005 and 2006, Chem.Phys.Lett. 436 (2007) 327–330
2.V.A.Alekseev, and N.Schwentner, Chem.Phys.Lett. 463 (2008) 47-49
3.V.A.Alekseev, J.Grosser, O.Hoffmann, and F.Rebentrost, J.Chem.Phys. 129 (2008) 201102
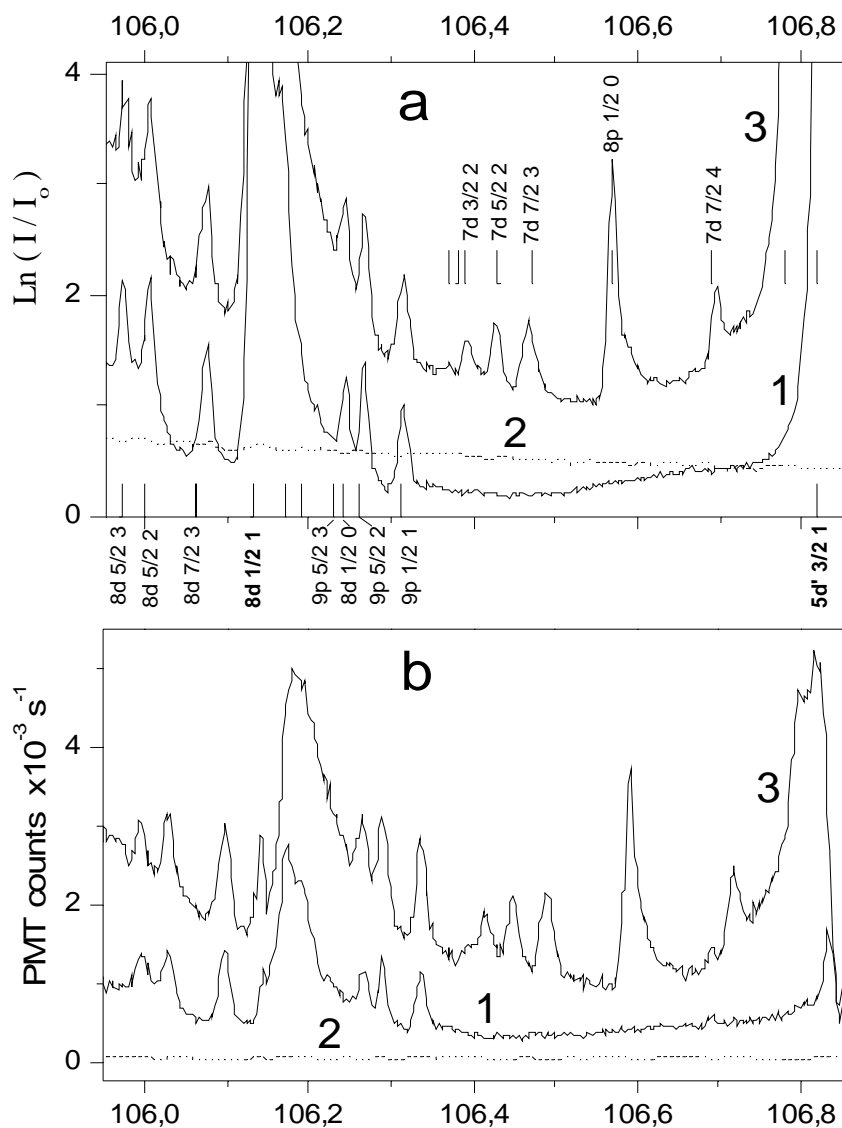
FIGURE 1. Absorption (*a*) and fluorescence excitation (*b*) spectra of **1** - Xe 35 mbar, **2** - CF$_4$ 70 mbar, and **3** – Xe 35 mbar + CF$_4$ 70 mbar. Undispersed fluorescence was recorded by a solar blind PMT. The lower set of sticks shows energies of Xe atom levels, the upper sticks shows the energies of lower lying Xe levels displaced by the ν_3 quantum energy.
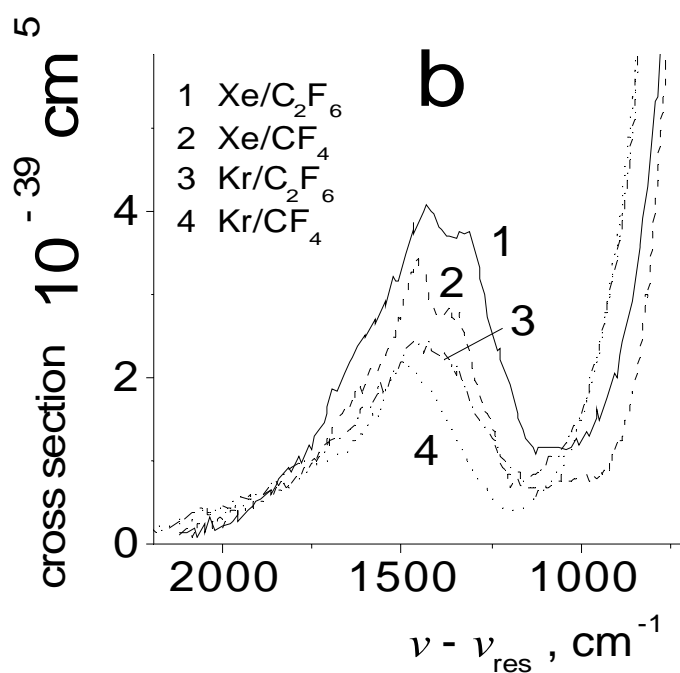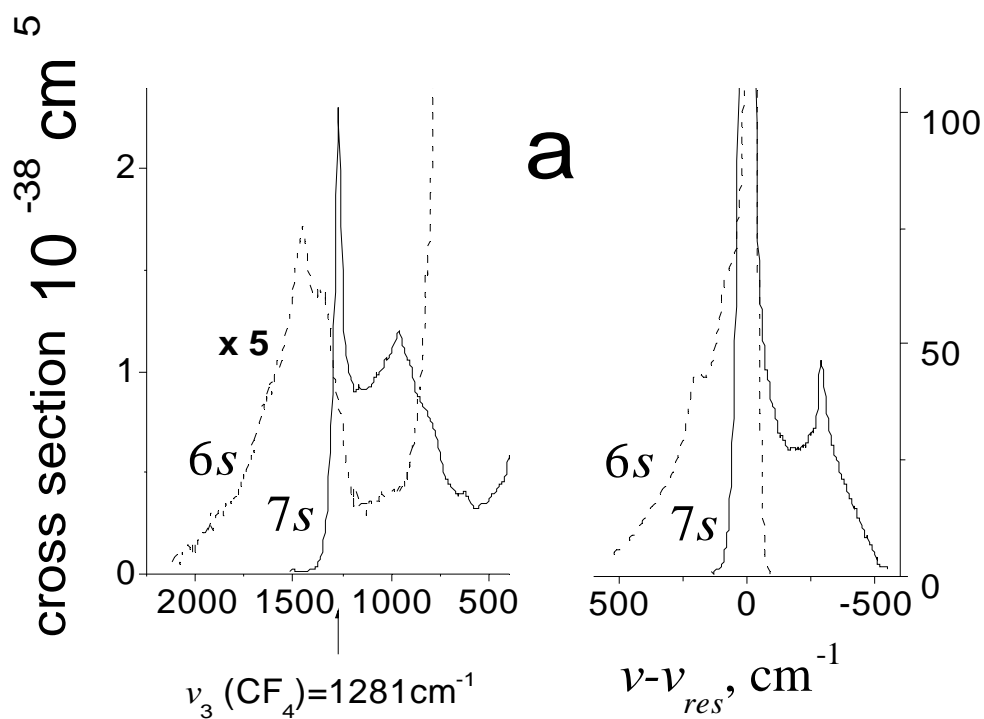
FIGURE 2. **a:** Xe $6s[3/2]_1$ (ν_{res}=68045.7 cm^{-1}) and Xe $7s[3/2]_1$ (ν_{res}=85440.5 cm^{-1}) resonance transitions in mixture with CF$_4$ **(right)** and their ν_3-satellite bands **(left)**.
b: ν_3 (CF$_4$) and ν_{10} (C$_2$F$_6$) satellites of Xe $6s[3/2]_1$ and Kr $5s[3/2]_1$ (ν_{res}=80917.6cm^{-1}) resonance transitions in mixtures with CF$_4$ and C$_2$F$_6$. (ν_3 =1281, ν_{10}=1250 cm^{-1}).

Core-Level Spectroscopy of Size-Selected Free Silicon Clusters

M. Vogel[1], K. Hirsch[1], Ph. Klar[1], A. Langenberg[1], F. Lofink[1], J. Probst[1], R. Richter[1],
J. Rittmann[1], V. Zamudio-Bayer[1], B. von Issendorff[2], T. Möller[1], and J.T. Lau[1]

[1] Technische Universität Berlin, Institut für Optik und Atomare Physik, EW 3-1, Hardenbergstraße
36, 10623 Berlin

[2] Albert-Ludwigs-Universität Freiburg, Fakultät für Physik/FMF, Stefan-Meier Straße 21, 79104
Freiburg

e-mail: tobias.lau@tu-berlin.de
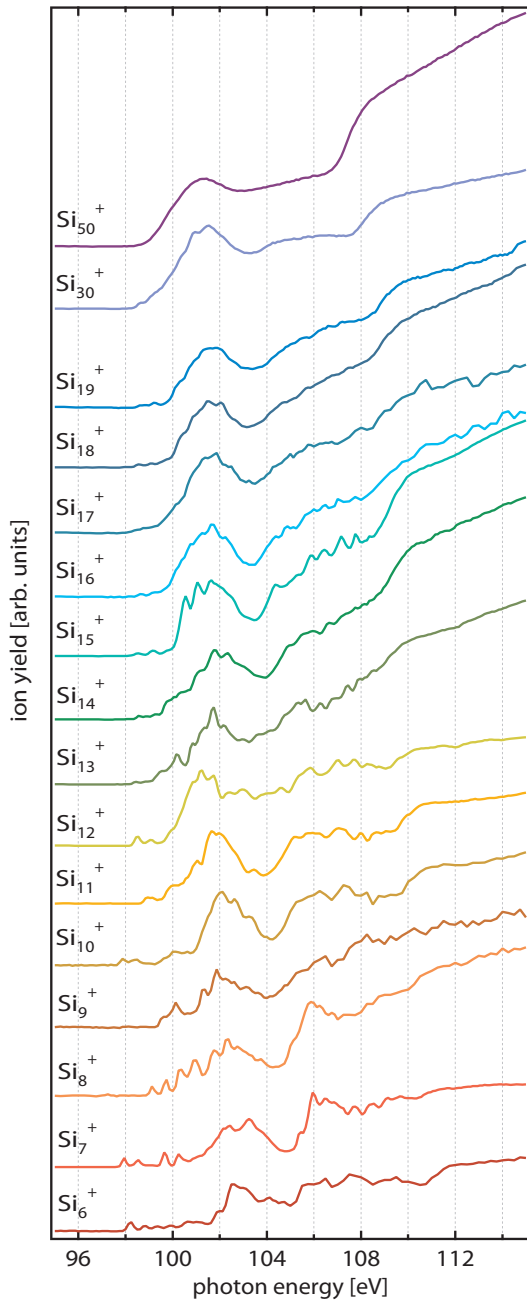
FIG. 1: Total ion yield spectra of Si_n^+ for $n = 6 - 50$.

X-Ray absorption spectroscopy of free nanoparticles has been and still is challenging because of the very low target density. By using a linear ion trap and the synchrotron beam at beamline U125/2 - SGM we were able to gather sufficient counting rates for investigating the $2p$ X-ray absorption of size selected free silicon clusters.

The cluster cations Si_n^+ are produced in a magentron sputter gas aggregation source, size selected in a quadrupol mass filter and accumulated in a liquid nitrogen cooled linear ion trap. The synchrotron beam overlaps with the trapped cluster beam along the trap axis, inducing a resonant transition $2p \rightarrow 3d$ or a direct transition from $2p$ into the continuum. In both cases the generated $2p$-hole is filled through a non-radiative decay process in which one or more Auger electrons are emitted. The multiply charged cluster ions may subsequently undergo fragmentation yielding differently sized and charged fragments. The fragments including the multiply charged clusters are detected with a double stage pulsed time-of-flight mass spectrometer. Adding up the ion yield for all fragments gives the total ion yield, which is proportional to the absorption cross section.

We investigated silicon clusters with a size of $n = 6$ up to a size of $n = 60$. The total ion yield spectra can be seen in figure 1. Different from metal clusters and due to the different bonding type, the spectra show distinct features up to clusters as big as $n = 16$ and the gradual change towards more bulk-like character can be seen clearly. The first main feature shifts towards smaller energies for larger clusters and the dip between the first and the second feature becomes washed out. But still the bulk character has not evolved completely for Si_{50}^+ (cp. [1]).

Interestingly the partial ion yield spectra are quite different for different fragments and hence the composition of fragments changes with energy. For parent cluster Si_6^+ these partial ion yield spectra are shown in figure 2. The fragments can be classified into
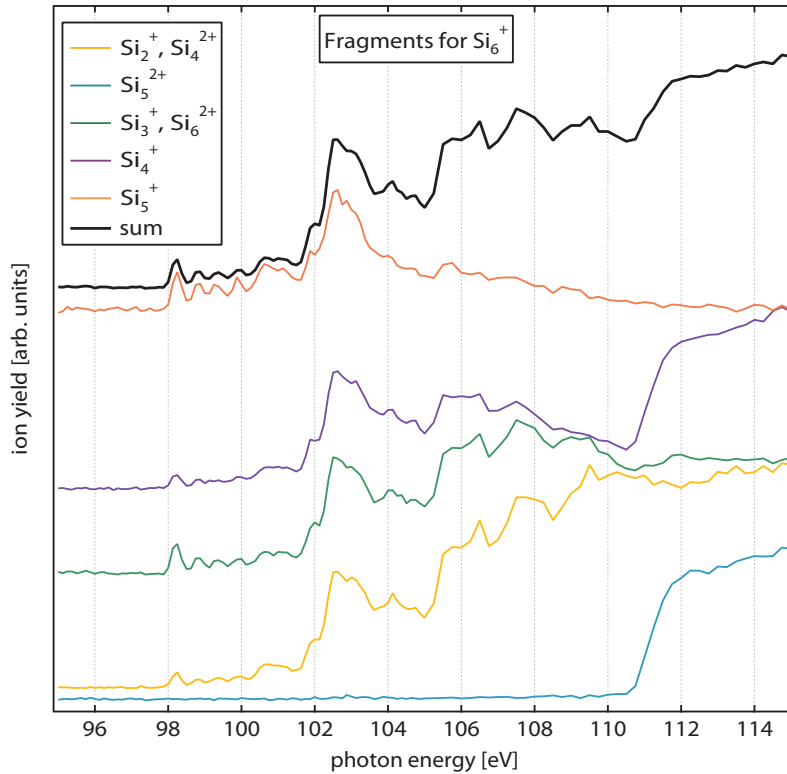
FIG. 2: Partial ion yield spectra for different fragments for parent cluster Si_6^+.

three categories. Fragments only generated for small energies from resonant excitation, fragments only generated for high energies from direct photoionization, and fragments generated from both resonant excitation and direct ionization (cp. Si_5^+, Si_5^{2+}, and Si_4^+ in figure 2, respectively). The fragments in the second category exhibit a quite abrupt rise in intensity at the 2p ionization threshold, which can directly be extracted from our data. We determined this threshold for clusters Si_n^+ ($n = 6 - 60$), which is plotted against the inverse radius together with values for the atom [2] and the bulk [3] in figure 3. As expected the threshold gets smaller for larger clusters. But moreover it evolves in a linear manner, which is perfectly in agreement with a metallic droplet model. In contradiction to earlier investigations on the valence band ionization of neutral silicon clusters [4] we see no significant step between Si_{20}^+ and Si_{22}^+ which was for the neutral clusters suggested to occur due to changes in isomer geometries [4].
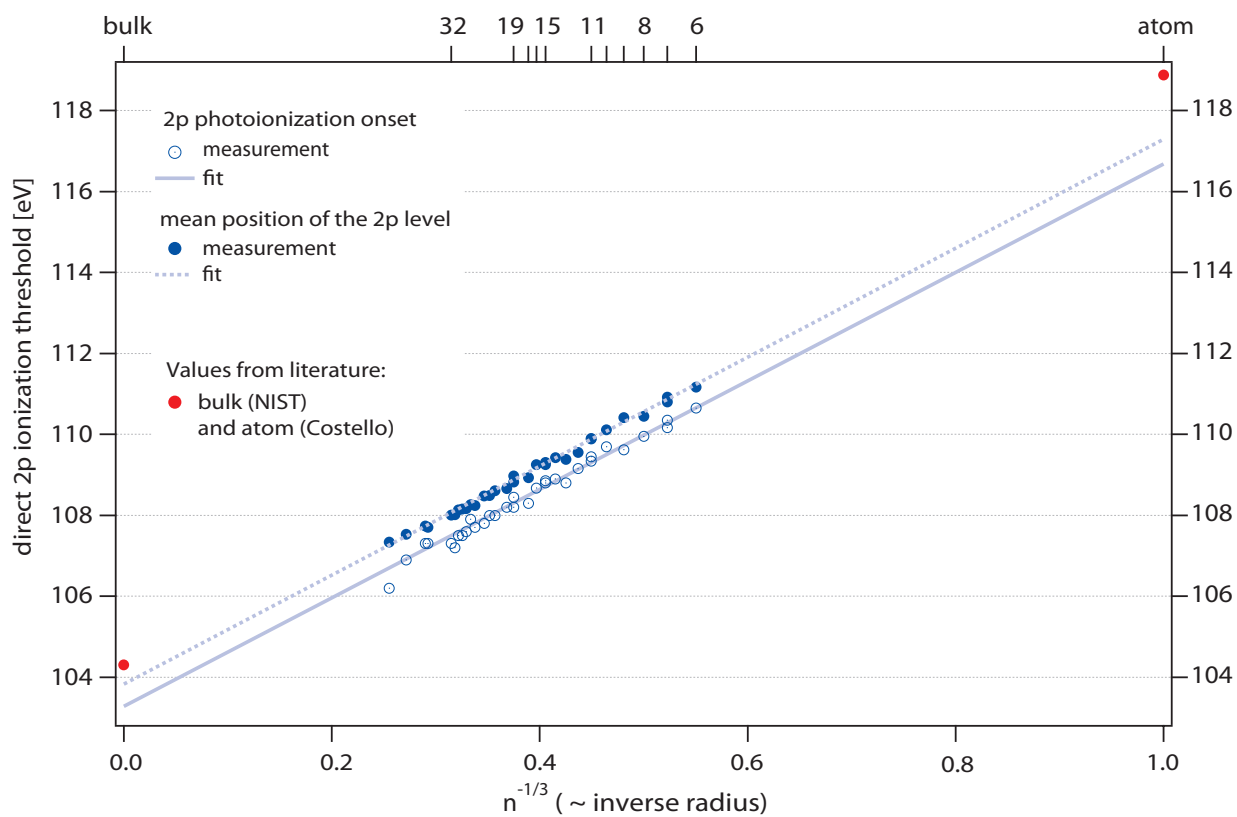
FIG. 3: Direct 2p photoionization threshold for silicon clusters.

[1] S. Shin, A. Agui, M. Watanabe, M. Fujisawa, Y. Tezuka, and T. Ishii, Phys. Rev. B **53**, 15 660 (1996).

[2] J. T. Costello, E. T. Kennedy, J.-P. Mosnier, and M. H. Sayyad, J. Phys. B: At. Mol. Opt. Phys. **31**, 677 (1998).

[3] XPS - NIST X-Ray Photoelectron Spectroscopy Database, URL `http://srdata.nist.gov/`.

[4] K. Fuke, K. Tsukamoto, F. Misaizu, and M. Sanekata, J. Chem. Phys. **99**, 7807 (1993).

X-ray Spectroscopy Reveals High Symmetry and Electronic Shell Structure of Transition Metal Doped Silicon Clusters

J. Rittmann[1], K. Hirsch[1], Ph. Klar[1], A. Langenberg[1], F. Lofink[1], J. Probst[1], R. Richter[1], M. Vogel[1], V. Zamudio-Bayer[1], T. Möller[1], Bernd v. Issendorff[2], and J.T. Lau[1]

[1] Technische Universität Berlin, Institut für Optik und Atomare Physik, EW 3-1, Hardenbergstraße 36, D-10623 Berlin

[2] Albert-Ludwigs-Universität Freiburg, Fakultät für Physik/FMF, Stefan-Meier-Straße 21, D-79104 Freiburg

e-mail: tobias.lau@tu-berlin.de

Doped silicon clusters are perfect examples of tailoring nanoparticle properties by choice of size and composition. Since silicon prefers sp^3 bonding or even higher coordinated bonds, pure silicon clusters tend to form complex and rather compact structures. Incorporation of a single impurity atom, however, rearranges the geometric and electronic structure of small silicon clusters completely. In particular, this can lead to a stabilization of otherwise unfavorable cage structures [1]. Prominent examples are $ScSi_{16}^-$, $TiSi_{16}$, and VSi_{16}^+, which are highly stable and therefore largely abundant in mass spectra [2,3] because of simultaneous electronic and geometric shell closure [4,5].

Despite a wealth of of theoretical and experimental work the electronic structure and nature of bonding in these silicon cages is still controversial. Two competing models are commonly used, rationalizing the electronic structure obtained from *ab initio* calculations either on the basis of the empirical 18 (in this case rather 20) electron rule known for transition metal compounds in chemistry, or on electronic shell closure of delocalized electrons in a spherical potential model combined with an approximate selection rule for the angular momentum. In a simplified description, the first model explains stability on the grounds of electronic shell closure at the transition metal atom, while the second model considers electronic shell closure in the spherical potential of the entire cluster cage.
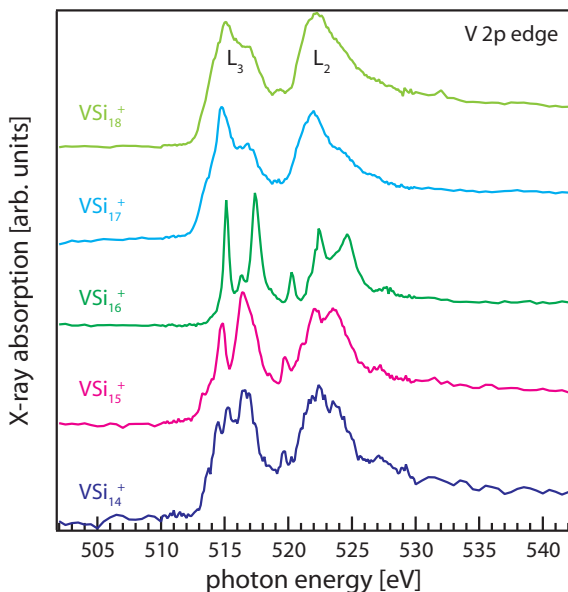
Figure 1: $L_{2,3}$ x-ray absorption spectra of size-selected VSi_n^+ clusters ($n = 14-18$). The VSi_{16}^+ spectrum is characterized by the sharpest lines, indicating a high symmetry cage and high degeneracy of the electronic levels. The double peak structure can be linked to the electronic density of states in tetrahedral symmetry.

We have used element-specific x-ray absorption spectroscopy on size-selected free clusters [6,7] to clarify the local electronic structure of the dopant atom that leads to the exceptional stability of doped silicon cages. Transition metal doped silicon cluster cations are produced in a magnetron sputtering source by co-sputtering of two targets. After size-selection in a quadrupole mass selector, clusters are stored in a liquid nitrogen cooled linear Paul trap. Along the trap axis, electronic transitions are excited by a collinear beam of tuneable soft x-ray radiation. Ions are subsequently extracted from the trap and are analyzed in a time-of-flight mass spectrometer. X-ray absorption spectra are obtained in ion yield mode by monitoring the yield of cluster fragment ions as a function
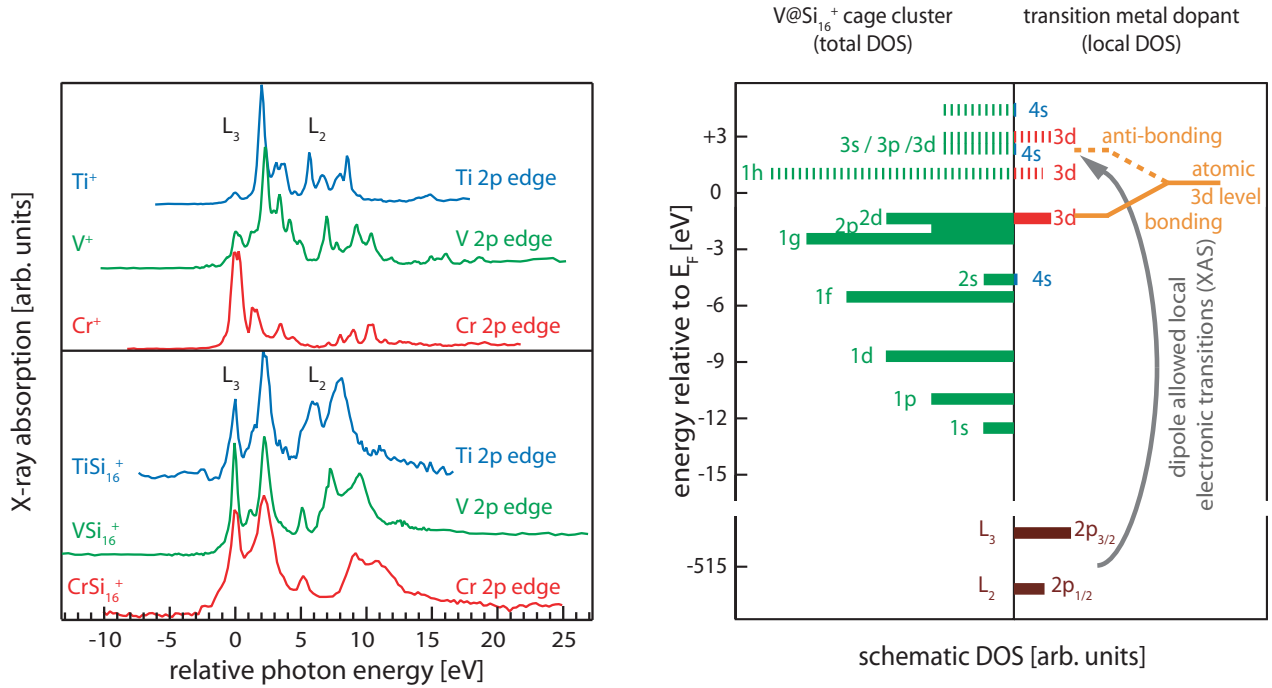
Figure 2: Left: Transition metal $L_{2,3}$ x-ray absorption spectra of $TiSi_{16}^+$, VSi_{16}^+, and $CrSi_{16}^+$ in the lower panel, and of bare Ti^+, V^+, and Cr^+ [6] in the upper panel. The spectra are aligned at the first peak position. While bare ions show differing spectra, the relative excitation energy in doped silicon clusters is nearly identical. In the titanium spectrum, the 5 eV feature of the L_3 line is partially masked by overlapping L_2 intensity. Right: Schematic view of the VSi_{16}^+ density of states. The total DOS is shown in the left panel while the local l-projected DOS at the dopant site [5] is shown in the right panel. In XAS at the spin-orbit split metal 2p levels, only transitions into *local*, d- or s-projected states are allowed. Therefore, only states marked in dashed blue ($4s$) and dashed red ($3d$) are probed.

of incident photon energy.

Vanadium $L_{2,3}$ x-ray absorption spectra of free, size-selected VSi_n^+ clusters with n=14–18 are presented in Fig. 1. In comparison to other clusters, the spectrum of VSi_{16}^+ exhibits the best resolved structure, which indicates a high degeneracy of electronic levels and a high symmetry of this cluster. Adding or removing silicon cage atoms lowers the symmetry and broadens electronic transitions as in VSi_{17}^+ or VSi_{15}^+.

When keeping the number of silicon atoms constant but changing the dopant atom from vanadium to titanium and chromium, the number of valence electrons in the cluster is changed by ± 1. The resulting x-ray absorption spectra of $TiSi_{16}^+$, VSi_{16}^+, and $CrSi_{16}^+$ are shown in the lower panel of Fig. 2. For ease of comparison, the spectra are aligned at the first peak position of the transition metal L_3 excitation and are given on a relative photon energy scale. Surprisingly, titanium, vanadium, and chromium exhibit a very similar fine structure in their x-ray absorption spectra; the relative excitation energies are practically identical for all three dopant atoms. Not only the intense lines at 0 eV and 2.1 eV, but also the less intense features at 1.1 eV and 5.0 eV are reproduced in all spectra. This indicates a nearly identical local electronic density of states at the transition metal atoms and a very similar geometry of their environment, as x-ray absorption spectroscopy is very sensitive to both [8]. For comparison, the spectra of the bare transition metal ions are displayed in the upper panel of Fig. 2. As expected, the multiplet structure is characteristic for each element and reflects the differences in electronic structure, namely the different d-orbital occupancies. Apparently, these differences disappear when the atoms are embedded into Si_{16} cages. Here, titanium and chromium adopt the the local electronic structure of vanadium in VSi_{16}^+ in spite of their differing number of valence electrons. Obviously, the interaction with the highly symmetric cage determines the elec-

tronic structure of the dopant.

These findings can be well understood within the spherical potential model [5, 9–11], which was originally developed to explain the nature of bonding in pure and endohedral fullerenes.The resulting schematic density of states of VSi_{16}^+ [5, 11] is shown in Fig. 2: A total of 68 valence electrons occupy all states of the 'σ' ($n = 1$) system up to $1g$ and of the 'π' ($n = 2$) system up to $2d$, which forms the highest occupied molecular orbital of the cluster. The lowest unoccupied molecular orbital has $1h$ character [5], and there is a large $2d$–$1h$ gap. The metal atom $3d$ orbitals contribute to the completely filled cage $2d$ orbital as well as to two narrow groups of unoccupied levels above the gap, which are about 2 eV apart. Since the $2p$ core hole is created locally at the vanadium dopant, and transitions are allowed from a vanadium $2p$ initial state into final states with d or s angular momentum character, these sharp features of the electron density of states show up in the x-ray absorption spectra.

In the case of 'non-magic' $TiSi_{16}^+$ and $CrSi_{16}^+$ cage clusters with 67 and 69 valence electrons, respectively, the energetic ordering of the orbitals should remain very similar, as the nearly identical spectra in Fig. 2 demonstrate that the silicon cage retains its highly symmetric structure. In $CrSi_{16}^+$, the additional valence electron is then accommodated in the $1h$ orbital above the $2d$–$1h$ gap. Because of the dominant silicon contribution to this $1h$ orbital, the electron can be expected to reside mainly at the silicon cage. The local $4s$ and $3d$ electronic states which are probed by chromium $L_{2,3}$ x-ray absorption spectroscopy are therefore hardly affected by the additional valence electron, for which reason the $CrSi_{16}^+$ and VSi_{16}^+ x-ray absorption spectra are nearly identical in their main features. The slight broadening observed for $CrSi_{16}^+$ is probably due to Jahn-Teller deformation because of the open electronic shell situation. Similarly, in the case of $TiSi_{16}^+$ with its 67 valence electrons, the electron missing to the closed electronic shell leads to a $2d^9$ configuration. Since the $2d$ orbital has most of its weight at the Si_{16} cage [5], only a fraction of the hole is located at the titanium dopant. Again, the small change in the local $3d$ occupancy has a negligible influence on the absorption spectrum. In the three cases of $TiSi_{16}^+$, VSi_{16}^+, and $CrSi_{16}^+$ considered here, the interaction with the electronic structure of the highly symmetric silicon cage results in a nearly identical local electronic structure of the dopant and leads to the very similar x-ray absorption spectra observed experimentally.

References

[1] V. Kumar and Y. Kawazoe, Phys. Rev. Lett. **87**, 045503 (2001).

[2] S. M. Beck, J. Chem. Phys. **87**, 4233 (1987).

[3] K. Koyasu, M. Akutsu, M. Mitsui, and A. Nakajima, J. Am. Chem. Soc. **127**, 4998 (2005).

[4] J. Ulises Reveles and S. N. Khanna, Phys. Rev. B **74**, 035435 (2006).

[5] M. B. Torres, E. M. Fernández, and L. C. Balbás, Phys. Rev. B **75**, 205425 (2007).

[6] J. T. Lau, J. Rittmann, V. Zamudio-Bayer, M. Vogel, K. Hirsch, P. Klar, F. Lofink, T. Möller, and B. v. Issendorff, Phys. Rev. Lett. **101**, 153401 (2008).

[7] K. Hirsch, J. T. Lau, P. Klar, A. Langenberg, F. Lofink, R. Richter, J. Rittmann, M. Vogel, V. Zamudio-Bayer, T. Möller, and B. v. Issendorff, submitted to J. Phys. B: At. Mol. Opt. Phys., (2009).

[8] F. M. F. de Groot, J. Electron Spectrosc. Relat. Phenom. **67**, 529 (1994).

[9] C. Yannouleas and U. Landman, Chem. Phys. Lett. **217**, 175 (1994).

[10] K. Jackson and B. Nellermoe, Chem. Phys. Lett. **254**, 249 (1996).

[11] V. Kumar, Comp. Mater. Sci. **36**, 1 (2006).

Atomic Localization of 3d Valence Electrons in Cr_2^+, Mn_2^+, and $CrMn_2^+$ Dimer Cations

K. Hirsch[1], Ph. Klar[1], A. Langenberg[1], F. Lofink[1], J. Probst[1], R. Richter[1], J. Rittmann[1], M. Vogel[1], V. Zamudio-Bayer[1], T. Möller[1], Bernd v. Issendorff[2], and J.T. Lau[1]

[1] Technische Universität Berlin, Institut für Optik und Atomare Physik, EW 3-1, Hardenbergstraße 36, D-10623 Berlin

[2] Albert-Ludwigs-Universität Freiburg, Fakultät für Physik/FMF, Stefan-Meier-Straße 21, D-79104 Freiburg

e-mail: tobias.lau@tu-berlin.de

X-ray absorption spectroscopy provides direct evidence for atomic localization of $3d$ valence electrons in Cr_2^+, Mn_2^+, and $CrMn^+$ dimer cations. Bonding in these transition metal molecules is solely mediated by $4s$ electrons. This can be ascribed to the stable $3d^5$ configuration in chromium and manganese atoms and is markedly different from other $3d$ transition metal dimers with open $3d$ sub-shells, where $3d$ valence electrons participate in bonding.

In $3d$ transition metals, $3d$ electrons are usually considered valence electrons which participate in chemical bonding. This is because of their binding energy, which is close to that of the $4s$ electrons. Considering their radial distribution function, however, $3d$ electrons could also be considered core electrons because of the contracted $3d$ wave function. Among the $3d$ transition metals, chromium and manganese are unique because of their half filled $3d$ shell and stable $3d^5$ configurations with high spin ^7S and ^6S ground states. Apart from single atoms, dimers are the simplest transition metal species, but even these are not fully understood. Again, especially chromium and manganese with their half-filled $3d$ shell still pose problems to theoreticians.
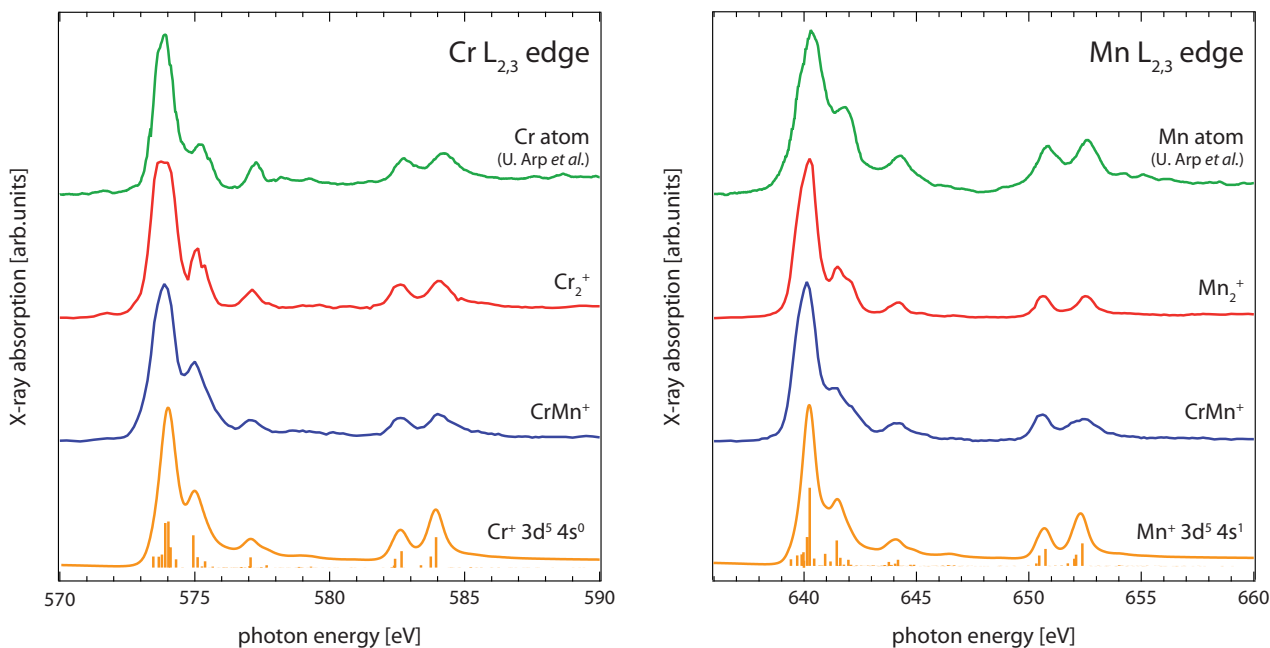
Figure 1: Left: Resonant X-ray absorption spectra of atomic chromium [1], Cr_2^+, and $CrMn^+$ at the chromium $2p$ edge. **Right:** Resonant X-ray absorption spectra of atomic manganese [2], Mn_2^+, and $CrMn^+$ at the manganese $2p$ edge. All spectra are dominated by $2p \rightarrow 3d$ transitions and can be reproduced by atomic multiplet calculations assuming a $3d^5$ initial state configuration. This directly shows an atomic localization of $3d$ electrons.

X-ray absorption spectroscopy can be used as a fingerprint method, where the electronic configuration can in many cases be deduced directly from the spectrum without the need for extensive theoretical calculation. This is especially true for distinguished configurations with empty, filled, of

half-filled electronic shells. We have performed X-ray absorption spectroscopy on pure and mixed chromium and manganese dimer cations to clarify the degree of $3d$ electron localization. The experimental setup is described in detail elsewhere [3, 4]. Briefly, cationic transition metal dimer molecules are produced by magnetron sputtering, mass separated, and stored in a buffer gas filled ion trap at liquid nitrogen temperature. X-ray absorption spectra are taken in ion yield mode, monitoring the yield of photo-generated daughter ions as a function of incident photon energy.

Chromium and manganese dimer cations are markedly different from other transition metal dimers with respect to their X-ray absorption spectrum. While the spectra of $3d$ transition metals with open $3d$ shells differ from their atomic counterparts, Cr_2^+ and Mn_2^+ show strikingly spectra strikingly similar to their neutral atoms, as is evident from Figures 1 and 2.
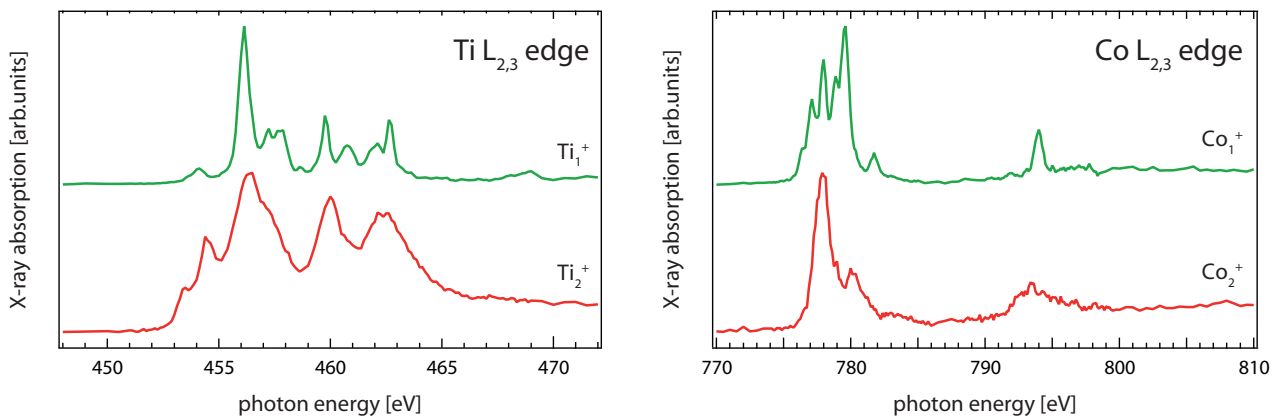
Figure 2: 2p X-ray absorption spectra of Ti_1^+ and Ti_2^+ (left) and of Co_1^+ and Co_2^+ (right). In titanium and cobalt dimer cations, $3d$ electrons participate in bonding.

Resonant X-ray absorption spectra taken at the chromium $2p$ edge of chromium atoms [1], Cr_2^+, and $CrMn^+$ are shown in Fig. 1. All three spectra are nearly identical in their transition energies and intensities. Compared to the atomic chromium spectrum [1], features in Cr_2+ are better resolved because of a higher monochromator resolution of 150 meV as compared to 290 meV. As in atomic chromium, the Cr_2^+ spectrum represents a purely atomic $[Ar]3d^54s^0$ or $[Ar]3d^54s^1$ initial state configuration, as can be seen by comparison with an atomic multiplet calculation. The experimental spectrum can be reproduced by calculating transitions from a cationic $[Ar]3d^54s^0$ initial state configuration into a $2p^53d^64s^0$ final state configuration. Final states with $3d^54s^1$ or $3d^54s^04d^1$ configurations do not contribute significantly to the spectrum, as can be understood from the much smaller overlap of the $2p$ wave function with $4s$ or $4d$ as compared to $3d$. Varying the initial state to $[Ar]3d^54s^1$ does not lead to changes in the spectrum, as transitions from $2p$ into $4s$ states do not contribute significantly. A lifetime broadening of 250 meV together with the experimental resolution of 150 meV was used in the calculations.

From the spectral fingerprint of Cr_2^+, we conclude that all $3d$ electrons are atomically localized at their ionic cores and do not participate in bonding. Bonding in Cr_2^+ is mediated solely by the remaining $4s$ electron, shared between the two atoms in a bonding $(4s\sigma_g)^1$ configuration. This is consistent with an anti-ferrimagnetic $^2\Sigma_g^+$ ground state predicted from theory [5] as well as from collision induced dissociation [6].

Very similar results are found for manganese, the second element in the $3d$ row with a half-filled $3d$ shell. Manganese $2p$ x-ray absorption spectra of Mn_2^+, $CrMn^+$, and atomic manganese [2] are shown in Fig. 1, together with an atomic multiplet calculation. Again, the dimer cation spectrum shows more details because of a higher monochromator resolution. Similar to chromium, the experimental spectrum can be reproduced with an atomic multiplet calculation taking $3d^54s^1$ as the initial state configuration and $3d^64s^1$ as the final state configuration. In all cases, the spectrum is dominated by $2p \rightarrow 3d$ transitions; taking also $2p \rightarrow 4s$ or $2p \rightarrow 4d$ transitions into account does

not further improve of the already very good agreement between theory and experiment. As in Cr_2^+, $3d$ electrons in Mn_2^+ are non-bonding, localized at their ionic cores. The remaining three $4s$ electrons are situated in a fully occupied ($4s\ \sigma$) bonding orbital and a singly occupied antibonding ($4s\ \sigma^*$) orbital. The experimental result is consistent with a ferromagnetically coupled $^{12}\Sigma_g^+$ high spin state found by electron spin resonance on matrix isolated Mn_2^+ [7, 8] and by photodissociation spectroscopy [9].

Given the results on Cr_2^+ and Mn_2^+, the question arises of how $3d$ electrons behave in mixed $CrMn^+$ dimer cations. Considering the number of $4s$ electrons, these mixed dimer cations are in between pure Cr_2^+ and Mn_2^+. This question can again be answered by resonant $2p$ x-ray absorption spectroscopy because of its element specific nature. The spectra of mixed dimer cations are also shown in Fig. 1. Although these are recorded with the same energy resolution of 150 meV, the lines in the mixed dimer cations are broadened but can still be reproduced by atomic multiplet calculation with $3d^5$ initial state configurations and $2p \rightarrow 3d$ transitions, indicating atomic localization of $3d$ electrons also in the mixed dimer cation.

In summary, we have shown how X-ray absorption spectroscopy on size-selected cluster and molecular ions can contribute to the understanding of bonding. Addressing the interesting question of magnetic coupling in gas phase transition metal dimer cations and clusters will become feasible with further developments of ion trapping techniques for X-ray magnetic circular dichroism spectroscopy, so far only applicable to supported species [10].

References

[1] U. Arp, K. Iemura, G. Kutluk, T. Nagata, S. Yagi, and A. Yagishita, J. Phys. B: At. Mol. Opt. Phys. **28**, 225 (1995).

[2] U. Arp, F. Federmann, E. Källne, B. Sonntag, and S. L. Sorensen, J. Phys. B: At. Mol. Opt. Phys. **25**, 3747 (1992).

[3] J. T. Lau, J. Rittmann, V. Zamudio-Bayer, M. Vogel, K. Hirsch, P. Klar, F. Lofink, T. Möller, and B. v. Issendorff, Phys. Rev. Lett. **101**, 153401 (2008).

[4] K. Hirsch, J. T. Lau, P. Klar, A. Langenberg, F. Lofink, R. Richter, J. Rittmann, M. Vogel, V. Zamudio-Bayer, T. Möller, and B. v. Issendorff, submitted to J. Phys. B: At. Mol. Opt. Phys., (2009).

[5] G. Gutsev and C. Bauschlicher, J. Phys. Chem. A **107**, 4755 (2003).

[6] C.-X. Su, D. A. Hales, and P. B. Armentrout, Chem. Phys. Lett. **201**, 199 (1993).

[7] R. J. van Zee and W. Weltner, Jr., The Journal of Chemical Physics **89**, 4444 (1988).

[8] M. Cheeseman, R. J. V. Zee, H. L. Flanagan, and J. W. Weltner, J. Chem. Phys. **92**, 1553 (1990).

[9] A. Terasaki, A. Matsushita, K. Tono, R. T. Yadav, T. M. Briere, and T. Kondow, J. Chem. Phys. **114**, 9367 (2001).

[10] J. T. Lau, A. Föhlisch, R. Nietubyc̀, M. Reif, and W. Wurth, Phys. Rev. Lett. **89**, 057201 (2002).

Core-level structure of $C_{60}F_{18}$ and $C_{60}F_{36}$ studied by photoelectron spectroscopy

V.M. Mikoushkin[1], V.V. Shnitov[1], V.V. Bryzgalov[1], Yu.S. Gordeev[1], O.V. Boltalina[2,3],
I.V. Gol'dt[2], S.L. Molodtsov[4,5], D.V. Vyalikh[4]

[1] *Ioffe Physical-Technical Institute RAS, St.-Petersburg, 194021, Russia*
[2] *Chemistry Department, Moscow State University, Moscow, 119899, Russia*
[3] *Chemistry Department, Colorado State University, Fort Collins, 80523, USA*
[4] *Institut für Festkörperphysik, Technische Universität Dresden, D-01062 Dresden, Germany*
[5] *Institute of Physics, St. Petersburg State University, 198904 St. Petersburg, Russia*

Abstract. X-ray photoelectron spectra of solid fluorinated fullerenes $C_{60}F_x$ (x = 18, 36) were measured in comparison with parent C_{60} using synchrotron radiation. Core-level binding energies of carbon and fluorine were measured and the former data were revised. It was revealed that the binding energy of 1s electron in fluorine atoms and in the carbon atoms bounded with fluorine does not practically depend on the number of fluorine atoms in molecule. It was shown that C-F link has ionic type and does not change the character in variation of the number of fluorine atoms in molecule.

Introduction

Fluorination of carbon nanotubes and fullerenes has been considered as potentially important modification method for novel material applications. Of particular interest are stable fluorinated fullerenes $C_{60}F_x$ with certain number of fluorine atoms per fullerene *x* = 18, 36, 48, for which synthetic methodologies have been perfected in the recent years [1-3]. Core-level structure of these molecules in the condensed state has been intensively studied by X-ray photoelectron spectroscopy (XPS) to control the element composition and to characterize chemical bondings [4-9]. Two peaks were observed in the C1s XPS spectra of carbon. One of them is connected with C-C bonding of carbon atoms only and another one was attributed to C-F bonding of carbon with fluorine atom. The binding energy of C1s electron corresponding to the second peak is higher then that of the first one. Relative intensities of these peaks gave the number of fluorine atoms in molecule and made possible rather accurate element control of fluorofullerenes under study. Unfortunately, reliability of the information about binding energies proved to be unsatisfactory. For example, the C-F binding energy of C1s in $C_{60}F_{43-48}$ measured in Ref. [4, 8, 7, 5, 6] are E_b (C1s, C-F) = 287.2, 287.4, 288.4, 290.5, and 291.1 eV correspondingly. Wide range of the obtained values (3.9 eV) evidences for systematic errors made at list in some of the researches. The main goal of this study was to verify the binding energies of carbon and fluorine C1s electrons in fluorofullerens $C_{60}F_{18}$ and $C_{60}F_{36}$ taking into account that these molecules are characterized by dielectric properties and by low radiation stability [9, 10].

Experimental details

The experiment was performed at the BESSY storage ring at the Russian-German synchrotron radiation (SR) beamline equipped with the plane-grating monochromator (PGM) and with the experimental station of the Russian-German laboratory [11]. Photoelectron spectra were collected using a hemispherical analyzer VG CLAM-4. Thin films of C_{60}, $C_{60}F_{18}$ and $C_{60}F_{36}$ were grown in the preparation chamber of the spectrometer by evaporation of the high-purity solid compounds onto Si and gold substrates just before measurements. The vacuum during deposition falls up to ~ $5 \cdot 10^{-9}$ Torr. Powders of $C_{60}F_{18}$ and $C_{60}F_{36}$ were synthesized by the technology described earlier [3]. Thin SiO_2 interlayer was used to prevent both chemical interaction of fullerenes with Si substrate. This layer was a part of the layer of thin (~ 1 nm) native oxide remained after annealing the substrate at ~ 1000 °C. Heating at ~
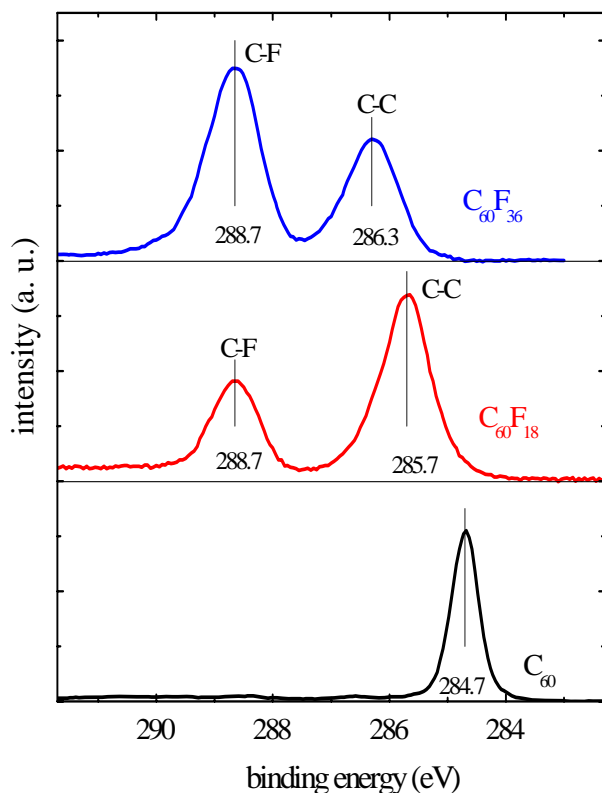
700 °C was used for cleaning the substrate and removal of fullerene films. Thickness of fullerene films was estimated by the control of the weakening the substrate photoelectron lines. The energy scale of the photoelectron (PE) spectra of fluorinated fullerenes was calibrated by measuring the spectra of thin films grown on the atomically clean surface of gold. The thickness of the film was small enough to detect Au $4f_{7/2}$ line. At the same time, the thickness was made larger than the mean free path $\lambda \sim$ 1 ML of ejected electrons to significantly diminish the contribution of the interface layer of molecules to PE spectrum. The binding energy $E_b = 84.0$ eV of the Au $4f_{7/2}$ electrons relative to the Fermi level was used as a reference energy. The accuracy of the obtained binding energies does not exceed ± 0.2 eV.

Fig. 1. C1s photoelectron spectra of the films of C_{60}, $C_{60}F_{18}$ and $C_{60}F_{36}$.

Core-level structure of $C_{60}F_{18}$ and $C_{60}F_{36}$

Fig. 1 demonstrates carbon C1s X-ray photoelectron spectra of the $C_{60}F_{18}$ and $C_{60}F_{36}$ films measured at the photon energy $h\nu = 800$ eV with relatively low energy resolution (FWHM = 1.0 – 1.1 eV) to shorten the exposition and to prevent modification of the materials. These XPS spectra are compared with the spectrum of C_{60} film previously measured by us at the photon energy $h\nu = 500$ eV with better energy resolution (FWHM = 0.55 eV). Two peaks corresponding to C-C and C-F bonds are seen in the spectra of fluorofullerenes in accordance with former data. Relative intensities of these peaks give reasonable composition of studied molecules: $C_{60}F_{20\pm1}$ and $C_{60}F_{36\pm1}$. However, values of the binding energies obtained in this work and represented in Table 1 are far from the data of Ref. [4, 5, 6, 8] excepting the binding energies E_b(C-C) = 286.2 eV and E_b(C-F) = 288.4 eV measured in Ref. [7] for $C_{60}F_{48}$ which proved to be close to our data for $C_{60}F_{36}$. The core-level binding energy of fluorine E_b (F1s) = 687.1– 687.3 eV measured in this work also differs noticeably from those obtained earlier: E_b (F1s) = 685.3 - 686.1 eV [8]. The possible reason of the discussed discrepancies may be in different ways of spectra calibration in different studies. Using insulator reference samples could result in systematic errors.

Table 1. Binding energies of 1s core electrons of carbon and fluorine in fluorofullerenes.

	E_b (C1s), eV			E_b (F1s), eV
	C-C	C-F	ΔE_b	F-C
$C_{60}F_{36}$	286.3	288.7	2.4	687.3
$C_{60}F_{18}$	285.7	288.7	3.0	687.1
C_{60}	284.7			
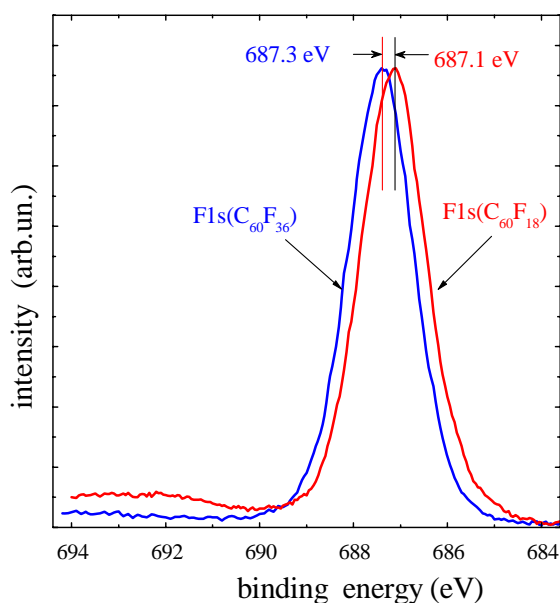
Fig. 2. F1s photoelectron spectra of the films of $C_{60}F_{18}$ and $C_{60}F_{36}$.

Fig.1 shows that the binding energy $E_b(C1s, C-F) = 288.7$ eV of 1s electron of carbon atom bounded with fluorine does not depend on the number of fluorine atoms in molecule. Fluorine F1s spectra of $C_{60}F_{18}$ and $C_{60}F_{36}$ represented in Fig.2 also show the practical absence of the dependence of the binding energy $E_b(F1s, F-C) = 687.1 - 687.3$ eV on the extent of fluorination of molecule. The observed independence of the binding energies evidences for identity of C-F bonds in different fluorofullerens with different number of fluorine atoms and different atomic structure. The conclusion can be made about the identical type of C-F chemical bonding in different fluorofullerenes. Large chemical shift $\Delta E_b(C-F) = 288.7 - 284.7 = 4.0$ eV of the C-F chemical state relative to the C-C state in parent fullerene C_{60} points out to ionic type of the link. Notice, that C1s C-F binding energies were dependent on fluorination extent in Ref. [6, 8].

Fig.1 and Table 1 show that the difference ΔE_b between C1s C-C and C-F peaks decreases in enhancement of the number of fluorine atoms in molecule similarly to Ref. [6, 8]. This difference was assigned in Ref. [6, 8] to be a measure of the strength of C-F bond. The variation of the binding energy difference ΔE_b was interpreted in Ref. [6, 8] as a result of transformation of the character of chemical C-F bonding form semi-ionically type in the compounds with lower fluorine content to covalent type links for highly fluorinated fullerenes. We came above to different conclusion about invariability of the C-F link and believe that the discussed difference can not be used as a characteristic of C-F bonding. The chemical shift of the C1s C-F photoelectron peak should be counted from the reference chemical C-C state in parent fullerene C_{60}. The reason of the shift of C1s C-C peak to higher binding energies resulting in decrease of the difference ΔE_b on fluorination was assumed to be in diminution of relaxation energy due to reduction of the number of π-electrons on fluorination.

References:

[1] O.V. Boltalina, S.H. Strauss, "Fluorinated Fullerenes", in Dekker Encyclopedia of Nanoscience and Nanotechnology: New York, Marcel Dekker, 2004, eds. J. A. Schwarz, C. Contescu, K. Putyera, p. 1175-1190.

[2] O.V. Boltalina, N.A. Galeva, Russ. Chem. Rev. 69 (2000) 609.

[3] I.V.Goldt, O.V. Boltalina, E. Kemnitz, I. Troyanov, Solid State Sci. 4 (2002) 1395.

[4] P.J. Benning, T.R. Ohno, J.H. Weaver, et al., Phys. Rev. B 47 (1993) 1589.

[5] D.M. Cox, S.D. Cameron, A. Tuinman, et al., J.Am. Chem. Soc. 116 (1994) 1115.

[6] Y. Matsuo, T. Nakajima, S. Kasamatsu, et al., J. Fluor. Chem. 78 (1996) 7.

[7] R. Mitsumoto, T. Araki, E. Ito, et al., J. Phys. Chem. A 102 (1998) 552.

[8] A.P. Dement'ev, O.V. Boltalina, D.B. Ponomarev, N.A. Galeva, Proceedings - Electrochemical Society, 2001-11 (2001) 559.

[9] V.M. Mikoushkin, M.S. Galaktionov, V.V. Shnitov, et al., Bulletin of the BESSY Annual Report (2006), Berlin, 2007, 202.

[10] V.V. Shnitov, V.M. Mikoushkin, Yu.S. Gordeev, et al., Fullerenes, Nanotubes and Carbon nanostrucrutes 14 (2006) 297.

[11] S.I. Fedoseenko, D.V. Vyalikh, I.E.Iossifov, et al., Nucl. Instr. Meth. A 505 (2003) 718.

The electron energy band structure of graphene formed on different nickel single crystal surfaces

D. Usachov[1], D. Marchenko[1], A.M. Shikin[1], V.K. Adamchuk[1], A. Varykhalov[1,2], O. Rader[2]

[1]St. Petersburg State University, 198504 St. Petersburg, Russia
[2]BESSY, 12489 Berlin, Germany

Graphene is considered to be a perspective material for nanoelectronics [1]. It can be formed on a number of materials with different crystal structure. The substrate on which graphene is synthesized can have a substantial influence on its morphology and electronic structure. This gives the possibility to modify graphene the way we want choosing an appropriate substrate. But to do this we have to know how a certain substrate affects the properties of graphene. We have carried out investigations of the crystal structure of graphene formed on different crystal faces of nickel [2]. It is well known that on the Ni(111) surface having a hexagonal surface lattice, graphene forms a commensurate (1x1) structure as a result of the similarity of their lattice parameters. Our theoretical study of the graphene atomic structure on single-crystal surface Ni(110) with rectangular unit cell shows that graphene in such a system appears to be incommensurate with respect to the substrate. Moreover, due to strong chemical interaction with the substrate its crystal lattice is deformed reflecting the substrate relief. This result is confirmed by our STM investigations. Strong interaction in the adsorbate-substrate system also should inevitably have an influence on the graphene electronic structure. This work is devoted to the investigation of this influence. In order to study the influence of the nickel substrate structure on the graphene electronic structure we carried out investigations of the valence band electronic structure of the graphene formed on different nickel faces, namely on Ni(110), Ni(755) and Ni(771). Crystal faces Ni(755) and Ni(771) are stepped surfaces vicinal to planar faces (111) and (110), respectively. Our previous investigations showed that during graphene synthesis these surfaces undergo faceting. As a result the Ni(755) surface appears to be formed by crystal faces (111) and (311), while the Ni(771) surface – by faces (110) and (331). This gives the possibility to study the graphene structure on these four different surfaces.

(a)   (b)
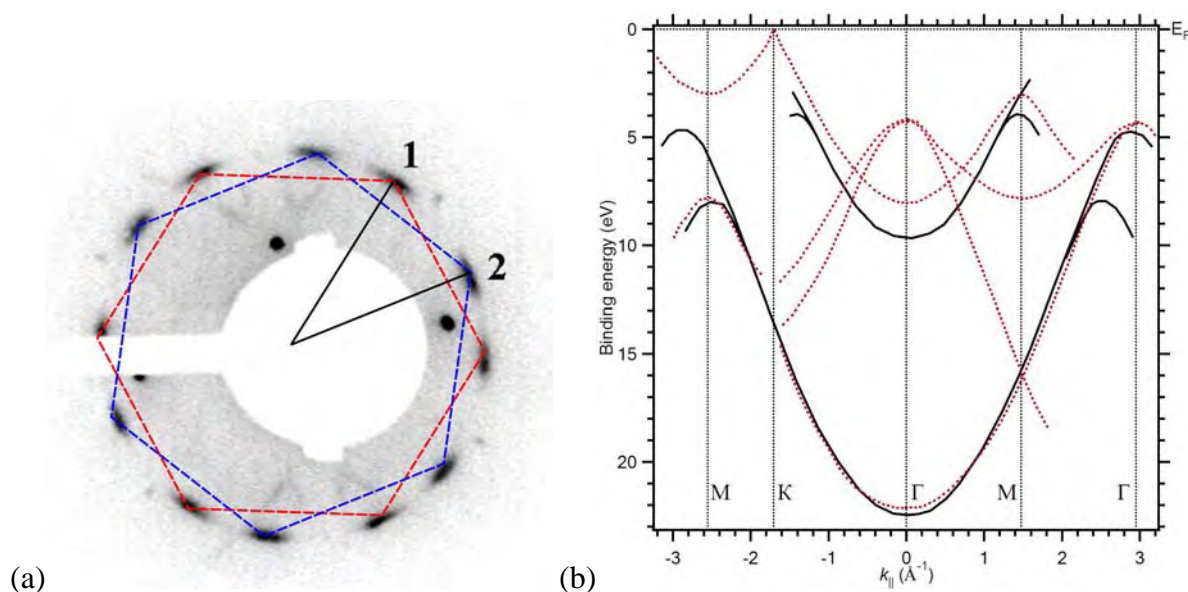
Fig. 1. (a) LEED pattern of the system graphene/Ni(110). (b) Experimentally measured electronic structure of the graphene valence band at photon energy 50 eV in the case of Ni(110) substrate (solid line) in comparison with the experimental graphite band structure (dotted line) taken from Ref. [3].

Atomically clean, well ordered Ni(110), Ni(755) and Ni(771) surfaces were prepared in ultrahigh vacuum by alternately subjecting single-crystal surfaces to Ar ion sputtering and short heating, and characterized by LEED. The graphene layer was synthesized by propylene cracking at partial pressure 10^{-6} mbar and temperature 500º C. To measure the graphene valence band electronic structure we used ultra-violet angle-resolved photoelectron spectroscopy. All measurements were carried out on the Russian-German beamline.

Graphene formed on the Ni(110) surface has a domain structure with two most preferred orientations with respect to the substrate. For this reason, in the LEED pattern there are two series of reflexes formed by two hexagons rotated with respect to each other (fig 1a). This makes the investigations of the electronic structure more complex, because both types of domains should contribute to the photoelectron spectra measured in a certain direction. Fortunately the rotation angle between the domains is close to 30º, that is why if we measure the graphene electronic structure in the high symmetry Brillouin zone direction ΓK of the first domain, then with respect to the second domain we measure in the other high symmetry Brillouin zone direction ΓM and we always get these two directions superimposed. This circumstance allows measuring the graphene electronic structure in both high symmetry directions simultaneously. In fig. 1b the solid line represents the results of measurements of the graphene electronic structure on the Ni(110) surface in the direction of one of the graphene LEED spots. For comparison the dotted line in the figure shows the graphite band structure in the two high symmetry directions ΓK (left half of the figure) and ΓM (right half of the figure). One can see that the graphene σ-band in its form and energy position is very close to the graphite σ-band. In contrast to the σ-band, the graphene π-band is shifted towards higher binding energies by nearly 1.7 eV. This shift is a result of the interaction between the graphene π-states and nickel d-states.
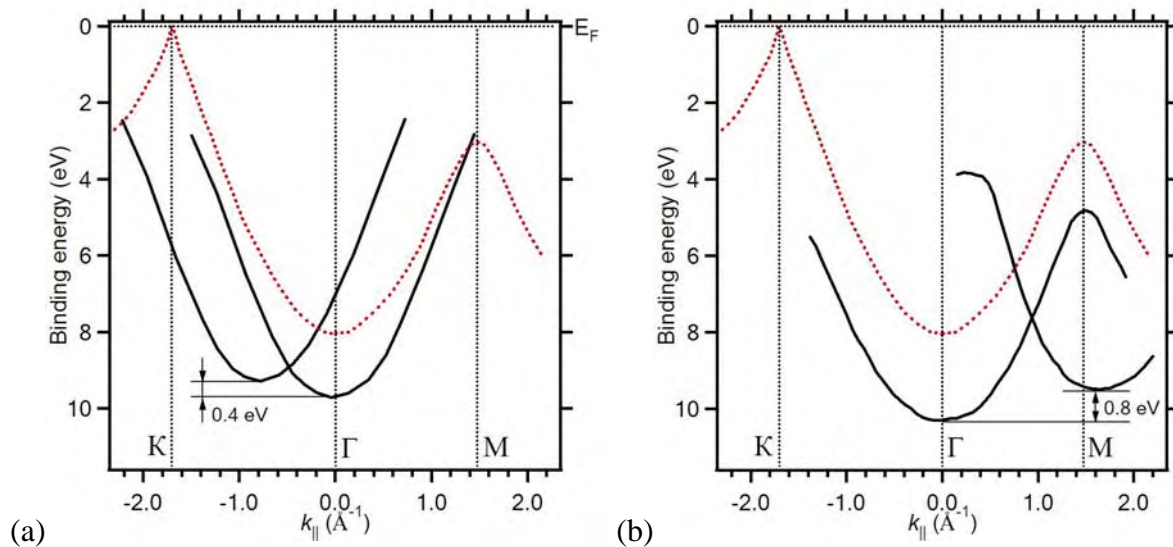
Fig. 2. Dispersion of graphene π-states (solid line) obtained experimentally (a) in the case of a Ni(771) substrate at a photon energy of 50 eV, (b) in the case of a Ni(755) substrate at a photon energy of 55 eV. For comparison the dispersion of the graphite π-states taken from Ref. [3] is shown with dotted lines.

The measured dispersion of the π-states of graphene on the faceted Ni(771) surface (fig. 2a) consists of two branches corresponding to graphene on the facets (110) and (331). The direction of measurements was chosen along the [001] direction, perpendicular to the facet edges. During calculation of the $k_{\parallel}$ the normal to the sample surface was chosen perpendicular to the (110) crystal plane. This is why the branch of π-states of the graphene on the (110) surface is symmetrical with respect to the Γ point and its energy position coincides

with the position of the branch obtained in measurements of the graphene/Ni(110) system. The π-branch of graphene on the (331) face is shifted by 13º away from the normal, which corresponds to the angle between the crystal faces (110) and (331). Its energy position differs from the position of the branch from the (110) surface on nearly 0.4 eV towards lower binding energies. This means the interaction of graphene with the (110) surface is stronger than with (331).

The results of measurements of the graphene electronic structure in the case of the Ni(755) substrate (fig. 2b) have nearly the same behavior. Here the normal to the sample surface was chosen perpendicular to the (111) crystal plane and the measurements were done in the direction perpendicular to facet edges. That is why the π-branch of the graphene on the (111) face is symmetrical with respect to the Γ point, and the branch of graphene on the (331) face is shifted by 29º away from normal, which corresponds to the angle between these faces. The energy position of the graphene π-band on the (311) face differs from the position on the (111) face by 0.8 eV, again towards lower binding energies.

The obtained data allow us to conclude that interaction of the graphene with nickel substrate results in a modification of the graphene electronic structure which appears mainly in the form of a shift of graphene π-states towards higher binding energies with respect to bulk graphite. The value of this shift depends on the crystal structure of the nickel surface and appears to be higher for more densely packed crystal faces, so the strength of the interaction increases in the set of nickel faces (331), (311), (110) and (111).

[1] K. S. Novoselov *et al.*, Science, **306**, 666 (2004).
[2] D. Usachov *et al.*, Phys. Rev. B **78**, 085403 (2008)
[3] Th. Seyller *et al.*, Surf. Sci. **600**, 3906 (2006)

Synchrotron Measurements of Residual Stresses in Thermal Barrier Coating Systems

André M.G. Luz

Department of Mechanical Engineering, Imperial College London,
South Kensington Campus, London SW7 2AZ, United Kingdom

1. Introduction

During the last two decades there has been an enormous effort to introduce thermal barrier coating (TBC) technologies for the manufacture of high temperature components for advanced gas turbine engines used in aircraft propulsion and land-based power generation. One of the main driving forces for this development is the desire to increase fuel gas temperatures, resulting in an improved thermal efficiency and thus making a primary contribution to the conservation of energy resources and to the limitation of CO_2 and other greenhouse gas emissions.

Current thermal barrier coatings are multilayered systems, where an aluminium-rich metallic bond coat (e.g. MCrAlY, where M is a combination of Ni and Co) is deposited on the superalloy, followed by ceramic top coat deposited on the bond coat and in contact with the hot gas. During processing and thermal exposure, a third layer is formed between the bond coat and the top coat. This layer is commonly referred to as the thermally grown oxide (TGO), primarily made up by alumina (Al_2O_3). Yttira-stabilised zirconia (7-8 wt.% Y_2O_3 + ZrO_2 (YSZ)) is the most frequently used top coat material. The thermal barrier coating provides a temperature drop of up to 200 $^{\circ}$C due to its low thermal conductivity, which is enhanced by the intentionally porous microstructure. This porous design also allows for strain tolerance during thermal cycling, thereby preventing instantaneous spallation.

A major weakness of TBC systems is the interface between the metallic bond coat and the ceramic top coat. At this interface an in-service degradation is observed caused by debonding (delamination) of the coating, leading to a macroscopic spallation of the ceramic layer. The interface region undergoes high stresses due to the mismatch of thermal expansion between the layers. Additionally, growth stresses due to the development of the TGO at the interface and stresses due to interface roughness are superimposed. Stress relaxation at high temperature leads to reduced stress levels at the interface, but gives rise to enhanced stress accumulation after cooling down to room temperature, resulting in early crack initiation at the interface and spallation failure afterwards. Consequently, most current approaches relate TBC failure to the evolution of the stress levels at or near the TGO.

2. Residual Stress Close to Failure

The emphasis of the present study is to measure non-destructively the evolution of the local stresses within the TGO, as the TBC approaches the end of life. The depth-resolved analysis of the residual stresses in the near surface zone of the TBCs was carried out at the materials science beamline EDDI (Energy Dispersive DIffraction) at the Berlin synchrotron storage ring BESSY II. The high resolution ED synchrotron diffraction experiments were performed during a beamtime period of 10 days.

The oxide layer is more than one order of magnitude thinner than the two adjacent layers, bond coat and ceramic top coat, which makes its detection quite challenging. The TGO grows with thermal cycling following a parabolic law, so it is easier to start analysing the sample close to failure, as this

sample has the thickest oxide layer. Figure 1 plots a series of diffraction lines recorded by depth scanning the small gauge volume through the near surface of the TBC sample close to failure.
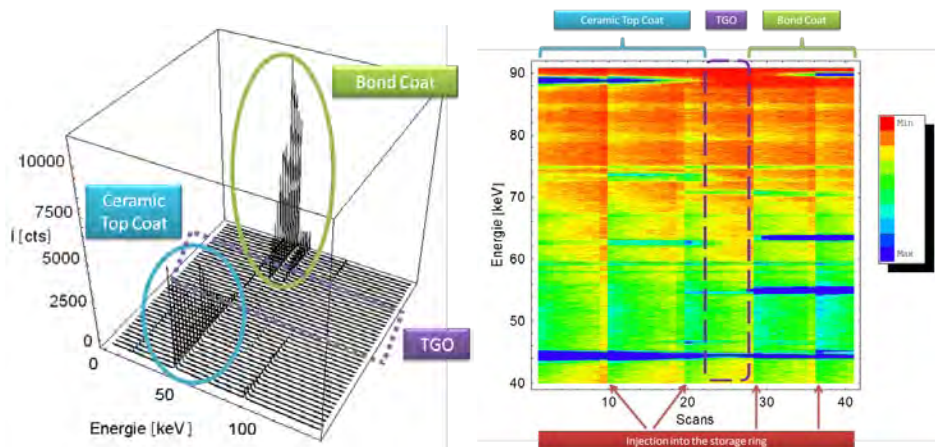
Figure 1 - 3D and 2D plots of a series of ED diffraction patterns recorded by depth scanning

The ceramic top coat and the bond coat show strong distinctive reflections, but even after an extremely long exposure time, the TGO exhibits very weak diffraction patterns. Figure 2 shows typical energy dispersive diffractograms for the three layers.
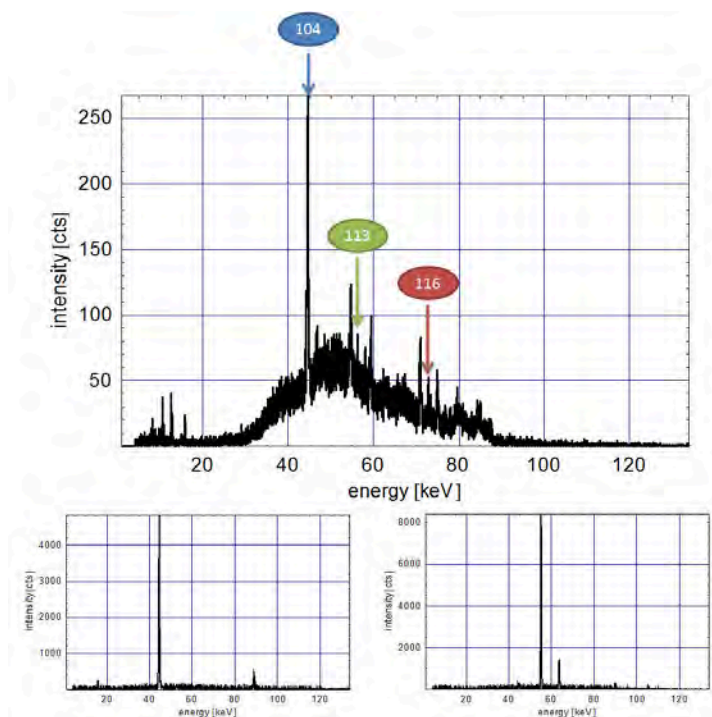
Figure 2 - ED diffractogram of the TGO (upper chart), ceramic top coat (left chart) and bond coat (right chart) for the TBC sample close to failure

Alumina has the strongest diffraction peak located at the 104 reflection, with an unstrained lattice energy $E_0 = 45.170\ keV$. However, as this peak overlaps with the reflection peak from the ceramic top coat, it is not appropriate for stress evaluation. The 113 reflection ($E_0 = 55.152\ keV$) displays the second highest intensity. In this case, the diffraction line is quite close to the reflection peak from the bond coat, so the 113 reflection was not considered suitable for strain measurement. The third biggest diffraction line occurs in the 116 reflection. As the unstrained lattice energy is $E_0 = 71.926\ keV$, the ED diffractogram in Figure 2 proves this peak is not overlapped with neighbouring

peaks. Therefore, the 116 reflection peak was chosen for strain depth profiling. The strained lattice energy measured in Figure 2 is $E = 72.619\ keV$. This means that the lattice strain of the TGO in the sample close to failure is $\varepsilon = -0.00954$, which corresponds to a residual stress of $\sigma = -3.624\ GPa$.

3. Residual Stress at Half-Life

The procedure described above for high resolution strain depth profiling was also followed for the TBC sample at half-life. The energy dispersive diffractogram of the TGO is depicted in Figure 3. The TGO at half-life is considerably thinner than the one close to failure. Thus, it is not possible to distinguish the 113 reflection from the background and the diffraction peak belonging to the bond coat. The 116 diffraction line is also quite close to another peak, but it is still clearly separated from its neighbours.
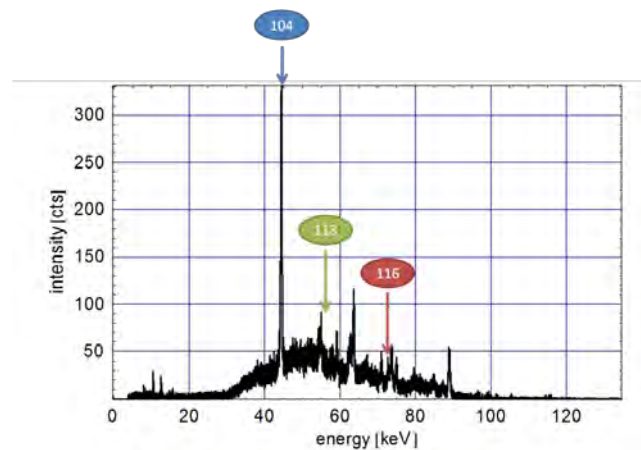
Figure 3 - ED diffractogram of the TGO for the TBC sample at half-life

The strained lattice energy measured in Figure 3 for the 116 reflection peak is $E = 72.808\ keV$. This means that the lattice strain of the TGO in the sample at half-life is $\varepsilon = -0.0121$, which corresponds to a residual stress of $\sigma = -4.603\ GPa$.

4. Conclusions

The residual stresses of the oxide layer in thermal barrier coating systems were measured non-destructively by high-resolution depth strain profiling using the energy dispersive technique. The experiments were carried out at the materials science beamline EDDI at the Berlin synchrotron storage ring BESSY II during a beamtime period of 10 days. The results show that the TGO in undamaged TBCs is subjected to a compressive stress of 4.6 GPa at room temperature. Though, when close to failure, the TGO reveals a much lower compressive stress of 3.6 GPa. This demonstrates that there is a close relationship between relaxation of compressive stress in the TGO and damage within the TBC. Raman spectroscopy is a non-destructive technique where the shape of the spectrum changes with the stress level within the TGO. Hence, this tool has the potential to be used as a non-destructive method to indicate the damaged regions in the TBC.

5. Acknowledgement

Analysis of X-ray absorption spectra of functional proteins on the basis of their amino acid composition

Yan Zubavichus,[1,2] Andrey Shaporenko,[1] Michael Grunze,[1] and Michael Zharnikov[1]

[1] *Angewandte Physikalische Chemie, Universität Heidelberg, Im Neuenheimer Feld 253, 69120 Heidelberg, Germany*

[2] *Russian Research Centre "Kurchatov Institute", Kurchatov sq. 1, 123182 Moscow, Russia*

Near edge X-ray absorption fine structure (NEXAFS) spectroscopy is widely appreciated as a versatile experimental tool to elucidate the chemical structure of organic materials and nanostructures and films based on them. Over the last years, biological macromolecules, such as proteins and DNA, have come into the focus of interest as objects to be probed. The mere spectral information, *i.e.*, positions and intensities of spectral features, from NEXAFS can easily be supplemented with an analysis of the polarization dependence of spectra (*i.e.*, the linear dichrosim effects) in order to assess the real-space orientation of specific functional groups in an anisotropic system. NEXAFS spectromicroscopy with soft X-ray synchrotron microbeams or X-PEEM setups efficiently maps the distribution of chemically different species in an inhomogeneous sample with a spatial resolution of a few tens nm.

Recently, we have compiled a comprehensive library of the NEXAFS spectra for 22 most abundant protein-constituting amino acids[1] as well as for a representative group of homopolypeptides[2]. Here (see ref 3 for details), we report and compare the NEXAFS spectra of four different functional proteins in an attempt to qualitatively correlate differences between these spectra, which appeared to be minor, with the respective variations in their amino acid compositions. The proteins under study include lysozyme, ovalbumin both from hen egg-white, bovine serum albumin (BSA), and type I collagen from rat tail. They are representative for different classes of functional proteins.
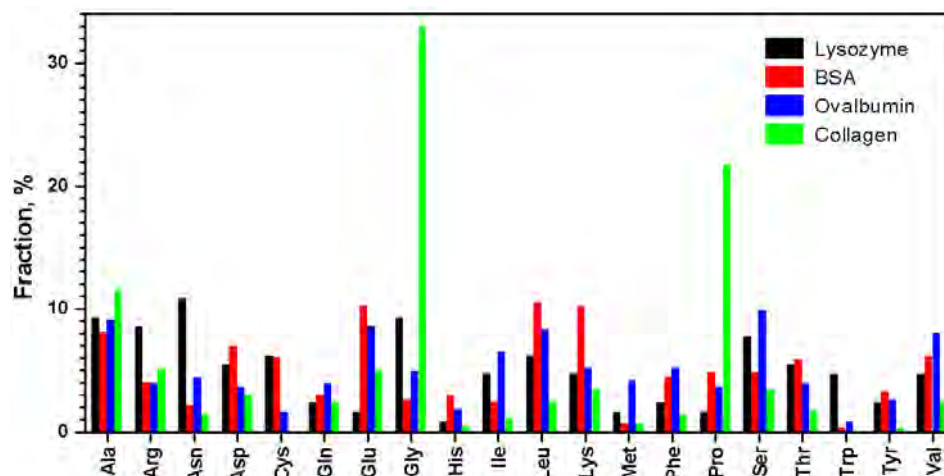
Fig. 1. A histogram of the overall amino acid compositions for the proteins under study, viz. lysozyme (black), BSA (red), ovalbumin (blue), and type I collagen from rat tail (green).

The overall amino acid compositions of the proteins under study are shown as a histogram in Fig. 1. Commonly adopted three-letter notations of the residues are used. As can be judged from the figure, lysozyme and albumins manifest rather even distributions of the amino acid residues, whereas collagen is characterized by the prominent prevalence of glycine (Gly) and proline (Pro).

The experimental spectra of the four studied proteins at the carbon, nitrogen, and oxygen *K*-edges are shown in Fig. 2. As expected, these spectra are similar to previously measured spectra of pristine amino acids and peptides. Further, the spectra of the individual proteins are reasonably similar to each other, which is understandable taking into account a large amount

of the individual amino acid residues constituting these proteins. Within the building block approach,[1] a spectrum of a protein can be represented by a weighted sum of the spectra of its constituent amino acids. However, such an approach cannot be applied to proteins in the straightforward way. First of all, the NEXAFS spectra, especially at the carbon and nitrogen edges, are noticeably modified by the introduction of the peptide bonds.[2] Furthermore, the conformational flexibility of a macro-molecule, which gives rise to the co-existence of different local configurations of nominally identical moieties, tends to broaden and smear out the respective spectral features.

Taking into account these general considerations, we have precisely analyzed the C, N, and O K-edge spectra of the proteins in Fig. 1 on the basis of their exact amino acid composition as shown in Fig. 2.[3] In particular, in the pre-edge region A of the nitrogen K-edge NEXAFS spectra, weak peaks at 398.5 eV and 399.9 eV can be resolved in the spectrum of BSA. Similar features sometimes observed in the spectra of pristine glycine were tentatively attributed[2] to the free uncharged NH_2-groups (in contrast to the NH_3^+-groups typically present in the zwitter-ionic amino acids). They also occur in the spectrum of pristine lysine (Lys),[1] which contains an additional amino group in the side chain. Thus the increased intensity of the pre-

Fig. 2. Experimental C, N, and O K-edge NEXAFS spectra of the proteins under study, viz. lysozyme (black), BSA (red), ovalbumin (blue), and type I collagen from rat tail (green). The distinct spectral regions, where potentially useful variations can occur, are labeled A-E.

edge region A in the case of BSA can be correlated with the highest content of lysine (10.2%) in BSA among the proteins studied. The most significant difference in the N K-edge spectra of the four functional proteins consists of some intensity redistribution between the high-lying $\sigma^*(N–C)$ contributions D and E. For the majority of pristine amino acids, only feature D is present in the N K-edge spectra, whereas the feature E appears only upon the peptide bond formation due to the partial double character of the C–N bonds in peptide bridges. Only in the cases of proline and hydroxyproline, the spectral feature E is already present in the spectra of pristine amino acids. Thus the maximum intensity of the feature E with respect to that of D in the case of collagen can be explained by the prominent abundance of the proline residues.

In summary, we demonstrated that different functional proteins are characterized by distinguishable NEXAFS spectra and some of the respective differences clearly correlate with their amino acid compositions. Nevertheless, in order to enable quantitative analyses of the protein spectra, a lot of further efforts, both experimental and computational, are necessary.

References:

1. Y. Zubavichus, A. Shaporenko, M. Grunze, and M. Zharnikov, *J. Phys. Chem. A* **109,** 6998 (2005).
2. Y. Zubavichus, A. Shaporenko, M. Grunze, and M. Zharnikov, *J. Phys. Chem. B* **111,** 9803, (2007); *ibid* **111,** 11866 (2007).
3. Y. Zubavichus, A. Shaporenko, M. Grunze, and M. Zharnikov, *J. Phys. Chem. B* **112,** 4478 (2008).

Densely packed monomolecular films of molecular switches

M. Elbing,[1] A. Błaszczyk,[1] C. von Hänisch,[1] M. Mayor,[1,2] V. Ferri,[3] C. Grave,[3] M. A. Rampi,[3] G. Pace,[4] P. Samorì,[4] A. Shaporenko,[5] and M. Zharnikov[5]

[1]*Forschungszentrum Karlsruhe GmbH, Institute for Nanotechnology, D-76021 Karlsruhe, Germany*
[2]*Department of Chemistry University of Basel, St. Johannsring 19, CH-4056 Basel, Switzerland*
[3]*Dipartimento di Chimica, Università di Ferrara, I-44100 Ferrara, Italy*
[4]*Institut de Science et d'Ingénierie Supramoléculaires / CNRS UMR 7006, Université Louis Pasteur, 8 allée Gaspard Monge, F-67000 Strasbourg, France*
[5]*Angewandte Physikalische Chemie, Universität Heidelberg, Im Neuenheimer Feld 253, D-69120 Heidelberg, Germany*

The development of molecular electronics is considered to be one of the major challenges of modern science and technology. Perspective objects in this context are photochromic materials. Among such materials azobenzene and related compounds represent one of the most widely studied systems due to their ease of synthesis and facile detection of photo-isomerization. The isomerisation occurs at the N=N double bond yielding two different states, viz. the *trans*- and the *cis*-isomer. The two isomers exhibit different chemical and physical properties and can be interconverted reversibly by irradiation with UV (from *trans* to *cis*) and visible (from *cis* to *trans*) light. The practical utilization of these proposed functions requires the arrangement of the molecules containing the photo-active azo-group in a medium other than solution, e.g. as either Langmuir-Blodgett (LB) films or self-assembled monolayers (SAMs). However, early studies performed on both LB-films and SAMs of azo-containing compounds showed a poor yield of photo-isomerization. This behavior is generally explained by the flexibility of the aliphatic backbone commonly used as a foot for the azobenzene moiety and by change in the occupied cross-sectional area that is due to isomerization from the almost planar/extended *trans*- to the non-planar/contracted *cis*-isomer. While the solution properties are well-established, in densely packed molecular assemblies at surfaces the lack of "free volume" may hinder the isomerization.

To diminish the above problems, we designed a rigid and fully conjugated azobenzene-based
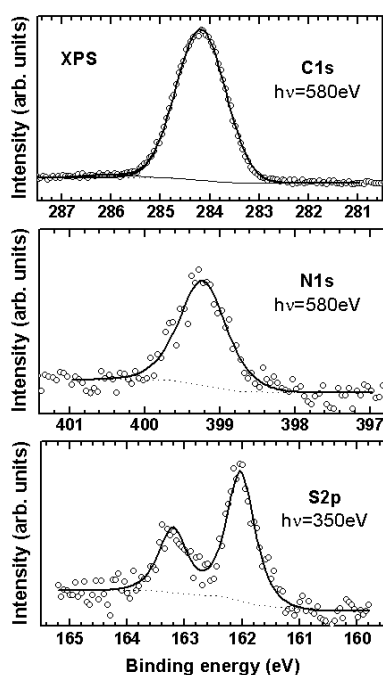
Fig. 1. C 1s, N 1s, and S 2p XPS spectra of AZO1/Au.[2]
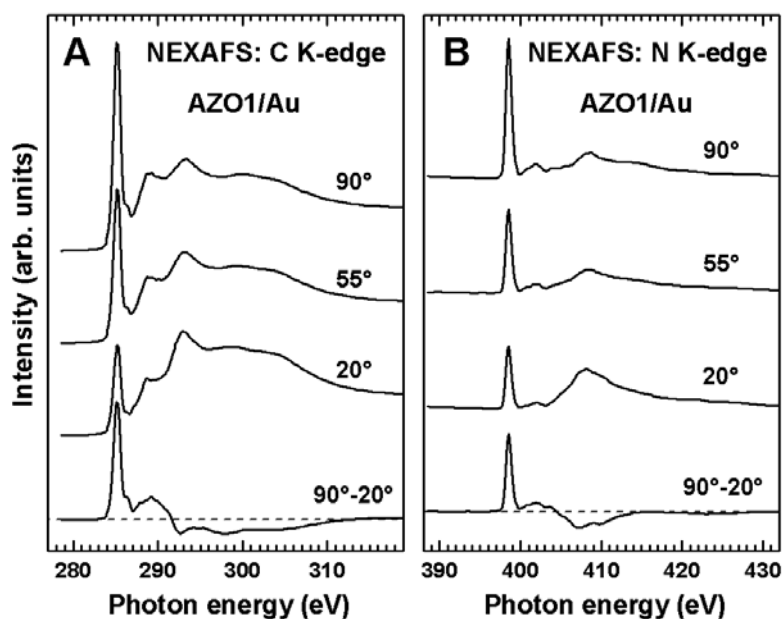
Fig. 2. C K-edge (A) and N K-edge (B) NEXAFS spectra of AZO1/Au.[2]
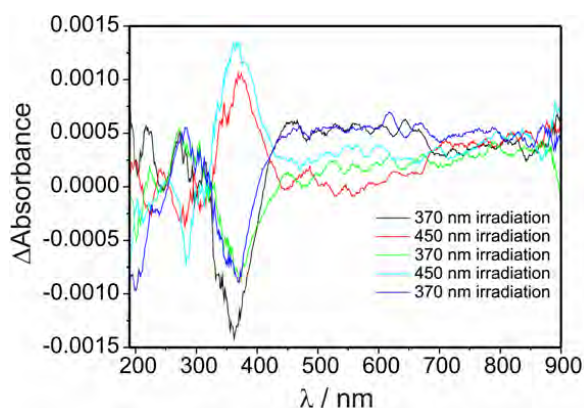
Fig. 3. Difference between UV-Vis absorption spectra of AZO1/Pd successively acquired after UV (370 nm) and Vis (450 nm) illumination.[2]
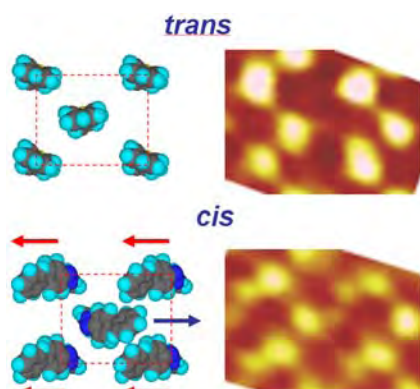
Fig. 4. STM images of AZO1/Au films in the case of cis and trans conformation.[1] Schematic cartoons of the molecular arrangement within the unit cell with the directions of isomerization (arrows) are shown.
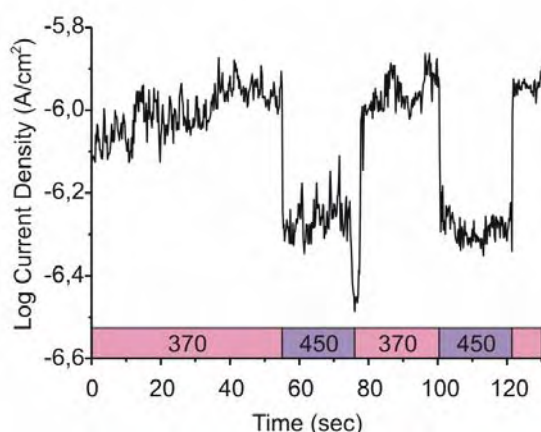
Fig. 5. Light-induced switching of current through an AZO1 SAM upon UV/Vis illumination. The measurements were performed in Au-AZO1//dodecane-thiolate-Hg junction.[3]

molecule (abbreviated below as AZO1), in which two biphenyl rods are connected by azo unit, and which can be attached to the substrate by a thiol anchoring group.[1] According to the X-ray photoelectron spectroscopy (XPS) and near-edge X-ray absorption fine structure (NEXAFS) spectroscopy data (see Figs. 1 and 2), AZO1 form densely packed and highly ordered SAMs on Au(111), with a coplanar arrangement of both biphenyl subunits in the trans case.[2] However, in spite of the dense molecular packing, the molecular conformation in these SAMs can be reproducibly changed by their irradiation with UV and visible light (see Fig. 3).[2] The reason that the sterical constrains do not hinder the isomerisation in the AZO1 SAMs is a correlation of the conformational changes of the individual molecules. As shown by scanning tunnelling microscopy (STM), the geometrical parameters of the molecular unit cell are not affected by the isomerisation (see Fig. 4).[1] But most important, the isomerisation occurs in a correlated manner: the adjacent molecular rows isomerise in the opposite directions (see Fig. 4), which does not requires "free volume".

The change of molecular conformation affects the electric properties of the AZO1 molecules. As shown by the mercury drop measurements, the conductivity of an AZO1 SAM in the *cis* state is significantly higher than that for the *trans* conformation, which is predominately related to a shorter pathway for the current.[3] Direct measurements of light-induced switching of current through an AZO1 SAM upon UV/Vis illumination were performed: consecutive changes of the current by ca. 1.5 order of the magnitude were observed (Fig. 5).[3] This work has been supported by DFG (ZH 63/9-2 and ZH 63/10-1).

References:

1. G. Pace, V. Ferri, C. Grave, M. Elbing, M. Zharnikov, M. Mayor, M. A. Rampi, and P. Samorì, PNAS **104**, 9937 (2007).
2. C. Grave, C. Risko, A. Shaporenko, Y. Wang, C. Nuckolls, M. A. Ratner, M. A. Rampi, and M. Zharnikov, Adv. Func. Mat. **17**, 3816 (2007).
3. V. Ferri, M. Elbing, G. Pace, M. Zharnikov, P. Samorì, M. Mayor, M. A. Rampi, Ang. Chem. Int. Ed. **47**, 3407 (2008).

The local structure of benzene on Si(001)(2x1): a scanned-energy mode photoelectron diffraction investigation

G. Nisbet[1],C. L. A. Lamont[1] ,M. Polcik[2], R. Terborg[2], D. I. Sayago[2], M. Kittel[2], J.T. Hoeft[2], R.L. Toomes[3], D. P. Woodruff[3]

[2] *Dept. of Chemical & Biological. Sciences, University of Huddersfield, Queensgate, Huddersfield HD1 3DH, UK*
[2] *Fritz-Haber-Institut der Max-Planck-Gesellschaft, Faradayweg 4-6, 14195 Berlin*
[3] *Physics Department, University of Warwick, Coventry CV4 7AL, UK*

Since the early 1990's there has been considerable interest in the interaction of unsaturated hydrocarbons with semiconductor surfaces, as they offer a potential route to the manufacture of optoelectronic and bioanalytical devices. One such model system is that of benzene on Si(001)(2x1). The clean Si(001) surface undergoes a reconstruction such that adjacent atoms pair together to form rows of dimers. Strictly, these dimers are asymmetric, but they flip rapidly between the two opposite local asymmetry states to produce only the average (2x1) periodicity; most adsorbates on this surface appear to remove or strongly suppress this asymmetry.
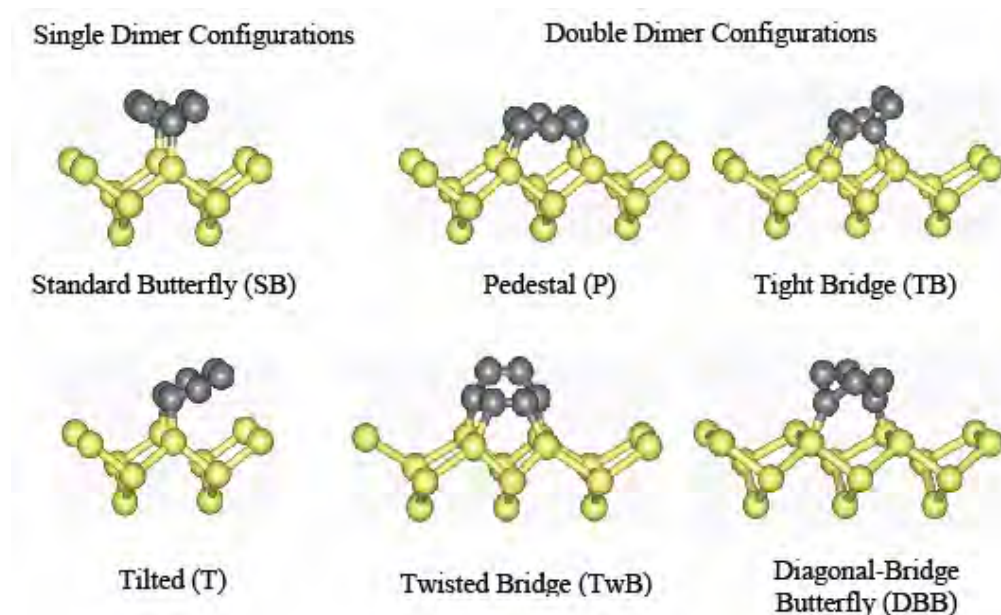
While there are no previous complete quantitative experimental determinations of the local chemisorption structure of benzene on Si(001), a number of different geometries have been proposed. These are illustrated in the figure and can be categorised into two groups – those bonded to a single Si dimer and those bonded to two adjacent Si dimers (referred to here as double-dimer configurations). There are just two bonding configurations in the first category, referred to as the 'standard butterfly' (SB) and 'tilted' (T) species. In the SB form the interaction with the dimer is through the C_1 and C_4 atoms of the benzene ring. Two double bonds are retained and the molecule has C_{2v} symmetry. The T species is formed through the interaction of two adjacent C atoms in the benzene ring with the dimer and the plane of the molecule is tilted away from the surface. Four double-dimer species have been suggested. In the 'pedestal'

(P) form the C_1, C_2, C_4 and C_5 atoms bond to adjacent Si dimers and the plane of the molecule is essentially flat and parallel to the surface. The 'tight bridge' (TB) and 'twisted bridge' (TwB) species both involve bonding of the C_{1-4} atoms with Si dimers and they retain one C=C bond, the bond axis of which is parallel to the surface. They are azimuthally rotated through 90° with respect to one another and both species have C_s symmetry; the mirror plane is perpendicular to the dimers in the case of TB and parallel to them in the case of TwB. The final structure is the 'diagonal-bridge butterfly' (DBB) species which is similar to the SB, in that only the C_1 and C_4 atoms of the benzene molecule are involved in the surface bonding, but the two Si atoms are in different dimers.

While there have been numerous previous experimental studies of this system by thermal desorption, vibrational and electronic spectroscopy, and STM, but the only prior quantitative structural information is derived from theoretical total energy calculations, mainly using DFT. Here we present the results of the first quantitative experimental structural study of this system using scanned-energy mode photoelectron diffraction (PhD [1]). PhD exploits the coherent interference of the directly-emitted photoelectron wavefield from a core level of an atom with other components of the same wavefield elastically scattered by the neighbouring atoms. In the ~50-400 eV kinetic energy range used, backscattering is strong and the PhD spectra from an adsorbate atom provide quantitative information on the adsorbate-substrate registry. Here we use C 1s PhD data emitted from the adsorbed benzene to determine its local geometry.

Our key conclusion is that the saturated monolayer of benzene on Si(001)-(2x1) contains both 'standard butterfly' and 'tilted bridge' forms of benzene, with a composition of 58±29% of the SB species. Detailed structural parameter values have been obtained for both species [2], including Si-C bondlengths and out of plane tilt angles of the benzene molecules, both with quite a high degree of precision. Intramolecular bondlengths and Si dimer bondlengths and separations have also been determined, but with less precision. The results for the SB species agree well with previous theoretical studies. The structural parameters for the TB species suggest considerable distortion of both the benzene molecule and the Si substrate. Our conclusion regarding the co-occupation of the SB and TB adsorbed species is consistent with the results of several previous studies by other methods, suggesting that at high coverage benzene initially adsorbs on this surface in the SB form at room temperature, but then partially converts to the TB form with time. We suggest that the reason that the conversion is not complete may not only be due to thermodynamics, but also to a combination of steric effects and a sensitivity of the adsorption energies of the adsorbed SB and TB forms to the nature of the surrounding benzene molecules.

References

1 D. P. Woodruff, *Surf. Sci. Rep.* **62** (2007) 1.
2 G. Nisbet, C.L.A.Lamont, M. Polcik, R. Terborg, D.I.Sayago, M. Kittel, J. T. Hoeft, R.L. Toomes, D.P. Woodruff, *J. Phys.: Condens. Matter*, **20** (2008) 304206

The local structure of OH species on the V_2O_3(0001) surface: a scanned-energy mode photoelectron diffraction study

E. A. Kröger[1], D. I. Sayago[1], F. Allegretti[2], M. J. Knight[2], M. Polcik[1], W. Unterberger[1], T. J. Lerotholi[2], K. A. Hogan[3], C. L. A. Lamont[3], M. Cavalleri[1], K. Hermann[1], D. P. Woodruff[2]

[1] *Fritz-Haber-Institut der Max-Planck-Gesellschaft, Faradayweg 4-6, 14195 Berlin*

[2] *Physics Department, University of Warwick, Coventry CV4 7AL, UK*

[3] *Dept. of Chem. & Biol. Sciences, University of Huddersfield, Huddersfield, UK*

Oxide surfaces in general, and those of vanadium oxides in particular, play a major role in practical heterogeneous catalysis. As such there have been many investigations of model oxide surfaces using surface science methods, although very few of these have involved quantitative surface structure determination, and even fewer have led to quantitative information on adsorbate structures. A particularly interesting problem in understanding the role of oxides in surface reactions is the influence of surface hydroxyl (OH) species. Some published literature suggests that hydroxyl termination of oxide surfaces is ubiquitous, particularly in aqueous environments, but also when exposed to air at atmospheric pressure. Insofar as some oxides have potential applications as catalysts in hydrogen production by water dissociation, surface hydroxyl species may also play a direct role in at least one important surface reaction. Our particular interest has been in the adsorption properties of the surfaces of ultra-thin V_2O_3(0001) films grown epitaxially onto Pd(111), and the application of the technique of scanned-energy mode photoelectron diffraction (PhD) to elucidate these adsorption structures. Here we present the results of an investigation of the local structure of OH species on the V_2O_3(0001) surface, produced either by water dissociation or by reaction with atomic hydrogen, using the PhD technique [1].

PhD exploits the coherent interference of the directly-emitted photoelectron wavefield from a core level of an atom with other components of the same wavefield elastically scattered by the neighbouring atoms. In the ~50-400 eV kinetic energy range used, backscattering is strong and the PhD spectra from an adsorbate atom provide quantitative information on the adsorbate-substrate registry. Here we exploit the fact that the O 1s photoelectron binding energy of the OH species differs by ~1.3 eV from that of the oxidic state in the substrate. We therefore collected PhD data from the O atom within the hydroxyl species alone, and thus can locate this hydroxylated O atom on the surface.

Bulk V_2O_3(0001) has a layer structure of the form … V.O₃.V'V.O₃.V'V.O₃V'… and the surface is believed to correspond to cutting the crystal between the two halves of the buckled V'V layer, thus being terminated by a 'half-metal' layer. Under standard preparation conditions, in an excess of oxygen gas, total energy calculations indicate that the lowest-energy structure involves O atoms bonded atop these surface half-layer V_{top} atoms to form local vanadyl (V=O) species. This means that there are two

different types of O atoms that are exposed at the surface and available for hydroxylation, namely the vanadyl O atoms, $O_{vanadyl}$ that sit atop the outermost half-metal layer V atoms, and the outermost O atomic layer of three-fold coordinated bridging O_{top} atoms of the bulk structure. Our PhD data show that the preferred sites are independent of the mode of hydroxylation (atomic H exposure or water reaction), the two preparation methods yielding essentially identical spectra. Note that we find clear evidence for photon-stimulated dissociation of a surface water layer, so the detailed chemistry at the oxide/water interface appears to be complex.

Our PhD results (reinforced by measurements of the OH coverage) show clearly [2] that it is *not* the atop vanadyl O atoms that are exclusively or primarily hydroxylated, but rather all or the great majority (~90%) of the hydroxyl O atoms are in O_{top} sites. This result is surprising in the context of conventional wisdom for this surface.

Fig. 1
Schematic diagram of the $V_2O_3(0001)$ surface structure, showing the two possible hydroxylation sites.

Ab initio density-functional theory cluster calculations provide partial rationalisation of this result, indicating that the chemisorption energies of atomic H at these two distinct oxygen sites are too similar to be reliably distinguished. Our experimental results may suggest that the O_1 site is in general more reactive than O_t. This would be analogous to earlier findings for V_2O_5 surfaces for which it was argued, both on experimental [3] and theoretical [4] grounds, that bridging oxygen sites exhibit higher reactivity that terminal ones.
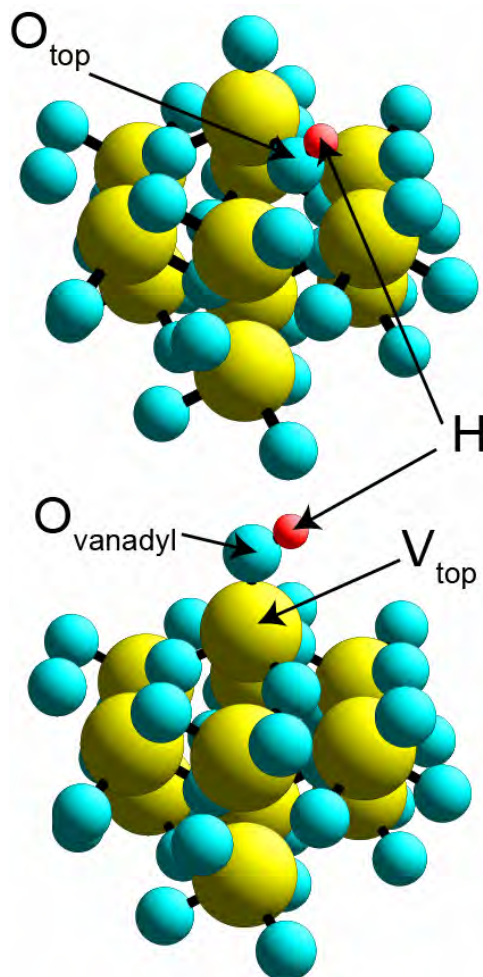
References

1 D. P. Woodruff, *Surf. Sci. Rep*. **62** (2007) 1.
2 E. A. Kröger, D. I. Sayago, F. Allegretti, M. J. Knight, M. Polcik, W. Unterberger, T. J. Lerotholi, K. A. Hogan, C. L. A. Lamont, M. Cavalleri, K. Hermann, D. P. Woodruff *Surf. Sci.* **602** (2008) 1267
3 J. Haber, in C. Mortena, A. Zecchina, and G. Costa (eds.), "Structure and Reactivity of Surfaces", Elsevier, Amsterdam, 1989.
4 M. Witko, K. Hermann, *J. Mol. Catal*. **81** (1993) 279.

The local structure of furan and its dissociation products on Pd(111)

M. J. Knight[1], F. Allegretti[1], E. A. Kröger[2], M. Polcik[2], C. L. A. Lamont[3], D. P. Woodruff[1]

[1] *Physics Department, University of Warwick, Coventry CV4 7AL, UK*

[2] *Fritz-Haber-Institut der Max-Planck-Gesellschaft, Faradayweg 4-6, 14195 Berlin*

[3] *Dept. of Chem. & Biol. Sciences, University of Huddersfield, Huddersfield, UK*

Furan, C_4H_4O, is the simplest oxygen-containing aromatic hydrocarbon, and is often used as a model in hydrodeoxygenation studies of such compounds that need to be removed from crude petroleum and liquids derived from coal and biomass. Surface science investigations on well-characterised single crystal surfaces have shown that on Pd(111) furan adsorbs intact at low temperatures, but around room temperature deoxygenation occurs with the production of CO; there is some evidence of partial formation of surface benzene on this surface, through coupling of a C_3H_3 surface intermediate, indicating that the surface species produced by initial heading are coadsorbed CO and C_3H_3. Despite characterisation by thermal desorption, vibrational spectroscopy and STM, leading to an indication that molecular furan lies essentially flat on the surface at low coverage, there is no detailed understanding of the local adsorption geometry of either the intact furan or the reaction products.

Here we present the results of a quantitative experimental structural study of this system using scanned-energy mode photoelectron diffraction (PhD [1]). PhD exploits the coherent interference of the directly-emitted photoelectron wavefield from a core level of an atom with other components of the same wavefield elastically scattered by the neighbouring atoms. In the ~50-400 eV kinetic energy range used, backscattering is strong and the PhD spectra from an adsorbate atom provide quantitative information on the adsorbate-substrate registry. The fact that C 1s XPS spectra from the Pd(111)/furan system resolve two distinct chemical states in both the intact molecule (from the C atoms adjacent to, and not adjacent to, the O atom), and the reaction products (from CO and from C_3H_3) means that we are able to obtain chemical-state-specific PhD data from these four distinct C atoms, providing enhanced specificity in the structural information.
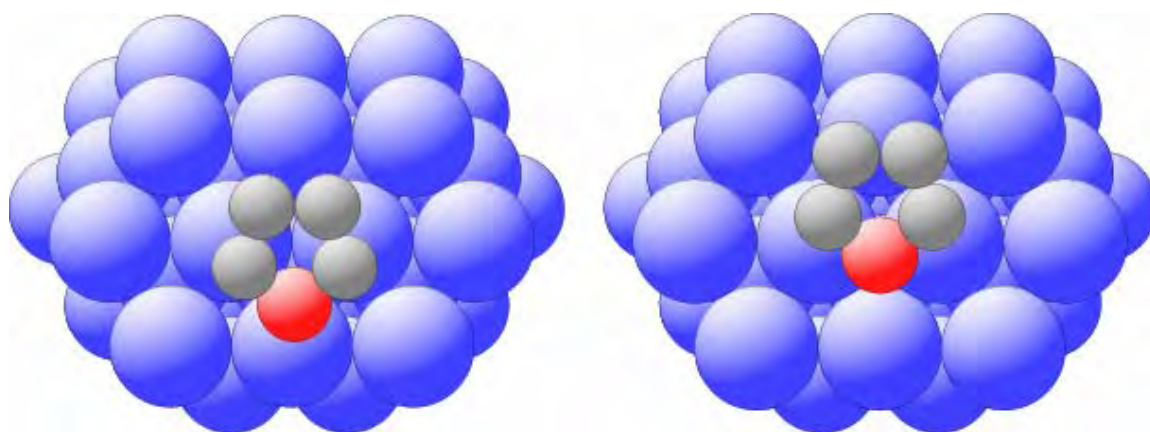
Fig. 1 Two of the four preferred structural models for furan on Pd(111).

O K-edge NEXAFS data interpretation leads to the conclusion that the intact furan molecule lies with its molecular plane essentially parallel to the surface, and an exhaustive search comparing the PhD data with simulations based on different possible lateral positions of the molecule on the surface led to four best-fit structure, two of which differed only from the other two in their location relative to the subsurface (being positioned relative to hcp and fcc hollow sites, respectively). The remaining ambiguity is between the structures shown in Fig. 1. In both cases the α-C atoms, adjacent to the O atom, occupy off-atop sites and show the shortest Pd-C bonds (2.13 ± 0.03 Å), but the O atoms are in differently-coordinated sites [2].

In the case of the coadsorbed CO and C_3H_3 fragments, the CO is found to occupy the same mixed hollow sites as in the Pd(111)c(4x2)-CO phase, with closely similar bondlengths. PhD analysis of the data from the C_3H_3 species leads to two possible best-fit structures, as in the case of intact furan. These are shown in Fig. 2. In one structure, one C atom is in an off-atop sites and the remaining two are in off-bridge sites, while in the other structure this occupation is reversed. In both models it is the off-atop C atoms that form the shortest Pd-C bondlengths (2.12 ± 0.04 Å), but the molecular plane is only weakly tilted relative to the surface [3].
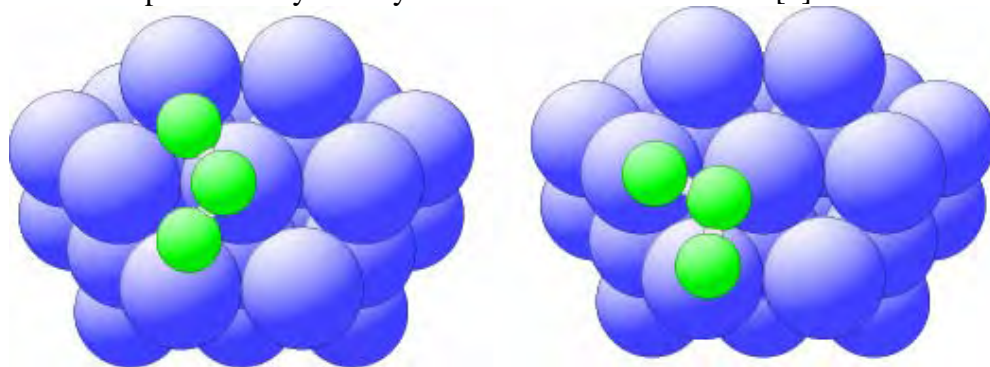
Fig. 2. The preferred structural models for C_3H_3 on Pd(111).

This local structure on the surface is somewhat similar to that found in an organometallic carbonyl cluster compound in which a fully methylated C_3 species (i.e. $(CCH_3)_3$ rather than (CH_3)) is bonded to a triangular group of three Ru atoms [4]. However, in this species the C_3 plane is significantly more tilted relative to the plane defined by the three Ru atoms.

References

1 D. P. Woodruff, *Surf. Sci. Rep.* **62** (2007) 1.
2 M. J. Knight, F. Allegretti, E. A. Kröger, M. Polcik, C. L. A. Lamont, D. P. Woodruff, *Surf. Sci.* **602** (2008) 2524
3 M. J. Knight, F. Allegretti, E. A. Kröger, M. Polcik, C. L. A. Lamont, D. P. Woodruff, *Surf. Sci.* **602** (2008) 2743
4 M. R. Churchill, L. A. Buttrey, J. B. Keister, J. W. Ziller, T. S. Janik, W. S. Striejewske, *Organometallics*, **9** (1990) 766

Kinetics of Volmer-Weber Growth:
Early stages of Fe_3Si/GaAs(001) epitaxy

Vladimir M. Kaganer, Bernd Jenichen, Roman Shayduk, Wolfgang Braun

Paul-Drude-Institut für Festkörperelektronik
Hausvogteiplatz 5–7, D–10117 Berlin, Germany

We grow Fe_3Si films by molecular beam epitaxy and simultaneously study their evolution by grazing incidence x-ray diffraction in our MBE/diffractometer system at the wiggler beamline U125/2 KMC. The x-ray diffraction data show that the growth begins by the abrupt formation of 3 monolayer (ML) high islands and approaches two-dimensional layer-by-layer growth at a thickness of 7 ML. A surface energy increase obtained by *ab initio* calculations allows us to identify the growth as a strain-free Volmer–Weber transient. Kinetic Monte Carlo simulations point to an optimum growth rate for Volmer–Weber growth in between two limits, the appearance of trenches at slow growth and surface roughening at fast growth [1].
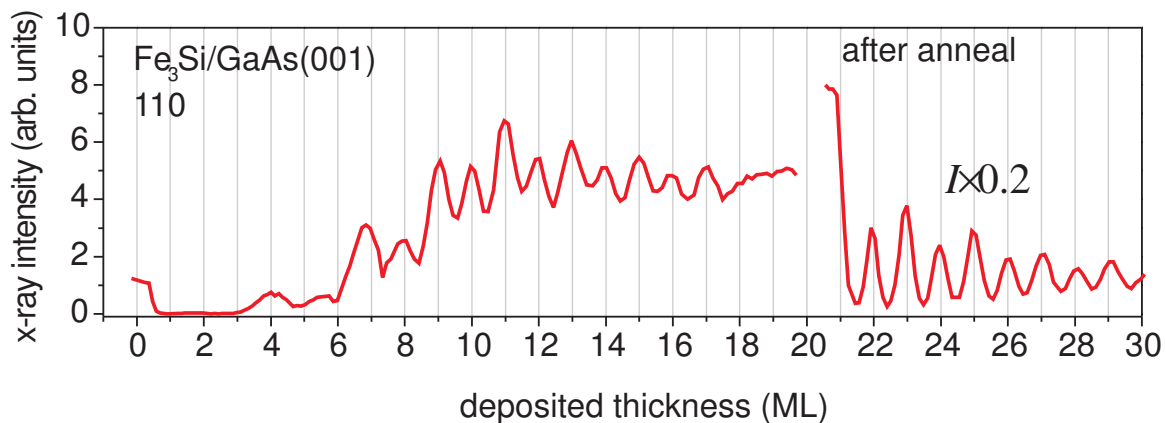
Figure 1: Diffraction intensity oscillations during epitaxial growth of Fe_3Si on GaAs(001). In addition to the heteroepitaxy on the substrate, homoepitaxial growth after an anneal is also shown.

The time dependence of the diffracted intensity we observe is presented in Fig. 1. Growth begins with an initial plateau of low intensity. It is followed by several irregular oscillations with maxima shifted from the integer layer positions. These irregular oscillations are reproducibly the same on three samples grown under the same conditions. The regular layer-by-layer oscillations are established only after the deposition of 7–8 ML. After the sample is annealed, further growth oscillations are periodic.

More detailed information on the initial growth is obtained by continuously measuring crystal truncation rods (CTRs) during growth. Figure 2 shows some of the CTRs. The reflections are measured in turn, with one scan taking approximately 8 minutes (the deposition time of 0.4 ML). The CTR intensities are fitted by calculations using both multibeam dynamical and distorted wave Born approximations [2]. The thickness interference oscillations of the CTR intensity provide information on the thickness of the crystalline film during growth. The measured film thickness is plotted in Fig. 3. After the deposition of 1 ML, crystalline Fe_3Si forms with a thickness just over 3 ML. Obviously, such a film can cover only part of the surface. This is in agreement with the fitted intensity curves in Fig. 2. Since the curves are properly scaled by adjusting the substrate maxima, the lower
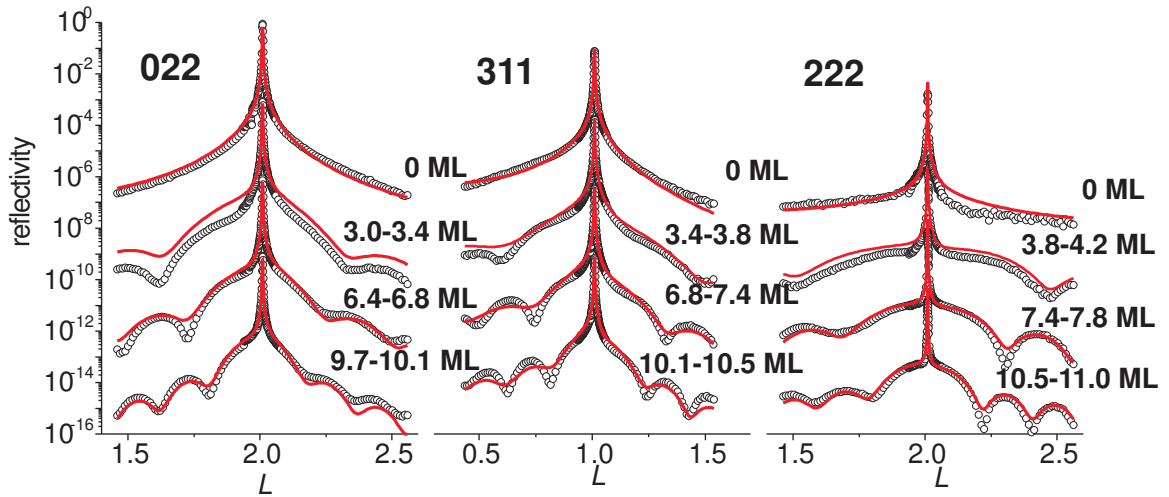
Figure 2: Crystal truncation rods measured during growth (circles) together with theoretical fits (red lines). The substrate temperature is 180 °C, the x-ray diffraction measurements are performed with an energy of 10 keV at a grazing incidence angle of 0.3°.

measured film intensity compared to the calculated one implies an average film density that is below solid Fe_3Si. The film thickness becomes equal to the deposited amount of material only after deposition of about 7 ML. Thus, Fe_3Si growth on GaAs begins by the formation of 3D islands at least 3 ML high.
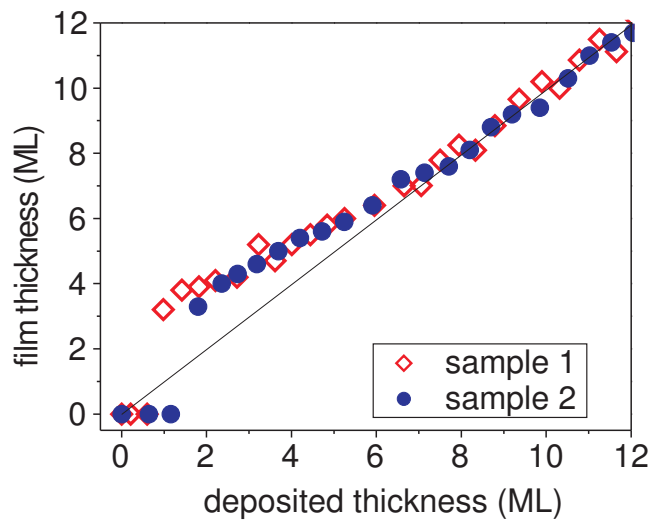
Figure 3: Fe_3Si epitaxial film thickness obtained from the CTR measurements.

Since we already know the atomic arrangement of Fe_3Si on GaAs(001) from our previous work [3], we have performed *ab initio* calculations of the epitaxial system. We find that the surface energy increases by ≈ 0.1 eV/Å^2, with respect to the GaAs surface energy. Hence, the energy calculations indicate a Volmer–Weber growth mode. We explore the growth kinetics by Monte Carlo simulations in a generic solid-on-solid model. We modify the standard calculations by decreasing the surface diffusion energy at the heterointerface, only for the first deposited layer. In this way, the bonding of the film to the substrate becomes weaker than the bonding within the film. The reduction of the surface diffusion barrier for the first layer by 0.11 eV drastically changes the initial growth compared to
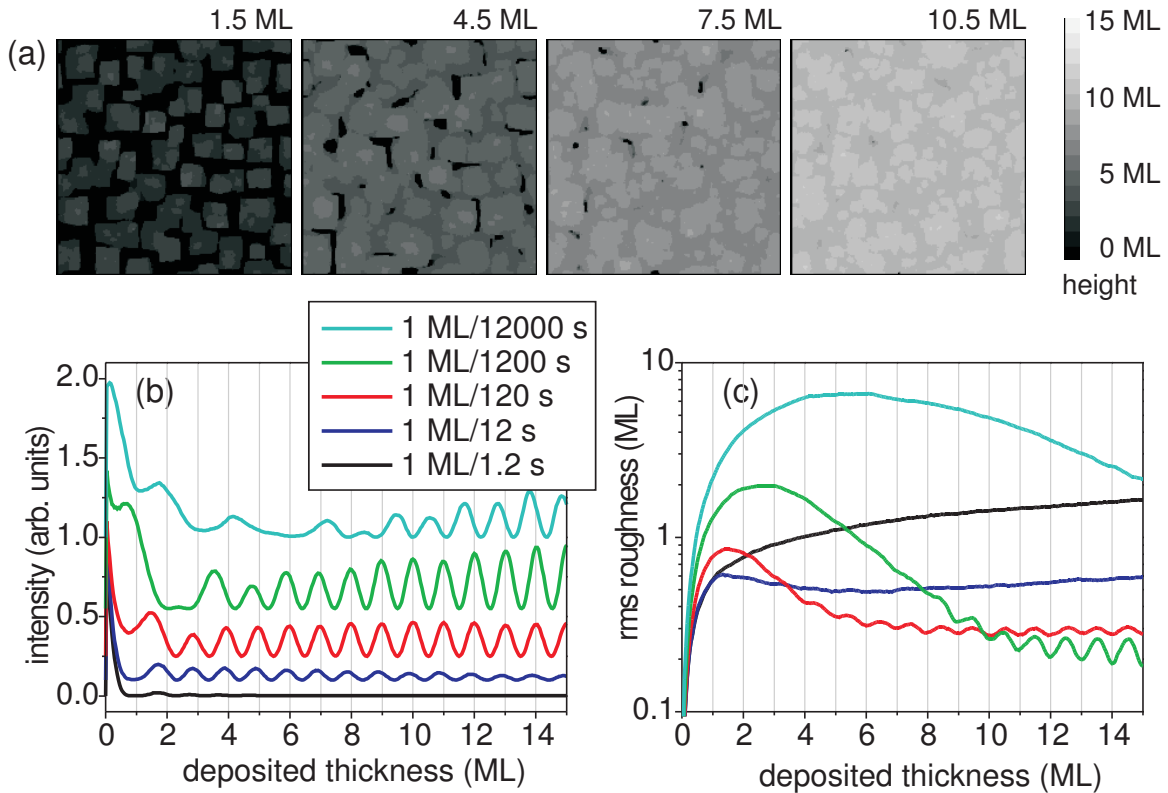
Figure 4: Kinetic Monte Carlo simulations for different growth rates: (a) snapshots of the surface after different depositions for the growth rate 1 ML/1200 s, (b) calculated intensity oscillations during deposition, and (c) time evolution of the root-mean-squared (rms) roughness.

homoepitaxy, see Fig. 4(a). After the deposition of several monolayers, the substrate is not completely covered. Rather, 2–3 ML high islands form as a result of the favored upward jumps from the substrate to the film. Even after the deposition of 8 ML, trenches and pits down to the substrate persist. The film becomes continuous and smooth only after about 10 ML of deposition.

Simulations for different growth rates and otherwise identical parameters are shown in Fig. 4(b,c). Low growth rates closer to thermal equilibrium lead to large surface features, but also to deep trenches between them that persist up to large thicknesses. By increasing the growth rate, the formation of trenches and pits is reduced. At still higher growth rates the surface roughness increases monotonically due to kinetic roughening. An optimum growth rate needs to be found for an experimental system as a compromise between formation of three-dimensional islands and trenches at low growth rates and roughening at high growth rates.

[1] V. M. Kaganer, B. Jenichen, R. Shayduk, W. Braun, and H. Riechert, Phys. Rev. Lett. **102**, 016103 (2009).

[2] V. M. Kaganer, Phys. Rev. B **75** (2007) 245425.

[3] V. M. Kaganer, B. Jenichen, R. Shayduk, and W. Braun, Phys. Rev. B **77**, 125325 (2009).

Spin- and angle resolved photoemission spectroscopy of the graphene/Ni(111) system

Yu. S. Dedkov[1], M. Fonin[2], M. Weser[1], O. Zander[2], U. Rüdiger[2], and C. Laubschat[1]

[1]*Institut für Festkörperphysik, Technische Universität Dresden, Germany*
[2]*Fachbereich Physik, Universität Konstanz, Germany*

Graphene, a monolayer of graphite, has recently attracted a considerable interest due to its unusual electronic properties. Being referred to as a zero-gap semiconductor or semi-metal, graphene exhibits a linear dispersion near the Fermi edge yielding mass-less Dirac-fermion behavior of the charge carriers, which gives rise to fascinating electronic transport properties such as anomalous Quantum-Hall effect or phase-shifted Shubnikov-de Haas oscillations. Moreover, graphene is also suggested to be a promising candidate for future carbon-based electronic or even spintronic devices.

In the present study we investigate the electronic and magnetic properties of high-quality graphene layers on a Ni(111) substrate prepared by chemical vapor deposition. By means of spin- and angle-resolved photoemission spectroscopy we observe (i) a considerable spin-polarization of the π-states of graphene and (ii) a large shift of the π-band upon magnetization reversal of the underlying Ni(111) substrate. We attribute the latter finding to the manifestation of a Rashba-like effect. The idea of the observation of Rashba-type interaction for the 2D electron gas of π-electrons in the graphene/Ni(111) system is analogous to the recent observation of the Rashba effect on Gd(0001) and O/Gd(0001) [1].

Photoelectron spectra were recorded at room temperature in angle-resolved mode with a 180° hemispherical energy analyzer SPECS PHOIBOS 150 combined with mini-Mott spin-detector. The energy resolution of the analyzer was set to 50 meV and the angular resolution was 0.5^o. Angle-resolved measurements were performed in magnetic remanence after having applied a magnetic field pulse of about 500 Oe along the <1-10> easy magnetization axis of the Ni(111) thin film. Magnetic field in the proximity of the W(110) single crystal after having applied a magnetic field pulse was measured by a Hall-sensor and found to be less than 0.1 Oe. A well ordered Ni(111) surface was prepared by the thermal deposition of Ni films with a thickness of more than 150Å on to the clean W(110) substrate followed by a subsequent annealing at about 300°C. Prior to the film preparation the tungsten substrate was cleaned by several cycles of oxygen treatment and subsequent flashes at about 2300°C. An ordered graphene overlayer on Ni(111) was prepared via cracking of propene gas (C_3H_6) [4].

After the cracking procedure the Ni(111) surface is completely covered by the graphene film as demonstrated by STM [Fig. 1 (a,b)]. All investigated terraces display the same atomic structure confirming high crystalline quality of the prepared graphene layer [Fig. 1 (b)]. Investigations by means of angle-resolved photoemission are in excellent agreement with previous studies and demonstrate the presence of a single graphene layer on the Ni(111) surface [4]. The modification of the valence band of the system was studied by means of spin-resolved photoelectron spectroscopy [Fig. 1 (c)]. The presence of a graphene overlayer on top of Ni(111) leads to drastic changes in the spin-resolved electronic structure which is due to the strong hybridization between Ni $3d$ and graphene π states in this system.

Fig. 1 (d) shows the spin-resolved spectra of the graphene π states of the graphene/Ni(111) system measured at room temperature. The observed difference between the spin-up (solid triangle up) and spin-down (open triangle down) indicates that the graphene layer is spin polarized with the calculated spin-polarization value of about (-12±2) %. The spin moment is aligned antiparallel to the magnetization of Ni meaning antiparallel magnetic
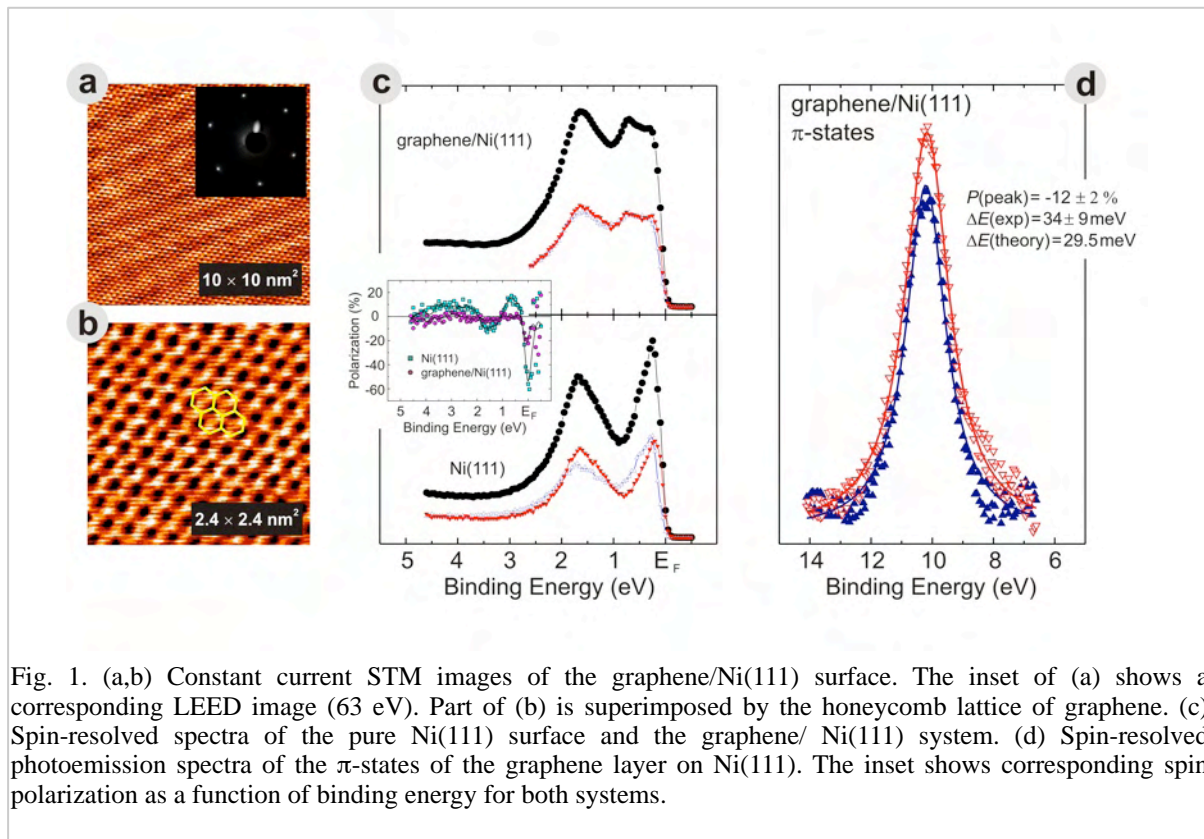
Fig. 1. (a,b) Constant current STM images of the graphene/Ni(111) surface. The inset of (a) shows a corresponding LEED image (63 eV). Part of (b) is superimposed by the honeycomb lattice of graphene. (c) Spin-resolved spectra of the pure Ni(111) surface and the graphene/ Ni(111) system. (d) Spin-resolved photoemission spectra of the π-states of the graphene layer on Ni(111). The inset shows corresponding spin polarization as a function of binding energy for both systems.

coupling of graphene to Ni. The spin splitting value of about 34±9 meV is observed. In the further discussion we will show that the results presented above are essential for the interpretation of the observed Rashba-type effect in the graphene/Ni(111) system.

Fig. 2 shows the results of angle-resolved photoemission measurements of the graphene/Ni(111) system upon magnetization reversal of the Ni(111) film. The experimental geometry is presented in Fig. 2 (a) (here we would like to emphasize that according to the geometry of the experiment residual magnetic field, if any, will produce effect opposite to that observed in this study). Two representative pairs of photoemission spectra measured for two opposite magnetization directions are shown in Fig. 2 (b). A clear shift of $\Delta E = 200$ meV in the peak position of the π states upon magnetization reversal is observed for spectra taken in off- normal emission geometry, whereas no shift is observed for spectra measured at normal emission. Although the states for opposite magnetization directions do not exist simultaneously, the observed energy shift is equivalent to the Rashba splitting at a nonmagnetic surface, and we shall refer to it further as the Rashba splitting. The energy dispersions extracted from the photoemission spectra measured for two opposite directions of magnetization are shown in Fig. 3 (c) together with a magnified plot of the region around the Γ point. In Fig. 3 (d) we plot the magnitude of the Rashba splitting $\Delta E(k)$ obtained from the data shown in Fig. 3 (c) as a function of the wave vector k along the Γ-M direction of the surface Brillouin zone. The large Rashba-like splitting of the π states observed in this experiment is possibly due to the asymmetry of the charge distribution at the graphene/ Ni(111) interface. The hybridization between the π states of graphene and the Ni 3d states leads to a considerable charge transfer from the 3d states of Ni surface atoms to the unoccupied π states of the graphene monolayer. As a consequence, a large potential gradient is formed at the interface and the electrons in the interface state are subject to an effective spatially averaged crystal electric field that leads to the Rashba effect. A similar effect was recently observed for the not fully spin-polarized surface states of Gd and oxygen/Gd(0001)
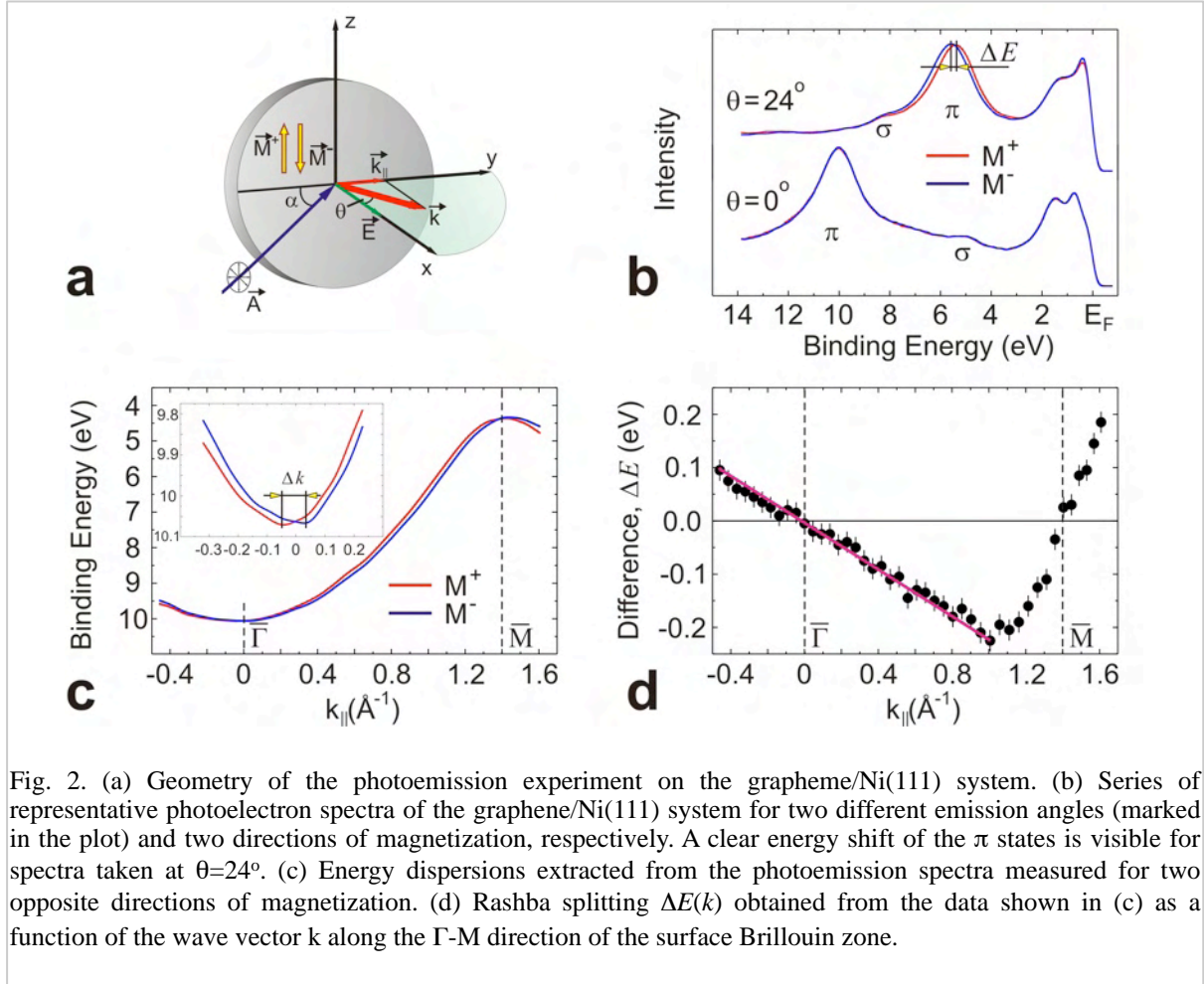
Fig. 2. (a) Geometry of the photoemission experiment on the grapheme/Ni(111) system. (b) Series of representative photoelectron spectra of the graphene/Ni(111) system for two different emission angles (marked in the plot) and two directions of magnetization, respectively. A clear energy shift of the π states is visible for spectra taken at θ=24°. (c) Energy dispersions extracted from the photoemission spectra measured for two opposite directions of magnetization. (d) Rashba splitting ΔE(k) obtained from the data shown in (c) as a function of the wave vector k along the Γ-M direction of the surface Brillouin zone.

systems [1] (T_C(Gd)=293K and T_N(O/Gd) is even lower), where *ab initio* calculations show that in this case the gradient of the potential plays the crucial role as the origin of the Rashba splitting but not the spin-orbit interaction. Experiments on these systems were performed at 80 K where surface states of Gd or O/Gd are not fully spin-polarized showing a spin-polarization value of about 30% [2,3]. As discussed in [1], the calculations performed without inclusion of spin-orbit interaction in the observed charge transfer at the interface covers almost 70% of the total Rashba splitting. This fact emphasizes the importance of the strong gradient of the electric field at the interface. This model can be implemented for the graphene/Ni(111) system as graphene layer on Ni(111) was found to be spin-polarized. The observed spin-polarization (Fig. 2) originates most probably from hybridization or the proximity effect. Since the Fermi surface of graphene is centered around the K point in reciprocal space where the Ni substrate has states of pure minority spin character one may expect that predominantly spin-down electrons will fill π states and produce the spin polarization of these states which leads in turn to the observed antiparallel alignment of the spin moment of graphene with respect to Ni(111).

1. O. Krupin *et al.*, Phys. Rev. B **71**, 201403 (2005).
2. A. V. Fedorov *et al.*, Phys. Rev. B **65**, 212409 (2002).
3. D. Li *et al.*, Phys. Rev. B **51**, 13895 (1995).
4. Yu. S. Dedkov *et al.*, Phys. Rev. Lett. **100,** 107602 (2008).

Hard x-ray photoemission: Depth-resolution with standing-wave excitation

S. Döring[1], F. Schönbohm[1], U. Berges[1], M. Gorgoi[2], F. Schäfers[2], S.-H. Yang[3], B. Balke[4], C. Papp[4], R. Schreiber[5], D. E. Bürgler[5], C. M. Schneider[5], W. Braun[2], C. S. Fadley[4,6], C. Westphal[1]

[1]TU Dortmund, Experimentelle Physik 1, Otto-Hahn-Str. 4, 44221 Dortmund, Germany
[2]Helmholtz Zentrum Berlin, Albert-Einstein-Str. 15, 12489 Berlin, Germany
[3]IBM Almaden, USA
[4]Lawrence Berkeley National Laboratory, Berkeley, CA 94720, USA
[5]Forschungzentrum Jülich, IFF-9, 52425 Jülich, Germany
[6]University of California, Davis, CA 95616, USA

MgO/Fe as an example for a magnetic tunnel junction

Magnetic tunnel junctions (MTJs) are systems which show the tunnel magnetoresistance (TMR) effect. These structures are used in magnetic storage devices like hard-drive read-write heads and in increasing applications, also magnetic random access memory (MRAM). The quality of the MgO/Fe interface is crucial for the strength of the TMR effect and thus for the performance of the MTJs. Therefore, its exact composition and structure are of primary importance and are a primary focus of interest. Presently, a few experimental results suggest the existence of FeO at the interface. Other studies could not find any metal oxide. Therefore, we tried to clarify the question of whether FeO exists at the interface between MgO and Fe [1] using the new method of hard x-ray photoemission with standing wave excitation.

X-ray standing wave excitation

The photoemission process is excited by an x-ray standing wave field. This field results from the interference of the incoming wave with the reflected wave. In order to gain a high reflectivity for soft x-rays we use multilayer mirrors, in first order of the Bragg reflection. At this angle the periodicity of the standing wave equals the multilayer period. Thus, the length scale of the probing field can be adjusted by the chosen mirror and it can be tuned to the interesting dimension of the sample under investigation, e.g. in our case a few nm.
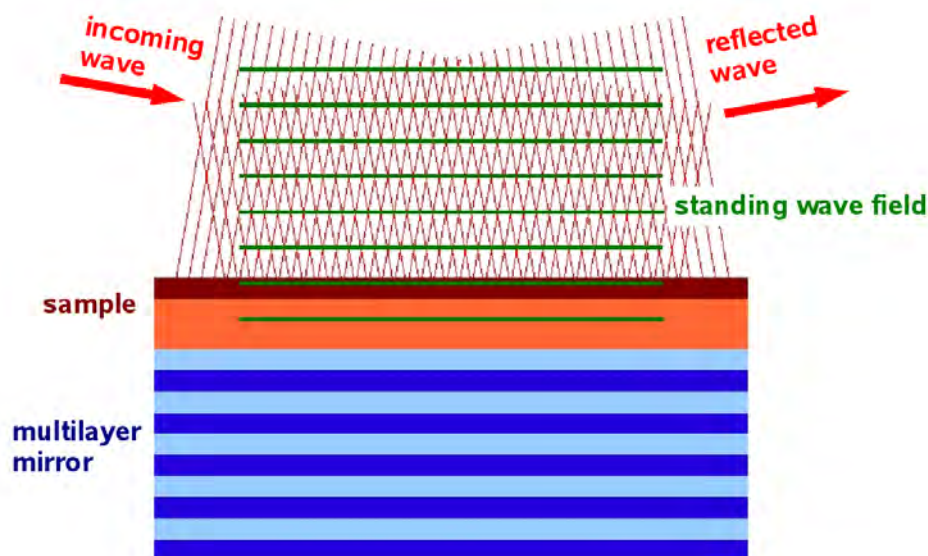
Figure 1: Schematic setup for the standing wave experiments. The incoming and the reflected wave form a standing wave field above the mirror. The sample is grown directly on the mirror and the standing wave can be moved through the sample.

During the experiment various XPS signal intensities are recorded either as a function of the incidence angle or as a function of the thickness in the wedge-type samples. These photoemission experiments provide elemental sensitivity as well as sensitivity for different chemical states of a given element.

In the first case the sample is rotated in small steps through the Bragg angle. At the Bragg angle the x-ray field intensity is amplified and modulated by the reflected wave leading to a resulting standing wave field. The actual modulation depends on the phase of the interference field around the emitting atoms within the sample. This phase is shifted as a function of the height above the multilayer mirror.

The shape and strength of this so-called rocking curve contain information on the layer thickness, the height above the mirror, and the interface roughness at the site of the emitting atoms [2].

A complementary, and in some ways more powerful, way of investigating buried interface structures is a combination of a wedge shaped sample with x-ray standing waves, as shown in Figure 2. The wedge changes its thickness by a few standing wave periods over the full width of the sample. An x-ray beam of < 1 mm height illuminates a small fraction of the sample which is macroscopically practically flat. The sample is moved perpendicular to the incoming light which moves the x-ray standing wave field along the slope of the wedge. Thus the intensity field of the x-ray standing wave field can be adjusted to coincide with different layers of the sample or with a specific interface. We choose the Bragg angle as the angle of incidence [3]. Figure 2 shows our actual wedge-type sample.
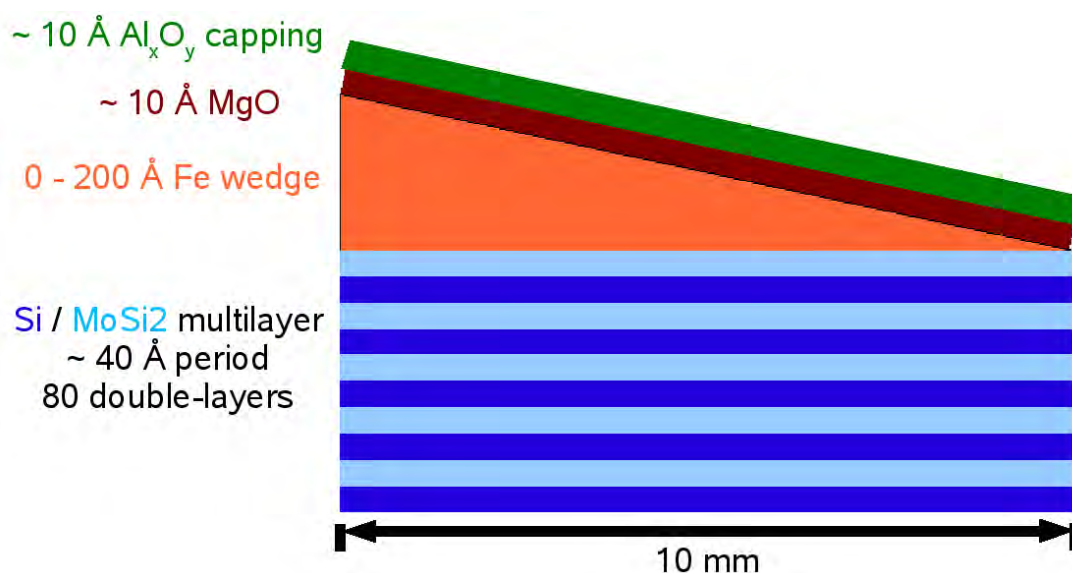
Figure 2: Schematic view of our wedge sample. The interface between the Fe wedge and the MgO layer above can be moved through the standing wave field. The photoemission signals is modulated as a function of the sample position.

Preliminary results

The wedge shaped Fe-layer provides direct access to the relative phase of the standing wave field. We recorded the XPS signals of Al 1s, O 1s, and Mg 1s as a function of the lateral position of the sample relative to the beam. The phase in each layer changes with the thickness of the Fe wedge below the sample.

The relative phase of the signals can directly be determined from the wedge scans, also the relative heights are accessible if the periodicity of the standing wave is known. At the Bragg angle this periodicity equals the period of the multilayer, which is known to be ~ 40 Å. It is possible to determine the thickness of the Al_xO_y layer to be ~ 10 Å directly from Fig. 3. Furthermore, the two components of the O 1s signal at 3463 eV and 3464.5 eV can easily be assigned to MgO and the Al_xO_y capping layer, respectively.
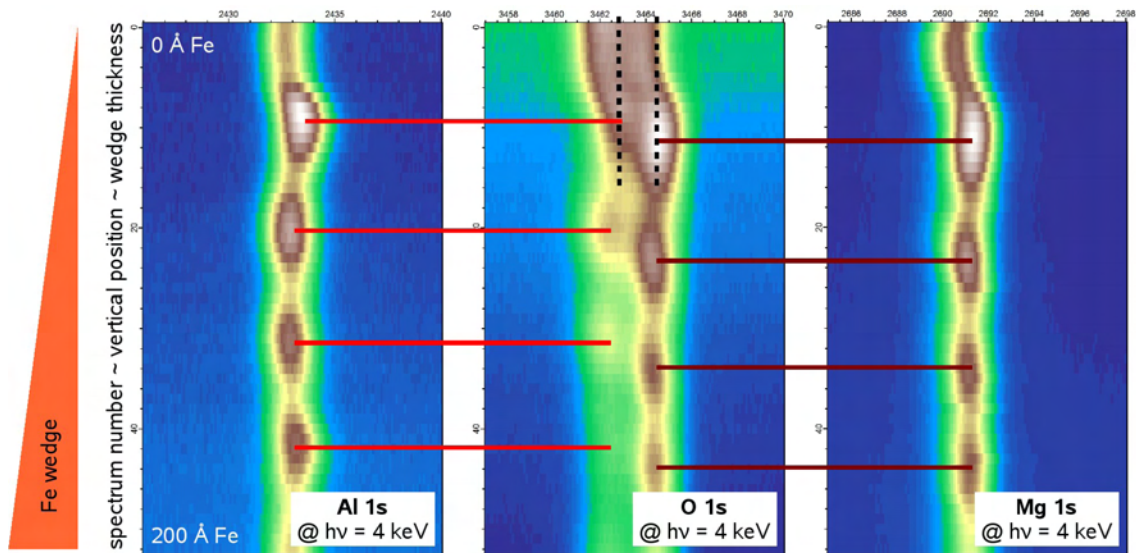
Figure 3: Raw data analysis of the experimental data. The modulation of the XPS intensities are color coded here. The horizontal lines connect equal phases.

So far we could not find any hint for the formation of FeO at the interface between the Fe wedge and the MgO layer above. There is no visible oxide component close to the Fe signals and there is also no component in the O 1s signal that could not be assigned to the MgO or Al_xO_y layers. The detailed quantitative analysis is still in progress.

Acknowledgments

[1] L. Plucinski et al., Phys. Rev. B **75**, 214411 (2007)
[2] S.H. Yang et al., J. Appl. Phys. **103**, 07C519 (2008)
[3] S.H. Yang et al., J. Phys. Cond. Matt. 14, L406 (2002)

Emission of a correlated electron-pair from a clean W(001) surface upon absorption of one photon

M. Muñoz-Navia, C. Winkler M. Birke, F.O. Schumann and J. Kirschner

Max-Planck-Institut für Mikrostrukturphysik, Weinberg 2, D-06120 Halle

The correlation between electrons influences the electronic structure of bulk and, even more, of low-dimensional materials. It manifests itself in enhanced or suppressed magnetic susceptibilities of paramagnetic metals, large electronic coefficients of the heat capacity, or in differences between experimental and theoretical one-electron band widths, to name a few examples. An external perturbation like electrons or photons that are introduced to the specimen by use of an external source to probe a system may excite simultaneously many degrees of freedom. For example in the case, when electrons in the valence band of the specimen share the energy of an absorbed photon and then the compound as a whole is excited. Resolving the excited state of one of the electrons, as in single photo-electron emission, yields integral information on the influence of the coupling to the surrounding medium. Obviously, more details are revealed on whether and how the particles are correlated, if the states of two photon-excited particles are measured [1]. A quite promising way to investigate these correlation effects is to study the double photo-electron emission (DPE). It has been established theoretically that the double photo-electron emission (direct excitation process) is forbidden in the absence of correlation (electron-electron interaction) [2]. Within the dipole approximation, the selection rule leads to a deep minimum in the cross section for equal energy sharing in a symmetric detection geometry under normal incidence. Alternatively, pair emission can happen via a two-step process, where the incoming photon is absorbed by a single electron which further scatters from another valence electron [3]. This process can be seen as an *internal (e,2e)*.

Experimental details

Electron coincidence spectroscopy (γ,2e) has been carried out utilising a pair of reflection time-of-flight (TOF) spectrometers. The TOF distributions of the electron pairs were measured, and from that the corresponding energy distribution was calculated. Data were taken on a W(001) single crystal surface at a photon energy of 25.0 eV. These data are compared to results from a previous single bunch run at BESSY II, and it will be discussed with respect to the possible collision processes that were mentioned above. The current setup was already described in detail in one of our previous reports [4]. Briefly, the experiment was carried out under UHV conditions (base pressure in the chamber was $< 10^{-10}$ mbar) at a photon energy of $h\nu = 25$ eV by utilising the TOF-technique. We used the monochromatized synchrotron radiation of the CPNIM dipole beam line at the BESSY II storage ring as an excitation source. Due to the TOF-technique, the single bunch mode of BESSY II is required. The incoming light of the monochromator was aligned parallel to the W(100) single crystal normal, and two channel-plate (MCP) detectors were positioned symmetrically ($\pm 40°$) with respect to the normal. With this setup an energy resolution of $\Delta E \approx 0.5$ eV for $E_{kin} = 20$ eV can be achieved [5]. The yield of electrons ejected from the surface of a clean tungsten crystal upon the absorption

of an incoming pulsed photon flux were detected in coincidence pairs through a logic circuit. The W(001) surface was cleaned by standard procedures which included oxygen treatment followed by high temperature flashes. The surface cleanness was monitored by Auger spectroscopy. The sample was periodically (about every 45 minutes) heated up to $\approx 1000°$ C between measurements to remove adsorbed gases from the sample surface.

Results

In order to analyze the measured data, we calculated the kinetic energies of the two electrons E_1 and E_2 that form an electron pair from its measured TOFs, and we plotted the abundance of corresponding pairs as a function of the respective kinetic energies in a 2D-plot, Fig. 1. In the following, we refer to those graphs as *2D-energy distributions*. Fig. 1 (b) shows data taken with $h\nu = 29.5$ eV from a previous single bunch run, while the current results ($h\nu = 25.0$ eV) are given in Fig. 1 (a).

(a) $h\nu = 25.0$ eV (b) $h\nu = 29.5$ eV
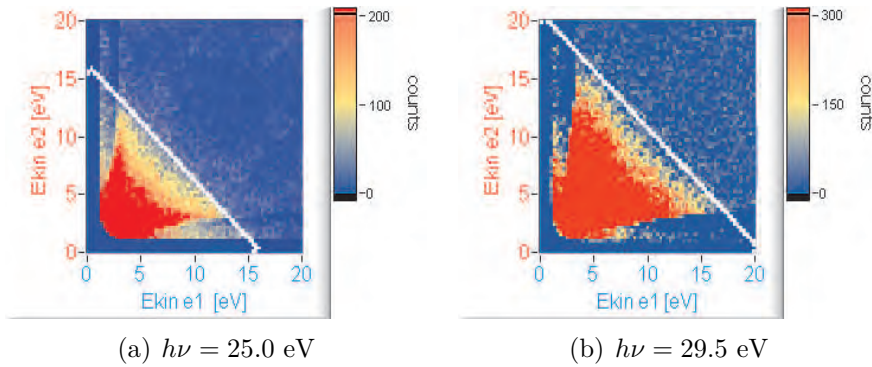
Figure 1: (γ,2e) 2D-energy distributions of correlated photoelectrons for W(001) taken at $h\nu = 25.0$ eV (a) and $h\nu = 29.5$ eV (b), respectively. The white lines indicate the onset of pair emission.

According to the law of energy conservation, the emission onset of the pair is given by $h\nu - 2 \cdot W_A = E_1 + E_2 = E_{sum}$, where $h\nu$ is the incident photon energy and W_A is the work function of the sample (4.6 eV for W(001)). The emission onset is indicated by white lines in Fig. 1.

Following the intensity distribution in Fig. 1 it turns out that the intensity basically increases rapidly as soon as the law of energy conservation is satisfied, however, it has to be noted that the increase of intensity does not follow equally all possible energy pairs, i.e. the white lines in Fig 1, but electron pairs with very different energies appears more likely. This seems to be even more significant for lower incident photon energies (Fig. 1a). In oder to illustrate this observation further, the data were replotted by considering only the intensity distribution in the range of $E_{sum} \pm 0.3$ eV along the onset of emission. This results in *energy sharing curves*, see Fig. 2. The minimum in the sharing curves at equal energies indicates that (γ,2e) scattering process is dominated by the DPE process [2]. It should be noted that the presence of the absorption of a photon by a single electron which scatters from another electron (the so call two-step process or internal (e,2e)) has generally to be assumed [3]. However, to get a deeper insight into the involved collision
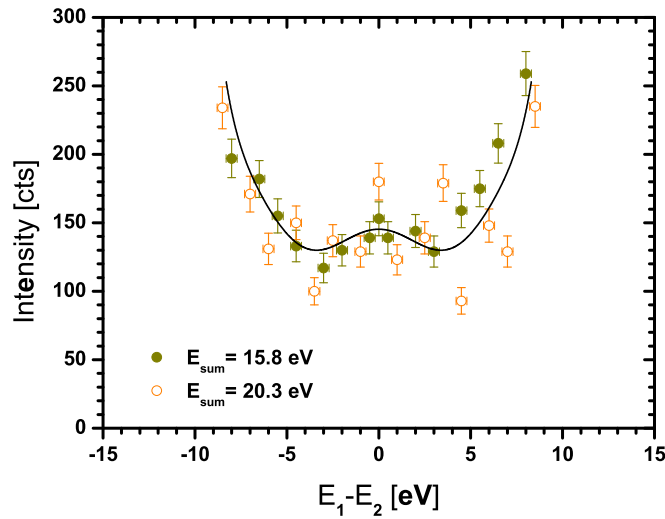
Figure 2: Energy-sharing distributions for a clean W(001) surface at photon energies of 25.0 eV (dark-yellow dots) and 29.5 eV (orange circles). The black solid-line is a guide a to the eye. The measurements where carried out with incoming light parallel to the surface normal.

processes, further measurements at BESSY II in single bunch mode are necessary.

We would like to take the opportunity to thank the BESSY staff for the excellent support.

References

[1] N. Fominykh, J. Berakdar, J. Henk and P. Bruno, Phys. Rev. Lett. **89**, 086402 (2002).

[2] J. Berakdar, Phys. Rev B **58**, 9808 (1998).

[3] Theoretical curves (after J. Berakdar) shown in R. Herrman, S. Samarin, H. Schwabe and J, Kirschner, J. Phys. IV France **9**, 127 (1999).

[4] C. Winkler M. Muñoz-Navia, K. Hünlich, H. Chang, R. Patel and J. Kirschner, BESSY Annual Report, 458 (2006).

[5] J. Kirschner, G. Kerherve and C. Winkler, Rev. Sci. Instrum. **79**, 073302 (2008).

Detailed electronic structure of copper phthalocyanine thin films

J. Ivanco,[a] T. Toader,[a] G. Gavrila,[b] W. Braun,[b] and D.R.T. Zahn[a]

[a] Institut für Physik - Halbleiterphysik, Technische Universität Chemnitz, D-09107 Chemnitz, Germany

[b] Helmholtz-Zentrum Berlin für Materialien und Energie GmbH, Albert-Einstein-Straße 15, D-12489 Berlin, Germany

The electronic structure of highly-ordered copper phthalocyanine (CuPc) thin films is unravelled. Particular molecular orbitals were identified via the deconvolution of the well-resolved valence band and their character in terms of the contribution of constituent atoms is addressed. The line shape of the valence band was found to be closely related to the molecular orientation in the films.

The electronic structure of copper phthalocyanine (CuPc) molecules has been extensively studied over the last decades both theoretically and experimentally.[1-5] Obviously, the experimental studies are lacking experimental resolution incommensurate to particular details on molecular orbitals provided by theoretical models. The reason resides in the complexity of the valence band (VB) consisting of many partly overlapping molecular orbitals.

Here, we report on the electronic structure of the CuPc thin films. The entire sample preparation and its characterization by photoelectron spectroscopy and NEXAFS were performed *in situ* at the Russian-German Beam Line using the MUSTANG experimental end station.

Fig. 1 shows the VB spectra of CuPc thin films with distinct molecular orientation achieved via the specific substrate surface preparation.[6] Upon first inspection, besides the HOMO and HOMO-1 orbitals, three individual bands, B, D, and E, can be recognized along with an apparently single peak denoted C. These examples suggest that the changing line shape is indicative of the varying molecular orientation. While all indicated bands display changes in their line profiles, the most pronounced variations are discernable in the band B located at about 8 eV with respect to the vacuum level.

That the indicated changes in the VB line shape are rather an angular effect and not due to the varying electronic structure is evidenced in Fig. 2, where a qualitatively similar trend in the band B is observed upon varying the take-off angle of a particular film. In other words, the centroid of the band *B* shifts towards higher BE with increasing angle between the take-off angle

and the normal to the CuPc molecular plane. The well-identified HOMO, HOMO-1, and the peak C, the variations of the band B and the experimental resolution allow an unambiguous determination and parameterization of particular orbitals in this region of the VB.

The spectra plotted in Fig. 2 were deconvoluted as follows: The HOMO, which is
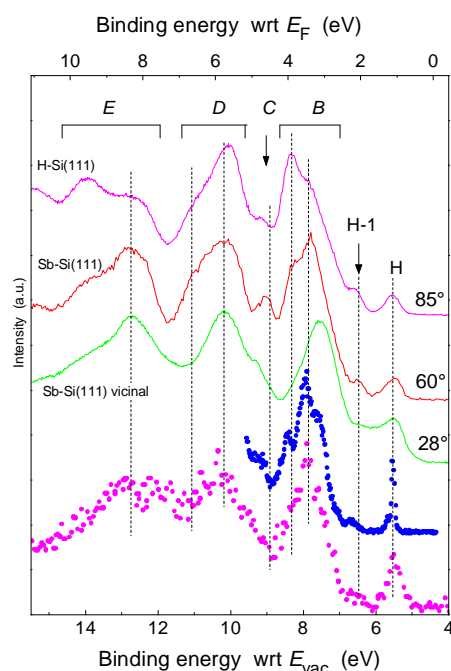
FIG. 1 Valence bands of about 10 nm thick CuPc films (lines) with various molecular orientations with respect to the substrate (indicated next to the curves), as determined by NEXAFS. The spectra were recorded at normal emission and with photon energy of 55 eV and are referenced to the vacuum level. The gas-phase CuPc valence band spectra (points) recorded either with HeII (Ref. 1, the bottom spectrum) or with 21 eV irradiation (Ref. 3, the "short" spectrum) are also given for comparison. The gas-phase spectra were shifted by 0.9 eV towards lower binding energies.
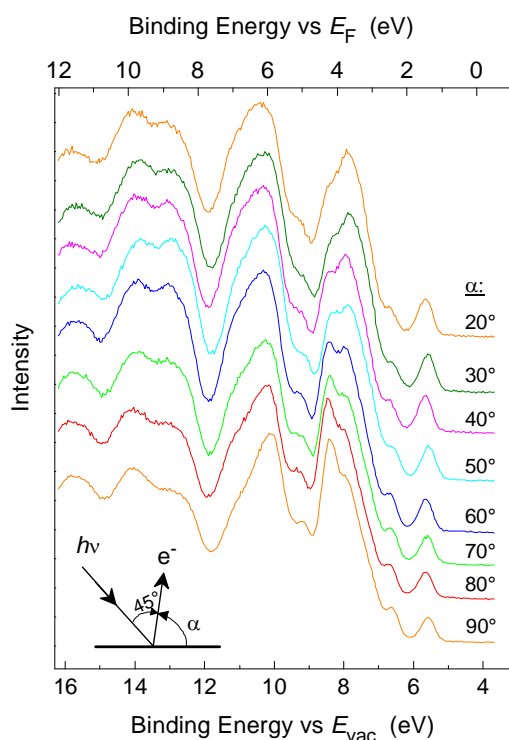
FIG. 2 Angle-resolved valence band spectra of 4.8 nm thick CuPc; the take-off angles are indicated next to the curves. The molecular orientation evaluated by NEXAFS was 70±2°. The spectra were obtained with an incidence photon energy $h\nu$ = 55 eV. All spectra are normalized by the intensity of noise at the Fermi level, no smoothing was performed. Spectra are set off for clarity.

FIG. 3 Deconvolution of valence band spectra exemplified for the spectra recorded at take-off angles of 90, 60, and 30°. Prior to the deconvolution the spectra were stripped of the background being assumed to be of the Shirley form, which accounts for inelastic electron scattering. All spectra were normalized to the noise level at the Fermi level. The top spectrum contains labels of the particular orbitals; see Table I for numerical values of binding energies.

well isolated from the rest of the spectra, allowed an explicit evaluation of the Lorentzian contribution of 40 % and full width at half-maximum (FWHM) being 0.58 eV. The same value for the Lorentzian was employed for all orbitals, while marginally increased FWHMs were required to obtain a good fit when going to orbitals with higher BE. The peak locations and intensities were free parameters in the fitting and the number of orbitals was the minimal one required to get a good fit. Finally, the resulting number of orbitals in the band B agreed with the number of orbitals detected in the highly-resolved gas-phase spectra.[3] At least five components were required to fit the band D. Even though the orbitals are less apparent than in the band B at a coarse look, the fitting converged to the presented values. The fidelity of the fitting procedure is illustrated in Fig. 3, where spectra for three various take-off angles are exemplified. Table I presents the obtained particular energy levels obtained from the deconvolution of the valence band spectra. Molecular orbitals were labelled by numerical order starting with the HOMO, HOMO-1, etc. Even though the spectra

recorded at all take-off angles were deconvoluted, the orbital energies given in the table come from the fitting of the spectrum recorded at normal emission, since the work function evaluation required for the vacuum level reference was accomplished for this case.

The dependence of the photoionization cross section on the photon energy can be employed for an assessment of contributions from constituent atoms to molecular orbitals. For example, the C $2p$- and N $2p$-derived states quench by a factor of about 8 faster than Cu-derived states upon varying photon energy ranging from 55 to 150 eV.[7] Thus, the evolution of the intensity with the photon energy may allow assorting the particular orbital with atoms of the molecule. Admittedly, the method does not allow separating contributions of C $2p$ and N $2p$ orbitals due to their very similar cross section variations upon photon energy in the investigated range. Consequently, we can differentiate between the contribution from the central copper atom and the ring atoms only.

TABLE I The binding energies (BE) of molecular orbitals of the condensed CuPc films (obtained in this work) and free CuPc molecules (Refs. 1 and 3). The BEs are given either with respect to the Fermi level (BE wrt E_F) or with respect to vacuum level (BE wrt E_{vac}). Note that the latter corresponds to ionization energies.

Molecular orbitals (bands, numerical order)		Condensed films [a]		Gas phase	
		BE wrt E_F (eV)	BE wrt E_{vac} (eV)	BE wrt E_{vac} (eV)	
				Ref. 1	Ref. 3
HOMO		1.39	5.58	6.38	6.38
HOMO-1		2.42	6.61	7.45	7.59
B	-2	2.93	7.12	-	~8
	-3	3.29	7.48	8.31	8.46
	-4	3.69	7.88	8.79	8.79
	-5	4.22	8.41	9.39	9.28
C	-6	4.97	9.16	10.26	~10.1
D	-7	5.53	9.72	~10.6	
	-8	5.84	10.03		
	-9	6.29	10.48	~11.4	
	-10	6.75	10.94		
	-11	7.07	11.26		

[a] This work

* Note that the orbital binding energies gleaned from the gas phase are as measured, i.e. they were not corrected for the polarization energy inherent to solid films.

Figure 4 shows valence bands of an about 1.8 nm thick CuPc film grown on H-Si(111)-7×7 probed with different incidence photon energies. The spectra were normalized with respect to their D-band maximum to contrast the photon energy dependence of particular bands and peaks. The differences in relative peak intensities are due to the different $h\nu$-dependences of the photoionization cross section of particular orbitals. It is obvious that similar tendencies can be observed between (a) the most dominant MO in the band D and the HOMO-1 and (b) between the HOMO and the band B. A quantitative analysis of the intensity dependences of particular orbitals on the photon energy can be found elsewhere.[8] In short, we found that the HOMO and the band B have a purely ring character, while the HOMO-8 and HOMO-1 have the entirely and mostly Cu-derived character.
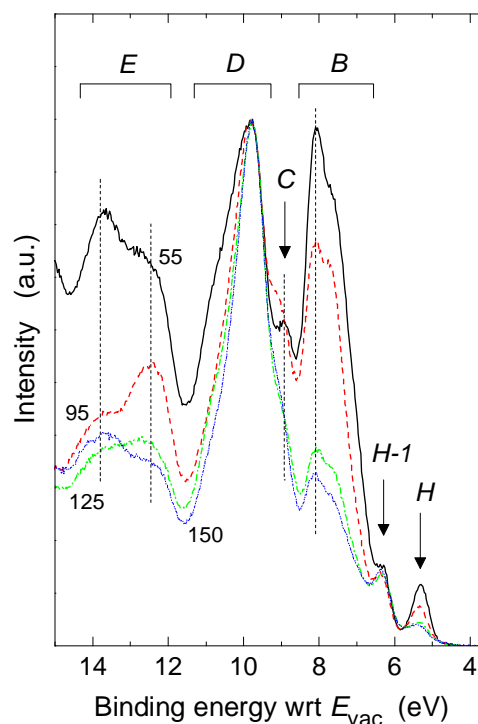
FIG. 4 Evolution of the valence band of an about 1.8 nm thick CuPc film grown on H-Si(111)-7×7 with the incidence photon energy being 55, 95, 125, and 150 eV. The molecular orientation was found to be 65±3° with respect to the substrate surface. The spectra were recorded at normal emission. The spectra were normalized to unity at the band D to visualise the evolution of relative intensities of particular molecular orbitals

1   J. Berkowitz, J. Chem. Phys. 70, 2819 (1979).

2   M.-S. Liao and S. Scheiner, J. Chem. Phys. 114, 9780 (2001).

3   F. Evangelista, V. Carravetta, G. Stefani, B. Jansik, M. Alagia, S. Stranges, and A. Ruocco, J. Chem. Phys. 126, 124709 (2007).

4   H. Peisert, M. Knupfer, T. Schwieger, J. M. Auerhammer, M. S. Golden, and J. Fink, J. Appl. Phys. 91, 4872 (2002).

5   V. Y. Aristov, O. V. Molodtsova, V. Maslyuk, D. V. Vyalikh, V. M. Zhilin, Y. A. Ossipyan, T. Bredow, I. Mertig, and M. Knupfer, Appl. Surf. Sci. 254, 20 (2007).

6   T. Toader, G. Gavrila, J. Ivanco, W. Braun, and D. R. T. Zahn, submitted to Appl. Surf. Sci.

7   J. J. Yeh and I. Lindau, Atomic Data and Nuclear Data Tables 32, 1 (1985).

8   T. Toader, G. Gavrila, W. Braun, J. Ivanco, and D. R. T. Zahn, submitted to phys. stat. sol. (b).

Ultra-thin films of α-NPD: A VUV ellipsometry analysis

S. Rudra[1], C. Himcinschi[1], S. J. Louis[1], M. Friedrich[1], C. Cobet[2], N. Esser[2] and D.R.T. Zahn[1]

[1]*Chemnitz University of Technology, Semiconductor Physics, D-09107 Chemnitz, Germany*
[2] *Institute for Analytical Sciences, D-12489 Berlin, Germany*

Introduction

Organic light emitting devices (OLED) have attracted much attention because of their superior characteristics such as high brightness, wide viewing angle, fast response time and low operating voltage [1,2]. Small molecules based OLEDs often include N, N'- Di (napthalen-1-yl)-N, N'-diphenylbenzidine (**α-NPD**) as a hole transporting layer [3], sometimes it is also used as a blue-emitter [4,5]. Considering the optical properties of these organic materials, the bulk dielectric function is always approximated to represent the thick film but determination of the optical properties of ultra-thin films is a most challenging and interesting task because in this regime the substrate and molecular interaction plays the most dominant role.

The aim of this work is to use vacuum ultraviolet (VUV) ellipsometry to study the growth of NPD from ultra-thin thicknesses to bulk-like thicknesses and to address the reason behind the difference in the optical response of the ultra-thin thickness regime compared to the bulk one.

Experimental

NPD films were grown by organic molecular beam deposition (OMBD) on three different substrates: H-Si (111), Zn- and O- terminated ZnO (0001). High quality sublimed NPD from Sensient Technologies was evaporated in a UHV chamber at a base pressure of 5×10^{-9} mbar from a Knudsen cell situated 20 cm away from the substrate holder. After deposition the samples were transferred to the analysis chamber (base pressure 6×10^{-9} mbar). *In situ* VUV-SE measurements were performed in the spectral range from 4.0 -9.0 eV photon range using the 3m-NIM1 monochromator in BESSY. The spectra were recorded using a rotating analyzer type ellipsometer at a fixed angle of incidence of (68°±0.5°). A more detailed description of the ellipsometer can be found elsewhere [6].

Results and discussions

The thickness of the NPD film was calibrated in the absorption free range of 0.73-2.5 eV using a VASE Ellipsometer from Woollam employing a single Cauchy dispersion relation as the deposited film was found to be isotropic in properties [7,8]. The dielectric function of the deposited film was found using a three phase model within the spectral range from 4.0-9.0 eV. An initial point by point fit was used to simulate the optical properties in which the data are fitted at each energy position separately, and then a general oscillator model using a number of Gaussian oscillators were used to fit the dielectric function.

It was found that the optical response of the NPD film is independent of the nature of the substrate in the bulk regime. To check whether this is the same for ultra-thin films, we also studied films with thicknesses in the submonolayer range on three different substrates.

Fig. 1 shows that the absorption feature of the NPD films for the ultra-thin thickness is sharper and spectrally blue-shifted compared to that of the thicker ones.
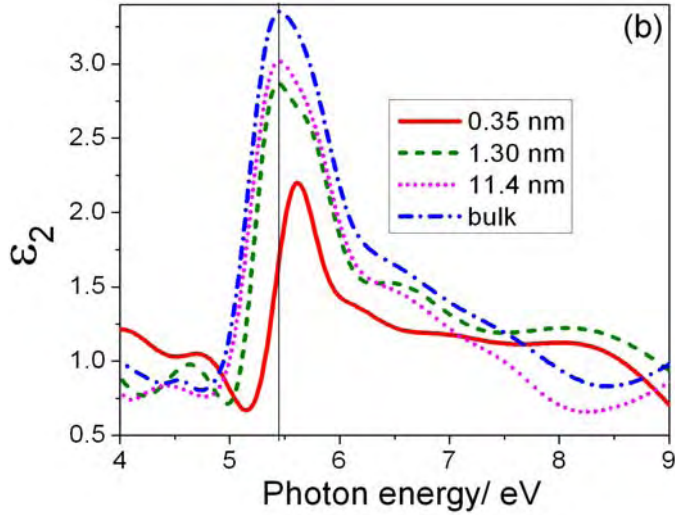
Fig. 1 Dielectric function of NPD films on ZnO-Zn starting from submonolayer regime to bulk thickness.

Further inspection shows that optical transitions of the 1.3 nm thick NPD film arise at the same energy as of the bulk one. A similar spectral blue-shift in optical transitions was reported in earlier work for ultra-thin Alq$_3$ films on H-Si (111) [9] and only reduced intermolecular interaction was given as a reason behind this phenomenon. To confirm the influence of the substrate on the spectral blue-shift, deposition of ultra-thin NPD films on two other substrates of ZnO-O and H-Si (111) was also studied.

In order to find out the optical response a separate approach for ultra-thin films in submonolayer coverage proposed by Aspnes was used. According to this approach the effective dielectric function can be determined by the following equation [10]:

$$< \varepsilon > = \varepsilon_s + \frac{4\pi i d}{\lambda} \sqrt{\varepsilon_s - \sin^2 \phi} \frac{\varepsilon_s (\varepsilon_s - \varepsilon_L)(\varepsilon_L - 1)}{\varepsilon_L (\varepsilon_s - 1)}$$

where, d is the thickness, λ is the wavelength of incident radiation, φ is the angle of incidence, ε_s is the substrate dielectric function and ε_L is the layer dielectric function. Once all other parameters are known ε_L can be found by using a quadratic equation, provided d<1 nm which is the submonolayer region for NPD films. Fig. 2 shows the comparison between the optical responses of the ultra-thin films deposited on different substrates as found from the ellipsometric simulation using the three phase model as well as Aspnes formula. It can be seen that the two different approaches are in good agreement showing that the separation of the dielectric response of the substrate and the overlayer is accurate.

The blue-shift in the optical spectra in figure 2 is clearly substrate dependent. (0.16 eV for Zn-O and 0.34 eV for H-Si). Reduced intermolecular interaction and the influence of the local field imposed by the substrate are supposed to be the reasons behind the spectral blue-shift [11] in the submonolayer regime.
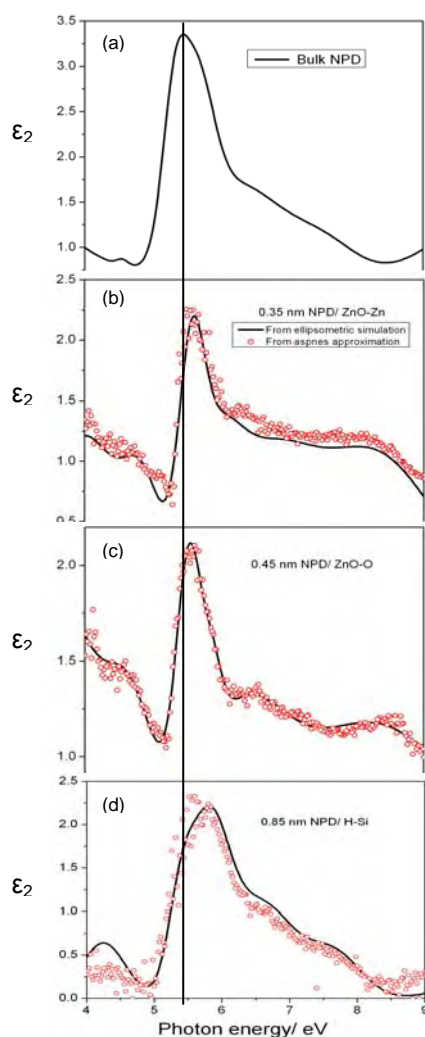
Fig. 2. Optical response of (a) bulk and ultra-thin films in the submonolayer regime on (b) ZnO-Zn, (c) ZnO-O and (d) H-Si.

Whithin the first monolayer the molecules themselves interact very weakly with each other and hence the influence of the local field imposed by the substrate on the molecules dominates but the amplitude of the local field is substrate dependent [12] and hence the extent of spectral blue-shift is influenced by the nature of the substrate. Now with increasing coverage, the local field imposed on a single molecule changes due to increased polarizability of the layer and the resonances are shifted to lower energies, showing increasing dielectric screening in the layer.

Conclusions

Good agreement between the optical responses obtained by two different methods shows the accuracy of ellipsometry in the submonolayer thickness regime. Even though reduced intermolecular interaction is supposed to be the primary reason behind the spectral blue-shift in the submonolayer region, the substrate dependence stems from different local fields present due to different surrounding polarizing media, i.e. different substrates.

Acknowledgements

[1] J. Kido, M. Kimura, K. Nagai, Science 267 (1995) 1332.
[2] J. Kido, C. Ohtaki, K. Hongawa, K. Okuyama, and K. Nagai, J. Appl. Phys. 32 (1993) L917.
[3] W. Helfrisch and W. G. Schneider, Phys. Rev. Lett. 14 (1965) 229.
[3M.Aonuma, T. Oyamada, H. Sasabe, T. Miki, and C. Adachi, Appl. Phys. Lett. 90 (2007) 183503.
[4] Y. Kijima, N. Asai and S. I. Tamura, Jpn. J. Appl. Phys., Part 1, 38 (1999) 5274.
[5] T. Tsuji, S. Naka, H. Okada and H. Onnagawa, Appl. Phys. Lett. 81 (2002) 3329.
[6] T. Wethkamp, K. Wilmers, N. Esser, W. Richter, O. Ambecher, N. Angerer, G. Jungk, R. L. Johnson and M. Cardona, Thin Solid Films, 313 (1998) 745.
[7] Sugiyama *et al,* Chem. Phys. Lett. 405 (2005), 330-333.
[8] Himcinschi *et al,* App. Phys. A 80 (2005), 551-555.
[9] O. D. Gordan, C. Himcinschi, D. R. T. Zahn, C. Cobet, N. Esser and W. Braun, Appl. Phys. Lett. 88 (2006) 141913.
[10] D. Aspnes, Spectroscopic Ellipsometry of Solids, edited by B. Seraphin (North-Holland, Amsterdam, 1976) Chap 15.
[11] H. Proehl, T. Dienel, R. Nitsche and T. Fritz, Phys. Rev. Lett. 93 (2004) 097403.
[12] A. Bagchi, R. Barrera and B. Dasgupta, Phys. Rev. Lett. 44, (1980) 147.

Structural and magnetic properties of Fe$_3$Si on MgO(001) and GaAs(001)

B. Krumme, C. Weis, E. Schuster, A. Warland, C. Antoniak, F. Stromberg

W. Keune, and H. Wende

Universität Duisburg-Essen, Fachbereich Physik, Experimentalphysik – AG Wende
and Center for Nanointegration Duisburg-Essen (CeNIDE)

Lotharstraße 1, D-47048 Duisburg, Germany
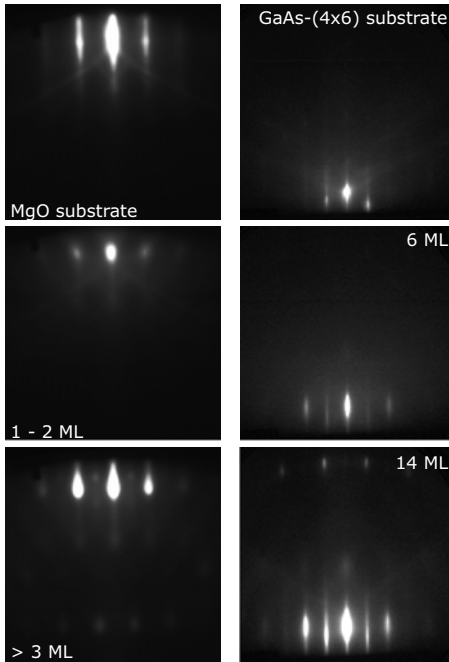
Figure 1: RHEED patterns of the Fe$_3$Si film growth on MgO (left column) and GaAs-(4 × 6) (right column) measured at 520 K with an electron energy of 15 keV.

In spintronic devices a spin-polarized current is injected from a ferromagnetic electrode into a semiconductor. This process is called spin injection. Heusler compounds are predicted to be half-metallic and therefore should exhibit a very high degree of spin polarization at the Fermi energy E$_F$ up to 100 % [1]. Fe$_3$Si is a binary Heusler compound which crystallizes in a D0$_3$ structure. Since spin injection from Fe$_3$Si into GaAs has been demonstrated successfully [2] Fe$_3$Si is a promising candidate as a material for ferromagnetic electrodes in spintronic applications. The highest degree of spin polarization current injected into a semiconductor can only be achieved with a perfect interface between ferromagnet and semiconductor. Therefore we studied the effect of different substrate surfaces on the growth and magnetism of Fe$_3$Si films.

Here we show our results from 80 Å Fe$_3$Si films on three different substrates, i.e. MgO(001) and GaAs with either a Ga-terminated (4 × 6) or an As-terminated (2 × 2) surface reconstruction. The sample prepared on MgO was used as a reference since we know from previous work that Fe$_3$Si films grow highly ordered on MgO. To compare the growth modes on the different surfaces the films were all prepared with identical parameters, i.e. substrate temperature of 520 K and equal deposition rates. The growth was monitored by reflection high energy electron diffraction (RHEED) (Fig. 1). On MgO (left column) we observed a direct change of substrate reflexes into Fe$_3$Si reflexes when initiating the film growth. In contrast, on GaAs-(4 × 6) the substrate reflexes totally vanish. At a film thickness of 6 ML the first Fe$_3$Si reflexes appear. This could be a first indication for an imperfect growth of Fe$_3$Si on GaAs-(4 × 6).

The x-ray absorption spectroscopy (XAS) and x-ray magnetic circular dichroism (XMCD) measurements were carried out at the PM3 dipole beamline at BESSY, whereas the chemical order-

ing of the films was investigated via conversion electron Mössbauer spectroscopy (CEMS) [6]. CEMS allows us to investigate the hyperfinefield distribution site-dependent, whereas XMCD yields the averaged magnetic moments of the Fe atoms.

Fig. 2 shows a comparison of the CEM spectra of the different substrates. The solid circles represent the experimental data and the red lines are the final fits to the data. In the case of MgO (top) we were able to fit the experimental data by a calculated spectrum of perfectly ordered Fe_3Si with a procedure based on [3]. On GaAs for both surface reconstructions it was necessary to include a second hyperfine field distribution (green line) in addition to the calculated one (blue line) to obtain a proper fit. It is likely that this additional contribution (green line) originates from the interface. This indicates a more disordered structure of Fe_3Si on GaAs than on MgO. Even the change of the surface shows a strong change in the CEM spectra suggesting a much better chemical ordering on the GaAs-(2×2) surface.

Figure 2: CEM spectra of 80 Å Fe_3Si on MgO (top), GaAs-(4×6), and GaAs-(2×2) measured at room temperature [6].

The results from the XAS and XMCD measurements are shown in Fig. 3. On the left we present a comparison of the data obtained for the Fe_3Si films on MgO (green line) and GaAs-(4×6) (red line) with an Fe reference (black line). The magnitude of the absorption signal at the L_3 edge compared to that of the Fe reference is reduced by ~ 8 % for Fe_3Si on MgO and reduced by ~ 17 % on GaAs-(4×6) indicating a change in the electronic structure. The absorption lines are broadened for Fe_3Si and a shoulder occurs 2 eV above the L_3 edge. Similar features are also found by Kallmayer et al. in the XAS of $Co_2Mn_{1-x}Fe_xSi$ [4]. They ascribed this feature to a very high order in the Heusler compound. The XAS for Fe_3Si on the different GaAs surfaces (on the right) is nearly identical. For the XMCD intensity at the L_3 edge we observed a reduction by 15 % for Fe_3Si on MgO in comparison to the Fe reference. In contrast, on GaAs-(4×6) this reduction becomes 31 % and on GaAs-(2×2) it increases to 38 %. From a sum rule analysis we calculated the magnetic moment per Fe atom. We obtained an averaged magnetic moment of 1.6 μ_B per Fe atom for Fe_3Si on MgO which is in good agreement with values from the literature, i.e. 1.63 μ_B [5]. For Fe_3Si on GaAs-(4×6) we obtained 1.5 μ_B which is whithin the error bar of the sum rules and on GaAs-(2×2) the magnetic moment is a bit reduced to 1.3 μ_B.

In conclusion, we determine similar averaged magnetic moments for Fe_3Si films on all substrates. However, from CEMS we could reveal considerable differences in the chemical ordering of the films. The averaged magnetic moments are obviously not dramatically influenced by disorder and therefore this property does not directly reflect the structural quality of Fe_3Si films. This is an important result since it reveals that the analysis of the averaged magnetic moment by magnetometries like XMCD or SQUID is not sufficient to judge on the chemical ordering of the Fe_3Si films.
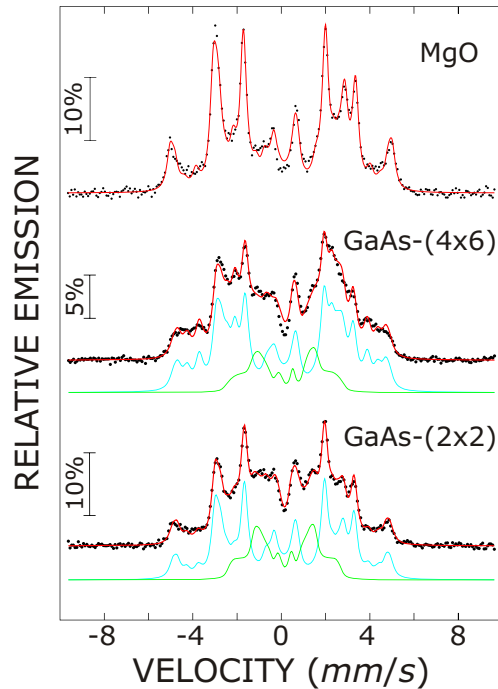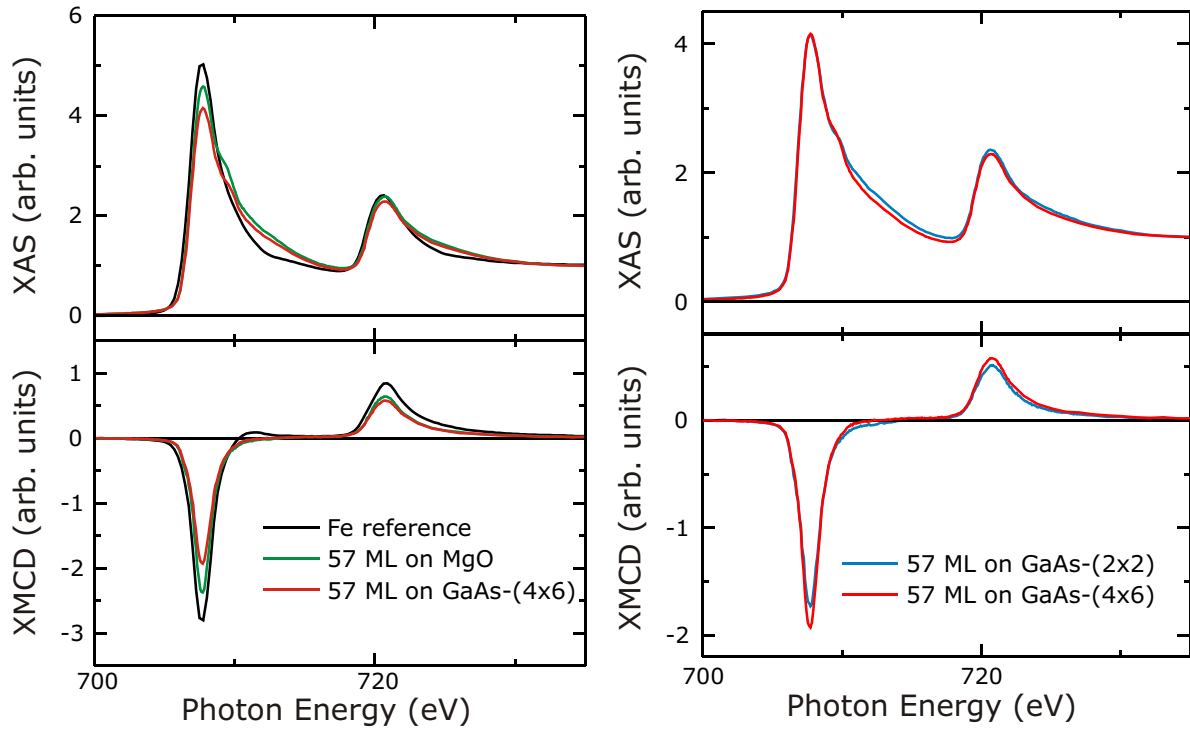
Figure 3: Left: Normalized XAS and XMCD of an Fe reference (black) and Fe₃Si on MgO (green) and GaAs-(4 × 6) (red). Right: Normalized XAS and XMCD Fe₃Si on GaAs-(4 × 6) (red) and GaAs-(2 × 2) (blue). All spectra measured at room temperature [6].

References

[1] R. A. de Groot, F. M. Mueller, P. G. van Engen, and K. H. J. Buschow, PRL **50**, 2024 (1983).

[2] A. Kawaharazuka, M. Ramsteiner, J. Herfort, H.-P. Schönherr, H. Kostial, and K. H. Ploog, Appl. Phys. Lett. **85**, 3492 (2004).

[3] M. Arita, S. Nasu, and F.E. Fujita, Trans. Jap. Inst. Met. **26**, 710 (1985).

[4] M. Kallmayer, H. J. Elmers, B. Balke, S. Wurmehl, F. Emmerling, G. H. Fecher, and C. Felser, J. Phys. D: Appl. Phys. **39**, 786 (2006).

[5] W. A. Hines, A. H. Menotti, J. I. Budnick, T. J. Burch, T. Litrenta, V. Niculescu, and K. Raj, PRB **13**, 4060 (1976).

[6] B. Krumme, submitted (2009).

Cobalt magnetic moment in Co_xPt_{1-x} clusters as a function of size, concentration and chemical order.

N. Blanc[1], M. Hillenkamp[1], A. Tamion[1], F. Tournus[1] and V. Dupuis[1]
C. Praetorius[2], T. Lödding[2] and K. Fauth[2]

[1] *Université Claude Bernard Lyon; CNRS; LPMCN, 69622 Villeurbanne, France*
[2] *Universität Würzburg, Department Physikalisches Institut, Germany*

Bimetallic Co_xPt_{1-x} nanoparticles are excellent candidates to achieve the Magnetic Anisotropy Energy (MAE) increase necessary for room temperature data storage applications. In our case, the samples were prepared at LPMCN (Lyon) using the LECBD (Low Energy Cluster Beam Deposition) technique [1, 2]. The stoichiometry of clusters has been tuned from pure Co clusters to Pt rich mixed clusters by using four targets with different cobalt compositions: Co, $Co_{0.75}Pt_{0.25}$, $Co_{0.5}Pt_{0.5}$ and $Co_{0.25}Pt_{0.75}$. In order to avoid interactions, clusters are embedded in various matrices thanks to an *in-situ* electron gun evaporator, and the cluster volume concentration is kept lower than 5%. For each composition, clusters samples have been previously characterized using transmission electron microscopy[3]: in each case, as-prepared clusters have a mean diameter of about a few of nanometers and are crystallized in the fcc chemically disordered phase. Their lattice parameter roughly follows a Végard law and their shape displays the typical facets of a truncated octahedron. After annealing, CoPt clusters coated with a-C layer exhibit the chemically ordered $L1_0$ tetragonal phase without coalescence effects[4]. The magnetic properties of the same samples have been systematically studied using SQUID magnetometry before or after the presented Co $L_{2, 3}$ edge XMCD measurements.

In this work, our aim was to address the role of the cobalt spin and orbital magnetic moments in the magnetic properties of well characterized Co_xPt_{1-x} clusters containing a few hundreds of atoms with adjustable size, chemical composition and order parameter, embedded in carbon matrices. For this purpose, we used X-ray Magnetic Circular Dichroism (XMCD) spectroscopy at the Co $L_{2, 3}$ edges (778 and 794 eV) under ± 3 T on the PM–3 beam line at BESSY to probe the effect of varying size (for a given stoichiometry x=0.5) and concentration (x=1, 0.25 and 0.75). For all samples the influence of chemical order on the magnetic properties is addressed. By performing XMCD measurements at both 12 K and room temperature, we have been able to measure the magnetic moments per Co atom on six samples of assemblies of non-interacting Co_xPt_{1-x} nanoclusters embedded in a carbon matrix, as-prepared and after *local* 2 hours 650°C annealing under vacuum. More precisely, the samples with a concentration x=0.5 are size-selected[5] meaning that the relative size-dispersion σ is limited to only 10%, while σ is around 40% for the other concentrations.

Size-selected CoPt Clusters in amorphous C matrices (diameter)	Co_xPt_{1-x} Clusters in amorphous C matrices
CoPt- 100V (2 nm)	Co
CoPt- 300V (3 nm)	Co_3Pt
CoPt- 500V (4 nm)	$CoPt_3$

Table I: *List of studied samples: 1) size-selected CoPt clusters with various diameters with a size dispersion σ about 10% and 2) Co_xPt_{1-x} clusters with a size dispersion σ about 40%, both embedded in C matrix as prepared and after annealing for 2 hours at 650°C.*

[1]**"Structural and magnetic properties of mixed CoPt clusters"** L. Favre, V. Dupuis, E. Bernstein, S. Stanescu, P. Melinon, A. Perez, T. Epicier, J.P. Simon, J.M.Tonnerre, D. Babonneau, Phys. Rev. B 74 014439 (2006)

[2] **"Magnetic anisotropy of Co_xPt_{1-x} clusters embedded in matrix"**, S. Rohart, C. Raufast, L. Favre, E. Bernstein, E. Bonet, V. Dupuis, Phys. Rev. B *74, 104408* (2006)

[3]**"Model predictions and experimental characterization of Co-Pt alloy clusters"** P. Moskovkin, S. Pisov, M Hou, C. Raufast, F. Tournus, L. Favre and V. Dupuis, European Phys. Journal D 43, 27–32 (2007)

[4] **"Evidence of $L1_0$ chemical order in CoPt nanoclusters : direct observation and magnetic signature"** F. Tournus F. Tournus, A. Tamion, N. Blanc, A. Hannour, L. Bardotti, B. Prével, P. Ohresser, E. Bonet, T. Epicier, and V. Dupuis, Phys. Rev. B, 77, 144411 (2008)

[5] R. Alayan et al., Rev sci instrum 75, 2461 (2004)

We used the total electron yield detection mode, which is essentially sensitive to the first surface layers. One can underline the absence of oxide signal at the *Co L₂, ₃* edge obtained for these samples. We can thus claim that thanks to the carbon "capping layers" our very reactive magnetic cluster samples are well protected from oxidation upon air exposure[6]. This is true for all samples under study here except for the CoPt-500V (4 nm) sample where an abnormal aging and oxidization effects have been seen on the Co $L_{2,3}$ edge, an effect that still has to be explained.

A preliminary treatment of the obtained data shows that the experiments were successful, as demonstrated by the values for spin and orbital momentum as derived for an annealed Co_3Pt sample, which are of the correct order of magnitude. The measured signals remain, however, small and an unambiguous quantitative evaluation demands a more sophisticated treatment and background correction, which are under way.

An example of experimental curves obtained on 3 nm Co_3Pt clusters diluted in an amorphous carbon matrix after annealing is given in figure 1.

a)   b)
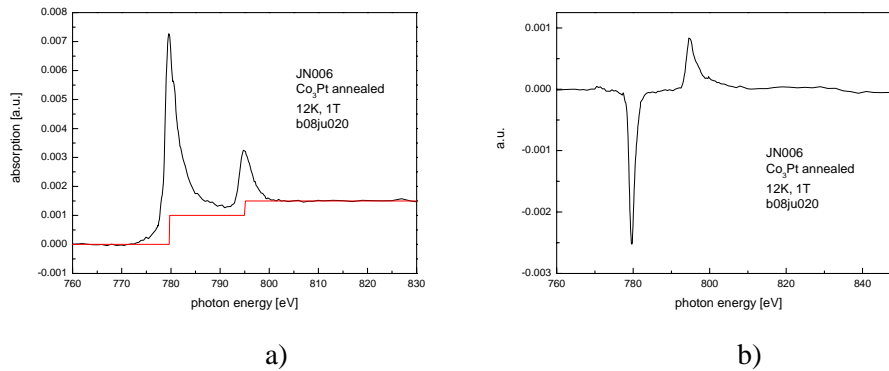
Figure 1: Co $L_{2,3}$ edges XMCD spectroscopy measurements at 12K under ± 1 T performed on a sample with Co_3Pt clusters 3 nm in diameter diluted in an amorphous carbon matrix after 2 hours 650°C annealing a) absorption spectra (in black) and the used two-step function (in red) b) normalized XMCD spectra to extract the m_L and m_S values from the sum rules.

By applying the sum rules, we present in *Table II* the spin magnetic moment m_S per Co atom and the orbital on spin moment m_L/m_S ratio for 12K and room temperature measurements on an annealed Co_3Pt sample. The number of holes per Co atom, is taken to be equal to $N_{holes} = 2.49$. For comparison, in the case of Co bulk phase[7], m_S, m_L/m_S, and N_{holes} are respectively equal to 1.62 μ_B/at, 0.095 and 2.49; while they are measured to be respectively 1.44 μ_B/at, 0.208 and 2.25 for a thin film of $CoPt_3$ alloy[8] and 1.76 μ_B/at, 0.068 and 2.628 for a presumably $L1_0$ CoPt thin film[9].

Temperature	annealed Co₃Pt sample
	m_S ($\mu_{B/at}$) - m_L /m_S
300 K	**1.7** - 0.086
12 K	**1.78** - 0.062

Table II: *Co₃Pt clusters diluted in an amorphous carbon matrix before and after 2 hours annealing at 650°C*

We previously mentioned that the increase of m_L/m_S in CoPt clusters is related to thermally assisted chemical ordering in such bimetallic clusters[4]. We claim that the protective carbon matrix allows us to both perform annealing on well-protected samples without nanoparticle coalescence and to reach a striking increase of the Co spin moment going with the $A1 \rightarrow L1_0$ transition for the CoPt samples. We hope to find evidence for a similar crystallographic transition into the $L1_2$ alloy phase also

[6] **"XMCD study of CoPt nanoparticles embedded in MgO and amorphous carbon matrices",** F. TOURNUS, A. TAMION, N. BLANC, P. OHRESSER, V. DUPUIS, Journal of Electron Spectroscopy and Related Phenomena <u>166-167</u> (2008) 84

[7] Chen, PRL75, p152 (1995)

[8] Grange, PRB58, p6298 (1998)

[9] Grange, PRB62, p1157 (2000)

for the Co_3Pt samples studied here, as evidenced by a systematic variation of spin and orbital momentum of the Co atoms.

One has to keep in mind that previous electron diffraction measurements on Co_xPt_{1-x} clusters protected by a thin amorphous silicon layer seemed to indicate surface segregation of the species in excess for the as prepared Co-rich phase[3], in agreement with theoretical predictions. So in this case, the effects of annealing treatments might be dependent of the stoichiometry x. A very careful examination of the present results on Co_xPt_{1-x} clusters embedded in a amorphous carbon matrix is in progress to avoid hazardous interpretation of the results as a function of size.

We have furthermore been able to measure the element specific magnetic response at the Co L_3 edge as a function of temperature. At 12 K hysteresis loops show that the ensemble is at least partially blocked whereas at RT purely superparamagnetic responses are seen. These results are important for an unambiguous corroboration of SQUID magnetization measurements that are always superposed by an important contribution from the substrate and possibly the matrix.

Finally, complementary experiments performed with hard X-rays beams delivered at the ESRF in Grenoble (GISAXS, XRD, EXAFS, XANES and XMCD measurements, at the *Pt L* and *Co K* edges) should shortly allow us to publish results concerning the effect of chemical order, cluster composition and size on the magnetic properties and to unravel the influence of Co and Pt atoms on the MAE.

Electronic and magnetic properties of iron nanostructures formed on a stepped silicon surface

I.I. Pronin[1], M.V. Gomoyunova[1], D.E. Malygin[1], S.M. Solov'ev[1], D.V. Vyalikh[2],
Yu.S. Dedkov[2], S.L. Molodtsov[2,3]

[1] Ioffe Physico-technical Institute, Russian Academy of Sciences, 194021 St. Petersburg,
Russia
[2] Institut für Festkörperphysik, Technische Universität Dresden, D-01309 Dresden, Germany
[3] Fock Institute of Physics, St. Petersburg State University, 198504 St. Petersburg, Russia

Thin iron and iron silicide films on silicon have been widely studied during the past twenty years due to a rapid development of solid-state electronics based on silicon technology [1]. The nanosize magnetic layers, lines, and dots formed on silicon are of the high potential for future applications as well [2]. However, tailoring of magnetic nanostructures requires a detailed knowledge of chemical, structural, electronic and magnetic properties of the Fe/Si interface at initial stages of their formation. Recently we have studied the magnetic behavior of ultrathin iron layers formed on the singular silicon surfaces [3]. The aim of the present work was to study the growth of iron nanostructures on the vicinal silicon surface and to investigate their electronic and magnetic properties.

The experiments were carried out at Russian–German beamline in a vacuum of 10^{-10} mbar. At first, the clean Si surfaces with regular arrays of bunched steps were prepared in UHV by thermal treatment of the vicinal Si(556) wafers. Characterization of the samples was performed by LEED. The nanostructures were fabricated by deposition of iron onto the stepped Si surfaces passivated by silver. The $\sqrt{3}\times\sqrt{3}$-Ag surface phase was formed on the substrates to suppress strong chemical reaction at the Fe/Si interface and to enhance the migration of Fe adatoms to the edges of the steps. The phase was grown by deposition of 0.8 Å of Ag on the samples heated to 500°C. The information about chemical composition and electronic structure of the deposited layers was obtained from core-level and valence-band photoelectron spectra taken at hν = 135 eV with the energy resolution of 100 meV.
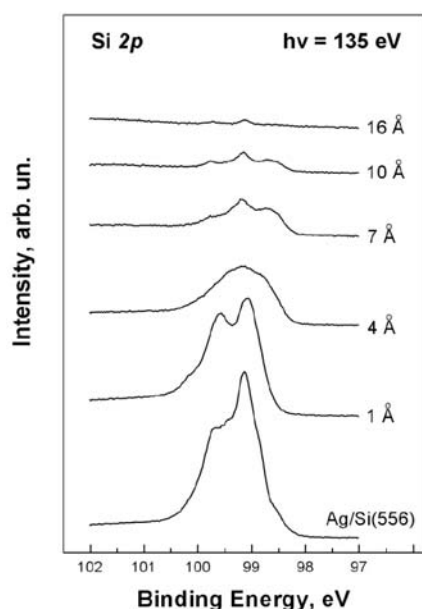
Fig. 1. The Si 2p spectra measured during Fe deposition on the Ag/Si(556) surface.
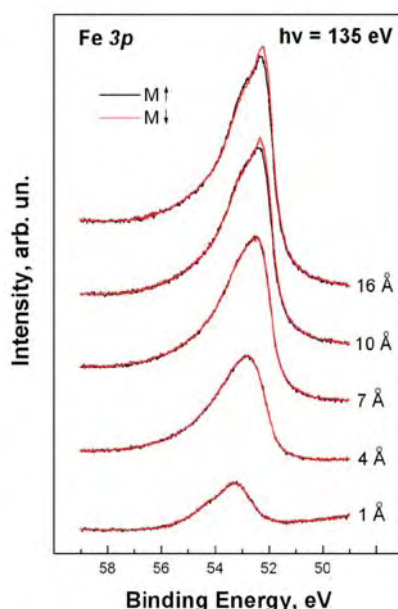
Fig. 2. The Fe 3p spectra measured during Fe deposition on the Ag/Si(556) surface for two opposite directions of the magnetic field.

The ferromagnetic ordering of the formed nanostructures was examined by magnetic linear dichroism (MLD) in the angular distribution of Fe 3p photoelectrons, as it was done in Ref. [3]. The samples were magnetized with a pair of Helmholtz coils fixed in the vacuum chamber. By passing pulsed current through the coils, one could generate a magnetic field parallel to the sample surface. The azimuthal <112> axis of the samples was collinear with the magnetization direction to within ± 5°.

The magnetic field of 10^3 Oe was applied to saturate the sample magnetization. The measurements of Fe *3p* spectra were performed in remanence at room temperature. The morphology of the grown structures was studied *ex situ* by atomic force microscopy (AFM).

The data obtained are illustrated in Fig. 1. The evolution of Si *2p* and valence-band spectra during the deposition of iron proved to be very similar to the one of the Fe/Si(111) system described in Ref. [3]. Analysis of the data obtained has shown that the √3×√3-Ag surface phase formed on the vicinal Si(556) surface does not influence considerably on the chemical composition of the growing layer. At the initial stage of iron deposition (1 Å Fe) the surface reconstruction disappears and the metastable FeSi silicide (with the CsCl structure) is formed at the interface. The process is followed by the island growth of the solid solution Fe-Si covered with segregated Si.
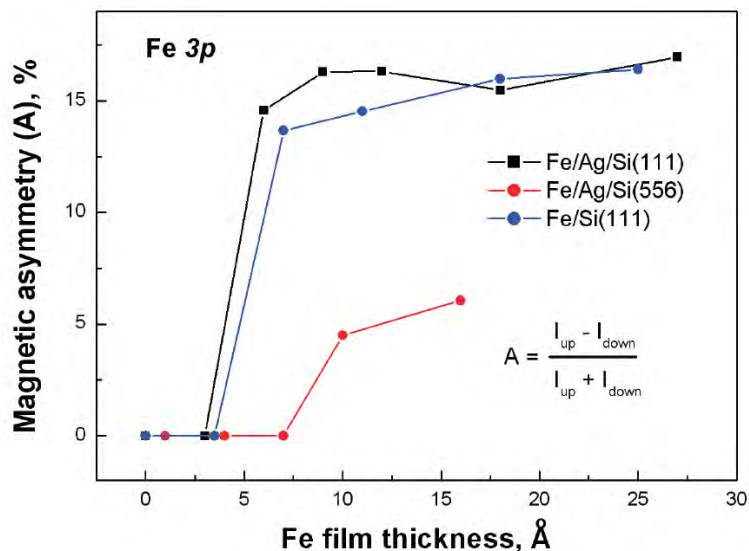
Fig. 3. The magnetic asymmetry amplitude *(A)* of the Fe *3p* spectra vs the Fe dose for the three interfaces.

At the same time, the stepped structure of the Si(556) substrate has great influence on the morphology of the growing layer. The AFM images have shown that at the initial stage of Fe deposition a regular system of stripes is formed on the sample surface. The stripes oriented along the steps consist of the clusters of Fe-Si solid solution with the average diameter of 30 nm. Besides, at coverages more than 7 Å the large iron islands (~100 nm) are formed on the sample surface.

The data illustrating magnetic properties of the formed nanostructures are presented in Fig. 2. The Fe *3p* photoelectron spectra were measured for two opposite magnetization directions oriented perpendicular to the substrate steps. No MLD effect is observed for the coverage range up to 7 Å, indicating the absence of in-plane ferromagnetic ordering of the nanostructures. The onset of the ferromagnetism was found after deposition of 10 Å Fe. It should be emphasized that the value of the threshold is considerable higher than the one observed in the case of iron layers grown on the singular Si surfaces. This fact is clearly seen from Fig. 3, where the magnetic asymmetry amplitude of the Fe *3p* spectra is shown as a function of the coverage for three systems investigated in identical conditions. Besides, the magnitude of the MLD effect is much smaller for the vicinal surface. Our findings can be explained by the strong magnetic anisotropy of the formed nanostructures.

References

1. M.V. Gomoyunova, I.I. Pronin, D.E. Malygin, A.S. Voronchihin, D.V. Vyalikh, S.L. Molodtsov. Surf. Sci. **601**, 5069 (2007).
2. D. Sander. J. Phys.: Condens. Condens. Matter. **16**, R603 (2004).
3. I.I. Pronin, M.V. Gomoyunova, D.E. Malygin, D.V. Vyalikh, Yu.S. Dedkov and S.L. Molodtsov. J. Appl. Phys. **104**, 104914 (2008).

Structure of Chromium monolayers studied by soft x-ray absorption spectroscopy

H.H. Rossner, D. Schmitz, and E. Weschke
Helmholtz-Zentrum Berlin für Materialien und Energie
Glienicker Str. 100, D-14109 Berlin, Germany

Magnetism at surfaces and interfaces has attracted much attention due to the prediction of greatly enhanced moments and large magnetic anisotropy in ultra thin films and due to the prospect of studying clean model cases of two-dimensional magnetism. Because of the strong relation between magnetic properties and crystallographic structure we investigated the possibility to study the structure of the 3d-transition metals in the soft x-ray energy regime using x-ray absorption at and above the overlapping L-edges. X-ray absorption fine structure (XAFS) studies performed by total electron yield detection enable the observation of surface phenomena due to the surface sensitivity inherent in low energy electron experiments. This capability is applied to chromium monolayers on Ag(100) surface. The Cr-Ag system has a very low lattice mismatch of ≈ 0.2 %, a wide miscibility gap above the melting point, and Cr can be grown epitaxially on Ag(100) without amalgamation and Ag segregation [1].

Cr films with average thicknesses of 1.0, 1.5, 2 and 4 Å were grown *in situ* at a pressure of $5*10^{-10}$ mbar and a substrate temperature of 440 K using an electron beam evaporator calibrated to a quartz balance. The experiment was performed with linearly polarized light at beamline UE46-PGM measuring energy scans of absorption coefficients $\boldsymbol{\mu}$ of the substrate and film-substrate systems separately, within photon energy range of $\Delta E = 550 - 1190$ eV at incident angles of $\theta = 30^o$ and $\theta = 90^o$ with respect to the surface plane. Signals of thin films contain large components from the substrate and are very sensitive to beamline systematic errors. In order to correct for intensity variations of the incident photons in time and energy the measured electron signals were normalized to the drain current of the last beamline mirror. To correct for energy dependence of monochromator transmission function and detector response the normalized film-substrate signal was divided by the normalized substrate signal.

The Bayes-Turchin method [2] was used in the analysis of the EXAFS spectra. This method allows to analyze simultaneously overlapping L-edge absorption spectra and the atomic like background component, takes into account the uncertainties of experimental data and model functions, and yields *a posteriori* parameters, *a posteriori* errors, and error correlations. In particular the method allows to include a large number of scattering paths which is indeed necessary at low wave numbers k of the EXAFS signal.

In our analysis we do not fit shell parameters to Fourier-filtered spectra of EXAFS oscillations, as usually done, but instead use the multiple-path expansion to extract average structure parameters from unfiltered $\boldsymbol{\mu}$ spectra. In the following we report upon results of 1.5 Å and 4 Å Cr films. The models we applied represent an idealistic view of the film-substrate system, i.e. we assumed one or three perfect monolayers of Cr on a perfect Ag(100) surface. For one monolayer of Cr the surface atoms of Ag were replaced by Cr atoms sitting in the most probable fourfold hollow site of Ag(100). The second and third layers of Cr were modeled according to the bcc-Cr crystal structure. The distance parameters d_i used in the

fit were the in plane Cr-Cr distance $d_{\text{Cr-Cr}}^{\text{ip}}$, the out-of-plane Cr-Ag distance $d_{\text{Cr-Ag}}^{\text{op}}$, and in case of three monolayers, we added the out-of-plane Cr-Cr distance $d_{\text{Cr-Cr}}^{\text{op}}$. All path-length parameters of the EXAFS formula were expressed in terms of d_i. Roughly 100 paths were treated considering a half-sphere cluster with radius 9 Å where the absorbing atom of the Cr monolayer was sitting between vacuum and Ag substrate. For multilayers the different sites of the absorbing Cr atom were taken into account. For the three-layer system, for instance, three sets of path expansions were averaged with the absorbing atom being placed in one of the layers separately. The disorder parameter of each path length is often written as sum of thermal and structural components. To disentangle the two contributions, one generally needs measurements at least at two different temperatures. For our measurements of overlapping L-edges at room temperature we assumed that the structural-disorder component can be neglected with reference to our idealistic model. We described the thermal vibrations by Debye-Waller parameters determined by a force-field model with spring constants κ_j : $\kappa_{\text{Cr-Cr}}$ for the nearest-neighbor Cr-Cr bond, $\kappa_{\text{Cr-Ag}}$ for the nearest-neighbor Cr-Ag bond, and $\kappa_{\text{Ag-Ag}}$ for the nearest-neighbor Ag-Ag bond. The start values of κ_j were set close to the values which describe the vibrational density of states (VDOS) of bcc-Cr and fcc-Ag extracted from inelastic neutron scattering. For fcc-Ag one spring constant of $\kappa_{\text{Ag-Ag}} = 21.5$ N/m was sufficient to approximate VDOS_{Ag}, and for the monolayer-substrate system we started the fit with $\kappa_{\text{Cr-Cr}} = \kappa_{\text{Cr-Ag}} = \kappa_{\text{Ag-Ag}}$. In case of bcc-Cr two spring constants were needed for an approximation of VDOS_{Cr}: $\kappa_{1,\text{Cr-Cr}} = 47.5$ N/m for the nearest neighbor bond and $\kappa_{2,\text{Cr-Cr}} = 25.5$ N/m for the next-nearest neighbor bond. The data sets measured at $\theta = 30^o$ and $\theta = 90^o$ were used in a bootstrap procedure to determine the structural parameters of the monolayer-substrate system successively. For the analysis of the 30° data and the 90° data the parameter vectors $\mathbf{x}$ were $\mathbf{x}_{30^o} = \left(\Delta\mu_{0,1} \ldots \Delta\mu_{0,14}, E_0, d_{\text{Cr-Ag}}^{\text{op}}, \kappa_{\text{Cr-Ag}}, \kappa_{\text{Ag-Ag}} \right)$ and $\mathbf{x}_{90^o} = \left(\Delta\mu_{0,1} \ldots \Delta\mu_{0,14}, E_0, d_{\text{Cr-Cr}}^{\text{ip}}, \kappa_{\text{Cr-Cr}} \right)$. For the multilayer-substrate system we took $\mathbf{x} = \left(\Delta\mu_{0,1} \ldots \Delta\mu_{0,14}, E_0, d_{\text{Cr-Ag}}^{\text{op}}, d_{\text{Cr-Cr}}^{\text{op}}, d_{\text{Cr-Cr}}^{\text{ip}}, \kappa_{1,\text{Cr-Cr}}, \kappa_{2,\text{Cr-Cr}}, \kappa_{\text{Cr-Ag}}, \kappa_{\text{Ag-Ag}} \right)$. The 14 parameters $\Delta\mu_{0,i}$, used for atomic like background correction, were equally spaced within the fitted k range.

The comparison of the experimental EXAFS oscillations with fit results is shown in Fig. 1. Uncertainties of experimental data are indicated by error bars which correspond to 0.3% of $\boldsymbol{\mu}$. Large error bars at $k \approx 6$ Å^{-1} are used for the L_1-edge region to account for uncertainties of the multiple-path expansion in edge regions. Uncertainties of the model were treated as described in Ref. [2]. In addition to the models of pure Cr layers we also applied models were an extra Ag monolayer is placed on top of Cr, with equal distances $d_{\text{Cr-Ag}}^{\text{op}}$ and equal spring constants $\kappa_{\text{Cr-Ag}}$ and $\kappa_{\text{Ag-Ag}}$ above and below the Cr film. Due to our simple model of ideal monolayers on an ideal surface we do not expect to reproduce the measured data in detail. However, it is clearly demonstrated that EXAFS can discriminate between one Cr monolayer and three Cr monolayer films. The differences show up in the region $k < 6$ Å^{-1} were the L_3 and L_2 components contribute, as well as in the region $k > 6$ Å^{-1}, where the L_1 component is added. In the second region we observe significant discrepancies between experimental data and models for the monolayer film at $\theta = 90^o$. At this angle the photon polarization vector is in the monolayer plane and sensitive to the inplane atom positions. Obviously our model of an ideal monolayer would need modifications. In case of three Cr monolayers this discrepancy is less pronounced. We further recognize that the models with Ag coverage give a slightly better fit in contradiction to the observation of Krembel et al. [1]. It is noted that data of overlapping L-edges are not very sensitive to κ_j. In these cases a priori information from inelastic neutron scattering is essential. Preliminary results of our analysis for 4 Å Cr on Ag are $d_{\text{Cr-Ag}}^{\text{op}} = 1.94 \pm 0.02$ Å , $d_{\text{Cr-Cr}}^{\text{op}} = 1.37 \pm 0.01$ Å , and $d_{\text{Cr-Cr}}^{\text{ip}} = 2.87 \pm 0.01$ Å . For 1.5 Å Cr on Ag we get $d_{\text{Cr-Ag}}^{\text{op}} = 2.05 \pm 0.01$ Å and $d_{\text{Cr-Cr}}^{\text{ip}} = 2.89 \pm 0.01$ Å .

References

[1] C. Krembel, M.C. Hanf, J.C. Peruchetti, D. Bolmont, and G. Gewinner, Phys. Rev. B **44**, 8407 (1991).

[2] H.J. Krappe and H.H. Rossner, Phys. Rev. B **70**, 104102 (2004).
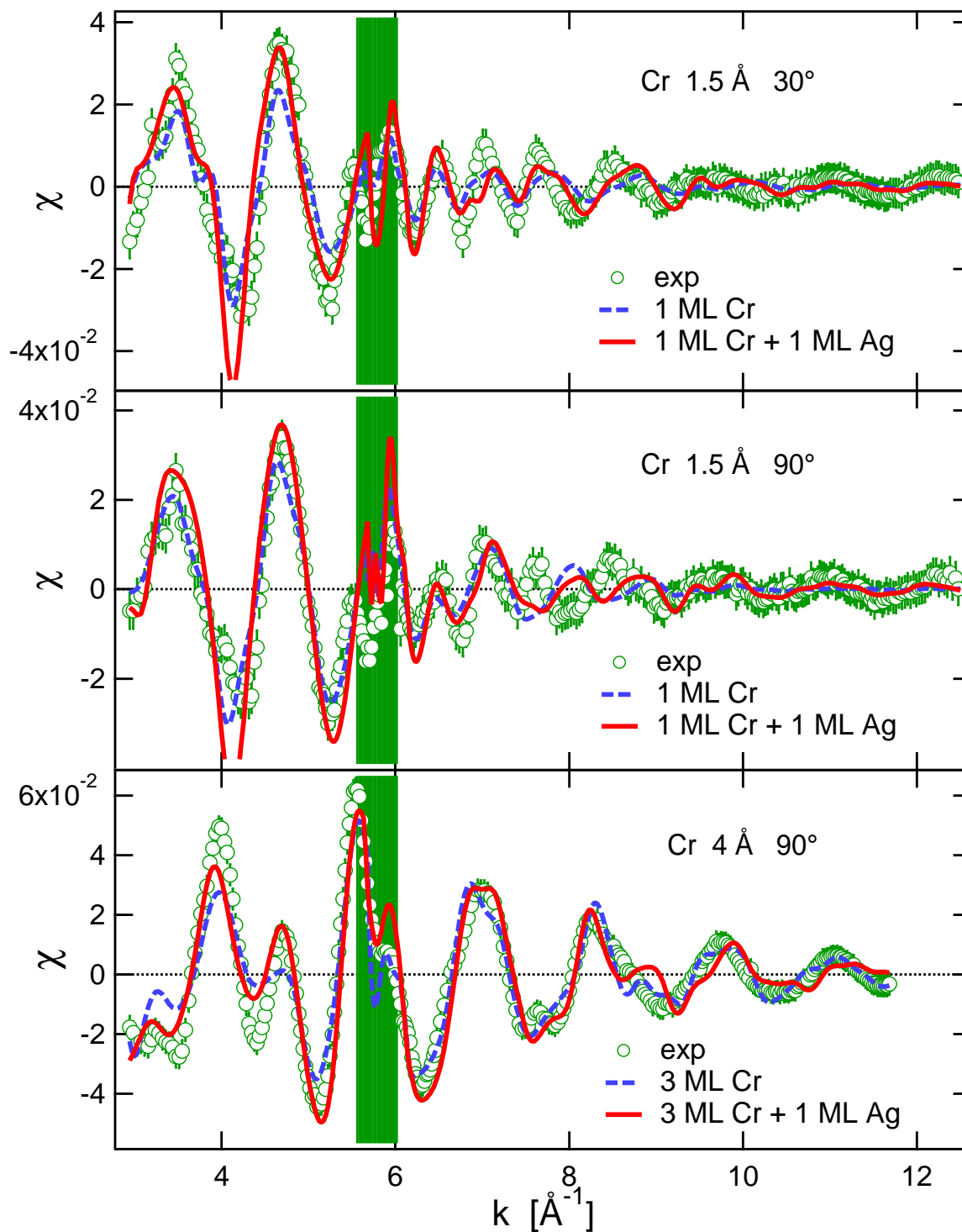
Figure 1: EXAFS oscillations χ of data (open dots) and models (lines). The model results of Cr layers on Ag substrate are shown by dashed lines, the model results with an extra Ag monolayer on top of the film-substrate system are shown by solid lines.

Self-assembled monolayers of azobenzene alkanethiols: Structure and optical properties

R. Schmidt[1,2], D. Brete[1,2], R. Carley[1], W. Freyer[1], C. Gahl[1], and M. Weinelt[1,2]

1. Max-Born-Institut, Max-Born-Straße 2 A, 12489 Berlin, Germany

2. Freie Universität Berlin, Fachbereich Physik, Arnimallee 14, 14195 Berlin, Germany

The functionalization of surfaces with molecular switches is a rapidly growing field in today's research. In this context self-assembled monolayers (SAMs) have often been considered ideal platforms to align and order molecules at surfaces. [1] Aromatic endgroups linked to a metal surface via alkanethiols represent here a versatile class of systems to control structure and energetics within the SAM. The balance of adsorbate-substrate and adsorbate-adsorbate interactions rules not only the supramolecular structure of the SAM [2] but has also strong influence on the optical properties and as a consequence the functional efficiency of the molecular switches.

By near-edge X-ray absorption fine structure (NEXAFS) spectroscopy and UV/Vis spectroscopy we investigated the geometric structure and the optical properties of wet-chemically prepared, well-ordered self-assembled monolayers of azobenzene linked via hexanethiol to a gold surface. By attaching a trifluoro-methyl endgroup to the chromophore both the molecular tilt and twist angles of the azobenzene moiety become accessible. Fig. 1 shows NEXAFS spectra of such 4-trifluoro-methyl-azobenzene-4'-methyleneoxy-hexanethiolat (TF-Az6) SAMs for the C1s and N1s edges, respectively, both for s- and p-polarized X-rays at an angle of incidence $\beta = 70°$. Experiments were performed at the U41-PGM beamline at BESSY. To reduce radiation damage the sample was kept at liquid nitrogen temperature and a fast shutter was used to block the beam during the scan of monochromator and undulator. The X-ray flux is measured at every wavelength with a GaAs photodiode integrated into the fast shutter.

The strongly polarization dependent NEXAFS signal is dominated by absorption from the azobenzene moiety since Auger electron emission from the buried alkane chains is strongly damped. At the carbon edge the dominant peak at around 285.7 eV corresponds to the transition from the C1s to π^*(LUMO) (lowest unoccupied molecular orbital), which extends over the two phenyl rings and the azo bridge. The width of 1.4 eV of this transition is attributed to the distinct chemical shifts of the C1s core levels in different environments within the chromophore. At the nitrogen edge the corresponding π^* resonance at 399.0 eV exhibits a much smaller width of 0.4 eV. From the respective polarization dependencies a mean tilt angle of the 1s to π^* transition dipole moment of $\alpha_{C1s} = 75 \pm 3°$ and $\alpha_{N1s} = 77 \pm 3°$ is deduced according to [3]. Since NEXAFS is a local probe of the electronic structure the comparable angles α_{C1s} and α_{N1s} indicate that the azobenzene moiety favors the *trans* conformation in thermal equilibrium.

Besides the pronounced π^* transitions the C1s NEXAFS spectra show sharp resonances in the energy range of 294 to 300 eV which are attributed to excitations at the CF_3 group since they are missing for the corresponding molecule without the marker group (not shown). In analogy to hexafluoro-ethane the main NEXAFS resonances are assigned to transitions to the σ^*(C-F) orbitals in the photon energy range of $295-298$ eV and to the σ^*(C-CF$_3$) resonance at 299 eV [4]. The polarization dependence of the latter is extracted by subtracting a background stemming from carbon shape resonances associated with the phenyl rings. It yields a tilt angle of $\vartheta(C - CF_3) = 17° \pm 5°$. The error bar accounts for the uncertainty of the background subtraction. From the measured orientation α of the
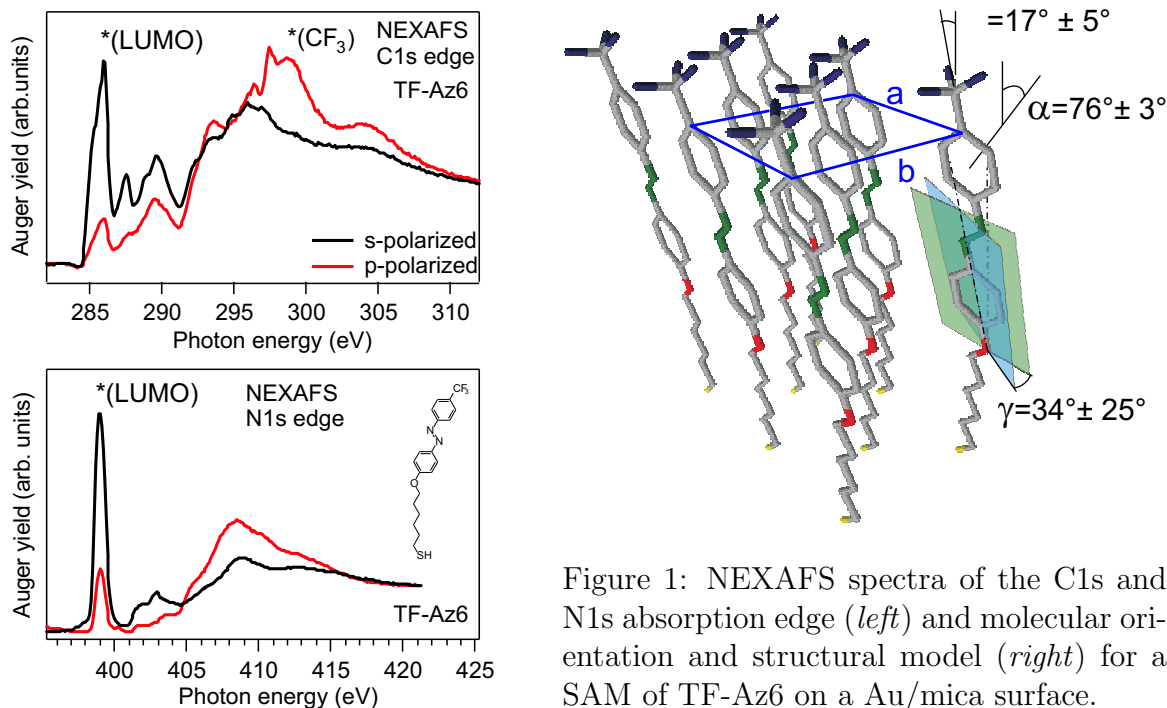
Figure 1: NEXAFS spectra of the C1s and N1s absorption edge (*left*) and molecular orientation and structural model (*right*) for a SAM of TF-Az6 on a Au/mica surface.

C1s to π^* transition dipole moment with respect to the surface normal and the tilt angle ϑ of the C-CF$_3$ axis, we derive the twist angle γ of the azobenzene moiety (cf. Fig.1(*right*) to be $34° \pm 25°$, using the relation

$$\cos\alpha = \sin\vartheta \cdot \cos\gamma. \tag{1}$$

Due to the almost vertical orientation of the C-CF$_3$ axis the twist angle γ is not well established as can be seen from the large uncertainty.

In Fig. 1c a structural model of the SAM is depicted. It is based on the molecular orientation deduced from our NEXAFS measurements and the centered rectangular unit cell derived from the AFM measurements of Jaschke *et al.* [5].

The close proximity of the chromophores has also significant consequences for the optical properties of the SAM. Fig. 2 shows UV/Vis absorption spectra of TF-Az6 in ethanolic solution as well as reflection spectra from the SAM. In solution the spectra exhibit three main absorption features: The $n - \pi^*$(LUMO) transition at a photon energy of 2.8 eV, which is dipole forbidden in the thermally stable, inversion-symmetric *trans* conformation of azobenzene, the strong $\pi - \pi^*$ (LUMO) transition at 3.5 eV, and a broad absorption line around 5 eV corresponding to higher $\pi - \pi^*$ transitions. Similar to the representation of the transmission as absorbance, the reflection spectra of the SAMs on Au/mica are plotted as $\log(R_{\text{ref}}) - \log(R_{\text{SAM}})$, where R is the particular reflectivity. The overall increase of the background to shorter wavelengths can be explained by the modification of the Au reflectivity due to a dielectric overlayer as shown by the dashed curve calculated from a dielectric continuum model with $\varepsilon = 2.5$ and a layer thickness of 2.0 nm. Especially the strong broadening of the $\pi - \pi^*$ (LUMO) to the high-energy side with a maximum shifted by 650 meV is striking. Such spectral shifts are typical signatures of an excitonic coupling among the chromophores as found in molecular aggregates.[6] The magnitude of the shift can be taken as a measure of the delocalization time of the optical excitation. In the case of the well-ordered TF-Az6 SAM this time is in the order of one femtosecond.
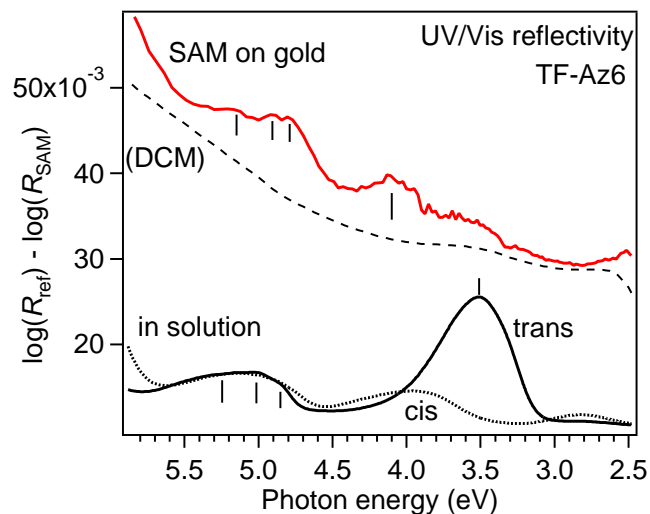
Figure 2: UV/Vis spectra of TF-Az6 in ethanolic solution (measured in transmission, *black*) and in the well-ordered SAM (measured in reflection and plotted as difference spectra of SAM-covered and clean Au substrate, *red*). The dashed line represents the calculated change of reflectivity due to a dielectric overlayer on gold.

As optical excitation of this π to π^* transition triggers the *trans* to *cis* isomerization of the azobenzene in solution, photoswitching in the SAM is ineffective. Quenching of the excitation on the femtosecond timescale might constitute here even a stronger constraint to photoswitching than steric hinderance.

In conclusion, we have determined the orientation of the azobenzene moiety within well-ordered TF-Az6 SAMs on gold by NEXAFS spectroscopy and have correlated this to the optical properties. A detailed insight into the intermolecular coupling will help to design structures with proper functionality. While dilution of the switch has been recently shown to restore functionality [7], many applications ask for switching a larger fraction of molecules.[8] Here excitonic coupling may open a new perspective to imitate light harvesting complexes and control excitation flow in a SAM by tuning the optical properties of the chromophores.

[1] M. Zharnikov, and M. Grunze, *J. Phys.: Condens. Mat.* **13**, 11333 (2001); S. F. Bent, *ACS Nano* **1**, 10 (2007)

[2] P. Cyganik, M. Buck, T. Strunskus, A. Shaporenko, J. D. E. T. Wilton-Ely, M. Zharnikov, and Ch. Wöll, *J. Am. Chem. Soc.* **128**, 13868 (2006)

[3] J. Stöhr, and D. A. Outka, *Phys. Rev. B* **36**, 7891 (1987)

[4] I. Ishii, R. McLaren, A. P. Hitchcock, K. D. Jordan, Y. Choi, and M. B. Robin, *Can. J. Chem.* **66**, 2104 (1988); H. Ågren, V. Carravetta, O. Vahtras, and L. G. M. Pettersson, *Phys. Rev. B* **51**, 17848 (1995)

[5] M. Jaschke, H. Schönherr, H. Wolf, H.-J. Butt, E. Bamberg, M. K. Besocke, and H. Ringsdorf, *J. Phys. Chem.* **100**, 2290 (1996)

[6] A. Eisfeld, and J. S. Briggs, *Chem. Phys.* **324**, 376 (2006)

[7] A. S. Kumar, T. Ye, T. Takami, B.-C. Yu, A. K. Flatt, J. M. Tour, and P. S. Weiss, *Nano Lett.* **8**, 1644 (2008)

[8] G. Pace, V. Ferri, Ch. Grave, M. Elbing, C. von Hanisch, M. Zharnikov, M. Mayor, M. A. Rampi, and P. Samori, *PNAS* **104**, 9937 (2007)

The alignment of tetra-phenyl-porphyrins on substrate templates

S. Fleming, T. Haber, M.G. Ramsey, G. Koller

Institute of Physics, Karl-Franzens-Universität Graz, A-8010 Graz, Austria

EU, R II 3-CT-2004-506008

Porphyrin based materials are not only important and common molecules in nature, they also attract interest because of their possible applications in organic solar cells and other opto-electronic devices. Here the orientation and electronic structure of meso-tetraphenylporphyrin (H_2-TPP) and its organo metallic complex Pt(II)-TPP grown on patterned/corrugated substrates, has been investigated from submonolayer to tens of nanometer thick films on clean Cu(110), Cu(110)-(2x1)O and crystalline films of chain-like molecules such as 6P(20-3).
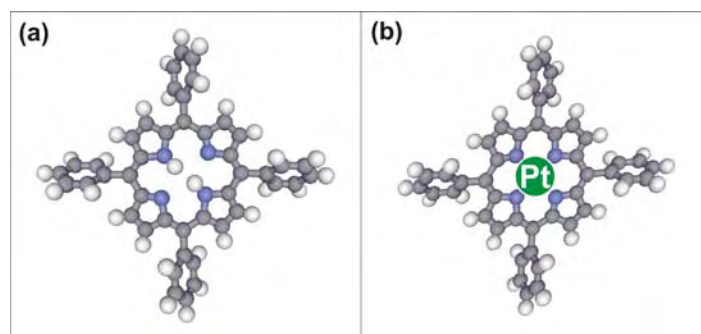
Fig.1: Schematics of H_2-TPP (a) and Pt(II)TPP (b).

The surfaces were prepared and investigated in the MUSTANG end station attached to the Russian-German beamline. The MUSTANG chamber is equipped with standard sample cleaning and a Phoibos 150 electron spectrometer from SPECS. This allowed UPS and XPS measurements in addition to polarisation dependent CK- and NK- edge Auger yield Near Edge X-ray Absorption Spectroscopy (NEXAFS), where the molecular orientation could be obtained. The molecules were evaporated from a home made triple evaporator using deposition rates of 1 to 5 Å per minute.

The Nis core level spectra of Pt(II)-TPP and H_2-TPP displayed in fig. 2(a) are notably different. Pt-TPP shows a single emission due to the four N-atoms being equivalently bound to the Pt core atom, whereas the nitrogens in H_2-TPP are chemically different and consequently two peaks are observed due to two of the four N-atoms being bound to hydrogen atoms. The double peak structure of the N1s core level is also expressed in the N_K-edge NEXAFS spectrum of H_2-TPP shown in fig 2 (b), which may be viewed as the superposition of two spectra offset by two eV, the energy separation of the N1s core levels. For azimuthally oriented films of H_2-TPP these two

N excitations will bear opposite dichroism as the hydrogen bound nitrogen atoms are diagonal to each other and at 90° to the lone pair nitrogens. In contrast to the N_K-edge, the C_K-edge NEXAFS spectra of Pt(II)-TPP and H_2-TPP are quite similar and dominated by the carbon atoms sitting in the phenyl rings. Transitions from the porphyrin macrocycle carbon atoms presumably constitute the shoulder at lower excitation energy of the main peak.
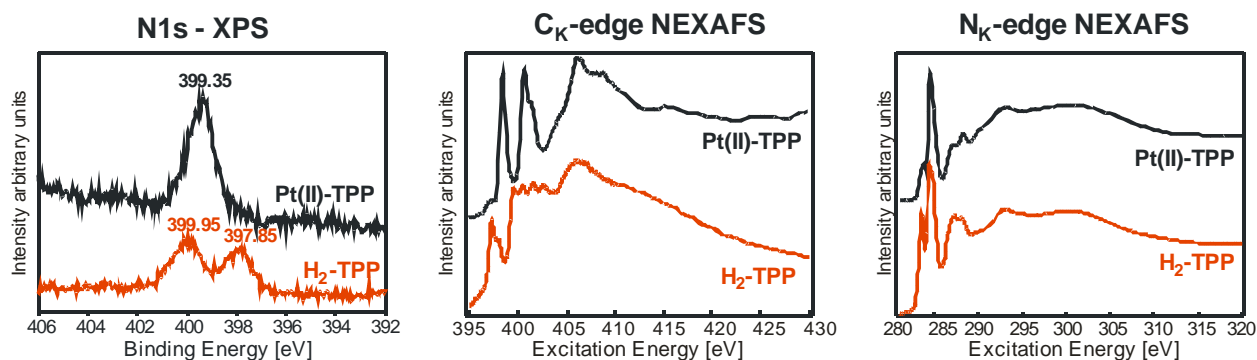
Fig. 2: (a) XPS of the N1s region of Pt(II)-TPP and H_2-TPP, (b) C_K- and (c) N_K-edge NEXAFS spectra of 120 Å thick Pt(II)-TPP and H_2-TPP films grown on a (2x1)O reconstructed Cu(110) surface in a gracing incidence geometry.

To grow azimuthally oriented films of tetra-phenyl porphyrins we have used the Cu(110)-p(2x1)O reconstructed single crystal substrate and a (20-3) oriented 300 Å thick sexiphenyl crystalline film as anisotropic templates. The results of NEXAFS taken in the two principle azimuths on these substrates are qualitatively the same and will be discussed here for H_2-TPP on Cu-(2x1)O only.

The C_K-edge NEXAFS spectra of Fig. 3 (a) and (b) are dominated for all experimental geometries by the C1s to π^* excitation at 285 eV, which is attributed to the phenyl carbons. In contrast, the shoulder at ~284 eV (attributed to porphyrin macrocycle carbons) is very weak at normal incidence and strong at glancing incidence geometry. This suggests that the porphyrin macrocycle lies flat on the CuO substrate, whereas the four phenyl rings are at a significant tilt. In contrast to the C_K-NEXAFS spectra the N_K-NEXAFS spectra show distinct angular and azimuthal dependencies. The observed relative shift in weight of the individual spectra can be attributed to the two different initial state nitrogen atoms. It is thus indicated that not only are all molecules lying with their macrocycle flat on the substrate, they are also azimuthally aligned, with the alignment driven by the nitrogen atoms. This is also in line with the Pt-TPP results (four identical nitrogen atoms), where no preferred alignment was observed.
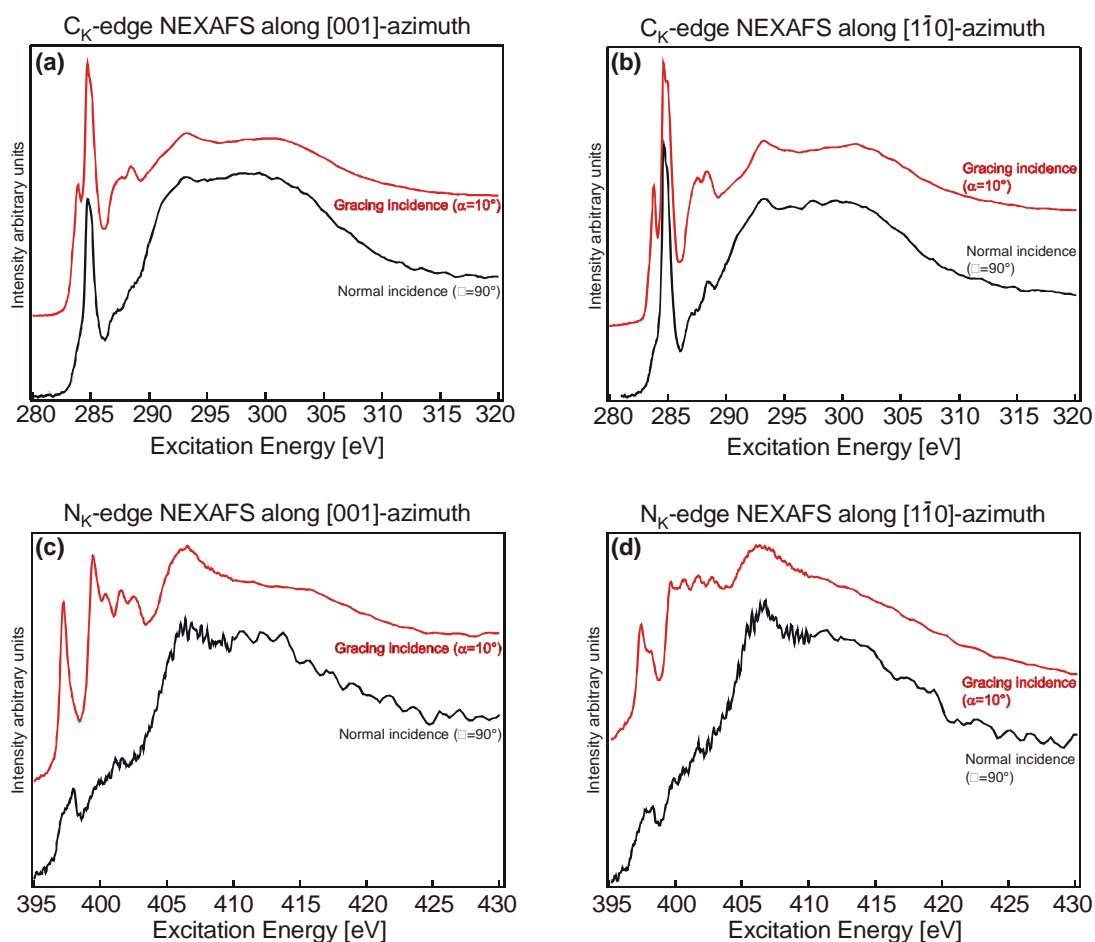
Fig. 3. C_K-edge ((a), (b)) and N_K-edge ((c), (d)) NEXAFS spectra of a 123 Å thick H_2-TPP film on Cu(110)-(2x1)O. The spectra were taken in normal and glancing incidence geometry, with the light being polarised in the [001]- ((a), (c)) and [110]- azimuths ((b), (d)), respectively.

We have investigated the bonding and orientation of H_2-TPP and Pt(II)-TPP on various inorganic and organic substrate templates. The results show that films of aligned Pt-TPP could not be achieved whereas for H_2-TPP, from monolayer to multilayer, films could be grown with the macrocycles parallel to the substrate and also aligned along the substrate corrugation, with this azimuthal alignment driven by the inequivalent nitrogen atoms.

An In-situ Investigation into Silica Scale Growth and Nucleation

Prof. B.K. Hodnett, Dr. Tim O'Sullivan, Laura O'Shea

University of Limerick

Introduction and Background

Sodium aluminosilicate scale formation in heat exchangers is a major issue in the day-to-day running of an alumina refinery. As well as aluminium, the liquor in which the raw material, bauxite, is dissolved contains a high level of impurities, such as silica and sodium. In areas of the plant where there are temperature differences (such as heat exchangers) these impurities can precipitate out of the liquor in the form of sodium aluminosilicate scales. Two forms of this scale are encountered: Sodalite and cancrinite. Sodalite generally forms at lower temperatures and can, over time, convert into cancrinite. These aluminosilicate scales act as excellent insulators, resulting in the need for greater amounts of energy to be added to the system. Removal of these scales is very problematic, resulting in loss-time and damage to equipment. This project was initiated in order to firstly understand the mechanism of scale nucleation and growth and secondly to attempt to mitigate the effects of this scale formation.

Experimental Equipment and Methods:

Examining the growth of silica scale required the commissioning of a specialised scaling studies cell.

The scaling studies cell is a piece of equipment designed to form sodium aluminium silicate scales from real and synthetic liquors at elevated temperatures. This allows the scientific study of the scaling process and factors affecting it. The system is designed to mirror as closely as possible the operating conditions in the heat exchangers at Rusal Aughinish.

The equipment was designed so that it is suitable for standalone work in Rusal Aughinish or the University of Limerick laboratory areas as well as being operated in a high-energy synchrotron beam at BESSY facilities. Specifically, glazing angle X-ray diffraction was used to examine the nucleation and growth of the silica scale species (namely sodalite and cancrinite) on a steel substrate.

The unit is a pumped recirculating system that will be able heat aluminosilicate liquors up to a maximum temperature of 250°C with suitable controls and safety systems to allow it to operate unattended for long periods of time, e.g. 24 hours.

The system is designed to circulate fluid from a stainless steel reservoir by means of an air driven liquid pump to the first heat exchanger, where returning fluid helps to per-warm the fluid. Following on from this, the pre-heater raises the temperature to near the target temperature before the fluid enters the cell. The cell is fitted with a cartridge heater, the purpose of which is to ensure that silica scaling occurs on the sample coupon.

As the fluid leaves the cell it passes again through the first heat exchanger before entering the second. This heat exchanger is plumbed to a cold water supply and cools the fluid to 60°C before returning it to the reservoir. A schematic showing the process units and their arrangement is shown in Fig. 1.
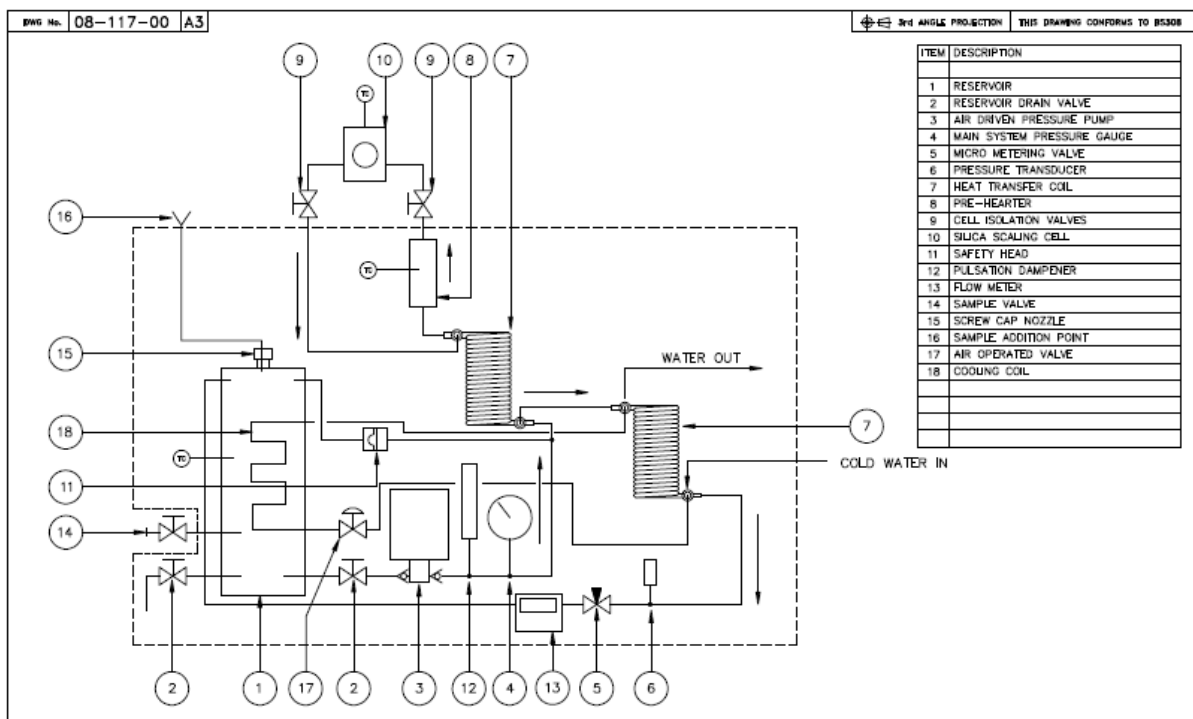
Figure 1: Schematic of the Units Contained in the Silica Scaling Rig

Results:

The rig enabled us to monitor the nucleation and growth of both sodium aluminosilicate phases (Sodalite and Cancrinite) on a carbon steel substrate using glancing-angle X-ray diffraction at the EDDI beamline at BESSY. The first experiment carried out aimed to determine how sodium aluminosilicate scale nucleates on a carbon steel test piece, and

identification of the phases present at nucleation. A total of 3 litres of liquor was circulated through the rig at 150°C and 23 bar pressure for 49 hours. Results are presented in Fig. 2.
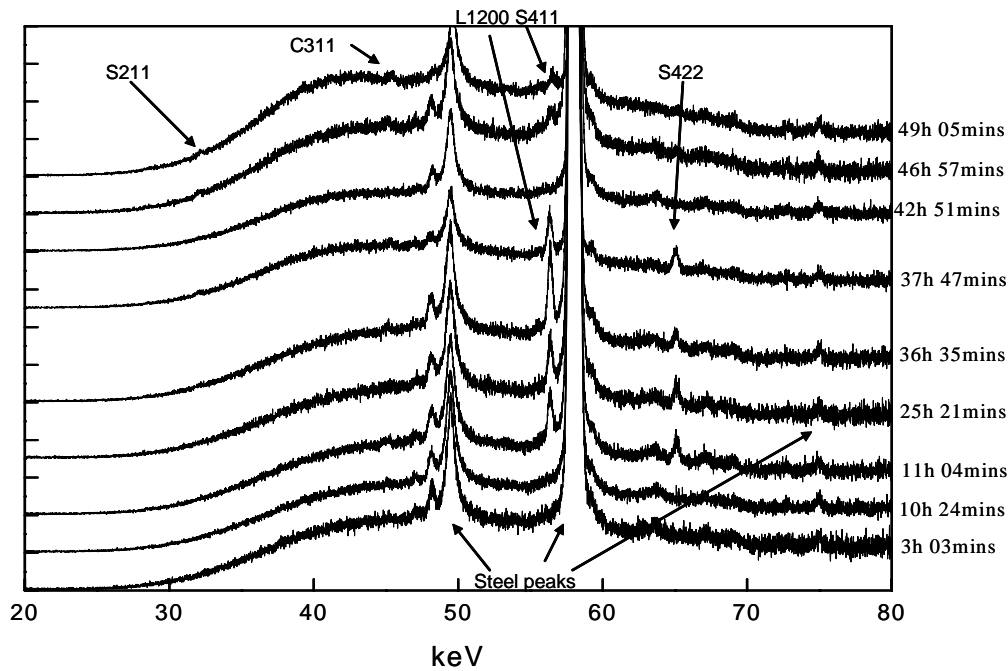
Figure 2: X-ray diffractograms tracing the nucleation of sodalite (S*hkl*) and its subsequent conversion to cancrinite (C*hkl*)

Of note in these results is the peak at 56.3 keV. It appears at 11 hours, disappears after 43 hours and reappears after 45 hours. This corresponds to the *hkl* = 200 peak of a Linde Type-zeolite (L1200). It is also characteristic of Sodalite (*hkl* = 411) and cancrinite (*hkl* = 330). Sodalite can be distinguished from Linde Type A zeolite by peaks corresponding to *hkl* = 211 and 422. Evaluation of these results and others are in an early stage, but the verification of the presence of a zeolite prior to the appearance of sodalite is interesting.

Future Work

After the success of our team's last visit to BESSY (December 2008), plans are underway to submit another proposal for the EDDI beamline to continue these studies.

This project was sponsored by RUSAL Aughinish and Enterprise Ireland.

SRPES Investigation of Noble Metal Electrodepositon onto n-Si(111)

T. Stempel, K. Skorupska, M. Lublow, A.G. Muñoz, M. Kanis, H.J. Lewerenz
Division of Solar Energy
Helmholtz Center Berlin for Materials and Energy
Glienicker Str. 100
D-14109 Berlin

The concept of nanoemitter solar cells [1], applicable to photovoltaic and photoelectrocatalytic energy conversion, comprises in its realization the site selective deposition of nano-dimensioned metal islands into pores of silicon oxide that have been formed during (photo)current oscillations of Si electrodes in dilute ammonium fluoride solutions. Because of the small dimensions of the nanopores, the change in surface chemistry upon electrodeposition of metals such as Pt and Ir is difficult to assess. Therefore, model experiments on the electrodeposition at H-terminated single crystalline Si samples have been carried out. H-termination can be achieved in (a) by etching in concentrated NH_4F solution, (b) by a two-step procedure with a successive HF etch after NH_4F etching [2] and (c) by the electrochemical hydrogen termination method [3]. Comparison of the Si 2p lines for the aforementioned treatments (Fig.1) shows that the two-step chemical and the electrochemical H-termination procedure result in a high quality H-termination evidenced by the missing signals for higher oxidation states of Si at the high energy side of the Si $2p_{1/2}$ peak. The treatment labelled (a) gives a small intensity at $E_B \sim 100.3$ eV that has been attributed to Si surface atoms with two backbonds to the lattice and termination with H and OH or F, respectively, which occur at kink and defect sites on (111) surfaces [4].
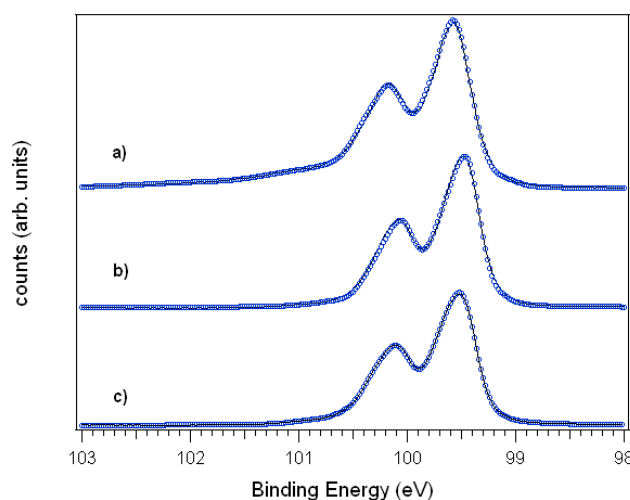
Fig.1: Synchrotron radiation photoelectron spectroscopy data of the Si $2p_{3/2-1/2}$ line; (a) two-step etching in conc. NH_4F and subsequently in conc. HF; (b) electrochemical hydrogenation procedure using dark current transients; (c) etching in conc. NH_4F; $h\nu$ = 150eV.

Electrodeposition has been performed at the Solid-Liquid Analysis System (SoLiAS) at the U49/2 beamline at BESSY using an *in-system* arrangement where the electrochemical cell has been directly attached to the UHV surface analysis apparatus. The procedure, using a fully electrochemically equipped glass vessel is established and allows surface sensitive measurements at samples that were submitted to electrochemical current flow with very low contamination levels [5]. Fig.2 shows the electrodeposition scans for Pt and Ir deposition from $PtCl_6^{2-}$ and $IrCl_6^{2-}$ containing solutions on H-terminated (111) surfaces and on the step-bunched Si surface which is nanostructured with step heights that are multiples of the atomic bilayer height. Since the Ir deposition occurs at a larger overpotential, the deposition scan was ended shortly after reaching the reduction peak of Ir. The Pt reduction occurs at less negative potentials and was carried out at -0.65V vs. SCE (saturated calomel reference electrode). It should be noted that more charge has passed in the deposition of Ir which has

to be considered when interpreting the SRPE spectra. For the step bunched surface, a potential jump was applied in an attempt to maintain the original substrate structure which might be altered by a potential scanning procedure.
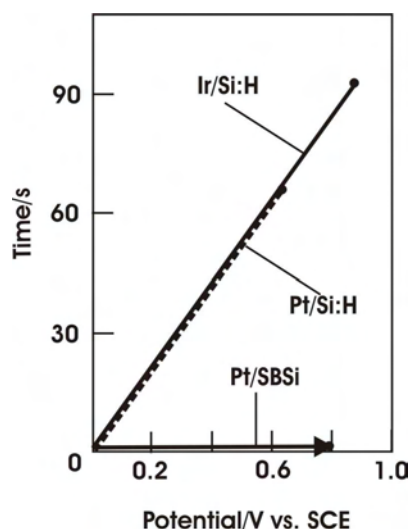
Fig.2: Potential scan for electrodeposition of Pt and Ir on n-Si(111); for H-terminated surfaces, a potential scan has been used. The scan velocity can be inferred from the graph. For the step-bunched Si surface (SBSi), a potential jump to -0.8V was made, indicated by the arrow.

The Pt and Ir 4f lines are shown in Fig.3 for increased excitation energies compared to the highly surface sensitive photon energy adjustment for the Si 2p lines, because the Pt 4f line is characterized by a distinct drop in the photoionization cross section around photon energies of 150eV. Because of the rather minute amounts of the metal nanoislands on the surface, photon energies have been adjusted to provide good 4f line intensity and, under these circumstances, the highest possible surface sensitivity. The asymmetric line shape for Pt is known since long and is attributed to the screening properties of the metal d-electrons. The effect is here slightly more pronounced than on the Pt films that were investigated earlier; this is attributed to the small size of the Pt nanodots where screening becomes less efficient. The line positions for the $4f_{7/2}$ line are those of the respective elements at binding energies of 71.2eV (Pt) and 60.9eV (Ir).
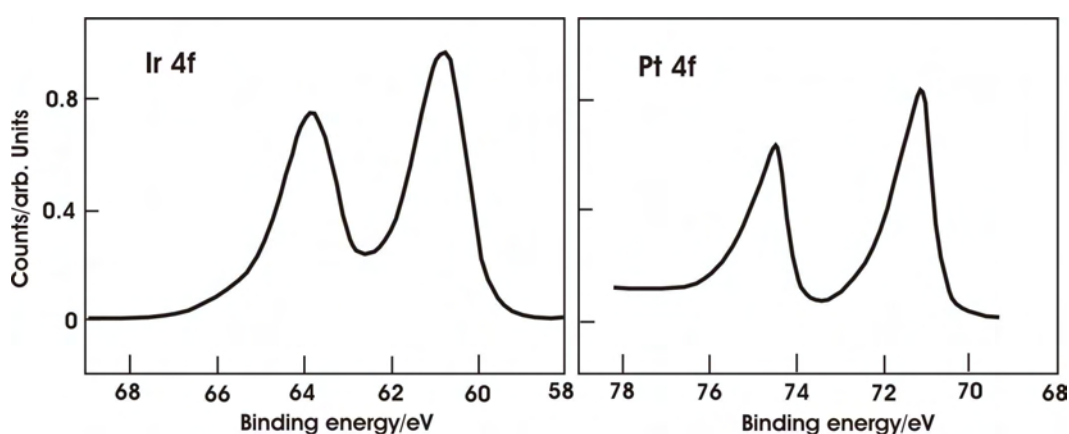
Fig.3: Ir (left) and Pt 4f lines (right) after electrodeposition onto H-terminated Si according to the data in Fig.2; photon energies were 630eV (Ir 4f) and 570eV (Pt 4f).

The Si 2p lines at high surface sensitivity are shown for the three treatment of Fig.2 in Fig.4. The envelope curves show that distinct signals for oxidized silicon are visible, with the especially pronounced Si(IV) line at $E_B = 103.4$eV. An estimate for the oxide thickness can be obtained by

comparison of the peak heights of the Si $2p_{3/2}$ lines. One sees that the thickest oxide is formed at the step bunched surface despite the potential jump technique that ensured only short time exposure to the electrolyte.
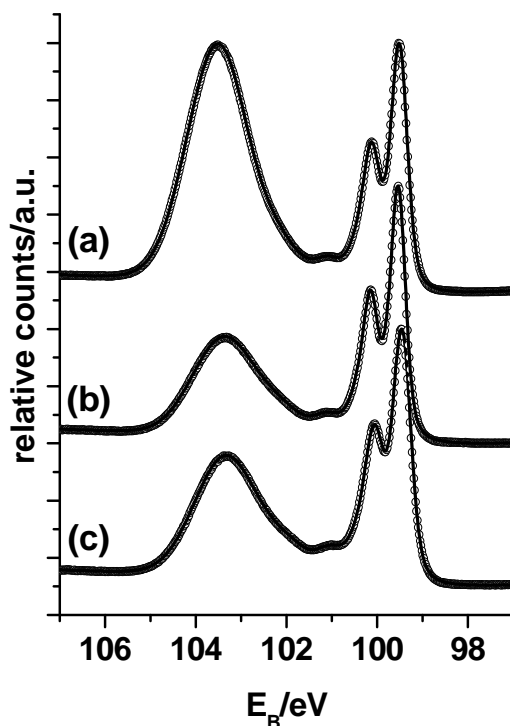
Fig.4: Si 2p lines for various surface treatments; (a) Pt on step bunched Si, prepared by potential jump; (b) Pt on H-terminated Si; (c) Ir on H-terminated Si; hν = 150eV.

This behaviour is attributed to the lower surface energy of the (100) terraces that form on the step edges and which oxidize more rapidly than the (111) surfaces in Fig.4b and Fig.4c. The increased charge flux on the Ir samples appears to be connected also with an increase in silicon oxide formation as can be seen by comparing Fig.4b and Fig.4c. The effect is explained by the energetically low lying levels of the redox solution from which the metals are deposited. Whereas oxide formation occurs by hole injection into the valence band and, depending on the Fermi level position, from emptying of charged surface states, metal deposition is particularly prominent when the n-type semiconductor is in an accumulation condition where a high number of carriers (electrons) from the conduction band drive the metal deposition reaction. The increased signal for Ir on Si(111):H (Fig.4c) compared to that of Pt (Fig.4.b) is likely due to the longer exposure time of the samples to the respective metal deposition solution (compare Fig.2).

References

1. H.J. Lewerenz, *Trans. IMF*, **86**, 19 (2008).
2. M. Lublow, T. Stempel, K. Skorupska, A.G. Muñoz, M. Kanis, and H. J. Lewerenz, Appl. Phys. Lett. **93** (2008) 62112
3. H.J. Lewerenz, T. Bitzer, J. Electrochem. Soc. **139** (1992) L21.
4. H. J. Lewerenz, M. Aggour, C. Murrell, M. Kanis, H. Jungblut, J. Jakubowicz, P. A. Cox, S. A. Campbell, P. Hoffmann and D. Schmeisser, J. Electrochem. Soc. **150** (2003) E185.
5. H.J. Lewerenz, Chem. Soc. Rev., **26**, 239 (1997).

Substrate influences on molecular self-assembly: complementary studies with STM and NEXAFS/XPS

Florian Klappenberger[1], Alexander Weber-Bargioni[2], Willi Auwärter[1], Thomas Strunskus,[3] Alexei Nevedof,[3] Christof Wöll,[3] Mario Ruben[4], and Johannes V. Barth[1]

1   Physik Department E20, Technische Universität München, James-Franck Str. 1, 85748 Garching, Germany
2   PHAS-AMPEL, The University of British Columbia, 2355 East Mall, Vancouver, Canada,
3   Lehrstuhl für Physikalische Chemie I, Ruhr-Universität Bochum, Bochum, Germany
4   Institute of Nanotechnology, Forschungszentrum Karlsruhe, Karlsruhe, Germany

Spontaneous supramolecular structure formation based on the self-assembly of suitably designed molecular components provides a promising way for the bottom-up construction of molecular devices. The emergence of specific functionalities can be controlled by the appropriate design of the molecular functional groups. Unfortunately, the deep knowledge on three-dimensional (3D) self-assembly cannot be transferred to two-dimensional (2D) in a straightforward way. The geometric restrictions to a surface and the chemical interactions with the surface have an enormous effect on the way supramolecular assembly takes place. A profound understanding of these influences is necessary to turn spontaneous structure formation into a useful tool for the production of future nanodevices.

Here we present a combined scanning tunneling microscopy (STM), near-edge X-ray-absorption fine-structure (NEXAFS) and x-ray photoemission (XPS) study on substrate induced effects on the self-assembly of flexible organic molecules on metal surfaces of different chemical reactivity. All NEXAFS and XPS data were obtained at the HE-SGM beamline at BESSY II. In the various examples we exploit the complex interplay of adsorption and structure formation with the properties of the different surfaces. The complementary information of local and integrating techniques is a key ingredient for the understanding of such processes.

In our first project we studied the chain-formation of diphenyl oxalic amide molecules in 3D and 2D environments. The X-ray crystal structure (Fig. 1a) demonstrates that the 3D phase consists of chains of molecules aligned along the direction **a** of the unit cell and that each molecule is approximately aligned within the **b-c** plane. Chains are ordered in a zigzag structure. The molecular conformation is dominated by a tilt of the phenyl rings with respect to the planar central functional group. A top view of a chain segment (Fig. 1b) highlights that the chains are held together by hydrogen bonding employing a complementary double bond motif of the NH¨O type. NEXAFS data were obtained for the C1s and the O1s range for a multilayer (approximately 10 monolayers) and a monolayer on Ag(111). The strongest resonance of the carbon edge (Fig. 1c) indicates the orientation of the phenyl rings, the resonance at 532 eV in the O1s range (Fig. 1d) originates from the two carbonyl bonds of the inner functional group and is a measure for its orientation. The conformation of the molecules in the multilayer is consistent with the 3D conformation. Thus the influence of the substrate is eliminated after several layers. The monolayer data (Fig. 1e and f) indicate a stronger tilt of the phenyl rings for molecules in direct contact with the substrate, contrary to the expected effect that the adsorption on the metal surface would lead to more planar molecules as the adsorption
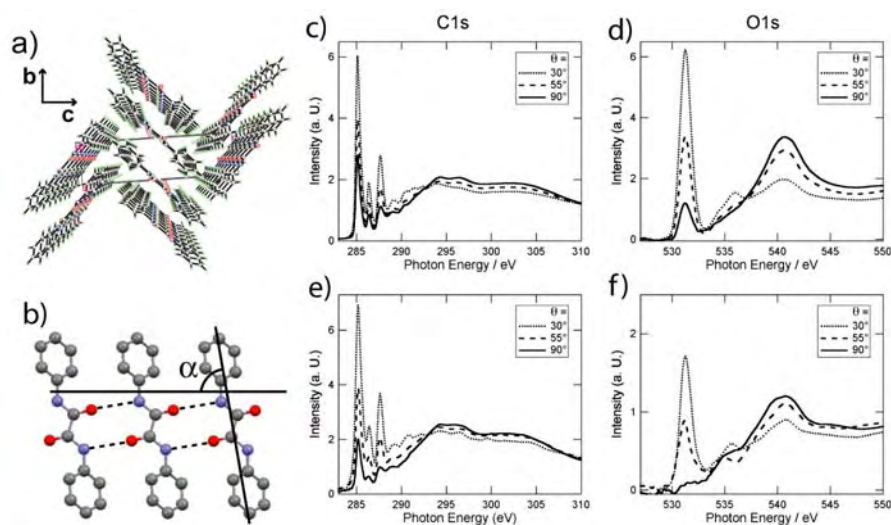
Fig. 1: a) and b) Crystal structure of diphenyl oxalic amide as obtained by X-ray structure analysis. Molecules line up in chains via two hydrogen bonds (dashed lines) per molecule. c) and d) NEXAFS data for a multilayer on Au(111). e) and f) NEXAFS data for a monolayer on Au(111).

energy would then be maximized.

STM data for a submonolayer coverage on the Ag(111) surface (Fig. 2a) demonstrates that chain formation prevails in the 2D environment. Chain lengths of up to 200 nm were found and indicate that the limit is given by the boundaries of the terraces. On the reconstructed Au(111) substrate (Fig. 2b) chains are found to selectively decorate the zigzag-shaped fcc regions (highlighted with bright transparence). With the help of Monte-Carlo simulations, which based on the experimental fact that molecules avoid the reconstruction transition regions, we were able to explain this preference by a fluctuation-triggered extinction of the shorter hcp chains during cooling. The hcp chains, which exist only at higher temperature are shorter because the hcp regions are smaller than the fcc regions.
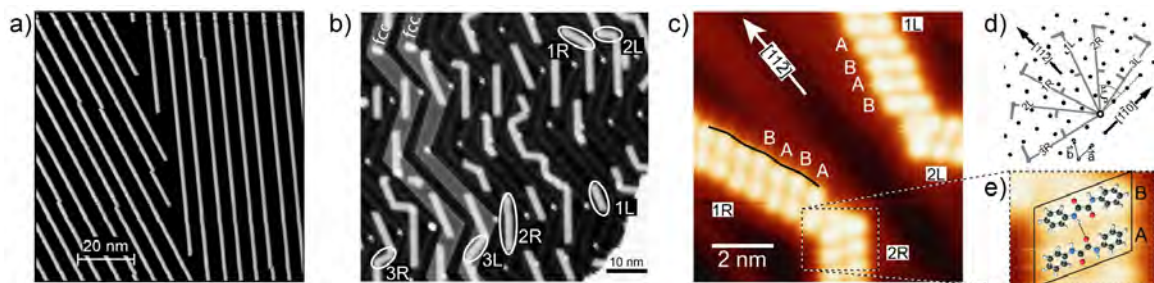
Figure 2: STM images of diphenyl oxalic amid chains on Ag(111) (a) and Au(111) (b). c) A high-resolution image shows chiral chains consisting of racemic mixtures of molecules of 2D chirality A and B. The underlying epitaxy model (d) is the same for both substrates and the hydrogen bonding motif is changed in comparison to the 3D structures

On both substrates chains in six direction were found, three of chirality R and three of chirality L (Fig. 2b), where R refers to the fact that the right hand side in front of the left hand side when going along the chain growth direction (Fig. 2c). The angles of the chains with respect to the [1-10] direction are consistent with the model presented in Fig. 2d. Chains grow commensurate to the substrate with the two enantiomers A and B of the 2D chiral molecule in one unit cell. The bonding motif now features a single hydrogen bond. This model elaborated from experimental fact is also supported by DFT calculations. With the help of the model the driving force for the distortion of the molecules in the monolayer can be understood. Due to the substrate induced change of the relative positions of adjacent molecules phenyl ring have to tilt stronger to avoid otherwise steric hindrance of the hydrogen atoms of neighboring phenyl rings.

In summary, the influence of the substrate manifests itself in various aspects. A novel molecular conformation is employed counter-intuitively featuring more distorted isomeres, the hydrogen-bonding motif is changed from two to one bond per molecule, chains now exhibit chirality even though they are made of racemic mixtures.

In a second project we studied the temperature dependence of the self-assembly of tetrapyridyl-porphyrin (TPyP) molecules on the Cu(111) surface in the range from 300 K to 500 K. After evaporation onto the substrate at 300 K STM data (Fig. 3a) reveal single molecules as bright protrusions dominated by two pronounced lobes near the center. The random distribution of adsorption places indicates that the molecules get immediately anchored when arriving on the substrate. After annealing to 390 K (Fig. 3b) short chain segments are present in which the terminal pyridyl groups of adjacent molecules point towards each other. After annealing to 500 K (Fig. 3c) the appearance of the molecules is drastically changed, now a dip in the center is surrounded by four lobes at the positions of the endgroups (Fig. 3c, inset).

The leading edge of the N1s NEXAFS data (Fig. 3d) can be decomposed into signals stemming from the two iminic (-N=) nitrogen atoms (red dotted line), from the two pyrrolic (-NH-) nitrogen atoms (green dash-dotted line) and the four pyridylic nitrogen atoms (blue solid line). The angle dependence of these peaks (Fig. 3e) qualifies the adsorbed TPyP molecules as being strongly distorted into a saddle-shape with the pyridyl group pointing towards the substrate. After annealing to 450 K (Fig. 3f) the shape of the measured resonances (black circles) is changed. Instead of the single strong pyridyl resonance, now two resonances with approximately half the intensity are present (blue solid and dashed lines). We attribute the higher lying resonance to pyridylic nitrogen atoms that are coordinated to metal adatoms. The angle dependence after annealing (Fig. 3g) indicates again a strong saddle-shape very similar to the one found before and only minor changes for the pyridyl groups. Thus the dramatic change of the molecular appearance in the STM data is unlikely the result of such a small conformational adaption.
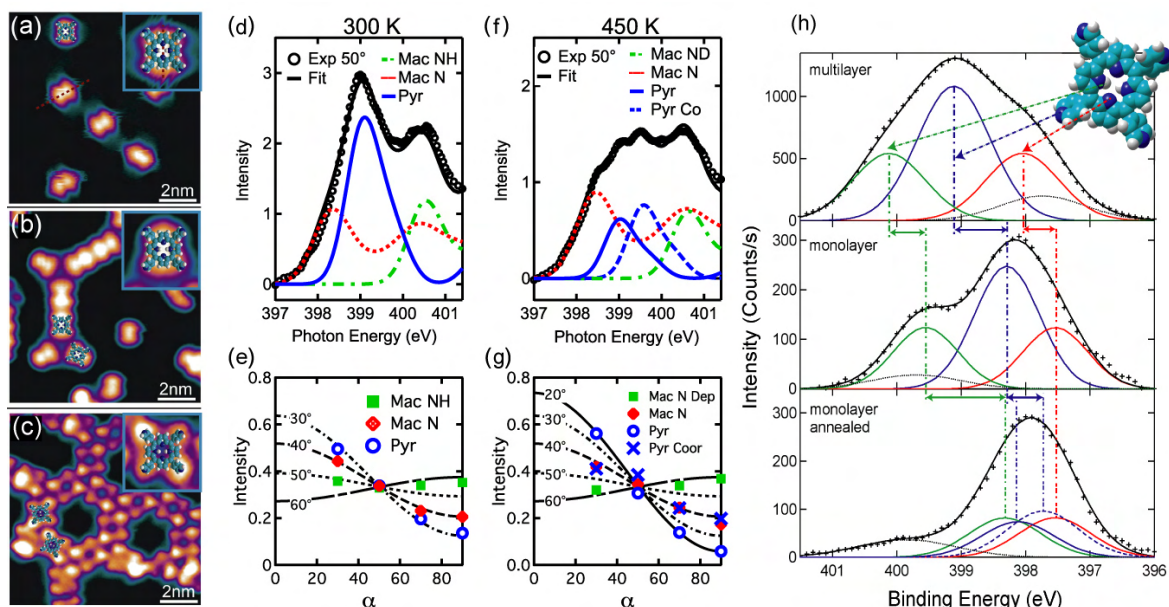
Fig 3: STM images of TPyP adsorbed on Cu(111) at 300 K (a) and after annealing to 390 K (b) and to 500 K (c). d) N1s NEXAFS data for a submonolayer coverage at the magic angle of 50° and its decomposition into signals stemming from the different N types. e) The angle dependence of the three components of d). f) After annealing to 450 K a forth component (dashed blue) is present in the NEXAFS signal. g) The angle dependence of the four components of d). h) XPS data (symbols) and components (green, blue and red) for mulitlayer (upper panel), monolayer adsorbed at 300 K, and monolayer after annealing to 450 K.

The N1s region of the XPS data (Fig. 3h) is again dominated by three components stemming from the three nitrogen atom types (pyrrolic green, pyridylic blue and iminic red). The comparison of the peak energies for a multilayer (upper panel) and a monolayer adsorbed at 300 K (middle panel) reveals a general shift towards smaller binding energies during adsorption. This shift is attributed to a combination of screening by the substrate and chemical interaction with the substrate. The largest shift appears for the pyridylic nitrogen atoms indicating that their position is nearest to the Cu surface. This is consistent with the model concluded by NEXAFS. After annealing to 450 K the most prominent change is the missing shoulder at the high binding energy side. We attribute the strong shift of the pyrrolic peak (green arrow) to a deprotonation of the corresponding nitrogen atoms. The XPS data is also conform to the presence of stronger coordinated pyridylic nitrogen species as indicated by the blue dashed peak.

The combined information indicates the following scenario. At 300 K the strongly distorted molecules are anchored individually, whereas at 390 K metal-ligand interactions between pyridylic N and copper adatoms result in linear and triangular supramolecular arrangements. The third phase occurred by heating the sample to 450 K and is characterized by a significant change in molecular appearance. The porphyrin's molecular conformation undergoes only minor changes during annealing and the modified STM appearance is explained by a change in the electronic structure initiated by the deprotonation of the pyrrolic nitrogens.

In conclusion, with a combination of complementary techniques we were able to quantify and understand for two different systems the substrate influence on the supramolecular structure formation. Our results help to understand the complex process of applying 3D supramolecular design knowledge to 2D self-assembly.

References:
[1] F. Klappenberger, M. E. Cañas-Ventura, S. Clair, S. Pons, U. Schlickum, Z.-R. Qu, T. Strunskus, A. Comisso, C. Wöll, H. Brune, K. Kern, A. DeVita, M. Ruben, and J. V. Barth, ChemPhysChem **9**, 2522 (2008).
[2] F. Klappenberger, A. Weber-Bargioni, W. Auwärter, M. Marschall, A. Schiffrin, and J. V. Barth, J. Chem. Phys. **129**, 214702 (2008).
[3] G. Tomba, M. Lingenfelder, G. Costantini, K. Kern, F. Klappenberger, J. V. Barth, L. C. Ciacchi, and A. DeVita, J. Phys. Chem. A **111**, 12740 (2007).

The Two-Dimensional Electron System Au/Ge(111)
Studied by Fermi Surface Mapping

P. Höpfner, M. Heßmann, J. Schäfer, S. Meyer, C. Blumenstein, and R. Claessen

Experimentelle Physik IV, Phys. Inst., Universität Würzburg, D-97074 Würzburg

C. Enderlein, T. Braun, and K. Horn

Fritz-Haber-Institut der Max-Planck Gesellschaft, D-14195 Berlin

Metallic reconstructions on semiconductor surfaces of (111)-orientation display an intriguing realization of electron confinement in two dimensions (2D). The interest in this research field was stirred by Carpinelli *et al.*, who reported the investigation of a charge density wave (CDW) on Pb/Ge(111) in 1996 [1]. Nevertheless, these studies were followed by experiments on related surface systems, as the enhanced many-body interaction in 2D may lead to the occurrence of exotic physical phenomena like CDWs, a Mott-Hubbard phase or superconductivity. These phenomena depend highly on the degree of correlation, which can be tuned by varying the adatom species. Examples range from In/Si(111) [2] as a non-correlated case to Sn/Ge(111) [3] showing high correlation effects, namely a Mott-Hubbard insulating phase.

In this report, we present data from angle-resolved photoemission on the two-dimensional electron system (2DES) Au/Ge(111)-($\sqrt{3} \times \sqrt{3}$)$R30°$. These include the Fermi surface topology and band structures along the main symmetry directions. The results presented here are part of a larger research program, concerned with 2DES for the investigation of the above mentioned physical phenomena. In this report, we present the first high resolution ARPES data of this interesting adsorbate system.

Experiments were carried out at beamline UE112-PGM-1 at the chamber of Prof. K. Horn equipped with a motorized six-axis-manipulator and a SPECS state-of-the-art 2D electron analyzer (total energy-resolution 20 meV).
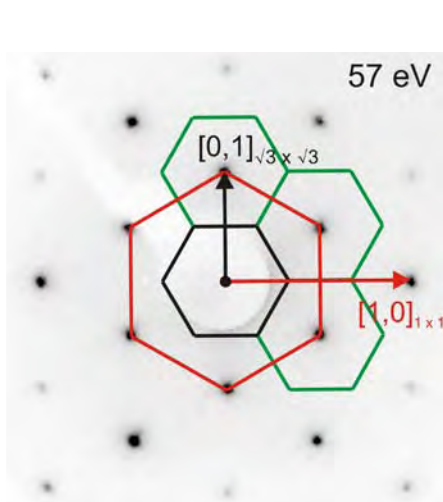
FIG. 1 LEED image at 57 eV and T = 80 K, showing spots originating from $\sqrt{3}$-reconstruction (black arrow) and the underlying substrate (red arrow). Surface Brillouin Zones are added for clarity (red: 1×1; black and green: $\sqrt{3}$).
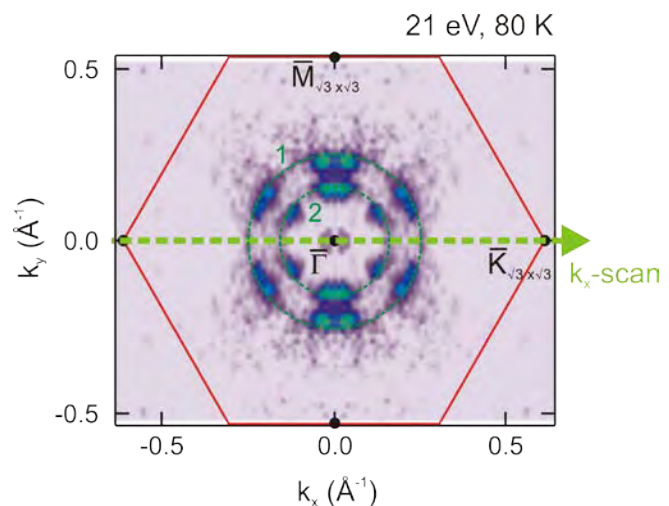
FIG. 2 Fermi surface map at photon energy 21 eV and T = 80 K. Circular features 1 and 2 are indicated by green dashed lines as guide to the eye. The scanning direction of the single band map in FIG. 3 is marked by the arrow.

Ge(111) samples were prepared by several cycles of sputtering and annealing. An estimated amount of 1 ML Au was evaporated. The ($\sqrt{3} \times \sqrt{3}$)-reconstruction could be verified by sharp LEED spots, as shown in FIG. 1. According to prior studies by SXRD [4], Au trimers are supposed to dominate the surface topology, while STM studies are ongoing for further insight.

Metallic character of Au/Ge(111) is proven by the Fermi surface in FIG. 2 taken at 80 K, which consists of two separated circular features. The intensity is lowered in $\overline{\Gamma}$-$\overline{K}$ direction, which is assumed to be affected by matrix elements, while intensity is highly increased along $\overline{\Gamma}$-$\overline{M}$.

Detailed insight is gained by mapping the band structure along high symmetry directions, as presented in FIG. 3. For $\overline{\Gamma}$-$\overline{K}$ two metallic bands (S1 and S2) are observed crossing the Fermi level at $k_F = 0.25$ Å^{-1} and 0.16 Å^{-1} respectively. These metallic bands are identified to form the Fermi surface presented in FIG. 2 as k_F values are consistent in both data sets. The band filling is calculated to 20 percent for S1 and approximately 92 percent for S2. The effective electron masses are $0.6 \times m_e$ for S1 and $1.2 \times m_e$ S2 respectively, which is close to the mass of a free electron. The close-up in FIG. 3 unveils an indication of a third metallic hole-like band at $k_F = 0.04$ Å^{-1}. Its contributions to the Fermi surface should be rather low, as visible in FIG. 2.

The findings presented in this report are reminiscent of recent results from Pb/Ge(111), where metallicity was demonstrated as well [5]. However, a CDW induced band gap was not observed in that case. Such a coupling of charge carriers and surface lattice may not be excluded at this moment for Au/Ge(111) and thus we will focus on this aspect in further experiments.

In summary, ARPES data reveal the metallic character of the 2DES Au/Ge(111) even at 80 K. At least two metallic bands are clearly identified, while a third band needs additional investigation. Up to this point the 2 DES Au/Ge(111) demonstrates metallic behaviour for transition metals on ($\sqrt{3} \times \sqrt{3}$)$R30°$ reconstructed semiconductor surface without additional doping. Regarding the above determined effective electron masses one may conclude that Au/Ge(111) shows a rather free electron like behaviour

Further research activities will focus on possible phase transitions at lower temperatures or on quasi-particle effects (electron-phonon-coupling). Therefore we plan to reproduce our results in an even higher resolution by use of synchrotron light. Our next beamtime at BESSY II in the first half of 2009 is dedicated to this aim.
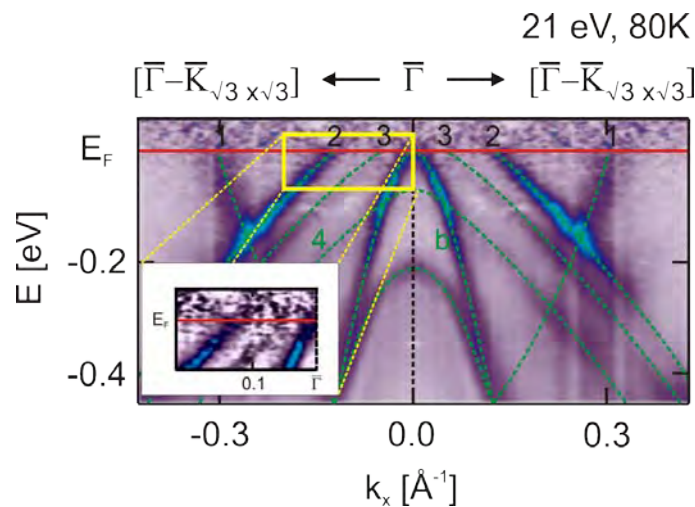
FIG. 3 Single band map at photon energy 21 eV and T = 80 K. Green dashed lines highlight the observed bands. The inset presents an enlargement at the Fermi level, showing a slight indication of a third metallic band.

[1] J. M. Carpinelli *et al.*, Nature **381**, 398 (1996)

[2] E. Rotenberg *et al.*, Phys. Rev. Lett. **91**, 246404 (2003)

[3] R. Cortés *et al.*, Phys. Rev. Lett. **96**, 126103 (2006)

[4] P. B. Howes *et al.*, Phys. Rev. B **48**, 1632 (1993)

[5] H. Morikawa *et al.*, Phys. Rev. B **77**, 193310 (2008)

Tailoring magnetic properties at the interface of a tunneling magnetoresistance device

P. Klaer,[1] E. Arbelo,[1] M. Kallmayer,[1] C. Herbort,[1] M. Jourdan,[1] H.J. Elmers,[1, *] and S. Cramm[2]

[1] *Institut für Physik, Johannes Gutenberg-Universität, D-55099 Mainz, Germany*
[2] *Institut für Festkörperforschung, Forschungszentrum Jülich GmbH, D-52425 Jülich, Germany*

Tunneling magnetoresistance devices consisting of two ferromagnetic layers (FM) separated by a thin insulator layer are crucial elements for spintronics. The resistance of this device strongly varies with the relative magnetization orientation of the two FM layers. According to Jullière's model, this tunneling magnetoresistance (TMR) effect is determined by the spin polarisation of the two FM layers. Large TMR effects result from FM layers with large effective spin-polarization values. Therefore, half-metallic ferromagnets (HMF) are ideal materials as electrodes for TMR devices. Co-based full-Heusler alloys with a chemical composition Co_2YZ (Y: transition metal, Z: main group element) possess high Curie temperatures and many of them have been predicted to be HFMs even at room temperature (RT) [1, 2]. Since the first TMR devices with $Co_2(Cr_{0.6}Fe_{0.4})Al$ as electrode material showing only moderate TMR values of 16% at RT [3], recently considerably larger TMR values have been reported for TMR devices using $Co_2(Cr_{0.6}Fe_{0.4})Al$, Co_2FeAl and Co_2MnSi electrodes [4]. $Co_2Fe(Al_{0.6}Si_{0.4})$ is especially promising because ab-initio calculations predict that the Fermi energy E_F lies in the center of the minority gap in contrast to Co_2FeAl and Co_2FeSi, where E_F is close to the upper or lower boundary of the gap [5, 6].

The large TMR values for $Co_2Fe(Al_{0.6}Si_{0.4})$ based TMR devices are considered to be caused rather by selective tunneling via the epitaxial MgO barrier than by the half-metallic properties of the electrodes.
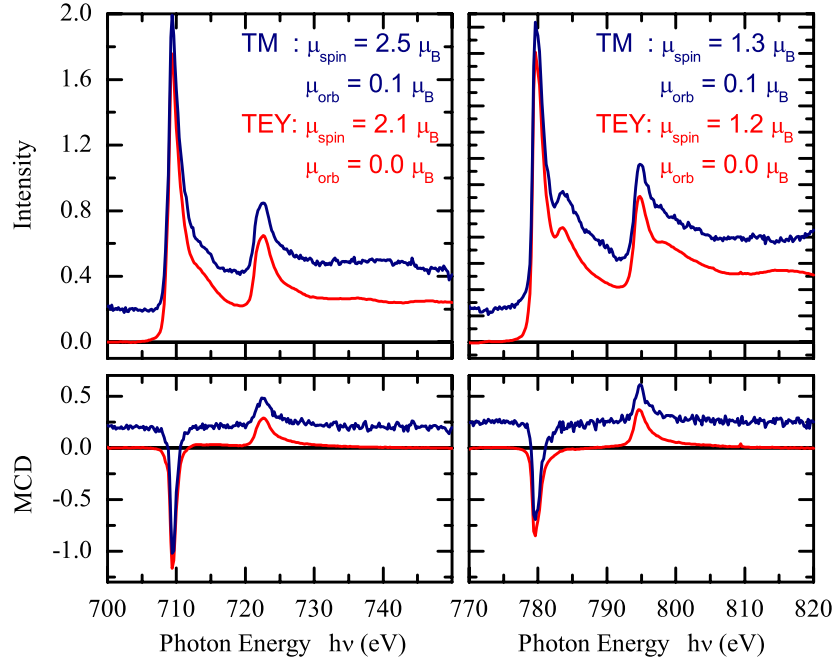
FIG. 1: Comparison of x-ray absorption data measured in transmission (TM, blue lines) and total electron yield (TEY, red lines) at the Fe (left) and Co (right) $L_{3,2}$ edges. The mean value for parallel and antiparallel magnetization is shown in the top panels while the difference (XMCD) is shown below. The sample is a 50 nm $Co_2Fe(Al_{0.6}Si_{0.4})$ film annealed at $T_a = 973$ K. Magnetic moments have been calculated by a sum rule analysis neglecting the dipole term and assuming numbers of unoccupied d-states for Co $N_h = 2.5$ and Fe $N_h = 3.5$. The direct comparison of TM and TEY data reveals smaller spin and orbital moments at the films surface compared to the bulk values.
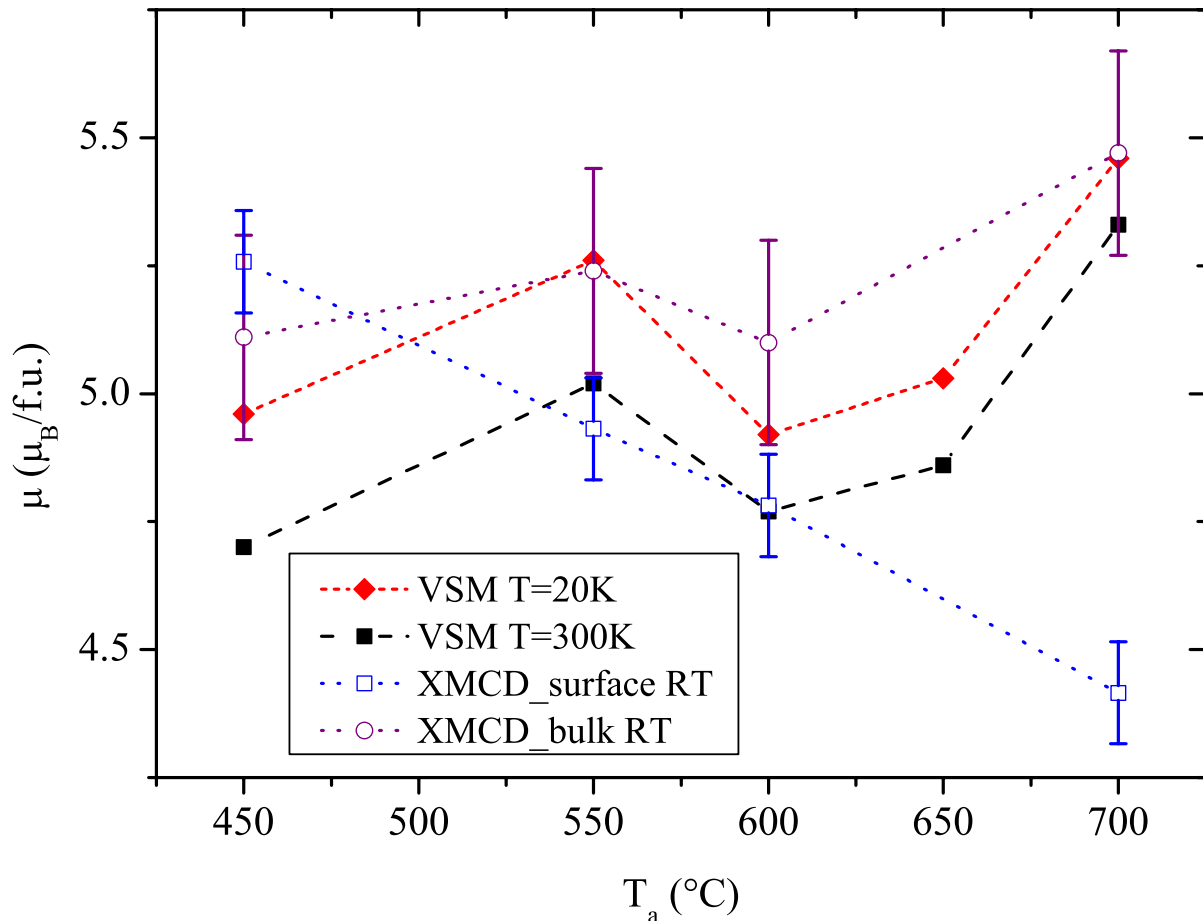
FIG. 2: Magnetization (m) in units of μ_B per formula unit (f.u.) of $Co_2Fe(Al_{0.6}Si_{0.4})$ thin films annealed at various temperatures as measured by VSM and x-ray absorption. Values from x-ray absorption were derived from adding up the element-specific moments per atom assuming the denoted stoichiometry. Values calculated from TEY (blue open squares) give information about the surface with an information depth of roughly 2.5 nm and data derived from transmission (red open circles) denote the bulk properties of the films. At $T_a = 973$ K, m fits with theoretical predictions, but the surface magnetization is considerably decreased.

Consequently, TMR devices using amorphous Al_2O_3 barriers have shown considerably lower values in the past. However, the reason may also be found in degraded interface properties at the HMF/Al_2O_3 interface. Our purpose in the present study was to tailor the interface properties as close as possible to the ideal bulk properties using x-ray absorption spectroscopy (XAS/XMCD) as the selective method. Comparing simultaneously measured transmission and total-electron yield signal [7–9], we were able to directly compare bulk and interface properties of the same sample (see Fig. 1).

We fabricated epitaxial $Co_2Fe(Al_{0.6}Si_{0.4})$ films on MgO(100) substrates including a MgO buffer layer using magnetron sputtering with a base pressure of 1×10^{-9} mbar. After an annealing process the tunneling barrier was prepared by deposition of metallic Al and reactive oxidation. Finally the films were capped in-situ by 2 nm metallic Al in order to prevent a contamination of the interface. Characterization of films involved x-ray diffraction (XRD), reflection of high energy electrons (RHEED), scanning tunneling microscopy (STM) and vibrating sample magnetometry (VSM).

A crucial parameter for the fabrication of the HMF film is the substrate temperature during deposition and post-deposition annealing. Following previous studies we deposited the films at $T_d = 300$ K in order to obtain a smooth and continuous film morphology [10]. After annealing at $T_a = 723$ K XRD reveals a B2-ordered structure, i.e. a random occupation of Fe and Z sites. Further annealing at higher temperature $T_a > 823$ K seems to improve local order in the direction of a $L2_1$ order of an ideal Heusler compound. The (111) XRD intensity increases with increasing T_a up to the highest applied value of

923 K. Also RHEED and STM investigations point to an increasing order with increasing annealing temperature. The Slater-Pauling rule relating the magnetic moment per formula unit to the number of valence electrons poses a necessary condition for a HMF. For $Co_2Fe(Al_{0.6}Si_{0.4})$ one expects a value of $\mu = 5.5\mu_B$/f.u.. At $T_a = 923$ K, μ as measured by VSM fits with this prediction. A lower annealing temperature results in smaller magnetic bulk moments. The dependence of μ on T_a is confirmed by an element-specific measurement of atomic magnetic moments applying a XMCD sum rule analysis to the transmission data (see Fig. 2).

The non-monotonous dependence of the magnetization on T_a is surprising as it was not observed for Co_2FeAl and Co_2FeSi films. For Co_2FeAl we observed a maximum magnetization at an intermediate temperature of $T_a = 723$ K, which might be explained by the increase of B2 order with increasing T_a as observed by XRD and an onset of an A-type disorder, i.e. random occupation of all lattice sites, at higher temperatures. For Co_2FeSi films a monotonous increase of the magnetization up to $T_a = 973$ K was interpreted as an increased $L2_1$ order [11]. Since the magnetization of the films is in all cases below the value predicted from the Slater-Pauling rule, one expects higher spin-polarization with increasing magnetization. This is in conflict with the observation of a decreasing TMR effect at annealing temperatures exceeding $T_a = 723$ K.

An analysis of the surface sensitive TEY data provides a clear-cut explanation for this disagreement. It clearly reveals a monotonous decrease of the magnetization at the $Co_2Fe(Al_{0.6}Si_{0.4})/Al_2O_3$ interface with increasing T_a. The best approach to the expected magnetization value of 5.5 μ_B is achieved for the lowest annealing temperature $T_a = 723$ K. A speculative explanation might be given by a depression of local atomic order at the interface with increasing T_a while the local atomic order behaves differently in the bulk of the film, or even by a change of composition at the interface indicating the beginning of a phase separation along the film normal [12]. Further investigations to clarify this open question are underway.

* eMail:`elmers@uni-mainz.de`

[1] I. Galanakis, Ph. Mavropoulos. J. Phys.: Condens. Matter 19, 315213 (2007).

[2] C. Felser, G. Fecher, and B. Balke, Angew. Chem., Int. Ed. 46, 668 (2007).

[3] K. Inomata, S. Okamura, R. Goto, and N. Tezuka, Jpn. J. Appl. Phys. 42, L419 (2003).

[4] W. Wang, H. Sukegawa, R. Shan, and K. Inomata, Appl. Phys. Lett. 93, 122506 (2008) and references therein.

[5] G. H. Fecher and C. Felser, J. Phys. D 40, 1582 (2007).

[6] Z. Gercsi and K. Hono, J. Phys.: Condens. Matter 19, 326216 (2007).

[7] M. Kallmayer, H. Schneider, G. Jakob, H. J. Elmers, K. Kroth, H. Kandpal, U. Stumm, and C. Cramm, Appl. Phys. Lett. 88, 072506 (2006).

[8] M. Kallmayer, K. Hild, T. Eichhorn, H. Schneider, G. Jakob, A. Conca, M. Jourdan, H.J. Elmers, A. Gloskovskii, S. Schuppler, P. Nagel, Appl. Phys. Lett. 91, 192501 (2007).

[9] P. Pörsch, M. Kallmayer, T. Eichhorn, G. Jakob, H. J. Elmers, C. A. Jenkins, C. Felser, R. Ramesh, and M. Huth, Appl. Phys. Lett. 93, 022501 (2008).

[10] A. Conca, M. Jourdan, H. Adrian, J. Phys. D: Appl. Phys. 40, 1534 (2007).

[11] M. Kallmayer, H. Schneider, G. Jakob, H. Elmers, B. Balke, S. Cramm, J. Phys. D: Appl. Phys. 40, 1552 (2007).

[12] V. Ksenofontov, C. Herbort, M. Jourdan, C. Felser C, Appl. Phys. Lett. 92, 262501 (2008).

Electronic structure of buried interfaces: resonant soft x-ray reflectivity studies

J. Geck[1], E. Schierle[2], H. Wadati[3], L. Alff[4], P. Komissinskiy[4], E. Weschke[2],
C. Schüßler-Langeheine[5] and G.A. Sawatzky[3]

[1]*IFW Dresden, P.O. Box 270116, 01171 Dresden, Germany*
[2]*Helmholtz-Zentrum Berlin, Albert-Einstein-Str. 15, 12489 Berlin, Germany*
[3]*Department of Physics and Astronomy, University of British Columbia, Vancouver, Canada*
[4]*Darmstadt University of Technology, Petersenstr. 23,64287 Darmstadt, Germany*
[5] *II. Physikalisches Institut, Universität zu Köln, Zülpicher Str. 77, 50937 Cologne, Germany*

Introduction: Heterostructures made of conventional metals and semiconductors play an important role for today's leading-edge technologies. Their electronic properties are often very different from those displayed by its constituents in bulk form and it is well established that this is due to the interfaces between the different compounds.

Correlated electron materials, like the transition metal oxides (TMOs), display a zoo of different electronic phases including those exhibiting superconductivity, multiferroicity, colossal magnetoresistance (CMR) as well as spin charge and orbital order. Based on this large diversity of the electronic properties it is anticipated that the new quantum phenomena and functionalities of TMO-heterostructures go well beyond the effects known from semiconductors or metals [1,2]. Of major importance for the properties of a TMO-heterostructure is the electronic or ionic reconstruction that occurs at the interfaces in order to prevent the so-called polar catastrophe [3]. These reconstruction effects alter not only the charge carrier density, but can also affect the magnetism or the orbital occupations at an interface. Hence the electronic properties at the interface can be dramatically different from those of both adjacent bulk materials, a prominent example being the occurrence of superconductivity in heterostructures made of materials with insulating bulk properties [4]. Recent experiments now demonstrate that such effects can be created and tuned in a controlled way at the interface between two TMOs.

In order to understand the physical mechanisms that are at play at an interface, it is necessary to examine the electronic structure at buried interfaces in detail. This creates a compelling need for experimental techniques, which can selectively and directly access the electronic structure of buried interfaces in heterostructures. In the case of TMOs, resonant soft-x-ray scattering provides unique experimental probes that meet these requirements.

In this specific project we use resonant soft x-ray reflectivity (RSXR) to study the electronic properties of the buried interfaces realized in heterostructures containing doped CMR-manganites. Since the electronic structure of manganites depends strongly on the local symmetry of the Mn-site, electronic reconstruction effects involving the charge, orbital and spin are expected to occur at the interfaces.

Experimental: We studied the interface-electronic structure in heterostructures consisting of a $La_{0.67}(Ba,Ca)_{0.33}MnO_3$ (L(B,C)MO) films, sandwiched in between the substrate and a capping layer. The substrate and capping layer material were identical for each sample and either $NdGaO_3$ (NGO) or $SrTiO_3$ (STO). The epitaxial manganite films as well as the capping layer were grown by pulsed laser deposition.
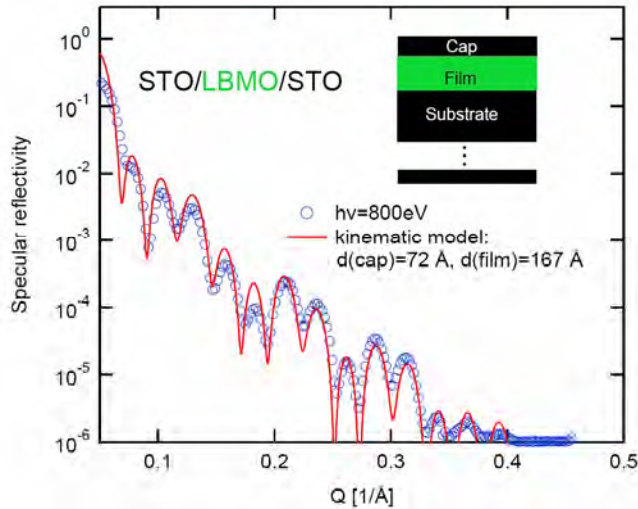
Figure 1: Non-resonant reflectivity curve of a STO/LBMO/STO hetero-structure (T=20 Kelvin, B=0.5 Tesla, π-polarization). A kinematical calculation gives a good description of the experimental data and was used to characterize structural properties of the samples.

The RSXR experiment was conducted at the UE46-PGM undulator beamline operated by the Helmholtz-Zentrum Berlin, using the two-circle UHV diffractometer built at the Freie Universität Berlin. A continuous flow He cryostat was used for cooling the samples. The detector was a silicon diode which had an angular acceptance of about 0.8° in the scattering plane and 4° perpendicular to it. The measurements were performed in the temperature range between 300K and 60K. Below the magnetic ordering temperature the manganite films were magnetized perpendicular to the film surface by means of a constant applied magnetic field of 0.5 Tesla.

Results: Figure 1 shows a non-resonant soft x-ray reflectivity measurement done with 800eV photons of a STO(substrate)/LBMO(167nm)/STO(72nm) sample. The non-resonant measurements were performed in order to characterize structural properties of the samples. In order to do so, we used a kinematical model calculation to extract structural parameters like layer thicknesses and the averaged width of the interface regions. As can be observed in Fig. 1, the kinematical model reproduces the experimental data quite well at angles above the critical angle. For all studied samples the intensity variations could be observed over a large Q-range, implying sharp interfaces between the different materials. Indeed the kinematical model yielded an interface thickness of 5-9 Angströms.

RSXR results are presented in Fig.2. We performed a comprehensive RSXR study as a function of temperature, applied magnetic field and photon polarization. As an example, RSXR measurements of a STO/LCMO/STO heterostructure in the vicinity of the Mn L_3-edges are shown. Close to the Mn L_3-edge at 643 eV, the reflectivity profile R as a function momentum Q changes strongly with the photon energy, as illustrated in Fig.2 (a),(b). Not only the intensities but also the position of the maxima in $R(Q)$ changes considerably around the Mn L_3-edge. These changes are due to the energy dependence of the index of refraction n in the interface region. We are currently analyzing $R(Q)$ for the different
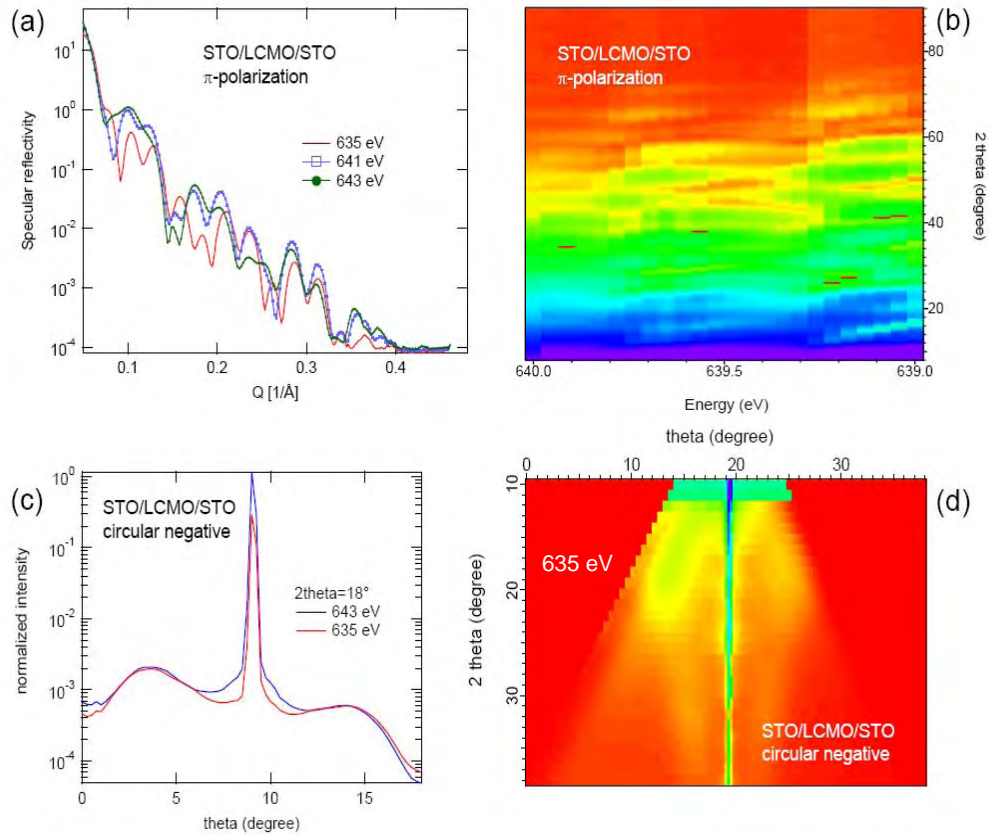
Figure 2: RSXR measurements of a STO/LCMO/STO heterostructure (T=20 Kelvin, B=0.5 Tesla).
(a),(b): Reflectivity profiles R(Q) measured at different photon energies. R(Q) on-resonance (641eV, 643eV) and off-resonance (635 eV) show clear differences. (c),(d): Off-specular RSXR measurements.

photon energies in order to extract *n*, which will then be compared to the bulk values determined from reference samples. In this way RSXR provides unique information about the electronic structure at the interfaces of the studied heterostructures.

In Fig. 2 (c),(d) the off-specular RSXS of the STO/LCMO/STO sample is shown. The off-specular reflectivity is related to the roughness of the interfaces. As can clearly be observed in Fig.2 (c), there is an additional contribution to the diffuse off-specular scattering, indicating the presence of an additional electronic roughness. By analyzing RSXS data as a function of energy and polarization, we aim to extract detailed information about the electronic structure at the interfaces of the studied heterostructures.

References:
[1]   H. Yamada *et al.*, Science **305**, 646 (2004)
[2]   A.P. Ramirez, Science **315**, 1377 (2007)
[3]   N. Nakagawa *et al.*, Nature Materials 5, 204 (2006)
[4]   N. Reyren *et al.*, Science **317**, 1196 (2007)

Tailoring the nature of magnetic coupling
of Fe-porphyrins to ferromagnetic substrates

M. Bernien[1], J. Miguel[1], C. Weis[2], J. Kurde[1], B. Krumme[2], M. Piantek[1], K. Baberschke[1],
W. Kuch[1], and H. Wende[2]

[1]*Institut für Experimentalphysik, Freie Universität Berlin, Arnimallee 14, 14195 Berlin, Germany*
[2]*Fachbereich Physik, Experimentalphysik - AG Wende and Center for Nanointegration*
Duisburg-Essen (CeNIDE), Universität Duisburg-Essen, Lotharstrasse 1, 47048 Duisburg,
Germany

Organic molecules as building blocks of surface-mounted nanoscale systems have reached tremendous impact in solid state physics. Metallo-porphyrins display a quasi-planar geometry, allowing for a two-dimensional assembly as electronic circuits or devices [1], while the four-ligated metal center can be accessed by two additional adsorption sites. This can be used to gain control on the metal center spin of paramagnetic porphyrin molecules. For instance, if metallo-porphyrins are deposited directly on a ferromagnetic (FM) metal surface, the spin of the central ion aligns parallel to the substrate magnetization [2-4].

Here, we demonstrate that an antiferromagnetic (AFM) coupling between the metal center of paramagnetic Fe-octaethylporphyrin molecules and ultrathin FM Co and Ni films can be realized by placing oxygen atoms between the molecules and the magnetic substrate. The strength of the AFM iron-oxygen-substrate interaction is estimated from the temperature dependence of the induced magnetization of the molecules. We have carried out x-ray absorption spectroscopy (XAS) and x-ray magnetic circular dichroism (XMCD) investigations of sub-monolayers of 2,3,7,8,12,13,17,18-Octaethylporphyrin-Fe(III) chloride (Fe-OEP) on oxygen-covered FM Ni and Co thin films [5]. The measurements were carried out at the beam line UE56/2-PGM2. Ni and Co films were epitaxially grown on a preoxidized Cu(100) single crystal. The oxygen atoms act as a surfactant for the growth of the FM film, floating on top of the surface [6, 7]. This results in a well-characterized $c(2{\times}2)$ superstructure of 0.5 ML atomic oxygen on top of the ferromagnetic films. Successively, we deposited Fe-OEP molecules by sublimation at 490 K
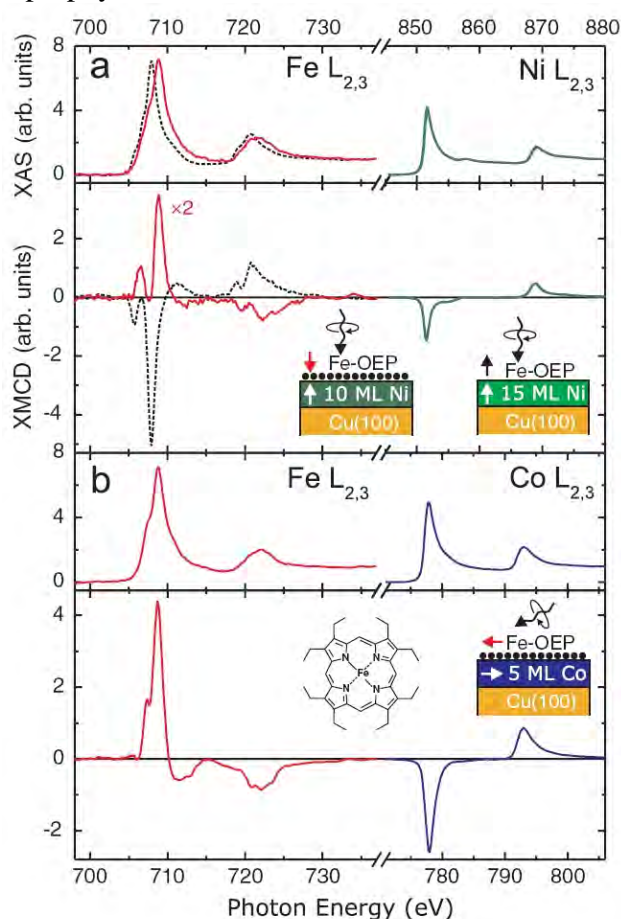
FIG. 1: Fe-$L_{2,3}$ XAS and XMCD spectra of 0.6 ML Fe-OEP on O/Ni (a) and O/Co (b) (red lines), and on Ni (black dotted lines, panel a). The corresponding Ni and Co spectra are shown on the right [5]. Insets: sketches of the corresponding samples and of the Fe-porphyrin molecule.

from a Knudsen cell. From an angular-dependent analysis of the N *K* edge π* resonances, we conclude on a planar adsorption geometry in both cases.

Figure 1 shows the Fe-L$_{2,3}$ XAS and XMCD spectra for 0.6 ML Fe-OEP on O/10 ML Ni/Cu(100), O/5 ML Co/Cu(100) (red lines), and 15 ML Ni/Cu(100) (black dotted line), measured at normal (grazing) incidence for the Ni (Co) samples at T = 40 K. XMCD measurements were performed in an applied magnetic field of 20 mT along the easy axes of the Ni and Co films, *i.e.* the surface normal and the [110] in-plane direction, respectively. Grazing and normal incidence geometries were used with angles of 70° and 0° between the incoming x-ray wave vector and the surface normal, respectively. An opposite sign of the Fe XMCD signals on the oxygen-covered Ni and Co films with respect to the substrate magnetization is observed, evidencing an antiparallel alignment of the Fe spin with the substrate. By sweeping the external magnetic field, the Fe magnetization reverses at the same field as the substrate while maintaining the antiparallel alignment. This AFM coupling is found only in the presence of the oxygen layer. In contrast, the Fe XMCD on the bare Ni film shows the same sign as the XMCD of the Ni substrate. We identify superexchange across oxygen atoms to be responsible for the antiparallel alignment [5].

The energy position of the Fe XAS peaks can be used as an indicator for the Fe valence state [8]. Charge-transfer processes that may occur during the evaporation and adsorption of Fe-OEP onto the O/metal substrates would affect the Fe valence state. In the case of the surfactant-grown substrates (red lines in Fig. 1), the Fe-L$_3$ XAS peak positions coincide with those of an Fe(III)-OEP-Cl bulk sample (data not shown), implying a trivalent Fe ion. On the contrary, a red-shift of about 1 eV is visible on the bare metallic substrates, suggesting an increase of the number of 3*d* electrons at the Fe site.

In order to estimate the coupling energy E$_{ex}$ of the Fe magnetic moment to the O/Ni, Ni and O/Co substrates, we have studied the temperature dependence of the magnetizations of the FM films and of the Fe centers in the molecules. In Fig. 2 the Fe, Ni and Co XMCD signals at fixed photon energies, normalized to the extrapolated saturation values, are plotted *vs.* temperature. The evolution of the Fe magnetization deviates drastically from that of the substrate for all samples. For Fe-OEP on O/Co, the Fe magnetization is closer to the substrate than for the Ni samples, indicating a stronger coupling energy. The temperature dependence of the relative Fe magnetization M$_r$(T)= M(T)/M(T=0) has been modeled with a Brillouin function B$_J$(α) accounting for the coupling to the magnetic substrate as an effective magnetic field [5]:

$$M_r^{Fe}(T)= M_r^{sub}B_J(E_{ex}/k_BT).$$

Here we have assumed a divalent (trivalent)
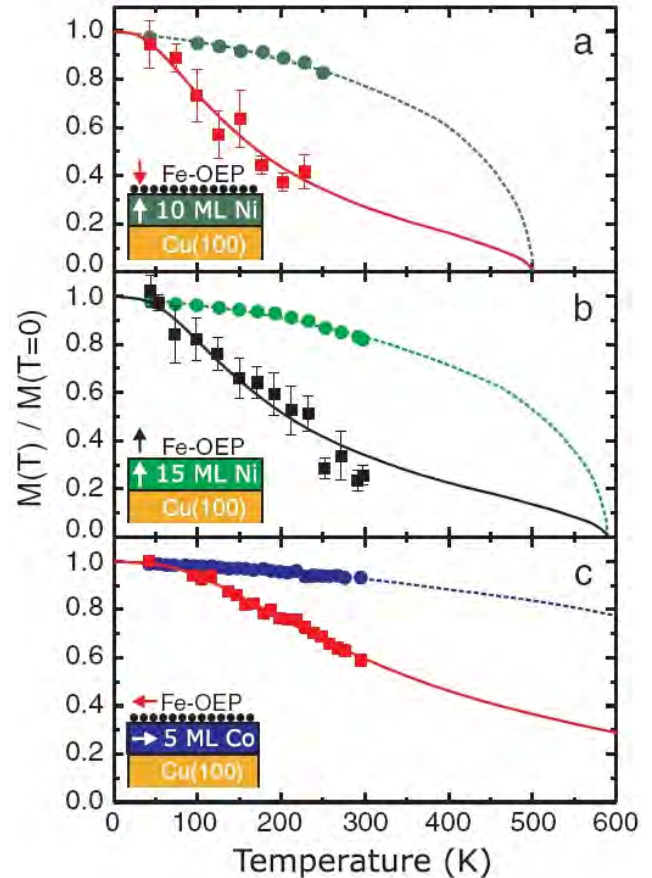
FIG. 2: Temperature dependence of Fe XMCD (squares; full lines: fit of Brillouin-type model) and Ni or Co XMCD [5] (circles; dashed lines: empirical curve taken from Ref. 10) for 0.6 ML Fe-OEP on (a) O/10 ML Ni/Cu(100), (b) 15 ML Ni/Cu(100) and (c) O/5 ML Co/Cu(100).

Fe oxidation state on the metallic (oxygen-covered) surfaces, as suggested by the XAS peak positions, and Fe intermediate spin states that result in spin moments S=1 (S= 3/2). For Fe-OEP on O/Co we obtain a coupling energy of 37 meV, being about half of that for the direct adsorption of the molecules on a Co substrate [4] (E_{ex} =70meV). In contrast, identical values of 17 meV are found for Fe-OEP on the oxygen-covered and bare Ni substrates. These values are of the same order of magnitude as in transition metal monoxides (*e.g.* E_{ex}^{NiO} =17meV/bond [9]).

To conclude, we showed how to tailor the magnetic coupling between ferromagnetic Ni and Co substrates and the Fe spin at the center of porphyrin molecules. When mediated by half a monolayer of atomic oxygen, the Fe–substrate coupling is antiferromagnetic. This situation is in contrast to the previously found ferromagnetic coupling of Fe-porphyrin molecules directly adsorbed onto the magnetic substrates. The corresponding coupling energies have been obtained from the temperature dependence of the Fe and substrate magnetic moments.

[1] L. Grill, M. Dyer, L. Lafferentz, M. Persson, M. V. Peters, and S. Hecht, Nature Nanotech. **2**, 687 (2007).

[2] A. Scheybal, T. Ramsvik, R. Bertschinger, M. Putero, F. Nolting, and T. A. Jung, Chem. Phys. Lett. **411**, 214 (2005).

[3] H. Wende, M. Bernien, J. Luo, C. Sorg, N. Ponpandian, J. Kurde, J. Miguel, M. Piantek, X. Xu, P. Eckhold, W. Kuch, K. Baberschke, P. M. Panchmatia, B. Sanyal, P. M. Oppeneer, and O. Eriksson, Nat. Mater. **6**, 516 (2007).

[4] M. Bernien, X. Xu, J. Miguel, M. Piantek, P. Eckhold, J. Luo, J. Kurde, W. Kuch, K. Baberschke, H. Wende, and P. Srivastava, Phys. Rev. B **76**, 214406 (2007).

[5] M. Bernien, J. Miguel, C. Weis, Md. E. Ali, J. Kurde, B. Krumme, P. M. Panchmatia, B. Sanyal, M. Piantek, P. Srivastava, K. Baberschke, P. M. Oppeneer, O. Eriksson, W. Kuch, and H. Wende, Phys. Rev. Lett. **102**, 047202 (2009).

[6] C. Sorg, N. Ponpandian, M. Bernien, K. Baberschke, H. Wende, and R. Q. Wu, Phys. Rev. B **73**, 064409 (2006).

[7] R. Nünthel, T. Gleitsmann, P. Poulopoulos, A. Scherz, J. Lindner, E. Kosubek, C. Litwinski, Z. Li, H. Wende, K. Baberschke, S. Stolbov, and T. S. Rahman, Surf. Sci. **531**, 53 (2003).

[8] A. S. Vinogradov, A. B. Preobrajenski, S. A. Krasnikov, T. Chassé, R. Szargan, A. Knop-Gericke, R. Schlögl, and P. Bressler, Surf. Rev. Lett. **9**, 359 (2002).

[9] M. S. Seehra and T. M. Giebultowicz, Phys. Rev. B **38**, 11898 (1988).

[10] A. Scherz, C. Sorg, M. Bernien, N. Ponpandian, K. Baberschke, H. Wende, and P. J. Jensen, Phys. Rev. B **72**, 054447 (2005).

Ring opening reaction of Spiropyranes on a Au(111) single crystal surface

M. Piantek, A. Krüger, Ch. Navío, J. Miguel, M. Bernien, and W. Kuch

Institut für Experimentalphysik, Freie Universität Berlin, Arnimallee 14, 14195 Berlin, Germany
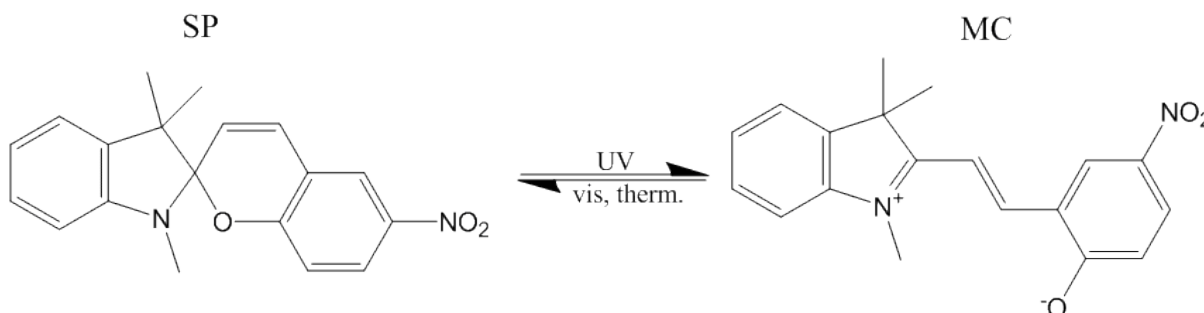
Figure 1: Structures and reaction paths of the two photo-isomers of 1',3',3'-trimethyl-6-nitrospiro[chromene-2,2'-indole].

Molecules that exhibit a photon-induced reversible transition between two isomeric states entail an enormous potential for applications in electronics, photonics, and computing. 1',3',3'-trimethyl-6-nitrospiro[chromene-2,2'-indole] (BIPS) undergoes such a reversible photoreaction from Spiropyran (SP) to Merocaynine (MC) involving a heterolytic cleavage of the C–O bond in the pyran ring (see Fig. 1), which goes along with a drastic change of the molecular electronic properties. Planning on the access of such functionalities, we follow the aim of furnishing a metallic surface with those photochromic switches. In the gas phase, in solution, and in the crystalline form, this ring opening/closing mechanism of BIPS is well understood, whereas in the adsorbed phase it still has to be investigated. In order to avoid the chemical interaction with the substrate, we used a comparatively inert Au(111) single crystal surface. All experimental data have been measured at the BESSY beamline UE56/2 PGM2.

Figure 2: X-ray photoelectron spectra of a monolayer of BIPS on Au(111), taken during a heating sequence from 230 K to 330 K.

Temperature-dependent XPS spectra of 1 ML BIPS evaporated on a Au(111) surface at 150 K during a heating sequence from 230 K to 330 K are shown in Fig. 2. From each spectrum a linear background was subtracted. At 230 K one sharp peak is visible at 399.0 eV and a

broad one around 405.3 eV. Due to the ionic character of the ON^+O^- nitro group, the corresponding N 1s core level should be lower in energy than the one of the indoline nitrogen. Thus the broader peak at higher binding energy can be attributed to the nitro group, while the peak at 399.0 eV corresponds to the indoline N 1s photoelectrons. These energies are in good agreement with those found in literature [1, 2].

Above 300 K a new component at 400.4 eV comes up while the peak at 399.0 eV vanishes almost completely at 330 K. Assuming a complete transition from SP to MC, an additional π bond at the triply bonded indoline nitrogen atom (>N$^+$=) will be formed. This causes a partial positive charging of the nitrogen atom, and such explains the shift of the XPS peak to higher binding energies.

Figure 3a shows the near edge X-ray absorption spectra (NEXAFS) of a mono layer of Spiropyran on Au(111) measured for the same heating sequence. The spectra are shifted vertically by multiples of 0.015 for clarity. All spectra taken at grazing incidence (dashed lines) show a pronounced π^* resonance around 403 eV. This resonance can be assigned to the transition from the N 1s (NO$_2$) core level into the lowest π^*(NO$_2$) orbital [3]. Since this resonance is not present in any of the spectra taken at normal incidence, we conclude that the nitrobenzopyrane moiety lies flat on the surface at all temperatures measured here.

Going to higher temperatures a second resonance appears at 400 eV in the spectra of grazing incidence at 300 K and more prominent at 330 K. This can only be caused by the formation of an additional π bond, as it is expected during the ring-opening reaction. Spectra calculated for the free SP and MC molecules using the StoBe code [4] are shown in Fig. 3b. They confirm the interpretation of the experimental data: The stronger resonance at 403 eV in both calculated spectra comes from the transition of the N 1s (NO$_2$) electron into the π^* orbital of the nitro-benzopyran moiety. The ring-opening reaction causes this π^* obital to be linked to the π system of the indole moiety of the MC making an N 1s (indole) $\rightarrow \pi^*$ transition at 400 eV possible. The orientation of
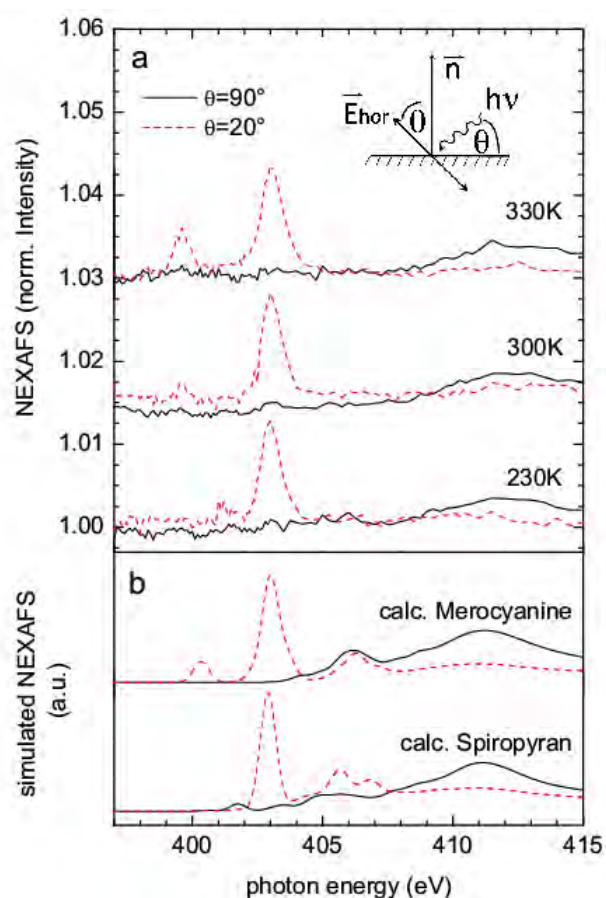
Figure 3: a): Experimental N K edge absorption spectra of a monolayer of BIPS on Au(111), taken during a heating sequence from 230 K to 330 K (simultaneously to the data of Figure 2). Continuous (dashed) lines correspond to spectra acquired at 90° normal (20° grazing) incidence of p-polarized X-rays. b) Calculated NEXAFS for the free SP and MC molecules. For the calculated spectra the angle of light incidence is given with respect to the molecular plane of the nitrobenzene moiety. The spectra are shifted vertically for clarity.

this new π bond is the same as for the $\pi^*(NO_2)$ orbital.

In conclusion, we find that the BIPS molecules deposited at 150 K are in the closed-ring configuration. During heating the sample up to 330 K the molecules transform to the ring opened configuration. Since we did not find a back transformation by cooling back to 150 K, the opened-ring geometry is the preferred conformation on the surface, in contrast to gas phase and solution.

[1] D. Schulze, K. H. Hallmeier, D. Wett, and R. Szargan J. Elec. Spec. Relat. Phenom. **151** (2006) 204

[2] H. Ågren, B. O. Roos, P. S. Bagus, U. Gelius, P.-Å. Malmquist, S. Svensson, R. Maripuu, and K. Siegbahn, J. Chem. Phys. **77** (1982) 3893

[3] C. C. Turci, S. G. Urquhart, and A. P. Hitchcock, Can. J. Chem. **74** (1996) 851

[4] K. Hermann and L. G. M. Pettersson, program package StoBe (Stockholm,Berlin, 2005), a modified version of the DFT-LCGTO program package deMon by A. St.-Amant and D. Salahub (University of Montreal)

Ultrafast Electron Transfer Dynamics at Phosphorus-Metal Interfaces

S. Neppl, F. Blobner, P. Feulner

Physikdepartment E20, TU-München, D-85748 Garching

Ultrafast charge transfer (CT) in heterogeneous systems is of key importance in both fundamental research and technology. However, for reliable interpretation of CT data, it is mandatory to identify the impact of the interfacial electronic structure on the electron transfer dynamics. To gain a better understanding of the mechanisms underlying ultrafast charge transfer processes, we focus on the simplest model system, a reactive atom on a surface, Using polarization-resolved core hole clock spectroscopy (CHC) at the P2s absorption edge, we studied the electron transfer dynamics from phosphorus atoms on surfaces to their metallic substrates. In particular, we analyzed the sensitivity of the resulting electron transfer times to changes in the structural and electronic properties at these interfaces.

In the CHC approach, the lifetime of a resonantly excited core hole state is used as an internal reference clock for the electron dynamics to be investigated [1]. The very short-lived P2s core hole (lifetime ~ 550as [2]) enables access to dynamical processes proceeding on a low femtosecond to attosecond time scale.

The CHC method yields values for the charge delocalization time, but does not allow continuous tracking of the charge dynamics in the time domain. This will be possible in future experiments utilizing XUV lasers with attosecond pulse lengths and appropriate detection schemes [3].

Atomic phosphorus (P) layers on Ru(0001) and Cu(111) were prepared by electron-induced decomposition of molecularly adsorbed PF_3. Upon annealing, we observed two ordered phases of P on Ru(0001): a p(2x1) superstructure at 300K and a $\sqrt{7}$x$\sqrt{7}$R19.2° phase at 700K (most likely due to formation of ruthenium phosphide [4]). Both phases exhibit a re-

Fig.1 : Left: P2p photoemisson; Right: P-induced Ru3d$_{5/2}$ surface core level shift (red arrow)

markable different electronic charge distribution between the adsorbate and the topmost Ru layer, which is directly reflected in the binding energy shift of the P2p photoemisson and the P-induced Ru3d5/2 surface core level shift with opposite sign as the temperature is increased (Fig.1).

Decay of the [P2s]P3p* resonance *before* delocalization for the P3p* electron yields [P2p] participator and [P2pP3p]P3p* (denoted L) spectator final states with constant binding energy, *after* delocalization [P2pP3p] Auger states (denoted D). A similar scenario was observed for S/Ru(0001) [5,6]. In our case, the [2p3s]3p* spectator channel was much weaker than for S/Ru(0001). A quantitative analysis in terms of CT times, i.e. $\tau_{CT} = \tau_{[P2s]}$ x (L/D) (Fig.2) is possible by phenomenological fits with two Gaussian line shapes with constrained peak parameters to the D and L channels as a function of incoming photon energy, for L after subtraction of non-resonant shake-up contributions S (see Fig.2) [5] . Exemplary fits are shown in Fig.3.
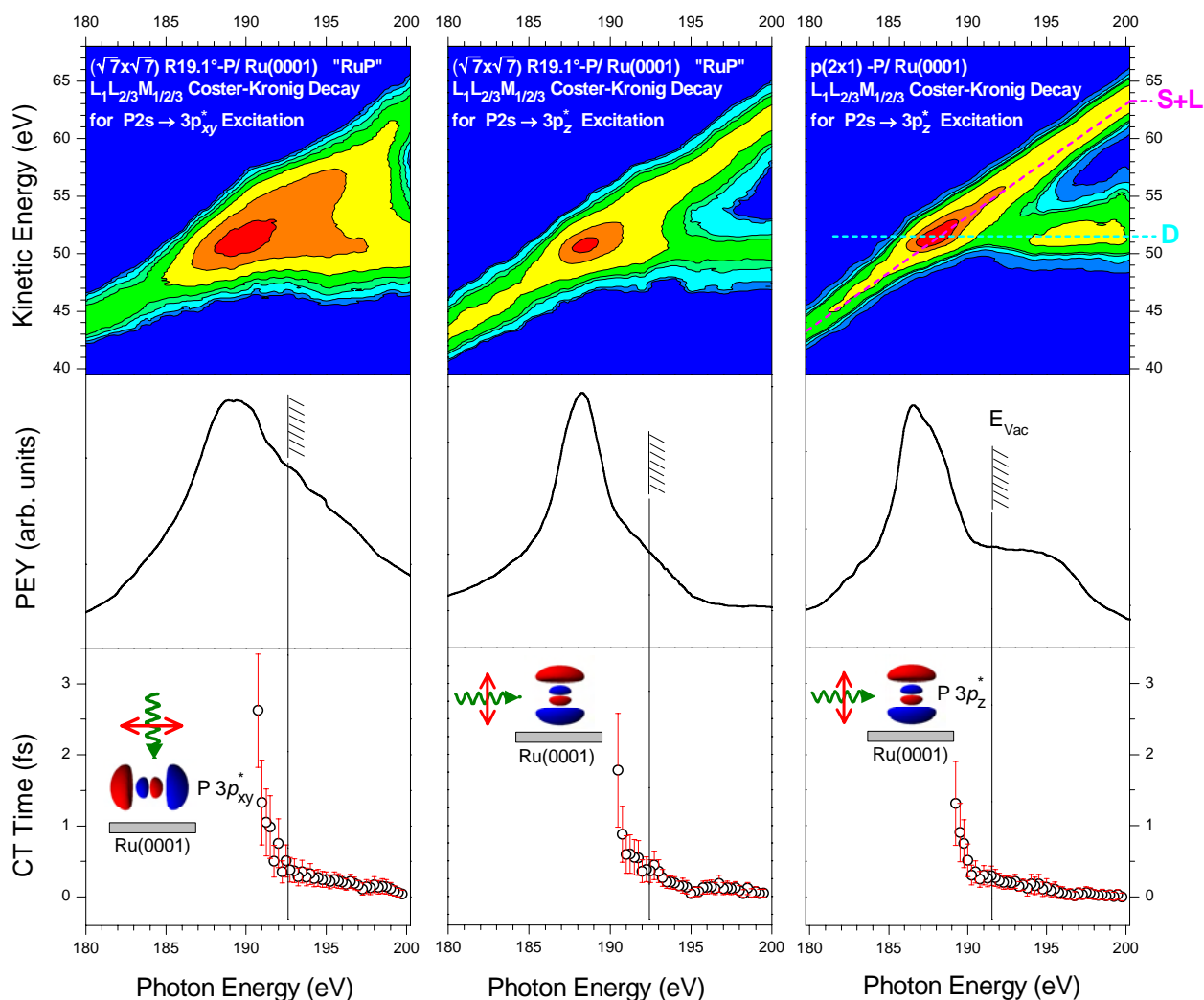
Fig.2 : LLM autoionization spectra, XAS data and derived electron transfer times for the two different P/Ru(0001) interfaces. The insets in the bottom panels indicate the polarization of the exciting radiation.

Both P/Ru(0001) systems exhibit similar electron transfer times in the low-fs to sub-fs regime that show the same *hv*-dependence. In contrast to previous results on S/Ru(0001) [6], we find no indication of a polarization effect in the CT.

For P on Cu(111) we observe a complete quenching of the P2s → 3p* resonance. The step-like XAS line shape (Fig.4), centered at the Fermi energy, implies the direct injection of the excited electrons into extended Cu(111) conduction band states with-

out any localization — in agreement with LLM autoionization spectra (data not shown).
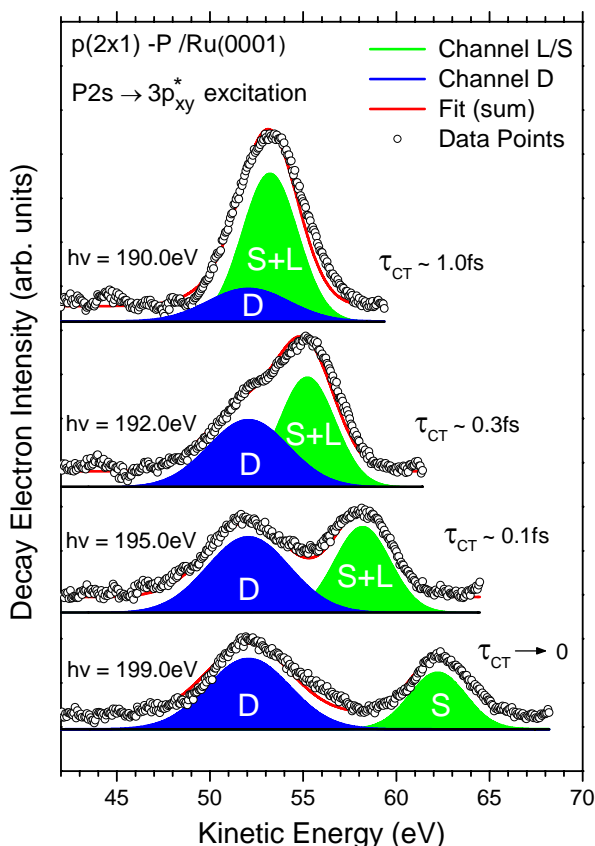
Fig.3 : Quantitative analysis of electron transfer times by phenomenological curve fitting to the channels S,L and D.
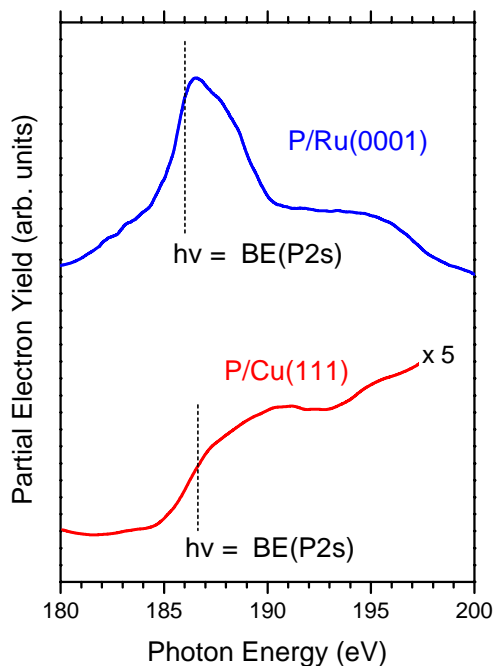
Fig.4 : Comparison of XAS obtained from P/Ru(0001) and P/Cu(111). Dashed lines indicate direct P2s excitation to the Fermi level.

References:

1. see, e.g. D. Menzel, Chem.Soc.Rev. 37, 2212; P.A. Brühwiler, O. Karis, N. Martensson, Rev. Mod. Phys., 74, 703.
2. J.L. Campbell, T. Papp, Atomic Data and Nuclear Data Tables 77, 1.
3. A.L. Cavalieri et al., Nature 449, 1029.
4. H.-S. Tao *et al.*, Surf.Sci., 312, 323.
5. A. Föhlisch *et al.*, Nature, 436, 373.
6. M. Deppe *et al.*, J.Chem.Phys. 127, 174708.

High-pressure photemission study of the SrTiO$_3$/Pt interface

R. Schafranek, C. Körber, A. Wachau, A. Klein

Darmstadt University of Technology, Institute of Materials Science, Darmstadt, Germany

M. Hävecker, A. Knop-Gericke, R. Schlögl

Fritz-Haber-Institute, Dept. of Inorganic Chemistry, Berlin, Germany

Metal/oxide interfaces are important for a wide range of applications. The interface between (Ba,Sr)TiO$_3$ and Pt, e.g., is used as electrode/dielectric combination in tunable capacitors for microwave applications [1]. The properties of the capacitors depend crucially on the electrode preparation, which can be related to a variation of the Schottky barrier height. It has been shown by photoemission experiments that the barrier height can be reversibly switched between a reduced state with a low barrier height (~0.5 eV) and an oxidized state with a high barrier height (>1.2 eV) by annealing at 400°C in vacuum and oxygen, respectively [2].

The aim of the synchrotron experiments was to obtain more detailed insights into the dependence of the barrier height on the environment. For the studies, Nb-doped SrTiO$_3$(100) single crystals were prepared at TU Darmstadt by heating in oxygen pressure of 1 Pa pressure. The samples were free of hydrocarbon contaminations as checked in-situ by XPS. After cleaning and XPS measurement a ~3 nm Pt layer was deposited without breaking vacuum by magnetron sputtering. The details of the interface formation are described in [2]. After Pt deposition the samples are removed from vacuum and transferred to the high-pressure XPS setup at the ISISS dipole beamline. The experiment was performed by stepwise heating the sample up to 400°C. The sample temperature was held constant at 100, 150, 200, 300, and 400°C, respectively, while the oxygen pressure was varied between high vacuum (p~10^{-5} Pa) and 10 Pa O$_2$. The temperature and pressure conditions during the experiment are shown in Fig. 1.
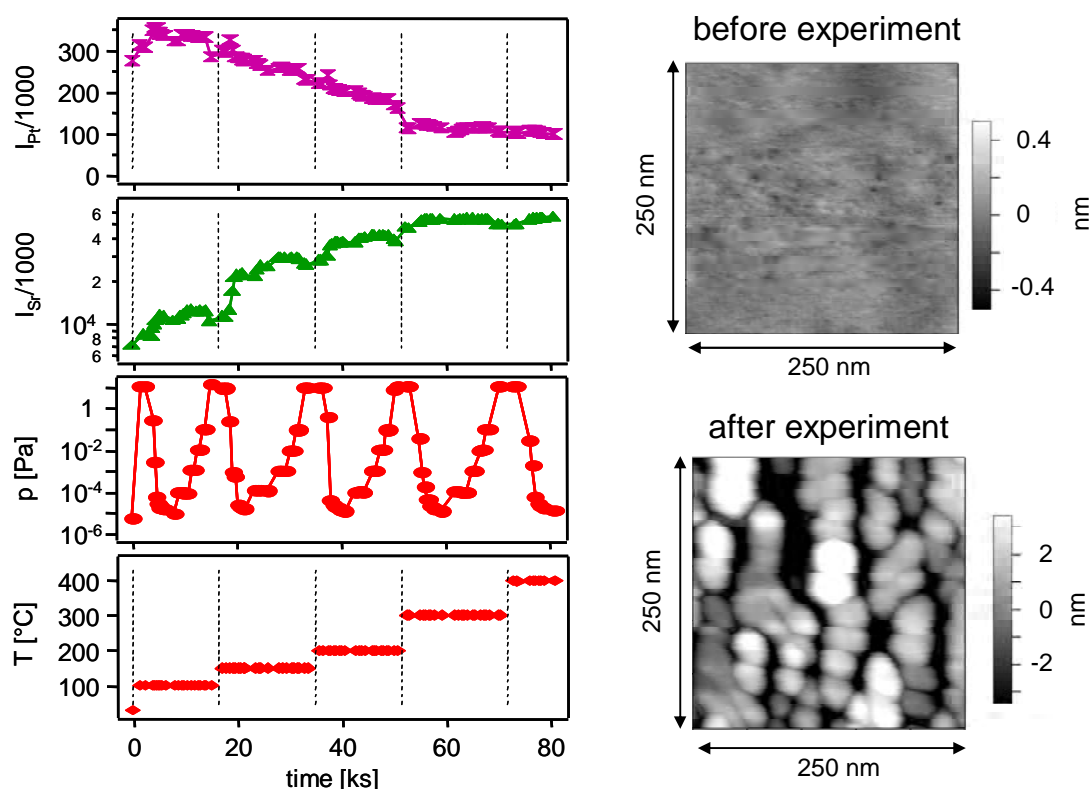
Fig. 1: (left) Installed temperature and pressure and measured substrate (Sr 3d) and overlayer (Pt 4f) intensities in the course of the experiment. The pressure was controlled by variation of pumping speed and oxygen gas inlet; (right) AFM images of an unheated SrTiO$_3$/Pt sample (top) and the SrTiO$_3$/Pt after the experiment shown on the left side (bottom).

The Sr 3d substrate and Pt 4f overlayer intensities recorded during the experiment are included in Fig. 1. The intensities have been normalized by the mirror current of the refocusing mirror of the beamline. With increasing substrate temperature, the Sr 3d intensity increases while the Pt 4f intensity

decreases. This indicates islands formation of the Pt film, which is also evident from the AFM images shown in the right part of Fig. 1. While the unheated $SrTiO_3$/Pt shows an extremely flat surface, Pt islands with a typical height of 4 nm are clearly identified on the surface of the sample used for the experiment.

The peak shape of the substrate emissions did not change at any temperature and pressure. Also no formation of Pt-oxides can be identified. The carbon peak, which is observed on the sample after introduction from air, is quickly removed after heating to 100°C in an oxygen pressure of 10 Pa. However, after removal of the oxygen the carbon emission reappears for sample temperatures up to 300°C. The reappearance of the carbon peak is attributed to adsorption of organic compounds which are present in the residual gas from previous experiments.

Calibration of binding energies has been performed by setting the peak of the Pt 4f emission to a binding energy of 71.15 eV, which resulted in zero binding energy of the Fermi edge of the metal film/islands. The evolution of the corrected substrate Sr 3d and Ti 2p core level binding energies is shown in Fig. 2. Binding energy differences between core levels and valence band maximum derived from a large set of samples have been subtracted to quantify the variation of the Fermi energy with respect to the valence band maximum of $SrTiO_3$.
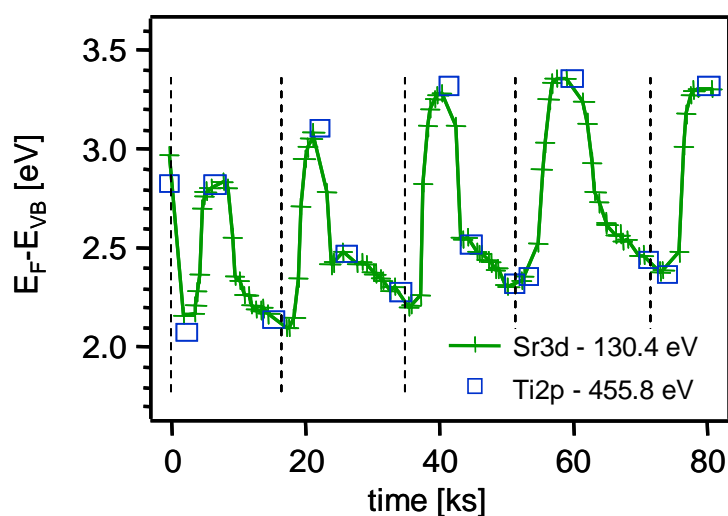
Fig. 2: Variation of Sr 3d and Ti 2p binding energies recorded in the course of the experiment. The dashed lines indicate the changes of substrate temperature and correspond to those in Fig. 1. Valence band maximum to core level binding energy differences as indicated in the graph have been subtracted from the core levels in order to show the variation of the Fermi level with respect to the valence band maximum.

Both core levels exhibit parallel shifts of ~1eV magnitude. The binding energies directly follow the oxygen pressure in the chamber. It is evident that the changes occur already at the lowest used substrate temperature of 100°C, where clustering of the Pt film is not yet pronounced. The change of Schottky barrier height, directly given by the changes of core level binding energies and attributed to a change of defect concentration at the interface [2], evidently occurs through a closed Pt film. No three-phase boundary (substrate-film-gas) seems to be required as often quoted in literature.

1. R. Schafranek, A. Giere, A.G. Balogh, T. Enz, Y. Zheng, P. Scheele, R. Jakoby, and A. Klein, J. Eur. Ceram. Soc. (2009),
2. R. Schafranek, S. Payan, M. Maglione, and A. Klein, Phys. Rev. B **77** (2008), 195310.

Molecular Orientation in Pentacene films on Pd

D. Käfer[1], G. Witte[2], and Ch. Wöll[1]

[1]Physical Chemistry I, Ruhr-University Bochum, Universitätsstr. 150, 44801 Bochum
[2]Molecular Solids, Department of Physics, Philipps-University, Renthof 5, 35032 Marburg

Due to its high charge carrier mobility pentacene is a promising molecular semiconductor for the fabrication of organic field-effect transistors (OFETs). While gold has been commonly used as electrode material in pentacene-based thin film transistors, a strong increase in the charge carrier mobility and decrease in contact resistance can be achieved using Pd electrodes instead [1]. The morphology and microscopic orientation for pentacene on Au has been investigated in detail [2], while it is still unknown on a Pd substrate. Since the charge transport in the organic active layer depends on the molecular ordering, morphology and crystallinity, it is therefore important to study the molecular orientation of pentacene on Pd(111) and polycrystalline Pd (as this is used in devices), which was done using NEXAFS spectroscopy. The experiments were carried out at the HESGM beamline of the BESSY II synchrotron facility.
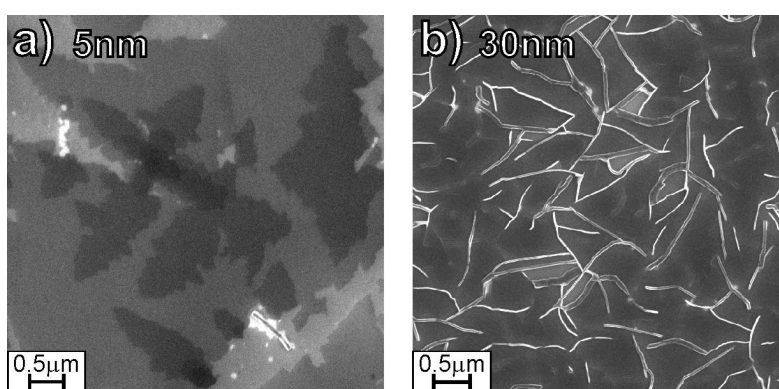
Fig. 1: SEM images of a) 5 nm and b) 30 nm pentacene films (300 K, 10Å/min) on Pd(111)

First, the macroscopic morphology of thin pentacene films on Pd substrates has been characterized by recording SEM images (LEO 1530 Gemini) of 5 and 30 nm pentacene films on Pd(111) (see fig. 1). Remarkably, a thin pentacene film of 5 nm thickness deposited on Pd(111) shows a completely different growth behavior than on Au(111), where a pronounced Stranski-Krastanov growth and 3D island formation (even a post-deposition dewetting) has been observed [2]. In case of Pd(111) serving as substrate, a more layer-by-layer growth type, at least for low film thicknesses, is found as indicated by the different gray shades corresponding to different individual pentacene layer heights (fig. 1a). The shape of the growing layers can be classified as dendritic. Noticeably, a full coverage of the substrate is achieved already at such low film thicknesses, which is in contrast to films on Au or Ag. The rather layered growth on Pd (and additional AFM data not shown) already indicate that in agreement with pentacene grown on SiO_2 but in contrast to pentacene on Au an upright orientation of the molecules seems to be present.

Increasing the film thickness to 30 nm, the SEM image (fig. 1b) reveals the appearance of thin needles of up to 2 μm length on top of the homogenous pentacene film. In between these needles a magnification and contrast amplification reveals small pyramids of around 0.4 μm size. Compared to pentacene films on Au, the films on Pd(111) grow not only in different orientations and cover the surface, but also are much smoother and more homogenous with strongly reduced 3D island growth behavior.

To clearly determine the molecular orientation of such thick films also used in devices, a 30 nm pentacene film on clean Pd(111) has been investigated using NEXAFS spectroscopy (see fig. 2a). The magnification in the π^* region of the C1s absorption edge shows at least 6 π^* resonances at 283.78, 284.28, 284.66, 285.79, 286.24, and 286.97 eV, which agrees well with gas phase NEXAFS spectra of pentacene [3] and those obtained for thick films on non-interacting surfaces like SiO_2 [2]. For quantitative analysis of the dichroism the peak areas of these resonances, obtained by fitting the spectra recorded at 5 different angles θ of incoming

synchrotron light, have been analyzed using the relationship (3-folded symmetry) $I_{vec,\sigma\geq3} = P\cos^2\theta(3\cos^2\alpha-1)+1-\cos^2\alpha$ [4]. The resulting angle $\alpha = 69°$ of the transition dipole moment to the surface normal can be translated into a tilt of the aromatic backbone of $\varphi = 24°$, indicating standing geometry. This result is in pronounced contrast to the orientation in thick pentacene films on Au(111) [2] and on Ag(111) [5], where rather lying geometries have been found ($\alpha = 31/34°$) in thicker films, but nearly agrees with the value observed for bulk samples on SiO_2 ($\alpha = 79°$) [2].
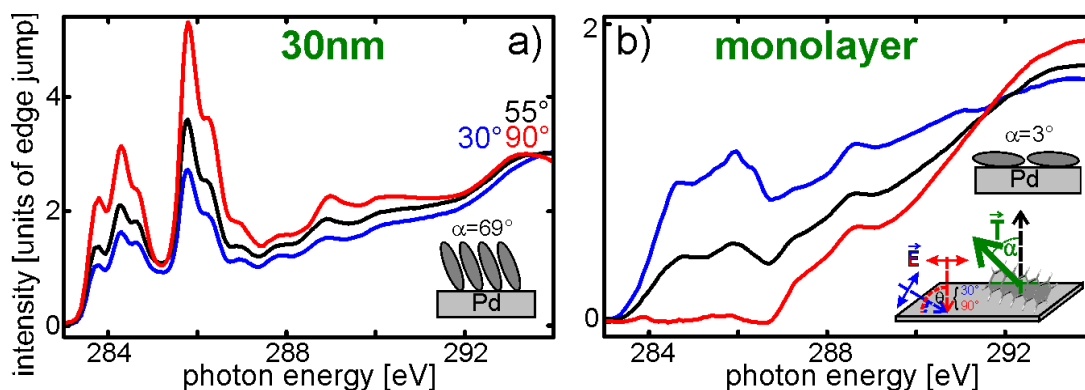
Fig. 2: magnification in the π^* region of NEXAFS spectra of a) 30 nm pentacene on Pd(111) (300 K, 10 Å/min), and b) of a monolayer (prepared by heating to 420 K)

As the current is mostly transported in the first (few) layer(s) of the pentacene film in a device and as it is known that the monolayer can adopt an orientation different from all following layers [5], also the monolayer pentacene, prepared by heating off the physisorbed layers of a 3 nm film at 420 K, is investigated. The pentacene monolayer on Pd(111) shows a different NEXAFS spectrum (see fig. 2b) as the dichroism is inverted and furthermore the 6 individual π^* resonances are not visible anymore. Instead, two rather broad peaks appear at 284.7 and 285.9 eV. This broadening has been observed for pentacene on Au and Ag [2,5] as well and is assigned to a strong interaction and electronic coupling of the aromatic π-system with the metal surface, indicative for chemisorption. The quantitative analysis of the dichroism yields an angle $\alpha = 3°$ and thus a tilt of $\varphi = 87°$, indicating a flat lying chemisorbed pentacene wetting layer on Pd(111). This wetting layer has also been observed on other metal surfaces, e.g. on Au(111) ($\alpha = 13°$) [2] and on Ag(111) ($\alpha = 13°$) [5].
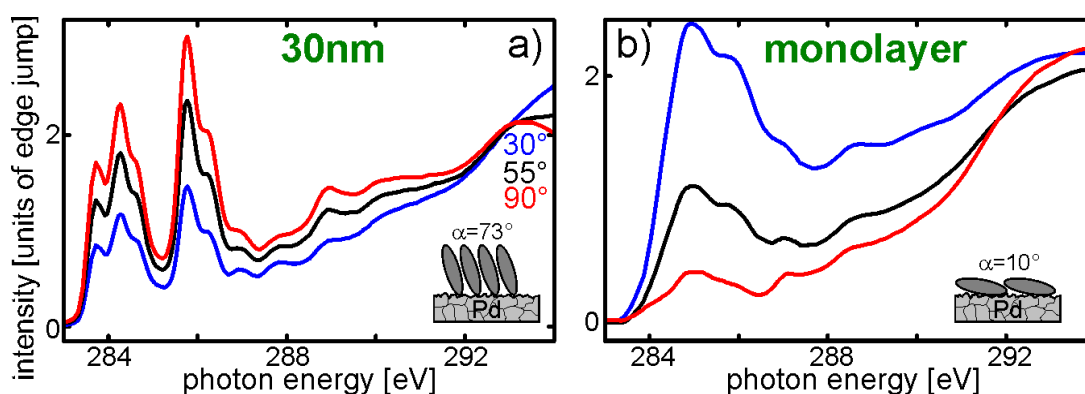
Fig. 3: magnification in the π^* region of NEXAFS spectra of a) 30 nm pentacene on a clean polycrystalline Pd sheet (300 K, 10 Å/min), and b) of a monolayer (heating to 420 K)

However, the electrodes used in a pentacene OFET will have polycrystalline nature. Therefore, NEXAFS spectra have also been recorded for 30 nm and a monolayer pentacene on a UHV-cleaned polycrystalline Pd sheet. For thick films (see fig. 3a) the quantitative analysis yields $\alpha = 73°$, translating into a tilt angle of $\varphi = 19°$, i.e. standing orientation just like in case of clean Pd(111) or on polycrystalline Au [2]. For these thicker films again 6 π^* resonances appear, while for the monolayer film of pentacene on Pd(111) again a strong peak broaden-

ing occurs resulting in only two resonances left in the π^* region at 284.9 and 285.8 eV (see fig. 3b). The analysis of the dichroism yields an angle $\alpha = 10°$ corresponding to a tilt angle of $\varphi = 80°$ for a pentacene monolayer on a clean polycrystalline Pd sheet.

The NEXAFS spectrum thus indicates a rather flat lying monolayer, as far as this is possible on a rough surface, as there will always be molecules that stick to step edges also in standing geometry. As this scenario has also been observed for pentacene on polycrystalline Au surfaces, the molecular orientation within the crystalline films seems to depend in general distinctly on the roughness of the substrate surface. While for thick films on Au(111) and on Ag(111) the molecules keep a rather lying geometry representing a preferred bulk crystal orientation, pentacene films on polycrystalline Au and Pd surfaces will adapt the thermodynamically most stable (001) crystal growth direction, i.e. upright standing orientation. The intrinsic difference is that on rough polycrystalline surfaces larger diffusion barriers are present and an enhanced tilting of linear shaped molecules in sum results in initial disorder, causing the further growth to proceed not in a templated way but simply in the energetically most favorable c-direction.

References

[1] C. Bock, D.V. Pham, U. Kunze, D. Käfer, G. Witte, Ch. Wöll, Physica E **40**, 2107 (2008)

[2] D. Käfer, L. Ruppel, G. Witte, Phys. Rev. B **75**, 085309 (2007)

[3] M. Alagia, C. Baldacchini, M. G. Betti, F. Bussolotti, V. Carravetta, U. Ekström, C. Mariani, S. Stranges, J. Chem. Phys. **122**, 124305 (2005)

[4] J. Stöhr, NEXAFS Spectroscopy, vol. 25 (Springer Series in Surface Science, 1992)

[5] D. Käfer, G. Witte, Chem. Phys. Lett. **442**, 376 (2007)

Time–resolved XRMS experiments with ALICE

Stefan Buschhorn, Frank A. Brüssing, Radu Abrudan, Hartmut Zabel

Experimentalphysik IV, Ruhr-Universität Bochum,
Universitätsstrasse 150,
44780 Bochum, Germany

Magnetism on short timescales has attracted strong interest within the last years, for both a fundamental understanding and for technical reasons, as precessional motion is the lower limit for switching. X-Ray Resonant Magnetic Scattering (XRMS) provides a powerful tool: Different layers in a magnetic structure are distinguishd by element selectivity, and a time resolution of less than 100 ps is achieved by a stroboscopic technique. In this way both precession frequencies and phase relation between differnet layers can be extracted. We present first time resolved data taken in reflection geometry with the ALICE chamber [1] during single bunch mode at BESSY, Berlin. A sketch of the setup is shown in figure 1. In this geometry we are sensitive to the precessional motion of individual magentic moments in thin films, and we can distinguish between different and deeply buried layers in magnetic heterostructures. The sample is excited by a magnetic field pulse and the instant magnetization is probed by single bunch generated x-rays in a stroboscopic manner: A photodiode records the reflected intensity for a variable delay between excitation and probe pulse, thus probing the magnetizaion as a function of delaytime. This technique is sensitive to repeated processes, as the signal is averaged over many excitations. From such time scans the element specific precessional frequency and damping constant can be determined.
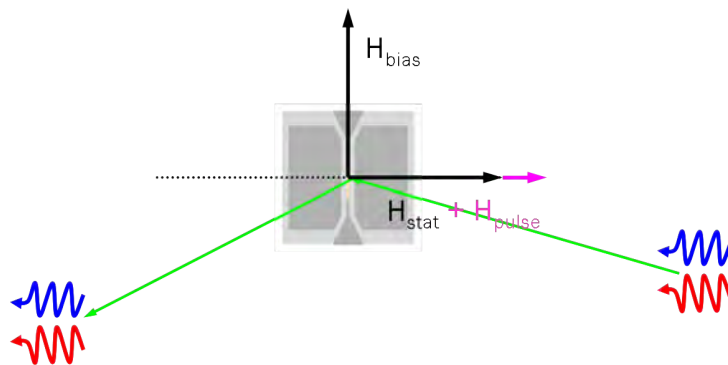
Fig. 1: Geometry of the sample, scattering plane and magnetic fields is shown: The stripline is aligned perpendicular to the scattering plane, thus the pulsed field H_{pulse} is parallel to the external static field H_{stat}. H_{bias} is applied by the Helmholtz coils.

Measurements have been done on a polycrystalline 25 nm Py ($Ni_{80}Fe_{20}$) film on top of a Cr stripline, deposited on a Si substrate. The sample has been prepared by ion beam sputtering through a mask, which has been shown to work best for our experiments. A triggered pulse generator delivers a 10 ns current pulse through the stripline, providing a pulsed Oersted field at the sample for excitation in the x-direction parallel to the scattering plane. The sample holder provides SMA type contacts to connect the stripline, and a pair of coils for a static bias field H_b to align the magnetization in y-direction parallel to the stripline and perpendicular to the scattering plane. With circularly polarized light, the horizontal or x-component of the magnetization is detected under $\sim 7°$ incidence. All data

are normalized to the quasi-static situation without a field pulse applied, to correct for background oscillations and the ring decay.

Figure 2 shows resulting data as measured at the Fe edge. In the upper graph the bias field is kept constant at 11.5 Oe, and the pulser output is varied from 10 V to 2.5 V, leading to a varying amplitude of H_p. The overall step in the data arises from the 10 ns current pulse, and the step height represents the new equilibrium direction for the magnetization, given by the superposition of internal fields, bias field and pulsed field. For smaller H_p we expect a smaller step height, a behaviour clearly shown by our data. The lower part of figure 2 shows the effect for different bias fields. Again, the decrease in step height is expected for higher bias fields, as the effective field direction comes closer to being perpendicular to the scattering plane. At the same time we observe an increase in frequency for higher bias fields. This is expected according to the Landau-Lifshitz-Gilbert equation, as the frequency is increasing with larger effective field. The sample geometry, field direction and helicity were observed to have no effect on the detected oscillations.
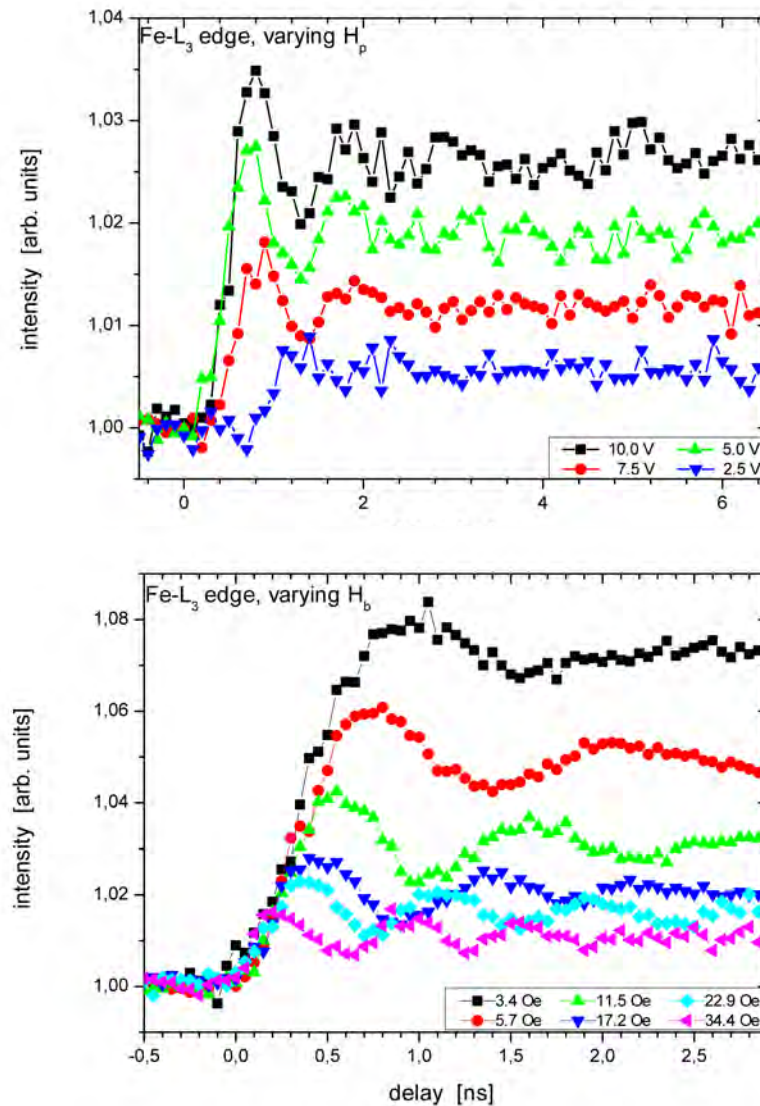
Fig. 2: The upper graph shows the signal for different pulse amplitudes and a bias field of 11.5 Oe. For the lower graph the amplitude is maximal, and the bias field is varied. In both cases the expected behaviour of the step height upon the current pulse is observed.

Finally, in figure 3 we compare the data for Fe and Ni precession at different bias fields, where Ni and Fe are plotted with different scales on the left and right side of each graph, respectively, to match in final step hight. All four graphs are chosen to have the same scaling. It is clearly seen that the oscillations are in phase with the given resolution, a result observed previously by Bailey et.al. [3]. A detailed analysis of the data is still in progress, and a careful comparison with simulations will be carried out.
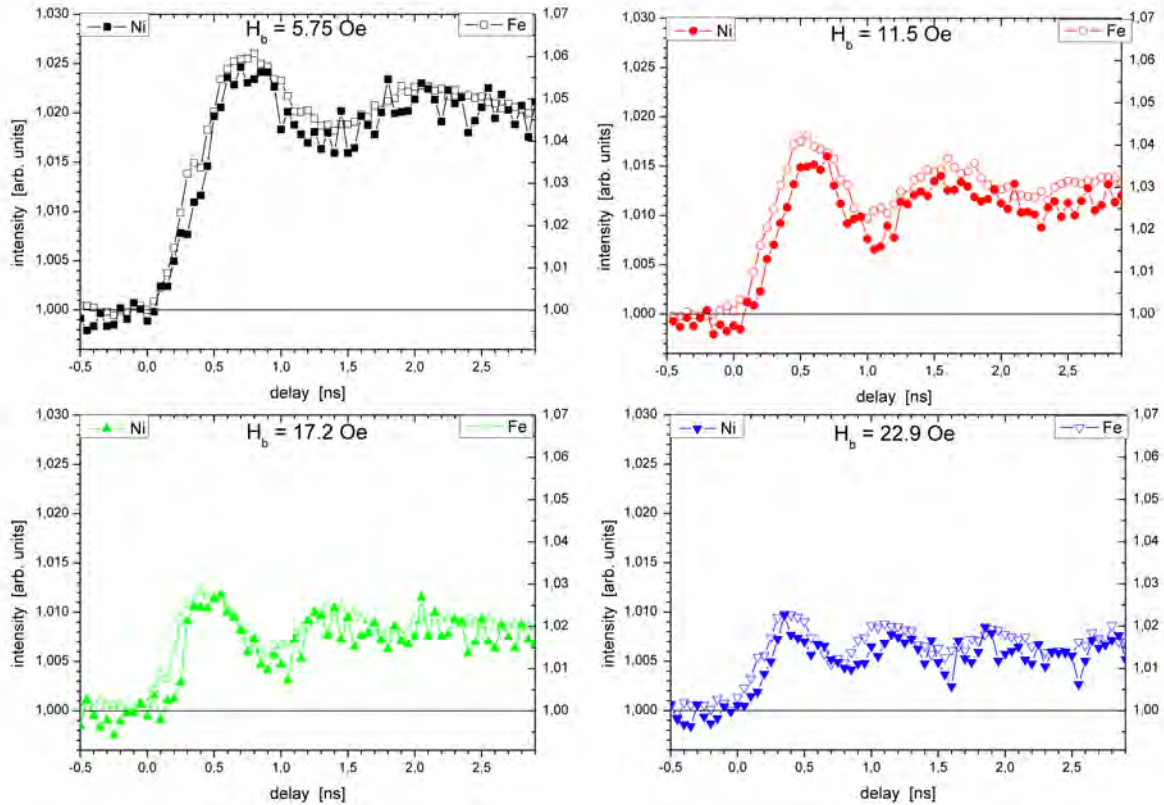
Fig. 3: The graphs show the Ni and Fe signals for four different bias fields. The Fe and Ni axes are adjusted to match, but are chosen the same for all four graphs. The signals clearly oscillate in phase.

References

[1] J. Grabis, A. Nefedov, and H.Zabel, *Rev. Sci. Inst.* **74**, 4048 (2003)

[2] A. Neudert, J. McCord, D.Chumakov, R. Schäfer, and L. Schultz, *Phys. Rev. B* **71**, 134405 (2005)

[3] W. Bailey, L. Cheng, D. Keavney, C.-C. Kao, E. Vescovo, and D. Arena, *Phys. Rev. B* **70**, 172403 (2004)

NEXAFS characterization of the self-limiting monolayer growth of terephtalic acid on rutile TiO$_2$ (110)

A. Nefedov, M. Naboka, Ch. Wöll

Physikalische Chemie I, Ruhr -Universität Bochum, Universitätstr. 150, 44801 Bochum

Chemically functionalized surfaces play an important role in many nanotechnological applications. However, not too many attempts have been made so far to create a chemically functionalized metal oxide surface by adsorption of organic molecules, even though metal oxide surfaces provide anisotropy and special adsorption sites that lead to well-ordered monolayers. Terephthalic acid [C$_6$H$_4$(COOH)$_2$, TPA] is a versatile molecular linker and has, consequently, received considerable attention in designing of three-dimensional self-assembled porous frameworks stabilized by metal-carboxylate bonds [1], as well as in two-dimensional supramolecular architectures at surfaces [2,3,4]. In particular, TPA/TiO$_2$ (110)(1×1) is a promising system to create an overlayer of upright oriented molecules terminated with carboxyl groups. This kind of chemical functionalization could have wide-ranging applications, similar to those of carboxyl-terminated SAMs [5].

For the NEXAFS experiment the TiO$_2$ crystal was introduced into the UHV system with a base pressure better than 10^{-9} mbar attached to the HE-SGM beamline. Sample cleaning was performed by cycles of argon ion sputtering (P$_{Ar}$ ~ 1 × 10^{-4} mbar, E = 800 V, T = 300 K, I=1μA) and annealing at 600 K in vacuum. The deposition rate was measured with a Quartz crystal microbalance and was adjusted to 0.07 Å/sec by heating the crucible to 445 K. The distance between the crucible and the TiO$_2$ crystal was about 20 mm.

In order to determine the dependence of monolayer coverage on deposition time we deposited the TPA molecule in several steps, each lasting 5 – 15 s. After each deposition step the sample was transferred from the preparation chamber to the main chamber and the measurement of the NEXAFS spectra for the C K- edge as well as a long spectra including the C K, Ti $L_{2,3}$ and O K adsorption edges were performed. By measuring such spectra it is possible to monitor the growth of the film thickness taking into account that the jump at the C K adsorption edge, i.e. the difference of intensities measured before (E=278 eV) and after (E=340 eV) the edge, is proportional to the amount of carbon atoms. At the same time the signal measured around Ti $L_{2,3}$ absorption edges (E=420 eV and E= 480 eV, correspondingly) remains the same and therefore can be used for normalization. In Fig. 1 we present the dependence of the ratio of the C/Ti signals on deposition time. We can clearly observe a saturation after about 70 sec of deposition at 455 K, which we assign to 1 ML of TPA. Based on the saturation behavior we can also conclude that a second layer of TPA cannot be grown or, at least, is very unstable.
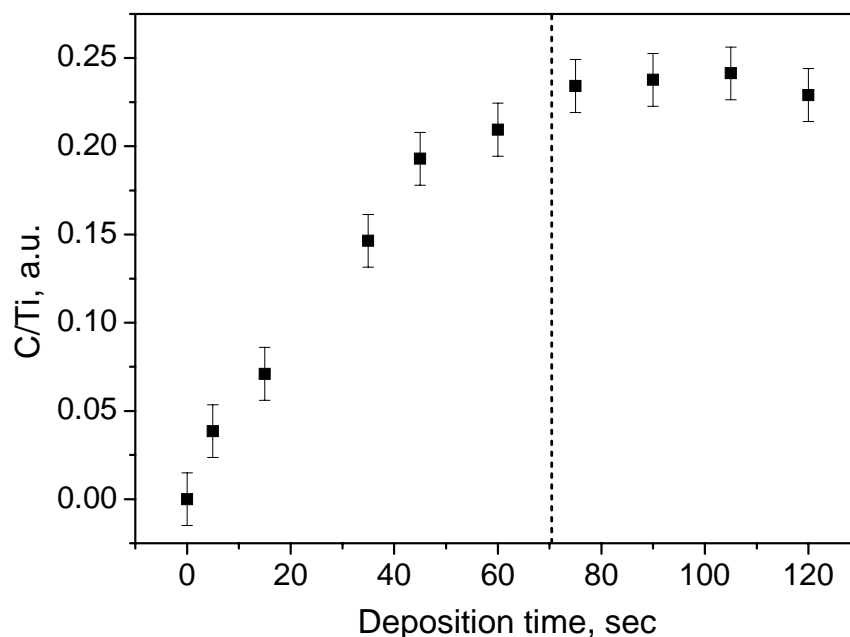
Fig. 1 : C/Ti ratio dependence on deposition time. The dashed line correspond to the deposition time of 1 ML.

For a precise determination of the orientation of the TPA molecule the measurements in case of the lowest (0.03 – 0.07) and the highest (1ML) coverages were carried out at $\theta = 20°$, $30°$, $55°$, $70°$ and $90°$ and at different azimuthal orientation of the TiO_2 crystal with azimuthal angles $\varphi = 0°$ and $90°$, with respect to the [001] direction of the (110) surface.

Figure 2 (a) (left panel) shows a series of carbon K-edge NEXAFS spectra taken on TiO_2 (110) covered with 0.07 ML of TPA molecule corresponding to a deposition time of 5 sec at 445 K. The set of spectra shows a clear dependence of the peak intensities on the incident angle θ. In particular, the pronounced dichroism of the peaks at E = 284.9 eV and 285.5 eV, which are related to the phenyl ring, and the peak at E = 288.3 in Fig. 2 (b) (left panel), which is connected to the carbonyl groups, indicates almost flat lying molecules. The NEXAFS spectra of the 1 ML sample Fig. 2 (right panel) present features similar to these observed for the 0.07 ML sample in Fig. 2 (left panel), but the angular dependence of the peak intensities is opposite. A difference signal for $\pi*$ resonance becomes positive (Fig. 2, right panel, (b)) and thus provides a clear evidence for an upright orientation of TPA molecule on TiO_2 (110).

In conclusion, the absorption of TPA on rutile TiO_2 (110) was investigated by means of near-edge x-ray absorption fine structure spectroscopy (NEXAFS) under ultrahigh vacuum conditions in a range from very low coverages to saturation corresponding to 1 monolayer (ML). We found flat – lying TPA molecules at low coverages (up to ~0.3 ML), while when saturation coverage is achieved TPA molecules adsorb in a upright position.
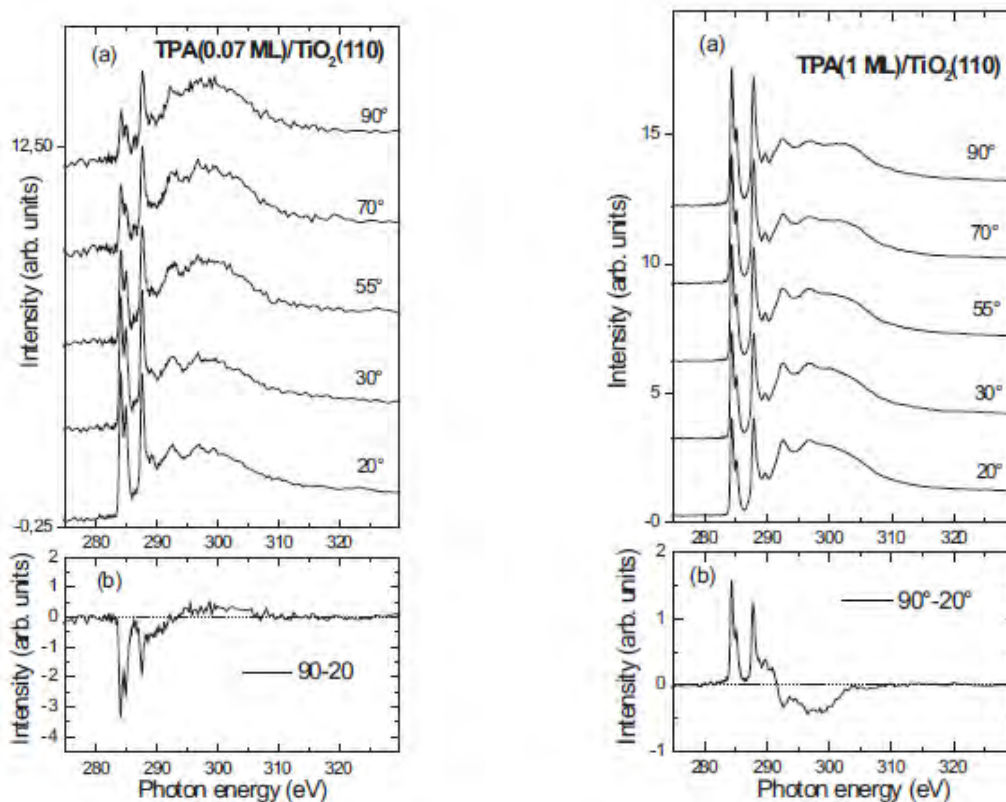
Fig 2: (a) NEXAFS spectra for the 0.07 ML (left panel) and 1 ML of TPA (right panel) measured at different photon incidence angles. (b) Difference of the spectra measured at θ = 90° and θ = 20° .

[1] O. M. Yaghi, M. O'Keeffe, N. W. Ockwig, H. K. Chae, M. Eddaoudi, and J. Kim, Nature, **423**, 705, 2003.

[2] S. Stepanow, T. Strunskus, M. Lingenfelder, A. Dmitriev, H. Spillmann, N. Lin, J. V. Barth, C. Wöll, and K. Kern, J. Chem. Phys. B, **108**, 19392, 2004.

[3] J. V. Barth, G. Costantini, and K. Kern, Nature, **437**, 671, 2005.

[4] M. E. Cañas-Ventura, F. Klappenberger, S. Clair, S. Pons, K. Kern, H. Brune, T. Strunskus, C. Wöll, R. Fasel, and J. V. Barth, J. Chem. Phys, **125**, 184710, 2006.

[5] J. C. Love, L. A. Estroff, J. K. Kriebel, R. G. Nuzzo, and G. M. Whitesides, Chemical Reviews, **105**, 1103, 2005

The induction of ordering effects in 3D colloidal layers on structured substrates

Th. Geue[1], P. Huber[1], W. Leitenberger[2] and M. Textor[3]
1 Laboratory for Neutron Scattering, ETH Zurich & PSI, CH-5232 Villigen PSI, Switzerland
2 Institute of Physics, University of Potsdam, D-14415 Potsdam, Germany
3 Materials Science Dept., ETH Zurich, CH-8093 Zurich, Switzerland.

Ordered colloidal assemblies are three-dimensional periodic structures formed from small polystyrene spheres suspended in solution. These assemblies attract considerable attention when used as optical filters, switches and materials with photonic band gaps.

Unfortunately, a broad application of ordered colloidal assemblies is greatly restricted by numerous difficulties in the formation of large area ordered crystalline assemblies with uniform crystal orientation. We present an approach using a holographically manufactured template (surface relief grating – SRG) made from a photopolymer which is pre-structured. The aim of these templates is to allow the growing of ordered colloidal assemblies by slow sedimentation to direct the crystallization of colloids towards bulky crystals and to allow a tailoring of the final lattice structure, orientation and size of the final colloidal assemblies. The understanding of the sedimentation process is hereby of great importance.

To fully monitor the crystallization process in 3 dimensions, energy dispersive X-ray reflectometry was used to describe the phenomena taking place on the formation of colloidal layering. X-ray techniques are rarely used to investigate the formation of ordered colloidal assemblies so far [1-2].

The surface relief grating has been fabricated by exposing a pdr1m-thin film to an interference pattern of a green laser [3] Polystyrene Colloids from (Microparticles GmbH, Berlin) with a polydispersity index of 0.03 have been used. For homogeneity reasons a very small concentration of the colloids (about 0.01…0.06 %) was chosen. In order to guarantee stable conditions in temperature and humidity the sedimentation process was performed in a spatially limited, closed volume of 104 cm^3. Because of the small cell volume the deposition process takes place close to the thermodynamic equilibrium between solid phase and colloidal droplet. The sedimentation velocity of spherical particles is estimated to be in the order of v = 20µm/h. Therefore several hours of stable experimental conditions are needed to follow the deposition process.

In the displayed results, an incident angle α_I of 0.3° and exit angles α_F ranging from 0.36° (top) to 0.38° (down) have been used resulting in a slightly off-specular measurement position. The intensity is scaled individually for each plot. The individual graphs show the evolution of normalized energy dispersive scattering signal as a topologically structured surface grating is turned around its surface normal. The change in the effective grating periodicity seen by the x-ray beam leads to the change in the peak positions marked with black lines. The graphs show the scattering before (right) and after (left) the evaporation of a droplet of colloidal dispersion on top of the grating. The grating periodicity of the substrate (680nm) had thereby been chosen to match the lattice constant of a close packed arrangement of colloidal particles with a diameter of 760nm. The main change in the scattering signal after the droplet evaporation is a broadening of the peaks and an equalization of the peak intensities. A more detailed analysis is underway.

Scattering from covered and bare pdr1m Surface Gratings

covered

uncovered
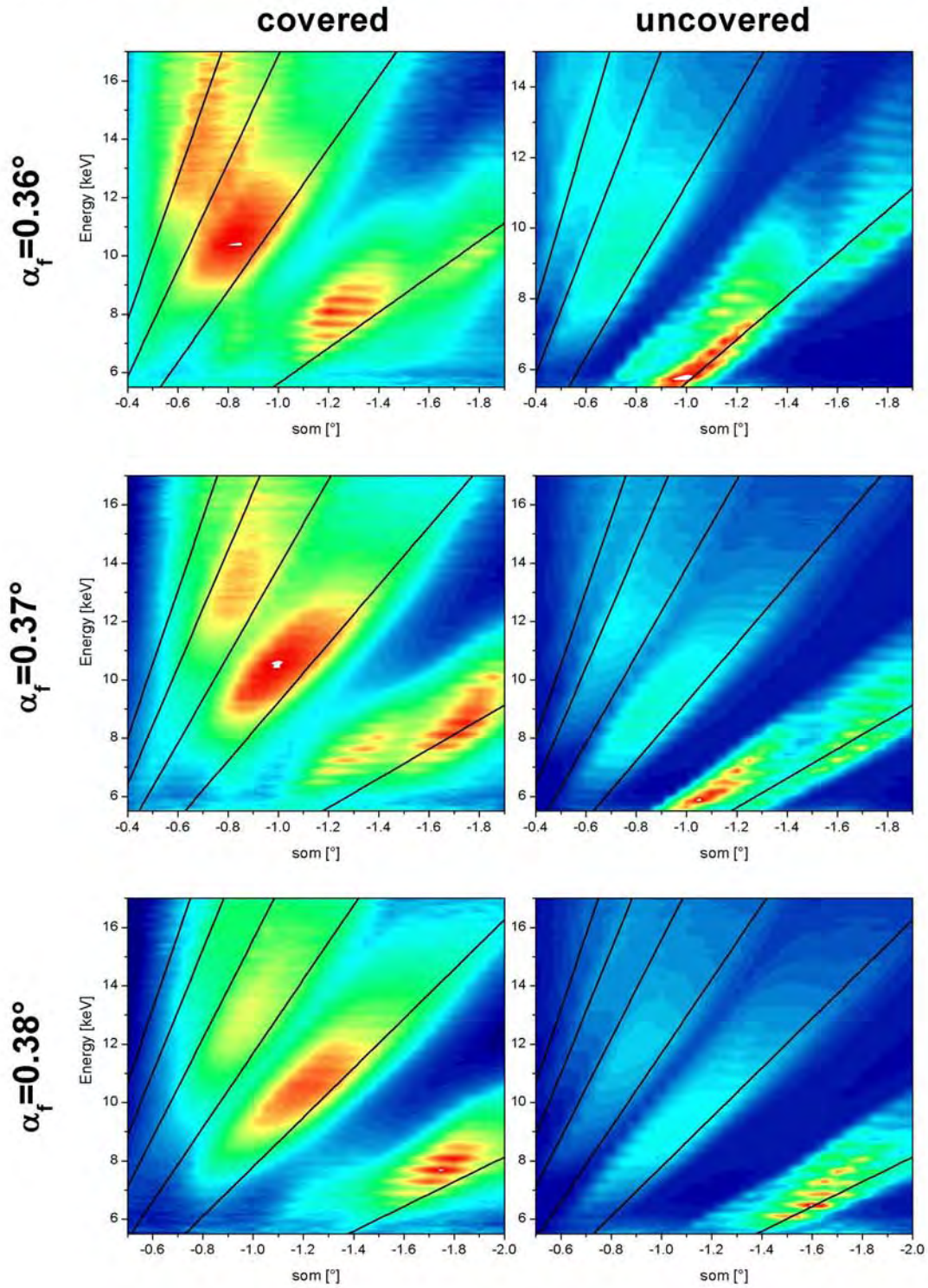
[1] Narayanan, S., Wang, J., Lin, X.-M. *Phys. Rev. Lett.*, 93, 135503 (2004)

[2] Reinhold B., Geue T., Huber, P., Sant T., Pietsch U., Sztucki M. , *Langmuir* 2009 accepted

[3] P. Rochon, E. Batalla, A. Natansohn, Applied Physics Letters 66 (1995) 136

Feasibiliy study of using a radial infrared furnace at the SoLiAS-system

S. Hümann, D. Vogel, F. Renner, M. Stratmann, M. Rohwerder
Max-Planck-Institut für Eisenforschung GmbH - 40237 Düsseldorf
T. Mayer, W. Jaegermann
Technische Universität Darmstadt - Petersenstr. 23 - 64287 Darmstadt
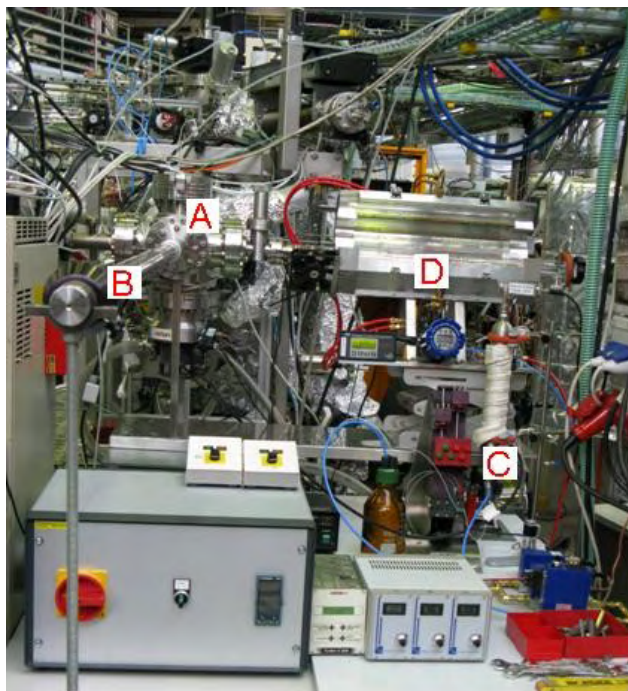
Figure 2.1: Experimental setup for short term annealing experiments connected to the SoLiAS-system.

One of the great advantages of the synchrotron XPS is the high brilliance of the applied x-ray beam especially at lower energies. This enables experiments at low kinetic energies, thereby varying the information depth of the resulting XPS-spectra. To investigate the segregation behavior of alloying metals within steels, such as aluminium, silicon, manganese etc. some of the model alloys have been investigated in detail at the SoLiAS-station (BESSY II in Berlin). In Figure 2.1 the experimental setup for the short term annealing experiments, which have been added to the SoLiAS-station, can be seen. One can see the transfer-chamber (A), the transfer tubes (B), the gas- and water-supply (C) and the quartz reaction tube within the radial infrared-furnace (D). The aim of this experiment was to do the annealing experiments under the same conditions as in the high-temperature lab at MPIE with the possibilities of a contemporary surface analysis by means of synchrotron x-ray photoemission spectroscopy (SXPS). One great advantage of the direct connection of the short term annealing setup to an UHV-system is the possibility to transfer samples without any further oxygen contamination.

Figure 2.2: Manipulator and sample holder for SXPS-experiments at BESSY II.

Figure 2.2 shows the sample holder and the manipulator which was used for the SXPS experiments at BESSY II. The transfer of the iron samples is realized by means of an omicron-sample holder (sample plate). To avoid any pollution the reaction chamber was completely built out of quartz glass. For the connection of the reaction chamber to the SoLiAS-station CF-flanges were used to guarantee to have gas leakages.

Figure 2.3 shows one set of high resolution survey SXPS-spectra of to different silicon containing model alloys at a kinetic energy of 1150 eV. Before starting the SXPS measurements all samples have been sputtered to clean up the surface.

The Fe2p-emission can be seen at 710 eV, the corresponding Auger-emission of Fe can be found at binding energies between 400 and 600 eV. Due to the fact that all model alloys have been sputtered with argon in the UHV-chamber to get a clean surface no carbon (C1s ~ 286 eV) and also no oxygen (O1s ~ 530 eV) could be found.

Additionally at lower binding energies the Si2p emission at 92.3 eV and the Fe3p emission at 54.4 eV can be found. Especially these emissions at low binding energy values can be investigated with SXPS due to the brilliant energy dispersion.

Another advantage while using synchrotron radiation as the x-ray source is the possibility to choose a certain kinetic energy and thereby varying the information depth of the data. A detailed analysis of the survey spectra of the sample holder, stainless steel, shows only a very small Fe2p signal at 710 eV BE. But in contrast to the sputtered model alloys a large amount of oxygen (O1s-emission) and carbon (C1s-emission) can be seen easily at 532 eV and 287 eV, respectively.
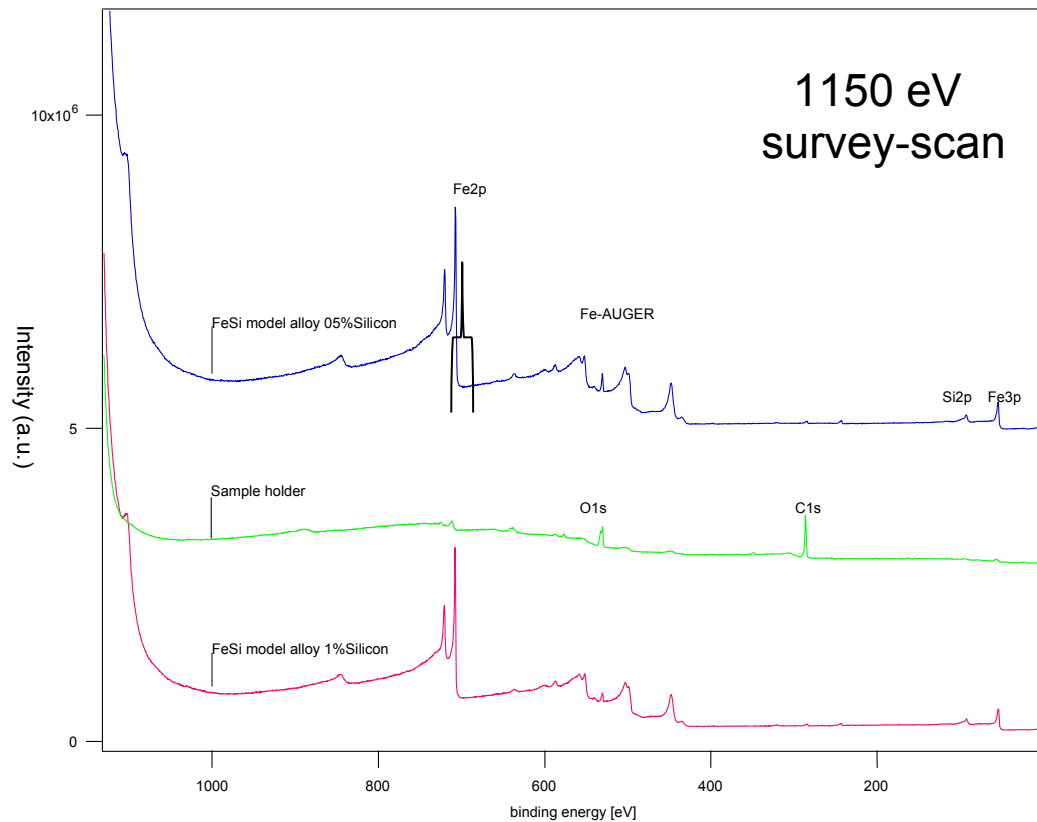
Figure 2.3: Sputtered model alloys. SXPS-survey spectra of the sample holder and silicon containing model alloys at a kinetic energy of 1150 eV.

The SXPS-spectra which are shown in figure 2.4 were obtained after an annealing procedure at at DP (dew point) of -44.4°C. Figure 2.4 shows (a) the spectra of the Fermi-edge and the O2s emission, respectively. The figures 2.4b and 2.4.c compare show the Fe2p and Fe3p PES-emissions.

The analysis of the PES-spectra in figure 2.4a reveals the following. All model alloys show a sharp Fermi-edge at 0 eV BE. Additionally 4 different PES-emissions can be detected in the range between 0 and 40 eV BE. The PES-emission at 30.8 eV (A) is due to a pollution effect by means of sodium. The PES-spectra at 22 eV (b) and 17.3 eV (c) can be assigned to an O2s-emission. A detailed look at the spectra shows a higher amount of surface oxygen in the case of a aluminum containing model alloy. A close look to the Fe 2p- and Fe3p-emmisions (Figs. 2.4b and 2.4c) shows one of the great advantages of SXPS. Due to the fact that the kinetic energy is not fixed the operator is able to get spectra with different information depts. This can be seen here in a very impressive way. The spectra of the Fe2p-emission in Fig. 2.4b consist clearly of a least 2 iron species. The first Fe2p-emission at 708.3 eV BE (A) can be assigned to the PES-emission of pure iron, the second one at 710.3 eV BE (B) results from oxidized iron. In contrast to the Fe2p-emission (Fig. 2.4.b) the Fe3p-emission (Fig. 2.4.c) does not show any signal of pure Iron. This is due to the fact, that the corresponding PES-spectra were recorded with a kinetic energy of 230 eV, which enables a real surface sensitive measurement.
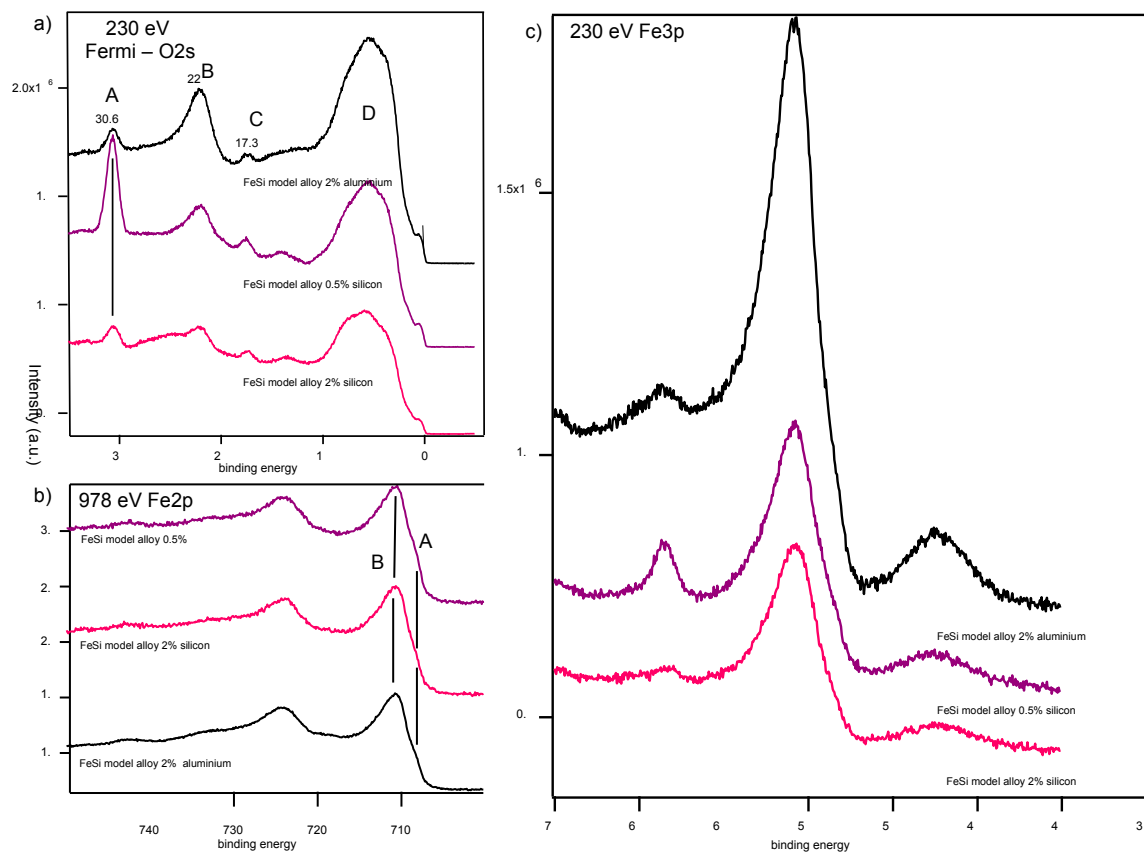
Figure 2.4: Model alloys annealed at DP -44.5°C. SXPS-spetra of a) Fermi edge at 230 eV; b) Fe2p at 978 eV; c) Fe3p at 230 eV.

Results

This short overview of the XPS-data shows that it is possible to install the radial infrared furnace with its gas dosing system directly to a high preformance SXPS-system such as the SoLiAS-system at BESSY II.

This allows to combine the great advantages of SXPS (possibility to preform experiments with different depth information for the same photoelectron emission, e.g. Fe3p, O1s, Fe2p, etc. as a function of the applied kinetic energy) with the advantages of the infrared furnaces (very high heating and colling rates, defined gas atmospheres).

Interestingly the amount of the alloying metal in the model alloys (here silicon and aluminium) has a very strong non-linear influence on the segregation behavior (compare 0.5 % Al with 1 % Al content). After the dry annealing cycles dramatic changes concerning the SXPS-signal intensities (Al2p and Si2p) can be obtained. In these cases an enrichment of the alloying metal on the surface can be observed.

Intermixing of Pt capping and Ni/Cu multilayers

S. Granroth[*], R. Knut, S. Svensson, G. Andersson, M. Marcellini, O. Karis
Dept. of Physics, Box 530, SE-751 21 Uppsala, Sweden

M. Gorgoi, F. Schäfers, W. Braun, and W. Eberhardt
BESSY Gmbh, Berlin, Germany

High Kinetic Energy Photoelectron Spectroscopy (HIKE) has been used to observe interface roughening and alloying in multilayers. First results of Ni/Cu multilayers [1] measured at the KMC-1 beamline convincingly demonstrated that HIKE is an excellent tool to investigate the alloying process as a function of temperature. Here we present an extended study where the aim has been to obtain more data to investigate more carefully the intermixing of the multilayer compounds and the capping material [2]. In addition, we wanted to explore the role of Cu segregation the binding energy shifts.

Multilayer samples were grown on MgO (001) by UHV-based dc magnetron sputtering and composed of a Fe/Pt/Cu buffer layer and repeated Ni_5Cu_5 bilayer units where the subscripts refer to the thickness of the Cu and Ni layers in monolayers. Samples were protected by a Pt or Ni cap. Multilayers were heated to temperatures between 20 and 530 ℃ and then subsequently cooled to room temperature at which point the spectra were measured. The photoemission spectra were taken at the HIKE end-station at KMC-1 using 2010 eV and 6030 eV photon energies at normal photoelectron emission. The overall resolution at these photon energies was determined to be 0.26 eV and below 0.4 eV, respectively.

The Cu $2p$ spectra of Pt capped sample shifted about 0.45 eV towards lower binding energy (Fig. 1). The most dramatic changes take place above 200 ℃ with a rapid evolvement of both line profile and chemical shift between 200 and 250 ℃. No significant shift was observed in Ni $2p$ core-level spectra of the same sample.
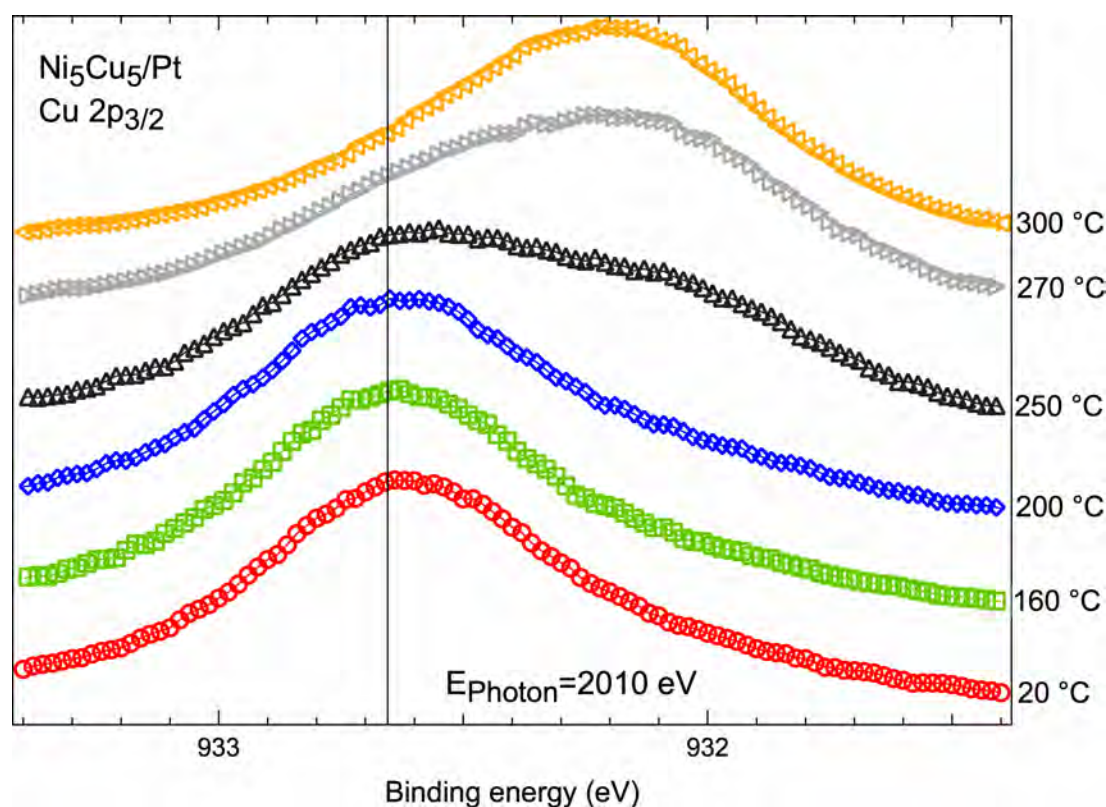
Fig. 1. *Cu $2p_{3/2}$ spectra of Pt capped Ni_5Cu_5 as a function of temperature. The black line at 932,65 eV marks the binding energy of bulk Cu $2p_{3/2}$ (100 ML Cu).*

The obvious way to confirm that the observed distinctly different behaviour compared to our previous study could be attributed to the formation of a ternary Pt-Ni-Cu alloy was to repeat the experiments with a sample without a Pt cap. We chose to study a Ni_5Cu_5 sample where Pt capping layer was replaced by 2 nm thick Ni(100) layer that was gently sputtered until all signs of NiO was removed in the spectra. The resulting Cu $2p_{3/2}$ spectra, which were measured with 2010 eV photon energy, are presented in Fig. 2. The binding energy shift of Cu $2p$ is still negative but has decreased considerably being maximum -0.1 eV at temperatures between 320 and 400 ºC. At this time more obvious changes were also observed in Ni $2p_{3/2}$ spectra which shifted towards lower binding energy reaching -0.2 eV shift at higher temperatures.
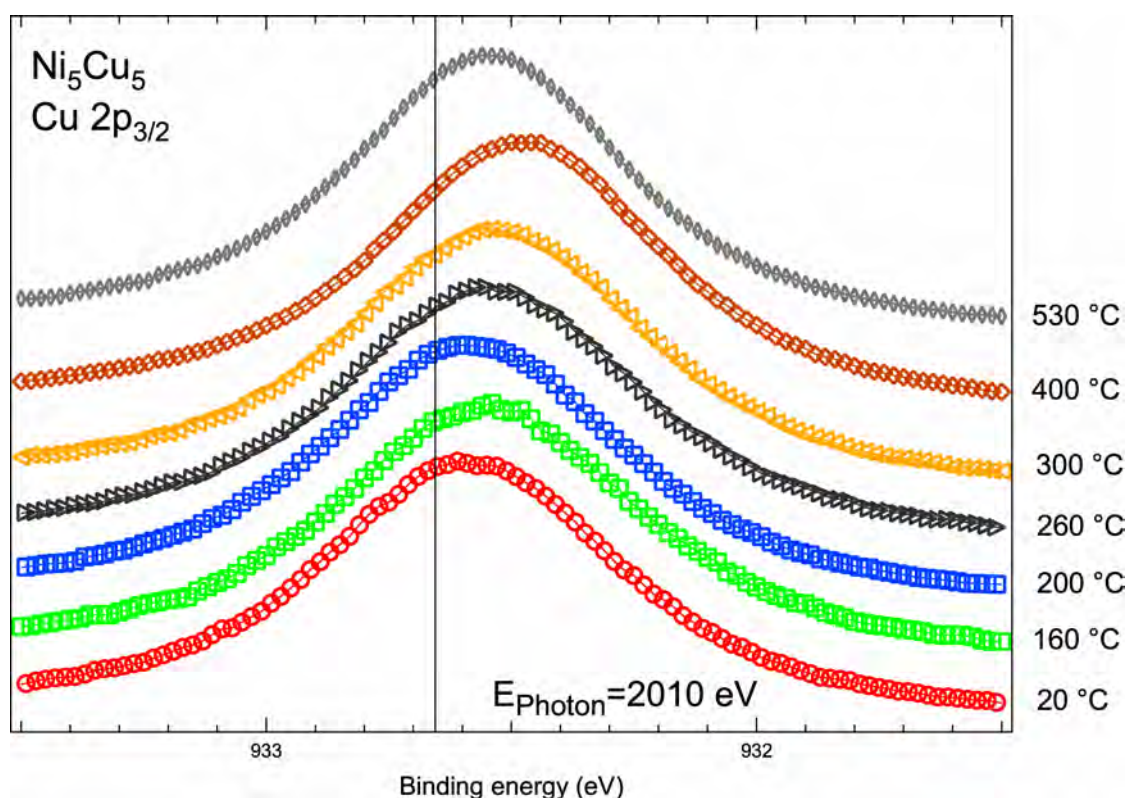
Fig. 2. *Cu $2p_{3/2}$ spectra of uncapped Ni_5Cu_5 as a function of temperature.*

The sizable shift (almost -0.5 eV) of Cu $2p$ core-level for the Pt capped sample is much larger than the corresponding shift for the uncapped sample. This difference suggests that we are studying a ternary alloy instead of a binary Ni-Cu alloy in the case of the Pt capped sample. This conclusion was further confirmed by comparing the core-level intensities of Cu $2p$ and Ni $2p$ relative to the intensity of Pt $4f$ as a function temperature. Reported core level shifts of Cu $2p$ and Ni $2p$ in $Pt_{1-x}Cu_x$ and $Ni_{1-x}Pt_x$ alloys support the conclusion as well.

In Fig. 2 it can be seen that the Cu $2p$ spectrum measured at 530 ºC has slightly shifted backwards because of incipient Cu segregation, which is known to be very pronounced in the uppermost atom layers. To study the formation of the Ni-Cu alloy where the effect of segregation of Cu is not contributing to the binding energy shift, we measured Cu $2p$ spectra using 6030 eV photon energy. Then the Cu $2p$ shift were -0.2 eV in accordance with reported binding energy shifts in $Ni_{1-x}Cu_x$ alloys.

[*] Also at *Department of Physics, FIN-20014 University of Turku, Finland*
[1] E. Holmström et al., *Phys. Rev. Lett.* **97** (2006) 266106.
[2] S. Granroth, R. Knut, M. Marcellini, G. Andersson, S. Svensson, O. Karis, M.Gorgoi, F. Shäfers, W. Braun, W. Eberhardt, in manuscript.

Probing synchrotron radiation induced local surface potential modifications on the semiconductor p-WSe$_2$:Rb using PEEM

Jens Buck*, Dirk Rahn*, Erik Kröger*, Florian Kronast†,
Hermann Dürr†, Kai Rossnagel*, Lutz Kipp*
* Christian-Albrechts-Universität zu Kiel, † BESSY

Introduction

Tungsten diselenide belongs to the class of transition metal dichalcogenides and – like all of the compounds out of this class – has a layered structure with hexagonal symmetry. It is known to be a semiconductor with an indirect band gap of approximately 1.2 eV [1]. Therefore, it has been considered as substrate for novel solar cells, and remarkable quantum efficiencies could be achieved under laboratory conditions in the past [2]. Excellent carrier mobilities were reported for this material [3]. Besides possible applications, both the bulk and the surface of WSe$_2$ are also interesting subjects to basic research, because they show a variety of exotic effects, among them a strongly anisotropic electrical conductivity [4] due to the basically two-dimensional structure, an abnormal low thermal conductivity [5], or structure creation processes such as nanowire network formation [6]. The motivation of this work is to gain better insight into the behavior of the Rb-covered surface of WSe$_2$ at variable carrier injection rate.

Experiment

The surface potential of a semiconductor at constant illumination can be well understood in terms of a one-dimensional model [7] with an unstructured surface, if lateral inhomogenities can be neglected. The aim of the experiment was to probe an imperfect surface with spatial and chemical resolution. Furthermore, simultaneous access to the local surface potential of the sample is crucial. A photoemission electron microscope (PEEM) with synchrotron source – such as the Elmitec PEEM III at beamline UE49/PGMa at BESSY - is best suited for this purpose.

WSe$_2$, among other layered crystals is said to be difficult to prepare for microscopy experiments with the standard cleaving technique, because small flakes are likely to remain on the surface. These problems could be overcome and – to our knowledge – this is the first time a layered crystal was prepared successfully to withstand the high voltage in an electron microscope.

The clean sample surface shows no features,
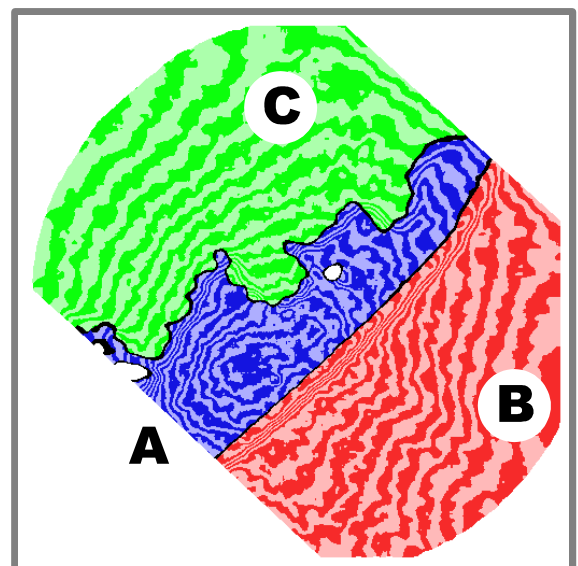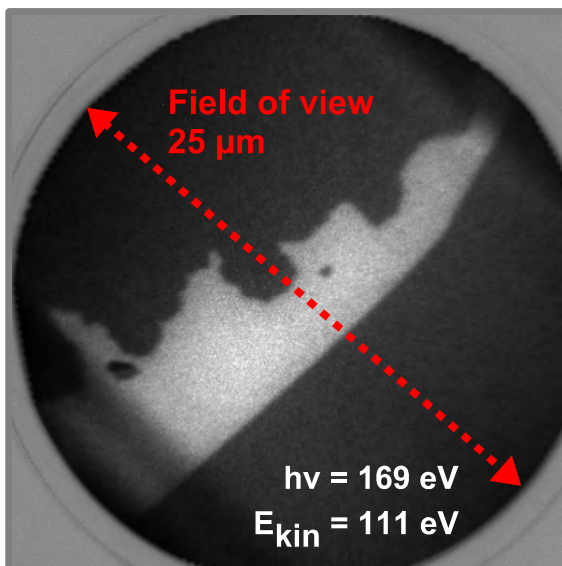
Figure 1 (left): *Raw PEEM image (Se 3d photoemission intensity) showing texturing of the WSe$_2$:Rb surface.*

Figure 2 (right): *3 regions, subdivided into bins of constant total intensity each, give flux - dependent information.*
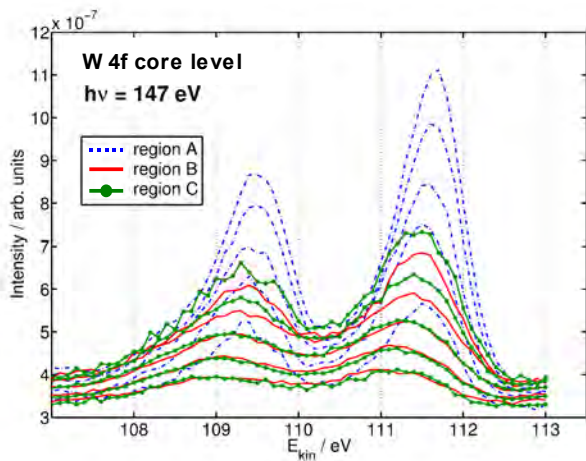
Figure 3 (left): *The peak positions of the W 4f core levels are used to probe the surface potential.*
Figure 4 (right): *Surface photovoltage effect on regions A to C.*
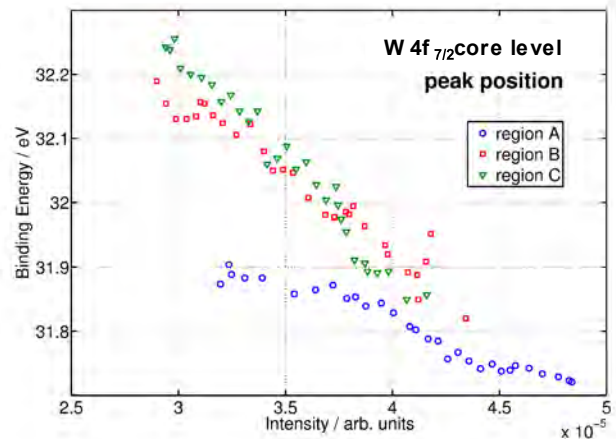
except for some step edges. After deposition of Rb, the surface is segmented into high-contrast regions of up to several 100 μm length and an irregular shape (fig.1). These regions clearly differ in the spectral features of the substrate, although XPS shows only small or even no differences in Rb concentration. Spectral details of the texture are not subject of this report and will be discussed elsewhere. The rather discrete contrast gives rise to the assumption of two distinct types of the surface, into which the spatial resolved spectrosopic data was binned in the following.

To study charging effects of the sample surface, the position of the W 4f substrate peak can be used to probe the surface potential. The injection rate of charge carriers is given by the local incident photon flux per unit area and is therefore proportional to the measured intensity. By subdividing the regions into sections with approximately constant intensity, several "intensity channels" can be detected in parallel. The resulting regions of interest are shown in figure 2. The channels obtained by this method are of course potentially interacting by lateral diffusion of carriers, but this influence is assumed to be rather small, because the carrier dynamics is expected to be much slower than the timing of the synchrotron light.

voltage can be ruled out by the sign of the shift. Therefore, the effect must be explained in terms of a surface photovoltage [7]. Earlier experiments revealed band bending towards higher binding energy on the surface of p-WSe2 upon Rb deposition. Injection of charge carriers will decrease the involved surface potential and thus give a shift to lower binding energy in this case. The lower magnitude of the effect in region A suggests a lower surface potential when no carriers are injected (compared to regions B and C). This can only be explained by a smaller charge transfer per unit area from the adsorbate to the substrate, even though XPS data shows a nearly constant Rb concentration all over the surface. Therefore, we conclude that the surface is not chemically homogeneous and is presumably covered locally by unbound surface atoms, e.g. self-intercalated tungsten or selenium.

Especially tungsten diselenide has a very high lateral electrical conductivity compared to the perpendicular direction. This fact and the observed lateral inhomogeneity make a true three-dimensional theoretical treatment of the surface photovoltage necessary. In conjuction with spectroscopic data acquired in the same beamtime, the influence of adsorbates on surface carrier dynamics can be studied in detail.

Results and Discussion

On the clean surface, there is no significant change of the peak position as the photon flux increases. On the Rb covered surface, all regions clearly show a shift towards lower binding energy at higher photon flux (figs. 3, 4), with the magnitude of this effect depending on the type of region. Charging due the ohmic resistance of the sample or a photodiffusion

References

[1] Traving *et al.*, Phys. Rev. B **55**, 10392(1997).
[2] Prasad *et al.*, J. Phys. D **21**, 1028(1988)
[3] Podzorov *et al.*, App. Phys. Lett. **84**(17), 3301 (2004)
[4] Hu *et al.*, J. Phys.: Cond. Mat. **17,** 3575(2005)
[5] Goodson *et al.*, Science **315**, 342(2007)
[6] Adelung *et al.*, App. Phys. Lett. **74**, 3053 (1999)
[7] Trares-Wrobel *et al.*, App. Phys. Lett. **74**, 1836 (1999)

Cobalt phthalocyanine on Au(001): calculations and electron spectroscopy measurements

V.Yu. Aristov[1,2], O.V. Molodtsova[1], V.V. Maslyuk[3], Y.A. Ossipyan[3], T. Bredow[4], I. Mertig[3], M. Knupfer[1]

1 IFW Dresden, D-01069 Dresden, Germany
2 Institute of Solid State Physics, Russian Academy of Sciences, Chernogolovka, Moscow distr., 142432, Russia
3 Martin-Luther-Universität at Halle-Wittenberg, Fachbereich Physik, Germany
4 Institute for Physical and Theoretical Chemistry, Bonn University, D-53115 Bonn, Germany

The molecular magnets are assumed as possible candidates for potential applications in high-density information storage and quantum computers, while molecular spintronics devices have attracted enormous attention [1, 2]. Nowadays transition magnetic metal phthalocyanine CoPc is considered as a material for development of low dimensional molecular magnet. Such important potential applications give a strong motivation to characterize and investigate the electronic structure and morphology of cobalt phthalocynine thin films.

In this work we have studied the electronic properties of CoPc molecules and CoPc thin films. The molecular film of about 7 nm was deposited on (001) surface of a gold single crystal in UHV conditions and was characterized by photoemission spectroscopies (PES): valence band (VB) and core-level. The PES experiments were performed at BESSY using the soft-x-ray synchrotron light emitted by the Russian- German high energy resolution dipole beam line. The experimental results were simulated and have been explained in the framework of density functional theory (DFT) calculations, which were performed for the single molecule by using the linear combination of atomic orbitals (LCAO) formalism based on density functional theory and realized in the CRYSTAL code [3].Other details of the sample preparation as well as of the experimental measurements can be found elsewhere (see e.g. [4]).
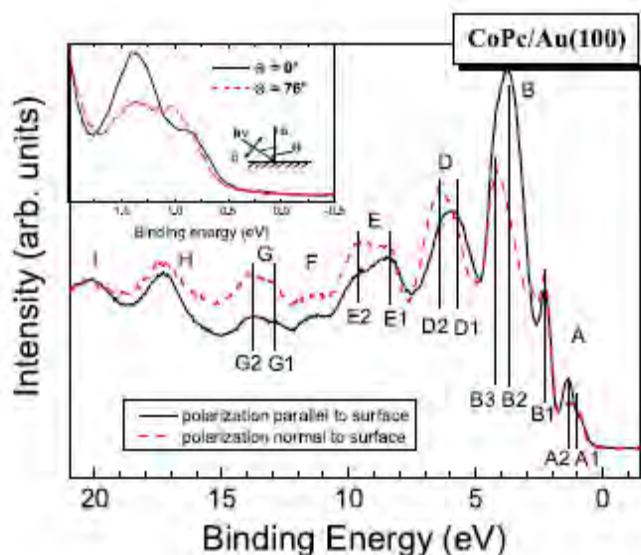
Fig. 1 shows the experimental VB photoemission spectra from CoPc thin films deposited on Au(001) and taken with a light polarization vector parallel (solid line) and normal (dash line) to the sample surface.

Fig. 1. VB PE spectra of CoPc thin film deposited on Au(001) taken with the **E** vector parallel (solid line) and normal (dashed line) to the sample surface (see inset).

As it was revealed from low energy electron diffraction and x-ray absorption investigations, the CoPc molecules are well ordered and positioned parallel to the Au(001) surface [5]. The states, which give contribution to the high BE side of each multi-component peak (G2, E2, D2 and B3) are more intense when the **E** vector is normal to the surface and probably stem from orbitals of π - symmetry. The states, which give contribution to the lower BE side of each multi-component peak (G1, E1, D1 and B2) are relatively more intense when the **E** vector is parallel to the surface and probably stem from orbitals of σ -symmetry. Peak B1 probably has both π and σ contributions. As far as the highest occupied molecular orbital (HOMO) is concerned,

subpeak A1 probably has contribution from π orbitals, while A2 stems from σ ones. This is more clearly seen in the top of valence band spectra presented in the inset of the Fig. 1 as a function of the polarization vector relative to the sample surface.
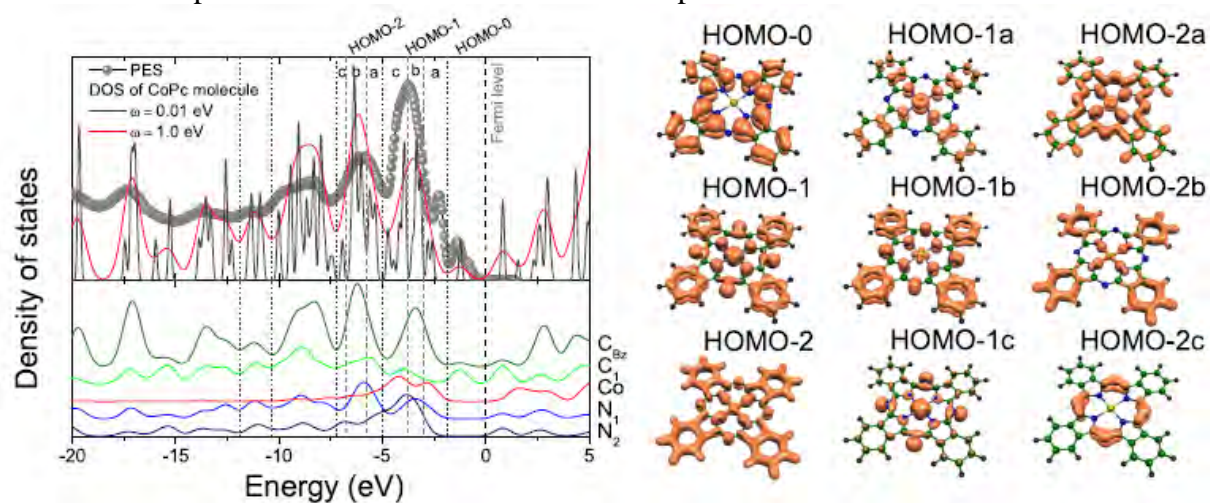
Fig. 2. Left upper panel, circles: PES of the VB of the CoPc film (normal emission, hν = 110 eV). Thick/thin line: calculated valence band spectrum of isolated CoPc molecules, after application of a Gaussian function to each calculated state with a FWHM=1.0/0.01 eV. The left lower panel presents the DOS projected onto various atomic species. Right panels: schematic presentation of the CoPc molecules and calculated charge distribution contributing to corresponding peaks of the valence band (see text).

In Fig. 2 one can see reasonable agreement between experiment and theory. All features of the experimental spectrum are reflected in the theoretical curve. For better understanding of the nature of the occupied states the isodensity surfaces for the HOMO-0, HOMO-1 and HOMO-2 features were plotted and shown in Fig. 2. The first feature (HOMO-0) includes π-states situated on both aromatic rings. The analysis of the projected DOS on the atomic species (Fig. 2, lower left panel) shows, that mostly the states from pyrolle carbon dominate here. We note that the present calculations do not reproduce the double peak near the Fermi level as seen in the photoemission spectra. This aspect has to be clarified in the future.

The second feature (labelled as HOMO-1) has contributions from π-states localized on benzene and hybrid Co-N states. The analysis of the molecular orbitals allows to separate the HOMO-1 region into three independent contributions. The first (HOMO-1a) has contributions from π-states localized on benzene and hybrid $Co(d_{xz},d_{yz})/N(p_{x/y})$ orbitals, where the dxz, dyz states are occupied for both spin-channels. Here, the density of the $N(p_{x/y})$ orbitals predominates over $Co(d_{xz}, d_{yz})$. The second part (HOMO-1b) consists of π-states with equally distributed density on benzene and on hybrid $Co(d_{xy})/N(p_{x/y})$ states which are occupied for the spin-down electrons. The spin-up $Co(d_{xy})/N(p_{x/y})$ orbital form the last part (HOMO-1c) of this series. Both spin components of the cobalt DOS are completely asymmetric. The spin-down states are shifted towards E_F in comparison with the spin-up states. The $Co(d_{xy})/N(p_{x/y})$, $Co(d_z^2)$ spin-up densities and $Co(d_{xz}, d_{yz})/N(p_{x/y})$, $Co(d_{x^2-y^2})$ states are related to the third group (HOMO-1c). The magnetic moment of the Co atom is 1.15 μ_B. Other atoms in the molecule are weakly polarized and a have negative magnetic moment up to 0.02 μ_B. The third feature (labelled as HOMO-2) consists of σ - states of benzene and pyrolle. The contribution of the d-orbitals of Co to this feature is small, and a separation into individual components is shown in Fig. 2 as HOMO-2a to HOMO-2c.

To obtain reliable experimental data in studies of the electronic structure of organic films one should be aware of the stability of the films exposed to irradiation by X-ray or electron beams. Therefore, we have performed additionally measurements of possible degradation of our samples. Fig. 3 depicts a series of LEED patterns, each taken from a 4 nm thick CoPc film

grown on Au(001) with the overall electron exposure time (going from Fig. 3a to Fig. 3f) amounting to 60 seconds. As can be clearly recognized from the Figure, the intensity of the diffraction spots from the CoPc film exposed to the electron beam typical for LEED measurements (~ 30 eV, 1 mA) decreases rapidly and almost vanishes. Thus, there is a very strong influence of the electron beam on the CoPc film.
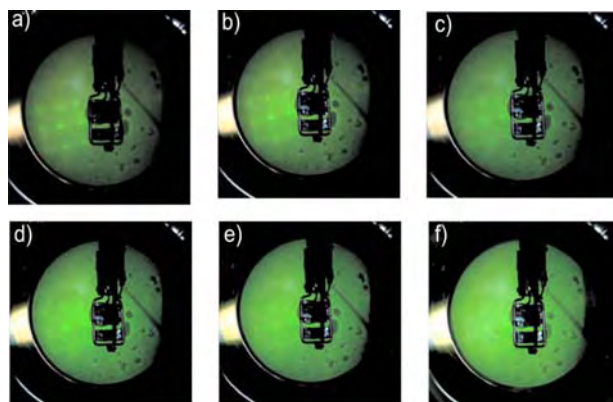
Fig. 3. A series of six ((a) – (f)) LEED patterns taken from a 4 nm thick CoPc film grown on Au(001) which demonstrates fading of the diffraction spots upon time (Ep = 28.3 eV).

Fig. 4. A series of N 1*s*, C 1*s* and Co 2*p* excitation spectra of a CoPc film grown on Au(001) as a function of exposure time to X-ray radiation typical for a bending magnet beamline at BESSY.
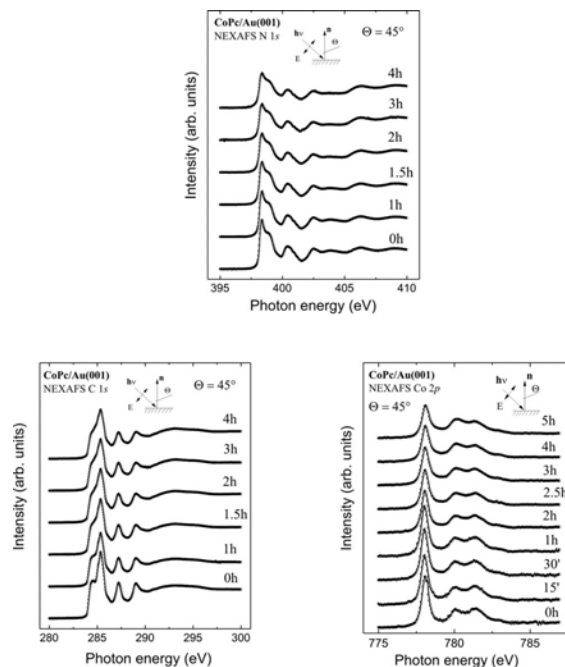
Unlike the previous case of damage by an electron beam we have found that the CoPc films are very resistant against X-ray irradiation at a bending magnet beamline. This is illustrated in Fig. 4, where a series of N 1*s*, C 1*s* and Co 2*p* excitation spectra from a CoPc film grown on Au(001) are shown as a function of exposure time typical for a bending magnet beamline at BESSY. It is clearly seen, that during the time typical for data acquisition (30 min, at most 1h) only small broadening of the characteristic features occurs. This observation proves, that CoPc films are much more stable with respect to exposure to X-ray radiation typical for NEXAFS or photoemission experiments if compared to irradiation by electron beams as used in LEED studies.

In summary, we have managed to associate the contributions of different atomic species as well as sites of the CoPc molecule to the electronic DOS, or in other words, we have achieved a qualitative assignment of different VB structures. A more thorough consideration of the VB features of materials, such as metal phthalocyanines, can be accomplished utilizing the cross-section dependence on the photon energy.

References

[1] S.A. Wolf et al. Science 294 (2001) 1488.

[2] R. Liu et al. Nano Lett. 5 (2006) 258.

[3] V.R. Saunders et al. (2003) CRYSTAL2003 User's Manual, (University of Turin, Turin).

[4] V.Yu. Aristov et al. J. Chem. Phys., 128 (2008) 034703.

[5] O.V. Molodtsova, M. Knupfer et al. J. Appl. Phys. 104 (2008) 083704.

Ultrafast demagnetization processes in Gd

A. Melnikov, M. Sultan, U. Bovensiepen

Freie Universität Berlin, Fachbereich Physik, Arnimallee 14, 14195 Berlin, Germany

M. Wietstruk, T. Kachel, N. Pontius, C. Stamm, W. Eberhardt, H. A. Dürr

BESSY GmbH Berlin, Albert-Einstein-Str. 15, 12489 Berlin, Germany

C. Gahl, M. Weinelt

Max-Born-Institut, Max-Born-Str. 2 A, 12489 Berlin, Germany

Magnetization dynamics driven by femtosecond (fs) laser pulses has for more than a decade challenged our understanding of magnetism [1,2]. It represents the fastest magnetization dynamics for elementary transition metal ferromagnets thus exploring the ultimate writing speed-limit for magnetic data-storage applications [3]. In Materials such as Fe, Co and Ni demagnetization times of a few 100 fs have been realized [4], timescales clearly shorter than conventional spin angular momentum transfer to the lattice [5]. Various attempts have been made to identify the microscopic origin of this phenomenon [6-8]. However, in 3d ferromagnets the optically excited valence electrons carry the magnetic moment and the complex interplay between itinerant electron behavior and magnetic interactions remains an unresolved problem.

To further the understanding of femtomagnetism, it seems necessary to separate optical excitation from spin dynamics. Therefore we focus on the rare earth ferromagnet Gd, whose magnetic moment $\mu = 7,55\ \mu_B$ mainly originates from the $4f^7$ electrons localized at the ion core. The ferromagnetic order is mediated by indirect exchange interaction via the $5d6s$ conduction band which contributes $\mu_{5d6s} = 0,55\ \mu_B$ to μ. This separation is facilitated in Gd by employing an IR-laser pump x-ray probe technique [4]. With an 800 nm fs-laser pulse we optically excite the $5d6s$ valence electrons, while probing with 1182 eV x-ray pulses and using the x-ray circular dichroism (XMCD) measures the magnetization of the localized $4f$ electrons. As a sample we used a 10 nm Gd film evaporated under UHV conditions onto a free standing 500 nm Al foil with additional 50 nm buffer and 5 nm Yttrium cap layer.
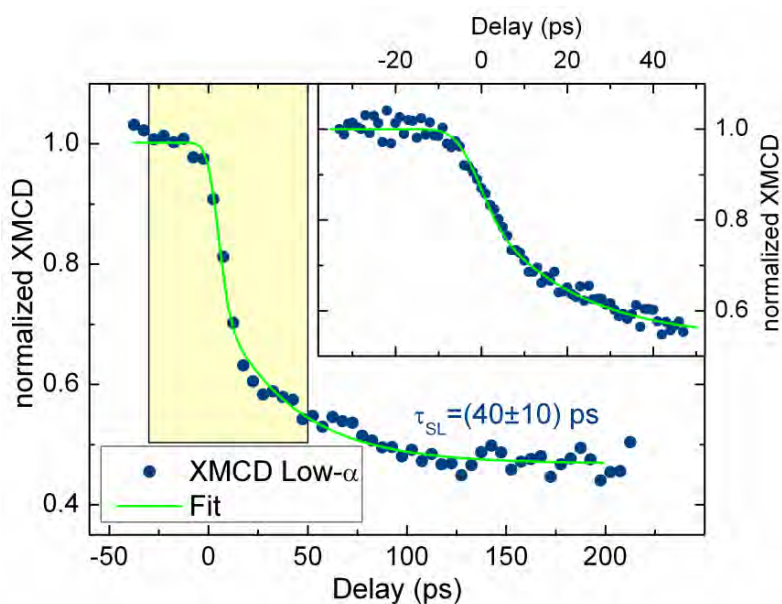
Fig. 1: XMCD signal, representing the $4f$ magnetization measured in low-α mode with x-ray pulse width of 12 ps. The main panel shows the reduction of the magnetization with a time constant of 40 ps, attributed to spin-lattice relaxation. The inset shows an additional drop of magnetization within the probe pulse length.

Time-resolved studies have been carried out with a temporal resolution of 12 ps in the low-α operation mode of BESSY. Figure 1 depicts the transient XMCD signal which is a measure of the 4*f* magnetic moment μ_{4f}. The transient drop in the magnetization is the result of laser-heating the valence electrons to temperatures above 1000 K [9]. After typically 1 ps this energy is transferred via electron-phonon scattering to the lattice [9,10], which will slowly cool off via heat transport in the free-standing film. Within the 12 ps time resolution the Gd lattice is heated instantaneously and remains hot thereafter. If the magnetization follows the lattice temperature, a fast drop not resolved in the low-alpha mode and a transient plateau of the XMCD signal would occur. We indeed observe such a fast initial drop, but followed by a slower decrease. Analyzing the latter by a single exponential fit gives a decay time of $\tau_{SL} =$ 40±10 ps. Since the lattice temperature rises within 1 ps after excitation, the larger time constant τ_{SL} describes the equilibration of the 4*f* spin and phonon systems. Our measurements thus corroborate earlier results that the 4*f* spin subsystem does not instantaneously follow the lattice temperature [5,9] and establish a spin-lattice relaxation time of 40 ps in accordance with theory [11]. As highlighted in the inset of Fig. 1 the transient XMCD trace shows in addition a faster drop and clear kink around zero delay. Consequently, an additional step function convolved with the x-ray pulse duration is needed to fit the data (green line). Since the above spin-lattice relaxation does not act on this timescale, this initial drop of the XMCD signal must be attributed to a second, faster demagnetization process, occurring during the 12 ps x-ray pulse duration.

This faster demagnetization process is resolved in Fig. 2 where 120 fs x-ray pulses generated by the femtosecond slicing technique [4,12] are used to record the transient XMCD. We find a characteristic timescale of $\tau = 1.0 \pm 0.2$ ps for the demagnetization of μ_{4f} demonstrating that after optical excitation 4*f* angular momentum is dissipated on a much faster timescale than τ_{SL}. Since we probe the total 4*f* magnetic moment, the 27 % drop in Fig. 2 corresponds to a decrease in μ_{4f} of $1\hbar \approx 0.27 \cdot 7/2 \, \hbar$. Suppose this angular momentum change is compensated by the valence electrons, μ_{5d6s} should increase by $1\hbar$ to 280% of the equilibrium value. In additional experiments at the FU Berlin we could prove, using magneto-optical Kerr effect (MOKE) with 1.5 eV Laser pulses in order to analyze the magnetization dynamics of the valence band, that there is no such increase of μ_{5d6s}. Furthermore, the magnetic moment of the valence band decreases concomitantly with μ_{4f}, regarding the timescale as well as the magnitude.

This leads to the conclusion, that the angular momentum change in the 4*f* is not accumulated by the 5*d*6*s* valence electrons but transferred to the lattice on a timescale of 1 ps. The microscopic origin of this new fast demagnetization process is still debated. The current concept of this process can be divided into two
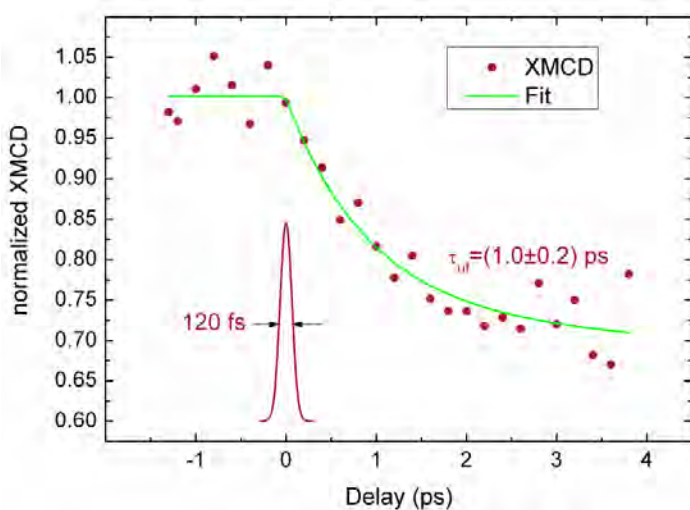
Fig. 2: Transient XMCD signal, measured with 120 fs x-ray pulses at the Gd M_5 absorption edge in the fs-slicing mode. From the exponential Fit (green line) a time constant of $\tau = 1.0 \pm 0.2$ ps was derived.

parts. After thermalization of the optically excited electrons, the process of emitting magnons is strongly enhanced by the population of electronic states above the Fermi energy. This leads to a demagnetization of the 4*f* spin system and transfers the angular momentum from the 4*f* to the valence electrons. At the same time the angular momentum is transferred from the 5*d*6*s* valence electrons to the lattice via electron-phonon scattering. Since the magnon emission process should occur on the timescale of 10 fs and the electron lattice equilibration time is about 1 ps, we conclude that the angular momentum transfer from the valence electrons to the lattice is the bottleneck in this demagnetization process and determines the demagnetization time constant of 1 ps.

[1] Beaurepaire, E *et al*. 1996. *Phys. Rev. Lett.* **76** (22): 4250-4253.

[2] Kimel, AV *et al.* 2005. *Nature* **435** (7042): 655-657.

[3] Tudosa, I *et al.* 2004. *Nature* **428** (6985): 831-833.

[4] Stamm, C *et al.* 2007. *Nature Mater.* **6** (10): 740-743.

[5] Vaterlaus, A *et al*. 1992. *Phys. Rev. B* **46** (9): 5280-5286.

[6] Zhang, GP; Hübner, W. 2000. *Phys. Rev. Lett.* **85** (14): 3025-3028.

[7] Schmidt, AB *et al*. 2005 *Phys. Rev. Lett.* **95** (10): 107402.

[8] Koopmans, B *et al*. 2005 *Phys. Rev. Lett.* **95** (26): 267207.

[9] Melnikov, A *et al*. 2008 *Phys. Rev. Lett.* **100** (10): 107202.

[10] Rhie, HS; Dürr, HA; Eberhardt, W. 2003. *Phys. Rev. Lett.* **90** (24): 247201.

[11] Hübner, W; Bennemann, KH. 1996. *Phys. Rev. B* **53** (6): 3422-3427.

CoPc and FePc thin films ordering on Au(001)

V.Yu. Aristov[1,2] , O.V. Molodtsova[1], Yu.A. Ossipyan[2], and M. Knupfer[1]

[1]*IFW Dresden, D-01069 Dresden, Germany*
[2]*Institute of Solid State Physics, Russian Academy of Sciences, Chernogolovka,
Moscow distr., 142432, Russia*

Magnetic transition metal phthalocyanines (TM-Pc), which are organometallic complexes, have already obtained substantial attention of researchers due to many different potential applications [1-3]. More recently, they have also been considered as a material for development of low dimensional molecular magnets [4] which are possible candidates for applications in high-density information storage and quantum computers (see review [5] and Refs. therein). In many of these applications the electronic structure, as well as molecular orientation and ordering in thin films of TM-Pc are important pre-requisites for the development of devices.

In present work we have studied the molecular orientation and ordering in thin films of CoPc and FePc deposited on a Au(001) substrate. The molecular films were characterized by LEED (low energy electron diffraction) and NEXAFS (near edge absorption fine structure), which represent ideal tools for studies of the geometry of molecular adsorbates and thin films.

NEXAFS measurements were performed at the Berliner Elektronen-Speicherring für Synchrotronstrahlung (BESSY) using soft x-ray synchrotron light provided by the Russian-German high-energy resolution dipole beamline. The LEED patterns were taken using an OMICRON back view setup. We have used Au (001)-5x20 surface of a gold single crystal as a substrate for phthalocyanine film growth. The CoPc and FePc films were deposited in a sample preparation chamber till the thicknesses varied between a few Å and 9 nm. The soft x-ray absorption spectra were recorded in the total electron yield mode and normalized to the incident photon flux. Other details of the sample preparation as well as of the experimental measurements can be found elsewhere (see e.g. [6]).

The LEED patterns were taken at each preparation stage, from the clean Au(001) surface with a 5x20 surface reconstruction to the organic thin films of different thicknesses deposited on this clean Au(001) surface. After inspection of the diffraction pattern of each CoPc(FePc)/Au sample, the organic film was desorbed by sputtering and annealing, and the clean gold substrate was prepared again. The organic films were investigated for substrate temperatures of 250 °C (ET) and room temperature (RT) during film growth. Fig. 1 presents typical LEED patterns taken at nearly normal electron beam incidence from the clean 5x20 Au(001) substrate and the TM-Pc films grown at RT and at ET.

The LEED pattern of the clean Au(001)5x20 surface presented in Fig. 1(a) reveals sharp and high-contrast 1/5 and 1/20 fractional order diffraction spots in agreement with LEED patterns published elsewhere [7-9]. Upon TM-Pc film deposition the observed 5x20 diffraction spots fade rapidly and disappear, while simultaneously another, rather pronounced diffraction pattern arises. The structure of this LEED pattern does not significantly change with molecular film thickness up to at least 9 nm, which is the maximum value in the present study.

The diffraction spots from the TM-Pc overlayers indicate a square unit cell in reciprocal space. The LEED patterns presented in Figs. 1(c-g) demonstrate that these overlayers are highly ordered (in particular for deposition at the elevated temperature). From the LEED pattern we derive a real space unit cell of 14.2 Å x 14.2 Å, which is aligned along the <110> and <1 $\bar{1}$0> axes of the Au(001) surface. We emphasize that up to films thicknesses of 5 nm we obtain this square unit cell also for growth at RT for both phthalocyanines.
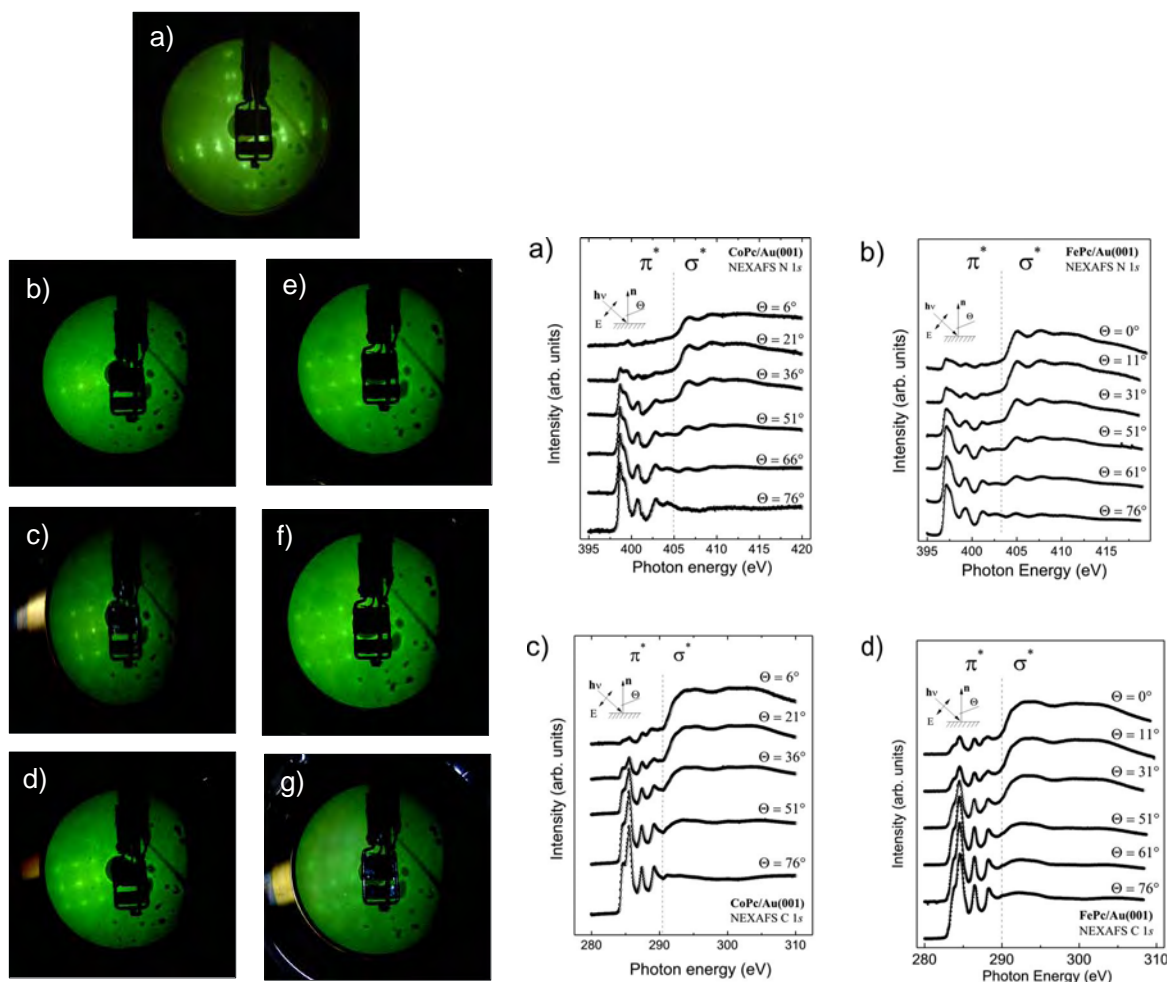
Fig. 1. (Color on line). LEED patterns taken from the clean Au(001)-5x20 substrate and from various CoPc and FePc films grown on this substrate. (a) Au(001)-5x20, the incident electron energy E_p = 37 eV; (b)-(d) CoPc films: (b) 5 nm CoPc deposited on Au(001) at RT, E_p = 31.7 eV; (c) 5 nm CoPc deposited on Au(001) at ~ 250 °C, E_p = 32 eV; (d) 8 nm CoPc deposited on Au(001) at ~ 250 °C, E_p = 28.3 eV. (e)-(g) FePc films: (e) 2.5 nm FePc deposited on Au(001) at RT, E_p = 28.2 eV; (f) 5 nm FePc deposited on Au(001) at RT, E_p = 29.3 eV; (d) 9 nm FePc deposited on Au(001) at ~ 250 °C, E_p = 28.1 eV.

Fig. 2. N $1s$ and C $1s$ NEXAFS spectra taken from CoPc (a, c) and FePc (b, d) films (9 nm thick), deposited on the Au(001) surface, taken at different angles Θ between the light polarization vector E and the normal to the sample surface n. The insets indicate the experimental geometry. The lower energy features (396–404 eV) for N $1s$ and (283-290 eV) for C $1s$ represent the π^* resonances, whereas the features above 404 eV and 290 eV, respectively, are related to the σ^* resonances.

Consequently, we conclude, that CoPc and FePc deposition up to coverage of 5 nm at RT and of 9 nm at ET on Au(001)5x20 gives rise to formation of highly ordered molecular films with square unit cells of approximately 14.2 Å x 14.2 Å aligned along the <110> and <1 $\overline{1}$0> axes of the Au(001) surface. We note, that our results are not in line with the LEED data for a CoPc film deposited on an Au(001) substrate [10], where two domains have been found to be rotationally invariant by 16°. We attribute this difference to differences in the preparation process. In order to obtain deeper insight into the TM-Pc film structure we have performed polarization dependent NEXAFS experiments.

Fig. 2 shows the N $1s$ NEXAFS spectra recorded from the 9 nm thick CoPc (a) and FePc (b) films. The spectra were taken as a function of the incidence angle of polarized X-ray radiation. It was shown for other Pc's [11-13], that the rather sharp N1s NEXAFS peaks in the region between 398 and 405 eV can be assigned to transitions from the N $1s$ core-level into the unoccupied π^* orbitals with N 2p orbital contributions, which are oriented perpendicular to the molecular plane. The high-energy structures above 405 eV, are related to N $1s$ - σ^* transitions. These σ^* orbitals lie parallel to the plane of the molecule.

2

Fig. 2 ((a)-(b)) reveal a very strong angular dependence of the N 1s - π* intensities (396 – 404 eV). At grazing incidence the intensities of these π* signals show a maximum and decrease with increasing Θ reaching a minimum at normal incidence. The angular dependence of the N 1s - σ* intensities (404 – 420 eV) reveals the opposite trend. This behavior demonstrates, that the CoPc and FePc molecules are well ordered with the molecular planes lying parallel to the Au(001) substrate. If the synchrotron radiation beam is 100% linearly polarized and the molecules lie flat on the substrate, the intensity of 1s - σ* resonances should be described by a $\sin^2\Theta$ function, while the 1s - π* resonances follow a $\cos^2\Theta$ dependence [14]. Fig. 3 shows the angular dependent intensity of the 1s core level excitations into the main π* resonances for the CoPc and FePc thin films deposited on Au(001)-5x20. It is obvious from Fig. 3 that the CoPc data follow the theoretical curves expected for lying molecules well. A deviation of the experimental curve from the expectation for FePc (Fig. 3, right panel) can be explained by DFT calculations [15].
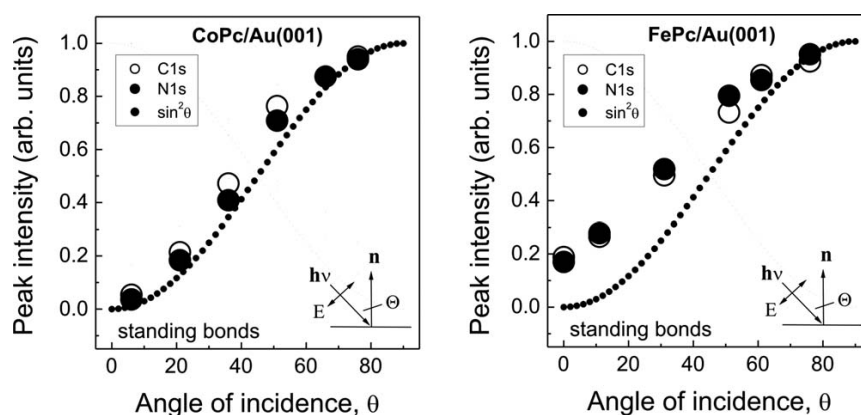
Fig. 3. Filled and open circles: angular dependence of the intensity of the main π* resonances of CoPc and FePc deposited on Au(001)-5x20 (left-hand and right-hand panels respectively). The expected intensity profiles for flat lying molecules are also indicated by small dots.

Thus, our results prove that the CoPc and FePc films grown on the Au(001) substrate at the elevated temperature (at least up to the thickness of ~ 9 nm) are well ordered with the molecular planes parallel to the substrate surface. This might also result in well defined electronic properties.

References
[1] M. Trometer, et al, Sens. Actuators B **8** (1992) 129.
[2] C.C. Leznoff, A.B.P. Lever, Phthalocyanines: Properties and Appl., Vols. 1–4, VCH, New York, 1989–1996.
[3] A.R. Harutyunyan, et al., J. Magn. Magn. Mater. **194** 16 (1999); A.A. Kuznetsov, et al., ibid. **225** (2001) 95.
[4] J. Ribas i Gispert, Contributions to Science **1** (1999) 39.
[5] W.J.M. Naber, S. Faez and W.G. van der Wiel, J. Phys. D: Appl. Phys. **40** (2007) R205.
[6] V.Yu. Aristov, O.V. Molodtsova, V.M. Zhilin, D.V.Vyalikh, and M. Knupfer, Phys. Rev. **B72** (2005) 165318.
[7] D.G. Fedak and N.A. Gjostein, Surf. Sci. **8** (1967) 77.
[8] M.A. Van Hove, et al, Surf. Sci. **103** (1981) 189.
[9] M.A. Van Hove, et al, Surf. Sci. **103** (1981) 218.
[10] T.S. Ellis, et al, J. Appl. Phys. **100** (2006) 093515.
[11] T. Okajima, et al, Surf. Rev. Lett. **9** (2002) 441.
[12] H. Peisert, T. Schwieger, J.M. Auerhammer, M. Knupfer et al, J. Appl. Phys. **90**, (2001) 466.
[13] G. Cabailh, et al, Appl. Surf. Sci. **234** (2004) 144.
[14] J. Stöhr, NEAFS Spectroscopy (Springer, Berlin, 1992).
[15] J. Åhlund, et al., J. Chem. Phys. **125** (2006) 034709.

Pinned uncompensated moments in Fe/MnPd and their relation to the exchange bias loop shift

Sebastian Brück[1], Xiaosong Ji[2], Kannan M. Krishnan[2], Eberhard Goering[1]

[1]*Max-Planck-Institut für Metallforschung, Heisenbergstraße 3, 70569 Stuttgart, Germany*

[2]*Materials Science and Engineering, University of Washington, Seattle, Washington 98195, USA*

Abstract

X-ray magnetic reflectivity (XRMR) and x-ray magnetic circular dichroism (XMCD) have been used to investigate the magnetic configuration in the Fe/MnPd exchange bias system. From the XRMR investigation, a precise element selective magnetic depth profile of the Mn in the antiferromagnet is obtained which reveals a complex interfacial magnetic configuration with rotatable and pinned uncompensated Mn moments. Rotatable moments are only located at the interface to the ferromagnet in a very narrow region of 4Å. Pinned uncompensated Mn moments are found directly below the rotatable Mn moments reaching roughly 13Å deep into the antiferromagnet. A direct correlation of pinned moments and hysteresis loop shift is found from comparing measurements parallel and perpendicular to H_E.

The exchange bias effect [1] which occurs when a ferromagnet is in direct contact to an antiferromagnet has attracted much attention recently. The coupling with the antiferromagnet induces a shift of the hysteresis loop accompanied by an increase of the coercive field. While it is widely accepted that uncompensated pinned moments in the antiferromagnet are responsible for the observed loop shift [2], direct evidence for this relation is still missing for most exchange bias systems.

The sample investigated here is a film with a nominal thickness of 750Å $Mn_{52}Pd_{48}$ followed by 75Å Fe and finally a 15Å Pt capping layer. It is grown epitaxially on a MgO(001) substrate by ion-beam sputtering. The base pressure of the preparation chamber was 10^{-9}mbar and the substrate was heated to 85°C during preparation. At this temperature, MnPd grows chemically disordered. The sample then was annealed for 1h at 250°C to order it chemically and establish a good crystallographic orientation where the a-axis lies perpendicular to the film surface

[3]. A magnetic field was applied during the annealing to induce a well defined unidirectional anisotropy in the sample. From subsequent vibrating sample magnetometry a room temperature exchange bias of H_E=-4.5mT and a coercive field of H_C=12.1mT is found.

The XRMR and XMCD investigations were carried out at the UE56/2-PGM1 beamline at BESSY II in Berlin using the groups own dedicated 3-axis reflectometer [4]. To obtain the structural and magnetic depth profile from the measured magnetic reflectivity spectra, a special simulation software developed in our group [5] is used. It allows simulating and fitting normal and magnetic reflectivity curves as well as magnetic asymmetries by providing two different algorithms: the Parratt algorithm or a magneto optical approach based on 4x4 matrices. To account for roughness and especially allow local variations of the magnetic moment, ReMagX uses an adaptive multi slicing approach which enables local variations of

the magneto-optical properties, i.e. artificial magnetic moments.

The chemical profile has been obtained from fitting linear polarized reflectivity curves at the Fe and Mn L_3 edges [6,7]. It is found that the relevant Fe to MnPd interface in the sample is of exceptional quality showing a RMS roughness of only $\sigma_{RMS}=1.8$Å. The real thicknesses of the individual layers as obtained from fitting the resonant reflectivity curves are Fe(87.3Å) and Pt(16.4Å) which is in good agreement with the nominal values. The magnetic reflectivity curves were measured using circular polarized light with 90% degree of polarization. An external magnetic field of +/-67mT was used to align the magnetic moments in the sample. The reflectivity was measured at the maximum of the Mn L_3 edge, at an energy of 639.5eV for both magnetic field directions, parallel and antiparallel, and both helicities of the incident x-rays. From comparing the reflectivity for the two magnetic field directions a clear magnetic asymmetry is found which proofs the existence of rotatable Mn moments in the antiferromagnet [6,7]. It is found that these rotatable moments are only present in a very narrow region directly at the interface. In Ref. [7] it is shown that the presence of the ferromagnet induces this rotatable Mn layer in the antiferromagnet.

The observed rotatable Mn moments explain the increase of the coercive field but they cannot explain the loop shift related to exchange bias. The shift can only be related to pinned uncompensated Mn moments with unidirectional character. To derive the signal of those pinned moments, the asymmetry has to be calculated in a way that blanks out rotatable moments. This can be achieved by the following scheme: $A_{pin}=(I^{++}-I^{--})/(I^{++}+I^{--})$ where the index (++) refers to the reflectivity for parallel magnetic field and positive helicity while (--) refers to the opposite alignment of field and helicity.

The *pinned asymmetry* obtained from applying this calculus is shown in Figure 1 as black curve. The red curve shown in the graph is the result from fitting the magnetic signal of the pinned Mn moments.
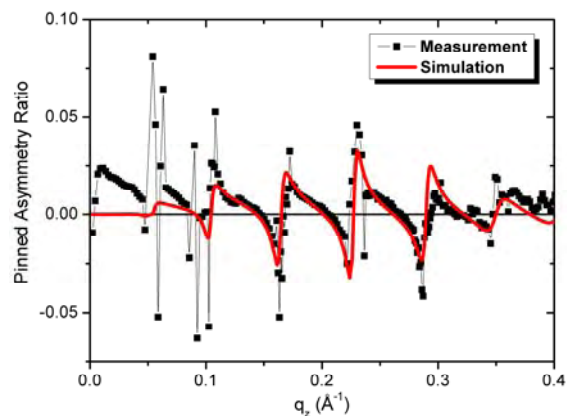
Figure 1 Asymmetry from pinned uncompensated Mn moments in the sample. The spectra have been measured at the maximum of the L_3 edge of Mn (639.5eV) using circular polarized light. The red curve is the fit solution discussed in the text.

From the simulation it is found that the pinned Mn moments are located in a region, slightly below the interface to the ferromagnet reaching roughly 13Å deep into the antiferromagnet. Compared to the rotatable Mn, the pinned moments are located deeper in the antiferromagnet and the magnitude of the signal is a factor of 5 smaller. The small signal is either related to fewer atoms contributing to the signal or different magneto-optical properties for the pinned moments. The latter cannot be excluded since the spectroscopic properties of these moments are unknown.

To test the relation of the found pinned uncompensated Mn moments with the loop shift of exchange bias, the measurement was repeated perpendicular to the field cooling, i.e. H_E, direction. The hysteresis loop properties were checked by measuring element selective loops in reflection. Therefore the reflectivity is measured at a fixed angle and energy

while sweeping the magnetic field from positive to negative saturation and vice versa. The resulting hysteresis for Fe as measured at an energy of 707.2eV at an angle of incidence of $\Theta=11°$ with positive helicity is shown in Figure 2.
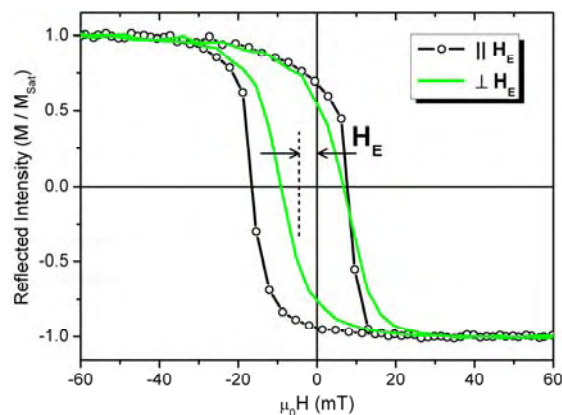
Figure 2 Element selective hysteresis loops obtained from measuring the reflectivity at a fixed angle while varying the magnetic field. Both loops are measured at the Fe L_3 edge (707.2eV) at an angle of incidence of $\Theta=11°$ using positive circular polarized light. The black curve is measured along the field cooling, i.e. H_E direction, while the green one is measured perpendicular to it.

The black curve shows the hysteresis measured parallel to H_E while the green one is measured in perpendicular orientation. Nearly no loop shift is found in the perpendicular direction as expected from the unidirectional character of exchange bias. The corresponding pinned asymmetries for the two orientations are shown in Figure 3 as black and green curve accordingly. The pinned asymmetry for the perpendicular orientation is strongly reduced, clearly indicating the relation between the pinned uncompensated Mn moments in the antiferromagnet and the loop shift H_E.

In summary we have shown that pinned uncompensated Mn moments exist in the exchange bias system Fe/MnPd. A direct correlation of these pinned moments with the loop shift is found from comparing measurements parallel and perpendicular to the exchange bias direction.
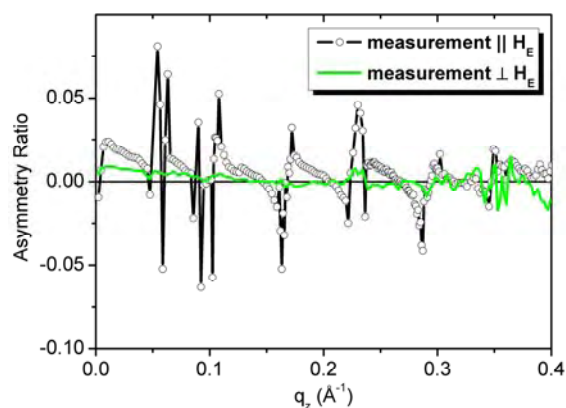
Figure 3 Comparison of the asymmetry signal from pinned uncompensated Mn moments depending on the alignment of the sample. The black curve is the asymmetry parallel to H_E (same as in Fig. 1), the green one is perpendicular to H_E direction.

Acknowledgements

References

[1] W.H. Meiklejohn and C.P. Bean, Phys. Rev. **105**, 904 (1957).

[2] J. Nogués and I.K. Schuller, J. Magn. Magn. Mater. **192**, 203-232 (1999).

[3] P. Blomqvist, K.M. Krishnan and D.E. McCready, J. Appl. Phys. **95**, 8019-8022 (2004).

[1] S. Brück et al., Rev. Sci. Instrum. **79**, 083109-6 (2008).

[5] S. Macke, S. Brück and E. Goering ReMagX - x-ray magnetic reflectivity tool URL: www.mf.mpg.de/remagx.html

[6] S. Brück et al., BESSY Yearbook 2007 pages 183-185 (2007).

[7] S. Brück et al., Phys. Rev. Lett. **101**, 126402-4 (2008).

ADSOPRTION OF L- AND D-SERINE AMINO ACIDS ON THE BIMETALLIC CHIRAL AU-CU{531} SURFACE

T. Eralp[1], A. Cornish[1], D. Batchelor[2] and G. Held[1]

[1]*University of Reading, Department of Chemistry, Reading RG6 6AD, UK.*
[2]*BESSY and Universität Würzburg, Experimental-Physik II, Am Hubland, Würzburg, Germany*

Surface systems involving chiral molecules adsorbed on chiral single crystal surfaces are model systems for potential enentioselective heterogeneous catalysts and could provide a route to the selection of enantiopure chiral bio-relevant molecules. Recently, the adsorption of aminoacids has been studied on different gold single crystal surfaces. In particular, the adsorption of cysteine is well studied because of the strong bond between its thiol group and the gold surface atoms [1-3]. There are, however, no studies related to the adsorption of aminoacids on bimetallic surfaces containing gold.

At our previous beamtime at BESSY, L- and D-serine adsorption on the intrinsically chiral Cu{531} surface was extensively studied by XPS and NEXAFS. It has been found that there is a strong angular difference in the orientations of the two enantiomers on this chiral surface.

In this study, by depositing gold on the chiral Cu{531} surface, the surface was transformed layer-by-layer from copper-like to gold-like while preserving the chiral surface structure. Depending on the coverage of Au atoms, the surface shows gold properties as well as copper, which is expected to lead to different adsorption bonds and different orientations of the two enantiomers affecting the enantioselectivity of the surface.

The experiments were performed at the BESSY beamline UE52-PGM at a base pressure of $3x10^{-10}$ mbar. O1s, N1s and C1s XPS data were recorded at room temperature using a Scienta 200 mm electron energy analyser with pass energy 100 eV and a photon energy of 630 eV; for the Au4f spectra a photon energy of 300eV was used. The binding energies (BE) were calibrated by measuring a spectrum at the Fermi energy with the same photon energy and pass energy. The NEXAFS experiments were done at normal incidence; the orientation of the electrical field vector, within the surface plane was controlled by the undulator settings to be parallel or perpendicular to the [$1\overline{12}$] direction of the {531} surface as well as angles of 15°, 30°, 45°, 60° and 75° from parallel [4]. A partial yield detector (PYD) was used with the retarding voltage set to accept electrons in the kinetic energy range up to 50 eV below the lowest photon energy. The raw C and O K-edge NEXAFS data were normalised with respect to the ring current and spectra of the clean sample.

Uptake curves for gold on Cu{531} are displayed in Figure 1. Au4f spectra were recorded after each dosing step. With increasing coverage, a new peak starts rising at around 84.2eV, which represent the bulk Au atoms, near the main Au4f7/2 peak (surface) indicating that monolayer coverage

is exceeded. The appearance of this peak was used to calibrate the Au coverage. Layers of 1ML and 2ML were prepared to investigate the adsorption of L-and D-serine on these bimetallic surfaces.

The O1s, C1s and N1s spectra for L-serine and D-serine were found similar to each other for 1ML and 2ML Au on Cu{531}. For 40% saturation coverage the O1s XPS spectrum has a main peak at 531.5eV and a shoulder at a lower BE (530.7 eV), as in the case of adsorption on the clean Cu{531} surface (Figure 2a). As the coverage increases, this shoulder disappears and a new peak appears at higher BE (532.8 eV). The main peak is assigned to the overlapping signal of the two oxygen atoms in the deprotonated carboxylate (COO) group, which form a bond to one Cu atom each [5, 6]. The peak that appears at low BE for low coverage and high BE for higher coverages is assigned to the OH side group which changes from making a bond with the Cu surface (low BE) to dangling away from the surface (high BE). In the N1s region, there is an additional small peak at a binding energy of 402eV, which is assigned to the NH_3^+ state of the amino group [6]. This indicates that there exist two states of the aminoacids for adsorption on the gold covered surface, zwitterionic and anionic, which is different from the adsorption on clean Cu{531} (Figure 2b).

In order to determine the orientation of the molecules on the surface, NEXAFS spectra were measured for different in-plane polarization. On the clean Cu{531}surface an angular difference of 39.3° and 25° (for {311} and {110} microfacets respectively) has been found between the orientation of the two enantiomers. Whereas on the gold-covered surfaces this difference decreases to 9.2° and 11.3° (for 1ML Au coverage) and 3.1° and 4.3° (for 2ML Au coverage) for {311} and {110} microfacets respectively (Figure 3). This is a significant decrease in the enantioselectivity as compared to Cu{531} with respect to orientational differences between two enantiomers.

REFERENCES

1. A. Kühnle, T. R. Linderoth, B. Hammer, F. Besenbacher , *Nature,* **2002,** *415,* 892
2. O. Cavalleri, G. Gonella, S. Terreni, M. Vignolo, L. Floreano, A. Morgante, M. Canepa, R. Rolandi, , *Phys . Chem. Chem. Phys .* , **2004**, *6*, 4042
3. T. Greber, Z. Sljivancanin, R. Schillinger, J. Wider, B. Hammer, *Phys. Rev. Lett.,* **2006***, 96,* 056103
4. M. J Gladys, A. V Stevens.; N. R Scott, G.; Jones, D. Batchelor, , G. Held *J. Phys. Chem. C* **2007**; *111(23)*, 8331.
5. G. Jones et al., *Surface Science*, **2006**, *600*, 1924-1935
6. O. Cavalleri, G. Gonellą,S. Terreni, D. Cvetko, A. Cossaro, L. Mattera, O. Cavalleri, R. Rolandi, A. Morgante, L. Floreano, M. Canepa, *Journal of Physical Chemistry*, **2005** , *109* , 18003
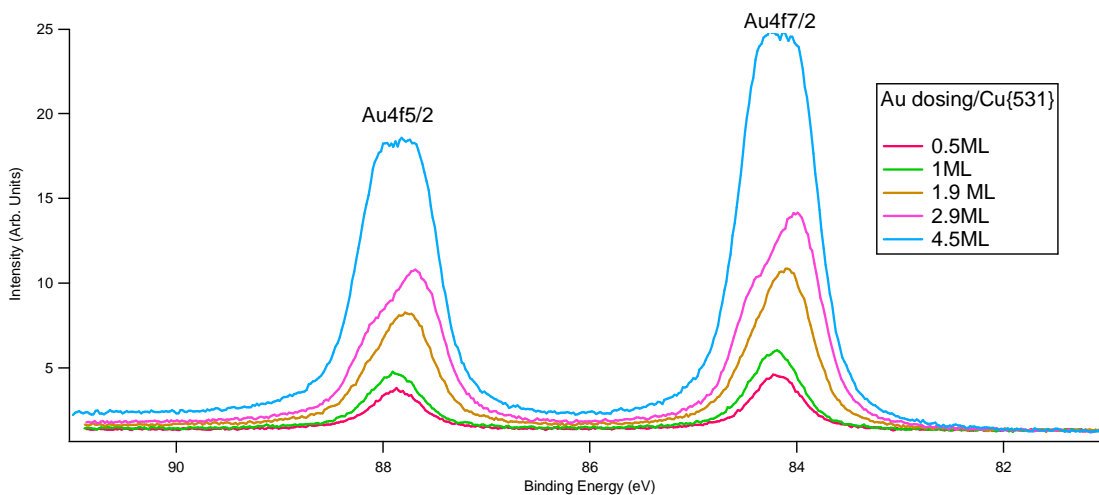
Figure 1. Au uptake curves, h*v*=300eV.

a)

b)
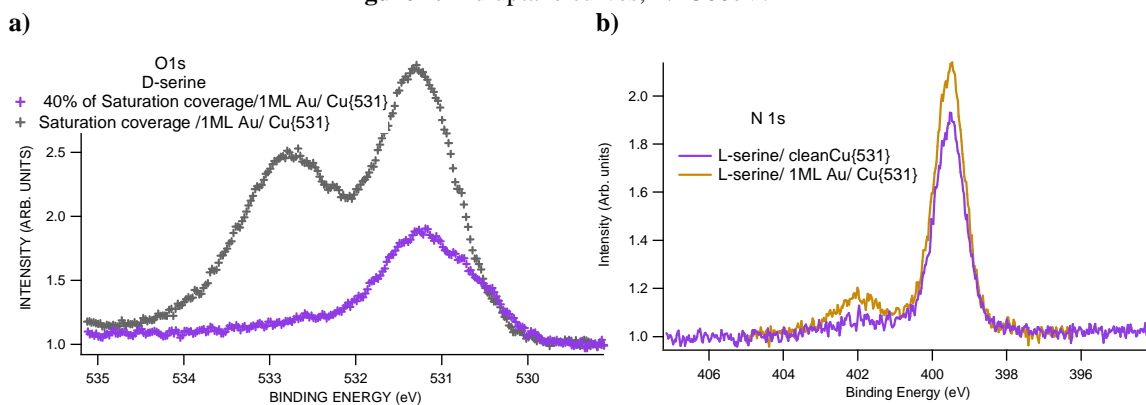
Figure 2. a) O1s peaks for two different D-serine coverages on 1ML Au/Cu{531}, h*v*=630eV; **b)** N1s peaks for saturation coverage of L-serine on clean Cu{531} and 1ML Au covered Cu{531}, h*v*=630eV
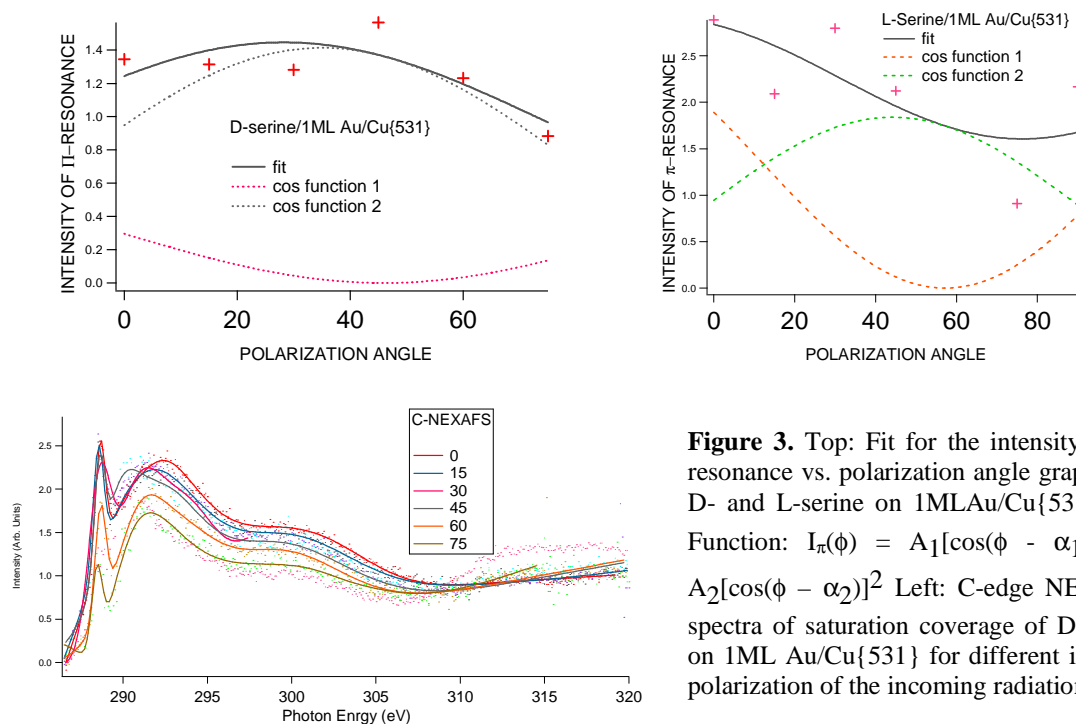
Figure 3. Top: Fit for the intensity of π-resonance vs. polarization angle graphs for D- and L-serine on 1MLAu/Cu{531}. Fit Function: $I_\pi(\phi) = A_1[\cos(\phi - \alpha_1)]^2 + A_2[\cos(\phi - \alpha_2)]^2$ Left: C-edge NEXAFS spectra of saturation coverage of D-serine on 1ML Au/Cu{531} for different in-pane polarization of the incoming radiation.

Magnetic structure of antiferromagnetic and ferrimagnetic thin semiconducting films.

E. Schierle[1], D. Schmitz[1], V. Soltwisch[1], G. Springholz[2], E. Weschke[1]

[1]*Helmholtz-Zentrum Berlin für Materialien und Energie, 12489 Berlin, Germany*
[2]*Institut für Halbleiterphysik, Johannes Kepler Universität, A-4040 Linz, Austria*

Introduction: Current thin film devices exploit the properties of multilayer structures, where functionality is caused by phenomena strongly related to the material properties close to the interfaces. In the vicinity of such symmetry-breaking interfaces of two materials, astonishing local deviations of material properties can be found, e.g. the occurrence of superconductivity at the interface between two insulators [1]. Already at the surface of a single material, the local electronic and magnetic structure can differ from the bulk [2]. In magnetic thin films, the influence of interfaces may become dominant and can even change the spin structure of the entire film. Therefore, depth-resolved studies of interface-induced changes of material properties have become an interesting but also challenging topic in basic research. As shown recently, resonant magnetic soft x-ray diffraction from thin films enables to determine the temperature-dependent magnetization profiles of an entire film with atomic-layer resolution [3]. Here, we apply this method to study the field- and temperature-dependent magnetic order of thin films of semiconducting EuSe. Magnetic semiconductors are of particular interest since their electronic and magnetic properties can be tuned by purposeful doping. EuSe is characterized by a complex phase diagram including ferro-, antiferro- and ferrimagnetic phases, which is caused by the near balance between ferromagnetic (FM) nearest neighbor (nn) exchange J_1 and antiferromagnetic (AFM) next-nearest neighbor (nnn) exchange J_2 [4]. Consequently, the magnetic structure of EuSe is very sensitive to small changes of the degree of epitaxial strain and to applied external magnetic fields, which enables to study interface-related modifications of various magnetic structures even from the same sample.

Experimental: High-quality single-crystalline films of EuSe(111) with thicknesses between 10 and 60 monolayers (ML) were grown by molecular beam epitaxy on a $PbSe_xTe_{1-x}$ buffer predeposited on a BaF_2 substrate and finally capped with a thin $PbSe_xTe_{1-x}$ layer to prevent oxidation and to provide two identical interfaces. By varying the ratio of Se and Te of the buffer and capping layers, films with compressive, tensile and vanishing epitaxial strain could be realized. We studied the magnetic structures of these films by means of resonant magnetic soft x-ray diffraction, exploiting the large magnetic scattering cross section at the Eu-M_5 absorption threshold. The experiment was performed at the UE46-PGM-1 beam line, using the UHV diffractometer built at the Freie Universität Berlin. Magnetic fields up to 250 mT could be applied by a system of permanent magnets and a Helmholtz-like electromagnet without limitation of the accessible scattering angles. Using a sample holder directly attached to a continuous flow He cryostat and with optimized shielding, the scattering experiment could be performed at sample temperatures down to 3 K.

Results: The magnetic structure of EuSe consists of ferromagnetically ordered (111) layers, with either AFM or FM coupling of neighbouring layers. Since each Eu^{2+} ion has an equal number of nn and nnn Eu^{2+} ions in the adjacent (111) layer, the effective coupling between two neighbouring layers, J_{eff}, strongly depends on the ratio of J_1 and J_2. In thin films, only domains with FM (111) layers parallel to the surface exist. Therefore, magnetic scattering along the [111] direction of our (111) films shows magnetic superstructure reflections, with a position given by the inverse of the magnetic period along [111]. In films with compressive strain, we observed magnetic (½ ½ ½) reflections as shown in the inset of Fig. 1(a). This corresponds to a simple AFM structure of type II (↑↓). In contrast, films without strain show magnetic reflections at (¼ ¼ ¼), i.e. the bulk EuSe zero-field AFM structure of type I (↑↑↓↓) is realized. From films with applied tensile strain no magnetic signal could be observed along [111]. This strain dependence of the magnetic structure is caused by the influence of strain on J_1: Changing the strain from compressive towards tensile, the FM intra-layer coupling of the (111) layers decreases, while J_{eff} changes from AFM towards FM coupling. With increasing external field H, both observed types of AFM structure undergo metamagnetic phase transitions into a ferrimagnetic (FiM) phase, characterized by a ($^1/_3$ $^1/_3$ $^1/_3$) reflection (↑↑↓) as can be seen in the inset of Fig. 1(c). Fig. 1 shows the intensity of the FiM and AFM reflections from a 36ML-thin EuSe film with compressive strain. The AFM/FiM transition temperature strongly depends on H. In the presented experimented we studied this AFM/FiM and the AFM/paramagnetic (PM) as well as the FiM/PM transition in detail. The polarization dependence of the scattered magnetic intensity contains information on the orientation of the spins and the distribution of domains. Without applied field the AFM structure is characterized by an equal distribution of all six possible in-plane orientations of the spins. From the evolution of the scattered intensities with increasing field, shown in the inset of Fig. 1(b), one can conclude, that for small H the AFM structure remains but the spins start to align perpendicular to the direction of H, until a phase transition into the FiM phase occurs, with spins now essentially oriented along H. Further conclusions can be drawn from the shape of the magnetic reflections as illustrated in Fig. 2. Due to the finite thickness of the films, the reflections are

Figure 1: Temperature and field-dependent magnetic scattering intensities from 36 ML of EuSe recorded at the position of the AFM and FiM reflections shown in the insets of (a) and (c).
(a) Intensities for zero external field;
(b) same as (a) but for an external field of 35 mT, π and σ denotes the polarization of the incident light; inset: intensity of AFM reflection for different external fields;
(c) same as (a) but for an external field of 125 mT.

characterized by side (Laue) oscillations with a period given by the inverse of the effective number of contributing magnetic layers. Close to the FiM/PM transition, the period of the Laue oscillations increases with temperature (Fig. 2(a)). Hence, the effective number of contributing magnetic layers decreases with temperature, i.e. the magnetization does not vanish homogeneously across the film. An analogous inhomogeneous albeit inverse behaviour is observed at temperatures slightly above the AFM/FiM transition (Fig. 2(b)): the period of the Laue oscillations of the FiM reflection decreases with increasing temperature. A direct comparison of the AFM and FiM reflection (Fig. 2(c)) shows different periods of the Laue oscillations for the FiM and AFM reflections from the same film, even at the lowest temperature. While the AFM reflection corresponds to a magnetic thickness which equals the film thickness, the FiM reflection is significant broader. This can be understood, assuming that the outermost 4 layers at both interfaces are coupled ferromagnetically and therefore do not contribute to the scattering signal from the FiM structure, which points towards a rather complex magnetic behaviour at the interface.
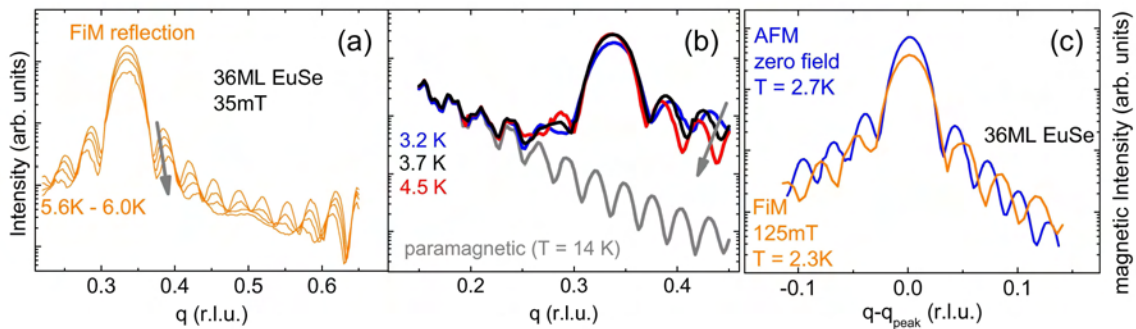
Figure 2: Temperature-dependent magnetic reflections from 36 ML of EuSe. (a) Evolution of the FiM reflection close to the FiM/PM transition. The gray arrow indicates the peak broadening with increasing temperature. (b) Same as (a) but for temperatures slightly above the AFM/FiM transition. The gray arrow indicates the sharpening with increasing temperature. (c) Comparison of AFM and FiM reflection.

Our detailed study on the strain-, field- and temperature-dependent magnetic structure of thin films of EuSe shows that all magnetic phase transitions in these films do not proceed homogeneously, but are characterized by a distinct depth dependence. From the recorded high-quality magnetic reflections through various magnetic phase transitions, detailed information on the microscopic behaviour of the magnetic structure, especially close to the interfaces, is obtained. In particular, an atomic-layer resolved reconstruction of the magnetic structure as demonstrated in Ref. 3 should be feasible. Corresponding simulations are performed at present.

References:
[1]   N. Reyren et al., Science **317**, 1196 (2007)
[2]   E. Weschke et al., Phys. Rev. Lett. **93**, 157204 (2004)
[3]   E. Schierle et al., Phys. Rev. Lett. **101**, 267202 (2008)
[4]   R. T. Lechner et al., Phys. Rev. Lett. **94**, 157201 (2005)

Resonant Photoemission studies of Rutile (110) TiO$_2$ single crystals and TiO$_2$ thin films

Sebastian Müller*, Dieter Schmeißer

Brandenburgische Technische Universität Cottbus, Angewandte Physik – Sensorik, Konrad-Wachsmann-Allee 17, 03046 Cottbus

*Sebastian.Mueller@TU-Cottbus.De

1. Introduction

Today there is still very high interest in the research related to Titanium Dioxide [1]. One reason is the wide range of possible applications, like catalysis [2, 3], opto-electronics [4], anti-fog coatings and self cleaning surfaces [5]. Besides this, there are still many activities in the field of fundamental research. The nominal d^0 configuration in TiO$_2$ makes it a suitable model substance for the studies of fundamental properties and interactions like model catalysts [6]. Titanium Dioxide single crystals in the Rutile phase, usually with the most stable (110) surface are widely available and can be easily prepared for photoemission experiments. In this report, we present resonant photoemission studies of single crystals and thin films of TiO$_2$.

2. Experimental details and sample preparation

The rutile single crystals were purchased from SurfaceNet. In order to prepare them for photoemission experiments, they were etched in diluted HNO$_3$ to remove surface contaminations and subsequently rinsed with water. Carbon contaminations were removed by heating the crystal in UHV conditions to around 900°C. During this step, the stoichiometric TiO$_2$ was also reduced to under-stoichiometric TiO$_{2-x}$. The color of the crystal turned from pale yellow to grey indicating reduced bulk material. The stoichiometric surface is restored by annealing it in ambient air at 900°C. Despite the step in ambient air, there is no significant amount of carbon contamination on the surface. The thin films are prepared by evaporation of Ti onto a SiC substrate in UHV from a Ti filament which is heated to 1000°C. This metallic film is then oxidized in ambient air at a temperature of 900°C as well. Similar to the results obtained from single crystals, there was no significant carbon contamination on the thin films as well. The estimated thickness of these films is 10 nm. The samples are prepared and analyzed at the ASAM end station at beamline U49/2–PGM2 which is operated by BTU Cottbus.

3. Results and Discussion

The Ti 2p photoelectron spectra of the single crystal (black curve) and the thin film (red curve) are shown in Fig. 1, left panel. The Ti 2p$_{3/2}$ binding energy is observed at –459.3 eV in case of the single crystal with a spin orbit split of 5.7 eV. The spectrum of the thin film shows a shift of 0.4 eV towards lower binding energy, while the FWHM values are the same in both spectra (about 1 eV) as well as the spin orbit split. Like in the spectrum of the single crystal, no contributions at lower binding energies, that would correspond to Ti^{3+}, are observed. The satellite structure is also present in the
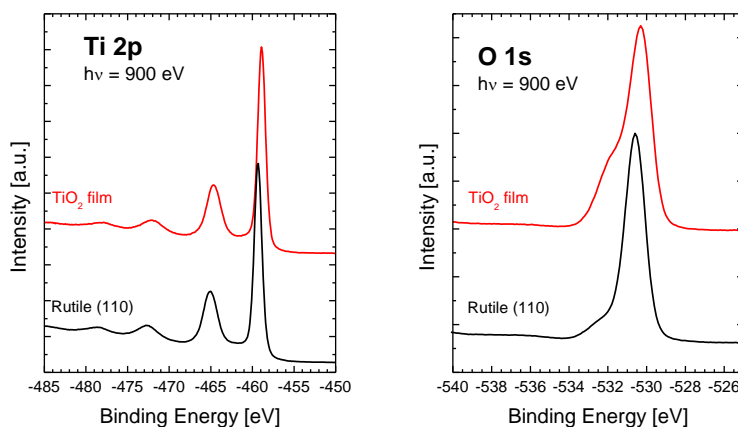
Fig. 1 PES spectra of Ti 2p (left panel) and O 1s (right panel) from Rutile (110) single crystal (black curve) and TiO$_2$ thin film (red curve) measured with photon energy of 900 eV.

thin film. In the O 1s spectra (Fig. 1, right panel) we observe the same shift of 0.4 eV between the single crystal (–530.6 eV) and the thin film. However, the shape of both spectra shows significant differences. In case of the single crystal, a small feature at high binding energy side (around –533 eV) is observed. This feature can be attributed to adsorbed water respectively to some –OH groups that are bond to the surface. The same asymmetry was found for example in sputtered and doped TiO_2 films [4]. In the thin film this feature is present more clearly indicating a higher amount of adsorbed water or –OH groups despite both samples had to undergo the same annealing step in ambient air.

The valence band spectra presented in Fig. 2 also show some differences between both samples. In the single crystal the intensity of the valence band feature at lower binding energy (–4.8 eV) is higher than that from the feature at high binding energy (–7.5 eV). In the thin film, both features have almost the same intensity. The high energy feature is found at –6.8 eV instead of –7.5 eV in the single crystal. Additionally, the valence band edge is more clearly pronounced in case of the thin film while it seems to be more smoothed out in the other spectrum.

Finally, XAS is used to identify the phase of the TiO_2 thin film (Fig. 3). The XAS spectrum of the single crystal shows the typical shape of the rutile modification of TiO_2 [1]. In the corresponding spectrum of the thin film again significant
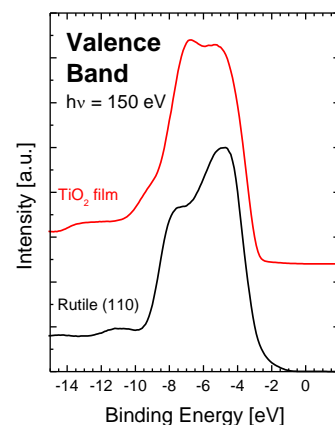
Fig. 2 Valence band photo-emission spectra of Rutile(110) single crystal and TiO_2 thin film ($h\nu = 150$ eV).
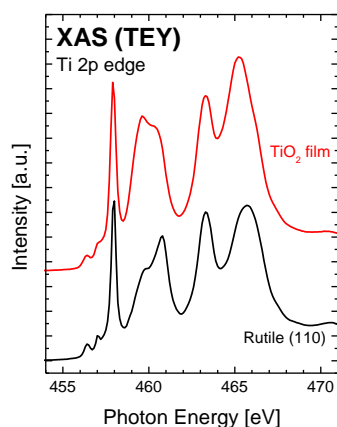
Fig. 3 XAS spectra of single crystal and thin film measured at Ti 2p edge in TEY mode.

differences are present. The first feature appears at the same excitation energy of 458 eV in both spectra. It represents the transitions from Ti 2p to Ti 3d states with a t_{2g} symmetry in the octahedral crystal field of the O^{2-} ions [1]. The features at higher excitation energies differ only in the spectral shape, but the energie positions are the same. Comparison with reference data [1] indicates that the thin film is composed from a mixture of rutile and. The temperature during the annealing and oxidation step in ambient air should be high enough for the transition from anatase to rutile, but most likely the time is to short to fully convert the film to rutile.

The next step is measurement of resonant photoemission spectra which means that a set of valence band spectra is aquired with photon energies around the Ti 2p absorption edge, which in principle means that it is energy resolved XAS. The representation of the obtained data is shown in Fig. 4. Vertical cross sections i.e. at fixed excitation energies represent valence band spectra (EDC curves). Horizontal cross sections are constant initial state (CIS) spectra that represent the intensity of a photoemission line as a function of the excitation energy. Electrons with a fixed kinetic energy (constant final sate, CFS) appear under an angle of 45°. Low intensity is represented by blue color, high intensity is represented by red, white represents regions where the intensity is cut off. The diagonal lines from top left to low right that are observed in the gap region are due to Ti 2p lines that are excited by the 2nd order of the monochromator.

We focus on the region from 0 eV to –20 eV binding energy. In case of the single crystal (Fig. 4, left panel) we only observe the 2nd order contribution in the band gap region but no resonance from any gap states. In contrast to that, we observe a resonance from the valence band i.e. the signal intensity increases when the Ti 2p edge is reached. Similar to the results from the valence band spectra above, we also observe that the band edge which is smoothed out in the single crystal spectra. Additionally, a new feature between –10 eV and –15 eV appears when the Ti 2p absorption edge at 458 eV photon energy is reached. As this feature continues under an angle of 45°, an Auger-like character has to be assumed. The kinetic energy corresponds to that of the Ti LVV respectively Ti 2p3d3d Auger. In case of the thin film (Fig. 4, right panel) the same Auger-like feature is observed, but differences ar present
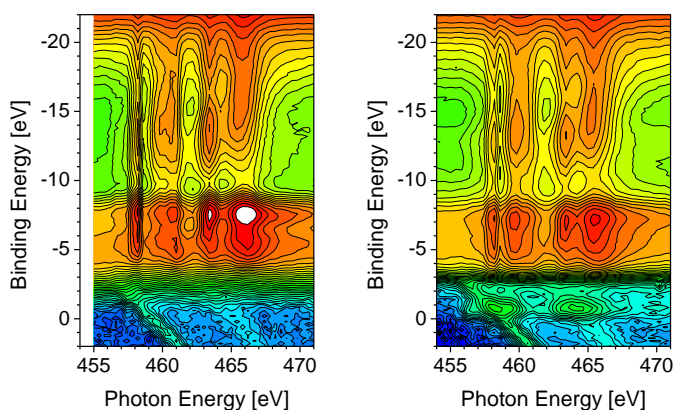
Fig. 4 Datasets of valence band spectra excited with photon energies around the Ti 2p absorption edge for Rutile single crystal (left panel) and TiO_2 thin film (right panel). The intensity is color coded (blue = low, red = high, white = cut off) on a logarithmic scale.

as well. One contrast is the appearance of a resonance in the band gap region which can be clearly distinguished from the pure influence of the 2nd order light observed in case of the single crystal. The gap state appears at a binding energy of around –0.8 eV. In the references, this feature is found around –1 eV [1, 7]. It is attributed to occupied Ti 3d states in the gap region due to some oxygen deficiency which is not observed in the photoemission from the core levels or the valence band. However, the more striking result is the presence of the Ti 2p3d3d related Auger line. During XAS process an electron from the Ti 2p core level is excited to an empty Ti 3d state. This excited state decays via a spectator channel which means that the excited electron remains in a Ti 3d state and does not participate in the de-excitation process. It can be described as follows:

$$2p^6\ [3d^2L^2] + h\upsilon\ \rightarrow 2p^5\ [3d^2L^2]^{e^-}\ \xrightarrow{Spectator}\ 2p^6\ [3d^0L^2]^{e^-}\ +\ e^-\ Auger$$
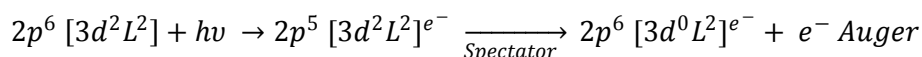
The described process requires two electrons in Ti 3d states with two ligand holes which is a contradiction to the nominal $3d^0$ configuration in TiO_2. This can be interpreted as a reflection of the covalent bonding properties in TiO_2. As this is observed in the single crystal as well as in the thin film, a relation to the gap states can be excluded.

4. Summary

The comparative studies presented here show that although we come close to stoichiometry in the thin film i.e. no gap states or Ti^{3+} contributions are observed in normal photoemission, the spectra at resonance reveal the presence of defects with Ti 3d character. The step from studies of single crystals towards thin films allows studies of such systems under more realistic conditions that are closer to application than the single crystalline model substances.

5. References

[1] U. Diebold, Surf. Sci. Rep. 48 (2003) 53-229
[2] Y. Shao et al., Langmuir 10 (1994) 178
[3] F. Morales et al., BESSY Annual Report 2007 249 and references therein
[4] J. Domaradzki et al., Vacuum 82 (2008) 1007-1012
[5] P.C. Maness et al., Appl. Environ. Microbiol. 65 (1999) 4094
[6] M. Della Negra et al., Surf. Sci. 540 (2003) 117
[7] A.G. Thomas et al., Phys. Rev. B 67, 035110 (2003)

IN-SITU STUDY OF THE ATOMIC LAYER DEPOSITION OF HfO$_2$

Massimo Tallarida, Konstantin Karavaev, and Dieter Schmeisser

Brandenburgische Technische Universität, Cottbus

Abstract

We studied the atomic layer deposition of HfO$_2$ by means of core level and valence band photoemission at the beamline U49/2-PGM2. Our novel approach, making use of a self-made ALD reactor attached to the UHV measurement chamber, permitted us to study the HfO$_2$ growth after each ALD cycle avoiding the contamination of the thin film and determining its electronic properties as a function of the film thickness. The in-situ investigations, revealed the influence of the Hf-precursor and its reactivity to water on the electrical properties of the interfaces Si/SiO$_2$/HfO$_2$. For these experiments we used HfCl$_4$ and tetrakis-di-methyl-amino-Hf (TDMAHf) as Hf-precursors and water as oxygen source. We determined the role of the Cl contamination on the valence band offset present at the Si/SiO$_2$ interface after the growth of HfO$_2$. The presence of Cl in that interface was due to the reduced reactivity of the chemisorbed HfCl$_4$ species to H$_2$O. We also observed the abrupt change in the valence band offset as the HfO$_2$ film reached the thickness of 2 complete layers.

Introduction

Atomic layer deposition (ALD) is the most promising industrial method for growing conformal thin films of high-k oxides [1]. Hafnium oxide (HfO$_2$) is probably the most important high-k material for future Si-based nanotechnology.
The ALD of HfO$_2$ consists in the chemisorption of the metal precursor onto the substrate and its consequent hydrolysis. The two steps are separated by the introduction of a purging inert gas, which is needed to remove the non-reacted molecules of the metal precursor and the byproduct of the reacted molecules. In this way, with the introduction of the oxygen source, the reactions take place only at the surface of the substrate, avoiding the CVD growth.

We investigated the ALD of HfO$_2$ in-situ, measuring XPS and XAS spectra just after each complete cycle (metal precursor+H$_2$O) looking at the chemical and physical properties of the just formed HfO$_2$. For understanding the role of the high-k material in the total gate stack (gate oxide+gate metal) we started studying the role of the metal precursor in the valence band offset between the high-k material and the Si substrate. As already known, during the growth of HfO$_2$ on Si substrates there is the formation of an interfacial layer made by Si-O bonds. The presence of such layer is often an issue as it reduces the equivalent oxide thickness. Moreover, it could have an influence on the valence band offset between the high-k material and the Si substrate because of the possible interfacial dipole [2]. We studied the valence band offset using our in-situ set-up. With respect to the ex situ experiments, our procedure gives the possibility to follow the electronic properties of the semiconductor-interfacial oxide-High-k oxide during the formation of the first layers of the high-k material, without the introduction of external contaminations.

Experimental set up

We used two different Hf precursors: HfCl$_4$ and tetrakis-di-methyl-amino-Hf (TDMAHf). As oxygen source we used in both cases H$_2$O. The purging gas was N$_2$ in both cases. The

pressure reached during the introduction of $HfCl_4$ was $2x10^{-5}$mbar, as this precursor has a very small volatility and the heating of the Hf-precursor at about 150-170°C was necessary in order to reach reasonable vapor pressures. The more volatile TDMAHf was heated to only 60°C, reaching a pressure during the Hf-precursor of about 10^{-2}mBar. The pressure during the H_2O introduction was $2x10^{-2}$mbar. The pulse time for the $HfCl_4$ step was of 6 minutes, while that of TDMAHf was only 0.5seconds. This difference is due to the different vapor pressures of the two precursors. As ALD is supposed to work in saturation conditions, the different pulse time assured almost the same quantity of Hf-precursor. The pulse times of H_2O were 20s. in the case of $HfCl_4$ and 0.5s. in the case of TDMAHf. Also the purging times were different in the two cases: 2minutes for the $HfCl_4$-based ALD and 1second in the TDMAHf-based ALD. The different times were due to the different reactor geometry used in the two experiments that allowed the decrease of N_2 and H_2O exposure maintaining the same quality of the ALD films.

The photoemission experiments were all performed at the synchrotron source BESSY in Berlin, at the beamline U49/2. The synchrotron light permits to achieve high photon intensity and high resolution in a wide range of energy, leading to a high surface sensitivity of the photoemission experiments, much higher compared to the usual Al K-α lab source. This is important because the films we are interested in are of the order of less than to a few nanometers.

Experimental results I ($HfCl_4$+H_2O)

In fig. 1 we show the Si2p spectra measured at 150eV. It is possible to observe the spin-orbit splitting of the substrate related (Si^0) component of the Si2p at about 99.6eV, which is about 0.6eV. Also the intermediate oxidation components (Si^{+1}, Si^{+2}, and Si^{+3}) can be observed at binding energies between 100eV and 103eV, while the stoichiometric SiO_2 component is detected at about 103.5eV. All features present in this figure shift in binding energy as the ALD of HfO_2 proceeds. To analyze those shifts we performed a multi-peak fit. The result of that fit for the Si substrate is presented in figure 2. In figure 3 the binding energies of all components forming the Si2p spectra are depicted for each ALD cycle.

The binding energies shown in figure 3 are referred to the valence band maxima of the corresponding ALD cycle. These are found to shift, as it can be observed in figure 4. From the binding energies of the various components and the valence band maxima we could determine the valence band offset changes during the formation of the first two layers of HfO_2, as shown in figure 5.
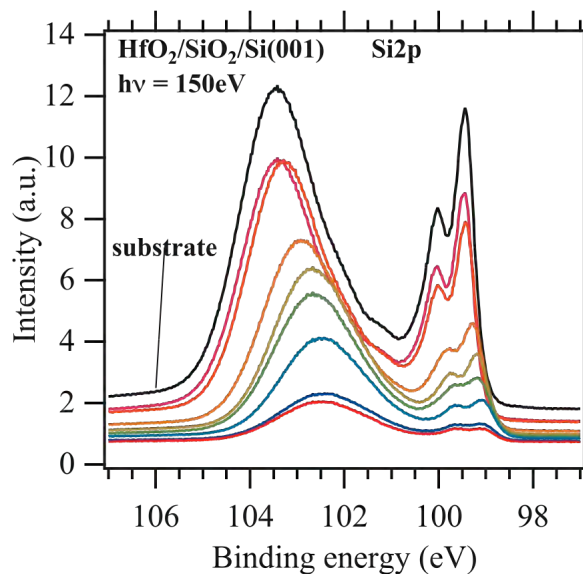
Figure 1: Si2p spectra of the Si substrate and after each (HfCl₄+H₂O) ALD cycle. All features shift in binding energy as the ALD proceeds. The intensity decrease is due to the coverage of the Si substrate by HfO₂.
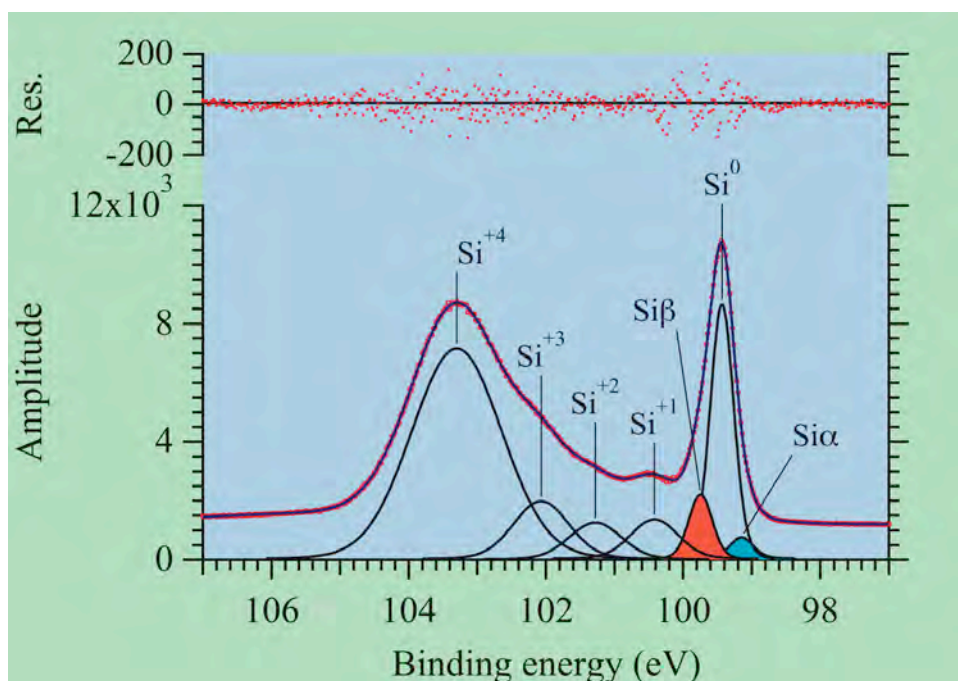
Figure 2: Fit of the Si2p spectrum of the substrate before ALD using Voigt functions. The Si^0 component represents the bulk Si, the $Si^{+1 \div +4}$ all oxidation states of Si. The Siβ and Siα are due to Si-Si bonds at the interface with the Si-oxide.
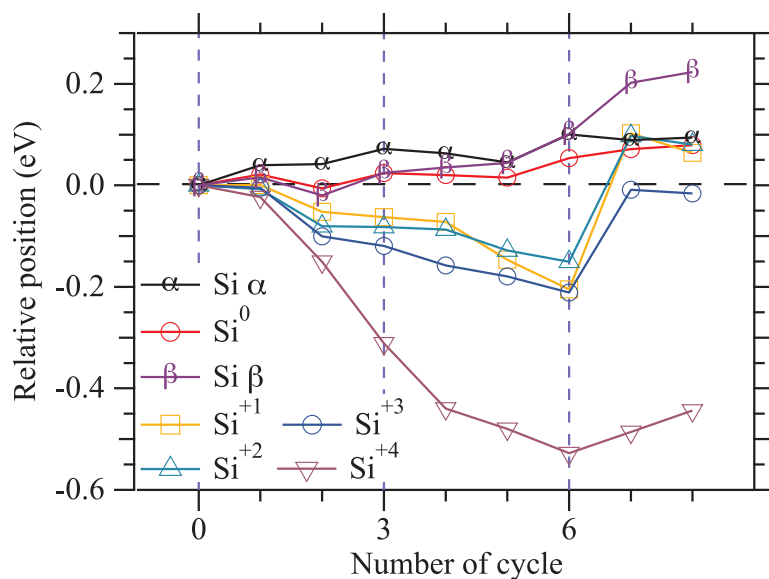
Figure 3: Binding energy of each Si2p component after each ALD cycle. The reference positions are those of the substrate (cycle 0).
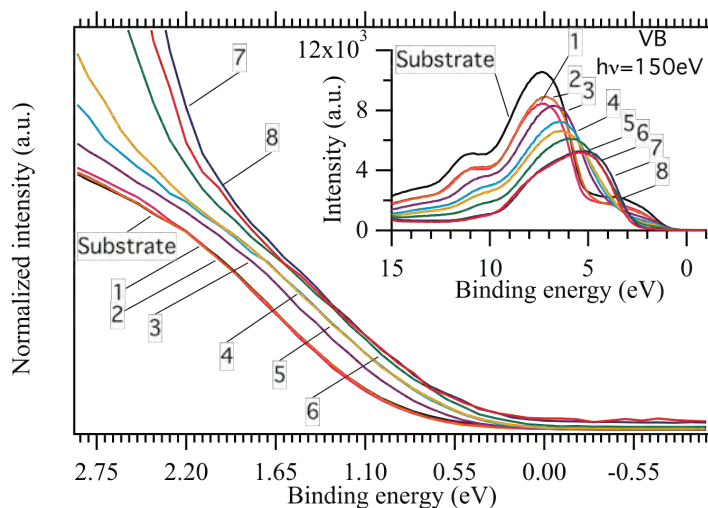
Figure 4: Valence band spectra for the substrate and after each ALD cycle. The binding energy region is limited to the valence band maximum (VBM). A larger range of the same spectra is shown in the inset. In order to determine the shift of the VBM the spectra were normalized to the same slope near the maxima.
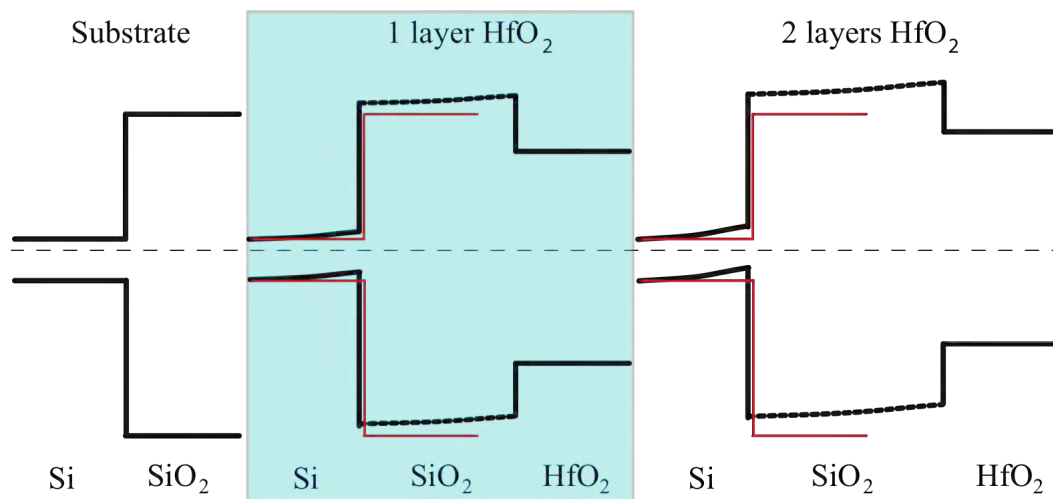
Figure 5: Valence band offset determined from the binding energy of the Si2p components and the HfO$_2$-related component in the O1s and Hf4f spectra (not shown).

Experimental results II (TDMAHf+H$_2$O)

In figure 6 we show the results of in-situ experiments using TDMAHf as Hf-precursor. Similarly as in the case of HfCl$_4$ we measured the Si2p spectra before starting the ALD and after each cycle. Anyway, for clarity we show only the spectra after each 2 cycles. Similarly to the HfCl$_4$ ALD, the Si2p components related to the oxidized Si shift as the ALD proceeds, but clearly, the substrate-related components do not shift. Moreover, the Siα component in this case is very strong compared to the ALD with HfCl$_4$.
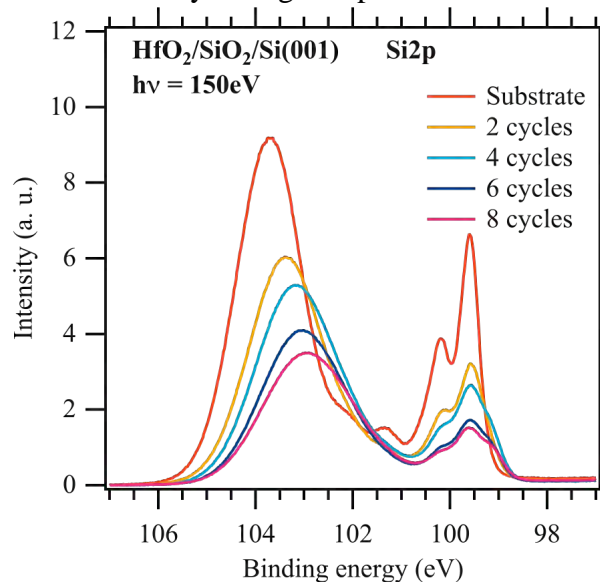
Figure 6: Si2p spectra of the substrate and after each 2 (TDMAHf+H$_2$O)-ALD cycles. The Si$^{+1\div+4}$ components shift as in the case of HfCl$_4$-based ALD, while the substrate-related components behave in a different way: The bulk component does not shift, but the Sia component becomes very strong.

Discussion

We compared the behavior of the Si2p spectra after each ALD cycle for two different Hf-precursors. From the intensity attenuation of the substrate-related components (Si^0, Sia, and Sib) we could determine the growth rate per cycle (GPC) to be very similar on both cases, and, more precisely, to be 0.33layer/cycle and 0.25layer/cycle, respectively. In both cases we

observed the shift of the oxidized components of Si, while only when using $HfCl_4$ we observed a shift of the bulk Si component and of the VBM. For the ALD of HfO_2 with $HfCl_4$ we also observed the presence of a large quantity of Cl contamination (not shown) [3, 4]. The use of a different precursor not containing Cl reveals the importance of that contamination to the electronic properties of HfO_2. The chemical formula of TDMAHf is in fact $Hf(N(CH_3)_2)_4$, the methyl groups are bond to N, each nitrogen is bond to Hf. The possible contaminations are due to the decomposition of the CH_3 groups and the formation of Si-C-type bonds. Anyway, from the measurement of the C1s before ALD and after each cycle we didn't detect any increase of the C1s intensity. Also the N1s intensity did not change during the ALD. This result shows that the band bending observed in the ALD with $HfCl_4$ was due to the presence of Cl species at the Si-SiO_2 interface. Anyway, the shift at the SiO_2/HfO_2 was not affected by the presence of Cl. From this result it can be concluded that the chemistry governing the ALD of HfO_2 does not influence the SiO_2/HfO_2 interface, but it may induce a band bending at the Si/SiO_2 interface that can change the total electrical behavior, in fact the valence band offset between the substrate and the high-k material results increased when an extra band bending is present in the substrate. The shift of the Si^{+4} component shows also the presence of a charge near the SiO_2/HfO_2, inducing the shift towards lower binding energy. This could be due to the interfacial dipole between the two oxides. The formation of the interfacial dipole was predicted by Robertson [2] and was attributed to the different charge neutralization level (CNL) of the two oxides. Here we can see how the dipole at the SiO_2/HfO_2 interface grows with the growth of HfO_2, gaining an insight into the electronic nature of that dipole. In fact, as the HfO_2 grows and attains its bulk properties the CNL also changes, reaching the bulk level with the completion of two HfO_2 layers. Only at this point the interfacial layer reaches its stable value.

Conclusions

Finally, we could compare the chemical-physical properties of the material for different chemicals used in the ADL reactions. We observed a similar behavior in the oxidized components of Si2p spectra, while the substrate-related components behaved differently depending on the ALD chemistry. In particular, the role of Cl contamination on the valence band offset between HfO_2 and Si could be evidenced. This result is important to correctly interpret the spectra after the final formation of the gate stack with the coverage of the high-k oxide with the gate metal and to determine the correct work function of the high-k material.

References

1) M. Leskelä, M. Ritala, Thin Solid Films **409**, 138 (2002);
2) J. Robertson, Eur. Phys. J. Appl. Phys. **28**, 265 (2004);
3) M. Tallarida, K. Karavaev, and D. Schmeisser, J. Appl. Phys. **104**, 064116 (2008);
4) M. Tallarida, K. Karavaev, and D. Schmeisser, JVST B, **27**, 300 (2009).

Profiling the interface electron gas of LaAlO$_3$/SrTiO$_3$ heterostructures by hard X-ray photoelectron spectroscopy

G. Berner,[1] M. Sing,[1] K. Goß,[1] A. Müller,[1] A. Ruff,[1] A. Wetscherek,[1] S. Thiel,[2] J. Mannhart,[2] S. A. Pauli,[3] C. W. Schneider,[3] P. R. Willmott,[3] M. Gorgoi,[4] F. Schäfers,[4] and R. Claessen[1]

[1]*Experimentelle Physik 4, Universität Würzburg, Am Hubland, D-97074 Würzburg, Germany*
[2]*Institute of Physics, Universität Augsburg, Electronic Correlations and Magnetism, Experimentalphysik VI, Universitätsstrasse 1, D-86135 Augsburg, Germany*
[3]*Paul Scherrer Institut, CH-5232 Villigen, Switzerland*
[4]*Berliner Elektronenspeicherring-Gesellschaft für Synchrotronstrahlung m.b.H., Albert-Einstein-Str. 15, D-12489 Berlin, Germany*

Novel phases with often unexpected electronic and magnetic properties may form at the interfaces of epitaxial heterostructures made out of complex insulating oxides. A case in point is LaAlO$_3$ (LAO) on TiO$_2$-terminated SrTiO$_3$ (STO), for which a metallic interface state was found at room temperature (RT) [1]. While two-dimensional (2D) superconducting behavior below 200mK [2, 3] and indications of ferromagnetism below 1K [4] have been reported, the origin and nature of the metallic state have been matter of intense debate [1, 2, 4–13]. The metallic state could be either of extrinsic origin, i.e., due to effective n-doping by oxygen vacancies, or be intrinsic, i.e., owing to electronic reconstruction. In the latter case, the polar structure of LAO with alternating (LaO)+ and (AlO$_2$)− planes leads to a monotonically increasing potential with increasing number of monolayers [5]. To avoid this polar catastrophe, in the most simple picture half an electron charge per 2D unit cell is transferred to the interface [14], corresponding to a sheet carrier density $n_{2D} \approx 3.4 \times 10^{14}$ cm^{-2}. However, depending on sample growing conditions, in particular the oxygen partial pressure during deposition, experimentally determined sheet carrier densities of ~10^{13}–10^{17}cm^{-2} [4, 8, 10, 13, 15] have been measured. Likewise, considerable efforts have been made to determine the thickness of the conducting layer. Values between 7nm and 600μm were found [2, 5, 9, 10, 13, 16]. Unfortunately, simultaneous information on layer thickness and charge carrier concentration is scarce [2, 10, 13].

LAO/STO heterostructures have been grown by pulsed laser deposition (PLD) on TiO$_2$ terminated (001) STO surfaces. One set of samples — with 2, 4, 5, 6 unit cell (uc) thick LAO overlayers — was grown at the University of Augsburg as described elsewhere [8]. Here we only point out that after deposition in an O$_2$ atmosphere of 2×10^{-5}mbar around 800°C these samples were cooled to RT in 400mbar of O$_2$ with an extra one hour oxidation step at 600°C (hence these samples are denoted "annealed" throughout this report) in order to avoid oxygen vacancies. The other sample is 5uc thick and was prepared at the Paul Scherrer Institute under 5×10^{-6}mbar of O$_2$ and otherwise similar conditions, but without a particular oxidation treatment ("not-annealed"). In addition, a commercial undoped STO single crystal was measured as reference.

Hard X-ray photoemission was performed at beamline KMC-1 [17] of BESSY using the HIKE endstation. The total energy resolution using 3keV photons amounted to ≈500meV. Binding energies were calibrated with reference to the Au 4f core-level at 84.0eV. Due to the large probing depth no particular surface preparation was necessary. The annealed 4uc sample has been contacted as described in Ref. 8 and allowed for *in situ* conductivity measurements. All data was recorded at RT and is normalized to the background intensity at higher binding energies or, equivalently, to equal integrated intensity.
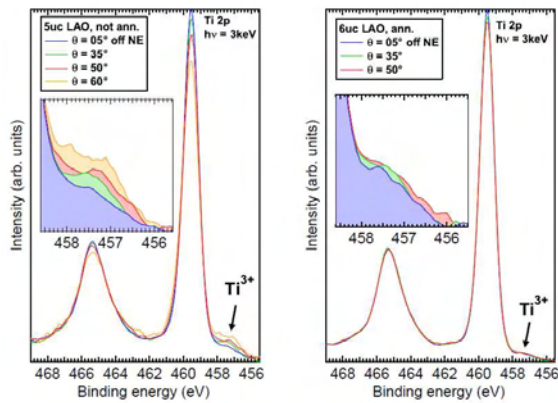
Fig. 1: Ti 2p spectra of two different LAO/STO samples as function of photoelectron emission angle θ. The Ti^{3+} signal is a direct manifestation of the Ti 3d charge in the interface.

In Fig. 1, HAXPES spectra are presented of the Ti 2p doublet at different emission angles θ with respect to the surface normal (normal emission – NE). The data sets were recorded on not-annealed (left panel) and annealed (right panel) samples exhibiting an interface 2DEG. The low spectral weight at the lower binding energy side of the main line, detailed in the insets of Fig. 1, can be attributed to emission from the 2p level of Ti^{3+} as evidenced by its energetic shift of 2.2eV. Thus it represents a direct manifestation of additional electrons hosted in the otherwise empty 3d shell of Ti^{4+} in STO. No anomalies could be seen in any other core-level spectra (not shown), indicating that essentially all extra electrons reside on the Ti sites. Going to larger emission angles the Ti^{3+} signal increases in relation to the Ti^{4+} main line, which corresponds to a decrease in the effective electron escape depth as $\lambda_{eff} = \lambda \cdot \cos\theta$ (see Fig. 2).

For a more quantitative analysis we use the following simple model (cf. Fig. 2): The 2DEG extends from the
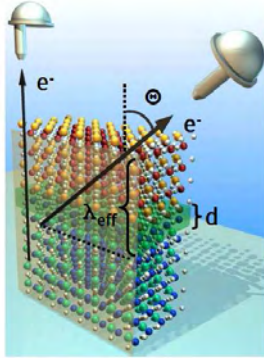
Fig. 2: Schematic illustrating depth profiling by angle-dependent HAXPES.

interface to a depth d into the STO substrate. The interface region is stoichiometric and characterized by a constant fraction p of Ti^{3+} ions per unit cell. Taking into account the exponential damping factor $e^{-z/\lambda_{eff}}$ for photoelectrons created in depth z one can easily calculate the ratio of Ti^{3+} to Ti^{4+} signal as a function of emission angle θ:

$$\frac{I(3+)}{I(4+)} = \frac{p(1-\exp(-d/\lambda\cos\theta)}{1-p(1-\exp(-d/\lambda\cos(\theta))} \quad (1)$$

Note that in Eq. 1 p and d are not independent. The electron escape depth λ in STO was fixed to 40Å according to the NIST database [18]. The analysis shows that the 2DEG thickness amounts to only a few STO unit cells. The carrier concentration is far below the expected 0.5 e^- per 2D unit cell derived from simple electrostatics. There is even a clear trend discernible of the 2DEG being confined to only 1 uc.

A qualitative comparison of various samples and bare STO based on their Ti $2p_{3/2}$ spectra (left panel) and their Ti^{3+}-related part (right panel) are shown in Fig. 3. All spectra were measured at an emission angle of 50° which represents the best compromise between data statistics and interface sensitivity. The bare STO substrate shows no sign of Ti^{3+}-related spectral weight, while there is small but finite weight discernible for the annealed sample with 2uc LAO. The Ti^{3+} intensity steadily increases with the number of LAO overlayers for annealed samples and reaches a maximum for the non annealed 5uc sample indicating the importance of growth conditions for the interface charge carrier concentration.

It is noteworthy that the 2uc sample exhibits finite charge carrier concentration, although from transport it is insulating [8]. The finite charge density is in line with *in situ* conductivity measurements on a 4uc sample which shows a sharp increase by roughly a factor of two upon X-ray exposure. After switching the X-rays off, the conductivity relaxes with a time constant of several hours. Interestingly, the bare STO substrate does not show any sizeable Ti^{3+} spectral weight indicating that the LAO/STO interface is important to collect the mobile amount of photogenerated electrons.
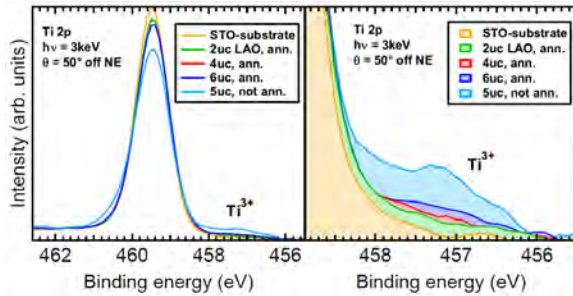
Fig. 3: Ti $2p$ spectra at fixed emission angle ($\theta = 50°$) of various samples with respect to LAO thickness and preparation conditions plus bare STO.

To extract total charge carrier concentrations n_{2D} one has to divide $p\cdot d$ as obtained from the best fit curves by a^2, where a is the STO lattice constant. The resulting values for n_{2D} are in the same order of magnitude, as described in [8], but show a gradual increase corresponding to the increase of numbers of LAO overlayers, at variance with Hall measurements. A jump at a critical thickness of 4uc is observed followed by a plateau reaching up to 15uc [8]. This discrepancy could be due to the fact that the photogenerated charge carrier contribution is not constant, since with increasing LAO thickness and concomitant increasing electric potential more electrons photoexcited to trap states are released. The non annealed sample shows a high charge carrier density. Extrinsic doping by oxygen vacancies could be an explanation.

References:

[1] A. Ohtomo and H. Y. Hwang, Nature 427, 423 (2004). (2008).

[2] N. Reyren *et al.*, Science 317, 1196 (2007).

[3] A. D. Caviglia *et al.*, Nature 456, 624 (2008).

[4] A. Brinkman *et al.*, Nat. Mater. 6, 493 (2007).

[5] N. Nakagawa *et al.*, Nat. Mater. 5, 204 (2006).

[6] M. Huijben *et al.*, Nat. Mater. 5, 556 (2006).

[7] R. Pentcheva and W. E. Pickett, Phys. Rev. B 74, 035112 (2006).

[8] S. Thiel *et al.*, Science 313, 1942 (2006).

[9] G. Herranz *et al.*, Phys. Rev. Lett. 98, 216803 (2007).

[10] W. Siemons *et al.*, Phys. Rev. Lett. 98, 196802 (2007).

[11] V. Vonk *et al.*, Phys. Rev. B 75, 235417 (2007).

[12] K. Yoshimatsu *et al.*, Phys. Rev. Lett. 101, 026802.

[13] M. Basletic *et al.*, Nat. Mater. 7, 621 (2008).

[14] C. Noguera, J. Phys.: Condens. Matter 12, R367 (2000).

[15] A. Kalabukhov *et al.*, Phys. Rev. B 75, 121404(R) (2007).

[16] P. R. Willmott *et al.*, Phys. Rev. Lett. 99, 155502 (2007).

[17] F. Schäfers *et al.*, Rev. Sci. Instrum. 78, 123102 (2007).

[18] NIST Standard Reference Database 71, Ver. 1.1, http://www.nist.gov/srd/nist71.htm.

Electronic structure of autoassembled TCNQ molecules deposited on Cu (100)

C. Urban[b], I. Preda[a], G. Domínguez-Cañizares[a], D. Díaz-Fernández[a], A. Vollmer[d], A. Gutiérrez[a], D. Ecija[b], M. Trelka[b], R. Otero[b,c], J.M. Gallego[e], L. Soriano[a] and R. Miranda[b,c]

[a] *Departamento de Física Aplicada e Instituto de Ciencia de Materiales Nicolás Cabrera, Universidad Autónoma de Madrid, 28049 Madrid, Spain*
[b] *Departamento de Física de la Materia Condensada e Instituto de Ciencia de Materiales Nicolás Cabrera, Universidad Autónoma de Madrid, 28049 Madrid, Spain*
[c] *IMDEA-Nanociencia, 28049 Madrid, Spain*
[d] *BESSY GmbH, Albert-Einstein-Strasse 15, 12489 Berlin, Germany*
[e] *ICMM-CSIC, 28049 madrid, Spain*
[*] Corresponding author: l.soriano@uam.es

The main purpose of this project is the study of the electronic structure of TCNQ organic molecules deposited on a clean Cu (100) surface. These molecules are characterized by their electronic properties, being electron acceptor.[1] It is known that when deposited on a Cu (100) surface, these molecules become autoassembled [2] (Fig.1) however the electronic interaction of these
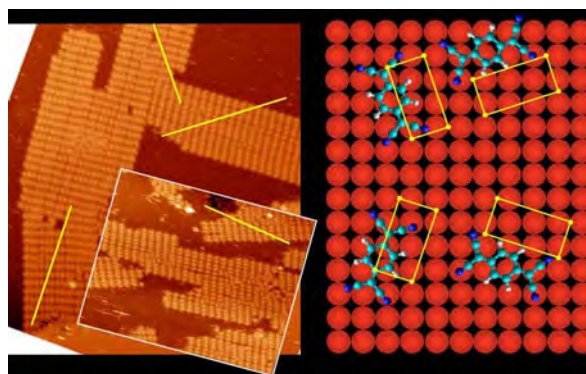
Fig. 1: STM images and orientation derived model of TCNQ/Cu (100).

molecules with the substrate is an important topic that is not yet understood. We present preliminary results on this system obtained by X-ray absorption (XAS) and X-ray photoemission (PES) spectroscopies at the PM4 beamline at BESSY.

The C 1s x-ray absorption spectra at normal incidence of the TCNQ/Cu (100) surface as a function of the coverage are shown in Fig.2. The spectra are also compared to those obtained by Fraxedas et al[3] for bulk TCNQ. According to the assignments made by these authors, the main peak of both, C 1s and N 1s spectra, which are derived from the

Fig. 2: C 1s and N 1s XAS spectra at normal incidence as a function of the coverage

CN groups of the TCNQ molecule, are broadened with respect to those of the bulk molecule. This seems to indicate, as expected, a significant charge transfer from the Cu substrate to the TCNQ molecule.

This is also confirmed by angle dependent XAS spectra at the N 1s edge for a coverage of 0.5 ML shown in Fig. 3. Indeed, the broad peak assigned to the CN groups changes its intensity with the incidence angle. This is consistent with the splitting of these levels due to the charge transfer in the direction towards the Cu substrate.

Fig. 3: N 1s XAS spectra for 0.5 ML TCNQ/Cu (100) as a function of the incident angle

The photoemission C1s and N 1s spectra of the TCNQ molecule as a function of the coverage are presented in Fig. 4. The spectra have been normalized for comparison purposes. For the C 1s
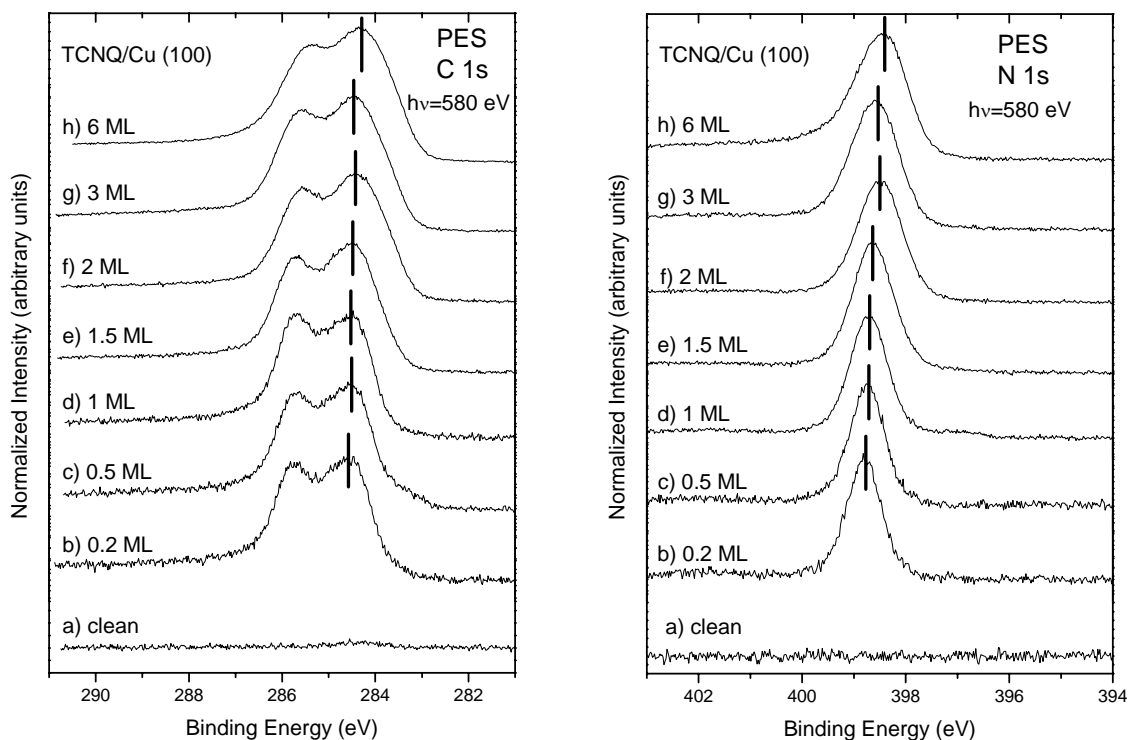
Fig. 4: C 1s and N 1s photoemission spectra of TCNQ molecules deposited on a Cu (100) substrate as a function of the coverage

spectra, they are formed by two different clearly observable peaks and a third peak hidden in between them. This agrees with the three different C atoms present in the TCNQ molecule,

i.e, benzoic ring, CN groups and intermediate C atoms. The higher binding energy peak, which is associated to the CN groups, is progressively shifting towards lower binding energies as the coverage increases. This is also consistent with the charge transfer produced from the Cu substrate to the CN groups. The above results are also corroborated by the N 1s XPS spectra shown in Fig.4. In this case, the spectra are formed by a single peak, as corresponds to the only N position in the TCNQ molecule. It can also be seen a similar shift towards lower binding energies of the peak as the coverage increases.

Finally, we have also measured the work function of the analyzed surface as a function of the coverage. The results are presented in Fig. 5. As the coverage increases up to 2 ML, the work function increases linearly from 4.5 to 5.05 eV. Then it remains almost constant for further depositions. This is again in agreement with the charge transfer produced from the Cu substrate to the first monolayer. Further coverages do not produce any significant change of the work function indicating that upon addition of the upper TCNQ monolayers the molecules do not receive any extra charge from the substrate.
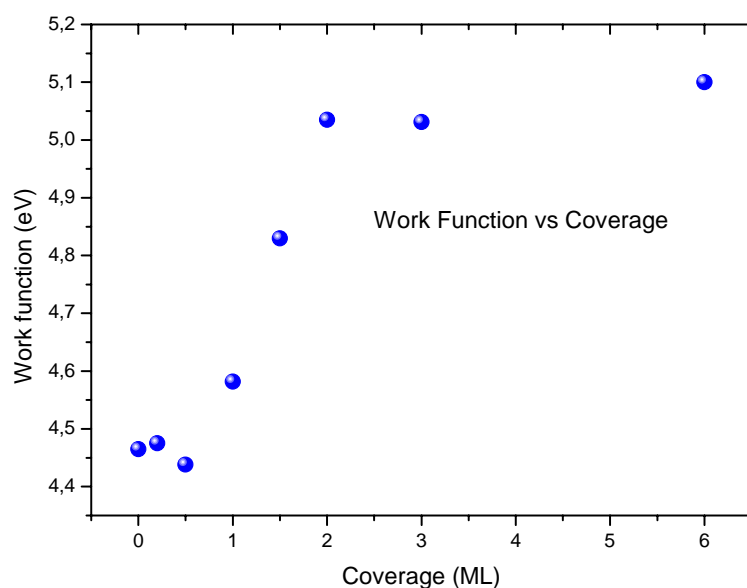
Fig. 5: Work function of the TCNQ/Cu (100) surface as a function of the TCNQ coverage.

References:

[1] Martin, N. et al. J. Org. Chem. **63**, 1268-1279 (1998).

[2] J.M. Gallego et al, unpublished results.

[3] J. Fraxedas, Y. J. Lee, I. Jiménez, R. Gago, R. M. Nieminen, P. Ordejón, E. Canadell, PRB 68, 195115 (2003).

Angle-resolved photoemission studies of Y-AlNiCo(100)

R. Mäder,[1] R. Widmer,[1] O. Gröning,[1] Th. Braun,[2] Yu. S. Dedkov,[2] and K. Horn[2]

[1]*Swiss Federal Laboratories for Materials Testing and Research, Dübendorf, Switzerland*
[2]*Fritz-Haber Institute of the Max-Planck Society, Berlin, Germany*

Quasicrystals and approximants belong to the class of intermetallic compounds known as complex metallic alloys (CMA) [1]. The complex crystallographic structure of CMA is based on highly symmetric clusters (elementary building blocks) which decorate large unit cells, which contain up to thousands atoms. Quasicrystal samples represent the ultimate case where the unit cell can be considered as infinite.

Decagonal quasicrytsls (*d*-QCs) can be structurally considered as a periodic stack of quasiperiodic atomic planes, so that *d*-QCs are two-dimensional quasicrystals, whereas they are periodic crystals in a direction perpendicular to the quasiperiodic planes. This duality makes *d*-QCs especially suitable to study the effect of quasiperiodicity in the physical properties of the material, as a given property can be investigated on the same sample along the quasiperiodic and periodic directions. Experiments report that *d*-QCs exhibit anisotropy in their electrical and thermal transport properties (electrical resistivity, thermoelectric power, Hall coefficient, thermal conductivity, and optical conductivity) when measured along the quasiperiodic and periodic directions. The basic question here is whether the observed anisotropy is a consequence of the quasiperiodic structural order within the 2D atomic layers versus the periodic order in the perpendicular direction or the anisotropy is rather a consequence of complex local atomic order on the scale of near-neighbor atoms with no direct relationship to the quasiperiodicity.

While this question has so far not been answered satisfactorily for the *d*-QCs, the situation is clearer for approximants of the decagonal phase. Approximant phases are characterized by large unit cells, which periodically repeat in space, but the structure of the unit cell closely resembles *d*-QCs. Atomic layers are again stacked periodically and the periodicity lengths along the stacking direction are almost identical to those along the periodic direction of *d*-QCs. Moreover, atomic planes of approximants and *d*-QCs show locally similar quasiperiodic patterns, so that their structures on the scale of near-neighbor atoms closely resemble each other. Decagonal approximants thus offer valid comparison of the physical properties to the *d*-QCs with the advantage that theoretical simulations for the approximants are straightforward to perform, whereas this is not the case for the nonperiodic *d*-QCs.

In this report we present a photoemission study of a single-crystalline complex metallic alloy $Al_{13-x}(Co_{1-y}Ni_y)_4$, also known as the Y-Al-Ni-Co phase, which is a monoclinic approximant of the decagonal phase with two atomic layers within one periodic unit along the stacking direction and a relatively small unit cell, comprising 32 atoms. The measurements of the anisotropy in Y-AlNiCo thus allow comparison of this simple decagonal approximant to the $Al_4(Cr,Fe)$ phase, a decagonal approximant with a considerably higher structural complexity. Moreover, Y-AlNiCo allows comparison to the closely related *d*-Al-Ni-Co quasicrystal.
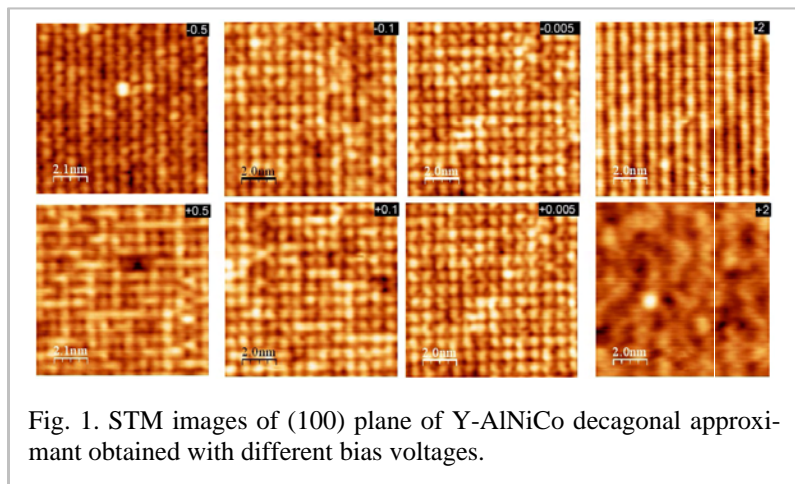
Fig. 1. STM images of (100) plane of Y-AlNiCo decagonal approximant obtained with different bias voltages.

Fig. 1 shows an STM images of the Y-AlNiCo(100) surface. These images were obtained at different bias voltages and demonstrate strong variation of the conducting map depending on the applied voltage. These changes can be understood on the basis of the existing band structure calculations [3] as probing different valence band states in the vicinity of the Fermi level.

Angle-resolved photoemission studies of Y-AlNiCo(100) were performed at the UE56/1-SGM beamline with a display-type energy analyzer SPECS PHOIBOS 100. Spectra were collected in the wide-angle-mode at a photon energy of $h\nu = 100$ eV and a temperature of the sample of about $T = 120$ K yielding an energy reso-

Fig. 2. (a) Fermi surface of Y-AlNiCo in the first Brillouin zone, calculated ab initio for the structural model of Zhang *et al.* [4]. (b) Fermi surface cut measured for the freshly prepared Y-AlNiCo(100) surface. Experiments were performed at the temperature of $T = 120$ K with photon energy of $h\nu = 100$ eV. The yellow rectangular marks the surface projection of the first Brillouin zone.

lution of about 50 meV. The sample was oriented in a way that the *E*-vector of the synchrotron radiation was along the b^*-vector of the reciprocal lattice of Y-AlNiCo (see Fig. 2). Surfaces of the Y-AlNiCo(100) crystal were cleaned by repeated cycles of Ar^+-sputtering and annealing until sharp LEED spots were obtained demonstrating high structural order of the surface. The cleanness of the sample was checked via monitoring of C 1*s* and O 1*s* core-levels as well as valence band spectroscopy.

The calculated Fermi surface in the first Brillouin zone taken from Ref. [3] is shown in Fig. 2(a). Calculations were based on the Y-AlNiCo structural model proposed by Zhang *et al.* [4]. The Fermi surface is contributed to by 11 bands that cross the Fermi level, resulting in a significant complexity. It is highly anisotropic, explaining the experimentally observed anisotropy in the electrical conductivity.

The Fermi surface of the freshly prepared Y-AlNiCo(100) crystal measured at a photon energy of 100 eV is shown in Fig. 2(b). These data were obtained in the wide-angle-mode (acceptance angle of $\pm15^o$) of the analyzer, allowing to collect the full range of wave vectors in the Brillouin zone at this photon energy. The Fermi surface data were obtained by changing only the tilt-angle (β). The experimental data were found to be in a rather good agreement with the theoretically obtained Fermi surface [Fig. 2(a,b)]. The central rings around the Γ point of the Brillouin zone, as well as nearly flat sheets of the Fermi surface, are clearly resolved in the data. The energy resolved data are quite complex and require an additional analysis which is being performed in a close collaboration with theoretical groups.

References:

1. K. Urban and M. Feuerbacher, J. Non-Cryst. Solids **334&335**, 143 (2004).
2. J. Dolinsek *et al.*, Phys. Rev. B **76**, 174207 (2007).
3. A. Smontara *et al.*, Phys. Rev. B **78**, 104204 (2008).
4. B. Zhang *et al.*, Z. Kristallogr. **210**, 498 (1995).

Structural analysis of epitaxial rare-earth oxides grown on Si(001) and Si(111)

Tatsuro Watahiki, Bernd Jenichen, Roman Shayduk, Wolfgang Braun and Henning Riechert

Paul-Drude-Institut für Festkörperelektronik, Hausvogteiplatz 5-7, D-10117 Berlin, Germany

As a replacement for the conventional gate insulator SiO_2 in metal-oxide-semiconductor field effect transistors (MOSFETs), several high-κ dielectric materials are currently studied. Hf-related oxides offer good performance and are already used in the current CMOS generation. However, the further miniaturization of MOSFETs requires smaller effective oxide thicknesses, and it remains difficult to reduce the SiO_2 interface layer between Si and Hf oxides without adversely affecting the carrier mobility. Rare earth metal oxides, including La_2O_3, Gd_2O_3 and Pr_2O_3, are promising alternative high-κ gate dielectrics for future CMOS technology. Owing to their small lattice mismatch, they can be epitaxially grown on Si(001) and Si(111), which enables us to introduce interface engineering to control the interface structure. We have determined the structure of Gd_2O_3 thin films with in-situ reflection high-energy electron diffraction (RHEED) and grazing-incidence x-ray diffraction (GIXRD) with 10 keV x-rays at our beamline at the synchrotron BESSY in Berlin. The layers are grown on Si(001) and (111) substrates by molecular-beam epitaxy (MBE) using a high-temperature effusion cell for evaporating Gd_2O_3. During growth, an adjustable flux of molecular oxygen is admitted into the growth chamber.

We have investigated the impact of the oxygen partial pressure P_{O2} during growth on the resulting structure. Figure 1 shows the dependence of (a) the intensities of the Gd_2O_3(404) and the silicide peaks in RHEED and (b) the variation of the integrated intensities of Gd_2O_3(040) and silicide peaks in GIXRD with changing P_{O2}. The layers were grown at 650 ^{o}C on Si(001) substrates. By increasing P_{O2} from 2.7×10^{-8} to 5.0×10^{-8} mbar, the integrated intensity of the silicide peak in GIXRD decreases nearly by one order of magnitude but is still clearly detectable. In RHEED, the silicide peak can no longer be resolved. This indicates that the silicide phase forms at the interface. At $P_{O2}=6.5 \times 10^{-8}$ mbar, the silicide peak has disappeared. However, at the same time the increase in P_{O2} leads to a rapid degradation of the crystallinity of the Gd_2O_3. Thus, the structure of the epitaxial Gd_2O_3 strongly depends on P_{O2}.
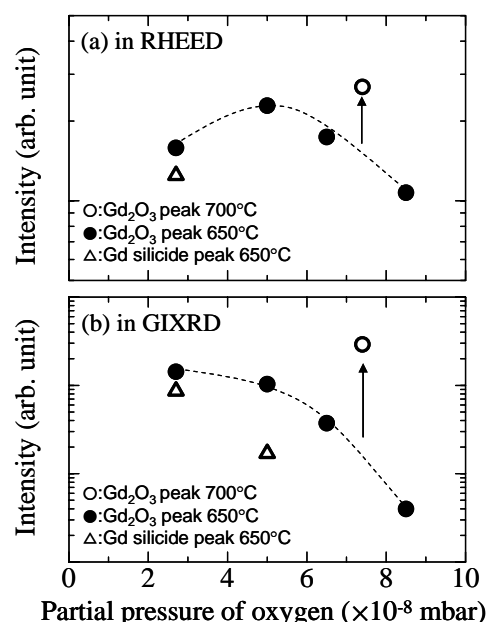
Figure 1. Dependence of (a) the intensity of Gd_2O_3(404) (closed circles) and silicide peaks (open triangles) in RHEED and (b) the integrated intensities of the Gd_2O_3(040) and silicide peaks in GIXRD on P_{O2}. RHEED intensities are measured during growth with oxygen flow and are normalized to the background. The results for layers grown at 700 ^{o}C are shown with open circles. The dashed lines and arrows are guides to the eye.

The presence of oxygen adversely affects the nucleation of the crystalline structure during the initial stage of growth. To enhance the quality of the epitaxial Gd_2O_3 layer, we have increased the substrate temperature to improve the nucleation of Gd_2O_3. From RHEED and GIXRD, it is obvious that the intensity contrast of the diffraction peaks increases by increasing T_{sub} to 700 ^{o}C. Also, no silicide peak is detected by GIXRD. An increase in the substrate temperature therefore enhances the nucleation and the diffusion length of the surface mobile species.

We have also investigated the epitaxial growth of Gd_2O_3 on Si(111). Figure 2 shows the intensity of the RHEED specular spot during growth. The intensity decreases drastically at the intitial stage of growth, probably due to the roughnening of the surface. It then recovers after a few monolayers of growth, indicating a flat surface of the layer. Intensity oscillations are due to layer-by-layer growth. The oscillation period can be deduced from the thickness measured by x-ray reflectivity. It is around 0.3 nm, which agrees well with Gd_2O_3(222) (0.312 nm). The 12 nm thick layer shows a streaky pattern in RHEED, indicating a smooth surface. Figure 3 shows the in-plane x-ray reciprocal space map of a Gd_2O_3 layer

Figure 2. Intensity profile of the specular spot in RHEED for a Gd_2O_3 layer grown on Si(111). T_{sub} and P_{O2} are 700 ^{o}C and 8.0×10^{-8} mbar, respectively.
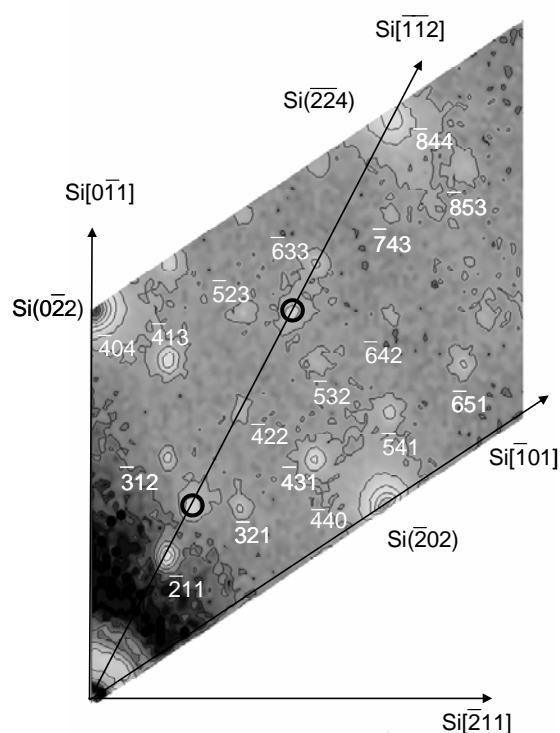
Figure 3. In-plane GIXRD reciprocal space map of the sample shown in figure 2.

grown on Si(111) with a thickness of 7-8 nm. Most of the reflections can be assigned to cubic Gd_2O_3 as shown in Fig. 3. These results show that Gd_2O_3 (111) grows epitaxially on Si(111), but the layer is rotated 60 degree in-plane with respect to the Si(111) substrate. The peaks marked with a circle do not originate from cubic Gd_2O_3. They may be due to an interface structure. Further investigations are necessary to clarify their origin in the Gd_2O_3 (111)/Si(111) system.

Strain dependence of AlN optical properties

C. Cobet, C. Werner, M. Röppischer, N. Esser

ISAS – Institute for Analytical Sciences, Department Berlin, Albert-Einstein-Str. 9, 12489 Berlin, Germany

New light emitting devices for the green, blue, and ultraviolet spectral region are based on wurtzite-nitride heterostructures of InN, GaN, AlN, and their alloys. The single crystalline nitride layers are grown on substrates like SiC or sapphire, which are not lattice matched and differ significantly in their thermal expansion coefficients. A remarkable strain and a high amount of defects is the consequence. Especially, the strain in the active layer has a big influence on the electronic structure and thus influence e.g. the emission wavelength and the efficiency of the light emitting device.

The main aim of our study was a detailed analysis of strain related changes in the dielectric function of AlN by means of synchrotron spectroscopic ellipsometry in the spectral range of electronic excitations. Similar measurements of GaN-bandgap excitons are recently done [Dju02], but there are only a very few other experiments for AlN [Si05], [Dad06]. Theoretical predictions indicated that especially the bandgap excitons of AlN around 6.2eV are very sensitive to strain in the material (Fig.1), which directly influences the emission wavelength and potentially the polarization. But also changes among the higher

Fig. 1: Transition energies of the three band edge excitons calculated for different biaxial strains with the k-p-theory. Due to compressive (tensile) strain, all excitons shift to higher (lower) energies. Furthermore, a band crossing of the two upper most valence bands is found at compressive strain.

interband transitions influence the device properties. According to the Lyddane-Sachs-Teller relation, the refractive index around and below the band gap is hardly affected by this transitions. The measurements were performed with a home made synchrotron ellipsometer setup [Weth98] at the 3m-NIM and the TGM4 beamline at BESSY II. This instrument allows a determination of the real and imaginary part of the dielectric function in the VUV-spectral range, with high spectral resolution (<0.5meV), and in an UHV environment. The later allows surface preparation and low temperature measurements.

In order to study strain depended changes in the optical properties, we have measure the room temperature dielectric function of three (0001) AlN-layers grown by MOCVD on an Al_2O_3 substrate (Fig. 2a) [Re08]. They are grown at 1300, 1400, and 1500°C, respectively. Among these three different samples, a clear shift of the exciton related structures around 6.2eV is observed. AlN excitons reveal a spin-orbit and crystal field

Fig. 2: a) Imaginary part of the dielectric function measured on AlN layers grown on Al$_2$O$_3$ at three different temperatures. b) The observe energy shift of the excitonic features is plotted against growth temperature (dashed lines) in comparison the respective k-p-theory predictions (solid lines).

related splitting of the uppermost valence states at the Γ-point in a Γ_{7+}, Γ_9, and Γ_{7-} band (insertion of Fig.1). The associated excitons FX^B, FX^A, and FX^C are denoted in figure 2a with arrows. The clear overall and relative shift of the three bandgap excitons is induced by an increasing biaxial strain in the AlN layers. Due to a different thermal expansion coefficient of the substrate material ($8.3 \cdot 10^{-6}$ K^{-1}) and AlN ($4.15 \cdot 10^{-6}$ K^{-1}), all these films exhibit an unintentional strain after cooling down from growth temperature. A theoretical prediction within a k-p-theory according to [Chu96] for the strain related shift of the AlN excitons is shown in figure 2b in comparison with the experimental results. The agreement is very good concerning direction and strength of the strain related energy shift. The remaining energy offset could be attributed to the well known bandgap mismatch if quasi particle effects and the exciton binding contribution are not considered in the theoretical calculations.

Figure 3a shows the dielectric function in the band gap region of AlN measured at different temperature between 300 and 10K. This AlN layer was grown on a SiC substrate. All three excitonic features show a clear shift to higher transition energies with decreasing measurement temperature. This specific shift is well known even in unstrained bulk material and can be attributed to the thermal expansion of the crystal and to electron phonon coupling effects [Lau87]. But the band ordering and the relative position of the three excitons should be almost constant in case of an isotropic thermal expansion i.e. hydrostatic strain. However, the different thermal expansion coefficient of SiC ($4.3 \cdot 10^{-6}$ K^{-1}) and AlN ($4.15 \cdot 10^{-6}$ K^{-1}) leads to an additional variation of the biaxial strain in the AlN layer. These relative shifts are clearly visible in figure 3b, if the energy position of excitonic structures is plotted against the measurement temperature. The general line shape e.g. of the FX^B exciton is well described by an average Bose-Einstein statistical factor for phonons [Lau87]. The dashed lines in figure 3b emulate the temperature behavior for the combined FX^A and FX^C structure as well as for the exciton related structure B by using the same fit parameters as for FX^B. The obvious deviations clearly demonstrate the increasing influence of strain with decreasing temperature.
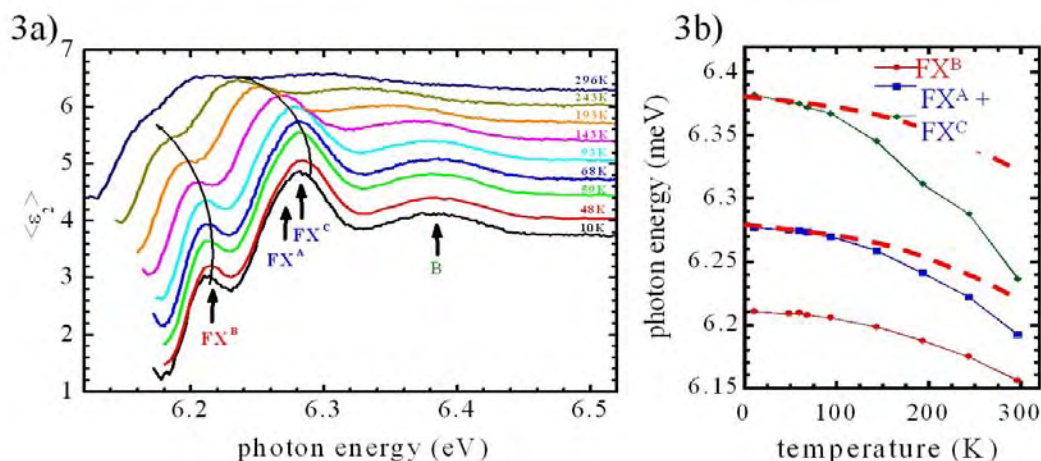
Fig. 3: a) Temperature dependency of the dielectric function (imaginary part) of an AlN layer grown on SiC. b) The observe energy shift of the excitonic features is plotted against the measurement temperature (solid lines). The dashed lines denote emulate the temperature behavior for FX^A/FX^C and the exciton related structure B by using the fit parameters obtained for FX^B with an average Bose-Einstein statistical factor.

Acknowledgements

References

[Dju02]   A.B. Djurisić et. al.: Mat. Sci. Engineering R **38**, 237 (2002)
[Si05]   E. Silveira et. al.: Phys. Rev. B **71**, 041201(R) (2005)
[Dad06]   A. Dadgar et. al.: J. Cryst. Growth **297**, 306 (2006)
[Weth98] T. Wethkamp et. al.: Thin Solid Films **313-314**, 745 (1998)
[Re08]   O.Reentilä et. al.: J. Cryst. Growth **310**, 4932 (2008)
[Chu96]   S.L. Chuang et. al.: Phys. Rev. B **54**, 2491 (1996)
[Lau87]   P. Lautenschlager et. al.: Phys. Rev. B **36**, 4821 (1987)

SXPS Studies of Porphyrin-Adsorption at Copper/ Electrolyte Interfaces

Stephan Breuer[1]*, Duc-Thanh Pham[1], Gennady Cherkashinin[2], Thomas Mayer[2], Peter Broekmann[1,3], Klaus Wandelt[1]

1 Universität Bonn, Institut für Physikalische und Theoretische Chemie, Wegelerstraße 12, 53115 Bonn
2 Technische Universität Darmstadt, Institut für Materialforschung, Petersenstraße 23, 64287 Darmstadt
3 Universität Bern, Departement für Chemie und Biochemie, Freiestraße 3, CH 3012 Bern
* BreuerStephan@uni-bonn.de

Introduction

Electrochemistry offers a path to desposit and manipulate organic molecules on surfaces, alternative to the deposition from vapour, which is often limited by the thermolability of the molecules. Anion modified copper single crystal surfaces are well proven templates for the self-assembly of supramolecular structures of adsorbed organic molecules (Fig 1). The adsorbed anions on a positively charged copper surface lead to a charge inversion which favors the adsorption of cations [Safarowsky et al 2004].
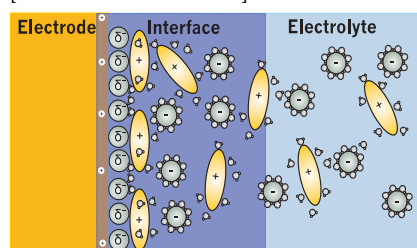
Fig. 1 Schematical sketch of the template effect for the adsorption of organic cations on a anion precovered metal surface. The anion coverage causes a charge inversion.

Due to their biological, e.g. chlorophyll in green leaves or haem in haemoglobin, as well as their technological relevance porphyrins are interesting objects to study. Former EC-STM studies in our group allowed the direct visualization of the adsorption structures of porphyrins at the solid-liquid interface correlated with their electrochemical behaviour [Hai, 2007a,b]. These studies used mainely Tetramethyl-pyridinium-porphyrin tetratosylat (TMPyP, Fig. 2a) and revealed many different structures depending on the underlying substrate, anion layer and the applied potential.
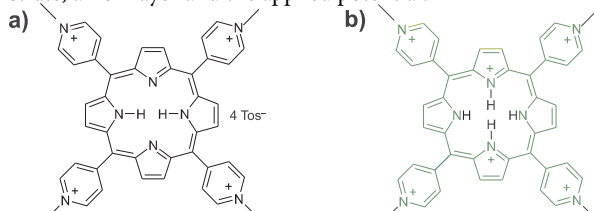
Fig. 2 a) The free porphyrin base Tetramethylpyridinium-porphyrin tetratosylat (TMPyP). b) The porphyrin diacid which is stable under acidic conditions. Due to mesomerism all core nitrogen atoms are equivalent.

The present SXPS study, correlated with the known electrochemical and structural data, gives a deeper insight in both the chemical and redox state of the adsorbate and the interaction with the substrate and coadsorbed anions using TMPyP on chloride and sulphate precovered Cu(100) and Cu(111).

Experimental

The experiments are performed at the SoLiAS-Station (Solid-Liquid Analysis System) which is designed for the analysis of electrochemically prepared surfaces and interfaces [Meyer et al., 2005].

The undulator beamline U 49/2-PGM-2 has been used for our experiments. Spectra are mainly obtained with an excitation energy of 730 eV. The spectra (acquired by a Phoibos 150 MCD 9 analyzer (Specs)) are referenced to the $Cu3p_{3/2}$ line ($E_B = 75$ eV) or to the Fermi edge. The photoelectron spectra are fitted with Voigt profiles after subtraction of a Tougaard type background.

The Cu (100) and Cu (111) are obtained from MaTeck (orientation accuracy < 0,5°). Before each experiment the crystals are electropolished in 50 % orthophosphoric acid by applying an anodic potential of 2 V between the crystal and a platinum foil. The crystal is mounted in an electrochemical cell that allows the preparation under argon atmosphere and a fast and contaminationless transfer to UHV. Prior to each experiment the status of the crystal has been checked by acquiring a CV in the pure supporting electrolyte (10 mM HCl or 5 mM H_2SO_4). The EC cell is equipped with a three electrode design which is connected with a potentiostate in order to identify emersion potentials by taking a CV. The change between the supporting and TMPyP containing working electrolyte has been carried out under potential control. The following electrochemical data refer to the reversible hydrogen electrode (RHE) unless otherwise noted.

All electrolyte solutions are prepared from Millipore water (> 18MΩ) and reagent grade substances (Merck). The Tetramethyl-pyridinium-porphyrin Tetratosylat is obtained by FrontierScientific.

Results and Discussion

TMPyP adsorbed on chloride precovered copper electrodes

Chloride adsorbs specifically on copper surfaces. Depending on the underlying symmetry a c (2 × 2)-Cl on Cu (100) and a (√3 × √3) R30°-Cl superstructure on Cu (111) is formed and *in situ* observable by STM over the whole potential range between hydrogen evolution and copper dissolution. Both surfaces are able to enforce the self-assembly of adsorbed porphyrins and other organic molecules (e.g. viologens) [Safarowsky et al 2004]. In case of chloride on Cu (100) recent *in-situ* surface x-ray scattering experiments has shown that the chloride ions remain to a large extension negatively charged [Huemann et al 2007]. This fact induces the charge reversal across the interface.
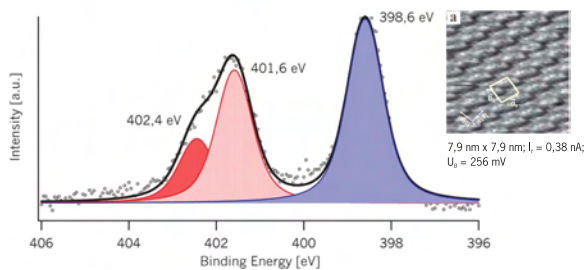
Fig. 3 N1s spectrum, emersion potential +100 mV vs RHE. Core N atoms at 398,6 eV, pyridinium N atoms at 401,4 eV and 402,4 eV. Small inset: STM image of TMPyP on Cu(100)-c(2×2)-Cl.

The N1s signal is a sensitive probe for changes in the chemical environment of the N-atoms. Consequently, N1s spectra provide important information about intra- and intermolecular changes. The following interpretation of our *ex situ* spectra is based on the assumption that the chemical composition and the charge state will be unaltered after transfer into UHV.

TMPyP adsorbs on the c(2×2) structure in flat lying, but distorted rows as shown by *in situ* STM. The N1s spectrum (Fig. 3) after emersion at +100 mV shows two peaks. One at 398,6 eV and the other at around 402 eV. The peak at 398,6 eV is ascribed to the core nitrogen atoms. Fig 2a shows two groups of inequivalent core nitrogen atoms in the free porphyrin base. In this case a deconvolution of the signal in two, clearly distinguishable components, of the same intensity should be expected [MACQUET, MILLARD 1978; SAMO et al 2001]. But under acidic conditions the porphyrin core is fully protonated [YOSHIMOTO, SAWAGUCHI 2008], hence all core nitrogen atoms are equivalent. The fact that we find only one signal is in agreement with this complete protonation. The other peak at around 402 eV is split in two signals at 401,6 eV and 402,4 eV. These signals are asigned to the (cationic) pyridinium groups [BREUER et al 2008]. The splitting in two signal contributions
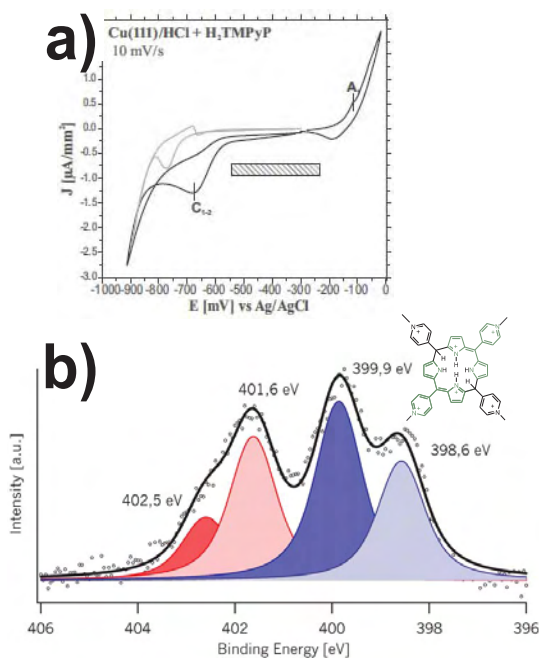
is consistent with the non-quadratic appearence of the molecules in the STM image (see inset Fig. 3).

The situation is more complex in case of TMPyP adsorption on Cu(111)/Cl (emersion potential +100 mV). The N1s spectrum (Fig. 3b) consists of four contributions. The signals at around 402 eV are ascribed again to the pyridinium groups. But, interestingly, there are now two signals at lower binding energy. The already known signal at 398,6 eV and a new signal at 399,9 eV. The CV (Fig 4a) of the system shows a permanent cathodic background current indicating a proceeding reduction of the porphyrin which leads to the porphodimethene (small inset in Fig. 4b). Changes of the bonding situation due to the reduction process occur only at carbon core atoms, but not at the core nitrogen atoms, however the extension of the mesomeric system over the whole molecule is broken up. The decrease of the mesomeric stabilization causes a higher binding energy of the core nitrogen atoms. Therefore we ascribe the signal at 399,9 eV to the core nitrogen atoms in the reduced porphodimethene. Hence, the adsorbate on Cu(111) is partially reduced, also at higher potentials.

Another interesting aspect, which we have studied, is the possible coadsorption of anions within the organic layer. Former EC-STM studies suggested a coadsorption of anions that stabilize the adsorbate, but they give no hint of their chemical identity. In the present study we analysed the Cl2p and S2p spectra. In case of coadsorbed chloride we expect two chloride species. One arises from the underlying chloride layer, and another one, with a different binding energy, due to coadsorbed chloride within the organic layer. However our Cl2p spectra are well fitted with one component only. Because there are no other sulphur containing components in the electrolyte except the tosylat counterion, the S2p signal at 167,4 eV must originate from coadsorbed toyslat ions. The chemical shift is in agreement with the literature data of tosylat [MOULDER et al, 1992].

TMPyP adsorbed on sulphate precovered copper surfaces

Sulphate ions adsorb not so strongly on copper surfaces as chloride. On Cu(100) only a mobile adsorbate layer is formed on the surface that cannot be imaged by STM or diffraction techniques. On Cu(111) a Moiré structure can be imaged, but only at higher potentials (>0 V). The CV of the Cu(111) surface in the pure sulphuric acid shows adsorption and desorption waves. The big potential difference of 400 mV between these two waves is attributed to the kinetical hindrance of at least one of these processes. *In situ* IRRAS (Infrared Reflective

Fig. 4 a) CV of TMPyP, Cu(111), 10 mM HCl showing the permanent cathodic background. b) N1s spectra of TMPyP adsorbed on Cu(111)/Cl, emersion potential +100 mV. The signal at 399,9 eV represents the core nitrogen atoms of porphodimethene (small constitutional formula as inset).
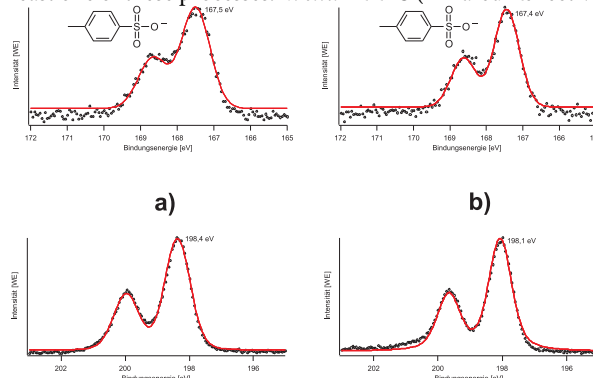
Fig. 5 S2p (representing the tosylate anion) and Cl2p spectra (representing only the underlying chloride layer) well fitted with one component on a) Cu(100)/Cl and b) Cu(111)/Cl.
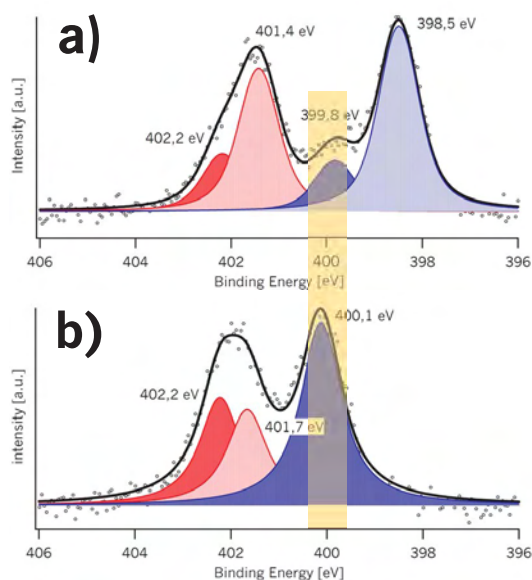
Fig. 6 *TMPyP adsorption on sulphate precovered Cu(100) N1s spectra after adsorption at a) +100 mV and b) –300 mV vs. RHE. The disappearence of the signal at 398,5 eV in favour of the signal at 400,1 eV indicates the reduction of the adsorbed porphyrin.*

Fig. 7 *The N1s spectrum after adsorption a) at + 100 mV vs. RHE and c) at – 300 mV vs. RHE. The intensity distribution for the core N1s atoms has inverted. b) STM image of TMPyP adsorbed on sulphate precovered Cu(111). Showing both the TMPyP molecules (bright dots) and the Moiré structure. 41 nm × 41 nm, $E = – 100$ mV vs. RHE, $U_b = 210$ to 20 mV, $I_t = 0,1$ nA*

Absorbance Spectroscopy) has shown sulphate ions which are already present on the Cu(111) surface below the onset potential for Moiré formation, but as a mobile phase not detectable with STM [Arenz et al. 2001].

Although on Cu(100) an ordered sulphate adlayer can also not be imaged, the modified surface does act as template for the self-assembly of well ordered porphyrin layers forming flat lying rows. The N1s spectrum after TMPyP adsorption at + 100 mV (Fig. 6a) can be deconvoluted into four signals. The signals at 401,4 and 402,2 eV are ascribed to the pyridinium groups. The signal at 398,5 eV is ascribed to the porphyrin core nitrogen atoms; the signal at 399,8 eV again indicates the formation of the reduced porphodimethene as suggested by the permanent reduction background current (CV data not shown here) as mentioned above. In the spectrum after emersion at – 300 mV the signal at 398,5 eV completely disappears, in favour of a signal at 400,1 eV. This shows that the adsorbate is completely reduced at this potential in agreemant with our above assignment.

In situ STM studies have shown that on Cu(111)/SO$_4^{2-}$ TMPyP adsorbs only on the Moiré structure, but in a less ordered mode (Fig 7b). Variation of the tunneling parameters (bias voltage) has enabled the simultaneous imaging of the adsorbed TMPyP and the underlying sulphate Moiré structure. The N1s spectrum after adsorption at + 100 mV (Fig 7a) is similar to that one obtained on Cu(100). If the potential is decreased under the desorption potential of sulphate the spectrum changes. Even so *in situ* STM experiments do no longer show adsorbed TMPyP, the N1s spectrum (emersion potential – 300 mV, Fig 7c) does show adsorbed porphyrin, but obviously in a completely disordered manner. The intensity distribution for the core nitrogen atoms has been inverted, relative to that one obtained after emersion at higher potentials, indicating an advanced reduction.
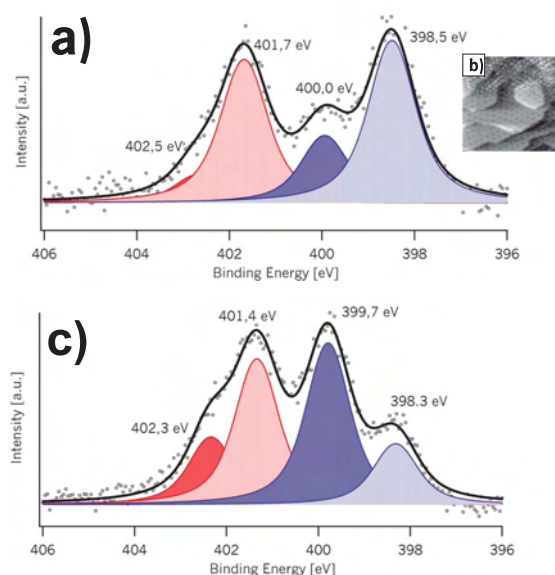
Conclusion

This study presents the fruitful complementarity of *ex situ* SXPS and *in situ* techniques (STM, CV) exemplarily shown for the porphyrin adsorption on anion modified copper electrodes. The SXPS studies add information about the chemical composition which gives a deeper insight in the adsorbate-adsorbate interactions (tosylat coadsorption) as well as the redox behaviour (indicated by N1s signals at approx 398,5 eV and 399,9 eV correlated with changes in the TMPyP core) of the porphyrin under defined adsorption conditions (potential, surface symmetry and precoverage).

References

Arenz M., Broekmann P., Lennarz M., Vogler E, Wandelt K, **2001**, *Phys. Status Solidi*, 187, 63–74.

Breuer S., Pham D. T., Huemann S., Gentz K., Zoerlein C., Hunger R., Wandelt K., Broekmann P, **2008**, *N. J. Phys.*, 10, 125033.

Hai N.T.M., **2007a**, Dissertation, Universität Bonn.

Hai N.T.M., Gasparovic B., Wandelt K., Broekmann P., **2007b**, *Surf. Sci.*, 601, 2597–2602.

Huemann S., Hai N.T.M., Broekmann P., Wandelt K., Zajonz H., Dosch H., Renner F, **2007**, *J. Phys. Chem. B*. 110, 24955–24963.

Macquet J.M., Millard M.M., **1978**, *JACS*, 100, 4741–4746.

Meyer T., Lebedev M., Hunger R., Jaegermann W., **2005**, *Appl. Surf. Sci.*, 252, 31–42.

Moulder W.F., Stickle J.F., Sobol W.E., Bomben K.D., **1992**, *Handbook of X-ray Photoelectron Spectroscopy*, Perkin Elmer Corp.

Safarowsky C., Wandelt K., Broekmann P., **2004**, *Langmuir*, 20, 8261–8269.

Samo D.M., Malienzo L.J., Jones W.E., **2001**, *Inorg. Chem.*, 40, 6308–6315.

Yoshimotu S., Sawaguchi T., **2008**, *JACS*, 130, 15944–15949.

Tailoring electronic interface properties by means of fluorinated aromatic SAMs: a model system investigated with C1s-NEXAFS

Christian Schmidt, Gregor Witte

Molekulare Festkörperphysik, Fachbereich Physik, Philipps-Universität Marburg (Germany)

One of the key issues of organic electronic devices is a precise control of metal-organic heterojunctions. Recently, Gundlach et al. demonstrated that pre-treatment of Au-electrodes with pentafluorobenzenethiol (PFBT) largely improves device characteristics of dif-TESADT based OTFTs which was attributed to enhanced crystal growth and a lowering of injection barrier [1]. However, our previous works revealed only a poor ordering for benzenethiol-SAMs [2] which seems to become even worse for PFBT, shown by C1s-NEXAFS. In the afore mentioned study we were able to show, that changing the anchoring group to Se improves ordering of the film. Apparently this concept does not work for pentafluorinated benzene-SAMs because neither PFBT nor PFBS form ordered films on Au-substrates as indicated by the absence of orientational ordering in the corresponding NEXAFS spectra (shown in Fig. 1a). To unravel the origin of this behaviour and to provide a well defined model system for further theoretical analysis, we have further investigated various differently substituted aromatic thiols on Cu(100) since benzenethiols is reported to form long range ordered films on this particular surface [3]. In fact by controlled adsorption under UHV-conditions well ordered SAMs have been prepared for non-, partially and even for fully-fluorinated molecules which in all cases are upright oriented as derived from the dichroism of the C1s-NEXAFS signal (see Fig. 1b). By employing further additional techniques (UPS, LEED, TDS) the structure of the films and their effect on the electronic properties of the interface is being presently characterized in order to understand the tailoring of electronic interfaces in organic semiconductor devices.
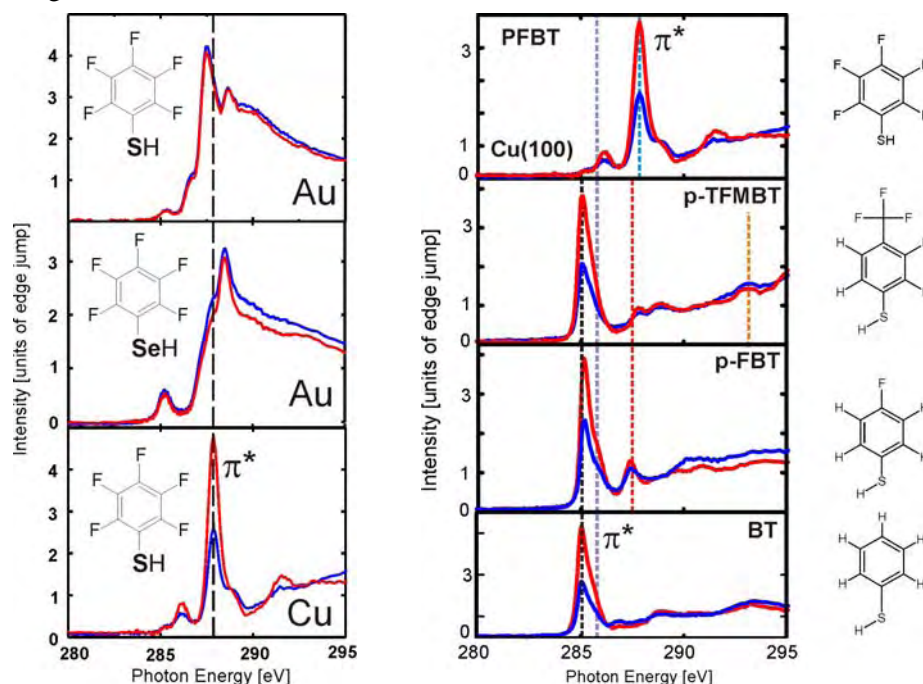
Fig. 1 *C1s-NEXAFS of perfluorinated benezene-SAMs on Au(111) and Cu(100) (left) and for differently substituted benzenethiols on Cu(100) (right). The red (blue) curves are measured for perpendicular and grazing incidence of the electric field.*

[1] D. J. Gundlach et al., Nature Materials **7**, 216 (2008)
[2] D. Käfer, A. Bashir and G. Witte, J. Phys. Chem. C **111**, 10546 (2007)
[3] F. Allegretti et al., Surf. Sci. **602**, 2453 (2008)

List of Projects 2008

Project Leader	Institute	Project Title
Adam Lewera	University of Illinois at Urbana-Champaign	Studies of Novel Catalysts for a New Generation Fuel Cells by Synchrotron High-Resolution XPS: Electrochemical Deposition of Platinum on Rh(111)
Adnane Achour	Karolinska Institutet	Structural Studies of TCR/MHC class I-dependent mechanisms for viral escape and virus-induced autoimmune diseases.
Adriana Miele	University of Rome La Sapienza	Structures of biotechnologically relevant proteins from bacteria, human pathologies and pathogens: identification of mechanism of action, of targets for drugs and vaccines, and exploitation for the biosynthesis and processing of antibiotics.
Ahmad Ariffin	Humboldt-Universität zu Berlin	XANES experiments on overdoped Bi(Pb)-2201 and Bi-2201 single crystals.
Ajay Gupta	Inter-University Consortium for DAEF facilities	Study of interface structure in multilayers with perpandicular magnetic anisotropy
Alan Michette	King's College London	Characterisation of Photonic Band Gap Phosphors
Alessandra Beltrami	Freie Universität Berlin	Structural studies of BMP receptor II LF and SF
Alexander Gottberg	Freie Universität Berlin	Electronic structure of 3d transition metal monoxide thin films
Alexander Gottberg	Freie Universität Berlin	Electronic Structure of Mg Thin Films Grown on Mo(110) and W(110)
Alexander Gottberg	Freie Universität Berlin	Electronic structure of MgO films
Alexander Okotrub	Russian Academy of Sciences	Probing of vertical alignment of carbon nanotubes by X-ray absorption spectroscopy
Alexander Okotrub	Russian Academy of Sciences	Spectroscopic study how the synthetic conditions influence the electronic structure of the fluorinated double-wall carbon nanotubes
Alexander Schnegg	Helmholtz Zentrum Berlin für Materialien und Energie	Mapping zero-field splitting parameters of single molecular magnets: a THz FDMR study
Alexander Schnegg	Helmholtz Zentrum Berlin für Materialien und Energie	Studying THz zero field splittings in paramagnetic multiatom metal centres: A Fourier Transform Electron paramagnetic resonance study
Alexander Shikin	St. Petersburg State University	Influence of substrate on quantum-well spectra developed in ultrathin layers of Al on W(110) and Ta(110)
Alexander Shikin	St. Petersburg State University	Substrate-induced spin-orbit splitting of states formed in thin films of Au and Ag on W(100).
Alexander Soldatov	Rostov State University	Cu doped AlN nanorods: active materials for nanospintronics (local 3D and electronic structure)
Alexander Vinogradov	St. Petersburg State University	Comparative study of electronic structure for cobalt and nickel phthalocyanine complexes, CoPc and NiPc, with resonant photoemission spectroscopy: effects of partly filled HOMO and 3d-3d exchange interaction on decay processes of cobalt 2p excitations.
Alexander Vinogradov	St. Petersburg State University	Resonant photoemission study of the hybridization effect between Ti 3d and F 2p electron states in valence band of titanium fluorides, TiF_{3} and TiF_{4}.
Alexander Wanner	Universität Karlsruhe (TH)	Internal Load Transfer in novel metal matrix composites exhibiting a lamellar microstructure
Alexander Wanner	Universität Karlsruhe (TH)	Residual stresses in novel metal matrix composites exhibiting a lamellar microstructure
Alexei Nefedov	Ruhr-Universität Bochum	Characterization of the reactivity of ZnO single crystal surfaces towards small molecules
Alexey Nikulin	Institute of Protein Research RAS	Structural aspects of regulation of ribosomal protein L1 synthesis in Bacteria and Archaea
Alexey Nikulin	Institute of Protein Research RAS	Studies of the interactions of translation IF2 from Archaea with nucleotides and initiator tRNA
Anders Sandell	Uppsala University	Bulk Electronic Properties of Multiferroic Materials
André Heinemann	Helmholtz Zentrum Berlin für Materialien und Energie	A long term decomposition kinetic study of the Ni34Fe66 Invar alloy by element sensitive SAXS.
Andre Luz	Imperial College	Measurement of the Residual Strains Within Thermal Barrier Coating for Several Fractions of Life Using High Energy X-Ray Diffraction
Andreas Eichinger	Technische Universität München	Structure determination of Alpha-1-acid glycoprotein in complex with different ligands
Andreas Eichinger	Technische Universität München	Structure determination of an anticalin-VEGF-complex
Andreas Eichinger	Technische Universität München	Structure determination of human odorant binding protein (hOBP)

List of Projects 2008

Project Leader	Institute	Project Title
Andreas Heine	Philipps-Universität Marburg	De novo structure determination of Prephenate Dehydratase (PDT)
Andreas Heine	Philipps-Universität Marburg	Structure determination of aldose reductase mutants in complex with potent inhibitors
Andreas Heine	Philipps-Universität Marburg	Thrombin Inhibitors: Cooperativity in binding of small ligands to a macromolecular target
Andreas Karydas	N.C.S.R Demokritos	Elemental and structural characterization of ancient Greek glassy nano-materials
Andreas Klein	Technische Universität Darmstadt	Lattice mismatch and interdiffusion at CdTe/CdS heterointerfaces
Andreas Klein	Technische Universität Darmstadt	Pressure dependence of barrier height at SrTiO3/Pt interface
Andreas Koitzsch	IFW Dresden	Electronic properties of interfaces for organic spintronic
Andreas Koitzsch	IFW Dresden	Electronic structure of thin transition metal oxide films
Andreas Koitzsch	IFW Dresden	High Energy Photoemission Spectroscopy on CeTIn5 (T = Co, Rh, Ir)
Andreas Koitzsch	IFW Dresden	Superconducting gap of the heavy fermion superconductor CeCoIn5 and antiferromagnetic state of CeRhIn5
Andreas Müller	Universität Würzburg	Hard x-ray photoemission spectroscopy of LaAlO3/SrTiO3 heterostructures
Andrei Varykhalov	BESSY GmbH	Commissioning of new 5-axis Cryomanipulator "PenteAx"
Andrey Ionov	Russian Academy of Sciences	Electronic structure and bonding in tetrakis-arilphenyl porphyrins
Andrey Yakshin	FOM Institute for Plasma Physics Rijnhuizen	Mo/Si interdiffusion and B4C diffusion barrier interaction studies using High Kinetic Energy Photoelectron Spectroscopy
Anna Zimina	BESSY GmbH	Investigation of the electronic structure of KI@CNTs by photon-in photon-out soft X-ray spectroscopy.
Anna Zimina	BESSY GmbH	Investigation of the electronic structure of nanotubes and nanoribbons based on anatase phase of TiO2 by photon-in photon-out soft X-ray spectroscopy.
Antje Vollmer	BESSY GmbH	Why do Cs2Te Photo Cathodes die? - A combined XPS, UPS, and Work Function Investigation
Anton Stampfl	Australian Nuclear Science and Technology Organisation	The surface and bulk Fermi surfaces of the paramagnetic and spin-glass phases of Cu3Mn(100) [1]
Ardeschir Vahedi-Faridi	Freie Universität Berlin	PX-CRG proposal: X-ray Structure Analysis of ICOS Receptor and ICOS Ligand
Ardeschir Vahedi-Faridi	Freie Universität Berlin	PX-CRG: Crystallographic studies of human major histocompatibility complexes
Ardeschir Vahedi-Faridi	Freie Universität Berlin	PX-CRG: Structural Studies of a sulfate transporter of the thermoacidophilic bacterium Alicyclobacillus acidocaldarius
Armin Hoell	Helmholtz Zentrum Berlin für Materialien und Energie	Nanostructure and Composition of molten silver-free photochromic particles in a glass studied by ASAXS
Armin Hoell	Helmholtz Zentrum Berlin für Materialien und Energie	Particle constitution of selenium modified noble metal nanoparticles - anelement sensitive nano-structure analysis by ASAXS
Armin Kleibert	Universität Rostock	Exploring the origin of the high temperature magnetic stability of iron nanostructures on Cu(111)
Arnaldo de Brito	Laboratorio Nacional de Luz Sincrotron	Photoelectron angular distribution of laser excited, cooled and trapped Cesium
Arne Kromm	Bundesanstalt f. Materialforschung und -prüfung	Investigations into the transformation kinetics of low transformation temperature filler materials using high-energy synchrotron radiation
Attila Bóta	Budapest University of Technology and Economics	Nanoparticle formation in multilamellar vesicles
Augusto Marcelli	Instituto Nazionale di Fisica Nucleare	Time resolved investigation of water and ethanol evaporation processes in the THz range
Axel Rosenhahn	Universität Heidelberg	Correlation of intracellular organization with x-ray contrast in holography
Axel Scheidig	Christian-Albrechts-Universität zu Kiel	Structural investigations of two redox-active enzymes (AFR and GatDH), one aminopeptidase and one outer membrane protein.
Barbara Niemeyer	Staatliche Museen zu Berlin	Analysis of the Scythian gold treasures from Vettersfelde and Maikop in the collections of the Antikensammlung Berlin

List of Projects 2008

Project Leader	Institute	Project Title
Ben Schuler	Universität Zürich	Investigating rapid protein folding kinetics with SRCD and microfluidic mixing devices
Benedetta Casu	Eberhard Karls Universität Tübingen	Role of the substrate in the growth of organic thin films: a spectromicroscopy investigation
Benedikt Klobes	Rheinische Friedrich-Wilhelms-Universität Bonn	The origin of precipitation hardening in AlCuMg alloys - an investigation of the early stages of precipitation by anomalous small-angle x-ray scattering
Benjamin Schmid	Universität Würzburg	Bulk sensitive hard X-ray photoemission spectroscopy on oxide hetereointerfaces
Benjamin Schmid	Universität Würzburg	Valence state hybridization in diluted magnetic semiconductors probed by resonant photoemission spectroscopy
Bernard Leyh	Université de Liège	Photoabsorption, fluorescence and dissociative photoionization spectroscopy of bromine and dibromoethene
Bernd von Issendorff	Universität Freiburg	Doped Gold Clusters: Impurity Atoms in a Nanoscale Matrix
Bernd Winter	BESSY GmbH	Photoelectron Spectroscopy at Liquid Aqueous Surfaces
Berta Martins	Universität Bayreuth	Glycyl-radical catalysis by the 4-hydroxyphenylacetat decarboxylase
Berta Martins	Universität Bayreuth	Radical-dependent Catalysis of 4-hydroxybyturyl-CoA dehydratase
Bettina König	Max-Delbrück-Centrum für Molekulare Medizin	PX-CRG Proposal: Protein-nucleic acid interaction
Bjorn Dalhus	Institute of Medical Microbiology	Mechanism of endonuclease IV incision next to oxidized bases
Bjorn Dalhus	Institute of Medical Microbiology	Structural characterization of a MMR protein involved in repair of abasic sites in DNA
Bogdan Constantinescu	National Institute for Nuclear Physics and Egineering 'Horia Hulubei'	Archaeological gold provenance studies - the case of Carpathian Mountains native gold
Bohdan Andriyevskyy	Technical University of Koszalin	Dielectric functions of the ammonium sulfate crystal in the range of 4-10 eV and its changes at the ferroelectric phase transition
Britta Bohnenbuck	Max-Planck-Institut für Festkörperforschung	Investigation of Ca3Ru2O7 and RuSr2GdCu2O8 using Resonant X-Ray Diffraction
Burkhard Ziemer	Humboldt-Universität zu Berlin	Determination of the absolute structure of mandelic acid derivatives
Cameliu Himcinschi	Technische Universität Chemnitz	VUV Ellipsometry of ultrathin dielectric and metallic layers for advanced interconnects
Carla Bittencourt	University of Mons-Hainaut	Electronic Structure of Metal Nanoparticles Evaporated on Plasma-Treated Carbon Nanotubes
Carla Bittencourt	University of Mons-Hainaut	Scanning Transmission X-ray Microscopy studies of carbon nanotubes (CNTs)
Carla Bittencourt	University of Mons-Hainaut	Transmission X-ray Microscopy Studies of One Dimensional Nanostructures (ODN)
Carolin Antoniak	Universität Duisburg-Essen	Forcing ferromagnetism between Fe and Tb thin films via Cr interlayer
Carolin Antoniak	Universität Duisburg-Essen	Revealing the origin of the enhanced orbital magnetism in L10 ordered FePt nanoparticles
Carsten Kamenz	Humboldt-Universität zu Berlin	3D in-situ comparisons of scorpion book-lung architecture
Carsten Lehmann	Helmholtz Zentrum Berlin für Materialien und Energie	Valence band discontinuities and electronic structure of epitaxial CuInSe2 (112)
Carsten Winkler	Max-Planck-Institut für Mikrostrukturphysik	Two-Electron Photoemission (gamma,2e) from Solids
Catherine Amiens	LCC-CNRS	Magnetism of the Co 3d states in core/shell Co@Rh bimetallic nanoparticles
Celine Chadefaux	Centre de Recherche et de Restauration des Musées de France- UMR 171	SAXS/WAXS studies of the effects of consolidation treatment on archaeological bone and antler from the Neolithic lake site of Chalain (France)
Celine Chadefaux	Centre de Recherche et de Restauration des Musées de France- UMR 171	Synchrotron infrared microspectroscopy studies of the effect of consolidation treatment on archaeological ivory and reindeer antler
Charles Fadley	University of California Davis	Probing spintronic structures in three dimensions via standing-wave photoemission microscopy
Christian Pettenkofer	Helmholtz Zentrum Berlin für Materialien und Energie	PES studies of the doping of ZnO by nitrogen

List of Projects 2008

Project Leader	Institute	Project Title
Christian Pettenkofer	Helmholtz Zentrum Berlin für Materialien und Energie	Valence band dicontinuities and electronic structure of epitaxial CuInSe2 (CIGSE).
Christian Pettenkofer	Helmholtz Zentrum Berlin für Materialien und Energie	XPEEM investigations of chalcopyrite absorber materials for solar cells
Christian Pettenkofer	Helmholtz Zentrum Berlin für Materialien und Energie	XPEEM investigations of polycristalline thin film solar cell absorbers
Christian Schüßler-Langeheine	Universität zu Köln	Metal insulator transition and phase separation in perovskite titatanates
Christian Schüßler-Langeheine	Universität zu Köln	Resonant diffraction from SDW/CDW in Ti-doped Sr2RuO4
Christian Schüßler-Langeheine	Universität zu Köln	Resonant diffraction from static and fluctuating stripe order
Christian Schüßler-Langeheine	Universität zu Köln	Spectroscopic investigation of orbital order in Ca2RuO4
Christian Schüßler-Langeheine	Universität zu Köln	Stripe order in layered cobaltates / Time scales in K-edge resonant diffraction
Christian Stamm	BESSY GmbH	Spin dynamics in ferromagnets explored with femtosecond x-ray spectroscopy
Christian Stamm	BESSY GmbH	Two-dimensional photon detection in the energy-dispersion plane at the Femtoslicing beamline
Christian-Herbert Fischer	Helmholtz Zentrum Berlin für Materialien und Energie	Band alignment and depth profiling of composition in chalcopyrite thin film solar cell components by high energy high resolution x-ray photoemission (HIKE)
Christian-Herbert Fischer	Helmholtz Zentrum Berlin für Materialien und Energie	Depth-resolved analysis of chalcopyrite thin film solar cell components via angle resolved soft X-ray emission spectroscopy (ARXES) and photoelectron spectroscopy (PES)
Christine Boeglin	Université Louis Pasteur Strasbourg	TEMPERATURE DEPENDENT MAGNETIC DOMAINS IN COUPLED NiO/Fe3O4(100).
Christine Boeglin	Université Louis Pasteur Strasbourg	Time resolved electronic structures at the CoL3 edge in super-paramagnetic Co clusters.
Christine Boeglin	Université Louis Pasteur Strasbourg	ULTRAFAST MAGNETIZATION DYNAMICS OF FERRO-SUPERPARAMAGNETIC NANOPARTICLES.
Christoph Bostedt	Technische Universität Berlin	VUV absorption spectroscopy on pristine and functionalized (doped) diamondoids
Christoph Cobet	ISAS - Institutsteil Berlin	Strain dependency of excitons in bulk AlN and (Al,GaN) layer structures investigated by means of synchrotron ellipsometry
Claudia Felser	Johannes-Gutenberg-Universität Mainz	High energy photoemission of Heusler compounds and thin films for magneto-electronic devices: From materials to TMR devices.
Claudia Felser	Johannes-Gutenberg-Universität Mainz	VUV photoemission studies on ionic liquids
Claudia Fleck	Technische Universität Berlin Fachgebiet Werkstofftechnik	Influence of the microstructure and the residual stress state on the mechanical properties of magnesium-hydroxyapatite metal matrix composites
Claus Schneider	Forschungszentrum Jülich GmbH	Compositional analysis of heteroepitaxial ferroelectric nanoislands for ultrahigh-density memory cells
Claus Schneider	Forschungszentrum Jülich GmbH	Current-induced magnetization dynamics in thin film systems
Claus Schneider	Forschungszentrum Jülich GmbH	Magnetic Coupling in MgO-Based Tunneling Trilayers with Heusler Electrodes
Claus Schneider	Forschungszentrum Jülich GmbH	Magnetodynamic Response of Heusler Thin Films
Claus Schneider	Forschungszentrum Jülich GmbH	Role of magnetic coupling on the fast magnetization dynamics in wedge-type metallic trilayer systems.
Claus Schneider	Forschungszentrum Jülich GmbH	Time-resolved element-selective magnetooptical measurements of magnetization dynamics in magnetic films and multilayers
Cornelius Gahl	Max-Born-Institut für Nichtlineare Optik und Kurzzeitspektroskopie	Core-level spectroscopy of photochromic molecular switches - functionalized azobenzene derivatives at surfaces
Daniel Kuemmel	Max-Delbrück-Centrum für Molekulare Medizin	Proteins involved in vesicle transport & tethering
Daniel Martinez Molina	Karolinska Institutet	Structural characterization of central Herpes-virus proteins
Daniel Martinez Molina	Karolinska Institutet	Structural determination of membrane proteins
Daniel Martinez Molina	Karolinska Institutet	Substrate and inhibitor interaction studies of human Leukotriene C4 Synthase

List of Projects 2008

Project Leader	Institute	Project Title
Daniel Wohlwend	Institut für Mikrobiologie und Genetik GZMB	Structure determination of Importin7 and of the complex Importin-beta/Importin7/H1, Structure determination of the complex Importin-beta/Importin-alpha/Nup153
Daniela Schneeberger	Universität Würzburg	Structural studies of the Cdc42 specific and gephyrin-binding guanine nucleotide exchange factor collybistin
Daniele Di Castro	University of Rome La Sapienza	Investigation of the superconducting state of high-Tc superconductors by crossed infrared spectroscopy and muon spin relaxation experiments
David Batchelor	Forschungszentrum Karlsruhe	Further Commissioning of the Soft X-Ray Dispersive photoelelectron spectroscopy beamline UE52-PGM
David Batchelor	Forschungszentrum Karlsruhe	Photon Swept mode: Dispersive NEXAFS
David Cobessi	Ecole Superieure de Biotechnologie de Strasbourg UMR7100	Crystallographic studies of the outer membrane heme receptor ShuA of the human pathogen Shigella dysenteria.
David Ensling	Uppsala University	Photoelectron spectroscopic investigation of the electrochemical intercalation/deintercalation reaction of Li2FeSiO4-type cathodes for lithium-ion batteries
Debashis Mukherji	Technische Universität Braunschweig	In-situ XRD measurement of surface oxidation of an experimental Co-Re alloy
Debdutta Lahiri	Bhabha Atomic Research Centre	Local structural understanding of the glass formation process in Zr-based glasses, using XAFS.
Denis Kudlinzki	Institut für Mikrobiologie und Genetik GZMB	Structural characterization of truncated fragments from the human spliceosomal DExD/H-Box Protein hPRP22
Denis Vyalikh	Technische Universität Dresden	Parity of electron wave functions in heavy-fermion YbRh2Si2 compound probed by quantum well states of an overlayer
Detlef Schmitz	Helmholtz Zentrum Berlin für Materialien und Energie	Commissioning of the high-field end station
Detre Teschner	Fritz-Haber-Institut der Max-Planck-Gesellschaft	Summary of FHI proposals at Beamline ISISS-PGM
Dirk Volkmer	Universität Ulm	Redox-active Metal-organic frameworks
Djordje Francuski	Freie Universität Berlin	Crystal structure of aspartic proteinase-FeAP9 and aspartic proteinase like protein-FeAPl1 from buckwheat
Dmitry Roshchupkin	Russian Academy of Sciences	X-ray diffraction study of periodically poled LiNbO3 crystal
Dmitry Zemlyanov	University of Limerick	Effective control of palladium catalytic selectivity by surface doping and structure
Dmytro Usachov	St. Petersburg State University	The electron energy band structure of graphene layers formed on commensurate and incommensurate surfaces of nickel single crystal
Eckart Rühl	Freie Universität Berlin	Angle-Resolved Elastic Light Scattering from Free Structured Nanoparticles
Eckart Rühl	Freie Universität Berlin	Multiple Fragmentation of Covalent Clusters using the COLTRIMS Reaction Microscope
Eckart Rühl	Freie Universität Berlin	Non-linear Binding Properties of Multivalent Linkers Bound to Isolated Nanoparticles
Eckart Rühl	Freie Universität Berlin	Radiative Relaxation of free Nitrogen Clusters in the N 1s-regime
Eckart Rühl	Freie Universität Berlin	Shape resonances in core-excited sulfur hexafluoride clusters
Eckart Rühl	Freie Universität Berlin	Soft X-Ray Spectroscopy of Metastable Solution Droplets
Eike Schulz	Institut für Mikrobiologie und Genetik GZMB	Structural and Functional Characterization of Intramolecular Chaperone Domains Conserved in Bacteriophage Tailspike Proteins
Eike Schulz	Institut für Mikrobiologie und Genetik GZMB	Structural and Functional Characterization of the Active Site of Endoneuramidase F
Eike Schulz	Institut für Mikrobiologie und Genetik GZMB	Structural and functional characterization of the phi-29 homologous bacteriophage GA-1 neck appendage protein gp12
Elena Filatova	St. Petersburg State University	X-ray photoelectron spectroscopic analysis of HfO2/Si structure synthesized by atomic layer deposition (ALD) method.
Elena Filatova	St. Petersburg State University	X-ray reflection spectroscopic characterization of HfO2/Si structure synthesized by atomic layer deposition (ALD) method

List of Projects 2008

Project Leader	Institute	Project Title
Elena Reznikova	Forschungszentrum Karlsruhe	Transmission hard X-ray Microscope for 15-35 keV monochromatic energies with 50-100 µm field of view, exposure time of < 1 sec, resolution of < 100 nm, with use of planar sets of X-ray refractive objectives and condensers with large apertures
Elena Tereschenko	Russian Academy of Sciences	A TRXSW study of quasicrystal formation in layered nanostructures under heat treatment.
Eleni Paloura	Aristotle University of Thessaloniki	Study of nanocomposite Ni-TiN and Cu-TiN coatings by means of micro-XRF and XAFS
Emad Aziz Bekhit	BESSY GmbH	XAFS studies of metal oxide nanoparticles in aqueous enviroment
Emmanuel Kentzinger	Forschungszentrum Jülich GmbH	Origin of the coupling between the spin polarizations of Mn and Tb in the bulk and thin films of the multiferroic TbMnO3
Emmanuelle Montarges-Pelletier	CNRS	Organic matter fingerprints in suspended particulate matter from industrial and agricultural watersheds.
Enrico Schierle	Helmholtz Zentrum Berlin für Materialien und Energie	Layer-resolved magnetic structure across an antiferromagnetic/ferromagnetic semiconductor interface.
Enrico Schierle	Helmholtz Zentrum Berlin für Materialien und Energie	Magnetization profiles of antiferromagnetic and ferrimagnetic thin semiconducting films.
Enrique Ortega	NanoPhysics Lab San Sebastian	Testing molecular levels with distinct supramolecular environements in self-assembled monolayers
Erik Nibbering	Max-Born-Institut für Nichtlineare Optik und Kurzzeitspektroskopie	Ultrafast infrared-pump/x-ray probe spectroscopy of water
Eugen Weschke	Helmholtz Zentrum Berlin für Materialien und Energie	Interplay of RE and Mn magnetic ordering in the multiferroic compounds REMnO3
Eugen Weschke	Helmholtz Zentrum Berlin für Materialien und Energie	Magnetic ordering in multiferroic REMnO3 (RE= Tb, Dy) studied by soft x-ray resonant scattering
Eva Kovacevic	GREMI - Université d'Orléans	NEXAFS spectroscopy on plasma polymerized hydrogenated carbon-nitride nanoparticles
Eva Pereiro-Lopez	ALBA Synchrotron Light Source	X-ray microscopy investigation of Intracellular Mature Vaccinia Virus
Florian Klappenberger	Technische Universität München	Substrate induced change of conformational and electronic structure of large organic molecules (Continuation)
Florian Kronast	BESSY GmbH	Microscopic investigation of exchange bias in Ni/FeMn bilayers
Florin Radu	BESSY GmbH	Superparamagnetism of CoO and Co3O4 AF nanoparticles
Florin Radu	BESSY GmbH	The mechanism for positive exchange bias in IrMn/NiFe bilayers
Francisco Garcia-Moreno	Helmholtz Zentrum Berlin für Materialien und Energie	Decomposition and oxidation behaviour of TiH2 and ZrH2 powder for metal foaming
Francisco Garcia-Moreno	Helmholtz Zentrum Berlin für Materialien und Energie	Phase transformation and decomposition behaviour of ZrHx powder for metal foaming
Frank Bruessing	Ruhr-Universität Bochum	Highly-symmetric magnetic order in as-grown epitaxial spin-valve structures
Frank de Groot	Universität Utrecht	On the origin of the cobalt particle size effect in Fischer-Tropsch synthesis: An in-situ soft X-ray absorption study
Frank Schreiber	Eberhard Karls Universität Tübingen	Counterion distribution around charged proteins in aqueous solution studied using ASAXS
Frank Schumann	Max-Planck-Institut für Mikrostrukturphysik	Two-dimensional angle-resolved photoelectron spectroscopy
Frank Wien	Synchrotron Soleil	High throughput protein refolding screening
Franz Bartl	Universitätsklinikum Charité	FTIR spectroscopic investigations of the biological signal transduction in rhodopsin and of the dynamic of hydrogen bonds
Franz Bartl	Universitätsklinikum Charité	Phospholipid Transport by the intracellular parasite T. gondii
Franz Schaefers	BESSY GmbH	Broadband Multilayer-based Polarimetry at the Fe, Co and Ni 2p edges
Franziska Emmerling	Bundesanstalt f. Materialforschung und -prüfung	In situ investigation of aggregation mechanism using SAXS/WAXS techniques
Franziska Emmerling	Bundesanstalt f. Materialforschung und -prüfung	In situ SAXS/WAXS studies of aggregation processes
Friedrich Reinert	Universität Würzburg	Core-level spectroscopy of organic thin films and interfaces

List of Projects 2008

Project Leader	Institute	Project Title
Gaspar Gonzalez-Doncel	CENIM, C.S.I.C.	Residual Stress Profiles in friction stir welds in MMCŽs
Georg Held	University of Reading	Characterising chiral interfaces by synchrotron radiation: serine and cysteine adsorption on Au-Cu{531}
Georg Koller	Karl-Franzens-Universität Graz	Heterostructures of chain- and plate-like conjugated molecules
Georg Koller	Karl-Franzens-Universität Graz	Interfacial and bulk electronic structure of crystalline organic monolayers and films
Georg Schulz	Universität Freiburg	Structure determination of a complex consisting of PEX19 and the membrane protein PEX3, two human proteins involved in peroxisome biogenesis
Georg Schulz	Universität Freiburg	Structure determination of Pex3, a human membrane protein involved in peroxisome biogenesis
Georg Schulz	Universität Freiburg	Structure solution of Early B-Cell Factor (EBF), a transcription factor that contains a novel type of DNA-binding domain
Georg Schulz	Universität Freiburg	Structure determination of a complex consisting of PEX19 and the membrane protein PEX3, two human proteins involved in peroxisome biogenesis
Georg Woltersdorf	Universität Regensburg	Layer Resolved Ferromagnetic Resonanceprobed by time resolved XMCD
George Sheldrick	Max-Planck-Institut für Biophysikalische Chemie	Design of lignad for phasing
George Sheldrick	Max-Planck-Institut für Biophysikalische Chemie	Protein-tag design
George Sheldrick	Max-Planck-Institut für Biophysikalische Chemie	Structural information of oligonucleotide (DNA) complexes with antibiotics
Gerald Bunke	Technische Universität Berlin	Quantitative Charakterisierung der Blei- und Kupferisothermen einzeln und im Gemisch an immobilisierter Makroalgen Biomasse mit Röntgenfluoreszens, Untersuchung der Bindungsstruktur (Antrag auf Fortsetzung des bereits genehmigten Projektes)
Gerald Bunke	Technische Universität Berlin	Quantitative Charakterisierung der Schwermetallverteilung von Mehrkomponenten Isothermen an immobilisierter Makroalgen Biomasse mit Röntgenfluoreszenz, Untersuchung der Bindungsstruktur
Gerald Zehl	Helmholtz Zentrum Berlin für Materialien und Energie	Novel Electrocatalysts for Fuel Cell Application: Formation of Catalytically Active Phases monitored by In-Situ X-Ray Diffraction Analysis
Gerardo Garcés	CENIM, C.S.I.C.	Evolution of internal stress in magnesium matrix composites
Gerd Schoenhense	Johannes-Gutenberg-Universität Mainz	Photoemission Studies on newly-designed Charge-Transfer Salts
Gerd Schoenhense	Johannes-Gutenberg-Universität Mainz	Spin-resolved photoemission electron spectromicroscopy of Heusler compounds.
Gereon Niedner-Schatteburg	Technische Universität Kaiserslautern	The spin and orbit contributions to the magnetic moments of isolated clusters (GAMBIT)
Gerhard Schumacher	Helmholtz Zentrum Berlin für Materialien und Energie	Temperature and oxygen partial pressure dependent Lattice distortion in perovskite
Gheorghe Chiuzbaian	Université Pierre et Marie Curie	Local electronic structure of diluted magnetic systems
Gregor Witte	Philipps-Universität Marburg	Cross-linking of benzene-based SAMs
Gregor Witte	Philipps-Universität Marburg	Structure and stability of fluorinated aromatic SAMs
Greta Patzke	Universität Zürich	Structural Environment of Tungsten Atoms in Mixed Nanostructured W/Mo-Oxides
Grzegorz Bujacz	Technical University of Lodz	Complexes of chagasin with cysteine proteases
Grzegorz Lupina	IHP-Microelectronics	Band alignment and chemical reactivity at the interface of perovskite type BaHfO3 and TiN
Guenther Maier	University of Leoben	Determination of Hierarchical Strains in Intercalated clay-Polypropylene nano-Composites
Hanna-Kirsti S. Leiros	University of Tromsø Norwegian Structural Biology Centre	DNA modification, Quorum sensing and acetyl transferase proteins from Vibrio salmonicida.
Hannelore Hoch	Humboldt-Universität zu Berlin	Evolutionary transformation of sensory systems during cave adaptation
Hans Bartunik	Max-Planck-Arbeitsgruppen fuer Strukturelle Molekularbiologie	Structural analysis of the target proteins phytanoyl-CoA dioxygenase, prephenate dehydratase and Mrr restriction endonuclease from Mycobacterium tuberculosis
Hans Bartunik	Max-Planck-Arbeitsgruppen fuer Strukturelle Molekularbiologie	Structural studies of Parkinson-disease related proteins

List of Projects 2008

Project Leader	Institute	Project Title
Hans Brandstetter	Universität Salzburg	Structure and function of clostridial collagenases
Hans Lewerenz	Helmholtz Zentrum Berlin für Materialien und Energie	Combined SRPES/SPM Investigation on Metal Electrodeposition on Nanostructured Si Surfaces
Hans Siegbahn	Uppsala University	Metal-Ligand interaction in the valence electronic structure of metal-organic complexes for solar cell applications
Hans-Joachim Elmers	Johannes-Gutenberg-Universität Mainz	Tailoring of interface magnetization at surfaces of Heusler films
Hans-Peter Steinrück	Universität Erlangen-Nürnberg	Adsorption of hydrocarbons on NiO investigated by in-situ high-resolution XPS
Harald Otto	Freie Universität Berlin	Light-induced structural changes in the photoreceptors PYP, Cph1 and Agp1 detected with SRCD
Haroldo Pinto	Max-Planck-Institut für Eisenforschung GmbH	Evolution of Internal Stresses and Phase Composition in Oxide Layers grown on Iron Aluminides
Hartmut Zabel	Ruhr-Universität Bochum	Antiferromagnetic order in Py/Al2O3 patterned multilayers
Hartmut Zabel	Ruhr-Universität Bochum	Commissioning of the ALICE chamber
Hartmut Zabel	Ruhr-Universität Bochum	XRMS study of CoFeB/MgO multilayers for spintronic applications
Heiko Wende	Universität Duisburg-Essen	Magnetic coupling of Fe-porphyrin molecules to ferromagnetic films studied by temperature-dependent XMCD investigations
Heiko Wende	Universität Duisburg-Essen	Magnetism of ultrathin Fe_3Si films on GaAs(001): a thickness-dependent XMCD study of a Heusler-like system
Heiko Wende	Universität Duisburg-Essen	Reliable element-specific magnetic properties of Mn-containing Heusler compounds: XMCD investigations beyond standard analysis procedures
Heinrich Riesemeier	Bundesanstalt f. Materialforschung und -prüfung	Materials research based on Synchrotron-micro-CT, Synchrotron-Refraction-Topography and Synchrotron-XRF
Heinz-Guenter Brokmeier	Technische Universität Clausthal	Investigation on the residual stress distribution after mechanical surface treatments and after the cyclic fatigue test
Helmut Kuhlenbeck	Fritz-Haber-Institut der Max-Planck-Gesellschaft	Electronic properties of thin film ceria, nano-ceria, and metal particles deposited on ceria
Heon-Jung Kim	Max-Planck-Institut für Festkörperforschung	Interfacial electronic structure and magnetism in hybrid structures of LCMO and YBCO.
Hermann Dürr	BESSY GmbH	Characterization of FEL photocathodes with XPS
Hermann Dürr	BESSY GmbH	Chemical and magnetic spectromicroscopy of individual nanoparticles
Hermann Dürr	BESSY GmbH	Electron-magnon coupling at the Cr(110) surface probed by high-resolution photoemission spectroscopy
Hermann Dürr	BESSY GmbH	Is there a spin-dependent quasiparticle renormalization in 3d ferromangets?
Hermann Dürr	BESSY GmbH	Microscopic origin of giant magnetic anisotropy in tetragonal FeCo alloys
Hermann Dürr	BESSY GmbH	Probing Ce 4f valence fluctuations in real time
Hideaki Ogata	Max-Planck-Institut für Bioanorganische Chemie	X-ray crystallographic study of sulfate/sulfite reductases and [NiFe]hydrogenases
Holger Dau	Freie Universität Berlin	Binuclear metal sites in enzymes and model compounds studied by EXAFS
Holger Dau	Freie Universität Berlin	XANES and high-quality EXAFS on ultra-dilute protein suspensions and biomimetic model complexes of importance for light-driven H2 production from water
Holger Dobbek	Universität Bayreuth	Assembly intermediates of cluster C
Holger Dobbek	Universität Bayreuth	Carbon dioxide activation at the Ni,Fe-cluster of Carbon Monoxide Dehydrogenase (CODH)
Holger Dobbek	Universität Bayreuth	Crystal structure of the Mo- and Se-containing enzyme Nicotinate Dehydrogenase
Holger Dobbek	Universität Bayreuth	Dioxygen activation at mononuclear Fe-containing oxygenases
Holger Dobbek	Universität Bayreuth	Radical catalysis in the 2-hydroxyacyl-CoA dehydratase family: structural and functional investigations
Holger Dobbek	Universität Bayreuth	Structural characterization of the nickel accessory protein CooC from Carboxydothermus hydrogenoformans

List of Projects 2008

Project Leader	Institute	Project Title
Holger Dobbek	Universität Bayreuth	Structural identification of Fe-S clusters of CooF and complex formation with its partner carbon monoxide dehydrogenase II
Holger Dobbek	Universität Bayreuth	Structural investigation of CO oxidation/CO2 reduction mechanism at the active site cluster C of Carbon Monox-ide Dehydrogenase
Holger Dobbek	Universität Bayreuth	The Ni-binding ATPase CooC from Carboxydothermus hydrogenoformans
Holger Dobbek	Universität Bayreuth	Xenobiotica reductase A in the degradation of quinoline
Holger Stiel	Max-Born-Institut für Nichtlineare Optik und Kurzzeitspektroskopie	Test und Anwendung eines auf neuartigen HOPG-Kristallen basierenden wellenlängendispersiven Röntgenspektrometers für die chemische Speziation von Übergangsmetallverbindungen
Horst-Artur Crostack	Universität Dortmund	Residual stresses in multilayer-steel composites
Horst-Artur Crostack	Universität Dortmund	Tomographic strain analysis of microstructured Al materials
Horst-Artur Crostack	Universität Dortmund	Tomographic strain analysis of particle reinforced metal matrix composites
Humberto Rodriguez Alvarez	Helmholtz Zentrum Berlin für Materialien und Energie	Real time in-situ growth studies of Cu(In,Ga)(S,Se)2 thin films
Ignacio Jimenez	Instituto de Ciencia de Materiales de Madrid	XANES analysis of bond deformation in strained cBN nanostructures.
Igor Konovalov	Universität Leipzig	Defect-related modulated x-ray photoconductivity of intentionally doped semiconductors
Immo Kötschau	Helmholtz Zentrum Berlin für Materialien und Energie	Real time in-situ growth studies of Cu(In,Ga)(S,Se)2 and Cu2(Zn,Sn)S4 thin films
Ingo Manke	Technische Universität Berlin	In-situ investigation of the discharge of alkaline Zn-MnO2 batteries with synchrotron X-ray tomography
Ingwer Denks	Helmholtz Zentrum Berlin für Materialien und Energie	Application of the ¿stress-scanning¿-method to materials with complex near surface stress states
Ingwer Denks	Helmholtz Zentrum Berlin für Materialien und Energie	Development of the stress scanning method
Irina Sluchinskaya	Moscow State University	EXAFS studies of local structure of Pb atoms in perovskites and SnSe crystals
Irina Sluchinskaya	Moscow State University	EXAFS study of Cu-doped CdSe and CdSe/CdS core/shell quantum dots as promising materials for nanobiotechnology
Ivana Kuta-Smatanova	University of South Bohemia	Crystallization study of several halogenalkane dehalogenases
Iver Lauermann	Helmholtz Zentrum Berlin für Materialien und Energie	In-situ monitoring of chemical reactions in liquids and at interfaces between chalcopyrite surfaces and liquids by x-ray emission spectroscopy
Iver Lauermann	Helmholtz Zentrum Berlin für Materialien und Energie	In-situ NEXAFS measurements of homogeneous and heterogeneous reactions of zinc complex compounds in the LIQUIDROM end station
Jan Dohnalek	Institute of Macromolecular Chemistry of the Academy of Sciences of the Czech Republic	Structural studies of proteins involved in adaptive immune system and proteins operating on nucleic acids.
Jan Honolka	Max-Planck-Institut für Festkörperforschung	XMCD study of ordered Co nanoclusters covered by a thin MnPt wedge
Jan Ivanco	Technische Universität Chemnitz	Influence of the molecular orientation on the electronic properties of organic/inorganic heterostructures
Jan Ivanco	Technische Universität Chemnitz	Injection barrier height at organic-inorganic semiconductor interfaces - The mechanism of the formation
Jan Lengefeld	Universität Potsdam	CaF2 cells for ultra-violet circular dichroism spectroscopy on proteins
Jan Lengefeld	Universität Potsdam	Database, extended ultra-violet circular dichroism spectroscopy on proteins
Jan Luning	Université Pierre et Marie Curie	Investigation of surface and interface dynamics in thin polymer films by resonant soft x-ray photon correlation spectroscopy
Jana Harizanova	Bulgarian Academy of Sciences	Investigation of spatial distribution of telomeres in mouse cells
Jana Schmitzova	Institut für Mikrobiologie und Genetik GZMB	Crystallographic studies on yeast DExD/H-box proteins yPrp28p, yPrp22p, yPrp2p, their deletion mutants and complexes with their interaction partners

List of Projects 2008

Project Leader	Institute	Project Title
Jan-Erik Rubensson	BESSY GmbH	Resonant Inelastic Photon Scattering at Double Excitations of Helium
Jan-Erik Rubensson	BESSY GmbH	Resonant Inelastic Soft X-ray Scattering at the Ge 3p Edges Applied to New Materials and Nanostructures
Jark Böttcher	Philipps-Universität Marburg	Optimization of two spacegroup dependent bindingmodes of an equal composited HIV-protease ligand complex.
Jens Brinkmann	Institut für Mikrobiologie und Genetik GZMB	Crystal structure determination of the translation repression complex at the msl-2 mRNA 3ŽUTR consisting of Sex-lethal and the co-repressor UNR
Jens Gibmeier	Universität Karlsruhe (TH)	Commissioning: setting-up operation of a new detector electronic
Jens Gibmeier	Universität Karlsruhe (TH)	Determination of diffraction elastic constants and stress factors using energy dispersive diffraction
Joachim Haug	Universität Ulm	3D-modelling of inner and outer structures of living and fossil arthropods
Jochen Geck	IFW Dresden	Resonant soft x-ray reflectivity studies of manganite-insulator interfaces
Jochen Geck	IFW Dresden	Spectroscopic study of the charge density wave order in two-dimensional dichalcogenides
Jochen Kuper	Universität Würzburg	X-ray structure of the XPD protein
Jochen Maul	Johannes-Gutenberg-Universität Mainz	NEXAFS spectroscopy of the metalloprotein hemocyanin in a flow cell
Joerg Haug	Martin-Luther-Universität Halle-Wittenberg	ASAXS study on the structure of Ag/Au nanoparticles in glasses produced by ion implantation.
Joerg Radnik	Leibniz-Institut für Katalyse e.V. an der Universität Rostock	ASAXS study of the influence of Cu and Bi on the properties of TiO_2 supported Pd nanoparticles used in acetoxylation of toluene
Joerg Schäfer	Universität Würzburg	Electrons Confined to Atomic Nanowires of Au on Ge(001)
John Hemminger	University of California, Irvine	Acid-Base Equilibria at the Surface of Aqueous Solutions
Jongseok Lee	Seoul National University	Anisotropy of the condensed matters studied by the polarization-modulated infrared microspectroscopy
Jongseok Lee	Seoul National University	Coherent electrodynamics in the density wave state of the double-layered perovskite ruthenate $Ca_3Ru_2O_7$
Jordi Fraxedas	CSIC	Experimental determination of the band diagrams of donor polyfunctionalized TTF-derivatives on gold: donor-metal charge transfer.
Jörg Fink	BESSY GmbH	ARPES on the Pseudogap State in High Tc Superconductors
Jörg Fink	BESSY GmbH	ARPES studies of the high-Tc superconductor $Ba_{1-x}K_xBiO_3$
Jörg Fink	BESSY GmbH	Is there a stripe-like charge ordering in Ni-doped high-Tc superconductors?
Jörg Fink	BESSY GmbH	Metal-Insulator Transition in Doped Mott-Hubbard Systems and Surface Electronic Structure of Cleaved $YBa_2Cu_3O_{7-d}$
Jörg Fink	BESSY GmbH	Static Electronic Stripes in $(La,Eu)_2-xSr_xCuO_4$
Jörg Fink	BESSY GmbH	Static stripe order in $(LaEu)_2-xSr_xCuO_4$ studied by high-energy X-ray scattering
Jörg Fink	BESSY GmbH	Time-dependence of rhe photoinduced metal-insulator transition in a Mott-Hubbard system
Jörg Winter	Ruhr-Universität Bochum	NEXAFS spectroscopy on plasma polymerized nanoparticles
José Crespo López-Urrutia	Max-Planck-Institut für Kernphysik	Resonant photoexcitation and photoionization of highly charged ions by synchrotron radiation
Jose Endrino	Instituto de Cienca de Materiales de Madrid	XANES Study of Novel $NaPt_3O_4$ films Deposited by Pulsed Magnetron Sputtering
Jose Serra	Instituto de Tecnología Química	INVESTIGATIONS ON HIGH-TEMPERATURE PROTON CONDUCTION IN NEW CRYSTALLINE OXIDES (doped-Ln_6WO_{12})
Jozef Keckes	University of Leoben	Residual Stresses in Laser-Cycled Steel Coated with a Hard Coating
Juergen Thieme	Universität Göttingen	Characterization of organic sulfur binding forms in soils
Juergen Thieme	Universität Göttingen	Humic substances and the electron transfer process of bacteria and iron minerals

List of Projects 2008

Project Leader	Institute	Project Title
Juergen Thieme	Universität Göttingen	Iron particles and their influence on the dynamics of colloidal systems in soils
Juergen Thieme	Universität Göttingen	Stereo imaging and elemental mapping to study the dynamics of a colloidal structures in the environment
Juergen Thieme	Universität Göttingen	Study of humic substances from soil and groundwater with the Scanning Transmission X-ray Microscope at Undulator U41
Julia Sedlmair	Universität Göttingen	Imaging actin filaments of muscle cells and spatially resolved spectroscopy of these cytoskeleton constituents by x-ray spectromicroscopy.
Jürgen Behnen	Philipps-Universität Marburg	New probe molecules for the experimental hotspot analysis
Jürgen Lindner	Universität Duisburg-Essen	In situ combination of PEEM and magneto-resistance measurements to monitor the magnetization reversal in epitaxial Fe nanowires and extract the resistance of single domain-walls
Jürgen Müller	Max-Delbrück-Centrum für Molekulare Medizin	PX-CRG: Structural determinants of protein folding, stability, assembling, and activity
Kai Bechstein	Leibniz Universität Hannover	Investigation of lacquer systems and paint layers with regard to layer thickness and elemental distribution
Kai Bechstein	Leibniz Universität Hannover	Spectroscopic investigations of organic functionalities and compounds in biomineralisation products of marine specimens with spatially high resolved Synchrotron-FTIR technique
Kai Fauth	Universität Würzburg	Magnetic moments in 3d-5d transition metal alloy clusters
Kai Rossnagel	Christian-Albrechts-Universität zu Kiel	Combined ARPES and SEXAFS study of molecular switches on layered compounds
Kai Rossnagel	Christian-Albrechts-Universität zu Kiel	Electronic and geometric structure of Cu adsorbed TaS2 surfaces
Kai Rossnagel	Christian-Albrechts-Universität zu Kiel	Ultrahigh-resolution ARPES on the Fermi liquid reference system TiTe2
Kai Tittmann	Martin-Luther-Universität Halle-Wittenberg	Structural analysis of reaction intermediates in transketolases and transaldolases
Karel Prokes	Helmholtz Zentrum Berlin für Materialien und Energie	Magnetic order in UNiSi single crystal
Karin Föttinger	Technische Universität Wien	Mechanism and quantification of carbonate formation on Pd catalysts: an approach to characterize surface defect sites.
Karl Gruber	Karl-Franzens-Universität Graz	Structural determinants of the substrate specificity of dipeptidyl-peptidases III (DPP-III)
Karl Gruber	Karl-Franzens-Universität Graz	Structures of berberine-bridge enzyme (BBE) from california poppy: substrate complexes and active site mutants
Karl Gruber	Karl-Franzens-Universität Graz	The roles of human ALDH1 and ALDH2 in bioactivation of glycerole-trinitrate (GTN)
Karsten Hinrichs	ISAS - Institutsteil Berlin	Biofunctionalization of thin films of Nitrocompounds on silicon and gold
Karsten Hinrichs	ISAS - Institutsteil Berlin	In-situ IR synchrotron mapping ellipsometry on stimuli-responsive mixed polymer brushes
Karsten Hinrichs	ISAS - Institutsteil Berlin	Molecular Orientation in organic films for Au-molecular layer-GaAs Diodes
Karsten Hinrichs	ISAS - Institutsteil Berlin	Study of the peptide/linker interface for biosensors by IR synchrotron mapping ellipsometry
Karsten Horn	Fritz-Haber-Institut der Max-Planck-Gesellschaft	Electron and hole doping in single and few layer graphene
Karsten Niefind	Universität zu Köln	Structure determination of components of the dialkyl ketone degradation pathway from Pseudomonas veronii
Karsten Niefind	Universität zu Köln	Structure/function-relationships of protein kinase CK2 (casein kinase 2)
Katja Fälber	Forschungsinstitut für Molekulare Pharmakologie	A-kinase-anchoring proteins (AKAPs) as scaffolds of multiprotein complexes
Katrin Fischer	Universität zu Köln	Crystal structure of Arabidopsis nitrate reductase catalytic domains and holo-enzyme
Katrin Fischer	Universität zu Köln	Structural analysis of holo-gephyrin and gephyrin splice variants
Kay-Oliver Thiel	Freie Universität Berlin	Metal monolayer depostion on the modified Au(111) electrode

List of Projects 2008

Project Leader	Institute	Project Title
Kejin Zhou	Université Pierre et Marie Curie	Electronic and magnetic structure of Co-doped ZnO diluted magnetic semiconductors probed by soft x-ray spectrosopies
Kenneth Johnson	University of St. Andrews	Scottish Structural Proteomics Facility(www.sspf.ac.uk): Focus on Drug targets in Drug-resistant Bacteria
Klaus Piontek	Universität Freiburg	BIORENEW: An European Integrated Project for the Design of Tailor-made Biocatalysts
Klaus Wandelt	Universität Bonn	Redox-Chemistry of Self-Assembled Porphyrin Layers Monitored by SXPS
Klaus Wandelt	Universität Bonn	Surface Redox-Chemistry of Viologens monitores by SXPS
Kristina Edström	Uppsala University	Non destructive depth profile studies of the electrode/electrolyte interface in Li-ion batteries using HIKE
Kristina Lakomek	Institut für Mikrobiologie und Genetik GZMB	The transferRNA modifying enzyme ThiI in complex with full-length tRNA
Lada Yashina	Moscow State University	The mechanism of H2/O2 oxidation/reduction on Pt and Ag catalysts prepared on different supports for fuel cell applications
Laurent Duda	Uppsala University	Electrochemical in situ soft x-ray spectroscopy of Li-ion batteries and copper corrosion at varied electrochemical potentials
Laurent Duda	Uppsala University	Ultrahigh resolution resonant inelastic x-ray scattering at the oxygen K-resonances of highly correlated materials
Laurent Michot	CNRS	X-ray tomographic study of Mushroom Bodies in Drosophila brains. Relationships between 3D structure and long-term memory.
Lenka Zajickova	Masaryk University / Faculty of Science	Band structure of hard carbon films assessed from the optical measurement
Leonardo Soriano	Universidad Autonoma de Madrid	Electronic structure of organic molecules on metallic surfaces:TTF and TCNQ on Cu (100)
Lia Addadi	Weizmann Institute of Science	Mapping temporal and spatial phase distribution of minerals in vertebrate and invertebrate skeletons using micro-focus x-ray beam scattering and diffraction.
Lia Addadi	Weizmann Institute of Science	Mg K-edge NEXAFS study of magnesium/calcium carbonate minerals. Relevance to the stabilization of metastable phases in biomineralization.
Lisa Englert	Philipps-Universität Marburg	Catalysis of in situ Click-Chemistry by metalloenzymes
Lisa Englert	Philipps-Universität Marburg	Fragment-;based lead discovery: Screening and evolving fragments for the inhibition of thermolysin
Liu Tjeng	Universität zu Köln	Polarization dependent soft-x-ray absorption spectroscopy on Ce and Yb Heavy-Fermion systems: a new approach to determine the symmetry of the lowest crystal-field states.
Liubov Moroz	Deutsches Zentrum für Luft-und Raumfahrt e.V.	Infrared Microspectroscopy of Rare Metamorphosed Carbonaceous Chondrites
Lubomir Smrcok	Slovak Academy of Sciences	Solid state chemical reactions in rapidly quenched Na3AlF6-Al2O3 melts
Lutz Heyne	Universität Konstanz	Current-induced vortex-core displacement in ferromagnetic disks.
Malte Behrens	Fritz-Haber-Institut der Max-Planck-Gesellschaft	Photoemission spectroscopy of active copper in Cu/ZnO/Al2O3 catalysts for methanol sysnthesis
Manfred Schreiner	Academy of Fine Arts	Non-destructive SR-XRF Analysis of Silver Coins of the Roman Emperor Trajan (AD 98-117)
Manuela Klaus	Technische Universität Berlin Fakultät III Prozesswissenschaften	Energy dispersive residual stress analysis in multilayer structures on the basis of the sin2psi-technique - investigations at high temperature
Manuela Klaus	Technische Universität Berlin Fakultät III Prozesswissenschaften	Residual stress analysis on CVD-diamond coated cutting tools
Marcella Passos Felicissimo	University of Groningen	Vertical phase separation in polymer:fullerene solar cell blends
Marek Przybylski	Max-Planck-Institut für Mikrostrukturphysik	Orbital moments in tetragonally distorted Fe(1-x)Co(x) alloy films on Pd(001), Ir(001) and Rh(001)
Maria Brzhezinskaya	ALBA Synchrotron Light Source	Lateral superlattice and quantum-size effects in pentacene-derived regular stripes formed on flat and stepped Ni(110)
Maria Brzhezinskaya	ALBA Synchrotron Light Source	Study of hydrogenated and fluorinated single-wall carbon nanotubes by x-ray photoelectron and absorption spectroscopy

List of Projects 2008

Project Leader	Institute	Project Title
Maria Brzhezinskaya	ALBA Synchrotron Light Source	Study of single-walled carbon nanotubes filled by CuI one-dimensional nanocrystals with core-level spectroscopies
Maria Christine Richter	Universite de Cergy-Pontoise	Resonant photoemission with circularly polarized light at 2p edges of magnetic transition-metal oxides exhibiting half-metallic properties
Marie-Claire Gazeau	Université Paris 12	VUV absorption spectroscopy of planetary molecules at low temperatures
Marina Gomoyunova	Russian Academy of Sciences	Electronic and magnetic properties of iron silicide nanostructures formed on a stepped silicon surface
Mario Dähne	Technische Universität Berlin	Anisotropic electronic structure of one-dimensional silicide nanostructures on high-index silicon surfaces
Mario Dähne	Technische Universität Berlin	K-parallel imaging of the electronic structure of one-dimensional silicide nanostructures
Mark Golden	University of Amsterdam	Bulk sensitive core level spectroscopy of novel correlated transition metal oxides: layered CMR manganites and perovskite multilayers.
Mark Golden	University of Amsterdam	k-space microscopy of quantum electron matter: layered colossal magnetoresistant manganates.
Markus Braune	Fritz-Haber-Institut der Max-Planck-Gesellschaft	Partial cross section oscillations in the valence photoionization of N2 and O2
Markus Wahl	Max-Planck-Institut für Biophysikalische Chemie	Structural analysis of 5'-splice site binding by Prp8
Markus Wahl	Max-Planck-Institut für Biophysikalische Chemie	Structural basis for metal-independent phosphoryl transfer by CASK
Markus Wahl	Max-Planck-Institut für Biophysikalische Chemie	Structural basis for reversible photoswitching in fluorescent protein Dronpa and variants
Markus Wahl	Max-Planck-Institut für Biophysikalische Chemie	Structural investigation of spliceosomal components
Martin Lommel -4864	Johann Wolfgang Goethe-Universität Frankfurt	PTB-Kooperationsprojekt
Martin Moche	Karolinska Institutet/Structural Genomics Consortium	Structural genomics of Human Proteins
Martin Oberkofler	Max-Planck-Institut für Plasmaphysik	NEXAFS and photoemission study of amorphous carbon films relevant to nuclear fusion applications
Martin Radtke	Bundesanstalt f. Materialforschung und -prüfung	Materials research based on Sy-XRF
Martin Weinelt	Max-Born-Institut für Nichtlineare Optik und Kurzzeitspektroskopie	Probing ultrafast magnetization dynamics in gadolinium with X-ray magnetic circular dichroism
Martin Weinelt	Max-Born-Institut für Nichtlineare Optik und Kurzzeitspektroskopie	Rumpfniveauspektroskopie an photochromen Schaltermolekülen - funktionalisierte Azobenzolderivate an Oberflächen
Massimo Tallarida	Brandenburgische Technische Universität Cottbus	ALD growth of high-K dielectrics (HfO2) on Si(001) in the sub-monolayer range
Matthias Bochtler	Cardiff University	Restriction endonucleases that can cleave RNA-DNA hybrids
Matthias Bochtler	Cardiff University	Unusual type II Restriction endonucleases
Matthias Neeb	BESSY GmbH	Setup of Penning trap at Beamline UE52-PGM
Matthias Neeb	BESSY GmbH	XPS and Auger spectroscopy on deposited metal clusters
Melanie Oschlies	Institut für Mikrobiologie und Genetik GZMB	Structural and Functional Characterisation of murine CMP-Sialic acid Synthetase C-terminus
Michael Krumrey	Physikalisch-Technische Bundesanstalt	PTB Radiometry
Michael Krumrey	Physikalisch-Technische Bundesanstalt	Traceable Charcterization of Nanoparticles
Michael Elbaum	Weizmann Institute of Science	Biological X-ray microscopy: imaging of cell growth and motility apparatus
Michael Gradzielski	Technische Universität Berlin	Mesoscopic Characterisation of DNA/RNA-Polycation Complexes with Tailor-made Polycations
Michael Hävecker	Fritz-Haber-Institut der Max-Planck-Gesellschaft	Commissioning of ISISS, the catalysis beamline at BESSY
Michael Huppmann	Technische Universität Berlin	Hot extruded magnesium alloy AZ31: deformation mechanisms and behaviour at cyclic loading
Michael Kolbe	Max-Planck-Institut für Infektionsbiologie	Structural studies of the needle tip of Type Three Secretion Systems
Michael Kolbe	Max-Planck-Institut für Infektionsbiologie	Structural studies on chaperone-effector complexes involved in Type Three Secretion

List of Projects 2008

Project Leader	Institute	Project Title
Michael Kolbe	Max-Planck-Institut für Infektionsbiologie	Structural studies on IpaB from Shigella flexneri
Michael Martins	Universität Hamburg	Magnetic properties of small, size-selected, deposited transition metal and alloy clusters
Michael Meyer	Centre Universitaire Paris-Sud	Photoionization studies of highly excited atoms
Michael Meyer	Centre Universitaire Paris-Sud	Rotational and vibrational energy of molecular fragments formed after resonant inner-shell excitation
Michael Zharnikov	Universität Heidelberg	Molekulare Gradienten auf der Mikro- und Nanometerskala
Michele Glass-Maujean	Université Pierre et Marie Curie	Photon-energy calibration for the 10m-NIM beamline by establishing an atlas of H2 absorption lines between 85 - 72 nm (14.5 - 17.3 eV)
Michele Ortolani	University of Rome La Sapienza	Terahertz spectrum of plasma oscillations in a 2-dimensional electron gas
Mihaela Gorgoi	BESSY GmbH	Comissioning beamtime for the HIKE system and KMC-1 beamline
Mihaela Gorgoi	BESSY GmbH	Relative Sub-shell Photoionization Cross-sections of Selected Metals Determined by High Kinetic Energy Photoemission
Mikhail Fonin	Universität Konstanz	Spin-resolved photoemission of ferromagnetic ordered MnxGey alloys
Mikhail Mazuritskiy	Southern Federal University	Interaction of channeling x-ray radiation in the policapillary structures with excited electronic states for energy near Si L - absorption edge
Miklós Fried	MFA Research Institute for Technical Physics and Materials Science	Investigation of ion implantation caused decfects in SiC crystals by means of synchrotron ellipsometry
Milton Stubbs	Martin-Luther-Universität Halle-Wittenberg	Structure determination of Spatzle isoforms.
Milton Stubbs	Martin-Luther-Universität Halle-Wittenberg	Structure determination of the thermophilic prolyl isomerase and chaperone SlyD
Milton Stubbs	Martin-Luther-Universität Halle-Wittenberg	Structure determination of TobS2 from Streptomyces tenebrarius - an aminotransferase in the kanamycin biosynthetic pathway
Minghong Yang	ISAS - Institutsteil Berlin	Application of synchrotron ellipsometry for the spectral region between 30 - 60 eV
Monika Koch-Mueller	GeoForschungsZentrum Potsdam	Crystal chemistry and high-pressure stability of OH-bearing minerals II
Nicholas Allsop	Helmholtz Zentrum Berlin für Materialien und Energie	Direct measurement of the electric field and band bending in semiconductor junctions using high energy, high resolution x-ray photoemission (HIKE).
Nicholas Barrett	CEA/Saclay	X-ray photoelectron emission microscopy study of p-doped diamond films over the full range of boron concentrations
Niko Pontius	BESSY GmbH	Optical control of the magnetization state in metallic magnets studied by time-resolved X-ray Magnetic Circular Dichroism
Nils Nawrath	Technische Universität Berlin	Phase formation in the interface region of Magnesium AZ 31 and Aluminium AA 6060
Nora Darowski	Helmholtz Zentrum Berlin für Materialien und Energie	Interlayer coupling in Fe/FeSi multilayers studied by means of depth-selective x-ray magnetic dichroism
Norbert Koch	Humboldt-Universität zu Berlin	High kinetic energy photoemission on conjugated organic materials
Norbert Koch	Humboldt-Universität zu Berlin	Localized charge transfer between molecular acceptors and polymer donors
Norbert Koch	Humboldt-Universität zu Berlin	Molecular acceptors and donors adsorbed on metal surfaces
Norbert Sträter	Universität Leipzig	6-phosphofructokinase from Pichia pastoris
Norbert Sträter	Universität Leipzig	Crystal structure of 5-Chlormuconolacton dehalogenase ClcF
Norbert Sträter	Universität Leipzig	Inhibition of E-NTPDases to interfere with purinergic signalling and to study the catalytic mechanism
Norbert Sträter	Universität Leipzig	Inhibition of PDE4A involved in inflammatory diseases
Norbert Sträter	Universität Leipzig	Stereospecificity of the 2-oxoglutarate dependent dioxygenase RdpA
Norbert Sträter	Universität Leipzig	Substrate binding mode and catalytic mechanism of arylmalonate decarboxylase
Norbert Sträter	Universität Leipzig	Substrate binding mode of E-NTPDase 2 involved in purinergic signaling

List of Projects 2008

Project Leader	Institute	Project Title
Olaf Seifarth	IHP GmbH	Electronic structure of strained Si overlayers prepared via lattice mismatched oxide heterostructures on Si
Olav Hellwig	Hitachi Global Storage Technologies	Imaging the reversal and switching mechanism in prototype patterned media via magnetic Spectro-Holography and resonant soft X-ray scattering
Olav Hellwig	Hitachi Global Storage Technologies	Magnetic reversal and dynamics in perpendicular anisotropy systems when approaching the Curie point using coherent scattering and spectro holography
Oliver Daumke	Max-Delbrück-Centrum für Molekulare Medizin	Functional insights into the GIMAP family
Oliver Daumke	Max-Delbrück-Centrum für Molekulare Medizin	Mechanisms of membrane deformation and viral resistance by Mx-Proteins
Oliver Daumke	Max-Delbrück-Centrum für Molekulare Medizin	PX-CRG: EHD proteins as molecular model systems for membrane remodelling NTPases
Oliver Daumke	Max-Delbrück-Centrum für Molekulare Medizin	PX-CRG: Structural studies on the GAP activation of Centaurin-beta
Oliver Daumke	Max-Delbrück-Centrum für Molekulare Medizin	PX-CRG: Structure and function of the GIMAP family
Oliver Ernst	Universitätsklinikum Charité	PX-CRG: The crystal structure of GPCR rhodopsin in its active state
Oliver Hahn	Bundesanstalt f. Materialforschung und -prüfung	Non-destructive Investigation of parchment and writing materials of the Qumran Scrolls Part II: Synchrotron based Fourier Transform Infrared Spectroscopy (FTIR)
Oliver Henneberg	Universität Potsdam	Determination of the Spatial Resolved Crystal Structure of Waveguides in Laser Crystals
Oliver Rader	BESSY GmbH	Electronic structure of a novel magnetic phase: spin-resolved photoemission of bcc Ni
Oliver Rader	BESSY GmbH	Evolution of the spin-dependent electronic structures in 3d transition metals from monolayers to bulk: the case of Fe and Ni
Oliver Rader	BESSY GmbH	Is the (100) surface of fcc Fe really ferromagnetic?
Oliver Rader	BESSY GmbH	Origin of spin polarization of spin-orbit split quantum-well states
Oliver Rader	BESSY GmbH	Spin-polarized density of states in graphene
Oliver Rader	BESSY GmbH	What causes really the different temperature dependences of Fermi surface features of the Pb monolayer on Cu(111)?
Olivier Renault	CEA	X-ray Photo-Electron Emission Microscopy (XPEEM) study of the metal catalyst diffusion at the surface of single silicon nanowires using the NanoESCA spectromicroscope
Olle Björneholm	Uppsala University	Microscopic mechanisms of preferential solvation of metal ions in water/acetonitrile solutions
Olle Björneholm	Uppsala University	Soft X-ray absorption (SXA) of water and aqueous solutions study with synchrotron radiation
Olle Björneholm	Uppsala University	X-ray photoelectron spectroscopy of divalent metal-ions in aqueous solutions
Oskar Paris	University of Leoben	Position-resolved and in-situ structural investigations of biological and bio-inspired materials
Oskar Paris	University of Leoben	Structure-function relationships in biological and bio-inspired materials
Pagona Papakonstantinou	University ol Ulster	Role of nitrogen on the electronic structure and electron transport propoerties of diamond nanowires deposited in nitrogen rich CH4 plamas
Paolo Calvani	University of Rome La Sapienza	Search for charge-order excitations in the very-far-infrared conductivity of manganite single crystals.
Pascal Lablanquie	Université Pierre et Marie Curie	Highly correlated multi-photoionisation processes studied by electron spectrometry with a magnetic bottle electron spectrometer: Auger processes in selected metallic atoms (alkali, Hg) and triple ionisation in Lithium
Patrick Cramer	Ludwig-Maximilians-Universität München	Structure of multiprotein transcription complexes (2)
Patrick Hoffmann	Helmholtz Zentrum Berlin für Materialien und Energie	Chemical nature of nitrogen incorporated into epitaxial ZnO
Patrick Huber	Universität des Saarlandes	Spontaneous capillary filling of silica nanochannels arrays studied by energy-dispersive small-angle x-ray diffraction measurements
Patrick Scheerer	Universitätsklinikum Charité	PX-CRG Structure analysis of bacterial phytochromes

List of Projects 2008

Project Leader	Institute	Project Title
Paul Bingham	University of Sheffield	Fe K-edge XAS studies of medium range ordering of Fe in oxide glasses
Peter Baumgärtel	Universität Potsdam	Calibration standards for SRCD spectroscopy bemlines
Peter Baumgärtel	Universität Potsdam	Extension of the UVIS Experimental Station by the Method of Multiple Polarisation Modulation (MPM)
Peter Feulner	Technische Universität München	One- and two-electron excitations of physisorbed He: Inter- and intra-layer coupling and charge and energy transfer processes.
Peter Feulner	Technische Universität München	Photon stimulated desorption of ions and neutrals from thin layers of He atoms and hydrogen molecules on metal surfaces
Peter Feulner	Technische Universität München	Thin layers on surfaces: Investigations of electron dynamics and bonding by inner shell excitations.
Peter Guttmann	BESSY GmbH	Development and x-ray optics performance test for the x-ray microscopes at the U41
Peter Guttmann	BESSY GmbH	Implementation of phase contrast mode into the full-field x-ray microscope, x-ray optics performance test and further development of the x-ray microscopes at the U41
Peter Guttmann	BESSY GmbH	In-situ x-ray microscopy studies of electromigration in copper interconnects
Peter Guttmann	BESSY GmbH	X-ray nano-tomography of higher order chromatin structure in a transcriptionally active domain
Peter Zimmermann	Technische Universität Berlin	Photoionisation studies of aligned alkaline atoms excited by an intensive CW laser field: Pump-probe experiments in a strongly driven (coupled) two-level system
Petra Hellwig	Université Louis Pasteur, Inst. de Chimie, UMR 7177	Far infrared spectroscopic evidence on low frequency movements of signaling and adhesion proteins (Integrins) and their models
Petra Hellwig	Université Louis Pasteur, Inst. de Chimie, UMR 7177	Far infrared spectroscopic study on hydrogen bonding patterns in membrane proteins and their models
Philippe Leininger	Max-Planck-Institut für Festkörperforschung	Resonant x-ray diffraction from the spin-chain compound NaCu2O2
Raimund Feifel	Uppsala University	Multi-electron-ion coincidence spectroscopy of atoms and molecules both below and above inner shell excitations
Rainer Fink	Universität Erlangen-Nürnberg	Electronic relaxations in metalloporhyrin-fullerene dyads
Rainer Fink	Universität Erlangen-Nürnberg	Substrate-molecule interactions in metalloporphyrin monolayers
Ralf Feyerherm	Helmholtz Zentrum Berlin für Materialien und Energie	Interplay between charge- and spin-ordering in TbBaFe2O5
Ralf Feyerherm	Helmholtz Zentrum Berlin für Materialien und Energie	Magnetic-field dependent interplay of RE and Mn magnetic ordering in the multiferroic REMnO3 (RE= Tb, Dy, Gd)
Ralf Feyerherm	Helmholtz Zentrum Berlin für Materialien und Energie	Study of the interplay of RE and Mn magnetic ordering in the multiferroic RE(Mn,Ga)O3 (RE= Tb, Dy, Gd) by X-ray resonant magnetic scattering
Ralf Ficner	Institut für Mikrobiologie und Genetik GZMB	Structural investigations of a highly tissue-dependent processed, glycosylated lysosomal matrix protein
Ralf Ficner	Institut für Mikrobiologie und Genetik GZMB	Structure determination of the hydratase of unsaturated fatty acids from Lactobacillus acidophilus (LAH)
Ralph Puettner	Freie Universität Berlin	Inner valence photoelectron spectroscopy of small molecules
Ralph Puettner	Freie Universität Berlin	Valence band structure of clean and oxidized (100) surfaces of cubic PbS, PbSe and orthorhombic SnS, SnSe single crystals
Reinhard Denecke	Universität Leipzig	Adsorption and reaction studies on oxidized surfaces using in-situ high-resolution XPS in combination with a supersonic molecular beam
Reinhard Denecke	Universität Leipzig	Investigation of the magnetic order in multiferroic layer systems
Reinhard Denecke	Universität Leipzig	Tuning terrace width and reactive properties of stepped surfaces by step decoration
Ricardo Bernhardt	Technische Universität Dresden	Analysis of local bone mineralisation differences around biofunctionalised titanium implants with high spatial resolution
Ricardo Bernhardt	Technische Universität Dresden	Analysis of the extent and spatial distribution of bone tissue mineralization in relation to anabolic and anti-resorptive agents in an osteoporotic rat model

List of Projects 2008

Project Leader	Institute	Project Title
Rita Wiesinger	Academy of Fine Arts	In-situ FT-IRRAS investigations of the metal/atmosphere interface
Robert Kolodziejczyk	Adam Mickiewicz University	Crystallographic studies of human cystatin C mutants
Robert Mikutta	Martin-Luther-Universität Halle-Wittenberg	Transformation of minerals during progressive basalt weathering determines the structural composition of mineral-bound humic substances
Robert Wallauer	Johann Wolfgang Goethe-Universität Frankfurt	Double Photoemission from a High Temperature Superconductor
Robert Wallauer	Johann Wolfgang Goethe-Universität Frankfurt	Double Photoemission from superconducting Lead(111)
Roland Widmer	Laboratory for High Performance Ceramics	High resolution ARPES investigation on Al-rich complex metallic alloys: What is the relation between the real and the pseudo-Brillouion Zone
Rolf Hilgenfeld	Universität zu Lübeck	3-deoxy-D-manno-oct-2-ulosonic-acid (Kdo) Glycosyltransferase of Aquifex aeolicus (WaaA)
Rolf Hilgenfeld	Universität zu Lübeck	The "SARS-unique" domain (SUD) of SARS coronavirus: an oligo(G)-binding protein
Rolf Zehbe	Technische Universität Berlin	Morphological Characterization of Biological Samples on the Cellular Level
Roman Adam	Forschungszentrum Jülich GmbH	Time-resolved element-selective magnetooptical measurements of magnetization dynamics in magnetic films and multilayers.
Ronny Helland	University of Tromsø Norwegian Structural Biology Centre	Structure-function studies of molecules involved in copper homeostasis in methanotroph bacteria.
Rotraut Merkle	Max-Planck-Institut für Festkörperforschung	In-situ XPS/XAS study of adsorbed oxygen species on (La,Sr)(Fe,Co)O3-d perovskites under applied electrical bias
Rüdiger Goldhahn	Technische Universität Ilmenau	Influence of electric fields and strain on the electron-hole interaction for ZnO and MgZnO alloys
Rudolf Winter	University of Wales Aberystwyth	In-situ anomalous GISAXS of the ZrO2 dip-coating process of glass surfaces
Sander Smits	Heinrich Heine Universität Düsseldorf	Structure determination of NisT (ABC transporter), TehA (TRAP transporter) and the octopin dehydrogenase.
Sanja Korica	Fritz-Haber-Institut der Max-Planck-Gesellschaft	Photoionization of free C60 molecules in the low photon energy region
Sascha Hümann	Max-Planck-Institut für Eisenforschung GmbH	Surface oxidation of steels and model alloys in N2-H2-H2O gas mixtures
Satoshi Kera	Chiba University	Electronic dynamics and intermolecular interaction of organic semiconductor film by energy-dispersive NEXAFS measurement
Savvas Savvides	Ghent University	Biochemistry and protein engineering of bacterial disaccharide phosphorylases
Savvas Savvides	Ghent University	Structural studies of AggA: a bacterial membrane protein important for biofilm formation.
Savvas Savvides	Ghent University	Structural studies of hematopoietic cytokine-receptor interactions
Savvas Savvides	Ghent University	Structural studies of Old Yellow Enzyme from S. Oneidensis at ultra-high resolution
Sebastian Glawion	Universität Würzburg	Resonant photoemission spectroscopy on doped and undoped transition metal oxyhalides
Sebastian Müller	Brandenburgische Technische Universität Cottbus	Adsorption of ultrathin Chromium and Cobalt layers on Titanium Dioxide
Sebastian Müller	Brandenburgische Technische Universität Cottbus	Properties of ultrathin Cobalt films on TiO2
Sébastien Bonhommeau	BESSY GmbH	Soft x-ray resonant scattering on orbital order in Magnetite
Sébastien Bonhommeau	BESSY GmbH	Thin films of MnFe Prussian blue analogues investigated by x-ray magnetic circular dichroism
Sebastien Moniot	Freie Universität Berlin	PX-CRG: Crystallographic studies of cyanobacterial photosystem II
Sebastien Moniot	Freie Universität Berlin	PX-CRG: Demonstration of structural molecular mimicry in HLA class I/peptide complexes
Sebastien Moniot	Freie Universität Berlin	PX-CRG: Structural studies of proteins required for homeostasis of copper in Enterococcus hirae
Sebastien Moniot	Freie Universität Berlin	PX-CRG: Structure and Function of the Replisome of Plasmid RSF1010

List of Projects 2008

Project Leader	Institute	Project Title
Sergej Borisenko	IFW Dresden	Commissioning of the He3 cryostat for the "one-cubed" endstation of the UE112-PGM-2b beamline.
Sergej Borisenko	IFW Dresden	Investigation of the high-energy kinks in high-Tc superconducting cuprates.
Sergey Subach	Forschungszentrum Jülich GmbH	Investigating the molecular orientation in complex organic phases: Tetracene on Ag(111)
Sergey Troyanov	Humboldt-Universität zu Berlin	Crystal and molecular structures of organic derivatives of fullerenes
Sergey Troyanov	Humboldt-Universität zu Berlin	Molecular structure of perfluoroalkylated fullerenes
Sergio Valencia Molina	Helmholtz Zentrum Berlin für Materialien und Energie	A resonant X-ray scattering study of magnetic ordering and electromagnetic properties in multiferroic BiFeO3 thin films
Serguei Molodtsov	Technische Universität Dresden	Hybridization of 4f and valence-band states in heavy rare-earth systems
Serguei Molodtsov	Technische Universität Dresden	Photoemission and NEXAFS study of electronic structure and electron transfer in pristine and metallized DNA
Serguei Molodtsov	Technische Universität Dresden	Size-dependent electronic structure of Au nanoclusters embedded in protein matrices
Serguei Molodtsov	Technische Universität Dresden	Ultra-high resolution photoemission study of Eu-derived heavy-fermion systems
Shin Imada	Osaka university	XMCD-PEEM study of the mechanism for the disappearence of remanent perpendicular magnetization below Curie temperature in subnanometer-thick L10 FePt film
Silvia Dante	Helmholtz Zentrum Berlin für Materialien und Energie	Interaction of the Alzheimer's peptide Abeta(1-42) with unilamellar vesicles of phospholipids
Sina Möhlmann	Institut für Mikrobiologie und Genetik GZMB	Crystallographic studies on the human spliceosomal DEAD-box protein hPrp28 (U5-100k)
Socrates Tzartos	Hellenic Pasteur Institute	Determination of the crystal structures of human nicotinic acetylcholine receptor extracellular domains.
Sofia Macedo	University of Vienna - Max F. Perutz Laboratories	Reduction of metalloproteins by incoming X-rays
Sohail Khoshnevis	Institut für Mikrobiologie und Genetik GZMB	structural investigation of translation initiation factors 3 in yeast: structure determination of Tif34
Sophie Canton	University of Lund	X-Ray Absorption Spectroscopy on new symmetric and asymmetric biomimetic complexes modelling active sites in metalloenzymes
Souren Grigorian	Universität Siegen	Measurements the reflectivity properties of various multilayer structures in soft x-ray range
Stefan Buschhorn	Ruhr-Universität Bochum	Precession of magnetic moments in patterned magnetic films
Stefan Buschhorn	Ruhr-Universität Bochum	time-resolved XRMS experiments on Invar
Stefan Cramm	Forschungszentrum Jülich GmbH	Detection of voltage-controlled magnetization switching in Fe/Si/Fe trilayers by linear and circular magnetic X-ray dichroism.
Stefan Eisebitt	BESSY GmbH	High Resolution X-ray Holographic Imaging of Cells
Stefan Eisebitt	BESSY GmbH	Lensless Imaging of Magnetic Domains via Resonant Scattering at the M-Edges of 3d Transition Metals
Stefan Eisebitt	BESSY GmbH	Magnetization Dynamics in Ferromagnetic Multilayer Materials studied by Photon Correlation Spectroscopy
Stefan Eisebitt	BESSY GmbH	Polarization Dependence in Holographic Imaging of Magnetic Structures
Stefan Eisebitt	BESSY GmbH	X-Ray Holographic Imaging of Low-Contrast Objects
Stefan Eisebitt	BESSY GmbH	X-ray Spectro-Holography in Reflection Geometry
Stefan Hendel	Universität Bielefeld	At-wavelength reflectivity measurements of La/B4C-multilayer stacks at the energy range up to 190 eV
Stefano Agrestini	ENSICAEN	spin transition and chemical state in the Colossal Magneto-Resistive GdBaCo2O5+x
Steven Tait	Max-Planck-Institut für Festkörperforschung	Structure and Coordination Geometry of 2D Cu-TCNQ Coordination Systems on Cu(100) by Near Edge X-ray Absorption Fine Structure
Sung Seok Seo	Oak Ridge National Laboratory	Soft x-ray scattering of two-dimensional LaTiO3/LaAlO3 superlattices
Svante Svensson	Uppsala University	HIKE studies of mutilayers and nanostructured materials for applications in magnetism, solar cell devices, Li ion batteries and fuel cells

List of Projects 2008

Project Leader	Institute	Project Title
Sven Döring	Universität Dortmund	Hard x-ray photoemission: depth-resolution with standing-wave excitation and angle- resolved measurements
Sylvia Luckner	Universität Würzburg	X-Ray structures of Mycobacterium tuberculosis KasA inhibitor complexes
Sylvia Wenmackers	Hasselt University	Vacuum Ultra-Violet Spectroscopic Ellipsometry of DNA Layers Covalently Attached onto Synthetic Diamond Films for Biosensor Application
Sylvio Haas	Helmholtz Zentrum Berlin für Materialien und Energie	Further developments of the SAXS-instrument: Improvements of the calibration procedure for the position-sensitive multi-wire proportional counter (MWPC) detector with delay line readout
Sylvio Haas	Helmholtz Zentrum Berlin für Materialien und Energie	Nano-structure investigations of transparent glass ceramics codoped with Er3+ and Yb3+ ions for efficient frequency upconversion by ASAXS
Tamas Haraszti	Universität Heidelberg	Melanosomal ultrastructure imaging with TXM
Tatiana Sukhanova	Institute of Macromolecular Compounds (Russian Academy of Sciences)	ELECTRONIC STRUCTURE OF PLATINUM NANOPARTICLES STABILIZED BY WATER SOLUBLE POLYMERS
Thalia Deniozou	Fritz-Haber-Institut der Max-Planck-Gesellschaft	Core and Valence level studies on the T-Al3(Mn, Pd) complex metallic alloy and thin films
Thomas Elsaesser	Max-Born-Institut für Nichtlineare Optik und Kurzzeitspektroskopie	Ultrafast infrared-pump/x-ray probe spectroscopy of water
Thomas Geue	Paul Scherrer Institut	Formation of 3D colloidal layers on structured substrates from colloidal dispersions
Thomas Kroll	IFW Dresden	Electronic structure of doped metal phthalocyanine complexes
Thomas Mayer	Technische Universität Darmstadt	Electronic structure of organic/inorganic composites for photovoltaic application
Thomas Mayer	Technische Universität Darmstadt	Photo-electron-spectroscopic analysis of energy-converting interfaces for optimization in long-living powerful organic solar cells
Thomas Monecke	Institut für Mikrobiologie und Genetik GZMB	3D crystal structure of the ternary export complex consisiting of the export factor Crm1 bound to RanGTP and its substrate Snurportin1
Thomas Monecke	Institut für Mikrobiologie und Genetik GZMB	Determination of the crystal structure of the active m7G-cap specific dimethyltransferase Tgs1 in complex with its substrates m7GTP and S-adenosyl-L-methionine.
Thomas Nitschke-Pagel	Technische Universität Braunschweig	Determination of residual stress depth fields in welded joints after different mechanical surface treatments
Thomas Pichler	Universität Wien	Charge transfer versus hybridisation in alkaline earth intercalated graphite and implications to superconductivity in CaC6
Thomas Pichler	Universität Wien	Doping dependence of basic correlation effects in graphite
Thomas Pichler	Universität Wien	Tracing nanochemical reactions inside the 1D confinement of single wall carbon nanotubes
Thomas Schmidt	Fritz-Haber-Institut der Max-Planck-Gesellschaft	High resolution electron spectroscopy with the aberration corrected SMART-spectro-microscope at a high flux density beamline
Thomas Seyller	Universität Erlangen-Nürnberg	Electronic structure of Au nano-wires on SiC(1-100)
Thomas Seyller	Universität Erlangen-Nürnberg	Electronic structure of cleaved SiC{0001} surfaces
Thomas Seyller	Universität Erlangen-Nürnberg	Graphene on SiC - doping and intercalation
Thomas Seyller	Universität Erlangen-Nürnberg	Metal overlayers on SiC surfaces
Thomas Strunskus	Christian-Albrechts-Universität zu Kiel	Attachment of Mo- and W-metal complexes to self assembled monolayers on gold surfaces
Till Jahnke	Johann Wolfgang Goethe-Universität Frankfurt	Investigation And Complete Characterization Of Interatomic Coulombic Decay In Water Dimers
Tim O'Sullivan	University of Limerick	Further Investigation into the Mechanism of Nucleation and Growth of Silica Scale on Steel Substrate.
Tim O'Sullivan	University of Limerick	Investigation into the Mechanism of Nucleation and Growth of Silica Scale on Steel Substrate.
Tim Salditt	Universität Göttingen	Transmission X-ray microscopy of olfactory neural cells: The ultrastructure of ciliae
Tina Ritschel	Philipps-Universität Marburg	Structure-based Drug Design for TGT, an Enzyme linked to the Pathogenicity of the Shigella Bacterium

List of Projects 2008

Project Leader	Institute	Project Title
Tobias Lau	Technische Universität Berlin	Charge and Energy Transfer in Transition Metal Doped Endohedral Silicon Clusters: A Systematic Photofragmentation Study
Tobias Lau	Technische Universität Berlin	Quantum size effects in doped silicon clusters
Tobias Lau	Technische Universität Berlin	Transition Metal Clusters at the Molecular Limit
Tobias Lau	Technische Universität Berlin	Transition Metal Molecules: Electronic Configuration and Bonding in very small Chromium and Manganese Clusters
Tobias Panzner	Universität Siegen	Development and application of an energy dispersive CCD-Devise for hard x-ray synchrotron radiation
Tobias Panzner	Universität Siegen	Energy dispersive X-ray-Photon-Correlation-Spectroscopy using a energy dispersive CCD-Devise
Torsten Staab	Rheinische Friedrich-Wilhelms-Universität Bonn	The Role of Magnesium in the Formation of Nano-Clusters in Aluminum-MgSi alloys
Ulf Wiedwald	Universität Ulm	Non-interacting FePt Nanoparticles: Suppression of L10 order below a critical diameter?
Ulla Vainio	HASYLAB at DESY	Distribution of charged groups in lignosulfonate particles
Ulrike Wagner	Karl-Franzens-Universität Graz	Deciphering catalytic promiscuity between beta-lactamases and family VIII esterases.
Uwe Hergenhahn	Max-Planck-Institut für Plasmaphysik	Charakterisierung molekularer Auger-Zerfälle
Uwe Hergenhahn	Max-Planck-Institut für Plasmaphysik	Koinzidente Photoelektron-Auger Elektron Messungen
Uwe Hergenhahn	Max-Planck-Institut für Plasmaphysik	Photoionization and autoionization of weakly bonded clusters
Uzuki Matsushima	Iwate University	Development of a combination method of synchrotron X-ray tomography and cold neutron tomography to observe structure and water flow in plant stems -Part III-
Vadim Alekseev	St. Petersburg State University	Spectroscopy and photochemistry of gas phase mixtures of halogens with rare gases.
Vadim Galakhov	Russian Academy of Sciences - Ural Division	X-ray photoelectron and absorption spectroscopic studies of the electronic states of 3d nanooxides obtained by different high pressure treatment
Valeri Nazin	Kurchatov Synchrotron Radiation Source	UPS study of Ti-Zr-Ni quasicrystal system
Valerii Bukhtiyarov	Boreskov Institute of Catalysis	In situ X-ray photoelectron spectroscopy (XPS) and mass-spectrometry study of olefin (ethylene and propylene) epoxidation over supported silver catalysts
Valerii Bukhtiyarov	Boreskov Institute of Catalysis	In-situ XPS study of Pt/Al2O3 and Pd/Al2O3 catalysts for total methane oxidation
Valerii Bukhtiyarov	Boreskov Institute of Catalysis	XPS and Auger study of nano-sized gold particles on iron oxides
Valery Mikoushkin	Ioffe Physico-Technical Institute	Why fullerene becomes a dielectric in fluorination?
Vasily Kaichev	Boreskov Institute of Catalysis	In situ XPS and mass-spectrometry study of deactivation of palladium catalysts in propylene oxidation
Veronique Dupuis	Universite Claude Bernard Lyon I	Co-magnetic moment in CoxPt1-x clusters as a function of size, concentration and chemical order.
Victor Aristov	Russian Academy of Sciences	Is the atomically clean Si(100) surface of paramount practical importance metallic below 10K?
Victor Sivkov	Komi Science Center Ural Division Russian Academy of Sciences	The oscillator strength distributions in the NEXAFS spectra of bacterial surface protein layers: X-ray damage.
Vladimir Komlev	Università Politecnica delle Marche	X-ray Microtomography Analysis for Engineered Heart Tissue
Volker Schmidt	Universität Ulm	Examination of stochastic structures and structure related transport processes in porous media
Volodymyr Zabolotnyy	IFW Dresden	Investigation of charge density waves and superconductivity in NbSe2
Walther Schwarzacher	University of Bristol	GISAXS of electrodeposited Pb island films
Werner Unterberger	Fritz-Haber-Institut der Max-Planck-Gesellschaft	High pressure' surface structure determination: a test of a new method
Werner Unterberger	Fritz-Haber-Institut der Max-Planck-Gesellschaft	Biologically-related molecules, chirality and oxide surfaces: photoelectron diffraction determination of local adsorption geometries.
Werner Unterberger	Fritz-Haber-Institut der Max-Planck-Gesellschaft	Complex molecules, chirality and oxide surfaces: photoelectron diffraction determination of local adsorption geometries
Wilko Rauert	Universität Würzburg	Structural studies of the ubiquitin activating enzyme E1
Willy Mahler	Fritz-Haber-Institut der Max-Planck-Gesellschaft	Optimierung des Zweistrahbetriebes an den UE56/2-Strahlrohren bei BESSY

List of Projects 2008

Project Leader	Institute	Project Title
Winfried Seifert	IHP-Microelectronics	Analysis of transition metal contamination in solar-grade Si: interaction processes and impact on electrical properties
Witoslaw Kielich	Universität Kassel	Bestimmung von Potenzialkurven angeregter CO^2+ Zustände über deren Fluoreszenzzerfall.
Witoslaw Kielich	Universität Kassel	Determination of fluorescence cascades and branching ratios of fluorescence transitions in singly ionized Xe after autoionization of doubly excited neutral Xe-states
Witoslaw Kielich	Universität Kassel	Interferenzeffekte zwischen Zerfallskanälen benachbarter lebensdauerverbreiterter vibronischer Zustände nach Innerschalenelektronenanregung von CO.
Wolf-Dieter Schubert	Helmholtz Zentrum für Infektionsforschung (HZI)	Structural and Functional Analysis of virulence associated proteins of bacteria and viruses, and enzymes of heme biosynthesis.
Wolfgang Braun	Paul-Drude-Institut für Festkörperelektronik	Analysis of the growth and interface structure of rare earth oxide compounds on Si (001)
Wolfgang Braun	Paul-Drude-Institut für Festkörperelektronik	Formation of interface dislocation network during the growth of antimonides on GaAs and Si
Wolfgang Braun	Paul-Drude-Institut für Festkörperelektronik	III-V channels on Si for future CMOS devices
Wolfgang Braun	Paul-Drude-Institut für Festkörperelektronik	Interface and layer structure of Gd2O3 epitaxy on Si(111)
Wolfgang Braun	Paul-Drude-Institut für Festkörperelektronik	Synthesis and in-situ structural analysis of epitaxial phase change materials for nanoscale storage applications
Wolfgang Höhne	Humboldt-Universität zu Berlin, Charité	PX-CRG Studies on enzyme mechanisms and investigation of protein-ligand interactions by crystallographic methods.
Wolfgang Höhne	Humboldt-Universität zu Berlin, Charité	Structural analysis of maturation and accessory proteins of bacterial [NiFe] hydrogenases
Wolfgang Kuch	Freie Universität Berlin	Layer-resolved XMCD-PEEM study of magnetic domains in coupled trilayered structures with the highest spatial resolution
Wolfgang Kuch	Freie Universität Berlin	Substrate- and ligand-dependent changes in the electronic properties of adsorbed spin crossover molecules
Wolfgang Kuch	Freie Universität Berlin	X-ray absorption spectroscopic and spectro-microscopic investigation of adsorbed switchable molecules
Wolfgang Kuch	Freie Universität Berlin	Zeit- und örtlich hochaufgelöste Magnetisierungsdynamik in magnetischen Nano- und Mehrschichtsystemen
Wolfgang Unger	Bundesanstalt f. Materialforschung und -prüfung	Determination of unsaturated CN species and amino groups at complex functional organic surfaces prepared by plasma techniques using a "two step analysis" NEXAFS approach
Wolfgang Unger	Bundesanstalt f. Materialforschung und -prüfung	Development of analytical methods for smart ultra-thin films with tailored surface properties
Wolfgang Unger	Bundesanstalt f. Materialforschung und -prüfung	Signatures of amine species at aminated surfaces used as platforms for microarray based diagnostic devices (lab-on-the-chip) developed for life science applications
Wolfgang Unger	Bundesanstalt f. Materialforschung und -prüfung	Validated test sample and derivatization reaction for the assessment of quantitative surface analytical protocols for the determination of amines by inter-laboratory comparison
Yael Politi	Weizmann Institute of Science	Time dependent Mg K-edge NEXAFS study on the transformation of Mg-ACC to Mg-calcite in developing sea urchin larval spicules.
Yurii Ossipyan	Russian Academy of Sciences	Investigation of electronic properties of transition metal phthalocianines by a combination of ResPES, PES, NEXAFS and first principles calculations
Yuriy Dedkov	Fritz-Haber-Institut der Max-Planck-Gesellschaft	Spin-resolved photoelectron spectroscopy of magnetic systems formed by intercalation: MG/TM/Rh(111) [MG=monolayer of graphite (graphene), TM=Fe,Co]
Yury Dobrovolsky	Russian Academy of Sciences	The mechanism of Pt cluster formation on different carbon materials for fuel cells application
Yves Muller	Universität Erlangen-Nürnberg	Allosteric mechanism of Tet-Repressor action (This is the continuation of the proposal: 2007_2_70347)
Yves Muller	Universität Erlangen-Nürnberg	Crystal structure determination of progesterone 5-beta-reductase from Digitalis lanata.

List of Projects 2008

Project Leader	Institute	Project Title
Yves Muller	Universität Erlangen-Nürnberg	Crystal structure determination of YvoA, a bacterial transcriptional regulator of the HutC-family
Yves Muller	Universität Erlangen-Nürnberg	Crystal structure of corticosteroid-binding globulin (CBG)
Yvette Roske	Max-Delbrück-Centrum für Molekulare Medizin	Human proteins of medical and pharmacological relevance
Yvette Roske	Max-Delbrück-Centrum für Molekulare Medizin	medical and pharmalogical relevant human and bacterial proteins and proteins involved in nucleocytoplasmic transport

Publication List 2008

Abrudan, R., J. Miguel, M. Bernien, C. Tieg, M. Piantek, J. Kirschner and W. Kuch (2008). "*Structural and magnetic properties of epitaxial Fe/CoO bilayers on Ag(001)*." Physical Review B **77**(1): 014411.

Aliouane, N., O. Prokhnenko, R. Feyerherm, M. Mostovoy, J. Strempfer, K. Habicht, K. C. Rule, E. Dudzik, A. U. B. Wolter, A. Maljuk and D. N. Argyriou (2008). "*Magnetic order and ferroelectricity in RMnO3 multiferroic manganites: coupling between R- and Mn-spins*." Journal of Physics-Condensed Matter **20**(43): 434215.

Andriyevsky, B., W. Ciepluch-Trojanek, C. Cobet, A. Patryn and N. Esser (2008). "*Optical spectra of triglycine sulfate crystals in the range of 7-33 eV and its changes at phase transition*." Phase Transitions **81**(10): 949-961.

Angelucci, F. (2008). "*Glutathione reductase and thioredoxin reductase at the crossroad: The structure of Schistosoma mansoni thioredoxin glutathione reductase*." Proteins **72**(3): 936-945.

Antoniak, C., A. Trunova, M. Spasova, M. Farle, H. Wende, F. Wilhelm and A. Rogalev (2008). "*Lattice expansion in nonoxidized FePt nanoparticles: X-ray absorption measurements*." Physical Review B **78**(4): 041406.

Arcovito, A., T. Moschetti, P. D'Angelo, G. Mancini, B. Vallone, M. Brunori and S. Della Longa (2008). "*An X-ray diffraction and X-ray absorption spectroscopy joint study of neuroglobin*." Archives of Biochemistry and Biophysics **475**(1): 7-13.

Arion, T., R. Flesch, T. Schlatholter, F. Alvarado, R. Hoekstra, R. Morgenstern and E. Ruhl (2008). "*Collision induced fragmentation of free sulfur clusters*." International Journal of Mass Spectrometry **277**(1-3): 197-205.

Aziz, E. F., N. Ottosson, S. Eisebitt, W. Eberhardt, B. Jagoda-Cwiklik, R. Vacha, P. Jungwirth and B. Winter (2008). "*Cation-specific interactions with carboxylate in amino acid and acetate*." Journal of Physical Chemistry B **112**(40): 12567-12570.

Aziz, E. F., N. Ottosson, M. Faubel, I. V. Hertel and B. Winter (2008). "*Interaction between liquid water and hydroxide revealed by core-hole*." Nature **455**(7209): 89-91.

Bagus, P. S., H. Freund, H. Kuhlenbeck and E. S. Ilton (2008). "*A new analysis of X-ray adsorption branching ratios: Use of Russell-Saunders coupling*." Chemical Physics Letters **455**(4-6): 331-334.

Balke, B., G. H. Fecher, A. Gloskovskii, J. Barth, K. Kroth, C. Felser, R. Robert and A. Weidenkaff (2008). "*Doped semiconductors as half-metallic materials: Experiments and first-principles calculations of CoTi1-xMxSb (M = Sc, V, Cr, Mn, Fe)*." Physical Review B **77**(4): 045209.

Ballav, N. and M. Zharnikov (2008). "*Reorientation-promoted exchange reaction in aromatic self-assembled monolayers*." Journal of Physical Chemistry C **112**(38): 15037-15044.

Balogh, Z., C. Cserhati, Z. Erdelyi, A. Csik, G. A. Langer, I. Zizak, N. Darowski, E. Dudzik, R. Feyerherm and D. L. Beke (2008). "*Silicide formation reactions in a-Si/Co multilayered samples.*" Diffusion and Diffusional Phase Transformations in Alloys **277**: 3-8.

Barbirz, S., J. J. Muller, C. Uetrecht, A. J. Clark, U. Heinemann and R. Seckler (2008). "*Crystal structure of Escherichia coli phage HK620 tailspike: podoviral tailspike endoglycosidase modules are evolutionarily related.*" Molecular Microbiology **69**(2): 303-316.

Bartoll, J., O. Hahn and U. Schade (2008). "*Application of Synchrotron Infrared Radiation in the Study of Organic Coatings in Cross-Sections.*" Studies in Conservation **53**(1): 1-8.

Beckhoff, B., M. Kolbe, O. Hahn, A. G. Karydas, C. Zarkadas, D. Sokaras and M. Mantler (2008). "*Reference-free x-ray fluorescence analysis of an ancient Chinese ceramic.*" X-Ray Spectrometry **37**(4): 462-465.

Beckhoff, B. (2008). "*Reference-free X-ray spectrometry based on metrology using synchrotron radiation.*" Journal of Analytical Atomic Spectrometry **23**(6): 845-853.

Beckhoff, B., R. Fliegauf, M. Kolbe, M. Muller, B. Pollakowski, J. Weser and G. Ulm (2008). "*X-ray spectrometry for wafer contamination analysis and speciation as well as for reference-free nanolayer characterization.*" Ultra Clean Processing of Semiconductor Surfaces Viii **134**: 277-280.

BenMoussa, A., A. Soltani, K. Haenen, U. Kroth, V. Mortet, H. A. Barkad, D. Bolsee, C. Hermans, M. Richter, J. C. De Jaeger and J. F. Hochedez (2008). "*New developments on diamond photodetector for VUV solar observations.*" Semiconductor Science and Technology **23**(3): 035026.

BenMoussa, A., J. F. Hochedez, R. Dahal, J. Li, J. Y. Lin, H. X. Jiang, A. Soltani, J. C. De Jaeger, U. Kroth and M. Richter (2008). "*Characterization of AlN metal-semiconductor-metal diodes in the spectral range of 44-360 nm: Photoemission assessments.*" Applied Physics Letters **92**(2): 022108.

Bohnenbuck, B., I. Zegkinoglou, J. Strempfer, C. Schussler-Langeheine, C. S. Nelson, P. Leininger, H. H. Wu, E. Schierle, J. C. Lang, G. Srajer, S. I. Ikeda, Y. Yoshida, K. Iwata, S. Katano, N. Kikugawa and B. Keimer (2008). "*Magnetic structure and orbital state of Ca3Ru2O7 investigated by resonant x-ray diffraction.*" Physical Review B **77**(22): 224412.

Bradeanu, I. L., N. Kosugi, R. Flesch and E. Ruhl (2008). "*Site-dependent spectral shifts in core-to-pi* excitations of pyridine clusters.*" Journal of Physical Chemistry A **112**(39): 9192-9199.

Breuer, S., D. T. Pham, S. Huemann, K. Gentz, C. Zoerlein, R. Hunger, K. Wandelt and P. Broekmann (2008). "*Organic layers at metal/electrolyte interfaces: molecular structure and reactivity of viologen monolayers.*" New Journal of Physics **10**(12): 125033.

Bruck, S., G. Schutz, E. Goering, X. S. Ji and K. M. Krishnan (2008). "*Uncompensated moments in the MnPd/Fe exchange bias system.*" Physical Review Letters **101**(12): 126402.

Bruck, S., S. Bauknecht, B. Ludescher, E. Goering and G. Schutz (2008). "*An advanced magnetic reflectometer.*" Review of Scientific Instruments **79**(8): 083109.

Brzhezinskaya, M. M., N. A. Vinogradov, V. E. Muradyan, Y. M. Shul'ga and A. S. Vinogradov (2008). "*Electronic structure of fluorinated carbon nanotubes studied by X-ray absorption and photoelectron spectroscopy.*" Fullerenes Nanotubes and Carbon Nanostructures **16**(5-6): 335-339.

Brzhezinskaya, M. M., N. A. Vinogradov, V. E. Muradyan, Y. M. Shul'ga, N. V. Polyakova and A. S. Vinogradov (2008). "*Characterization of fluorinated multiwalled carbon nanotubes by x-ray absorption spectroscopy.*" Physics of the Solid State **50**(3): 587-594.

Bugoi, R., V. Cojocaru, B. Constantinescu, T. Calligaro, L. Pichon, S. Rohrs and J. Salomon (2008). "*Compositional studies on Transylvanian gold nuggets: Advantages and limitations of PIXE-PIGE analysis.*" Nuclear Instruments & Methods in Physics Research Section B-Beam Interactions with Materials and Atoms **266**(10): 2316-2319.

Cabarcos, O. M., A. Shaporenko, T. Weidner, S. Uppili, L. S. Dake, M. Zharnikov and D. L. Allara (2008). "*Physical and electronic structure effects of embedded dipoles in self-assembled monolayers: Characterization of mid-chain ester functionalized alkanethiols on Au{111}.*" Journal of Physical Chemistry C **112**(29): 10842-10854.

Calvani, P., S. Lupi, M. Ortolani, L. Baldassarre, C. Mirri, R. Sopracase, U. Schade, Y. Takano and T. Tamegai (2008). "*Study of the optical gap in novel superconductors by coherent THz radiation.*" Infrared Physics & Technology **51**(5): 429-432.

Cattani-Scholz, A., D. Pedone, M. Dubey, S. Neppl, B. Nickel, P. Feulner, J. Schwartz, G. Abstreiter and M. Tornow (2008). "*Organophosphonate-based PNA-functionalization of silicon nanowires for label-free DNA detection.*" Acs Nano **2**(8): 1653-1660.

Conard, T., S. List, M. Claes and B. Beckhoff (2008). "*Advanced metrologies for cleans characterization: ARXPS, GIXF and NEXAFS.*" Ultra Clean Processing of Semiconductor Surfaces Viii **134**: 281-284.

Cserhati, C., Z. Balogh, A. Csik, G. A. Langer, Z. Erdelyi, G. Y. Glodan, G. L. Katona, D. L. Beke, I. Zizak, N. Darowski, E. Dudzik and R. Feyerherm (2008). "*Linear growth kinetics of nanometric silicides in Co/amorphous-Si and Co/CoSi/amorphous-Si thin films.*" Journal of Applied Physics **104**(2): 024311.

Cyganik, P., K. Szelagowska-Kunstman, A. Terfort and M. Zharnikov (2008). "*Odd-even effect in molecular packing of biphenyl-substituted alkaneselenolate self-assembled monolayers on Au(111): Scanning tunneling microscopy study.*" Journal of Physical Chemistry C **112**(39): 15466-15473.

Dau, H. and M. Haumann (2008). "*The manganese complex of photosystem II in its reaction cycle - Basic framework and possible realization at the atomic level*." Coordination Chemistry Reviews **252**(3-4): 273-295.

Dorr, S., U. Schade and P. Hellwig (2008). "*Far infrared spectroscopy on hemoproteins: A model compound study from 1800-100 cm(-1)*." Vibrational Spectroscopy **47**(1): 59-65.

Dubiel, M., J. Haug, H. Kruth, H. Hofmeister and K.-D. Schicke (2008). "*Ag/Na ion exchange in soda-lime glasses and the formation of small Ag nanoparticles*." Materials Science and Engineering: B, E-MRS 2007 Fall Conference Symposium F: The binary ion exchange process in materials science and chemistry: application, characterization and modelling. **149**(2): 146-151.

Durr, H. A., C. Stamm, T. Kachel, N. Pontius, R. Mitzner, T. Quast, K. Holldack, S. Khan, C. Lupulescu, E. F. Aziz, M. Wietstruk and W. Eberhardt (2008). "*Ultrafast electron and spin dynamics in nickel probed with femtosecond X-ray pulses*." Ieee Transactions on Magnetics **44**(7): 1957-1961.

Eimuller, T., P. Guttmann and S. N. Gorb (2008). "*Terminal contact elements of insect attachment devices studied by transmission X-ray microscopy*." Journal of Experimental Biology **211**(12): 1958-1963.

Elbing, M., A. Blaszczyk, C. von Haenisch, M. Mayor, V. Ferri, C. Grave, M. A. Rampi, G. Pace, P. Samori, A. Shaporenko and M. Zharnikov (2008). "*Single Component Self-Assembled Monolayers of Aromatic Azo-Biphenyl: Influence of the Packing Tightness on the SAM Structure and Light-Induced Molecular Movements*." Advanced Functional Materials **18**(19): 2972-2983.

Eriksson, F., N. Ghafoor, F. Schafers, E. M. Gullikson, S. Aouadi, S. Rohde, L. Hultman and J. Birch (2008). "*Atomic scale interface engineering by modulated ion-assisted deposition applied to soft x-ray multilayer optics*." Applied Optics **47**(23): 4196-4204.

Feng, D., J. Liu, A. P. Hitchcock, A. L. D. Kilcoyne, T. Tyliszczak, N. F. Riehs, E. Ruhl, J. D. Bozek, D. McIlroy and P. A. Dowben (2008). "*Photofragmentation of closo-carboranes. part 1: Energetics of decomposition*." Journal of Physical Chemistry A **112**(15): 3311-3318.

Flesch, R., A. Wirsing, M. Barthel, J. Plenge and E. Ruhl (2008). "*Inner-valence photoionization of O(D-1): Experimental evidence for the 2s(2)2p(4)(D-1)-> 2s(1)2p(5)(P-1) transition*." Journal of Chemical Physics **128**(7): 074307.

Fuchs, M. R., K. Holldack, M. Bullough, S. Walsh, C. Wilburn, A. Erko, F. Schafers and U. Mueller (2008). "*Transmissive x-ray beam position monitors with submicron position- and submillisecond time resolution*." Review of Scientific Instruments **79**(6): 063103.

Gaal, P., W. Kuehn, K. Reimann, M. Woerner, T. Elsaesser, R. Hey, J. S. Lee and U. Schade (2008). "*Carrier-wave Rabi flopping on radiatively coupled shallow donor transitions in n-type GaAs*." Physical Review B **77**(23): 235204.

Galakhov, V. R., M. A. Melkozerova, T. I. Chupakhina, G. V. Bazuev, M. Raekers, M. Neumann and S. L. Molodtsov (2008). "*Valence states of 3d ions in lanthanum manganites-cobaltites, determined by X-ray spectroscopy.*" Bulletin of the Russian Academy of Sciences: Physics **72**(10): 1403-1405.

Galakhov, V. R., M. Neumann and D. G. Kellerman (2008). "*Electronic structure of defective lithium cobaltites Li x CoO2.*" Applied Physics A: Materials Science and Processing: 1-4.

Gaudin, J., S. Rehbein, P. Guttmann, S. Gode, G. Schneider, P. Wernet and W. Eberhardt (2008). "*Selection of a single femtosecond high-order harmonic using a zone plate based monochromator.*" Journal of Applied Physics **104**(3): 033112.

Gerlach, M., M. Krumrey, L. Cibik, P. Muller, H. Rabus and G. Ulm (2008). "*Cryogenic radiometry in the hard x-ray range.*" Metrologia **45**(5): 577-585.

Girard-Lauriault, P. L., P. Desjardins, W. E. S. Unger, A. Lippitz and M. R. Wertheimer (2008). "*Chemical characterisation of nitrogen-rich plasma-polymer films deposited in dielectric barrier discharges at atmospheric pressure.*" Plasma Processes and Polymers **5**(7): 631-644.

Gomoyunova, M. V., D. E. Malygin and I. I. Pronin (2008). "*Processes of silicide formation in the Fe/Si(111)7x7 system.*" Physics of the Solid State **50**(8): 1579-1584.

Graf, N., E. Yegen, A. Lippitz, D. Treu, T. Wirth and W. E. S. Unger (2008). "*Optimization of cleaning and amino-silanization protocols for Si wafers to be used as platforms for biochip microarrays by surface analysis (XPS, ToF-SIMS and NEXAFS spectroscopy).*" Surface and Interface Analysis **40**(3-4): 180-183.

Graf, C., B. Langer, M. Grimm, R. Lewinski, M. Grom and E. Ruhl (2008). "*Investigation of trapped metallo-dielectric core-shell colloidal particles using soft X-rays.*" Journal of Electron Spectroscopy and Related Phenomena **166**: 74-80.

Gruneis, A., C. Attaccalite, T. Pichler, V. Zabolotnyy, H. Shiozawa, S. L. Molodtsov, D. Inosov, A. Koitzsch, M. Knupfer, J. Schiessling, R. Follath, R. Weber, P. Rudolf, L. Wirtz and A. Rubio (2008). "*Electron-electron correlation in graphite: A combined angle-resolved photoemission and first-principles study.*" Physical Review Letters **100**(3): 037601.

Guerra, M. F., M. Radtke, I. Reiche, H. Riesemeier and E. Strub (2008). "*Analysis of trace elements in gold alloys by SR-XRF at high energy at the BAMline.*" Nuclear Instruments & Methods in Physics Research Section B-Beam Interactions with Materials and Atoms **266**(10): 2334-2338.

Guimond, S., J. M. Sturm, D. Gobke, Y. Romanyshyn, M. Naschitzki, H. Kuhlenbeck and H. J. Freund (2008). "*Well-ordered V2O5(001) thin films on Au(111): Growth and thermal stability.*" Journal of Physical Chemistry C **112**(31): 11835-11846.

Guimond, S., D. Gobke, Y. Romanyshyn, J. M. Sturm, M. Naschitzki, H. Kuhlenbeck and H. J. Freund (2008). "*Growth and characterization of ultrathin V2Oy (y approximate to 5) films on Au(111).*" Journal of Physical Chemistry C **112**(32): 12363-12373.

Gutsche, R. and G. Bunke (2008). "*Modelling the liquid-phase adsorption in packed beds at low Reynolds numbers: An improved hydrodynamic model.*" Chemical Engineering Science **63**(16): 4203-4217.

Hallmann, L., A. Bashir, T. Strunskus, R. Adelung, V. Staemmler, C. Woll and F. Tuczek (2008). "*Self-assembled monolayers of benzylmercaptan and p-cyanobenzylmereaptan on Au(111) surfaces: Structural and spectroscopic characterization.*" Langmuir **24**(11): 5726-5733.

Hartnig, C., R. Kuhn, P. Kruger, I. Manke, N. Kardjilov, J. Goebbels, B. R. Muller and H. Riesemeier (2008). "*Water management in fuel cells - a challenge for non-desctructive high resolution methods.*" Mp Materials Testing-Materials and Components Technology and Application **50**(10): 609-614.

Held, G. and M. J. Gladys (2008). "*The chemistry of intrinsically chiral surfaces.*" Topics in Catalysis **48**(1-4): 128-136.

Ivanova, M. (2008). "*NWA 4757: metamorphosed carbonaceous CM chondrite.*" Meteoritics and Planetary Science **43**(Supplement): A66-A66.

Jagoda-Cwiklik, B. (2008). "*Ionization of aqueous cations: Photoelectron spectroscopy and ab initio.*" Journal of Physical Chemistry B **112**(25): 7355-7358.

Jagoda-Cwiklik, B. and P. Jungwirth (2008). "*Ionization of imidazole in the gas phase, microhydrated environments.*" Journal of Physical Chemistry A **112**(16): 3499-3505.

Jenichen, B., V. M. Kaganer, W. Braun, R. Shayduk, B. Tinkham and J. Herfort (2008). "*In situ X-ray diffraction study of epitaxial growth of ordered Fe3Si films.*" Journal of Materials Science-Materials in Electronics **19**: S199-S202.

Jenkins, C. A., R. Ramesh, M. Huth, T. Eichhorn, P. Porsch, H. J. Elmers and G. Jakob (2008). "*Growth and magnetic control of twinning structure in thin films of Heusler shape memory compound Ni2MnGa.*" Applied Physics Letters **93**(23): 234101.

Johansson, E. M. J., M. Odelius, M. Gorgoi, O. Karis, R. Ovsyannikov, F. Schafers, S. Svensson, H. Siegbahn and H. Rensmo (2008). "*Valence electronic structure of ruthenium based complexes probed by photoelectron spectroscopy at high kinetic energy (HIKE) and modeled by DFT calculations.*" Chemical Physics Letters **464**(4-6): 192-197.

Jungwirth, P. (2008). "*Ions at aqueous interfaces: From water surface to hydrated proteins.*" Annual Review of Physical Chemistry **59**: 343-366.

Kaganer, V. M., B. Jenichen, R. Shayduk and W. Braun (2008). "*Structure of Fe3Si/GaAs(001) epitaxial films from x-ray crystal truncation rods.*" Physical Review B **77**(12): 125325.

Kallmayer, M., K. Hild, H. J. Elmers, S. K. Arora, H. C. Wu, R. G. S. Sofin and I. V. Shvets (2008). "*Magnetic moment investigations of epitaxial magnetite thin films.*" Journal of Applied Physics **103**(7): 07D715.

Karis, O., S. Svensson, J. Rusz, P. M. Oppeneer, M. Gorgoi, F. Schafers, W. Braun, W. Eberhardt and N. Martensson (2008). "*High-kinetic-energy photoemission spectroscopy of Ni at 1s: 6-eV satellite at 4 eV.*" Physical Review B **78**(23): 233105.

Katsikini, M., F. Pinakidou, E. C. Paloura, F. Boscherini, E. Wendler and W. Wesch (2008). "*X-ray absorption fine structure study of In implanted GaN: Effect of annealing.*" Materials Science and Engineering B-Advanced Functional Solid-State Materials **152**(1-3): 132-135.

Katsikini, M., F. Pinakidou, E. C. Paloura, P. Komninou, E. Iliopoulos, A. Adikimenakis, A. Georgakilas and E. Welter (2008). "*Effect of composition on the bonding environment of In in InAlN and InGaN epilayers.*" Physica Status Solidi a-Applications and Materials Science **205**(11): 2593-2597.

Katsikini, M., F. Pinakidou, E. C. Paloura, P. Komninou, A. Georgakilas and E. Welter (2008). "*Temperature dependent EXAFS of InN.*" Physica Status Solidi a-Applications and Materials Science **205**(11): 2611-2614.

Kaya, S., J. Weissenrieder, D. Stacchiola, T. K. Todorova, M. Sierka, J. Sauer, S. Shaikhutdinov and H. J. Freund (2008). "*Formation of one-dimensional molybdenum oxide on Mo(112).*" Surface Science **602**(21): 3338-3342.

Khyzhun, O. Y., T. Strunskus, C. Woll, H. Gies and V. Staemmler (2008). "*Comparison of the OK alpha x-ray emission bands in micro- and mesoporous silica materials and in alpha-quartz.*" Journal of Chemical Physics **129**(8): 084711.

Klappenberger, F., A. Weber-Bargioni, W. Auwärter, M. Marschall, A. Schiffrin and J. V. Barth (2008). "*Temperature dependence of conformation, chemical state and metal-directed assembly of tetrapyridyl-porphyrin on Cu(111).*" J. Chem. Phys. **129**: 214702-1-10.

Klappenberger, F., M. E. Canas-Ventura, S. Clair, S. Pons, U. Schlickum, Z. R. Qu, T. Strunskus, A. Comisso, C. Woll, H. Brune, K. Kern, A. De Vita, M. Ruben and J. V. Bartha (2008). "*Does the Surface Matter? Hydrogen-Bonded Chain Formation of an Oxalic Amide Derivative in a Two- and Three-Dimensional Environment.*" Chemphyschem **9**(17): 2522-2530.

Koitzsch, A., D. Inosov, J. Fink, M. Knupfer, H. Eschrig, S. V. Borisenko, G. Behr, A. Kohler, J. Werner, B. Buchner, R. Follath and H. A. Durr (2008). "*Valence-band and core-level photoemission spectroscopy of LaFeAsO1-xFx.*" Physical Review B **78**(18): 180506.

Koitzsch, A., S. V. Borisenko, D. Inosov, J. Geck, V. B. Zabolotnyy, H. Shiozawa, M. Knupfer, J. Fink, B. Buchner, E. D. Bauer, J. L. Sarrao and R. Follath (2008). "*Hybridization effects in CeCoIn5 observed by angle-resolved photoemission.*" Physical Review B **77**(15): 155128.

Kotzsch, A., J. Nickel, A. Seher, K. Heinecke, L. van Geersdaele, T. Herrmann, W. Sebald and T. D. Mueller (2008). "*Structure analysis of bone morphogenetic protein-2 type I receptor complexes reveals a mechanism of receptor inactivation in juvenile polyposis syndrome.*" Journal of Biological Chemistry **283**(9): 5876-5887.

Krasnikov, S. A., N. N. Sergeeva, M. M. Brzhezinskaya, A. B. Preobrajenski, Y. N. Sergeeva, N. A. Vinogradov, A. A. Cafolla, M. O. Senge and A. S. Vinogradov (2008). "*An x-ray absorption and photoemission study of the electronic structure of Ni porphyrins and NiN-confused porphyrin.*" Journal of Physics-Condensed Matter **20**(23): 235207.

Kroll, T., S. Bonhommeau, T. Kachel, H. A. Durr, J. Werner, G. Behr, A. Koitzsch, R. Hubel, S. Leger, R. Schonfelder, A. K. Ariffin, R. Manzke, F. M. F. de Groot, J. Fink, H. Eschrig, B. Buchner and M. Knupfer (2008). "*Electronic structure of LaFeAsO[sub 1 - x]F[sub x] from x-ray absorption spectroscopy.*" Physical Review B **78**(22): 220502-4.

Kuettner, E. B., A. Keim, M. Kircher, S. Rosmus and N. Strater (2008). "*Active-site mobility revealed by the crystal structure of arylmalonate decarboxylase from Bordetella bronchiseptica.*" **377**(2): 386-394.

Lau, J. T., J. Rittmann, V. Zamudio-Bayer, M. Vogel, K. Hirsch, P. Klar, F. Lofink, T. Moller and B. Von Issendorff (2008). "*Size Dependence of L-2,L-3 Branching Ratio and 2p Core-Hole Screening in X-Ray Absorption of Metal Clusters.*" Physical Review Letters **101**(15): 153401.

Lee, J. S., M. Gensch, K. Hinrichs, W. Seidel and U. Schade (2008). "*Determination of the polarization characteristics of the ELBE free electron laser.*" Infrared Physics & Technology **51**(6): 537-540.

Lee, J. S., M. Ortolani, J. Kouba, A. Firsov, Y. J. Chang, T. W. Noh and U. Schade (2008). "*Electric-pulse-induced local conducting area and joule heating effect in VO2/Al2O3 films.*" Infrared Physics & Technology **51**(5): 443-445.

Lerer, A. M., M. I. Mazuritskii, P. V. Makhno and D. A. Noranovich (2008). "*Theoretical calculation of the angular distribution of radiation at the output of a flat nanodimensional X-ray waveguide.*" Technical Physics Letters **34**(3): 228-230.

Lewin, E., P. O. A. Persson, M. Lattemann, M. Stuber, M. Gorgoi, A. Sandell, C. Ziebert, F. Schadfers, W. Braun, J. Halbritter, S. Ulrich, W. Eberhardt, L. Hultman, H. Siegbahn, S. Svensson and U. Jansson (2008). "*On the origin of a third spectral component of C1s XPS-spectra for nc-TiC/a-C nanocomposite thin films.*" Surface & Coatings Technology **202**(15): 3563-3570.

Lewin, E., P. O. A. Persson, M. Lattemann, M. Stuber, M. Gorgoi, A. Sandell, C. Ziebert, F. Schäfers, W. Braun, J. Halbritter, S. Ulrich, W. Eberhardt, L. Hultman, H. Siegbahn, S. Svensson and U. Jansson (2008). "*On the origin of a third spectral component of C1s XPS-spectra for nc-TiC/a-C nanocomposite thin films.*" Surface & Coatings Technology **202**(15): 3563-3570.

Luo, Y., M. Piantek, J. Miguel, M. Bernien, W. Kuch and R. Haag (2008). "*In-situ formation and detailed analysis of imine bonds for the construction of conjugated aromatic monolayers on Au(111).*" Applied Physics a-Materials Science & Processing **93**(2): 293-301.

Lupi, S., L. Baldassarre, M. Ortolani, C. Mirri, U. Schade, R. Sopracase, T. Tamegai, R. Fittipaldi, A. Vecchione and P. Calvani (2008). "*Subterahertz electrodynamics of the graphenelike superconductor CaAlSi.*" Physical Review B **77**(5): 054510.

MacDonald, M. A., F. Schaefers, R. Pohl, I. B. Poole, A. Gaupp and F. M. Quinn (2008). "*A W : B4C multilayer phase retarder for broadband polarization analysis of soft x-ray radiation.*" Review of Scientific Instruments **79**(2): 025108.

Martin, T., G. Woltersdorf, C. Stamm, H. A. Duerr, R. Mattheis, C. H. Back and G. Bayreuther (2008). "*Layer resolved magnetization dynamics in interlayer exchange coupled Ni81Fe19/Ru/Co90Fe10 by time resolved x-ray magnetic circular dichroism.*" Journal of Applied Physics **103**(7): 07B112.

Matyi, R. J., L. E. Depero, E. Bontempi, P. Colombi, A. Gibaud, M. Jergel, M. Krumrey, T. A. Lafford, A. Lamperti, M. Meduna, A. Van der Lee and C. Wiemer (2008). "*The international VAMAS project on X-ray reflectivity measurements for evaluation of thin films and multilayers - Preliminary results from the second round-robin.*" Thin Solid Films **516**(22): 7962-7966.

Mayer, G., M. Fonin, S. Voss, U. Rudiger and E. Goering (2008). "*X-Ray Spectroscopic Investigations of Zn0.94Co0.06O Thin Films.*" Ieee Transactions on Magnetics **44**(11): 2700-2703.

Mayer, T., U. Weller, E. Mankel, W. Jaegermann, C. Kelting, D. Schlettwein, N. Baziakina and D. Wohrle (2008). "*Organic-inorganic hybrid composites for photovoltaics: Organic guest molecules embedded in mu c-Si and ZnSe host matrices.*" Renewable Energy **33**(2): 262-266.

Mayer, T., R. Hunger, A. Klein and W. Jaegermann (2008). "*Engineering the line up of electronic energy levels at inorganic-organic semiconductor interfaces by variation of surface termination and by substitution.*" Physica Status Solidi B-Basic Solid State Physics **245**(9): 1838-1848.

Mazuritskiy, M. I. and P. V. Makhno (2008). "*Anomalous X-ray Scattering and Channeling inside Hollow Microcapillary Structures.*" Jetp Letters **88**(6): 351-354.

Merzlikin, S. V., N. N. Tolkachev, T. Strunskus, G. Witte, T. Glogowski, C. Woll and W. Grunert (2008). "*Resolving the depth coordinate in photoelectron spectroscopy - Comparison of excitation energy variation vs. angular-re solved XPS for the analysis of a self-assembled monolayer model system.*" Surface Science **602**(3): 755-767.

Merzlikin, S. V., N. N. Tolkachev, T. Strunskus, G. Witte, T. Glogowski, C. Wol and W. Grunert (2008). "*Reply to a comment of J. Zemek, Prague, regarding the paper +ACI-resolving the depth coordinate in photoelectron spectroscopy - comparison of excitation energy variation vs. angular-resolved XPS for the analysis of a self-assembled monolayer model system+ACI- Discussion.*" Surface Science **602**(23): 3634-3635.

Miguel, J., M. Bernien, D. Bayer, J. Sanchez-Barriga, F. Kronast, M. Aeschlimann, H. A. Durr and W. Kuch (2008). "*A new sample holder for laser-excited pump-probe magnetic measurements on a Focus photoelectron emission microscope.*" Review of Scientific Instruments **79**(3): 033702.

Mikoushkin, V. M., V. V. Shnitov, V. V. Bryzgalov, Y. S. Gordeev, O. V. Boltalina, I. V. Gol'dt, S. L. Molodtsov and D. V. Vyalykh (2008). "*Electronic structure of unoccupied states of fluorinated fullerenes C60F18 and C60F36*." Fullerenes Nanotubes and Carbon Nanostructures **16**(5-6): 588-592.

Mitrea, G., J. Thieme, P. Guttmann, S. Heim and S. Gleber (2008). "*X-ray spectromicroscopy with the scanning transmission X-ray microscope at BESSY II*." Journal of Synchrotron Radiation **15**: 26-35.

Muller, J. J., S. Barbirz, K. Heinle, A. Freiberg, R. Seckler and U. Heinemann (2008). "*An intersubunit active site between supercoiled parallel beta helices in the trimeric tailspike endorhamnosidase of Shigella flexneri phage Sf6*." Structure **16**(5): 766-775.

Nolting, D. (2008). "*Pseudoequivalent nitrogen atoms in aqueous imidazole distinguished by chemical shifts in photoelectron spectroscopy*." Journal of the American Chemical Society **130**(26): 8150-+.

Nucara, A., P. Maselli, P. Calvani, R. Sopracase, M. Ortolani, G. Gruener, M. C. Guidi, U. Schade and J. Garcia (2008). "*Observation of charge-density-wave excitations in manganites*." Physical Review Letters **101**(6): 066407.

Ortolani, M., J. S. Lee, U. Schade and H. W. Hubers (2008). "*Surface roughness effects on the terahertz reflectance of pure explosive materials*." Applied Physics Letters **93**(8): 081906.

Ortolani, M., J. S. Lee, U. Schade, I. Pallecchi, A. Gadaleta and D. Marre (2008). "*Infrared study of a La0.7Sr0.3MnO3-delta micrometric transistor channel*." Physica B-Condensed Matter **403**(10-11): 1922-1926.

Owens, A., B. Beckhoff, G. Fraser, M. Kolbe, M. Krumrey, A. Mantero, M. Mantler, A. Peacock, M. G. Pia, D. Pullan, U. G. Schneider and G. Ulms (2008). "*Measuring and Interpreting X-ray Fluorescence from Planetary Surfaces*." Analytical Chemistry **80**(22): 8398-8405.

Pasquo, A. (2008). "*Cloning, expression, crystallization and preliminary X-ray data analysis of*." Acta Crystallographica Section F **64**(PT4): 281-283.

Pavlychev, A. A., X. O. Brykalova, D. A. Mistrov, R. Flesch and E. Ruhl (2008). "*Position and line shape of the 2t(2g)-shape resonance in S 2p-excited sulfur hexafluoride clusters*." Journal of Electron Spectroscopy and Related Phenomena **166**: 45-52.

Piantek, M., J. Miguel, M. Bernien, C. Navio, A. Kruger, B. Priewisch, K. Ruck-Braun and W. Kuch (2008). "*Adsorption of carboxymethylester-azobenzene on copper and gold single crystal surfaces*." Applied Physics a-Materials Science & Processing **93**(2): 261-266.

Pinakidou, F., M. Katsikini and E. C. Paloura (2008). "*Determination of the crystallization ratio in a series of Fe-containing vitroceramic products by means of XAFS spectroscopies*." Journal of Non-Crystalline Solids **354**(45-46): 5053-5059.

Pinakidou, F., M. Katsikini, P. Kavouras, F. Komninou, T. Karakostas and E. C. Paloura (2008). "*Structural role and coordination environment of Fe in Fe2O3-PbO-SiO2-Na2O composite glasses.*" Journal of Non-Crystalline Solids **354**(2-9): 105-111.

Pollakowski, B., B. Beckhoff, F. Reinhardt, S. Braun and P. Gawlitza (2008). "*Speciation of deeply buried TiOx nanolayers with grazing-incidence x-ray fluorescence combined with a near-edge x-ray absorption fine-structure investigation.*" Physical Review B **77**(23): 235408.

Porsch, P., M. Kallmayer, T. Eichhorn, G. Jakob, H. J. Elmers, C. A. Jenkins, C. Felser, R. Ramesh and M. Huth (2008). "*Suppression of martensitic phase transition at the Ni2MnGa film surface.*" Applied Physics Letters **93**(2): 022501.

Powis, I., C. J. Harding, S. Barth, S. Joshi, V. Ulrich and U. Hergenhahn (2008). "*Chiral asymmetry in the angle-resolved O and C 1s(-1) core photoemissions of the R enantiomer of glycidol.*" Physical Review A **78**(5): 052501.

Pozdnyakov, A. O., M. M. Brzhezinskaya, A. S. Vinogradov and K. Friedrich (2008). "*NEXAFS spectra of polymer-nanocarbon composites.*" Fullerenes Nanotubes and Carbon Nanostructures **16**(5-6): 471-474.

Pronin, II, M. V. Gomoyunova, D. E. Malygin, D. V. Vyalykh, Y. S. Dedkov and S. L. Mollodtsov (2008). "*Magnetic linear dichroism in photoemission from an ultrathin iron silicide film.*" Physics of the Solid State **50**(3): 553-556.

Pronin, II, M. V. Gomoyunova, D. E. Malygin, D. V. Vyalykh, Y. S. Dedkov and S. L. Mollodtsov (2008). "*Magnetic ordering of the Fe/Si interface and its initial formation.*" Journal of Applied Physics **104**(10): 104914-1-104914-10.

Qiu, L. Y., J. L. Zhang, A. Kotzsch, W. Sebald and T. D. Mueller (2008). "*Crystallization and preliminary X-ray analysis of the complex of the first von Willebrand type C domain bound to bone morphogenetic protein 2.*" Acta Crystallographica Section F-Structural Biology and Crystallization Communications **64**: 307-312.

Rack, A., S. Zabler, B. R. Mueller, H. Riesemeier, G. Weldemann, A. Lange, J. Goebbels, M. Hentschel and W. Goerner (2008). "*High resolution synchrotron-based radiography and tomography using hard X-rays at the BAMline (BESSY II).*" Nuclear Instruments & Methods in Physics Research Section a-Accelerators Spectrometers Detectors and Associated Equipment **586**(2): 327-344.

Rajalingam, K., T. Strunskus, A. Terfort, R. A. Fischer and C. Woll (2008). "*Metallization of a thiol-terminated organic surface using chemical vapor deposition.*" Langmuir **24**(15): 7986-7994.

Ralf Thiedmann, F. F., Christoph Hartnig Werner Lehnert & Schmidt, Volker (2008). "*Stochastic 3D Modeling of the GDL Structure in PEMFCs Based on Thin Section Detection.*" J. Electrochem. Soc. **155**(4): B391-B399.

Richter, M., S. V. Bobashev, A. A. Sorokin and K. Tiedtke (2008). "*Nonlinear photoionization in the soft X-ray regime.*" Applied Physics a-Materials Science & Processing **92**(3): 473-478.

Romanyshyn, Y., S. Guimond, H. Kuhlenbeck, S. Kaya, R. P. Blum, H. Niehus, S. Shaikhutdinov, V. Simic-Milosevic, N. Nilius, H. J. Freund, M. V. Ganduglia-Pirovano, R. Fortrie, J. Dobler and J. Sauer (2008). "*Selectivity in Methanol Oxidation as Studied on Model Systems Involving Vanadium Oxides.*" Topics in Catalysis **50**(1-4): 106-115.

Romanyuk, O., V. M. Kaganer, R. Shayduk, B. P. Tinkham and W. Braun (2008). "*Staircase model of GaSb(001) (1x3) and c(2x6) phases.*" Physical Review B **77**(23): 235322.

Roodenko, K., Y. Mikhaylova, L. Ionov, M. Gensch, M. Stamm, S. Minko, U. Schade, K. J. Eichhorn, N. Esser and K. Hinrichs (2008). "*Ultrathin responsive polyelectrolyte brushes studied by infrared synchrotron mapping ellipsometry.*" Applied Physics Letters **92**(10): 103102.

Ruhl, E. (2008). "*Clusters and Nonoparticles Studied by Short-Wavelength Radiation.*" Journal of Electron Spectroscopy and Related Phenomena **166**: 1-2.

Saremba, S., J. Nickel, A. Seher, A. Kotzsch, W. Sebald and T. D. Mueller (2008). "*Type I receptor binding of bone morphogenetic protein 6 is dependent on N-glycosylation of the ligand.*" Febs Journal **275**(1): 172-183.

Savino, C. (2008). "*Cloning, expression, purification, crystallization and preliminary X-ray crystallographic analysis of C-12 hydroxylase.*" Protein and Peptide Letters **15**(10): 1138-1141.

Schäfers, F. (2008). *Ray - The BESSY Ray Trace Program* in Springer Series in Modern Optical Sciences: Modern Developments in X-Ray and Neutron Optics, Ed. A. Erko, M. Idir, T. Krist and A. G. Michette, Springer Berlin/Heidelberg, Vol.**137:** 9-41

Schierle, E., E. Weschke, A. Gottberg, W. Sollinger, W. Heiss, G. Springholz and G. Kaindl (2008). "*Antiferromagnetic Order with Atomic Layer Resolution In EuTe(111) Films.*" Physical Review Letters **101**(26): 267202.

Schlappa, J., C. Schussler-Langeheine, C. F. Chang, H. Ott, A. Tanaka, Z. Hu, M. W. Haverkort, E. Schierle, E. Weschke, G. Kaindl and L. H. Tjeng (2008). "*Direct observation of t(2g) orbital ordering in magnetite.*" Physical Review Letters **100**(2): 026406.

Schlickum, U., R. Decker, F. Klappenberger, G. Zoppellaro, S. Klyatskaya, W. Auwärter, S. Neppl, K. Kern, H. Brune, M. Ruben and J. V. Barth (2008). "*Chiral kagom lattice from simple ditopic molecular bricks.*" J. Am. Chem. Soc. **130**: 11776–11782.

Schmidt, M., J. S. Lee, M. Grunze, K. H. Kim and U. Schade (2008). "*Anisotropy studied by polarization-modulated Fourier transform infrared reflection difference microspectroscopy.*" Applied Spectroscopy **62**(2): 171-175.

Scholze, F., C. Laubisa, G. Ulm, U. Dersch, J. Pomplun, S. Burger and F. Schmidt (2008). "*Evaluation of EUV scatterometry for CD characterization of EUV masks using rigorous FEM-Simulation - art. no. 69213R.*" Emerging Lithographic Technologies Xii, Pts 1 and 2 **6921**: R9213-R9213.

Scholze, F. and M. Krumrey (2008). "*Characterization of nanostructured surfaces using EUV- and X-ray reflectometry.*" Nanofair 2008: New Ideas for Industry **2027**: 175-178.

Schönfeld, D. L., R. B. G. Ravelli, U. Mueller and A. Skerra (2008). "*The 1.8- Crystal Structure of [alpha]1-Acid Glycoprotein (Orosomucoid) Solved by UV RIP Reveals the Broad Drug-Binding Activity of This Human Plasma Lipocalin.*" Journal of Molecular Biology **384**(2): 393-405.

Seemayer, A., A. Hommes, S. Hümann, S. Schulz and K. Wandelt (2008). "*Characterization of GaSb thin films from tailor-made single-source precursors.*" Journal of Crystal Growth, The Fourteenth International conference on Metalorganic Vapor Phase Epitax **310**(23): 4831-4834.

Shayduk, R. and W. Braun (2008). "*Positioning errors during stepped scans in X-ray crystallography.*" Journal of Applied Crystallography **41**: 768-775.

Shen, C., M. Haryono, A. Grohmann, M. Buck, T. Weidner, N. Ballav and M. Zharnikov (2008). "*Self-Assembled Monolayers of a Bis(pyrazol-1-yl)pyridine-Substituted Thiol on Au(111).*" Langmuir **24**(22): 12883-12891.

Shikin, A. M., A. Varykhalov, G. V. Prudnikova, D. Usachov, V. K. Adamchuk, Y. Yamada, J. D. Riley and O. Rader (2008). "*Origin of spin-orbit splitting for monolayers of au and ag on W(110) and Mo(110).*" Physical Review Letters **100**(5): 057601.

Siepchen, B., A. Klein and W. Jaegermann (2008). "*Interface formation in CdTe solar cells: Nucleation of CdTe on CdS(0001) and (10-10).*" Physica Status Solidi (RRL) **2**(4): 169-171.

Sokolov, A. A., E. O. Filatova, V. V. Afanas'ev, E. Taracheva, M. M. Brzhezinskaya and A. A. Ovchinnikov (2008). "*Interface analysis of HfO2 films on (100)Si using x-ray photoelectron spectroscopy.*" Journal of Physics D: Applied Physics **42**(3): 035308-00.

Stamm, C., J. U. Thiele, T. Kachel, I. Radu, P. Ramm, M. Kosuth, J. Minar, H. Ebert, H. A. Durr, W. Eberhardt and C. H. Back (2008). "*Antiferromagnetic-ferromagnetic phase transition in FeRh probed by x-ray magnetic circular dichroism.*" Physical Review B **77**(18): 184401.

Steinrueck, H. P., J. Libuda and D. A. King (2008). "*Chemistry at surfaces.*" Chemical Society Reviews **37**(10): 2153-2154.

Swaraj, S., U. Oran, A. Lippitz and W. E. S. Unger (2008). "*Surface chemical analysis of plasma-deposited copolymer films prepared from feed gas mixtures of ethylene or styrene with allylamine.*" Plasma Processes and Polymers **5**(1): 92-104.

Thiedmann, R., F. Fleischer, C. Hartnig, W. Lehnert and V. Schmidt (2008). "*Stochastic 3D modeling of the GDL structure in PEMFCs based on thin section detection.*" Journal of the Electrochemical Society **155**(4): B391-B399.

Thieme, J., S. C. Gleber, P. Guttmann, J. Prietzel, I. McNulty and J. Coates (2008). "*Microscopy and spectroscopy with X-rays for studies in the environmental sciences.*" Mineralogical Magazine **72**(1): 211-216.

Thomas, S. M., M. Koch-Muller, V. Kahlenberg, R. Thomas, D. Rhede, R. Wirth and B. Wunder (2008). "*Protonation in germanium equivalents of ringwoodite, anhydrous phase B, and superhydrous phase B.*" American Mineralogist **93**(8-9): 1282-1294.

Thomas, S. M., R. Thomas, P. Davidson, P. Reichart, M. Koch-Muller and G. Dollinger (2008). "*Application of Raman spectroscopy to quantify trace water concentrations in glasses and garnets.*" American Mineralogist **93**(10): 1550-1557.

Tiedtke, K., J. Feldhaus, U. Hahn, U. Jastrow, T. Nunez, T. Tschentscher, S. V. Bobashev, A. A. Sorokin, J. B. Hastings, S. Moller, L. Cibik, A. Gottwald, A. Hoehl, U. Kroth, M. Krumrey, H. Schoppe, G. Ulm and M. Richter (2008). "*Gas detectors for x-ray lasers.*" Journal of Applied Physics **103**(9): 094511.

Tietze, T., M. Gacic, G. Schutz, G. Jakob, S. Bruck and E. Goering (2008). "*XMCD studies on Co and Li doped ZnO magnetic semiconductors.*" New Journal of Physics **10**: 055009.

Tinkham, B. P., O. Romanyuk, W. Braun, K. H. Ploog, F. Grosse, M. Takahasi, T. Kaizu and J. Mizuki (2008). "*GaSb(001) Surface Reconstructions Measured at the Growth Front by Surface X-ray Diffraction.*" Journal of Electronic Materials **37**(12): 1793-1798.

Tinkham, B. P., W. Braun, K. H. Ploog, M. Takahasi, J. Mizuki and F. Grosse (2008). "*As-rich InAs(001)-(2x4) phases investigated by in situ surface x-ray diffraction.*" Journal of Vacuum Science & Technology B **26**(4): 1516-1520.

Tinkham, B. P., B. Jenichen, V. M. Kaganer, R. Shayduk, W. Braun and K. H. Ploog (2008). "*Post-deposition growth kinetics of Ge on Ge(001).*" Journal of Crystal Growth **310**(15): 3416-3421.

Truica-Marasescu, F., P. L. Girard-Lauriault, A. Lippitz, W. E. S. Unger and M. R. Wertheimer (2008). "*Nitrogen-rich plasma polymers: Comparison of films deposited in atmospheric- and low-pressure plasmas.*" Thin Solid Films **516**(21): 7406-7417.

Ulrich, V., S. Barth, S. Joshi, T. Lischke, A. M. Bradshaw and U. Hergenhahn (2008). "*Separating the vibrationally resolved auger decay channels for a CO core hole state.*" Physical Review Letters **100**(14): 143003.

Ulrich, V., S. Barth, S. Joshi, U. Hergenhahn, E. Mikajlo, C. J. Harding and I. Powis (2008). "*Giant chiral asymmetry in the C 1s core level photoemission from randomly oriented fenchone enantiomers.*" Journal of Physical Chemistry A **112**(16): 3544-3549.

Unger, W. E. S. (2008). "*Surface chemical analysis of plasma polymer films: How far shines the light today?*" Vakuum in Forschung und Praxis **20**(4): 20-27.

Usachov, D., A. M. Dobrotvorskii, A. Varykhalov, O. Rader, W. Gudat, A. M. Shikin and V. K. Adamchuk (2008). "*Experimental and theoretical study of the morphology of commensurate and incommensurate graphene layers on Ni single-crystal surfaces.*" Physical Review B **78**(8): 085403.

Varykhalov, A., J. Sanchez-Barriga, A. M. Shikin, W. Gudat, W. Eberhardt and O. Rader (2008). "*Quantum Cavity for Spin due to Spin-Orbit Interaction at a Metal Boundary*." Physical Review Letters **101**(25): 256601.

Varykhalov, A., J. Sanchez-Barriga, A. M. Shikin, C. Biswas, E. Vescovo, A. Rybkin, D. Marchenko and O. Rader (2008). "*Electronic and Magnetic Properties of Quasifreestanding Graphene on Ni*." Physical Review Letters **101**(15): 157601.

Varykhalov, A., O. Rader and W. Gudat (2008). "*Origin of Au nanostructures on tungsten surface carbides*." Physical Review B **77**(3): 035412.

Voevodskaya, N., F. Lendzian, O. Sanganas, A. Grundmeier, A. Gräslund and M. Haumann (2008). "*Redox intermediates of the Mn-Fe site in subunit R2 of Chlamydia trachomatis ribonucleotide reductase: An X-ray absorption and EPR study*." Journal of Biological Chemistry J. Biol. Chem.: M807190200

Vogel, J., W. Kuch, K. Fukumoto, F. Romanens, S. Pizzini and J. Camarero (2008). "*Domain wall dynamics and interlayer interactions in magnetic trilayer systems studied by XMCD-PEEM*." Applied Physics a-Materials Science & Processing **92**(3): 505-510.

Watahiki, T., B. P. Tinkham, B. Jenichen, R. Shayduk, W. Braun and K. H. Ploog (2008). "*Praseodymium silicide formation at the Pr2O3/Si interface*." Applied Surface Science **255**(3): 758-760.

Watcharinyanon, S., D. Nilsson, E. Moons, A. Shaporenko, M. Zharnikov, B. Albinsson, J. Martensson and L. S. O. Johansson (2008). "*A spectroscopic study of self-assembled monolayer of porphyrin-functionalized oligo(phenyleneethynylene)s on gold: the influence of the anchor moiety*." Physical Chemistry Chemical Physics **10**(34): 5264-5275.

Weber-Bargioni, A., W. Auwarter, F. Klappenberger, J. Reichert, S. Lefrancois, T. Strunskus, C. Woll, A. Schiffrin, Y. Pennec and J. V. Barth (2008). "*Visualizing the frontier orbitals of a conformationally adapted metalloporphyrin*." Chemphyschem **9**(1): 89-94.

Weidner, T., F. Bretthauer, N. Ballav, H. Motschmann, H. Orendi, C. Bruhn, U. Siemeling and M. Zharnikov (2008). "*Correlation between the Molecular Structure and Photoresponse in Aliphatic Self-Assembled Monolayers with Azobenzene Tailgroups*." Langmuir **24**(20): 11691-11700.

Weidner, T., K. Rossler, P. Ecorchard, H. Lang, M. Grunze and M. Zharnikov (2008). "*Self-assembled monolayers of ruthenocene-substituted biphenyl ethynyl thiols on gold*." Journal of Electroanalytical Chemistry **621**(2): 159-170.

Weidner, T., A. Shaporenko, J. Muller, M. Schmid, P. Cyganik, A. Terfort and M. Zharnikov (2008). "*Effect of the bending potential on molecular arrangement in alkaneselenolate self-assembled monolayers*." Journal of Physical Chemistry C **112**(32): 12495-12506.

Weidner, T., N. Ballav, M. Zharnikov, A. Priebe, N. J. Long, J. Maurer, R. Winter, A. Rothenberger, D. Fenske, D. Rother, C. Bruhn, H. Fink and U. Siemeling (2008). "*Dipodal ferrocene-based adsorbate molecules for self-assembled monolayers on gold*." Chemistry-a European Journal **14**(14): 4346-4360.

Wenmackers, S., S. D. Pop, K. Roodenko, V. Vermeeren, O. A. Williams, M. Daenen, O. Douheret, J. D'Haen, A. Hardy, M. K. Van Bael, K. Hinrichs, C. Cobet, M. vandeVen, M. Ameloot, K. Haenen, L. Michiels, N. Esser and P. Wagner (2008). "*Structural and optical properties of DNA layers covalently attached to diamond surfaces.*" Langmuir **24**(14): 7269-7277.

Wernet, P., G. Gavrila, K. Godehusen, C. Weniger, E. T. J. Nibbering, T. Elsaesser and W. Eberhardt (2008). "*Ultrafast temperature jump in liquid water studied by a novel infrared pump-x-ray probe technique.*" Applied Physics a-Materials Science & Processing **92**(3): 511-516.

Winkler, T., N. Ballav, H. Thomas, M. Zharnikov and A. Terfort (2008). "*Micrometer-scale protein-resistance gradients by electron-beam lithography.*" Angewandte Chemie-International Edition **47**(38): 7238-7241.

Winter, B. (2008). "*Electron dynamics in charge-transfer-to-solvent states of aqueous.*" Journal of the American Chemical Society **130**(22): 7130-7138.

Yashina, L. V. (2008). "*X-ray photoelectron studies of clean and oxidised alpha-GeTe(111) surfaces.*" Journal of Applied Physics **103**: 094909-1-094909-12.

Yashina, L. V. (2008). "*A Combined Photoelectron Spectroscopy and ab Initio Study of the Adsorbate System O2/PbTe(001) and the Oxide Layer Growth Kinetics.*" Journal of Physical Chemistry C **112**(50): 19995-20006.

Yegen, E., A. Lippitz, D. Treu and W. E. S. Unger (2008). "*Derivatization of amino groups by pentafluorobenzaldehyde (PFB) as observed by XPS and NEXAFS spectroscopy on spin coated 4,4 '-methylenebis(2,6-diethylaniline) films.*" Surface and Interface Analysis **40**(3-4): 176-179.

Zebisch, M. and N. Strater (2008). "*Structural insight into signal conversion and inactivation by NTPDase2 in purinergic signaling.*" **105**(19): 6882-6887.

Zhang, J. L., L. Y. Qiu, A. Kotzsch, S. Weidauer, L. Patterson, M. Hammerschmidt, W. Sebald and T. D. Mueller (2008). "*Crystal structure analysis reveals how the chordin family member crossveinless 2 blocks BMP-2 receptor binding.*" Developmental Cell **14**(5): 739-750.

Zschech, E., W. B. Yun and G. Schneider (2008). "*High-resolution X-ray imaging - a powerful nondestructive technique for applications in semiconductor industry.*" Applied Physics a-Materials Science & Processing **92**(3): 423-429.

Zubavichus, Y., A. Shaporenko, V. Korolkov, M. Grunze and M. Zharnikov (2008). "*X-ray Absorption Spectroscopy of the Nucleotide Bases at the Carbon, Nitrogen, and Oxygen K-Edges.*" Journal of Physical Chemistry B **112**(44): 13711-13716.

Zubavichus, Y., A. Shaporenko, M. Grunze and M. Zharnikov (2008). "*Is X-ray absorption spectroscopy sensitive to the amino acid composition of functional proteins?*" Journal of Physical Chemistry B **112**(15): 4478-4480.

Zyubin, A. S. (2008). "*Theoretical and Experimental Study of the Reactivity of PbTe in Interaction with Oxygen: Effect of Germanium Impurity Atoms*." Russian Journal of Inorganic Chemistry **53**(1): 86-95.

Habilitations, Theses 2008

Ball, David K., *Röntgenspektroskopie an Spin-Crossover-Molekülen auf Metalloberflächen*, Diploma degree, Freie Universität Berlin, 2008

Bashir, Asif, *Growth and Structural Characterization of Self-Assembled Monolayers (SAMs) on Gold made from Functionalized Thiols and Selenols*, Ph.D. thesis, Ruhr-Universität Bochum, 2008

Berndt, Johannes, *Reactive complex plasmas,* Habilitation, Ruhr University Bochum, 2008

Blobner, Florian, *Adsorbat-Substrat-Ladungstransferdynamik von atomaren Phosphorschichten auf Metalloberflächen*, Diploma thesis, Technische Universität München, 2008

Buchholz, Marcel, *On the application of sum rules to soft x-ray resonant magnetic scattering*, Diploma thesis, Universitaet zu Koeln, 2008

Demund, Alexander, *Interface reactions: Fe/ZnO(000-1) and Fe/SrTiO3(001)*, Ph.D. thesis, Universität Leipzig, 2008

Eylenstein, Roy, *Untersuchungen zur Struktur und Inhibition der cAMP-spezifischen Phosphodiesterase 4A,* Ph.D. thesis, Universität Leipzig, 2008

Ferretti, N., Ph.D. thesis, Technische Universität Berlin, 2008

Hirsch, Konstantin, *Röntgenabsorptionsspektroskopie an freien, massenselektierten Metallclustern*, Diploma thesis, TU Berlin, 2008

Käfer, Daniel, *Characterization and Optimization of Growth and Electronic Structure of Organic Thin Films for organic Electronics Applications*, Ruhr-Universität Bochum, 2008

Kanygin, Mikhail, *Angle dependence of X-ray fluorescent spectra of massive from aligned carbon nanotubes*, Bachelor diploma, Physics Department Novosibirsk State University, 2008

Klaer, Peter, *Röntgenzirkulardichroismus an Heusler-Volumenproben*, Diploma thesis, 2008

Klar, Philipp, *Elektronische Struktur binärer Cluster*, Diploma thesis, TU Berlin, 2008.

Klopffleisch, Karsten, *Strukturelle Charakterisierung von Komplexen der Proteinkinase CK2 mit ATP-kompetitiven Inhibitoren*, Universität zu Köln, 2008

Kotzsch, Alexander, *BMP Ligand-Rezeptor Komplexe: Molekulare Erkennung am Beispiel der spezifischen Interaktion zwischen GDF-5 und BMPR-IB*, Ph.D. thesis University Würzburg, 2008

Kroetz, Kerstin, *Fehleranalyse bei der Simulation von EXAFS-Datensätzen biologischer Proben*, 2008

Krumme, B., *Magnetische Eigenschaften dünner Fe_3Si-Schichten auf GaAs(001) und MgO(001)*, Diploma thesis, Universität Duisburg-Essen, 2008

Lofink, Fabian, I*nnerschalenspektroskopie zur Untersuchung der elektronischen Eigenschaften dotierter Siliziumcluster*, Diploma thesis, TU Berlin, 2008.

Makhno, Pavel, *Electrodynamic analysis of nanostructures in optical and X-ray frequency ranges*, Ph.D. thesis, Southern Federal University, 2008.

Pal, Sonia, *Strukturelle Charakterisierung von Enzymen des Abbauweges für Alkylmethylketone aus Pseudomonas veronii*, Universität zu Köln, 2008

Pörsch, Peter, *Martensitischer Phasenübergang in Ni-Mn-Ga-Formgedächtnislegierungen*, Diploma thesis, University Mainz, 2008

Qui, Li-yan, *Structural and functional analysis of crossveinless 2 / BMP-2 /Chordin interaction*, Ph.D. thesis, University Würzburg, 2008

Rajalingam, Ketheeswari, *Reactions at an organic surface*, Ruhr-Universität Bochum, 2008

Rau, Daniel, *Strukturelle und thermodynamische Untersuchungen an Membransystemen*, Saarland University, 2009

Reinhardt, F., *Hochaufgelöste Röntgenabsorptions- und Röntgenemissionsspektroskopie an Titanverbindungen*, Technische Universität Berlin, 2008

Schmidt, Christian, *Charakterisierung aromatischer SAMs zur Elektrodenmodifikation in organischen Transistoren,* Masters thesis, Ruhr-Universität Bochum, 2008

Scholz, Markus, *Photoemissionsspektroskopie an niederdimensionalen korrelierten Elektronensystemen*, Universität Würzburg, 2008

Schöppke, Matthias, *Zeitabhängige Untersuchungen der benzol-Adsorption auf mit Silber modifizierten Pt(322)-Oberflächen*, Bachelor thesis, Universität Leipzig, 2008

Schwanitz, Konrad, *The TiO2/Dye/Electrolyte Interface in the Dye Sensitized Solar Cell - A Synchrotron Induced Photoelectron Spectroscopy Study*, PhD-Thesis, TU-Darmstadt, August 2008

Silber, David, *Untersuchungen der Adsorption von Kohlenmonoxid, Wasser und einfachen Alkoholen auf der TiO2(110)-Oberfläche*, Ph.D. thesis, Ruhr-Universität Bochum, 2008

Skrebtsov, R.Yu., *XAFS studies of local environment of Mn and Cd impurity atoms in SrTiO3*, Diploma paper, Physics Department, Moscow State University, 2008.

Trowitzsch, Simon, *Functional and structural investigation of spliceosomal snRNPs*, Ph.D. thesis, Universität Göttingen, 2008

Weber, Gert, *Purification and crystallization of spliceosomal snRNPs*, Ph.D. thesis, Universität Göttingen, 2008

Wenmackers, Sylvia, *Morphology, functionality and molecular conformation study of CVD diamond surfaces functionalised with organic linkers and DNA*, Ph.D. thesis, Hasselt University, 2008

Wett, Daniel, *Wachstum und chemische Veränderungen von Eisen- und Cobalt-Dünnschichen auf Zinkoxid(0001)*, Ph.D. thesis, Universität Leipzig, 2008

Zebisch, Matthias, *Biochemical and structural characterization of NTPDase ectodomains: Implications for Purinergic Signaling,* Ph.D. thesis, Universität Leipzig, 2008

Zimmermann, U., *Untersuchung zur Retention von Aminogruppen bei der Plasmapolymerisation von Allylamin in Abhängigkeit von Plasmaprozessparametern*, Diploma thesis, Technische Fachhochschule Wildau, 2008

Authors Index

(click on page number to open selected page)

Keyword Index

(click on page number to open selected page)